



10TH

AUSTRALASIAN
MASONRY
CONFERENCE

11 – 14 February, 2018
SYDNEY AUSTRALIA

PROCEEDINGS

EDITORS | MARK MASIA | DARIUSZ ALTERMAN | YURI TOTOEV | ADRIAN PAGE

Proceedings of the

10TH AUSTRALASIAN MASONRY CONFERENCE

Masonry Today and Tomorrow

EDITORS

MARK MASIA
DARIUSZ ALTERMAN
YURI TOTOEV
ADRIAN PAGE

Copyright © The University of Newcastle, NSW, Australia,
Think Brick Australia, the Concrete Masonry Association of
Australia and individual authors.

These proceedings may be reproduced in part or in whole for
educational or research purposes provided that appropriate
credit is given to the author(s) and reference is made to the
10th Australasian Masonry Conference. These proceedings
may not be reproduced for commercial purposes.

The editors, the organising and technical review committees
and the sponsors of the 10th Australasian Masonry Conference
accept no responsibility for damages resulting from the use,
application, or interpretation of the information presented,
discussed or referred to in the papers contained in these
proceedings. The information published in these proceedings
is presented in the form received from the contributing
authors. Mention of trade names or commercial products does
not constitute endorsement or recommendation for use.

ISBN 978-0-7259-0018-2

Published in 2018 by:

The University of Newcastle
University Drive
Callaghan, NSW, 2308, Australia

Think Brick Australia
Suite 7.01, Level 7, 154 Pacific Highway
St Leonards NSW 2065 Australia

Concrete Masonry Association of Australia
Suite 7.01, Level 7, 154 Pacific Highway
St Leonards NSW 2065 Australia

Cover image: Winner, Horbury Hunt Commercial Award,
Think Brick Awards 2015: **Dr Chau Chak Wing Building**.
Architects: Gehry Partners / Daryl Jackson / Robin Dyke.
Manufacturer: Bowral Bricks. Builder: Lend Lease.
Photographer: Jacqui Dean. www.deanphotographics.com.au

The Organising Committee would like to acknowledge the generous support provided by the following sponsors of the 10th Australasian Masonry Conference:

THINK BRICK & CMAA MEMBERS



BOWRAL BRICKS



PLATINUM SPONSORS



GOLD SPONSOR



SILVER SPONSOR



PREFACE

The 10th Australasian Masonry Conference is being hosted by The University of Newcastle, Think Brick Australia and the Concrete Masonry Association of Australia and is being held at the PARKROYAL Hotel, Darling Harbour, Sydney, from 11-14 February, 2018.

The AMC series began in 1991, first hosted by The University of Newcastle and, over the past 27 years, has grown into the leading forum in the Australasian region for the exchange of ideas between representatives across the masonry industry. Previous conferences were hosted by:

- The University of Auckland (2011)
- The University of Newcastle (2008)
- The University of Newcastle (2004)
- The University of Adelaide (2001)
- Central Queensland University, Gladstone (1998)
- The University of Technology Sydney (1995)
- Queensland University of Technology (1994)
- The University of Melbourne (1992)
- The University of Newcastle (1991)

MASONRY TODAY AND TOMORROW

In this 10th Edition, we hope to address many of the challenges associated with managing the large population of existing masonry buildings, including many wonderful examples contributing to our built cultural heritage. In addition, we will share the innovations and discuss the challenges surrounding the use and reuse of masonry products in new construction. The scope of the conference includes research and applications using all masonry products, including bricks, blocks and pavers.

These proceedings contain 57 papers. The papers cover a range of topics of both a fundamental and practical nature relating to: masonry architecture, seismic behaviour and assessment, structural retrofitting and strengthening, the performance and detailing of facades and veneers, energy performance, masonry materials and walling systems, dry stack masonry, reinforced masonry, analysis, design and design codes. The papers were subjected to a rigorous peer review process. Each paper was independently peer reviewed by two members of the technical review committee. Reviewer comments were returned to authors and final papers submitted. The final papers were then re-reviewed before being accepted.

The conference has attracted strong interest both nationally and internationally with delegates from countries across the world. The conference provides an excellent forum for an exchange of views between representatives across the masonry industry, and will help to ensure that Australasian expertise in masonry research and practice remains at the highest level by international standards.

Associate Professor Mark Masia

Co-Chairman, Conference Organising Committee

WELCOME TO SYDNEY

It gives me great pleasure to welcome you all to the 10th Australasian Masonry Conference.

Over the past ten years, Australia has seen a renewed enthusiasm for masonry and particularly its application. We as an association have witnessed this first hand through the interest in our Think Brick Awards and the projects on display, many of which advocate for advances in masonry design, incorporating such features as hit & miss and stackbonding.

Think Brick's collaboration with the University of Newcastle and research into Thermal Efficiency is well documented and its progress has been presented at previous international masonry conferences.

Last year CMAA commissioned research with Queensland University of Technology to substantiate masonry structural strength without having to restrain the vertical steel. This has resulted in changes to Australian Masonry Standards and we are excited to be able to share these results with you.

CMAA's DesignPave engineering software is also being launched at the conference, making it easier to design concrete segmental pavers.

We welcome our long-term partner Professor Simon Beecham from the University of South Australia who has been a long-term collaborator with the CMAA, in all our pavement research programs.

I do hope you enjoy the scenery and activities of one of the best cities in the world, and my home town, Sydney.

Keep thinking Brick, Block and Paver.

Elizabeth McIntyre

Group CEO

Think Brick Australia and Concrete Masonry Association of Australia

EDITORS

| | |
|------------------|-----------------------------|
| Mark Masia | The University of Newcastle |
| Dariusz Alterman | The University of Newcastle |
| Yuri Totoev | The University of Newcastle |
| Adrian Page | The University of Newcastle |

ORGANISING COMMITTEE

Co-chairs:

| | |
|--------------------|-----------------------------|
| Mark Masia | The University of Newcastle |
| Elizabeth McIntyre | Think Brick Australia |
| Yuri Totoev | The University of Newcastle |

| | |
|------------------|-----------------------------|
| Dariusz Alterman | The University of Newcastle |
| Glenn Hogan | Think Brick Australia |
| Adrian Page | The University of Newcastle |
| Goran Simundic | The University of Newcastle |

TECHNICAL REVIEW COMMITTEE

| | |
|--------------------|-------------|
| Clive Allen | Australia |
| Dariusz Alterman | Australia |
| Vlatko Bosiljkov | Slovenia |
| Marcio Correa | Brasil |
| Hossein Derakhshan | Australia |
| Manicka Dhanasekar | Australia |
| Dmytro Dizhur | New Zealand |
| Robert Drysdale | Canada |
| Fernando Fonseca | USA |
| Marta Giarretton | New Zealand |
| Michael Griffith | Australia |
| Jason Ingham | New Zealand |
| Andrea Isfeld | Canada |
| Shelley Lissel | Germany |
| Mark Masia | Australia |
| Nebojsa Mojsilovic | Switzerland |
| Paolo Morandi | Italy |
| Adrian Page | Australia |
| Andrea Penna | Italy |
| Nigel Shrive | Canada |
| Goran Simundic | Australia |
| Mark Stewart | Australia |
| Yuri Totoev | Australia |
| Jaroslav Vaculik | Australia |
| Kevin Walsh | USA |

TABLE OF CONTENTS

| | |
|---|----------------------------|
| List of Sponsors | <u>iii</u> |
| Preface | <u>iv</u> |
| Committee Structure | <u>v</u> |
| Table of Contents | <u>vi</u> |
| SECURING OF UNREINFORCED MASONRY PARAPETS AND FACADES - FROM FUNDAMENTAL RESEARCH TO NATIONAL POLICY J.M. Ingham, D. Dizhur, M. Giaretton, K.Q. Walsh, H. Derakhshan, R. Jafarzadeh, M.C. Griffith and M.J. Masia | 1 |
| SEISMIC RISK ASSESSMENT OF NEW ZEALAND URM CHURCH INVENTORY S.R. Abeling, S. Vallis, T. Goded, S. Giovinazzi and J.M. Ingham | 15 |
| PERFORMANCE BASED ASSESSMENT OF CULTURAL HERITAGE BUILDINGS IN CENTRAL EUROPE - CASE STUDIES FROM SLOVENIA V. Z. Bosiljkov | 32 |
| MASONRY BUILDING DESIGN FOR EARTHQUAKE-AFFECTED REMOTE AREAS OF NEPAL J. K. Bothara, D. Dizhur and J. Ingham | 48 |
| SEISMIC ASSESSMENT MODEL OF MASONRY INFILL WITH OPENINGS AND EXPERIMENTAL VERIFICATION T.C. Chiou, Y.H. Tu, Y.S. Tu, L.L. Chung and C.T. Huang | 63 |
| DESIGN OF IN-PLANE UNREINFORCED MASONRY WALL TESTING PROGRAM AND PRELIMINARY FINITE ELEMENT ANALYSIS (FEA) M.K. Howlader, M.J. Masia, M.C. Griffith and J.W. Jordan | 75 |
| MASONRY CLADDING DESIGN CONCEPTS FOR ENHANCED PERFORMANCE DURING EARTHQUAKES S. Dill and J. Hochwalt | 89 |
| HELIF ANGLE DESIGN FOR ANCHORED MASONRY VENEER W. Mark McGinley | 99 |
| A FIELD INVESTIGATION INTO LONG-TERM CORROSION OF METAL WALL TIES IN MASONRY VENEER CONSTRUCTION B. Jardim do Nascimento, I.A. Chaves, M.J. Masia and R.E. Melchers | 112 |
| MECHANICAL CHARACTERIZATION OF WALL TIE CONNECTION IN CAVITY WALLS G. Skroumpelou, F. Messali, R. Esposito and J.G. Rots | 124 |

| | |
|--|-----|
| CRITICAL REVIEW OF NUMERICAL MODELLING TECHNIQUES FOR SEISMIC RESPONSE OF COMPLEX URM BUILDINGS K. Ip, D. Dizhur, L. Sorrentino; M.J. Masia, M.C. Griffith and J.M. Ingham | 136 |
| PEAK FLOOR ACCELERATIONS IN UNREINFORCED MASONRY BUILDINGS WITH FLEXIBLE DIAPHRAGMS H. Derakhshan, Y. Nakamura, H. Goldsworthy, K.Q. Walsh, J.M. Ingham and M.C. Griffith | 150 |
| DAMAGE QUANTIFICATION IN PLASTERED UNREINFORCED MASONRY WALLS USING DIGITAL IMAGE CORRELATION M. Didier, G. Abbiati, F. Hefti, M. Broccardo and B. Stojadinovic | 162 |
| INFLUENCE OF THE BEHAVIOUR OF CALCIUM SILICATE BRICK AND ELEMENT MASONRY ON THE LATERAL CAPACITY OF STRUCTURES R. Esposito, S. Jafari, G.J.P. Ravenshorst, H.R. Schipper and J.G. Rots | 174 |
| USING THE MACRO-ELEMENT METHOD TO SEISMICALLY ASSESS COMPLEX URM BUILDINGS F. Gálvez, S. Abeling, K. Ip, S. Giovinazzi, D. Dizhur and J. Ingham | 185 |
| BASIC STUDY FOR SAFE MASONRY CONSTRUCTIONS AGAINST EARTHQUAKES IN DEVELOPING COUNTRIES - COMPARATIVE STUDY ON CEMENT MORTAR FOR JOINTS T. Narafu, H. Sugiyama, H. Imai and A. Tasaka | 198 |
| CALALSIL™ POLYMERIC SILICATES – A NOVEL GEOPOLYMER CONCRETE FOR A SUSTAINABLE FUTURE L.S. Burgess-Dean | 212 |
| COMPARISON OF CURING SYSTEMS FOR ZERO SLUMP CONCRETE MASONRY A. Reyes, A. Incera and M. Murillo | 224 |
| WATER LOSS INFLUENCE ON LAYING MORTAR COMPRESSIVE STRENGTH A. L. Temp, A. S. Milani, M. J. Oliveira, A. Lübeck and G. Mohamad | 237 |
| NEW ECO-FRIENDLY MASONRY UNITS FOR BETTER THERMAL AND ACOUSTIC INSULATION A.A. Gheni, M.A. ElGawady and J.J. Myers | 248 |
| EFFICIENCY RATIO OF HOLLOW CLAY BLOCK MASONRY R.P. Portella, G. Mohamad, F.S. Fonseca, A. Lübeck, R.P.B. Schmidt and L.E. Modler | 260 |

| | |
|--|-----|
| RESEARCH ON THE THERMAL PERFORMANCE OF AUSTRALIAN HOUSING AT THE UNIVERSITY OF NEWCASTLE D. Alterman, A. W. Page and B. Moghtaderi | 270 |
| THE USE OF COMPUTATIONAL FLUID DYNAMICS SIMULATION TO COMPARE THE THERMAL PERFORMANCE OF HOUSING MODULES INCORPORATING HEAVY OR LIGHTWEIGHT WALLING SYSTEMS C. Zhang, D. Alterman, A.W. Page and B. Moghtaderi | 283 |
| NUMERICAL SIMULATION OF THE EFFECT OF SLAB-EDGE INSULATION FOR SLAB-ON-GROUND MASONRY HOUSING Z. Liu, D. Alterman, A. Page, B. Moghtaderi and D. Chen | 296 |
| OPTIMIZATION OF THE SEISMIC PERFORMANCE OF CONTEMPORARY MASONRY CHIMNEY SYSTEMS V. Bosiljkov, D. Antolinc, G. Steinecker and S. Plaskan | 309 |
| PULL-OUT TESTING OF NEAR SURFACE MOUNTED STEEL WIRE ROPE IN UNREINFORCED MASONRY N. A. Misnon, D. Dizhur, M. Giaretton and J. M. Ingham | 322 |
| IN-PLANE TILT TESTS ON DRY STACK MASONRY WALLETES N. Mojsilović and M. Petrović | 334 |
| ENERGY DISSIPATION OF FRAMED SEMI INTERLOCKING MASONRY PANEL UNDER LARGE DISPLACEMENT M. A. Hossain, Y.Z. Totoev and M.J. Masia | 343 |
| PSEUDO-STATIC TESTS OF MORTAR-LESS MASONRY JOINT WITH DIFFERENT INTERLOCKING SHAPES K. Lin, H.J. Liu and W. Hou | 356 |
| NONLINEAR DYNAMIC RESPONSE OF DRY STACK SEMI-INTERLOCKING MASONRY WALL UNDER OUT-OF-PLANE LOAD H.J. Liu, K. Lin and D.X. Peng | 367 |
| THE OUT-OF-PLANE CAPACITY OF SEMI-INTERLOCKING INFILL PANELS: EXPERIMENTAL INVESTIGATION O. Zarrin, Y.Z. Totoev and M.J. Masia | 378 |

| | |
|--|-----|
| UNSHAKEN: RETAINING ARCHITECTURAL QUALITIES OF HISTORIC URM CHURCHES AND CHURCH PRECINCTS WITHIN THE NEW ZEALAND SEISMIC RETROFIT PROCESS S. Vallis, S. Giovinazzi, S. Abeling and J. Ingham | 388 |
| OUT-OF-PLANE RESPONSE OF AN INNOVATIVE MASONRY INFILL WITH SLIDING JOINTS SUBJECTED TO DYNAMIC TESTS ON SHAKING TABLE P. Morandi, R.R. Milanesi, C.F. Manzini and G. Magenes | 402 |
| COMPARISON BETWEEN PREDICTED URM WALL OUT-OF-PLANE DISPLACEMENT-BASED PERFORMANCE AND IN SITU PROOF TEST RESULTS K.Q. Walsh, D.Y. Dizhur, I. Giongo, H. Derakhshan and J.M. Ingham | 417 |
| AN IMPROVED MACROELEMENT MODEL FOR THE NONLINEAR ANALYSIS OF MASONRY BUILDINGS S. Bracchi, A. Galasco, A. Penna and G. Magenes | 431 |
| FULL-SCALE OUT-OF-PLANE SHAKING TABLE TESTS OF URM WALLS IN TWO-WAY BENDING F. Graziotti, U. Tomassetti, L. Grottoli, A. Penna and G. Magenes | 443 |
| OUT OF PLANE BEHAVIOUR OF CONCRETE BLOCK MASONRY WALL WITH DIFFERENT BASE SUPPORT CONDITIONS A.C. Isfeld, M. Hagel, A.L. Müller and N.G. Shrive | 455 |
| EFFECTS OF HORIZONTAL REINFORCEMENT DISTRIBUTION ON IN-PLANE PERFORMANCE AND POST-PEAK BEHAVIOUR OF MASONRY SHEAR WALLS O. Stathis, O. Fischer and S.L. Lissel | 467 |
| A FINITE ELEMENT INVESTIGATION ON STRUCTURAL PERFORMANCE OF FULLY GROUTED REINFORCED MASONRY BUILDING S. Noor-E-Khuda and M. Dhanasekar | 479 |
| EXPERIMENTAL STUDIES ON THE EFFECT OF GROUT CONFINEMENT TO THE REINFORCING BARS IN MASONRY WALLS UNDER CONCENTRIC COMPRESSION M. Song and M. Dhanasekar | 490 |
| ANALYSIS OF THE INFLUENCE OF HORIZONTAL REINFORCEMENT AND EFFECTIVE HEIGHT ON THE PEAK STRENGTH OF MASONRY SHEAR WALLS S. Rizaee and N.G. Shrive | 502 |

| | |
|--|-----|
| NUMERICAL AND EXPERIMENTAL STUDY ON UNREINFORCED MASONRY BUILDINGS WITH VARIOUS OPENING CONFIGURATIONS STRENGTHENED WITH STEEL BANDS T. Choudhury and H.B. Kaushik | 512 |
| IN-SITU EARTHQUAKE TESTING AND SECURING OF DOMESTIC URM CHIMNEYS D. Dizhur, M. Giaretton, H. Derakhshan, J. Ingham and M. Griffith | 523 |
| DYNAMIC TESTING OF MASONRY SHEAR WALLS STRENGTHENED WITH CORE-FILL RETROFITS A. Papadopoulou , O. Fischer and S.L. Lissel | 535 |
| ENVIRONMENTAL EFFECT ON REINFORCED MASONRY WALLS STRENGTHENED WITH NSM AND CEMENTITIOUS ADHESIVE Z. Al-Jaberi, J.J. Myers and M. ElGawady | 547 |
| MITIGATING IMPACT FAILURE OF MASONRY BOUNDARY WALLS USING AUXETIC COMPOSITES M. Asad, M. Dhanasekar, T. Zahra and D. Thambiratnam | 560 |
| EXPERIMENTAL AND ANALYTICAL STUDY OF SEISMIC LOW-COST RETROFITTED MASONRY BUILDING S. Ahmad, R. A. Khan, S. Shamim and M. Asad | 572 |
| COMMON SENSE APPROACH TO MASONRY QUALITY ASSURANCE J. Chrysler, K. Siggard and P. Samblanet | 581 |
| STRUCTURAL BRICK MASONRY IN THE WESTERN UNITED STATES J. Chrysler, J. G. Tawresey and P. J. Samblanet | 594 |
| DETERMINATION OF MODEL PARTIAL FACTOR FOR MASONRY UNREINFORCED SHEAR WALLS BASED ON ANNEX D OF EN-1990 H. Salehi and W. Jäger | 606 |
| ANALYSIS OF THE VERTICAL LOAD DISTRIBUTION BETWEEN THE STRUCTURAL MASONRY WALLS IN A SMALL SCALE MODEL M.R.S. Correa, W.J. Silva and J.S. Camacho | 621 |
| AS3700 MASONRY STRUCTURES CODE - A 2018 UPDATE A.W. Page | 634 |

| | |
|--|-----|
| SHOCK TABLE TEST ON MASONRY BUILDINGS STRENGTHENED USING WELDED WIRE MESH AND MICRO CONCRETE S. B. Kadam, Y. Singh and B. Li | 644 |
| FLEXURAL TESTS OF CLAY BLOCK MASONRY PRISMS REINFORCED WITH CARBON FIBER (CFRP) G.F. Medeiros; R. Bordinon, G. Mohamad, A.B.S. Santos Neto, J.F. Machado, V.M. Tombezi | 661 |
| BOND SLIP BEHAVIOUR OF DEEP MOUNTED CARBON FIBRE REINFORCED POLYMER STRIPS CONFINED WITH A DUCTILE ADHESIVE IN CLAY BRICK MASONRY Ö. S. Türkmen, S.N.M. Wijte, J.M. Ingham and A.T. Vermeltfoort | 672 |
| HERITAGE HOTEL CASE STUDY: SEISMIC RETROFIT OF AN UNREINFORCED MASONRY BUILDING PRIOR TO THE CANTERBURY EARTHQUAKES N. A. Misnon, S. Abeling, J.Hare, R. Jafarzadeh, J. M. Ingham and D. Dizhur | 587 |
| THE CHALLENGES OF DEVELOPING A BOND MODEL FOR FRP TO MASONRY JOINTS—A CLOSER LOOK AT EXISTING TEST RESULTS AND LIMITATIONS OF EXPERIMENTAL DESIGN J. Vaculik, P. Visintin and M.C. Griffith | 697 |

SECURING OF UNREINFORCED MASONRY PARAPETS AND FACADES – FROM FUNDAMENTAL RESEARCH TO NATIONAL POLICY

**J.M. Ingham¹, D. Dizhur², M. Giaretton³, K.Q. Walsh⁴, H. Derakhshan⁵, R. Jafarzadeh⁶,
M.C. Griffith⁷ and M.J. Masia⁸**

¹ Professor, Department of Civil and Environmental Engineering, The University of Auckland, Auckland 1023, New Zealand, j.ingham@auckland.ac.nz

² Lecturer, Department of Civil and Environmental Engineering, The University of Auckland, Auckland 1023, New Zealand, ddiz001@aucklanduni.ac.nz

³ Post-doctoral Researcher, Department of Civil and Environmental Engineering, The University of Auckland, Auckland 1023, New Zealand, mgia506@aucklanduni.ac.nz

⁴ Assistant Professor of Practice, Department of Civil & Environmental Engineering & Earth Sciences, University of Notre Dame, Indiana, United States; Senior Structural Engineer, Frost Engineering and Consulting, Mishawaka, Indiana, United States, kwash8@nd.edu

⁵ Post-doctoral Researcher, School of Civil, Environmental and Mining Engineering, The University of Adelaide, Adelaide, SA 5005, Australia, hossein.derakhshan@adelaide.edu.au

⁶ Engineer, Auckland Council, Private Bag 92300, Victoria Street West, Auckland 1142, New Zealand, reza.jafarzadeh@aucklandcouncil.govt.nz

⁷ Professor, School of Civil, Environmental and Mining Engineering, The University of Adelaide, Adelaide, SA 5005, Australia, michael.griffith@adelaide.edu.au

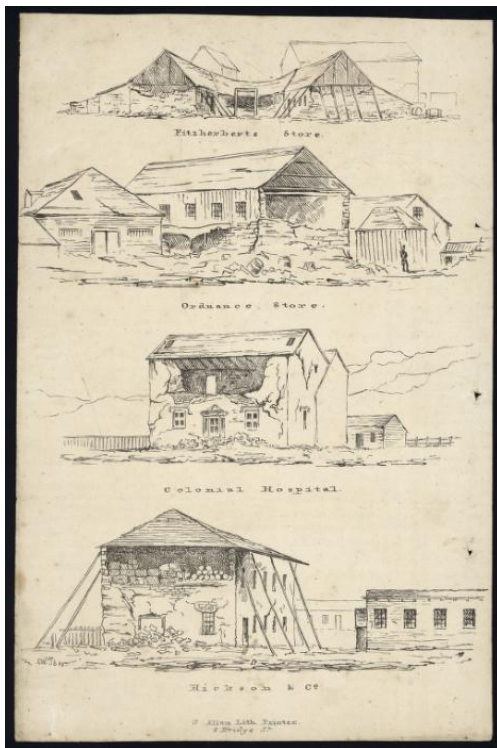
⁸ Associate Professor, Centre for Infrastructure Performance and Reliability, The University of Newcastle, Callaghan, NSW 2308, Australia, mark.masia@newcastle.edu.au

The study of unreinforced masonry buildings and their performance in earthquakes is a topic that has led to strong Australasian collaboration amongst masonry researchers over the last decade, that has resulted in significant advances in knowledge and empirical evidence, comprehensive capture of post-earthquake ‘perishable data’, the development of new numerical assessment and design procedures, and the training of a new generation of masonry researchers. These efforts have significantly influenced national policy and professional practice, particularly in New Zealand. A chronology of these events is reported.

Keywords: *Unreinforced masonry, parapet, façade, legislation*

INTRODUCTION

Since the time of European settlement, New Zealand has a sustained history of unreinforced masonry (URM) buildings having performed poorly in large earthquakes, with several notable examples from the mid-1800s and early 1900s shown in Figure 1. Although less seismically active, Australia also has a notable history of earthquakes having caused damage to URM buildings (see Figure 2). From the mid-1970s through until today research has been undertaken in New Zealand and Australia that has assisted in framing national policy and practice on the seismic assessment and improvement of URM buildings, with some of this research reviewed herein.



(a) 1848 Mw 7.8 Marlborough earthquake

(source: <http://www.geonet.org.nz/earthquake/historic-earthquakes/top-nz/quake-01.html>)



(b) 1929 Mw 7.8 Murchison earthquake

(source: <http://mp.natlib.govt.nz/detail/?id=42847&recordNum=4&q=earthquake&f=tapuhigroupref%24PAColl-3051&s=a&l=mi>)

Figure 1: The poor performance of unreinforced masonry buildings in past New Zealand earthquakes (magnitude data sourced from: https://en.wikipedia.org/wiki/List_of_earthquakes_in_New_Zealand)



(c) 1901 M_L 6.8 Cheviot earthquake

(Source: <http://christchurchcitylibraries.com/heritage/photos/disc5/img0067.asp>)



(d) 1931 M_w 7.8 Hawke's Bay earthquake

(Source: <http://www.teara.govt.nz/en/historic-earthquakes/8/1>)

Figure 1 (continued): The poor performance of unreinforced masonry buildings in past New Zealand earthquakes (magnitude data sourced from: https://en.wikipedia.org/wiki/List_of_earthquakes_in_New_Zealand)



(a) 1989 M_L 5.6 Newcastle, NSW earthquake



(b) 2010 M_w 5.2 Kalgoorlie-Boulder, WA earthquake

Figure 2: The poor performance of unreinforced masonry buildings in past Australian earthquakes (magnitude data sourced from https://en.wikipedia.org/wiki/1989_Newcastle_earthquake and https://en.wikipedia.org/wiki/2010_Kalgoorlie-Boulder_earthquake)

HONOURING THE CONTRIBUTIONS OF PROFESSOR NIGEL PRIESTLEY

Between 1974 and 1985 Professor Nigel Priestley undertook several landmark studies in New Zealand on clay brick masonry, first at the Ministry of Works Central Laboratories and then at the University of Canterbury, commencing with an investigation of reinforced clay brick masonry walls (Priestley and Bridgeman 1974) in collaboration with the New Zealand Pottery and Ceramics Research Association. In 1979 Nigel again collaborated with researchers from the New Zealand Pottery and Ceramics Research Association to investigate the dynamic performance of brick masonry veneer panels (Priestley et al. 1979). The 1979 study was motivated by the poor

reputation of unreinforced masonry veneers when subjected to earthquakes, with much of this reputation being attributed to the failure of brick masonry facades and walls during the 1931 Napier and the 1968 Inangahua earthquakes. Seven unreinforced and two reinforced clay brick masonry veneer walls tied to conventional timber-frame backings were subjected to out-of-plane sinusoidal accelerations in the appropriate frequency range imitating earthquake loading, see Figure 3, where the stud spacing, veneer-tie type and the initial distribution of pre-formed cracking were the main variables. Out-of-plane face loading was specifically considered because the draft Code of Practice for light timber frame construction required the entire in-plane load demands to be carried by the timber frame bracing to which the masonry veneer wall is fixed. From this testing, it was concluded that when unreinforced masonry veneers were built to the specifications prescribed in the draft Code of Practice, acceptable response could be expected for earthquake loading levels in excess of those expected for the highest seismic zone in New Zealand. Furthermore, it was found that pre-formed horizontal or diagonal panel cracking had little or no apparent influence on the ultimate performance of the veneers.

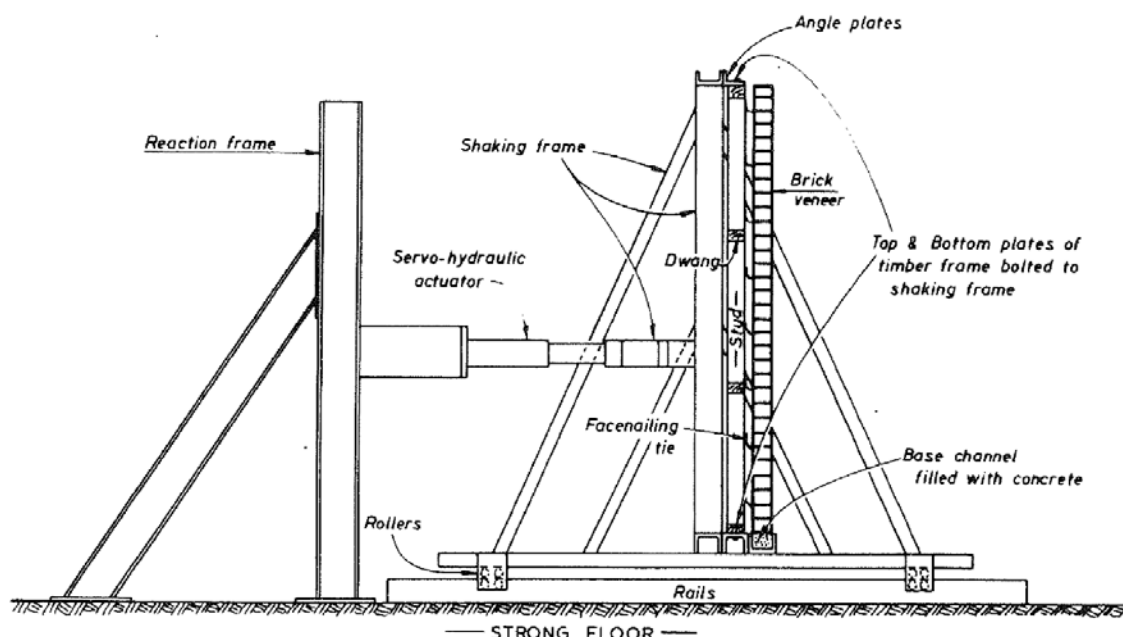


Figure 3: Test set-up for out-of-plane dynamic loading of clay brick masonry veneer walls (Priestley et al. 1979)

In 1985 Nigel added a new dimension to his masonry research by investigating the out-of-plane response of unreinforced masonry (URM) walls (Priestley 1985). This research was focused on assessing the earthquake characteristics of existing URM walls, rather than the design of new reinforced masonry buildings, and Nigel commented that:

“the response of unreinforced masonry walls to out-of-plane (face load) seismic excitation is one of the most complex and ill-understood areas of seismic analysis”.

It is noted that the elastic analysis technique that was commonly applied at that time was focused on masonry stress levels that were “rather insignificant for unreinforced masonry”, resulting in

(a) Forces

(b) Detail at Wall Centre

(c) Displacements at failure

SEISMIC RETROFIT SOLUTIONS PROJECT

5

THE CANTERBURY EARTHQUAKE SEQUENCE

The first event in the Canterbury earthquake sequence occurred on 4 September 2010. Researchers from the University Auckland collaborated with colleagues from Adelaide and Newcastle in Australia in the inspection and reporting of damage to URM buildings (Bailey et al. 2015; Dizhur et al. 2015; Giaretton et al. 2016a,d; Moon et al. 2014, 2015; Senaldi et al. 2015), with their efforts gaining significant media attention both in New Zealand and worldwide (see Figure 5). Further experimental studies were subsequently initiated as collaborations between New Zealand and Australia.



(a) Griffith (left) and Ingham (right) inspecting a collapsed canopy following the 2010 M_w 7.1 Darfield earthquake (https://en.wikipedia.org/wiki/2010_Canterbury_earthquake)

(b) Ingham (centre) doing live interview for national television channel following the 2011 M_L 6.3 Christchurch earthquake (https://en.wikipedia.org/wiki/2011_Christchurch_earthquake)

Figure 5: Members of the research team during the Canterbury earthquakes

THE CANTERBURY EARTHQUAKES ROYAL COMMISSION

Following the Canterbury earthquake sequence the research team was commissioned to prepare a report for the Canterbury Earthquakes Royal Commission (CERC). A decision was made that because of the potential legal implications surrounding the CERC, only Ingham and Griffith would be listed as authors of this work, with student members of the research team acknowledged in the published reports for their efforts (Ingham and Griffith 2011a). The CERC subsequently commissioned the research team to publish an addendum report that specifically addressed the performance of strengthened unreinforced masonry buildings in the Canterbury earthquake sequence (Ingham and Griffith 2011b). The joint Australasian authoring of these reports was testament to the strength of the trans-Tasman collaborative research relationship that had formed during the Seismic Retrofit Solutions project spanning 2004-2010.

On behalf of the research team Ingham reported findings at the Canterbury Earthquakes Royal Commission (see Figure 6), with many of the team's recommendations adopted in the formal recommendations of the Royal Commission (see CERC Interim Report (2011) and CERC Final Report (2011)). In turn, these recommendations eventually found their way into the Building (Earthquake-prone Buildings) Amendment Bill passed by the New Zealand Parliament and receiving Royal Assent on 13 May 2016 (New Zealand Parliament 2013).

The proceeding of the CERC were televised, and extracted news items appeared daily on national television and in newspapers (see stuff 2011 as an example).

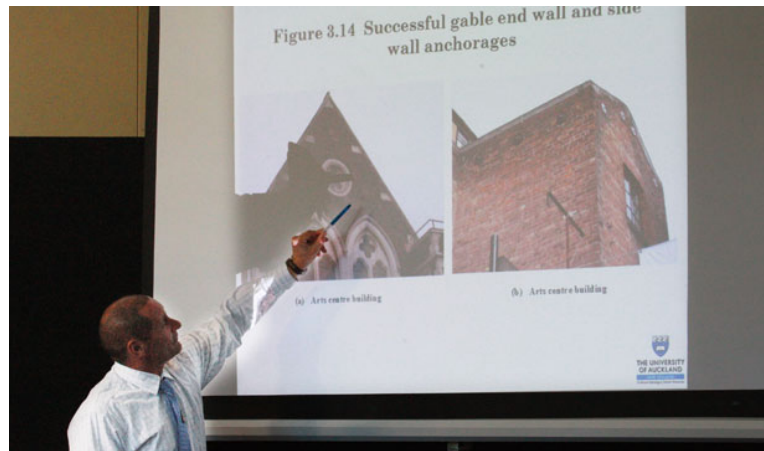


Figure 6: Ingham presenting findings at the Canterbury Earthquakes Royal Commission
(Source: <http://www.stuff.co.nz/the-press/news/5923532/Expert-says-earlier-quake-saved-lives>)

UPDATING OF NEW ZEALAND EARTHQUAKE PRONE BUILDING LEGISLATION

Following conclusion of the 2004-2010 Seismic Retrofit Solutions project, members of the research team participated in writing a national guidance document for professional engineers tasked with the seismic assessment and improvement of unreinforced masonry buildings. These guidelines are part of the national framework for seismic assessment of existing buildings, accessed at www.eq-assess.org.nz, with the URM guidance document accessed at <http://www.eq-assess.org.nz/new-home/part-c/c8/>. This guidance document extended upon but retained many of the recommendations from the draft document produced by the research team in 2010 and was adopted as the nationally-recognised procedure for consistency in practice across the profession, with nationwide seminars delivered to professional engineers to explain its usage.

SECURING OF PARAPETS AND FACADES

Recognising that the collapse of parapets, chimneys and façade walls of both cavity and solid URM construction were the primary contributors to deaths occurring in earthquakes due to collapsed earthquake prone URM buildings, attention then turned to the development of cost-effective and structurally validated solutions for securing of URM facades (Walsh et al. 2015). Solutions were

validated via testing on a low-cost purpose-built shake table designed and assembled by the research team (Giaretton et al. 2018b,c).

COLLABORATION WITH AUCKLAND COUNCIL

In early 2016 a project was initiated as a collaboration between the University of Auckland and Auckland Council, extending the already-existing collaborative relationship (Walsh et al. 2016, 2017) with the intent of using data from Council-owned URM buildings that had been the subject of earthquake assessment and strengthening designs, to extract details on the true costs of detailed seismic assessment and earthquake strengthening. Seismic retrofit costing and associated decision making strategies were already a topic of interest to the research team (Egbelakin et al. 2014, 2015; Jafarzadeh et al. 2014a,b,c, 2015), with the reason for collaborating with Auckland Council specifically being a response to the realisation that retrofit cost data was extremely difficult to secure from professional engineers and building owners due to commercial sensitivity, whereas Auckland Council had agreed to release this data as a public service. From a critique of the cost data it was established that securing of URM parapets cost approximately NZ\$1000 /m of façade, and that the cost was relatively insensitive to the level of seismicity at the site. This data was first communicated to the New Zealand Ministry of Culture and Heritage and helped to inform their development of a NZ\$12 million national fund to support earthquake prone heritage buildings, announced on 12 August 2016 (<http://heritageequip.govt.nz/>).

THE 2016 KAIKŌURA EARTHQUAKE

On 14 November 2016 the M_w 7.8 Kaikōura earthquake initiated a new round of building damage inspections, along with a realisation that the significant risk of a major aftershock in the Wellington region meant that the likelihood of deaths due to falling unreinforced masonry facades was elevated to roughly 10 times the usual risk, which was already high when recognising that the primary fault line separating the Pacific plate from the Australian plate passes through central Wellington. On 19 December 2016 a charrette was held between researchers, practitioners and representatives of central and local government to discuss possible strategies for how to address this elevated risk of fatalities due to URM facades. Data presented to policy writers included building inventories, validated structural solutions, and costings for implementation of securing solutions. The outcome from the day was a recommendation that efforts be instituted to secure URM facades in the lower North Island and upper South Island, with a particular focus on heritage precincts with high pedestrian traffic.

On 25 January 2017 the Minister for Building and Construction, the Hon Dr Nick Smith, used emergency powers introduced after the Kaikōura earthquake to require that owners of approximately 300 high-risk URM buildings in Wellington, Lower Hutt and Blenheim undertake earthquake strengthening by securing their street-facing parapets and facades. The Government set aside NZ\$3M for financial support for building owners, and owners had 12 months to complete their securing. Owners could apply for financial support from the Government up to a maximum of NZ\$15,000 for securing of a façade or NZ\$10,000 for a parapet.

ABOUT QUAKECORE

QuakeCoRE is a New Zealand national centre of research excellence for earthquake resilience (<http://www.quakecore.nz/about/>) that spans across multiple New Zealand research institutions. Within QuakeCoRE, Flagship 3 is associated with multi-disciplinary research associated with potentially earthquake-prone buildings, and has as one objective the undertaking of research to inform policy.

Although not an explicit goal when the research reported herein began in 2004, it has transpired that the research team have succeeded in promulgating a national methodology for the detailed seismic assessment of unreinforced masonry buildings, have produced research findings that have been reported in mainstream television and newspaper media, have made recommendations that were adopted by the Canterbury Earthquakes Royal Commission and subsequently by the New Zealand Parliament, and have undertaken research that aided in the development of post-earthquake emergency legislation.

CONCLUSIONS

There are extensive conclusions that have been developed and promulgated by the research team over the last 14 years, but conclusions specifically meaningful to the work presented herein are:

- 1) Although not specifically linked to the later URM research reported herein, the pioneering research of Professor Nigel Priestley is acknowledged.
- 2) The reported research activity has been a highly successful collaboration between masonry researchers in New Zealand and Australia. Whilst this research has found more immediate implementation in New Zealand in response to recent major earthquake activity, the knowledge gained and the tools developed are equally meaningful to Australia.
- 3) The obtained research funding has been translated into knowledge and tools that are now in everyday use in New Zealand amongst the wider public and the professional structural seismic consulting engineering profession.
- 4) Through a unique set of circumstances, the research team has continued to ‘stay one step ahead’ of the needs of consulting engineers, policy writers and the general public, and has seen much of their research efforts transposed into national policy and practice.

ACKNOWLEDGEMENTS

The members of the wider New Zealand-Australia research team are too numerous to specifically list, ranging from collaborating staff academics at universities worldwide, post-doctoral researchers from New Zealand and Australia, an extensive cohort of doctoral research students, and an even more extensive cohort of undergraduate research students and visiting international research interns. The authors wish to thank this collective for all their passion and commitment to this evolving programme of work. Whilst this narrative has intentionally focussed on research activity undertaken in New Zealand, it is acknowledged that significant companion studies have been undertaken in Australia led by Griffith and by Masia, and that funding secured from the Australian Research Council Discovery Project grant scheme has been an important enabler to the reported trans-Tasman research collaboration. The funding secured from the New Zealand and

Australian national funding agencies is gratefully acknowledged, as is all the industry funding, donated materials, and supplementary time and resources provided by industry personnel that have contributed to the success of this research. This is QuakeCoRE publication number 0259.

REFERENCES

Almesfer, N., Dizhur, D., Lumantarna, R., Ingham, J. M. (2014). Material properties of existing unreinforced clay brick masonry buildings in New Zealand, *Bulletin of the New Zealand Society for Earthquake Engineering*, 47, 2, June, 75-96.

Bailey, S., Dizhur, D., Trowsdale, J., Griffith, M., Ingham, J. (2015). Performance of Posttensioned Seismic Retrofit of Two Stone Masonry Buildings during the Canterbury Earthquakes, *ASCE Journal of Constructed Facilities*, 29, 4, 04014111.

Canterbury Earthquakes Royal Commission. (2011). Interim Report Section 3.3. <http://canterbury.royalcommission.govt.nz/Interim-Report-Section-3.3>. Accessed 3 Feb 2018.

Canterbury Earthquakes Royal Commission (2011). Final Report, Volume 4: Earthquake-prone Buildings, <http://canterbury.royalcommission.govt.nz/Final-Report---Part-Two>. Accessed 3 Feb 2018.

Derakhshan, H., Griffith, M. C., Ingham, J. M. (2013). Airbag testing of unreinforced masonry walls subjected to one-way bending, *Engineering Structures*, 57, 12, 512-522.

Dizhur, D., Ingham, J.M. (2013). Diagonal tension strength of vintage unreinforced clay brick masonry wall panels, *Construction and Building Materials*, 43, 6, 418-427.

Dizhur, D., Griffith, M. C., Ingham, J. M. (2013). In-plane shear improvement of unreinforced masonry wall panels using NSM CFRP strips, *ASCE Journal of Composites in Construction*, 16, 6, 04013010.

Dizhur, D., Bailey, S., Griffith, M., Ingham, J. (2015). Earthquake Performance of Two Vintage URM Buildings Retrofitted Using Surface Bonded GFRP: Case Study, *ASCE Journal of Composites for Construction*, 19, 5, 05015001.

Dizhur, D., Lumantarna, R., Biggs, D., Ingham, J. M. (2017). In-situ assessment of the physical and mechanical properties of vintage solid clay bricks, *Materials and Structures*, 50, 1, Article number 63.

Dizhur, D., Lumantarna, R., Ingham, J. M. (2016), Assessment of mortar properties in vintage clay brick unreinforced masonry buildings, *Materials and Structures*, 49, 5, 1677-1692.

Egbelakin, T. K.; Wilkinson, S., Ingham, J. M. (2014). Economic impediments to successful seismic retrofitting decisions, *Structural Survey*, 32, 5, 449-466.

Egbelakin, T., Wilkinson, S., Ingham, J. (2015). Integrated framework for enhancing earthquake

risk mitigation decisions, *International Journal of Construction Supply Chain Management*, 5, 2, 34-51.

Giaretton, M., Dizhur, D., Da Porto, F., Ingham, J. M. (2016). Construction Details and Observed Earthquake Performance of Unreinforced Clay Brick Masonry Cavity-walls, *Structures*, 6, 159-169.

Giaretton, M., Dizhur, D., Ingham, J. (2016a). Shaking table testing of as-built and retrofitted clay brick URM cavity-walls. *Engineering Structures*. 125, 70-79.

Giaretton, M., Dizhur, D., Ingham, J. (2016b). Dynamic testing of as-built clay brick unreinforced masonry parapets, *Engineering Structures*. 127, 676-685.

Giaretton, M., Dizhur, D., Da Porto, F., Ingham, J. M. (2016c). Post-Earthquake Reconnaissance of Unreinforced and Retrofitted Masonry Parapets, *Earthquake Spectra*, 32, 4, 2377-2397.

Giaretton, M., Ingham, J., Dizhur, D. (2018a). Experimental validation of seismic retrofit solutions for URM chimneys, *Bulletin of Earthquake Engineering*, 16, 1, 295-313.

Giaretton, M., Dizhur, D., Ingham, J. (2018b). Shake table testing of seismically restrained clay brick masonry parapets, *Earthquake Spectra*. Preprint available online.

Giongo, I., Dizhur, D., Tomasi, R., Ingham, J. M. (2013). In-plane assessment of existing timber diaphragms in URM buildings via quasi-static and dynamic in-situ tests, *Advanced Materials Research*, 778, 495-502.

Giongo, I., Dizhur, D., Tomasi, R., Ingham, J. M. (2015). 'Field testing of flexible timber diaphragms in an existing vintage URM building', *ASCE Journal of Structural Engineering*, 141, 1, SPECIAL ISSUE: Field Testing of Bridges and Buildings, D4014009.

Ingham, J. M., Griffith, M. C. (2011a). The Performance of Unreinforced Masonry Buildings in the 2010/2011 Canterbury Earthquake Swarm, Commissioned report to the Royal Commission of Inquiry into Building Failure Caused by the Canterbury Earthquake. <http://canterbury.royalcommission.govt.nz/documents-by-key/20110920.46>

Ingham, J. M., Griffith, M. C. (2011b). The Performance of Earthquake Strengthened URM Buildings in the Christchurch CBD in the 22 February 2011 Earthquake, Addendum report commissioned by Royal Commission of Inquiry into Building Failure Caused by the Canterbury Earthquake. <http://canterbury.royalcommission.govt.nz/documents-by-key/20111026.569>

Ismail, N. Petersen, R., Masia, M. J., Ingham, J. M. (2011). Diagonal shear behaviour of unreinforced masonry wallettes strengthened using twisted steel bars, *Construction and Building Materials*, 25, 12, 4386-4393.

Ismail, N., Ingham, J. M. (2012a). Cyclic out-of-plane behaviour of slender masonry walls seismically strengthened using posttensioning, *ASCE Journal of Structural Engineering*, 138, 10, 1255-1266.

Ismail, N., Ingham, J. M. (2012b). In-situ and laboratory based out-of-plane testing of unreinforced clay brick masonry walls strengthened using near surface mounted twisted steel bars, *Construction and Building Materials*, 36, 11, 119-128.

Ismail, N., Ingham, J. M. (2016). In-plane and out-of-plane testing of unreinforced masonry walls strengthened using polymer textile reinforced mortar, *Engineering Structures*, 118, 167-177.

Jafarzadeh, R., Ingham, J. M., Wilkinson, S., González, V., Aghakouchak, A. A. (2014a). Application of Artificial Neural Network Methodology for Predicting Seismic Retrofit Construction Cost, *ASCE Journal of Construction and Engineering Management*, 140, 2, 04013044.

Jafarzadeh, R., Wilkinson, S., González, V., Ingham, J. M., Ghodrati Amiri, G. (2014b). Predicting Seismic Retrofit Construction Cost for Buildings with Framed Structures Using Multi-Linear Regression Analysis, *ASCE Journal of Construction and Engineering Management*, 140, 3, 04013062.

Jafarzadeh, R., Ingham, J. M., Wilkinson, S. (2014c). A Seismic Retrofit Cost Database for Buildings Having a Framed Structure, *Earthquake Spectra*, 30, 2, 625-637.

Jafarzadeh, R., Ingham, J. M., Walsh, K. Q., Hassani, N., Ghodrati Amiri, G. R. (2015). Using statistical regression analysis to establish construction cost models for seismic retrofit of confined masonry buildings, *ASCE Journal of Construction and Engineering Management*. 141, 5, 04014098.

Knox, C., Dizhur, D., Ingham, J. (2017). Experimental cyclic testing of URM pier-spandrel substructures, *Journal of Structural Engineering*, 143, 2, 04016177.

Lin, Y.-W., Wotherspoon, L. Ingham, J. M. (2016). Out-of-plane testing of unreinforced masonry walls using ECC shotcrete, *Structures*, 7, 33-42.

Lumantarna, R., Biggs, D. T., Ingham, J. M. (2014a). Compressive, flexural bond and shear bond strengths of in-situ New Zealand unreinforced clay brick masonry constructed using lime mortar between the 1880s and 1940s, *ASCE Journal of Materials in Civil Engineering*, 26, 4, 559-566.

Lumantarna, R., Biggs, D. T., Ingham, J. M. (2014b). Uniaxial compressive strength and stiffness of field extracted and laboratory constructed masonry prisms, *ASCE Journal of Materials in Civil Engineering*, 26, 4, 567-575.

Mahmood, H., Ingham, J. M. (2011). Diagonal Compression Testing of FRP-retrofitted Unreinforced Clay Brick Masonry Wallettes, *ASCE Journal of Composites for Construction*, 15, 5, 810-820.

Moon, L., Dizhur, D., Senaldi, I., Derakhshan, H., Griffith, M., Magenes, G., Ingham, J. M. (2014). The demise of the URM building stock in Christchurch during the 2010/2011 Canterbury earthquake sequence, *Earthquake Spectra*, 30, 1, 253-276.

Moon, L., Biggs, D., Ingham, J., Griffith, M. (2015). Transect Survey as a Post-Disaster Global Rapid Damage Assessment Tool, *Earthquake Spectra*, 31, 4, 2443-2457.

New Zealand Parliament. (2013). Building (earthquake-prone buildings) Amendment Bill, Ministry of Business, Innovation, and & Employment (MBIE), Wellington, New Zealand.

NZSEE. (2016). Section C8 – Seismic assessment of unreinforced masonry buildings, The seismic assessment of existing buildings: Technical guidelines for engineering assessment, accessed at: <http://www.eq-assess.org.nz/new-home/part-c/c8/> 14 May 2017.

Oyarzo-Vera, C., Ingham, J., Chouw, N. (2017). Vibration-based damage identification of an unreinforced masonry house model, *Advances in Structural Engineering*, 20, 3, 331-351.

Priestley, M.J.N, Bridgeman, D.O. (1974). Seismic resistance of brick masonry walls, *Bulletin of the New Zealand National Society for Earthquake Engineering*, 7(4), pp. 167-187.

Priestley, M.J.N, Thorby, P.N., McLarin, M.W., Bridgeman, D.O. (1979). Dynamic performance of brick masonry veneer panels, *Bulletin of the New Zealand National Society for Earthquake Engineering*, 12 (4), pp. 314-323.

Priestley, M.J.N. (1985). Seismic behaviour of unreinforced masonry walls, *Bulletin of the New Zealand National Society for Earthquake Engineering*, 18 (2), pp. 191-205.

Russell, A. P., Ingham, J. M. (2010). Prevalence of New Zealand's Unreinforced Masonry Buildings, *Bulletin of the New Zealand Society for Earthquake Engineering*, 43, 3, Sept., 182-201.

Senaldi, I., Magenes, G., Ingham, J. M. (2015). Damage assessment of unreinforced stone masonry buildings after the 2010-2011 Canterbury earthquakes, *International Journal of Architectural Heritage: Conservation, Analysis, and Restoration*, 9, 5, 605-627.

Stuff (2011). September's quake 'saved 300 lives', <http://www.stuff.co.nz/the-press/news/christchurch-earthquake-2011/5919747/Septembers-quake-saved-300-lives>. Accessed 4 Feb 2018.

Walsh, K. Q., Dizhur, D., Shafaei, J., Derakhshan, H., Ingham, J. M. (2015). In situ out-of-plane testing of unreinforced masonry cavity walls in as-built and improved condition, *Structures*, 3, 187-199.

Walsh, K. Q., Jafarzadeh, R., Short, N., Ingham, J. M. (2016). Seismic risk management of a large public facilities portfolio: a New Zealand case study, *Facilities*, 34, 13/14, 809-827.

Walsh, K. Q., Cummuskey, P. A., Jafarsadeh, R., Ingham, J. M. (2017). Rapid identification and taxonomical classification of structural seismic attributes in a regionwide commercial building stock, *ASCE Journal of Constructed Facilities*, 31, 1, 04016067.

Wilson, A., Quenneville, P. J. H., Moon, F. L., Ingham, J. M. (2014a). Lateral performance of nail connections from century old timber floor diaphragms, *ASCE Journal of Materials in Civil*

Engineering, 26, 1, 202-205.

Wilson, A., Kelly, P. A., Quenneville, P. J. H., Ingham, J. M. (2014b). Non-linear in-plane deformation mechanics of timber floor diaphragms in unreinforced masonry buildings, ASCE Journal of Engineering Mechanics, 140, 4, 04013010.



**MASONRY TODAY
AND TOMORROW**

**11 - 14 February, 2018
SYDNEY AUSTRALIA**

www.10amc.com

SEISMIC RISK ASSESSMENT OF NEW ZEALAND URM CHURCH INVENTORY

S.R. Abeling¹, S. Vallis², T. Goded³, S. Giovinazzi⁴ and J.M. Ingham⁵

¹ Doctoral Candidate, Department of Civil and Environmental Engineering, The University of Auckland, Newmarket, Auckland, 1023, New Zealand, sabe321@aucklanduni.ac.nz

² Doctoral Candidate, School of Architecture and Planning, The University of Auckland, Grafton, Auckland 1010, New Zealand, sval034@aucklanduni.ac.nz

³ Seismic Hazard Modeller, GNS Science, Avalon, Lower Hutt, 5010, New Zealand, t.goded@gns.cri.nz

⁴ Senior Research Fellow, Department of Civil and Natural Resources Engineering, University of Canterbury, Christchurch, 4800, New Zealand, sonia.giovinazzi@canterbury.ac.nz

⁵ Professor, Department of Civil and Environmental Engineering, The University of Auckland, Newmarket, Auckland, 1023, New Zealand, j.ingham@auckland.ac.nz

A screening framework that identified the risk and vulnerability factors of unreinforced masonry (URM) churches was developed based on international literature and church damage observations following the 2010/2011 Canterbury earthquakes. This screening framework was applied to an inventory of church buildings located in the Waikato and Taranaki regions of New Zealand. The inventory contains 78 churches, including 9 churches that are primarily or partially composed of URM wall elements. General, architectural, structural, and seismic risk assessment information was gathered for each of the buildings in the inventory. A procedure using fuzzy rule based modelling was developed to evaluate the seismic risk of churches in the inventory in terms of the Scenario Projected Building Damage and the Building Importance/Exposure. Scenario Projected Building Damage was determined using vulnerability functions for URM churches and an estimated Modified Mercalli Intensity for the site. Building Importance/Exposure was determined by fuzzy rule based modelling and was composed of five basic risk items, being Importance Level, Occupancy, Economic Impact, Heritage Impact, and Timeframe for repair. Using the 9 URM churches as preliminary case studies, the seismic risk assessment procedure is presented herein. Based on the results of the assessment, each church was assigned a seismic risk rating that will be used by the stakeholders to prioritise seismic strengthening interventions.

Keywords: Churches, building inventory, seismic risk



INTRODUCTION

The inherent architectural characteristics of churches cause this building type to be particularly vulnerable in earthquakes. Churches are often comprised of large open plans and thrusting structures. These architectural attributes, combined with non-ductile materials such as unreinforced masonry (URM) and early reinforced concrete (RC), have been shown to performed poorly in earthquakes worldwide (Sofronie, 1982; Montilla et al., 1996; Guerreiro et al., 2000; Lagomarsino & Podesta, 2004; Lagomarsino, 2012; Sorrentino et al., 2014). In New Zealand, the Canterbury earthquake of 2010/11 caused damage to several clay brick and stone URM churches (Leite et al., 2014; Cattari et al., 2015). Damage from the earthquakes resulted in the demolition of several churches with significant historic, architectural, and social importance. In an effort to prevent further destruction of church architecture in New Zealand due to earthquakes, much research has been undertaken in terms of cataloguing and assessing URM churches. Research includes the development of a nationwide inventory of URM churches (Marotta et al., 2015) and research into the vulnerability assessment of URM churches in New Zealand (Leite et al., 2013; Goded et al., 2016; Marotta et al., 2016).

A pilot study was undertaken to identify the seismic risk of Anglican churches in the Waikato and Taranaki Regions of New Zealand. Churches of all construction materials were considered within the project, and URM churches are the focus of the research presented herein. An inventory of 70 churches, including 9 URM churches, is introduced and a procedure to determine seismic risk and to prioritise seismic interventions is proposed.

The inventory is comprised of churches located primarily in the Waikato and Taranaki regions of New Zealand. These regions have moderate to low seismicity according to the New Zealand Seismic Hazard Model (Stirling et al., 2012). The use of a rating system to prioritise retrofits may be considered particularly useful in areas of moderate to low seismicity given the extended timeframe for retrofitting buildings under the Building (Earthquake-prone Buildings) Amendment Act 2016 (New Zealand Parliament, 2016). The Act requires typical earthquake-prone building in areas of high seismicity to be retrofitted within a time frame of 15 years and offers an extended timeframe for earthquake-prone buildings in areas of moderate and low seismicity.

HISTORY OF ANGLICAN CHURCHES AND URM BUILDINGS IN NEW ZEALAND

Anglicanism was the first form of Christianity brought to New Zealand. The first European style churches were constructed in the 1830s, and the first URM church was St Paul's in Auckland, being a brick church completed in 1843 (McKay, 2015). Bishop George Augustus Selwyn (1809–1878) greatly influenced Anglican Church architecture in New Zealand. He was assisted by architects such as Frederik Thatcher (1814–1890) in the construction of several churches in the Gothic revival style of building, which is a style regarded by Selwyn to be the only acceptable style for ecclesiastical buildings. The Gothic revival is characterised by ornate decoration, with the most identifying feature of the style being the pointed arch used for windows, doors, and decorative elements. Steeply pitched roofs with exposed trusses and rafters are honest expressions of structure that were popular in Gothic revival churches. In Europe, Gothic revival is typically expressed in masonry construction. Architects of the late 19th and early 20th century generally kept within the Gothic revival style of building, with other notable architects of Anglican churches including

Benjamin Mountfort (1825–1898), Frederick Jersey De Clere (1856-1952), and Frank Messenger (1865-1945) (Thornton, 2003).

Masonry was viewed as a more permanent material as compared with timber and was the preferred construction method, but the cost of materials and lack of skilled masons made this type of construction prohibitive for early settlers. Therefore, a majority of early New Zealand churches were constructed from timber (Thornton, 2003). In the 1880s prosperity increased and clay bricks became more readily available. Masonry buildings increased in popularity, particularly in districts near brickworks, such as those in Auckland, or in districts near stone quarries, such as those in Otago. However, URM buildings fell out of popularity following the Mw 7.8 1931 Hawke's Bay earthquake, which resulted in the damage or destruction of many URM buildings (Dowrick, 1998). Damage occurred due to the inability of the URM buildings to resist lateral forces from the earthquake. The New Zealand Standards Institute was formed in 1935 and released by-laws that encouraged the use of RC elements in URM construction. In 1965, the New Zealand Standard Model Building By-Law NZSS 1900 Chapter 8:1965 explicitly prohibited construction of URM buildings in high seismic areas and imposed regulations on URM construction in areas of lower seismicity (Russell & Ingham, 2010).

Historically Anglicanism has been the largest religious denomination in New Zealand, with approximately 40% of the total New Zealand population identifying as Anglican during the time period 1871–1945 (Statistics New Zealand, 1871-1945). However, in recent years, the number of Anglicans has declined, and only about 12% of the New Zealand population identified as Anglican in the 2013 census (Statistics New Zealand, 2014). The declining number of practicing Anglicans has resulted in low weekly attendance of services and churches in smaller or rural communities now only offering services once or twice a month. There are few new churches being built and existing churches are falling into disuse and are not being maintained. Despite low attendance and fewer services, churches are still viewed as an integral part of many communities as venues to host functions such as weddings and funerals, and church buildings are often widely regarded as important heritage structures of the community.

PROCEDURE FOR ANGLICAN CHURCH INVENTORY DATA COLLECTION

The significant heritage and cultural value of churches made the task of cataloguing and mitigating seismic risk associated with these structures important. In order to determine the overall seismic risk of existing churches in New Zealand, it was essential to develop an inventory of churches. Marotta et al. (2015) presents an inventory of nearly 300 URM churches throughout New Zealand. For the inventory developed within this study, the dataset is comprised of 78 buildings that currently or formerly served as churches and are owned by the Anglican Diocese of Waikato and Taranaki (Figure 1). The Diocese offered full access to their building stock, including a list of building addresses and construction type and any archival information.

Information for the inventory was initially collected through the review of archival information, Heritage New Zealand records, and general histories from local historians when available. A field assessment of each church in the inventory was then conducted to verify and complete the dataset. The information for the inventory was divided into four primary categories: (i) general information, (ii) architectural information, (iii) structural information, and (iv) additional seismic risk assessment information. Multiple parameters made up each primary category, and the parameters

used for the seismic risk assessment discussed herein were the church name and location, building value, heritage rating, primary construction type, importance level, maximum occupancy, and seismic hazard factor (Z).

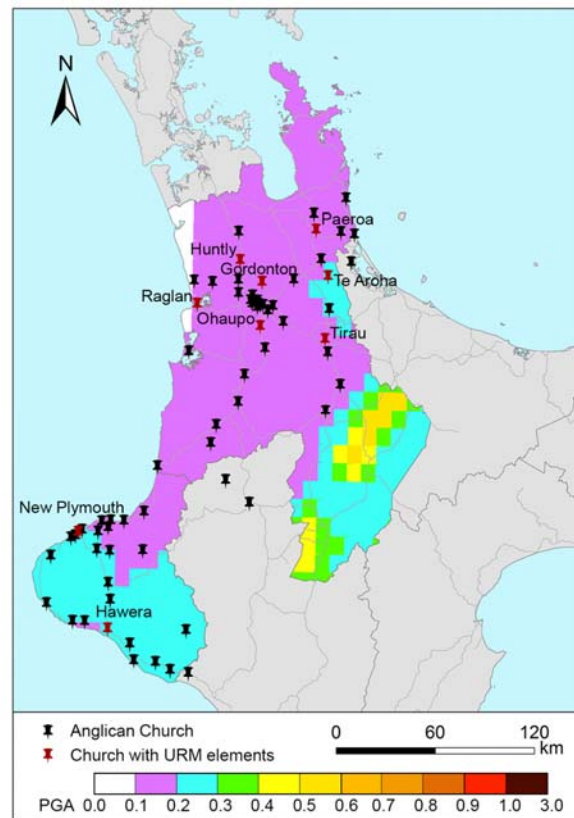


Figure 1: Location of Anglican churches in Waikato and Taranaki regions in relation to 475 year, shallow soil PGA (g) (Stirling et al., 2012)

URM CHURCHES IN THE BUILDING INVENTORY

URM churches account for about 11% of the churches in the Waikato and Taranaki inventory. This building type was immediately identified as the most vulnerable building type given the history of poor performance of URM churches in earthquakes. Therefore, the URM churches in the inventory were used as case study buildings to develop decision making tools for the diocese.

In a national context, Anglican churches account for approximately 33% of URM churches in New Zealand, but only about 5% of New Zealand's URM churches are located in the Waikato and Taranaki regions (Marotta et al., 2015). Nine churches were identified in the inventory that are primarily or partially composed of URM wall elements. Six of the URM churches have brick masonry walls (Figure 2a-f), one church has walls composed of an unknown URM type (Figure 2g), one church has cut stone URM walls (Figure 2h), and one church has random rubble stone URM walls (Figure 2i). Five of the churches have reinforced concrete (RC) elements such as an RC cap beam or RC in the buttresses. Most of the churches are small with a simple floor plan. one church has a footprint area of 50-100 m², three churches have a footprint area of 101-200 m²,

five churches have a footprint area of 201-500 m², and one church has a footprint area of 500-1000 m². Six of the churches have only one nave and no a transept, one church has one nave and a transept, and two churches are larger and have three naves and a transept.



Figure 2: URM churches in Waikato and Taranaki building inventory

SCENARIO PROJECTED BUILDING DAMAGE FOR URM CHURCHES

A building damage grade was assigned to each URM church based on the development of seismic scenarios and vulnerability functions. Damage grades were defined using the URM damage grades descriptions in the European Macroseismic Scale (EMS-98), with Grade 1 corresponding with slight damage and Grade 5 corresponding with destruction (Grünthal, 1998). The reason for using the EMS-98 scale instead of the New Zealand Modified Mercalli (MMI) scale, is that the MMI scale does not include damage grade descriptors for any building materials (e.g., timber, RC, masonry), thus making it very difficult to assign damage grades using the New Zealand MMI scale (Goded et al., 2014).

Scenarios were developed by choosing the fault source with the highest contribution to the seismic hazard for each location at the 500-year return period, using the latest version of the New Zealand National Seismic Hazard Model (NSHM) (Stirling et al., 2012). Once the seismic scenario was selected the magnitude of the fault source and its distance to the town centre were used to calculate the Modified Mercalli Intensity (MMI) by using New Zealand intensity attenuation equations (Dowrick & Rhoades, 2005). As an approximation of the site effects at each of the churches, intensity amplification factors were obtained using a site class map for the whole country (Perrin et al., 2015). A site class was assigned to each church and intensity amplification factors were derived from the amplification factors for each New Zealand site class obtained by Dowrick and Rhoades (2005). A final MMI was calculated and this intensity was used to estimate the expected damage grade using the individual vulnerability function for each church.

The vulnerability functions for URM churches were developed based on damage observed in the Canterbury earthquakes of 2010/2011 (Goded et al., 2016). Using these data, a macroseismic method was developed to obtain the seismic vulnerability of URM churches using vulnerability index modifiers specifically developed for New Zealand URM churches. The vulnerability function for a specific church was calibrated based on the building characteristics, such as masonry quality, state of maintenance, existing building damage, structural transformations, etc., and structural features such as the number of naves or the height of the lateral walls. A projected mean damage grade was output from the generated vulnerability function and seismic scenario. Complete details of the development of the vulnerability curves and associated methodology for URM churches are described in Cattari et al. (2015) and Goded et al. (2016).

RISK ASSESSMENT AND DECISION MAKING USING FUZZY LOGIC

Determining the projected building damage was only one aspect of assessing the seismic risk of the churches. Risk assessment is a complex process and often requires comparing quantitative values with qualitative concepts, such as the comparison of economic value and social significance. The risk items that must be compared are measured on separate, often ambiguous, scales. Characterizing risk for each risk item often relies on human judgement, which is subject to personal bias. Fuzzy set theory offers a mathematical way of managing the vagueness and fuzziness in humanistic systems such as with risk assessment and decision making (Ross, 2004).

Fuzzy set theory has been used within the earthquake engineering field for applications such as seismic inelastic analysis and design (Mistakidis & Georgiou, 2003), evaluation of seismic vulnerability (Tesfamariam & Saatcioglu, 2010) and post-earthquake damage assessment (Sanchez-Silva & Garcia, 2001). A method to use fuzzy set theory to prioritize seismic retrofits was developed by Tesfamariam and Saatcioglu (2008) and was applied to a case study of schools by Tesfamariam and Wang (2012).

Risk assessment using fuzzy logic can be simplified by the development of a hierarchical structure that subdivides primary criteria into definable risk items. Two primary criteria were identified as the major contributors to the seismic risk posed by building in the inventory: (i) Scenario Projected Building Damage and (ii) Building Importance/Exposure. The risk items identified that contribute to Building Importance/Exposure were Importance Level, Occupancy, Heritage Impact, Economic Impact, and Timeframe for Repair (Figure 3). Each risk item is described in the following sections.

The basic theory of fuzzy sets was first introduced by Zadeh (1965). The framework is a natural way of dealing with problems in which the source of imprecision originates from the inability to precisely define criteria for class membership (Zadeh, 1965). Fuzzy set theory differs from traditional set theory in that membership to a set is not binary (i.e. x is either a member or not a member of set A). Rather, x can be a member of set A with a certain degree of membership, μ , that ranges between 0 and 1. Linguistic variables, or variables with a values defined by words rather than numbers, are a key feature of fuzzy sets. The primary function of linguistic variables is to provide a way to approximately characterise complex or ill-defined phenomena (Zadeh, 1973). The use of a linguistic variable as a form of data compression is referred to as granulation (Zadeh, 1994). For Building Importance/Exposure, three granules (or fuzzy subsets) have been defined for each risk item, *low* (L), *medium* (M), and *high* (H). For Scenario Projected Building Damage, five granules have been defined to correspond with Damage Grades 1-5 of EMS-98.

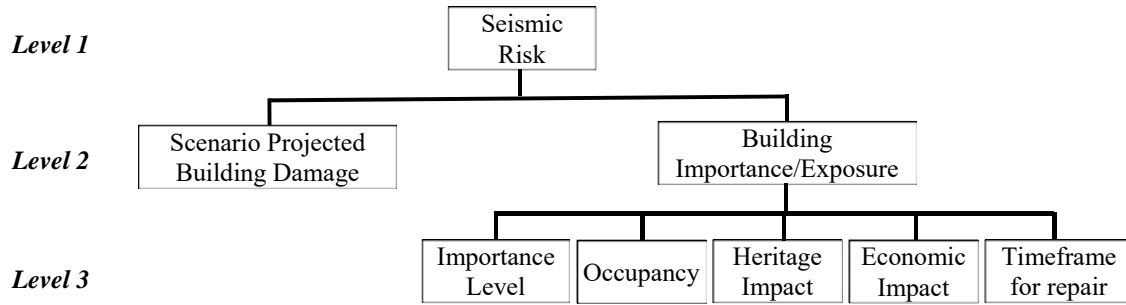


Figure 3: Hierarchical earthquake risk assessment

Fuzzification was used to transform the input parameters for each risk item into a homogenous scale. A value for each risk item was mapped on the corresponding fuzzy scale to determine the membership to each granule, μ . After fuzzification, the value of each risk item under Building Importance/Exposure was expressed by a three-tuple fuzzy set (μ_L, μ_M, μ_H) and Seismic Projected Building Damage was expressed by a five-tuple fuzzy set $(\mu_{G1}, \mu_{G2}, \mu_{G3}, \mu_{G4}, \mu_{G5})$. A membership to *high* (H), was indicative of high risk, whereas a membership to *low* (L) was indicative of low risk. For example, a building considered to have a “significant” economic impact had higher membership value to H and a lower membership value to L .

A fuzzy (rule-based) system was established to define the relationships between the input and the output parameters. Mamdani type fuzzy models are the most common inference method (Ross, 2004), and was the method used to define the input-output relationship. Equation 1 was used to describe a fuzzy system consisting of r linguistic IF-THEN propositions with two inputs and one output.

$$R^k: \text{IF } x_1 \text{ is } A_1^k \text{ and } x_2 \text{ is } A_2^k \text{ THEN } y \text{ is } B^k \quad \text{for } k = 1, 2, \dots, r \quad (1)$$

Where R^k represents the k th rule, x_1 and x_2 represent two noninteractive inputs (antecedents), A_1^k and A_2^k are the fuzzy sets representing the k th antecedent pairs, y is a single output (consequent) linguistic variable and B^k is the fuzzy set representing the k th consequent. The inputs, x_1 and x_2 , are conjunctive antecedents because the inputs are connected

by the AND connective. For the AND connective, the aggregated output is the fuzzy intersection of all individual rule consequents (membership values), where the fuzzy intersection involves the minimum operator. One technique to obtain a membership values of fuzzy relation R^k is Mamdani's implication method, which is given by Equation 2.

$$\mu_{R^k}(x_1, x_2) = \min[\mu_{A_1^k}(x_1), \mu_{A_2^k}(x_2)] \quad (2)$$

Given that the rule base r involved more than one rule, aggregation of rules was necessary to obtain an overall membership value. Each IF-THEN proposition that made up the rule base is considered a disjunctive antecedent. These antecedents are connected by the OR connective, and the aggregated output is found by the union of membership functions, where the fuzzy union involves the maximum operator. The aggregated output for the r rules using Mamdani implication method of inference for a set of disjunctive rules is given by Equation 3.

$$\mu_{B^k}(y) = \max_k[\min[\mu_{A_1^1}(x_1), \mu_{A_2^2}(x_2)], \min[\mu_{A_1^1}(x_1), \mu_{A_2^2}(x_2)], \dots, \min[\mu_{A_1^k}(x_1), \mu_{A_2^k}(x_2)]] \quad (3)$$

for $k = 1, 2, \dots, r$

After aggregation, the process of defuzzification was used to reduce a fuzzy set to a crisp number. The weighted average method was used as the defuzzification process, where a crisp value of a fuzzy set was obtained by assigning weights to its membership (Sadiq et al., 2004; Tesfamariam & Saatcioglu, 2008) as shown by Equation 4.

$$Z = \sum_{i=1}^n q_i * \mu_{B^i} \quad (4)$$

Where q_i is a quality order weight factor, $q_i \in [0,1]$, and Z is the defuzzification value of fuzzy set B^k . The q_i values are associated with the granules of the output rule base.

It is noted that the membership functions used for fuzzification and the quality order weight factors, q_i , have been assigned based on values suggested in Tesfamariam and Saatcioglu (2008). Further calibration of membership functions and quality ordered weight factors may be implemented in future research as more building are assessed.

BUILDING IMPORTANCE/EXPOSURE

The primary category Building Importance/Exposure was comprised of five risk items. The risk items were Importance Level, Occupancy, Economic Impact, Heritage Impact, and Timeframe for Repair. Each risk item is described in the following section, and transformation and fuzzification values for the risk items are presented in Table 1.

Importance Level

Buildings are assigned an Importance Level (IL) according to building use and occupancy in AS/NZS 1170.2 (2002). Importance Levels specify the serviceability limit state, or the level of damage that can be tolerated for a certain level of shaking. Importance levels vary between IL1 and IL4, with IL1 structures being the least likely to endanger human life and other property and IL4 buildings being structures with special post-disaster functions, such as hospitals or police stations.

Table 1: Building importance/exposure factors

| Parameter | Quantifier | Transformation | Fuzzification |
|---------------------|---------------------|----------------|--|
| Importance Level | IL1 | 0.10 | [L; M; H] → [TFN(0, 0, 0.5); TFN(0, 0.5, 1); TFN(0.5, 1, 1)] |
| | IL2 | 0.50 | |
| | IL3 | 0.60 | |
| | IL4 | 0.90 | |
| Occupancy | 0-10 | 0.10 | [L; M; H] → [TFN(0, 0, 0.5); TFN(0, 0.5, 1); TFN(0.5, 1, 1)] |
| | 11-100 | 0.40 | |
| | 101-1,000 | 0.75 | |
| | >1,000 | 0.90 | |
| Economic Impact | Below Average | 0.10 | [L; M; H] → [TFN(0, 0, 0.5); TFN(0, 0.5, 1); TFN(0.5, 1, 1)] |
| | Average | 0.50 | |
| | Significant | 0.90 | |
| Heritage Impact | Not Listed | 0.10 | [L; M; H] → [TFN(0, 0, 0.5); TFN(0, 0.5, 1); TFN(0.5, 1, 1)] |
| | NZHPT 2 | 0.50 | |
| | NZHPT 1 | 0.90 | |
| Timeline for repair | $Z < 0.15$ | 0.10 | [L; M; H] → [TFN(0, 0, 0.5); TFN(0, 0.5, 1); TFN(0.5, 1, 1)] |
| | $0.15 \leq Z < 0.3$ | 0.40 | |
| | $Z \geq 0.3$ | 0.75 | |
| | Priority Building | 0.90 | |

Note: L = Low, M = Medium, H = High, and TFN = Triangular fuzzy number

Occupancy

Occupancy, or number of people that may be within a structure, can be used to infer the number of casualties in an earthquake. Importance Level categorisation does take into account the occupancy rates within IL3. However, the occupancy of IL3 building may still vary greatly, and for this reason, occupancy is considered as its own category. The occupancy has been categorised into 4 groups, 0-10, 11-100, 100-1000, and more than 1000 as was specified in Tesfamariam and Saatcioglu (2008).

Economic Impact

For the purposes of determining a value for Building Importance/Exposure, Economic Impact was determined based on building value, where the building value was estimated based on property reports available on QV.co.nz and was taken to be the ‘capital value’ of the property minus the ‘land value’. Economic Impact was categorised as *Below Average*, *Average*, or *Significant*. Churches with a building value of less than \$100,000 were categorised as *Below Average* Economic Impact, churches with a building value of between \$100,001 and \$500,000 were categorised as *Average* Economic Impact, and churches with a building value of over \$500,000 were categorised as *Significant* Economic Impact.

Heritage Impact

The ‘Policy and Procedures Framework for Earthquake Prone Building’ of the Anglican Diocese of Waikato and Taranaki (2015) indicated prioritization given to buildings listed by Heritage New Zealand Pouhere Taonga (HNZPT). The HNZPT identifies historic places and lists them as either Category 1 or Category 2. Category 1 are historic places of special or outstanding historical or

cultural significance or value, and Category 2 are historic places of historical or cultural significance or value (Heritage New Zealand Pouhere Taonga Act 2014) .

Timeframe for Repair

The Building (Earthquake-prone Buildings) Amendment Act 2016 implements a timeframe in which buildings classified as ‘earthquake-prone’ must be seismically retrofitted. The timeframe varies based the priority of the building and the seismic risk of the area, where the seismic risk of an area is based on the seismic hazard factor, Z . Priority buildings include certain hospital, emergency, and education buildings as well as buildings that could impede important transport routes and URM buildings with parts that could fall in an earthquake onto thoroughfares with sufficient vehicular or pedestrian traffic. In low seismic risk areas ($Z < 0.15$), all buildings must be strengthened within 35 years. In medium seismic risk areas ($0.15 \leq Z < 0.3$), priority buildings must be strengthened within 12.5 years and all other buildings must be strengthened within 25 years. In high seismic risk areas ($Z \geq 0.3$), priority buildings must be strengthened within 7.5 years and all other buildings must be strengthened within 15 years. For the purposes of this study, priority buildings have been grouped into one category.

EXAMPLE

The process of determining Seismic Risk using Fuzzy Logic is outlined in the example below using St. Mary’s Church, Hawera. Step 1 describes the determination of the Scenario Projected Building Damage. Steps 3-6 describe the process used to determine Building Importance/Exposure using Fuzzy Logic. Step 7 describes the process used to determine a Seismic Risk Rank using fuzzy logic.

Step 1 was the process of determining the Scenario Projected Building Damage. Using the seismic scenario for St. Mary’s Church, Hawera, the intensity estimated to be MMI 8.5. The building sits on soil type C (shallow soils), and the intensity level with site effects was also estimated to be MMI 8.5. Figure 4 shows the vulnerability curves for St. Mary’s Church, Hawera. Given an MMI 8.5 earthquake, the projected building damage was a mean damage grade of 3. This mean damage grade was the input for the Scenario Projected Building Damage.

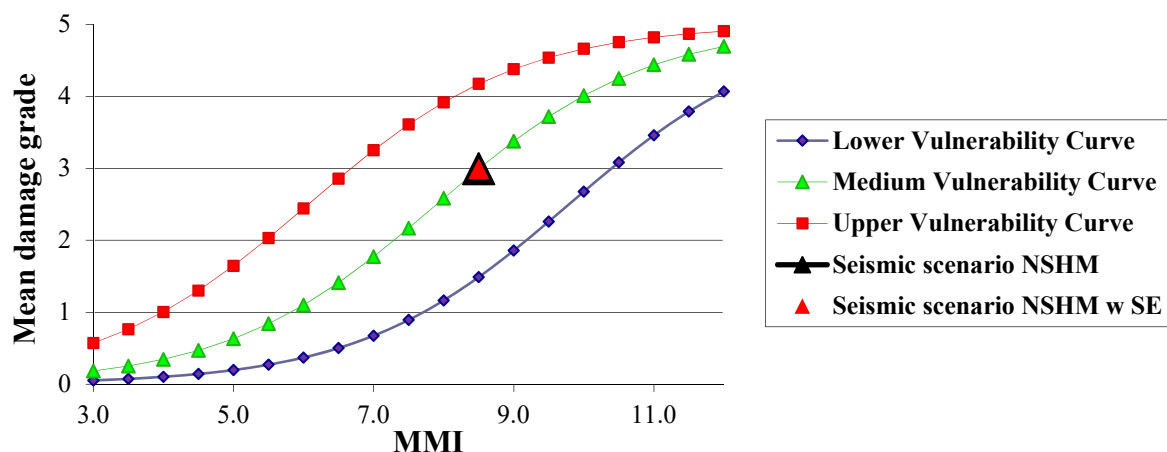


Figure 4: Vulnerability Curve for St. Mary’s Hawera

Step 2 in the evaluation process was to establish a fuzzy rule base hierarchy and the corresponding fuzzy rule bases. Building Importance/Exposure was comprised of five input parameters, or risk items. For the purposes of establishing a simplified rule base system, a hierarchical fuzzy rule base system was established (Figure 5). Three temporary rule bases (RB₁₁-RB₁₃) were defined, each with two three-tuple fuzzy sets. The output value from each temporary rule base served as an input to the next rule base in the hierarchy. An example of an IF-THEN fuzzy rule base for Importance Level and Occupancy (RB₁₁) is shown in Figure 5.

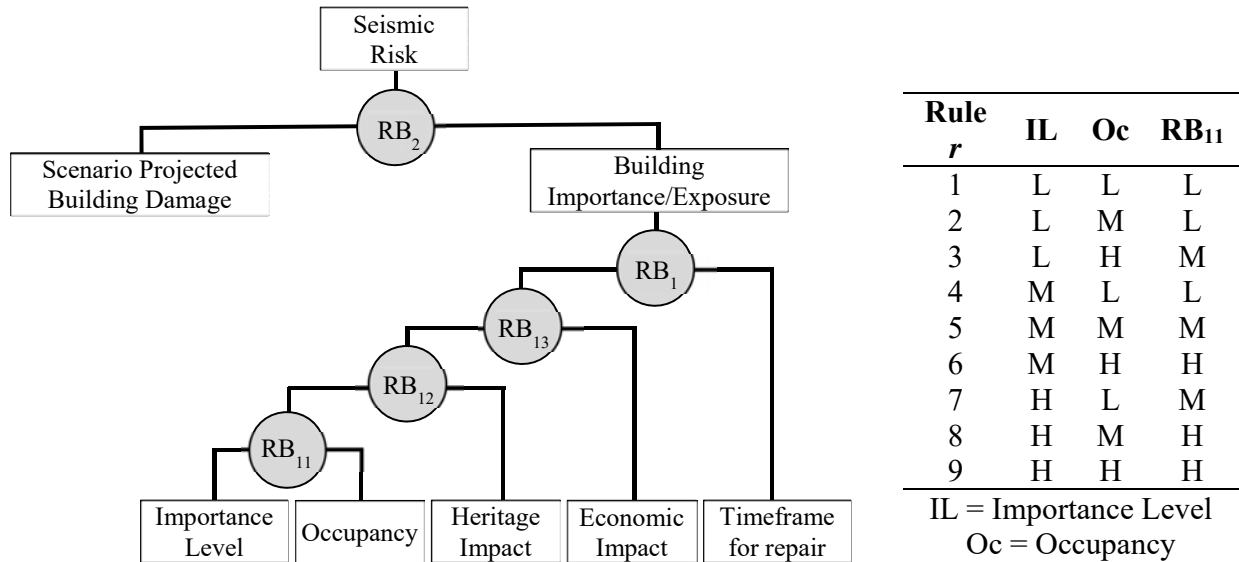


Figure 5: Fuzzy rule base hierarchy and example of fuzzy rule base set

Step 3 of the evaluation procedure was to transform the inputs for each risk items to a singular unit type using the quantifier and transformation parameters presented Table 1. The observed value of risk-based items and corresponding transformations for St. Mary's, Hawera are provided in Table 2.

Table 2: Risk items and transformation for St. Mary's, Hawera

| Risk Item | Input Column | Observation | Transformation |
|----------------------|---------------------------|-------------|----------------|
| Importance Level | Importance Level | IL3 | 0.60 |
| Occupancy | Maximum Occupancy | 300 | 0.75 |
| Economic Impact | Building Value | \$675,000 | 0.50 |
| Heritage Impact | HNZPT Category | 2 | 0.50 |
| Timeframe for Repair | Priority Building? | No | - |
| | Seismic Hazard Factor (Z) | 0.18 | 0.40 |

Step 4 of the evaluation procedure was the fuzzification process. The triangular fuzzy numbers given in Table 1 were depicted graphically in Figure 6 for the Importance Level and Occupancy risk items. The transformed value of the corresponding risk item was mapped onto the fuzzy

numbers, and the membership of each granule was determined to establish a fuzzy set. The fuzzification of the transformed values for each risk item using the corresponding granules were:

$$\begin{aligned}(\mu_L^{IL}, \mu_M^{IL}, \mu_H^{IL}) &= (0, 0.8, 0.2); \\(\mu_L^{OC}, \mu_M^{OC}, \mu_H^{OC}) &= (0, 0.5, 0.5); \\(\mu_L^{EI}, \mu_M^{EI}, \mu_H^{EI}) &= (0, 1, 0); \\(\mu_L^{HI}, \mu_M^{HI}, \mu_H^{HI}) &= (0, 1, 0); \\(\mu_L^{TF}, \mu_M^{TF}, \mu_H^{TF}) &= (0.2, 0.8, 0).\end{aligned}$$

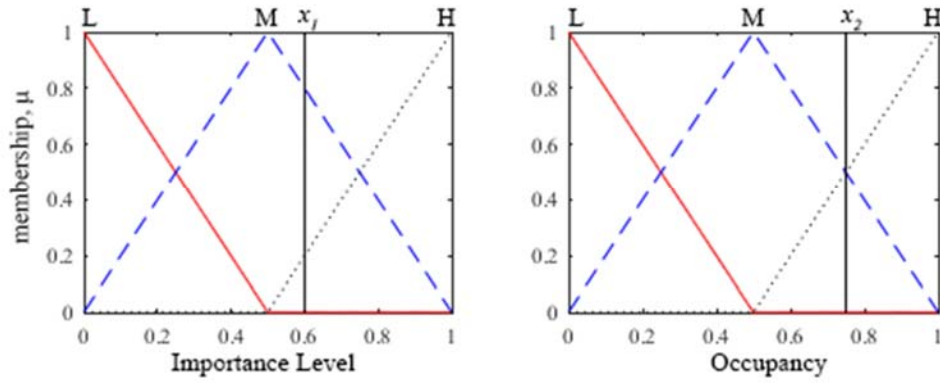


Figure 6: Fuzzification of Importance Level and Occupancy

Step 5 of the evaluation procedure was inferencing using the fuzzy rule bases defined within the rule base hierarchy. The inferencing was performed in a bottom up approach that starts with RB_{11} and finishes with R_2 . Using the rule base proved in Figure 5, the inferencing to quantify RB_{11} is shown below.

$$\begin{aligned}\mu_L^{RB_{11}} &= \max[\min(0,0), \min(0,0.5), \min(0.8,0)]=0 \\RB_{11} = \mu_M^{RB_{11}} &= \max[\min(0,0.5), \min(0.8,0.5), \min(0.2,0)]=0.5 \\ \mu_H^{RB_{11}} &= \max[\min(0.8,0.5), \min(0.2,0.5), \min(0.2,0.5)]=0.5\end{aligned}$$

Step 6 of the evaluation procedure was the defuzzification process. The q_i values for defuzzifying the output were $q_i(i = 1, 2, 3) = [0, 0.5, 1]$. RB_{11} was defuzzified as

$$Z_{11} = \sum_{i=1}^n q_i * \mu_i = 0 \times 0 + 0.5 \times 0.5 + 1 \times 0.5 = 0.75$$

Steps 4 through 6 were repeated for the remaining rule bases using the same quality order weight factor, q_i , to determine that $Z_{12} = 0.75$, $Z_{13} = 0.75$, and Building Importance/Exposure (Z_1) = 0.75.

Step 7 was the final step of the process and determined a crisp value for Seismic Risk between 0 and 1 using fuzzy logic. The fuzzification used for the Scenario Projected Building Damage was $[G1; G2; G3; G4; G5] \rightarrow [TFN(0, 0, 0.4); TFN(0.1, 0.4, 0.6); TFN(0.4, 0.6, 1.2); TFN(0.6, 0.9, 1); TFN(0.9, 1, 1)]$, and the fuzzification used for Building Importance/Exposure was $[L; M; H] \rightarrow$

[TFN(0, 0, 0.5); TFN(0, 0.5, 1); TFN(0.5, 1, 1)]. The q_i values for defuzzifying the output was $q_i(i = 1, 2, 3) = [0, 0.5, 1]$. The Seismic Risk (R_2) was then determined to be 0.75.

BUILDING RANK

The process outlined in the preceding example was repeated for each of the 9 URM churches in the inventory. A rank was assigned to each church based on the calculated value for Seismic Risk, with Rank 1 corresponding to the church with the highest seismic risk and Rank 9 corresponding to the church with the lowest seismic risk. Churches with the same Seismic Risk value were given the same rank. Input information for the risk assessment and the determined rank are shown in Table 3. St. Mary's Cathedral, New Plymouth was ranked first due to its occupancy, heritage classification, and building value. St. Mark's Church, Te Aroha had the highest estimated mean damage grade, and was ranked second along with St. Mary's, Hawera and St. Paul's, Huntly. Seismic retrofits of the URM churches can be prioritised based on the assigned rank.

CONCLUSIONS

An inventory was developed that contains general, architectural, structural, and seismic risk assessment information on 78 churches, including 9 churches that are primarily or partially composed of URM wall elements. A procedure using fuzzy rule based modelling was developed to evaluate the seismic risk of churches in the inventory in terms of the Scenario Projected Building Damage and the Building Importance/Exposure. The 9 URM churches were used as a preliminary case study for a seismic risk assessment. An example of the seismic risk assessment was presented, and each URM church was assigned a seismic risk rating. The fuzzy numbers used in the seismic risk assessment procedure will be further calibrated as necessary, and the seismic risk assessment will be applied to the entire church inventory as a tool for stakeholders to prioritise seismic strengthening interventions.

ACKNOWLEDGEMENTS

This project was supported by QuakeCoRE, a New Zealand Tertiary Education Commission-funded Centre. This is QuakeCoRE publication number 0221.

Table 3: URM Churches Risk Assessment Information

| Church Name | City | Primary Construction Type | Importance Level | Maximum Occupancy | Building Value (Capital Value - Land Value) | NZHPT Category | Priority Building? | Seismic Hazard Factor (Z) | Estimated Mean Damage Grade | Rank |
|-----------------------------|--------------|--|------------------|-------------------|--|----------------|--------------------|---------------------------|-----------------------------|------|
| St Mary's | Gordonton | Brick URM, RC elements | IL2 | 80 | \$80,000.00 | 2 | N | 0.16 | 2 | 7 |
| St Mary's | Hawera | Brick URM, timber elements | IL3 | 300 | \$675,000.00 | 2 | N | 0.18 | 3 | 2 |
| St Paul's | Huntly | Brick URM, RC elements | IL2 | 125 | \$86,000.00 | 1 | N | 0.15 | 3 | 2 |
| St Mark's | Te Aroha | Brick URM | IL2 | 140 | \$410,000.00 | 2 | N | 0.18 | 4 | 2 |
| Church of the Good Shepherd | Tirau | Brick URM, RC elements | IL2 | 130 | \$735,000.00 | N/A | N | 0.21 | 3 | 5 |
| St Paul's | Paeroa | Brick URM, RC elements (Original), RC and Brick (Addition) | IL2 | 150 | \$405,000.00 | N/A | N | 0.18 | 2 | 7 |
| St Peter's | Raglan | URM, unknown type | IL2 | 80 | \$260,000.00 | N/A | N | 0.15 | 1 | 7 |
| Christ Church | Ohaupo | Cut stone URM | IL2 | 50 | \$45,000.00 | N/A | N | 0.18 | 3 | 5 |
| St. Mary's Cathedral | New Plymouth | Random Rubble URM | IL3 | 400 | \$1,950,000.00 | 1 | N | 0.18 | 3 | 1 |

REFERENCES

- Cattari, S., Ottonelli, D., Pinna, M., Lagomarsino, S., Clark, W., Giovinazzi, S., et al. (2015). Damage and vulnerability analysis of URM churches after the Canterbury earthquake sequence 2010-2011. *Proceedings of SECED 2015 Conference: Earthquake Risk and Engineering towards a Resilient World*, 9-10 July, Cambridge UK.
- Diocese of Waikato and Taranaki. (2015), Policy and Procedures Framework for Earthquake Prone Buildings, Diocese of Waikato and Taranaki, Retrieved from http://www.taranakicathedral.org.nz/uploads/Seismic/Policy_on_Earthquake_Prone_Buildings_Final_to_Standing_Committee_08052015.pdf
- Dowrick, D. J. (1998). Damage and intensities in the magnitude 7.8 1931 Hawke's Bay, New Zealand, earthquake. *Bulletin of the New Zealand Society for Earthquake Engineering*, 31(3), pp. 139-163
- Dowrick, D. J., and Rhoades, D. A. (2005). Revised models for attenuation of modified mercalli intensity in New Zealand Earthquakes. *Bulletin of the New Zealand Society for Earthquake Engineering*, 38(4), pp. 185-214
- Goded, T., Cousins, W. J., and Fenaughty, K. F. (2014). Analysis of the Severe-Damage Online Felt Reports for the Canterbury (New Zealand) 2011 Aftershocks on 22 February Mw 6.2, 13 June Mw 6.0, and 23 December Mw 6.0. *Seismological Research Letters*, 85(3), pp. 678-691. 10.1785/0220130198
- Goded, T., Giovinazzi, S., Liberatore, D., Pinna, M., Cattari, S., Ingham, J. M., et al. (2016), Vulnerability assessment of unreinforced masonry churches (EQC 14/660) - Final Report, GNS, 132 pp.
- Grünthal, G. (1998). European Macroseismic Scale 1998. *Cahiers du centre Européen de Géodynamique et de Séismologie*, 15, pp. 1-99
- Guerreiro, L., Azevedo, J., Proença, J., Bento, R., and Lopes, M. (2000). Damage in ancient churches during the 9th of July 1998 Azores earthquake. *Proceedings of 12th World Conference on Earthquake Engineering*, 30 Jan - 4 Feb, Auckland, New Zealand.
- Lagomarsino, S. (2012). Damage assessment of churches after L'Aquila earthquake. *Bulletin of Earthquake Engineering*, 10, pp. 73-92. 10.1007/s10518-011-9307-x
- Lagomarsino, S., and Podesta, S. (2004). Damage and vulnerability assessment of churches after the 2002 Molise, Italy earthquake. *Earthquake Spectra*, 20(S1), pp. 271-283. 10.1193/1.1767161
- Leite, J., Ingham, J. M., and Lourenco, P. (2014). Damage inspection in churches - The Canterbury earthquake (New Zealand) experience. *Proceedings of Cultural Heritage and Loss Prevention (HELP) 2014*, 6-7 Oct, Porto, Portugal.

Leite, J., Lourenco, P., and Ingham, J. M. (2013). Statistical Assessment of Damage to Churches Affected by the 2010-2011 Canterbury (New Zealand) Earthquake Sequence. *Journal of Earthquake Engineering*, 17(1), pp. 73-97. 10.1080/13632469.2012.713562

Marotta, A., Goded, T., Giovinazzi, S., Lagomarsino, S., Liberatore, D., Sorrentino, L., et al. (2015). An inventory of unreinforced masonry churches in New Zealand. *Bulletin of the New Zealand Society for Earthquake Engineering*, 48(3), pp. 171-190

Marotta, A., Sorrentino, L., Liberatore, D., and Ingham, J. (2016). Vulnerability assessment of unreinforced masonry churches following the 2010-2011 Canterbury (New Zealand) earthquake sequence. *Journal of Earthquake Engineering*, pp. 1-23. 10.1080/13632469.2016.1206761

McKay, B. (2015). *Worship: A History of New Zealand Church Design*. New Zealand: Penguin Random House.

Mistakidis, E. S., and Georgiou, D. N. (2003). Fuzzy sets in seismic inelastic analysis and design of reinforced concrete frames. *Adv. Eng. Software*, 34, pp. 589-599

Montilla, P. J., Uzcategui, A. I., and Hernandez, S. M. (1996). Damages occurred to churches due to earthquake of February 8, 1995 in Pereira, Colombia. *Proceedings of 11th World Conference on Earthquake Engineering*, 23-28 June, Acapulco, Mexico.

New Zealand Parliament. (2014). Heritage New Zealand Pouhere Taonga Act 2014. Ministry for Culture and Heritage, Wellington, New Zealand. Retrieved from <http://legislation.govt.nz/act/public/1991/0069/latest/DLM230265.html>

New Zealand Parliament. (2016). Building (Earthquake-prone Buildings) Amendment Act 2016. Ministry of Business, Innovation and Employment, Wellington, New Zealand. Retrieved from <http://www.legislation.govt.nz/act/public/2016/0022/22.0/DLM5616102.html>

Perrin, N. D., Heron, D., Kaiser, A., and Van Houtte, C. (2015). Vs30 and NZS1170.5 site class maps of New Zealand. *Proceedings of New Zealand Society for Earthquake Engineering NZSEE 2015 Conference*, 10-12 April, Rotorua, New Zealand.

Ross, T. J. (2004). *Fuzzy Logic with Engineering Applications* (Second ed.). West Sussex, England: John Wiley & Sons Ltd.

Russell, A. P., and Ingham, J. M. (2010). Prevalence of New Zealand's unreinforced masonry buildings. *Bulletin of the New Zealand Society for Earthquake Engineering*, 43(3), pp. 182-202

Sadiq, R., Husain, T., Veitch, B., and Bose, N. (2004). Risk-based decision-making for drilling waste discharges using a fuzzy synthetic evaluation technique. *Ocean Engineering*, 31(16), pp. 1929-1953. 10.1016/j.oceaneng.2004.05.001

Sanchez-Silva, M., and Garcia, L. (2001). Earthquake damage assessment based on fuzzy logic and neural networks. *Earthquake Spectra*, 17(1), pp. 89-112

Sofronie, R. (1982). Behaviour of eastern churches in earthquakes. *Proceedings of 7th European Conference on Earthquake Engineering*, 20-25 Sept, Athens, Greece.

Sorrentino, L., Liberatore, L., Decanini, L. D., and Liberatore, D. (2014). The performance of churches in the 2012 Emilia earthquakes. *Bulletin of Earthquake Engineering*, 12(5), pp. 2299-2331. 10.1007/s10518-013-9519-3

Standards Australia, and Standards New Zealand. (2002). AS/NZS 1170.0:2002 Structural Design Actions *Part 0: Genertal Principles*. Wellington, New Zealand: Standards New Zealand.

Statistics New Zealand. (1871-1945), New Zealand Census, Wellington, New Zealand, Retrieved from http://m.stats.govt.nz/browse_for_stats/snapshots-of-nz/digitised-collections/census-collection.aspx

Statistics New Zealand. (2014), 2013 Census QuickStats about culture and identity - Religious Affiliation, Wellington, New Zealand, Retrieved from www.stats.govt.nz

Stirling, M. W., McVerry, G. H., Gerstenberger, M. C., Litchfield, N. J., Van Dissen, R. J., Berryman, K. R., et al. (2012). National seismic hazard model for New Zealand : 2010 update. *Bulletin of the Seismological Society of America*, 102(4), pp. 1514-1542. 10.1785/0120110170

Tesfamariam, S., and Saatcioglu, M. (2008). Risk-Based Seismic Evaluation of Reinforced Concrete Buildings. *Earthquake Spectra*, 24(3), pp. 795-821. 10.1193/1.2952767

Tesfamariam, S., and Saatcioglu, M. (2010). Seismic Vulnerability Assessment of Reinforced Concrete Buildings Using Hierarchical Fuzzy Rule Base Modeling. *Earthquake Spectra*, 26(1), pp. 235-256

Tesfamariam, S., and Wang, Y. (2012). Risk-Based Seismic Retrofit Prioritization of Reinforced Concrete Civic Infrastructure: Case Study for State of Oregon Schools and Emergency Facilities. *Natural Hazards Review*, 13, pp. 188-195. 10.1061/(ASCE)NH.1527-6996.0000060

Thornton, G. (2003). *Worship in the Wilderness: Early Country Churches of New Zealand* (C. Lagahetau Ed.). Birkenhead, Auckland, New Zealand: Reed Publishing (NZ) Ltd.

Zadeh, L. A. (1965). Fuzzy Sets. *Information and Control*, 8(3), pp. 338-353. 10.1016/S0019-9958(65)90241-X

Zadeh, L. A. (1973). Outline of a New Approach to the Analysis of Complex Systems and Decision Processes. *IEEE Transactions on Systems, Man, and Cybernetics*, SMC-3(1), pp. 28-44. 10.1109/TSMC.1973.5408575

Zadeh, L. A. (1994). Fuzzy logic, neural networks, and soft computing. *Communications of the ACM*, 37(3), pp. 77-84. 10.1145/175247.175255

PERFORMANCE BASED ASSESSMENT OF CULTURAL HERITAGE BUILDINGS IN CENTRAL EUROPE - CASE STUDIES FROM SLOVENIA

V. Z. Bosiljkov¹

¹ Professor, University of Ljubljana, Faculty of Civil and Geodetic Engineering, Jamova 2, SI-1000 Ljubljana, Slovenia, vbosiljk@fgg.uni-lj.si

The seismic assessment of old masonry buildings of cultural heritage value is subjected to many uncertainties that may be attributed not only to the randomness of earthquake motions but also to physical and modelling strategy uncertainties related to prediction of structural vulnerability. Main elements of vulnerability analysis are the capacity or resistance of the structure interpreted in the form of strength and deformation, and the seismic demand. In the case of cultural heritage assets or monuments this may be vague issues, since current code provisions cannot be always met due to numerous architectural and conservations protection demands. How to incorporate all these issues in effective performance based assessment and planning retrofitting actions will be discussed through two case studies typical for central Europe: Kolizej Palace and Kazina Palace both built in mid XIX c in Ljubljana, Slovenia.

Seismic demands for existing buildings though they all survived numerous earthquake events cannot be fulfilled as it concerns current code provisions. Thus rigorous strengthening measures should be introduced for the achievement of demanded seismic performance. Here the most important issues are how to solve the most vulnerable parts of the buildings while still preserving their architectural and historical values. For the palaces this is usually related to preservation of large halls with high floors considering the level of maintenance of the building and decay of built brickwork masonry. While for Kolizej Palace regardless the chosen methodology for the seismic assessment there were no efficient feasible strengthening solutions, for Kazina Palace different strengthening approaches were proposed corresponding to different desired seismic performances.

Keywords: *cultural heritage, palace, castle, structural performance, earthquake*

INTRODUCTION

The seismic assessment of old masonry cultural heritage buildings is subjected to many uncertainties, as the variety of material and architectural characteristics of the buildings is enormous and buildings are set to specific geological area and urban context. Furthermore, the knowledge regarding the exact geometry of the building and its main structural elements, details of construction and built in materials (material properties considered in the analysis) can extent from very limited to very good. In current European standards for earthquake resistant design; assessment and retrofitting of buildings EN 1998-3:2005 (2005) the uncertainties which arise from limited knowledge of the building are to be considered with confidence factors, which correspond to certain knowledge levels. These knowledge levels serve also for the purpose of choosing the admissible type of analysis.

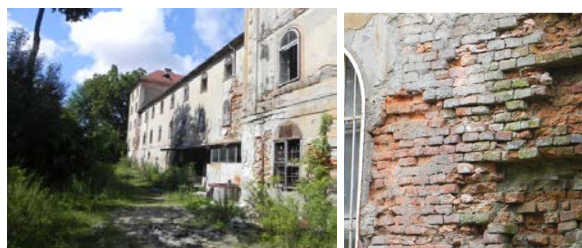
In this paper two individual architecturally similar buildings were investigated and assessed considering current code provisions. For the first one (Kolizej Palace) extensive in-situ investigation prior numerical analysis was necessary considering the state of long time neglected building. For the second one (Kazina Palace) limited in-situ investigation was feasible since the building is in use by numerous archives and governmental agencies. Main aim of analysis of Kolizej Palace was to assess its static and seismic load bearing capacity in its current condition. The building did not have the status of monument, thus according to Slovenian laws it was developers decision whether the building will be preserved or demolished. On the other hand Kazina Palace was in the process of getting the status of national monument thus following the assessment of the existing structure several strengthening scenarios were proposed regarding their impact and considering the future purpose of the building (Academy of Music) as well as demands of the owner (University of Ljubljana) and the Institute for the Protection of Cultural Heritage of Slovenia.

KOLIZEJ PALACE

Kolizej Palace in Ljubljana (Slovenia) was built after the plans of architect Josef Benedict Withalm in 1847 as a multipurpose building for soldiers and officers of the former Habsburg Monarchy (Figure 1-a). The building was erected very quickly within only two years and ever since it remained almost unchanged. In 1895 Ljubljana was struck by a strong earthquake but the records regarding the damage on Kolizej are unknown. From 1918, the building was turned into social apartments and its state went into worse. The building of Kolizej was 122 m long and from 29 to 32 m wide. Central part of the building had four stories, while the South part had five stories and was called “The South Tower”. The lowest level, to which we refer in our analysis as basement, was from two sides below the street level. The building’s walls and columns were made of brick and lime mortar and stood on brick masonry foundations. Vertical load bearing elements in the basement were outer walls and inner massive columns with a few partition walls. Above the basement horizontal bearing elements were masonry cap and barrel vaults. Upper storeys consisted of outer and inner brick walls and timber floors.



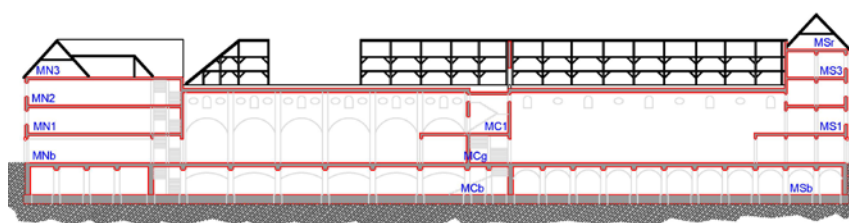
a) Kolizej in its former appearance (photo: Tomaž Lauko)



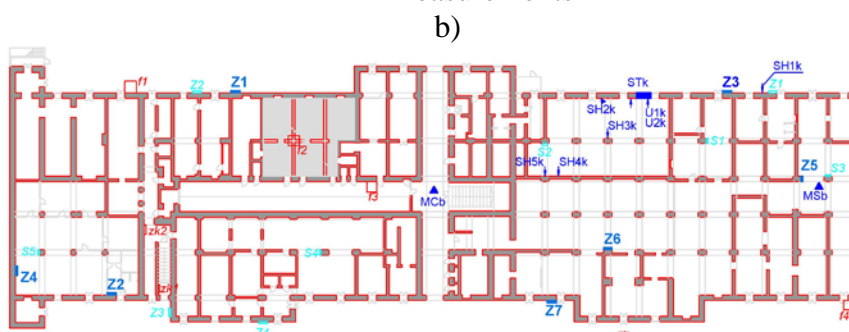
b) Kolizej in 2012 and the state of the masonry in basement (1st level)

Figure 1: Kolizej Palace in Ljubljana

In-situ inspections in 2008 revealed that the load bearing walls and columns were in some parts in very bad condition. Consequences of moisture due to capillary rise, unsuitable introduction of hydro isolation, damaged downpipes and damage due to freezing-thawing cycles were obvious (Figure 1-b). Deterioration due to moisture was extensive throughout the basement and partially in the ground floor, while in the upper floors along drainage at some positions on outer walls. In-situ tests consisted of microtremor measurements, in-situ shear and compressive tests, shove tests, moisture measurements as well as numerous laboratory tests on masonry components and assemblages (Figure 2).



a) Cross-section in S-N direction of Kolizej Palace and position of microtremor measurements



Z UL FGG SH shove test U additional samples of brick
 Z, S Report ZAG ST in-situ shear test M microtremor measurement
 ZP Report ZRMK D moisture content determined on all positions of SH and ST

b) Layout of the basement, testing positions and positions of masonry constituents sampling

Figure 2: Cross-section, layout and positions of in-situ tests at basement level

Shove tests were performed in three different floors in various positions. The in-situ shear test was performed on two walls, one representative for walls in normal condition and one and the other for walls in due to long term moisture exposure more deteriorated walls. Test setup for shove and shear test can be seen in Figure 3. The ratios between mechanical characteristics of walls in normal condition and walls in due to moisture more deteriorated walls (Table 1) exceed the confidence factors prescribed in EN 1998-3:2005 (2005) for case of lowest knowledge level of the building, which is $CF_{KL1}=1.35$.

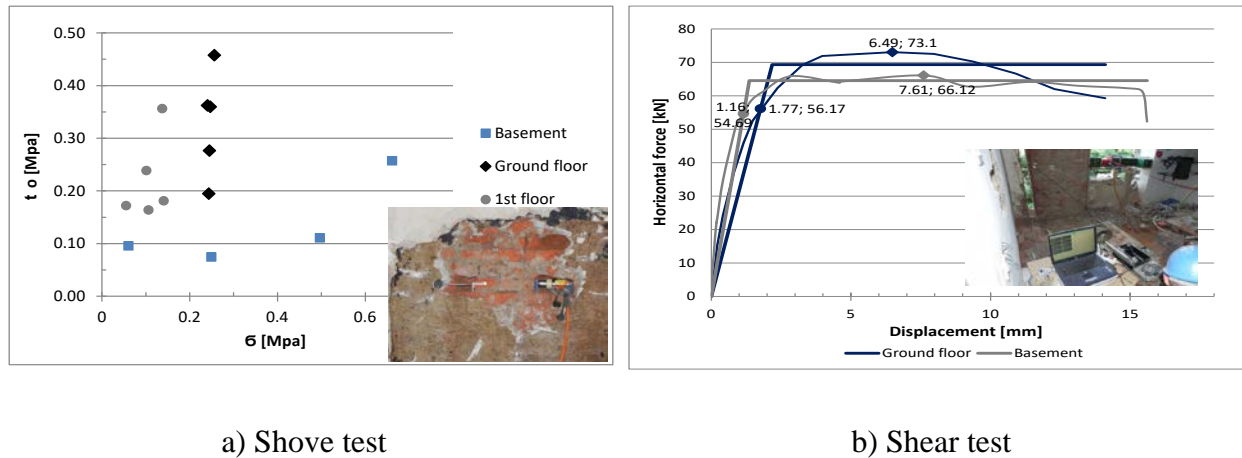


Figure 3: From shove tests calculated initial strengths of masonry joints a) and Hysteretic envelopes and idealized bilinear curves for wall in normal condition (blue) and wall in more deteriorated state (grey) from shear test b).

Table 1: Experimentally determined mechanical characteristics of less and more deteriorated brick masonry

| Mechanical characteristics | More deteriorated walls | Walls in normal condition | Ratio normal cond./more deteriorated |
|----------------------------|-------------------------|---------------------------|--------------------------------------|
| f_c [MPa] | 1.78 | 2.52 | 1.4 |
| f_t [MPa] | 0.046 | 0.072 | 1.6 |
| τ_0 [MPa] | 0.16 | 0.33 | 1.7 |
| E [MPa] | 132 | 236 | 1.8 |
| G [MPa] | 82.9 | 66.9 | 0.8 |

Following experimental campaign, a detailed numerical analysis was performed using structural element models (SEM) considering both storey mechanism response (SMR) by SREMB software (Tomažević 1987) and global response mechanism calculated with 3Muri (Galasco et al. 2009). Both methods are based on push over method.

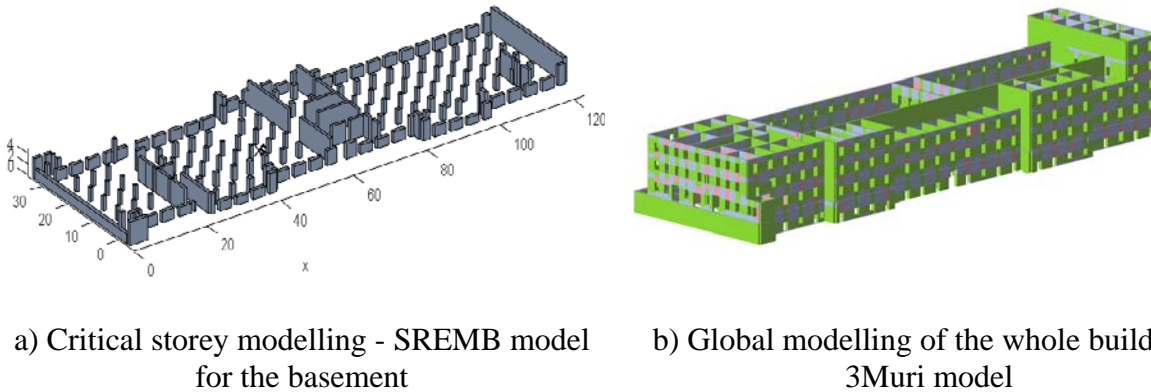


Figure 4: Numerical models for Kolizej Palace

Seismic demand was determined according to EC8-1 (EN 1998-1: 2004) provisions. Design ground acceleration for 475 years return period for this region of Ljubljana is 0.25 g. Considering soil factor for ground type C ($S = 1.15$), the peak ground acceleration amounts to $ULSPGA=0.288$ g. According to the results of analysis (Table 2) seismic demands for the building according to current standards were not satisfied regardless the type of chosen analysis. The resistance was calculated also as if all the walls had estimated characteristics of walls in normal condition and in other case of more deteriorated walls. Comparing these results, the influence of decay of material on the decrease of seismic capacity may be estimated between 29 and 37% for longitudinal X and transversal Y direction respectively (SREMB analysis).

Table 2: Seismic capacity of Kolizej Palace in both directions

| Material characteristics | Direction | ULSPGA [g] |
|--------------------------|-----------|------------|
| SREMB analysis | | |
| More deteriorated | + X | 0.05 |
| | + Y | 0.06 |
| Normal condition | + X | 0.06 |
| | + Y | 0.09 |
| 3Muri analysis* | | |
| Normal condition | + X | 0.12 |
| | + Y | 0.05 |

* for more deteriorated masonry characteristics the analyses did not achieve convergence

Following the outcome of our analysis, the owner had decided that it is not economically justified strengthening the building so, thus in yr. 2012 the palace was demolished, resulting in large public disapproval.

KAZINA PALACE

Kazina Palace was built in 1835-1837 after plans of architect Benedikt Müller as a protocalar building for upper class citizens of Ljubljana (Figure 5-a). The building is 59 m long and 29 m

wide. It has three stories and basement. Unlike Kolizaj palace the basement consists of solid massive walls made in stone masonry and is almost completely under ground level. The building is well maintained. The state of the masonry corresponds to the masonry of Kolizej Palace from upper floors (not deteriorated masonry). In the south part of the building there is a large dancing hall (The Grand Hall) located at the first floor with high slender piers and stone columns. Apart from some photo documentation there were no written records regarding the damage of the building following the earthquake in Ljubljana in 1985 (Figure 5-b).



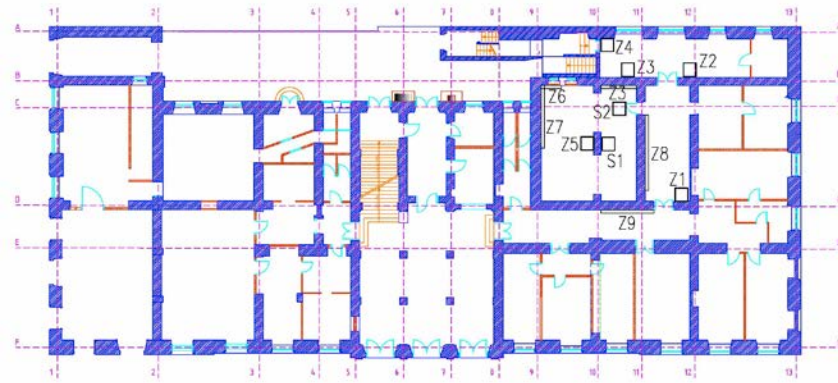
a) South facade of Kazina Palace



b) Remedial measures on S-W corner of Kazina Palace following earthquake in 1895

Figure 5. Kazina Palace in Ljubljana

Due to the current occupancy of the building limiting in-situ investigation (Figure 6) was feasible resulting in rather low knowledge level of the building ($CF_{KL1}=1.20$), meaning that strength parameters for this building were gained by reducing obtained values from Kolizej Palace (case for normal condition) by factor CF_{KL1} .



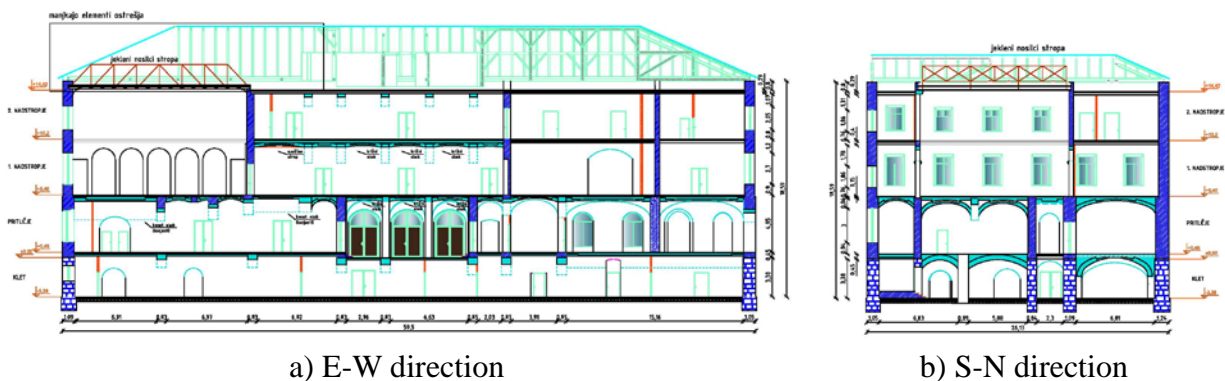
a) Ground level



b) 1st floor

Figure 6: Layout of two levels of Kazina Palace in Ljubljana with the position of in-situ investigation positions for walls (Z) and ceilings (S).

From the layouts (Figure 6) and cross-sections (Figure 7) of Kazina Palace it may be seen, that for this building analysis of critical storey (SMR modelling) would not provide realistic results. Thus seismic analysis was provided by global assessment with 3Muri software (Figure 9-a). Considering importance factor $\gamma_1 = 1.2$ for schools and important buildings, design ground acceleration for 475 years return period for this building was set to ULSPGA=0.346 g.



a) E-W direction

b) S-N direction

Figure 7: Cross-section of Kazina Palace in Ljubljana at position of the Grand Hall

Analysis of the building revealed that according to current code requirements for buildings and increased dead load that will be imposed in the building as well as considering replacement of old wooden roof structure with steel structural system, some additional measures should be provided regarding its static load bearing capacity. In piers encircled with red in Figure 8—a compressive stresses were above the limits provided according to EC6 (EN 1996-1-1: 2005) provisions. The most critical pier marked as Element 4 was already in current state 190% above the allowed limit. In addition to that above that pier the owner's intention was to install organ (6.5 tons heavy) in the Grand Hall situated above this critical pier. Because of that, urgent strengthening measures prior installation of organs were provided by jacketing of critical pier and providing RC frames as presented in Figure 8-b.

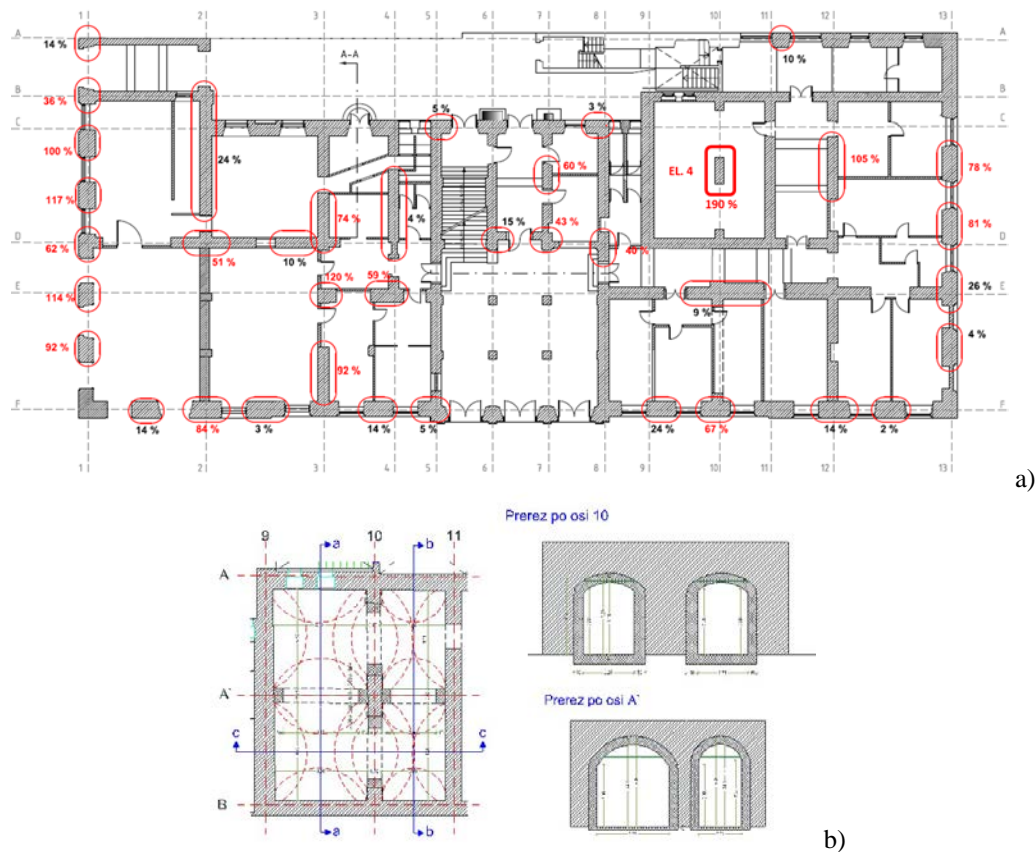


Figure 8: Critical state of compressive stresses in ground floor level a) and ad-hoc strengthening of critical pier b)

Following the results of static analysis additional measures for lowering mass of the building were foreseen. In the first step it was designed removal of heavy gravel infills over vaults and timber floors and its replacement with light-weight (styrofoam) concrete. With this intervention we shall decrease the overall weight of the building, providing stiffer floor diaphragms and tied walls on the floor levels. Composite action of timber and new concrete 7 cm thick RC slab will increase load-bearing capacity of floors enabling higher dead load as it was requested by the owner. These measures shall significantly reduce compressive stresses in critical piers at ground floor level.

For the purpose of seismic assessment over 50 different models each comprehending 24 analyses (12 analyses in positive and negative direction respectively) were performed. Here, results of four different analyses related to different performance levels are defined and presented as:

- 1st current state – represents the most critical result of analysis of the building in its current state;
- 2nd variant – Kazina is national monument of highest importance, i.e. it should fulfil requirements regarding static loading according to EC6, however it is not necessary to fulfil requirements of EC8-1 and EC8-3 regarding its seismic resistance considering 475 yr. return period. All requirements from the Institute for the Protection of Cultural Heritage of Slovenia (IPCHS) are fulfilled.
- 3rd variant – Kazina is national monument, it fulfils requirements of EC6, IPCHS requirements are mostly fulfilled and it fulfils resistance requirements according to EC8 for 100 yr. period but not for 475 yr. period.
- 4th variant – Kazina fulfils requirements in respect both to EC6 and EC8, while fulfils IPCHS requirements solely relating to south facade and Grand Hall.

Results from the analysis of the building in current state (Figure 9) reveal that its current seismic resistance achieves not more than 21% and 23% in X and Y direction respectively in respect to requirements of EC8. Moreover the most critical is torsion behaviour of the building due to slender elements of the Grand Hall (Figure 9 – b & c). The most critical walls are presented in Figure 9 – d & e, where in orange are marked walls failed in shear and in red those failed in flexure.

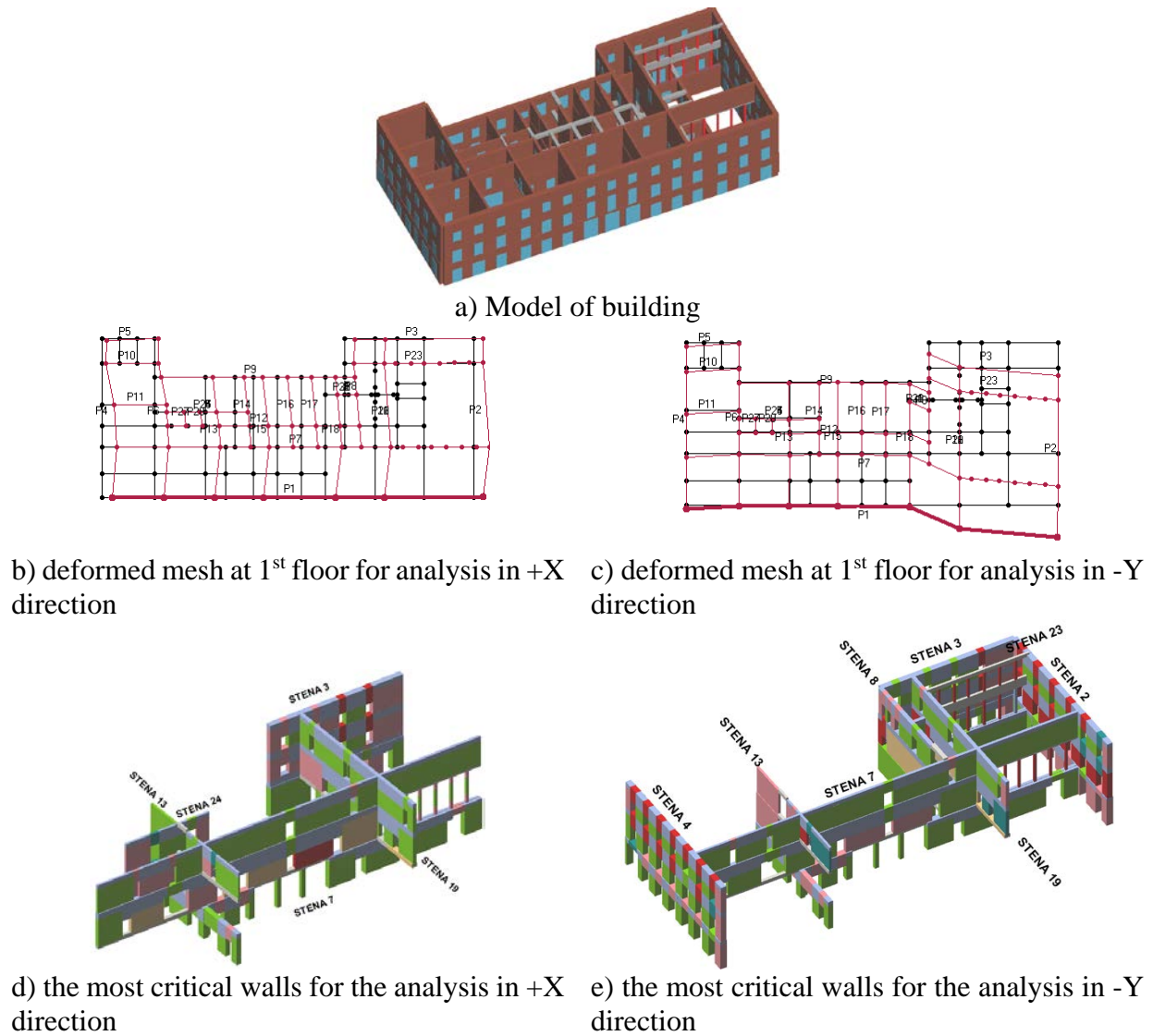
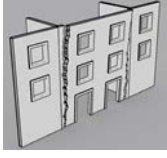
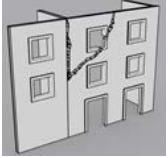
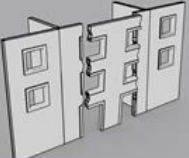
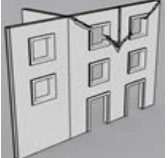


Figure 9: Kazina building in its current state – results of analysis

Additionally local out-of-plane resistance of facade walls provided with FaMIVE methodology (D'Ayala et al. 2002) revealed (Table 3), that for the most critical east facade the most critical mechanism is D (Table 3) and that the current resistance of high walls of Grand Hall is 35% of required resistance.

Table 3: Results of out-of-plane assessment for East facade according to FaMIVE methodology

| Critical out-of-plane mechanisms according to FaMIVE | A | D | E | G |
|--|---|---|--|---|
| |  |  |  |  |
| Resistance | 0.18 g | 0.12 g | 0.16 g | 0.15 g |

Following these outcomes, the 2nd variant was designed strictly following the instructions from IPCHS where interventions were allowed solely in North and East facade (Figure 10-a&b). Additionally, (in agreement with the architect) some existing openings were closed as well. North facade was strengthened with introducing additional RC walls (in Figure 10–a marked in grey) and jacketting (marked in red). Out-of-plane failure of the east facade was prevented with the grid of steel girder and posts (Figure 10-c) anchored in perpendicular walls and RC tie-beams at the top level (over the top of existing walls). Steel beams were built in the outer side of the facade between the openings and designed to support new roof steel structure.

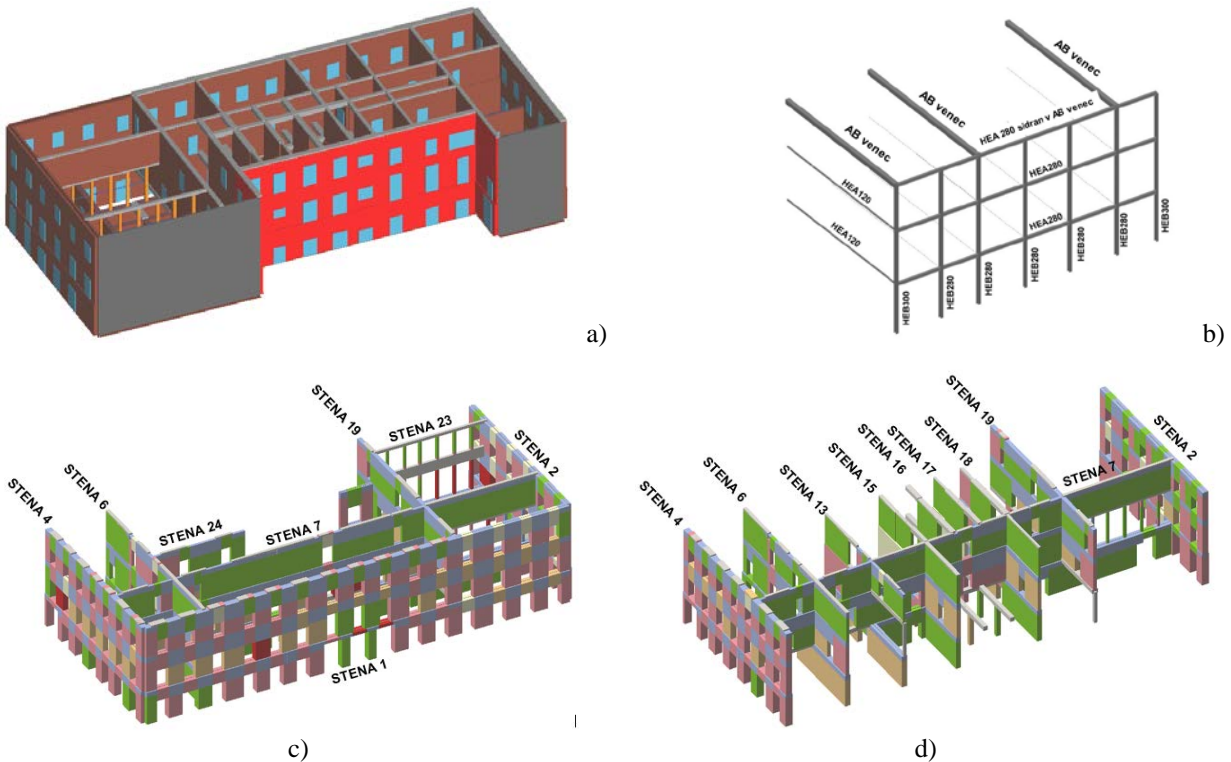


Figure 10: Strengthening measures for 2nd variant a) – b) and the most critical walls in X c) and Y d) direction of the analysis.

With designed strengthening measures resistance in X direction was increased on 54% while in Y direction we achieved only 35% of required resistance. Thus for the 3rd variant additional jacketting of some walls (where it was feasible and allowed, in Figure 11-b marked in red) in S-N direction

was designed together with introduction of the grid of steel elements also in west facade (previously not allowed by IPCHS) (Figure 11 - c). The size of steel columns both in East and West facade were designed to take over the load from new roof structure, thus lowering the compressive stresses in critical masonry piers as presented in Figure 8-a.

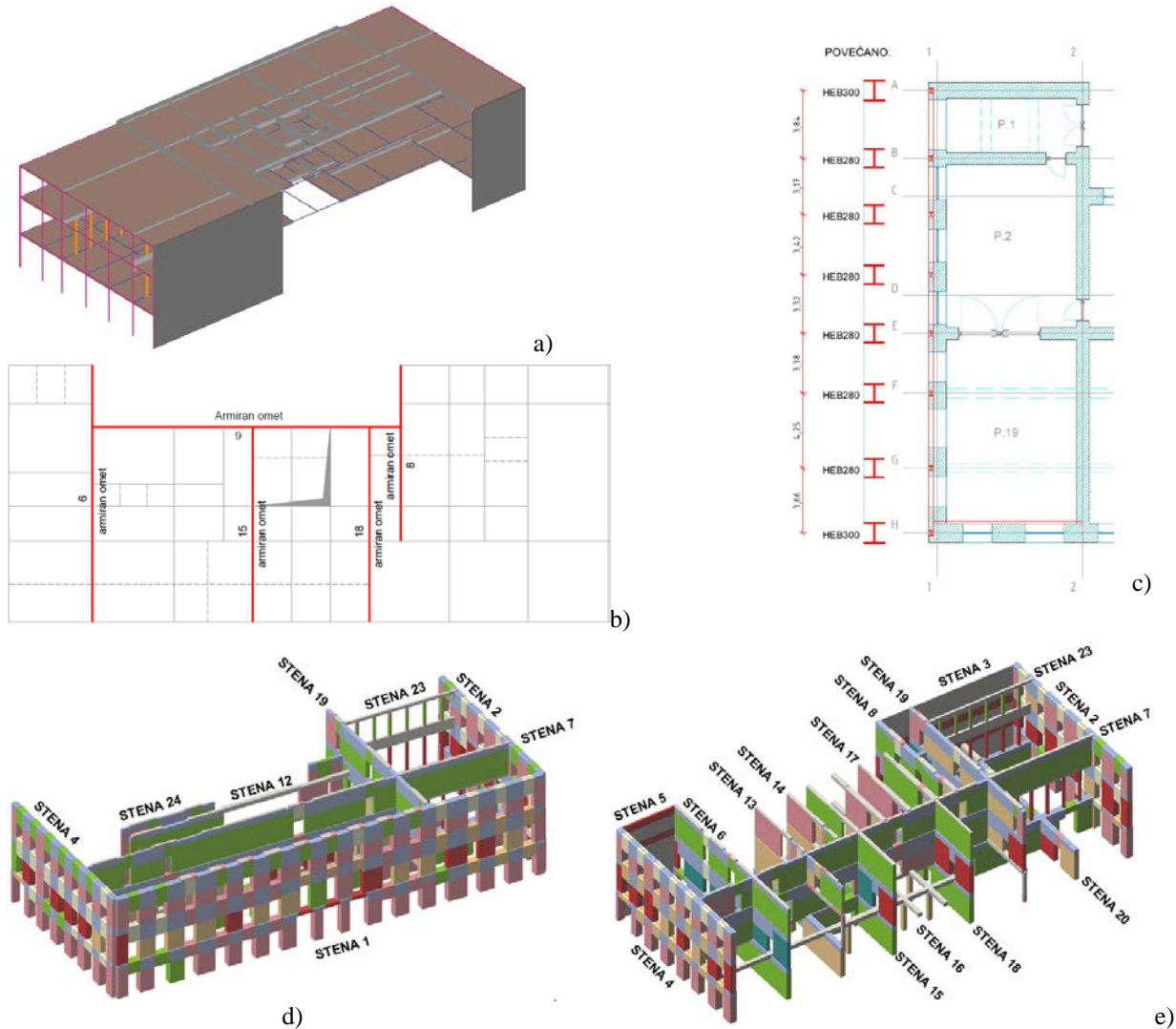


Figure 11: Strengthening measures for 3rd variant a) – c) and the most critical walls in X d) and Y e) direction of the analysis.

For 3rd variant the resistance in X direction was increased on 95%, while in Y direction it was less effective resulting of 60% of required resistance. Torsional effect was not critical anymore and the building would sustain seismic event with 475 yr. period in X direction and 100 yr. return period in Y direction according to EC8 requirements. Following this analysis, it was obvious that additional strength capacity should be added to the structure in Y direction. Thus for the 4th variant additionally RC frames with modest cross section of 40x40 cm² were introduced where it was feasible according to Figure 12–c. With this measure the resistance was increased on 113% and 93% for X and Y direction respectively. Ultimate displacement was increased for 48%.

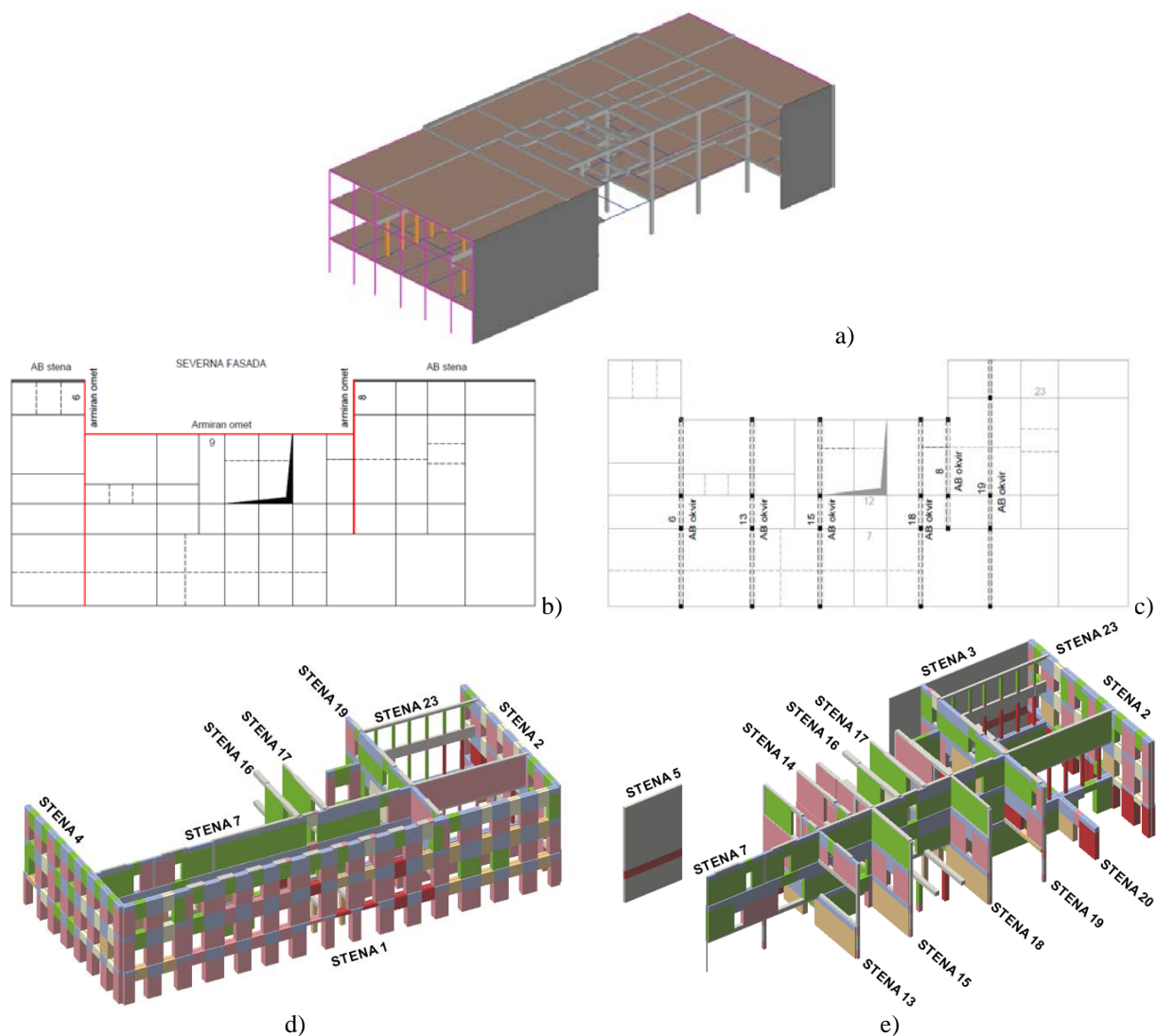


Figure 12: Strengthening measures for 4th variant a) – c) and the most critical walls in X d) and Y e) direction of the analysis

Results for all variants are summarized in following table (Table 4).

Table 4: Seismic capacity of Kazina Palace corresponding to current state and defined performance levels

| Analysis | Direction | ULSPGA [g] |
|-------------------------------|-----------|------------|
| 1 st Current state | + X | 0.06 |
| | - Y | 0.07 |
| 2 nd variant | + X | 0.19 |
| | + Y | 0.12 |
| 3 rd variant | + X | 0.33 |
| | + Y | 0.21 |
| 4 th variant | + X | 0.39 |
| | - Y | 0.32 |

Considering that the required ULSPGA for 100 yr. period is 0.21 g and 475 yr. period (corresponding to 10% probability of exceedance in 50 years) is 0.346 g. It may be concluded that without rigorous strengthening measures current code requirements for contemporary buildings would be hard to met (475 yr. period). On the other hand, building already survived moderate earthquake in yr. 1895 without significant damage (at least not recorded). This moderate earthquake from yr. 1895 may be classified as 100 yr. event, resulting according to EC8 provisions as PGA of 0.21 g. However, both global (3Muri) and local (FaMIVE) analysis provide significantly lower resistance of the building in current state resulting in 33% and 57% respectively in respect to required seismic resistance. Similar results were obtained also for Kolizej palace regardless the uncertainties related to chosen mechanical parameters for the analysis. Here one can conclude that either uncertainties regarding seismic events or complete methodology for the assessment according to EC8 are set too high and not quite appropriate for existing buildings. New forthcoming version of revised EC8-3 (draft is already prepared) should ease this problem.

Though the increase of seismic resistivity for masonry building is mostly related to improved strength characteristics, comparison of pushover curves for different variants in the X direction reveals that for the higher masonry buildings the increase of ductility has important role (Figure 13).

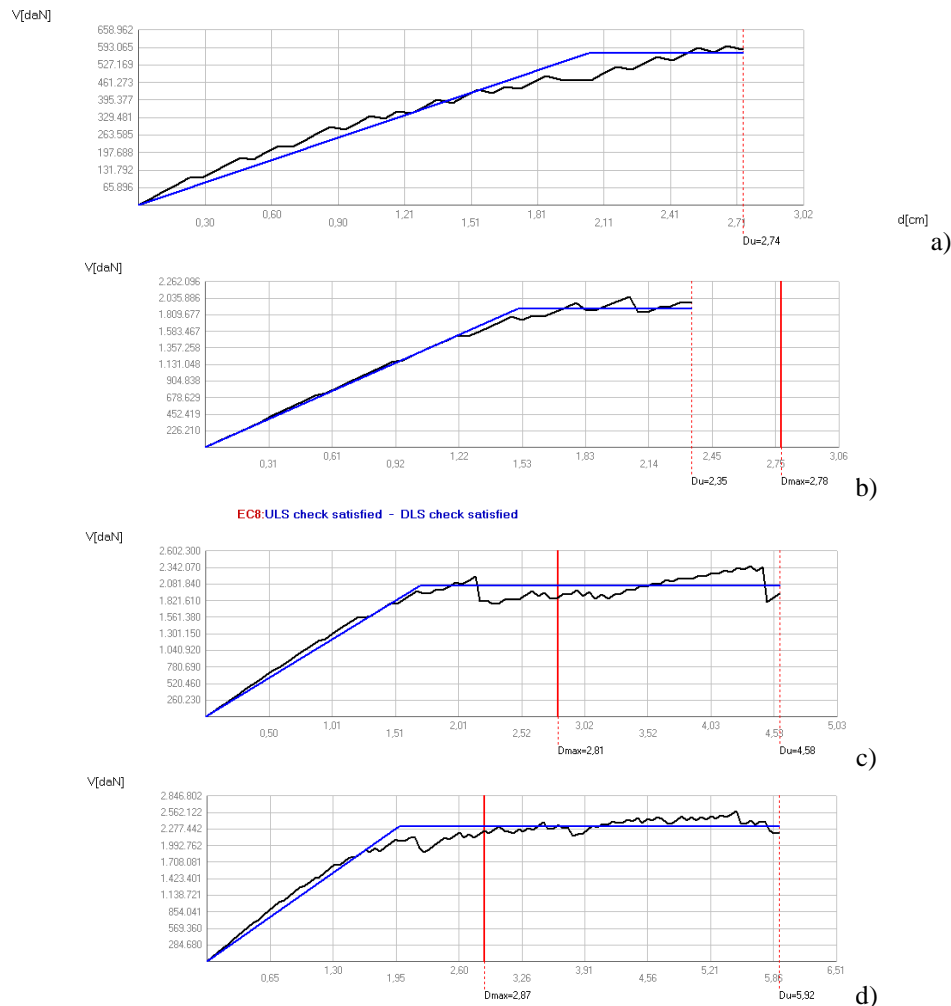


Figure 13: Pushover envelopes for X direction for 1st, 2nd, 3rd and 4th variant of analysis.

CONCLUSIONS

Study of the uncertainties regarding adopted modelling strategies and mechanical parameters on the seismic resistance of the building revealed that regardless of adopted modelling strategies and mechanical parameters for the analysis, the resistance of both palaces was far below seismic demand. On the other hand, both palaces survived moderate earthquake in yr. 1895 without significant damage. Results of seismic analysis revealed that according to current code provisions they fulfil not more than 30% of required resistance for 100 yr. return period according to EC8 requirements.

Following the results of in-situ tests and seismic assessment of two palaces built in approximately same period of time (mid XIX c.) and with similar architectural elements main conclusions regarding influence of deterioration of masonry may be set as:

- Influence of deterioration and ageing of brickwork masonry has significant effects on mechanical properties of masonry.
- Due to moistening and capillary rise, the infiltrating water leads to the mobilization and generation of salts that may significantly influence properties of the mortar and masonry bond. In this respect results of shove tests revealed reduction in strength of 40-60%.
- Reduction of strength properties due to decay of material may be up to 30% for compressive strength and 36% for reference tensile strength of the masonry.

Main problems in preserving old palaces in case of seismic design may be identified as state of preservation (that for Kolizej Palace led to the demolition of the building) and structural performance of structures with large halls and high slender pillars. Here due to insufficient accurate methodology for the assessment of buildings with the status of monuments (EC8), severe strengthening measures may jeopardize the most important architectural and historical elements of the building. Thus, for the assessment of buildings with status of monuments it is necessary to perform numerous analysis considering different performance levels. Once these levels are quantified both through imposed strengthening measures and their economic feasibility, final goal should be met through common agreement between civil engineers, conservators, architects and owners.

ACKNOWLEDGEMENTS

Part of herein presented results were achieved through the project PERPETUATE, funded by the European Commission in the 7th Framework Programme and by the Ministry of Science and Technology of the Republic of Slovenia. The author acknowledges the help of his students Meta Kržan, Neva Siebenreich, Doron Hekič and Amel Emkić as well as to prof. Dina D'Ayala from UCL, UK for generously providing FaMIVE software.

REFERENCES

Bosiljkov V.; Cotič P.; Uranjek M. & Kržan M. (2012) Uncertainties in the assessment of the seismic vulnerability of stone masonry buildings, In *Proceedings of the 15th International Brick and Block Masonry Conference : June 03rd to 06th, 2012, Florianópolis, Santa Caterina, Brazil.*

D'Ayala, D. and Speranza, E. (2002) An integrated procedure for the assessment of seismic vulnerability of historic buildings. *12th European Conference on Earthquake Engineering, London, UK*, 3 (1), Paper 561.

EN 1998-1:2004. Eurocode 8: Design of structures for earthquake resistance – Part 1: General rules, seismic actions and rules for buildings. CEN, 1998

EN 1998-3:2005. Eurocode 8: Design of structures for earthquake resistance – Part 3: Assessment and retrofitting of buildings. CEN, 2005.

EN 1996-1-1: 2005. Eurocode 6: Design of masonry structures – Part 1-1: General rules for reinforced and unreinforced masonry structures. Brussels, Belgium, CEN, 2005.

Galasco A.; Lagomarsino S.; Penna A. & Cattari S. (2009) TREMURI program: Seismic Analyses of 3D Masonry Buildings. University of Genoa.

Tomaževič, M. (1987). *Masonry buildings in seismic regions*. Ljubljana, UL FAGG. (in Slovenian)

MASONRY BUILDING DESIGN FOR EARTHQUAKE-AFFECTED REMOTE AREAS OF NEPAL

J. K. Bothara¹, D. Dizhur² and J. Ingham³

¹ Technical Director, Miyamoto International NZ Ltd., New Zealand,
jbothara@miyamotointernational.com

² Lecturer, Dept. of Civil and Environmental Engineering, The University of Auckland, Auckland, New Zealand,
ddiz001@aucklanduni.ac.nz

³ Professor, Dept. of Civil and Environmental Engineering, The University of Auckland, Auckland, New Zealand,
j.ingham@auckland.ac.nz

The 2015 Nepal earthquake sequence resulted in damage to or the destruction of more than 750,000 residential buildings in “most-affected” areas alone, of which 70% were low-strength masonry (LSM) buildings. In addition to residential buildings, thousands of schools and other institutional buildings were damaged or destroyed. Thirty-one of the country’s 75 districts were affected, with 14 districts declared most-affected areas. These most-affected areas were spread over more than 30,000 square kilometres of hills and mountains having rugged terrain, with a large portion containing scattered settlements that were inaccessible by land vehicular transport. The Government of Nepal has adopted the Build Back Better (BBB) reconstruction approach that requires all new buildings to be earthquake resilient. Meeting this provision generally requires the use of modern materials such as cement and steel, highly skilled construction techniques, and quality control. Stone and mud are commonly the only locally abundant reconstruction materials available. Hardwood is scarce in earthquake-affected areas, particularly at higher altitudes, and importing hardwood or treating local softwood is generally not an option. The situation is further worsened by limited availability of funds. These factors pose technical, logistical, and financial challenges for earthquake-resilient reconstruction. Consequently, innovative construction systems and techniques are required for optimal use of local materials and labour with minimal to no experience in using imported materials. Presented herein is first-hand experience with the development of such building techniques.

Keywords: *Nepal earthquake, earthquake-affected areas, reconstruction, vernacular materials, gabion bands, capacity building*

INTRODUCTION

In 2015 the Mid-western and Central regions of Nepal were hit by the M_w 7.8 Gorkha earthquake, which was followed by 484 aftershocks, the most significant of which was a M_w 7.3 earthquake (Figure 1) (NSC, 2015). The aftershocks substantially added to the damage and number of casualties from the initial earthquake. Of the 75 districts (an administrative unit) of Nepal, the earthquake sequence affected 31 districts in the western and central regions, with 14 of these 31 districts declared the ‘severely hit’ and ‘crisis hit’ in terms of casualties and infrastructural losses. To prioritise reconstruction, these 14 severely hit and crisis hit districts were reclassified by Government of Nepal as most affected. Another 17 districts deemed to be ‘hit with severe losses’, ‘hit’ and ‘slightly affected’ were reclassified as ‘affected’ districts (Figure 1). The majority of the earthquake-affected areas are rural. The earthquake sequence resulted in damage to or the destruction of approximately 750,000 residential buildings, 6,000 government buildings, and 30,000 school classrooms (NRA, 2016).

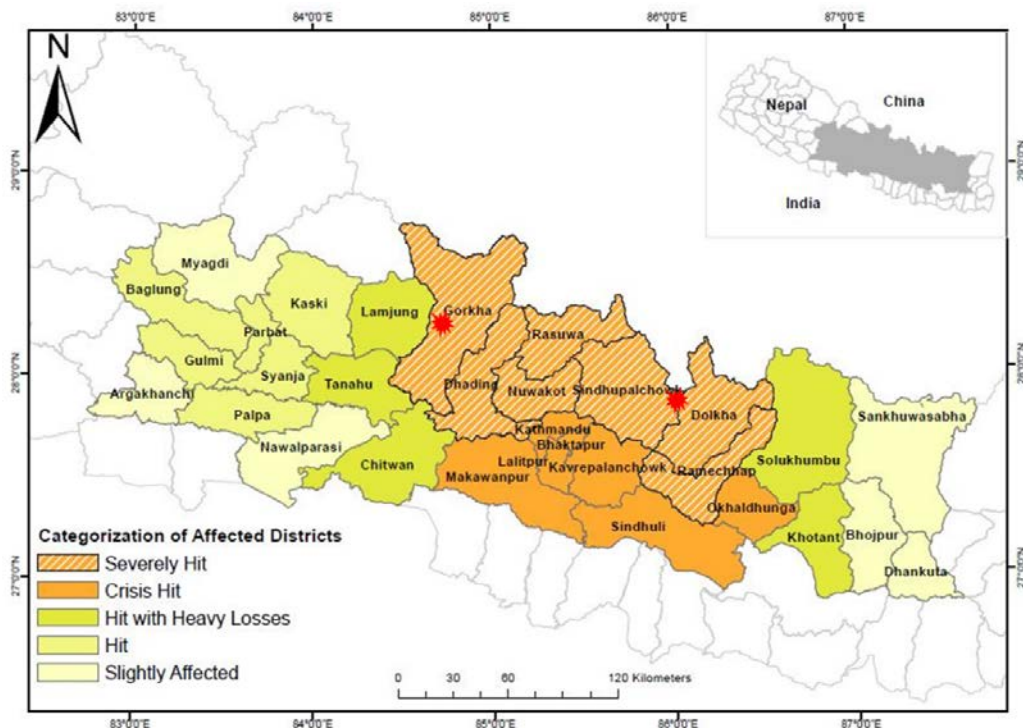


Figure 1: Location of earthquakes epicentres (red stars) and earthquake-affected areas

A set of ground motions recorded in Kathmandu from the main shock showed that the dominant shaking direction was north-south, although a comparable level of shaking took place in the east-west direction as well. The recorded peak ground displacement (PGD) and peak ground acceleration (PGA) were approximately 1.4 m and 0.16g, respectively. The Kathmandu Valley, however, is 77 km away from the epicentre and is a intermontane valley with deep fluvio-lacustrine sediments (Paudyal, Yatabe, Bhandary, & Dahal, 2013) and, hence, the motions recorded might not be representative of those of most of the earthquake-affected areas.

Considering Nepal's location in a high seismicity area and with a view towards "proofing" against future earthquakes, the post-earthquake reconstruction strategic plan — Post-Disaster Needs Assessment (PDNA) — prepared by the Government of Nepal (GoN) clearly emphasized "Build Back Better" (BBB) in accordance with the Sendai Framework for Disaster Risk Reduction (SFDRR) 2015-2030 (UN, 2015) for recovery, rehabilitation, and reconstruction. Taking a pragmatic approach, PDNA proposes owner-led reconstruction of houses, with owners allowed to choose construction materials and the size of the house. The Government of Nepal (GoN) offered financial assistance to individual house owners for reconstruction, with the precondition that the rebuilt house be earthquake resistant (NPC, 2015). Following the BBB philosophy, the GoN decided to reconstruct all institutional buildings such as schools and office buildings as earthquake resistant to mitigate future earthquake risk. This strategy is important for achieving the long-term goal of earthquake disaster risk reduction (EDRR) in Nepal, and is expected to have a profound effect on long-term seismic safety in the earthquake-affected area.

As evidenced by the 2015 earthquake sequence, the earthquake risk in the affected areas mainly originates from unreinforced masonry buildings typically constructed of locally sourced stones with mud mortar or no mortar (Bothara, Dhakal, Dizhur, & Ingham, 2016). Limited availability of funds and the physical inaccessibility of these areas limit the choice of materials for reconstruction. Hence, despite modern materials such as cement and steel being considered essential for earthquake-resilient reconstruction and the local population gravitating towards the use of these materials, stone masonry in mud mortar or no mortar will continue to be widely used in the near future in the majority of earthquake-affected areas in Nepal, particularly in remote areas. Construction of timber houses is another option for reconstruction, but this type of house is considered by the local population to be temporary, nondurable, and lacking in sturdiness. Further, hardwood is scarce in the earthquake-affected areas and treating local softwood or importing hardwood are not feasible options.

Although insignificant seismic improvements were implemented for residential buildings after the 1988 East Nepal earthquake, major interventions regarding earthquake resistance were achieved for the reconstruction of school buildings. Many one-storey, light steel-frame buildings (locally known as truss buildings) with light metal roofs, stone walls up to the sill level, and corrugated iron cladding above the sill level were constructed. Construction of buildings of this design (or variations of the design) continues in Nepal. Field visits completed after the 2015 earthquake showed that very few of these steel structures suffered structural damage. Contrary to their initial design intent, many of these buildings were constructed with full-height stone masonry cladding and partition walls in mud mortar. While these full-height walls suffered damage or were destroyed, the frame remained intact. After the 2015 earthquake, these buildings were used for emergency shelters, warehouses, health posts, and offices. This outcome shows that a small improvement to the building stock could alter damage and destruction scenarios and make a significant difference to post-earthquake situations.

The BBB philosophy proposed after the 2015 earthquake led to the development or proposal by various institutions for new earthquake-resilient building typologies — both vernacular and modern — and the strengthening of existing buildings. These typologies include framed buildings such as those with reinforced concrete (RC) frames with masonry infill walls; confined masonry and steel structures; RC/timber/gabion band technology; gabion mesh technology; mixed construction (bottom storey in stone and upper storey in timber); and polypropylene (PP) bands for

masonry buildings. As technical advisor for the reconstruction efforts, the Department of Urban Development and Building Construction (DUDBC) reviews and approves the proposed designs. The DUDBC requires an evidence-based design if the proposed typology is not included in the Nepal Building Code, which requires experimental and analytical validation of proposed building types. To assist with the review and approval process, DUDBC has published two compilations of designs for the reconstruction of houses. However, there remain very limited proposals for evidence-based designs for the reconstruction of residential buildings as well as important facilities such as schools in the earthquake-affected areas using cost-effective technologies. Observations on emerging typologies and first-hand experience of the development of typologies for seismic-resilient reconstruction in earthquake-affected areas of Nepal are presented herein.

FACTORS AFFECTING SELECTION OF BUILDING TYPOLOGY

Economic hardship and inaccessibility

The building typologies found in most of the earthquake-affected areas are mainly governed by the local availability of construction materials such as rubble stone, semi-fired or unfired brick, and mud (Figure 2). These materials are commonly used even though they are highly vulnerable to earthquake shaking (Dizhur, Dhakal, Bothara, & Ingham, 2016). This scenario is unlikely to change in the near future because of economic hardship and the inaccessibility of many areas. The per capita annual income of Nepal in 2015 was US\$761, which is equivalent to seventy five 50 kg bags of cement in markets that can be accessed by a vehicular transport corridor. A 2006 study (more recent data is unavailable) showed that the per capita income in rural areas of Nepal was less than half that of urban areas (Dillion, Sharma, & Zhang, 2011). The entrenched poverty of earthquake-affected rural areas means that there is little capacity to purchase modern construction materials. The GoN has provided financial assistance of NRs300,000 (\approx US\$3,000) and NRs100,000 (\approx US\$1,000) for the construction of a new house or the repair/retrofit of a damaged house, respectively. However, the available financial resources are insufficient to import modern construction materials required for improved construction to rural areas.



a) Residential structure with dry-stone (no mortar) masonry



b) Community health centre with stone and mud mortar



c) Typical school building with stone and mud mortar (note the high proportion of mud)

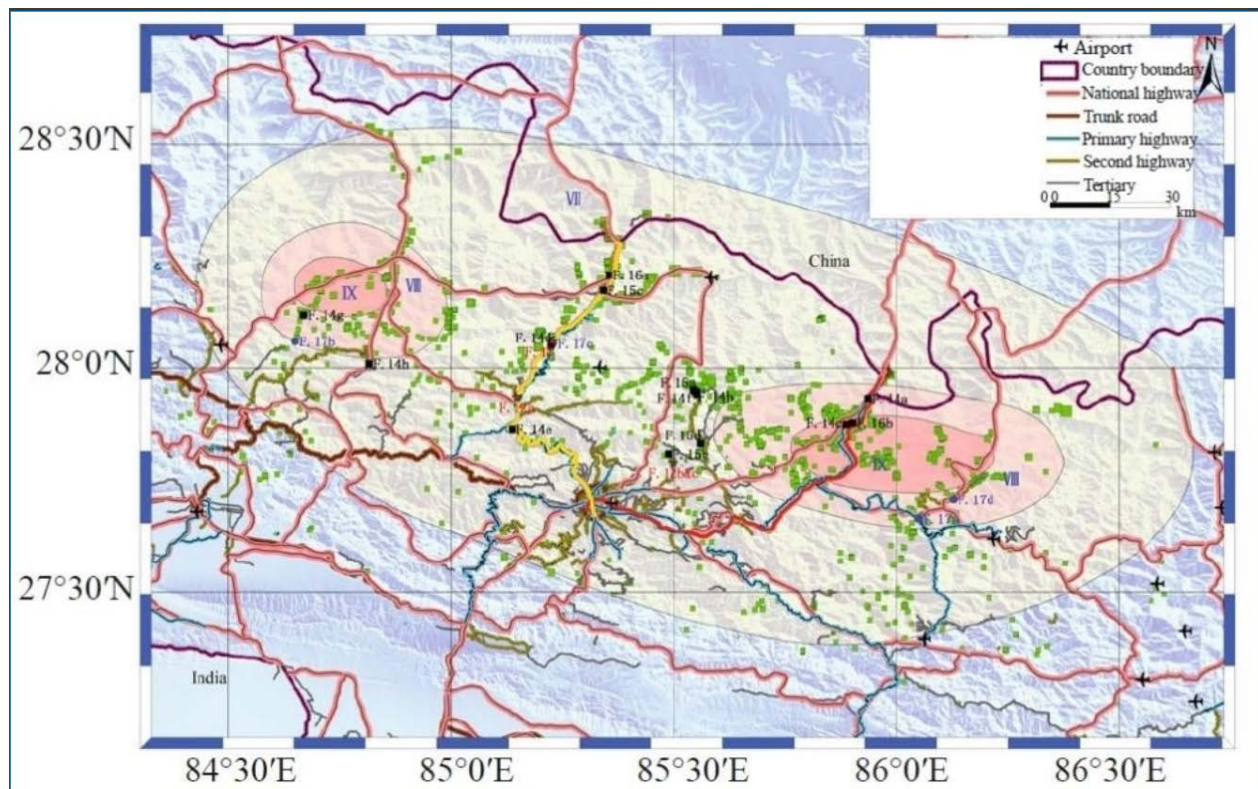


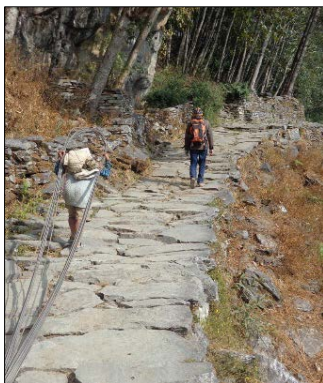
d) Steel 'truss' school building with full-height stone walls

Figure 2: Typical vernacular buildings in earthquake-affected areas

To present an example cost scenario, an average 700-square-foot house, the typical size of a Nepali house in the hills or mountains, requires approximately 15,000 bricks. At current market rates, the bricks alone would cost at least NRs225,000, if purchased from a brick manufacturing site. The bricks must then be transported, by vehicle, an average of 150 km from the southern plains or Kathmandu through mountainous roads and then manually carried for delivery at the construction site. For a stone masonry house of the same size, the cost of stone dressing alone is approximately NRs250,000. At the rates allocated by the Post-Disaster Needs assessment, an average 700-square-foot house constructed with cement masonry would cost more than NRs 1.0 million. Although remittances, money earned in foreign countries and sent back home, have significantly eased financial hardship in Nepal, available funds are insufficient in most cases for the use of dressed stone, cement, or rebar for construction.

Most earthquake-affected areas are inaccessible by vehicular land transport because of rugged topography, the remoteness of mountainous regions, and limited roads (Figure 3). In the last two decades, many new access roads to the areas have been constructed, but most of these roads are operable in dry weather only. This scenario limits access to markets for purchasing bricks, cement, rebar, and iron sheets and poses logistical challenges for transporting building materials, even if funds are available, as these construction materials have to be manually carried to construction sites (Figure 4a and 4b). Even the transporting of sand, which is available in local rivers, is a strenuous task because manual transportation by humans or on animals is required (Figure 4c).





a) Dragging rebar along a tourist route in the mid-mountains (source: Roshit Bothara)



b) Carrying plywood to a construction site [Ref: <https://s-media-cache-ak0.pinimg.com/originals/6e/3c/71/6e3c7148fc2a2caf930c9260fa71661b.jpg>]



c) Carrying sand along a tourist route in the mid-mountains (source: Roshit Bothara)

Figure 4: Transportation of construction materials in remote areas

Construction material hardship

Vernacular construction materials such as stone, mud, sand, and timber that are available in the earthquake-affected area are highly variable and their characteristics depend on local rock types and micro-climatic zone. Commonly available timber in the area is softwood such as pine (mostly *Pinus Wallichiana*) and uttis (*Alnus Nepalensis*), which are prone to termite attack. Hardwood, which takes longer to grow, is scarce, particularly in high-altitude areas. Importing hardwood or treating softwood to these areas for building construction is financially and logistically unfeasible.

The quality, shape, and size of stone depends on the rock type. Stone can be broadly classified into three categories based on size and shape (Figure 5). The stones shown in Figure 5a are soft, typically 100-150 mm largest dimension, and irregular in size and shape. This stone type is generally unsuitable for dressing because of the rock type and small size. Due to the small size and irregularity, this stone type requires a significant amount of mortar, in the order of 30-40% of volume. The irregularity of this type of stone makes walls unstable and, hence, this stone type is unsuitable for the construction of stone masonry walls. However, irregular stones are used when no alternative construction material is available (Figure 5a and 9c). In areas where sedimentary rock is available, stone can be quarried in large blocks. These stone types can be semi-dressed (Figure 5b) or fully dressed (Figure 5c) and are suitable for wall construction.

Similar to the available stone resources, the available soil in most of the earthquake-affected areas can be grouped into three broad categories, which are shown in Figure 6. The soil shown in Figure 6a and Figure 6b can sustain moisture, which is essential to maintain adhesion to masonry units and reduce brittleness. If funds are available, this type of soil can be stabilised using 5-8% of cement to improve masonry quality. However, the soil shown in Figure 6c has high silica content,

is powdery in nature, cannot sustain moisture, and, hence, does not adhere to masonry units and is highly brittle in nature. This type of soil is unsuitable for stabilisation using cement or lime because of its sandy nature and the requirement for high cement content. As a rule of thumb, any soil that is suitable for fired bricks is suitable for mud mortar, cement-stabilised mud mortar, or cement-stabilised bricks.



a) Irregular stone that requires a substantial amount of mortar



b) Semi-dressed stone with nominal mortar



c) Dressed stone with no/limited mortar

Figure 5: Stone for masonry construction



a) Cohesive soil



b) Semi-cohesive soil



c) Sandy, non-cohesive soil

Figure 6: Soil in the earthquake-affected areas

Sand can be either quarried from local streams or imported large distances from the southern plains and then carried by humans from the road to the construction site. Even if sand is quarried from local streams, it must be manually carried to construction sites that are not located along a road.

Skill hardship

Although stone masonry houses with timber bands (an earthquake-resistant feature found in some masonry buildings) are present in the earthquake-affected areas, local craftsman in most of these areas either lack knowledge and skills related to earthquake-resistant construction or have skills that have become diluted over time. Observed deficiencies of vernacular construction include the omission of through (bond) stones, failure to tie the outer wythe of an adobe wall to interior wythes, weak wall-to-wall connections, and lack of ties between floors/roof and walls (Gautam & Chaulagain, 2016) (Dizhur, Dhakal, Bothara, & Ingham, 2016).

Many craftsmen generally lack knowledge of modern construction materials and the construction skills required for using them, and have little appreciation of the limitations of and quality issues associated with these materials. Hence, even when modern materials are used, the quality of construction may be inferior because most local masons are used to working with stone and mud. Figure 7 presents some of the observed deficiencies in local construction practices using concrete and steel rebar.

Due to increased exposure to modern techniques and materials and recent training, local craftsmen have become more receptive to improved quality and earthquake-resistant construction. During field visits in 2016 to earthquake-affected areas, the first author witnessed improvement in the quality of construction and implementation of earthquake-resistant features (Figures 8 and 9), although these features still require significant improvement.



a) Manual mixing of concrete for bands



b) Compaction of concrete (note that one person is holding the formwork and another is compacting the concrete)



c) Laying bond-beam reinforcement (note the dirt in the formwork)

Figure 7: Typical observed deficiencies in construction technologies

BUILD BACK BETTER (BBB) FRAMEWORK

After the 2015 Ghorka earthquake, the GoN adopted the BBB approach for reconstruction. Accordingly, various funding agencies, local NGOs, international NGOs, international financial and development agencies, and the GoN have been supporting the reconstruction of residential buildings. In accordance with the GoN's guidance and supported by international partners, Nepal's Ministry of Education is promulgating earthquake-resistant reconstruction of schools and has, accordingly, developed designs for buildings that employ modern materials and technologies.

Nepal has its own building code, which includes non-engineered and engineered design and construction standards, rules of thumb, and guidelines, including guidelines on mud-based low-strength masonry (LSM) construction (MHPP, 1994). Nepal's building code permits the use of mud-based construction of residential buildings, but does not allow the use of mud for important facilities such as schools.

Many reconstruction partners and donor agencies were initially hesitant to allow the use stone masonry and mud-based reconstruction as part of the post-earthquake recovery, citing the high seismic vulnerability and risk posed by these building types. However, as part of a pragmatic solution, mud-based reconstruction techniques were accepted if they complied with the building code. Accordingly, many partner organisations have proposed various earthquake-resilient building typologies for the reconstruction of residential buildings. If a proposed design is not in compliance with Nepal's building code, the proposers are required to provide an evidence-based design for reconstruction. While this requirement has led to the analytical and experimental validation of a few of the proposed designs, further research is required.

The Ministry of Education has taken the opportunity to improve its portfolio and, accordingly, produced designs for the reconstruction of school buildings using modern materials and technologies, which it is currently implementing. However, there are still no designs that use LSM and other vernacular materials for school buildings. Funding and donor agencies require that any proposals for the reconstruction of school buildings must comply with the building code. This approach requires the validation of proposed LSM designs for school buildings.

Emerging building typologies

A large number of residential, institutional, and school buildings were inspected by the authors of this paper in 2015 and 2016 in many of the most severely-affected districts in the mid-mountain region to understand local construction materials and their availability, designs, construction technologies, and local skills. In addition to stone, mud, fired and unfired brick, and RC, the use of non-traditional materials such as interlocking blocks, cement-stabilised bricks and blocks, and sandbags was observed (Figures 8 and 10) in earthquake-affected areas.



a) Manufacturing of interlocking blocks for house construction



b) Cement-stabilised compressed brick ready for school construction



c) Hollow concrete blocks (note quality of the blocks)



d) Insulated wall panels for a school building

Figure 8: Emerging construction materials

A clear difference between accessible and remote earthquake-affected areas can be observed in post-earthquake construction practices. As observed by the authors during their field visits, the use of cement-based construction such as stone or brick masonry set in cement mortar and RC construction are on the rise (Figure 9e and f) along transport corridors whereas the use of stone in mud mortar (or no mortar) and timber bands (timber recycled from collapsed houses) are more common for houses in remote areas (Figure 9b and d). Because new reconstruction guidelines limit

houses with stone masonry and mud mortar to one storey plus an attic, a new building typology has emerged with a lighter upper structure (Figure 9a and f).

Meanwhile, to address needs in remote areas, new technologies with maximal use of local materials and minimal use of light-weight imported materials is emerging, including sand bag technology, stone houses with galvanised wire containment or gabion mesh bands, and cement-stabilised or compressed stabilised earth bricks (CSEB) (Figures 8a and b, 10c, 11, 12). These technologies are being used for both residential and school buildings.



a) Upper floor reconstructed and replaced by light metal cladding over a timber structure (R)



b) Dry-stone masonry building with timber bands (R)



c) Rubble-stone masonry in mud mortar with vertical bars and bands (R)



d) Semi-dressed stone masonry in mud mortar with bands, upper storey in timber (R)



e) Stone masonry in mud mortar with confining columns in the corners. RC bands on the ground storey, timber bands on the upper storey (R)



f) Stone masonry building with vertical rebar in the corners and RC bands on the ground floor and upper-storey timber structure (A)

Figure 9: New buildings in earthquake-affected areas (A: along roads accessible by vehicle, R: remote area)



a) School building with cement-stabilised earth bricks (A)



b) School building with confined masonry (brick in cement mortar) (A)



c) Earthbag technology (<http://earthbagbuilding.files.wordpress.com/2012/03/bond-beam-earthbag-school-nepal.jpg>)



d) Stone in mud mortar with RC bands (note the gable in timber) (R)

Figure 10: New school buildings in earthquake-affected areas (A: along road accessible by vehicle, R: remote area)

Proposed typologies

For the BBB approach, based on the socio-economic situation, remoteness, limited access to modern materials, and skill levels, any proposed building type for reconstruction in remote earthquake-affected areas should consider the following issues:

- Use of materials:
 - Maximise use of local materials and skills.
 - Minimise use of imported materials.
 - Use light and easy-to-transport imported materials.
- Proposed building type recommendations:
 - Easy to understand and implement, without requiring a radical change in local construction skills.
 - Minimum sensitivity to quality control.
 - Robust and resilient building structural system.
 - Accommodating variations in quality of local construction materials and skills.
 - Building type that could be replicated for different building occupancies.

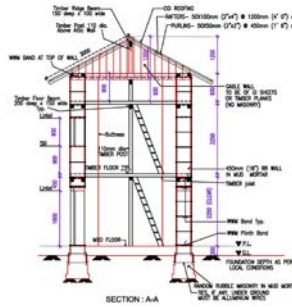
The steel truss buildings used for schools performed well, but culturally this building type would not be acceptable for residential buildings.

Considering the above criteria, the following loadbearing masonry building typologies have been proposed for remote earthquake-affected areas.

Semi-dressed stone masonry in stabilised mud mortar with RC/timber band, splints, and wire containment: This method follows the conventional way of strengthening stone masonry buildings with RC/timber bands, stitches, and vertical reinforcement in strategic locations in compliance with the relevant building standards in Nepal. It should be noted that delamination and mechanism failure are unique to stone masonry construction. These failure mechanisms occur because of a lack

of bond stones to tie multi-wythes of walls and irregular stone. To mitigate these deficiencies, the proposed method uses containment wires in the horizontal and vertical directions on both wall surfaces that are tied together with cross wires to basket the masonry. The method also requires further improvement with the use of cement-stabilised mortar (5-8% of cement mixture) to improve shear strength. Jagadish et al. (2015) validated the adequacy of this method by completing shock table (table shaken by impacts from a tractor or a large pendulum) tests of half-scale one-storey and two-storey models (Figure 10). However, they replaced the bands with interbedded welded steel mesh. Similarly, Pun (2015) completed tests of building sub-assemblages with containment and reported improved performance of stone masonry. Some efforts have also been made by other institutions, but the results of these validation programmes were not available at the time of publication of this paper.

Semi-dressed stone masonry with gabion mesh/geogrid bands, vertical bars, or wire containment: After the 2015 Nepal earthquake, Langenbach (2015) proposed the construction of stone masonry houses with gabion or geogrid bands (Figure 11). The benefit of this method is that the gabion or geogrids are easy to transport to remote areas and simple to install in stone masonry. However, the method does not address the issues of delamination and mechanism failure. Hence, containment wires, which would be tied together with cross wires, have been proposed in the vertical and horizontal directions on both wall surfaces. A potential issue with this system is the high flexibility of walls due to the flexibility of the bands. No validation programme for this system has yet been completed.



a) Proposed prototypes for stone masonry reconstruction with containment wires

b) Testing of proposed building on shock table

Figure 11: Proposed new building typologies in earthquake-affected areas (Jagadish, Desai, & Desai, 2015)



Figure 12: Examples of gabion/geogrid bands (Langenbach, 2015)

CSEB walls, RC bands, and vertical bars: This method follows a conventional procedure for strengthening brick masonry buildings with RC/timber bands, stitches, and vertical reinforcement in strategic locations and complies with the relevant building standards in Nepal. However, to maximise the use of local materials and minimise imported materials, fired bricks are replaced by CSEB (5-8% of cement mixture) and mortar. This method may be useful when a sufficient amount of soil is available. Srisanthi et al. (2014) reported improved seismic performance of small-scale models constructed of CSEB blocks and RC slabs with earthquake-resistant features such as horizontal and vertical bands.

Stabilised, rammed earth with geogrid and RC bands: Rammed earth technology is a simple, inexpensive, and sustainable method for building structures using ordinary soil found at the construction site. The technology consists of ramming stabilised or non-stabilised earth between formwork. Geogrids are interbedded in horizontal layers to improve shear strength and post-cracking behaviour of the walls. For increased durability the walls can be plastered with mud, cement-stabilised mud plaster, or cement sand plaster. No validation programme to determine the adequacy of this system's seismic resistance has yet been completed.

Earthbag construction: Earthbag technology is a simple, inexpensive, and sustainable method for building structures using ordinary soil found at the construction site. The technology consists of laying polypropylene bags filled with locally available soil, similarly to masonry (Figure 9c), with barbed wire serving as mortar and providing shear strength. This building typology is suitable where good-quality stone is unavailable. To protect the polypropylene bags and provide a more attractive appearance, the walls can be plastered with mud, cement-stabilised mud plaster, or cement sand plaster. Some pseudo-static experimental work (Croft, 2011) has been completed, but no validation programme to determine the adequacy of this system for earthquake shaking has yet been completed.

In general, limited research is available on unreinforced masonry building types in Nepal with less on proposed earthquake-resistant building typologies for remote areas. Nepal's building code restricts the use of mud mortar for important buildings (such as schools). Hence, validation of the adequacy of the above-listed building typologies during earthquake shaking through experimental and numerical simulations is required.

SUMMARY AND CONCLUSIONS

The vernacular construction materials and skills available in the earthquake-affected areas of Nepal are inadequate to meet building code requirements because of their inherent weaknesses or not available in sufficient quality locally. Reconstruction using modern materials is not yet feasible, particularly in remote rural areas of Nepal, due to financial and logistical challenges present in these areas. Any future proposed earthquake-resistant building types should maximise use of local materials and minimise use of imported materials. Any imported materials used should be light and easy to carry. The adequacy of future proposed building types needs to be validated through experimental and numerical testing. Some work in this direction is already underway.

REFERENCES

- Bothara, J. K., Dhakal, R. P., Dizhur, D., & Ingham, J. M. (2016). The Challenges of Housing Reconstruction after the April 2015 Gorkha, Nepal Earthquake. *Technical Journal of Nepal Engineers' Association, Special Issue on Gorkha Earthquake 2015, XLIII-EC30(1)*, 121-134.
- Croft, C. (2011). Structural Resistance of Earthbag Housing Subject to Horizontal Loading. *AR40223 MEng dissertation*, 62. Bath: Department of Architecture and Civil Engineering, The University of Bath.
- Dillion, A., Sharma, M., & Zhang, X. (2011). *Estimating the Impact of Access to Infrastructure and Extension Services Rural Nepal*. Wahington DC: International Food Policy Research Institute. doi:DOI: <http://dx.doi.org/10.2499/9780896291881>
- Dizhur, D., Dhakal, R. P., Bothara, J. K., & Ingham, J. M. (2016). Building Typologies and Failure Modes Observed in the 2015 Gorkha (Nepal) Earthquake. *Bulletin of the New Zealand Society for Earthquake Engineering*, 49(2), 211-232.
- Gautam, D., & Chaulagain, H. (2016). Structural Performance and Associated Lessons to be Learned from World Earthquakes in Nepal after 25 April 2015 (MW 7.8) Gorkha Earthquake. *Engineering Failure Analysis*, 68, 222-243. Retrieved May 16, 2017, from <http://dx.doi.org/10.1016/j.engfailanal.2016.06.002>
- Jagadish, K. S., Desai, R., & Desai, R. (2015). *Containment Reinforcement for Earthquake Resistant Technology (unpublished)*. National Centre for People's Action in Disaster Preparedness.
- Langenbach, R. (2015). "GABION BANDS": A Proposed Technology for Reconstructing Rural Rubble Stone Houses after the 2015 Nepal Earthquakes. Retrieved 09 04, 2017, from [http://www.traditional-is-modern.net/NEPAL/REPORTonGABION-BANDS\(Langenbach\)v2.pdf](http://www.traditional-is-modern.net/NEPAL/REPORTonGABION-BANDS(Langenbach)v2.pdf)
- Langenbach, R. (2015). Stone Masonry in Clay Mortar with Gabion Bands. A report submitted to the Nepal DUDBC by Randolph Langenbach, Conservationtech Consulting. Oakland. Retrieved 07 12, 2017, from <http://www.traditional-is-modern.net/NEPAL/DUDBC/ Conservationtech-GabionBands.pdf>
- MHPP. (1994). *A Management Plan for the Introduction of a National Building Code*. Kathmandu, Nepal: Nepal Building Code Dev. Project Nepal, His Majesty's Government of Nepal, Ministry of Housing and Physical Planning, UNCHS (UNDP Project # Nep.88.054-21.03).
- NPC. (2015). *Nepal Earthquake 2015: Post-Disaster Needs Assessment, Volume A: Key Findings*. Kathmandu, Nepal: National Planning Commission, Government of Nepal.
- NRA. (2016). *Nepal Earthquake 2015 : Post Disaster Recovery Framework 2016-2020*. Kathmandu, Nepal: National Planning Commission, Government of Nepal.
- NSC. (2015). *Nepal Earthquake*. (National Seismological Centre, Department of Mines and Geology, Government of Nepal) Retrieved 07 26, 2017, from Past Earthquakes: <http://seismonepal.gov.np/index.php?action=earthquakes&show=past>

Paudyal, Y. R., Yatabe, R., Bhandary, N. P., & Dahal, R. K. (2013). Basement topography of the Kathmandu Basin using microtremor observation. *Journal of Asian Earth Sciences*, 62, 627-637. doi:<https://doi.org/10.1016/j.jseaes.2012.11.011>

Pun, R. (2015). Improvement in Seismic Performance of Stone Masonry Using Galvanized Steel Wire. *A Thesis submitted in fulfilment of the requirement for the degree of Doctor of Philosophy*. School of Civil and Environmental Engineering, Faculty of Engineering and Information Technology, University of Technology, Sydney .

Quancai, X., Gaohu, L., Hao, C., & Chong, X. (2017). Seismic Damage to Road Networks Subjected to Earthquakes in Nepal, 2015. *Earthquake Engineering and Engineering Vibration*, 16(3), 649-670. doi:10.1007/s11803-017-0399-4

Srisanthi, V. G., Keshav, L., Kumar, P. P., & Jayakumar, T. (2014). Finite Element and Experimental Analysis of 3D Masonry Compressed Stabilised Earth Block and Brick Building Models against Earthquake Forces. *Periodica Polytechnica*, 58(3), 255-265. doi:10.3311/PPci.7443

UN. (2015). *Sendai Framework for Disaster Risk Reduction 2015 - 2030*. United Nations. Retrieved 01 31, 2017, from http://www.unisdr.org/files/43291_sendaiframeworkfordrren.pdf

SEISMIC ASSESSMENT MODEL OF MASONRY INFILL WITH OPENINGS AND EXPERIMENTAL VERIFICATION

T.C. Chiou¹, Y.H. Tu², Y.S. Tu³, L.L. Chung⁴ and C.T. Huang⁵

¹ Associate Researcher, National Centre for Research on Earthquake Engineering, Taipei, Taiwan,
tcchiou@ncree.narl.org.tw

² Associate Professor, Department of Architecture, National Cheng Kung University, Tainan, Taiwan,
yhtu@mail.ncku.edu.tw

³ Associate Professor, Department of Civil Engineering, Hungkuo Delin University of Technology, New Taipei,
Taiwan, tuysmail@gmail.com

⁴ Deputy Director, National Centre for Research on Earthquake Engineering, Taipei, Taiwan,
chung@ncree.narl.org.tw

⁵ Ph.D. Student, Department of Civil Engineering, National Taiwan University, Taipei, Taiwan,
d00521023@ntu.edu.tw

This paper reports on a simulation model of a masonry infill wall with openings. The proposed model adopts an equivalent compressive strut to represent the lateral load–deformation relationship of a masonry infill wall with openings. The in-plane stiffness of a masonry infill wall with openings is estimated in accordance with ASCE/SEI 41-13. Previous experimental results indicate that the major fracture path of a masonry infill wall occurs because of bed-joint sliding and/or vertical joint splitting. Therefore, the ultimate lateral strength of a masonry infill wall with openings is estimated from the bed-joint sliding shear, splitting strength of vertical (head) joints, and splitting strength of bricks. The deformation capacity of the masonry infill wall with openings is limited to no larger than 2% of the panel height.

The proposed model is verified by two cyclic loading tests of reinforced concrete frames with masonry infill. The first and second specimens have a door and window opening in the centre of the infill panel, respectively. The test results are briefly presented, discussed, and compared to the prediction results. Good correlation is observed between the experimental and analytical values of the lateral in-plane stiffness, ultimate strength, and deformation capacity of the infill frames.

Keywords: *masonry infill, openings, equivalent compressive strut, reinforced concrete frame, seismic assessment.*

INTRODUCTION

In Taiwan, most existing low-rise buildings use reinforced concrete (RC) frames as the skeleton and masonry panels as the partition walls. A masonry infill wall generally has door and window openings for access, ventilation, and lighting purposes. When a major earthquake occurs, masonry infill walls with openings may experience shear cracks that can extend to adjacent columns, as shown in Figure 1. Previous research indicated that masonry infill walls can contribute considerable lateral strength and stiffness to adjacent RC frames. Thus, masonry infill walls with openings become critical to the seismic resistance of buildings. Appropriately estimating the stiffness and strength of masonry infill walls with openings is therefore an essential issue.

Two characteristics of these RC buildings with masonry infill walls should be noted. One feature is that the construction sequence is similar to that of confined masonry (CM). This sequence begins with the construction of brick infill walls, followed by cast-in-place RC tie-members. The brick infill walls and the RC tie-members are integrated using a shear tooth interface. The second feature is that the dimensions of these tie-members are significantly larger than normal tie-members in CM structures. The typical size (width \times depth) of a column section is 300 mm \times 400 mm, and that of a beam section is 300 mm \times 600 mm. The thickness of the brick walls is approximately 200 mm. Since these tie-members are of a larger size, they are designed to be moment-resistant. Consequently, these confined brick walls are usually considered to be filled walls.

Most of studies on masonry panels have focused on intact panels with four sides of confinement (Tomaževič *et al.*, 1997; Sivarama Sarma *et al.*, 2003). There are some studies focusing on infill panels with openings (Kakaletsis *et al.*, 2008), but only a few on CM panels with openings. Therefore, the National Centre for Research on Earthquake Engineering (NCREE) has conducted a series of tests on brick infill panels with openings since 2009 (Tu *et al.*, 2015). These tests are designed to simulate the existing low-rise buildings consisting of RC frames with brick infill in Taiwan. This paper presents an experiment involving two cyclic loading tests of brick infill frames with door and window openings.

This paper presents a simulation model of a brick infill wall with openings. The proposed model adopts an equivalent compressive strut to represent the lateral load–deformation relationship of the wall. The in-plane stiffness will be estimated in accordance with ASCE/SEI 41-13. Previous research has shown that the major fracture path of a brick infill wall includes bed-joint sliding and vertical joint splitting. Therefore, the ultimate lateral strength of a brick infill wall with openings is estimated by the bed-joint sliding shear, splitting strength of vertical (head) joints, and splitting strength of bricks. The deformation capacity of a brick infill with openings is limited to no larger than 2% of the panel height. Following the experiment, the experimental and analytical results are compared and discussed.



Figure 1: Shear failure of brick wall with a window opening. Photo by Tsai (2014)

ASSESSMENT MODEL

The seismic behaviour of a brick infill wall with openings was simulated by effective brick infill piers. The effective brick infill pier was defined as a panel segment between openings and columns. An RC frame in-filled by a brick wall with a door opening, as shown in Figure 2(a), was simulated by a bare frame with two equivalent compressive struts. For a brick wall with a window opening, as shown in Figure 2(b), the captive column and brick infill pier were each simulated by shorter elements, owing to the restraining effect of the windowsill. In Figure 2, P represents the axial plastic hinge of the equivalent diagonal strut. The properties of the axial plastic hinge were calculated by the proposed skeleton curves of the brick infill piers in accordance with the findings of Chiou *et al.* (2016). Meanwhile, M3 and V2 in Figure 2 represent the moment plastic hinge and shear plastic hinge, respectively. These properties were calculated by the load–displacement relationship of the columns in accordance with TEASPA (Hsiao *et al.*, 2015).

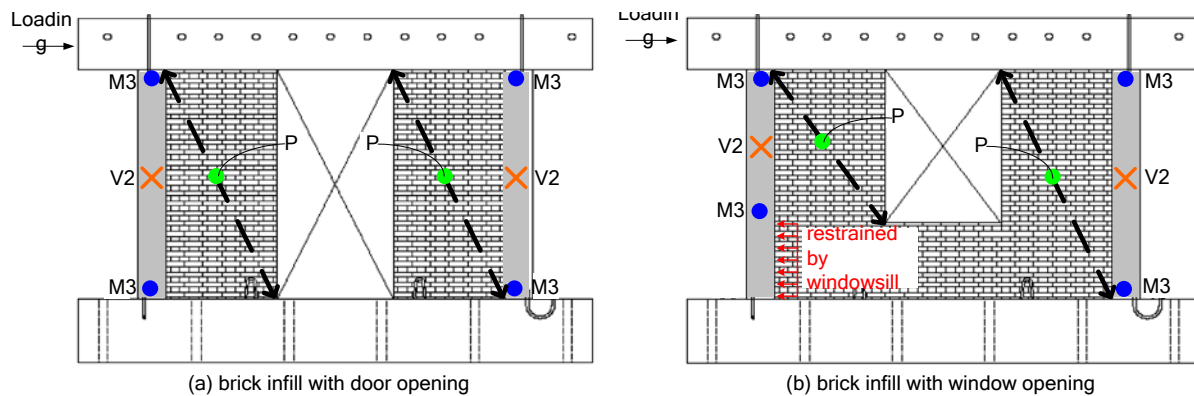


Figure 2: Simulation model of a brick wall with openings.

Chiou *et al.* (2016) proposed a model of an equivalent compressive strut to simulate the lateral load–deformation relationship of a brick infill pier. The proposed model establishes a triple linear curve to describe the load–deformation envelope curve for brick infill piers, as illustrated in

Figure 3. The stiffness of the triple linear curve is calculated in accordance with ASCE/SEI 41-13. The ultimate lateral strength of the infill piers is estimated based on the bed-joint sliding shear, the splitting strength of vertical (head) joints, and the splitting strength of bricks. These sources of strength are determined by the major fracture paths of the infill piers. The residual strength and ultimate deformation of the infill piers are empirically determined by experimental observations. The stiffness, ultimate lateral strength, and post ultimate strength behaviour of the simplified assessment model for brick infill piers are briefly introduced in the following paragraphs.

In accordance with ASCE/SEI 41-13 (2013), the in-plane lateral stiffness of an RC frame with a brick infill wall can be simulated by an equivalent column with a composite cantilever column, for which the adjacent columns are considered as the flanges of the equivalent column and the brick wall is considered as the web of the equivalent column. The stiffness of the equivalent column can be calculated by:

$$K_{ini} = \frac{1}{\frac{1}{K_{fl}} + \frac{1}{K_{sh}}} \quad (1)$$

where K_{fl} is the flexural stiffness of the equivalent composite cantilever column, which can be calculated as:

$$K_{fl} = \frac{3E_c I_{ce}}{h_{cb}^3} \quad (2)$$

where E_c is the elastic modulus of the concrete, I_{ce} is the equivalent moment of inertia of the transformed concrete section, and h_{cb} is the height of the equivalent column. If the shear stress is uniform across the wall, the shear stiffness (K_{sh}) of the equivalent column can be calculated by:

$$K_{sh} = \frac{G_m A_w}{h_w} \quad (3)$$

where A_w is the cross-section area of the brick infill wall, h_w is the height of the brick infill wall, and G_m is the shear modulus of the brick infill wall. This can be determined by:

$$G_m = 0.4E_m \quad (4)$$

where E_m is the elastic modulus of the brick infill wall, for which FEMA 356 (2000) suggests using $550f'_m$. The term f'_m denotes the compressive strength of a standard masonry pier in accordance with ASTM C1314-14 (2014).

Chiou *et al.* (2016) proposed that the lateral strength of infill piers should be based on the strength of the three cracking types, and can be calculated from:

$$V_{pier} = \tau_f \left(\frac{2}{3} \ell_b \times t_b \right) + 0.225 f_{mt} \left(\frac{2}{3} \ell_b \tan \theta_c \times t_b \right) + 0.225 \left(\frac{f_{mt} + f_{bt}}{2} \right) \left(h'_b - \frac{2}{3} \ell_b \tan \theta_c \right) \times t_b \quad (5)$$

The first term in Equation 5 represents the sliding shear strength of bed joints with an effective length of $2/3 \ell_b$, the second term represents the splitting strength of cross joints in inclined cracks with a length of $2/3 \ell_b \tan \theta_c$; and the third term represents the splitting strength of cross joints and the vertical splitting strength of a solid clay brick for vertical cracks with a length of $h'_b - 2/3 \ell_b \tan \theta_c$, as illustrated in the middle range of the strut in Figure 4. Since the loss of splitting strength of vertical cracks is categorised as brittle failure, and different locations on the fracture path cannot simultaneously reach the maximum, the strength provided by the splitting strength of cross joints (f_{mt}) and the vertical splitting strength of the solid clay brick (f_{bt}) is reduced by a coefficient of 0.225. In Equation 5, ℓ_b and t_b denote the length and thickness of the brick infill piers, respectively; and θ_c represents the critical crack angle of the brick wall, which depends on how the bricks have been laid. (Chen, 2003). The sliding shear strength of bed joints τ_f (MPa) can be computed by the following empirical equation proposed by Chen (2003).

$$\tau_f = 0.0258(f_{mc})^{0.885} + (0.654 + 0.00514 f_{mc}) \frac{N}{\ell_b \times t_b} \quad (6)$$

where f_{mc} is the compressive strength (MPa) of the mortar cubes and N is the axial force due to the gravity load (N). The splitting strength of cross joints, f_{mt} (MPa) can be calculated like so:

$$f_{mt} = 0.232(f_{mc})^{0.338} \quad (7)$$

The vertical splitting strength of the solid clay brick, f_{bt} (MPa), can be obtained using:

$$f_{bt} = 0.22 f_{bc} \quad (8)$$

where f_{bc} denotes the compressive strength (MPa) of the solid clay bricks obtained from a brick compression test performed in accordance with ASTM C67 (2007).

In Equation 5, h'_b represents the effective height of the major fracture path, as illustrated in Figure 4. This value is determined by the diagonal strut that crosses the boundary line between the column and pier. For a column with a single brick wall pier (Figure 4), the effective height of the major fracture path can be calculated as follows:

$$h'_b = \min\left(\frac{h_b}{\frac{2}{3} \ell_b + \ell_c - \frac{a_c}{3}} \times \frac{2}{3} \ell_b, \ell_b\right) \quad (9)$$

where a_c is the depth of the compressive zone of the column, which can be determined by the simplified equation proposed by Paulay *et al.* (1992):

$$a_c = (0.25 + 0.85 \frac{N}{A_g f'_c}) \ell_c \quad (10)$$

in which A_g denotes the cross-sectional area of the column.

The post ultimate strength behaviour of the brick infill pier is illustrated in Figure 3. According to the empirical observation by Chen (2003), the lateral strength of a masonry infill wall is based on horizontal slippage failure and vertical split failure. Vertical splitting cracks cause brittle failure; therefore, the splitting strength reduces rapidly after the peak strength, V_b , is reached, and becomes non-existent when the deflection reaches twice the lateral deflection at the maximum lateral strength ($2\Delta_b$). The residual strength, V_r , is calculated only from the sliding strength of bed joints and cannot exceed 0.6 times the maximum lateral strength:

$$V_r = \tau_f (\ell_b \times t_b) \leq 0.6V_b \quad (11)$$

In accordance with observations from tests of infill piers made by Tu *et al.* (2011), the residual strength of infill piers will rapidly decrease as a result of insufficient constraints on walls with an opening. The authors suggest that the residual strength will linearly descend to zero from the displacement of $2\Delta_b$ to the ultimate inter-story drift ratio of 2% (Figure 3).

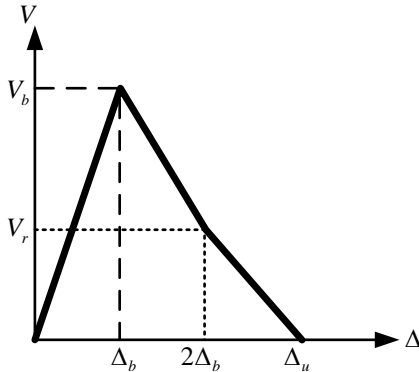


Figure 3: Proposed triple line model of a brick wall pier.

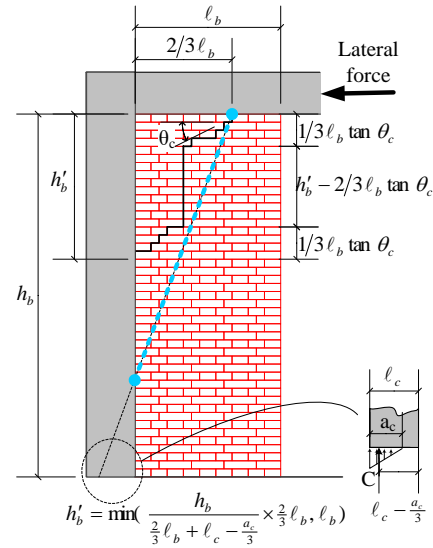


Figure 4: The idealised major fracture path of an RC column with a brick wall pier.

EXPERIMENTAL METHOD AND OBSERVATIONS

Two specimens of RC-frame in-filled brick walls with openings were subjected to lateral, cyclic in-plane loading tests at the NCRE. The first specimen (CD) was a brick wall with a door opening.

The other specimen (CW) was a brick wall with a window opening. Figure 5 shows the dimensions of the test specimens. Both specimens are full-scale. The brick walls were double-wythe and laid in English bond using solid clay bricks with dimensions of 200 mm \times 95 mm \times 53 mm. The column section is designed as a typical non-ductile column found in old buildings. The top beam section was purposely enlarged to simulate the strong-beam, weak-column, and shear-building behaviours of typical low-rise RC buildings. The dimensions of the identical RC column were 300 mm (depth) \times 400 mm (width) \times 2700 mm (height). The column cross-section contained non-ductile detailing with rebar of 8-#6, and a hoop of #3@ 250 mm. The end hooks were of the closed stirrup type at a 90° angle. Table 1 shows the parameters and material properties of the tests. The axial load in Table 1 was separated by column and infill piers in accordance with axial rigidity (EA).

Lateral cyclic in-plane loading was applied to the top beam. The loading was displacement-controlled by the increasing drift. Two vertical actuators provided vertical compression that simulated the dead load, and a force couple kept the top beam from rotating during the test to simulate the shear-building behaviour. Figure 6 shows the specimen and test setup. Vertical displacement gauges were installed at the top beam to monitor its rotation. Horizontal displacement gauges were installed at different heights along the columns and vertical edges of the opening to measure the deformation patterns. Strain gauges were attached to the longitudinal steel bars and hoops to study the stress condition in the columns. The material tests included tension tests for the steel, and compression tests for the bricks, mortar, prisms with five bricks, and concrete cylinders, as illustrated in Table.

Figure 1 shows lateral load–displacement hysteretic loops. The crack patterns at maximum strength are shown in Figure 8. The positive and negative load–displacement relationships of the specimens were not symmetrical, but the structural behaviours in the two directions were approximately the same. Specimens CW and CD showed similar damage progression and failure modes. The initial stiffness and drift at points of major damage are quite close for the two specimens. The masonry panels in both specimens failed in diagonal compression, causing toe crushing. The differences between the two specimens are that specimen CW exhibited higher strength overall and shear failure of columns, while the columns of Specimen CD only experienced flexural cracking. If the masonry panels are considered as equivalent diagonal struts, the difference in the crack pattern suggests that the presence of the windowsill allows the equivalent strut to develop with a gentler slope, which provides larger lateral resistance. This condition also induces larger shear at the intersection of the equivalent strut and the column, causing more severe damage to the column.

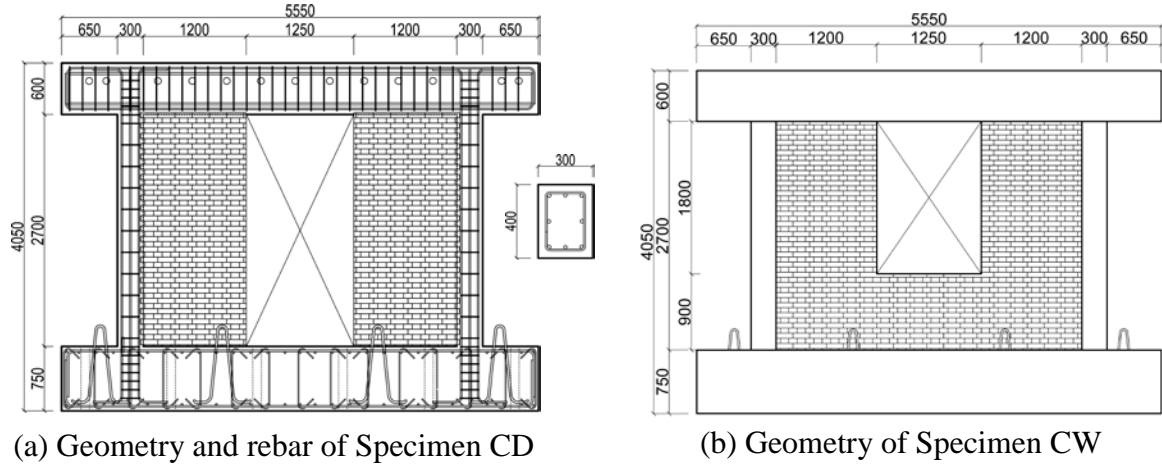


Figure 5: Elevation and reinforcement of specimens.



Figure 6: Test setup and specimen.

Table 1: Parameters and material properties.

| Specimen | Column | | | Wall | | | Axial load | |
|----------|--------|-------|-----|----------|----------|--------|------------|------------|
| | f'_c | f_y | | f_{mc} | f_{bc} | f'_m | column | brick wall |
| | | #6 | #3 | | | | | |
| | (MPa) | | | | | | (kN) | |
| CD | 28.8 | 443 | 360 | 17.6 | 20.2 | 11.6 | 156 | 79 |
| CW | 28.3 | 443 | 360 | 17.6 | 20.2 | 11.6 | 156 | 79 |

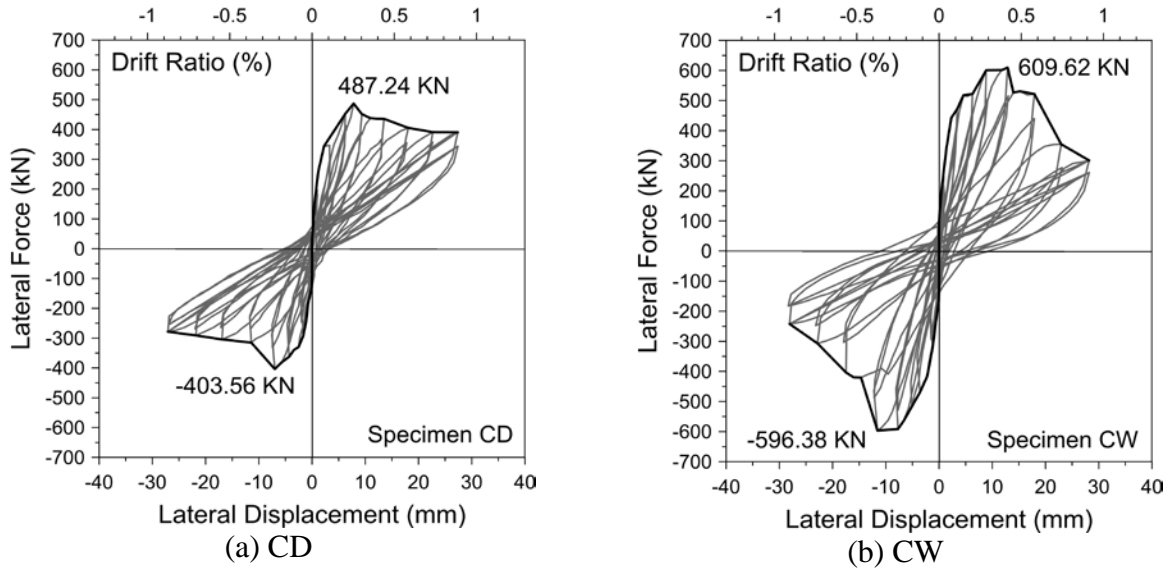


Figure 7: Lateral load–displacement hysteretic loops.

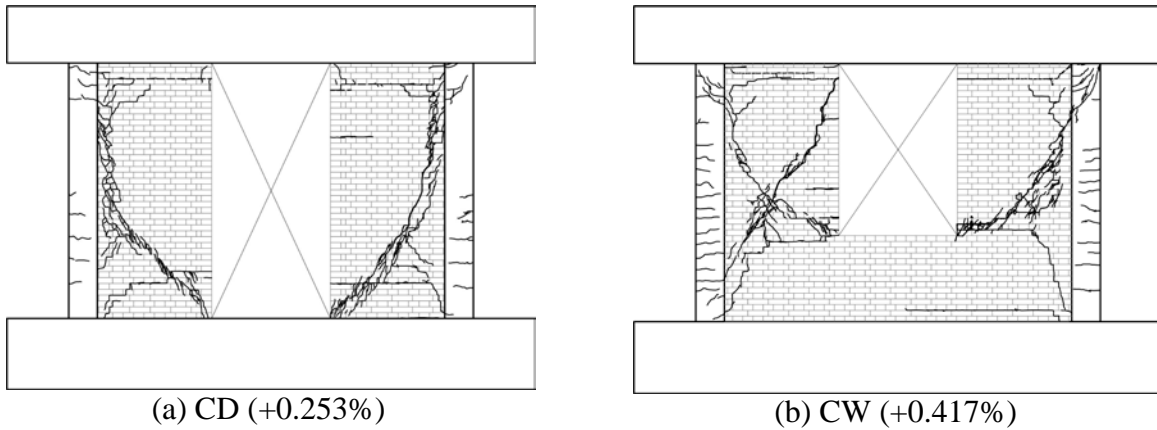


Figure 8: Crack patterns at maximum strength.

VERIFICATION OF THE ASSESSMENT MODEL

Engineers have known that the seismic behaviour of an RC frame with a brick infill wall can be simulated by an RC frame and an equivalent diagonal strut. For conservative simulation of a brick infill with openings, engineers may only simulate brick infill piers on the compressive side, assuming that the structure undergoes single curvature deflection. However, *Chiou et al.* (2016) indicated that the brick infill piers at either side of an opening can also have diagonal compressive struts under double curvature deformation. In this study, the seismic behaviour of RC in-filled frames with openings was simulated by an RC frame and two equivalent diagonal struts, as shown in Figure 2.

For in-plane lateral stiffness of a brick infill wall, the ASCE 41-13 model represents an uncracked initial stiffness of the equivalent column, as expressed in Equation 1. *Chiou et al.* (2016) indicated

that the stiffness of the equivalent column should be modified for simulation of the cracked stiffness. However, the reduction factor for cracked stiffness of the equivalent column is not given in ASCE/SEI 41-13 (2013). In accordance with experimental observation during this study, the cracked stiffness of Specimen CD is 152 kN/mm, which is 45% of the initial stiffness. Meanwhile, the cracked stiffness of Specimen CW is 192 kN/mm, which is 38% of the initial stiffness. As a result, a reduction factor of 0.35 is conservatively adopted for the cracked stiffness of the equivalent column in this study.

Figure 9 shows the predicted load–displacement curves compared with the experimental results. The experimental model reasonably predicted the initial stiffness of the experimental result. The prediction of the cracked stiffness for Specimen CD was 95 kN/mm, which is 63% of the experimental result. The prediction of the cracked stiffness for Specimen CW was 172 kN/mm, which is 90% of the experimental result. From this data, it can be concluded that the calculated initial stiffness conservatively estimates that of the tests.

For the maximum lateral strength, the calculated result for Specimen CD was 457 kN, which is 94% of the experimental result. The calculated result for Specimen CW was 486 kN, which is 80% of the experimental result. The strong correlation indicates that the proposed model can accurately predict the experimental results. It should be noted that, for Specimen CW, although the prediction model has simulated the constraint effect of a windowsill using a shorter column and a gently sloped diagonal strut, the simulation result of the columns still shows flexural failure. Experimental results, however, indicated that both columns underwent shear failure near their tops.

For the deformation at maximum lateral strength, the predicted deformation of Specimen CD is 4.8 mm, which is an underestimate compared to the experimental result of 7.8 mm. The calculated result for Specimen CW is 4.95 mm, which is also an underestimate compared to the experimental result of 12.9 mm. This data indicates that the prediction of deformation at maximum lateral strength by the model is conservative.

For the post ultimate strength behaviour, the skeleton prediction curve fits the experimental results of Specimen CD very well and conservatively fits those of Specimen CW.

Consequently, the proposed model can well predict seismic behaviour of an RC in-filled frame with door and window openings. The application of this model can improve the existing seismic assessment model of RC buildings.

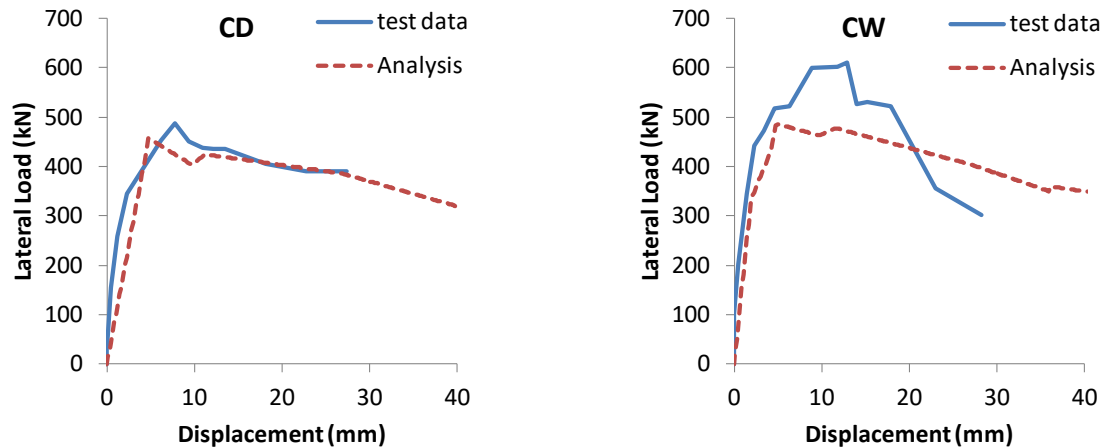


Figure 9: Comparison of the experimental and analytical results.

CONCLUSION

A simplified prediction model for infill piers was proposed in this paper and verified by experimental results. Based on the comparison of the analytical and experimental results, the following conclusions can be drawn.

The assessment model of masonry infill walls with openings was introduced and verified by testing. Consequently, the proposed model can well predict seismic behaviour of an RC in-filled frame with door and window openings.

The proposed simulation model could reflect the restraining effect of a windowsill and the contribution of brick infill piers at either side of an opening, which was consistent with the experimental observations.

A reduction factor of 0.35 for the cracked stiffness of the equivalent column was verified in the experiment. Verification of this factor by further test data should be a goal of future studies.

REFERENCES

ASCE/SEI 41-13 (2013), American Society of Civil Engineers, seismic evaluation and retrofit of existing buildings., American Society of Civil Engineers.

ASTM C67 (2007), Standard test methods for sampling and testing brick and structural clay tile, ASTM International, Place, Published, pp. 1-12.

ASTM C1314-14 (2014), Standard Test Method for Compressive Strength of Masonry Prisms, ASTM International, Place, Published,

Chen Y. H. (2003), Seismic Evaluation of RC Buildings Infilled with Brick Walls, Doctoral dissertation, M. S. Sheu, National Cheng Kung University Department of Civil Engineering, Tainan, Taiwan.

Chiou T. C., Hwang S. J., Tu Y. H., and Tu Y. S. (2016), A simplified assessment model of masonry infill piers, *Brick and Block Masonry: Proceedings of the 16th International Brick and Block Masonry Conference*, Taylor & Francis Group, Padova, Italy, pp. 1163-1171.

FEMA 356 (2000), Prestandard and Commentary for the Seismic Rehabilitation of Buildings. Federal Emergency Management Agency.

Hsiao F.-P., Oktavianus Y., Ou Y.-C., Luu C.-H., and Hwang S.-J. (2015), A Pushover Seismic Analysis and Retrofitting Method Applied to Low-Rise RC School Buildings. *Advances in Structural Engineering*, 18(3), pp. 311-324.

Kakaletsis D. J., and Karayannis C. G. (2008), Influence of Masonry Strength and Openings on Infilled R/C Frames Under Cycling Loading. *Journal of Earthquake Engineering*, 12(2), pp. 197-221.

Paulay T., and Priestley M. J. N. (1992), *Seismic Design of Reinforced Concrete and Masonry Buildings*. Wiley. ISBN: 0471549150

Sivarama Sarma B., Sreenath H., Bhagavan N., Ramachandra Murthy A., and Vimalanandam V. (2003), Experimental studies on in-plane ductility of confined masonry panels. *ACI Structural Journal*, 100(3), pp. 330-336.

Tomažević M., and Klemenc I. (1997), Seismic behaviour of confined masonry walls. *Earthquake Engineering & Structural Dynamics*, 26(10), pp. 1059-1071.

Tsai W.-L. (2014), Analysis and countermeasure of the failure mechanism of buildings in Chi-Chi Earthquake. Wan-Lai Tsai. ISBN: 978-957-43-1310-5

Tu Y.-H., Hsu Y.-H., and Chao Y.-F. (2015), Lateral load experiment for confined and in-filled unreinforced masonry panels with openings in RC frames, *Proceedings of the 12th North American Masonry Conference (NAMC)*, Denver, USA, pp. No. 206.

Tu Y. H., Chuang T. H., Lin P. C., Weng P. W., and Weng Y. T. (2011), Experiment of Slender Confined Masonry Panels under Monotonic and Cyclic Loading, *Proceedings of the 2011 Structure Congress*, Las Vegas, U.S., pp. 2730-2740.



**MASONRY TODAY
AND TOMORROW**

**11 - 14 February, 2018
SYDNEY AUSTRALIA**

www.10amc.com

DESIGN OF IN-PLANE UNREINFORCED MASONRY WALL TESTING PROGRAM AND PRELIMINARY FINITE ELEMENT ANALYSIS (FEA)

M.K. Howlader¹, M.J. Masia², M.C. Griffith³ and J.W. Jordan⁴

¹ PhD Student, Centre for Infrastructure Performance and Reliability, The University of Newcastle, Callaghan NSW 2308, Australia, MilonKanti.Howlader@uon.edu.au

² Associate Professor, Centre for Infrastructure Performance and Reliability, The University of Newcastle, Callaghan, NSW 2308, Australia, mark.masia@newcastle.edu.au

³ Professor, School of Civil, Environmental and Mining Engineering, The University of Adelaide, North Terrace Campus, SA 5005 Australia, michael.griffith@adelaide.edu.au

⁴ Bill Jordan & Associates Pty Ltd, Consulting Structural and Conservation Engineers, PO Box 141, Newcastle NSW 2300, bill@bjaeng.com.au

Heritage URM buildings represent the history, culture and identity of our towns and cities making them important assets to retain and preserve. However, they are vulnerable to damage during earthquakes. This vulnerability arises firstly from the building class to which they belong; unreinforced masonry, which performs poorly during earthquake shaking due to its high mass and stiffness and low tensile strength and ductility. When considering heritage URM construction the potential vulnerability is further complicated due to the often unique geometries, the unknown and potentially deteriorated material characteristics, and the lack of consideration of seismic design and detailing principles at the time of construction. During earthquake shaking, the URM walls loaded under a combination of vertical gravity forces and cyclic lateral in-plane forces play a crucial role in the seismic load path. To gain a better understanding regarding the horizontal load capacity of walls in heritage URM buildings, it is necessary to conduct experimental testing which correctly represents the typologies and materials present in heritage URM buildings. This paper presents the design of an experimental program of perforated URM walls subjected to quasi-static cyclic in-plane loading. A total of 8 perforated URM walls, two leaves thick common bond pattern, will be tested by varying the pier-spandrel geometry, applying two levels of vertical pre-compression stress, using low strength lime rich mortar and two repeats of each test. The selection of all the above parameters for the heritage URM walls in Australia are described in this paper. The paper also presents nonlinear FEA of the experimental design wall which was conducted to appraise the wall behaviour and failure modes due to cyclic in-plane loading.

Keywords: *heritage masonry, perforated wall, experimental program design, finite element modelling and analysis.*



INTRODUCTION

Unreinforced masonry (URM) was the most common form of building construction used in Australia throughout the 19th century and at the beginning of the 20th century. The structural configuration, considerable age and the construction materials of these URM buildings makes them more vulnerable to damage during earthquake loading than the more recently used reinforced concrete, masonry (designed to modern codes) or composite structures. The vulnerability of this form of construction in Australia was highlighted by the 1989 Newcastle earthquake which, despite being of only moderate magnitude (M5.6), caused extensive damage in older URM construction. During an earthquake, the excitation from the ground is transferred via the footing/foundation to the stiff in plane loaded URM walls, which are considered as the primary lateral load resisting component, and then transmitted to the out-of-plane walls through flexible floor and roof diaphragms.

Early research into the in-plane behaviour of perforated walls (that is, walls with window and door openings) subjected to earthquake loading focused on the failure of the piers (Magenes and Calvi, 1997; Tomaževič, 1999). However, previous earthquakes throughout the world have shown damage also within the spandrel of the perforated URM wall and so the spandrel behaviour under lateral load also has an impact on the overall wall performance. Although the effect of the spandrel in coupling the piers was considered in seismic analysis, the nonlinear response of the spandrel was usually not accounted for. For example, in the present simplified assessment (NZSEE, 2006), the seismic assessment method for perforated URM walls is based on the assumption of either weak (insignificant strength and stiffness) or strong (infinite strength and stiffness) spandrels and then the wall behaviour is solely dependent on the pier behaviour.

Recently extensive research has focussed on perforated walls to evaluate the global nonlinear behaviour of the URM structures under in-plane seismic loading. The findings show that the spandrel has a very important resistance capacity which affects the shear capacity of the wall. Experimental in-plane shear testing of full scale perforated walls (Allen et al., 2016) and solid URM walls (Konthesingha, 2012) has been conducted at The University of Newcastle using materials and construction details typical of contemporary wall construction in Australia. Also, numerous laboratory works on perforated URM walls with full and reduced scale were carried out representing new and old masonry practice in different countries of the world (Yi et al., 2006; Nateghi and Alemi, 2008; Bothara et al., 2010; Augenti et al., 2011; Knox, 2012; Vanin and Foraboschi, 2012; Triller et al., 2016). The material properties and the building configurations are different in old heritage buildings than contemporary practices in Australia. Therefore, the focus of this research is to design an experimental testing program and conduct preliminary finite element analyses (FEA) to better understand the seismic capacity of old heritage URM walls by assessing the load-displacement behaviour and the failure modes under in-plane loading.

SELECTION OF WALL GEOMETRY, MATERIALS AND PRECOMPRESSION LOAD

Specimen Geometry

Eight full-scale unreinforced masonry (URM) wall specimens with a centrally located semi-circular arch opening will be built in the laboratory and subjected to cyclic in-plane pseudo-static

loading. The specimens will be constructed with two different geometries by varying the spandrel depth, two vertical precompression loads and for each combination of test parameters two wall specimens will be tested, resulting in eight wall specimens in total. The dimensions of the chosen wall geometries for the proposed testing program (Figure 1) are similar to those previously tested in Auckland (Knox, 2012) and in Newcastle (Allen et al., 2016) and are further described below.

A study of the URM heritage buildings in New South Wales (NSW), Australia (Howlader et al., 2016) shows that more than 85% of the total heritage listed URM buildings were constructed prior to 1930 with the period of 1821-1900 containing more than 70% of the total heritage listed building stock. The URM building construction practice in Australia was similar to that of New-Zealand until the Napier earthquake in 1931 where clay brick was the prominent material for the construction of URM buildings. Masonry walls built in Australia in the nineteenth century were mostly solid walls without any cavity and the introduction of the cavity wall in some construction was seen in the last decade of the nineteenth century (Lucas, 1982). Based on these findings, solid load bearing clay brick walls were chosen as being most representative of heritage building walls for this testing program.

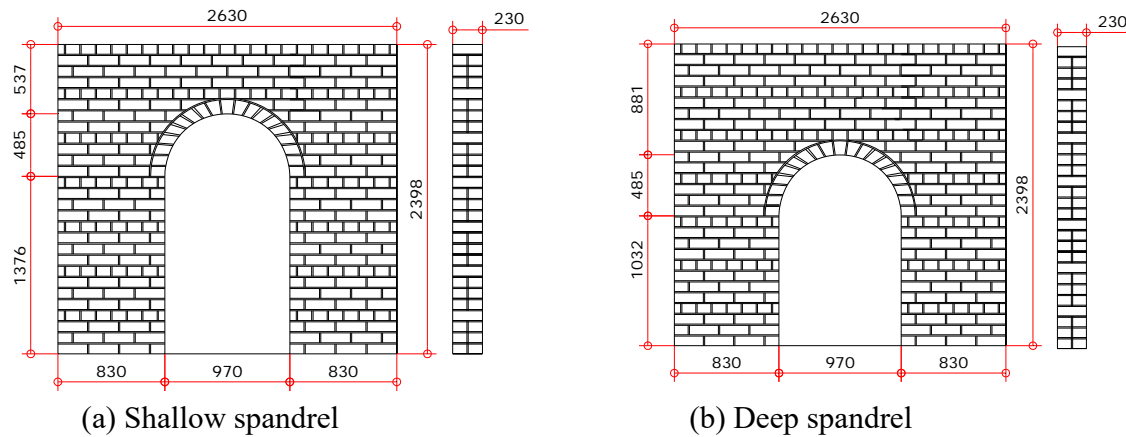


Figure 1: Proposed perforated URM wall geometry (all dimensions are in mm).

Solid masonry load bearing walls of multi-leaf thickness are more common in heritage building construction than single leaf walls. More than 75% of the heritage URM buildings in NSW are low rise buildings consisting of one and two storey height (Howlader et al., 2016). From the findings of Russell (2010), most of the solid load bearing walls of two storey URM buildings in New Zealand (two stories is the most common height for New-Zealand) are three leaves thick in the lower storey and reduce to two leaves thick in the top storey. The wall thickness for the current experimental study is chosen as two leaf wall with thickness of 230 mm. According to the bulletin of Australian Council of National Trust (Lucas, 1982), Common (American) bond was the most used bonding pattern in the 19th century, where headed courses are inserted at regular intervals to connect tightly the two leaves of the wall. In this testing program, Common bond is adopted, with courses of header bricks used at every fourth course. The shapes of openings for windows and doors in heritage listed buildings in the NSW region vary between rectangular, semi-circular, segmental and gothic (common in church buildings). The most common shape for openings in heritage buildings in Newcastle is the semicircular arch headed opening. Therefore, semi-circular arch opening was chosen for the experimental program here.

Constituent Materials

Brick: Howlader et al. (2016) found that the majority of load bearing heritage URM buildings in NSW were constructed using clay brick. Therefore, the specimens for the proposed study will be made using clay brick units of common available dimensions 230 mm x 110 mm x 76 mm. The bricks used in heritage buildings may have some differences in properties and characteristics compared to more modern bricks because of the modification of the manufacturing process (particularly the firing temperature). To replicate the behaviour of heritage masonry one approach would be to collect bricks from old buildings, remove the original mortar and use new mortar on the recycled brick. However, after removal of mortar from recycled bricks the mortar which is drawn into the surface of the bricks due to brick suction remains. This cannot be readily removed and its presence will change the suction properties of the bricks. Therefore, using recycled bricks with new mortar, it is not possible to replicate the correct nature of the bond between the brick unit and mortar which is very important for in-plane shear loading. Considering this, new brick units will be used to make the wall specimens. To provide the closest possible replication of heritage clay brick masonry the bricks sourced will be solid dry pressed units (typically higher suction) rather than extruded units, which typically have lower suction properties and usually contain cores.

Mortar: Tests on mortar collected from the field for URM buildings in New-Zealand by Lumantarna (2012) showed a great variation of compressive strength from 0.53 MPa to 25.88 MPa. Within this range, the higher strength mortars were found to be from the repointing of joints with cement based mortar. Excluding the repointing mortar, the compressive strength of the mortar samples varied from 0.53 MPa to 8.58 MPa which indicate mortars of lime and cement-lime based compositions. From the acid degradation test, Lumantarna (2012) found the volumetric binder to aggregate ratio of 1:3 was commonly used in the heritage building construction and the mineralogical separation showed that most of the field extracted mortar samples are lime dominated. Due to a shared history of settlement and similar periods of construction between Australia and New Zealand (Griffith et al. 2013), it has been assumed that mortars in heritage URM construction in Australia will share similar characteristics to those reported for New Zealand. There are different types of lime used to make the mortar for brick laying. To investigate a suitable mortar type for this experimental program, brick prisms were made in the laboratory with different types of lime with or without pozzolan and with cement. The materials used for making the mortar were ordinary Portland cement, rock lime or hydrated lime, pozzolan with different percentage by volume of lime and well graded river sand with maximum size of 4.75 mm. The gradation curve of the sand is shown in Figure 2. Flexural tensile strength of the mortar bed joint was determined using the bond wrench test in accordance with AS3700 (Standard Australia, 2011) for different ages to assess the rate of strength gain. Compressive strength of the mortar was also determined by making 70 mm x 70 mm x 70 mm mortar cubes and testing in accordance with ASTM C109/C109M-11 (ASTM, 2011). The flexural bond strength and mortar compressive strength results are summarised below in Table 1. Considering the above factors for previous heritage construction, and considering the need for a mortar with sufficient strength gain for testing of walls at 28 days, lime rich cement-lime mortar joints having 10 mm thickness was selected for the proposed testing program with mix proportions by volume of 1 cement : 2 lime (rock) : 9 sand. This mortar falls into the AS3700 'M2' classification (Standard Australia, 2011). This mortar is low in strength and can represent the weather deteriorated mortar of the heritage buildings.

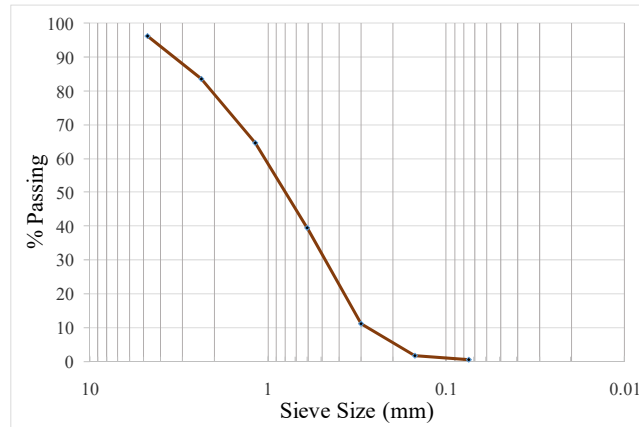


Figure 2: Gradation curve of used river sand.

Table 1: Strength of different types of mortar.

| Mortar Type | Flexure strength (MPa) (COV) | | | Compressive strength (MPa) (COV) | | |
|--|---------------------------------|------------------|------------------|-------------------------------------|------------------|------------------|
| Lime: Sand= (1:3) Pozzolan added as % volume of lime | Testing age | | | Testing age | | |
| | 21 days | 42 days | 90 days | 21 days | 42 days | 90 days |
| Rock lime without Pozzolan | -- | -- | 0.056 (0.252) | -- | -- | 0.199 (0.124) |
| Rock lime with 10% Pozzolan | -- | -- | 0.069 (0.257) | -- | -- | 0.241 (0.051) |
| Rock lime with 25% Pozzolan | 0.052 (0.290) | 0.071 (0.314) | 0.077 (0.277) | 0.245 (0.144) | 0.307 (0.036) | 0.309 (0.033) |
| Hydrated Lime | 0.070 (0.201) | 0.071 (0.097) | 0.077 (0.296) | 0.212 (0.036) | 0.251 (0.071) | 0.543 (0.001) |
| Cement: Lime: Sand = (1:2:9) | Testing age | | | Testing age | | |
| | 7 days | 14 days | 28 days | 7 days | 14 days | 28 days |
| Rock lime-cement | 0.212 (0.382) | 0.223 (0.306) | 0.201 (0.500) | 0.989 (0.016) | 1.229 (0.092) | 1.710 (0.013) |
| Hydrated Lime-cement | 0.621 (0.286) | 0.468 (0.454) | 0.402 (0.442) | 2.866 (0.037) | 4.120 (0.046) | 4.124 (0.078) |

Precompression Load

Two levels of vertical pre-compression stress will be used for each wall geometry. The variability of the axial stress on the pier is designed to represent walls at different positions within a building hence reflecting different levels of gravity loads supported by the walls. A pier located in the top floor will experience a lower axial stress than a pier which is located in the ground floor of a multistoried building. Knox (2012), calculated the axial compression stresses in perforated walls located at different floor levels of URM buildings. The lower axial stress (0.2 MPa) level on the

pier represents the walls located on the top storey and the higher (0.5 MPa) level corresponds to the piers of the ground floor of a three storey building. In some cases, the pier on the ground floor of the two storey building showed higher axial stress due to the position of the opening. In the NSW region most of the heritage buildings (76%) are one or two storey and three storey buildings occupy 10% of the total building stock (Howlader et al., 2016). Considering the prevalent building storey heights in the NSW region the axial stress levels of 0.2 MPa and 0.5 MPa are selected as low and high axial stress on the pier of the arched opening masonry wall.

PROPOSED EXPERIMENTAL TESTING PROGRAM

The experimental setup and instrumentation to be used in the proposed study are presented in Figure 3. This setup, including the chosen test boundary conditions, was designed by Allen et al. (2014) to simulate a single storey height section of masonry wall within a larger multi-storey building under axial compression and lateral in-plane loading. The walls will be constructed on a composite steel/reinforced concrete footing beam consisting of a steel channel (300 PFC) with its web laid flat on the laboratory floor and with a reinforced concrete beam cast between the flanges of the PFC such that the upper surface of the beam is concrete. This footing beam will be bolted to the laboratory strong floor. Fixed vertical pre-compression load resulting in either 0.2 MPa or 0.5 MPa average vertical compressive stress in the piers will be applied at the centre of each pier by the vertically aligned hydraulic jack, which reacts against the steel beam connected between the laboratory strong walls. The vertical load will be equally distributed from the hydraulic jack to centre line of each pier through the spreader beam (200 UC 46.2) and will be kept constant during the test.

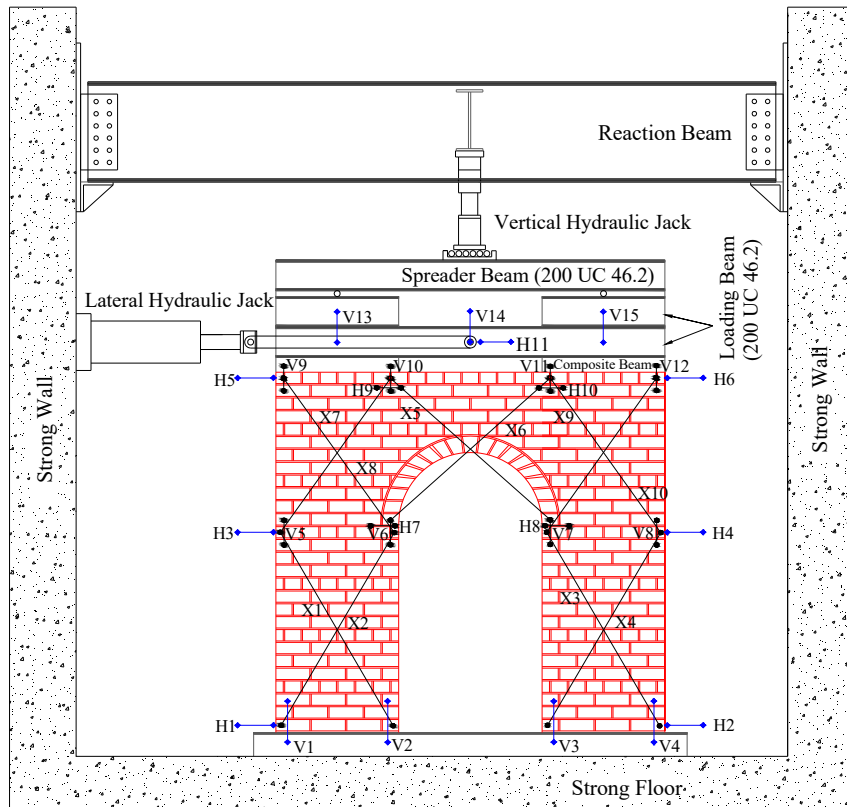


Figure 3: Elevation of the wall test setup and instrumentation (blue denotes absolute and black denotes relative displacement; H, V, X denotes horizontal, vertical and diagonal respectively).

Cyclic lateral displacement will be applied at the mid-length of the loading beam (200 UC 46.2) and due to its shallow depth another extra beam section (200 UC 46.2) will be joined by welding on top of the loading beam. The extra beam sections over the pier length will be located below the spreader beam and between them rollers will be set at the centre line of the pier to uniformly distribute the vertical load from the jack to the top of the pier throughout its length. This loading path will reduce the chance of local failure of the wall due to the applied vertical load. A composite section consisting of 300 PFC with top plate and stiffener will be placed in between the loading beam and the wall along the length of the pier which will allow a gap above the spandrel to allow vertical deformation of the spandrel during testing. The composite beam will be bolted to the loading beam and attached to the top edge of the wall specimens by using epoxy.

Lateral force applied to the URM wall will be measured using a load cell connected to the lateral hydraulic actuator. Linear variable differential transformers (LVDTs) will be added to measure and monitor the displacement at the key locations (Figure 3). Digital Image Correlation (DIC) technique will also be used to investigate the crack patterns and the displacement of the wall. The main controlling and monitoring lateral displacement transducer is H11 in Figure . Lateral displacement will be applied in reversing cycles with increasing amplitude and displacement rate and each cycle of the same amplitude will be repeated three times in the form of sinusoidal waves. In the displacement cycles of the testing program, push cycle will be denoted as negative

and pull direction as positive. The application of the lateral displacement will be terminated when the post-peak lateral load has reduced by 20% of the peak load or extreme damage or instability of the wall has been observed. The cyclic lateral displacement history to be used in the proposed testing program is presented here in Figure 4 and Table 2.

Table 2: Quasi-static cyclic displacement rates

| Displacement (mm), (Drift (%)) | Rate (mm/s) | Displacement (mm) (Drift (%)) | Rate (mm/s) |
|--------------------------------------|----------------|-------------------------------------|----------------|
| 0 (0) | 0.00 | ±7.0 (0.29) | 0.11 |
| ±0.5 (0.02) | 0.01 | ±8.0 (0.33) | 0.13 |
| ±1.0 (0.04) | 0.02 | ±10 (0.42) | 0.16 |
| ±1.5 (0.06) | 0.02 | ±12 (0.50) | 0.19 |
| ±2.0 (0.08) | 0.03 | ±16 (0.67) | 0.26 |
| ±3.0 (0.13) | 0.05 | ±20 (0.83) | 0.32 |
| ±4.0 (0.17) | 0.06 | ±24 (1.00) | 0.38 |
| ±5.0 (0.21) | 0.08 | ±30 (1.25) | 0.48 |
| ±6.0 (0.25) | 0.10 | -- | -- |

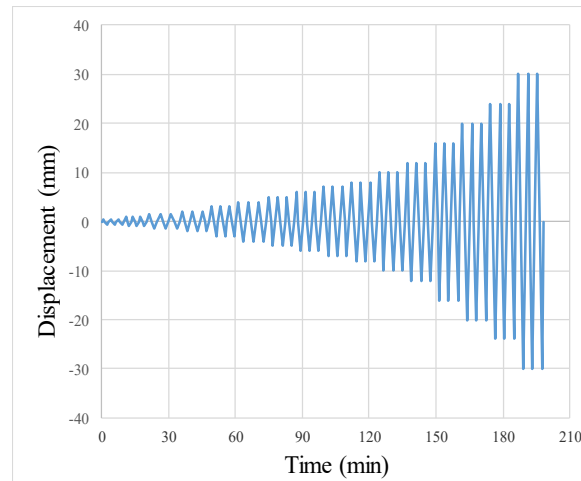


Figure 4: Proposed quasi-static cyclic displacement time history for tests.

NONLINEAR FINITE ELEMENT MODELLING OF THE WALL TESTS

Modelling Strategy

In the current study, the finite element simulation of the wall tests is performed using the commercially available software package DIANA 10.0 (TNO DIANA, 2016). The simplified micro-modelling approach is used to model the masonry wall, where the brick units are modelled using continuum elements and the mortar joints, brick/mortar interface and potential brick cracks are modelled with interface elements. Four noded quadratic (Q8MEM) rectangular isoparametric linear plane stress elements with thickness equal to the wall thickness of 230 mm are used for

modelling the solid brick units. As the mortar joints are modelled by zero thickness interface elements, the brick units are expanded both in height and length to keep the overall geometry of the wall consistent with the real masonry.

The zero thickness interface planes are modelled with the four-noded (L8IF) linear interface element. To model the potential crack planes through the brick, interface elements are used at each quarter length of the brick (Figure 5 (b)). In the previous FE micro-modelling the potential brick cracks were modelled using an interface only at the middle of the brick (Konthesingha, 2012; Allen et al., 2014). However, due to the use of common bond in the walls for the current study, the header courses are placed in every fourth course as shown in Figure 5 (a). To construct the header courses, the vertical joints are offset from the stretcher courses above and below by one quarter brick length, otherwise the vertical mortar joints would align over three adjacent courses, thus reducing integrity of the wall. Hence, considering the resulting masonry assemblage and to match properly with the nodes of the surrounding elements in the finite element model, potential crack surfaces (interface elements) at each quarter length of the brick is appropriate. Although the interface elements are zero thickness elements, for illustrative purposes a fake thickness 5 mm is used in the model (Figure 5(b)).

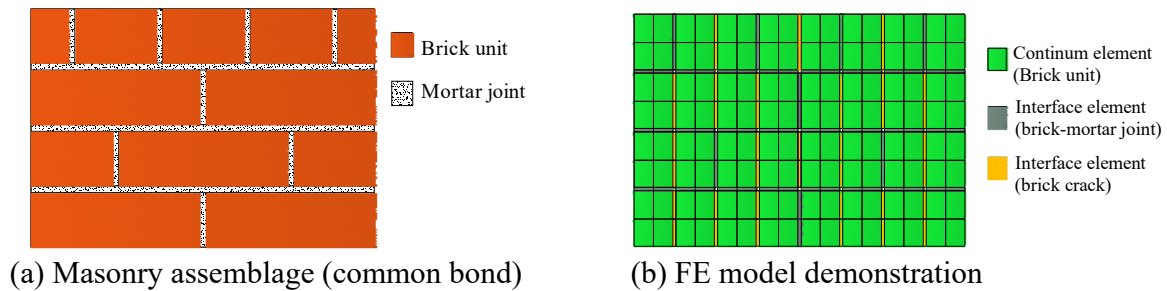


Figure 5: Simplified micro-modelling approach for the masonry wall.

Preliminary FE Results

The modelling was used to help design the experimental program and following the experimental testing phase, the models will be used to help interpret the experimental results and conduct parametric studies. Force-displacement behaviour and failure modes (crack patterns) for the modelled walls are presented in Figure 6 to Figure 8. Finite element modelling was performed for shallow and deep spandrel perforated URM walls with semicircular opening for four different pier axial precompression levels, i.e. 0.2 MPa, 0.5 MPa, 0.7 MPa and 1.0 MPa. In the analysis, the vertical precompression load was first applied at the centre of the loading beam (extra section) through the pier centreline in a single step and then held constant. Horizontal displacement was then applied at the centre of the loading beam with 500 steps by increasing with step size of 0.02 mm up to a maximum of 10 mm deflection. The displacement shown in Figure 6 is the applied displacement at the centre of the loading beam. Force-displacement behaviour of all the cases (Figure 6), showed extensive nonlinearity after the initial linear portion. With the increase of the precompression load both shallow and deep spandrel walls experienced a significantly higher base shear capacity. Also with the increase of the spandrel depth, the base shear capacity increased. Another observation is that at low axial load the walls show more ductile behaviour than at higher axial load.

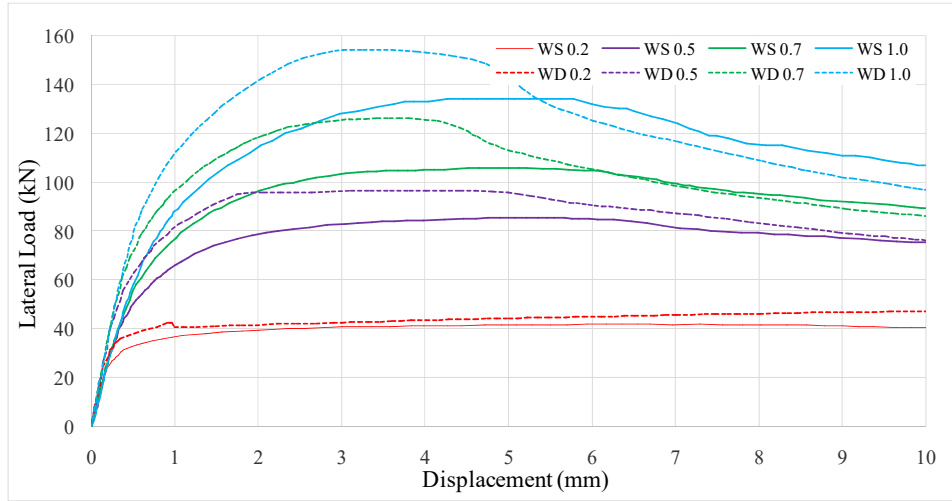


Figure 6: Lateral load-displacement behaviour of URM perforated wall.

For each case, the deformed shape of the wall at the ultimate base shear is presented in Figure 7 & Figure 8. In the case of shallow spandrel with low precompression load, rocking of the pier occurred with no significant damage of the spandrel. The flat plateau in the load-displacement behaviour after reaching the maximum load in the case of shallow spandrel is also consistent with the ductile behaviour associated with a stable rocking failure mechanism of the wall (Figure 7(a)). In case of the deep spandrel with low axial stress, the global coupling effect of the spandrel caused tension failure at the bottom of the left pier. The rocking failure was confined to the tension pier shown in Figure 8 (a), with no damage to the remaining part of the wall which formed a T shape together with the right pier and spandrel.

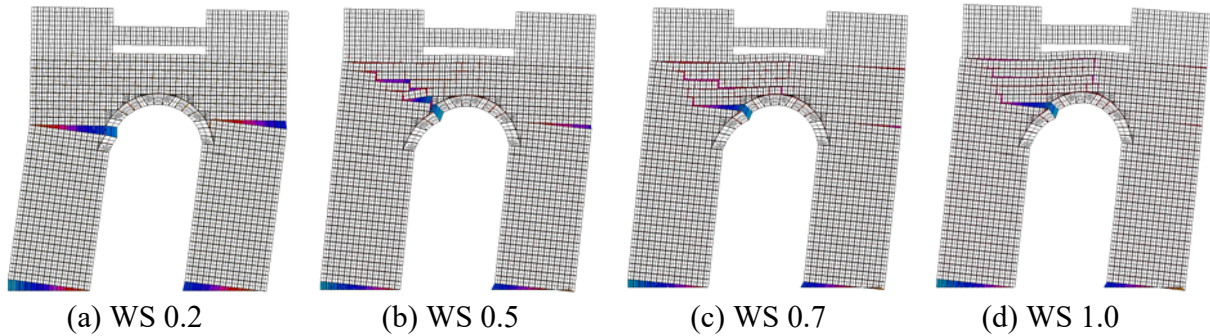


Figure 7: Crack pattern of shallow spandrel wall for different precompression levels.

The crack pattern in Figure 7 (b), shows that with the increase of the vertical precompression (0.5 MPa) for shallow spandrel, the failure pattern is no longer confined to pier rocking but also includes flexural failure of the spandrel. With further increases of the vertical axial load (0.7 MPa and 1.0 MPa) both flexural and shear cracking occurred in the spandrel. Stair stepped cracking also occurred in the joint region at the top of the tension pier which started nearly one third the height of the arch curve below the apex. Similar failure patterns are shown for the deep spandrel with a difference that flexural cracking in the spandrel started at precompression of 0.7 MPa. For

the highest precompression (1.0 MPa) in the deep spandrel wall, the spandrel also experienced stair stepped shear crack (Figure 8 (d)). These observations are consistent with reported earthquake damage which shows increased spandrel damage in the lower stories of multi-storey buildings (Knox et al., 2016).

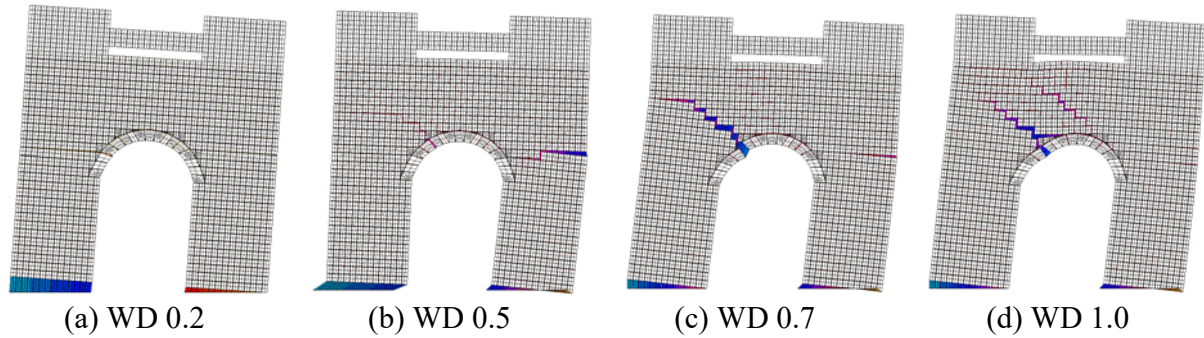


Figure 8: Crack pattern of deep spandrel wall for different precompression levels.

Finally, the wall base shear capacity obtained from the finite element analysis (FEA) was compared to capacity predictions made using the simplified pier capacity equations according to NZSEE (NZSEE, 2006) for each wall type assuming fixed-fixed pier boundary conditions (strong spandrel assumption). The FEA predicted capacities are presented with the values obtained from NZSEE (2006) in Table 3.

Table 3: Comparison of FEA predicted base shear result with NZSEE 2006.

| WALL | FEA (kN) | NZSEE (kN) | | |
|--------|----------|-----------------------|-------------|--------------|
| | | Different Pier Height | | |
| | | ST | TP | C8:URM |
| WS 0.2 | 41.7 | 46.6 (+12%) | 34.4 (-17%) | 37.7(-9%) |
| WS 0.5 | 85.5 | 108.8 (+26%) | 80.5 (-6%) | 88.1(+3%) |
| WS 0.7 | 106 | 147 (+38%) | 108 (+2%) | 119 (+12%) |
| WS 1.0 | 136 | 199 (46%) | 147 (+8%) | 161(+18%) |
| WD 0.2 | 47.0 | 62.1 (+32%) | 42.3 (-10%) | 47.3 (+0.6%) |
| WD 0.5 | 96.5 | 141.5 (+46%) | 98.7 (+2%) | 110.5 (+14%) |
| WD 0.7 | 126 | 176 (+39%) | 133 (+5%) | 149 (18%) |
| WD 1.0 | 154 | 229 (+43%) | 181 (+17%) | 202 (31%) |

In Table 3, the NZSEE values shown were calculated using different pier height assumptions as follows: straight portion (ST) of the pier, until the top of the opening (TP) and according to the Part C-Detailed Seismic Assessment, C8: Unreinforced Masonry Buildings (C8:URM) guidelines (NZSEE, 2017). According to C8:URM guidelines (NZSEE, 2017), for deep arched spandrels, equivalent rectangular spandrels are to be considered by extending the depth to one third of the depth of the arch below the arch apex. Hence the pier height is taken by extending the straight portion of the pier to two thirds of the arch depth. The percentage difference of the results obtained from the NZSEE equation compared to the FEA predicted shear capacities are presented in Table 3 in between parentheses.

It is shown that the FEA result agrees well with the NZSEE equations for the pier height according to C8:URM for the low precompression load but with the increase of the precompression load (greater than 0.5 MPa) pier height taken up to the top of the opening (TP) shows the best match with FEA. This observation is consistent with the modelled failure modes which seem to show that the cracking at the tops of the piers extends from a higher starting point on the piers as the precompression is increased. In the NZSEE equations, the capacity and failure mode was considered only for piers, hence this difference can be accepted as in FEA spandrel effects are also accounted for. In almost all of the cases, the pier rocking wall failure mode governed based on NZSEE guidelines which matches well with the FEA predicted pier failure. The FEA result is considered more realistic as damage observations from past earthquakes show that spandrel failure is not uncommon and hence the possibility for this failure mode must be represented in behaviour prediction models. Another observation which can be made is that as the precompression is increased the spandrel is more damaged and hence less able to provide coupling to the piers. This in turn means that the strong spandrel assumption starts to break down and perhaps the weak spandrel assumption in NZSEE may start to become more appropriate.

CONCLUSIONS

This paper presents the design of an experimental program for the cyclic in-plane testing of URM perforated walls including preliminary FE modelling and analysis for the walls. The key findings are below:

- The lime rich cement-lime mortar with mix proportions by volume of 1:2:9 (cement : lime : sand) is suitable to construct the wall considering its mechanical behaviour for the proposed experimental program.
- Load displacement behaviour varies with the change of spandrel depth and level of vertical precompression on the wall. The lateral load capacity of the wall increases with the increase of the precompression level and the spandrel depth. Another finding is that at low levels of precompression, the wall shows more ductile nature than at higher precompression load.
- At low precompression level, the crack pattern is confined to the piers and with the increase of the load, it extends to the spandrel with shear and flexural cracking.
- Spandrel crack initiates at lower axial load level for shallow spandrel depth than the deeper one.

ACKNOWLEDGEMENTS

The authors gratefully acknowledge the financial support provided by the Australian Research Council via Discovery Project DP160102070.

REFERENCES

Allen, C., Masia, M. J., & Page, A. W. (2014). Cyclic in-plane shear behaviour of unreinforced masonry walls with openings: Design of experimental testing programme. *9th International Masonry Conference*, Guimarães, Portugal.

Allen, C., Masia, M. J., & Page, A. W. (2016). Experimental Testing of Unreinforced Masonry Walls with Openings Subjected to Cyclic In-plane Shear. *16th International Brick & Block Masonry Conference (IBMAC)*, Padova, Italy.

ASTM (2011). Standard test method for compressive strength of hydraulic cement mortars (using 2-in or 50-mm cube specimens). *ASTM C109/C 109M-11*. ASTM International, West Conshohocken, PA.

Augenti, N., Parisi, F., Prota, A., & Manfredi, G. (2011). In-plane lateral response of a full-scale masonry subassembly with and without an inorganic matrix-grid strengthening system. *Journal of Composites for Construction*, 15(4), 578-590.

Bothara, J. K., Dhakal, R. P., & Mander, J. B. (2010). Seismic performance of an unreinforced masonry building: an experimental investigation. *Earthquake Engineering & Structural Dynamics*, 39(1), 45-68.

Griffith, M., Moon, L., Ingham, J. & Derakhsham, H. (2013). Implications of the Canterbury earthquake sequence for Adelaide, South Australia. *12th Canadian Masonry Symposium*, Vancouver, British Columbia.

Howlader, M., Masia, M., Griffith, M., Ingham, J., & Jordan, B. (2016). Characterisation of heritage masonry construction in NSW - State Heritage Register. *Australian Earthquake Engineering Society conference*, Melbourne, Australia.

Knox, C. L. (2012). Assessment of perforated unreinforced masonry walls responding in-plane. (*PhD Thesis*), Department of Civil and Environmental Engineering, The University of Auckland, New Zealand.

Knox, C. L., Dizhur, D., & Ingham, J. M. (2016). Experimental Cyclic Testing of URM Pier-Spandrel Substructures. *Journal of Structural Engineering*(04016177).

Konthesingha, C. (2012). Earthquake protection of masonry shear walls using Fibre Reinforced Polymer strengthening (*PhD Thesis*), School of Engineering, The University of Newcastle, Australia.

Lucas, C. (1982). *Conservation and restoration of buildings-preservation of masonry walls*. Australian Council of National Trust, Australia.

Lumantarna, R. (2012). Material characterisation of New Zealand's clay brick unreinforced masonry buildings. (*PhD Thesis*), Department of Civil and Environmental Engineering, The University of Auckland, New Zealand.

Magenes, G., & Calvi, G. M. (1997). In-plane seismic response of brick masonry walls. *Earthquake Engineering & Structural Dynamics*, 26(11), 1091-1112.

Nateghi, F. A., & Alemi, F. (2008). Experimental study of seismic behaviour of typical Iranian URM brick walls. *14th World Conference on Earthquake Engineering*, Beijing, China.

NZSEE (2006). Assessment and Improvement of the Structural Performance of Buildings in Earthquake -Prioritisation, Initial Evaluation, Detailed Assessment, Improvement Measures: Recommendations of a NZSEE Study Group on Earthquake Risk Buildings, New Zealand.

NZSEE (2017). The Seismic Assessment of Existing Buildings, Technical Guidelines for Engineering Assessments. *Section C8 – Seismic Assessment of Unreinforced Masonry Buildings*: New Zealand Society for Earthquake Engineering, New Zealand.

Russell, A. (2010). Characterisation and seismic assessment of unreinforced masonry buildings. (*PhD Thesis*), Department of Civil and Environmental Engineering, The University of Auckland, New Zealand.

Standard Australia (2011). Masonry structures. *AS-3700*: Standards Australia Limited, Australia.

TNO DIANA. (2016). DIANA Finite Element Analysis User's Manual Release 10.0, Delft, The Netherlands.

Tomažević, M. (1999). Earthquake resistant design of masonry buildings (Vol. 1), Imperial College Press, London. 1-86094-066-8.

Triller, P., Tomažević, M., & Gams, M. (2016). Seismic behaviour of multistorey plain masonry shear walls with openings: An experimental study. *16th International Brick and Block Masonry Conference*, Padova, Italy.

Vanin, A., & Foraboschi, P. (2012). In-plane behavior of perforated brick masonry walls. *Materials and Structures*, 45(7), 1019-1034.

Yi, T., Moon, F. L., Leon, R. T., & Kahn, L. F. (2006). Lateral load tests on a two-story unreinforced masonry building. *Journal of Structural Engineering*, 132(5), 643-652.

MASONRY CLADDING DESIGN CONCEPTS FOR ENHANCED PERFORMANCE DURING EARTHQUAKES

S. Dill¹ and J. Hochwalt²

¹ Structural Engineer, KPFF Consulting Engineers, 1601 5th Avenue Seattle WA, USA steve.dill@kpff.com

² Structural Engineer, KPFF Consulting Engineers, 1601 5th Avenue Seattle WA, USA john.hochwalt@kpff.com

When the owner and his/her architect decide that a building should be clad in brick, their aesthetic and functional objectives are frequently in conflict with seismic performance requirements. In conventional brick veneer construction, building corners, windows and other architectural features penetrating the veneer cannot accommodate the building design displacements, often as much as 2% of the story height, without sustaining significant damage.

Over the years, designers in the western United States have developed a variety strategies aimed at improving the seismic performance of masonry veneer. Some of those strategies include:

- Corner-panels that are detailed and connected to the backup structure in such a way they can accommodate building seismic deformation through warping action. A recent test program utilizing a full-size corner was conducted to verify the concept.
- Reinforced veneers have been utilized to create adequate panel strength to utilize strong, widely-spaced connections that enable more effective seismic isolation.
- Rocking veneer systems have been developed to accommodate building drifts using hinging planes built into the masonry that can accommodate limited rotations without damage utilizing neoprene bearing pads and unbonded dowels.

The paper will present essential concepts and design considerations drawn from constructed projects utilizing these approaches.

Keywords: *Masonry, reinforced, seismic, drift design*

INTRODUCTION

Designing masonry cladding systems for use in areas of high seismicity in combination with modern, frequently flexible, building systems, creates unique design challenges. In many parts of the world, the codes that govern the design and construction of masonry cladding systems either do not address the deformation compatibility of masonry, or address it in a very general fashion. As a result, these systems are typically constructed using industry standard details which are presumed to provide sufficient accommodation of building movements to ensure the safety of the occupants in the event of a code-level earthquake. For many buildings (and building owners) this approach is not adequate. Higher levels of cladding performance may be desirable for buildings that need to be operational following a natural disaster – hospitals, fire stations, etc. Special attention may be advisable for facilities used for public assembly where cladding failure could pose special risks to the public – schools, sports stadiums, etc. Moreover, an owner may decide that, for whatever reason, they want their building to achieve a more predictable, higher, level of performance than afforded by minimum compliance with a life-safety standard.

This paper was written to provide some insights to designers contemplating a more rigorous approach to masonry cladding design. The paper draws from the authors' years of experience in the design of brick cladding constructed for new buildings in the Western United States. It is based on the design of the anchored veneer and reinforced veneer systems that are common in that region. The information contained herein may not be applicable to the design of other masonry systems or in other parts of the world.

A description of the anchored brick veneer system as referenced in this paper may be found in Tawresey (2004) and a description of the reinforced brick veneer system may be found in Tawresey and Hochwalt (2011).

Generally, the structural design of cladding systems can be characterized as the process of identifying an arrangement of cladding components, and the connection of those components to the building, in such a way that the cladding both resists environmental loading and satisfactorily accommodates the building movements associated with earthquakes and other loads - without unacceptable compromise to the building envelope, aesthetics, constructability, or budget. This paper is structured around a four-step design process. The steps are loosely presented in the order in which a design might normally progress, but as in all design, circumstances may require that the designer revisit their preliminary assumptions and decisions as the building design develops (and changes!). The four steps of design that are the subject of this paper are: (1) Establish the performance criteria for the cladding (2) Consider alternate cladding systems and feasible configurations of those systems that might satisfy the performance criteria (3) Examine the actions of the cladding components associated with the candidate system(s) to confirm that they meet the performance criteria and (4) Design the cladding components and connections. The balance of this paper will expand on each of these four design steps.

PERFORMANCE CRITERIA

The first step in cladding design is establishing the performance expectations for the system. Minimally, cladding components must meet the requirements of any governing standards, which are generally aimed at maintaining life safety when the structure is subjected to the

effects of a rarely occurring earthquake. Beyond those minimum requirements, additional levels of performance may be established through jurisdictional requirements for specific building occupancies or simply by owner preference. These additional levels of performance may define a higher level of performance for the rarely occurring earthquake, or define performance expectations for more frequently occurring wind or seismic events. Of particular interest to the cladding designer are the design drifts (lateral building displacements) associated with the wind or seismic event under consideration.

One standard that defines performance levels for masonry structural systems and cladding is ASCE 41 (2013). While this standard is focused on the evaluation and retrofit of existing buildings, its descriptions of the performance of non-structural systems provides a useful framework for developing project specific design criteria. Combining the ASCE 41 performance levels for cladding and for masonry partitions suggests three categories of performance as Indicated in Table 1, below.

Table 1: Performance Categories for Cladding; Adapted from ASCE 41

| Performance Categories | Description of Condition |
|-------------------------------|---|
| Life Safety | Extensive distortion in connections and damage to cladding components may occur, including major cracking, crushing, localized dislodging, loss of weather-tightness and security. Overhead panels do not fall. |
| Position Retention | Cladding is damaged, but cladding remains in position. Damage may include yielding of connections, minor cracking at openings, minor cracking and crushing at corners, and minor dislodging, but no wall failure. Loss of weather-tightness is limited. |
| Operational | No loss of function or weather-tightness occurs. Damage is limited to yielding of connections, minor cracking at openings, minor cracking and crushing at corners. |

Review of this table brings to light two points regarding cladding performance in earthquakes. The first is that performance expectations for cladding systems at a Life-Safety performance level are quite low. It has been our experience that these low levels of performance surprise many building owners – they are not aware that their building’s cladding system may need extensive repair or replacement after a code-level earthquake. The second is that the more rigorous performance levels indicated, when combined with high seismic loading, are likely not achievable without careful, detailed design.

SYSTEMS AND CONFIGURATIONS

The broad types of the cladding systems used for a project (i.e. anchored veneer vs reinforced veneer, conventional window systems vs curtain walls, etc.) are usually selected early in the design, but may be changed later in the process for cost or performance reasons. The conundrum for the cladding designer is that the various cladding components are different – different system thicknesses, different connections to the building structure, different

interactions with air and water barriers, different costs, and different capacities to accommodate seismic forces and drift. For these reasons, the final selection of the cladding system components and the detailed design of those components are frequently performed late in the design process, or may be deferred until after building construction has begun. Unfortunately, delaying cladding design until very late in the design/construction process can so constrain the design, that higher levels of performance may be difficult to achieve.

The configuration of the cladding system should be thought of as the specific arrangement of the cladding components and their associated joints and is fundamental to the performance of the system. In many respects, cladding design consists of identifying configuration options, then examining the actions required for that configuration to accommodate design displacements, while meeting the prescribed performance requirements. In that light, identifying candidate cladding configurations that can accommodate the functional and aesthetic intent of the building is the first step in cladding design.

A few typical cladding configurations are shown in Figure 1, below.

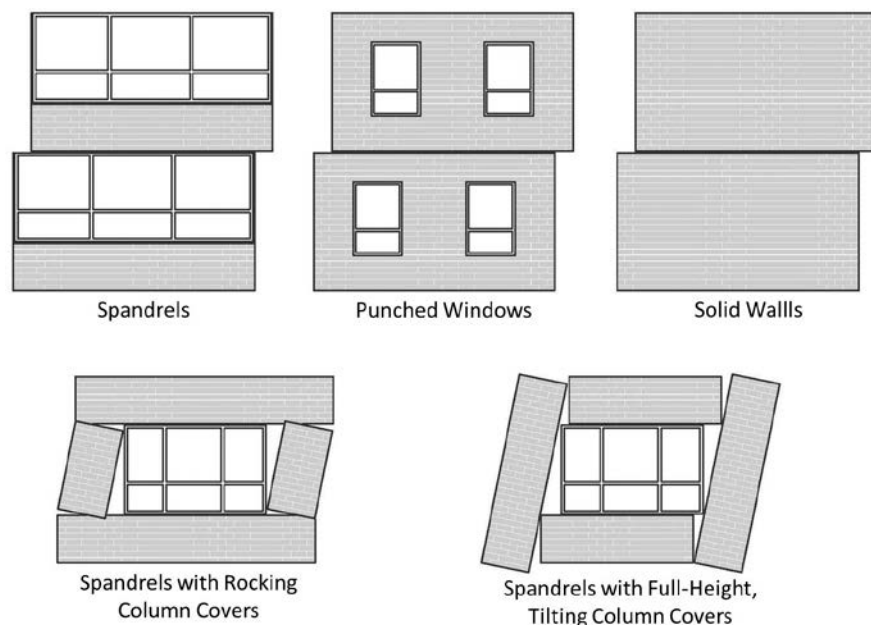


Figure 1: Typical Cladding Configurations

COMPONENT ACTIONS

The actions by which masonry cladding components can accommodate building movements are contingent upon the direction of movement relative to the plane of the cladding, as the behaviour of the masonry is significantly different in the in-plane and out-of-plane directions.

Masonry cladding in the in-plane direction typically has much less flexibility than the supporting structure; when accommodating building displacements, the masonry should be thought of as acting as a rigid element. The in-plane strength of the cladding to resist inertial forces due to its self-weight is not typically a critical parameter for design, but may need to be checked for unusual configurations.

Masonry cladding in the out-of-plane direction is often flexible enough that it can accommodate movements of the supporting structure without special detailing. The resistance of the out-of-plane inertia forces is typically a critical parameter for design; in anchored veneers the back-up wall is designed to provide out-of-plane support whereas reinforced veneers are designed so that the masonry has sufficient strength to span between points of attachment to the supporting structure.

Depending on their type and configuration, cladding components can accommodate building movements through a variety of actions. Some of those are described below.

Sliding Action

Sliding action involves one cladding component freely translating relative to an adjacent component in a properly designed joint to allow structural movements to occur without transmitting loads to the cladding. In Figure 2 below, two masonry components are isolated through sliding. Notice that the highlighted areas are detailed in such a way that the floor and panel above can freely translate along the length of the panel, without transmitting forces to the panel below. The exterior caulk joint would be destroyed by sliding action at modest levels of lateral displacement; that would, however, be considered acceptable for all but the most stringent performance levels.

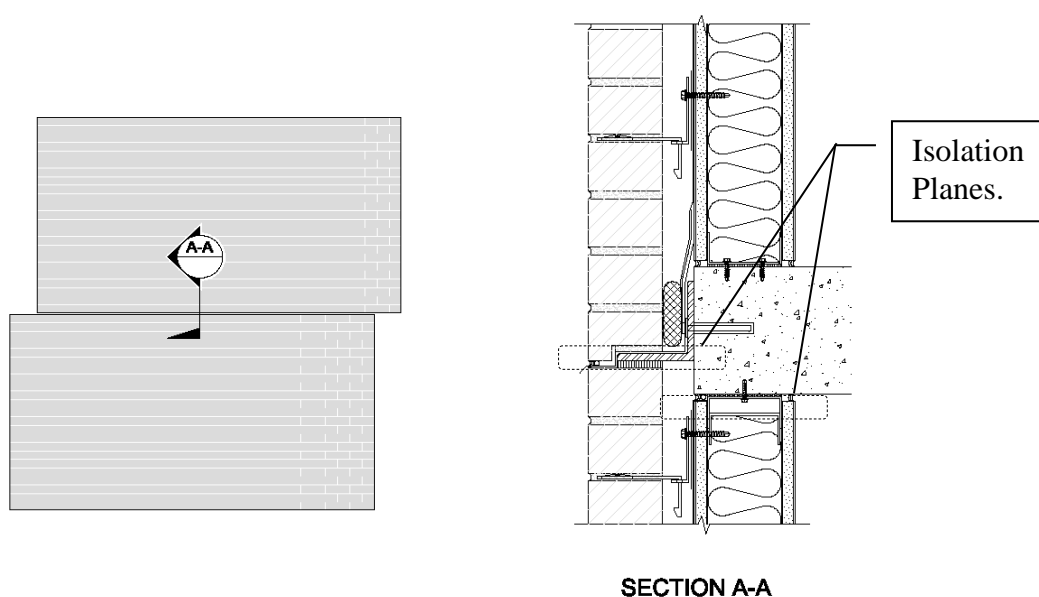


Figure 2: Sliding Joint; Anchored Veneer at Floor

In Figure 3 below, a Teflon bearing pad between polished, stainless steel plates is utilized to provide sliding action at the joint while transmitting vertical loading. In this way, the entire dead-load of the brick system can be transmitted to the ground, eliminating the need for intermediate dead-load connectors.

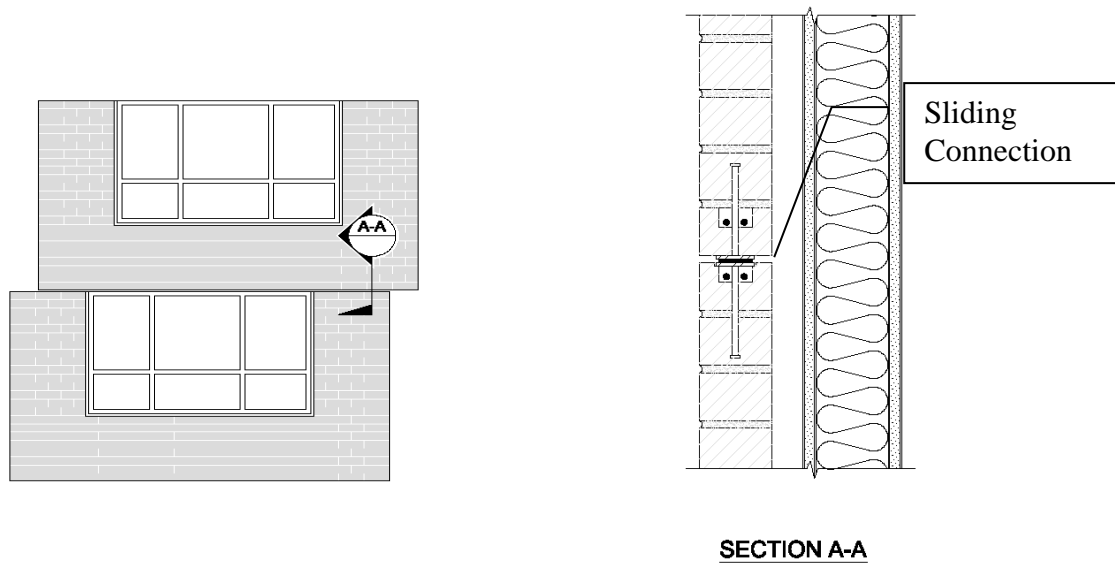


Figure 3: Sliding Joint; Reinforced Veneer at Sliding Joint

Tilting (or Rocking) Action

Tilting action involves constructing the cladding system in such a way that one cladding component can rotate relative to an adjacent component. This action allows the cladding to accommodate structural movement by rocking as a rigid body and is commonly used to accommodate out-of-plane deflections as shown in Figure 4. While the steel stud track anchorage, in the highlighted region of the detail, was not explicitly designed as a hinge, it is evident that small rotations can occur there with negligible damage to the cladding system.

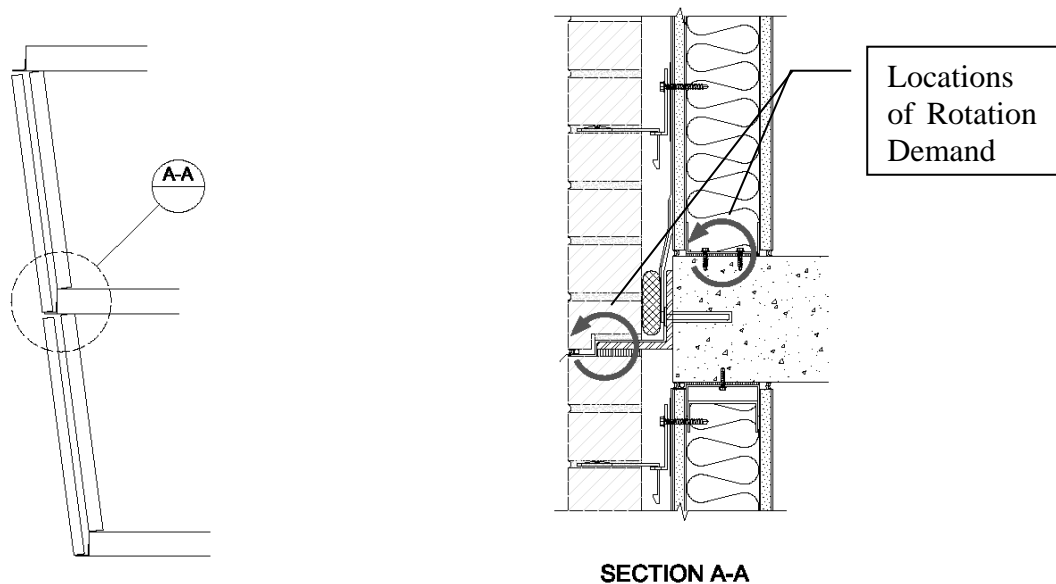


Figure 4: Tilting Action; Anchored Veneer at Floor

Alternatively, in Figure 5, tilting action (panel rotation) is utilized in-plane to accommodate building drifts in a reinforced veneer system through the introduction of neoprene bearing pads with unbonded bars used to keep the rocking joints aligned in-plane and to react the shear loads that are required to “trip” the panel rotation.

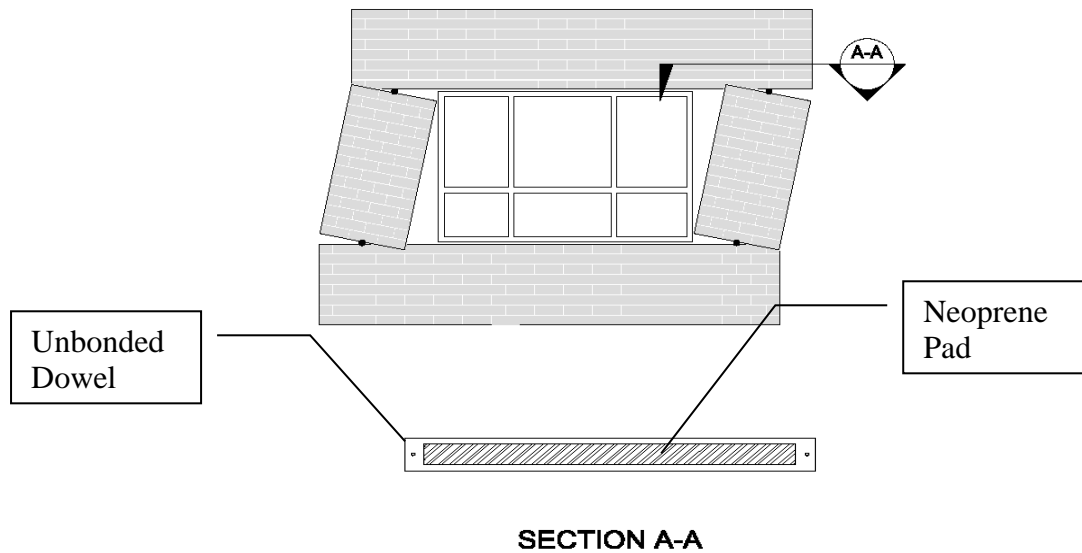


Figure 5: Rocking Action; Reinforced Veneer

Warping Action

Warping action involves a cladding component undergoing an out-of-plane curvature, generally induced by the relative displacement of an anchor point. Figure 6 below illustrates a cladding configuration utilizing warping corners. Warping is an action that generates internal stresses in the cladding materials and connection reactions based on the material properties of the cladding elements. In masonry materials, those properties vary significantly in pre-cracking vs. post-cracking conditions. For purposes of establishing design loads for component connections and for estimating the drift limits associated with cracking, the designer must develop estimates of panel stiffness before and after cracking, as well as, the warping limit associated with corner cracking. Research conducted by Tawresey and Twitchell (2009) tested corner warping of an anchored veneer. For the specific masonry materials and corner geometry tested, they noted a range of uncracked elastic behaviour at low levels of warping, followed by an extended range of warping capacity after cracking the panel to a condition requiring “only minor repair.”

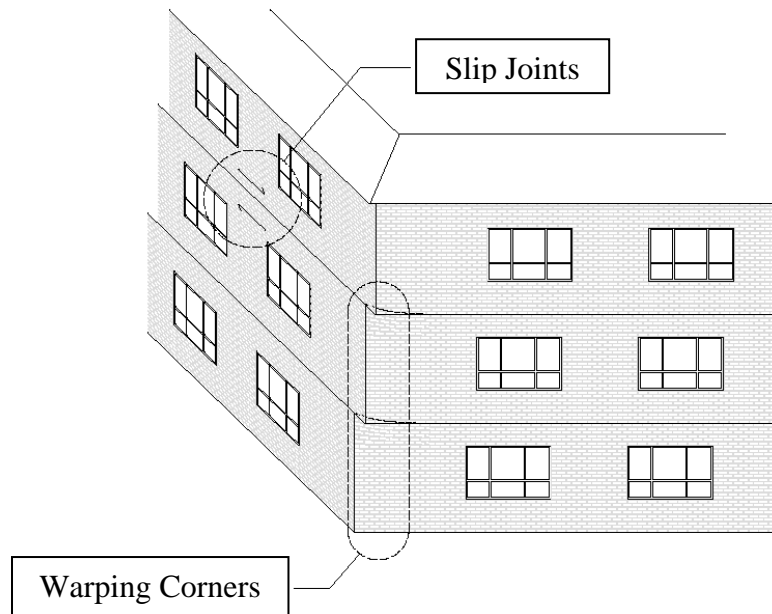


Figure 6: Anchored Veneer with sliding joints and warping corners

This action highlights the benefit of thinking about the required performance level of the cladding. Allowing some damage may result in a safer and more cost-effective design. It also may result in better performance than the conventional solution of placing a vertical control joint at the corner, as the incompatibility in movements of the cladding at the joint can result in pounding and the dislodging of masonry units.

Racking Action

Racking action is an in-plane shearing-deformation that can occur in cladding components as the result of story-drift. Masonry materials are typically too stiff and brittle to accommodate any significant building deformation in racking action. Window systems, on the other hand, are frequently detailed with clearance between the frame and the glass. The highlighted region in Figure 7 below shows free space within which the glazing can slip in the window seals until the glass impacts the aluminium assembly.

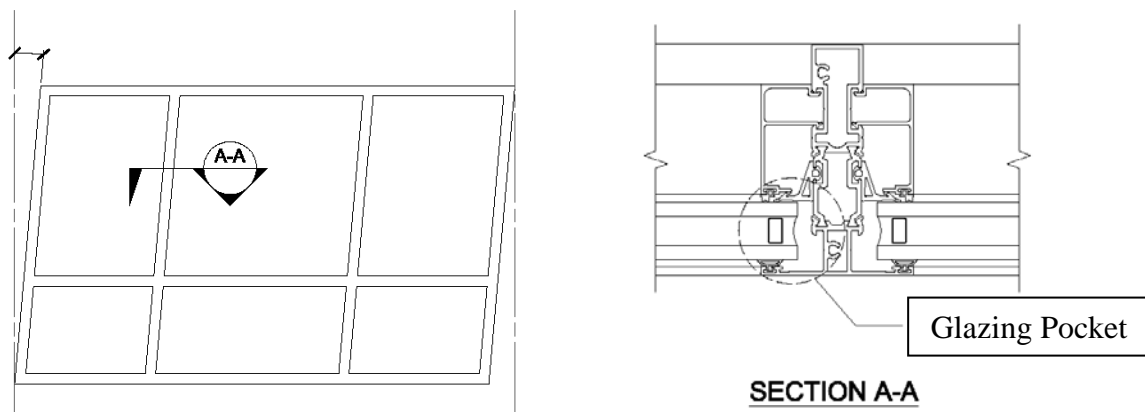


Figure 7: Racking Window System

The experienced designer will learn to identify problem areas in proposed configurations early in design and direct the cladding configuration toward workable solutions. In many cases, those problem areas may require a modification to the performance criteria and/or some compromise in the proposed cladding configuration. Common problem areas would include:

- Vertical misalignment of horizontal joints. Sliding horizontal joints generally connect continuously around the structure. Interruptions in this pattern are a source of problems.
- Corner conditions. Corners are the most damage prone locations in the building because they are the components of the cladding that are required to be compliant with both the in-plane and out-of-plane actions of the cladding system.
- Complex configurations. It can be very difficult, if not impossible, to definitively describe the resulting actions of very complex cladding configurations. When that situation exists, particularly on flexible buildings, it may not be possible (or wise) to indicate compliance with specific performance standards.
- Inadequate extent of isolation. It is not unusual that a cladding configuration can accommodate some seismic-induced motions, but have inadequate displacement capacity to meet the full required displacement demands of the performance criteria.

DETAILED DESIGN

Detailed design can begin once a workable configuration of cladding has been determined and the actions associated with the components of that configuration have been examined for compatibility with the accepted performance criteria the system. Detailed design includes designing the structural elements and connections associated with the cladding system. It also may include a review of the details associated with the air and water barriers to confirm that they are compatible with the performance expectations for the building.

SUMMARY

Many of the cladding systems and components used in new construction today are assembled with industry-standard details and little deliberate design. Not surprisingly, these cladding systems have often been significantly damaged in earthquakes. Better outcomes can be achieved with a better process.

REFERENCES

American Society of Civil Engineers (2013), *Seismic Evaluation and Retrofit of Existing Buildings*, ASCE/SEI 41-13, 2013.

Dill, S., (2006), Masonry Rocks, *Structure Magazine*, May, 2006, pp. 10-12

Tawresey, J. (2004). Design Guide for Anchored Brick Veneer Over Steel Studs, Western States Clay Products Association, 2004.

Tawresey, J., and Hochwalt, J. (2011). Design Guide for Structural Brick Veneer, Western States Clay Products Association, 2011.

Tawresey, J., and Twitchell, K. (2009). Warping of Brick Cladding Corners. *Structure Magazine*, January, 2009, pp. 20-21.



**MASONRY TODAY
AND TOMORROW**

**11 - 14 February, 2018
SYDNEY AUSTRALIA**

www.10amc.com

SHELF ANGLE DESIGN FOR ANCHORED MASONRY VENEER

W. Mark McGinley¹

¹ Professor, Department of Civil and Environmental Engineering, University of Louisville, Louisville KY, 40292, USA, m.mcginley@louisville.edu.

Anchored masonry veneer wall systems are commonly used in North America for residential, commercial and institutional construction. These exterior masonry veneers are nonload-bearing and are usually assumed to be little more than an exterior finish of the building envelope. Based on the US Building Codes, masonry veneer can be supported vertically by foundations for heights less than 30 feet, or supported by the building frame for taller structures. However, the increasing demands for higher amounts of insulation that have been the trend in energy code requirements, make designing shelf angle supports a challenge.

The purpose of this paper is to discuss the behaviour of these veneer support systems under typical loadings, and suggest a simple design methodology that may be applied under the current US building code provisions.

Keywords: *Masonry, veneer, support, shelf angle, design.*

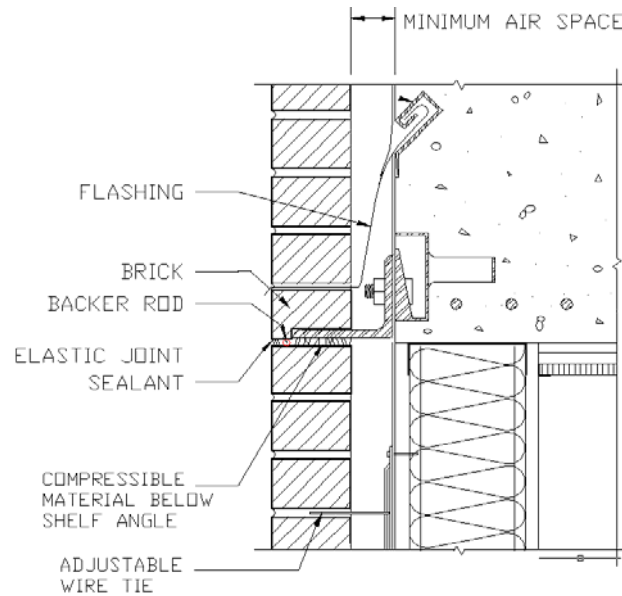
INTRODUCTION

Anchored masonry veneer wall systems are commonly used in North America in residential, commercial and institutional construction. Use of masonry veneers is also increasing in other parts of the world. In these systems, the exterior masonry veneers are non-load-bearing and are usually assumed to be little more than an exterior finish of the building envelope. Prescriptive design methods require that masonry veneer be supported vertically by foundations, for heights less than 9.14 m (30 feet), or supported by the building frame for taller structures (TMS 402/602 Committee, 2016). The purpose of this paper is to discuss the design of the vertical support of masonry veneers and how this design might be attempted under the current US building code provisions.

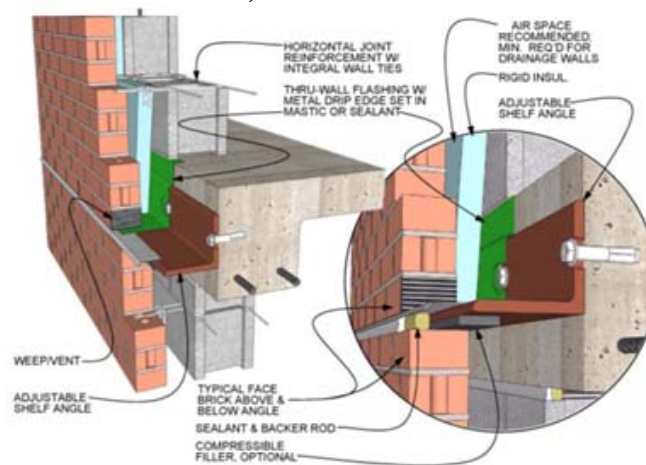
As shown in Figure 1, exterior wall veneer wall systems include an outer wythe (layer) of masonry veneer attached across an airspace to a backing wall by anchors. Typically these backing wall systems can include sheathed wood, or steel stud walls, or concrete masonry walls. Masonry veneers can also be attached to poured concrete walls. The veneer wythe is most commonly constructed



using units of clay or concrete masonry, bound together by mortar. These veneer masonry units vary from a nominal 67 mm to 102 mm (2-5/8 to 4 inches) in thickness.



a) Stud Backed



b) Concrete Masonry Wall Backed From (www.imi.org)

Figure 1: Anchored Masonry Veneer Wall Systems

For the design of masonry veneer systems, model building codes in the United States reference Chapter 12 of the Masonry Standards Joint Committees' *Building Code Requirements for Masonry Structures*, TMS402/602 -16 (TMS 402/602 Committee, 2016). The provisions in this standard describe two methods for veneer design, although the prescriptive method is used almost exclusively in North America. In these prescriptive design requirements, veneers backed by steel or wood stud wall systems, over 9.14 m (30 feet) in height, must be supported at each floor level. Even though not required for other backing systems, most all masonry veneer wall systems are routinely designed to be supported at each floor level to limit differential movement problems.

As shown in Figure 1, this vertical veneer support is typically provided by a steel (shelf) angle that is attached to the building structural system. This connection often uses anchors embedded in the floor slab. The slab edge is then supported by a spandrel beam. In steel structural systems, the shelf angle can also be attached to the spandrel beams directly using shear plates as shown in Figure 2 and the configurations vary widely (Parker, 2008). The beams and supports are designed to resist the applied loads with beam deflections limited to $L/600$ under service level live and dead loads (BIA, 1978).

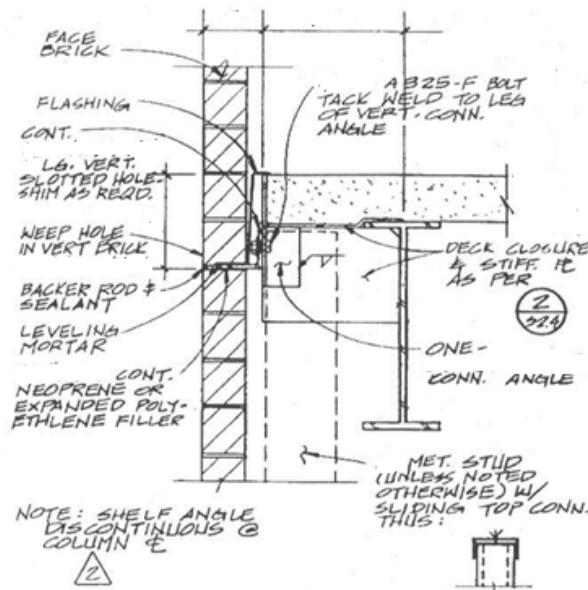


Figure 2: Steel Shear Plate Shelf Angle Support

DESIGN MODELS

The design of the shelf angle support is typically handled as part of the structural engineering design. During this design, a variety of analytical models are used. These models vary from modelling the steel angles as a simple span beam supported at anchor points loaded with a uniformly distributed dead load, to assuming the angle legs act as a bolted frame with an uniformly distributed vertical dead load applied to the end of the horizontal leg (Grimm and Yura, 1989), (BIA, 1987)(Tide and Krogstad, 1989) (see Figure 3).

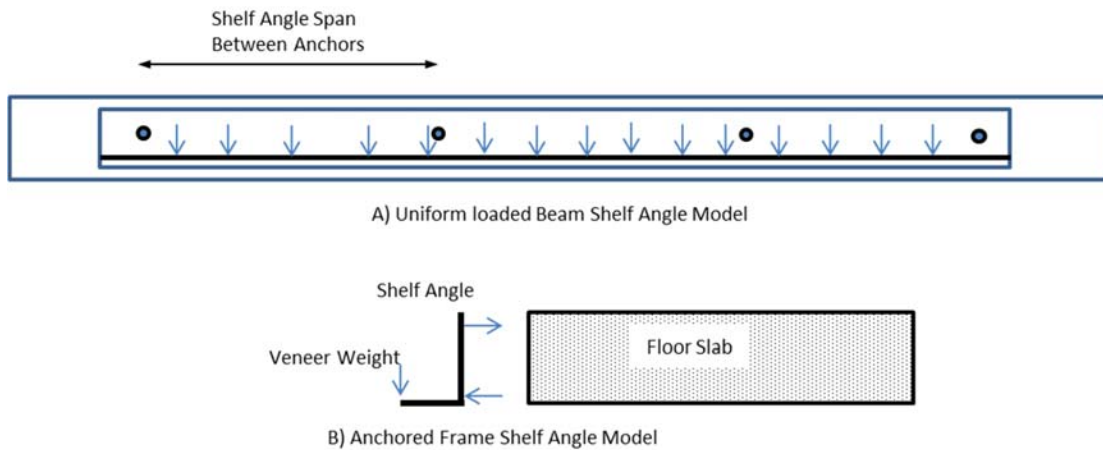


Figure 3: Shelf Angle Design Models.

Unfortunately, none of these models accurately describe how the support angle and veneer behave. The beam model ignores the significant torsion that is applied to the angle. Since angles have low torsional resistance they will rotate away from the slab, forcing greater loading on the angle sections near the anchors and ignoring this behavior may result in undersized shelf angle designs. Even though the frame model is more accurate and generally conservative, it also ignores the interaction of the brick and the shelf angle. In addition, the frame model requires assumptions be made relative to the effective width of the angle and tributary length wall. The thickness of the angle is highly dependent on these two assumptions, and designs often result in high angle thicknesses, especially as designers react to the higher insulation requirements of the new energy codes with longer horizontal leg lengths.

Although not usual, more sophisticated finite element models of the veneer wall system can be developed and, if the deformation of the ties and systems and supports are properly modelled, can be used to accurately predict the behavior of the wall system. Figure 4 shows a typical model of a veneer wall system. The veneer can be modelled using plate elements, the ties modelled as axial elements and the backing wall modelled as beam elements or plates as conditions warrant. These models can also be extended to incorporate models of the spandrel beams as well.

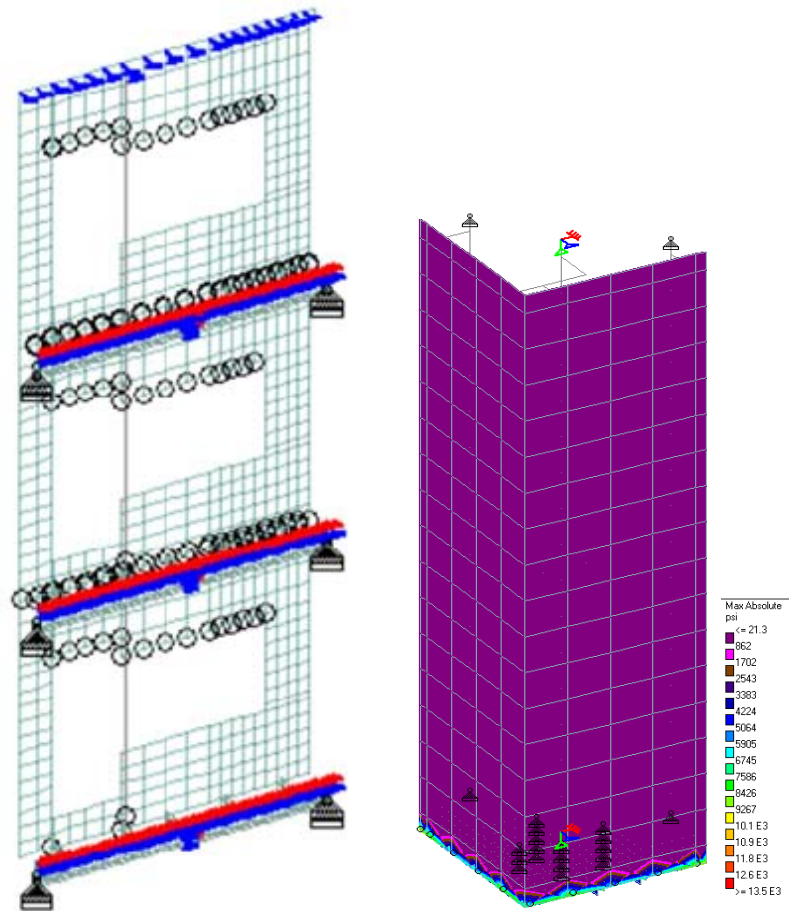


Figure 4: Typical Finite Element Models of Masonry Veneer Systems

Although finite element analyses can provide accurate prediction of the behavior of these systems, this level of analysis effort is not typically justified in most designs. However, the author has conducted a number of finite element analyses on these systems during the course of failure investigations and retrofit studies, and the results of these analyses suggest that the brick veneer under self-weight is not highly stressed (see Figure 4). These analyses also show a pattern of behavior that can be used to design shelf angles using more approximate analysis techniques.

The finite element analyses indicate that the veneer and shelf angle interact, and the veneer is much stiffer than the angle, especially away from the anchor locations. Thus, the shelf angle provides much less support away from the anchors as the angle twists away from the slab edge or shear plate connectors (see Figure 5). Away from the anchors, the veneer is essentially acting as a beam, transferring the veneer dead load to the stiffer angle section near each anchor. Using this behavior as a guide, a reasonable (and conservative) design approach would be to assume that the masonry veneer will act as a beam spanning horizontally in-plane between anchors.

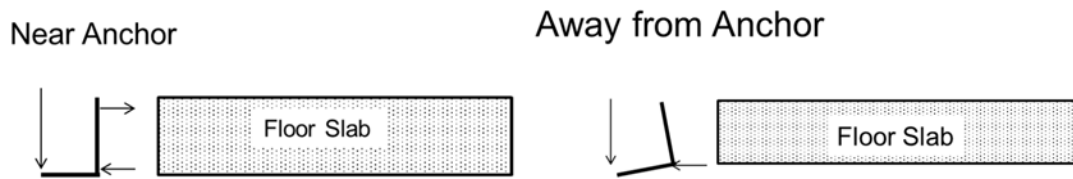


Figure 5 Action of the Steel Shelf Angle at Anchors and Away from Anchors

If it is conservatively assumed that the brick veneer spans between anchor supports as a simply-supported, uniformly-loaded beam, then an appropriate anchor spacing based on veneer flexural strength can be determined. Just how far a given height of veneer can span can be determined by applying the rational design methods described in the MSJC provisions.

To design the veneer as a beam, the allowable stress design procedures described in the masonry applicable design standards can be used (TMS 402/602 Committee, 2016). For example, if it is assumed that the dead load of a nominal 102 mm (4 inch) clay brick veneer produces a maximum vertical uniform load of 1.915 kPa (40 psf) for a unit area of the wall face, then a uniform load (w) of 1.915 (40) x height of brick above the angle must be resisted by the veneer acting as a beam. This load will produce a maximum moment and shear (M_{\max} and V_{\max}) of:

$$M_{\max} = w (L_{\text{span}})^2/8 \quad (1)$$

$$V_{\max} = h (L_{\text{span}})/2 \quad (2)$$

where $w = h \times 1.915$ kPa, h in meters (40 x $h \rightarrow h$ in feet).

If it is assumed that the brick supports itself over the anchor spacing in simple elastic bending, then the critical maximum flexural stress (f_t) produced by the moment (M_{\max}) can be limited to an allowable flexural tensile value (F_t) as shown in Equation 3 (TMS 402/602 Committee, 2016).

$$f_t = M_{\max} / S \leq F_t \quad (3)$$

$$\text{where } S (\text{section modulus}) = bd^2/6, \text{ for a rectangular section } S = t (h)^2/6 \quad (4)$$

The TMS 402/602 design standard for masonry structures (TMS 402/602 Committee, 2016) has no limits for in-plane flexural tensile stress parallel to the bed joint. The flexural tensile stress limits (F_t) that it does present in Table 8.2.4.2 are for out-of-plane loading, and these vary from 138 kPa to 731 kPa (20 to 106 psi) for solid masonry units. Even though the allowable in-plane flexural tensile stresses parallel to the bed joints are likely even higher than these values, the following analysis conservatively uses the lowest allowable out-of-plane strength value of 138 kPa (20 psi) (solid masonry, Type N Masonry Cement Mortar).

Equation (3) can be used to determine the maximum veneer spans (anchor spacing) for various uninterrupted heights of veneer as shown in Table 1. A similar analysis can be conducted with a 34.5kPa (5 psi) limit (1/4 of the previous limit) on the flexural stress and these opening heights are

also shown in Table 1. This lower F_t value is presented to illustrate that even if there is some question about the in-plane strength of the veneer, the veneer can still span a significant distance under its own deadweight, even if the masonry has low strength.

Table 1: Maximum Spans for Brick Supporting its Own Weight

| Height of Veneer, h – meters (ft) | Maximum Opening Span - meters for $F_t = 138 \text{ kPa}$ (20 psi) (ft) | Maximum Opening Span - meters for $F_t = 34.5 \text{ kPa}$ (5 psi) – (ft) |
|--|---|---|
| 0.305 (1.0) | 1.64 (5.39) | 0.82 (2.69) |
| 0.914 (3.0) | 2.84 (9.33) | 1.42 (4.66) |
| 1.524 (5.0) | 3.64 (12.04) | 1.83 (6.02) |
| 3.048 (10.0) | 5.19 (17.03) | 2.60 (8.52) |
| 6.096 (20.0) | 7.34 (24.08) | 3.67 (12.04) |
| 9.144 (30.0) | 8.99 (29.50) | 4.50 (14.75) |

Shear stress is not critical since calculations show brick sections will be able to support its own weight for spans over 15.2 m (50 ft) without exceeding allowable shear stresses (TMS 402/602 Committee, 2016), even for relatively low heights.

It should be noted that the analysis presented in Table 1 was based on simple beam theory. This theory becomes increasingly inaccurate as span to depth ratios drop below 2. For span to depth ratios below this value, the brick starts to act as a deep beam, or for very low values, as an arch. However, in these cases, the tensile stresses in the masonry will be quite small. However, Table 1 clearly indicates that, if there is sufficient height of brick, the brick is able to support its own deadweight, even if very conservative support and strength assumptions are used. Veneer heights of as little as 0.3 m (1 ft.) can support their own weight over a significant anchor spacing. Although the lower heights of brick can easily be supported by the angle, even if the relative stiffness would suggest the brick carries most of the load. Thus, anchor spacing will likely be determined by factors other than the flexural capacity (or arching action) of the veneer, although care must be exercised to account for any movement joints in the veneer to ensure they are not causing a break in veneer continuity and beam or arch analysis of the veneer sections should be undertaken in unusual conditions.

Based on the previous discussion, the veneer will be able to span between steel angle sections near anchors without veneer distress and thus will generally not determine anchor spacing. However, the anchor spacing will affect the loads on the angle anchors and the size of the steel angle. For a given anchor spacing, the angle must be designed to transfer the veneer loads to the structural support. More detailed analyses (McGinley, 2013) suggests that the load on the angle near each anchor is proportional to the tributary length of the veneer. These veneer loads are then transferred through the angle to the structural backing system. The length of the steel angle that resists this veneer loading is difficult to determine. Connection detailing, height of veneer, length of angle legs and angle thickness all will affect how much of the angle resists the veneer reactions. One method to determine the effective length of the steel angle is to assume it is 4 x (the nominal veneer thickness). This methodology comes from the procedures for determining the effective length of masonry wall under concentrated loads in older versions of the masonry standards (McGinley, 2013). More

detailed finite element analyses shows that this is a conservative assumption in most cases and can be used for the steel angle design. Another method for determining this effective steel angle length is suggested by the analysis conducted by Dillion (2017). The results of his analyses suggests that the effective loading of steel shelf angles drops off to near zero at approximately 20% of the anchor spacing away from each angle support (towards mid-span of the angle). This would suggest that the effective length of the angle around each support would be at most 40% of the anchor spacing. A reasonable conservative approximation for the effective steel angle length might be to assume that the effective length is about 25% of the anchor spacing.

Once the veneer loads and the effective length of the angle are determined, it is a simple matter to determine the thickness of the shelf angle using the simple frame model as described in Figure 3. This methodology is illustrated in the following design example.

DESIGN EXAMPLE

To show the application of the proposed steel angle design procedures, a shelf angle supporting a 3.05 m (10 ft.) height of 102 mm (4in.), clay brick veneer will be designed. The anchor spacing for the angle is assumed to be 1.83 m (6 ft.). This spacing would produce a veneer reaction loading of:

$$\text{Veneer Reaction} = 1.915 \text{ kPa} \times 3.05 \times 1.83 \text{ m} = 10.68 \text{ kN} \quad (40 \text{ psf} \times 10' \times 6' = 2400 \text{ lb}). \quad (5)$$

Adding 0.146 kN/m (10 lb/ft) for the angle weight results in $R = 10.94 \text{ kN}$ (2460 lb).

(note that Table 1 indicates that less than 1.0 m (1 ft.) of veneer would have more than sufficient flexural capacity to span the 1.83 m (6 ft.) anchor spacing, even if simple span supports and an allowable stress of 138 kPa (20 psi) was assumed.

To design the steel angle, the effective length of angle resisting this loading must be determined. If 25% of the angle between anchors can be assumed the effective, the angle's effective length would be 458 mm (18 in.)

If a 152 mm x 152 mm (6" x 6") equal legged angle was used to support the veneer, the approximate angle loading shown in Figure 6 can be assumed.

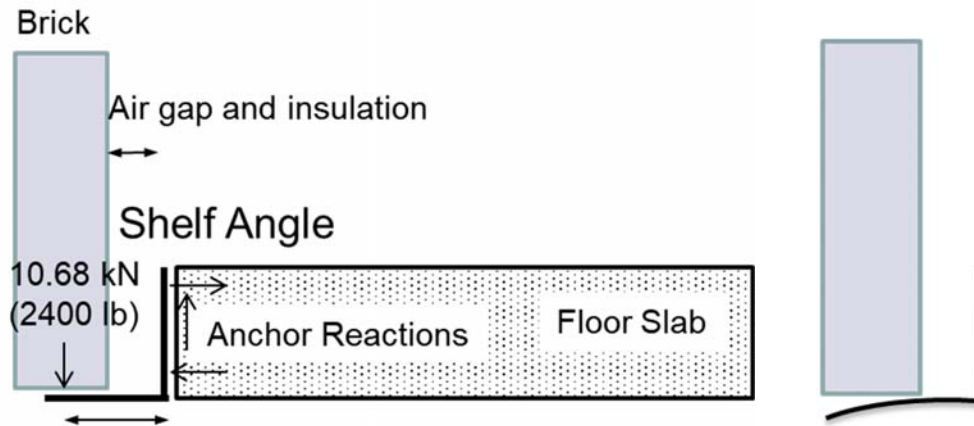


Figure 6: Angle Loading from Veneer and Assumed Angle Deformation

To determine the thickness of angle needed, the veneer weight is often assumed to be applied at the end of the horizontal angle leg. This condition will never happen since the angle will deform, forcing the effective loading point closer to the angle heel (see Figure 6). In most cases, it would be reasonable and conservative to assume that the veneer weight is applied in the center of the veneer. If this assumption is used and it is assumed that a 50 mm (2 in.) cavity is present (with a 13 mm (0.5 in.) angle thickness), then the resulting eccentricity of 0.102 m produces a maximum moment on the lower leg, M_{max} , of:

$$M_{max} = 10.68 \text{ kN} \times 0.102 \text{ m} = 1.089 \text{ kN.m} \quad (4.06 \text{ in.} \times 2400 \text{ lb} = 9,744 \text{ lb. in}) \quad (6)$$

The ASTM International (ASTM) A36/A36M-14 “Standard Specification for Carbon Structural Steel” is commonly used for steel angles. Assuming ASTM A36/A36M steel and using the AISC LRFD (AISC, 2010) design procedures, the section modulus of the steel angle, S_x , required to resist the factored dead load moment would be:

$$S_x = \frac{M_{max \text{ factored}}}{0.9 F_y} = \frac{1.2 (1.089 \text{ kN.m})}{0.9 (248.2 \text{ MPa})} = 5.916 \times 10^{-6} \text{ m}^3 = 5,916 \text{ mm}^3 \left(\frac{1.2 (9,744)}{0.9 (36,000)} = 0.361 \text{ in}^3 \right) \quad (7)$$

Since $S_x = bt^2/6$ and the effective length of the angle is 458 mm (18 in.), a minimum thickness of angle should be:

$$5,916 \text{ mm}^3 = 458 \times t^2/6 \quad \text{goes to } t = 8.80 \text{ mm} (0.347 \text{ in.}) \quad (8)$$

A 9.3 mm (3/8 in.) thick, A36 steel angle would work to support this load. Note that the eccentricity used in the above calculation has a significant impact on the thickness of the angle and will vary depending on the angle and cavity configuration. This distance should be minimized as much as possible. In addition, the steel angle capacity was conservatively limited to the yield moment, although an argument could be made that the angle leg could be designed to reach full plastic moment. However, it was felt that this lower limit is more appropriate, as inelastic deformation may negatively impact the performance of the movement joint below the angle.

The vertical leg of the angle would also have to be evaluated and sized. Equilibrium would suggest that the vertical leg would have to resist the same moment at the junction of the two legs, as well as the tension force produced by the shear force at the connection. For this case the tension stress on the same effective length of the angle would be less than 2% of the capacity and can safely be ignored. The vertical leg and horizontal leg would be designed for the same moment and thus be the same size. Note that this analysis ignores any shear lag effects.

The previously described design method requires that the masonry veneer remains intact over the assumed anchor spacing. This is likely to be the case. Even if the brick does crack, however, there will likely be at most two sections of brick acting over a given span. This configuration puts a much lower load on the steel shelf angle than a uniform loading, and in the extreme case will create an arch whose thrust will be balanced by masonry on each side and/or friction on the steel angle.

As can be seen from the analysis presented above, a reasonable angle thickness and support spacing can be determined. The deflection of the angles was not limited in the design. The purpose of the deflection limits in masonry design standards is to preclude excessive cracking of the hardened unreinforced masonry. As these angle deflections occur primarily before the masonry sets up, they can usually be ignored. Most importantly, there is no need to limit angle deformations to $L/600$ as the brick stress was limited to preclude flexural cracking. However, as discussed by Dillion (2017), the deformation of the shelf angle legs may need to be controlled to ensure an adequate movement joint is present below the angle. Dillion went on further to describe the deflections of the steel angle under the action of the veneer loading. The results of his analyses suggest the deflections at the angle toe at mid- angle span are just slightly greater than the deflection at the angle support locations. Depending on the attachment configuration of the angle, deformation at the toe of the horizontal leg can be estimated by combining of the rotational deformation allowed by the vertical leg and the flexural the flexural deformation of the vertical leg at angle support locations. However, this analysis would have to be conducted after the anchors have been designed and will vary significantly with the building configuration. This analyses was not included in this paper.

The next step in this process to design the anchor bolts. Figure 7 shows the possible configuration of a 152 mm x 152 mm x 9.5 mm (6 in. x 6 in. x 3/8 in.) angle under the 10.68 kN (2400 lb) veneer loading. The distance, d , from the center of bolt tension force and the center of the compression bearing force will vary significantly with bolt location and bearing configuration. If shims are used to force the bearing stress to be centered 13 mm (1/2 in.) above the angle toe, and the bolt is centered on the vertical leg (a typical but non-optimum location), d would be 64 mm (2.5 in.) for this steel shelf angle configuration. Based on equilibrium, the anchor and bearing couple must develop the same 1.089 kN.m moment about the toe of the steel angle. Thus, the tension on the anchor bolt can be obtained by dividing the moment induced by the veneer weight by d . This results in a tension force of 17.0 kN (3,820 lb). This bolt must also resist a shear load of 10.9 kN (veneer reaction and angle weight (2,460 lb).

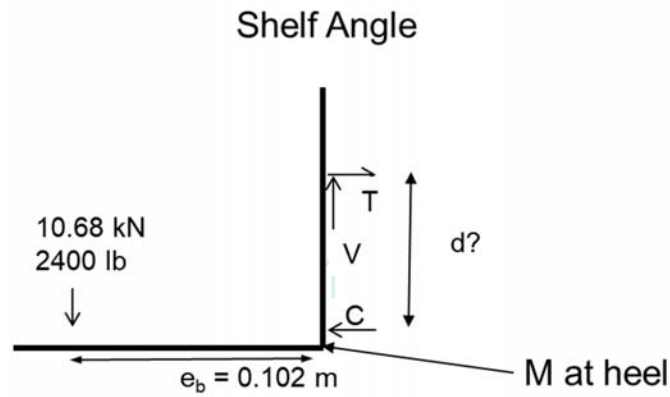


Figure 7: Angle Anchor and Loading Configuration

If post install anchors are used, these can then be designed for the combined shear and tension loading. Assuming the anchor configuration shown in Figures 7 and 8 and a concrete strength of 27.6 MPa (4000 psi), an anchor manufacture's published literature gives a factored shear strength of 75.6 kN (17,000 lb) and a factored tensile strength of 33.0 kN (7,400 lb) for a galvanized 15.9 mm x 111 mm (5/8 in. x 4-3/8 in.) expansion anchor. This would be compared to factored loads of:

$$\text{Factored Shear} = 1.4 (10.9) = 15.32 \text{ kN (3,444 lb)} \quad (9)$$

$$\text{Factored Tension} = 1.4 (17.0) = 23.8 \text{ kN (5,350 lb)} \quad (10)$$

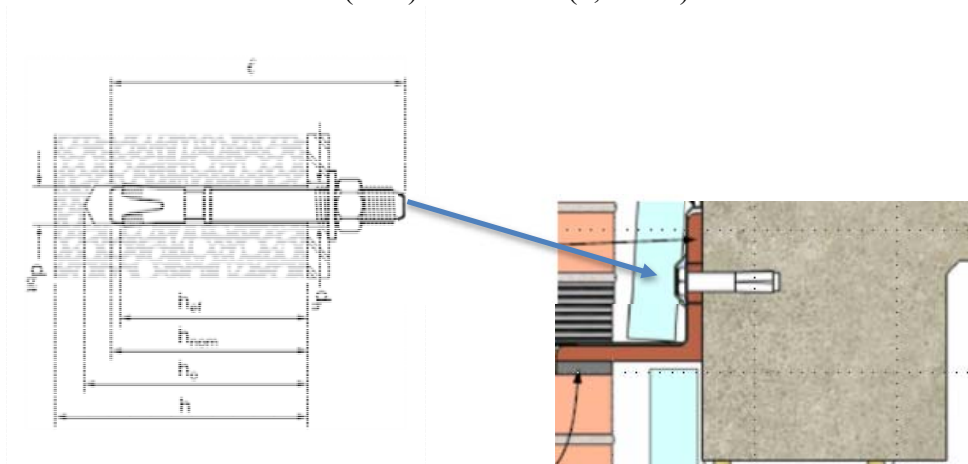


Figure 8: Post-installed Expansion Anchor for Steel Shelf Angle Attachment

As these are combined loadings these must be dealt with using an interaction equation (Eq. 12) as shown below (as per manufacturer's recommendations).

$$\left(\frac{N_u}{\phi N_n} \right)^{5/3} + \left(\frac{V_u}{\phi V_n} \right)^{5/3} = \left(\frac{23.8}{33.0} \right)^{5/3} + \left(\frac{15.32}{75.6} \right)^{5/3} = 0.65 < 1.0 \text{ thus OK.} \quad (12)$$

As shown by Equation 12, these anchors are adequate, although lower embedments are possible. Note that tear-out of the angle or bolt bearing should be checked, but these rarely govern the design. (As is the case here.)

The final aspect of steel shelf angle anchor design that must be evaluated is the bearing of the steel angle near the toe. To ensure adequate capacity and to account for construction tolerances, the angle must be shimmed to ensure adequate bearing capacity directly below the anchor bolt. Figure 9 shows the assumed bearing conditions.

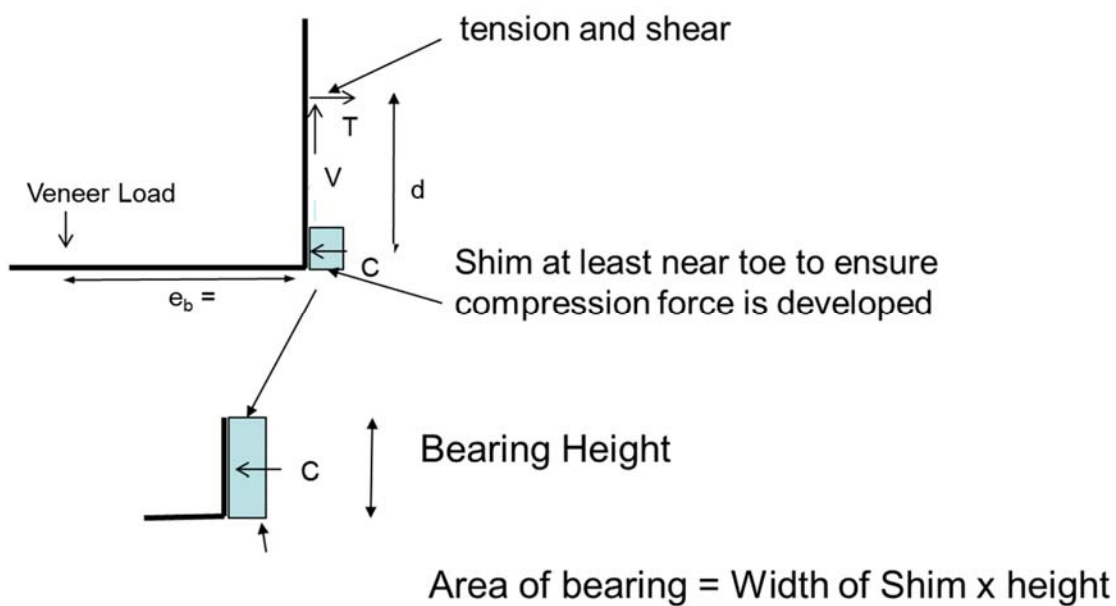


Figure 9: Assumed Bearing Conditions behind angle at Anchor Location

If the bearing of the steel is limited by the concrete bearing capacity, then the angle shim must provide sufficient area to limit the concrete bearing stress. Using the US, ACI 318 concrete bearing provisions (ACI 318, 2014), a 25 mm (1 in) high shim 76 mm wide would provide a bearing capacity of 29.3 kN (6,630 lb). This capacity is greater than the 23.8 kN compression force developed at this location. It should be noted that the shim height must be limited to 25 mm to be consistent with assumptions used to determine the tension and compression forces.

SUMMARY

The previous discussion presents a design method that can be used to design the steel shelf angle supports of masonry veneer wall systems. It should be noted that this design methodology is based on a number of conservative assumptions and is likely to result in conservative designs in most typical design conditions. Designers are encouraged to analyse the veneer wall systems, and their supports using a finite element modelling for more unusual conditions.

REFERENCES

- AISC (2010), Steel Construction Manual - 14th Edition, American Institute of Steel Construction, Chicago Ill.
- ACI 318 (2014), Building Code Requirements for Structural Concrete (ACI 318-14), American Concrete Institute, Farmington Hills, Michigan, USA
- ASTM A36/A36M (2014), Standard Specification for Carbon Structural Steel, ASTM International, West Conshohocken, PA, www.astm.org.
- BIA (1978). Structural Steel Angles Tech Note 31B, Brick Industry Association of America, Reston, VA.
- Dillion, P. B. (2017), Towards a Consistent and Economical Design of Shelf Angles, *Proceedings of the 13th Canadian Masonry Symposium*, Halifax, Canada, June 2017.
- Grimm, C. T. and Yura, J. A. (1989). Shelf Angles for Masonry Veneer, *J. Struct. Eng.*, 115(3), 509-525.
- TMS Committee 402/602 (2016). Building Code Requirements for Masonry Structures and Commentary, The Masonry Society, Longmont, CO.
- McGinley, W. M. (2013). "Design of Shelf Angles for Masonry Veneer." *Structure Magazine*, May, 2013, 10-12.
- [4] Parker, J. C. (2008). Façade Attachments to Steel-Framed Buildings, *Steel Design Guide 22*, American Institute of Steel Construction, Chicago.
- Tide, R. H. R. and Krogstad, N. V. (1993). "Economical design of shelf angles." *Masonry: Design and Construction, Problems and Repair, ASTM STP 1180*, John M. Melander and Lynn R. Laursdorf, Eds., American Society for Testing and Materials, Philadelphia.



**MASONRY TODAY
AND TOMORROW**

**11 - 14 February, 2018
SYDNEY AUSTRALIA**

www.10amc.com

A FIELD INVESTIGATION INTO LONG-TERM CORROSION OF METAL WALL TIES IN MASONRY VENEER CONSTRUCTION

B. Jardim do Nascimento¹, I.A. Chaves², M.J. Masia³ and R.E. Melchers⁴

¹ PhD Candidate, Centre for Infrastructure Performance and Reliability, The University of Newcastle, Callaghan, NSW 2308, Australia, barbara.jardimdonascimento@newcastle.edu.au

² Research Academic, Centre for Infrastructure Performance and Reliability, The University of Newcastle, Callaghan, NSW 2308, Australia, igor.chaves@newcastle.edu.au

³ Associate Professor, Centre for Infrastructure Performance and Reliability, The University of Newcastle, Callaghan, NSW 2308, Australia, mark.masia@newcastle.edu.au

⁴ Professor, Centre for Infrastructure Performance and Reliability, The University of Newcastle, Callaghan, NSW 2308, Australia, rob.melchers@newcastle.edu.au

With advances in corrosion resistant alloys and steels, masonry wall ties now can be specified to ensure longevity of brick veneer or cavity walls in modern construction. Some concern remains, however, about masonry veneer walls, many decades old, constructed using un-galvanised low carbon or mild steel structural ties. These are subject to corrosion. Improved understanding of how and when such wall ties might fail is important for estimating structural reliability, yet there is little, mainly anecdotal information available, largely unsuited for phenomenological modelling purposes or decision making. This study reports a field investigation of the corrosion of masonry brick veneer metal wall ties inspected in a variety of heritage listed masonry buildings in Newcastle, Australia. Visual inspection was used to identify corrosion damage. Some representative samples were collected to allow determination of remaining tie cross-section. The observations are compared to Code-specified life expectancy. This shows that localised corrosion damage of the ties when embedded in the mortar is significant and by implication could reduce structural reliability of the brick veneer construction. The implications for predicting potential long-term remaining wall tie structural capacity are discussed.

Keywords: *Corrosion, brick veneer, wall ties, structural reliability*



INTRODUCTION

Masonry construction has evolved through many centuries, being used to create several of the most significant architectural achievements of civilization, including the Pantheon in Rome, the Great Wall of China and the Egyptian Pyramids, now over 5,000 years old. The evolution in masonry construction resulted from the intersection of diverse factors, including standardization of the shapes of the blocks and the relationship between different components such as bricks, mortar and ties.

Masonry is known for its durability, resistance to fire and its sound and thermal properties. This extends also to brick veneer (Figure 1a) and cavity wall construction (Figure 1b). Importantly, these features depend directly on the materials involved. At first sight, wall ties (also known as brick ties) may appear to be relatively unimportant components in the overall wall system. However, they have an important role, as illustrated, for example, during extreme events such as the Newcastle Earthquake of 1989. It revealed the corrosion of brick ties was a major cause of loss of stability of masonry leaves and consequent failure of masonry walls (Page et al., 1990).

Veneer and cavity walls consist of an outer masonry leaf connected to an inner leaf by ties (Page et al., 1996). The cavity between the inner and outer leaves has the important function of preventing water ingress to the interior leaf. However, the cavity can retain moisture and this can lead to corrosion damage of the wall ties. The wall ties for both veneer and cavity systems are essentially similar. They provide a metal connection embedded in the mortar of the masonry leaf or leaves (Figure 1). Following standardised recommendation, the ideal type of tie to be designed will depend on the structural requirement of the masonry and geographical seismic conditions. This form of construction means that visual inspection of the ties is extreme difficult or impossible. Anecdotal evidence suggests they are seldom included in maintenance procedures. The difficulty of inspecting wall ties and any corrosion they might have suffered, as well as the incidence of masonry wall collapse in earthquake events, highlights a need for other approaches, including the possibility of predicting life-service of metal wall ties. This also may have benefits for decisions about building demolition, retrofitting or change of wall ties.



(a) Tie in Veneer wall



(b) Tie in Cavity wall

Figure 1: Examples of ties in Veneer and Cavity walls (Ancon, 2017)

The following discussions and suggestions survey existing knowledge and review some test observations with the aim to assist in improving the capability for prediction of masonry failure as a result of wall tie corrosion. Another factor to be considered due to the wall tie characteristic of transferring face loads between leaves is fatigue. Fatigue when in conjunction with corrosion can have an important role in understanding the degradation of the tie and this topic is yet to be further investigated.

The aim is to employ theoretical and non-destructive methods calibrated to field observations rather than empirical methods. While these might be useful for assessment of existing structures, they are unlikely to be feasible for extrapolation and thus for the prediction of likely future conditions and remaining life.

HISTORY OF BUILDING ACTIVITY

World-wide, more than 20 million homes were constructed in a 100-year period, between 1880 and 1980. It has been estimated that in that period, over 50% of the houses were built with a cavity form of wall construction (Malcolm, 1986). In Australia, the number of dwellings constructed after 1963 exceeded 100,000 per year and the average building activity grew over the following years (Figure 2). The materials used for walls in buildings also increased, and the use of brick for the outer walls went from 25% of usage in 1911 to over 58% in 1981. By 1993, bricks were the most common material for walls, with 87% of usage in new buildings, of which 67% were single-skin brick walls and 20% double-skin brick walls (Figure 3).

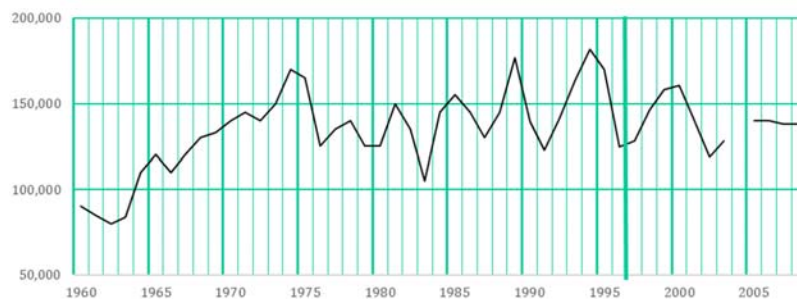


Figure 2: Number of dwellings commenced in Australia (BIS, 1998)

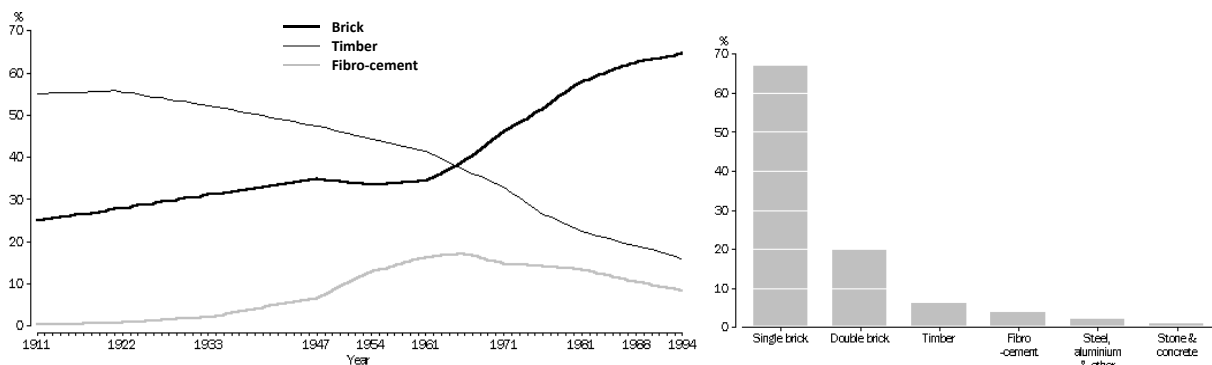


Figure 3: Materials of outer walls of occupied private dwellings (ABS, 2006)

The first use of wall ties, as wrought iron ties, inside cavity walls appears to have been in England in the mid-1800s (BIA, 2003). Also, it is known that bricks have been used for a long time and that a significant number of constructions over 100 years old are in bricks. Apart from the aging of masonry walls, problems such as water ingress, cracking, corrosion and collapse due to natural catastrophes have long been associated with brick construction. While for many

structures and constructions tools exist to permit prediction of durability based on factors such as materials, design, construction, environment, and maintenance, the situation for masonry construction is more complex (Grimm, 1985). Masonry systems have the additional complication that service-life depends on the individual as well as the blended performance of 3 or more dissimilar materials. These materials include those of the bricks of the inner and outer walls, the mortar and the wall ties. It follows that to analyse the overall performance of the system, it is necessary to analyse the individual components as well. For this possibly the best starting points are existing codes of practice and currently available standards.

CURRENT CODES AND REGULATIONS

With the increasing use of masonry construction many different metal wall tie systems began to be developed in the early 1960s (BIA, 2003). Modern wall ties are mainly stainless or galvanised steel, but before 1978 wall ties were mainly galvanised mild steel. These are known to be prone to corrosion after some 15-20 years and this could compromise the common expectation of a 50-year building service-life (Ancon, 2016).

Australian Standard AS/NZS 2699.1:2000 Wall Ties specifies the requirements for the design and manufacture of wall ties, ostensibly to assure a minimum design life of 50 years. Under current design requirements wall ties must meet defined durability classifications - namely, R0, R1, R2 and R3 for mild to moderate environments and R4 for aggressive environments (AS/NZS 2699, 2000). This tends to determine the material required for wall ties. Stainless steel is required only for R4 zones, while the R0, R1, R2 and R3 zones require at least galvanized steel ties, with the galvanised coating masses depending on (increasing with) the zone. Despite these prescriptive requirements, it has been recognized also that the service-life of a metal wall tie is difficult to predict as a result of the many factors that influence corrosion (Maurenbrecher et al., 1993).

Corrosion of metal ties can be tested as specified in Appendix C of AS/NZS 2699.1:2000. According to this standard specification, masonry samples must be prepared with wall ties embedded in mortar type M3 and then exposed to a simulated climate test in a chamber with controlled humidity, temperature and with application of a controlled rate of salt dosing. The samples must be exposed in the chamber for a total of 42 days divided in 6 cycles of 7 days each. At the end of the procedure the wall tie is removed from the mortar and the mass loss calculated from the final mass and the initial mass before exposure in the chamber. The mass loss per unit surface area is calculated as:

$$\text{mass loss per embedded surface area} = \frac{\text{total mass loss of tie}}{\text{area of tie embedded in mortar}} \quad (1)$$

According to AS 2699.1, 2000 if the mass loss per embedded area is less than 6% of total coating mass per area of the tie, the test is classified as successful. However, the question arises what 'success' in this sense means in terms of durability under field conditions.

To estimate the equivalence of chamber exposure tests to natural climatic exposures one approach is to assume that each cycle in the chamber is equivalent to 2.5 years of exposure in the field. Similarly, 12 cycles may be assumed equivalent to 5 years exposure and 18 cycles to 7.5 years, etc. (AS 2699.1, 2000). It is immediately obvious that the accuracy of extrapolation of

such test data becomes dubious for estimating the amount of corrosion after, say, 50 years. This also means that estimates of remaining tie capacity or resistance relative to an expected design life of 50 years is (highly) uncertain. The other problem with accelerated testing is that it provides little insight regarding the corrosion mechanisms and the quantification of the influencing factors that are likely to be involved in actual field exposures.

Factors other than corrosion may be important for the durability of wall ties. For that reason, AS 3700 (2011) addresses topics such as design properties and specifications for required strength, appropriate design rules for wall ties, their extent of embedment in the mortar, the space between ties, etc. Although important, there is a view that the information in the Standard is not enough to inhibit failures of the wall tie systems and that other factors may influence the correct functioning and life of the ties, factors such as the mortar type, the standard workmanship, local exposure and quality of protective coating (de Vekey, 2001).

EXPERIMENTAL OBSERVATIONS

The diagnosis of the condition of a wall tie is usually restricted to a surface inspection of the walls of a building, the assumption being that wall surface failures will indicate possible wall tie failure (Malcolm, 1986). Analyses to identify pathologies resulting from wall tie failures have been proposed (Malcolm 1986). In the proposed protocol, it is necessary first to examine the type of mortar used, the pattern of cracking, the presence of horizontal fractures in the mortar joints, and then, if considered necessary, to remove bricks in specific areas, located using a metal detector to then examine the condition of the wall ties by visual examination.

To provide some insight into the issues involved in actual field observations, an example is given here of such an examination, and of the application of the protocol, to walls of the Sanitarium Health Food building located at Cooranbong near Lake Macquarie, NSW. The work was conducted by Nicholas Guinane of Engenium Consulting Engineers and the University of Newcastle in April 2017. Visual inspections were made by removing masonry bricks in three different locations. Two brick extractions were in masonry walls from 1935 (Figure 4b,c) and one extraction was in a wall built in 1965 (Figure 4a) (Guinane, 2017).

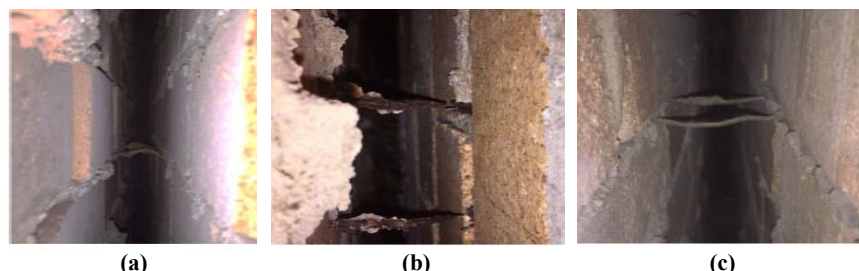


Figure 4: Wall tie inside a cavity wall (Guinane, 2017). The external wall for each image is on the left hand side.

The wall in Figure 4(a) was not damaged. The wall ties appeared to be in good condition with no visible corrosion after 50 years. In Figure 4(b) the wall had horizontal and stepped cracking. The wall ties in this region showed corrosion so severe that the ties had been rusted right through. The

wall shown in Figure 4(c) had some erosion in the mortar, some small stepped cracking and also a superficial outwards displacement. Although the wall ties appeared visually to be in good condition, the section of the tie at the interface of the external wall had lost about 20% of its diameter (Guinane, 2017).

Visual inspection of the tie within the cavity can be inefficient, resulting in potentially misleading results if not combined with other analysis. Based on previous experience, in cavity constructions the corrosion is severe at and within the mortar bed joints of the outer leaf (Page et al., 1990). Figure 5 illustrates failure at the part of the tie embedded in the mortar of the outer leaf.



Figure 5: Corrosion of the part of the tie embedded in mortar (Page, 1991)

The poor condition of the part of the tie embedded in the mortar is likely to affect the overall reliability of masonry walls. In extreme cases complete failure of the walls could occur. For example, in 2015, a wind storm in the Newcastle region caused damages to several properties, including the Bar Beach Bowling Club where the outer masonry leaves were dislodged (Figure 6a and 6b).



Figure 6: Collapse of a Masonry Veneer - Bar Beach Bowling Club

To throw some light on field observations and to determinate the rate of corrosion in different wall ties materials, Oke (2017) performed corrosion tests on light galvanised, heavy galvanised and stainless steel wall ties in a salt spray chamber during 4 weeks. The samples were examined before and after cleaning of rust products using a Zeiss SZ60 microscope. The samples were photographed using a digital camera (PixelINK) at 10x and 20x magnification (Figure 7 and 8). The results, after 4 weeks, showed a mass loss for all the samples. The light galvanised ties lost around 1.4% of their mass, the heavy galvanised ties lost 0.6% and the stainless-steel ties lost less than 0.01% (Oke, 2017).

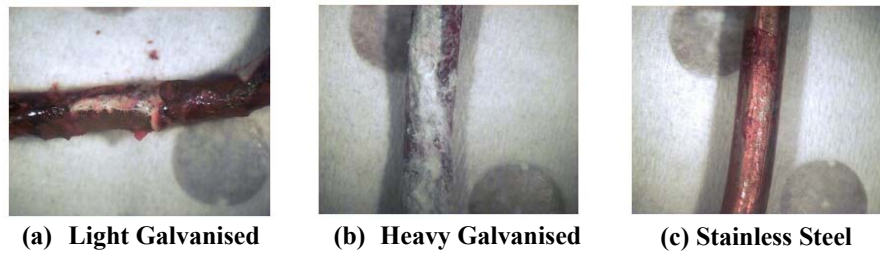


Figure 7: Close-up views of wall ties before cleaning (Oke, 2017)



Figure 8: Close-up views of wall ties after cleaning (Oke, 2017)

Obviously, mass loss of the tie causes cross-section reduction and thus loss of structural capacity in axial resistance or bending resistance or both and in turn these can affect structural reliability. Models for estimation of structural reliability and empirical information about corrosion rates are available for use in reliability analysis. (Melchers, 2005)

REVIEW OF ATMOSPHERIC CORROSION MODELS

The results obtained from the observation in the Sanitarium and the salt spray chamber might be compared to earlier studies on brick ties corrosion. Hagel et al. (2007) compared the corrosion rate (CR) and the estimated service life from two theoretical models from the International Organization for Standardization (ISO) with empirical results obtained by Keller et al. (1992) from the inspection of zinc galvanized specimens of masonry ties in buildings in Canada. The first model used by Hagel et al. (2007) was taken from ISO 9223-9226 and is based on the ISO 9226 (1992) method to determine corrosion rates integrated with the evaluation of ‘corrosivity’ according to ISO 9223 (1992). The second model used was the ISOCORRAG model (ASTM D571, 2010). In both cases, a number of assumptions were made in order to permit the use of the ISO models to predict service life of masonry ties. Irrespective of these, the approach used is questionable since the models are for atmospheric corrosion. It is very unlikely that the environment for masonry ties embedded in mortar bears a close relationship to atmospheric corrosion environments. Nevertheless, some of the issues and some of the variables may be relevant. For that reason, the approach used in some parts of the atmospheric corrosion literature may be relevant. A short review is presented below.

For the ISO 9223-9226 model, three parameters for the macro environment must be available to determine a so-called ‘corrosivity’ category. These parameters are the SO_2 and Cl deposition rates and the time of wetness (TOW). To make progress, the ‘corrosivity’ is taken as the

corrosion rate after 1 year of exposure. This is provided for each corrosion category. Also, the midpoint of the corrosion rate range is assumed. According to Hagel et al. (2007) the results may be used to calculate the predicted service life. However, this assumes that the 1 year corrosion rate applies for the whole of the service life.

The other model used by Hagel et al. (2007) is the ISOCORRAG model. It assumes a linear corrosion loss rate ($\mu\text{m}/\text{year}$) based on estimates of corrosion losses from 12-year exposures carried out with several coupons in 13 countries around the world, with a total of 53 exposure sites (Knotkova et al., 2010), and correlated with the TOW and the SO_2 and Cl deposition rates:

$$CR = a_1 + B_1 (\text{SO}_2) \mu\text{g}/\text{m}^3 + B_2 (\text{TOW}) \text{ h}/\text{years} + B_3 (\text{Cl}) \text{ mg}/(\text{m}^2.\text{d}) \quad (2)$$

Note: a_1 , $B_{1,2,3}$ are regression coefficients. $A_1 = 0.2098$; $B_1 = 0.0232$; $B_2 = 0.0002696$ and $B_3 = 0.0059$ (Hagel et al., 2007).

Comparative corrosion rates (CR) and service life estimates for the empirical and ISO models are shown in Table 1, based on Hagel et al. (2007). Hagel et al. (2007) noted that the results for the predicted CR and the expected service lives show wide variations. They considered this to be the result of the assumptions made for each model. When compared with the empirical results the differences compared with the model predictions are quite large. This can have significant implications if used for structural design.

Table 1: Comparative corrosion rates and service life estimations between empirical and ISO models (after Hagel et al., 2007).

| Specimen No. | Empirical results | | ISO 9223-9226 model | | ISOCORRAG model | |
|--------------|--|----------------------|--|----------------------|--|----------------------|
| | CR ($\text{g}/(\text{m}^2.\text{year})$) | Service life (years) | CR ($\text{g}/(\text{m}^2.\text{year})$) | Service life (years) | CR ($\text{g}/(\text{m}^2.\text{year})$) | Service life (years) |
| 1 | 34.0 | 7.5 | 45.0 | 5.7 | 48.3 | 5.3 |
| 2 | 48.0 | 7.5 | 45.0 | 8.0 | 48.3 | 7.5 |
| 3 | 22.2 | 9.0 | 45.0 | 4.4 | 35.9 | 5.6 |
| 4 | 55.0 | 4.0 | 45.0 | 4.9 | 35.9 | 6.1 |
| 5 | 12.0 | 7.7 | 45.0 | 2.0 | 38.2 | 2.4 |
| 6 | 8.0 | 11.5 | 45.0 | 2.0 | 38.2 | 2.4 |
| 7 | 25.0 | 8.8 | 10.0 | 22 | 24.1 | 9.1 |
| 8 | 28.0 | 8.4 | 10.0 | 23.4 | 24.1 | 9.7 |
| 9 | 31.0 | 8.7 | 10.0 | 26.9 | 24.1 | 11.2 |

More recent studies have focussed on what is considered by some investigators to be an improved prediction method, both for empirical and for ISO-based estimated corrosion rates. Chico et al. (2017) were of the opinion that the international programmes on atmospheric corrosion (ISOCORRAG, ICP/UNECE and MICAT) had many similarities and that therefore the results could be combined. To achieve this, the databases from the various programmes were collected and analysed to obtain an estimated evaluation of the first-year corrosion based on meteorological parameters, estimated time of wetness (TOW) and measurements of SO_2 and Cl deposition rates. The data collected from the international programs was then combined into one linear equation (Chico et al. 2017) to obtain an “universal” damage function based on the relationship between atmospheric corrosion rates and meteorological and pollution parameters:

$$C = a_1 + a_2 (RH) + a_3 (P) + a_4 (T) + a_5 (TOW) + a_6 (SO_2) + a_7 (Cl), \quad (3)$$

Where: C = carbon steel annual corrosion (μm); RH = annual average relative humidity (%); T = annual average temperature ($^{\circ}\text{C}$); P = annual precipitation (mm); TOW = annual fraction of number hours/year in which RH > 80% and T > 0 $^{\circ}\text{C}$; SO_2 = SO_2 pollution ($\text{mg}/\text{m}^2.\text{day}$); and Cl = chloride pollution ($\text{mg}/\text{m}^2.\text{day}$);

According to Eq. (3), every variable is accompanied by a coefficient ($a_2 - a_7$) that indicates the relative contribution of that variable to the overall corrosion C , with the highest coefficient for the variable of greatest significance. The coefficients were selected using a regression model in a computer programme (SSPS). In principle, additional variables could allow further comparison of estimates with other potentially related studies and it possible that such additions could result in improved estimates of 1 year corrosion rates. This remains a matter for further investigation.

DISCUSSION

A number of reservations should be apparent in the approaches used to obtain “mathematical” models as outlined above. Chief amongst these is the assumption that a 12-month corrosion rate is somehow relevant to longer term corrosion behaviour. Even in the atmospheric corrosion literature a linear model as implied by the 12-month rate has largely been discounted for estimation of realistic service lives (Leygraf et al. 2016). The power law is widely adopted instead. However, even this has deficiencies as it does not match longer term experimental field data as well as a more complex function, termed a ‘bi-model’ model and shown to be much more representative of longer term corrosion behaviour in a variety of exposure environments, including atmospheric corrosion (Melchers, 2007). Whether this model is also applicable to the corrosion of wall ties remains a topic for further investigation. Overall, it is clear that whatever modelling approach is chosen, much scope remains for more detailed and in-depth investigation of the proper empirical modelling of the long-term corrosion of metal wall ties.

In addition to the above, various other challenges can be identified:

- ❖ How should the various currently available mathematical models be improved to be sufficiently reliable to predict shorter- and longer-term corrosion of wall ties?
- ❖ How can the results of corrosion prediction models be properly incorporated into predictions of remaining service life?
- ❖ Is the use of stainless steel warranted, both in terms of potential improvement of the corrosion resistance of wall ties and the economics involved? Are experimental results available to support the use of stainless steels?
- ❖ In the occurrence of a natural catastrophe, are the wall ties from heritage masonry buildings adequate to resist the resulting loads?
- ❖ What solutions are available for the replacement of corroded ties? Are such solutions economically viable?

In terms of the last point, a number of methods are available for wall tie replacement. Recommendations for the method to use are based on the level of damage to the walls and can range from a simple tie replacement to the reinstatement of the building (Moore, 1982). If galvanized or carbon steel ties must be removed, replacement with stainless steel ties usually is

not recommended. This is because the contact of the stainless steel with carbon steel can result in a galvanic cell and increase the potential for corrosion (BIA, 2003).

From the results obtained in the investigations reviewed herein, it is likely that many differences remain the interpretation and prediction of corrosion results, mainly from the atmospheric literature, when applied to wall tie corrosion. Current empirical models can be misleading as the model parameters as well as the visual observation still demand a number of assumptions to make analysis possible. As noted, even for atmospheric corrosion, the integration of three international 12-month corrosion rate estimates (ISOCORRAGE, ICP/UNECE and MICAT) still produces generally inconclusive results.

Experimental testing of wall ties in harsh but artificial environmental conditions (e.g. Oke 2017) may be appropriate but such testing also has limitations, both in interpretation and in relating them to corrosion in realistic environments. Test results from corrosion chambers and from other accelerated processes may have application as comparative guides but should not be assumed to have relevance even for short-term corrosion. They require, at least, empirical comparison with relevant field exposure results under realistic exposure conditions. Such a scheme was proposed already many decades ago (Champion 1964) but appears still lacking.

Accelerated salt spray chamber tests of masonry ties embedded in mortar could be conducted and the results compared with relevant long-term field observations for masonry ties. On this basis, it should be possible to postulate a more realistic, empirically validated, corrosion loss trend with time. It can be anticipated, however, that such a model will have similarities with the more advanced models currently in existence for other corrosion environments.

In order to integrate all the discussed methods in this paper and to achieve more reliable results in terms of corrosion prediction and maintenance, the following experimental, field and analytic research program is proposed:

- ❖ Field investigation, particularly of heritage listed masonry buildings, with visual inspections and also collection of wall tie samples for laboratory examination;
- ❖ Longer term exposures of wall tie specimens in a salt spray chamber, with ties embedded in different types of mortar, use of different saline solutions, use of different tie steels and use of different mortar types;
- ❖ Comparison of the various results to correlate real time data with accelerated results for corresponding environmental conditions;
- ❖ Use of these results in potential mathematical models to develop improved corrosion prediction models suitable for and service-life prediction.

CONCLUSION

Because of the lack of models for the prediction of corrosion of masonry wall ties, much effort has been expended in trying to apply models based on atmospheric corrosion losses, using climate and pollution parameters. The international atmospheric corrosion models that have been developed to date for the prediction of 12 month corrosion losses produce very different results. They rely strongly on assumptions about the environment and about the progression of corrosion.

Since there are only tenuous links between atmospheric corrosion and the corrosion of wall ties, the present scenario for prediction of wall tie corrosion, and thus service life, prediction, is difficult.

The severe corrosion within the mortar bed joints suggest the necessity of corrosion tests based in the mortar environment instead of the atmosphere. These tests require natural and reliable empirical results for comparison and validation. To complement such work, a new research program is proposed herein. It proposes that short-term test regimes are compared with longer term exposures for brick ties embedded in different types of mortar, including use of accelerated tests in salt spray chambers, and using empirical comparisons to attempt to minimize uncertainty between the prediction models and field experience and observations.

ACKNOWLEDGEMENTS

The authors acknowledge the continued financial support provided by The University of Newcastle Faculty of Engineering and Built Environment. Advice from Professor Adrian Page, photographs taken by Goran Simundic, the experimental work by Nicholas Guinane and Isabella Oke and the support of the staff of the Civil Engineering Laboratory at The University of Newcastle is appreciated.

REFERENCES

- Ancon (2016), What is a wall tie. Ancon Building Products. Available from <https://www.ancon.co.uk/blog/what-is-a-wall-tie> [accessed 15 July 2017]
- Ancon (2017), Wall ties and Restraint Fixings. Ancon Building Products. Available from <https://www.ancon.co.uk/products/wall-ties-restraint-fixings> [accessed 15 July 2017]
- American Society for Testing and Materials (2010), ISOCORRAG International Atmospheric Exposure Program: Summary of Results, ASTM D571
- Australian Bureau of Statistics (2006), Housing Stock: Trends in Housing, Australian National Statistical Agency. Available from <http://www.abs.gov.au/AUSSTATS/abs@.nsf/> [accessed 19 July 2017]
- BIS Shrapnel (1998), Building in Australia, 18th Edition, BIS Shrapnel Pty Limited, pp. 101-166
- Brick Industry Association (2003), Wall Ties for Brick Masonry, Tech Notes 44B, Reston VA., pp 1-15
- Champion F. A., Corrosion testing procedures, Chapman and Hall, London, UK, 1964;
- Chico, B., de la Fuente D., Diaz I., Simancas J., Morcillo M. (2017), An Integration of ISOCORRAG, ICP/UNECE and MICAT Databases, Annual Atmospheric Corrosion of Carbon Steel Worldwide, National Centre for Metallurgical Research, Madrid, Spain, pp. 1-27
- de Vekey, R. C. (2001), Corrosion of metal components in walls, BRE Centre for Whole Life Construction and Conversation, pp. 1-8
- International Organization for Standardization (1992), Corrosion of metals and alloys – Corrosivity of

atmospheres – Classification, determination and estimation, Standard ISO 9223:1992

International Organization for Standardization (1992), Corrosion of metals and alloys – Corrosivity of atmospheres – Determination of corrosion rate of standard specimens for the evaluation of corrosivity, Standard ISO 9226:1992

Grimm, C. T., Durability of Brick Masonry (1985): A Review of the Literature, Masonry: Research, Application, and Problems, ASTM STP 871, j. C. Grogan and J. T. Conway, Eds., American Society for Testing and Materials, Philadelphia, pp 202-234

Guinane, N. (2017). A practical investigation into the corrosion of masonry brick metal wall ties. (Final year project). The University of Newcastle, NSW.

Hagel M. D., Lissel, S. L., Sturgeon G. R. (2007), Comparison of theoretical and empirically determined service lives for wall ties in brick veneer steel stud wall systems, *Canadian Journal of Civil Engineering*, Vol. 34, 11, pp. 1-9

Knotkova, D., Kreislova, K., Sheldon D (2010), DS71 – ISOCORRAG International Atmospheric Exposure Program: Summary of Results. American Society for Testing and Materials, West Conshohocken, PA. ASTM DS 71, pp 1-72

C. Leygraf, I.O. Wallinder, J. Tidblad, T. Graedel, Atmospheric Corrosion, Wiley, 2016.

Malcolm R.A. Hollis, (1986) Diagnosis and treatment of defective cavity wall ties, *Structural Survey*, Vol. 4 Issue: 4, pp. 332-345.

Maurenbrecher, A.H.P., Brousseau, R.J. (1993), Review of Corrosion Resistance of Metal Components in Masonry Cladding on Buildings, National Research Council Canada. Institute for Research in Construction, No. 640, Canada.

Melchers, R.E (2005) The effect of corrosion on the structural reliability of steel offshore structures, *Corrosion Science*, Vol. 47 Issue: 10, pp. 2391-2410.

Melchers, R.E (2007) The transition from marine immersion to coastal atmospheric corrosion for structural steels, *Corrosion*, 63, (6), pp. 500-514.

Moore, J. F. A. (1982), Corrosion and cavity wall ties, *Anti-Corrosion Methods and Materials*, Vol. 29 Issue 2, pp. 8-9

Oke, I (2017), An investigation into the corrosion of metal wall ties in masonry, (Final Year Project), University of Newcastle, pp. 1-62

Page, A. W. (1991), The behaviour of unreinforced masonry in the Newcastle Earthquake, Brick and block masonry: Proceedings of the 9th Int. Brick/Block Masonry Conference, Berlin, Germany, Volume 2, pp. 921-928

Page, A. W., Kautto, J., and Kleeman, P. W. (1996), A design procedure for cavity and veneer wall ties, Department of Civil Engineering and Surveying, The University of Newcastle, 22 pp.

Page, AW., Kleeman, PW., Stewart, MG., and Melchers, RE. (1990), Structural Aspects of the Newcastle Earthquake, National Structural Engineering Conference, 2nd, Adelaide, S. Aust, pp. 305-311

Standards Australia (2000), Wall Ties, Standard AS/NZS 2699.1:2000, Sydney, Australia

Standards Australia (2011), Masonry Structures, Standard AS 3700:2011, Sydney, Australia

MECHANICAL CHARACTERIZATION OF WALL TIE CONNECTION IN CAVITY WALLS

G. Skroumpelou¹, F. Messali², R. Esposito³ and J.G. Rots⁴

¹ Graduate student, Delft University of Technology, Section of Structural Mechanics, Delft, ZH, The Netherlands,
G.Skroumpelou@student.tudelft.nl

² Postdoctoral researcher, Delft University of Technology, Section of Structural Mechanics, Delft, ZH, The
Netherlands, F.Messali@tudelft.nl

³ Postdoctoral researcher, Delft University of Technology, Section of Structural Mechanics, Delft, ZH, The
Netherlands, R.Esposito@tudelft.nl

⁴ Full professor, Delft University of Technology, Section of Structural Mechanics, Delft, ZH, The Netherlands,
J.G.Rots@tudelft.nl

The assessment of the seismic response of unreinforced masonry (URM) buildings has been a popular topic all over the world in the last decades. In recent years, induced seismicity in the north of the Netherlands increased considerably and introduced seismic risk also in this country. The built environment in the region is mainly composed by unreinforced masonry buildings, which are not designed for seismic loading and have specific characteristics such as the use of cavity walls.

An extensive large-scale testing program has been recently carried out at Delft University of Technology to characterize the behaviour at material and structural level of the terraced house typology, which is characterised by the presence of cavity walls with loadbearing walls of calcium silicate bricks and veneer walls of perforated clay bricks. Experimental tests showed that the wall ties are able to connect the two leaves for small loads, but they may fail for higher accelerations and increase the probability of out-of-plane collapse of the wall. In this framework, the paper reports the outcomes of an extensive testing campaign on the connections between the two leaves of cavity walls under large imposed displacements, aiming at providing a complete characterization of the behaviour of the connections in terms of resistance, envelope curve and dissipated energy. The specimens were composed by the typical wall ties employed in Dutch terraced houses, embedded either in calcium silicate brick masonry or in perforated clay brick masonry. Different loading conditions (axial and shear, monotonic and cyclic loading) and different confining compressive loads on the couplets were considered.

Keywords: *Unreinforced masonry, Cavity walls, Wall ties, Quasi-static tests, Cyclic.*

INTRODUCTION

In the last years, the increasing seismicity in the northern part of the Netherlands has led to extensive research on the seismic assessment of the existing structures, as well as on possible strengthening methods. Most of the built environment in the area is composed of unreinforced masonry (URM) buildings. To provide benchmarks for the Dutch situation, an extensive testing campaign was performed at Delft University of Technology in 2015 (Esposito et al, 2017; Messali et al 2017; Esposito et al, 2018). The campaign focused on terraced houses (one of the most diffuse building typologies in the Netherlands) that is characterized by the use of cavity walls, similarly to URM buildings in other regions of the world, such as Australia, New Zealand, North America, and other parts of northern Europe. A cavity wall consists of two separate parallel walls cooperating as one wall, with a space between them, which is called cavity (Figure 1a). The inner and outer walls are also called leaves of the wall and are interconnected by means of metal ties, as described in NEN-EN 845-1 (2016). In comparison with solid walls, cavity walls offer better thermal and sound insulation, they prevent ambient moisture to enter the building and they are less expensive to construct (Products, 2016).

The out-of-plane mechanisms represent the primary cause of structural failure in URM buildings under seismic loading, particularly for poor wall-to diaphragm or wall-to-floor connections. Such failure can involve either the outer leaf or both leaves of the cavity wall, depending on the effectiveness of the connection provided by the wall ties. The ties should be placed in specific locations, spread almost uniformly over the area of the wall. The exact density and positioning of the ties vary according to different building regulations. As an indication of the distribution of the ties, BS EN 6697 (2010) suggests that, except around openings, not less than 2.5 ties per square meter (900 mm horizontal \times 450 mm centres) should be used for walls in which both leaves are 90 mm or thicker. Insufficient embedment of the tie in the mortar joint or inadequate number of ties could lead to reduction of the overall capacity of the cavity wall (Giaretton et al, 2016a).

This study aims at providing a complete description the seismic behaviour of the connections between the two wall leaves. The mechanical characterization of the connections in cavity walls can be achieved with tests at component level (Mertens et al, 2014) or for full scale structures (Walsh et al, 2015; Graziotti et al, 2016; Giaretton et al, 2016b). The latter tests showed that the connection may fail before the out-of-plane collapse of the wall.

The present study focuses on the component level. The simplest nevertheless realistic component of a URM wall consists of a couple of bricks connected by means of mortar, including an embedded wall tie. This component will be referred to as “the couplet” from this point onwards. The application of constant precompression will compensate for the absence of the surrounding wall. Assuming that one of the leaves is fixed, the relative motion of the free leaf can occur in three directions: two directions are parallel to the plane of the fixed leaf (vertical and horizontal shear loading) and one is perpendicular (axial loading) (Figure 1b). In the case of the couplets, the clamp will replace the free leaf. The testing setup allows only the application of vertical displacement. Therefore, the orientation of the couplets was adjusted accordingly to simulate the aforementioned relative displacements. At this point it should be noted that, in the framework of this research, the case of vertical shear loading was not tested, as the flexural failure of the tie would most probably be the governing failure mechanism. Besides, in real walls the ties are often

slightly bent to connect mortar layers at different height. This actual configuration has not been considered in the current testing campaign, and only straight ties have been tested.

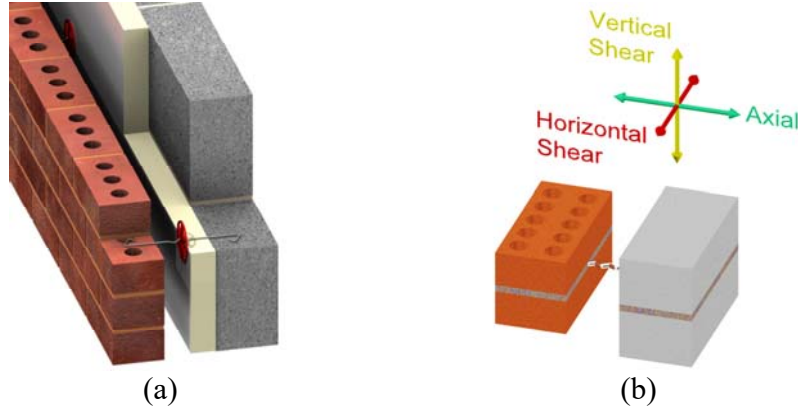


Figure 1: Cavity wall (a) and relative motions between wall leaves (b)

MATERIALS AND METHODS

Asymmetrical L-shaped ties with a diameter of 3.6 mm and a length of 200 mm are used. One end of the wall ties is hooked and the other one is zig-zagged. The couplets representative of the inner and outer leaves are composed of calcium silicate CS (102×212×71 mm) and perforated clay bricks (100×210×50 mm), respectively, and general purpose mortar. The cavity is 80 mm wide.

As components of the cavity walls, two types of couplets are investigated:

- CS specimens: the hooked part of the tie is embedded in a calcium silicate masonry couplet, with an anchoring length of 70 mm (Figure 2a).
- Clay specimens: the zig-zagged part of the tie is embedded in a clay masonry couplet with an anchoring length of 50 mm (Figure 2b).

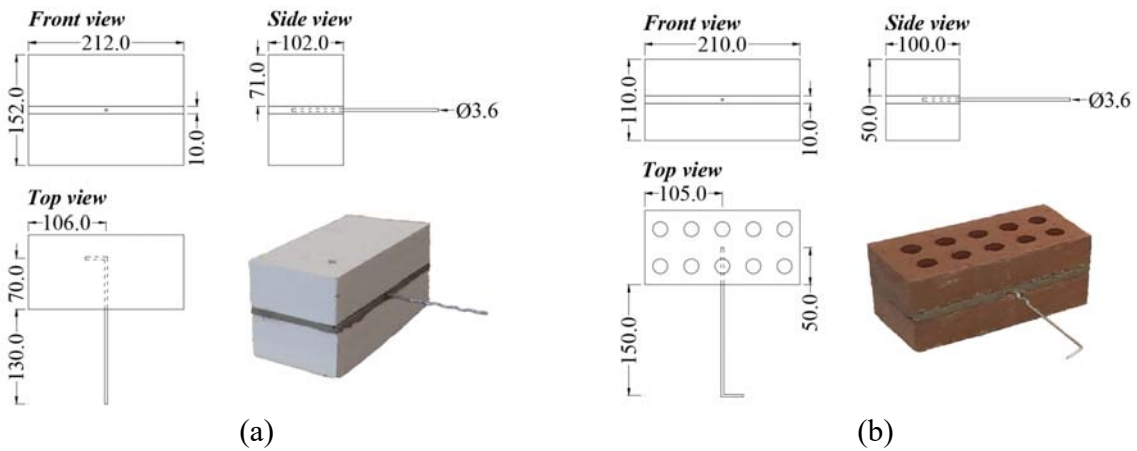


Figure 2: Couplets: CS specimens (a); Clay specimens (b)

The general testing setup for both the axial and shear tests was based on the recommendations reported in EN 846-5 (2012) and EN-846-7 (2012) and is presented in Figure 3a. It comprises:

- A horizontal steel plate, connected to a lower horizontal beam by means of steel threaded rods, to prevent the vertical displacements of the specimen. The specimen is supported by hardwood bearers that do not apply any restraint against splitting of the specimen.
- An apparatus to apply and maintain constant the lateral compressive stresses on the couplet. The force is provided by a hydraulic jack acting in the horizontal direction and perpendicular to the bed joint plane. The system is self-equilibrated by four threaded bars connecting the two vertical steel plates; the outer plate is fixed and the inner plate can slide when pushed by the piston.
- A test machine to apply the vertical load. The load is applied in a vertical direction using a displacement controlled apparatus, with a 4.5 t jack. The machine is provided with a clamp for gripping efficiently the free end of the tie, connected to the jack by means of a bolt.

The clamp and the orientation of the specimen in the setup depend on the type of test. Regarding the axial tests, a standard clamp. The specimen is oriented in such way that the long axis of the tie is vertical and the plane of the mortar parallel to the vertical steel plates (Figure 3b). As for the shear tests, a stiff clamp of custom design was manufactured to maintain the same general configuration of the setup. The specimen was placed in the setup with the tie being horizontal and, as for the axial tests, the plane of the mortar joint being vertical and parallel to the steel plates (Figure 3c). In both cases, the distance between the face of the bricks and the clamp was 80 mm, equal to the cavity width. In Figure 3b and Figure 3c the precompression and support systems are not included for the sake of clarity.

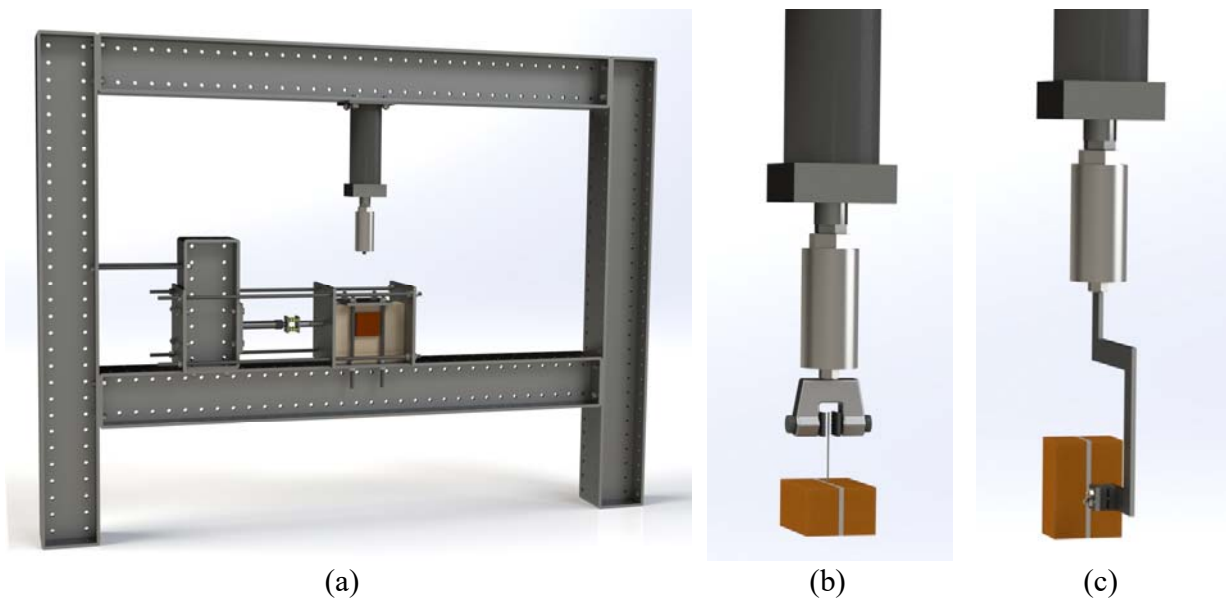


Figure 3: Testing setup: General setup (a); Axial setup (b); Shear setup (c)

Six different loading schemes are followed. The abbreviations used for naming the loading protocols are based on the following convention: **A**=**A**xial load, **S**=**S**hear load, **M**=**M**onotonic

load, **Cy**=Cyclic load, **T**=Tension load, **C**=Compression load. The description of each protocol is presented below.

- **Protocol A_{MT}** (monotonic tensile protocol): monotonic increase of the displacement with a rate of 0.1 mm/s up to failure.
- **Protocol A_{MC}** (monotonic compressive protocol): monotonic increase of the displacement with a rate of 0.1mm/s up to failure or up to maximum possible displacement.
- **Protocol A_{Cy}** (tensile-compressive protocol): the displacement is cyclically varied by applying both tensile and compressive loads on the tie.
- **Protocol S_M** (monotonic shear protocol): monotonic increase of the displacement with a rate of 0.1mm/s up to failure.
- **Protocol S_{Cy}** (cyclic shear protocol): the displacement is cyclically varied by applying both upward and downward (shear) loads on the tie up to failure.

All protocols are applied for two levels of precompression: $0.1 \pm 0.01 \text{ N/mm}^2$ and $0.3 \pm 0.01 \text{ N/mm}^2$. The number of tests performed according to each loading protocol for each campaign is presented in Table 1 below.

Table 1: Number of performed tests

| Loading protocol | A _{MT} | | A _{MC} | | A _{Cy} | | S _M | | S _{Cy} | |
|-------------------------------------|-----------------|-----|-----------------|-----|-----------------|-----|----------------|-----|-----------------|-----|
| Precompression (N/mm ²) | 0.1 | 0.3 | 0.1 | 0.3 | 0.1 | 0.3 | 0.1 | 0.3 | 0.1 | 0.3 |
| Performed tests on CS | 6 | 13 | 8 | 8 | 9 | 6 | 5 | 5 | 3 | 3 |
| Performed tests on clay | 7 | 10 | 7 | 6 | 4 | 7 | 5 | 4 | 3 | 3 |

The loading history for the cyclic tests can be subdivided into two phases (Figure 4). In phase 1, groups of three cycles are performed, each group of increased amplitude. In phase 2, each group is composed by two cycles of increased amplitude and two cycles with reduced amplitude (40% of the first two cycles). The loading rate is such that the duration of every cycle remains constant until reaching 1 mm/s; afterwards it is maintained constant. The exact number of groups of cycles for each cyclic protocol and their amplitudes are listed in Table 2. In all of the cyclic tests, the specimen is initially loaded upwards, that is referred as the positive direction.

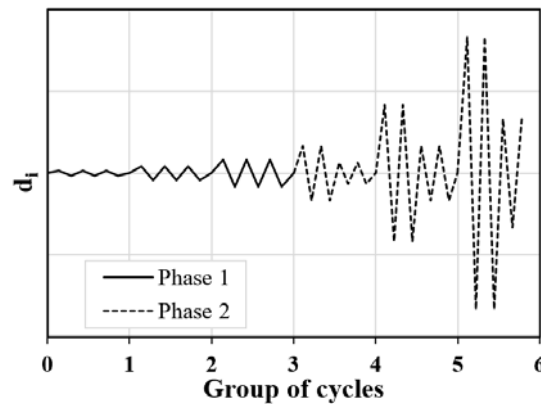


Figure 4: Cyclic protocols

Table 2: Protocols A_{Cy} and S_{Cy} – Sequence of loading

| A _{Cy} | Phase | 1 | | | 2 | | | | | | | | | | | | | | |
|-----------------|-----------------|-----|------|-----|----|-----|-----|----|----|----|----|---|----|---|----|---|----|----|--|
| | Group of cycles | 1 | 2 | 3 | 4 | 5 | 6 | 7 | 8 | 9 | 10 | | | | | | | | |
| | Amplitude (mm) | 0.1 | 0.25 | 0.5 | 1 | 0.4 | 2.5 | 1 | 5 | 2 | 10 | 4 | 15 | 6 | 20 | 8 | 30 | 12 | |
| S _{Cy} | Phase | 1 | | | | | | 2 | | | | | | | | | | | |
| | Group of cycles | 1 | 2 | 3 | 4 | 5 | 6 | 7 | | | | | | | | | | | |
| | Amplitude (mm) | 1 | 5 | 10 | 20 | 40 | 16 | 60 | 24 | 80 | 32 | | | | | | | | |

TEST RESULTS

First the different failure modes obtained for the axial tests are described (Figure 5). Regarding the CS masonry couplets, failure is characterized by cracking of the bed joint and straightening of the steel tie in tension (Protocol A_{MT}) and by piercing and expulsion of the cone of mortar next to the embedded steel tie in compression (Protocol A_{MC}). For clay masonry couplets, a dowel effect is provided by the mortar in the holes, giving higher resistance in tension (Protocol A_{MT}), while the tie buckles in compression (Protocol A_{MC}). The failure mode of the specimens tested according to Protocol A_{Cy} is a combination of the mechanisms of the monotonic tests, both for CS and clay couplets.

A representative force-displacement curve is presented in Figure 6 for each type of masonry and loading procedure. The ultimate failure of the specimen is defined when 20% of the peak force is reached in the post-peak phase. The tensile and compressive curve obtained for the monotonic protocols are shown together in the same diagram. The envelope curve was derived according to ASTM-E2126-11 (2011). The qualitative behaviour of the couplets does not change for different levels of precompression, therefore only one curve is presented for each loading protocol. Figure 7 shows the peak and the ultimate failure for all loading protocols and both precompression levels for both materials, and offers a complete overview of the results. The mean peak and ultimate force/displacement, along with the standard deviation, of each sample are reported in Table 3.

By comparing the behaviour of CS and clay couplets, the clay specimens presented consistently a more brittle behaviour and higher peak load at smaller displacements. For both materials, the cyclic loading determined the failure of the specimens for lower or similar loads than the corresponding monotonic tests, except for the case of tensile loading of clay couplets at a precompression of 0.3 MPa (for which the peak load for the cyclic loading is significantly higher than that for monotonic). However, in general the influence of the lateral precompression on the peak load (and related displacement) is rather limited for the CS specimens, whereas a larger peak forces are measured for clay couplets, probably due to the increased effectiveness of the observed dowel effect.

The values of the displacement at peak vary considerably from test to test. As a general indication, for CS masonry couplets displacements of 10 mm and 2 mm for tensile and compressive loading, respectively, can be considered reasonable reference values. Smaller displacements of 3 mm and 1.5 mm for tensile and compressive loading, respectively, are measured for clay masonry couplets.



Figure 5: Failure mechanisms for Protocol A_{MT} and Protocol A_{MC} (axial loading)

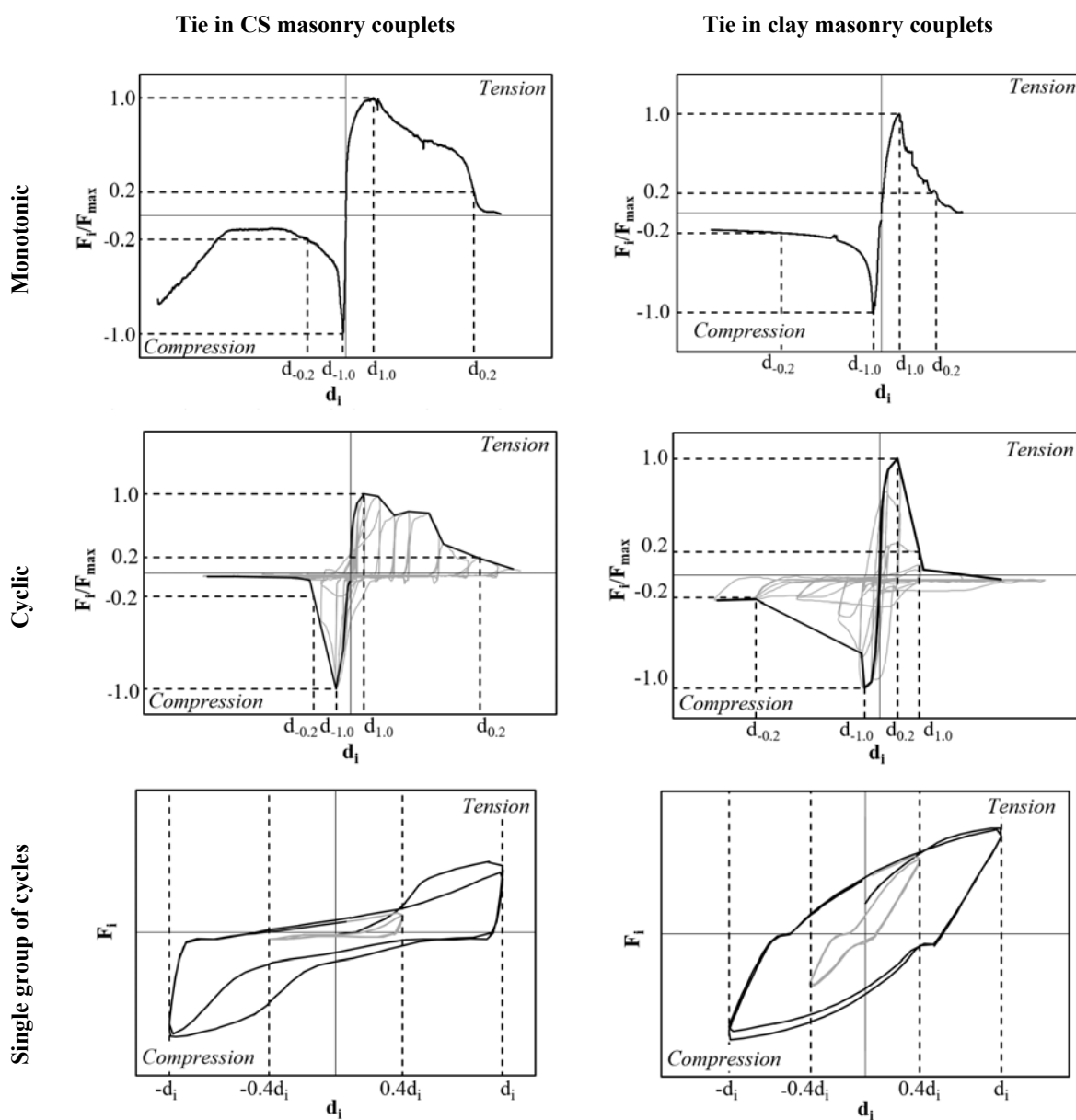


Figure 6: Indicative Force-Displacement curves for the different loading cases (axial tests)

Table 3: Results of axial tests

| Type of bricks | Loading protocol | | Precompression stress [MPa] | Peak force [kN] | Displacement [mm] | | |
|----------------|------------------|---|-----------------------------|-----------------|-------------------|----------------------|----------------------------------|
| | | | | | At peak force | At 20% of peak force | ni/n _{tot} ¹ |
| CS | A _{MT} | | 0.1 | 1.25±0.10 | 10.21±1.65 | 49.77 | 1/6 |
| | | | 0.3 | 1.34±0.14 | 8.44±0.80 | 45.23±5.61 | 12/13 |
| | A _{MC} | | 0.1 | 1.13±0.20 | 1.99±0.71 | 27.19±7.30 | 8/8 |
| | | | 0.3 | 1.04±0.32 | 1.38±1.11 | 30.32 | 1/8 |
| | A _{Cy} | T | 0.1 | 1.06±0.16 | 5.33±1.72 | 48.21±4.92 | 5/9 |
| | | | 0.3 | 0.97±0.08 | 10.54±9.19 | - | 0/6 |
| | | C | 0.1 | 1.05±0.30 | 3.41±1.05 | 12.02±5.43 | 9/9 |
| | | | 0.3 | 0.33±0.22 | 0.96±0.40 | 10.80±8.56 | 5/6 |
| Clay | A _{MT} | | 0.1 | 1.94±0.33 | 2.00±1.51 | 10.02±3.36 | 7/7 |
| | | | 0.3 | 2.35±0.83 | 3.63±2.53 | 13.19±5.52 | 10/10 |
| | A _{MC} | | 0.1 | 1.78±0.28 | 1.69±0.57 | 17.15±4.12 | 7/7 |
| | | | 0.3 | 1.76±0.30 | 1.49±0.59 | 17.77±7.01 | 5/6 |
| | A _{Cy} | T | 0.1 | 1.85±0.79 | 2.31±0.11 | 5.57±1.14 | 2/4 |
| | | | 0.3 | 3.10±0.49 | 6.53±2.67 | 19.52±2.16 | 2/7 |
| | | C | 0.1 | 1.65±0.30 | 1.02±0.59 | 14.60±0.46 | 4/4 |
| | | | 0.3 | 1.43±0.07 | 0.64±0.41 | 14.03±4.75 | 7/7 |

¹The number of specimens that reached this value (n_i) out of the total number of tested specimens for each loading protocol (n_{tot}) is presented since not all of the tests were carried out up to the point where the force reaches the 20% of its peak value.

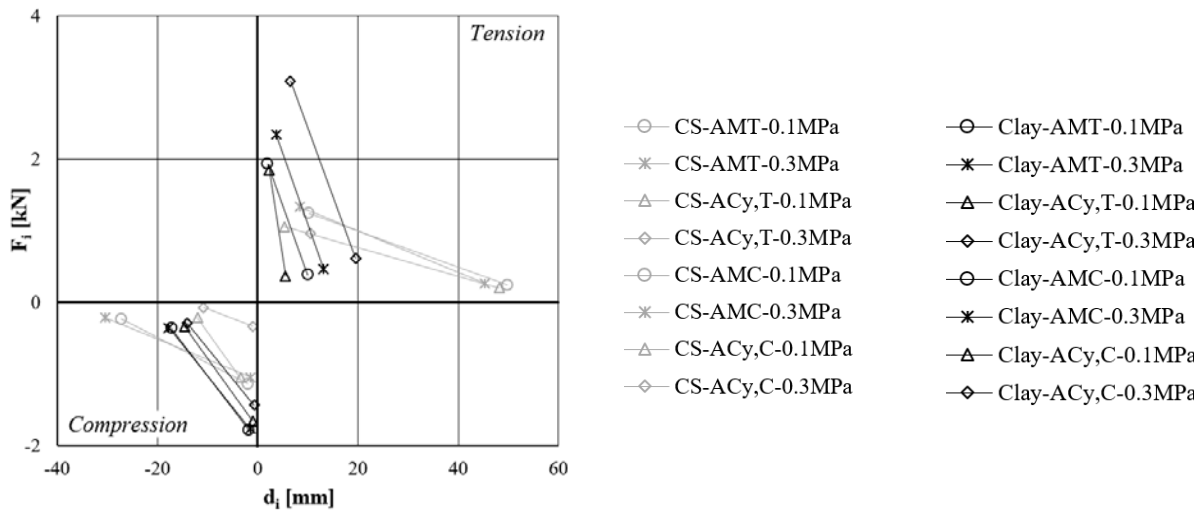


Figure 7: Peak force, 20% of peak force and corresponding displacements for the different loading cases (axial tests)

The results of the shear tests are hereinafter presented. As for the CS couplets, the observed failure mechanism for Protocol S_M was characterized by bending of the tie and often the expulsion of the cone of mortar next to the embedded steel tie. No difference was observed for

the cyclic Protocol S_{Cy} . The same failure mechanism was observed for the clay couplets for both Protocol S_M and Protocol S_{Cy} . An example of the described failure modes is shown in Figure 8.

For large displacements ($d_i \geq 20$ mm), pull-out of the ties was consistently observed, since the applied loading switched from pure shear to a combination of shear and tensile forces. This behaviour is due to the fixed horizontal distance between the clamp and the bricks, and the large imposed vertical displacements of the clamp. To avoid this coupling effect, the horizontal motion of either the specimen or the clamp should be allowed. A simple solution would be given by Teflon sheets between the specimen and the wooden supports: it may be challenging to maintain a constant precompression but the simplicity of this solution makes it noteworthy. Alternatively, the clamp may be redesigned to be free to move along the long axis of the tie. This approach is more complex but it would probably offer greater consistency of the results.

As a result of the discussed coupling effect, the shear resistance of the specimen is evaluated as the applied force for a lateral deflection of the tie of 20 mm, at which the second order effects were negligible in most of the cases. The results presented in the following figures and tables take into account this separation of loading phases. The curves on the left part of Figure 9 depict both the pure shear ($d_i < 20$ mm) and the combined ($d_i \geq 20$ mm) loading conditions. On the right part only the curves for pure shear are presented. The forces presented in Table 4 are those measured at an imposed displacement of 20 mm.

Tie in CS masonry couplets



Tie in clay masonry couplets



Figure 8: Failure mechanisms for Protocol S_M (shear loading)

Table 4: Results of shear tests

| Type of bricks | Loading protocol | Precompression stress [MPa] | Shear force at displacement 20 mm [kN] | |
|----------------|------------------|-----------------------------|--|-----------|
| | | | Upwards | Downwards |
| CS | S_M | 0.1 | 0.15±0.05 | |
| | | 0.3 | 0.09±0.01 | |
| | S_{Cy} | 0.1 | 0.10±0.01 | 0.10±0.02 |
| | | 0.3 | 0.11±0.05 | 0.11±0.03 |
| Clay | S_M | 0.1 | 0.13±0.10 | |
| | | 0.3 | 0.21±0.04 | |
| | S_{Cy} | 0.1 | 0.16±0.07 | 0.10±0.06 |
| | | 0.3 | 0.11±0.02 | 0.12±0.01 |

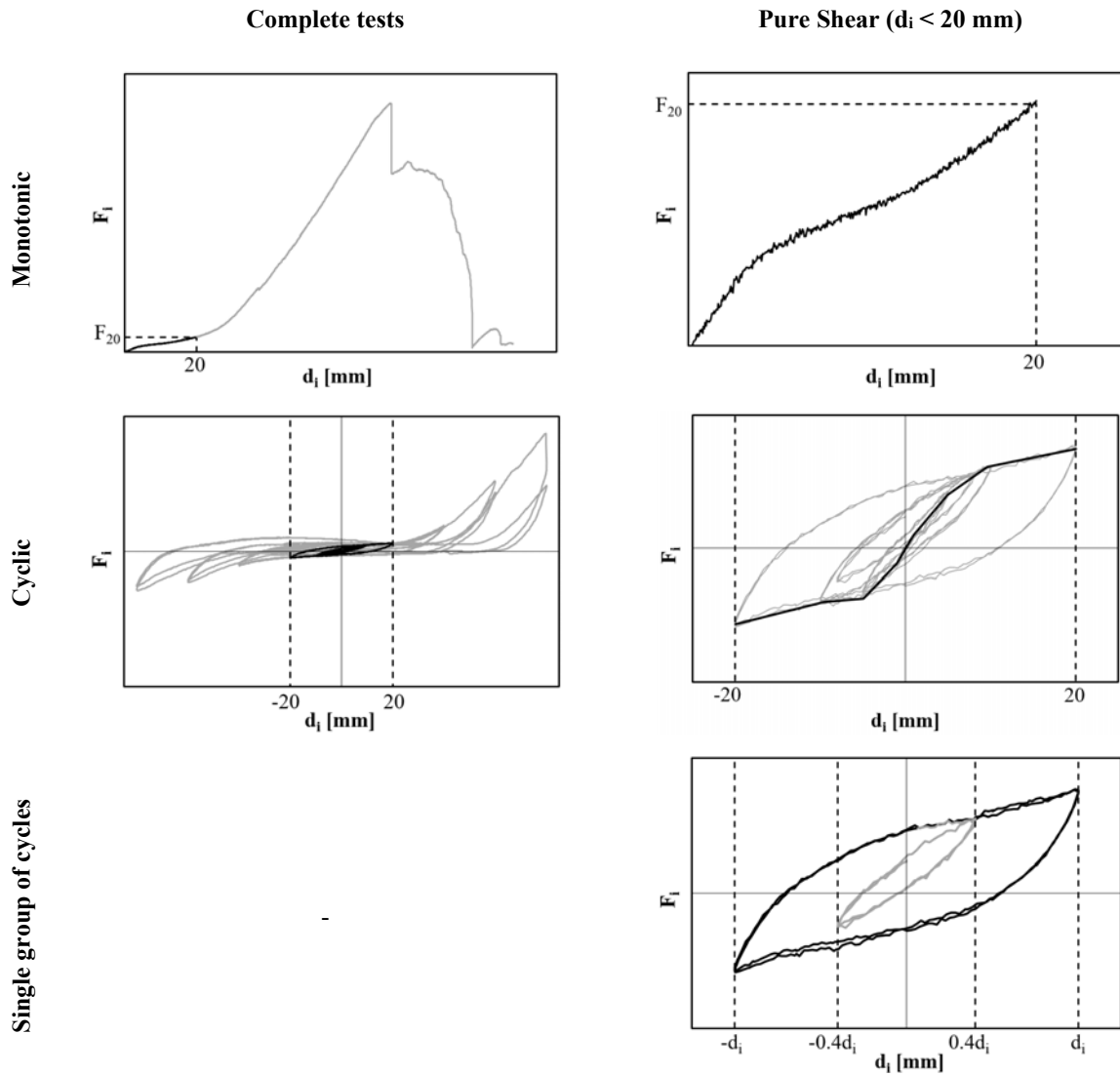


Figure 9: Indicative Force-Displacement curves for the different loading cases (shear tests) on both CS and clay specimens

The shear behaviour of the couplers (Table 4) was much more consistent than the axial (Table 3). Very similar forces were achieved at 20 mm displacement, regardless of the level of precompression and the type of loading (monotonic or cyclic), with clay couplers reaching an almost negligibly larger values. For the monotonic loading, the effect of the orientation of the embedded L-shaped end of the tie in the CS couplers was investigated. No difference was reported in the response of the two different orientations of the tie. The measured shear strength is so small that it can be easily neglected in the design of these connections, and the wall ties can be assumed able to transfer and withstand axial loading only.

CONCLUSIONS

As a part of a large-scale testing program of Delft University of Technology, this study aims at assessing the seismic response of wall tie connections in typical Dutch cavity walls.

Considering the axial tests, the clay couplets presented a more brittle behaviour and higher peak forces compared to the CS specimens. Hence, the embedment of the tie in the CS masonry would overall govern the behaviour of the connection. Cyclic loading determined a slight reduction of the peak load for both materials, while the level of precompression can be considered irrelevant to the behaviour of the connection. The compressive strength of the clay specimens, which is governed by buckling of the tie, may be lower if the tie is originally bent to connect two mortar joints at different heights, as in real walls. However, the overall connection behaviour would probably still be governed by the piercing and the expulsion of the mortar in the CS leaf, since this mechanism is significantly less resistant.

As for the shear tests, very consistent results were obtained for small displacements. The level of precompression did not affect the response of the specimens and the cyclic loading led to results similar to the monotonic. No significant difference was observed between the behaviour of the CS and clay couplets. The outcomes for large imposed displacements were affected by the coupling of axial and shear loading, a factor that should be taken into account for further testing; therefore, a new testing configuration for future campaigns should be considered.

The aforementioned results and conclusions are a first step towards the full comprehension of the seismic behaviour of connections in URM cavity walls, with specific focus to a building typology popular in the Northern part of the Netherlands.

ACKNOWLEDGEMENTS

A major part of this research was funded by NAM under contract numbers UI46268 “Physical testing and modelling – Masonry structures Groningen” and UI63654 “Testing program 2016 for Structural Upgrading of URM Structures”, which is gratefully acknowledged.

The authors are also grateful to master student Matteo Maragna for his assistance in carrying out the experimental work.

REFERENCES

BS EN 6697 (2010), Recommendations for the design of masonry structures to BS EN 1996-1-1 and BS EN 1996-2.

Esposito R., Terwel K.C., Ravenshorst G.J.P., Schipper H.R., Messali F., and Rots J.G. (2017), Cyclic pushover test on an unreinforced masonry structure resembling a typical Dutch terraced house. *Proceedings of 16th World Conference on Earthquake*, January 9-13, Santiago, Chile.

Esposito R., Safari S., Ravenshorst G.J.P., and Rots, J.G. (2018), Characterisation of calcium silicate brick and element masonry structures. *Proceedings of 10th Australasian Masonry Conference*, February 11-14, Sydney, Australia

Giaretton M., Dizhur D., Da Porto F., and Ingham J.M. (2016a), Construction details and observed earthquake performance of unreinforced clay brick masonry cavity-walls, *Structures*, Vol. 6, pp. 159-169

Giaretton M., Dizhur D., and Ingham J.M. (2016b), Shaking table testing of as-built and retrofitted clay brick URM cavity-walls, *Engineering Structures*, 125, pp. 70-79

Graziotti F., Tomassetti U., Penna A., and Magenes G. (2016), Out-of-plane shaking table tests on URM single leaf and cavity walls, *Engineering Structures*, vol. 125, pp. 455-470

Mertens S., Smits A., and Grégoire Y. (2014), Experimental parametric study on the performance of wall ties. *Proceedings of 9th International Masonry Conference*, July 7-9, Guimarães, Portugal

Messali F., Ravenshorst G., Esposito R. and Rots J.G. (2017), Large-scale testing program for the seismic characterization of Dutch masonry structures. *Proceedings of 16th World Conference on Earthquake*, January 9-13, Santiago, Chile.

NEN-EN 845-1 (2016), Specification for ancillary components for masonry - Part 1: Wall ties, tension straps, hangers and brackets, Nederlands Normalisatie-instituut (NEN).

NEN-EN 846-5 (2012), Methods of test for ancillary components for masonry - Part 5: Determination of tensile and compressive load capacity and load displacement characteristics of wall ties (couplet test), Nederlands Normalisatie-instituut (NEN).

NEN-EN 846-7 (2012), Methods of test for ancillary components for masonry - Part 7: Determination of shear load capacity and load displacement characteristics of shear ties and slip ties (couplet test for mortar joint connections), Nederlands Normalisatie-instituut (NEN).

Products, A.B. (2016), "Wall Ties & Restraint Fixings for the Construction Industry," ed, 2016.

Standard A.S.T.M. E2126-11 (2011), Standard Test Methods for Cyclic (Reversed) Load Test for Shear Resistance of Vertical Elements of the Lateral Force Resisting Systems for Buildings," ASTM International, West Conshohocken, PA.

Walsh K.Q., Dizhur D.Y., Shafaei J., Derakhshan H., and Ingham J.M. (2015), In situ out-of-plane testing of unreinforced masonry cavity walls in as-built and improved conditions. *Structures*, Vol. 3, pp. 187-199

CRITICAL REVIEW OF NUMERICAL MODELLING TECHNIQUES FOR SEISMIC RESPONSE OF COMPLEX URM BUILDINGS

K. Ip¹, D. Dizhur², L. Sorrentino³, M.J. Masia⁴; M.C. Griffith⁵ and J.M. Ingham⁶

¹ Master Student, Department of Civil and Environmental Engineering, University of Auckland, New Zealand, cip314@aucklanduni.ac.nz

² Lecturer, Department of Civil and Environmental Engineering, University of Auckland, New Zealand, ddiz001@aucklanduni.ac.nz

³ Assistant Professor, Department of Structural and Geotechnical Engineering, University of Rome, Italy, luigi.sorrentino@uniroma1.it

⁴ Associate Professor, Centre for Infrastructure Performance and Reliability, The University of Newcastle, Callaghan, NSW 2308, Australia, mark.masia@newcastle.edu.au

⁵ Professor, School of Civil, Environmental and Mining Engineering, The University of Adelaide, Australia, michael.griffith@adelaide.edu.au

⁶ Professor, Department of Civil and Environmental Engineering, University of Auckland, New Zealand, j.ingham@auckland.ac.nz

Masonry is a composite material with highly variable and relatively uncertain anisotropic mechanical properties. In contrast to other construction materials such as reinforced concrete and steel, common modelling approaches are not fully applicable to unreinforced masonry (URM) buildings, and serious mistakes can easily be made if practitioners lack fundamental knowledge on how to model the specific characteristic of URM buildings. A New Zealand methodology for the detailed seismic evaluation of simple one- and two-storey URM buildings where extensive numerical modelling is not required, has been published. However, there is currently no New Zealand guidance available to practicing engineers regarding appropriate strategies for the numerical modelling of complex URM buildings. In response to this situation, a literature review was undertaken to summarise appropriate URM modelling techniques and subsequently determine best practices using available resources in the structural engineering industry. Major components of a numerical modelling strategy are first addressed, including modelling methods and analysis procedures, with a focus on modelling complex URM buildings to determine their potential seismic deficiencies. Furthermore, a simplified numerical modelling framework is promulgated as an easy-to-follow guidance for modelling the seismic response of complex URM buildings. A case study of the Basilica of the Sacred Heart in Timaru, New Zealand is used to illustrate the application of URM modelling to an actual project and to provide a technical reference for practicing engineers.

Keywords: unreinforced masonry (URM), New Zealand, finite element (FE), discrete element (DE), basilica.

INTRODUCTION

During the 2010/2011 Canterbury earthquakes in New Zealand, the vulnerability of URM buildings to earthquake-induced shaking was once again highlighted. To minimise the risk posed by these structures, the Building (Earthquake-prone Buildings) Amendment Act 2016 was enacted in New Zealand. This Act identifies existing URM buildings as potentially earthquake-prone unless appropriate seismic strengthening work is undertaken or evidence is provided that demonstrates that a building's structural performance meets a minimum of 34% of the New Building Standard (NBS) requirements. Technical guidelines for engineering assessment of existing URM buildings were also updated to provide practicing engineers with the tools required for assessment (NZSEE 2017). These guidelines are largely aimed at the assessment of simple structural forms and prototypical one- and two-storey URM buildings that are commonly encountered throughout New Zealand. URM buildings with complex structural forms are typically outside the scope of the newly released assessment guidelines, and more sophisticated modelling techniques and strategies are generally required for adequate estimates of expected seismic performance. Large or complex URM buildings comprise approximately 14% of the total URM building stock in New Zealand (Russell and Ingham 2010) and have considerable financial value to owners as well as cultural and historic value to the public. The value of these buildings is one motivation for undertaking a detailed review of the modelling techniques applied to these complex URM buildings.

A new classification is introduced to define the types of URM buildings for the purpose of numerical modelling (refer to Table 1), which is based on the damage classification described by Lagomarsino et al. (2011) that identifies the typical failure mechanisms encountered for URM buildings. The building typology classification proposed by Russell and Ingham (2008) is modified with the focus on large (3+ storey) and complex URM buildings commonly found in New Zealand. For other complex structures outside the scope in this study, such as Roman theatres or Greek temples, it is recommended to refer to a more detailed building classification by Lagomarsino et al. (2011).

Table 1: URM Buildings Classification for Modelling Framework







| Type | Typology | Description | Photo |
|------|------------------------------|---|---|
| I | One- to two-storey buildings | Small scale buildings (individual or row) with regular geometry. Structure behaves as a 'box' in which the damage is mainly governed by in-plane shear loading on walls, although local out-of-plane overturning of walls may occur if adequate wall-to-diaphragm connections are not provided. |  |
| II | Three+ storey buildings | Large scale multi-storey buildings with regular geometry. Structure generally behaves as a 'box' with higher mode response. Damage is governed by in-plane shear and flexure of walls, and out-of-plane overturning of walls. |  |

Table 2: (Continued)

| Type | Typology | Description | Photo |
|------|---------------------------------|--|---|
| III | Institutional buildings | Buildings with large or irregular footprint, large open space or special features. Damage is governed by the in-plane shear and flexure of walls, out-of-plane overturning of walls, and partial collapse of parts (i.e. macroelements). |  |
| IV | Warehouse and factory buildings | Buildings with tall side walls and large open spaces inside. Structure responds locally due to highly flexible diaphragm. Damage is governed by the out-of-plane loaded walls and by the roof. |  |
| V | Churches | Churches with steeples, bell towers or other special features (i.e., dome, triumphal arch, portico, etc.). The failure mechanism is complex and usually consists of partial collapse of parts (i.e., macroelements) and local damage to individual components such as rocking of pillars, instability of arches and falling of roof or dome. |  |
| VI | Slender buildings | Slender buildings (i.e. water towers, chimneys, monument and lighthouses). Damage is governed by bending and shear, which may be preliminarily interpreted by referring to beam theory. |  |

LITERATURE REVIEW OF URM MODELLING STRATEGIES

URM modelling is a complex task due to material anisotropy, nonlinearity and spatially scattered characteristics, as well as large variations of geometries and connection types. As a result of these complexities, a large number of strategies have been proposed in the literature as summarised by Roca et al. (2010) and by Asteris et al. (2015). In the following a synopsis of the literature most relevant for the buildings described in Table 1 is given.

Tomazevic (1978) first proposed a simplified nonlinear analytical model for URM buildings using an equivalent static method. The model assumes that spandrels have infinite strength and stiffness, such that the failure mode is governed by the shear behaviour of piers only, which is similar to a soft-storey failure. Magenes and Della Fontana (1998) improved this basic approach with the introduction of a nonlinear method based on the equivalent frame (EF) idealisation. The EF model considers both piers and spandrels as idealised columns and beams connected by rigid joints. This approach is similar to the analysis method for modern concrete building designs, but the columns and beams are modelled as elastoplastic elements with stiffness and strength degradation corresponding to the constituent materials of the composite masonry. The approach provides a good estimation of the lateral load resistance of URM buildings and a more realistic prediction of the failure mechanism. Brencich et al. (1998) proposed a similar approach to that of the EF method using macroelements instead of

beam elements to model piers and spandrels. As an improvement of EF, the macroelement model includes damage and hysteretic dissipation, which allow a better estimation of dynamic response and the near-collapse mechanism. Recent research by Lagomarsino et al. (2013) further refined the nonlinear macroelement model and introduced several distinctive features in a numerical code named TREMURI, including the implementation of an orthotropic membrane element for the modelling of flexible diaphragms. Nevertheless, this method only addresses the in-plane behaviour of URM walls, similar to other EF approaches. The EF method has been successfully applied to the numerical modelling of multi-storey URM buildings, but these applications remain limited to buildings having a comparatively simple, regular geometry.

Nonlinear finite element (FE) modelling has become more popular in the structural engineering industry following the rapid development of computational power, allowing sophisticated analysis of complex problems. However, the application of complex analysis methods such as FE modelling has been focused mainly on modern building materials such as concrete and steel. Applications in URM modelling remain a challenge due to the complexity of constitutive models for masonry materials. In response to demand for more detailed nonlinear analysis of URM buildings, Lourenço (2002) proposed a micro- and macro-modelling approach for modelling masonry. Macro-modelling, also known as homogenisation, is based on the FE method in which masonry units, mortar, and joints are smeared in an FE continuum. The basic concepts of this modelling approach are similar to those of modelling for concrete, but a special anisotropic material model is assigned for masonry. The micro-modelling approach is divided into two categories—simplified and detailed. In the detailed micro-modelling approach, masonry units and mortar are modelled as an FE continuum, and the unit-mortar interface is modelled as discontinuous elements such as nonlinear springs or interface elements. In the simplified micro-modelling approach, only the masonry unit is modelled as an FE continuum, where the mortar and interface are smeared at the joint, which is represented by a discontinuous element. Lourenço (1996) combined different damage criteria for the masonry joint into a composite interface model, including a cap model for compressive failure, a tension cut-off for tensile failure, and a Coulomb friction envelope for shear failure, which allows cracking and softening of joints to be modelled in the simplified approach. The detailed approach can provide a closer inspection of the mortar damage mechanism, such as crushing and crack propagation.

The concept of discrete element (DE) modelling was first proposed by Cundall and Hart (1971) for the study of rock mechanics, and later extended by Lemos (1995) to the application of masonry modelling. The principal idea of DE is to idealize the masonry as a group of rigid blocks or particles. The interactions between the individual rigid bodies are represented by the constitutive law of contact, which is able to simulate physical phenomenon such as compression (pressure), friction and cohesion at the joints. Furthermore, DE allows full separation between bodies and detects new contacts automatically through the calculation process, thereby being suitable for modelling collapse mechanisms using a simplified micro-modelling approach. Lemos (2007) summarized the DE formulations that can be used in masonry modelling, such as Distinct Element Method (DEM), Discontinuous Deformation Analysis (DDA), Rigid Block (Limit) Analysis, Finite-Discrete method and particle model (i.e. SPH). These methods are a relatively new discipline in numerical analysis, which require significant expertise in order to generate the model and validate the results. The complexity of model preparation and long computational time limit the extent of application. Thus, DE modelling is not yet a practical tool for analysis of an entire complex URM building.

Finite and discrete element approaches can be combined within a general framework as shown by Munjiza (2004). With a focus on the collapse analysis of unreinforced masonry structures, the original taxonomy proposed by Bakeer (2009) can be revised as follows: (1) detailed finite-discrete micro model, (2) simplified finite-discrete micro model, (3) discrete micro model, and (4) finite-discrete macro model. The first and second approaches are based on the detailed and simplified micro-modelling proposed by Lourenço (1996). However, units and mortar (modelled with finite elements) are discrete elements that can slide, separate and come into new contacts. The third approach is equivalent to the discrete element modelling approach, where the units are usually modelled as rigid, and non-linear spring interfaces can be incorporated. The fourth approach has the advantages of both micro- and macro-modelling, as well as finite and discrete element approaches. The masonry is still subdivided into discrete elements, each being a homogenised continuum, but every discrete element models several units and joints (AlShawa et al. 2017). Thus, model preparation is significantly simplified without the need to model the masonry pattern and units explicitly. In addition, the computational effort is greatly reduced and it is thus feasible to apply the finite-discrete macro modelling approach to the whole building. Although crack formation cannot be captured in detail, damage and separation of structural components can be modelled such that collapse analysis is achievable on a whole building scale.

The macroblock approach using limit analysis (Heyman 1966) is a simplified approach to simulate the discretized behaviour in masonry structures. The masonry units are assumed as rigid with infinite strength and no tension or sliding is allowed at the joints, such that the structure can be analysed at equilibrium or in the kinematic state using linear programming techniques. In contrast to conventional modelling techniques, the estimated performance (i.e., safety factor) is based on a predefined collapse mechanism. Thus, the accuracy of the macroblock approach is dependent on engineer's experience and the database of damage patterns for similar masonry structures (Sorrentino et al. 2017).

SIMPLIFIED NUMERICAL MODELLING FRAMEWORK

The previous section briefly discussed the concepts of different URM modelling approaches. However, the capabilities, limitations, and complexities of these methods are difficult to capture in real-world applications, particularly for the modelling the seismic response of URM buildings. Furthermore, the differences in the discussed approaches are not evident without thoroughly examining the details and theories behind the individual approaches. To provide clear guidance to practitioners, a systematic framework is proposed to summarise these URM modelling approaches and corresponding practical applications.

The concept behind the proposed framework is the breakdown of previously outlined approaches into fundamental components, including the modelling approach and analysis methods, presented in an easy-to-follow framework (refer to Table 2). The proposed simplified framework is linked to the URM buildings typology in Table 1. Some of the combinations are voided because they are either irrelevant or not recommended. The matrix allows practitioners to quickly identify suitable strategies for different URM modelling purposes and the corresponding complexities, so that cost-effectiveness can be evaluated at an early stage. It is emphasised that this modelling framework mainly focuses on URM buildings in New Zealand. For application to other types of structures, Lagomarsino and Cattari (2015) developed the PERPETUATE guidelines which provide recommendations of modelling strategies for a broader range of architectural assets in Europe.

Table 3: Proposed Simplified Numerical Modelling Framework

| URM Typologies | | Modelling Approach | | | | |
|------------------|---------------------------|----------------------------|--|--|--|--|
| | | Equivalent Frame (EF) | Finite Element (FE) | Finite-Discrete Element (FDE) | Discrete Element (DE) | Macroblock (MB) |
| Analysis Methods | Linear Equivalent Static | I | I | | | |
| | Modal Response Spectrum | II, III, VI | II, III, VI | | | |
| | Static Nonlinear Pushover | <u>I</u> , II, III, VI | I, II, III, <u>IV</u> , <u>V</u> , VI | I, II, <u>III</u> , <u>IV</u> , <u>V</u> , VI | III, IV, <u>V</u> FOR LOCAL MECHANISM | |
| | Nonlinear Time History | <u>II</u> , III, <u>VI</u> | I, <u>II</u> , <u>III</u> , <u>IV</u> , <u>V</u> , <u>VI</u> | I, II, <u>III</u> , <u>IV</u> , <u>V</u> , <u>VI</u> | III, IV, <u>V</u> FOR LOCAL MECHANISM | |
| | Kinematic Limit Analysis | | | | | <u>I</u> , <u>II</u> , <u>III</u> , <u>IV</u> , <u>V</u> , VI FOR LOCAL MECHANISM |

* The recommended strategies are highlighted in green.

Suitable to model collapse mechanism

The recommended strategies for modelling large and complex URM buildings (Types II through VI) are highlighted in the table in green. The macroblock approach using limit analysis is always recommended to verify the local failure mechanism of the buildings, and in particular for structures without box behaviour, complementary to global analysis. The strategies for modelling a Type I building are also included in the table for completeness. The discussion of the recommended strategies for each typologies are provided below:

- **Type I**

Simple hand calculation (i.e., in-plane and axial capacity of piers) with the supplementary procedure being the macroelement approach (i.e., out-of-plane capacity) is normally sufficient for the assessment of one to two-storey URM buildings. Using linear equivalent static or modal response spectrum analysis to limit the member capacity within the elastic or limiting stress range is possible, but is not recommended because the global capacity of such buildings is significantly underestimated. For performance based assessment, nonlinear pushover using equivalent frame is recommended to allow stress redistribution.

- **Type II**

The equivalent frame approach is recommended to model the global (in-plane) failure mechanism (i.e., backbone curve) of large multi-storey URM buildings with regular

geometry and box behaviour. The finite element macro modelling approach is also practical but may not be the most cost-effective solution, and is only recommended if it is necessary to capture the out-of-plane damage. Static nonlinear pushover analysis is feasible and easy to perform but may not be able to correctly simulate the higher mode response, even if modal pushover is used (Lourenço et al. 2011). Nonlinear time-history analysis will give the best estimation for nonlinear dynamic response, but is computationally more expensive and requires the selection of appropriate records. In general, the application of EF to building assessment is relatively simple and can be completed using many commercial software packages available in the industry. Standard analysis methodology and verification procedures can be adopted for this basic level of modelling. Materials test may be required for model calibration.

- **Type III**

The finite element macro-modelling approach is recommended for multi-storey buildings with slender walls, large open spaces (without diaphragm), or some special features attached such as a tower or portico in which the equivalent frame may not be a suitable tool to model the out-of-plane or local response. The FE method with nonlinear time history analysis is suitable for modelling complex geometry, nonlinear local response (i.e., out-of-plane), nonlinear dynamic response (i.e., higher mode effect), and damage patterns (i.e., cracks). The finite-discrete element approach may provide extra information on the global post-peak collapse mechanism but may not be the most cost-effective solution. The macroblock approach shall also be used to verify the local failure or collapse of parts. Application of the FE approach to building assessment requires experienced engineers who are familiar with the features and constitutive laws of material models in specific software packages. A comprehensive analysis methodology, verification procedure, and materials test for model calibration are essential for this detailed level of modelling.

- **Type IV**

The finite element macro-modelling approach is recommended for buildings with tall side walls and large open spaces inside. Nonlinear static pushover analysis can capture the seismic response of both in-plane and out-of-plane loaded walls. The macroblock approach shall also be used to verify the local failure or collapse of parts. Application of the FE approach to building assessment requires experienced engineers who are familiar with the features and constitutive laws of material models in specific software packages. Planning and verification procedure are similar to Type III buildings.

- **Type V**

A finite-discrete macro-modelling approach is recommended to model the seismic response up to collapse of church buildings with steeples, bell towers or other special features. The combined finite-discrete element method is able to capture the crack pattern within the elements as well as the mechanical interaction at joints and connections. Typically, a church consists of different parts that respond to earthquakes independently due to poor connections and the absence of a rigid diaphragm, in which the capacity of the building cannot be represented by global performance. Multiple capacity curves are required to identify the seismic performance of each of the major parts or macroelements (i.e., tower, dome, etc.) when static pushover analysis is used.

Nonlinear time history analysis should give the most accurate assessment because the nonlinear dynamic response, in particular the rocking at joints and kinematic instability, can be modelled explicitly and transformation to a single degree of freedom is not required. However, it may be a challenge to obtain a sufficient number of suitable ground motions that match the dynamic characteristic of different parts of the church. The macroblock approach can be used to systematically verify the failure of each local macroelement. The discrete element micro-modelling approach can be considered as a verification of the macroelement capacity and collapse mechanism. Application of the FDE approach to building assessment requires experienced engineers and specialists to carry out the numerical analysis using advanced software with appropriate constitutive laws of material models and discrete interfaces (i.e., contacts). A specific analysis methodology, verification procedure, and materials tests for model calibration are mandatory for this advanced level of modelling.

- **Type VI**

The equivalent frame and finite element macro-modelling approaches are recommended for slender buildings for which the structural behaviour and damage are governed by bending and shear, which may be preliminarily interpreted by referring to beam theory and more thoroughly to FE. As the higher mode effect is significant for slender buildings, nonlinear time history shall be used for the assessment. Pushover analysis may underestimate the dynamic amplification at higher levels even if modal pushover is used (Lourenço et al. 2011). Planning and verification procedures are similar to those for Type III buildings.

CASE STUDY BUILDING

The Basilica of the Sacred Heart in Timaru, New Zealand was selected as a case study to apply the proposed simplified numerical modelling framework for complex URM churches. For other examples of modelling of churches, interested readers can refer to Endo et al. (2015) and Pantò et al. (2016). The building was constructed in the early 1900s and was listed as a Category 1 heritage building in 1985. Figures 1 and 2 show external and internal views of the Basilica. The scope of the assessment, performed by the first author when working for Opus International Consultants, includes determining the seismic resistance capacity of the Basilica according to the New Zealand procedure to assess the percentage of New Building Strength (%NBS). The structural performance and potential risk of collapse under earthquake loadings are also of interest. An overview of the strategy selection, methodology development, modelling application, and outcomes are provided as a demonstration of the modelling framework.

The Basilica has a typical Latin cross plan with a long main nave along with two lateral transepts and a semi-circular apse comprising the body of the church. At the end of the main nave, three connected rectangular rooms constitute the narthex, with bell towers flanking each side. The building was not designed for seismic resistance and is constructed mainly of URM. The lateral load-resisting system is difficult to identify, and is mainly governed by multi-leaf walls on the perimeter, which consist of three layers: an external layer of clay brick or limestone, unreinforced concrete infill, and a layer of clay brick or limestone on the interior. The walls are typically 900 mm thick at the piers, and approximately 500 mm thick between the piers. The free-standing height of the nave and transept walls from the ground to the roof

is approximately 12 m. The joints between structural components such as columns and spandrel beams are nonhomogeneous as they have a layer of mortar in the interface but are unreinforced. This construction detail allows rocking and sliding at the joints as well as at the foundation. The local stability of the nave, portico, and arch under dynamic loads is uncertain.



Figure 1: External View of Basilica of the Sacred Heart - Main Entrance



Figure 2: Internal View of Basilica of the Sacred Heart - Nave and Arch

The topology of the Basilica is classified as Type V based on its complex geometry. A wide range of modelling strategies are available for this type of building, as indicated in Table 2. The objectives and challenges of modelling the Basilica are listed below:

- Seismic assessment for the whole building, including local failure.
- Collapse mechanism identification.
- Complex geometry representation, including three-dimensional vault arches for supporting the dome.
- Multi-layer URM construction modelling.
- Mechanical interactions between components (i.e., rocking and sliding) modelling.

Judgement based on experience and cost-effectiveness is required to determine which approach should be adopted. Although the finite element macro-modelling approach is also practical, the combined finite-discrete element approach was chosen for modelling the collapse mechanism of this complex structure on a global scale. For the case study, a solid element was chosen to ensure a good representation of the building's complex geometry in three-dimensions that allows modelling of the actual mechanical interactions between components. Nonlinear pushover analysis was adopted to model the global and local collapse mechanisms for the whole structure. The identified local failure modes were verified by using the macroblock approach, although the details are not covered in this study.

The methodology adopted in the analysis was to individually model the structural components (i.e., columns, spandrels, walls) using macro models and to apply a contact surface between components such as joint interfaces, pre-existing cracks, weak planes, and supports. The smeared crack material model was used to simulate cracks and damage in the structural components. Contact surfaces were used to model element separation, rocking, sliding, and building collapse. This approach provided a powerful and cost-effective solution. The mortar has similar compressive and tensile strengths to the masonry units and thus an isotropic material was considered to further simplify the modelling procedure. A well-established smeared crack model, the Winfrith Concrete Model (Schwer 2011), was used to model the

stone and concrete layers. Stable and reliable contact algorithms (i.e., tiebreak, surface-to-surface) were used to model friction, cohesion, and energy dissipation in joint interfaces.

A three-dimensional CAD model was generated based on the point cloud obtained from site survey data collected from a laser scan. The geometry was then simplified and optimised by removing all unnecessary features. Modelling the thickness of multi-leaf walls is based on the existing drawings. Detailed FE meshing was carried out based on the simplified geometry. It took the first author four weeks to complete the entire process, including converting the point cloud to a meshed analytical model. Figure 3 shows the procedure.

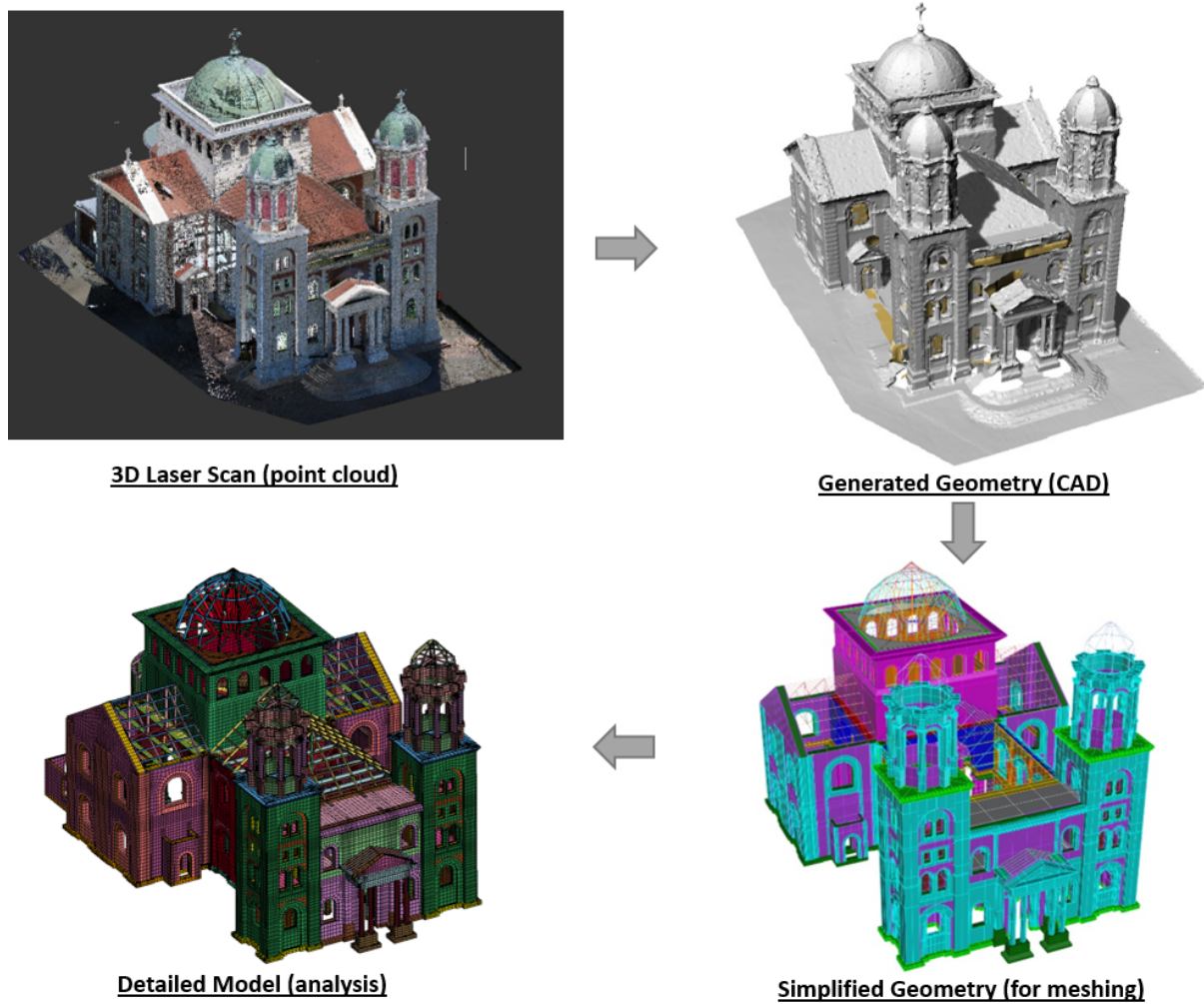


Figure 3: Procedures for Modelling the Complex Geometry of the Basilica

An explicit FE code package, LS-DYNA, was used for the numerical modelling. The major geometry was modelled with eight-node brick elements. The contact surfaces were modelled with a coefficient of friction of 0.75 (i.e., rock to rock) and an intentionally conservative zero tensile strength was assigned to the nonhomogeneous connections to model the separation of joints and capture the friction, rocking, and energy dissipation in the interface. The mesh was more refined in areas with contacts or a higher stress gradient to provide better and more stable contacts. A coarser mesh was used in other areas to reduce the total number of elements. For the less complex roof and slabs inside the sanctuary and bell towers, integrated beams and layered shell elements were used. The lateral load was simulated by applying a horizontal acceleration to the structure using nonlinear pushover analysis such that the load

distribution was proportional to the mass. Acceleration was slowly increased using a ramp function to achieve a quasi-static condition to avoid premature failure and local instability. The pushover curve showed that the existing Basilica is a brittle structure with little or no ductility. Two different assessment approaches—performance-based and code-based—were adopted to determine the capacity of the Basilica. For the purpose of conciseness, only the capacity curve of the nave walls is shown in Figure 4, with multiple capacity curves being used to assess other parts such as bell towers, dome, transepts, etc.

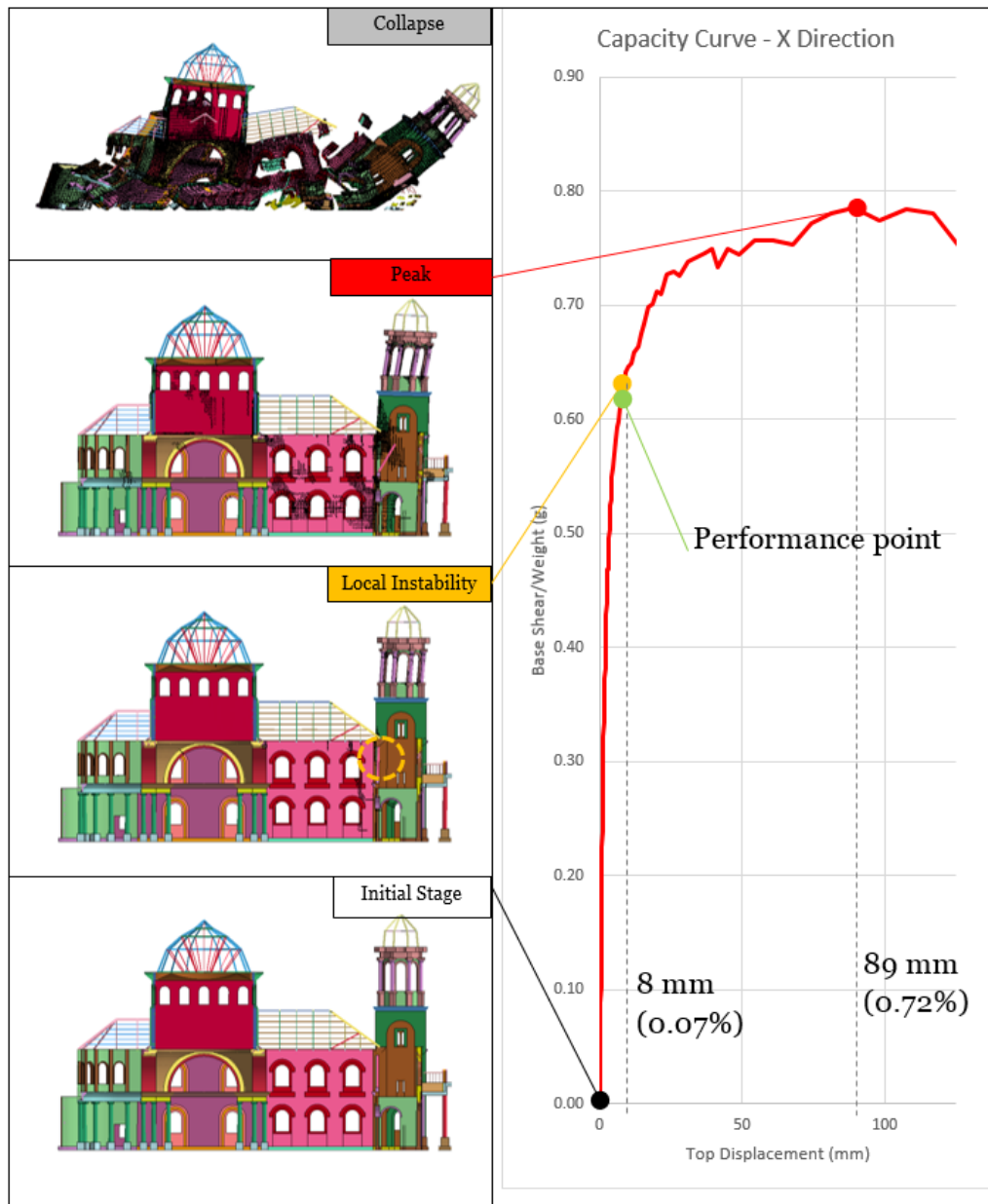


Figure 4: Capacity curve X-direction (Nave walls only)

The structural weaknesses of the system were identified by observing localized damage, stability, and failure modes through pushover analysis. Local failure and risks were identified in the model, such as instability of the stone columns under lateral loads and gable wall failed out-of-plane, which have a potential risk of collapse. These local failure modes were further

verified by application of the macroblock approach using limit analysis. Figure 5 shows the local failure modes of the bell tower.

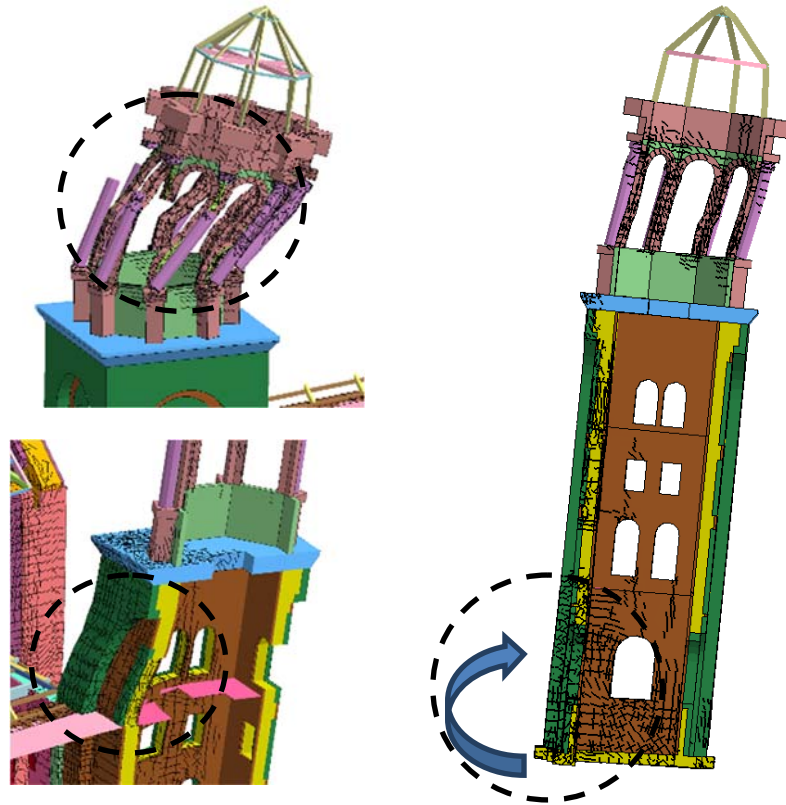


Figure 5: Local Failure and Instability of the Bell Tower

CONCLUSIONS

A critical review of the numerical modelling approaches for complex URM buildings was undertaken. A summary is provided of the practical methods developed in academia and applied in the structural engineering industry. The proposed simplified numerical modelling framework breaks down these approaches into fundamental components, including modelling approach and analysis methods, and is then presented in an easy-to-follow framework, which is linked to the URM building typologies in New Zealand. This framework enables practitioners to quickly identify appropriate modelling strategies and cost-effective solutions for URM modelling for various different purposes.

A case study of the Basilica of the Sacred Heart in Timaru, New Zealand was chosen to demonstrate application of the proposed simplified numerical modelling framework for complex URM buildings. The results show that the proposed framework is a user-friendly guideline that allows practitioners to explore a range of approaches for modelling a URM building (i.e., the Basilica) with complex geometry. An overview of the application, including the modelling methodology, geometry modelling, summary of the analytical model and analysis results, are provided as examples to illustrate the modelling procedures involved in assessment. This information serves as a reference for practitioners to evaluate the most cost-effective modelling approaches for similar URM buildings.

The proposed framework represents the best practices available in the engineering industry. This system can be further developed when it is applied in other projects with different

typologies. The future development of this framework will provide additional information and guidance to quantify the associated time and cost for projects at the preliminary stage.

ACKNOWLEDGEMENTS

The authors would like to acknowledge Opus International Consultants for providing information about the Basilica of the Sacred Heart in Timaru used in this study.

REFERENCES

- AlShawa O., Sorrentino L., & Liberatore D. (2017). Simulation Of Shake Table Tests on Out-of-Plane Masonry Buildings. Part (II): Combined Finite-Discrete Elements. *International Journal of Architectural Heritage*, 11(1), 79–93.
- Asteris P. G., Plevris V., Sarhosis V., Papaloizou L., Mohebkah A., & Komodromos P. (2015). Numerical modeling of historic masonry structures. In *Handbook of Research on Seismic Assessment and Rehabilitation of Historic Structures*, pp. 213–256.
- Bakeer T. (2009). Collapse analysis of masonry structures under earthquake actions, Ph.D. Thesis, Technische Universität Dresden.
- Brencich A., Gambarotta L. and Lagomarsino S. (1998). A macroelement approach to the three-dimensional seismic analysis of masonry buildings, 11th European Conference on Earthquake Engineering, Balkema, Rotterdam.
- Cundall P.A. and Hart P. (1971). A computer model for simulating progressive large scale movements in blocky rock systems, *Proc. of the symposium of the int. society of rock mechanics*, Nancy, France.
- Endo, Y., L. Pelà, P. Roca, F. da Porto, and C. Modena. 2015. “Comparison of Seismic Analysis Methods Applied to a Historical Church Struck by 2009 L’Aquila Earthquake.” *Bulletin of Earthquake Engineering* 13 (12): 3749–3778.
- Heyman J. (1966). The stone skeleton, *Int J Solids Struct*, 2 (2):249–79.
- Lagomarsino S, Abbas N, Calderini C, Cattari S, Rossi M. Ginanni Corradini R, Marghella G, Mattolin F, Piovanello V (2011). Classification of cultural heritage assets and seismic damage variables for the identification of performance levels. In: *Proceedings of 12th international conference on structural studies, repairs and maintenance of heritage architecture*, 5–7 September 2011, Chianciano Terme (Italy), WIT Trans Built Environ, vol. 118, pp 697–708.
- Lagomarsino S., Penna A., Galasco A. and Cattari S. (2013). TREMURI program: An equivalent frame model for the nonlinear seismic analysis of masonry buildings, *Engineering Structures*, 56, 1787–1799.
- Lagomarsino S., Cattari S. (2015). PERPETUATE guidelines for seismic performance-based assessment of cultural heritage masonry structures, *Bulletin of Earthquake Engineering*, 13 (1), pp. 13-47.

- Lemos J.V. (1995). Assessment of the ultimate load of a masonry arch using discrete elements, In J. Middleton & G. N. Pande (Eds.), *Computer Methods in Structural Masonry* – 3 (pp. 294–302). Swansea, UK: Books and Journals International.
- Lemos J.V. (2007). Discrete Element Modeling of Masonry Structures, *International Journal of Architectural Heritage*, 1:2, 190-213.
- Lourenço P.B. (1996). Computational strategies for masonry structures, Ph.D. Thesis, Delft University of Technology.
- Lourenço P.B. (2002). Computations on historic masonry structures. *Progress in Structural Engineering and Materials*, 4(3): 301–319.
- Lourenço P.B., Mendes N., Ramos L.F. and Oliveira D.V. (2011). Analysis of Masonry Structures Without Box Behavior, *International Journal of Architectural Heritage*, 5:4-5, 369-382.
- Magenes G. and Della Fontana A. (1998). Simplified non-linear seismic analysis of masonry buildings, Fifth International Masonry Conference, London, England.
- Munjiza A. (2004). *The combined finite-discrete element method*. Chichester: Wiley.
- NZSEE (2017). *The Seismic Assessment of Existing Buildings: Technical Guidelines for Engineering Assessments. Section C8 – Unreinforced Masonry Buildings*. Wellington, New Zealand: Co-ordinated by a Project Technical Group on behalf of NZSEE, SESOC, NZGS, MBIE and EQC. www.eq-assess.org.nz/new-home/part-c/c8/.
- Pantò, B., F. Cannizzaro, S. Caddemi, and I. Calì. 2016. “3D Macro-Element Modelling Approach for Seismic Assessment of Historical Masonry Churches.” *Advances in Engineering Software* 97: 40–59.
- Russell A. P. and Ingham J. M. (2008). Architectural Trends in the Characterisation of Unreinforced Masonry in New Zealand, 14th International Brick and Block Masonry Conference (14IBMAC), Sydney, Australia.
- Russell A. P. and Ingham J. M. (2010). Prevalence of New Zealand’s Unreinforced Masonry Buildings, *Bulletin of the New Zealand Society for Earthquake Engineering*, Vol. 43, No. 3, 182-201.
- Schwer L. (2011). The Winfrith Concrete Model: Beauty or Beast? Insights into the Winfrith Concrete Model, 8th European LS-DYNA Users Conference, Strasbourg, France.
- Sorrentino L., D’Ayala D., de Felice G., Griffith M.C., Lagomarsino S., Magenes G. (2017). Review of Out-of-Plane Seismic Assessment Techniques Applied To Existing Masonry Buildings, *International Journal of Architectural Heritage*, 11 (1), pp. 2-21.
- Tomazevic M. (1978). *The Computer Program POR; Report ZRMK*, Ljubljana, Slovenia. (in Slovene).

PEAK FLOOR ACCELERATIONS IN UNREINFORCED MASONRY BUILDINGS WITH FLEXIBLE DIAPHRAGMS

**H. Derakhshan¹, Y. Nakamura², H. Goldsworthy³, K.Q. Walsh⁴, J.M. Ingham⁵ and
M.C. Griffith⁶**

¹ Research Associate, School of Civil, Environmental and Mining Engineering, The University of Adelaide, 5005
Adelaide, Australia, hossein.derakhshan@adelaide.edu.au

² Structural Engineer, WSP Australia Pty Limited, Adelaide, Australia, Yasuto.Nakamura@wsp.com

³ Assoc. Professor, Melbourne School of Engineering, University of Melbourne, helenmg@unimelb.edu.au

⁴ Frost Engineering and Consulting, Mishawaka, Indiana, United States, kwash@frosteng.net

⁵ Professor, Department of Civil and Environmental Engineering, The University of Auckland, Auckland, New
Zealand, j.ingham@auckland.ac.nz

⁶ Professor, School of Civil, Environmental and Mining Engineering, The University of Adelaide, Adelaide,
Australia, michael.griffith@adelaide.edu.au

The non-structural components in buildings are often subject to greater earthquake accelerations than that of the ground. This acceleration amplification is due to the building's main lateral resisting system being subject to additional 'relative' accelerations as they deform when subjected to ground motion. Floor accelerations can be conservatively estimated using linear dynamic analysis, however even relatively simple modal analysis for buildings with flexible floor(s)/roof is often impractical. A simple modal analysis is proposed that is based upon the assumption of two vibration modes for the buildings, one being the first building mode if the diaphragm vibrations are excluded and the other being a diaphragm-related mode. These modal properties are simple to calculate and the results from the proposed method has practical value. For the evaluation of the method, parametric nonlinear time-history analyses were conducted on four building typologies with diaphragm flexibility being taken as a variable. Results show that significant increase in floor accelerations can occur due to the diaphragm vibrations, and that most of this increase can be captured by the proposed method.

Keywords: *unreinforced, masonry, accelerations, nonstructural, flexible, diaphragms*

INTRODUCTION

Excluding buildings having a very long fundamental period, the non-structural components within a building are typically subjected to greater earthquake accelerations than that of the ground due to the ‘relative’ accelerations within the building. Different approaches to the quantification of this acceleration amplification exist in the earthquake engineering literature. These methods include response spectrum analysis, e.g. Pozzi and Kiureghian (2015) and Miranda and Taghavi (2005), simple analytical formulations, e.g. Menon and Magenes (2011), and many studies using time-history analysis conducted on multi-degree-of-freedom (MDOF) systems, e.g. Shelton (2004).

Simple methods that preclude the need for complex analyses have been codified in various countries. For example, Eurocode 8 (CEN 2004), the New Zealand code NZS 1170.5 (NZS 2004), and the Australian code AS 1170.4 (AS 2007) all propose, with some exclusions, a linear increase in ‘peak floor acceleration’ (PFA) with building height, being a relationship that presumably reflects the first mode. The MDOF study by Shelton (2004) formed the basis for the methods in AS 1170.4 and NZS 1170.5 (NZS 2004) and included dynamic analyses of medium to high-rise (3 to 20 storeys) on RC and steel buildings with a ductility ranging from 3 to 6. It is clear that these properties do not match URM building properties that may include floor flexibility.

Previous experimental studies (Tena-Colunga and Abrams 1992; Costely and Abrams 1995) have reported increased building acceleration response due to the diaphragm flexibility. The timber diaphragms that are present in many of the older turn-of-the-century URM buildings are known (ASCE 2014) to have insignificant in-plane stiffness. The connected URM walls also lack considerable out-of-plane stiffness such that their mass can be assumed to be effectively lumped on the diaphragm edges. Therefore, it is realistic to assume that the earthquake response of these buildings is characterised by relatively longer-period vibrations of diaphragms within a relatively rigid URM shear wall response. The analysis of these buildings cannot be undertaken by following codified approaches, and the development of an alternative simple approach is necessary.

In a related subject, floor response spectra (FRS) that draws from building modal responses and also includes dynamic amplifications for the component response have been calculated. An example of these spectra is Equation (1) from Curti (2007) as referenced in Abbati (2016):

$$S_{az,k}(T) = \frac{PFA_k}{\sqrt{\left[1 - \left(\frac{T}{T_k}\right)^\alpha\right]^2 + A_1 \left(\frac{T}{T_k}\right)^\alpha}} \quad (1)$$

where PFA_k can be calculated using standard modal analysis from Equation 2:

$$PFA_k = \varphi_k \frac{L_k}{M_k} S_a(T_k) \quad (2)$$

The above equations have been written for the k^{th} mode of the building response and produce the spectral acceleration at the component period of T , i.e. $S_{az,k}(T)$. In these equations, PFA_k stands for the PFA in mode k , T_k is the building period at mode k , α is a spectral shape coefficient, A_1 is a damping-dependent factor, φ_k is the mode shape, L_k is the modal participation, M_k is the modal mass, and finally $S_a(T_k)$ is the building spectral acceleration at the modal period T_k . The

coefficients α and A_I were obtained in Lagomarsino (2015) for three ranges of T vs. T_k , and it was suggested to combine modal responses, i.e. $S_{az,k}(T)$, as an algebraic sum to obtain total component acceleration response, $S_{az}(T)$. A condition was imposed so that the sum is greater than the part acceleration response if subjected to unfiltered ground motion, i.e. $S_a(T)$. The sub-indices z in modal response $S_{az,k}(T)$ and total response $S_{az}(T)$ are to differentiate between the response of an elevated component subjected to filtered motions and the response assuming unfiltered motion.

Calculation of PFA for a building with flexible diaphragm requires computer analysis and can be impractical from many projects. Additionally, the PFA can also be significantly underestimated if only the first mode properties are used. It was the goal of this research to develop a simple method to estimate PFA (Equation 2) for low-rise URM buildings with flexible diaphragms. The calculation of $S_{az}(T)$ using the results from the proposed simple modal analysis, i.e. Equation 1, is beyond the scope of the current research but will be investigated later.

CASE STUDY BUILDINGS

The studied buildings and the schematics of wall numerical models are illustrated in Figure 1. The buildings are symmetrical in Direction 2, for which analyses were performed. The used computer software is Tremuri (Lagomarsino et al. 2013) that is capable of modelling failure mechanism of in-plane loaded URM walls. One of the limitations of the software is that the stiffness of the out-of-plane loaded walls are ignored and their mass is directly applied to in-plane loaded walls. However, the software can be used to study in-plane vibrations of the flexible floors by following an approach suggested by Nakamura et al. (2017).

Relatively smaller values of masonry Young's modulus and compressive strength (Table 1) were assumed, representing older URM buildings. Two other material data inputs for Tremuri are macro-element average cohesion and friction properties that depend on the dimensions of the individual piers and spandrels. These parameters were selected such that a mixed shear and rocking failure could occur in the buildings, with the obtained hysteresis behaviour being shown in Figure 2. A density of 1900 kg/m³ for masonry, a floor dead load of 1.8 kPa, a roof dead load of 1.5 kPa, and a reduced uniform floor live load of 1.2 kPa (including a seismic live load factor of 0.3 in accordance with AS 1170.1) were assumed.

LATERAL FORCE-DISPLACEMENT RESPONSE AND SDOF IDEALISATION

The building behavioural data (Figure 2) were obtained from pushover analyses of buildings with rigid diaphragm(s), with the control node being at the roof mid-span. The bilinear plateau force (H_u) was assumed to be equal to 0.85 time the maximum recorded strength. The initial stiffness was obtained by connecting the origin to a point on the backbone curve that corresponds to $0.75H_u$. The ultimate displacement corresponds to a reduction of 20% in the maximum recorded strength. These bilinear properties are summarised in Table 2. It is noted that irrespective of the building symmetry, the pushover curves in + and – directions are slightly different due to progressive URM damage. Both the bilinear models and the values in Table 2 correspond to loading in the + direction. Significant modal periods and corresponding effective mass ratios are detailed in Table 2. For three

of the buildings the effective mass ratio for the first mode is greater than 91%, but 2 modes were included in Table 2 for Building 4.

Table 1. Masonry material properties

| Young's modulus | Shear modulus | Compressive strength | cohesion | Friction coefficient |
|-----------------|---------------|----------------------|-----------|----------------------|
| 1385 MPa | 740 MPa | 5.74 MPa | 0.130 MPa | 0.111 |

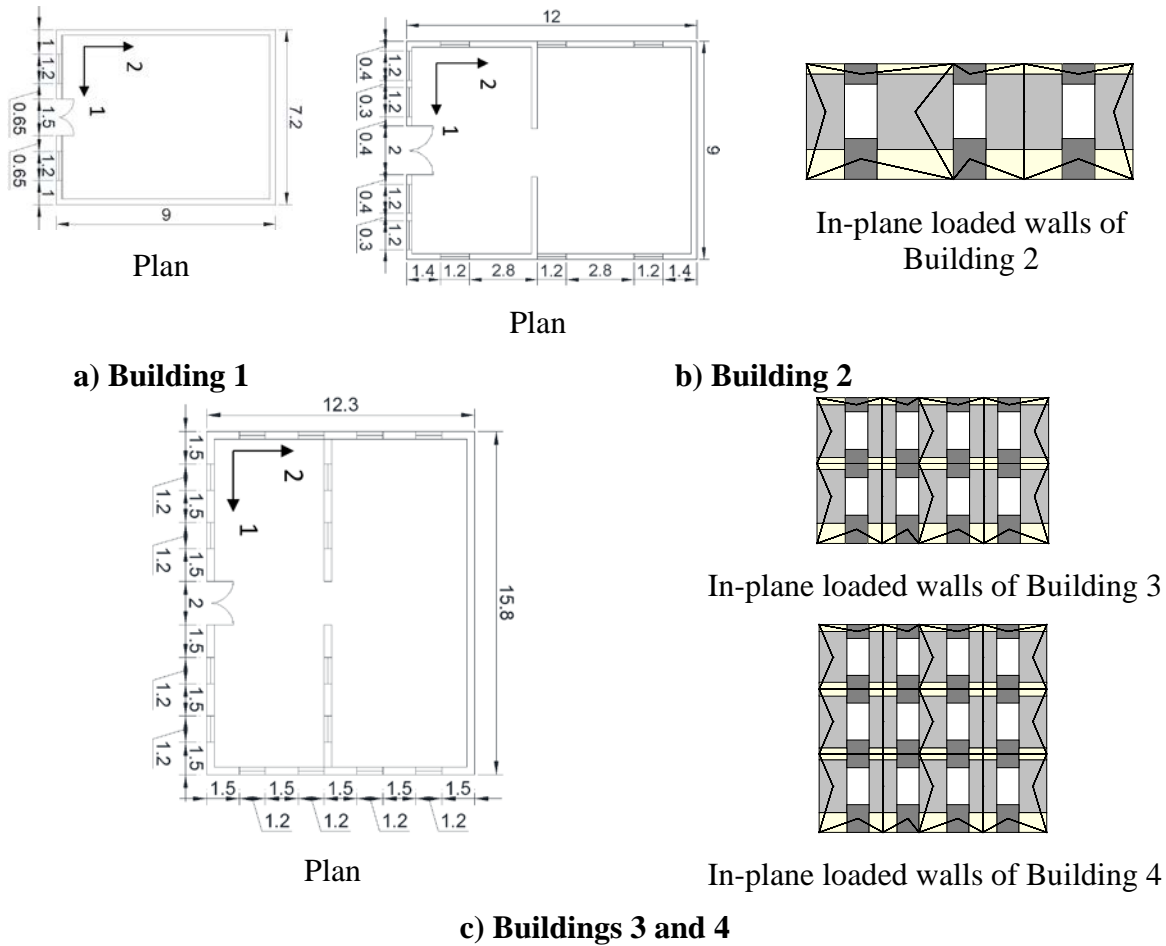


Figure 1: Case study buildings

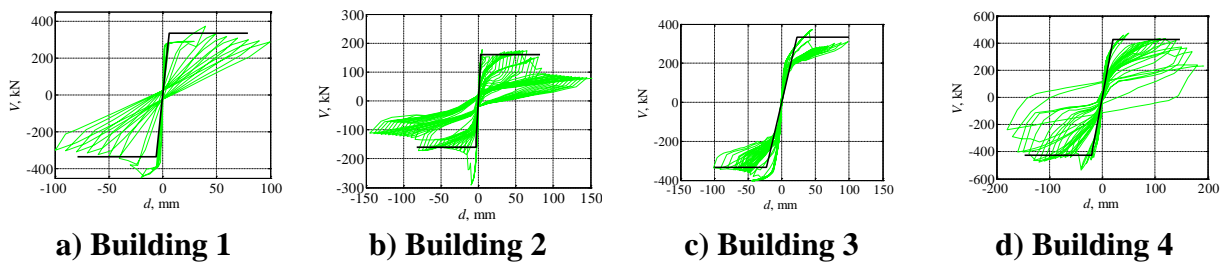


Figure 2: Building behavioural data from pushover analysis

Table 2. Bilinear and modal properties

| Model | H_u^1 , kN | d_e^2 , mm | d_u^3 , mm | μ | T_k^5 , sec | Effective mass ratio, $m_{eff,k}/M^6$ |
|---|-----------------|-----------------|-----------------|-------|---------------|---------------------------------------|
| 1 | 335.3 | 6.0 | 79 | 13.2 | 0.06 | 0.97 |
| 2 | 160.7 | 3.2 | 82 | 25.6 | 0.10 | 0.99 |
| 3 | 334.8 | 23.0 | 100 | 4.3 | 0.25 | 0.91 |
| 4 | 427.2 | 20.4 | 96 | 4.7 | 0.38; 0.15 | 0.84; 0.14 |
| 1: maximum bilinear force; 2: yield displacement; 3: ultimate displacement; 4: calculated from pushover curve as discussed in the text; 5: from modal analysis; 6: $m_{eff,k}$ is the effective mass in mode k and M is the building seismic mass | | | | | | |

ESTIMATION OF PFA USING SIMPLIFIED MODAL ANALYSIS

The acceleration response in masonry buildings is known to mostly reduce with increased inelasticity (Menon and Magenes 2011). Consistently, the PFA obtained using linear analyses is assumed to be an upper bound and suitable for assessing acceleration-sensitive non-structural components. This value can be calculated by combining modal acceleration responses.

As a diaphragm becomes flexible, its vibrations appear as a new mode in the building response. Some of the mass of the building that was excited with the original building period is now vibrated with the new diaphragm period, T_d , which can be larger than the original building period. With the appearance of this new mode and governed by the spectral shape of the applied ground motion (e.g. Figure 3), the related acceleration response, $S_a(T_d)$, can be significantly larger than the $S_a(T_1)$ for some buildings, especially for those buildings that have a relatively short period. For example, if the period of the building with a rigid diaphragm is $T_1=0.06$ sec, e.g. Building 1, the spectral acceleration is much smaller than the peak S_a obtained from Figure 3. If diaphragm-related modes have $T_d \approx 0.2$ sec, then the related spectral acceleration will be near the peak obtained from Figure 3. Therefore, the PFA calculated using modal combination will include this large contribution and can be significantly greater than the PFA for the building with rigid diaphragms. It is also important to note that because some of the building mass vibrates with new diaphragm modes, the ‘building’ first mode period reduces due to the reduced mass. However, parametric studies show that, for low rise buildings, the relatively small change in the building fundamental period results in an insignificant change in the related spectral acceleration so that the contribution of the in-plane wall vibrations to floor accelerations can still be assessed using the initial mode. This calculation becomes inaccurate for taller buildings, e.g. 2-storey or 3-storey buildings.

Conversely to the above discussion, if the original building period was close to that associated with peak S_a , e.g. in the range of 0.15 to 0.40 from Figure 3, then the appearance of new modes with other periods may not result in a significant increase in the PFA. This scenario could occur for Buildings 3 and 4, for which T_1 falls within that range. However, the modal shape factors also affects the relative accelerations in different floors. For example for Building 4, although the first mode period of 0.38 sec is associated with a large acceleration response, the magnitude of the acceleration response in the first level is about a third of that value (for a linear mode shape). If the new modes that appear in the first floor due to diaphragm vibrations are associated with

acceleration response of greater than a third of the $S_a(T_1)$, then the diaphragm flexibility increases the net PFA in the first level.

The above changes are considered to be automatic when employing a modal analysis, however a complete modal analysis is still impractical for many projects. Therefore, a simple modal analysis based on the first mode building vibration and uncoupled diaphragm vibrations is presented here.

Let us assume a two-storey building, e.g. Building 3, with a linear first mode shape. It is highlighted here that the assumption of a linear first mode shape automatically determines the second mode shape due to the orthogonality of the modes although both are in fact inaccurate. For this purpose the off-diagonal components of the modal mass matrix can be set as zero and the second mode shape is calculated accordingly. The approximate mode shape matrix is given by:

$$\Phi = \begin{bmatrix} 0.5 & 1 \\ 1 & -0.5 \frac{M_1}{M_2} \end{bmatrix} \quad (3)$$

Using this matrix the modal participation and modal masses can be calculated, and hence, the first mode PFA from Equation 1 can be calculated as:

$$PFA_1 = \left\{ \begin{matrix} \varphi_{11} \\ \varphi_{12} \end{matrix} \right\} \frac{\sum_{j=1}^2 \varphi_{1j} M_j}{\sum_{j=1}^2 \varphi_{1j}^2 M_j} S_a(T_1) = \left\{ \begin{matrix} 0.5 \\ 1 \end{matrix} \right\} \frac{0.5M_1 + M_2}{0.25M_1 + M_2} S_a(T_1) \quad (4)$$

In particular for Building 3, the normalised masses M_1 (ground floor) and M_2 (roof) were calculated as, respectively, 1 and 0.44. Therefore, Equation 4 is equivalent to:

$$PFA_1 = \left\{ \begin{matrix} 0.68 \\ 1.36 \end{matrix} \right\} S_a(T_1) \quad (5)$$

The PFA due to uncoupled diaphragm vibrations is:

$$PFA_d = \begin{bmatrix} 1 & 0 \\ 0 & 1 \end{bmatrix} \left\{ \begin{matrix} S_a(T_{df}) \\ S_a(T_{dr}) \end{matrix} \right\} \quad (6)$$

where $S_a(T_{df})$ and $S_a(T_{dr})$ are spectral acceleration of, respectively, the floor and roof diaphragms. The calculated PFA_1 and PFA_d can be combined using any of the existing modal combination methods, e.g. SRSS, CQC, or the algebraic sum. For SRSS, the final form for Building 3 is:

$$PFA = \sqrt{\left\{ \begin{matrix} 0.68 \\ 1.36 \end{matrix} \right\}^2 \{S_a(T_1)\}^2 + \left\{ \begin{matrix} S_a(T_{df}) \\ S_a(T_{dr}) \end{matrix} \right\}^2} \quad (7)$$

To estimate the absolute PFA, peak ground acceleration, PGA, is added to Equation 7:

$$PFA_{abs} = PGA + \sqrt{\left\{ \begin{matrix} 0.68 \\ 1.36 \end{matrix} \right\}^2 \{S_a(T_1)\}^2 + \left\{ \begin{matrix} S_a(T_{df}) \\ S_a(T_{dr}) \end{matrix} \right\}^2} \quad (8)$$

Similar derivation can be made for the three-storey Building 4, which has normalised masses of 1, 0.78, and 0.44, respectively in the first floor (M_1), second floor (M_2), and roof (M_3):

$$PFA_1 = \begin{Bmatrix} 0.33 \\ 0.67 \\ 1 \end{Bmatrix} \frac{0.33M_1 + 0.67M_2 + M_3}{0.109M_1 + 0.449M_2 + M_3} S_a(T_1) = \begin{Bmatrix} 0.48 \\ 0.96 \\ 1.44 \end{Bmatrix} S_a(T_1) \quad (9)$$

Using similar Equations to 6, 7, and 8, the contribution from diaphragm vibrations and the final PFA_{abs} can be calculated. For single-storey buildings, the predictive equation can be written as:

$$PFA = \sqrt{\{S_a(T_1)\}^2 + \{S_a(T_{dr})\}^2} \quad (10)$$

The method can be extended to include higher building modes, e.g. for Building 4, but it is highlighted that given the simplifications made in assuming uncoupled diaphragm vibration, inclusion of more building modes may be illogical.

NLTHA OF BUILDINGS WITH RIGID DIAPHRAGM

A total of 30 earthquake records (Oyarzo-Vera et al. 2012) were used to calculate the nonlinear building response through incremental dynamic analysis (IDA), with the IDA parameter being the spectral acceleration at the first mode period of the building, $S_a(T_1)$. Using three $S_a(T_1)$ increments of 0.05g, 0.5g, and 1.0g were sufficient to describe a reasonable range of elastic and inelastic building behaviour. The response spectra of the earthquake records normalised to peak ground acceleration (PGA) is shown in Figure 3. Rayleigh viscous damping was used with a 5% initial damping ratio assigned at two (lower and higher) frequencies corresponding to, respectively, the fundamental mode ($1/T_1$) and the lowest elastic mode containing 90% mass participation. The single-storey building analysis results (Figure 4) suggest that for most of the buildings the amplification factor slightly reduced with an increase in applied acceleration.

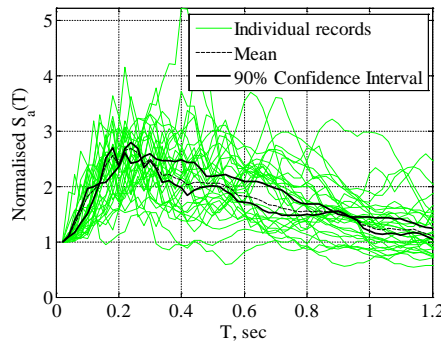


Figure 3: Absolute acceleration response spectra of the records normalised to PGA

As detailed in Table 3, ASCE/SEI 41-13 (ASCE 2014) specifies peak roof accelerations that are 3 times the PGA for all buildings. The related formula is $A=1+2x/h$, with A , h , and x being the amplification factor, building height, and part attachment height, respectively.

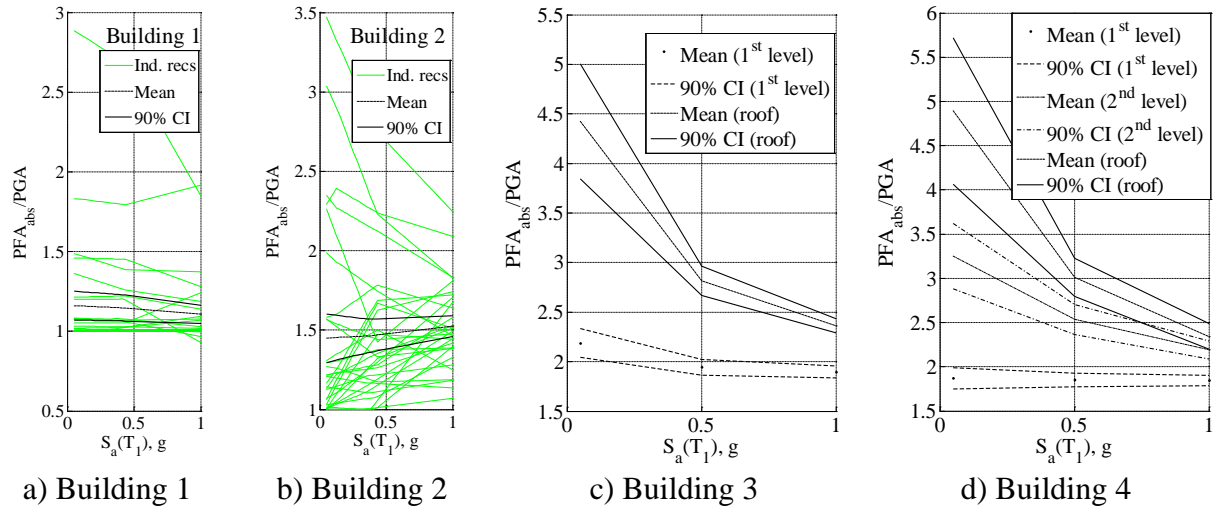


Figure 4: Peak floor accelerations normalised to PGA

Table 3: Roof acceleration amplification factor as per seismic codes

| | Building 1 | Building 2 | Building 3 | Building 4 |
|------------------------------------|------------|------------|------------|------------|
| | h=4.25m | h=4.25m | h=7.75m | h=11.25m |
| ASCE (ASCE 2014) | 3.00 | 3.00 | 3.00 | 3.00 |
| AS 1170.4 (AS 2007) | 1.72 | 1.72 | 2.32 | 2.91 |
| NZS 1170.5 (NZS 2004) | 1.71 | 1.71 | 2.29 | 2.88 |
| Current study (Mean); Sydney | 1.16 | 1.46 | 3.96 | 4.35 |
| Current study (upper 90%); Sydney | 1.24 | 1.59 | 4.41 | 5.00 |
| Current study (Mean); elastic | 1.20 | 1.45 | 4.40 | 4.90 |
| Current study (upper 90%); elastic | 1.25 | 1.60 | 5.00 | 5.75 |

The method has a potential to underestimate amplifications if relative accelerations are substantially greater than the ground acceleration, e.g. period range of $0.15 < T_1 < 0.4$ (absolute response acceleration of greater than 2 times PGA as seen in Figure 3). For example, an amplification factor of 3 is an overall underestimation when compared to 30-record average MDOF results of 4.4, 4.9 (Figure 4c and d; Table 3), obtained for relatively elastic response, i.e. $S_a(T_1)=0.05g$, of Buildings 3 and 4 that had a T_1 between 0.15 and 0.40 sec. The mean and upper 90% confidence interval of PFA_{abs}/PGA ratio interpolated from Figure 4 for Sydney or Melbourne, i.e. $S_a(T_1)=0.18$ for all buildings, is smaller than the ‘elastic’ values but can still be up to 4.35 and 5.00, respectively (see also Table 3). In contrast, for nearly rigid buildings, e.g. Building 1 and 2 with $T_1 < 0.13$ the smaller relative accelerations results in the ASCE method being conservative,

e.g. roof amplification factor of 3 from Table 3 compared to 1.20~1.45 obtained for the roof of Buildings 1 and 2 (Figure 4).

The roof acceleration from the NZS 1170.5 (NZS 2004) and AS 1170.4 (AS 2007) methods are dependent on the building height. For $h < 12$, the method follows a similar logic to ASCE/SEI 41-13, except that h has been replaced by 12, i.e. $PFA/PGA = 1 + x/6$. Therefore, this method produces substantially smaller amplification factors than the ASCE method for buildings shorter than 12 m. A comparison between these methods and the results obtained from this study (Table 3) shows that the methods underestimate PFA. For example, the mean roof amplification of 4.4 (Figure 4c and Table 3) for the small range of shaking of Building 3 is more than 90% greater than 2.29 from these methods (see Table 3). The underestimation of NLTHA results is about 54% if upper 90% confidence interval values are considered, i.e. 2.29 compared to 5.00 from Table 3. However, allowing for inelasticity, e.g. proportionate to the seismicity of Sydney or Melbourne, $S_a(T_1) = 0.18g$, the underestimation is reduced to 48%, e.g. 2.29 compared to 4.41 from Table 3. Underestimations also occur when these methods are used for lower floor accelerations.

BUILDINGS WITH FLEXIBLE DIAPHRAGMS

Several levels of diaphragm in-plane stiffness were assumed in the modelling. Default material properties for existing timber floors are set out in (ASCE 2014) in the form of a characteristic shear stiffness, G_d , with a minimum value of 350 kN/m. However, further in situ testing of URM buildings in New Zealand (Giongo et al. 2014) has suggested values up to a third of this stiffness depending on the condition (e.g. decay in timber joists) of the diaphragm. A lower bound of $G_d = 150$ kN/m (D1) was used in this research. As detailed in Table 4, four other cases of diaphragm stiffness were also studied, including a strengthened timber floor (D4) and the previously discussed case of rigid diaphragms (represented as D5 in Table 4).

Table 4: Range of diaphragm stiffnesses

| Designation | Description | Assumed G_d , kN/m | Ref. period T_d^* , sec |
|-------------|---|----------------------|---------------------------|
| D1 | As-built with single straight sheathing | 150 | 1.08 |
| D2 | As-built with single diagonal sheathing; unchorded | 600 | 0.54 |
| D3 | As-built with double straight sheathing; chorded | 2400 | 0.27 |
| D4 | Single straight sheathing strengthened with 19 mm plywood overlay with substantial edge nailing | 9600 | 0.13 |
| D5 | Large stiffness representing a rigid diaphragm | 3×10^6 | 0.01 |

* Calculated using the diaphragm stiffness and the combined mass of the diaphragm and the tributary mass of the out-of-plane loaded walls (little variations for different buildings ignored)

Modal analysis of the buildings with flexible diaphragms showed that several modes of vibration with insignificant individual modal mass, but with considerable overall modal mass appear in the building response. For example, in the response of Building 4 with D1, four of the initial modes

relate to the vibration of various diaphragm bays with effective modal mass ratios of about 15% in each mode and with a period of between 0.6 and 0.8 sec. These modes are followed by the characteristic mode, which has 30% mass contribution and is associated with a period of 0.24 sec. This latter period is smaller than the building period when floors are rigid, i.e. 0.38 sec from Table 2, due to the reduced mass that is mobilised in this mode. Hence, using the period of the building with rigid diaphragm in Equations 7 and 8 will involve a degree of error, depending on the acceleration response associated with $T_1=0.38$ sec in comparison to that for $T_1=0.24$ sec.

It can be seen from Figure 5 that for almost all the analysis cases, the amplification factor increases to reach a peak value and then reduces as the diaphragm become increasingly flexible. This effect is more pronounced for the single-storey buildings, where the first mode period of the building with rigid diaphragm was relatively small and the related spectral acceleration was much smaller than the plateau in the response spectra, e.g. in Figure 3. For Building 1, the amplification factor increased by 175% from 1.2 for diaphragm case D5 (rigid) to a value of 3.3 for the diaphragm case D2 as seen in Figure 4a. The PFA in lower floors of the multi-storey buildings is also affected by diaphragm vibrations as the wall-related vibrations are insignificant due to the first mode shape.

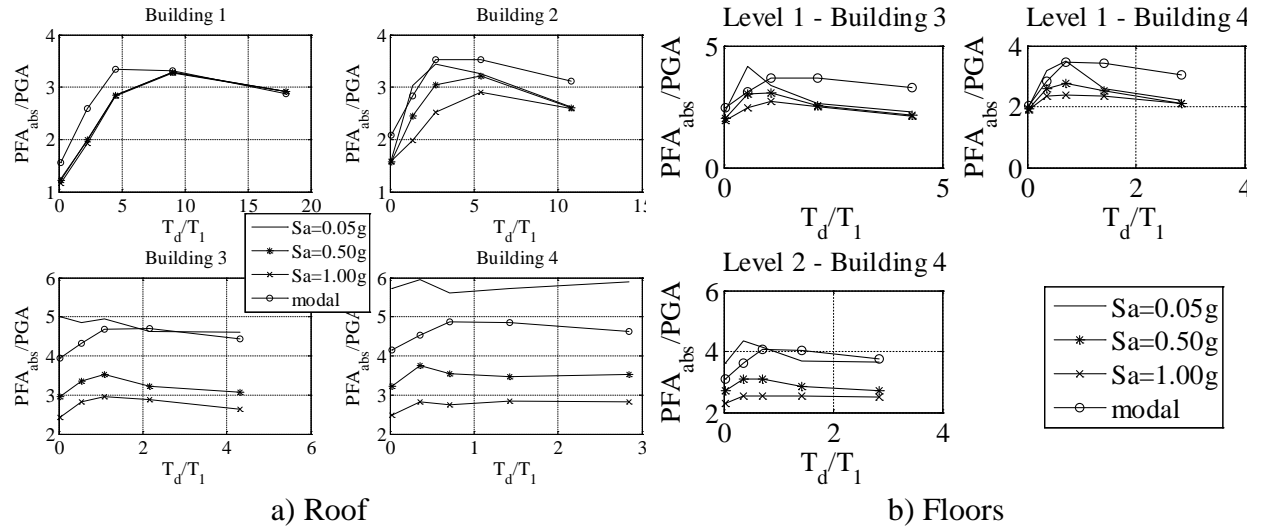


Figure 5: Peak floor accelerations for buildings with flexible diaphragms

The method described earlier can, with reasonable accuracy, address these effects. For example, the PFA are obtained to be in the range of 3.3~3.5 for Buildings 1 and 2. These values are slightly greater than the NLTHA estimates and are up to nearly 3 times the equivalent values when diaphragms are rigid, i.e. 1.2~1.5. However for the smallest T_d/T_1 ratio, i.e. case of rigid diaphragm, the method overestimates the PFA for Buildings 1 and 2 by up to about 30%. Conversely, for Buildings 3 and 4 the PFA for buildings with rigid diaphragm is underestimated by up to about 30%, and this underestimation is attributed to the wall-related components in Equations 7 and 8 only including the first mode. Furthermore, it is known that the SRSS method used can underestimate responses due to the cross-mode ‘moments’ being ignored.

SUMMARY AND CONCLUDING REMARKS

Four URM buildings were subjected to incremental dynamic analysis and the amplification of accelerations up the height of the buildings were investigated. A comparison of the results with Australian, New Zealand, and USA loading standards/guidelines suggests that various provisions underestimate floor accelerations for buildings with rigid floors. The underestimation can be by up to 54% if the code calculated values are compared to the upper 90% confidence intervals obtained for elastic building response. If some inelastic building response proportionate to seismicity of Sydney or Melbourne are assumed, then the underestimation is reduced to about 48%. It was found that the peak floor accelerations in buildings with flexible diaphragms can be up to nearly 2 times greater than that in a building with rigid floors. Therefore, it is clear that the code approaches cannot be applied to buildings that include flexible diaphragms. A simple modal combination method was proposed, which for the studied buildings could predict the peak floor acceleration with about 30% error.

ACKNOWLEDGEMENTS

The authors gratefully acknowledge the financial support provided by the Australian Government via the Bushfire and Natural Hazards CRC. The assistance of the TREMURI staff at the University of Pavia in providing academic licenses of Tremuri software is gratefully appreciated.

REFERENCES

Abbati, D., S. (2016), Seismic Assessment of Single-Block Rocking Elements in Masonry Structures. PhD thesis. Dipartimento di Ingegneria Civile, Chimica e Ambientale, Università Degli Studi Di Genova, Genoa, Italy.

AS (Australia Standards), (2007), AS 1170.4 Structural design actions, Part 4: Earthquake actions. Standards Australia.

ASCE (American Society of Civil Engineers), (2014), Seismic evaluation and retrofit of existing buildings. ASCE 41-13, Reston, Virginia.

CEN (Comité Européen de Normalisation), (2004), EN 1998-1 Eurocode 8: Design of structures for earthquake resistance -Part 1: General rules, Seismic actions and rules for buildings. Brussels, Belgium.

Costley AC and Abrams DP (1995) Dynamic response of unreinforced masonry buildings with flexible diaphragms. Dept. of Civil Eng., University of Illinois at Urbana-Champaign, 281 pp.

Curti E (2007). Vulnerabilità sismica delle torri campanarie: modelli meccanici e macrosismici. PhD Thesis, University of Genoa, Italy (in Italian).

Giongo, I., Wilson, A., Dizhur, D., Derakhshan, H., Tomasi, R., Griffith, M. C., Quenneville, P., and Ingham, J. M. (2014). Detailed seismic assessment and improvement procedure for vintage flexible timber diaphragms. *Bulletin of the New Zealand Society for Earthquake Engineering*, 47(2), 97-118.

Lagomarsino, S., Penna, A., Galasco, A. and Cattari, S. (2013) ,TREMURI program: an equivalent frame model for the nonlinear seismic analysis of masonry buildings, *Engineering Structures*, 56, 1787 – 1799.

Lagomarsino, S. (2015). Seismic assessment of rocking masonry structures. *Bulletin of Earthquake engineering*, 13(1):97-128.

Menon, A. and Magenes, G. (2011). Definition of Seismic Input for Out-of-Plane Response of Masonry Walls: II. Formulation. *Journal of Earthquake Engineering*, 15(2): 195-213.

Miranda, E., and Taghavi, S. (2005), Approximate floor acceleration demands in multi-story buildings. I: Formulation, *Journal of Structural Engineering*, 131(2), pp. 203-211.

Nakamura, Y., Derakhshan, H., Magenes, G., Griffith, M. (2017), Influence of diaphragm flexibility on seismic response of unreinforced masonry buildings, *Journal of Earthquake Engineering*, 21(6): 935-960.

NZS (New Zealand Standards), (2004), NZS 1170.5: Structural Design Actions: Part 5: Earthquake actions, New Zealand.

Oyarzo-Vera, C., McVerry, G., and Ingham, J. (2012), Seismic Zonation and Default Suite of Ground-Motion Records for Time-History Analysis in the North Island of New Zealand, *Earthquake Spectra*, 28 (2), 667-688.

Pozzi, M., and Der Kiureghian, A. (2015), Response spectrum analysis for floor acceleration, *Earthquake Engineering and Structural Dynamics*, 44(12), pp. 2111-2127.

Shelton, R.H. (2004), Seismic response of building parts and non-structural components. Study report, No. 124. BRANZ, Porirua City 5381, New Zealand. ISSN: 0113-3675.

Tena-Colunga A and Abrams DP (1992), Response of an unreinforced masonry building during the Loma Prieta earthquake. Structural Research Series 576, Department of Civil Engineering, University of Illinois at Urbana-Champaign, 288 pp.

DAMAGE QUANTIFICATION IN PLASTERED UNREINFORCED MASONRY WALLS USING DIGITAL IMAGE CORRELATION

M. Didier¹, G. Abbiati², F. Hefti³, M. Broccardo⁴ and B. Stojadinovic⁵

¹ PhD Student, Department of Civil, Environmental and Geomatic Engineering (D-BAUG), ETH Zurich, Switzerland didierm@ethz.ch

² PostDoc, D-BAUG, ETH Zurich, Switzerland, abbiati@ibk.baug.ethz.ch

³ Master Student, D-BAUG, ETH Zurich, Switzerland, heftif@student.ethz.ch

⁴ PostDoc, D-BAUG, ETH Zurich, Switzerland, broccardo@ibk.baug.ethz.ch

⁵ Professor, D-BAUG, ETH Zurich, Switzerland, stojadinovic@ibk.baug.ethz.ch

Pilot deep geothermal projects in St. Gallen and Basel, Switzerland, have induced long sequences of low-magnitude earthquakes with individual events up to a moment magnitude of 3.4 (Basel, 2006) and 3.5 (St. Gallen, 2013). In Basel, damage included mainly non-structural damage, e.g. small cosmetic cracks on plaster. Such damage can, however, still induce high financial losses, considering an aggregated building stock. Traditional seismic fragility functions for macroseismic events consider mainly structural damage and collapse damage states and are not applicable to quantify the risk in induced seismicity settings. Adapted fragility functions, focusing on high-probability low-consequence damage, like cosmetic cracks or plaster fall-off, are, thus, needed. To quantify such risk, plastered unreinforced masonry (URM) walls have been tested at ETH Zurich in a 3-actuator quasi-static cyclic test setup using load protocols representative of induced earthquake ground motion excitation. The strain and deformation fields on the plaster surface have been tracked during the tests by a Digital Image Correlation (DIC) measurement setup, and a procedure to compute two different damage scores has been developed. The Normalized Crack Area (NCA) quantifies the damaged area of the plaster surface and the Normalized Crack Length (NCL) the length of the cracks. Three damage states have been defined: *no crack*, *visible crack* and *plaster fall-off*. The damage scores have been related to the three damage states via an expert survey and a multivariate logistic regression. The probabilistic model was extended with a correlation of the displacement amplitudes to the calculated damage scores. This procedure allows to estimate the damage score for a given masonry wall displacement (e.g. caused by an induced ground motion sequence of interest) and to assess, then, the probability of observing a certain damage state and to quantify the risk of deep geothermal projects.

Keywords: unreinforced masonry, damage scores, fragility analysis, digital image correlation, crack detection

INTRODUCTION

Deep geothermal projects rely on hydro-fracking and hydro-shearing of rock to increase its permeability. Pilot projects in St. Gallen and Basel, Switzerland, have shown that these technologies cause long sequences of low-magnitude induced earthquakes with individual events up to a moment magnitude of 3.4 (Basel, 2006) and 3.5 (St. Gallen, 2013). In Basel, the resulting damage claims were estimated to be 7-10 million Swiss Francs (approximately 7-10 million USD). The observed damage included mainly non-structural damage, e.g. small cosmetic cracks on plaster. They can, however, as it has been the case in Basel, still induce high financial losses, if an aggregated building stock or building portfolio is considered. Traditional seismic fragility functions provided in literature for macroseismic events, considering mainly structural damage and collapse damage states, are not applicable to quantify the risk in such situations. Fragility functions, focusing on high-probability, low-consequence damage, like cosmetic cracks or plaster fall-off, rather than structural damage and life threatening consequences, are, thus, needed.

To quantify the non-structural damaging potential of such sequences of induced or triggered earthquakes, an experimental test campaign was led at ETH Zurich, Switzerland (Didier et al. 2017). A load protocol representative for sequences of small induced ground motions was designed and applied to plastered unreinforced masonry (URM) wall test specimens. A digital image correlation (DIC) setup (Mojsilovic and Salmanpour 2016) was used to track and analyze the occurrence and development of damage on the plastered surface of the walls. In detail, two damage scores, namely the Normalized Crack Area (NCA) and the Normalized Crack Length (NCL) were post-processed from von Mises strain maps obtained via DIC during the application of the load protocols. Then, three categorical damage states were defined to quantify the damage of the plaster of the URM walls: *no crack*, *visible crack* and *plaster fall-off*. The damage scores were then related to an expert classification using the defined damage states, obtained by a survey conducted for this study. Finally, a probabilistic model was derived to quantify the probability of occurrence of the different damage states for a wall exposed to induced seismic loads.

TEST CAMPAIGN

In total, 15 plastered URM walls have been tested at the Structural Testing Laboratory (Bauhalle) at ETH Zurich (Didier et al. 2017). Wall specimens of dimensions 1.20x1.20x0.15m have been built in running bond using conventional hollow Swiss clay bricks and mortar joints. The front side of the wall was plastered with a 12-14mm thick plaster layer (Figure 1 a), while the back side of the wall remained unplastered.

The goal of the test campaign was to quantify the damage observable on the plastered surface of the wall. The test specimens were placed on a concrete block (connected by a mortar joint at the bottom of the walls) into the test setup (Figure 2), and the top of the walls was connected to the loading frame, again by a mortar joint. The same mortar as for the joints of the walls was used. To avoid vertical loads on the plaster, the top mortar layer was only applied to the bricks, leaving the plaster disconnected from the loading frame.

Three servo-hydraulic actuators were connected to the loading frame. The two vertical actuators were used in force control mode to impose a vertical compression load corresponding to 10% of

the vertical compressive strength of the walls. A zero-moment condition was applied at the top of the test specimen, corresponding to a cantilever boundary condition. The horizontal actuator was used in displacement control and applied the horizontal displacement of the test or load protocol on the wall, through the steel loading beam.

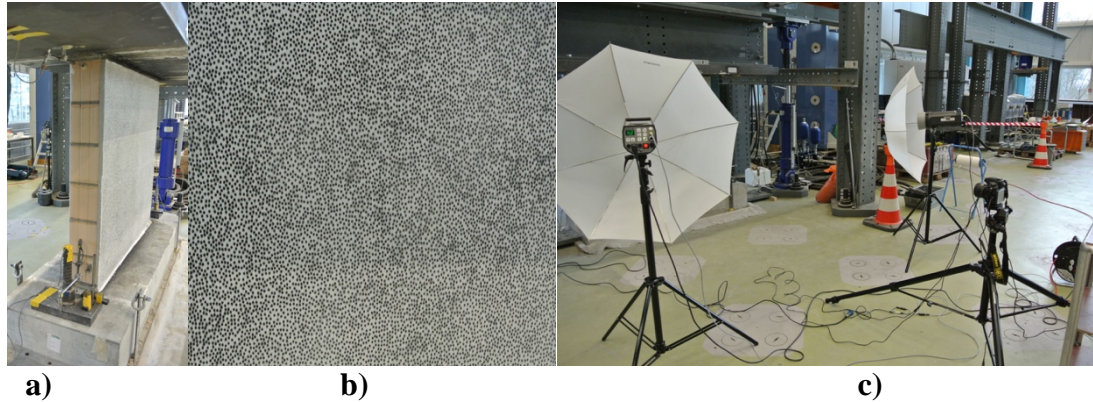


Figure 1: a) Plastered URM wall specimen, b) Random speckle pattern on plaster surface, c) DIC camera and flash setup

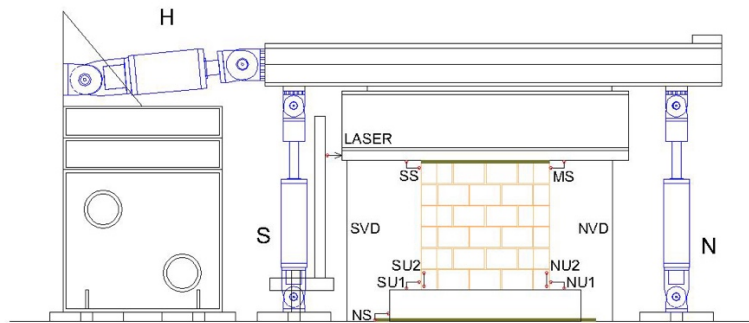


Figure 2: Experimental setup (H corresponds to horizontal, N to north, S to south) (from Didier et al. 2017)

Two different test protocols have been used in the experimental campaign: the BIN2_99 (Didier et al. 2017) and the NAMC protocol (Beyer and Mergos 2015). The BIN2_99 protocol (Figure 3 a) was derived from an augmented dataset consisting originally of records from the PEER-NGA-East database, the Basel 2007 and St. Gallen 2013 induced earthquake records, and a selection of West US induced motions. The NAMC test protocol (Figure 3 b) is representative for low-moderate seismicity. A constant actuator velocity of 2mm/min was used to apply the BIN2_99 protocol and a velocity of 1-4mm/min for the application of the NAMC protocol. The load application can, thus, be considered as quasi-static.

The displacement at the top of the wall was controlled and measured with a laser distance sensor. Additionally, 9 external Linear Variable Differential Transformers (LVDTs) measured local displacements at the bottom and top level of the wall, the foundation slip and the vertical displacement of the beam relative to the floor on both extremities of the beam.

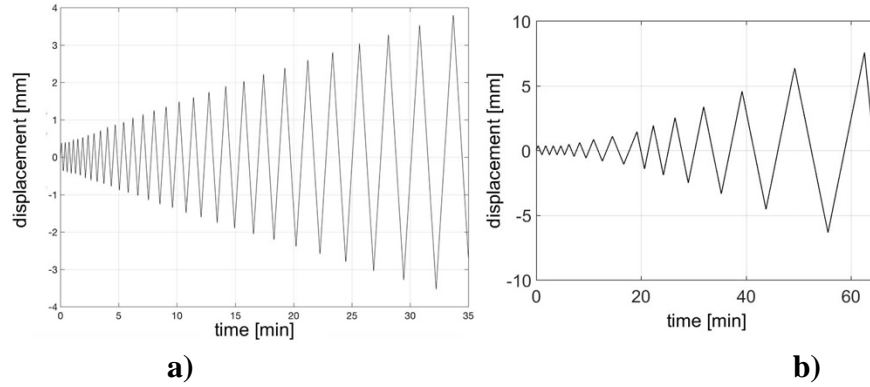


Figure 3: a) BIN2_99 test protocol, and b) NAMC test protocol (from Didier et al. 2017)

DIGITAL IMAGE CORRELATION (DIC)

Digital Image Correlation (DIC) was used to acquire the in-plane displacement and strain fields on the plaster surface of the specimens during the tests. A random speckle pattern was applied to the plaster surface using a thin plastic film with a laser-cut randomly distributed hole pattern to airbrush a thin layer of black paint on a white-painted plaster surface (Figure 1b). The obtained dot size of about 1.5mm was calibrated to obtain dots of 3-4 pixels in the digital images taken with a Nikon D810 (36.3 Megapixel) camera using a 50mm lens. The camera was computer-triggered at pre-defined displacement values at the top of the wall (measured with the laser), simultaneously with two flashes, used to guarantee a uniform light exposure of the plaster (Figure 1 c).

The obtained digital images of 4 walls, tested with the NAMC and the BIN2_99 load sequences (Table 1), were then post-processed and compared to each other to evaluate the damage of the plaster. The peak displacement and the zero displacement pictures were selected for subsequent analysis. The selection allowed a comparison between the damage observable at peak displacement and at residual displacement of a cycle (Figure 4). The residual and peak displacement pictures were processed separately, using the Vic2D software (Correlated Solutions 2017). The resulting strain and displacement data was exported as matrices from Vic2D and imported to Matlab (MathWorks 2015) to determine the two damage scores presented in the following sections.

Table 1: Test programs and final peak NCA and final peak NCL of the walls

| Wall ID | Test protocol | final peak NCA | final peak NCL |
|---------|----------------|----------------|----------------|
| Wall001 | NAMC | 0.09 | 2.6 |
| Wall002 | BIN2_99 & NAMC | 0.15 | 1.8 |
| Wall003 | BIN2_99 & NAMC | 0.15 | 3.6 |
| Wall004 | BIN2_99 & NAMC | 0.17 | 3.2 |

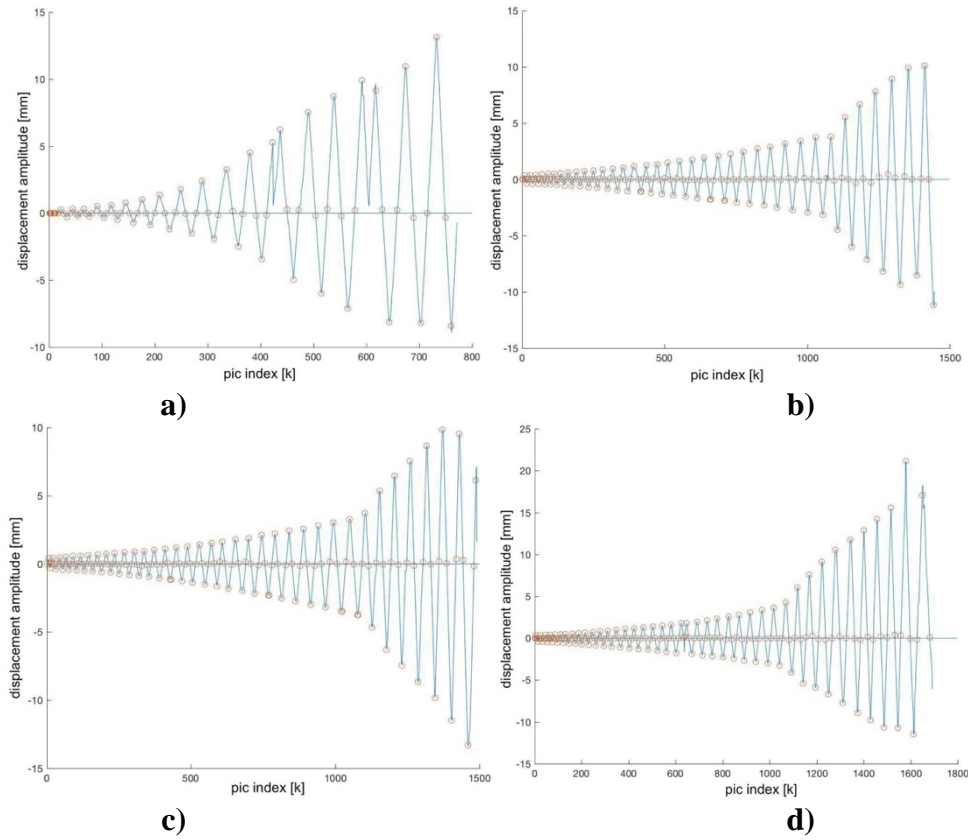


Figure 4: Applied load sequence and peak and near zero displacement pictures considered for the analysis a) Wall001, b) Wall002, c) Wall003, and d) Wall004

NORMALIZED CRACK AREA (NCA)

The Normalized Crack Area (NCA) corresponds to the ratio of the damaged plaster area to the total plastered wall area:

$$NCA = \frac{\text{damaged area of the plaster}}{\text{total area of the plaster}} = \frac{\text{number of white pixels on cumulative von Mises strain map}}{\text{total number of pixels on cumulative von Mises strain map}} \quad (1)$$

It is derived from the von Mises strain maps obtained from Vic2D, using the following procedure:

1. Import the von Mises strain maps as matrices into Matlab (Figure 5 a).
2. Convert the von Mises strain maps into grayscale (using a strain interval ranging between 0 and 0.1, values calibrated to maximize the signal-to-noise ratio over the different test protocols, Figure 5 b).
3. Select an optimal threshold value for black-to-white transition (using the *graythresh* function of the Image Processing Toolbox of Matlab, here: 0.05).
4. Convert the von Mises strain maps into binary (black-and-white) images: damage corresponds to white pixels, undamaged plaster to black pixels (using Matlab's *imbinarize* function with the selected threshold value for black-to-white transition).

5. Compile the cumulative binary von Mises strain map (Figure 5 c) through accumulation of the damage from all pictures of one test. Since masonry is a brittle material, it is assumed that damage, once inflicted to the wall, will not disappear again (logical OR operation applied to binary von Mises strain maps, assuming that a pixel once classified as damaged remains classified as such).
6. Calculate the NCA as the ratio of white pixels on the obtained cumulative binary von Mises strain map over the total plaster surface area, using Equation (1).

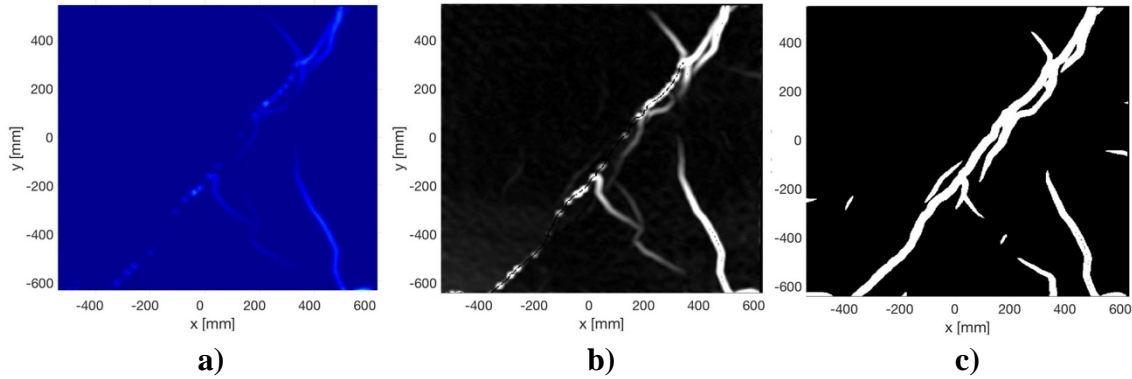


Figure 5: a) von Mises strain map, b) greyscale von Mises strain map, and c) cumulative binary von Mises strain map

Figure 6 shows the evolution of the residual and peak NCA for 4 selected walls. The peak NCA is computed from the picture taken at the maximum (peak) displacement of the cycle, at the moment when the cracks were open and plaster displacement was high. The following decreasing amplitude of the cycle closed the crack again (to a certain extent) giving the residual NCA at zero displacement. The picture index (pic index) corresponds to the picture index given on Figure 4. For the 4 walls, the largest crack formed from bottom south to top north of the wall (corresponding to the bottom left to top right), with the two areas at the edges showing widespread damage. Smaller damage in the horizontal direction was mainly visible on the north side of the walls. Wall003 and Wall004 showed additional cracks on the second diagonal. The observed crack pattern seemed to be sensitive to the direction of the first displacement (in this case from south to north), resulting in an asymmetric crack pattern.

During the first cycles of the test protocols, the four investigated walls showed little or no increase in the NCA. It could be clearly observed that the damage accumulated over the cycles and, thus, increased with the progression of the tests. Note that on Wall003 damage appeared much earlier than on Wall002 and Wall004, tested using the same load protocol (BIN2_99). The residual NCA progressed with a certain delay compared to the peak NCA. Over the evolution of the progression of damage, the value of the residual NCA corresponded to approximately 80% of the value of the peak NCA. The difference of the peak and residual NCA, as well as the stepwise increase of the NCA, can be accredited to the opening of the crack when pulling from north to south, and the closing of the crack when pushing from south to north. The sudden increase of the NCA towards the end of the test was due to plaster fall-off. The final peak NCA of the walls corresponded to 0.09 for Wall001 (i.e. 9% of the plaster surface were damaged after the application of the full load sequence), 0.15 for Wall002 and Wall003, and 0.17 for Wall004 (Table 1).

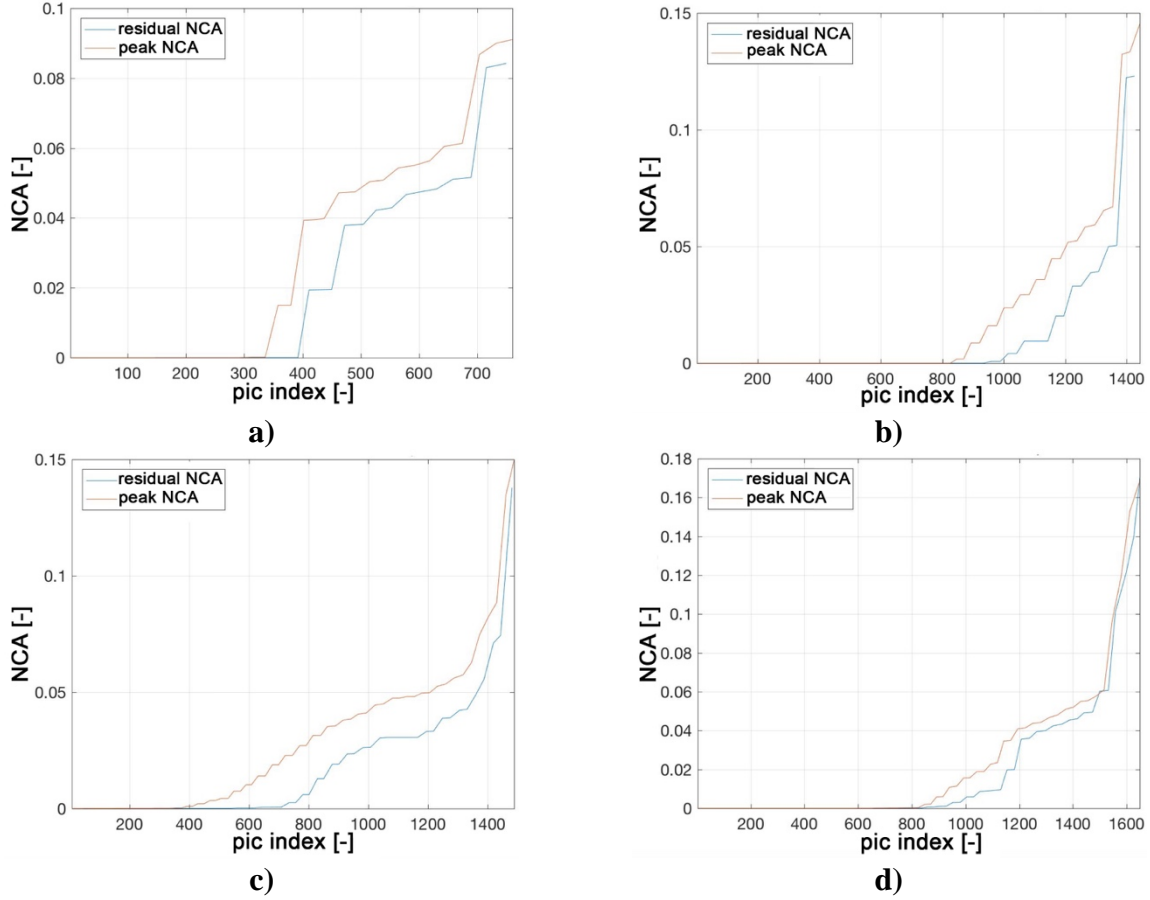


Figure 6: Residual and peak NCA for a) Wall001, b) Wall002, c) Wall003, and d) Wall004

NORMALIZED CRACK LENGTH (NCL)

The Normalized Crack Length (NCL) is the ratio of the sum of the length of all cracks observed on the plaster to the length of the diagonal of the wall:

$$NCL = \frac{\text{sum of length of all cracks}}{\text{length of wall diagonal}} = \frac{\text{sum of crack perimeters}/2}{\text{length of wall diagonal}} \quad (2)$$

A crack over the entire wall diagonal would, therefore, correspond to an NCL of 1. The NCL is derived as well from the cumulative von Mises strain maps, obtained using the same procedure as for the NCA. The crack length is approximated applying the edge detection method to the cumulative von Mises strain map of each wall. The crack length can be approximated as half of the crack perimeter (obtained with the edge detection method), assuming long and narrow cracks (i.e. crack length \gg crack width). The NCL is, thus, calculated using the following procedure:

1. Import the cumulative von Mises strain map into Matlab.
2. Frame the image by a black frame around the imported map to assure the recognition of crack edges coinciding with the border of the image by the edge detection algorithm.
3. Close the gaps in the white area with the *imclose* Matlab function.
4. Apply the Prewitt edge detection method on the image.

5. Calculate the crack length by dividing the crack perimeter obtained with the Prewitt edge detection by two.
6. Repeat steps 3.-5. on the same cumulative von Mises strain map, rotated by 30, 45, 60 and 90 degrees to reduce the influence of the crack direction on the obtained results.
7. Calculate the average crack length of all rotated images.
8. Normalize the total crack length by the number of pixels on the wall diagonal to obtain the NCL, using Equation (2).

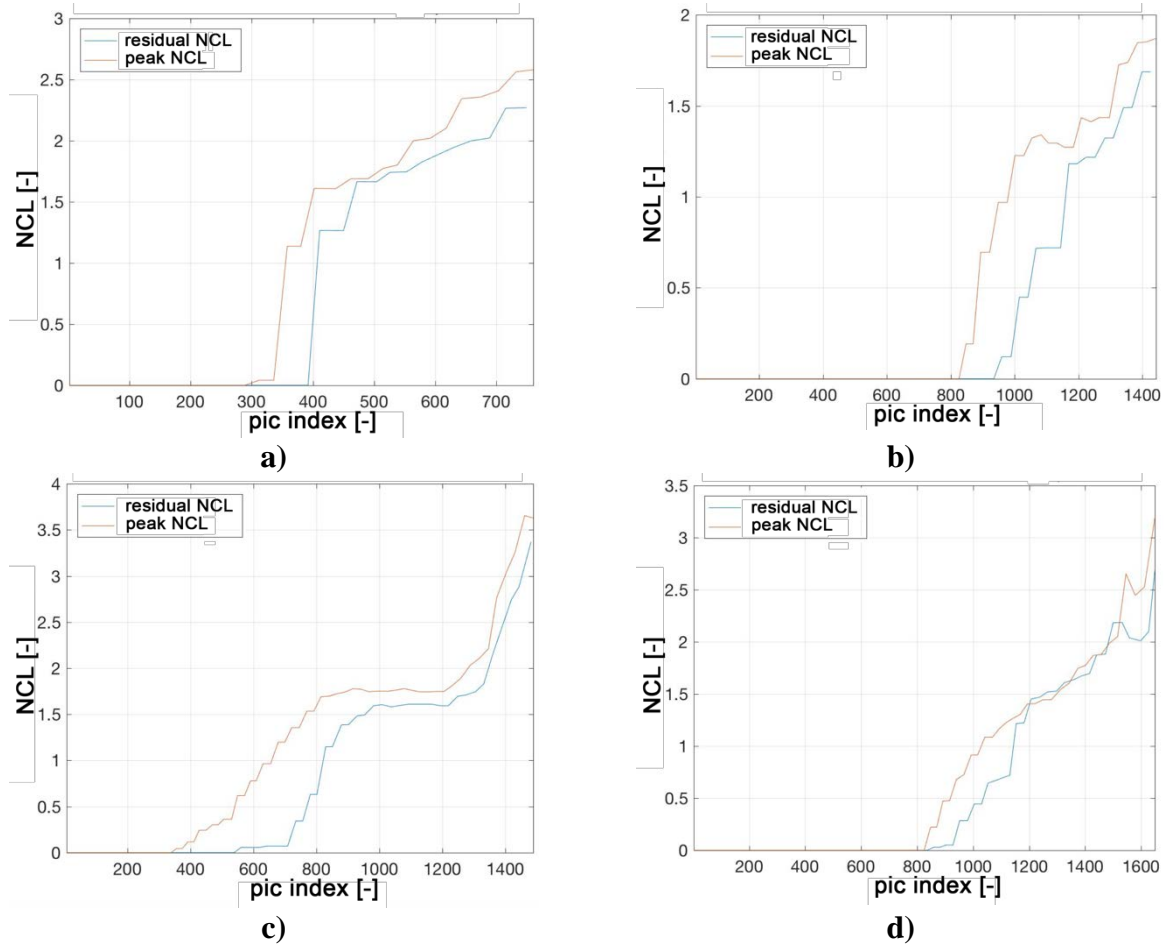


Figure 7: Residual and peak NCL for a) Wall001, b) Wall002, c) Wall003, and d) Wall004

Figure 7 shows the evolution of the residual and peak NCL (at maximum and at zero displacement) during the load sequence. The picture index corresponds to the picture index given on Figure 4. As for the NCA, the walls showed little or no increase in the NCL after the first cycles of the load protocol. After a certain point, the damage started to cumulate and the NCL increased with the progression of the test. Again, for Wall003, damage was observed much earlier than for Wall002 and Wall004, to which the same load protocol was applied. The peak NCL progressed faster than the residual NCL during most of the tests. This observation, as well as the stepwise increment of the NCL could, as for the NCA, be accredited to the opening and closing of the crack when pushing or pulling the wall. A decreasing NCL during the progression of the test could be explained by several cracks connecting and forming an area of damage instead of remaining individual cracks.

The perimeter of all the cracks, and consequently the NCL, decreased in such cases, although the damaged area increased. The same behavior explains the surpassing of the peak NCL by the residual NCL at some points of the load protocol (e.g. Wall004, Figure 7 d). Wall002 showed the smallest final peak NCL of 1.8, Wall001 had a final peak NCL of 2.6, Wall003 of 3.6, and Wall004 of 3.2 (Table 1).

Note that the walls with the highest/lowest final NCA and NCL were not necessarily the same walls (see Table 1). This was, again, due to several individual cracks connecting and forming a larger damaged area. The large increase in the NCA at the end of the tests, followed only by a slight increase of the NCL, could again be explained by this phenomenon: a large increase in the damaged area led often only to a limited increase in the parameter of the cracks. In fact, for small damage (i.e. in the *no crack* damage state) the relation between the NCA and the NCL was almost linear. In the *plaster fall-off* damage state, no correlation between the quantification of the NCA and NCL was anymore observable.

SURVEY

A survey has been conducted to relate the two physical damage scores, the NCA and the NCL, to an expert damage classification based on different damage states. The survey was conducted using 121 peak displacement pictures of the 4 walls presented above.

For the survey, the following damage states have been defined (Figure 8):

- *No crack*: no crack visually detected on the picture;
- *Visible crack*: crack can be detected by visual inspection;
- *Plaster fall-off*: fall-off of parts of the plaster.

Pictures showing significant damage, for which correlation of large parts of the picture using DIC was not possible due to excessive deformation, were assigned manually the *plaster fall-off* damage state, based on a sudden increase of the NCA. Multiple random sets including 40 or 41 pictures were generated to be shown to each participant of the survey. In total 30 participants were asked to take the survey, leading to 10 damage state assignments per picture.

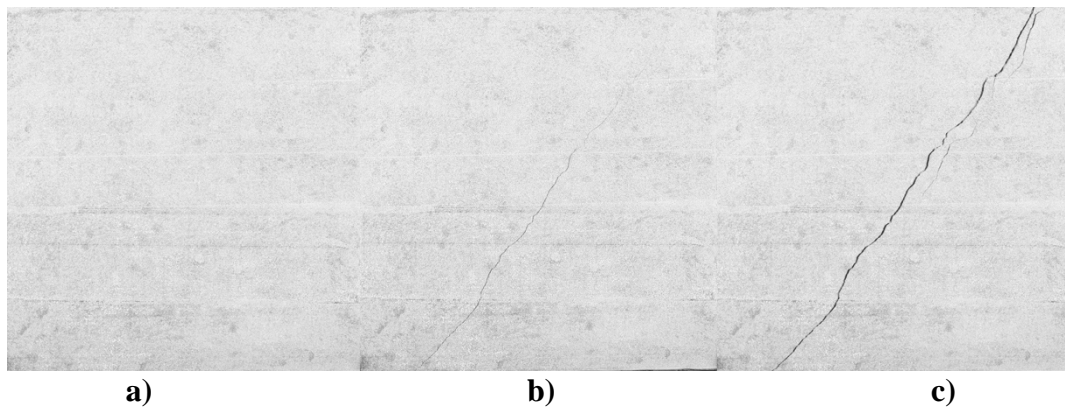


Figure 8: Example for each damage state (Wall004) a) *no crack*, b) *visible crack*, and c) *plaster fall-off*

A picture showing the full front side of the plastered URM wall was shown to the participants of the survey on a 15'' MacBook Pro with Retina Display. The individual participants were asked if they could detect a crack on the plaster. If a crack was detected, the *visible crack* damage state was assigned to the wall at the specific point in the loading sequence when the picture was taken. If no crack was detected on the picture, the image was classified into the *no crack* state. The survey answers were then evaluated in respect to the NCA and NCL, computed at the different points of the load protocol for each wall. The obtained data points from the survey are shown in Figure 9 a) and Figure 9 b) for NCA and NCL, respectively.

MULTIVARIATE LOGISTIC REGRESSION

A simple probabilistic model was derived to correlate the physical damage scores (i.e. the NCA and the NCL) and the expert damage classification, obtained from the survey. Figure 9 shows the results of the multivariate logistic regression for the peak NCA and peak NCL, respectively. The figure shows the probability of observing a certain damage state for a given peak NCA or peak NCL. For example, for a peak NCA of 0.035, the probability of the wall being in the *no crack* damage state is 90%, that of being in the *visible crack* damage state 10%, and that of being in the *plaster fall-off* damage state 0%. For the NCL, the main difference of the obtained probabilities, compared to the ones derived for the NCA, concerns the *plaster fall-off* damage state. For the NCA, a steep rise in the probability of the wall being in the *plaster fall-off* state is observed, while, for the NCL, the increase in probability of this damage state is more gradual, rising over a larger range. This can be explained by the manual classification of images to the plaster fall-off state, which was done considering a sudden increase of the NCA, and without consideration of the NCL. As described above, an increase of the damaged area, and, thus, the NCA, does not necessarily lead to an increased crack perimeter, and, thus, an increase of the NCL.

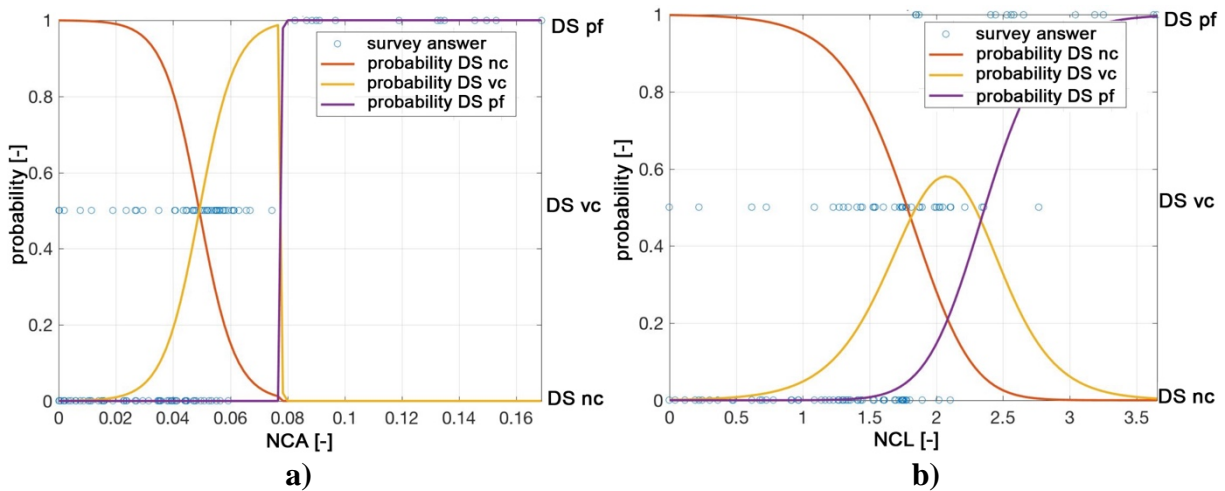


Figure 9: Survey answers and multivariate logistic regression for a) NCA and b) NCL (DS stands for damage state, pf, vc and nc for *plaster fall-off*, *visible crack* and *no crack*)

PROBABILISTIC MODEL OF PLASTER DAMAGE FOR FRAGILITY ANALYSIS

The probabilistic model was extended by correlating the wall displacement amplitudes to the calculated damage scores. This procedure allows to estimate the damage score for a given wall displacement (e.g. caused by an induced ground motion sequence at interest) to assess the probability of observing a certain damage state. Figure 10 a) and Figure 10 b) show the NCA and NCL observed for a given displacement during the test sequence. Additionally, a linear fit of the displacements and the observed NCA and NCL is depicted with the corresponding 95% confidence intervals. A clear trend can be observed in the data for the NCA, leading to a rather narrow confidence interval. The data points of the displacement and the observed NCL are spread over a larger value area, leading to a wider confidence interval. In combination with Figure 9 a) and Figure 9 b), the probability of observing the *no crack* damage state, the *visible crack* damage state and the *plaster fall-off* damage state can now be estimated for a given displacement amplitude.

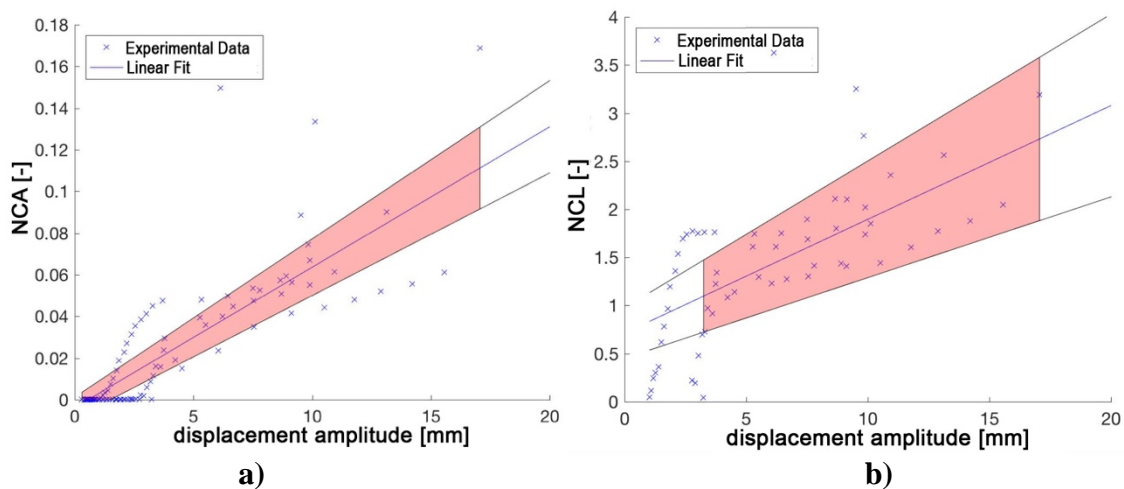


Figure 10: Displacement amplitude and computed a) NCA and b) NCL

First, the expected NCA or NCL is determined using Figure 10 a) or Figure 10 b) for a given wall displacement. For the estimated NCA or NCL, the probability of observing the different damage states can, then, be read from Figure 9 a) or Figure 9 b), respectively. Note that the same displacement amplitude does not necessarily lead to the same damage state probabilities, due to the differences in the quantification of the NCA and NCL. This is, again, mainly related to the fact that an increased damaged area does not necessarily lead to an increased NCL. The NCA is, thus, considered as the more reliable damage quantification score.

CONCLUSIONS

Plastered URM walls have been tested in the Structural Testing Laboratory at ETH Zurich in a 3-actuator quasi-static cyclic test setup. The walls were tested using two different load protocols: the BIN2_99 test protocol, representative of long induced seismicity sequences of low magnitude events, and the NAMC test protocol, representative of low-moderate seismicity. The strain and deformation fields on the plastered wall surface have been tracked during the application of the

load sequences using a DIC measurement setup. The obtained digital images have been post-processed using the Vic2D software, and a procedure to compute two damage scores, based on the obtained cumulative von Mises strain maps, has been developed. The NCA damage score quantifies the damaged area of the plaster surface, while the NCL damage score quantifies the length of the cracks. It has been shown that for higher damage, the NCA might be more representative of the actual damage than the NCL. Three observable damage states have been defined: *no crack*, *visible crack*, and *plaster fall-off*. A survey was done to relate the two damage scores to the three damage states via a multivariate logistic regression. A probabilistic damage model was extended with a correlation of the displacement amplitudes to the calculated damage scores. This procedure allows to estimate the damage score for a given wall displacement (e.g. caused by an induced ground motion sequence at interest) to assess the probability of observing a certain damage state. The methodology and results presented in this study need to be confirmed with the data from additional walls tested during the test campaign. The final goal of the project is to provide a methodology to develop fragility functions to quantify the risk of deep geothermal projects for a built agglomeration.

ACKNOWLEDGEMENTS

The authors wish to acknowledge the help of the technicians of the ETH Zurich Structural Testing Laboratory, Mr. Dominik Werne and Mr. Pius Herzog. The authors gratefully acknowledge the funding from the Swiss Competence Center for Energy Research: Supply of Electricity, NFP70 and ETH Zurich. The findings and conclusions presented in this paper are those of the authors and do not necessarily represent the views of the sponsors.

REFERENCES

Beyer K., and Mergos P. (2015). Sensitivity of drift capacities of URM Walls to Cumulative Damage Demands and Implication on Loading Protocols for Quasi-Static Cyclic Tests. *Proceedings of 12th North American Masonry Conference*, Denver, Colorado, USA.

Correlated Solutions – Vic2D (2017). Correlatedsolutions.com, Last checked: 26.01.2017.

Didier M., Abbiati G., Broccardo M., Beyer K., Danciu L., Petrovic M., Mojsilovic N. and Stojadinovic B. (2017). Quantification of Non-Structural Damage in Unreinforced Masonry Walls Induced by Geothermal Reservoir Exploration using Quasi-Static Cyclic Tests. *Proceedings of 13th Canadian Masonry Symposium*, June 4-7, Halifax, Canada.

The MathWorks Inc. – MatLAB (2015). Release 2015b, Natick, Massachusetts, USA.

Mojsilovic N., and Salmanpour A.H. (2016), Masonry walls subjected to in-plane cyclic loading: application of digital image correlation for deformation field measurement, *International Journal of Masonry Research and Innovation*, 1(2).

INFLUENCE OF THE BEHAVIOUR OF CALCIUM SILICATE BRICK AND ELEMENT MASONRY ON THE LATERAL CAPACITY OF STRUCTURES

R. Esposito¹, S. Jafari², G.J.P. Ravenshorst³, H.R. Schipper⁴ and J.G. Rots⁵

¹Postdoctoral researcher, Delft University of Technology, Delft, The Netherlands, R.Esposito@tudelft.nl

²PhD student, Delft University of Technology, Delft, The Netherlands, S.Jafari@tudelft.nl

³Assistant professor, Delft University of Technology, Delft, The Netherlands, G.J.P.Ravenshorst@tudelft.nl

⁴Assistant professor, Delft University of Technology, Delft, The Netherlands, H.R.Schipper@tudelft.nl

⁵Full professor, Delft University of Technology, Delft, The Netherlands, J.G.Rots@tudelft.nl

In recent years induced seismicity in the Netherlands considerably increased. This phenomenon has a wide impact on the built environment, which is mainly composed by unreinforced masonry (URM) structures. These buildings were not designed for seismic loading, and present peculiar characteristics include very slender walls (100 mm thickness and 2.5m in height), limited connections between walls and floors, and use of cavity walls. A large portion of the URM building stock consists of terraced houses in which the presence of calcium silicate (CS) masonry is often used. The CS masonry is used to build the loadbearing walls, which are part of the cavity wall system. The cavity walls are generally composed of two leaves of masonry separated by an empty cavity, having a thickness of 8-6 mm, and connected with steel anchors. On the basis of the construction year, different masonry unit were adopted to build the inner loadbearing leave: in the period 1960-1980 small CS brick and general purpose mortar were used, while after 1980, the presence of large CS elements and thin mortar layers is predominant. Although these materials are often used in the northern part of Europe, little information is available on their material and structural performance. In this paper, a comparison between the behaviour of CS brick and element masonry is presented. The results of two experimental campaigns carried out at Delft University of Technology are reported. Both masonry types have been characterised at the material level by performing standardised destructive tests, such as compression, shear, and bending tests on wallets. The characterisation at the structural level is carried out by performing quasi-static cyclic tests on full-scale two-story high assembled structures.

Keywords: *Calcium silicate brick masonry, calcium silicate element masonry, quasi-static cyclic tests, full-scale assembled structure*

INTRODUCTION

Due to the increase of the seismic activity in the northern part of the Netherlands, the assessment of the unreinforced masonry (URM) structures become a relevant topic. In this area, the majority of the structures are residential buildings among which the presence of terraced houses is substantial.

After the Second World War, the construction of terraced houses in URM became substantial in the Netherlands. Although many differences can be found from building to building, similar aspects characterise this typology. Terraced houses are usually composed of 5 to 10 housing units. Each of them is typically a two-story high masonry building. The units are characterised by a narrow floor plan being approximatively 5 m in width and 7-9 m in depth. The interstory height varies typically between 2.5 and 2.7 m. The construction is characterised by the presence of large daylight opening in the facades. Consequently, the loadbearing structure is composed of very slender piers and long transversal walls. The walls are mainly cavity walls, in which leaves are connected by steel ties. Different masonry types were used during the years including calcium silicate masonry for the inner leaf and clay brick masonry for the outer leaf. Generally the two leaves are separated by an empty cavity and they are connected with steel anchors. The majority of the buildings present concrete floors, which can be cast in-situ or prefabricated. The transversal walls are loadbearing and carry the floors, while the piers in the facades do not. The floors can span over a single house or be continuing for more than a housing unit. The timber roofs are usually adopted.

Despite the common characteristic illustrated in the previous paragraph, during the years differences can be found in the construction materials and thus the construction details; in particular the use of CS brick and element masonry is of importance. In the period 1960-1980 the mostly CS brick masonry was used to build the inner loadbearing part of the cavity wall, while in the period 1980-2000 the use of CS become popular due to the reduction and simplification in the construction process. Although calcium silicate masonry is diffused in the northern part of Europe, limited information can be found on the characterisation of brick and element masonry. In the past, Dutch researchers studied the behaviour of calcium silicate brick and element masonry (van der Pluijm, 1999; Vermeltfoort, 2007; Vermeltfoort, 2008); however they did not focus on seismic assessment of these structures. On the other hand, European researchers in the field of earthquake engineering (Salmanpour et al., 2015; Zilch et al., 2008) mainly studied the behaviour of CS block masonry having a thickness larger than 10 cm, which is not typically used in the Netherlands.

In order to provide benchmarks for the validation of assessment tools, experimental investigations have been carried out at Delft University of Technology to characterise from material to structural level the behaviour of typical Dutch terraced houses. Two experimental campaigns have been carried out with the focus on the two aforementioned construction periods. In this paper the quasi-static cyclic pushover tests on a CS brick masonry assemblage (Esposito et al. 2016, Esposito et al. 2017a) and on a CS element masonry assemblage (Esposito et al. 2017b) are presented and compared.

CASE STUDIES

Two specimens resembling typical Dutch terraced houses have been tested: a CS brick masonry assemblage and a CS element masonry assemblage. In both cases, the specimen represents only the loadbearing part of a single terraced house unit. As a consequence, only the inner leaf of the cavity wall was built and in the facades the masonry portion between the two piers was excluded.

The overall geometry of the two specimens was kept constant. The facades of the specimens have a length of 5.4 m. Due to limitation of the set-up; the depth of the specimen was restricted to 5 m. The total height of the specimen is 5.4 m. The south and north facades, which are identically, are represented only by the two piers connected to the transversal walls. Two sizes of the piers have been selected: on the western side the wide piers P1 and P3 have a width of 1.1 m, while on the eastern side the narrow piers P2 and P4 have a width of 0.6 m. In order to avoid sliding of the masonry at the bottom, the first course of brick masonry or the kicker layer was glued on the foundation beams. Each floor consisted of two separated prefabricated concrete slabs spanning between the loadbearing transversal walls. The floors were first laid up on the loadbearing walls in a mortar bed joint; subsequently the joints between the floor and the piers were filled by mortar. Consequently, the weight of the floor is not directly carried by the piers in the facades, but only by the transversal walls. The two separated concrete slabs per floor were then connected by cast-in-place reinforced concrete dowels, aiming to approach the behaviour of a monolithic floor.

The CS brick masonry assemblage (Figure 1a) was tested as representative of terraced houses built in 1960-1980 in the northern part of the Netherlands. Small masonry unit having dimensions 210x71x100-mm were used. A running bond pattern was adopted allowing for the interlocking of the bricks at the corners of the transversal walls and the piers. At the first floor level, the floor was connected horizontally to the piers by anchors of 6 mm diameter, cast in the floor and masoned in the piers. The narrow piers were connected by three anchors, while the wide piers by five anchors. These anchors are commonly used as horizontal buckling or wind load support of the pier, and they are not designed to withstand any vertical load. At the second floor level, the floor was laid on both the loadbearing transversal walls and the piers.

The CS element masonry assemblage (Figure 1b) was tested as representative of terraced houses built in 1980-2000 in the northern part of the Netherlands. Large masonry unit having dimensions 897x643x100-mm were used for the facade piers, while unit having dimensions 897x643x120-mm were used for the transversal wall. The masonry was made in stretcher bond. In order to ensure verticality of the wall, a kicker layer made of small masonry unit was adopted at the bottom of the masonry walls both at the ground and first floor. The connection between the façade piers and the transversal wall consisted of a vertical joint; additionally steel ties were placed in the bed joint in correspondence of the vertical joint. Both at the first and second floor level, the floor slabs were laid on both the loadbearing transversal walls and the piers.

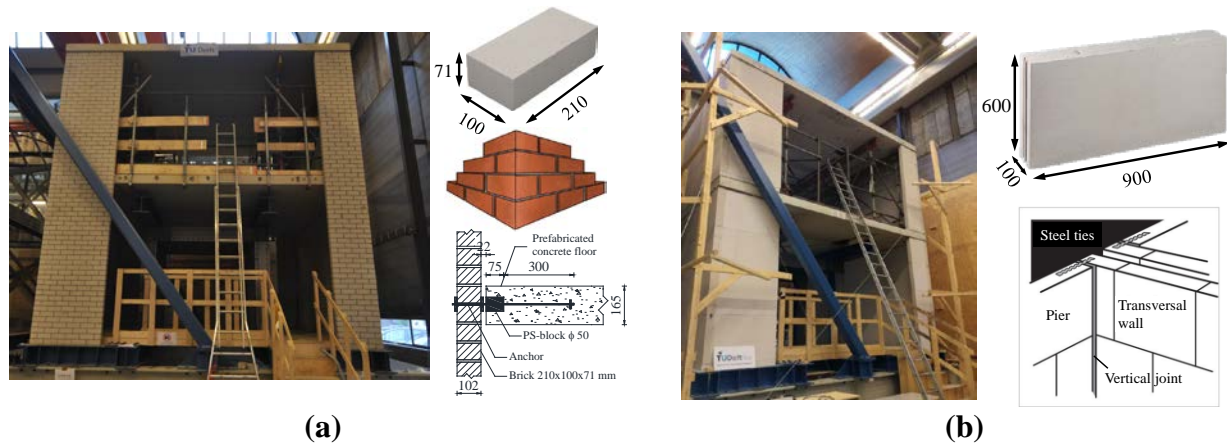


Figure 1: Specimens and main construction details: (a) CS brick masonry assemblage; (b) CS element masonry assemblage.

MATERIAL CHARACTERISATION

The material properties of calcium silicate masonry were selected to represent Dutch masonry used in the construction of terraced house before and after 1980. The compression, bending and shear properties of both masonry specimens were investigated in dedicated experimental campaigns (Esposito et al. 2016, Jafari et al. 2017). The test were mainly performed by following the European standard EN 1052, however a displacement controlled procedure was adopted to obtain an indication of the post-peak behaviour. Table 1 lists the mean material properties for the CS brick and element masonry and their constituents. The CS element masonry showed a higher compressive strength and Young's modulus with respect to the CS brick masonry. In both cases, the pre-peak stage was characterised by linear-elastic followed by a hardening behaviour until the peak. After the maximum stress was reached, a softening behaviour was observed for the calcium silicate brick masonry, while a brittle failure was reported for the element masonry. Both the out-of-plane masonry flexural strength parallel to the bed joint and the initial shear strength resulted higher for the CS element masonry with respect to the CS brick masonry. Consequently the bond between masonry unit and mortar can be considered stronger in the case of CS element masonry.

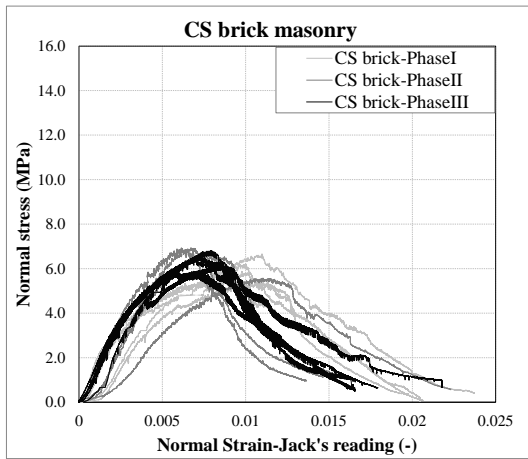
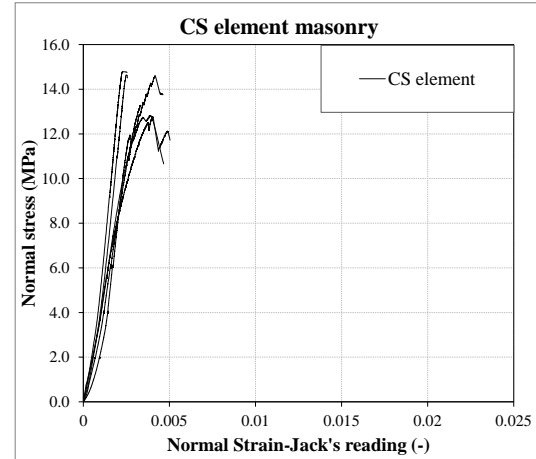
In both specimens the concrete floor was laid on the masonry wall by using a 10 mm thick joint made of general purpose mortar; the mortar adopted was the same of the one used for the CS brick masonry. To characterise the friction behaviour of the wall-to-floor connection, a shear-compression test was performed, similarly to the one for masonry, for the concrete to CS brick masonry interface. Table 2 lists the properties of the floor-to-wall connection. By comparing these properties with the shear properties of masonry specimens (Table 1), it is possible to conclude that the floor-to-wall connection present the same characteristics of any other bed joint in the case of the CS brick assemblage. On the contrary, in the case of the CS element masonry the floor-to-wall connection results weaker than the other mortar joints.

Table 1: Material properties of calcium silicate brick and element masonry.

| Material property | Symbol | Unit | CS brick | | CS element | |
|---|------------|------|----------|--------|------------|--------|
| | | | Average | C.o.V. | Average | C.o.V. |
| Compressive strength of mortar | f_m | MPa | 7.27 | 0.14 | 16.10 | 0.09 |
| Compressive strength of masonry unit | f_b | MPa | 13.26 | 0.13 | 19.50 | 0.06 |
| Compressive strength of masonry perpendicular to the bed joints | f'_m | MPa | 6.01 | 0.09 | 13.93 | 0.07 |
| Compressive strength of masonry parallel to the bed joints | $f'_{m,h}$ | MPa | 7.55 | 0.02 | 9.42 | 0.17 |
| Elastic modulus of masonry in the direction perpendicular to bed joints | E | MPa | 3339 | 0.25 | 8001 | 0.12 |
| Elastic modulus of masonry in the direction parallel to the bed joints | E_h | MPa | 2081 | 0.42 | 7400 | 0.13 |
| Out-of-plane masonry flexural strength parallel to the bed joint | $f_{x,1}$ | MPa | 0.21 | 0.25 | 0.58 | 0.14 |
| Out-of-plane masonry flexural strength perpendicular to the bed joint | $f_{x,2}$ | MPa | 0.76 | 0.47 | 0.73 | 0.04 |
| Masonry initial shear strength of calcium silicate masonry | f_{v0} | MPa | 0.12 | - | 0.83 | - |
| Masonry shear friction coefficient of calcium silicate masonry | μ | - | 0.49 | - | 1.49 | - |

Table 2: Material properties of concrete and floor-to-wall connection.

| Material property | Symbol | Unit | Average | C.o.V. |
|---|-------------|------|---------|--------|
| Cubic compressive strength of concrete | f_{cc} | MPa | 74.7 | 0.02 |
| Initial shear strength of bed joint between concrete floor and calcium silicate masonry | $f_{v0,cm}$ | MPa | 0.09 | - |
| Shear friction coefficient of bed joint between concrete floor and calcium silicate masonry | μ_{cm} | - | 0.52 | - |

**(a)****(b)****Figure 2: Stress-strain relationship in compression: (a) CS brick masonry; (b) CS element masonry.**

TESTING PROCEDURE

A quasi-static cyclic pushover test was performed on both assembled structures. The masonry structure was loaded by four actuators (Figure 3b), two per each floor, positioned at approximately 1.1 m inwards from the facades. A displacement was imposed at the second floor level, while a ratio 1:1 was maintained between the forces at the two floor levels ($F_1 + F_3 = F_2 + F_4$). To impose a constant ratio between the forces at the two floor levels, the forces in the actuators No. 1 and 3 at the second floor level were mechanically coupled to the forces at the first floor level ($F_1 = F_3$, $F_2 = F_4$).

The load was applied by mean of reversed cycles composed by 3 identical runs. A run is defined as the time needed to apply the maximum positive and negative target displacement starting and ending at zero. The speed of the imposed horizontal deformations was chosen for every cycle such that the cycle lasted 15 minutes. As a result of the increasing amplitude, the constant cycle time resulted in a deformation velocity increasing per cycle.

The deformation of the specimen was measured in absolute sense from a stiff wooden frame, which was connected neither to the steel reaction frame nor to the foundation beams (Figure 3b). The displacements along the X-axis, at the point of application of the loading, have been measured with draw wires with length of 150 mm.

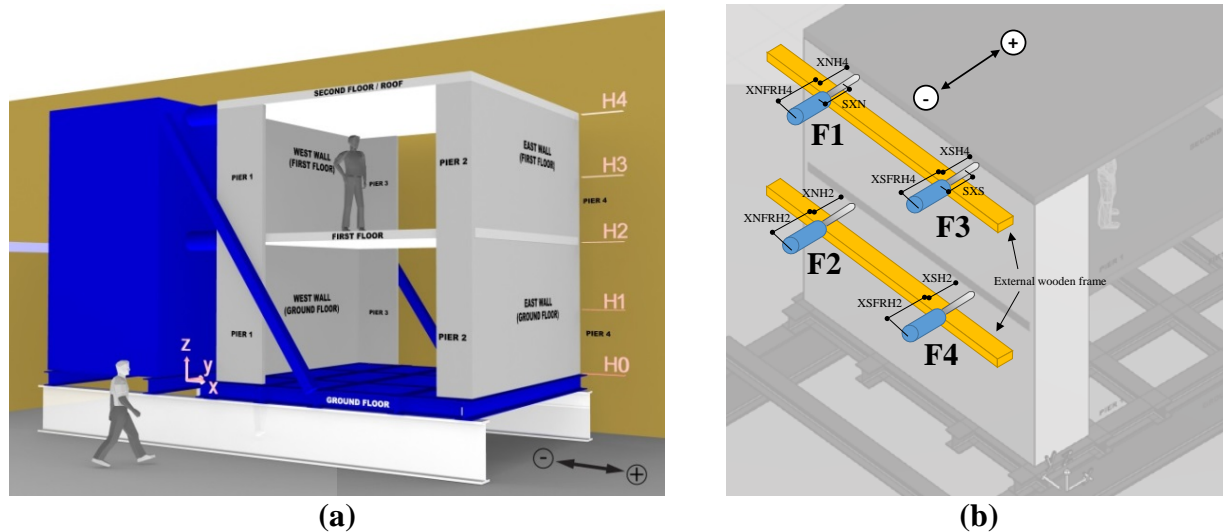


Figure 3: Test set-up

EXPERIMENTAL RESULTS

Figure 4 shows the response of the CS brick and element masonry assemblages in terms of base shear force versus displacement at the second floor level d₂. By comparing the two curves, it is possible to note that the CS brick masonry assemblage shows an higher displacement capacity, while the CS element masonry assemblage shows an higher maximum base shear force. In both cases a reduction of 20% in base shear force was achieved during the post-peak phase, but the test was continued until major damage (or even collapse) in the wide piers was observed. For the

CS brick masonry assemblage the 20% reduction in base shear force was obtained at a displacement of $d_2 = +43$ mm and $d_2 = -80$ mm, while for the CS element masonry assemblage it was reached at a displacement of $d_2 = -28$ mm and $d_2 = +50$ mm.

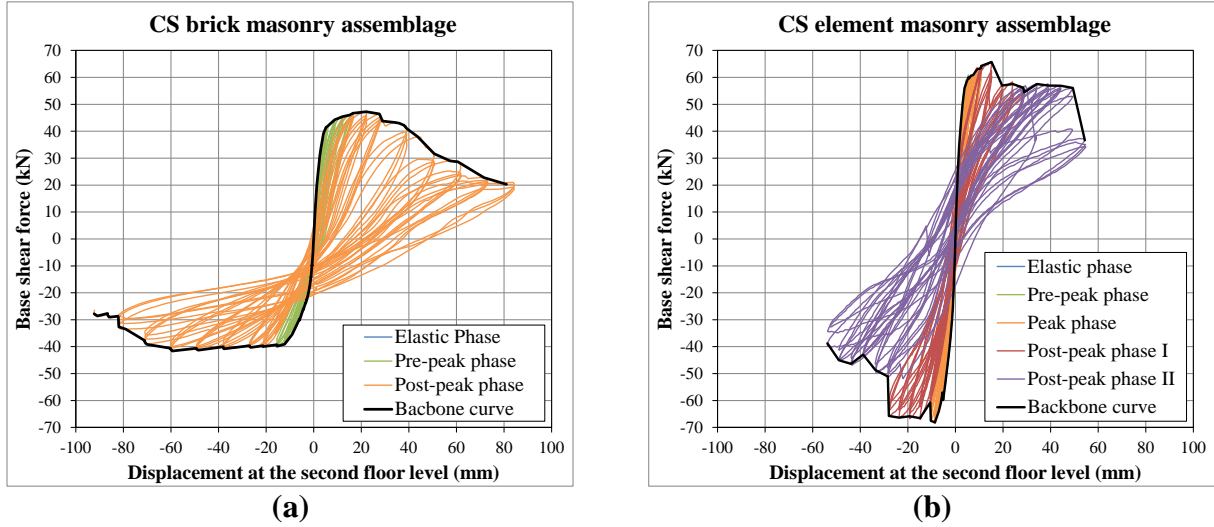


Figure 4: Capacity curve: (a) CS brick masonry; (b) CS element masonry.

In both cases, the failure mechanism was mainly governed by the in-plane damage of the facades piers at the ground floor (Figure 5, Figure 6). First, cracks occurred at the joint between the concrete floor and the masonry walls. Subsequently, diagonal/vertical cracks occurred in the wide pier P1 and P3 at the ground floor, while the rest of the structure was only slightly damaged. During the post-peak phase and prior to major damage in the narrow piers, the wide piers were subject also to a reduction in cross section that led to a further reduction in capacity. Both for the brick and element masonry the diagonal/vertical cracking occurred first in the head and bed joints. However, in the case of the CS element masonry assemblage, large out-of-plane deformation up to collapse of the piers occurred; this is caused by the large size of the masonry units.

By accommodating the in-plane deformation of the piers, the transversal walls deformed out-of-plane showing the effectiveness wall-to-wall connection in both cases. In the case of the CS brick masonry assemblage the running bond allowed a strong connection between the piers and the transversal walls and promoted the flange effect, which is of importance for the base shear capacity (Esposito et al., 2017a). In the case of the CS element masonry assemblage, although cracking occurred in correspondence of the vertical joints at approximately the peak load, the connection was still effective. This was caused by the presence of the steel ties and by the sliding friction mechanism at the vertical joint governed by the high friction coefficient of the CS element masonry. Additionally, the extensive damage of the pier and the detachment of masonry pieces that interlocked within the open cracked promoted local deformation at the end of the transversal wall for a length of approximately 1 m from each wide pier (Figure 6b).



(a)



(b)

Figure 5: Main damage in the wide piers at the ground floor: (a) CS brick masonry assemblage ($d_2 = 82$ mm); (b) CS element masonry assemblage ($d_2 = 54$ mm).

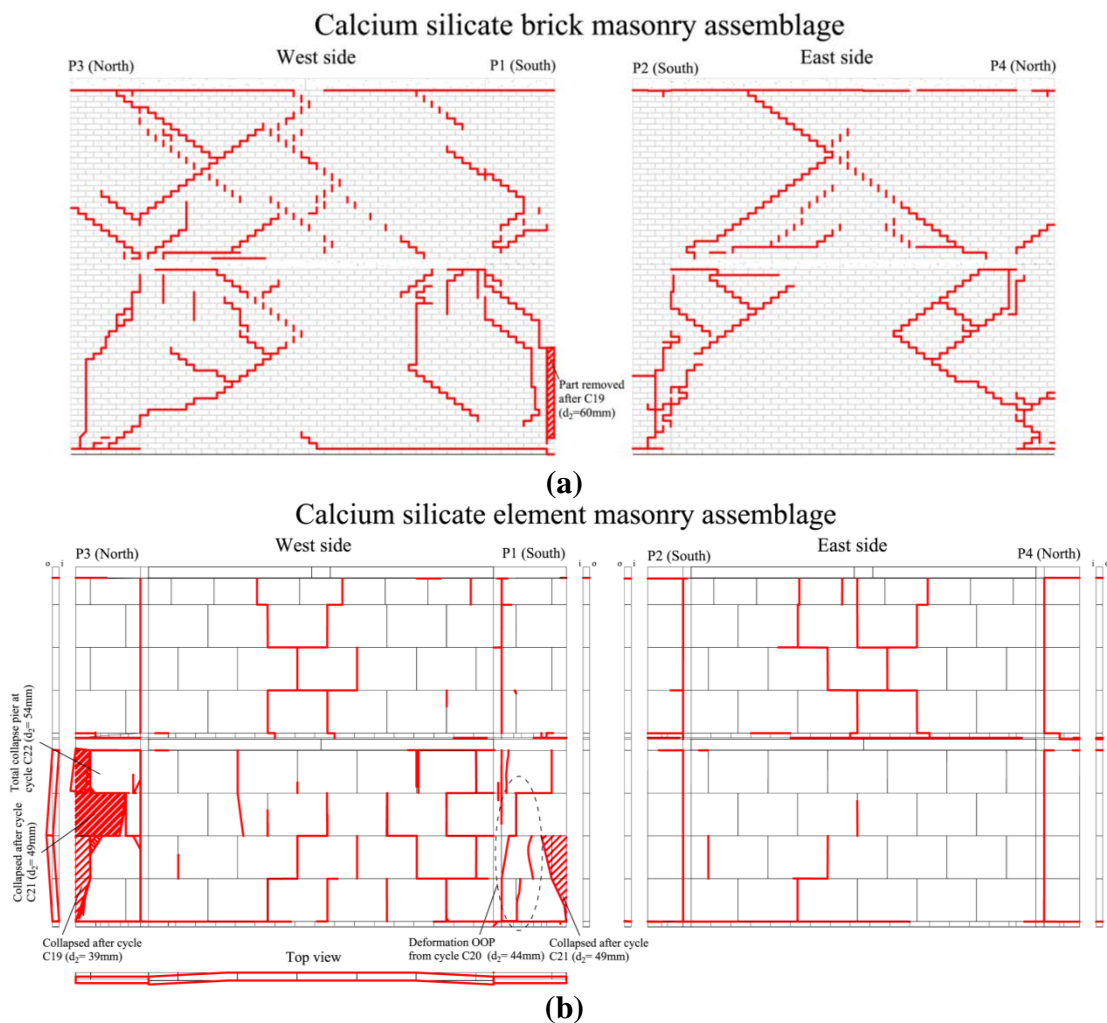


Figure 6: Crack pattern: (a) CS brick masonry; (b) CS element masonry.

Figure 7 shows the behaviour of the structure in terms of interstory drifts as a function of the displacement at the second floor level. They are calculated as the ratio between the relative floor displacement and the interstory height, which is 2.7 and 2.6 m for the first and second floor level, respectively. Although the CS brick masonry assemblage reached larger displacement at the second floor level (82 mm in comparison with the 54 mm of the CS element masonry assemblage), the two structures showed a similar interstory drift for the ground floor varying between 1.6% and 2.2%. A substantial different behaviour is observed at the first floor, where at the onset of damage of the wide pier the CS element masonry assemblage showed a nearly constant drift. This difference can be caused by the different load redistribution on the piers at the level of the first floor slab, which is consequence of the different construction detail. In the case of the CS brick masonry assemblage the piers are only horizontally connected to the floor by anchors, while for the CS element masonry assemblage the floor is laid on top of the piers. Although in both cases the piers do not bear the floor in the undamaged configuration, for relative large displacement the load transferred by the first floor slab is directly redistributed to the piers in the case of the CS element masonry assemblage, while it is indirectly transferred via the transversal walls in the case of the CS brick masonry assemblage. Consequently, in the former case a concentration of displacement is observed at the ground floor leading to a soft-story mechanism.

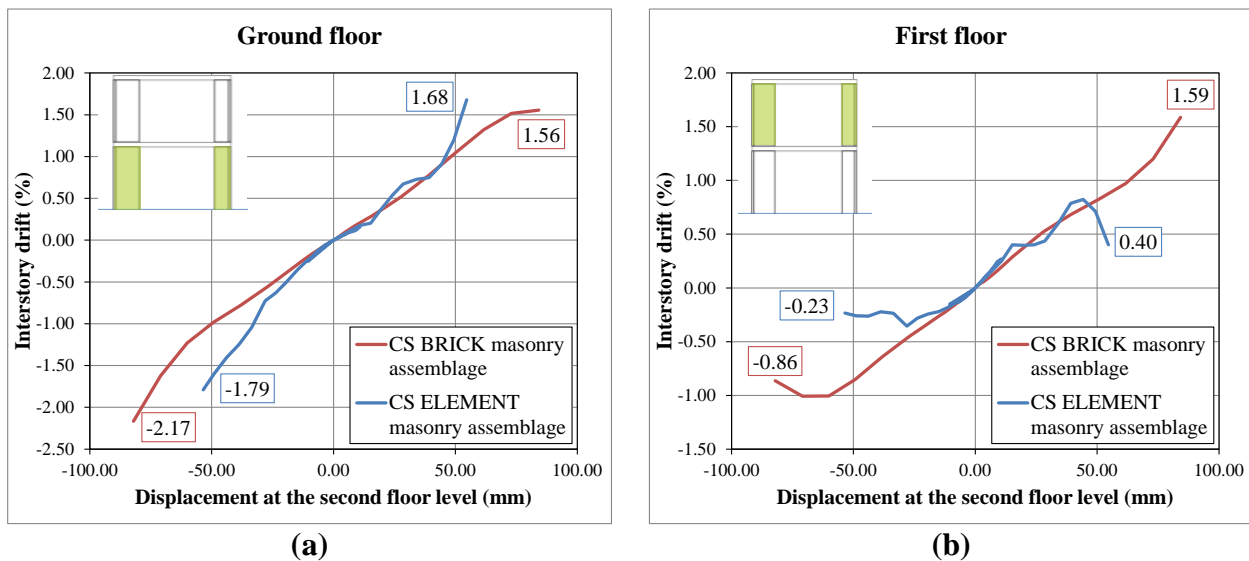


Figure 7: Comparison in terms of interstory drift: (a) Ground floor; (b) First floor.

CONCLUDING REMARKS

In the recent years the assessment of unreinforced masonry (URM) structures become of importance in the Netherlands due to the increase of seismic activity in a country in which earthquake resistant design criteria were not applied. The building stock in the area is mainly composed of low-rise URM structures among which terraced houses represent a large portion.

In order to study the behaviour of typical Dutch terraced houses and to provide benchmarks for the validation of models to be used in the assessment, quasi-static cyclic pushover tests on CS brick and CS element masonry assembled structures have been carried out and presented in this

paper. These tests are part of two large experimental campaigns carried out at Delft University of Technology between 2015 and 2017. The experimental investigation aimed at characterising the behaviour from material to structural level in the framework of the seismic assessment.

Despite the difference in unit size and construction details (e.g. wall-to-wall connection and floor-to-pier connection), similarity can be found in the behaviour of the CS brick masonry assemblage and CS element masonry assemblage. In both cases, the damage is localised at the ground floor and the structural response is mainly governed by the cracking in the wide piers. Although a different wall-to-wall connection is adopted, in both cases the transversal walls accommodate the deformation of the piers. If this can be easily predicted in the case of the CS brick masonry assemblage where the running bond is present, doubts could rise with respect to the vertical joint connection for the CS element masonry assemblage. In fact in this latter case, cracking at the vertical joint occurred approximatively at the peak load; however the transversal wall maintained its coupling with the pier thanks to the presence of the steel ties and the sliding friction mechanism.

A substantial difference can be noticed in the displacement capacity of the two structures. The maximum displacement reached at the second floor level was 82 mm and 54 mm for the CS brick masonry assemblage and the CS element masonry assemblage, respectively. Comparing the behaviour of the two structures in terms of the interstory drift, the difference in displacement capacity can be explained by the localisation of the deformation at the ground floor for the CS element masonry assemblage, which did not occurred for the CS brick masonry assemblage. This caused by the different load redistribution on the piers at the level of the first floor slab, which is consequence of the different construction detail. However, it should be mentioned that the difference in displacement capacity can also be influenced by the different material behaviour. In fact, the CS element masonry material has a more brittle behaviour with respect to the CS brick masonry.

ACKNOWLEDGEMENTS

This research was funded by NAM under contract numbers UI46268 “Physical testing and modelling – Masonry structures Groningen” and UI63654 “Testing program 2016 for Structural Upgrading of URM Structures”, which is gratefully acknowledged. Part of this research was developed in cooperation with the engineering company ARUP, the research centre EUCentre and the calcium silicate masonry association VNK.

REFERENCES

Esposito, R., Messali, F. and Rots, J.G., (2016). Material characterisation of replicated masonry and wall ties. Delft University of Technology. Final report 18 April 2016.

Esposito, R., Terwel, K.C., Ravenshorst, G.J.P., Schipper, H.R., Messali, F., and Rots, J.G., (2017a). Cyclic pushover test on an unreinforced masonry structure resembling a typical Dutch terraced house. *Proceedings of 16th World Conference on Earthquake Engineering*, January 9-13, Santiago, Chile

Esposito, R., Schipper, H.R., Ravenshorst, G.J.P. (2017b). Structural behaviour of calcium silicate element masonry assemblage: quasi-static cyclic pushover tests. Delft University of Technology. Preliminary report No. C31B67WP5-6, March 2017.

Jafari, S. and Esposito, R. (2017). Material tests for the characterisation of replicated calcium silicate element masonry. Delft University of Technology. Report No. C31B67WP1-11.

van der Pluijm, R. (1999). Out-of-plane bending of masonry behaviour and strength. Technische Universiteit Eindhoven, Eindhoven, the Netherlands.

Salmanpour, A. H., Mojsilović, N., & Schwartz, J. (2015). Displacement capacity of contemporary unreinforced masonry walls: An experimental study. *Engineering Structures*, 89, pp. 1-16.

Vermeltfoort, A.T. (2007). The response of calcium silicate element wallets to 2D compression loading. *Proceedings of 10th Canadian Masonry Symposium*, June 8-12, Banff, Alberta.

Vermeltfoort, A.T. (2008). Mechanical properties and application features of CASIELs. *Proceedings of 14th International Brick and Block Masonry Conference*, February 17-20, Sydney, Australia.

Zilch, K., Finckh, W., Grabowski, S., Schermer, D., & Scheufler, W. (2008). ESECMaSE–Deliverable D7. 1b–Test results on the behaviour of masonry under static cyclic in plane lateral loads. TU München, September.

USING THE MACRO-ELEMENT METHOD TO SEISMICALLY ASSESS COMPLEX URM BUILDINGS

F. Gálvez¹, S. Abeling¹, K. Ip¹, S. Giovinazzi², D. Dizhur³ and J. Ingham³

¹ PhD Candidate, Department of Civil & Environmental Engineering, The University of Auckland, Private Bag 92019, Auckland 1010, New Zealand, Fglv390@aucklanduni.ac.nz, Sabe321@aucklanduni.ac.nz, Cip314@aucklanduni.ac.nz,

² Research Fellow, Department of Civil and Natural resources Engineering, The University of Canterbury, Christchurch, New Zealand, Sonia.Giovinazzi@canterbury.ac.nz

³ Lecturer/Professor, Department of Civil & Environmental Engineering, The University of Auckland, Private Bag 92019, Auckland 1010, New Zealand, D.Dizhur@auckland.ac.nz, J.Ingham@auckland.ac.nz

Existing unreinforced masonry (URM) buildings are often composed of traditional construction techniques, with poor connections between walls and diaphragms that results in poor performance when subjected to seismic actions. In these cases the application of the common equivalent static procedure is not applicable because it is not possible to assure “box like” behaviour of the structure. In such conditions the ultimate strength of the structure relies on the behaviour of the macro-elements that compose the deformation mechanisms of the whole structure. These macroelements are a single or combination of structural elements of the structure which are bonded one to each other. Building damage that arose from the Canterbury earthquake sequence was taken as a reference to estimate the most commonly occurring collapse mechanisms found in New Zealand URM buildings in order to define the most appropriate macroelements.

When the macro-elements and their connections are defined, the next step is to impose equilibrium conditions and find the collapse mechanism most likely to be formed, via determination of the activation threshold ($\alpha = a/g$). The classification of a building into macroelements and collapse mechanisms allows the definition of analytical methods to assess the seismic vulnerability.

In addition to definition of the assessment process, the reported case study serves as an example for professionals around New Zealand. The level of considered earthquake shaking is consistent with New Zealand loading standards and is described in terms of the elastic site hazard spectrum C(T).

Keywords: *typologies, macroelements, URM, churches, earthquake, vulnerability*

INTRODUCTION

After the 2010-2011 Canterbury earthquakes an international team of researchers documented the observed earthquake damage to unreinforced masonry (URM) buildings in the Christchurch central business district (CBD). The result was a dataset illustrating the behaviour of URM buildings when subjected to earthquake loading conditions. One of the conclusions drawn from this exercise was that URM buildings are the construction type most vulnerable to seismic activity (Leite et al., 2013).

Current New Zealand regulations for seismic assessment enable many URM buildings to be assessed. However when the complexity of the building increases, it is recommended to utilise analysis techniques which are more appropriate for the real behaviour of the building and the specific individual behaviour of elements affected by inertial forces (NZSEE-Guidelines, 2016). Distinguishing between simple and complex building is not always possible and requires case study analysis. The factors that result in a building being classified as complex are implicit in the assessment methodology. The first mode of vibration is taken as dominant, thereby neglecting higher modes that condition the loading assumption in the assessment. This is the case for stiff or low rise buildings where the acceleration distribution acting on the mass of the URM structure may be assumed to be regular.

International researchers have developed an alternative methodology based on past earthquake experiences and the identification of repetitive patterns in the collapse mechanisms of URM buildings. The framework of the methodology begins with identification of the building typologies that can be found across the country where the assessments are being conducted. Each typology corresponds with a series of specific macroelements that will potentially collapse in observed mechanisms. Each mechanism is assessed using an analytical model based on static equilibrium, and the outcome is the capacity of the element that is then checked against the forecast seismic demand (NIKER, 2010). The main benefit of the macroelement method is that the assessment procedure is a reproduction of the observed collapse mechanisms. Therefore, higher modes of vibration are inherent in the assumptions. The first steps of an adaptation of the macroelement methodology to the historic URM architecture of New Zealand is proposed herein.

URM TYPOLOGY CLASSIFICATION

The macroelement methodology relies on the concept that buildings are composed of single elements or a combination of structural elements whose behaviour is almost autonomous (Lagomarsino, 1998). The repetition of similar structural damage patterns occurring in specific macroelements leads to the notion of determining families of buildings having similar seismic behaviour.

The proposed typological classification distinguishes between I_A (Isolated buildings), I_B (Row buildings), II (Buildings with longitudinal or central plan with one to three naves), III (Buildings having a longitudinal plan with three separated components, being the Foyer, Auditorium with upper gallery, and Stage) and IV (Institutional and industrial buildings that need to be further investigated). All the macroelements found are listed and described in Table 1. A more detailed classification of typology I can be seen in Russell (2010) and for typology II can be found in Marotta (2016).

The reported classification was based on three main sources. Binda et al. (2005) classified heritage buildings in relation to the mechanisms of damage and failure of European buildings when subjected to horizontal actions, and Russell (2010) made a first classification of the building stock found in New Zealand according to the footprint and storey height. Marotta (2016) identified the different New Zealand churches typologies based on their seismic behaviour and macroelements.

Typologies I_A and I_B have been extensively studied, and collapse mechanisms pertaining to these typologies have been identified in post-earthquake situations around the world. Examples from Nepal are studied in Dizhur et al. (2016) and the Italian case is reported in NIKER (2010). After the 2010-2011 Canterbury earthquakes similar collapse mechanisms were observed. Some examples are shown in Figure 1 and Figure 2.





Buildings belonging to Typology II are normally or were originally churches. However, cases of banks, court houses or museums have been documented. This typology is extensively studied and classified into different sub-typologies in Bazzurro et al. (2015) and Marotta (2016). However, all of these buildings share common macroelements (Figure 3) and a family group was defined.

Typology III buildings are composed of the foyer, the auditorium, and the stage. The foyer is the intermediate area between the street and the interior of the building hosting the lobby, the reception, the main stairs, and other multi-purpose spaces. Continuing towards the stage, the auditorium is situated at the space where the audience is seated. Over the ground floor a number of inclined galleries are provided to allow a proper visualization of the stage that are supported by metallic columns. Higher walls comprise the stage where the action takes place. Examples of the distribution are illustrated in Figure 4.

Table 1: Macroelements

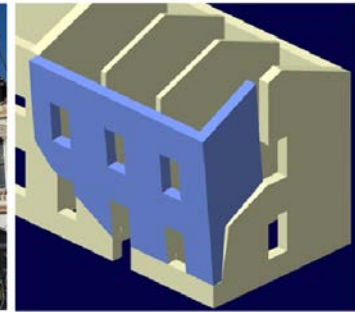
| ID | Macroelements | Description |
|-----|-----------------------|--|
| A | Apse | In a church, termination of the main building at the opposite side of the façade. |
| A-N | Atrium-Narthex | In a church, the lobby or entrance. |
| B | Boxes | Seating area in the auditorium, usually on both sides of the stage. |
| T | Tower | Slender structure normally taller than the rest of macroelements. Typically holds a bell or a clock. |
| C | Chapels | Space attached at either side of the transversal structure. |
| CO | Corner | Element that combines the F and TS. |
| D | Dome | Rounded vault with a circular base. |
| F | Façade | Front wall of the building facing the street. |
| LN | Lateral Nave | In a church, parallel nave to the central nave. |
| PR | Projections | Single blocks. E.g. balconies or ornamentation. |
| S | Stage | In a heritage civic building, termination of the main building on the opposite side of the façade. |
| SA | Separation Arch | Wall between two macroelements with an opening in the form of a curved or flat arch. (Chancel Arch, Proscenium Arch) |
| T | Transept | In a church, nave perpendicular to the central nave that forms the arms of the cross footprint. |
| TS | Transversal Structure | Main body of the building perpendicular to the façade. Central Nave in case of a church. |

Table 2: Building typologies and possible macroelements

| Name | Plan | Description | Possible macroelements |
|------|---|--|---------------------------------------|
| IA |  | Isolated buildings. Examples include stores, dwellings or offices. | F, CO, TS, PR |
| IB |  | Row buildings. Typical in commercial and industrial districts. | F, CO, TS, PR |
| II |  | Longitudinal or central plan with one to three naves. Normally churches but other examples include banks or museums. | TS, LN, F, T, D, SA, A, A-N, C, T, PR |
| III |  | Longitudinal plan with three separated components, the Foyer, the Auditorium with upper gallery, and the Stage. In the foyer the same macroelements as in the typology IB are identified. Examples are theatres, opera houses or event venues. | TS, B, F, CO, PR, SA, S |
| IV | Institutional, industrial (Russell, 2010) (To be classified) | | |



(a) Top of the façade overturning. F macroelement.



(b) Mixed overturning. F and CO macroelements.

Figure 1: Collapse mechanisms found in Christchurch. Schemes by Milano and Beolchini (2009).

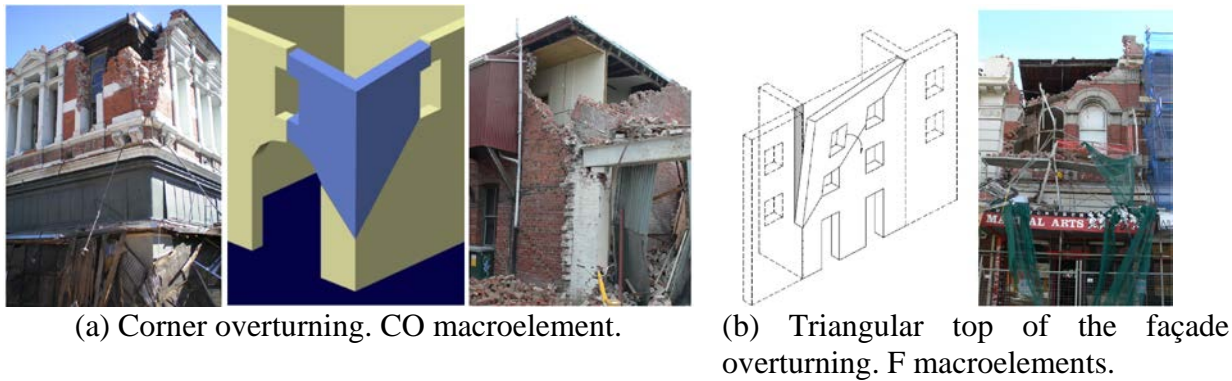


Figure 2: Collapse mechanisms found in Christchurch. Schemes by (Milano & Beolchini, 2009; NIKER, 2010).

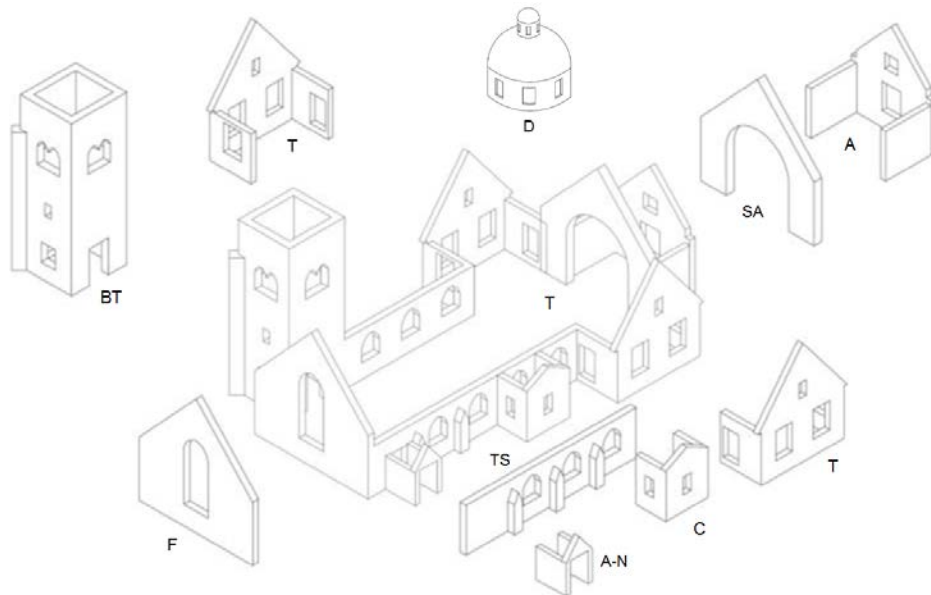


Figure 3: Macroelements composition of type II buildings (Bazzurro et al., 2015).

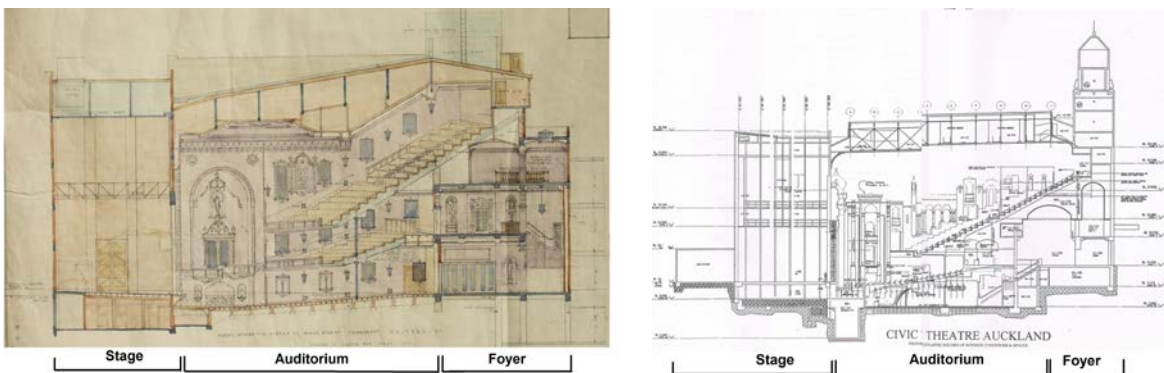


Figure 4: Cross section of typology III examples

Evidence of macroelement formation regarding typology III buildings was identified in the 2010-2011 Canterbury earthquakes as shown in Figure 5. The use of bounding reinforced concrete elements combined with URM (Figure 5) reflects a nationwide trend in utilizing reinforcing elements after the destructive M_s 7.8 1931 Hawkes Bay earthquake (Walsh et al., 2014). Several examples of HURM buildings can be found across the New Zealand context (Russell & Ingham, 2010). Despite the combination of materials, the macroelements are still noticeable, portraying their strong autonomous behaviour. The limited stock of theatres in Christchurch only allowed the identification of some macroelements, with some assumptions about the remaining macroelements being necessary until the rest are confirmed. Figure 6 represents the proposed discretization into macroelements of typology III buildings.



Figure 5: Odeon Theatre collapse mechanisms, Christchurch.

CASE STUDY IMPLEMENTATION OF THE VULNERABILITY ASSESSMENT

The selected case study building is St. Paul's Church in Huntly, Waikato. This building was chosen as a representative example of the URM type II within New Zealand building stock. The inherent

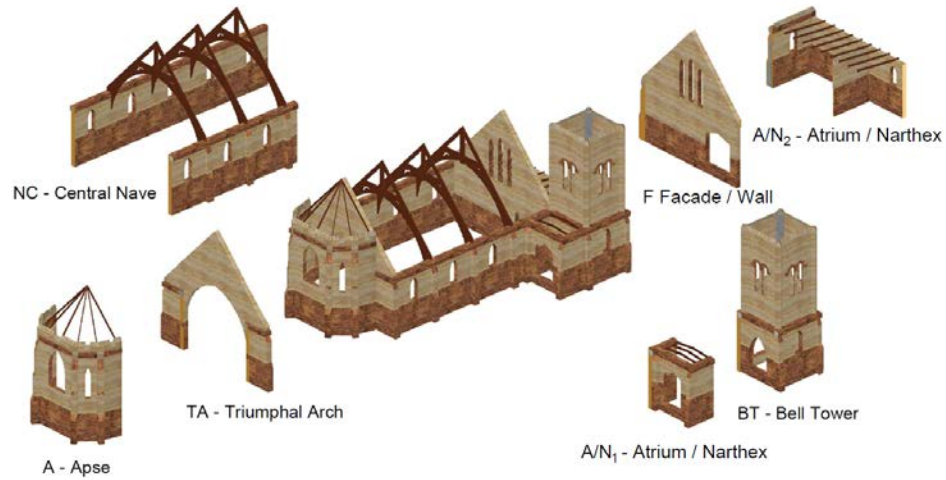


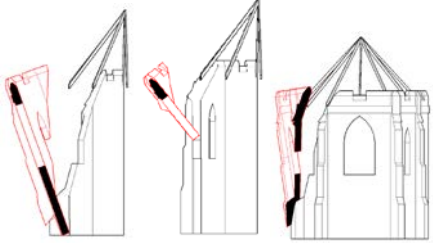
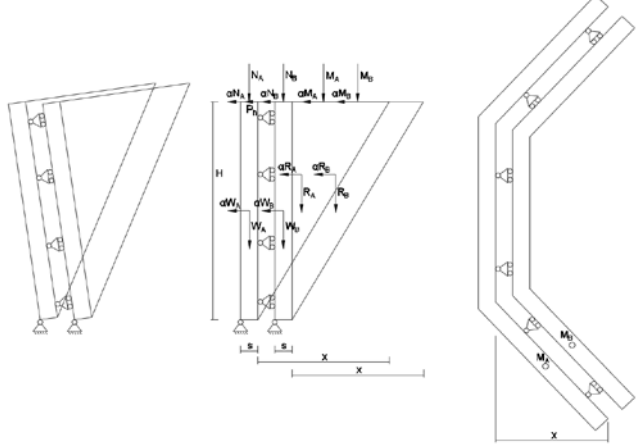
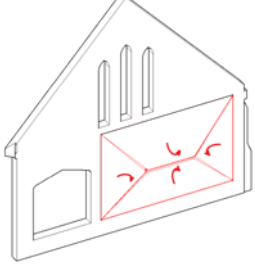
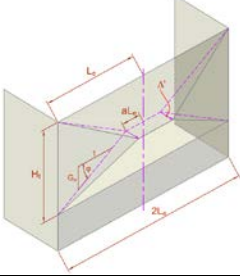
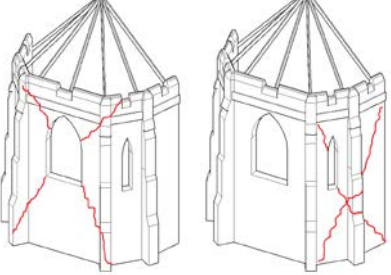
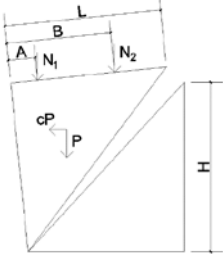
Figure 7: Division of the case study building into macroelements.

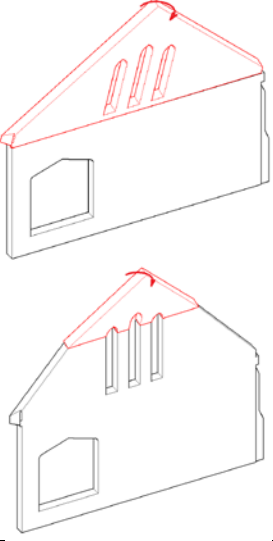
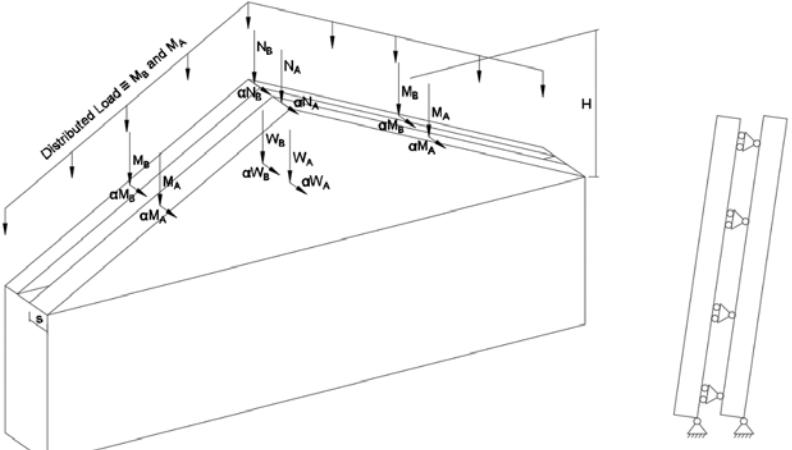
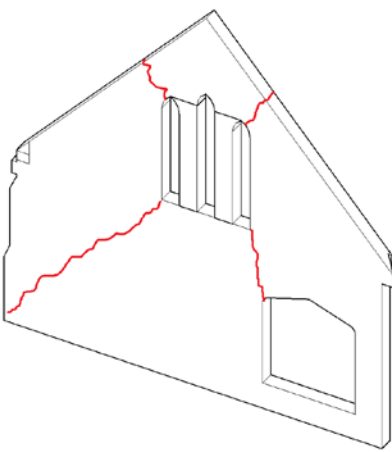
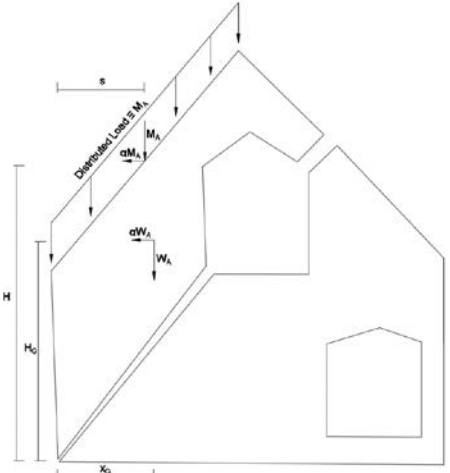
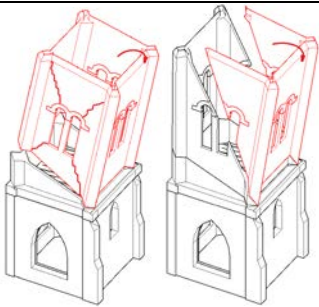

The vulnerability of the potential collapse mechanisms is represented by the activation threshold ($\alpha=a/g$), which is a horizontal multiplier of the lateral forces that activate the local damage mechanism. The calculations of α were conducted using kinematic models according to Milano et al. (2009), Bernardini et al. (1988), Avorio et al. (2002), De Felice et al. (1999) and Vaculik & Griffith (2017). The details are collected in Table 4.

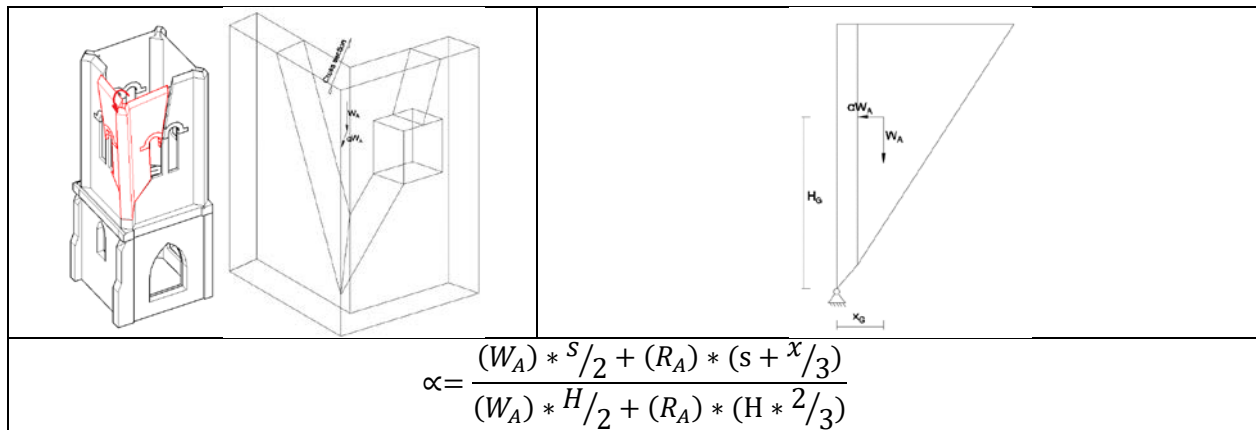
Table 3: Collapse mechanism for the A, F and T macroelements considering the direction of the seismic response and the direction of the earthquake.

| | Seismic Response: In-Plane | | Seismic Response: Out-of-plane | |
|--------|----------------------------|-------------|--------------------------------|------------------------|
| | Longitudinal | Transversal | Longitudinal | Transversal |
| APSE | | | | |
| FACADE | N/A | | | N/A |
| TOWER | Same as IP-T and OOP-L | | | Same as IP-T and OOP-L |

Table 4: Collapse mechanisms and kinematic models.

| A-OOP-L₁, A-OOP-L₂ and A-OOP-T | |
|--|--|
|  |  |
| $\alpha = \frac{(W_A + W_B + N_A + N_B) * \frac{s}{2} + (R_A + R_B) * (s + \frac{x}{3}) + (M_A + M_B) * (s + \frac{x}{2}) - P_H}{(W_A + W_B) * \frac{H}{2} + (N_A + N_B + M_A + M_B) * H + (R_A + R_B) * (H * \frac{2}{3})}$ | |
| F-OOP-L₂ | |
|  |  |
| $K_{2x} \lambda_{r0} = \frac{t}{H_t} \cdot \frac{4[1 + \psi(2 - \epsilon)]}{\frac{2}{3} + \frac{1}{3}a}$ | |
| Formulae developed in Vaculik and Griffith (2017). | |
| A-IP-L and A-IP-T | |
|  |  |
| $c = \frac{\frac{PxL}{3} + N_1xA + N_2xB}{PxHx\frac{2}{3}}$ | |
| F-OOP-L₁ and F-OOP-L₂ | |

| | |
|--|---|
|  |  |
| $\alpha = \frac{(W_A + W_B + N_A + N_B + M_A + M_B) * s/2}{(W_A + W_B + M_A + M_B) * H/2 + (N_A + N_B) * H}$ | |
| F-IP-T | |
|  |  |
| $\alpha = \frac{(W_A * x_G + M_A * s)}{(W_A * H_G + M_A * H)}$ | |
| T-OOP1 and T-OOP2 | |
|  |  |
| $\alpha = \frac{(W_A * s)}{(W_A * H)}$ | |
| T-IP-OOP | |



The seismic demand was calculated using the elastic site spectra according to NZS 1170.5. A soil type A or B was assumed and an estimated period of 0.25s was given to the structure. The hazard factor (Z) was assumed to be 0.15 and the return period as well as the near-fault factor were taken as 1.0.

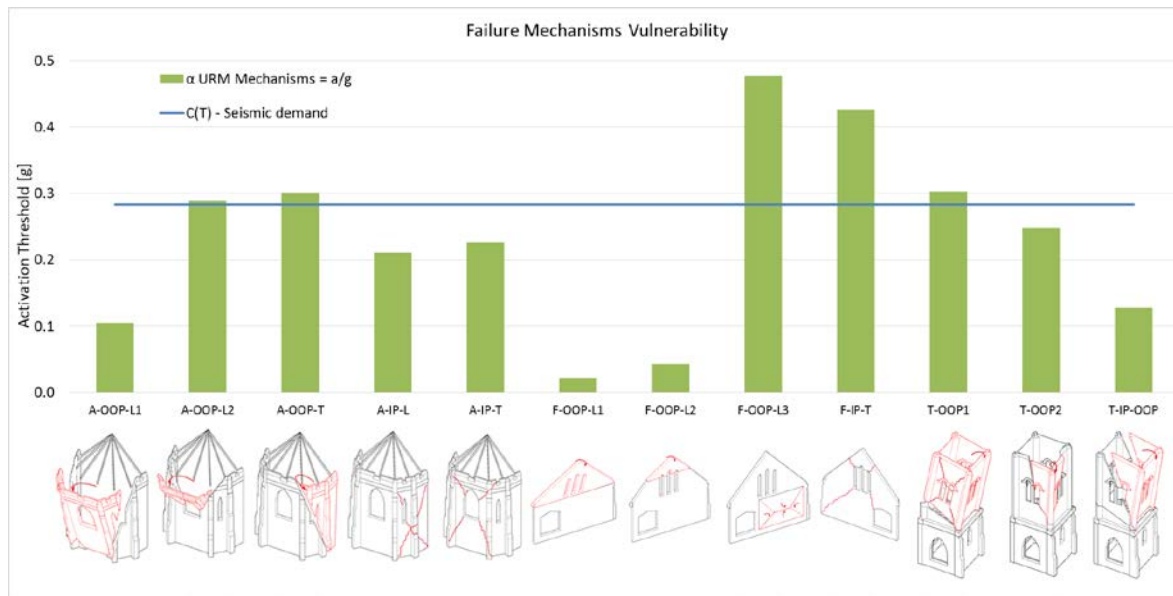


Figure 8: Activation threshold of the possible collapse mechanisms of three macroelements calculated and compared with the seismic demand.

CONCLUSIONS

Local and international approaches for the classification of URM buildings were revised to form a draft framework based on macroelements for the New Zealand historic URM building stock. Typologies I, II and IV were adapted from previous research whilst typology III was proposed to form a unique group.

The draft methodology for seismic assessment of complex URM buildings was presented and applied to a typology III building. Further research will be undertaken to verify the assumptions made for typology III, including a review of overseas investigations. Additional development of typology IV is to be conducted in order to expand the typological classification and implementation of the macroelements approach.

A typology II case study was implemented to describe the vulnerability assessment procedure. Post-earthquake damage analyses are essential for successful implementation of the macroelement method and identification of the most vulnerable elements of the building. The main objective of developing an alternative approach to the current regulations for simple URM buildings is to avoid to develop a consistent methodology and avoid any oversights that may result in missing potentially higher modes or collapse mechanisms.

ACKNOWLEDGEMENTS

This research was supported by QuakeCoRE, a New Zealand Tertiary Education Commission-funded Centre.

REFERENCES

Archives Research Guide to the St James Theatre Complex.

<http://temp.aucklandcouncil.govt.nz/EN/AboutCouncil/HowCouncilWorks/councilarchives/Documents/researchguidetothestjamestheatrecomplex.pdf>; Auckland Council.

Avorio, A., Borri, A., & Corradi, M. (2002). *Ricerche per la ricostruzione. Iniziative di carattere tecnico e scientifico a supporto della ricostruzione*. Roma: Regione dell'Umbria, DEI.

Bazzurro, A., Pinna, M., & Porta, F. (2015). *Seismic damage and vulnerability assessment of churches in New Zealand: proposal of a survey form for emergency management and models for the safety verification*. (Master theSIS), Genoa University (Italy).

Bernardini, A., Gori, R., & Modena, C. (1988). *Valutazioni di resistenza di nuclei di edifici in muratura per analisi di vulnerabilità sismica*.: University of Padova, Istituto di Scienza e Tecnica delle Costruzioni.

Binda, L., Cardani, G., & Saisi, A. (2005, 26th - 28th January 2005). *A Classification of Structures and Masonries for the Adequate Choice of Repair*. Paper presented at the International RILEM Workshop on Repair Mortars for Historic Masonry, Delft, The Netherlands

Cavell, F. B. (1969). *Civic Theatre; a report on the Civic Theatre*,. University of Auckland.

De Felice, G., Terenzi, P., & Tocci, C. (1999). *Criteri di progetto nel recupero strutturale. Codice di pratica per la sicurezza e la conservazione del centro storico di Palermo*.: Bari: Laterza.

Dizhur, D., Dhakal, R. P., Bothara, J., & Ingham, J. M. (2016). Building Typologies and Failure Modes Observed in the 2015 Gorkha (Nepal) Earthquake. *Bulletin of the New Zealand Society for Earthquake Engineering*, 49(2), 211-232.

Dizhur, D., Jiang, X., Qian, C., Almesfer, N., & Ingham, J. M. (2015). Historical development and observed Earthquake performance of unreinforced clay brick masonry cavity walls. *SESOC Journal*, 28(1), 55-67.

Lagomarsino, S. (1998, January 1998). *A new methodology for the post-earthquake investigation of ancient churches*. Paper presented at the 11th European Conference on Earthquake Engineering, Balkema, Rotterdam

Leite, J., Lourenco, P. B., & Ingham, J. M. (2013). Statistical Assessment of Damage to Churches Affected by the 2010–2011 Canterbury (New Zealand) Earthquake Sequence. *Journal of Earthquake Engineering*, 17(1), 73-97. 10.1080/13632469.2012.713562

Marotta, A. (2016). *Seismic vulnerability assessment of New Zealand unreinforced masonry churches*. (Dottorato in Ingegneria Strutturale e Geotecnica), Sapienza Università di Roma.

Milano, L., & Beolchini, G. C. (2009). *Condizioni d'Instabilità Negli Edifici*.

Milano, L., Mannella, A., Morisi, C., & Martinelli, A. (2009). Schede illustrative dei principali meccanismi di collasso locali negli edifici esistenti in muratura e dei relativi modelli cinematici di analisi *Allegato alle Linee Guida per la Riparazione e il Rafforzamento di elementi strutturali, Tamponature e Partizioni*: The Laboratories University Network of seismic engineering and Dipartimento della Protezione Civile.

NIKER. (2010). *Deliverable 3.1 - Inventory of earthquake-induced failure mechanisms related to construction types, structural elements, and materials*. Università di Padova - European Commission.

NZSEE-Guidelines. (2016). *The Seismic Assessment of Existing Buildings Section C8 – Seismic Assessment of Unreinforced Masonry Buildings*: Ministry of Business, Innovation and Employment, the Earthquake Commission, the New Zealand Society for Earthquake Engineering, the Structural Engineering Society and the New Zealand Geotechnical Society.

Russell, A. P. (2010). *Characterisation and Seismic Assessment of Unreinforced Masonry Buildings*. (PhD), University of Auckland.

Russell, A. P., & Ingham, J. M. (2010). Prevalence of New Zealand's Unreinforced Masonry Buildings. *Bulletin of the New Zealand Society for Earthquake Engineering*, 43(3)

Vaculik, J., & Griffith, M. C. (2017). Out-of-plane load–displacement model for two-way spanning masonry walls. *Engineering Structures*, 141, 328-343. 10.1016/j.engstruct.2017.03.024

Walsh, K. Q., Elwood, K. J., & Ingham, J. M. (2014). Seismic Considerations for the Art Deco Interwar Reinforced-Concrete Buildings of Napier, New Zealand. *Natural Hazards Review*, 16(4), 12. 10.1061/(asce)nh.1527-6996.0000169

BASIC STUDY FOR SAFE MASONRY CONSTRUCTIONS AGAINST EARTHQUAKES IN DEVELOPING COUNTRIES COMPARATIVE STUDY ON CEMENT MORTAR FOR JOINTS

T. Narafu¹, H. Sugiyama², H. Imai³ and A. Tasaka⁴

¹ Senior Advisor, Japan International Cooperation Agency(JICA), Chiyoda-ku, Tokyo, 102-8012, Japan,
Narafu.Tatsuo@jica.go.jp

² Professor, School of Regional Design, Utsunomiya University, Utsunomiya, Tochigi, 321-8585, Japan,
sugisugi@cc.utsunomiya-u.ac.jp

³ Senior Researcher, Mohri Architects & Associates. Inc., Chuo-ku, Tokyo, 103-0023, Japan, imai@mohri-aa.co.jp

⁴ Director, Japan Sport Council (JSC), Kita-Aoyama, Minato-ku, Tokyo, 107-0061, Japan, akihiko999@gmail.com

Many houses of middle- or low-income people in developing countries are masonry structures and often called “non-engineered” because there is little intervention by engineers in construction procedures. Those are usually very vulnerable against earthquakes and their collapse often kills people. Authors of this paper have been working on this issue by field surveys in affected areas and a series of experiments including shaking table tests. They found a big difference in performance during shaking motion among the structures on sites in developing countries and the specimens for laboratory experiments. It is assumed that strength of cement mortar is one of the key points which cause the difference. Therefore the authors implemented a comparative study to investigate the causes of the difference by compression tests of mortar specimens prepared with various cement samples from several countries in different distribution channels/storage conditions. They also conducted tests of specimens prepared under different conditions such as mixture proportion of cement/sand, remixing after several hours, and curing, which possibly affect the strength of mortar. The authors found that quality of cement by different countries/manufacturers is not so significant. On the other hand, mixture proportions of cement/sand, construction practice of remixing and curing methods affect the strength significantly.

Keywords: *Masonry, cement mortar, developing countries, earthquake, comparative study, mixture proportion*

BACKGROUND OF STUDY

Masonry structures in developing countries are heavily damaged by earthquakes and kill a large number of people again and again. “Guideline for Earthquake Resistant Non-engineered Construction” describes this situation. Figure 1 shows an unreinforced brick school building in Central Java, Indonesia, damaged by the Central Java Earthquake 2006. You can see the building was totally damaged while the furniture remained standing. This implies the building collapsed by shaking motion which could not make the furniture fall down such as MMI Intensity Scale 7 or 8, or JMA (Japan Meteorological Agency) Scale 5+. This kind of situation is often observed in affected areas in developing countries. On the other hand, a shaking table test at National Research Institute for Earth Science and Disaster Prevention in Tsukuba, Japan (NIED) in December 2007 on unreinforced brick masonry conducted by a research group including the authors showed the structure had high resilience. (“Collapse behavior of a masonry using a shaking table and numerical simulation” reports the result and analysis of the test) Table 1 is a list of major inputs for the shaking table tests. It shows the shaking motion of Iran/Bam and JMA Kobe could not cause any cracks (Input No. 1 and 2). A very strong artificial pulse wave of $1,719 \text{ cm/s}^2$ (No. 3) was given to cause damage and another Iran/Bam followed it. Finally collapse of the structure was realized by Input No. 5. The specimen was prepared using bricks of average quality in Pakistan, and mortar of a usual mixture proportion of local practice of C(cement):S(sand)=1:8 (compressive strength: 9.96 N/mm^2). Figure 2 is a photo just before the collapse during the final excitation of No. 5, JMA Kobe shaking motion. Even though quite large cracks appeared, the structure withstood and escaped collapse in rocking motion for several seconds.



Figure 1: Collapse of school building



Figure 2: Specimen of shaking table test



Figure 3: Debris of specimen for the shaking table test



Figure 4: Debris of an affected building by the Kashmir Earthquake 2005

Table 1: List of inputs of shaking table test

(National Research Institute for Earth Science and Disaster Prevention in Tsukuba, Japan (NEID) in December 2007)

| No of Inputs | Input types | Max. acceleration | Max. velocity | Condition of specimen |
|---------------------|--|---------------------------|----------------------|---|
| 1 | Iran/Bam(100%) | 761.7 cm/s ² | 100 cm/s | no crack |
| 2 | JMA Kobe NS (100%) | 809.5 cm/s ² | 100 cm/s | no crack |
| 3 | artificial strong pulse wave (3 times) | 1,719.1 cm/s ² | — | cracks appeared and grew |
| 4 | Iran/Bam (100%) | 742.0 cm/s ² | 100 cm/s | walls broke into segments and kept rocking motion |
| 5 | JMA Kobe NS (100%) | 793.3 cm/s ² | 100 cm/s | collapse of walls |

It seemed that strong bonding mortar kept all the bricks in the original position and effectuated rocking motion of the segments. Figure 3 shows debris of the specimen for the shaking table test and bricks in the debris are still connected by the mortar. On the other hand, debris of an affected building by the Kashmir Earthquake 2005 in Pakistan (Figure 4) shows that brick walls were broken into pieces. These facts imply that unreinforced brick masonry could possibly have high resilience and one of the key points for the resilience is bonding mortar. This study is conducted to identify key points for strength of bonding mortar for improving resilience of masonry structures. There are a large number of reference books such as “Properties of Concrete” and practical standards such as “Japanese Architectural Standard Specification for Reinforced Concrete Work JASS5”. However construction practice in developing countries on which this study focuses such as extremely high water/cement ratio and inadequate curing is out of scope of these references and the authors could not find a paper which covers the practice of developing countries.

Table 2: List of samples of cement

| Country | Sample | Manufacture | Collecting of samples |
|-----------|--------|-------------------|--|
| Indonesia | A | Holcim | Construction site in Yogyakarta |
| | B | Gresic | Laboratory in a university in Yogyakarta |
| | C | Gresic | small construction material shop No. 1 in Yogyakarta |
| | D | Gresic | small construction material shop No. 2 in Yogyakarta |
| | E | Gresic | small construction material shop No. 3 in Yogyakarta |
| | F | Inodocemnt | small construction material shop No. 4 in Yogyakarta |
| | G | Inodocemnt | large construction material shop in Jakarta |
| Iran | A | NA | ready-mixed concrete plant |
| | B | NA | Construction site No. 1 in Bam |
| | C | NA | Construction site No. 2 in Bam |
| Peru | A | SOL | large home center in Lima |
| | B | SOL | small construction material shop No. 1 in Lima |
| | C | SOL | small construction material shop No. 2 in Lima |
| Japan | A | Chichibu-Taiheiyo | whole sale company |

OUTLINE OF TESTS

Samples of cement for the tests

The authors collected samples of cement in four countries for strength tests of cement mortar through various distribution channels/storage conditions shown in Table 2. The basic principle to collect samples was to obtain usual types of cement for construction of small houses in each country for comparison purpose. As the samples of Indonesia, Peru and Iran were obtained from construction sites, a laboratory of a university, small material shops, home centers, and so on, data on the cement is limited to names of the manufacturers and physical properties or chemical composition were not obtained. Table 2 shows the data obtained on the samples.



Figure 5: Sites and situation of collecting cement samples in Indonesia

Indonesia A: at Construction site in Yogyakarta (left), Indonesia B : Laboratory in a university in Yogyakarta (right)



Figure 6: Shop and situation of collecting cement sample in Indonesia

Indonesia C: at a small construction material shop No. 1 in Yogyakarta. The shop front facing at a street (left) and measuring cement for sale upon request of customers (not by the bag) (right)



Figure 7: Shops and situation of collecting cement samples in Peru

Peru A: at a home center in Lima (left), Peru B: at a small building material shop No. 1 in Lima selling by measurement upon request of customers (right)



Figure 8: Sites and situation of collecting cement samples in Iran

Iran A: at a ready-mixed concrete plant (left), Iran B: at a construction site No. 1 (right)

Photos of examples of sites/shops and situation where samples were collected are shown in Figure 5 to 8. In addition to the samples from the three countries, cement manufactured by a Japanese company was obtained and tested in the same way as the samples from three countries for comparison purpose. The properties and chemical components of the Japanese sample are, density: 3.16 g/cm^3 , specific surface area: $3,310 \text{ cm}^2/\text{g}$, chemical components: C3S: 53%, C2S: 21%, C3A: 9%, C4AF: 9%.

Outline of specimens for the tests

To clarify difference caused by different manufactures, distribution channels/storage conditions, mixture proportions, mixing methods, remixing, and curing methods, specimens for strength tests

using cement samples listed in Table 2 were manufactured. Conditions and specifications for manufacturing the specimens such as mixture proportions and curing methods were decided based on field surveys on construction practice in developing countries reported in “Towards Resilient Non-engineered Construction Guideline for Risk-informed Policy Making”. Manufacturing work followed methods and procedures described below.

Sand: JIS (Japan Industrial Standard) standard sand satisfying requirements in 5.1.3 in Attachment 2, JIS R5201-1997 (density in oven-dry condition: 2.64g/cm^3 water absorption: 0.42%)

Mixing machine: a machine for mortar mixing satisfying JIS R5201-1997

Air condition during manufacturing: $20\pm 2^\circ\text{C}$ and $60\pm 5\%$ RH (relative humidity)

Mold: molds for cement mortar specimens for three pieces of size of $40\times 40\times 160\text{mm}$

The specimens were categorized into five groups as below based on aspects of comparison such as different manufactures, distribution channels or construction practices.

Group 1 for comparison of fourteen cement samples by different manufacturers or distribution channels listed in Table 2

Mixture proportion: cement: sand= 1:3, water: cement= 0.5: 1.0

Curing: removal of the molds at 20-24 hours after placing and curing in water of $20\pm 2^\circ\text{C}$

Group 2 for different mixture proportions (cement/sand ratio)

The specimens were manufactured with cement Japan A. Cement/sand ratios of the specimens are as follows,

Benchmark specimen (Japan A): cement: sand ratio= 1:3

MR(1:5): intermediate cement/sand ratio=1:5

MR(1:8): usual practice in developing countries, cement/sand ratio=1:8

Water/cement ratio: to be determined so as to have same level of Flow Values of the benchmark (The Flow Value of mortar must within the Value of the benchmark (Japan A) $\pm 10\text{mm}$)

Curing: same as Group 1

Group 3 for different mixing methods

It is a usual practice on construction site of small detached houses in developing countries that cement is mixed manually on site. In order to understand the difference in strength by using mixing machinery or not, specimens by manual mixing for four minutes were prepared (specimen name: MM).

Mixture proportion: same as Group 1

Cement: Japan A

Group 4 for influence by remixing

It is also a usual practice on construction site of small detached houses in developing countries that mortar is remixed with additional water when it becomes too viscous after several hours after the first mixing. In order to understand influence in mortar strength by remixing, specimens of following conditions were prepared (specimen names: RM1 and RM3).

Time of remixing: at one-hour (RM1) and three-hour (RM3) after the first mixing

Additional water: water necessary to make the Flow Values the same level of the initial mixing (within the Flow Values of the initial mixing $\pm 10\text{mm}$)

Group 5 for difference in curing methods

It is a common habit that almost no attention is paid for curing of mortar after the masonry work in developing countries. In order to clarify influence by different curing methods, specimens in two different curing methods were prepared. CA24 was cured in the molds for 24 hours and

CA72, cured in the molds for 72 hours. After removal of the molds, the specimens were cured in air of 20 ± 2 °C and $60\pm 5\%$ RH.

Cement: Japan A and Indonesia G

1) Flow Value tests

The Flow Value tests were conducted following JIS R5210-1997.

2) Compressive strength tests

Three pieces were tested for each of specimens at age of 3-day and 28-day. The average values were calculated and written in Table 3 in the column of Compressive strength.

RESULTS AND TEST ANALYSES

Group 1 for comparison of fourteen different cement samples

Results of compressive strength tests for Group 1 are shown in Table 3 and Figure 9. The strength of specimen using the cement Indonesia B was very low. The cement Indonesia B was collected in a laboratory of a university, being kept in an open cement bag for a long time and seemed to have already weathered judging from appearance. The specimen using cement manufactured by Gresik (Indonesia C, D and E) showed higher strength than those using cement by Indocement (Indonesia F and G) at age of both 3-day and 28-day.

Specimens using the cement Iran B and C showed rather lower strength compared with those of Indonesia and Peru. The specimens of Peru B and C using Peruvian cement showed high strength at 3-day age but increase of strength by aging from 3-day to 28-day is smaller compared to those using Indonesian and Iranian cement. The specimen of Japanese cement (Japan A) showed highest values both in 28-day strength and the increase by aging from 3-day to 28-day. It is assumed that it contains higher percentage of C2S which contribute to increase compressive strength for a long period.

In spite of difference observed above, all the compressive strength at age of 28-day do not have large difference except Indonesia B which had suffered from weathering. Small building material shops in developing countries usually sell in a small amount by measuring (not by the bag) such as cement samples of Indonesia C, D, E and F, and Peru B and C. Indonesia A was obtained at a construction site where the construction work had been completed about a week ago and the cement had been left in an open air. The result of the compressive tests shows those differences in storage and distribution channels do not influence the compressive strength of mortar specimens significantly in comparison with other conditions stated below such as mixture proportions, remixing and curing methods. (Details are reported in the following sections).

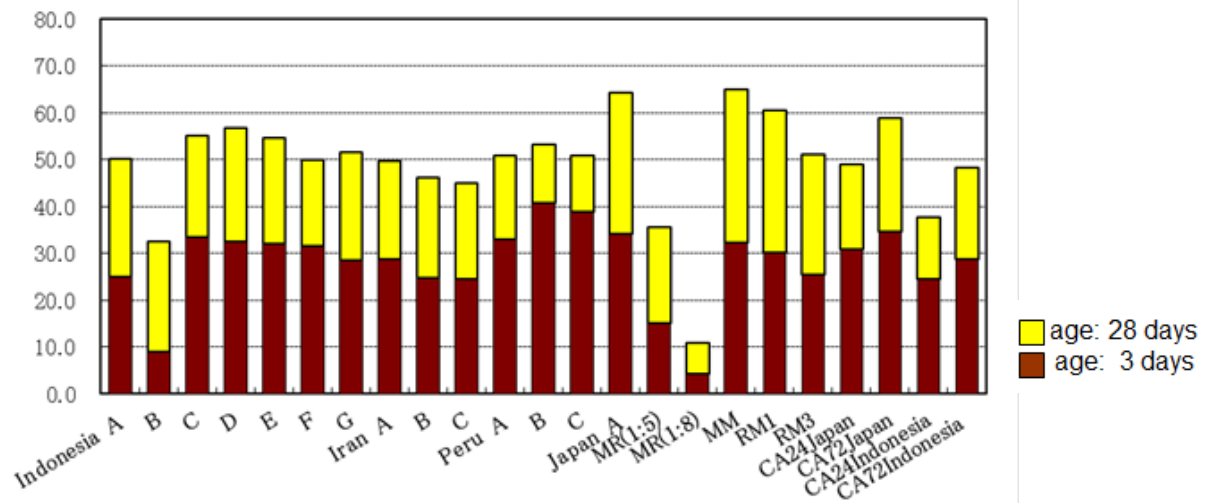


Figure 9: Compressive strength of mortar specimens

Table 3: Compressive strength of mortar specimens (mixture proportion C:S=1:3)

| Specimens | | Manufacturer | Flow Value | Compressive strength (N/mm ²) | | Ratio against Japan A | Increase of compressive strength 2) - 1) |
|-----------|---|-------------------|------------|---|------------------|-----------------------|--|
| | | | | 1) Age of 3-day | 2) Age of 28-day | | |
| Indonesia | A | Holcim | 198 | 25 | 50.1 | 78 | 25.1 |
| | B | Gresic | 128 | 9 | 32.6 | 51 | 23.6 |
| | C | Gresic | 181 | 33.5 | 55.1 | 86 | 21.6 |
| | D | Gresic | 180 | 32.5 | 56.8 | 88 | 24.3 |
| | E | Gresic | 184 | 32 | 54.6 | 85 | 22.6 |
| | F | Inodocemnt | 166 | 31.6 | 50 | 78 | 18.4 |
| | G | Inodocemnt | 188 | 28.6 | 51.7 | 80 | 23.1 |
| Iran | A | NA | 174 | 28.7 | 49.6 | 77 | 20.9 |
| | B | NA | 170 | 24.7 | 46.2 | 72 | 21.5 |
| | C | NA | 173 | 24.5 | 45.1 | 70 | 20.6 |
| Peru | A | SOL | 188 | 33.1 | 50.8 | 79 | 17.7 |
| | B | SOL | 188 | 40.8 | 53.3 | 83 | 12.5 |
| | C | SOL | 186 | 39 | 50.8 | 79 | 11.8 |
| Japan | A | Chichibu-Taiheiyo | 195 | 34.1 | 64.4 | 100 | 30.3 |

Group 2 for different mixture proportions

In usual practice in developing countries, low mixing ratio of cement/sand such as 1:8 is applied. Usually people involved in construction work pay attention to cement/sand ratio, not to cement/water ratio. They just add water so as to make the workability of mortar good for construction work without measuring amount of water. Mixing mortar for the specimens of Group 2 followed similar way by adding water to make Flow Values similar to the mortar of the

benchmark of Japan A. The results of strength tests are shown in Figure 9 and other data such as Flow Values, water/cement ratios and compressive strengths are shown in Table 4. The compressive strength of MR(1:5) (ratio C:S=1:5) and MR(1:8) (ratio C:S=1:8) are both much smaller than the benchmark of Japan A (ratio C:S=1:3). Figure 10 shows these data with cement/water ratio on horizontal axis and compressive strength at age of 28-day on vertical axis. It is clearly observed that points of three specimens are on a line. This means smaller ratio of C:S ratio leads to smaller compressive strength and cement/water ratio is the dominant explanatory factor rather than cement/sand ratio.

The compressive strength of MR (1:8) at age of 28-day is 10.8 N/mm² and around same value as the mortar strength used for the specimen for the shaking table experiment stated in “Background of Study” (9.96 N/mm²), which showed good performance against shaking motion.

Table 4: Results of tests of Group 2

| Specimens | Cement/sand | Water/cement | Cement/water | Compressive strength | Ratio against Japan A |
|----------------------|-------------|--------------|--------------|----------------------|-----------------------|
| | C/S | W/C(%) | C/W | N/mm ² | % |
| Japan A (bench mark) | 1:3 | 50 | 2 | 64.4 | 100 |
| MR (1:5) | 1:5 | 80 | 1.25 | 35.7 | 55 |
| MR (1:8) | 1:8 | 142.2 | 0.7 | 10.8 | 17 |

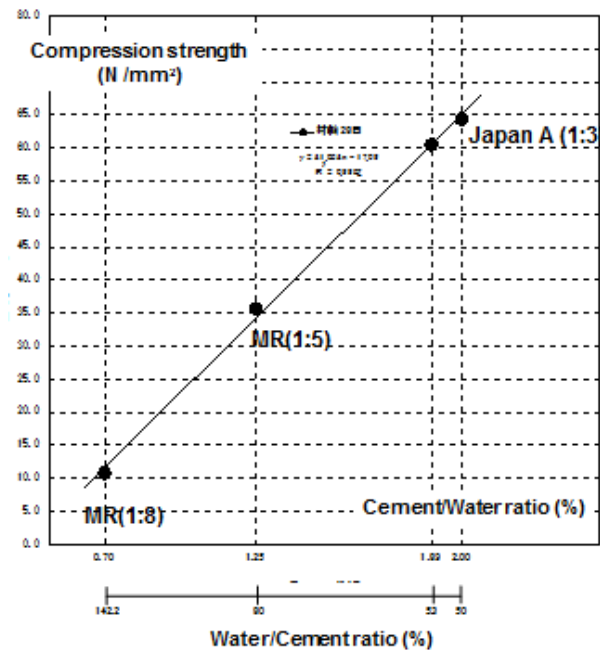


Figure 10: Relation between compressive strength and cement/water ratio

It implies that even mortar of poor cement ratio such as C:S=1:8 could make the brick masonry structure rather resilient compared to the affected masonry structures by earthquakes in developing countries such as Figure 1 and there might be other conditions which would cause the extreme vulnerability observed in those damaged buildings.

Group 3 for different mixing methods

The specimens of mortar by manual mixing (specimen name: MM) has compressive strength of 65.0 N/mm^2 at age of 28-day, which is similar level to that by machine mixing (the benchmark of Japan A) of 64.4 N/mm^2 . Amount of mortar for MM is small and mixing work were done well, which might make the mortar condition similar to that of machine mixing. Further tests under condition similar to actual situation on site are necessary to identify actual influence caused by the mixing methods.

Group 4 for influence by remixing

Mixing conditions of specimens for Group 4 are shown in Table 5. By adding water to keep similar level of workability of the mortar, the water/cement ratio of RM1 (remixing at 1 hour later) became 53% and RM3 (at 3 hours later) became 56%. Remixing invited the reduction of compressive strength by 6% in remixing at 1 hour later (RM1) and 20% at 3 hours later (RM3). As is observed in Figure 10, cement/water ratio and compressive strength are in the linear relation. Both of the results of compressive test of RM1 and RM2 follow this relation but the reduction is larger than the linear relation in Figure 10 especially in the case of RM3. The cause of this result is considered that hardening of fresh mortar already started when the remixing was conducted and the remixing work crushed hardened part of mortar and led to larger reduction of the strength compared to mortar of the same cement/water ratio without remixing.

Table 5: Comparison of influence by remixing (Group 4)

| Specimen | Cement/sand | Water/cement (%) | Flow Value | Compressive strength (28-day)(N/mm^2) | Ratio to Japan A (%) |
|----------|-------------|------------------|------------|--|----------------------|
| Japan A | 1:3 | 50 | 195 | 64.4 | 100 |
| RM1 | 1:3 | 53 | 195 | 60.5 | 94 |
| RM3 | 1:3 | 56 | 194.5 | 51.2 | 80 |

Group 5 for difference by curing methods

The test results of the specimens in different curing methods are shown in Table 6. Two kinds of cement were used (Japan A and Indonesia G).

Table 6: Comparison of influence by different curing methods (Group 5)

| Specimen | Water/cement (%) | Flow Value | Curing | Compression (28 days) (N/mm²) | Ratio to Japan A (%) |
|-----------------|-------------------------|-------------------|-----------------------|---|-----------------------------|
| Japan A | 50 | 195 | in water | 64.4 | 100 |
| CA24Japan | 50 | 195 | in air after 24 hours | 49.1 | 76 |
| CA72Japan | 50 | 195 | in air after 72 hours | 58.9 | 91 |
| Indonesia G | 50 | 188 | in water | 51.7 | 100 |
| CA24Indonesia | 50 | 187 | in air after 24 hours | 37.7 | 73 |
| CA72Indonesia | 50 | 187 | in air after 72 hours | 48.2 | 93 |

The specimens with the both kinds of cement have common tendency that the longer in air, the smaller the compressive strength. In case the specimens were taken off from molds at 24 hours after casting and left in air afterwards, the reduction of the compressive strength is 24 to 27%, and in case taken off at 72 hours, the reduction is 7 to 9%. In many cases in developing countries curing is not considered important. Therefore joint mortar in masonry walls is usually not cured and could not keep humidity being left in hot and dry air, which invites lack of water necessary for cement hardening.

SUMMARY OF RESULTS OF TESTS

It is widely recognized that masonry structures in developing countries are quite vulnerable and kill many people. One of the dominant causes of the vulnerability is considered to be the weak bonding strength of mortar used for the masonry joints. This study is conducted to clarify factors which influence the mortar strength by a series of compressive strength tests of the mortar specimens under various conditions such as different manufacturers, different distribution channel/storage conditions, construction practice such as mixture proportions, remixing, curing methods and so on. Followings are the significant findings of the tests.

- 1) The difference in compressive strength by the different manufactures and distribution channel/storage condition is not significant except the sample under the extremely bad condition (Indonesia B). Those differences are not large and could not account for the extreme vulnerability of actual masonry construction in developing countries and there must be other factors for that.
- 2) Construction practice in developing countries usually applies poor cement ratio such as C:S= 1:8. It is confirmed by the results of tests that the poor cement ratio reduces compressive strength drastically. It is also analysed that the appropriate explanatory variables on compressive strength is not cement/sand ratio, but cement/water ratio.
- 3) As to mixing methods (machine or manual), the test results by the two methods did not show a significant difference in this study.
- 4) One of typical construction practices in masonry works in developing countries is remixing of mortar at several hours after the initial mixing. It is confirmed that remixing caused

decrease of strength, which is caused mainly by increase of water/cement ratio by added water in remixing. The reduction of strength is 6% in case of remixing after one hour, and 20% in case of three hours, which are somewhat larger than mortar strength with the same water/cement ratio without remixing, calculated by the linear relation in Figure 10. The reason of this result is considered that the remixing work crushed hardened part in the mortar which had been already created at the time of remixing.

5) In construction work of masonry structures in developing countries, curing of joint mortar usually does not attract attention and is left in air without any treatment. It is assumed that no curing may affect the strength of mortar and the strength tests were conducted to identify the effects. It is confirmed that curing in air affected in considerable level of reduction of 7 to 9% when left in air after 72 hours and 24 to 27% left in air after 24 hours because of lack of water necessary for cement hardening.

REMAINING ISSUES WHICH NEED FURTHER RESEARCH

The authors have identified several points which affect strength of bonding mortar such as mixture proportions, remixing and curing. In order to prepare complete recommendation for safer masonry structures in developing countries, following points must be explored.

1) Remaining points concerning joint mortar

Quality of sand for mortar might be another critical points for strength of mortar. In most cases in developing countries, sand available near construction site is used without any quality control. Therefore it is assumed that quality of sand differs from site to site and tests on several typical kinds of sand are necessary. Another possible critical point is quality of water. Usually water for mortar mixing is also obtained near the site without any quality control. Effects by salt or organic components should be clarified. The effects by manual mixing are not clarified in this study and need further study.

Identification of acceptable rational mixture proportion could be a very important research topic. It is clarified mixture proportion of cement/sand or cement/water is critical for strength but the idealistic proportion might not be accepted by low income people in developing countries from a view point of cost. As is observed in the shaking table test reported in “BACKGROUND OF STUDY”, considerable resilience of total masonry structure would be realized by certain level of strength of bonding mortar. This topic needs approach on balance between cost of cement and expected strength considering the other factors such as remixing and curing.

2) Construction workmanship

One of the dominant factors of resilience of masonry structure is workmanship of laying work of joint mortar which needs to be filled completely between bricks or concrete blocks. In many cases workers do not care this matter and insufficient filling is often observed like Figure 11, where the mortar does not fill the space between bricks and a void goes through to the other side. Soaking of brick before laying work is another key procedure to obtain good bonding but often ignored on site. Those effects need to be studied to be quantitative manners for analysis considering all the relevant critical points.

3) Quality of materials

Manufacturing procedures and quality of materials such as bricks and concrete blocks are different from those in developed countries. In many cases small scale manufacturers by family

members produce them without quality control such as control of burning temperature of brick manufacturing procedures (Figure 12) and mixing proportion of cement, compaction and curing of concrete block manufacturing. In addition to the strength of the materials, shape/size (critical for precise laying) and condition of surface which contacts bonding mortar need to be studied.



Figure 11: Brick laying in developing countries



Figure 12: Melting brick by rain water

CONCLUDING REMARKS

Most of masonry detached houses in developing countries are constructed by local workers without engineering knowledge using materials without quality control. In order to enhance resilience of structures by improving materials, construction practice, and workmanship, it is impossible to improve all the points to desired level similar to that in developed countries for a short time. Under the situation, the authors would like to take a strategic approach to find an effective and practical way which are acceptable for house owners who are low- or middle-income people, and understandable and feasible for local workers with limited skills and engineering knowledge. In the context this study is conducted to clarify key points for resilience of structures focusing on bonding mortar for masonry joints in a quantitative manner. This study clarifies remixing and curing methods have significant influence to strength of mortar, which could be improved with little cost compared to increase of the cement ratio. Those acceptable recommendations should be delivered to construction site immediately. Since the damage to masonry structures is the dominant causes of the human casualties and property loss caused by earthquakes, further studies should be conducted on the remaining points such as the rational cement/sand ratio, the construction practice and workmanship on site, and the quality of materials by inter-disciplinary studies with participation of more researchers and engineers.

ACKNOWLEDGEMENTS

The authors express sincere gratitude to Mr. Yukiyasu Kamemura, Mr. Kazushi Shirakawa, and Mr. Hiroshi Hirakawa from JICA Expert Team working in Indonesia (at the time of the study) for collecting cement samples and HACHIYO Consultant Co. Ltd. for the excellent mortar tests.

REFERENCES

Takafumi N. , Tatsuo N., Hiroshi.I., Toshikazu H., Qaisar A., Chikahiro M (2012)., Collapse behavior of a masonry using a shaking table and numerical simulation, Bulletin of Earthquake Engineering Volume 10, N.. 1, Springer, pp. 269-283

Anand S. A., Teddy B., Yuji I. (2013), Guideline for Earthquake Resistant Non-engineered Construction, UNESCO, pp. 18-45, 62-95

Japanese Architectural Standard Specification for Reinforced Concrete Work JASS5, Section 4, 5, and 8 (2015), Architectural Institute of Japan (AIJ)

Adam M. N., Properties of Concrete, Chapter 4, 6 and 7 (2012), Prentice Hall

Kenji O., Tatsuo N. and Shizuko M (2016), Towards Resilient Non-engineered Construction Guideline for Risk-informed Policy Making Section 3.2 Constructon Practice of Non-Engineered Cosntructions, UNESCO, pp. 76-83



**MASONRY TODAY
AND TOMORROW**

**11 - 14 February, 2018
SYDNEY AUSTRALIA**

www.10amc.com

CALALSIL™ POLYMERIC SILICATES – A NOVEL GEOPOLYMER CONCRETE FOR A SUSTAINABLE FUTURE

L.S. Burgess-Dean¹

¹ Director, CalAlSi™ Queensland, Australia, leon@bricktec.com.au

Sustainable construction materials using an analogue of silicate mineral paints can lead the way towards a future without the need to use fossil fuels. Silicate mineral paints, cement coatings, geopolymer and calcium silicate coatings have been used for decades to protect and provide aesthetic value to rocks, concrete and fired clay products. Lately, polymer layered silicate nanocomposites have used organic polymers between clay layers to combine the properties of organic polymers with phyllosilicates for use in oil and gas operations. This paper describes water-stabilised polysilicate gels that have been used as the base for geopolymer and the specific case of calcium silicate geopolymer. Ceramic gel-based geopolymers have the advantage of not requiring an organic polymer to act as the double layer that provides ionic stabilisation. Stabilisation of the ionic charge is achieved through symmetry of the silicate chain, counter alkali ions in the aqueous double layer which is supported by symmetrical hydrogen bonding across the chemical surface. Stabilised gel-based geopolymers have been shown to adhere as single-pack coatings to polar substrates including silicates, rocks, concretes, fired clay, glass, metals including aluminium, steel and zinc and polyamides such as nylon. Each coating forms a hard and durable surface by simple evaporation. This development indicates the wide range of fire-proof and fire-resistant products can be produced through basic manufacturing and even construction processes. Additionally the ceramic gel can be coupled with a range of metals and metal oxides to provide all the colours currently available for concrete applications. The sustainability of these mixtures is derived from low temperature preparation of dehydrated clays and the use of chemical bases that can be produced using renewable energy.

Keywords: CalAlSi™, geopolymer concrete, polysilicate, paint, grout, mortar, floor leveller



INTRODUCTION

Sustainability of construction materials supply is often deemed less important than the economics of producing the material to service the largest construction zone. This concept is developed as a value for money proposition when engaged in construction and manufacturing projects. Recently innovation has had a greater focus in construction projects. However, innovative materials are seldom considered as part of the value for money equation.

The main reason for this is the inherent need for construction projects to use the most cost effective method to deliver the construction in the limited time available for the project. The availability of materials such as gravels, aggregates and sand is plentiful around most parts of a construction zone. As a result, these materials are considered as commodities that are interchangeable depending on the economics of extraction and delivery to site. Binder materials such as cement and bitumen or asphalt are generally mass produced by well-established firms who are known for their business outputs and have the abilities to take a long view of future market needs. Therefore, the incentive to change material type is limited even if the materials technology is more than hundreds of years old.

Ordinary Portland cement began its development in the United Kingdom around 1750 and was developed to include a range of calcium silicates up to 1850. Modern cement contains a range of admixtures that produce specific properties in the finished concrete but all rely on the hydraulic process of water adding to cement to create the hardened product. Fired clay and asphalt are even more ancient materials dating back to the year 5000BC. These two types of materials have one common aspect which is that the bulk of the material is held together by a small fraction that acts as a binder.

Most highly regarded opinion about modern uses of these materials splits the applications between structural purposes where concrete and a little fired clay are the materials of choice and water resistant shielding constructions such as road construction where asphalt is preferred. Modern mixtures of course have a variety of admixtures that improves the physical, chemical and microstructural properties of concrete.

Sustainability in the design of buildings and infrastructure involve striking a sensible balance of social, environmental and economic considerations. Considerations include:

- Structural integrity
- Vibration
- Weather protection
- Fire resistance
- Acoustic performance.
- Thermal mass considerations compared with insulation.
- Use of recycled materials from waste streams
- Whole of life value in life-cycle assessment

Recently, modern economies have initiated the concept of advanced manufacturing to produce high performance materials to service industries involved in electronic communications, medical

devices and aerospace applications (Goennemann, 2017). Advanced manufacturing is closely related to sustainability in economies due to the need to develop better technologies to manufacture solutions that make societies more sustainable.

Advanced and traditional manufacturing have largely been considered as quite distinct due to the greater emphasis advanced manufacturing has on the value of research and development, prototyping, market development and servicing (Figure 1).

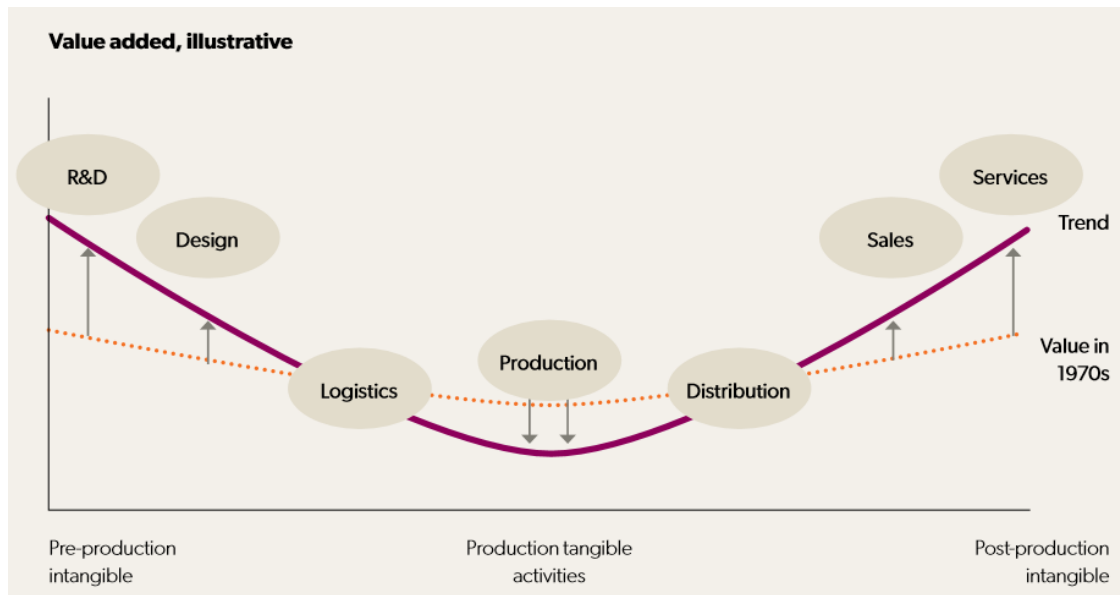


Figure 1: Value in manufacturing is shifting from production to pre- and post-production intangibles such as R&D and Services (Goennemann, 2017)

Sustainability in advanced manufacturing of construction materials has the aim of producing technology that will provide beneficial uses of existing waste streams and better use existing resources. Construction materials must look to waste streams of existing processes due to the clear economic benefit from lower transportation and establishment costs involved in opening new quarries and resource areas compared with using closer sources of material if possible.

Advanced materials also have the benefit of advanced performance characteristic with regards to strength, toughness, insulation, durability and performance in emergency conditions such as a natural disaster. Geopolymers including calcium silicates use adhesion rather than random hydraulic forces to bind aggregate particles together. Unlike asphaltic concretes geopolymers are fire proof, have excellent resistance to acids and bases and can be easily made to be water-proof through the addition of silicone polymers without affecting their fire-proofing properties.

Geopolymer materials technology was first discussed in terms of macro molecules containing the same bonding as silicon-oxygen oligomers contained in clay molecules and quartz. Joseph Davidovits first patented a geopolymer resin formulation in 1979. From this first formulation, numerous academic works have been published regarding the fire, chemical resistance and general durability of geopolymers compared with Ordinary Portland Cement (OPC), fired clay

products and asphaltic concretes. In Australia there have been some constructions projects that used geopolymer concretes such as the Cube at the Queensland University of Technology. Even though these developments have been significant, there does not seem to be any move away from OPC as the material of choice for general concrete applications.

When innovation of construction materials is considered in the context of a value for money proposition, it is often determined through simple calculations that the economics of changing construction material type from OPC to some alternative like geopolymer concrete requires more cost than any single project can reasonably absorb. The reason for this is the extreme cost effectiveness of OPC and asphaltic concretes when compared with the establishment costs of starting up a new extraction, processing and distribution chain involving geopolymers or other advanced composite material. Without innovation incentives such as those offered in high profile construction projects, it is difficult to see where advances in materials technology can enter the construction and manufacturing market given the enormous establishment costs.

A major advantage geopolymers have over OPC and fired clay is the processing temperature required to prepare raw materials prior to the binding reaction. OPC and fired clay both require temperatures above 1000°C to develop the base material from which the final product is derived. The world has undergone a step change in the cost of energy derived from fossil fuels over the past twenty years (Figures 2 and 3). These increased costs of fossil fuels will have an economic impact on the viability of OPC and fired clay products.

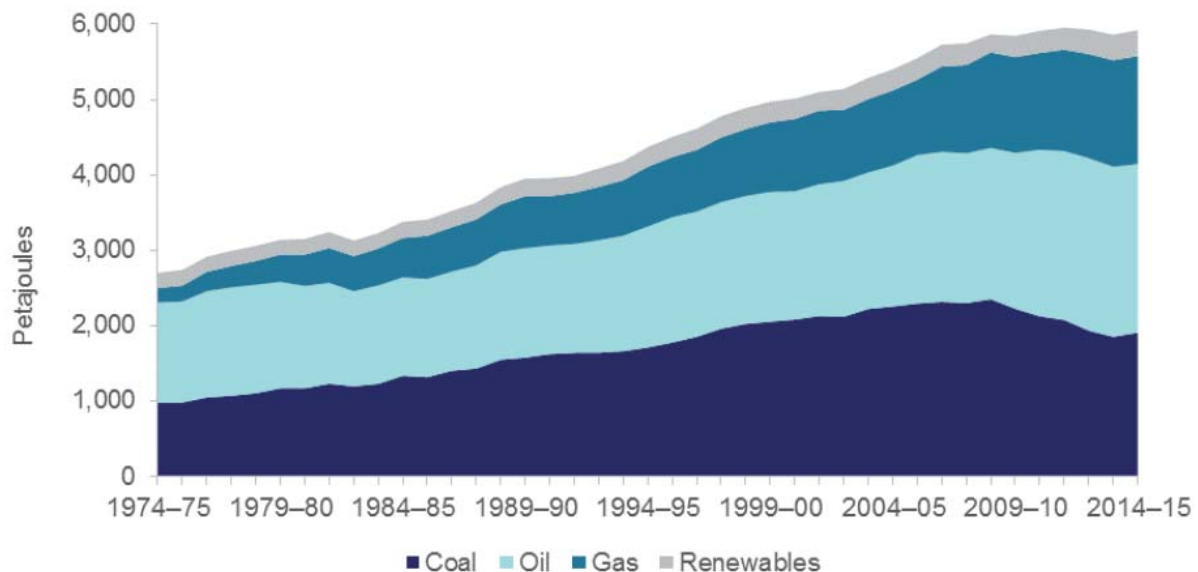


Figure 2: Australian Energy Consumption by Sector (Chief Economists 2016)

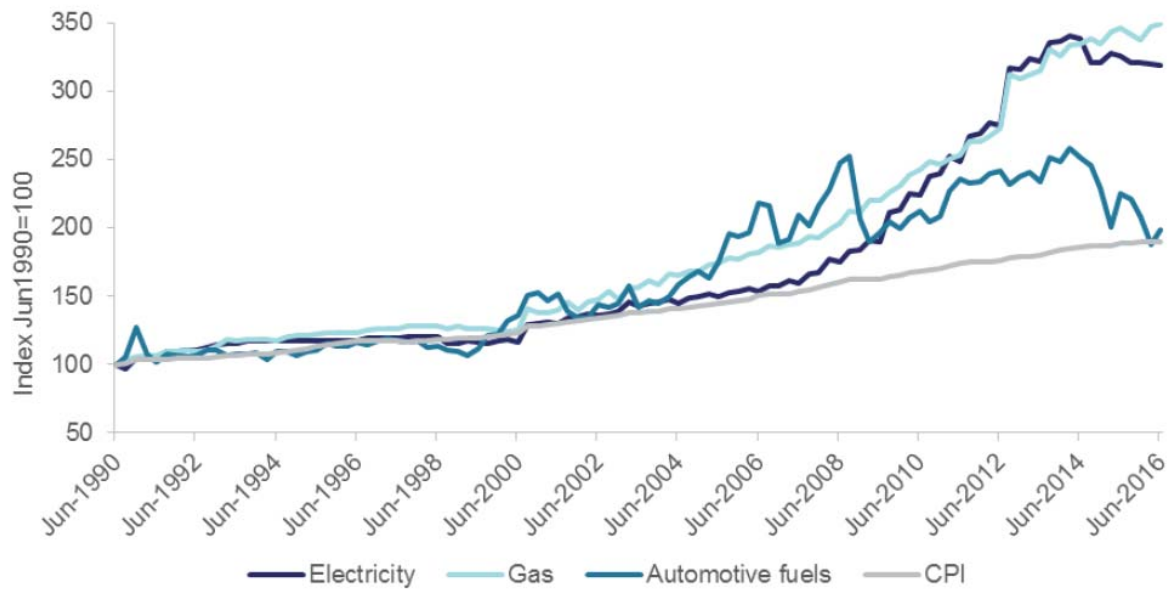


Figure 3: Australian household energy price index (Chief Economists 2016)

Simple modelling suggests that the value for money prospect for using low heat intensive, fire-proof composites like geopolymers improves when compared with OPC and fired clay as the both price and scarcity of fossil fuels increase. Geopolymer production relies on the use of either sodium or potassium hydroxide. These chemicals are produced by hydrolysis which uses a large and expensive quantity of electricity.

This aspect of geopolymer production has been cited as the main reason why large scale production is not economical when compared with gas fired kilns production of OPC and fired clay. However, with the advent of cost effective renewable energy sources such as wind and thermal solar, the sustainability argument for large scale geopolymer production improves when electricity for electrolysis is provided by these renewable energy production.

Geopolymer production has been shown to be possible using coal combustion products (CCPs) such as fly ash and bottom ash from all currently operating coal fired power plants in Australia. The Australian production volume of CCPs is approximately 13 million tonnes per year. The total amount of concrete, aggregate and quarry products required to service housing, building and infrastructure construction is approximately 170 million tonnes across Australia (Slattery, 2013). This equates to approximately 7.5% of the total construction material used each year in Australia can be supplemented by CCPs.

Economics dictate that the best use of resources provides the best outcome for society. Given the need to re-use waste streams such as CCPs, there is a large incentive to determine whether there is an advance material use for CCPs that can be accommodated within less than 10% of the construction materials industry. This paper intends to address some fundamental improvements to material processing and applications that can be achieved using a geopolymer and calcium silicate style of adhesive polymer. The use of innovative silicate gel technology with CCPs

produce advanced geopolymer construction materials will show how advanced materials technologies can provide a significant improvement in sustainability in the construction industry.

BACKGROUND SCIENCE AND ENGINEERING

Silicate mineral paints, geopolymers, calcium silicate and OPC coatings have been used for many decades to protect and provide aesthetic value to rocks, concrete and fired clay products. Rarely have these coatings been used to protect metals, plastics, fibreglass or any other engineering material. This paper discusses an alumina-silicate (CCP) and calcium silicate geopolymer that adheres to polar substrates other than silicates by building in the silicate microstructure into the wet coating.

A review of geopolymer and calcium silicate technology indicates that reactant materials coagulate into a durable solid through adhesive forces followed by coalescence at the chemical and physico-chemical level to produce stable microstructures. This is opposite to the hydraulic processes that create hydrated calcium silicate hydrate crystals from producing most of the cohesion obtained when OPC cures.

For decades hydraulic processes have been considered superior due to their ability to create strength by consuming water rather than leaving pores due to loss. However, to produce the best hydraulic concrete possible there needs to be a combination of both hydraulic and adhesive forces. This has been demonstrated by the additional use of pozzolanic materials that allow water better adhesion to them so that it can be more efficiently used in the hydraulic reaction that produces calcium silicate hydrate and heat.

Concrete also uses metal and plastic fibres to overcome particular property flaws when encountering extreme conditions such as fire or high heat. Plastic fibres are included in concrete to first melt allowing open passage for steam which will be released by the concrete above approximately 300°C. Pozzolans are added to reduce initial water requirements and metal fibres are added for strength during a fire event.

Geopolymers rely exclusively on the pozzolanic and chemical reactions to produce a microstructure built from long chained macromolecules of re-hydrated amorphous pozzolans. Geopolymers do not release a quantum of water at any particular temperature when heated because the curing process eliminates water to allow particles to coalesce. For this reason geopolymers based on either CCPs or calcium hydroxide (silicate) are much more resistant to fire and extreme heat.

To understand more about the adhesive forces that occur during geopolymer reactions it is best to describe some of the common forms of silicon dioxide otherwise known as silica. The most common form is the crystalline mineral quartz. This form is relatively unreactive and often acts as chemically protective filler in geopolymer microstructures. However, many amorphous forms of silica are either reactive or pozzolanic components in the geopolymer microstructure.

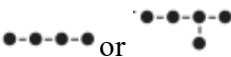
Amorphous silica comes in many forms. Some are listed below:

- Silica xerogel –is the dried out version of silica that is tough, hard and solid. Silica gel contains a nano-porous silica micro-structure, suspended inside a liquid. As a desiccant, it has an average pore size of 2.4 nanometres and has a strong affinity for water.
 - Type A - clear pellets, approximate pore diameter: 2.5 nm.
 - Type B - translucent white pellets, pore diameter: 4.5-7.0 nm,
 - Type C - translucent, micro-pored structure, raw material for preparation of silica gel cat litter.
 - Stabilizing silica gel - non-crystalline micro-porous solid powder, nontoxic, flame-resisting.
- Silica alumina gel - light yellow, chemically stable, flame-resistant, insoluble except in alkali or hydrofluoric acid. Superficial polarity, thermal stability, performance greater than fine-pored silica gel.
- Silica fume – CAS number 69012-64-2 sometimes called microsilica amorphous spherical particles of silica which is a by-product of the ferrosilicon process. Silica fume is often porous and sized at approximately 150 nm. This is the most economical form of amorphous silica and can be a primary source of reactants in geopolymer products.
- Fumed silica – (CAS number 112945-52-5), also known as pyrogenic silica because it is produced in a flame, consists of microscopic droplets of amorphous silica fused into branched, chainlike, three-dimensional secondary particles which then agglomerate into tertiary particles. Size is between 5-50nm.
- Colloidal silicas – are suspensions of fine amorphous, nonporous, and typically spherical silica particles in a liquid phase. Size range 1-5nm. This size approximates to between 64-8000 silica chemical units per particle.
- Precipitated silica or Micronised – is silica that has been precipitated from an alkali silicate solution. Particle sizes range from 5-150nm
- Hydrophobic silica – is an aerosol assisted self-assembly of colloidal silica all having their surfaces fused with a hydrophobic chemical, typically polydimethyl siloxane.
- Silica gel – is a granular, vitreous, porous form of silicon dioxide made synthetically from sodium silicate.

Since all processes (OPC, geopolymer, calcium silicate) are created from an initial aqueous solution, it is best to understand the formation of the reactive species in solution that allows the hydraulic and adhesive reactions to create solid, stable and durable microstructures.

The formation of silicate gel may be divided into three steps (Zhu, 2007):

- (a) The enlargement of sol particle. The smaller the sol particle size is, the stronger the binding strength of the gel.
- (b) The enlarged particles are linked together into a straight or branch chain.
- (c) The gel forms a frame network with steric skeleton like following (Figure 4).



 coalesce into the following network.



Figure 4: Coalescence of sol particles from straight line, branched into a network

If a particle is linked with one or two other particles, its coordinate number is 1 or 2. If a particle is linked with three or more other colloid particles, its coordinate number is 3 or 4. As the average coordinate number increases, the strength and rigidity of the gel also increases. However, the collapsibility and reclaimability decreases with increasing coordination number (Zhu, 2007). Alkali silicate solutions are soluble using either lithium, sodium or potassium cations. The relative size of the cation changes the solubility and reactivity of each silicate. When silicic anion forms a pair of electron charge with these cations, the following phenomena will result in:

Si-O ----- K⁺ ← (9-11) H₂O
 Si-O ----- Na⁺ ← (5-7) H₂O
 Si-O ----- Li⁺ ← 3 H₂O

Typically potassium silicate has higher solubility in water followed by sodium silicate and lithium silicate is insoluble in water. The focus of this study is on the most sustainable combination of materials. That is sodium silicate due to the high availability of sodium in the oceans and across the terrestrial Earth.

Silica gel can be formed using a variety of techniques. When commercially available sodium silicate solutions are mixed with CCPs or calcium silicate a fast and irreversible reaction occurs that causes both reactants to coalesce into a porous solid. It is difficult to control the porosity and therefore, physical properties of the final product when the adhesion reaction takes place too fast for water to be diffused away from the reactants to allow particles to adhere in a nanostructural then microstructural pattern that enhance the finished products properties.

MATERIALS AND METHODS

Technical grade of powdered sodium silicate was obtained from PQ Australia in the ratio of Na₂O:SiO₂ of 3.2:1. Technical grade sodium hydroxide pearls were obtained from Industrial Cleansers. Fly ash from a number of power stations was obtained to perform the same geopolymer reaction. Calcium hydroxide powder was obtained from the local hardware store as produced by Cement Australia.

Fly ash was obtained from Millmerran power station which is characterised as acidic through the higher proportion of iron and aluminium oxides in the amorphous mixture. A second sample of fly ash/bottom ash was obtained from Kogan Creek Power Station which is characterised as an

alkali fly ash that contains a large content of calcium, sodium and potassium ions in the amorphous mineral mixture.

A combination of Linear alkylbenzene acids, linear olefinic acids and alkali metal and ammonium bases were used as the initiators of the gelation reaction that produced a repeatable aqueous silica gel with eight waters of coordination rather than the typical 6 that commercially available sodium silicate solutions have.

The geopolymer formulation was provided in Table 1. Initially the silica gel is mixed with the fly ash with the addition of approximately half of the total; water content to ensure complete mixing. The silica micro particles and silica fume, sodium hydroxide and coloured oxide are then added prior to the final aliquot of water to ensure the gelatinous slurry is completely formed. Mixing was achieved through the use of a helical mixing paddle attached to a rotary drill with a maximum rotational velocity of 1100 rpm.

Table 1 Geopolymer and Calcium Silicate Formulation

| Geopolymer | % | Calcium Silicate | % |
|-----------------------|------|-----------------------|-------|
| Silicate Gel 8 waters | 5.7 | Silicate Gel 8 waters | 16.8% |
| Fly Ash | 35.9 | Calcium Hydroxide | 26.3% |
| Silica 400 | 18.3 | Silica 400 | 12.4% |
| Silica Fume | 9.7 | Silica Fume | 11.8% |
| NaOH | 3.4 | NaOH | 1.6% |
| Coloured oxide | 1.9 | Coloured oxide | 2.2% |
| H2O | 25.1 | H2O | 28.9% |

Each mixture was applied using a paint brush to the following substrates:

1. Fired clay brick
2. OPC concrete
3. Aluminium metal (surface roughened using P180 grit paper)
4. Galvanised steel
5. Mild steel (1040)
6. Stainless steel (304)
7. Untreated timber

RESULTS

Each geopolymer mixture demonstrated excellent adhesion to each substrate. Adhesion was best demonstrated on the fired clay brick and concrete. However, each metal and timber piece showed significant adhesion using all three mixtures. Each mixture was completely water resistant after three days of curing in the Brisbane Autumn conditions without rain. Time to touch was between 1 and 1.5 hours for each mixture for dry film thicknesses between 0.5 to 1.0mm.

There were a small difference in viscosity between the Milmerran fly ash and the Kogan Creek fly ash/bottom ash mixture where the former was more viscous than the latter. This was attributed to the higher acidic character of the Milmerran fly ash. Each mixture displayed significant thixotropic behaviour showing initial viscosity of above 20000 cP which dropped to below 10000 cP after more than 5 minutes of constant stirring.

DISCUSSION

Polymer layered silicate nanocomposites have been developed from hydrated expandable phyllosilicates like montmorillonite that have organic polymers layered between silicate sheets. The class of geopolymers described in this paper are best described as a hybrid between layered phyllosilicates and standard geopolymer concretes. Using silicate gels that have advanced water coordination allow for nano-sized materials to be layered so that adhesion is formed between sheets of alkali activated geopolymer reactant materials.

Geopolymer ceramics uses polymeric joining of amorphous phyllosilicate particles to improve the sustainability and reduce carbon dioxide emissions for concrete production. However, the fundamental challenge of storage, transportation to site and curing time remain the same as concrete made using OPC. The results of this work introduced a new class of polysilicate aquagels that adhere to a range of medium to high surface energy materials.

These composites can be made as bulk mixtures through to nano-composites. Metals, cellulose, wood, stone, crusher dust, sand and recycled concrete are all aggregates that can be bonded with polysilicate aquagels to make a range of stable building products such as grouts, mortars, concrete, paints and putties.

The properties of these polysilicate materials improve on the typical properties of geopolymer materials by using a layered bonded nanostructure to surround aggregate particles. This improves the resulting microstructure by layering each particle to create ordered nano-porosity that reduces density without reducing thermal mass. This improved microstructure has been found through rudimentary experiments to exhibit substantially better insulation to sound, heat while remaining fire-proof.

The layered nanostructure provides resistance to the transmission of sound and heat waves when compared with standard geopolymer formulations that contains micro-pores that are randomly positioned throughout the material. Additionally the storage of polysilicate aquagels and their composites are similar to those of paints, making this the most accessible material for use in remote areas.

The Silicate gel used in this investigation has been trademarked as CalAlSi™. CalAlSi™ gel-based geopolymer formulations are the newest way to chemically align particles so that reaction is delayed while in the wet state and can be allowed to progress when left exposed to evaporate at the application site.

CONCLUSIONS

Ceramic gels have the capability to produce fire-proof ceramic mixtures that can be used as coatings, resins for composites and as binders to metal and polar organic powders. Gelatinising silicate minerals in a form that can separate reactant particles in a water-based solution provides a critical improvement to the usability of these mixtures for both manufacturing and construction purposes.

Geopolymer mixtures can be combined with metal and organic polymer powders to produce high performance aqueous composite mixtures and coatings. As a binder with crystalline silica, the CalAlSi™ gel can be used as a binder in numerous concrete mixtures with CCPs. These mixtures are high performance with regards to strength, durability, thermal and sound insulation, water and fire resistance. These properties are attributed to the nano-structural symmetry of CalAlSi™ gel to align reactant fly ash particles in the finished product.

The use of CalAlSi™ gels as the basis to formulating concrete mix designs provides for a step change in embodied energy when compared with OPC concrete, conventional geopolymer mixtures and fired clay ceramics. The improved sustainability is derived by the ability to improve strength through nano-structural symmetry of the reactant dehydrated clays or fly ash which reduces the amount of binder required for a given set of physical properties. Sustainability is also improved dramatically when the binder which is based on sodium chloride is developed using renewable energy sources to electrolyse sodium hydroxide and hydrochloric acid. Sustainability is further improved when dehydration of clays is achieved at temperatures that can be developed by concentrating solar heat by simple light concentration using mirrors as is currently done in concentrated solar energy converters.

The economics of manufacture are excellent when compared with OPC or fired clay since the mineral resource is similar to fired clay and the extra costs of using sodium hydroxide is offset by the reduced costs of using renewable energy for almost all aspects of the materials manufacture.

Sustainable use of gel-based geopolymers is best demonstrated by the ease of application that a safe, water-based mixture provides to the end user. Construction materials have long been used by the least trained members of the supply chain. Making the process to deliver an aesthetically pleasing construction material allows the application process to be transferred from the trained trade person to the do it yourself enthusiast and creative applicator. These two features will likely drive construction practices in the near to medium term across the world, making CalAlSi™ gel-based geopolymers the material of choice for sustainable and economically affordable manufacturing and construction.

REFERENCES

Goennemann, J. (2017), *Advanced Manufacturing Growth Centre Sector Competitiveness Plan*, Advanced Manufacturing Growth Centre, 2017.

Office of the Chief Economist, (2016), *Australian Energy Update 2016*, Department of Industry, Innovation and Science, Canberra.

Sika http://www.sika.com/en/solutions_products/construction-markets/concrete-additives/concrete-handbook-2013/concrete-types/fire-resistant-concrete.html, (2017).

Slattery, K. (2013), *CCAA Submission Productivity Commission Inquiry: Public Infrastructure*, Cement Concrete & Aggregates Australia.

Zhu C. (2007), *Recent advances in waterglass sand technologies*, China Foundry, Vol 4, No 1.

COMPARISON OF CURING SYSTEMS FOR ZERO SLUMP CONCRETE MASONRY

A. Reyes¹, A. Incera² and M. Murillo³

¹ Master, Professor, Universidad Latina de Costa Rica, Civil Engineering Department; Productos de Concreto, Civil Engineering Department, andres.reyes@ulatina.cr

² Dipl.-Ing., Universidad Latina de Costa Rica, Civil Engineering Department, antonioincera@hotmail.com

³ Professor, Universidad Latina de Costa Rica, Civil Engineering Department, minor.murillo@ pc.cr

Given that the current complementary requirements for structural masonry and the growth of the industry in Costa Rica has arisen, a need to implement production processes that allow to obtain improvements in the compressive strengths of concrete blocks without incurring huge economic changes. As a result, the task of analysing the effect of curing in concrete blocks with dry mixtures has been given by the experimental proposal of 13 methods in laboratory, by testing a batch of 5 blocks in 24 hours, 8 and 28 days. From the implemented systems a comparison was made between pieces without any cure and others exposed to a method assigned as the ideal.

The proposed systems were determined considering the weather, the manufacture site characteristics, economic feasibility, place and accessibility to the materials. Finally, a comparative table of the methods with the greater projection and practicality in its application at industrial level has been made. With the results obtained it is possible to determine the importance of the cure in early stages in concrete blocks with dry mixtures, including the methods of convenience application at industrial level and the compressive strength increase due to the correct application in the curing times.

Keywords: *curing methods, curing concrete blocks, comparison methods, zero slump concrete*

INTRODUCTION

The manufacture of existing concrete blocks and the need of developed production systems with greater benefits, without the need to incur in large economic investments has led to the task of studying the agents of the greatest incidence in the final strength of concrete blocks. Since concrete blocks are made up by dry mixtures their low plasticity and low settlement do not allow a good

adhesion between their physical components. As a consequence, a suitable compaction percentage is required for the mixture to present the physical bonding of the aggregates and a homogeneous behaviour. As the cement hydrates, the relative humidity of the mixture is reduced, causing the paste to lose a significant percentage in its moisture content if no water is supplied by an external medium. This loss of moisture in the paste can alter the final desired properties of the concrete, especially if it falls below 80% in the first 7 days. Under these conditions the curing membranes cannot retain the amount of water needed in the concrete. In this circumstance the use of additional water curing or fogging used by and after the placement of the concrete is recommended, a process that benefits the reduction of cracks by contraction in concretes with a water/cement ratio around 0.3. Concretes with a high cement content and a water/cement ratio below 0.40 require additional special curing processes. Considering the climatic conditions of a tropical country like Costa Rica where there are only two well defined seasons (dry and rainy for 6 months each), the presence of high temperatures, excessive winds and the scarcity of rainfall in the dry season, causes an additional decrease in the strengths reached by the blocks.

Compared with the cure methods of other cement elements, curing the blocks is especially delicate due to the extreme conditions from which these components are dosed. When using minimum amounts of water and cement in the manufacturing of blocks it requires the constant presence of water in order to ensure that the reactions of the existing cement in the mixture are produced completely. The most commonly used curing systems for the production of concrete blocks are natural curing or steam curing.

In order to evaluate the importance of curing on dry mixes and the selection of an ideal method at the industrial production level, thirteen methods of curing in the laboratory were carried out, which allowed to analyse the strength of early stages and their impact on the development of the blocks.

EXPERIMENTAL TEST PROPOSAL

The curing process fulfils three functions depending on its application method; retain the water in the concrete mixture during the early hardening process, reducing the water loss of the concrete surface mixture, and accelerating the gain of the compressive strength using additional heat and moisture. Although heat by steam is one of the most used methods for curing block production, it is a process that has been left out due to its high cost at an industrial production level, in addition to being a method that promotes the gain of strengths at early ages and a slight reduction at 28 days.

After analysing the three functionalities, a series of curing alternatives were proposed based on the requirements of the dry mixes. As we know concrete blocks have a minimum moisture content in their mixture, analysed methods of curing that involve incorporation of water through external agents were indispensable. Based on the proposed methods, the blocks extraction of the curing chambers were carried out without affecting the integrity of the blocks, providing a reasonable time in which the samples had the necessary consistency to be removed from the test areas.

Due to the difficulties of extracting the blocks from the curing chambers, once they have been demolded the application of the methods in laboratory presents an approximate loss of 5 to 6 hours (21-25%) in the cure at early stages (24 hours), primarily taking into account the initial four hours of the concrete setting, as well as the placement in each of the respective areas of the method. In

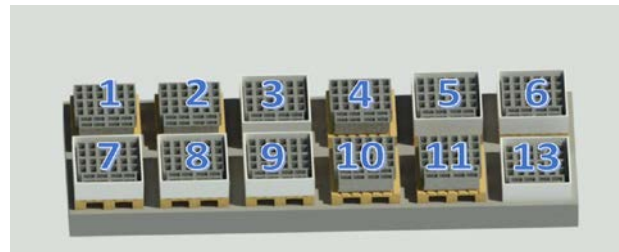
the initial period of dry mixtures, it is necessary to avoid the loss of moisture to the blocks due to the hydration process. In order to perform the analysis of 5 blocks of concrete were extracted from the curing chambers for the compression test at 24 hours, 8 and 28 days, which equals a total of 195 units in the 13 methods. It is important to consider that all the blocks had a density of approximately 2110 km/m^3 and a net area of 260 cm^2 . For the test at 8 and 28 days the capping process was performed according to the INTE 06-02-16 standard, meanwhile, for the test at 24 hours the imperfections and rough areas were removed with a paddle or blade. It is important to make an emphasis on the curing and compressive strengths tests periods, the main reason for an 8 day compressive strength test is trying to resemble the production process in the Factory. Which means a 7 day curing process, and ready to dispatch on the 8th day, however, for this investigation there must be a 7 day curing method applied, proceeding with a capping process to finally begin testing on the 8th day. For the 28 day compressive strength test as well, it is required to extract the blocks from the curing process on the 25th day, then it is necessary to make the capping procedure and test on the 28th day.

Figure 1(a) shows the different methods proposed in site followed by Figure 1(b) which has the initial (suggested) scheme of placement of the different proposals. As can be observed there is a variability in their locations, this is due to the fact that the wet chambers were placed as a micro sprinkler serial system, which we could ensure that the water flow could be decreased being distributed among several curing chambers. In addition, the spray systems were placed in one area and the covers in another trying to avoid the direct contact of the water from one method to another.

Otherwise, in Figure 1 (a) most of the pallets have different methods attached together, being allowed as long as the curing process during that period was related; for example, blocks exposed to sprinklers in method 6 were together with the blocks exposed to sprinklers in method 5, and so on depending on each curing method.



(a)



(b)

Figure 1: (a) On-site methods, (b) Initial proposed methods sketch

Details of the curing methods are presented in Figures 2-14, corresponding to Figure 1b and Table 1.

1. Non-curing outdoor concrete blocks for 28 days (NCO).



Figure 2: NCO

2. Non-curing indoor concrete blocks for 28 days (NCI).



Figure 3: NCI

3. Concrete blocks cured in moist chamber simulation * for 28 days (MC).



Figure 4: MC

4. Concrete blocks cured with sprinklers for 7 days, followed by 21 days outdoors with no curing processes (S+NCO).

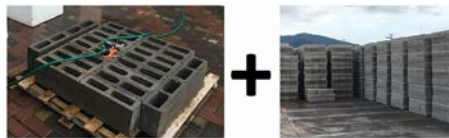


Figure 5: S + NCO

5. Concrete blocks cured in moist chamber simulation * for 24 hours, followed by 27 days of outdoor water sprinklers (MC+S).



Figure 6: MC + S

6. Concrete blocks cured in moist chamber simulation * for 24 hours, followed by 6 days of outdoor water sprinklers and finally 21 days outdoors with no curing processes (MC+S+NCO).



Figure 7: MC + S + NCO

7. Concrete blocks cured in moist chamber simulation * for 24 hours, followed by 6 days of cure using saturated coverings (burlap according AASHTO M182) with a polyethylene film on top, and finally 21 days outdoors with no curing process (MC+SC+NCO).



Figure 8: MC + SC + NCO

8. Concrete blocks cured in moist chamber simulation * for 24 hours, followed by 6 days of cure using saturated coverings (burlap according AASHTO M182) with a polyethylene film on top, and finally 21 days of outdoor water sprinklers (MC+SC+S).



Figure 9: MC + SC + S

9. Concrete blocks cured in moist chamber simulation * for 24 hours, followed by 27 days of curing by saturated coverings (burlap according AASHTO M182) with a polyethylene sheet on top (MC+SC).



Figure 10: MC + SC

10. Concrete blocks cured with saturated coverings with a polyethylene film on top for 7 days, followed by 21 days outdoors with no curing process (SC+NCO).



Figure 11: SC + NCO

11. Concrete blocks cured with saturated coverings with a polyethylene film on top for 28 days (SC).



Figure 12: SC

12. Concrete blocks cured with a Prodex ** thermal insulation cover for 28 days (P) [not illustrated method in Figure 1 (b)].



Figure 13: P

13. Concrete blocks cured in a polystyrene foam case with a sheet of water in the bottom of the box without direct contact of the blocks for 28 days (PWB).



Figure 14: PWB

Note:

* Polystyrene case with the ability to retain the temperature (21-25 °C) and relative humidity (greater than 95%). Fogging applied.

** Thermal insulation produced in Costa Rica used in roofs.

BLOCK TEST ACCORDING TO ASTM C140 / C140M - 14B STANDARD

From the tested blocks an average of 5 strengths achieved in each of the different stages were realized, including a more accurate result of the sampling that the INTE 06-02-13 demands with 3 blocks. In order to have a better perspective of the acquired results, a summary table is made that contains the 13 methods with their average strength, respective curing period, amplitude, minimum and maximum strengths with their respective graph.

As can be seen, the methods with more relevant results are those which include additional water at the 24 hours mark, inclusive the saturated coverings brings sensitive gains in the blocks strength, however, the saturated burlap and Prodex cover imply a difficult placement process.

Table 1: Summary fc of blocks exposed to different times and methods of cure

| Summary fc of blocks exposed to different times and methods of cure. | | | | | | | | | | |
|--|-------------|------------|------------------|--------|-----------------------|--------|-----------------------|--------|-------------------------|--------------------|
| Method | Cure (days) | fc (days). | fc, Kg/cm2 (MPa) | | Max. fc, Kg/cm2 (MPa) | | Min. fc, Kg/cm2 (MPa) | | Amplitude, Kg/cm2 (MPa) | Standard Deviation |
| 1. NCO | 1 | 1 | 52.1 | (5.1) | 56.3 | (5.5) | 45.8 | (4.5) | 10.5 (1) | 4.10 |
| | 7 | 8 | 102.3 | (10.0) | 107.9 | (10.6) | 96.8 | (9.5) | 11.2 (1.1) | 4.24 |
| | 25 | 28 (f'c) | 144 | (14.1) | 150.4 | (14.8) | 135.1 | (13.3) | 15.3 (1.5) | 7.46 |
| 2. NCI | 1 | 1 | 54 | (5.3) | 58.6 | (5.7) | 51.4 | (5.0) | 7.2 (0.7) | 2.85 |
| | 7 | 8 | 111 | (10.9) | 117.7 | (11.6) | 102 | (10.0) | 15.8 (1.6) | 6.17 |
| | 25 | 28 (f'c) | 128.8 | (12.6) | 138.0 | (13.5) | 115.6 | (11.3) | 22.4 (2.2) | 10.45 |
| 3. MC | 1 | 1 | 61.9 | (6.1) | 63.8 | (6.3) | 59.4 | (5.8) | 4.4 (0.5) | 1.91 |
| | 7 | 8 | 134.2 | (13.2) | 144.4 | (14.2) | 127.9 | (12.5) | 16.5 (1.7) | 6.71 |
| | 25 | 28 (f'c) | 176.6 | (17.3) | 191.2 | (18.8) | 157.5 | (15.5) | 33.7 (3.3) | 13.93 |
| 4. S+NCO | 1 | 1 | 53.6 | (5.3) | 56.6 | (5.6) | 51.9 | (5.1) | 4.8 (0.5) | 1.79 |
| | 7 | 8 | 111.7 | (11.0) | 119.7 | (11.7) | 101.5 | (10.0) | 18.2 (1.7) | 6.55 |
| | 25 | 28 (f'c) | 163.1 | (16.0) | 179.6 | (17.6) | 145.2 | (14.2) | 34.4 (3.4) | 15.51 |
| 5. MC+S | 1 | 1 | 62.3 | (6.1) | 69.5 | (6.8) | 56 | (5.5) | 13.5 (1.3) | 4.84 |
| | 7 | 8 | 128.5 | (12.6) | 142.9 | (14.0) | 118.2 | (11.6) | 24.8 (2.4) | 10.97 |
| | 25 | 28 (f'c) | 208 | (20.4) | 214.7 | (21.1) | 191.0 | (18.7) | 23.6 (2.4) | 9.76 |
| 6. WC+S+NCO | 1 | 1 | 62 | (6.1) | 68.3 | (6.7) | 57.5 | (5.6) | 10.8 (1.1) | 4.61 |
| | 7 | 8 | 125 | (12.3) | 142.6 | (14.0) | 111.4 | (10.9) | 31.2 (3.1) | 12.28 |
| | 25 | 28 (f'c) | 188.5 | (18.5) | 207.7 | (20.4) | 169.7 | (16.7) | 38.0 (3.7) | 14.10 |
| 7. WC+SC+NCO | 1 | 1 | 56.5 | (5.5) | 60.6 | (5.9) | 53.3 | (5.2) | 7.3 (0.7) | 2.69 |
| | 7 | 8 | 117.2 | (11.5) | 128.6 | (12.6) | 107.3 | (10.5) | 21.4 (2.1) | 8.89 |
| | 25 | 28 (f'c) | 165.7 | (16.3) | 172.1 | (16.9) | 159.1 | (15.6) | 13.0 (1.3) | 5.24 |
| 8. WC+SC+S | 1 | 1 | 53.6 | (5.3) | 57.3 | (5.6) | 50.62 | (5.0) | 6.68 (0.6) | 3.40 |
| | 7 | 8 | 114.4 | (11.2) | 129.9 | (12.6) | 108.9 | (10.5) | 21 (2.1) | 8.96 |
| | 25 | 28 (f'c) | 155.1 | (15.2) | 172.8 | (17.0) | 139.9 | (13.7) | 32.9 (3.3) | 11.70 |
| 9. WC+SC | 1 | 1 | 60.4 | (5.9) | 62.8 | (6.2) | 56.7 | (5.6) | 6.1 (0.6) | 2.50 |
| | 7 | 8 | 119.1 | (11.7) | 121.9 | (12.0) | 113.5 | (11.1) | 8.5 (0.9) | 3.25 |
| | 25 | 28 (f'c) | 163.7 | (16.1) | 183.7 | (18.0) | 142 | (13.9) | 41.7 (4.1) | 15.60 |
| 10. SC+NCO | 1 | 1 | 60.7 | (6.0) | 62.9 | (6.2) | 57.8 | (5.7) | 5.1 (0.5) | 1.97 |
| | 7 | 8 | 116.2 | (11.4) | 126.4 | (12.4) | 104.5 | (10.2) | 21.9 (2.2) | 7.94 |
| | 25 | 28 (f'c) | 147.9 | (14.5) | 154.6 | (15.2) | 138.7 | (13.6) | 15.9 (1.6) | 5.85 |
| 11. SC | 1 | 1 | 61.5 | (6.0) | 64.9 | (6.4) | 57.9 | (5.7) | 7.0 (0.7) | 3.03 |
| | 7 | 8 | 112.2 | (11.0) | 116.4 | (11.4) | 100 | (9.8) | 16.4 (1.6) | 7.02 |
| | 25 | 28 (f'c) | 163.8 | (16.1) | 169.7 | (16.7) | 158.6 | (15.6) | 11.2 (1.1) | 3.97 |
| 12. P | 1 | 1 | 61.2 | (6.0) | 65.0 | (6.4) | 59.4 | (5.8) | 5.6 (0.6) | 2.28 |
| | 7 | 8 | 112.7 | (11.1) | 124.4 | (12.2) | 104.6 | (10.3) | 19.8 (1.9) | 7.51 |
| | 25 | 28 (f'c) | 163 | (16.0) | 176.6 | (17.3) | 150.8 | (14.8) | 25.8 (2.5) | 11.98 |
| 13. PWB | 1 | 1 | 64.2 | (6.3) | 68.8 | (6.7) | 58.2 | (5.7) | 10.6 (1.0) | 5.14 |
| | 7 | 8 | 128.7 | (12.6) | 131.9 | (12.9) | 123.8 | (12.1) | 8.1 (0.8) | 3.24 |
| | 25 | 28 (f'c) | 154.6 | (15.2) | 168.5 | (16.5) | 147.1 | (13.4) | 21.4 (3.1) | 8.63 |

From the graph “*average fc vs. curing time*” in figure 15, it is possible to have a more specific idea of the strengths reached by the dry mixtures in presence of a series of number of curing methods, at one side this graph allows to extract the methods with more projection at a production level, in another side is possible to recognize the most critical systems.

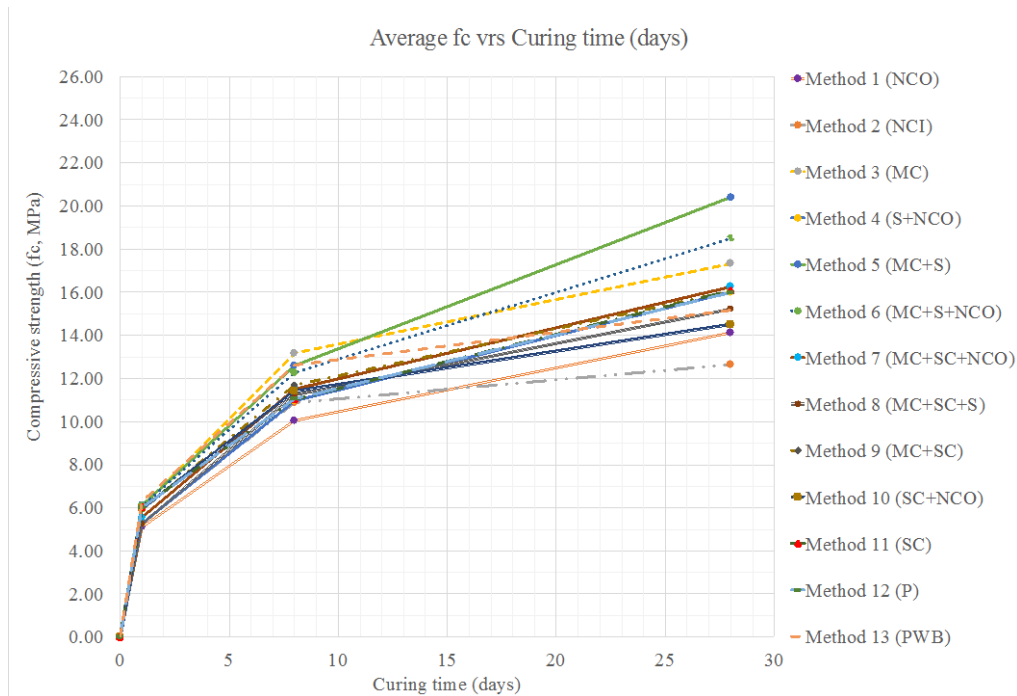


Figure 15: fc average of blocks exposed to different times and methods of cure

In table 1 the methods with the greatest projection are those which incur in moisture adhesion at the early stages of the blocks, such as method 5, 6, 7, 8. Applying the curing system by means of a wet chamber in the first hours of the block allows a partial hardening, a contribution to the humidity necessary for a continuous hydration process and a gain of the compressive strengths at early stages. Figure 16 shows the lower part of the wet chamber simulations (polystyrene) once all have been placed in each respective site, it is necessary to place the whole serial system of micro sprinklers as soon as possible.



Figure 16: Blocks placed in the wet chambers simulation

In presence of methods with satisfactory results that demonstrated the positive effect of a well-defined curing process as one of the fundamental agents that compose the compressive strength of the dry mixtures, it is possible to define method 5 as the most efficient in terms of compressive strengths gains, although, it is not a viable system in an industrial process. A non-viable method is the one that incurs in a curing systems period up to more than 7 days, which corresponds approximately at a 70% of the expected compressive strengths in some types of cement according to the recommendations of the ACI (American Concrete Institute) and the PCA (The Portland Cement Association). At a manufacturing level, reducing the delivery time of the blocks provided a sensible economic improvement, the application of curing for 28 days incurs an over cost in the production processes.

For this and more reasons method 6 has been assigned as the most feasible process, which means the easiest, more effective and economical way a method can be applied, based on this a series of comparisons between a critical method and the one of greater importance were carried out in order to obtain a percentage reflected in the increase of compressive strengths due to the application of a suitable cure, which means a correction factor between a well done cured system and slightly curing.

Method 2 did not incur any additional cure, however, the blocks were also exposed to no weather or controlled temperature as can be observed in the results, this system has the lowest strength. Although at the production level the blocks are always exposed to at least a minimal cure in order to emphasize the importance of the cure in dry mixtures, this system has been considered as the critical method and will be the reference against the ideal system. In addition, method 2 is intended to refer to a cure performed in the yard in the summer period, which corresponds to high temperatures and lower precipitations.

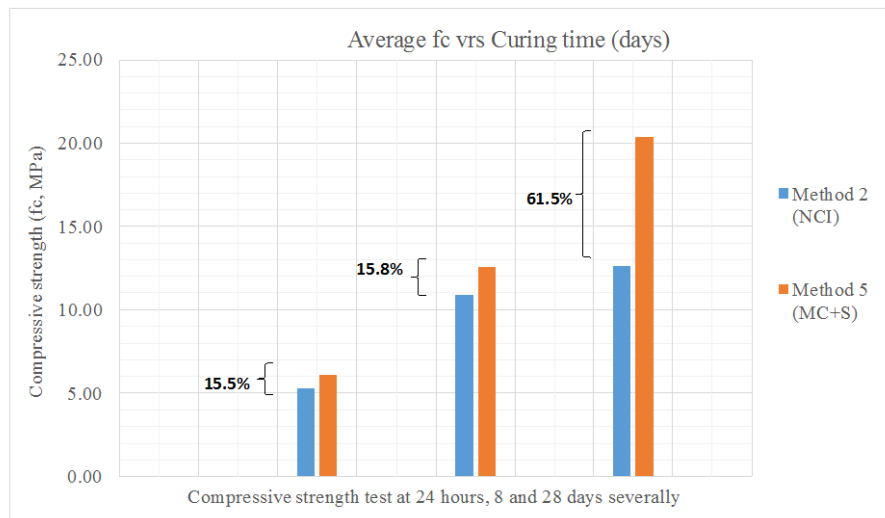


Figure 17: Comparison of method 2 against method 5 in the compression strengths obtained at 24 hours, 8 and 28 days

Although method 5 is not considered to be the most viable in its application, it is ideal in terms of the results obtained. A comparative was carried out in order to have a parameter of the benefit of the cure against a null curing system. As can be seen in figure 17 there is a considerable increase at 24 hours and 8 days, and an excessive increase at 28 days of up to 61.5%. Although the blocks are not dispatched at 28 days, their quality control is analysed at 28 days.

Table 2: Summary of methods of higher projection in the application of industrial production

| fc, MPa (days) | | 1 | 8 | 28 |
|----------------|----------------------|-----|------|------|
| Average fc | | | | |
| Methods | Method 2 (NCI) | 5.3 | 10.9 | 12.6 |
| | Method 5 (MR+S) | 6.1 | 12.6 | 20.4 |
| | Method 6 (MR+S+NCO) | 6.1 | 12.3 | 18.5 |
| | Method 7 (MR+WC+NCO) | 5.5 | 11.5 | 16.3 |
| | Method 8 (MR+WC+S) | 5.3 | 11.2 | 15.2 |
| | Method 12 (P) | 6.0 | 11.1 | 16.0 |

As can be seen in Table 2, these are the 6 methods that meet the characteristics to be implemented at a production level (including the critical method number two), were assigned in this way not only by the compressive strengths obtained, but also because of their low cost in terms of improvements and ease of application. Once again it is necessary to emphasize the importance of cure concrete blocks at early ages (first 24 hours). For the type of mixtures composed by a low water content, much of that moisture is consumed through the hydration process and the relative humidity of the environment, which reduces considerably the strengths gains. In addition to this, the wet tarpaulin system allows the presence of water in the early hours of the concrete hardening as well as the proper water of the mixture; However, it can damage the initial consistency of the blocks, also requires keeping it moist for continuous periods, which is inconvenient for long processes.

From Table 2, it's possible to extract the analysis of method 2 (critical) vs. the system 6 (ideal).

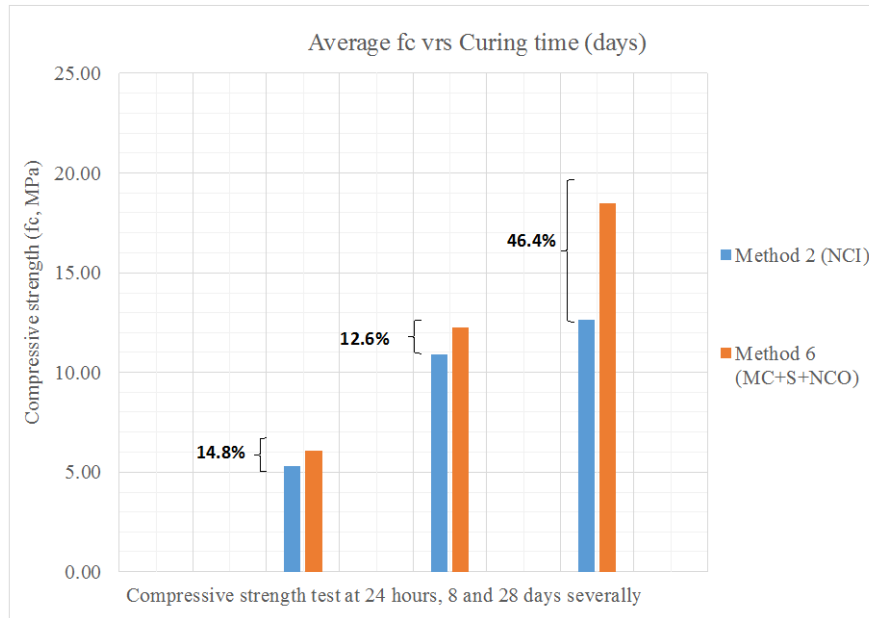


Figure 18: Comparison of method 2 vs. method 6 at different ages

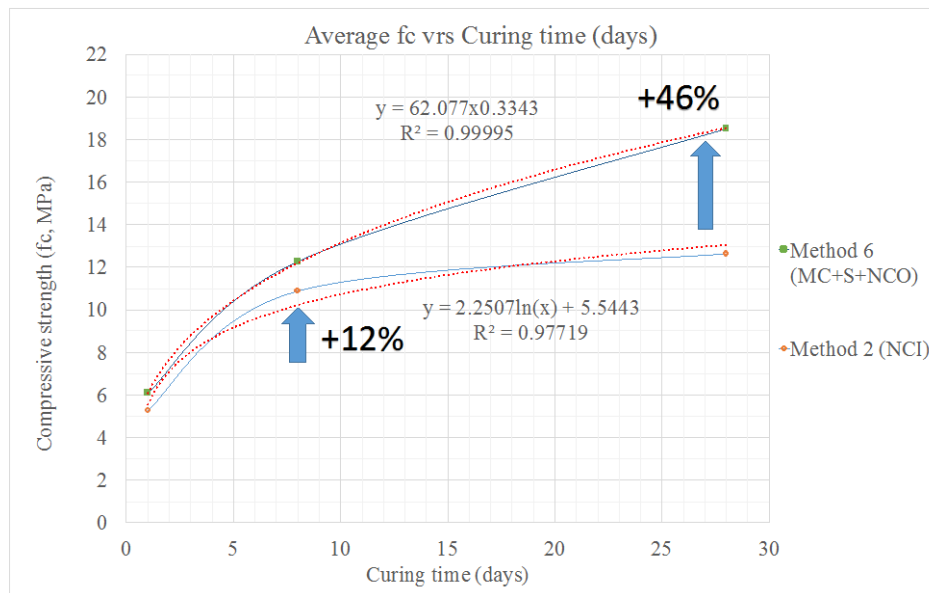


Figure 19: Comparison of the compressive strength of the method 6 vs method 2 with their respective trendline and coefficient of determination.

According to figure 18 and 19 a percentage of the most viable method against the critical method has been obtained, which provides an accurate value of the corrections that can be made in the blocks manufactured without any additional cure. As can be observed in figure 20 the obtained values at 28 days shows a 46% increase of the strengths generated in relation to a non-curing system, also demonstrates a gain of 12.6% at 8 days.

For a recommendation, a graph of the methods with better results at 7 days of curing have been proposed (including method 2 with the critical strengths), which allows a projection of the dispatch times that can be performed in the plant with the improvements in cure. It is extremely important to emphasize that these results can improve due to the methodology used in the project to extract the blocks from the curing chambers which reduced the curing time of the first 24 hours up to a 20-25%.

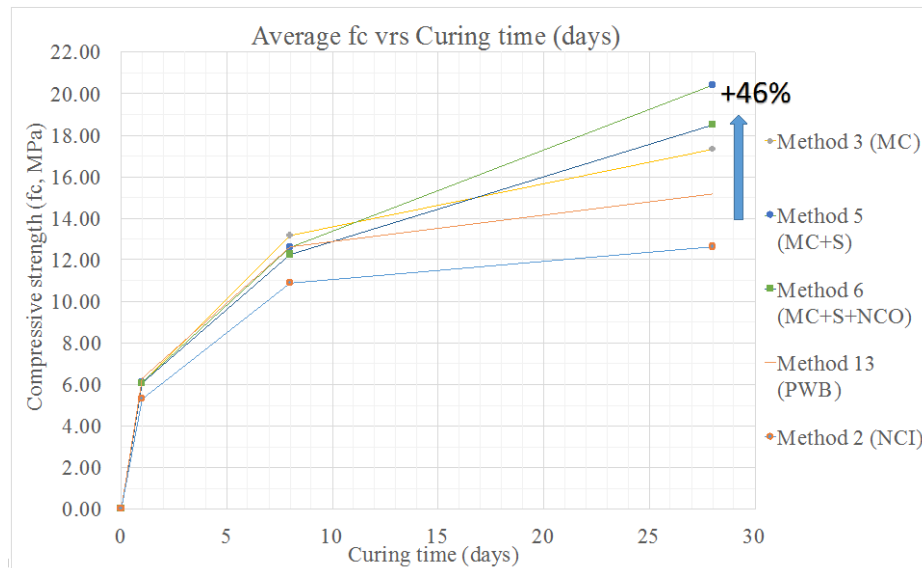


Figure 20: Methods with the highest compressive strengths obtained at 8 days

CONCLUSIONS

As it can be observed in the strengths obtained from the concrete blocks tested and subjected to different curing methods, taking into consideration a zero-cure method in relation to parts subjected to a curing in the yard only through daily precipitations (45 minutes daily per 18 days), ensures that a minimum curing process can increase the compressive strength of specimens made with dry mixtures up to 12% at 28 days. From the same data collected it has been demonstrated that the low water content of a dry mix is not enough for the hydration process to occur during the initial 24 hours of the block, an aspect that is reflected in the compressive strengths of the blocks at 28 days. A situation that has allowed to determine the importance in the application of curing by additional water in dry mixes in the early stages.

The presence of high temperatures, excessive winds and the scarcity of rainfall in the dry season, causes a decrease in the strength reached by the blocks. In the comparison between outdoors and no curing indoors method, this situation can be verified.

With the methodologies implemented, it has been possible to define an ideal method of cure applicable to the area of dry mixtures, allowing a low cost in its application at industrial level and a considerable increase in the compressive strengths, which corresponds to an increase of a 46 % of the strengths at 28 days in relation to uncured concrete blocks.

The application of 24 hour wet chamber cure method followed by 6 days with sprinklers, is considered the ideal method for block production in Costa Rica, since most of the factories have block storage rooms for early stages that can be adapted with micro sprinklers, in addition to the relatively economic adjustment that needs to be done to set sprinklers in the yards. Also, because of the conditions of the country, water can be gathered by means of wells and recycling, which turns out to be a simple and low cost method that contributes to the development of the “ideal method”.

ACKNOWLEDGMENTS

Thanks to the constant collaboration and advice of the technicians in the area of quality control of “Productos de Concreto SA”, likewise to the Universidad Latina which brings part of the budget for the assistance to the 10 th Australian Masonry Conference, and last but not least, to Productos de Concreto itself, which contributes with their facilities, laboratories and all the materials and equipment required for this investigation.

REFERENCES

ACI (American Concrete Institute) committee 308R-01 (R19). (2001). *ACI Standards and Technical Documents on ACI 308*. Obtain from ACI: www.concrete.org

Incera, A. (2017). *Comparación de los métodos de curado de bloques de concreto y adaptación del método de diseño de Frasson Jr. para mezclas secas (Tesis de Licenciatura)*. Miraflores: Universidad Latina de Costa Rica Sede Heredia.

INTE 06-02-13 (2015). *INTECO Catálogo de normas*. Recuperado el 20 de Octubre de 2015, de INTECO: <http://www.inteco.or.cr/>

INTE 06-02-16 (2007). *INTECO Catálogo de normas*. Recuperado el 20 de Octubre de 2015, de INTECO: <http://www.inteco.or.cr/>

Portland Cement Association. (2008). Curing Concrete. En S. H. Kosmatka, B. Kerkhoff, & W. C. Panarese, *Design and control of concrete mixtures* (págs. 219-226). Skokie, Illinois, USA: Library of Congress Cataloging-in-Publication Data.



**MASONRY TODAY
AND TOMORROW**

**11 - 14 February, 2018
SYDNEY AUSTRALIA**

www.10amc.com

WATER LOSS INFLUENCE ON LAYING MORTAR COMPRESSIVE STRENGTH

A. L. Temp¹, A. S. Milani², M. J. Oliveira³, A. Lübeck⁴ and G. Mohamad⁵

¹ Assistant Professor, Federal University of Pampa, RS, Brasil. aldotemp@unipampa.edu.br

² Assistant Professor, Federal University of Pampa, RS, Brasil. alisson.unipampa@gmail.com

³ Civil Engineer, Federal University of Pampa, RS, Brasil. marcelooliveira@unipampa.edu.br

⁴ Adjunct Professor, Federal University of Pampa, RS, Brasil. andrelubeck@gmail.com

⁵ Adjunct Professor, Federal University of Santa Maria, RS, Brasil. gihad.civil@gmail.com

Masonry is a composite material which results from the union of blocks by mortar and shows a dependent behavior on the individual properties of blocks and mortar and on their interaction. The compatibility of strains between components results in a complex state of stresses on the elements, especially on mortar, which is in a confined compressive state due to its greater deformability in comparison with blocks. The blocks avidity for humidity makes them draw water from the just-laid mortar, reducing its water-cement ratio and increasing its compressive strength, in comparison with the control specimens usually moulded during laying. However, it is still unknown how much the mortar mechanical properties are modified due to this water exchange. In order to represent the blocks water-absorption effect on the laying mortar properties, cylindrical specimens (tablets) were moulded with a 4cm diameter and two different heights, 1.5cm and 4cm, in circumstances similar to the masonry laying joints, on either concrete or ceramic blocks surfaces. The results show that the mortar properties are modified due to drying, caused by the blocks absorption and, also, by the confinement, caused by the bonding and small height of the joint, resulting in different mechanical properties from those measured in the control specimens, and thus making it difficult to predict the material behavior when it is structurally used.

Keywords: *masonry; laying mortar; water loss; compressive strength.*



THE UNIVERSITY OF
NEWCASTLE
AUSTRALIA



CMAA
CONCRETE MASONRY
ASSOCIATION OF AUSTRALIA

INTRODUCTION

Masonry is a composite material which results from the blocks union by mortar. The behaviour of this composite material depends on the blocks and mortar individual properties and on their interaction. Knowing the factors that influence the interaction between masonry components is thus key to understanding masonry behaviour.

Laying mortar is a mixture of binder and aggregates which serves to various functions in masonry, from binding the units and ensuring the water sealing, when it is hardened, to allowing laying in fresh state. Therefore, mortar properties in fresh and hardened state affect masonry behavior and its strength.

The bonding between blocks and mortar plays a fundamental role on masonry performance. The compatibility of strains between elements results in a complex state of stresses on the elements, especially on mortar, which is in a confined state due to its greater deformability if compared with the blocks. This confined stress state tends to modify mortar behavior, when compared with the one observed at the axially-loaded specimens test. (Atkinson et al., 1985; Hayen, Van Balen e Van Gemert, 2003; Mohamad et al., 2009; Mohamad et al., 2015).

Another important aspect that makes it difficult to predict mortar behavior is the blocks tendency to absorb water from mortar. Blocks avidity for humidity makes them remove water from mortar, reducing its water-cement ratio and increasing its compressive strength if compared to specimens usually moulded during laying. Authors like Mohamad (2013), Parsekian, Hamid and Drysdale (2012), Carasek (2010) and Parsekian and Soares (2010) have also pointed out that one of the most desirable properties for mortar is the water-retention capacity, so that there is no bond weakening between the joint and the blocks due to mortar fast drying. However, in order to ensure mortar workability, more water than necessary for cement hydration should be added while mixing, allowing exceeding water to be absorbed by the blocks.

The recognition of mortar behavior changes in joints also reflect on some standard texts. ACI 530-05 (2005) standard prescribes that mortar compressive strength in masonry joints, with an approximate 10mm height, exceeds more than two times the strength measured in 50mm-side cubes. Eurocode 6, EN 1996-1-1 (2002), suggests that mortar choice should result from an analysis of its exposition conditions and of the block properties, especially regarding to the water retention capacity and workability.

There is a great variety of blocks and mortar available for use in masonry construction. There are blocks of various materials and geometries, while masonry mortars can be manufactured or in-situ mixed, with different components and properties. Also, the laying procedure influences on components interaction. If the blocks are soaked before laying, their avidity for water will be smaller. This variety of possibilities results in very diverse behaviors for masonry. Perhaps that is the reason why there are few studies which have attempted to characterize mortar strength change due to the blocks tendency to absorb water from mortar.

In literature review there is great variation between the results and the influence of the blocks properties or of the mortar type on the strength improvement is not clear. The strength improvement observed was between 50 and 100%.

LITERATURE REVIEW

There are few studies that have evaluated mortar strength variation due to blocks water absorption, and among the researched studies, there is great variation in the implementing procedures.

Bierwirth et al. (1991) have developed a test method to evaluate mortar strength improvement in laying joints. Mortar was laid between blocks in order to be subject to the same humidity loss conditions that happen in masonry joints. In order to allow water movement but to ease the sample drawing as well, filter paper was placed between the block and the mortar. Two sample-drawing methods were tested, one using a cup saw for drawing and the other using plastic rings placed between the blocks with the fresh mortar. The authors have achieved strength increases greater than 50%.

Bierwirth, Stöckl and Kupfer (1993) have evaluated the confined strength of mortar samples drilled out from masonry joints. Four types of mortar and three types of blocks were tested. The specimens were drawn from mortar joints between blocks. They were 30mm in diameter and 12mm height. In order to avoid the influence of the confinement caused by the plates of the load machine, two steel brushes were used to load the specimen. Researchers have concluded that the block saturation rate and its avidity for water are influent on mortar strength.

Stöckl, Bierwirth and Kupfer (1994) have compared the previous test results (Bierwirth et al, 1993) with the results of prismatic specimens of 4x4x16cm. Specimens were moulded between two blocks using filter paper to ensure the liquid migration without the complete binding of the mortar and the block. The mortar samples were 12mm high. The blocks were tested in two humidity conditions, either saturated after immersed in water for one hour or humid after immersed in water for one minute. One mortar type was tested, with mix proportions by cement, lime and sand of 1:1:17.9, measured in volume, and with an uniaxial compressive strength of 2.84 MPa. The mortar strength in joints was more than 100% greater than the one measured in the 4x4x16cm specimens.

Barbosa et al. (2011) have studied the influence of water loss on mortar compressive strength. The researchers have evaluated the tendency of concrete blocks of taking water from laying mortars with 1:1:5 and 1:0.25:3 volume proportions of cement, lime and sand. Two specimens geometries were evaluated, Ø5x10cm cylinders and 10cm-side cubes. The researchers have concluded that the water-cement ratio change can be significant enough to double the mortar compressive strength.

Lübeck (2016) has evaluated the indirect strength growth of two manufactured mortars, with 4 and 15 MPa nominal strengths, when used to lay ceramic and concrete blocks. One type of concrete blocks and two different geometries of ceramic blocks were tested. The concrete blocks absorption rate was 6%, while for the ceramic blocks rates were 11% and 13% in hollow and massive blocks, respectively. The strength growth was determined based on the mortar confined strength when compared with the control specimens. The researcher concluded that the mortar strength increase reached, in average, 70%.

Steil et al. (2001) have evaluated the mechanical properties of masonry moulded with different mortar types, two of them manufactured (I-1 and I-2) and two mixed in laboratory (C-1 and C-2). The mix proportions for those mortars were chosen aiming to obtain compressive strengths similar to the manufactured ones. During masonry compression tests, the manufactured mortar I-1 ($f_c=5,27\text{MPa}$ and $E=6,6\text{GPa}$) showed smaller transversal strains than the mortar mixed in laboratory C-1 ($f_c=6,28\text{MPa}$ and $E=6,6\text{GPa}$). I-1 e C-1 had similar compressive strength and elasticity modulus, which does not explain the observed behavior. Steil et al. (2001) justified the observation by the block-joint bonding. The I-1 mortar showed greater water retention than C-1 and, consequently, greater water-cement ratio and smaller compressive and bonding strengths. The smaller the bonding, the less the capacity to transmit strains by contact, and thus the prisms I-1 joints resulted in smaller transversal strains, for they were not capable to transmit strains to the adjacent blocks, leading to the break of the joint-block bonding and to joint crushing. It is thus evident the importance of the humidity migration between mortar and blocks in order to predict masonry behavior.

EXPERIMENTAL PROGRAM AND MATERIAL PROPERTIES

In order to represent the water loss effect on the mortar strength, cylindrical specimens (tablets) were moulded, with diameter of features and two different heights, 1.5 and 4cm, in circumstances similar to those in masonry joints. The tablets were moulded between blocks so that it was possible for water to migrate from mortar to blocks. Two mortar types with similar compressive strengths were tested, one of them manufactured, with a 6MPa nominal strength, and the other one mixed in laboratory, with 1:0.51:6:0.9 volume proportions of cement, lime, sand and water, respectively. The mixed mortar had proportions defined in order to result in the same compressive strength of the manufactured one. Two hollow block types, ceramic and concrete, were tested.

The same workability was defined for modelling both mortars, 260mm measured on the flow table (NBR 13276, 2002). The mortar water retention was determined according to NBR 13277 (2005) and standard compressive strength was tested with 4x4x16cm prismatic samples. The results are shown in Table 1.

Reference specimens were moulded with different geometries, in order to analyse the confinement effect over the compressive strength. Cylindrical samples with 5cm diameter and 10cm height and tablets with a 4cm diameter and two different heights. Those tablets were moulded between glass plates, in order to prevent water migration from mortar.

The blocks characterization was accomplished according to the standards NBR 15270-3 (2005), in the case of ceramic blocks, and NBR 12118 (2011), in the case of concrete blocks. In Table 2 the blocks-characterization results are shown. The table shows the gross area (A_g), the net area (A_{net}), the net area-gross area ratio (A_{net}/A_g), the water-absorption rate (IAA) and the initial absorption rate (IRA), the compressive strengths in gross area ($f_{c,g}$) and in net area ($f_{c,net}$), in addition to the measured standard deviation (s.d) and variation coefficient (C.V).

Table 1. Water retention in mortar.

| Mortar | Water retention (%) | Compressive strength (MPa) |
|---------------------|---------------------|----------------------------|
| Manufactured | 95.7 | 6,23 |
| Mixed in laboratory | 88.8 | 6,24 |

Table 2. Blocks physical properties.

| Block type | A_g (cm ²) | A_{net} (cm ²) | A_{net}/A_g | IAA (%) | IRA | $f_{c,g}$ (MPa) | $f_{c,net}$ (MPa) | s.d. (MPa) | C.V. (%) |
|------------|--------------------------|------------------------------|---------------|---------|-------|-----------------|-------------------|------------|----------|
| Ceramic | 408.43 | 169.29 | 0.41 | 11.0 | 12.41 | 12.32 | 29.73 | 4.56 | 15.0 |
| Concrete | 552.34 | 323.29 | 0.59 | 6.0 | 25.81 | 12.29 | 21.00 | 2.70 | 13.0 |

The cylindrical tablets of Ø4x4cm and Ø4x1.5cm were moulded inside PVC rings and placed between two blocks (either ceramic or concrete). In order to ease the drying of samples moulded between blocks, but to maintain the water exchange as well, filter-paper layers were placed at the mortar-block interfaces, both at the base and at the top. The specimens were removed from the moulds and from the contact with blocks after 48 hours of exposure, and they were left curing in natural conditions in laboratory until the compressive test. All samples were tested 28 days after moulded. Figure 1 illustrates the specimens during moulding. In Figure 1(a) it is possible to visualize the control specimens; in Figure 1(b), the specimens moulded on the glass plate, and in Figure 1(c), the specimens during moulding between ceramic blocks.



a) 4x4x16cm and Ø5x10cm



b) Ø4x4cm and Ø4x1.5 cm on glass



c) Ø4x4cm and Ø4x1.5 cm with ceramic block

Figure 1: Specimens moulding.

In Figures 2(a) and 2(b) it is possible to visualize the specimens positioned between the ceramic and concrete blocks, respectively. The blocks were always used in natural dried conditions.



a) Ceramic blocks



b) Concrete blocks

Figure 2: Specimens moulding between the blocks.

RESULTS AND DISCUSSION

The average compressive strength results obtained with 4x4x16cm specimens, tested according Brazilian standard NBR 13279 (2005), Ø5x10cm cylindrical specimens and Ø4cm tablets are shown in Table 3, with the standard deviation (s.d) and the variation coefficient (C.V.) obtained in tests, and graphically in Figure 3.

Table 3. Compressive strengths of mortar specimens.

| | Manufactured | | | Mixed in laboratory | | |
|----------------------|--------------|-----------|----------|---------------------|-----------|----------|
| Group | f_c (MPa) | s.d (MPa) | C.V. (%) | f_c (MPa) | s.d (MPa) | C.V. (%) |
| 4x4x16cm | 6.23 | 0.22 | 3.55 | 6.24 | 0.46 | 7.32 |
| Ø5x10cm | 4.26 | 0.34 | 7.97 | 3.95 | 0.37 | 9.31 |
| Ø4x4cm – Reference | 3.95 | 0.39 | 9.98 | 3.03 | 0.37 | 12.35 |
| Ø4x4cm – Ceramic | 4.97 | 0.97 | 19.50 | 5.18 | 0.60 | 11.61 |
| Ø4x4cm – Concrete | 5.44 | 0.79 | 14.61 | 4.56 | 0.23 | 5.11 |
| Ø4x1.5cm – Reference | 12.11 | 0.58 | 4.82 | 6.35 | 0.83 | 13.08 |
| Ø4x1.5cm – Ceramic | 20.49 | 2.07 | 10.09 | 15.34 | 1.03 | 6.69 |
| Ø4x1.5cm - Concrete | 23.78 | 1.84 | 7.75 | 16.10 | 0.63 | 3.93 |

In Figure 3, the variation given by the measured standard deviation is represented at the extremity of each column. The two first columns of each group are the reference specimens, the 4x4x16cm

prismatic ones and the Ø5x10cm cylindrical ones. The other columns are for the cylindrical tablets. The nomenclature indicates the tablet dimension and the surface characteristic: reference, ceramic or concrete. Those named as “Reference” are the ones moulded between glass plates. The manufactured mortar resulted in a 4.26 MPa average strength in the cylindrical specimens and 6.23 MPa in the 4x4x16cm prismatic ones. The mortar mixed in laboratory resulted in a 3.95 MPa average strength in the cylindrical specimens and in 6.24 MPa in the prismatic ones. Considering the observed standard deviation, it is possible to affirm that the compressive strengths of both mortars were equal in the control specimens and for the 4cm-high ceramic tablets. Only in 1.5cm-high tablets it was possible to observe a significant difference between the two mortar types, due to a bigger contact area available for water exchange in comparison to the sample volume. Therefore, it is possible to affirm that the specimen drying caused by the blocks was more effective in the 1.5cm-high tablets.

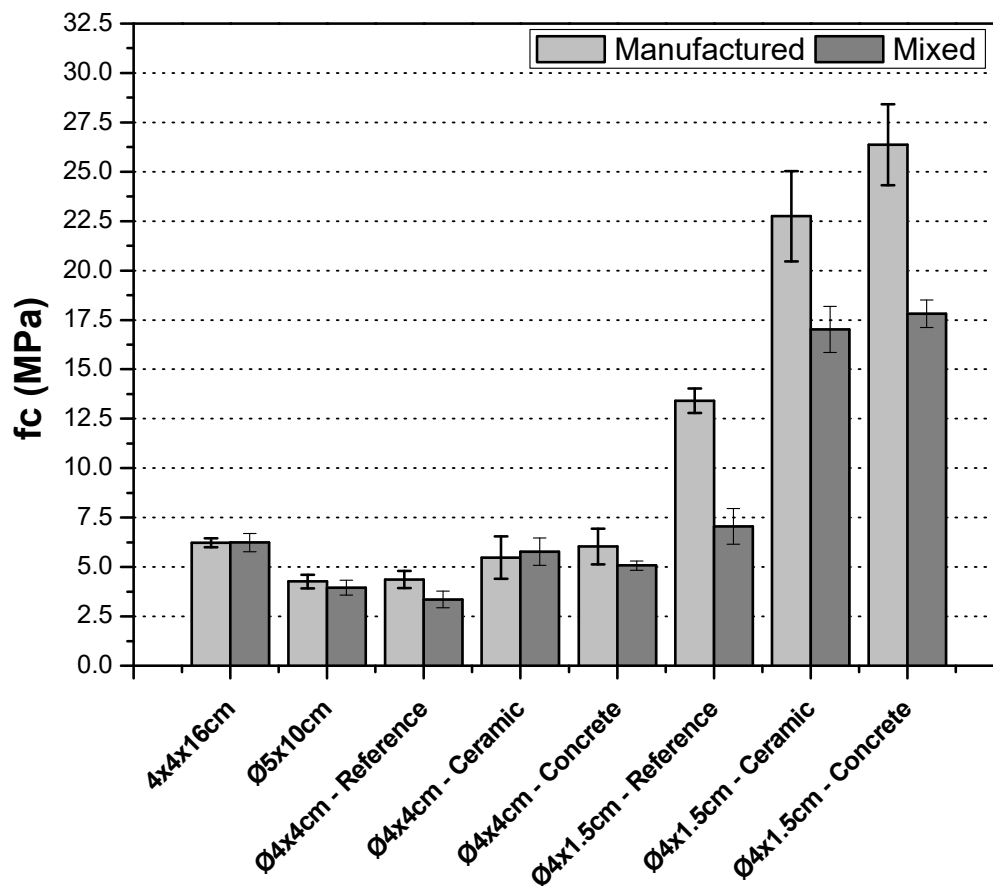


Figure 3: Strength of the studied specimens.

The comparison between compressive strengths of Ø4cm tablets and control specimens shows a strength decrease for the 4cm-high ones and a strength increase for the 1.5cm-high ones. That variation is due to the specimen shape and its combination with confinement, which results from the side friction caused by the load-application plates of the test equipment. The Ø4x1.5cm specimens showed a greater strength than the Ø4x4cm ones, for both mortar types, which

indicates that the friction caused by the load plates resulted in a greater confinement in the tested samples.

The comparison of strengths between different surfaces for each of the specimens heights and mortar types is presented in Figure 4. It also shows the ratios between the reference specimens and the strengths obtained with the different block types.

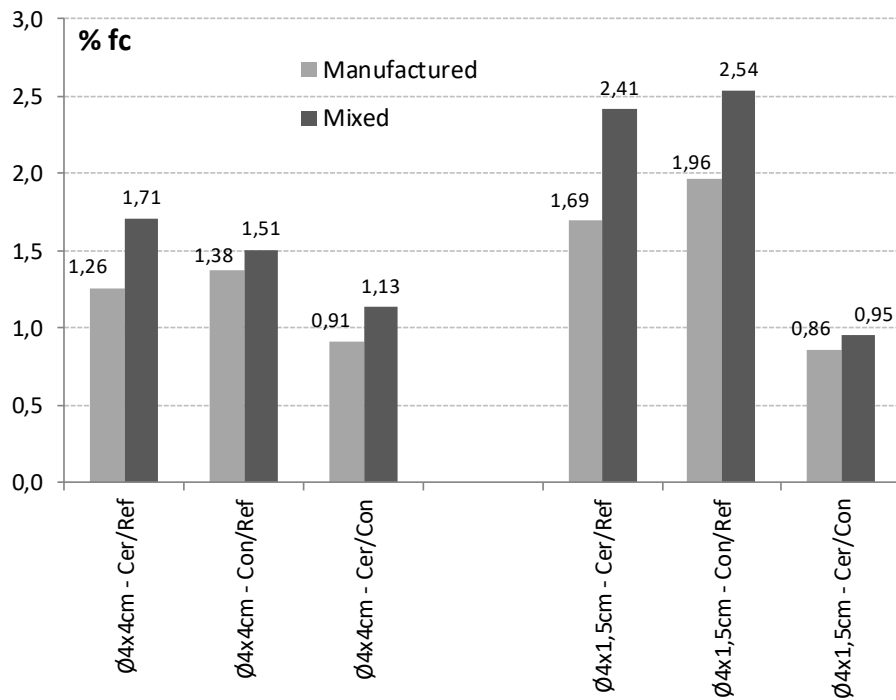


Figure 4. Comparison between compressive strengths for each mortar type and specimen geometry.

For both Ø4x4cm and Ø4x1.5cm specimens, it was verified that the strength of tablets exposed to drying conditions was greater than the strength of control tablets, independently of the block type, either ceramic or concrete, which indicates a strength improvement, for both manufactured and mixed mortars, due to water loss. The strength increase of mortars mixed in laboratory was greater than the increase of manufactured mortars, although the latter had greater absolute measured strength. The lowest strength improvement in the manufactured mortar was consequence of the greatest water retention, as already pointed out.

By comparing the strength improvement of 4cm-high specimens with the 1.5cm ones, it was noticed that the latter had a bigger strength improvement, because the smaller thickness results in a more effective drying of the specimen, increasing its strength. For the height of 1.5cm, the maximum strength improvement observed for manufactured mortar was 96% for concrete blocks, while for the mixed mortar it was 154% for the same block type. For ceramic blocks and the same specimen's height, the improvement observed for manufactured mortar was 69% and for mixed mortar the improvement was 141%.

The block type was not determinant on the strength improvement, which may have been an influence of the need to use filter paper so that there was not bonding between mortar and block.

CONCLUSIONS

The mortar strength change caused by the blocks tendency to absorb water from the laying mortar was evaluated by comparing compressive strengths of mortar tablets, with a 4cm diameter and two different heights, 4cm and 1.5cm. From that analysis it is possible to conclude:

- There was greater strength improvement in the 1.5cm-high tablets than in the 4cm-high ones, which indicates that the difference in the contact area-specimen volume ratio was determinant on the results. The 1.5cm-high specimens, with greatest contact area for water exchange in comparison to the sample volume, tend to proportionally have more water loss to the block, resulting in a more effective and homogenous drying, and in greater compressive strength increases.
- The Ø4x1.5cm specimens showed an average compressive strength superior than the others, due to the greatest confinement effect caused by friction with the test-equipment plates.
- It was verified that mortars mixed in laboratory showed a greater strength improvement than the manufactured mortar, due to the presence of water-retention admixtures, which are common in manufactured mortars.
- No behavior change was observed in the mortar water absorption due to the block type used, perhaps because of the filter paper between the mortar and the block during moulding.
- Results demonstrates that mortar properties are modified due to drying caused by the blocks absorption and also by the confinement caused by the joint bonding and small height, resulting in mechanical properties different than those measured in the control specimens. The maximum strength improvement observed for manufactured mortar was 96%, while for the mixed mortar it was 154%, both for concrete blocks and 1.5-high mortar specimens.

REFERENCES

ABNT. Associação Brasileira de Normas Técnicas. NBR 12118 (2014). "Blocos vazados de concreto simples para alvenaria - Método de ensaio". (in Portuguese). Rio de Janeiro, Brazil.

ABNT. Associação Brasileira de Normas Técnicas. NBR 15270-3 (2005). "Componentes cerâmicos. Parte 3: Blocos cerâmicos para alvenaria estrutural e de vedação - Métodos de ensaio". (in Portuguese). Rio de Janeiro, Brazil.

ABNT. Associação Brasileira de Normas Técnicas. NBR 13276 (2006). "Argamassa para assentamento e revestimento de paredes e tetos - Determinação do índice de consistência". (in Portuguese). Rio de Janeiro, Brazil.

ABNT. Associação Brasileira de Normas Técnicas. NBR 13277 (2005). "Argamassa para assentamento e revestimento de paredes e tetos - Determinação da retenção de água". (in Portuguese). Rio de Janeiro, Brazil.

ACI. American Concrete Institute. ACI 530-05 (2005). Building Code Requirements for Masonry Structures. Farmington Hills, USA. 158 p.

Atkinson, R. H.; Noland, J. L.; Abrams, D. P. (1985). A deformation failure theory for stack-bond brick masonry prism in compression. In: International Brick Masonry Conference, 7, 1985, Melbourne, Proceedings. v. 1, Melbourne: IBMAC. p. 577-592.

Barbosa, C. S.; Hanai, J. B.; Lourenço, P. B.; Mohamad, G. (2011). "Influência da perda de água e das tensões confinantes nas propriedades físicas e mecânicas da argamassa de assentamento para alvenaria estrutural". In: Proceedings of IX "Simpósio Brasileiro de Tecnologia das Argamassas". (in Portuguese). Belo Horizonte, Brazil.

Bierwirth, H.; Dieler, C. H.; Stöckl, S.; Kupfer, H. (1991). Development of a Test Equipment for Triaxial Loaded Mortar Specimens. In: Proceedings of the 9th International Brick/Block Masonry Conference, Berlin, Germany, p. 584-591.

Bierwirth, H.; Stöckl, S.; Kupfer, H. (1993). Triaxial tests on mortar specimens taken from bed joints. In: Proceedings of the 6th North American Masonry Conference. Philadelphia, Pennsylvania.

Carasek, H. Argamassas. In: ISAIA, G. C. (Coordinator). (2010). "Materiais de Construção Civil e Princípios de Ciência e Engenharia de Materiais". (in Portuguese). Brazilian Concrete Institute - Ibracon, São Paulo. Brazil.

Eurocode 6. EN 1996-1-1 (2002). Design of masonry structures - Part 1-1: Common rules for reinforced and unreinforced masonry structures. Brussels. 131 p.

Hayen, R.; Van Balen, K.; Van Gemert, D. (2003). The mechanical behaviour of mortars in triaxial compression. In: Proceedings of the 6th International Conference on Materials Science and Restoration, Karlsruhe, p. 295-302.

Lübeck, A. (2016). "Comportamento mecânico e influência da argamassa no modo de ruptura da alvenaria estrutural". (in Portuguese). Doctoral thesis, Federal University of Santa Maria, Brazil.

Mohamad, G.; Neto, A. B. S. S.; Pelisser, F.; Lourenço, P. B.; Roman, H. R. (2009). "Caracterização mecânica das argamassas de assentamento para alvenaria estrutural – previsão e modo de ruptura". (in Portuguese). Revista Matéria, v. 14, n. 2, p. 824-844.

Mohamad, G. (Coordinator). (2013). "Alvenaria estrutural". (in Portuguese). Ed. Edgard Blucher, Brazil.

Mohamad, G.; Fonseca, F. S.; Roman, H. R.; Vermeltfoort, A. T.; Rizzatti, E. (2015). Behavior Of Mortar Under Multi-Axial Stress. In: Proceedings of 12th North American Masonry Conference. Denver, Colorado, USA.

Parsekian, G.; Soares, M. M. (2010). "Alvenaria Estrutural em Blocos Cerâmicos: Projeto, Execução e Controle". (in Portuguese) Ed. O Nome da Rosa. São Paulo, Brazil.

Parsekian, G. A.; Hamid, A. A.; Drysdale, R. G. (2012). "Comportamento e dimensionamento de alvenaria estrutural".(in Portuguese). Ed. Edufscar, São Carlos, Brazil.

Steil, R. O.; Calçada, L. M. L.; Oliveira, A. L.; Martins, V. C.; Prudêncio Jr., L. R. (2001). "Influência do tipo de argamassa no fator de eficiência e na deformabilidade de alvenarias estruturais de blocos de concreto". (in Portuguese) In: Proceedings of IV "Simpósio Brasileiro de Tecnologia das Argamassas", IV SBTA. Brasília, Brazil.

Stöckl, S.; Bierwirth, H.; Kupfer, H. (1994). The influence of test method on the results of compression tests on mortar. In: Proceedings of the 10th International Brick and Block Masonry Conference, Calgary, Canada. p. 1397-1406.

NEW ECO-FRIENDLY MASONRY UNITS FOR BETTER THERMAL AND ACOUSTIC INSULATION

A.A. Gheni¹, M.A. ElGawady² and J.J. Myers³

¹ Ph.D. Candidate, Dept. of Civil, Architectural, and Environmental Engineering, Missouri University of Science and Technology, Rolla, MO 65409, aagmr6@mst.edu

² Benavides Associate Professor, Dept. of Civil, Architectural, and Environmental Engineering, Missouri University of Science and Technology, Rolla, MO 65409, elgawadym@mst.edu

³ Professor and Associate Dean, Department of Civil, Architectural & Environmental Engineering, Missouri University of Science and Technology, Rolla, MO 65409, jmyers@mst.edu

The low thermal and sound insulation capacity of a concrete masonry unit (CMU) motivated the researchers to investigate the impact of using the crumb rubber that came from scrap tires as an aggregate replacement in the concrete masonry unit's production. Using scrap tire rubber resulted in more sustainable construction units by using recycled materials and reduces the buildings' energy consumption. An experimental investigation was conducted to explore the impact of using various ratios of crumb rubber in concrete masonry units on the thermal conductivity and the sound insulation. The thermal conductivity at the masonry material level test was performed according to the Whole Building Design Guide CRD-C 45-65 to evaluate after that the thermal insulation for the whole masonry unit. The sound absorption test was performed according to the requirements of ASTM E1050 using a tube, two microphones, and a digital frequency analysis system. The results indicated that adding the crumb rubber to masonry units had a positive impact on reducing the thermal conductivity. Units with 37% rubber replacement ratio reduced the thermal conductivity by 48% compared to a conventional masonry unit. The new rubberized material exhibited a clear increase in sound absorption and noise reduction compared to standard conventional and lightweight masonry units. The mechanical characterization and dimension requirements were reported to show that the new eco-friendly masonry units met the ASTM requirements for loadbearing and non-loadbearing concrete masonry units based on the rubber content.

Keywords: masonry, Thermal insulation, Crumb rubber, Sustainable material, Eco-friendly, sound absorption.

INTRODUCTION

With a growing sustainable society, the interest to produce and use more sustainable and energy efficient construction materials has accelerated in recent years. Despite the importance of the concrete masonry unit (CMU) as a worldwide construction material, it is still generally produced using conventional materials such as mineral aggregates and Portland cement. The construction industry uses the largest amount of materials by weight compared to other industries in the United States (Horvath 2004). Using these materials in massive quantities has a negative impact on the environment. The negative contribution of these materials comes from two sources. The first source is the impact of the production process. For example, 5% of carbon dioxide emissions are derived from the cement production industry (Worrell et al. 2001). Most of the activities associated with aggregate extraction and processing are responsible for increasing environmental devastations through increasing noise, dust, and impacts on surface and groundwater. The increase in desertification is related to the steady alternation of landscapes and habits. The second negative contribution is the high energy consumption of buildings that were constructed using these materials. Hence, a pressing need exists to develop construction masonry units that use sustainable and energy-efficient raw materials. Using crumb rubber produced from scrap tires as a replacement for mineral aggregate is one approach toward achieving this goal.

The Rubber Manufacturer's Association reported that 242.8 million scrap tires were generated in the U.S. in 2015 (RMA 2016). Scrap tires serve as a home for mosquitoes, rats, and snakes and they are a tremendous fire hazard. Once a tire pile catches fire, it is very difficult to extinguish. Burning waste tires emits dangerous toxic gases, such as CO, NO₂, SO₂, and oil runoff, that could result in severe pollution problems. Therefore, effectively recovering and reusing waste tires is an urgent and important issue (Po 2004). Most states in the U.S. have enacted legislation that either restricts or bans the disposal of tires in landfills.

A wide range of research has been devoted to investigating the impact of adding crumb rubber to concrete. A reduction was noted in the unit weight of rubberized concrete because of the rubber particle's low specific gravity and increased entrapped air contents. In term of slump, researchers reported an increase and then decrease with the increase of rubber content due to the hydrophobic nature of rubber which causes a water film coating on the rubber particles that reduce the friction with other particles. With the high rubber content, the low unit weight of the rubberized concrete causes a reduction in slump (Siddique and Naik 2004, Gou and Liu 2014).

Both the compressive and flexural strengths were negatively affected when crumb rubber was used as one of the concrete components due to rubber's relatively low stiffness and the poor bond between the rubber particles and cement paste (Batayneh et al. 2008, Najim and Hall 2010). From the durability perspective, using crumb rubber in concrete improved the concrete's resistance to freezing and thawing (Skripkiūnas et al. 2010, Thomas and Gupta 2013). For dynamic loading applications, the energy dissipation, viscous damping, and hysteric damping properties improved significantly when rubber replaced aggregate in concrete (Zheng et al. 2008, Moustafa and ElGawady 2017).

Rubberized concrete provides sound and heat insulation, a higher sound absorption, a higher noise reduction coefficient, and lower heat transfer properties (Turgut and Yesilata 2008, Sukontasukkul 2009, Hall et al. 2012, Ghenni et al. 2017). Both load-bearing and non-load-bearing masonry hollow blocks were produced with a partial replacement of the mineral

aggregate by crumb rubber (Isler 2012, Sadek and El-Attar 2015, Gheni et al. 2017). Mohammed et al. (2012) reported an improvement in thermal, acoustic, and electrical properties of rubberized CMU compared to the conventional masonry blocks. Al-Jabri et al. (2005) and Gheni et al. (2016) investigated using by-product materials, i.e., vermiculite, polystyrene beads, and wood to improve the thermal insulation properties of CMU. They compared the thermal insulation of three types of concrete blocks. They noted that polystyrene beads and wood improved the thermal insulation of the blocks.

EXPERIMENTAL PROGRAM

Crumb rubber was used as an aggregate replacement to produce masonry blocks with four different ratios of rubber (0%, 10%, 20%, and 37%). All of the blocks were manufactured in a masonry plant in Jefferson City, Missouri using the standard masonry manufacturing process for producing a rubberized concrete masonry block (RCMU). The aim of this study was to investigate the thermal and acoustic characterization of RCMUs. The thermal conductivity of the new masonry material itself was examined according to Whole Building Design Guide CRD-C 45-65. Sound absorption test was performed according to the requirements of ASTM E1050. Finally, the thermal and sound characterizations of RCMUs with different rubber ratios were compared with standard conventional and lightweight masonry unit.

MATERIAL PROPERTIES

All materials used in this research were sampled and tested according to standard test methods (Table 1). Three varied sizes of crumb rubber namely #30, #14-30, and #6-7 (Fig. 1) were used to create the mix of rubber that had the closest ingredients to the replaced fine aggregate. Fig. 2 shows the sieve analysis results for the used rubber mix and mineral fine aggregate. Three masonry block units for each rubber replacement were placed in an oven at 113 °C for 25 hours. Following heat treatment, units were then soaked in a large water container for 24 hours. The absorption rate of each unit with a different amount of rubber replacement, according to ASTM C140/C140M–14b was measured.

Table 1. Material properties

| Items | Tests type | Results | ASTM limits |
|--------|---------------------------------------|---|---|
| RCMU | Compressive strength ASTM C90–12 | 0% rubber 29.8 MPa 10% rubber 25.3 MPa 20% rubber 15.4 MPa 37% rubber 6.7 MPa | 13.1 MPa |
| RCMU | Absorption Test ASTM C90–12 | 0% rubber 109 kg/m ³ 10% rubber 133 kg/m ³ 20% rubber 151 kg/m ³ 37% rubber 176 kg/m ³ | 208 kg/m ³ (Max) |
| RCMU | Density Classification ASTM C90–12 | 0% rubber 2206 kg/m ³ 10% rubber 2122 kg/m ³ 20% rubber 2050 kg/m ³ 37% rubber 1913 kg/m ³ | Lightweight less than 1680 kg/m ³ Medium weight 1680–2000 kg/m ³ Normal weight 2000 kg/m ³ or more |
| Rubber | Unit weight | 641 kg/m ³ | ----- |

As shown in Table 1, increasing the rubber replacement ratio in RCMUs increased the water absorption. This increase in water absorption was related to the increase in air content because of the rubber particles' tendency to entrap air at their rough surface due to the particles' non-polar nature (Fedroff et al. 1996). The compressive strength results showed that RCMUs with both 10% and 20% rubber replacement ratios met the ASTM C90-12 for concrete masonry bearing units while the 37% replacement met ASTM C129-14a for non-loadbearing units.



Figure 1: The different sizes of crumb rubber that used in RCMU's production

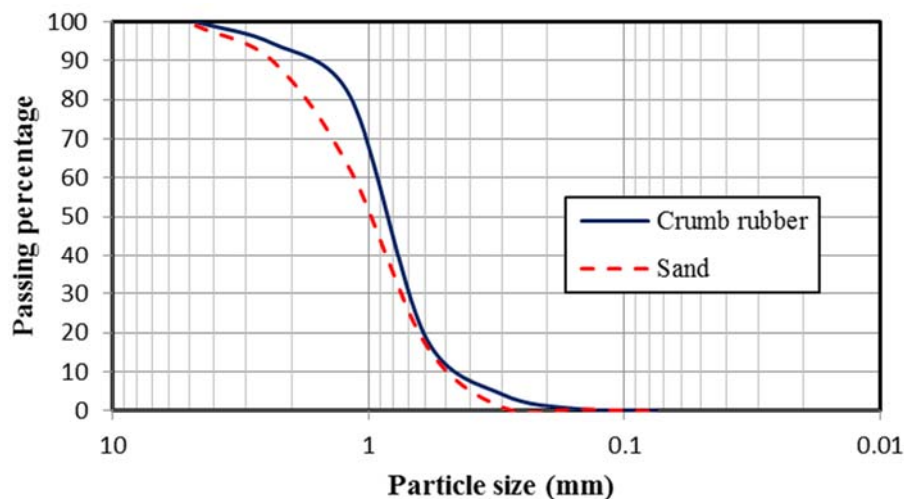


Figure 2: Sieve analysis of the used mix of crumb rubber

THERMAL CONDUCTIVITY

During this experimental work, the thermal characteristics of the rubberized concrete masonry units (RCMU) were determined using guarded hot plate assembly method. This test was conducted according to the Whole Building Design Guide CRD-C 45-65 (WBDG 1965). This

method deals with plates of material rather than masonry units with dimensions of 100 mm x 100 mm. x 25 mm. As shown in Fig. 3, and Fig. 4 the apparatus used in this test consisted of a guarded hot plate, controlled heat source, and temperature measurement system. The guarded hot plate was fabricated using 51 mm thick corkboard for the interior faces and 19 mm thick plywood for the exterior faces. The corkboard was preferred to Styrofoam because of its ability to insulate even if in full contact with the hot plate. The corkboard pieces were arranged around the tested sample so that all the heat would pass vertically through only the tested samples without any dissipation through the walls in the other directions. A 102 mm x 102 mm aluminum plate with a slim heat sheet was used as a controlled heat source that was kept the temperature at $60\text{ }^{\circ}\text{C} \pm 2\text{ }^{\circ}\text{C}$. This constant temperature was achieved using a proportional–integral–derivative controller (PID) that was connected to the slim heat sheet to produce the required temperature at this side of the sample.

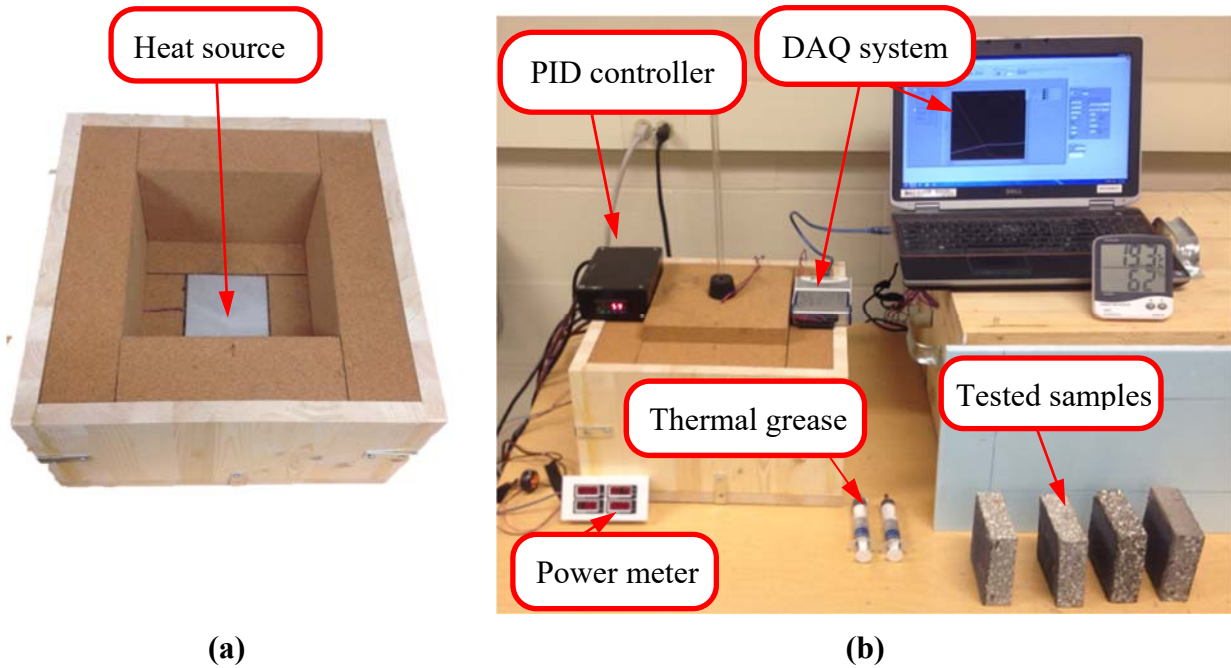


Figure 3: Thermal conductivity measuring system: (a) Testing box (b) The whole system

The temperature measurement system consisted of two thermocouple wires connected to a sensitive computerized data acquisition system. This system was used to monitor the temperature of the aluminum plate in full contact with the tested sample and in the room above it. To achieve full contact between the aluminum plates and the tested sample, thermal grease was used to cover the contact areas.

Thermal conductivity was then calculated as follows:

$$k = \frac{qL}{A(t_1 - t_2)} \quad (1)$$

Heat resistivity was then calculated as follows:

$$r = \frac{L}{k} \quad (2)$$

where:

k: thermal conductivity factor, (W/m K).

r: heat resistivity, ($\text{m}^2\text{ K/W}$).

L: thickness of the tested specimen, (m).

A: area of the tested specimen, (m^2).

t_1 : the temperature of hot plate face in contact with the specimen, K.

t_2 : the temperature at the heat collecting plate on the top face of the sample, K.

q : heat flow rate within the tested specimen, W/m^2 . ($q = 3.41$ times the rate of electrical energy input to the hot plate, Watts).

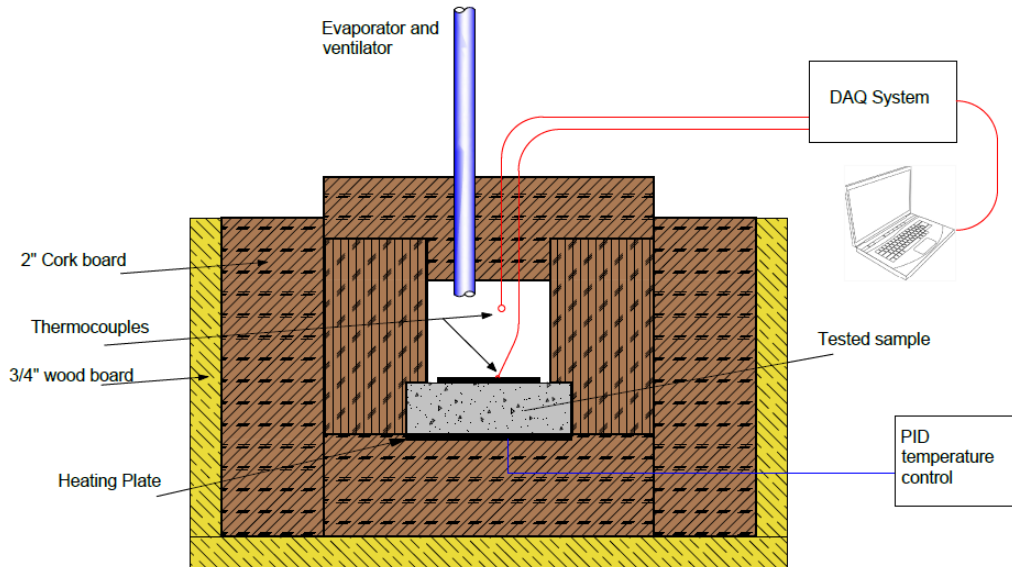


Figure 4: Thermal conductivity apparatus general layout

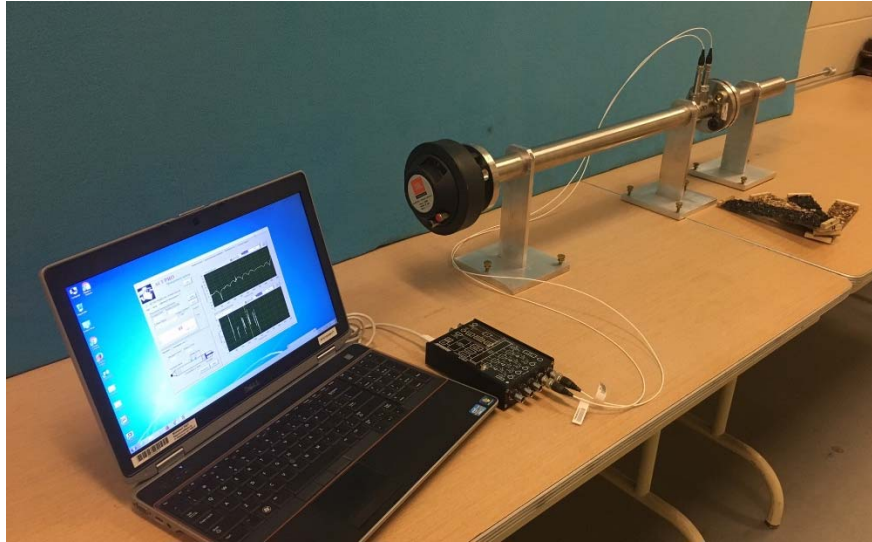
SOUND ABSORPTION

The ability of a material to absorb sound can be measured using the sound absorption coefficient (α). According to ASTM E1050–12, the Acoustical Properties of Materials and Systems (ACUPRO) was used to measure both absorption coefficient under varied frequencies and noise reduction coefficient. The plane wave tube was carefully machined using stainless steel tube with a wall thickness of 3.2 mm for an accurate measurement of sound pressure amplitude and phase (Fig. 5a). The phase response of the tube is less than 0.1 degrees over the operating range from 50-5650 Hz. The precision machined flanges, side ports, and microphone holders accurately maintain microphone alignment. A 16 ohms high-frequency compression JBL compression driver was used to produce sound (Fig. 5b). Two 13 mm high accuracy microphones were used with microphone holders to ensure stable posting the testing apparatus (Fig. 5c). A fully integrated ACUPRO Software and DT 9837A data acquisition module was used to collect and analyze the output data from the testing apparatus (Fig. 5d).

Since the sound absorption of materials is varied under different frequency ranges, it required using a single value that evaluates the sound absorption of the particular material. To solve this problem, the noise reduction coefficient (NRC) was calculated for each masonry material with different rubber ratio. The NRC can be calculated using the following equation (Thumann and Miller 1986, Sukontasukkul 2009):

$$NRC = (\alpha_{250} + \alpha_{500} + \alpha_{1000} + \alpha_{2000}) / 4 \quad (3)$$

Where α_{250} , α_{500} , α_{1000} , α_{2000} are the sound absorption coefficients (α) at 250, 500, 1000, and 2000 Hz respectively.



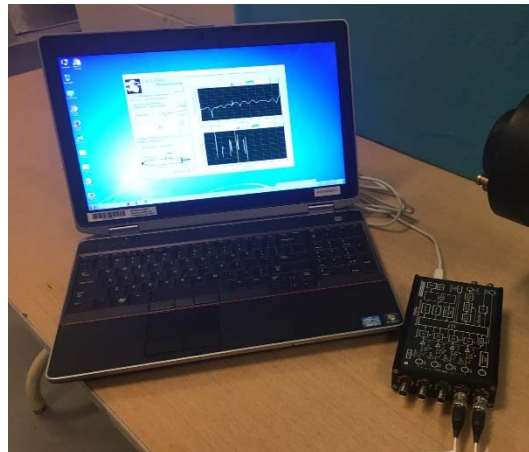
(a)



(b)



(c)



(d)

Figure 5: Acoustic absorption test: (a) testing apparatus, (b) Sound source (compression driver), (c) microphones with holders, (d) ACUPRO Software with data acquisition module

The tested samples were prepared by using a high precision water jet cutter (Fig. 6a) to cut masonry specimens that fit tightly inside the ACUPRO testing system (Fig. 6b).



(a)



(b)

Figure 6: (a) using water jet cutter to cut masonry specimens and (b) masonry specimen to be used in ACUPRO testing system

THERMAL CONDUCTIVITY RESULTS

Fig. 7 shows the influence of having the crumb rubber in masonry plate. The thermal conductivity dropped from 1.6 to 0.92 (w/m·k) by replacing 37% of the mineral aggregate with the same size of crumb rubber. This represents a reduction of 42.5% in thermal conductivity. Similarly, using 10% and 20% rubber replacement resulted in a reduction of 8.75% and 17.5% in thermal conductivity respectively compared to conventional CMU. This reduction in thermal conductivity will be reflected in the same trend on the energy consumption of building using this type of masonry units.

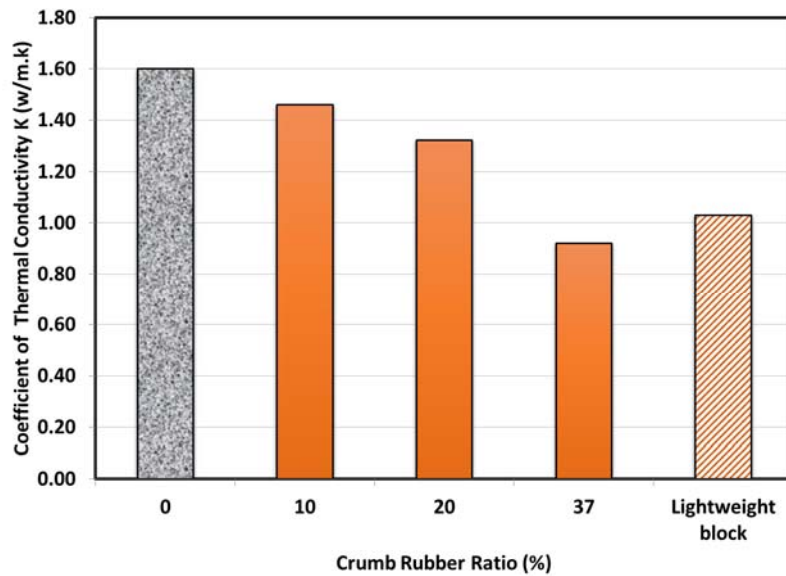


Figure 7: Thermal conductivity factor for masonry materials with varied rubber content

Additionally, the rubberized masonry units exhibited higher heat resistance compared with conventional CMU as shown in Fig. 8.

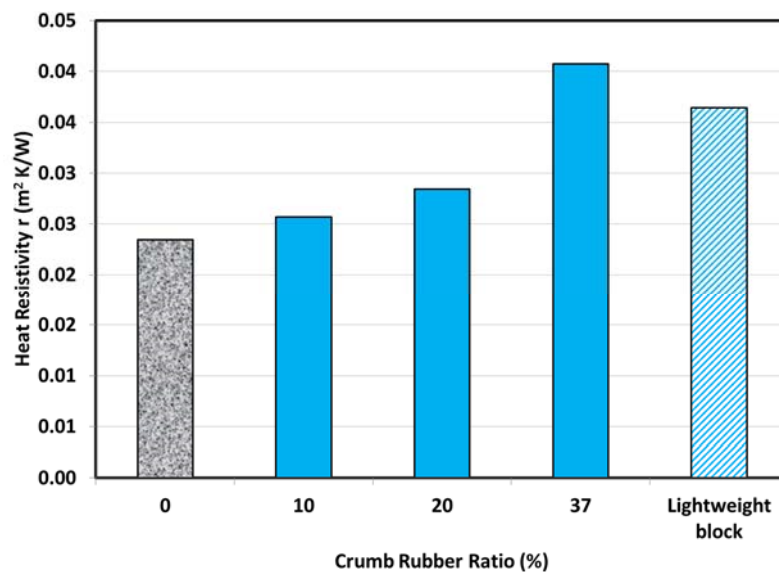


Figure 8: Heat resistivity factor for masonry materials with varied rubber content

SOUND ABSORPTION RESULTS

As shown in Fig. 9, the rubberized masonry materials showed a better sound absorption under both low and high frequency. In addition, results also being compared with lightweight masonry material. The sound absorption of rubberized masonry material was found to be lower than that of lightweight masonry at low frequency. However, rubberized masonry with both 20% and 37% rubber ratio had a higher sound absorption under high frequency.

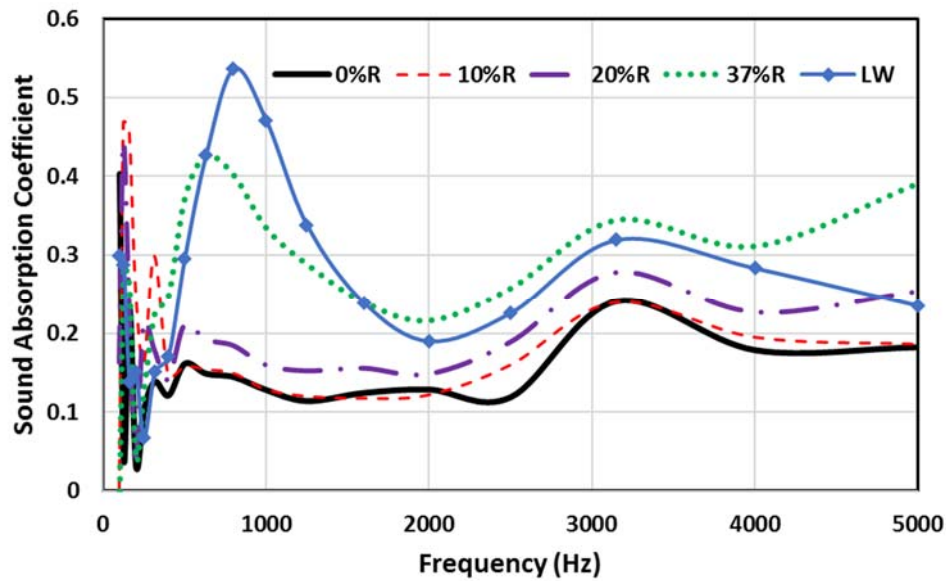


Figure 9: Sound absorption coefficient of rubberized masonry materials

The noise reduction factor increased with all rubber replacement ratio as shown in Fig. 10. Masonry materials with 10, 20, 37% rubber ratios exhibited an increase in the noise reduction coefficient of 9, 40, 101% respectively.

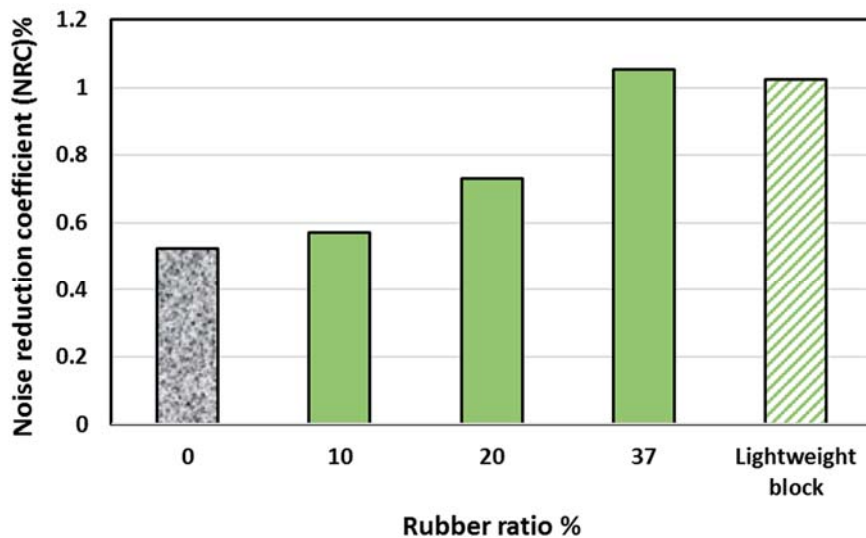


Figure 10: Noise reduction coefficient of rubberized masonry materials

FINDINGS AND CONCLUSIONS

Crumb rubber was used as a replacement of mineral fine aggregates to manufacture rubberized concrete masonry units (RCMU). The thermal and sound characteristics of RCMUs having of rubber replacement ratio of 0%, 10%, 20%, and 37% were examined using guarded hot plate assembly method according to the Whole Building Design Guide CRD-C 45-65 and the sound absorption according to ASTM E1050-12. The thermal and sound performance of lightweight CMU was also investigated as another reference.

Based on the experimental investigation, the following conclusions can be drawn:

- Up to 20% crumb rubber can be used as a partial replacement for fine aggregate to produce load bearing rubberized masonry units that meet the requirements of the ASTM C90. Units with 37% rubber ratio met ASTM C129 requirements for non-loadbearing CMUs.
- The thermal conductivity for rubberized masonry decreased with increasing the rubber content. For example, replace the fine aggregate with 10%, 20%, and 37% crumb rubber reduced the thermal conductivity of RCMU by 8.75%, 17.5%, and 42.5% respectively.
- The sound absorption increased with the increase of rubber ratio under both low and high frequency. Furthermore, the rubberized masonry materials exhibited higher noise reduction coefficient with an increase of 9, 40, and 101% for rubber ratio of 10, 20, and 37% respectively.

ACKNOWLEDGEMENTS

This research was conducted at Missouri University of Science and Technology and was supported by Midwest Block & Brick Inc. This support is gratefully appreciated. However, any opinions, findings, conclusions, and recommendations presented in this paper are those of the authors and do not necessarily reflect the views of the sponsors.

REFERENCES

- Al-Jabri, K. S., A. Hago, A. Al-Nuaimi and A. Al-Saidy (2005). "Concrete blocks for thermal insulation in hot climate." *Cement and Concrete Research* 35(8): 1472-1479.
- Batayneh, M. K., I. Marie and I. Asi (2008). "Promoting the use of crumb rubber concrete in developing countries." *Waste Management* 28(11): 2171-2176.
- Fedroff, D., S. Ahmad and B. Savas (1996). "Mechanical properties of concrete with ground waste tire rubber." *Transportation Research Record: Journal of the Transportation Research Board*(1532): 66-72.
- Gheni, A., M. A. ElGawady and J. J. Myers (2017). "Thermal Characterization of Cleaner and Eco-Efficient Masonry Units Using Sustainable Aggregates." *Journal of Cleaner Production*.
- Gheni, A. A., Z. K. Aljaberi, M. E. ElGawady and J. J. Myers (2016). Energy efficiency and thermal characterization of eco-friendly wood fiber masonry blocks. *Brick and Block Masonry*, CRC Press: 895-901.
- Gheni, A. A., M. A. ElGawady and J. J. Myers (2017). "Mechanical Characterization of Concrete Masonry Units Manufactured with Crumb Rubber Aggregate." *ACI Materials Journal* 114(01).
- Gou, M. and X. Liu (2014). "Effect of rubber particle modification on properties of rubberized concrete." *Journal of Wuhan University of Technology-Mater. Sci. Ed.* 29(4): 763-768.
- Hall, M. R., K. B. Najim and C. J. Hopfe (2012). "Transient thermal behaviour of crumb rubber-modified concrete and implications for thermal response and energy efficiency in buildings." *Applied thermal engineering* 33: 77-85.

- Horvath, A. (2004). "Construction materials and the environment." *Annu. Rev. Environ. Resour.* 29: 181-204.
- Isler, J. W. (2012). Assessment of concrete masonry units containing aggregate replacements of waste glass and rubber tire particles, University of Colorado at Denver.
- Mohammed, S., K. Hossain, J. Swee, G. Wong and M. Abdullahi (2012). "Properties of crumb rubber hollow concrete block." *Journal of Cleaner Production* 23(1): 57-67.
- Moustafa, A. and M. A. ElGawady (2017). "Dynamic properties of high strength rubberized concrete." *ACI Spec. Publ* 314: 1-22.
- Najim, K. and M. Hall (2010). "A review of the fresh/hardened properties and applications for plain-(PRC) and self-compacting rubberised concrete (SCRC)." *Construction and building materials* 24(11): 2043-2051.
- Po, Y. (2004). Analysis on the stability and economies of use of waste tires for construction of retaining wall, Master's thesis. Department of Civil Engineering, National Central University.
- RMA, R. M. A. (2016). 2015 U.S. Scrap Tire Management Summary. Wasington, DC.
- Sadek, D. M. and M. M. El-Attar (2015). "Structural behavior of rubberized masonry walls." *Journal of Cleaner Production* 89: 174-186.
- Siddique, R. and T. R. Naik (2004). "Properties of concrete containing scrap-tire rubber—an overview." *Waste management* 24(6): 563-569.
- Skripkiūnas, G., A. Grinys and E. Janavičius (2010). Porosity and durability of rubberized concrete. *Second International Conference on sustainable construction materials and technologies*.
- Sukontasukkul, P. (2009). "Use of crumb rubber to improve thermal and sound properties of pre-cast concrete panel." *Construction and Building Materials* 23(2): 1084-1092.
- Thomas, B. S. and R. C. Gupta (2013). "Mechanical properties and durability characteristics of concrete containing solid waste materials." *Journal of Cleaner Production* 48: 1-6.
- Thumann, A. and R. K. Miller (1986). "Fundamentals of noise control engineering."
- Turgut, P. and B. Yesilata (2008). "Physico-mechanical and thermal performances of newly developed rubber-added bricks." *Energy and Buildings* 40(5): 679-688.
- WBDG (1965). Method of Test for Thermal Conductivity of Lightweight Insulating Concrete. Whole Building Design Guide National Institute of Building Sciences, US Army Corps of Engineers: 5.
- Worrell, E., L. Price, N. Martin, C. Hendriks and L. O. Meida (2001). "Carbon dioxide emissions from the global cement industry." *Annual review of energy and the environment* 26(1): 303-329.
- Zheng, L., X. S. Huo and Y. Yuan (2008). "Experimental investigation on dynamic properties of rubberized concrete." *Construction and building materials* 22(5): 939-947.

EFFICIENCY RATIO OF HOLLOW CLAY BLOCK MASONRY

R.P. Portella¹, G. Mohamad², F.S. Fonseca³, A. Lübeck⁴, R.P.B. Schmidt⁵ and L.E. Modler⁶

¹ Professor, Franciscan University Center UNIFRA, Department of Architecture and Urbanism, Santa Maria, Brazil.
portellarafael@unifra.br

² Associate Professor, Federal University of Santa Maria, Department of Civil Engineering, Santa Maria, Brazil,
gihad@ufsm.br

³ Associate Professor, Department of Civil and Environmental Engineering, Brigham Young University, 368 Clyde Building, Provo, UT 84602, ffonseca@et.byu.edu

⁴ Assistant Professor, Federal University of Santa Maria, Department of Civil Engineering, Santa Maria, Brazil,
andrelubeck@gmail.com

⁵ Assistant Professor, Federal University of Santa Maria, Cachoeira do Sul Campus, Cachoeira do Sul, Brazil,
raquelbrondani@gmail.com

⁶ Assistant Professor, Federal University of Fronteira Sul, Department of Civil Engineering, Santa Maria, Brazil,
luismodler@gmail.com

The compressive strength of masonry prisms is one of the most important and common parameters used by designers of masonry structures. The study presented herein is related specifically to hollow clay block masonry and presents a relationship between the compressive strength of prisms and blocks developed from a database of mortar, block and prism tests conducted between the years of 2007 and 2014. Hollow masonry prisms, blocks and mortars were tested at the age of 7 and 28 days. The results were divided into five groups according to the block compressive strength: 6.0 to 8.5 MPa, 8.5 to 10.0 MPa, 10.0 to 12.0 MPa, 12.0 to 15.0 MPa, and above 15.0 MPa. The results were used to determine the ratio between the compressive strengths of the hollow clay prisms and blocks, which can be used as a measure of the efficiency of the block. The calculated block efficiencies for the compressive strength ranges at 7 days were 0.40, 0.28, 0.29, 0.29 and 0.25, respectively. For the age of 28 days, the block efficiencies for the compressive strength ranges were 0.50, 0.48, 0.37, 0.33 and 0.31, respectively. These results show that there was a decrease in efficiency with the increase of block strength. The results were also used to establish a correlation between prism and block compressive strengths.

Keywords: *hollow clay masonry prism, specified compressive strength, hollow clay blocks, structural masonry, ungrouted masonry, efficiency ratio.*

MASONRY CONSTRUCTION SYSTEM IN BRAZIL

The gradual increase in the competitions between building companies and the demands by the purchaser, forced some builders to search new strategic change, like improving the production process and trying to find out more rational and sustainable constructions techniques. The masonry construction has several advantages and the two most important is the economy and the easily flexibility to plan the different construction phase. A comparative example of the differences in constructions costs of masonry structures and reinforce concrete buildings is given in Table 1. From the results of Table 1 it is possible to conclude that there is a significant reduction of the structure costs when it is comparing the masonry building with the reinforced concrete. For instance, for the most common building in Brazil (four floor without transition in reinforcing concrete) the differences in the structural costs were between 25 to 30%. Because of this, the masonry buildings are the most popular construction system for social dwelling.

Table 1: Differences in structural costs of masonry and reinforce concrete buildings

| Building characteristics | Structural differences costs (%) |
|---|---|
| Four floors without transition in reinforce concrete | 25-30 |
| Non-reinforced masonry walls with seven floor without transition in reinforce concrete in the first floor | 20-25 |
| Reinforce walls with seven floor without transition in reinforce concrete in the first floor | 15-20 |
| Seven floor with transition in reinforce concrete in the first floor | 12-20 |
| Twelve floor without transition in reinforce concrete in the first floor | 10-15 |
| Twelve floor with transition in reinforce concrete in the two first floor | 8-12 |

Clay blockwork masonry is the most used construction system in Brazil for buildings up to four floors. In masonry construction system, the walls should function like a fence, supporting vertical and horizontal load from slabs, walls and wind. The designer, who adopt the masonry as a construction system, should consider in his plan some technical aspects for the success of the enterprise. Some design measurements are: follow a modular mesh coordination between load bearing walls; design compatibilities between structural elements and water and sewer systems; appropriate material and component specifications and a rigid plane of quality control for each floor for the components and for production.

One of the most significant problems for the masonry structures designer is how to determine the correlation between the compressive strength of the block and masonry, especially due to the wide range of blocks in Brazilian market. The Figure 1 shows the different types of block. In Figure 1(a) it is presented the hollow clay block with hollows in faceshell and crossweb, which the inner crossweb has the double of the thickness of the crossweb from the edges. The Figure 1(b) presents the hollow block with solid faceshell and crossweb with the same overall thickness. The block of Figure 1(c) is quite similar from the block of Figure 1(b), and the difference is regarding the

thickness and the presence of hollows in the inner crosswebs. The Figure 1(d) presents the perforated block.

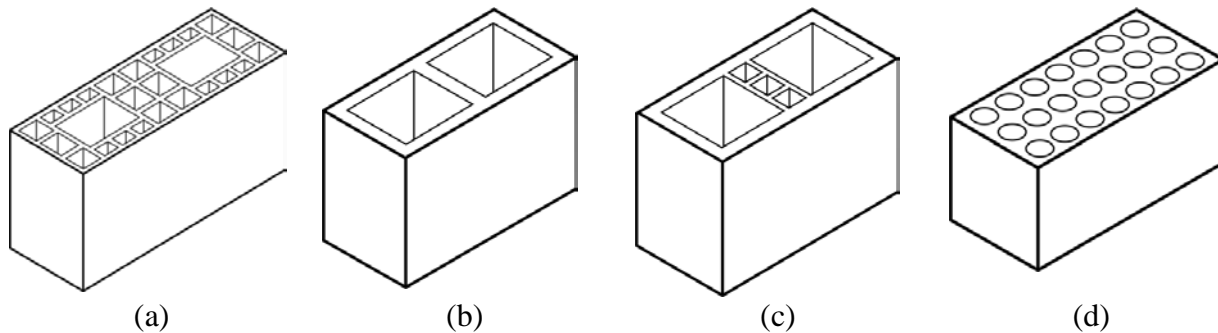


Figure 1: Hollow clay block masonry units

Regarding the lack of efficiency ratio between prisms and blocks in Brazilian code, the main objective of this research was determine from experimental results of hollow clay block showed in Figure 1(a) the global efficiency ratio for mean and characteristic values between prisms and blocks tested during 2007 and 2014 at Building and Materials Laboratory (LMCC) of Federal University of Santa Maria (UFSM).

EXPERIMENTAL TEST

Standards and buildings codes establish two methods to determine the load bearing capacity of masonry. One of the methods consists of testing specimens such as prisms, wallets, or walls and then correlate the compressive strength of the masonry with experimental results of testing. This correlation between strengths it is called an efficiency ratio, which is important for the masonry designers to preview the block and mortar type. The other method consists of using an empirical formula and graphs to determine the masonry strength from correlations between compressive strength of units and mortar (BS 5628-1 (1992) and Eurocode 6 (2005)). More specifically the Brazilian standard code NBR 15812-1 (2010) establish the first methods as design parameters to adopt on masonry projects. The Brazilian code set the ratio between the compressive strength of a wall and prism of 0.70, however the standard does not indicate any prism/block relation leaving the decision for the designers to carry tests at the certified laboratories.

The main goal of this research is to calculate the prism/block efficiency ratio of hollow clay blocks and nongROUTED prisms tested between 2007 and 2014 at the Building and Materials Laboratory (LMCC) of Federal University of Santa Maria (UFSM). The prisms test were done at 7 and 28 days. In Figure 2 is showed the block and the two high block stack bond prism. The nominal block dimension was 150 mm (thicknes), 300 mm (length) and 200 mm (height). The compressive strength of the block and prism was calculated using always the gross area, as recommended by NBR 15812-1 (2010).



Figure 2: Hollow clay block masonry unit and the stack bond prism

To get an efficiency ratio, due to the wide range of block compressive strength from 6 MPa to above 15 MPa, the blocks were divided into five groups, according to the compressive strength range. The Table 2 presents the different groups corresponding to each block strength range and the number of prisms tested at 7 and 28 days. For both ages a total of 919 of two high stack bond prisms was tested under compression.

Table 2: Prism tests quantities

| Group | Block strength range (MPa) | Prisms test quantities (units) | |
|-------|----------------------------|--------------------------------|------------|
| | | 7 days | 28 days |
| 1 | 6.0 to 8.5 | 34 | 34 |
| 2 | 8.5 to 10.0 | 104 | 121 |
| 3 | 10.0 to 12.0 | 189 | 231 |
| 4 | 12.0 to 15.0 | 74 | 94 |
| 5 | Above 15.0 | 19 | 19 |
| | Total | 420 | 499 |

EXPERIMENTAL RESULTS

For each block and prism group, it was calculated the mean and characteristic strength values at 7 and 28 days. The Table 3 presents the experimental results of compressive strength of mortar, block and prism, for each group of block strength range. The Figure 3 to 7 present the normal distribution results for block and prism compressive strength, with the mean and characteristic values for the confidence interval between 5% to 95% at 7 and 28 days.

Table 3: Prism and block test results

| Group | Block strength range (MPa) | f mortar (MPa) | | f_{block} (MPa) | | f_{prism} (MPa) | | | |
|-------|----------------------------|----------------|---------|-------------------|---|-------------------|---------|---|---------|
| | | | | Mean value | Characteristic value for 5% of confidence | Mean value | | Characteristic value for 5% of confidence | |
| | | 7 days | 28 days | 28 days | 28 days | 7 days | 28 days | 7 days | 28 days |
| 1 | 6.0 to 8.5 | 3.7 | 5.0 | 7.4 | 6.4 | 3.6 | 4.3 | 2.6 | 3.4 |
| 2 | 8.5 to 10.0 | 3.8 | 5.4 | 9.6 | 9.0 | 3.5 | 4.4 | 2.6 | 3.3 |
| 3 | 10.0 to 12.0 | 4.1 | 5.6 | 10.7 | 9.9 | 4.1 | 5.0 | 2.8 | 3.8 |
| 4 | 12.0 to 15.0 | 3.5 | 5.4 | 13.0 | 11.9 | 4.6 | 5.4 | 3.4 | 3.9 |
| 5 | Above 15.0 | 5.2 | 5.6 | 15.8 | 15.7 | 5.2 | 6.2 | 3.9 | 4.9 |

The Figures 3 to 7 show individual results, the mean and characteristic value for confidence level of 5% to 95%. The results were separated according to the block compressive strength range and the age of tests.

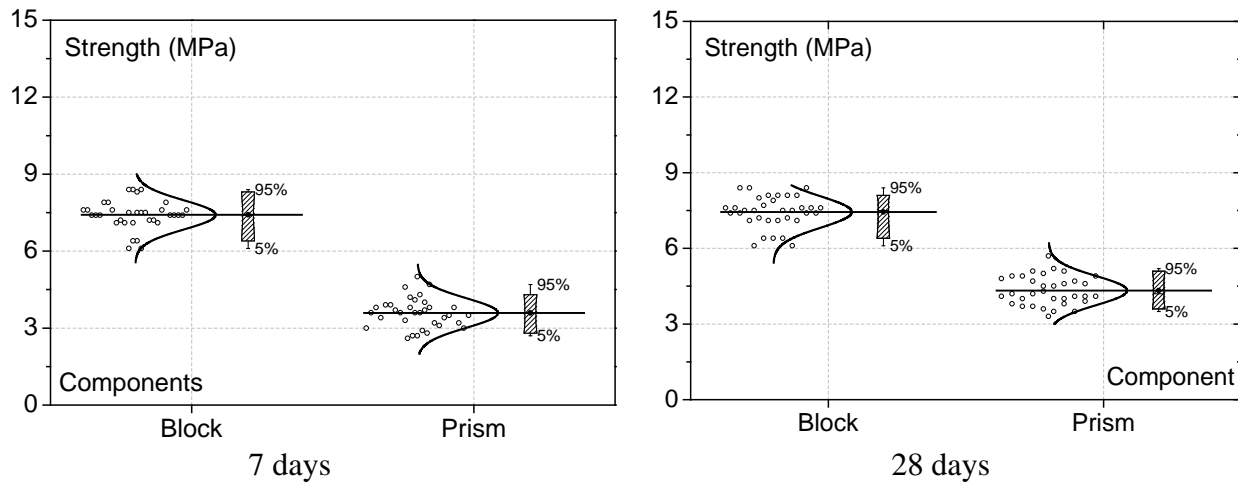


Figure 3: Clay block masonry unit with compressive strength range of 6.0 to 8.5 MPa.

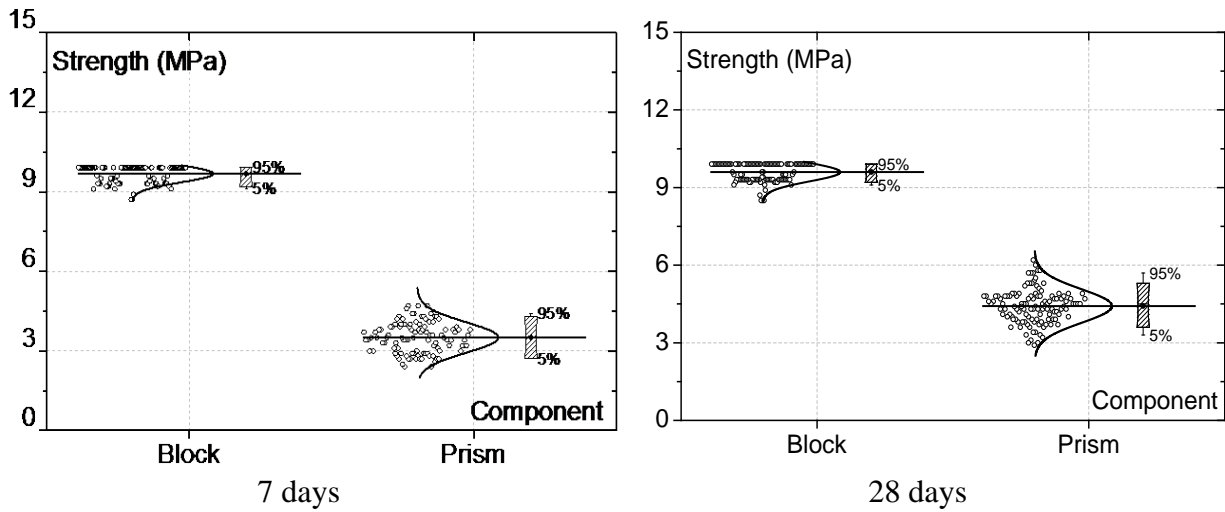


Figure 4: Clay block masonry unit with compressive strength range of 8.5 to 10.0 MPa.

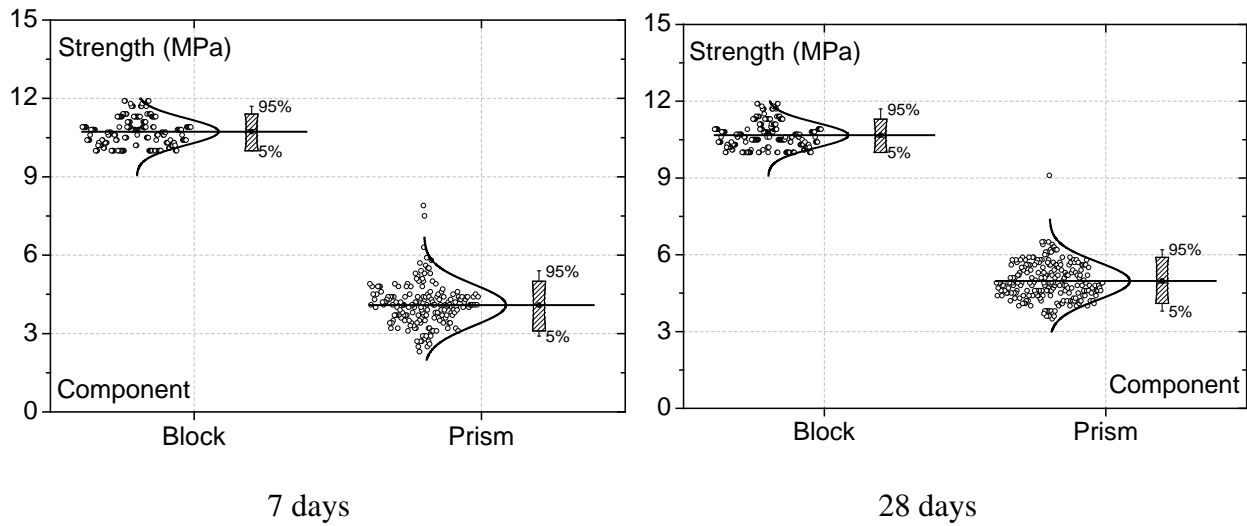


Figure 5: Clay block masonry unit with compressive strength range of 10.0 to 12.5 MPa.

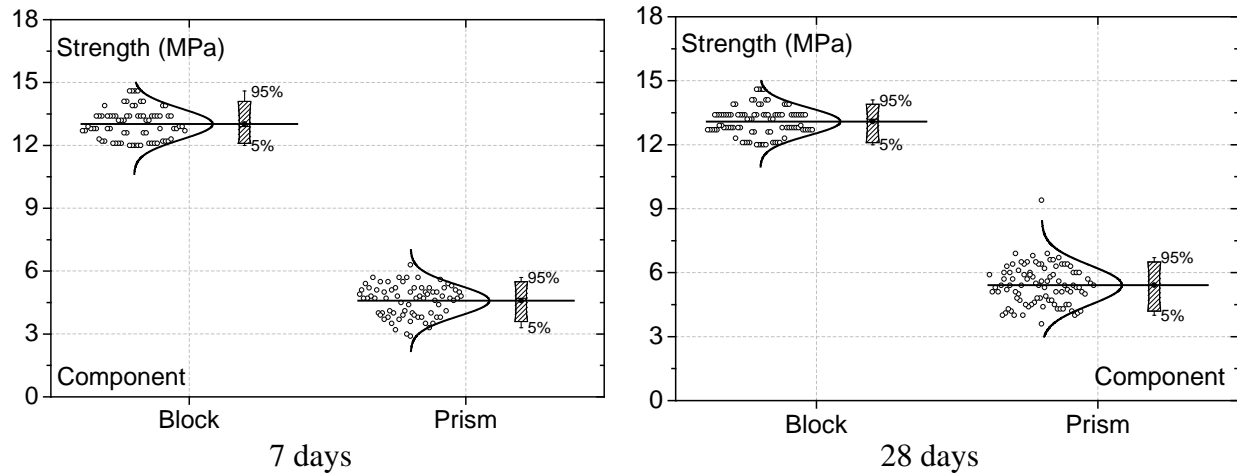


Figure 6: Clay block masonry unit with compressive strength range of 12.5 to 15.0 MPa.

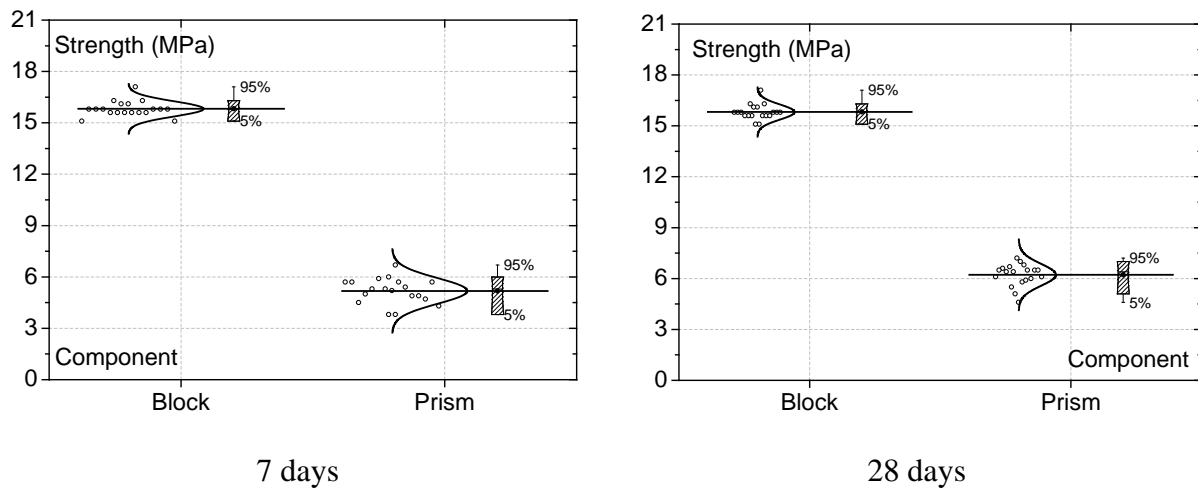


Figure 7: Clay block masonry unit with compressive strength above 15.0 MPa.

Table 4 presents the efficiency ratio between prism and block at 7 and 28 days. It was possible to observe that, with the increase on the block compressive strength, there was a decreasing in the efficiency ratio between prism and block. For test at 28 days, the most common block in Brazilian market (group 1) presents a global efficiency ratio of about 0.50. For blocks from groups 2 and 3 a good approximation for the efficiency ratio were about 0.35, and for blocks from groups 4 and 5 the efficiency ratio were about 0.30. For test at 7 days, the blocks of group 1 presents a global efficiency ratio about 0.40. The others blocks groups the efficiency ratio were about 0.25.

Table 4: Efficiency ratio between prisms and blocks

| Group | Block strength range (MPa) | f_{prism} / f_{block} | | f_{prism} / f_{block} | |
|-------|----------------------------|-------------------------|----------------|-------------------------|----------------|
| | | 7 days | 7 days | 28 days | 28 days |
| | | Mean | Characteristic | Mean | Characteristic |
| 1 | 6.0 to 8.5 | 0.49 | 0.41 | 0.58 | 0.53 |
| 2 | 8.5 to 10.0 | 0.36 | 0.29 | 0.46 | 0.37 |
| 3 | 10.0 to 12.0 | 0.38 | 0.28 | 0.47 | 0.38 |
| 4 | 12.0 to 15.0 | 0.35 | 0.28 | 0.41 | 0.33 |
| 5 | Above 15.0 | 0.33 | 0.25 | 0.39 | 0.31 |

Table 5 presents the results between mortar and block compressive strength. As more close to 1.0 is the mortar and block compressive strength ratio, much stronger is the mortar. From table 3 and 4 it possible to conclude that much higher is the f_{mortar} / f_{block} ratio, higher is efficiency ratio between prism and block. For instance, considering only the characteristic value and block strength range from group, the f_{mortar} / f_{block} ratio was 0.78, and the f_{prism} / f_{block} ratio was 0.53. For others block group the decrease in f_{mortar} / f_{block} ratio did not affect significantly the efficiency ratio between prism and block. Probably this could be due to the failure process of the prisms. The presence of voids in faceshell and crosswebs decrease the mortar confinement between mortar and block, producing localized crushing on bedding mortar.

Table 5: Mortar and block compressive strength ratio

| Group | Block strength range (MPa) | f_{mortar} / f_{block} | | f_{mortar} / f_{block} | |
|-------|----------------------------|--------------------------|----------------|--------------------------|----------------|
| | | 7 days | 7 days | 28 days | 28 days |
| | | Mean | Characteristic | Mean | Characteristic |
| 1 | 6.0 to 8.5 | 0.50 | 0.58 | 0.67 | 0.78 |
| 2 | 8.5 to 10.0 | 0.39 | 0.42 | 0.56 | 0.60 |
| 3 | 10.0 to 12.0 | 0.38 | 0.41 | 0.52 | 0.56 |
| 4 | 12.0 to 15.0 | 0.27 | 0.29 | 0.41 | 0.45 |
| 5 | Above 15.0 | 0.33 | 0.33 | 0.35 | 0.36 |

Figure 8 presents the characteristic compressive strength relation between prism and block at 7 and 28 days for blocks from 6.5 MPa to 15.0 MPa, with the corresponding polynomial function and coefficient of correlation.

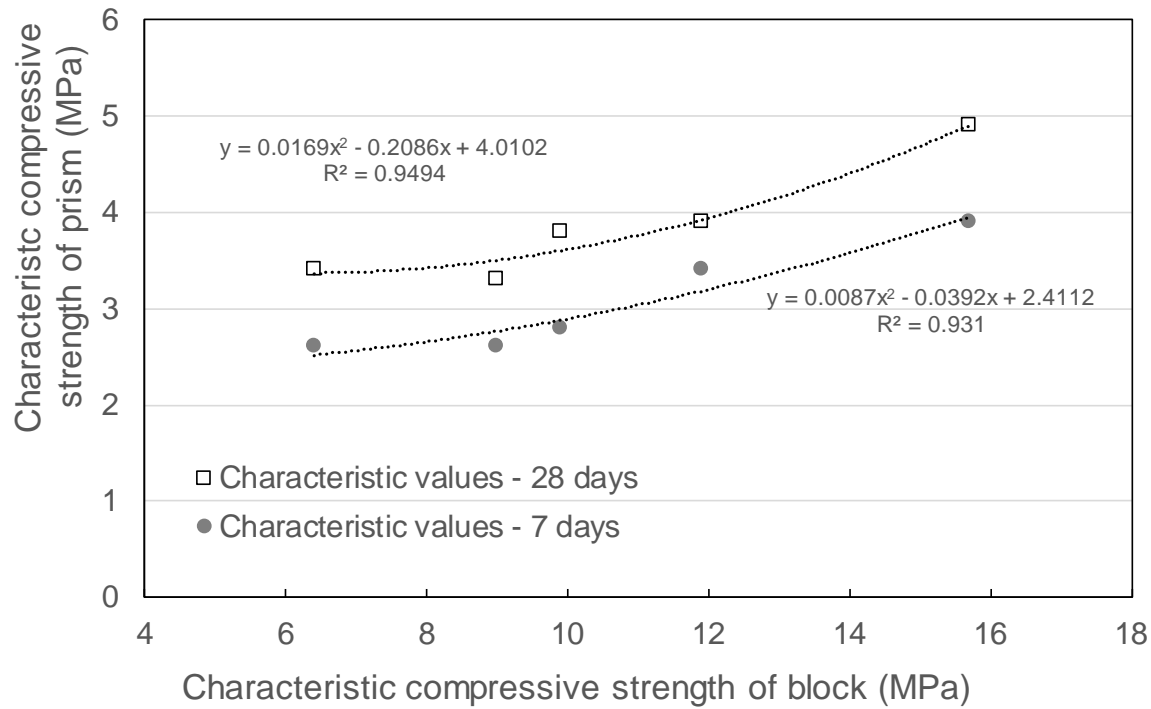


Figure 8: Characteristic compressive strength of prism and blocks.

CONCLUSIONS

The main conclusions from the work presented herein are:

- It is possible to establish a global efficiency ratio between prism and block;
- The efficiency ratio decreases with the increase of the block compressive strength;
- The efficiency ratio calculated with mean values was higher when compared with characteristic values for tests at 7 and 28 days;
- For tests at 28 days and block strength range from group 1 the global efficiency ratio was about 0.50. For blocks from groups 2 and 3 a good approximation for the efficiency ratio were about 0.35, and for blocks from groups 4 and 5 the efficiency ratio were about 0.30;
- For tests at 7 days, the blocks from group 1 present a global efficiency ratio of about 0.40. The others block groups the efficiency ratio were about 0.25;
- Significant difference was found in the efficiency ratio for f_{prism} / f_{block} ratio of block strength range from group 1.

ACKNOWLEDGEMENT

The authors would like to thank to the CAPES Foundation, Ministry of Education of Brazil, Brasilia, DF, for supporting this study.

REFERENCES

ABNT, NBR 15812-1. Masonry – Hollow Blocks, Part 1: Design. São Paulo – BR, 2010.

BS 5628-1. Code of practice for use of masonry – Part 1: Structural use of unreinforced masonry. BSI, 1992.

EN 1996-1 – 1. Eurocode 6 – Design of masonry structure – Part 1-1: General rules for reinforced and unreinforced masonry structures. ES, 2005.

Mohamad, G. Mechanism failure of concrete block masonry under compression. PhD Thesis. Department of Civil Engineering. University of Minho, Portugal, 2007.

Mohamad, G. Masonry Buildings – Materials, designs and performance. 1^a Ed., São Paulo: Blücher, 2015.

Portella, R. P. Efficiency ratio prism/hollow clay blocks. Dissertation (Civil Engineering Masters) – PPGEC, Federal University of Santa Maria, Santa Maria, 2015.



MASONRY TODAY AND TOMORROW

11 - 14 February, 2018
SYDNEY AUSTRALIA

www.10amc.com

RESEARCH ON THE THERMAL PERFORMANCE OF AUSTRALIAN HOUSING AT THE UNIVERSITY OF NEWCASTLE

Dariusz Alterman¹, Adrian Page² and Behdad Moghtaderi³

¹ Senior Research Academic, Centre for Infrastructure Performance and Reliability, The University of Newcastle, Callaghan, NSW 2308, Australia, dariusz.alterman@newcastle.edu.au

² Professor Emeritus, Centre for Frontier Energy Technologies & Utilisation, The University of Newcastle, Callaghan, NSW 2308, Australia, adrian.page@newcastle.edu.au

³ Professor, Centre for Frontier Energy Technologies & Utilisation, The University of Newcastle, Callaghan, NSW 2308, Australia, behdad.moghtaderi@newcastle.edu.au

The increased emphasis on Green House Gas (GHG) emissions and Global Warming has given greater impetus to the development of energy efficient housing in Australia, including the introduction of mandatory requirements for the energy performance of new construction through a star rating performance system. However, the emphasis in design has traditionally been placed on the thermal resistance (R-value) of the building components with little consideration of the benefits of thermal mass in ameliorating the effects of the extremes of temperature experienced during the normal diurnal cycle. The full benefit of the thermal mass of masonry walling systems has therefore not been obtained.

To address this issue, the Thermal Research Group at the University of Newcastle in collaboration with Think Brick Australia has been involved in an on-going 15 year study of the thermal performance of the common Australian housing wall systems (cavity brick, conventional and reverse brick veneer and lightweight). This research has involved the construction and monitoring of four full scale housing test modules, as well as the development of a sophisticated hot box system capable of testing walls and their components under both static and dynamic temperature cycles. The principal aim of this research has been to develop a convenient combined measure of wall performance reflecting the contribution of both thermal mass and thermal resistance with the potential for incorporation in the appropriate building regulations. This paper provides an overview of the investigation together with some of the key research outcomes.

Keywords: *masonry, thermal performance, energy, housing*



INTRODUCTION

The increased emphasis on GHG emissions and global warming has given greater impetus to the development of energy efficient housing in Australia. However, the emphasis in design has traditionally been placed on the thermal resistance (R-value) of the building components with little consideration of the benefits of thermal mass in ameliorating the effects of the extremes of temperature experienced during the normal diurnal cycle. The full benefit of the thermal mass of masonry walling systems has therefore not been obtained. The principal shortcoming of current simulations of thermal performance is the lack of real data on the performance of various housing walling systems under Australian climatic conditions. One particularly important aspect is the consideration of the contribution and interaction of the thermal resistance and thermal mass of each wall, which directly influences the wall and building performance under each (dynamic) diurnal temperature cycle.

With a view to overcoming the shortage of real data, over the past 15 years the Thermal Research Group at the University of Newcastle, in partnership with Think Brick Australia, has undertaken a major theoretical and experimental study of the thermal performance of housing wall systems (insulated and uninsulated cavity brick (InsCB & CB), conventional and reverse brick veneer (InsBV & InsRVB) and lightweight (InsLW)) in a typical moderate Australian climate. The research has involved the construction and monitoring of four full scale housing test modules, as well as the development of a sophisticated hot box system capable of testing walls and their components under both static and dynamic temperature cycles. The principal aim of this research has been to develop a convenient combined measure of wall performance reflecting the contribution of both thermal mass and thermal resistance with the potential for incorporation in the appropriate building regulations. Detailed reports on this research have been published recently (Alterman et al 2017, Page et al 2009). This paper provides an overview of the research together with the principal outcomes.

The research has had two major strands:

Strand 1: The observation and analysis of the performance of four full scale housing test modules located on the University of Newcastle campus. Over the testing period, incorporating all seasons and weather conditions, modules incorporating various walling systems (with and without a north facing window and internal partitions) have been used, with the interior of the modules being allowed to either “free float” or be “controlled” within a given temperature range by the use of artificial heating or cooling.

Strand 2: the detailed study of the performance of walling systems and their components when subjected to dynamic temperature cycles simulating various Australian climate zones (in particular, the development of measures reflecting the contribution of both thermal resistance and thermal mass to the wall and building performance).

STRAND 1 - HOUSING TEST MODULE STUDY

The housing module tests were used to provide qualitative and quantitative data on the thermal performance of the walling systems under real climatic conditions. The modules were

comparable in size to other buildings used in similar overseas studies. Note that the intent of the module tests was not to reproduce the behaviour of an actual house but rather to observe and quantify the typical heat flow mechanisms for walls in a realistic context.

The modules were constructed on the University of Newcastle Callaghan Campus in suburban Newcastle (Newcastle is located on the east coast of Australia at latitude 33°south). Over the testing period, a range of walling systems have been used (cavity brick, insulated cavity brick, brick veneer with and without insulation, lightweight construction and insulated reverse brick veneer – see Table 1). The modules are shown in Figure 1. In each case the response of the modules incorporating a particular walling system was observed with the interior being either in a ‘free-floating’ state (where the response of the module is influenced by the weather conditions and the recent thermal history), or with the interior heated or cooled to pre-set levels of comfort. The latter allowed the heating/cooling energy requirements for each walling system to be assessed. Heating energy was measured directly from electricity consumption whilst a chilled water heat exchanger system was used to measure the cooling demand.



Figure 1: View of modules: (a) from Northern view and (b) from Southern view. Note: Module 1 – InsBV, Module 2 – InsCB, Module 3 – CB, Module 4 – InsRBV.

The modules had a square floor plan of 6 m x 6 m and were spaced 7 m apart to avoid shading and minimise wind obstruction. With the exception of the walls and roof, the buildings were of identical construction following normal Australian practice, being built on a concrete slab-on-ground and aligned in a manner so that the north wall of each building was perpendicular to astronomical north. Timber trusses were used to support the roof which consisted of tiles for the InsCB and InsBV modules and steel sheeting for the InsLW and InsRBV modules, in both cases placed over a layer of sarking. The buildings had a ceiling height of 2450 mm. The ceiling consisted of 10mm thick plasterboard with glasswool insulation batts (R3.5 m².K.W-1) placed between the rafters. Since the emphasis of the investigation was on wall performance, the R3.5 insulation was selected to minimise the “through-ceiling” heat flow. Entry to the buildings was

via tight fitting, insulated solid timber doors located on the southern face of the buildings. The roof was supported by an independent steel frame which allowed the removal and replacement of walls as required.

Table 1: Details of Module Components
(*R values – air to air*)

| Building Element | Material(s) | Insulation |
|--|---|--|
| Cavity Brick wall (CB) R=0.62 | 2x110mm brickwork skins with 50mm cavity; 10mm internal render | Nil - standard 50mm cavity |
| Insulated Cavity Brick wall (InsCB) R=1.48 | 2x110mm brickwork skins with 50mm cavity; 10mm internal render | Standard 50mm cavity and R1 polystyrene insulation fixed to cavity side of interior brick skin |
| Brick Veneer wall (BV) R=1.14 | 110mm external brickwork skin; 50mm cavity; internal pine stud timber frame; 10mm interior plasterboard | Low glare reflective foil on timber frame |
| Insulated Brick Veneer wall (InsBV) R=1.72 | 110mm external brickwork skin; 50mm cavity; internal pine stud timber frame; 10mm interior plasterboard | Low glare reflective foil on timber frame with R1.5 glasswool batts |
| Insulated Reverse Brick Veneer wall (InsRBV) R=1.93 | 2-3mm acrylic render on 7mm fibro-cement sheets on timber stud frame; internal 110mm brick skin; 10mm internal Render | Low glare reflective foil on timber frame with R1.5 glasswool batts |
| Insulated Lightweight wall (InsLW) R=1.86 | External 7 mm fibro- cement sheeting finished with polymer render; breathable membrane fixed to pine stud frame; 10mm internal plasterboard | Low glare reflective foil on timber frame with R1.5 glasswool batts |
| Heavy internal partition walls (HPW) R=0.25 | 110mm brickwork | No insulation |
| Lightweight internal partition walls (LPW) R=0.52 | 10mm plasterboard on 90mm timber stud frame | No insulation |

Initial tests were performed on windowless modules, and subsequently a major window opening was installed in the northern wall of each module to allow solar ingress. Later in the investigation, some internal partition walls were also included to investigate the influence of internal thermal mass on the overall thermal performance. Window effects were reproduced by the insertion of a north-facing 3-panel sliding door assembly, 2050 mm high x 2840 mm wide, representing $\approx 20\%$ of the floor area which is a typical living room window/floor area ratio. The door consisted of clear, 6.38 mm laminated glass, set in a light coloured aluminium frame.

Module Instrumentation

The instrumentation recorded the external weather conditions including wind speed and direction, air temperature, relative humidity and the incident solar radiation on each wall (vertical plane) and on the roof (horizontal plane). For each module, temperature and heat flux profiles through the walls, slab and ceiling were recorded in conjunction with the internal air temperature and relative humidity. Heat flux sensors were placed on the walls, ceilings and concrete slab, adjacent to the window (in direct sunlight) and at the rear south-east corner. Thermocouples were placed on the surface of the slab at various locations between the window and the centre of the room. For the window, three net radiation sensors were placed at heights of 600, 1200 and 1800mm up the glass panel to assess the incoming/outgoing radiation. The surface temperature of the glass was recorded and additional heat flux sensors were placed on the aluminium frame to assess the influence of the frame itself. Internal air space temperatures were also monitored at heights of 600, 1200 and 1800mm with the relative humidity and globe temperatures being measured centrally. In total, 105 data channels were scanned and logged every 5 minutes for each of the modules for the duration of the testing program.

Module Testing Program

As previously described, each module was designed to allow the selective replacement of walling systems without disturbing the roof structure. This has allowed a range of wall types and opening conditions to be considered. As the modules were constructed progressively, an increasing number of variables were considered over the testing period. A summary of the module history and testing schedule is given in Figure 2. Testing commenced in February 2003 and has been ongoing since that date. For each of the main wall types, at some stage during the investigation, the internal conditions of the module were held constant and monitored for approximately 12 months to cover all four seasons. Because of time constraints the length of tests for the various combinations of other variables was reduced, but in all cases each testing period included both hot and cold conditions.

The key factor used to assess the relative thermal performance was the interior thermal comfort of the occupants. Whilst it is realised that thermal comfort is influenced by a range of factors such as humidity, radiant energy, air speed, individual preferences etc., for simplicity in this comparative study the variations in internal air space temperature were used to assess the relative performance, with temperatures between 18 - 24°C assumed to lie within a satisfactory thermal comfort range. The following aspects of the behaviour of the modules and wall behaviour were studied over the testing period – full results are reported in the Phase 1 and Phase 2 Reports (2011, Page et al; 2017 Alterman et al.) :

- Windowless modules - Comparison of BV and CB and Ins.LW and Ins.CB modules under hot and cold weather conditions.
- Impact of north facing window on internal temperature and relative performance of the various modules under hot and cold conditions for both free floating and controlled internal conditions.
- 12 month relative study of the performance of CB, InsCB, InsBV and InsRVB modules over all four seasons for both free floating and controlled conditions.

The Phase 2 investigation also focussed on some of the mechanisms of heat transfer and the influence of various aspects of the house on that performance. These included:

- study of the significance and interaction of wall thermal mass and thermal resistance;
- significance of wall thermal mass location;
- influence of internal lightweight or heavy weight partitions;
- influence of carpet on thermal performance;
- influence of a major window opening in the northern wall and the associated mechanisms of heat transfer;
- seasonal energy demands for the various walling systems to maintain reasonable internal comfort levels.

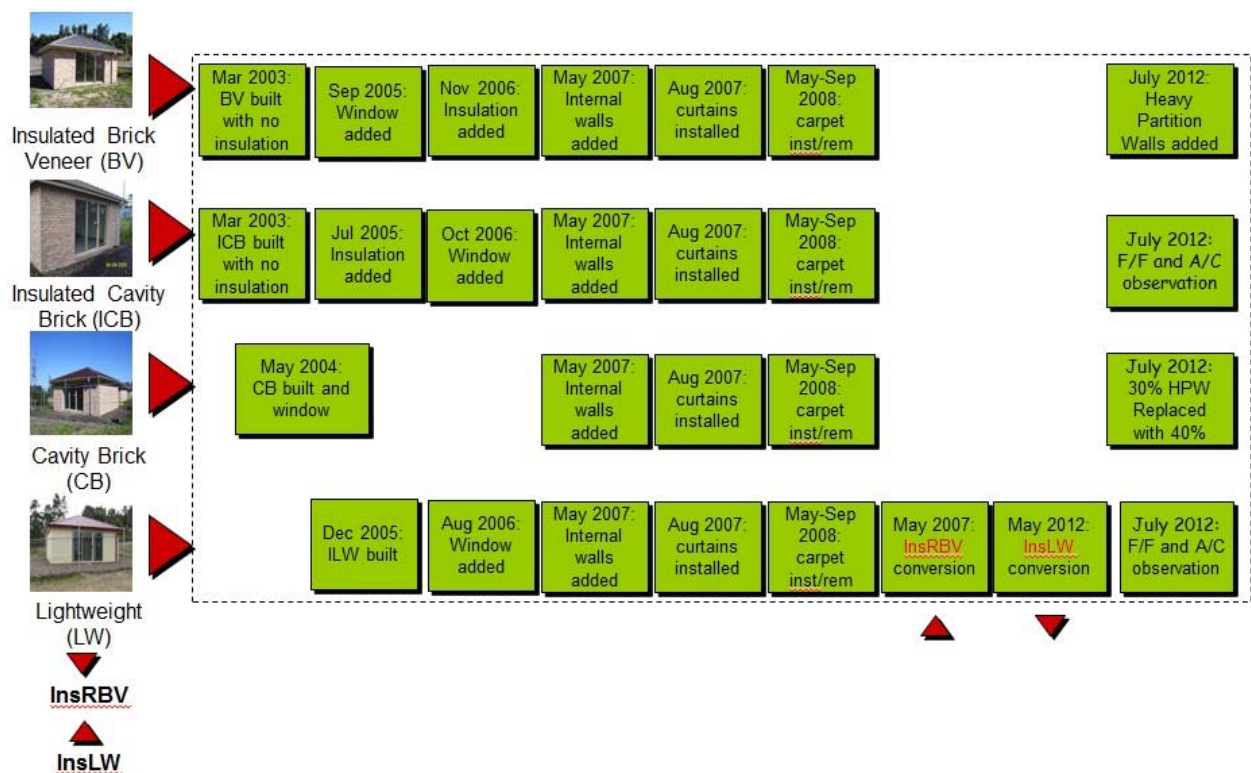


Figure 2: Module Testing Schedule
(Note: external wall types remained constant from 2012)

SOME TYPICAL RESULTS OF THE MODULE TESTS

Internal Temperature Response for Different Walling Systems

For each of the modules, under free floating conditions, the internal temperature variations were continuously monitored for all seasons, with consistent patterns emerging. The InsLW modules consistently exhibited greater temperature variations with longer periods outside of the comfort zone. The best overall performer for all seasons was the InsCB module both in terms of temperature variation and periods outside of the nominal comfort zone. Some typical temperature responses are shown in Figures 3 and 4.

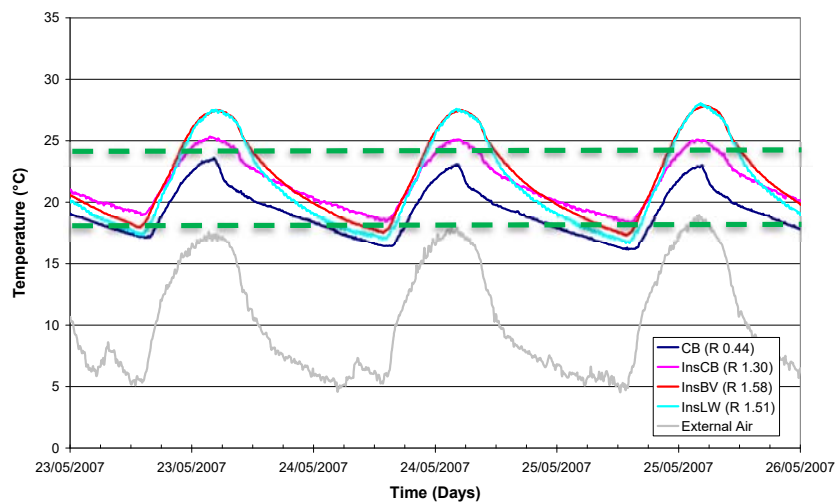


Figure 3: Free floating temperatures under winter conditions

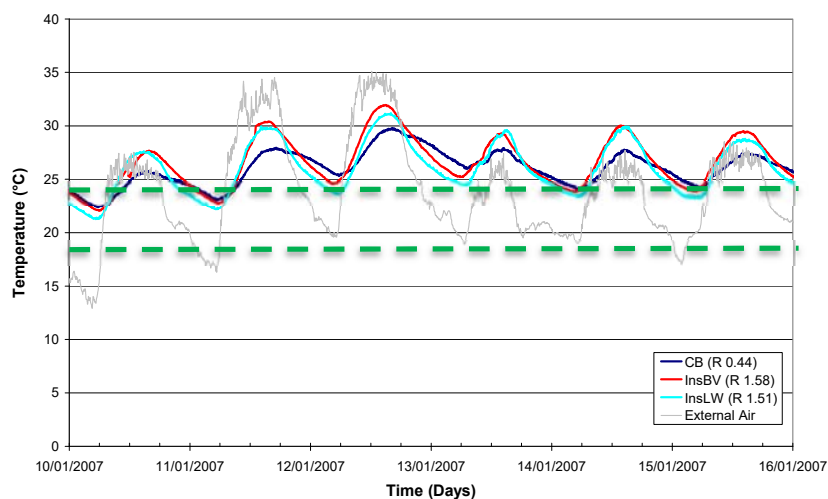


Figure 4: Free floating temperatures under summer conditions

Contribution of thermal mass to wall performance

Figure 5 shows the external and internal module temperatures for a 24 hour summer cycle for the free floating InsCB and InsLW modules (with R-values of 1.30 and 1.51 respectively). The results clearly indicate that R-value does not directly correlate with wall performance, with the thermal mass also playing a significant role, particularly in relation to thermal lag.

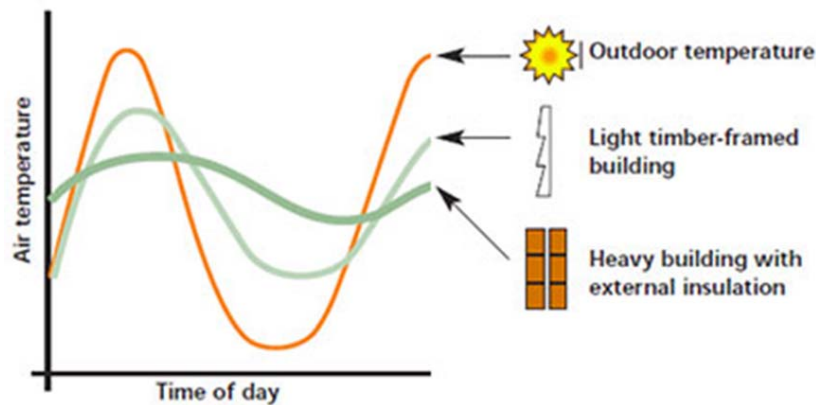


Figure 5: Performance of InsCB & InsLW modules under free floating, summer conditions

Comparison of the performance of the InsCB, InsBV and InsLW modules shown in Figure 6 again illustrates the important contribution of thermal mass, and in particular, the significance of the location of the thermal mass in relation to the wall insulation. The performance of the InsCB and InsRBV, with the internal brickwork skin on the interior side of the insulation layer is significantly better than the InsBV and InsLW modules.

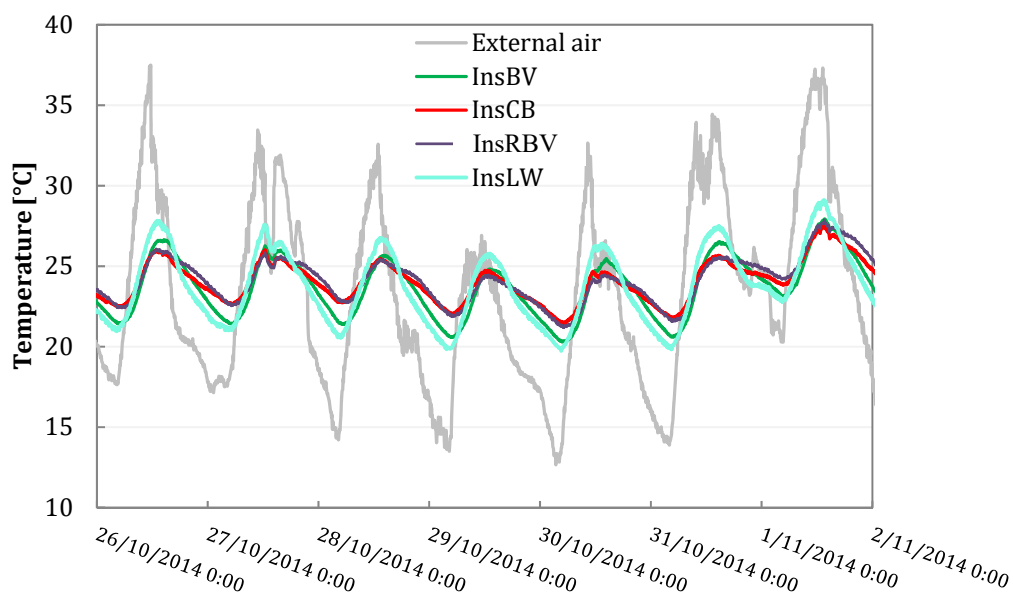


Figure 6: Performance of InsCB, InsBV & InsRBV under free floating, spring conditions

Interior partitions also play a role in the thermal response of the module, particularly if they are constructed from a material with significant thermal mass. Figure 7 shows the significant difference between the energy absorbed and released by internal lightweight and heavy internal partitions for a typical 24 cycle.

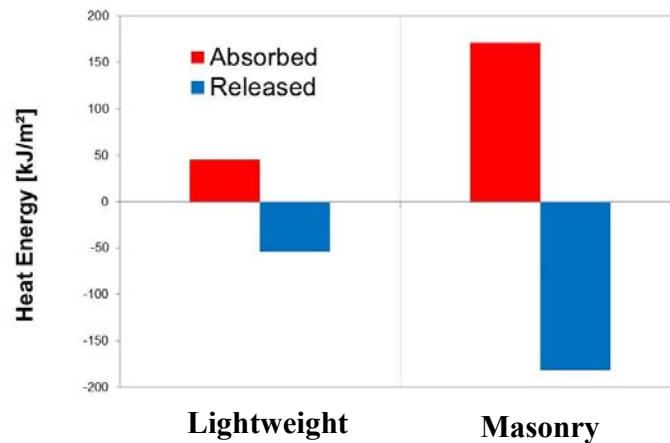


Figure 7: Energy absorbed & released by internal partition walls

Module Performance Under Controlled Interior Conditions

As previously indicated, for some of the observation period, the interior temperature of each module was maintained between 18 and 24 degrees by heating/cooling with the consumed energy being continuously monitored. This again allowed the detailed study of the role of the various wall components and the role of insulation and thermal mass. Typical results for annual performance are shown in Figure 8. Note that again there is no direct relationship between R-value and thermal performance (e.g. comparison of the energy requirements for CB (R=0.62) and InsLW (R=1.69)).

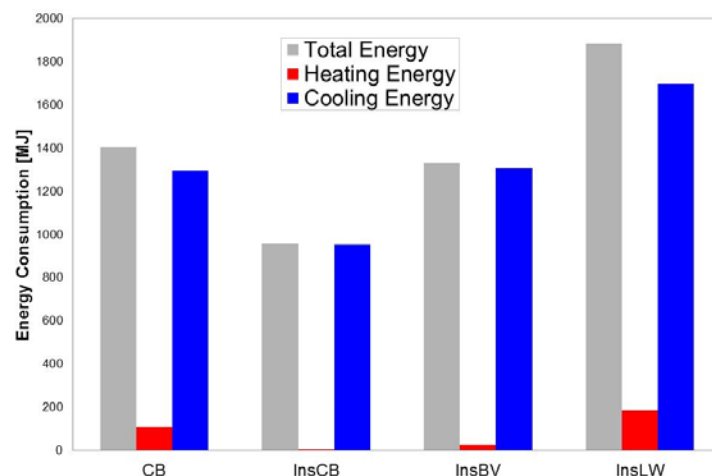


Figure 8: Energy use for controlled conditions (CB, InsCB, InsBV & InsLW modules)

STRAND 2 – DYNAMIC PERFORMANCE OF WALLING SYSTEMS

The dynamic thermal tests were carried out using a modified Hot Box apparatus that was originally designed to measure the thermal resistance of wall assemblies under steady-state conditions. This apparatus consisted of two separate chambers with each enclosure surrounded by R3.5 insulation to maintain a constant temperature gradient across the 2.4m x 2.4m test panels. The apparatus included specialised instrumentation for temperature control, temperature and power consumption measurement. Both chambers and test panel were located in a controlled (constant temperature) space to create a steady ambient external environment for the test without any influence of external temperature variations. This also allows heat flux attenuation studies to be performed under cyclic (transient) temperature conditions which mimic day-night temperature variations. A schematic arrangement of the modified Hot Box apparatus is shown in Figure 9.

The dynamic cycles, which represent the outdoor temperature conditions, are created in one chamber, called the “external” chamber. The other uncontrolled free-floating chamber (the “response” chamber) is used to observe the response of the panel under the external temperature profiles. Unlike the steady-state test, no specialised instruments to measure the energy requirements were installed as the temperature profile is the only input parameter. This realistically reflects the real conditions as the performance of a building depends on the outdoor diurnal temperature which is mainly affected by the solar radiation.

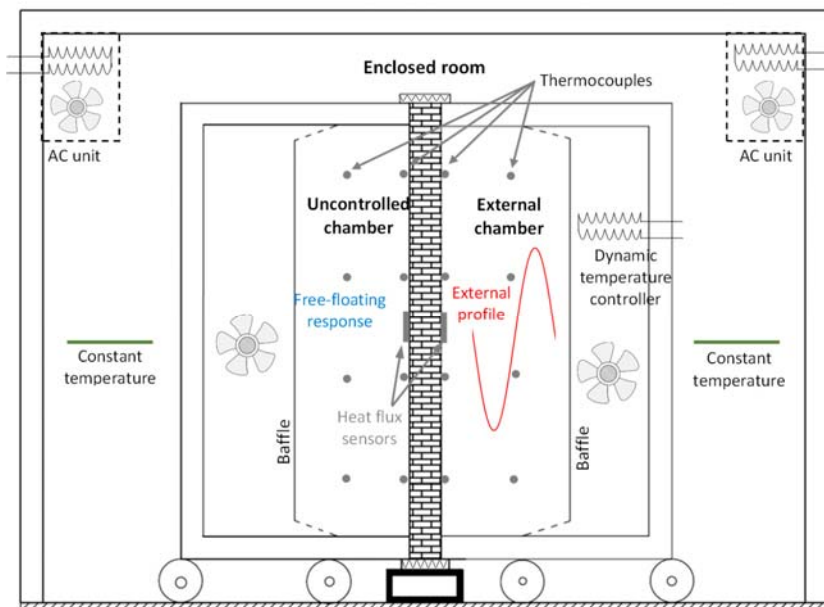


Figure 9: Schematic Arrangement of the Hot Box Apparatus

The dynamic thermal performance can be analysed using a concept, based on temperature measurements; the internal and external surface temperatures for the analysis of a material/panel response and the external and internal air temperatures for a building response [Alterman et al, 2012]. The concept therefore captures the response of the internal surfaces of walls which are being exposed to the external environment of a diurnal cycle. In general, the internal side of a

material or wall panel represents the effect of the energy exchanged between the external and internal environment. This process therefore encapsulates and captures the entire mechanism of heat transfer from the external to the internal surface, including the influence of the physical properties of the surface and the thermal properties of the materials. Thus, the Dynamic Thermal Response (DTR) concept inherently takes into account all the parameters involved in the heat transfer such as thermal mass and thermal resistance as well as the dynamics of the temperature cycle, solar radiation and wind effects. The basic assumptions of the concept are presented here and more details of the concept and its verification have been previously published (Alterman et al, 2012).

The dynamic temperature response profile is created by plotting the external and the internal wall surface temperatures for a single diurnal cycle within the Cartesian coordinate system. The response generates an elliptical shape in which the angle of the principal axis of the ellipse is measured. The response of a panel is characterized by this slope which varies depending on the external conditions and the thermal properties of the wall (see Figure 10).

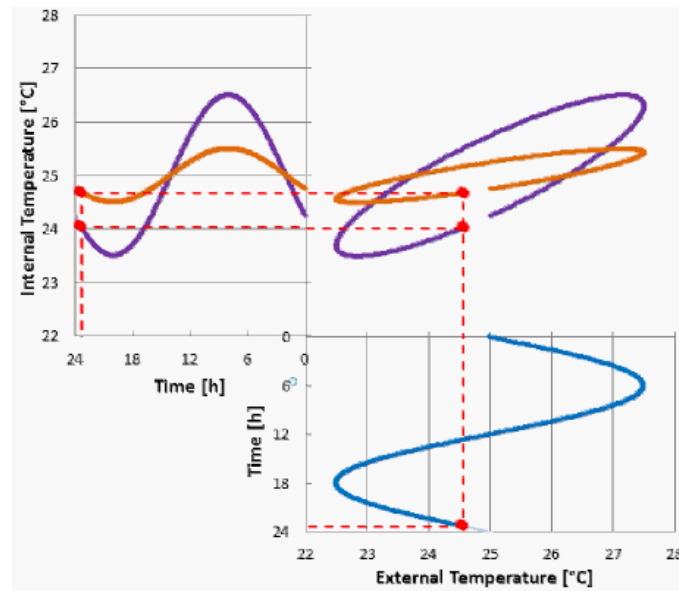


Figure 10: Dynamic temperature response (DTR) concept relating external to internal wall surface temperatures

This phenomenon was first observed for the walls in the housing test modules (see Figure 11), with the concept then being extended to the study of individual walls.

The dynamic hot box tests have systematically studied the performance of all of the common walling types when subjected to a range of temperature cycles corresponding to the Australian climate zones. For each wall type, the steady state R-value and the DTR (T-value) evaluated for the wall element alone and with insulation on the outer and then the inner face. The influence of thermal mass and thermal resistance were also studied by testing a range of wall panels from a solid concrete wall (high thermal mass, low R-value), various masonry walling systems and to a polystyrene panel (high R-value, low thermal mass). Typical results for a 110 mm brickwork wall (28% coring) for various climate zones are shown in Figure 12. It is significant to note that

the T-value is independent of climate zone and therefore an inherent property of the walling system. Detailed results for all walling systems have been reported recently (Alterman et al, 2017).

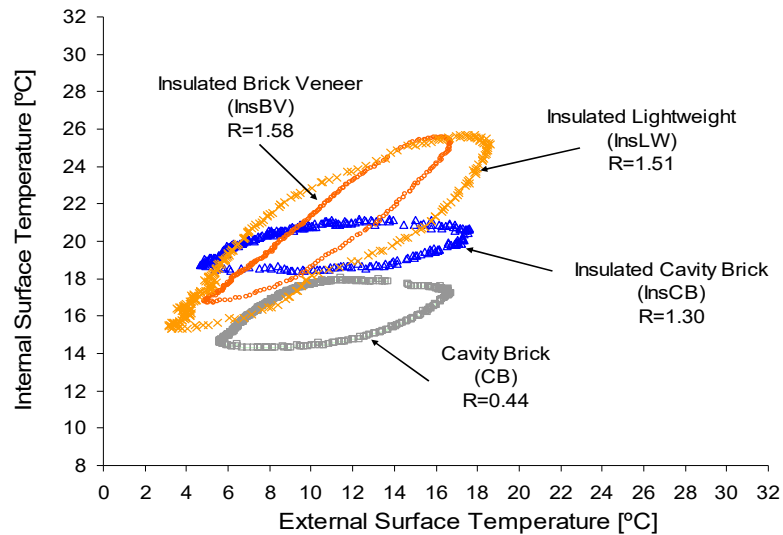


Figure 11: DTR concept (T-values) from housing module tests

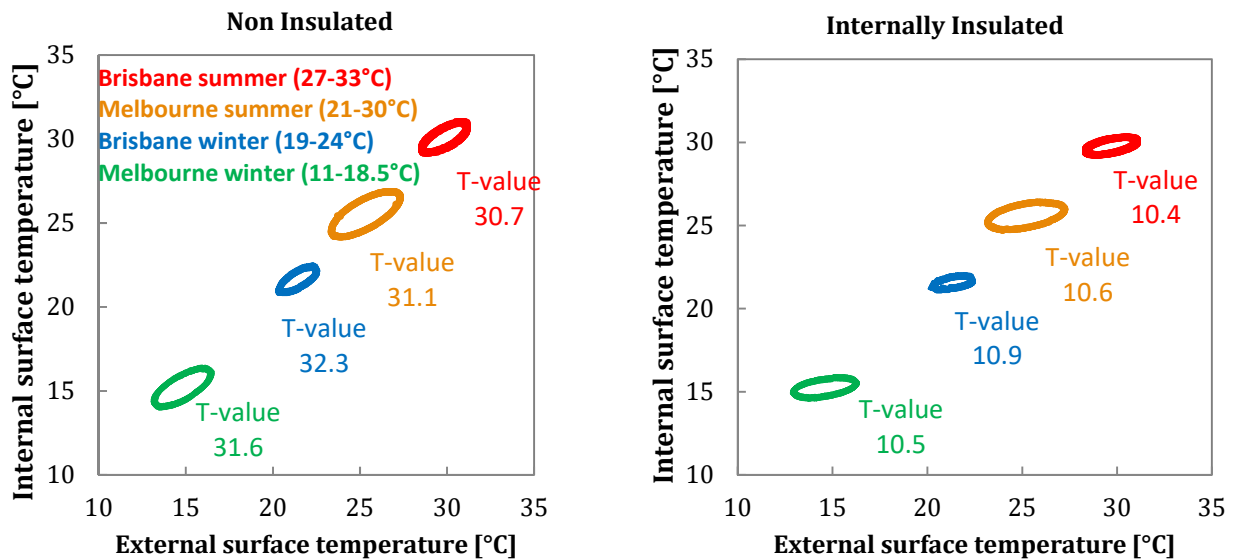


Figure 12: DTR (T-values) for brick masonry wall with 28% cored bricks

CONCLUSIONS

This paper has provided an overview of a major research program on the thermal performance of Australian housing wall systems which has been carried out over the past 15 years. The research has involved the study of the performance of housing modules incorporating a range of walling systems, as well as the development of a wall performance measure which incorporates the influence of both thermal resistance and thermal mass. Full details have been published elsewhere (Page et al 2011, Alterman et al, 2017), with only some of the key outcomes being presented here.

The most important feature of the research has been the confirmation that the thermal performance is inherently dependent on both the thermal resistance and thermal mass of the building components, and not the thermal resistance alone. The key outcome has been the development of a combined measure which directly reflects both these effects (the DTR or T-value) which has the potential to be used as a direct measure of the wall performance both in thermal modelling applications and the regulatory environment.

ACKNOWLEDGEMENTS

This research has been supported by Think Brick Australia and Australian Research Council. Their support and the assistance of Civil Engineering laboratory staff are gratefully acknowledged.

REFERENCES

- Page A. W., Moghtaderi B., Alterman D. and Hands S. (2011), A Study of the Thermal Performance of Australian Housing, Priority Research Centre for Energy, the University of Newcastle, (available on: <http://www.thinkbrick.com.au/thermal-performance-and-climate-design>).
- Alterman D., Page A.W. and Moghtaderi B. (2017), A Study of the Thermal Performance of Australian Housing – Phase 2, Priority Research Centre for Frontier Energy Technologies and Utilisation, the University of Newcastle.
- Alterman D., Moffiet T., Hands S., Page A.W, Luo C., and Moghtaderi B. (2012), A Concept for a Potential Metric to Characterise the Dynamic Thermal Performance of Walls, Energy and Buildings, 54, pp. 52-60
- Alterman D., Page A., Moghtaderi, B., Zhang, C. (2015). Contribution of thermal resistance and thermal mass to the energy demand of walling systems, *Mauerwerk*, 19(1), 64-73.

THE USE OF COMPUTATIONAL FLUID DYNAMICS SIMULATION TO COMPARE THE THERMAL PERFORMANCE OF HOUSING MODULES INCORPORATING HEAVY OR LIGHTWEIGHT WALLING SYSTEMS

C. Zhang¹, D. Alterman², A.W. Page³ and B. Moghtaderi⁴

¹ PhD student, PRC for Frontier Energy Technologies and Utilisation, The University of Newcastle, Callaghan, NSW 2308, Australia, c3086961@uon.edu.au

² Senior Research Academic, Centre for Infrastructure Performance and Reliability, The University of Newcastle, Callaghan, NSW 2308, Australia, Dariusz.Alterman@newcastle.edu.au

³ Professor Emeritus, PRC for Frontier Energy Technologies and Utilisation, The University of Newcastle, Callaghan, NSW 2308, Australia, Adrian.Page@newcastle.edu.au

⁴ Professor, PRC for Frontier Energy Technologies and Utilisation, The University of Newcastle, Callaghan, NSW 2308, Australia, Behdad.Moghtaderi@newcastle.edu.au

This paper provides a detailed study on the use of computational fluid dynamics (CFD) simulations to predict the thermal performance of housing modules constructed from cavity brickwork or lightweight walling systems. The housing test modules were built on the University of Newcastle (Australia) campus and the detailed thermal performance of each system was measured for a range of seasonal conditions. The CFD simulations were able to accurately reproduce the observed behaviour and provided an increased understanding of the dynamic response and behaviour of the two walling systems. It is shown that the thermal mass of the masonry components play a major role in reducing the internal temperature fluctuations resulting in more stable internal conditions.

Keywords: *thermal performance, CFD simulation, walling system*

INTRODUCTION

In the context of growing energy crisis, energy conservation has become a critical consideration in building design. In cold or hot climatic zones where air conditioning system is always required to maintain the thermal comfort of the indoor environment, the energy efficiency of buildings, i.e. the ability to reduce the loss of heating or cooling energy, is a very important measure to assess the building thermal performance. However, for buildings in moderate climatic zones, there is a

potential to use smart design to achieve comfortable room temperatures for occupants without the use of air conditioning even in summer and winter seasons.

“Smart design” requires consideration of many aspects that may affect the housing thermal performance, and this paper focuses on the study of how different walling systems, consisting of lightweight and heavy components, influence the overall thermal performance of houses located in moderate climatic zone under free-floating conditions. This can be done by comparing the thermal behaviour of two full-scale housing modules constructed from the lightweight timber framed and cavity brickwork walling systems. The two housing modules were tested on site under a range of real weather conditions on the Callaghan campus of the University of Newcastle, Australia (latitude 32.9°S, Longitude 151.7°E). Details of the housing module tests have been published previously (Page et al. (2011)).

Numerical simulation using computational fluid dynamics (CFD) analysis is used to simulate the full-scale in-situ housing module tests and to predict the thermal performance of the modules. The use of CFD analysis for the prediction of housing thermal performance has been limited, although there have been some studies analysing the behaviour of buildings or building elements. Malvoni et al. (2016) and Santos et al. (2014) utilised CFD simulations to assess the thermal performance of various window frames and a lightweight steel framed wall respectively. Bajc et al. (2015), Paris et al. (2016) and Kristianto et al. (2014) focused on passive house behaviour using CFD simulations, while Papadopoulos and Soebarto (2015) and Zhang et al. (2015) investigated houses with a ventilation system. Yang et al. (2009) and Aryal and Leephakpreeda (2015), developed precise CFD models for air-conditioned buildings to study factors that may have influence thermal comfort and energy consumption of the buildings. However, in most of the previous studies, the accuracy of the CFD simulation results could not be validated using real experimental data. This shortcoming is overcome in this study by comparing the CFD simulation results with the actual measured data from the in-situ tests.

The difference in response between the two housing modules with lightweight and heavy wall systems can be clearly identify from both the experimental and simulation data, demonstrating the positive role of the brick masonry components with high thermal mass played in improving the overall module thermal performance.

IN-SITU HOUSING TEST MODULES

The housing module tests were carried out over a number of years under real weather conditions on the Callaghan campus of the University of Newcastle (Australia) in a moderate climatic zone. The study reported here is based on the performance of two housing modules, one constructed with Insulated Lightweight (InsLW) walls and the other with Insulated Cavity Brick (InsCB) walls, (see Figure 1) Both modules were built on a concrete slab-on-ground with a 6m x 6m floor plan, with a ceiling height of 2450mm. The northern wall of modules contained a window (2050mm high × 2840mm wide) and was oriented perpendicular to astronomical north. The inclusion of a window enabled the study of the passive solar behaviour of each module. In order to more realistically reflect real construction, two internal partition walls (2m high and 2m × 1m in plan located as in Figure 2) were installed in the internal module space. The only differences between the InsLW and InsCB modules were the roofing materials and the walling systems

(including the external walls and internal partition walls). Because the ceiling was heavily insulated by a layer of R3.5 glasswool batts to minimise the heat exchange between the roof space, the influence of the walling systems could be studied independently.



Figure 1: The Insulated Lightweight (InsLW) and Insulated Cavity Brick (InsCB) modules

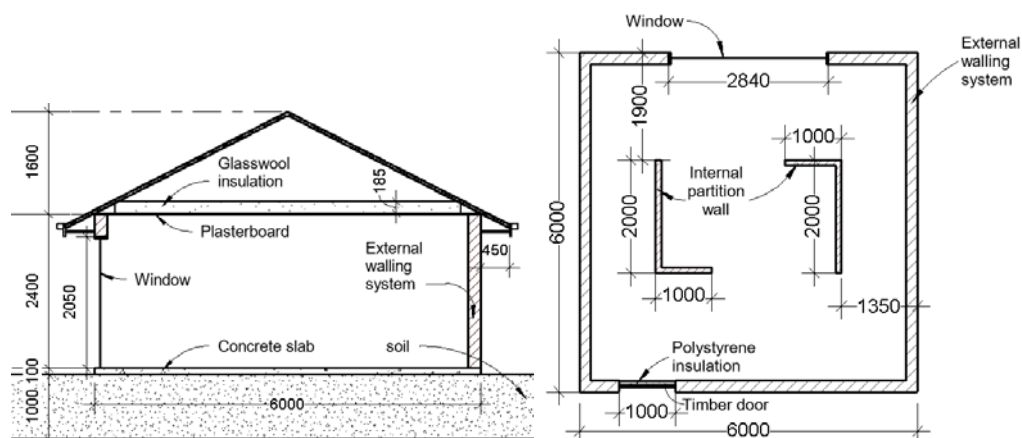


Figure 2: Details of the housing modules

Details of the external walling system and internal partition walls of the InsLW and InsCB modules are presented in Figure 3. All walls of the InsLW module were timber-framed with and without insulation for the external and internal walls respectively. The external walling system of the InsCB module mainly consisted of two brick masonry skins 75mm apart and a 25mm polystyrene insulation in between the two brick skins attached to the interior skin creating a 50mm air gap. The internal partition wall of the InsCB module was a single layer brick masonry wall.

The thermal properties regarding thermal resistance (R-value) and thermal mass of external walling system and internal partition walls for the InsLW and InsCB modules are given in Table 1. The thermal resistance (or R-values) of the two modules are very similar. The R-values of the external walling systems are 1.3 for the InsCB and 1.5 for the InsLW module, and that of the internal partition walls are 0.14 for both modules. However, there is significant difference in thermal mass between the InsLW and InsCB modules. The thermal masses of the external walling system and internal partition walls of the InsCB module are 16.8 and 1.9 MJ/ °C respectively, about 9 times higher than the InsLW module (1.8 and 0.2 MJ/ °C). The thermal mass of the InsCB module is mainly contributed by the brick masonry components. Therefore, the influence of thermal mass contributed by heavy mass components on the overall thermal

performance of housing can be studied by the comparing the performance of the InsLW and InsCB modules.

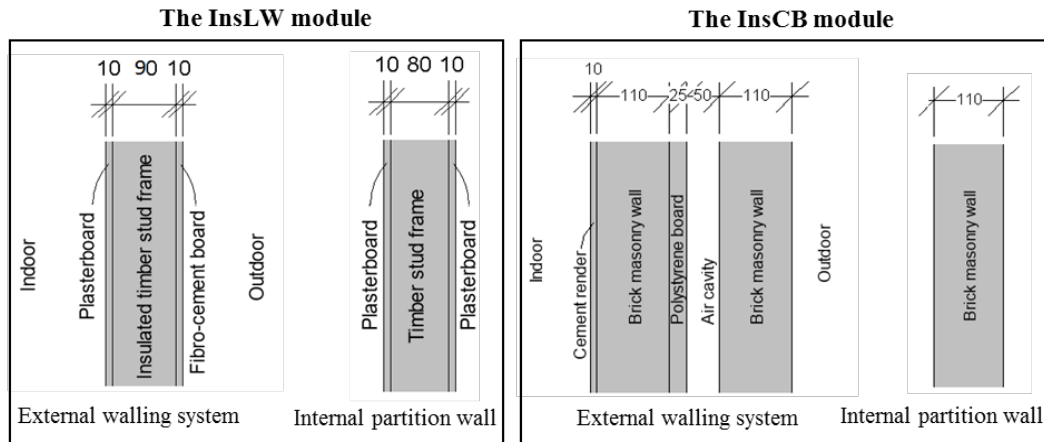


Figure 3: The external walling system and internal partition walls for the InsLW and InsCB modules

Table 1: The thermal resistance (R-value) and thermal mass for InsLW and InsCB modules

| Module | Wall | R-value [$\text{m}^2 \cdot \text{K}/\text{W}$] | Thermal mass [$\text{MJ}/^\circ\text{C}$] |
|---------------------------------------|-------------------------|--|---|
| Insulated lightweight (InsLW) module | External walling system | 1.5 | 1.8 |
| | Internal partition wall | 0.14 | 0.2 |
| Insulated Cavity Brick (InsCB) Module | External walling system | 1.3 | 16.8 |
| | Internal partition wall | 0.14 | 1.9 |

COMPUTATIONAL FLUID DYNAMICS (CFD) SIMULATION

This study utilised the numerical simulation based on computational fluid dynamics (CFD) analysis to simulate the in-situ housing module tests and to predict the housing thermal performance. CFD is a branch of fluid mechanics that analyses and solves fluid flow problems using numerical methods. The software “Autodesk CFD”, which provides computational fluid dynamics and thermal simulation tools, was chosen for this study. The air can be defined as a liquid whose properties (including density, viscosity and conductivity) vary with the change of temperature during the simulation. The natural convection analysis can be enabled in such a “variable” environment, and this can significantly increase the accuracy of the simulation. In addition, the Autodesk CFD is able to include the solar heating analysis, which is important for simulating the housing module tests under real weather conditions.

COMPARISON STUDY UNDER HOT WEATHER CONDITIONS

The thermal performance of the InLW and InsCB modules without controlled interior conditions (e.g. air conditioning) was compared under hot weather conditions. A two-week time period of

the in-situ module test in the summer season in December 2013 was used for the analysis, and the actual external air temperature profile measured in the test is shown in Figure 4. The day-time peak temperatures of the two hottest days were about 37 and 38°C, with the remainder ranging from 25 to 32°C, representing typical Newcastle summer conditions. The night-time minimum temperatures of the two summer weeks ranged between 12 and 25°C.

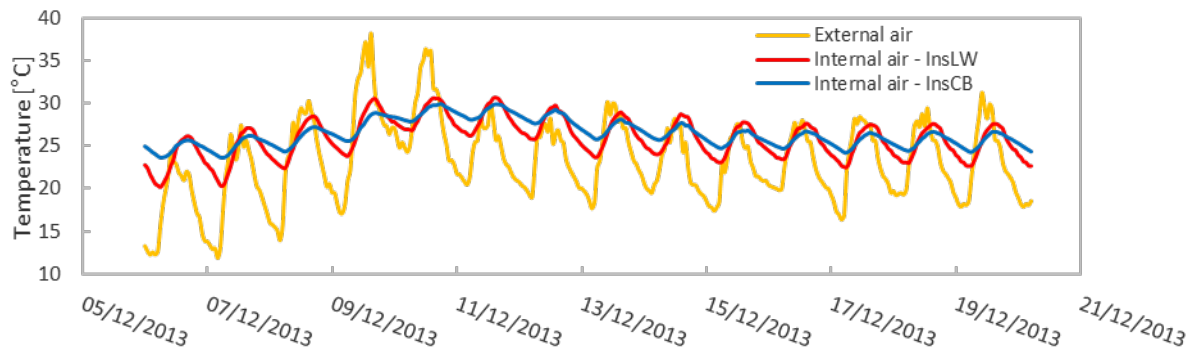


Figure 4: The external and internal air temperatures for the InsLW and InsCB modules, 06/12/2013 - 20/12/2013

The internal air temperature profiles for the InsLW and InsCB modules in response to the external weather conditions between 06/12/2013 and 20/12/2013 are shown in Figure 4. The most obvious difference of the internal air temperature between the two modules is the diurnal temperature fluctuations. Overall, the internal temperature of the InsCB module fluctuated less (about 2.8°C on average) than the InsLW module, but there was no significant difference (<0.5°C) between the average internal temperatures for the InsLW and InsCB modules. As a result, the daytime internal temperature of the InsCB module was cooler than the InsLW module in this hot summer time period. Compared with the InsLW module, the InsCB module was warmer during night time with an average minimum temperature of approximately 25°C which was not excessive. Therefore, the InsCB module with steadier indoor environment and cooler daytime temperature had better thermal performance than the InsLW module, demonstrating the benefits of the high thermal mass walling system without the need for air conditioning.

Depending on the solar elevation angle, the solar impact on the modules varies. At a certain location, the solar elevation angle changes, following a sinusoidal curve during different time of the year, with the largest and smallest angles occurring in summer and winter season respectively. The solar elevation angle curve for the test site on the campus of the University of Newcastle (Australia) during a year is shown in Figure 5. During the hot summer time period from 06/12/2013 to 20/12/2013, the average solar elevation angle is about the 79.5°C, and such a large angle means that the solar energy is not transmitted into the internal module space through the window.

The temperature distributions predicted by CFD simulations on the external and internal surfaces of the InsLW and InsCB modules at different times (9:00am, 12:00pm and 3:00pm) of a typical day between 06/12/2013 and 20/12/2013 are shown in Figures 6 and 7. During the daytime from 9am to 3pm, the external surfaces (including the roof and exterior wall surfaces) of the two

housing modules are significantly influenced by the solar radiation so that the temperature is unevenly distributed and is much hotter externally than on the internal surfaces. In addition, the temperatures distributions for the external surfaces of the InsLW and InsCB modules have noticeable differences due to the difference in thermal properties between the two modules. Compared with the external surfaces, the temperature distributions of the internal surfaces (especially the slab and partition walls) are relatively uniform for both modules. This demonstrates that the internal module space is not affected by the solar radiation because of the high solar elevation angle in December.

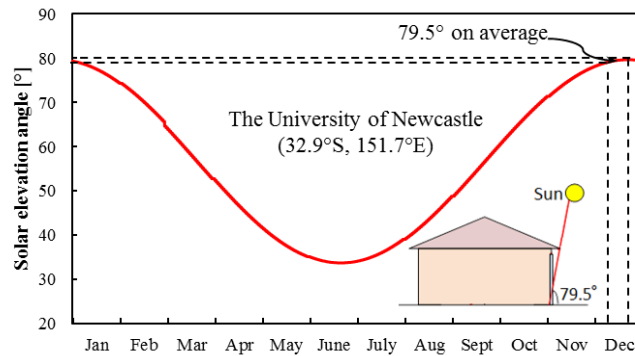


Figure 5: The average solar elevation angle at test site, 06/12/2013 - 20/12/2013

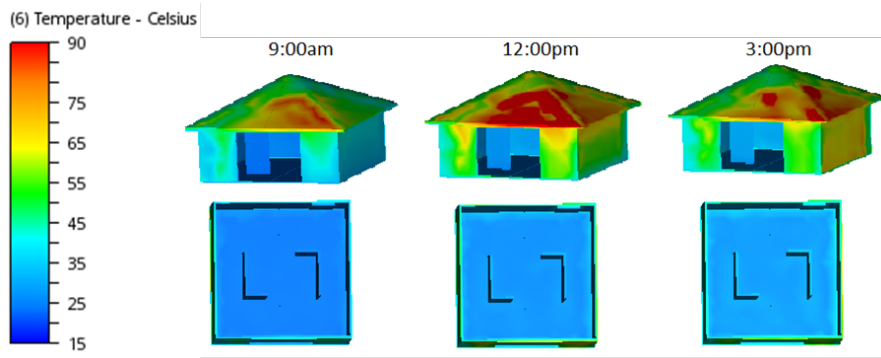


Figure 6: Temperature distributions for the InsLW module at 9:00am, 12:00pm and 3:00pm on 11/12/2013

Comparisons between the measured and simulation predicted internal air temperatures for the InsLW and InsCB modules are shown in Figures 8 and 9 respectively. For both modules, the actual and predicted internal temperature profiles for most days follow a similar diurnal fluctuation trend. The internal air temperature predicted by the CFD simulation for the InsLW module during the two days 09/12/2013 and 10/12/2013 has obvious larger diurnal fluctuations than the real temperature, but the diurnal fluctuations of the actual and predicted internal air temperatures for the other days are consistent. For the InsCB module, the internal temperature

profile predicted by CFD simulation during the first two days are less fluctuated, and after that became more consistent with the real profile, as in Figure 9. During the second half of the time period from 03/12/2013, the predicted internal air temperature became slightly higher ($\approx 2^{\circ}\text{C}$) than the real data for both modules but more clear for the InsCB module, as in Figure 8 and 9. The major reason caused this discrepancy is that the diurnal solar energy applied during simulation for this summer period was excessive and might not be fully dissipated due to the limitation of the external air volume and ground sizes for the CFD models, this effected an overall temperature increase. Overall, the discrepancies between the actual and simulation predicted internal air temperatures are acceptable, and the CFD simulation predicted relatively accurate internal air temperatures for both the InsLW and InsCB modules under hot climatic conditions.

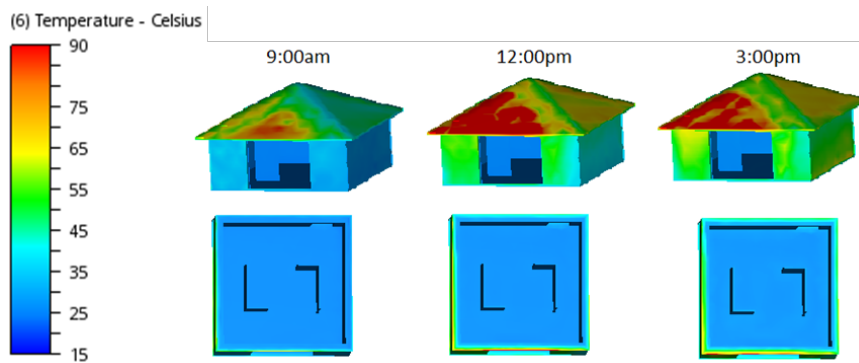


Figure 7: Temperature distributions for the InsCB module at 9:00am, 12:00pm and 3:00pm on 11/12/2013

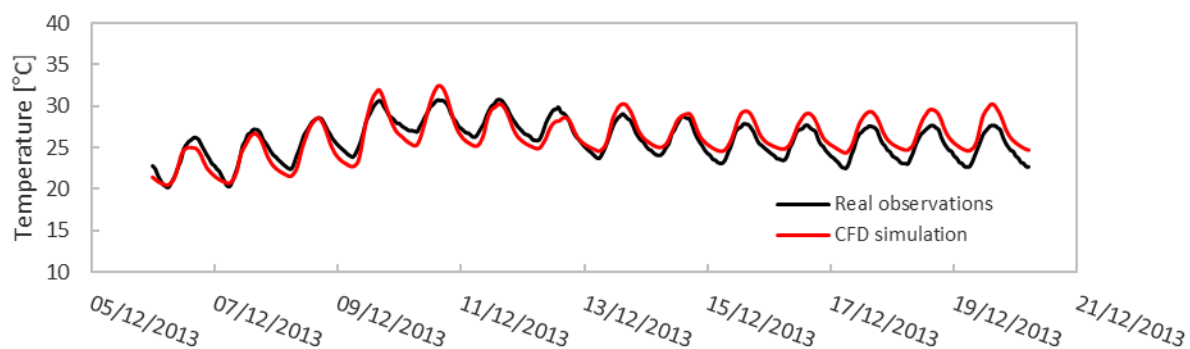


Figure 8: The actual measured and simulation predicted internal air temperature of the InsLW module, 06/12/2013 - 20/12/2013

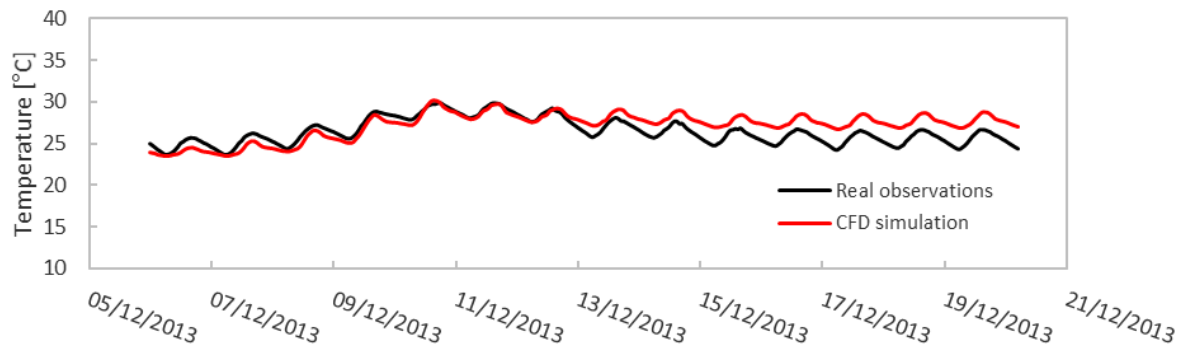


Figure 9: The actual measured and simulation predicted internal air temperature of the InsCB module, 06/12/2013 - 20/12/2013

Comparisons of the internal air temperatures for the InsLW and InsCB modules based on the CFD simulations are shown in Figure 10. Similar to the real observations (in Figure 4), the simulation results also show that the InsCB module has a steadier indoor environment with less diurnal temperature fluctuations compared with the InsLW module. On average, the diurnal fluctuations of the internal temperature predicted by the simulation for the InsCB module are about 3.6°C smaller than for the InsLW module, while that based on the real observations are about 2.8°C. The extra reduction of indoor temperature fluctuations in the InsCB module is caused by the heavy brick masonry components with high thermal mass. Therefore, under Newcastle summer weather conditions, the CFD simulation successfully captured the difference in dynamic thermal performance of the InsLW and InsCB modules and thus the effect of thermal mass of the walling system on the overall module performance (which is slightly overestimated).

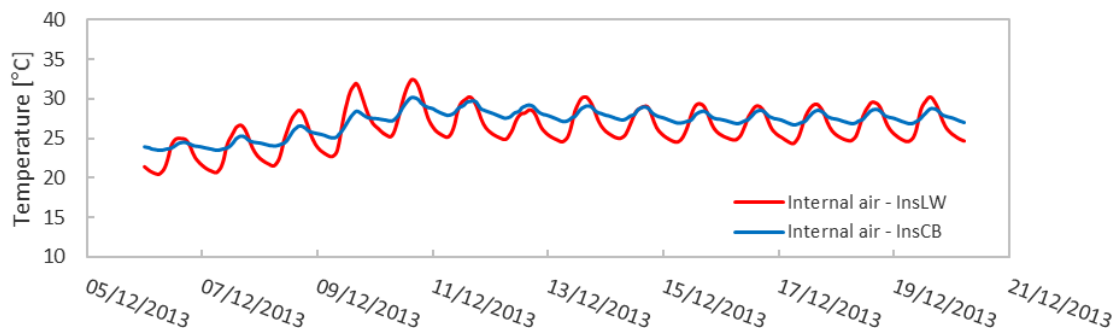


Figure 10: Predicted internal air temperatures by simulations for the InsLW and InsCB modules, 06/12/2013 - 20/12/2013

COMPARISON STUDY UNDER COLD WEATHER CONDITIONS

The thermal performance of the InsLW and InsCB modules under cold weather conditions were measured in-situ and predicted by CFD simulations from 19/05/2007 to 05/06/2007, as shown in Figure 11. Most of the days in this time period have a daytime peak temperature below 20°C, and the highest peak temperature of about 23°C occurred on 29/05/2007. About half of the days had a minimum temperature below 5°C with the lowest of 2°C occurring on 31/05/2007.

The internal air temperature profiles measured during the in-situ tests for the InsLW and InsCB modules from 19/05/2007 to 05/06/2007 are shown in Figure 11. The InsLW and InsCB modules had very similar average internal air temperatures of 21.9 and 21.8°C. However, there was a big difference in the internal temperature fluctuations between the InsLW and InsCB modules. The internal air temperature during this time period for the InsLW module ranged from 16.5 to 30°C, while that for the InsCB module ranged from 18 to 27°C. On average, the diurnal fluctuations of the internal air temperature for the InsCB module were 3.5°C smaller than for the InsLW module, demonstrating the steadier indoor environment of the InsCB module. In addition, the night-time temperature in the InsCB module was warmer than the InsLW module, which provided better thermal comfort at cold winter nights. The steadier and “night-time” warmer temperature in the InsCB module demonstrates the better thermal performance under cold weather conditions, due to the contribution of the high thermal mass of the brick masonry walling system.

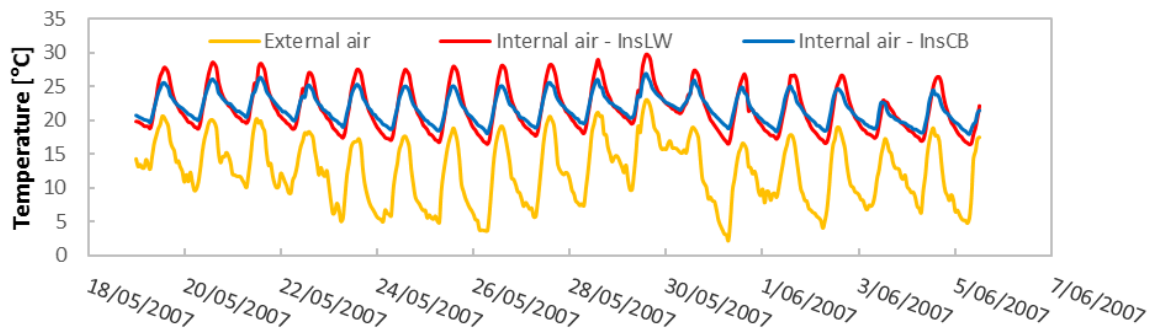


Figure 11: The external and internal air temperatures for the InsLW and InsCB modules, 19/05/2007 - 05/06/2007

The average solar elevation angle during the period from 19/05/2007 to 05/06/2007 is very low, (about 35°), close to the annual minimum value, as shown in Figure 12. When the housing modules are exposed to such “low solar angle” conditions, the sunlight can shine through the window and fall on the concrete slab and partition walls so that the indoor environment can be directly influenced by the solar radiation. Consequently, the internal air temperatures are warmed by this extra solar energy and as shown in Figure 11, are higher than the external temperature.

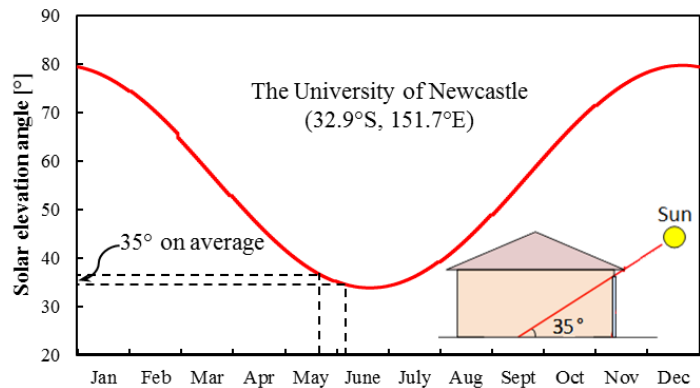


Figure 12: The average solar elevation angle at test site, 19/05/2007 - 05/06/2007

The CFD simulation correctly predicted the effect of solar radiation on the interior space of modules, as seen in Figures 13 and 14 which present the temperature distributions for the InsLW and InsCB modules at different times (9am, 12pm and 3pm) from two different views. For both modules, the solar affected areas of the concrete slab and internal partition walls change with time and always have higher temperatures than the unaffected areas. In addition, the temperature distributions on the external surfaces of modules are also time dependant. Overall, the housing modules exposed to the noon (12pm) sun have the highest external surface temperature. It is noticeable that the external surfaces of the InsCB module are always warmer than the InsLW module at 9am, 12pm and 3pm, because of the different thermal properties of the two modules.

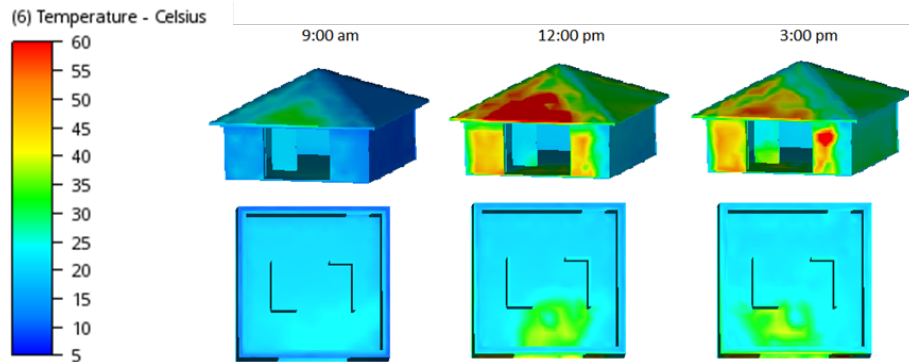


Figure 13: Temperature distributions for the InsLW module at 9:00am, 12:00pm and 3:00pm on 24/05/2007

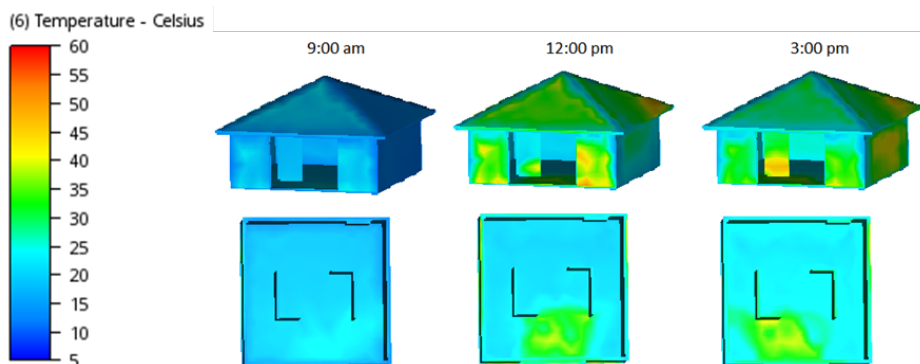


Figure 14: Temperature distributions for the InsCB module at 9:00am, 12:00pm and 3:00pm on 24/05/2007

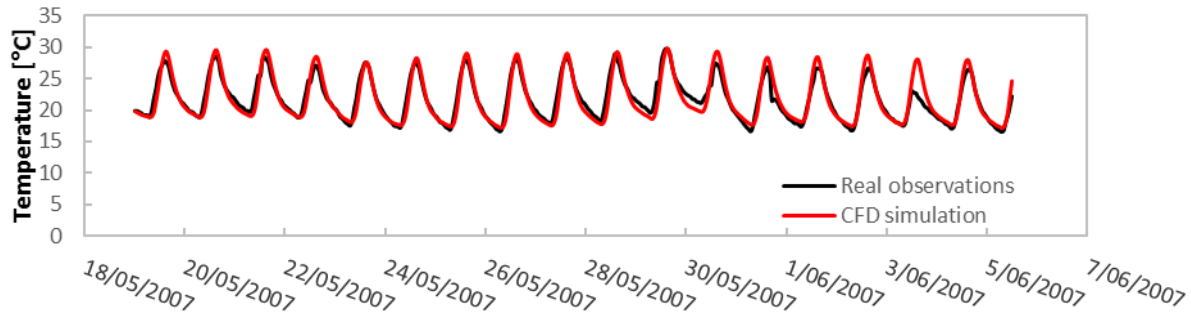


Figure 15: The actual measured and simulation predicted internal air temperature of the InsLW module, 19/05/2007 - 05/06/2007

Comparisons between the actual measured and simulation predicted internal temperatures for the InsLW and InsCB modules from 19/05/2007 to 05/06/2007 are shown in Figure 15 and 16 respectively. For both modules, the predicted internal air temperature profile by simulation matches the actual profile reasonably well during this time period except for the day 03/06/2007, when the diurnal fluctuations of the actual internal air temperature for the InsLW and InsCB modules are much smaller than that of the predicted temperature by CFD simulation. This is because the cloudy weather on that day allowed less solar radiation to reach the test site, the effects of which were not taken into consideration by the CFD simulation.

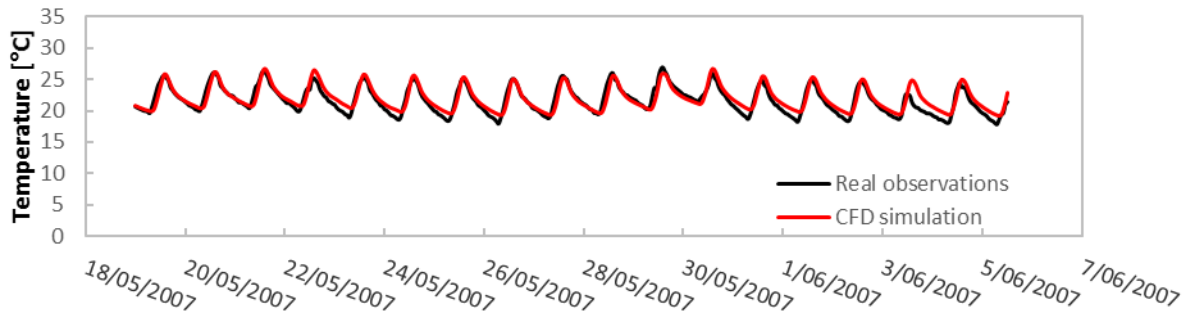


Figure 16: The actual measured and simulation predicted internal air temperature of the InsCB module, 19/05/2007 - 05/06/2007

The thermal performance of the InsLW and InsCB module under cold weather conditions is compared in Figure 17 using the internal air temperature profiles for the two modules predicted by CFD simulations. During the time period from 19/05/2007 to 05/06/2007, the predicted internal air temperature for the InsLW module varied between 17 and 30°C, while that for the InsCB module was between 19 and 27°C. On average, the diurnal fluctuations of the internal air temperature for the InsLW module was about 5°C larger than for the InsCB module according to the CFD simulation results, but only 3.5°C larger in the real observation data. Therefore, the CFD simulation was able to confirm the ability of the InsCB module to maintain a more stable indoor environment, with warmer night-time temperatures in cold weather than for the InsLW module with light timber-framed structures. However, the effect of the brick masonry components in reducing the indoor temperature fluctuations was overestimated.

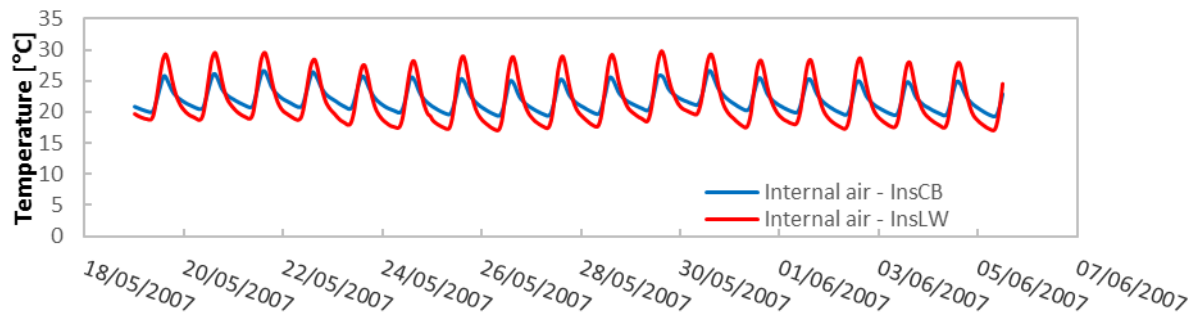


Figure 17: Predicted internal air temperatures for the InsLW and InsCB modules, 19/05/2007 - 05/06/2007

CONCLUSIONS

It has been shown that the free floating dynamic thermal performance of the InsLW and InsCB modules under either hot or cold weather conditions can be predicted using a CFD simulation, with the simulation results being in relatively good accordance with the experimental data. The simulations were also able to reproduce the influence of the thermal mass of the heavier walling components as well realistic predictions of the internal conditions of the housing test modules under both summer and winter conditions.

ACKNOWLEDGEMENTS

This research has been supported by Think Brick Australia and Australian Research Council.

REFERENCES

- Aryal P., Leephakpreeda T. (2015), CFD Analysis on Thermal Comfort and Energy Consumption Effected by Partitions in Air-Conditioned Building, *Energy Procedia* 79, pp. 183-188.
- Bajc T., Todorovi M. N., Svorcan J.(2015), CFD analyses for passive house with Trombe wall and impact to energy demand, *Energy and Buildings*, 98, pp. 39–44.
- Kristianto M. A., Utama N. A., Fathoni A.M. (2014), Analysing Indoor Environment of Minahasa Traditional House Using CFD, *Procedia Environmental Sciences*, 20, pp. 172-179.
- Malvoni M., Baglivo C., Congedo P. M., Laforgia D. (2016), CFD modeling to evaluate the thermal performances of window frames in accordance with the ISO 10077, *Energy*, 111, pp. 430-438.
- Page A.W., Moghtaderi B., Alterman D. and Hands S. (2011), A Study of the Thermal Performance of Australian Housing, Priority Research Centre for Energy, the University of

Newcastle, (available on: <http://www.thinkbrick.com.au/thermal-performance-and-climate-design>).

Papadopoulos Y., Soebarto V. (2015), Investigation of thermal comfort and air flow in a naturally ventilated lightweight house in as bush fire prone area, Proceedings of BS2015:14th Conference of International Building Performance Simulation Association, Hyderabad, India.

Paris A. Fokaides P. A., Christoforou E., Ilic M. (2016), Papadopoulos A., Performance of a Passive House under subtropical climatic conditions, *Energy and Buildings*, 133, pp. 14-31.

Santos P., Martins C., Silva L. S. and Braganca L. (2014), Thermal performance of lightweight steel framed wall: The importance of flanking thermal losses, *Journal of Building Physics*, 38, pp. 81–98

Yang J. H., Seok H. T., Lee S. J. (2009), A Study on the Application of a Ceiling Plenum Ventilation System in an Apartment House, *Indoor Built Environment*, 18, pp. 234–244.

Zhang Y., Huang L., Zhou Y. (2015), Analysis of Indoor Thermal Comfort of Test Model Building Installing Double-Glazed Window with Curtains Based on CFD, *Procedia Engineering*, 121, pp. 1990 -1997.

NUMERICAL SIMULATION OF THE EFFECT OF SLAB-EDGE INSULATION FOR SLAB-ON-GROUND MASONRY HOUSING

Z. Liu¹, D. Alterman², A. Page³, B. Moghtaderi⁴ and D. Chen⁵

¹ PhD candidate, Priority Research Centre for Frontier Energy Technologies and Utilization, The University of Newcastle, Callaghan, NSW 2308, Australia, zhang.liu@uon.edu.au

² Senior Research Academic, School of Engineering, The University of Newcastle, Callaghan, NSW 2308, Australia, dariusz.alterman@newcastle.edu.au

³ Emeritus Professor, Centre for Infrastructure Performance and Reliability, The University of Newcastle, Callaghan, NSW 2308, Australia, adrian.page@newcastle.edu.au

⁴ Professor, Centre for Infrastructure Performance and Reliability, The University of Newcastle, Callaghan, NSW 2308, Australia, behdad.moghtaderi@newcastle.edu.au

⁵ Principal Research Scientist, CSIRO Land and Water, Commonwealth Scientific and Industrial Research Organisation (CSIRO), Private Bag 10, Clayton South, Victoria 3169, Australia, Dong.Chen@csiro.au

Slab-edge insulation (SEI) can effectively reduce the operational energy of slab-on-ground houses, especially in areas with extreme weather conditions. The SEI has the potential to reduce the heat flow through the interior floor surface, with this effect being different for houses with different walling systems. In order to investigate the thermal effect of SEI in combination with different masonry walling systems, a simulation tool developed at the University of Newcastle was used to investigate the effect of SEI for houses with three different walling systems – Cavity Brick (CB), Insulated Cavity Brick (InsCB) and Insulated Brick Veneer (InsBV). The annual temperature profile used for the numerical simulations was from the weather records for Newcastle, Australia. The simulation results indicated that the SEI was most effective in improving the energy performance of the InsBV house, followed by the CB house. The least improvement was for the InsCB house, but the energy saving was still substantial, accounting for a potential annual edge slab energy loss of 15.42%.

Keywords: *heat loss, walling system, slab-edge insulation, FVM.*

INTRODUCTION

Energy conservation, greenhouse gases reduction and sustainability have drawn increasing attention and efforts worldwide for many years. According to Ball et al. (2017), end energy usage in domestic building accounts for 11.1% of the total greenhouse gas emissions in Australia. The energy usage for heating and cooling accounts for 40% of the total energy consumption in domestic buildings. Therefore, the achievement of better energy efficiency in housing has become a very important topic for engineers and architects. Many factors which influence the thermal performance of residential buildings (such as insulation, roof and walling systems, orientation and locality) have been widely investigated through theoretical and experimental methods. For example, to investigate the thermal performance of Australian housing, in recent years an extensive range of theoretical and experimental studies of housing systems has been undertaken at the University of Newcastle (UON) (Page et al. (2011), Alterman et al. (2012), Alterman et al. (2015)). As part of the study, four full scale housing testing modules have been built on the university campus. Over the testing period, a range of common walling systems have been considered, including modules incorporating CB, InsCB and BV walling systems. Housing thermal performance is influenced by factors such as insulation, roof and walling systems, orientation and locality. The floor slab also has a significant influence on the thermal performance of slab-on-ground houses. It has been found that 30% (Hagentoft, 1988) to 50% (Neymark et al., 2008, Chen, 2013, Zoras, 2009) of residential energy consumption can be attributed to the heat transfer through the ground. Many studies have been conducted on how to reduce this ground heat loss. For example, Yoshino et al. (1992) tested the effect of ground insulation with a semi-underground test house at Tohoku University, Sendai, Japan. The experiment results indicated the side with horizontal insulation had lower temperature variations and lower heating loads.

In this study, the effect of slab-edge insulation (SEI) was investigated experimentally using the housing testing modules at the UON over a 2-year period as well as numerically using the Finite Volume Method (FVM). The results of the experimental study indicated that the SEI could effectively reduce the energy loss through the ground floor of the Insulated Cavity Brick module. Using SEI, the heat loss through the ground floor can be reduced by changing the thermal response of the adjacent part of the ground and by changing the boundary conditions of the ground and slab edges. In fact, not only the boundary conditions of ground surface and slab edges could be changed by the SEI, but also the boundary conditions of the walling system. These different boundary conditions will also lead to a different temperature distribution within the house, and especially the walls. Because of the close contact between the wall and ground floor, the floor heat transfer process is significantly influenced by the temperature variation of the wall. Therefore, the coupled thermal effect of the SEI and the wall will vary for different walling systems. Using numerical simulations, the effect of SEI were investigated for houses with the three different masonry walling systems in the Newcastle climate.

HOUSING TEST MODULES

The testing modules built on the university campus incorporated the common forms of domestic walling construction in Australia - Cavity Brick (CB), Insulated Cavity Brick (InsCB) and Insulated Brick Veneer (InsBV) as shown in Figure 1. More details of each construction

(including the walling system, the ground floor slab, the SEI and the ground foundation) are shown in Figure 2 to Figure 4. The numerical simulations described in this paper reflect the same configurations as the real testing modules.



Figure 1: Testing facilities

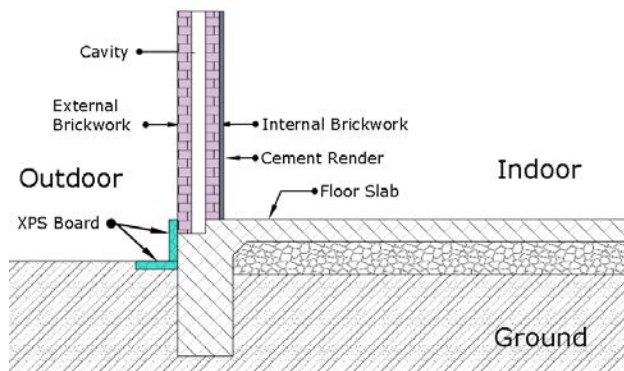


Figure 2: Cross-section of Cavity Brick module

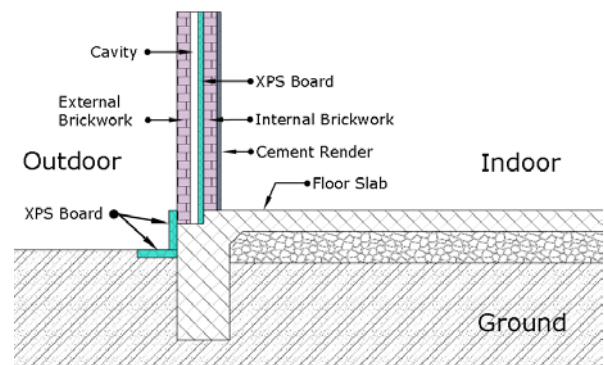


Figure 3: Cross-section of Insulated Cavity Brick module

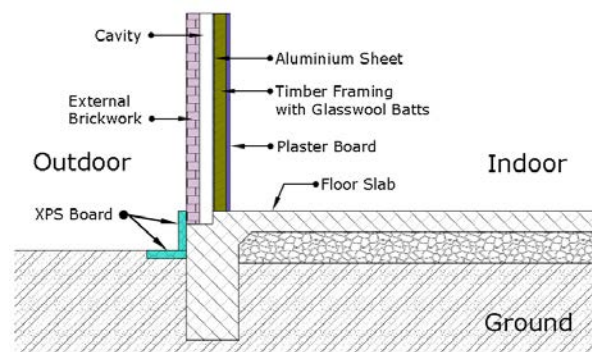


Figure 4: Cross-section of Insulated Brick Veneer module

Extruded Polystyrene (XPS) panels were used as SEI which were installed around the perimeter of slab edges of the InsCB module in the vertical and horizontal directions as show in Figure 5. More detailed information about the dimension and position of the SEI of the InsCB module are shown in Figure 5. The dimensions and installation of the XPS panels for the other two testing

modules were similar. During this period, the interior temperature of the modules was held constant at 21°C by means of a heating/cooling system.

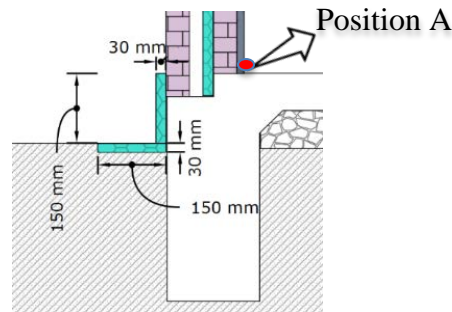


Figure 5: Configuration of SEI

The thermal properties of the construction materials used in the numerical simulations are summarised in Table 1.

Table 1: Properties of materials

| Walling systems | Thermal Conductivity (W / (m · K)) | Density * Specific Heat Capacity (J / (m ³ · K)) |
|--|---------------------------------------|--|
| Soil (of ground) | 1. 21 | 1613000.0 |
| Concrete (of floor) | 1. 45 | 2112000.0 |
| Brick | 0.65 | 1197000.0 |
| Cement Render | 1.00 | 1450800.0 |
| Extruded Polystyrene (XPS) (at slab edge) | 0.03 | 79861.5 |
| Glass Wool Batts | 0.13 | 29440.0 |
| Plaster Board (at wall surface) | 0.17 | 924000.0 |

CLIMATE CHARACTERISTICS

The annual and daily outdoor air temperature fluctuations significantly influence the temperature fluctuation of the indoor environment as well as the operational energy. Thus, the outdoor air temperature fluctuation profile is normally used as the boundary condition at the upper surface of the ground soil and the external surface of the wall. Newcastle has a humid subtropical climate, typical of the Australian east coast. The climate is generally moderated by the Pacific Ocean to the east. Summers are mostly warm and humid with periods of very dry and hot weather occasionally due to hot west to north-westerly winds, which can result in temperatures in excess of 40 °C (104 °F). Winters are generally cool with drier conditions than summer on average. The air temperature profile in Newcastle in a whole year is shown in Figure 6. The daily temperature fluctuation over a week in spring is shown in Figure 7. All the temperature data for Newcastle were collected at the experimental site on the university's Callaghan campus. The collected data of Newcastle outdoor air temperature over a whole year was used in the numerical simulation process in this paper.

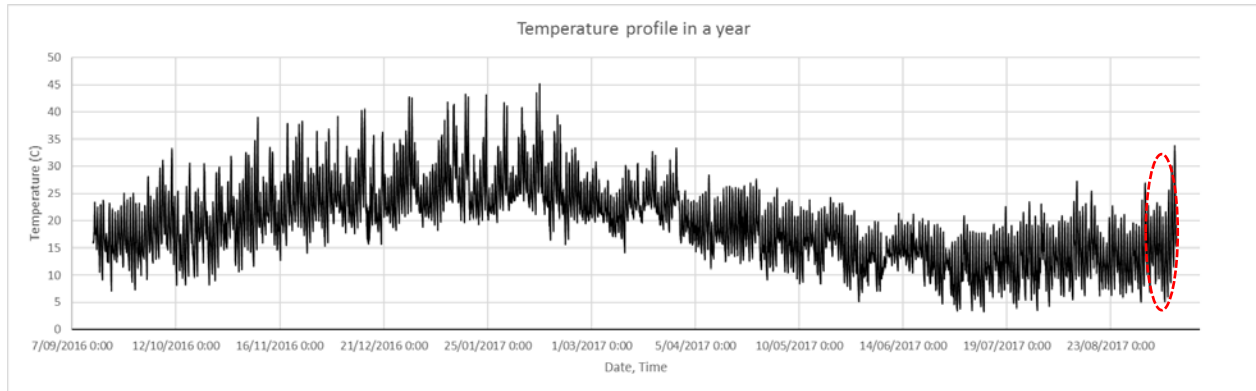


Figure 6: Annual external air temperature profile (2016-2017)

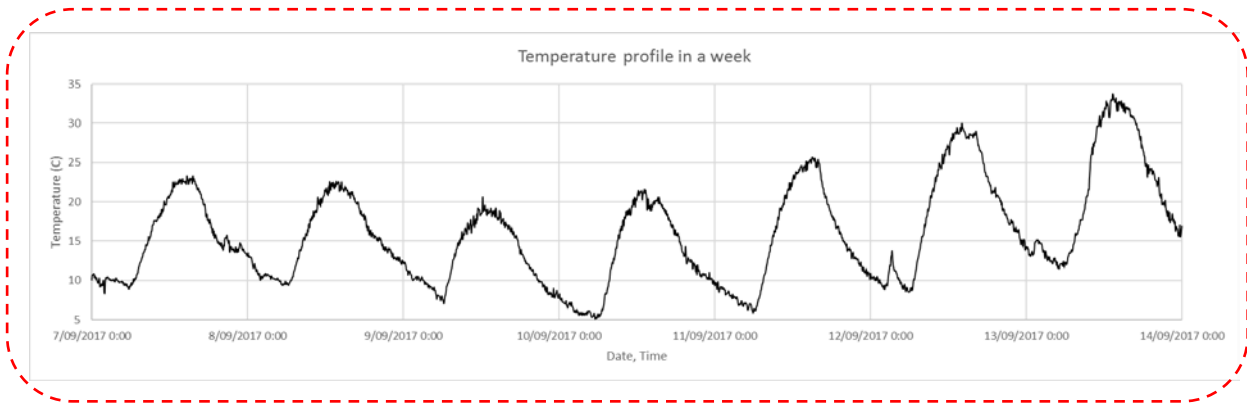


Figure 7: Weekly external air temperature profile for highlighted period in Figure 6

NUMERICAL SIMULATION MODEL

Heat conduction is a process whereby heat is transferred from one region of the medium to another. The heat flux per unit area – q , by conduction, can be written as Equation (1):

$$q = -k \cdot \text{grad}T, \text{ or } q = -k \cdot \nabla T \quad (1)$$

Where:

k - thermal conductivity of the medium,
 T - temperature.

From consideration of conservation of heat energy in a representative control volume, it is possible to derive the basic heat conduction equations based on Equation (1). For example, the heat conduction equation can be posed in the following general form:

$$\frac{\partial(\rho \cdot C \cdot T)}{\partial t} + \text{div}(\rho \cdot U \cdot T) = \text{div}(k \cdot \text{grad}T) + S_{\phi} \quad (2)$$

Where:

- ρ - density of the material,
- C - specific heat capacity of material,
- t - time,
- S_{ϕ} - rate of heat generation within the medium.

The Finite Volume Method (FVM) is commonly used to accurately and quickly solve Equation (2) in practical problems. FVM is a fast-developing calculation method because its good adaptability to complex boundary conditions and complicated configurations of the solution domain, and high computational efficiency. The general procedure of FVM is:

- 1). Discretise the solution domain, and establish the control volume around each node,
- 2). Obtain a set of discrete equations by integrating governing equations at each control volume,
- 3). Solve the discrete equations under specific initial and boundary conditions and then acquire approximate solutions of the governing differential equations in the solution domain.

In this paper, FVM is used to model the testing module heat transfer process involving the ground, the floor slab, the wall and the slab edge insulation.

Figure 8 shows the solution domain which was discretized by a cell centred scheme. To save computation time, the cell dimensions increased geometrically towards the far-field and deep-ground. The cell growth and distribution are illustrated in Figure 8.

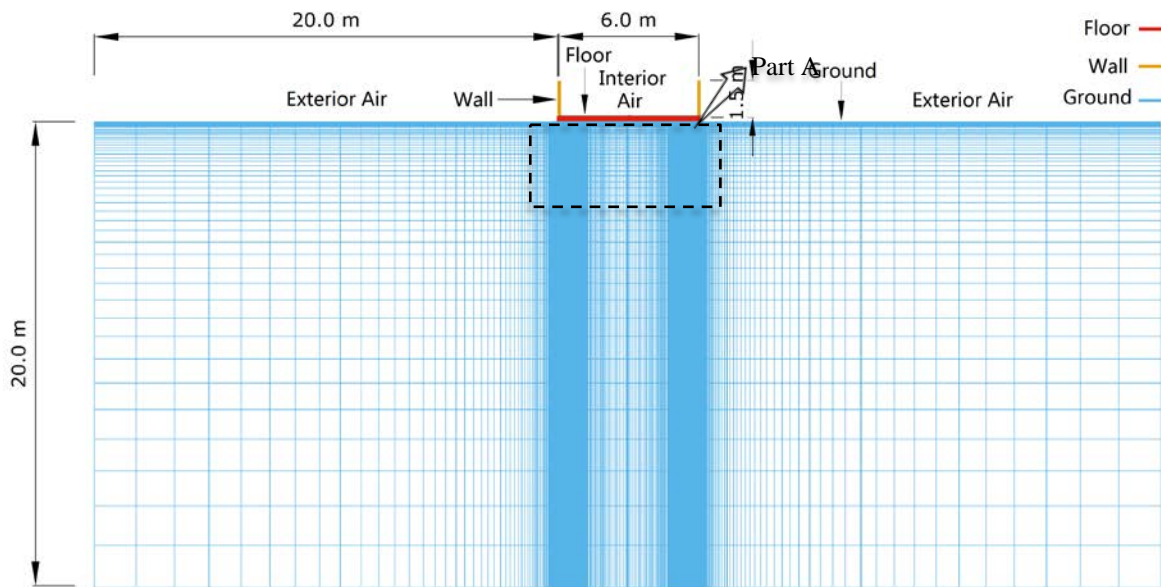


Figure 8: Grid of solution domain

A proper initial condition (which is the initial temperature distribution in this study) can reduce the running cycles of simulation required to reach a 'quasi steady state' (that is, the same temperature profile at the same point in time during a yearly cycle). For the floor and walling

system, the initial temperature is assumed as the interior air temperature of 21 °C . The ground soil under the test house is regarded as a half-infinite soil volume, thus, the initial temperature distribution of ground follows the formula (3) as:

$$\begin{aligned}
 T(z,t) = & T_{mean} + T_{amp,daily} \cdot \exp\left(-z \cdot \sqrt{\frac{\pi}{1 \cdot 24 \cdot 60 \cdot 60 \cdot \alpha}}\right) \\
 & \cdot \sin\left[\frac{2\pi \cdot (t - t_{0,daily})}{1 \cdot 24 \cdot 60 \cdot 60} - z \cdot \sqrt{\frac{\pi}{1 \cdot 24 \cdot 60 \cdot 60 \cdot \alpha}} - \frac{\pi}{2}\right] \\
 & + T_{amp,yearly} \cdot \exp\left(-z \cdot \sqrt{\frac{\pi}{356.25 \cdot 24 \cdot 60 \cdot 60 \cdot \alpha}}\right) \\
 & \cdot \sin\left[\frac{2\pi \cdot (t - t_{0,yearly})}{356.25 \cdot 24 \cdot 60 \cdot 60} - z \cdot \sqrt{\frac{\pi}{356.25 \cdot 24 \cdot 60 \cdot 60 \cdot \alpha}} - \frac{\pi}{2}\right]
 \end{aligned} \tag{3}$$

Where:

$T(z,t)$ - soil temperature at specific time t (s) and depth z (m), (°C).

z - depth of soil below the ground surface (m).

t - time in a year (s).

T_{mean} - mean surface temperature (average air temperature) (°C).

$T_{amp,daily}$ - amplitude of ground surface temperature in a day (°C).

α is thermal diffusivity of the ground (soil), i.e. $\lambda / (\rho \cdot C)$.

$t_{0,daily}$ - time lag (seconds) from an arbitrary starting time (taken as 2.35 a.m.) to the occurrence of the minimum temperature in a day, (s).

$T_{amp,yearly}$ - amplitude of ground surface temperature in a year (°C).

$t_{0,yearly}$ - time lag (seconds) from an arbitrary starting time (taken as 2.35 a.m. 14th Sep) to the occurrence of the minimum temperature in a year, (s).

As for the boundary conditions, the boundary conditions at the far-field and deep-ground areas are adiabatic. The meteorological data measured on the university campus as shown in Figure 6 was used as the boundary conditions of the upper surface of the ground soil and the external surface of the wall. The auxiliary heating and cooling in the test houses maintained a constant indoor temperature (21±3 °C). The boundary conditions at the internal surface of the wall and the indoor slab surface were assumed as third-type boundary condition with indoor temperature and overall heat transfer coefficient as 5.744 W/(m²·K). In the simulation process, a time step size of 3600s (1h) was maintained. Alternating - Direction - Implicit method (ADI) was utilized to solve the discrete governing differential equations in the solution domain.

After running eleven yearly simulation cycles, the quasi steady state annual periodic solution was obtained. The simulated temperature fluctuations of the solution domain in the very last year (11th year) was used for analysing the thermal effect of the SEI.

ANALYSIS OF NUMERICAL SIMULATION RESULTS

Figure 9 presents the temperature distribution of the CB module without the SEI in profile view. The corresponding time of Figure 9 is at 2:30 a.m., 14th September. The enlarged and clearer thermal picture of Part B (which is the right of the ground floor as indicated in Figure 9) of the CB module without SEI as well as with SEI are shown in Figure 10.

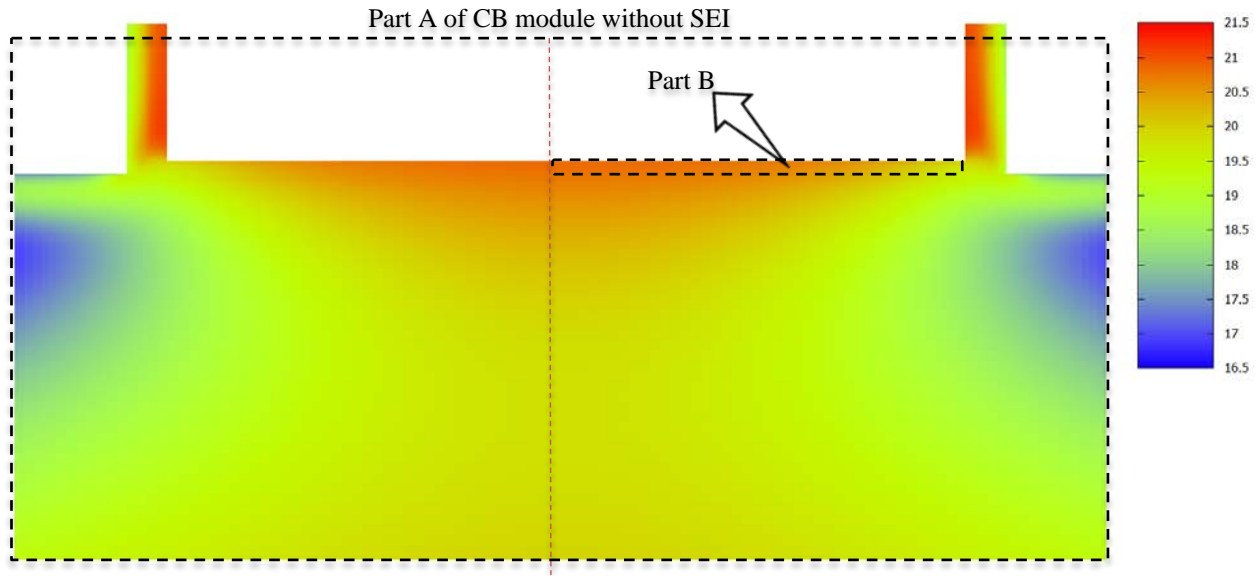


Figure 9: Thermal picture of Part A of CB module without SEI in profile view

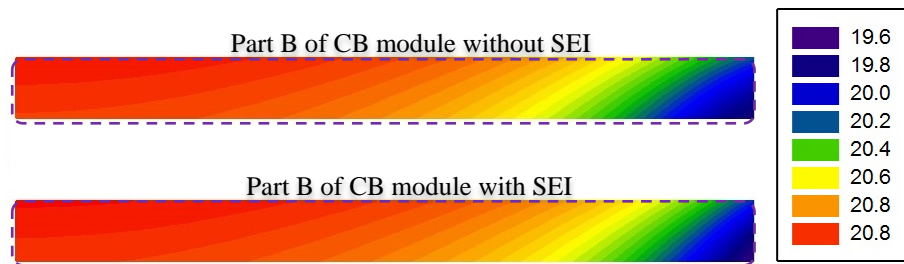


Figure 10: Enlarged thermal picture of Part B of CB module without/with SEI

Compared to the temperature distribution of Part B for the CB module without SEI, the temperature distribution of the corresponding Part B with SEI is more evenly-distributed, especially for the area close to the wall and the slab edge (as can be seen from Figure 10). Compared to the CB module without SEI, the CB module with SEI has a larger area of slab surface with temperatures closer to the indoor air temperature (21°C). This means there is less heat flow from the interior of the module through the surface of slab to the far-field, deep-ground area and the outdoor air. As shown in Figure 11 to Figure 14, a similar thermal effect of the SEI was found for the other two masonry housing modules (InsCB and InsBV).

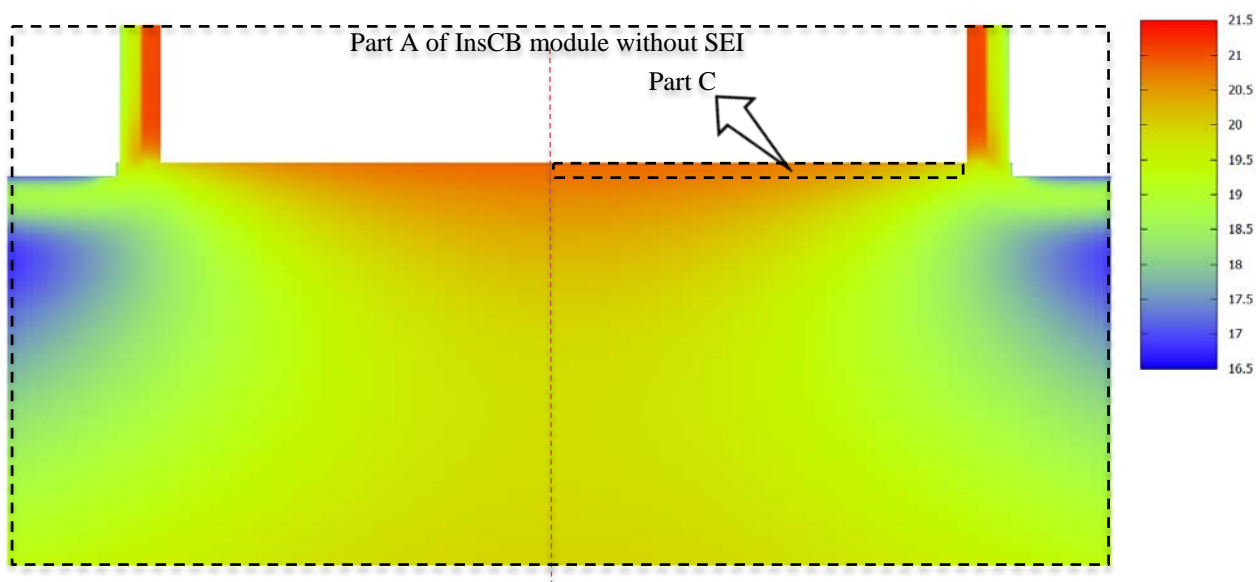


Figure 11: Thermal picture of Part A of InsCB module without SEI in profile view

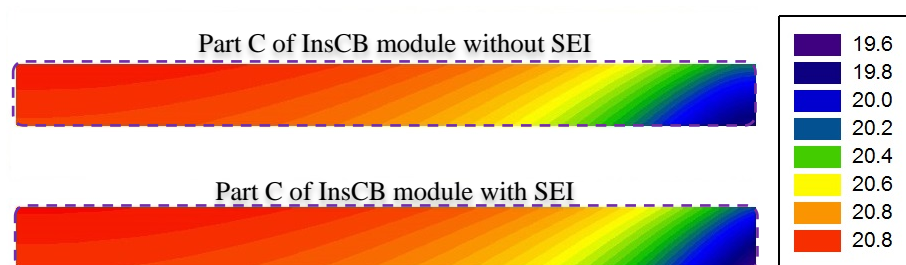


Figure 12: Enlarged thermal picture of Part C of InsCB module without/with SEI

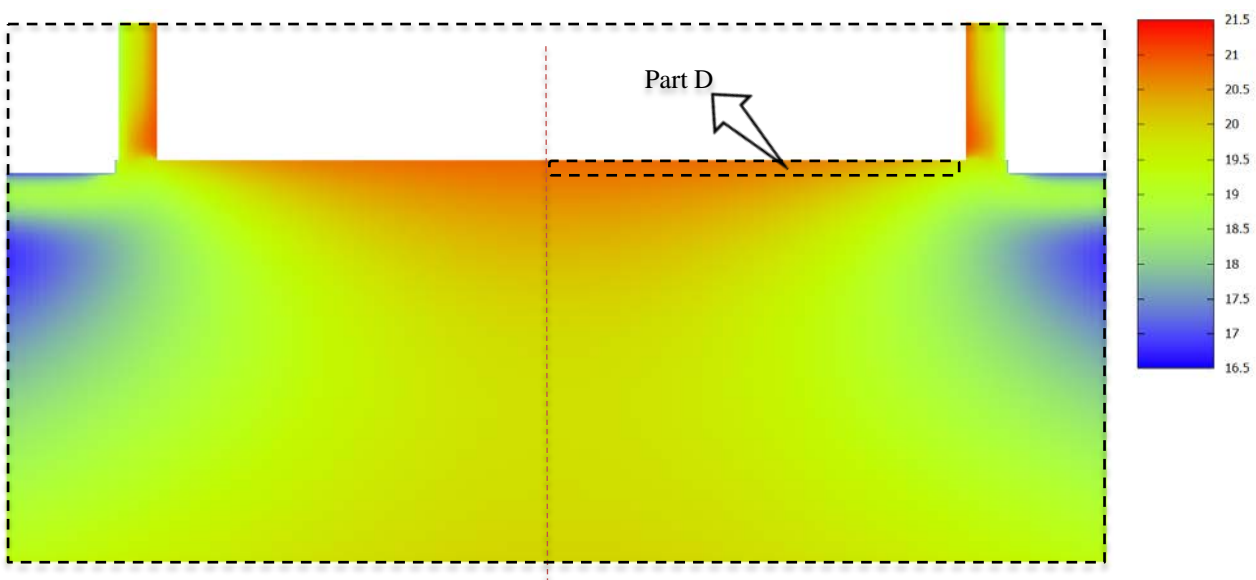


Figure 13: Thermal picture of Part A of InsBV module without SEI in profile view

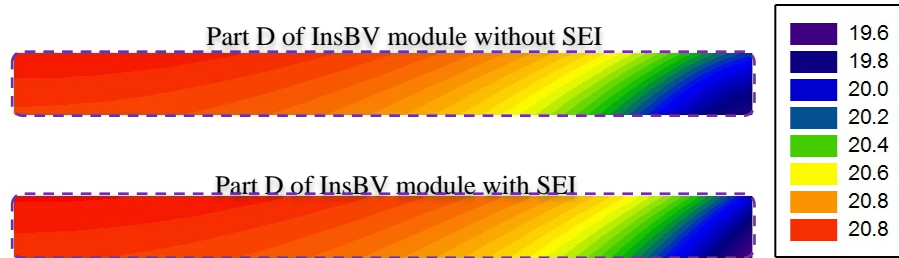


Figure 14: Enlarged thermal picture of Part D of InsBV module without/with SEI

The yearly and weekly temperature fluctuations at Position A (corner position at interior slab surface, as indicated in Figure 5) for three testing modules are shown in Figure 15 to Figure 17. All three figures clearly indicate that the temperature fluctuations at Position A for all three modules with SEI were much less significant than the temperature fluctuations with no SEI. Among six temperature variation profiles, the temperature profile at Position A in InsBV without SEI presented the most significant fluctuation in both an annual and daily period. The least significant temperature fluctuation was in the InsCB module with SEI.

By comparing the temperature fluctuation of the InsBV module (with SEI) with the temperature fluctuation of the InsCB module (without SEI), it was found that the temperature fluctuation in InsBV with SEI was steadier and closer to the indoor temperature than the temperature fluctuation in the InsCB module without SEI for a large proportion of a year (especially in summer days). That is, the heat flow from the interior slab surface of the InsBV module with SEI is less than the heat flow through purely the floor slab of the InsCB module. This means that by using SEI, the thermal performance of the slab of the InsBV module can match or even exceed the thermal performance of the slab of the InsCB module.

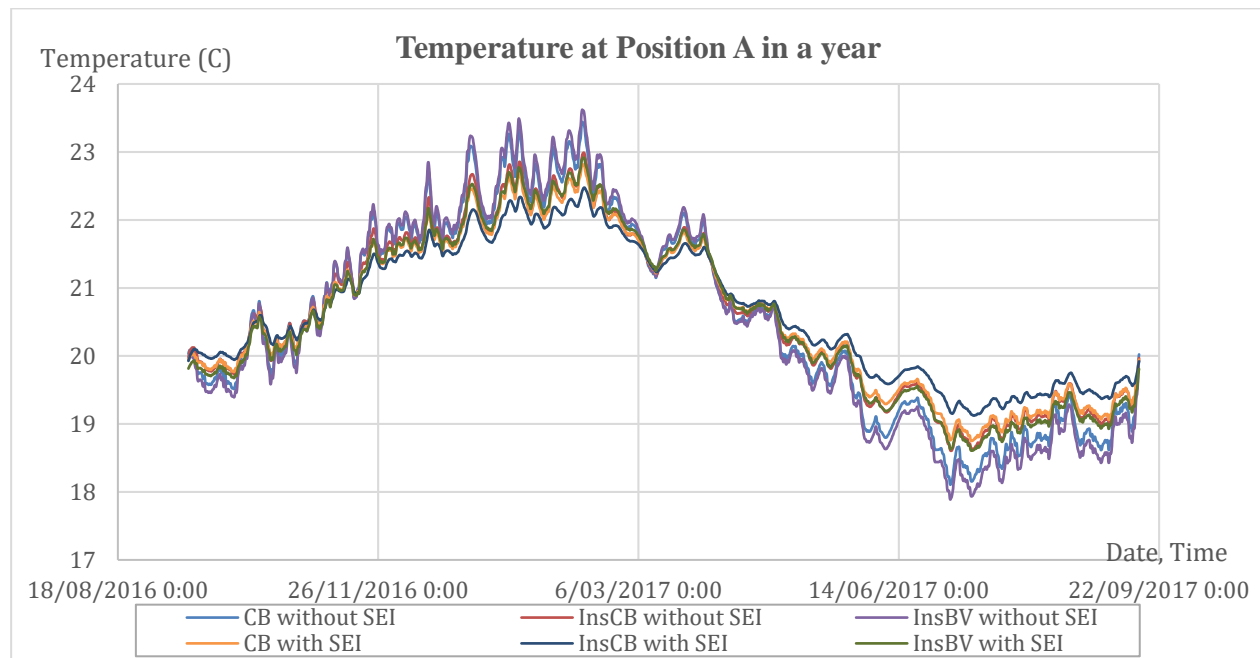


Figure 15: Yearly temperature fluctuation at Position A

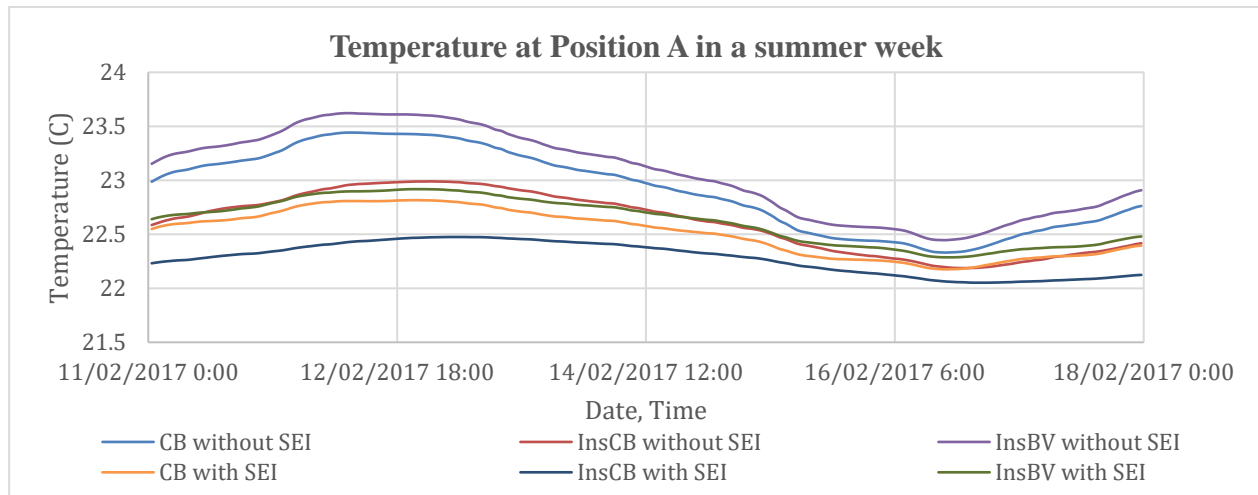


Figure 16: Weekly temperature fluctuation at Position A

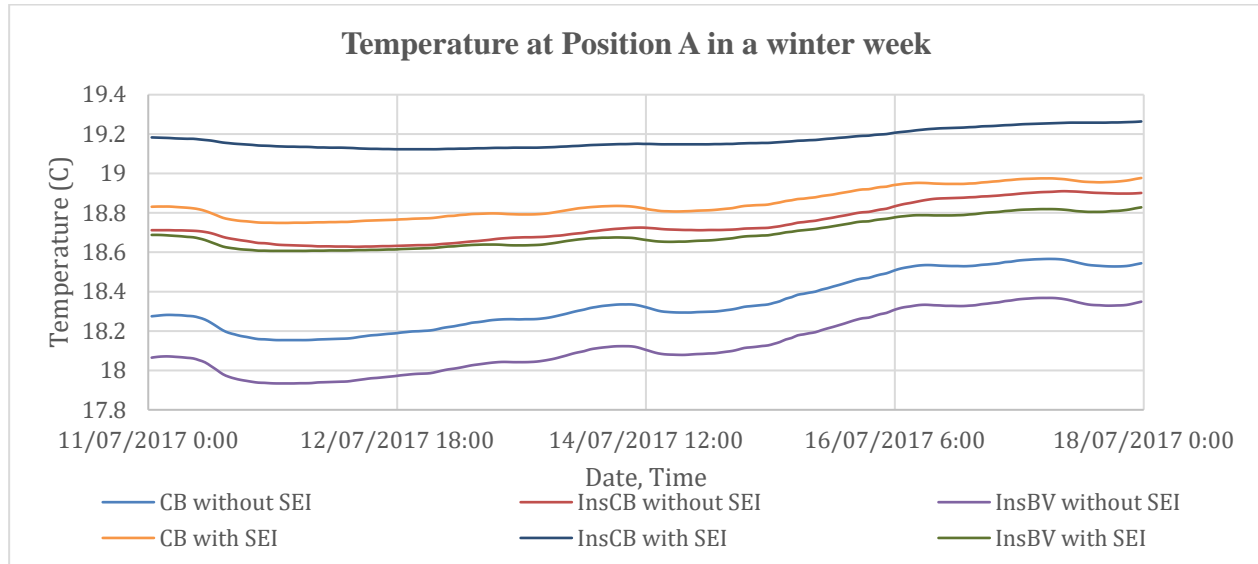


Figure 17: Weekly temperature fluctuation at Position A

The heat flow from the interior of the module through the surface of the slab to far-field, ground beneath and air outside in a whole year (the 11th yearly simulation cycle) for three testing modules (without and with SEI) is shown in Table 2.

From Table 2 it can be seen that, whether there is SEI or not, the accumulated heat flux (lost energy) through the interior slab surface of the InsCB module in a year is least among the three modules, followed by the CB module, with the most energy loss in the InsBV module.

Based on numerical simulation, the better thermal performance of floor slab for all modules was observed after utilizing the SEI, with the best improvement for the InsBV module. The annual heat flow for the InsBV module with installed SEI panels through the slab was lower of 16.30%

than its counterpart. This resulted in better thermal performance than even the InsCB module without the SEI panels installed around the slab as presented in Table 2.

Table 2: Numerical simulation results

| Walling systems | Accumulated heat flux through interior floor surface in a year | | Saved energy per year | Proportion of saved energy |
|-----------------|--|-----------|-----------------------|----------------------------|
| | Without SEI | With SEI | | |
| CB | 1.965E+09 | 1.647E+09 | 0.317E+09 | 16.15% |
| InsCB | 1.840E+09 | 1.556E+09 | 0.284E+09 | 15.42% |
| InsBV | 2.092E+09 | 1.751E+09 | 0.341E+09 | 16.30% |

CONCLUSIONS

In this paper, the effect of slab-edge insulation (SEI) in combination with three types of masonry walling systems (Cavity Brick, Insulated Cavity Brick and Insulated Brick Veneer) has been investigated. The analysis includes annual simulations based on the Finite Volume Method to assess the energy savings in housing with a temperature controlled internal combined space combined with slab edge insulation (SEI). From the study, it can be seen that SEI can reduce the heat flux and the temperature fluctuations at the interior floor surface in all three housing test modules. For the Insulated Brick Veneer module, which had poorest thermal performance among the three testing modules, the most energy (in terms of net energy saving and percentage of energy saving) can be saved by installing SEI. The SEI had the least effect for the Insulated Cavity Brick module, although significant energy savings were still obtained with the use of the SEI.

ACKNOWLEDGEMENTS

This research project has been supported by the Commonwealth Scientific and Industrial Research Organisation (CSIRO) and the University of Newcastle.

REFERENCES

- Alterman, D., Moffiet, T., Hands, S., Page, A., Luo, C., & Moghtaderi, B. (2012). A concept for a potential metric to characterise the dynamic thermal performance of walls. *Energy and Buildings*, 54, 52-60.
- Alterman, D., Page, A., Moghtaderi, B., & Zhang, C. (2015). Contribution of thermal resistance and thermal mass to the energy demand of walling systems/Beitrag des Wärmedurchlasswiderstandes und der thermischen Masse zum Energiebedarf von Wandsystemen. *Mauerwerk*, 19(1), 64-73.
- Ball, A., Ahmad, S., McCluskey, C., Pham, P., Pittman, O., Starr, A., Nowakowski, D., &

Lambert, N. (2017). Australian Energy Update 2015. Australia Government Department of Industry and Science: Canberra, ACT.

Chen, D. (2013). Dynamic three-dimensional heat transfer calculation for uninsulated slab-on-ground constructions. *Energy and Buildings*, 60, 420-428.

Hagentoft, C. E. (1988). Heat loss to the ground from a building: slab on the ground and cellar (Vol. 1004). *Byggnadsfysik LTH*, Lunds Tekniska Högskola.

Neymark, J., Judkoff, R., Beausoleil-Morrison, I., Ben-Nakhi, A., Crowley, M., Deru, M., ... & Witte, M. (2008). International Energy Agency Building Energy Simulation Test and Diagnostic Method (IEA BESTEST): In-Depth Diagnostic Cases for Ground Coupled Heat Transfer Related to Slab-on-Grade Construction (No. NREL/TP-550-43388). National Renewable Energy Laboratory (NREL), Golden, CO..

Page A.W., Moghtaderi B., Alterman D. and Hands S. (2011), A Study of the Thermal Performance of Australian Housing, Priority Research Centre for Energy, the University of Newcastle, 220pp.

Yoshino, H., Matsumoto, S., Nagatomo, M., & Sakanishi, T. (1992). Five-year measurements of thermal performance for a semi-underground test house. *Tunnelling and Underground Space Technology*, 7(4), 339-346.

Zoras, S. (2009). A review of building earth-contact heat transfer. *Advances in Building Energy Research*, 3(1), 289-313.

OPTIMIZATION OF THE SEISMIC PERFORMANCE OF CONTEMPORARY MASONRY CHIMNEY SYSTEMS

V. Bosiljkov¹, D. Antolinc², G. Steinecker³ and S. Plaskan⁴

¹ Professor, University of Ljubljana, Faculty of Civil and Geodetic Engineering, Jamova 2, SI-1000 Ljubljana, Slovenia, vbosiljk@fgg.uni-lj.si

² Assistant, University of Ljubljana, Faculty of Civil and Geodetic Engineering, Jamova 2, SI-1000 Ljubljana, Slovenia, david.antolinc@fgg.uni-lj.si

³ Schiedel GmbH, Friedrich-Schiedel-Straße 2-6, A-4542 Nußbach, Austria, Gerald.Steinecker@schiedel.com

⁴ Schiedel GmbH, Friedrich-Schiedel-Straße 2-6, A-4542 Nußbach, Austria, sandi.plaskan@schiedel.si

Traditional masonry chimney systems are regarded as highly vulnerable due to earthquakes. The general perception is that they will fail even in the case of moderate earthquake. Virtually all post-earthquake reports mention significant number of damaged or toppled chimneys, while there are no data on the number of chimneys that were undamaged. Following the outcome of the results from the first part of tests on two types of contemporary chimney systems under the influence of cyclic lateral loading, optimization of existing system was made by placing the reinforcement bars along all four corners of the chimney from the top of the chimney down to RC plate. Tested chimneys were of the height of 400 cm and were subjected to cyclic horizontal load, acting on the top module of the specimens while the bracing system at the roof level was provided according to producer requirements. Horizontal load was applied in the form of programmed displacements, cyclically imposed in both directions until the collapse of the specimens. At each displacement amplitude corresponding to major cracking event, vibration tests for the evaluation of natural frequency and damping of the system were performed. By extending rebars the failure mechanism was changed halving the mass of the chimney that could be activated during earthquake resulting with significantly higher resistance. In comparison to existing chimney systems the new hysteresis behaviour of the whole system was significantly improved. Considering coupling effect with the typical primary masonry structure - conservative values regarding seismic resistance of the optimized system were obtained.

Keywords: masonry chimney, contemporary, structural performance, earthquake

INTRODUCTION

Traditionally masonry chimneys are regarded as highly vulnerable to seismic events. A general perception among designers is that they will fail even in the case of moderate-strong earthquake that may provoke solely minor damages to structural elements. In the current code of practice chimneys as secondary structural elements are not of concern in seismic design for contemporary buildings. Virtually all post-earthquake reconnaissance reports mention significant numbers of damaged or toppled chimneys. Following the recent New Zealand Canterbury earthquake (2010/2011), it has been reported (Giaretton et al. 2017) that 15,400 chimneys were damaged or destroyed resulting with estimate of NZ\$70 million losses. City of Los Angeles records for the Northridge earthquake identify approximately 30,000 chimneys for which repair permits were issued while other sources report a total of 60,000 damaged chimneys. While these data reinforce the fragile nature of masonry chimneys, there are no data on the number of chimneys that were undamaged (Osteraas et al. 2010). Recently finished study on the probability of exceeding a certain economic loss, and the loss dependent on a given seismic intensity for masonry buildings revealed that for the low seismic events costs for retrofitting of chimney systems may significantly contribute to the overall costs of repairs for non-collapsed buildings (Snoj et al. 2017). Estimation for limiting values of acceleration for near collapse state for traditional brickwork chimney failure differs depending from the primary load bearing structure to which they are attached to. Thus in the literature for the single storey building they may be set as low as $a_g = 0.11$ g (Osteraas et al. 2010) up to 0.30 – 0.60 g for brickwork masonry chimneys made with lime and cement-lime mortar respectively (Giaretton et al. 2017).

According to European building codes (Eurocodes), seismic performance requirements for unreinforced and reinforced masonry chimneys for the construction in seismic areas are not set as obligatory. In EN 1998-6 (EN 1998-6 2005), obligatory provisions are provided only for concrete and steel chimneys as well as for steel towers and guyed masts. In the Informative Annex E information and guidance for the seismic design of Masonry chimneys of interests for this research study are set as:

- Behaviour factor is set as for the unreinforced masonry ($q=1.5$) though according to EN 1998-1 for chimneys, acting as unbraced cantilevers along less than one half of their total height, or braced or guyed to the structure at or above their centre of mass, q could be set to 2.0
- Minimum vertical reinforcement - for chimneys with a horizontal dimension up to 1 m, a total of four 12 mm diameter continuous vertical bars anchored in the foundation should be placed in concrete between leaves of solid masonry or placed and grouted within the cells of hollow masonry units.
- Minimum horizontal reinforcement - vertical reinforcement should be enclosed within 6 mm diameter ties, or other reinforcement of equivalent cross-sectional area, at a spacing of not more than 400 mm.
- Minimum seismic anchorage should be provided at each level of floor or roof which is more than 2 m above the ground, except where constructed completely within the exterior walls.
- Cantilevering - should not project as a corbel from a wall or foundation by more than half of the chimney wall thickness.

Whether some clauses from Eurocode are obligatory or informative is set through National Document for the Application (NAD) of Eurocode. The most of contemporary masonry chimney systems do not fulfil some of these requirements and it exist reasonable fear amongst chimney producers that structural requirements as stated in informative annex of EN 1998-6 may jeopardize their position on the market.

RESEARCH PROGRAMME

Being aware of the lack of experimental data on the lateral behaviour of contemporary masonry chimneys structurally attached to the primary structure i.e. the building, the research program was set in the first phase on the assessment of the behaviour of two different types of chimney systems built and tested in laboratory conditions (type A and B). Two tested types of chimneys had same dimensions but differ in used light-weight concrete masonry blocks, ceramic flue liners and consequently their masses. Both systems were partly reinforced along the height with diagonally placed and grouted rebars (3m long reinforcing bars). Their cross-sections are presented in following figures (Figure 1), while the length of reinforcement in Figure 2.

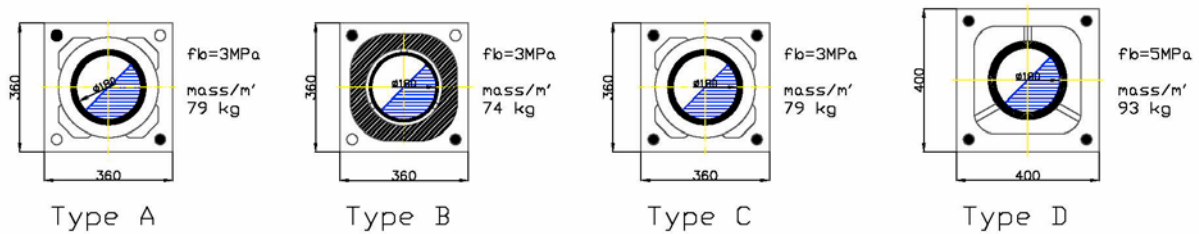


Figure 1: Horizontal cross-sections for tested types of contemporary masonry chimney systems with main characteristics.

In the second phase of research programme type A system was improved by providing reinforcement along all four corners and extending steel bars down to the RC slab (Type C in Figure 1), which in practice would mean fully reinforced masonry chimney from the top down to foundation level. In the last step of the optimization this improvement was repeated for type D system, where the load from the masonry units is transferred to ceramic liners simply through randomly placed spacers.

All systems have the same system of lateral bracing as presented in Figure 2. For systems A&B it was set (current building practice according to manufacturer requirements) that steel bars will span 1.5 m above roof structure and 1.5 m below, resulting with 3 m length as presented in Figure 2. Lateral bracing of the system at the roof structure level was provided through elastic response of two steel bars laid at different height and fixed into rafters (Figure 6). At the level of RC plate (bottom of the chimney), the contact between chimney and RC plate was provided through thermal insulation layer (fire safety requirements) placed between chimney and RC plate. All specimens were built by skilled masons provided by industrial partner. Prior the testing, RC plate was casted in the laboratory and fixed to the strong floor of the laboratory. Chimneys were built from light-weight concrete masonry units with thin bed mortar in laboratory conditions and mature there for at least 28 days.

The main aims of this study were set as:

- identification of failure mechanisms – this was completely unknown to us. Conservative approach of designing chimney systems is considering them as cantilever systems standing from the RC slab upward. However, tested systems have some additional supports and bracing systems that may significantly influence the response of the chimney due to lateral loading;

- identification of the resistance of chimney in term of its strength and displacement depending from desired performance targets;
- application of obtained results in term of verifying resistance of chimney systems considering type and behaviour of primary structure both in elastic and in-elastic state.

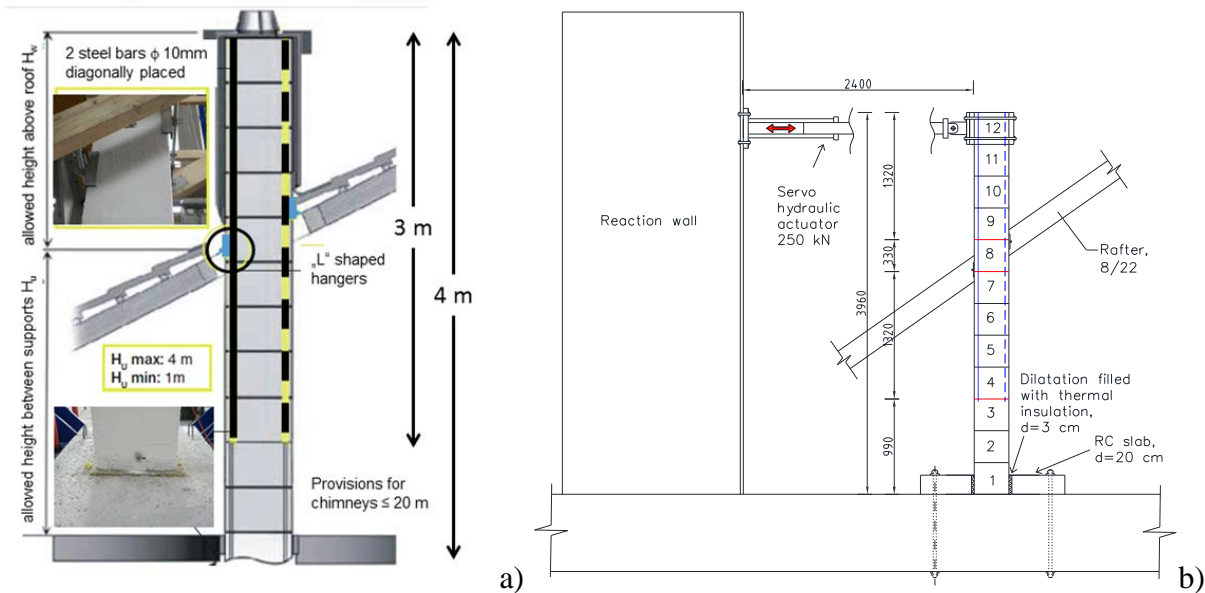


Figure 2: Reinforcement for chimney systems type A and B, lateral support system of the chimney at the roof level and detail of connection through RC slab a), test set-up for laboratory testing b).

EXPERIMENTAL SET-UP

The chimneys have been tested as vertical cantilevers. Programmed lateral displacements have been imposed at the top level of the chimney. Though the chosen distribution of loading does not correspond with the mass distribution of the chimney it is the close approximation to the first natural shape of the chimney system as it has been numerically investigated (Bosiljkov et al. 2016).

The test set-up consisted of a steel testing frame and one programmable hydraulic actuator (Figure 2-b). Horizontal load was imposed by means of a programmable, static capacity hydraulic actuator type Instron 250 kN, fixed on strong wall and connected to the chimney at the top with a steel connector that braced both sides of the chimney. Cyclic lateral displacements with step-wise increased amplitudes, repeated three times at each displacement peak, have been used to simulate the lateral seismic loads.

All specimens have been instrumented with displacement transducers (LVDT-s) to measure horizontal displacements. Load cells have been placed between the chimney and actuators in order to measure the forces acting on the chimney at each instant of time. The instrumentation of a typical specimen for lateral resistance test is shown in Figure 3, where D – refer to LVDT measurement devices, while A relate to accelerometers. LVDT's were placed to measure deformed shape of

chimney system from one side of the chimney in the direction of loading. Four accelerometers A1-4 were placed along the height in the direction of loading, while two accelerometers A5-6 were placed perpendicular to the direction of loading. Accelerometers A1-4 were placed at different height positions in order to evaluate different frequencies of parts of chimneys once the cracking occurred. Acquisition systems for LVDT's and accelerometers were separated.

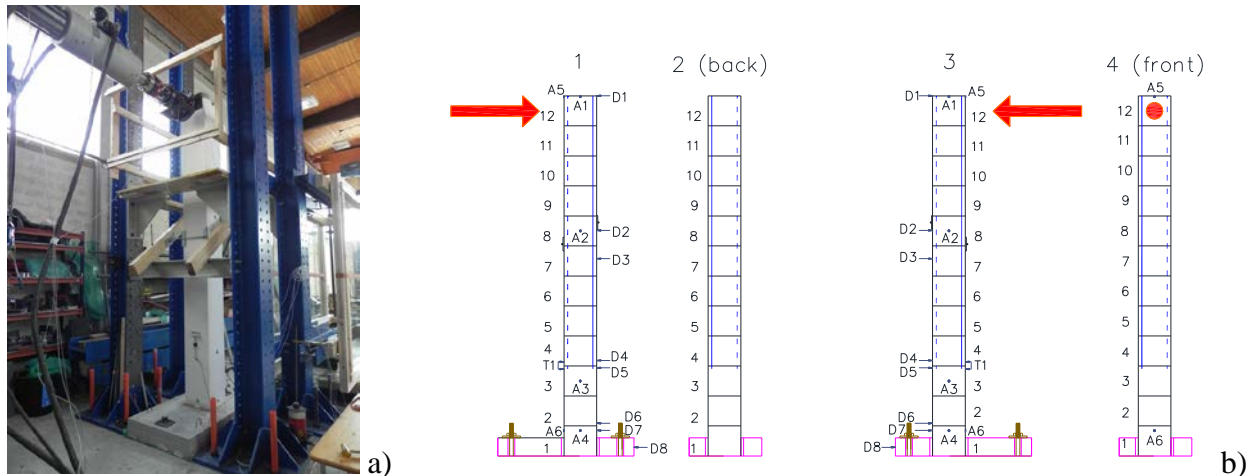


Figure 3: Typical chimney during lateral resistance test a) and positions of measuring devices b)

In order to assess dynamic characteristics of different chimney systems, vibration tests by means of superimposed (forced) initial amplitude provided either by hammer impact or by pulling force at the top of the chimney was considered for the structural characterization and damage detection. For this purpose, free vibration and natural frequencies as well as damping of different chimney systems in dependence from recorded levels of damage were measured. This was done following the occurrence of particular crack pattern (performance limit). Measurements were done following the detachment of the chimney from the actuator and by pulling the top of the chimney with controlled force of 0.05 kN regardless the level of damage in the chimney. Once the force was released the accelerations were recorded and analysed.

RESULTS OF TESTING

All types of chimney failed in flexure. Lateral bracing system at roof line provided effective elastic support for chimney system. Bars of bracing system were largely deformed. No failure occurred in bracing system, however since it was not firmly attached to chimney it allowed limited lateral movement of chimney system at points D and E (see Figure 6) and free rotation. Vertical cracks along masonry units were mainly due to the low tensile strength of units and very stiff behaviour of grout and steel bars in relation to masonry units. Good cohesion between grout and masonry units was observed and no yielding of steel bars were observed following dismantling of the chimney. Ceramic flue liners were not damaged during tests.

Characteristic deformed shapes of chimney systems in dependence on recorded damage and steps of loading are presented Figure 4. It can be seen, that for type A and B systems resistance of the

chimney is significantly lower in the positive direction of loading. This is mainly due to the asymmetrical position of bracing system at the roof line and limited length of reinforcing bars along the height of the chimney (see Figure 2-a). In negative direction the lever arm is shorter and thus the stiffness as well as resistance was higher. Failure of both chimney systems is largely influenced by the presence of reinforcement solely in the upper part of the chimney. Soon, after the so called “plastic hinge” (point C in Figure 6) is formed, the system turns into two kinematic bodies loosely attached with ceramic flue liners. Bracing system at roof line is effective; however, it allowed limited translation and almost free rotation. Thus for the purpose of seismic design the whole mass of the upper part of the chimney above plastic hinge should be used for the calculation of seismic force.

By introducing reinforcement along all four corners and extending bars down to RC slab (new bar length is from point F to A in Figure 6), the crack pattern propagation and consequently failure mechanism was changed. Chimney behaved as rigid body till its maximum resistance. As soon as bracing system at roof level came into yielding phase, masonry units exhibited cracking along the reinforcement bars. For the last test set-up (Type D) LVDT's D2-D6 were replaced with new devices of max range of ± 50 mm, thus for higher displacements their results are missing in Figure 4-d.

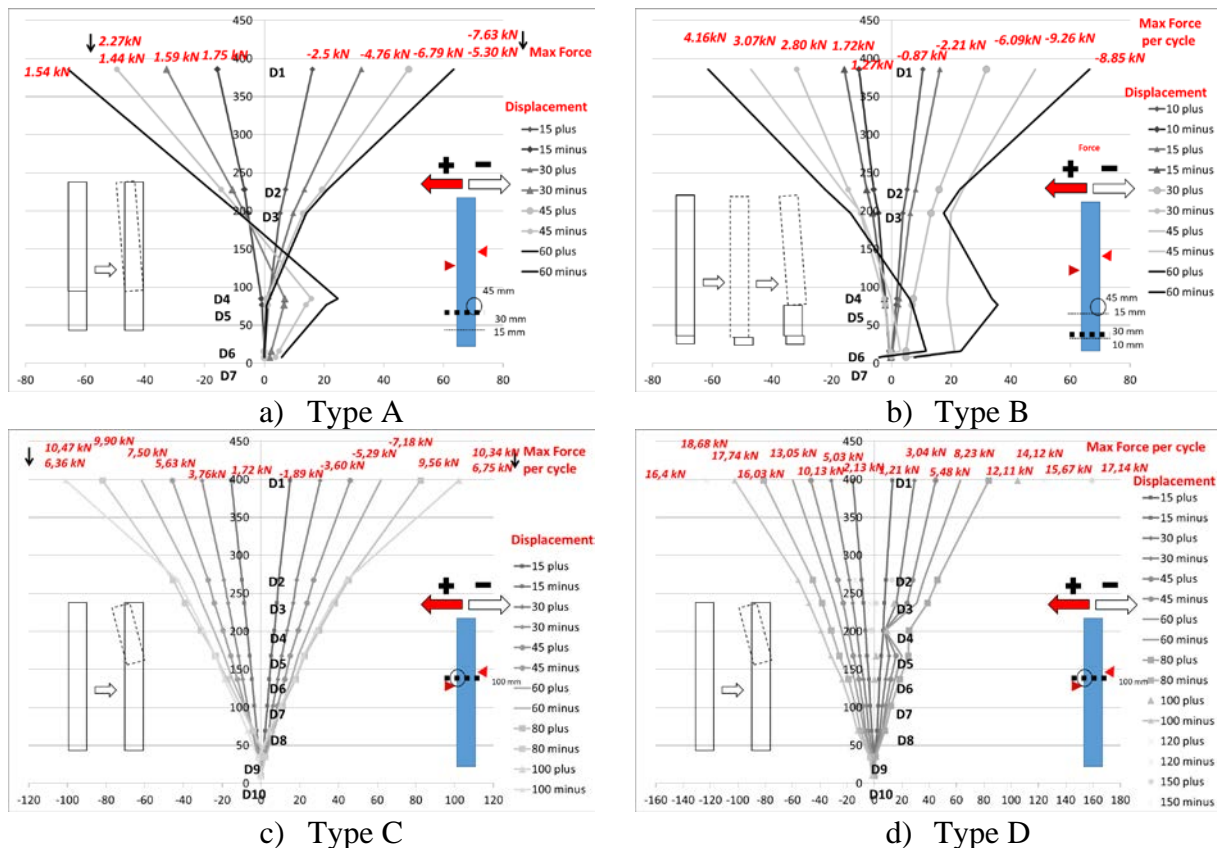


Figure 4: Deformed shapes of chimney systems in dependence on obtained displacement with maximum resistance in each direction of loading.

With the introduction of improvements hysteresis behaviour of the system was changed. While type A and B system exhibited typical hysteresis behaviour characteristic for URM systems (Maison et al. 2017), improved systems (C and D) showed symmetrical behaviour with large energy dissipation (Figure 5) and shape of hysteresis loops more characteristic for RM systems.

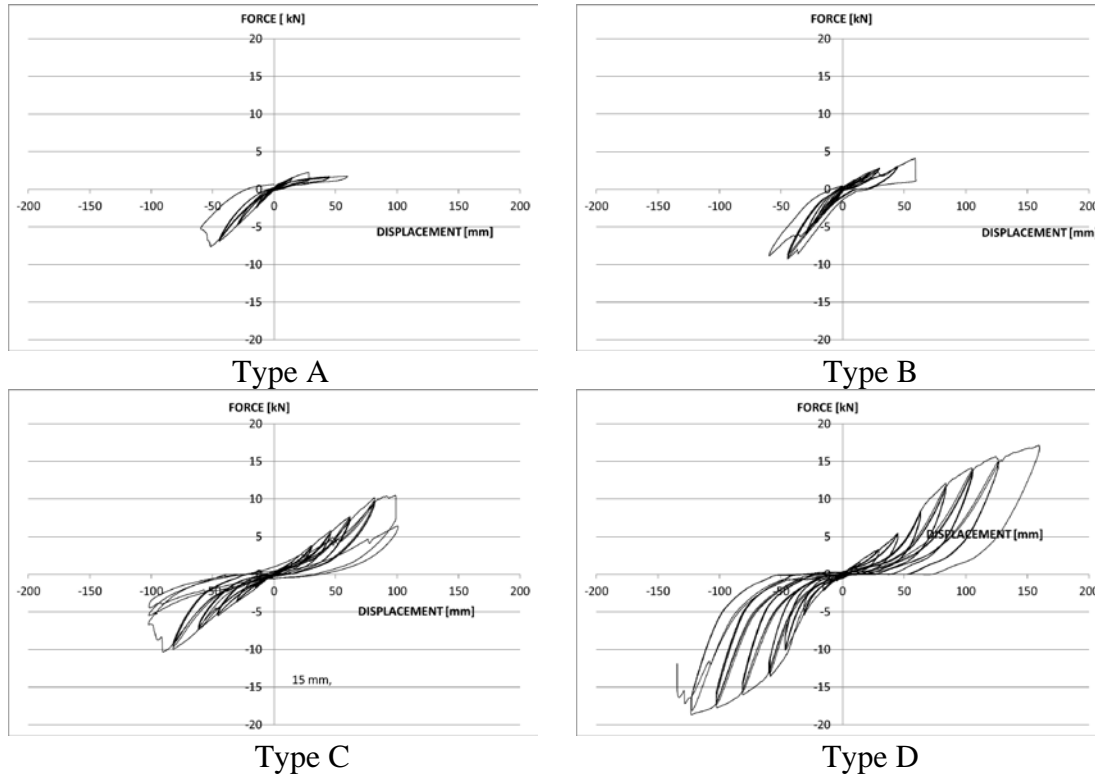


Figure 5: Hysteresis behaviour of all tested chimney systems

On the basis of the observed damage propagation, four limit states (*FC*, *DL*, *SD* and *NC*) have been defined which characterize the behaviour of the tested chimney specimens under lateral loads:

- Flexural cracking related to URM, defined by the initiation of horizontal cracks either at the bottom of the specimen or in the first or second mortar bed joint (point B in Figure 6) as a result of exceeding bond strength of the mortar (H_{fx} , d_{fx}). From the performance point of view this state may be defined as *FC* (First Crack);
- Flexural cracking related to partly RM, defined by the initiation of horizontal cracks at the point where reinforcement end (H_{cr} , d_{cr}) and formation of kinematic system consisted of upper body (C-F) and lower body (B-C) (see Figure 6). For type B system, this system occurred following the large sliding over the bottom of the specimen (point B). For fully RM specimen this state is related to first cracking in masonry unit. From the performance point of view this state may be defined as *DL* (Damage Limitation);
- Crushing of the unit, defined by the initiation of vertically oriented cracks, passing along the reinforcement and is related to maximum resistance defined by the maximum attained resisting lateral force (H_{max} , d_{H-max}).

- Maximum resistance, defined with the maximum attained resisting lateral force in the direction with longer lever arm (H_{max}^+ , d_{H+max}). From the performance point of view this state may be defined as *SD* (Significant Damage);
- Ultimate limit, defined by the maximum attained displacement of the chimney just before collapse (d_u). From the performance point of view this state may be defined as *NC* (Near Collapse).

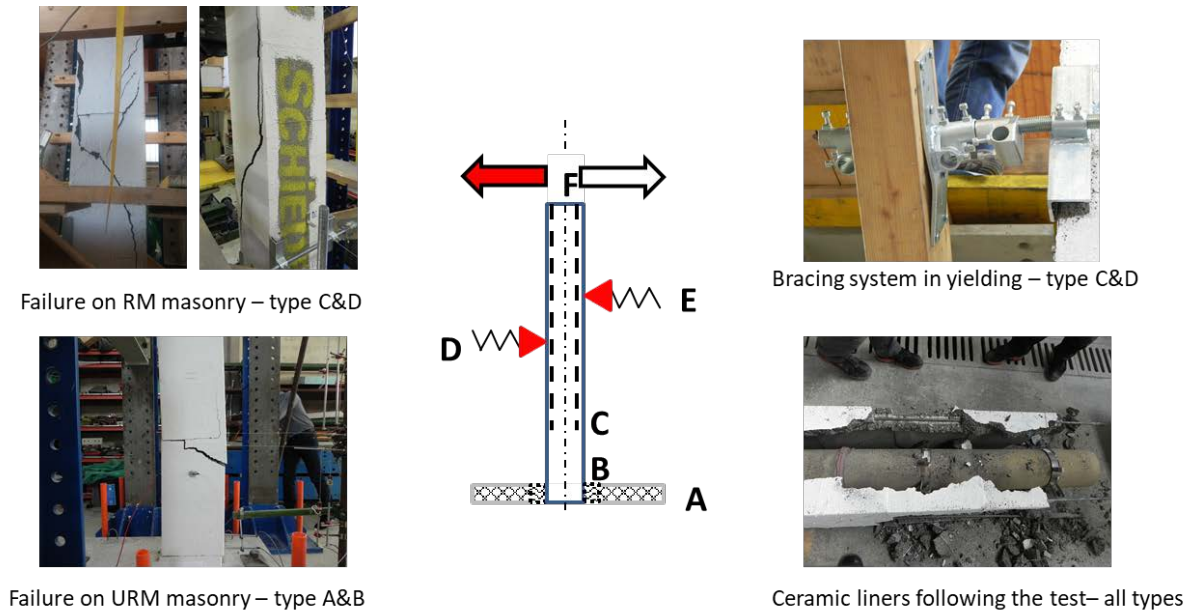


Figure 6: Identified resisting system and typical damage patterns.

Earthquake induced chimney failures pose a life safety hazard only as a result of toppling or collapse of the whole chimney. Since in our tests we have not provoked complete collapse of the chimney, in our analysis performance limits are solely related to the structural performance of the chimney. As it concerns functional performance it should be noted that following dismantling of chimneys no visible cracks were observed on ceramic flue liners. Results for performance limits are presented in Table 1.

Table 1: Performance limits for chimney systems.

| | Type A | | | Type B | | | Type C | | | Type D | | |
|-----------|--------|-------|----------|--------|-------|----------|--------|--------|----------|--------|------|----------|
| | H | d | θ | H | d | θ | H | d | θ | H | d | θ |
| | [kN] | [mm] | [%] | [kN] | [mm] | [%] | [kN] | [mm] | [%] | [kN] | [mm] | [%] |
| FC | 1.42 | 9.81 | 0.25 | 1.27 | 10.60 | 0.27 | - | - | - | - | - | - |
| DL | 2.27 | 28.10 | 0.70 | 2.34 | 28.60 | 0.72 | 10.33 | 90.26 | 2.26 | 14.12 | 100 | 2.50 |
| H_{max} | 7.63 | 55.43 | 1.39 | 9.26 | 48.25 | 1.21 | 10.40 | 90.50 | 2.54 | 18.68 | 120 | 3.00 |
| SD | 2.27 | 22.38 | 0.56 | 4.15 | 58.92 | 1.47 | 6.74 | 101.50 | 2.54 | 18.68 | 120 | 3.00 |
| NC | 1.75 | 66.09 | 1.65 | 1.15 | 59.45 | 1.49 | 3.95 | 101.80 | 2.55 | 17.14 | 150 | 3.75 |

The results for first two types show slightly better performance of type B system. *FC* and *DL* states are close for both systems in respect to their drifts. Resistance for *FC* is better for type A system.

For the seismic analysis of the chimney the key parameters are maximum resistance, here defined as *SD* state and ductility defined by the ratio of rotations for *NC* and *DL* states. For *SD* state type B system obtained better resistance. Ductility for first two systems was around two. Rotations for both systems and all performance states were in absolute values very low. For secondary masonry elements that are expected to fail in flexure, according to EC8-3 (see Annex C) design values are much higher (for secondary elements for *SD* limit state defined as $0.012 h_0/D$, where D is the in-plane horizontal dimension of the wall (depth), while h_0 is the distance between the section where the flexural capacity is attained and the contraflexure point which in this case it was the roof level).

For optimized systems (C&D) both resistance and rotations were significantly improved with better performance of type D systems. Both systems are stiffer resulting in almost symmetrical response of the chimney system. Performance levels *DL*, *SD* and *NC* for type C system are very close resulting in lower ductility of the system in comparison to system D.

For tested chimney systems dynamic identification was done through Fast Fourier Transformation (FFT) analysis of the recorded amplifications along the height of chimney in both directions. For the analysed signals from top accelerometers results corresponding different damage levels that in some cases were correlated to the characteristic performance limit states are presented in following figure.

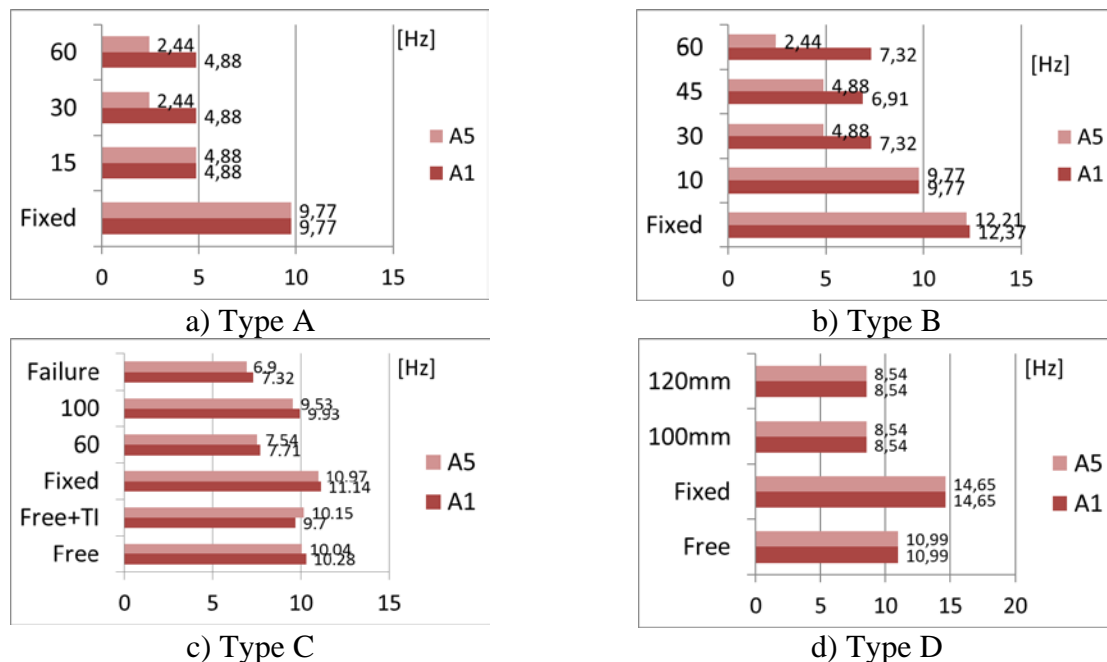


Figure 7: Measured frequencies

Results for damping for all types of chimney systems obtained from the accelerometer A1 (top of the chimney) are presented in the following table. Initial damping is already very high (as it was expected). Due to progression of damage it increases, however for highly damaged chimney ($d=60$ mm), chosen methodology for determination of dampness was not applicable.

Table 3: Evaluated damping (ξ).

| | Type A | | Type B | | Type C | | Type D | |
|----------|--------|------|--------|-------|--------|-------|--------|-------|
| | A1 | A5 | A1 | A5 | A1 | A5 | A1 | A5 |
| | [%] | [%] | [%] | [%] | [%] | [%] | [%] | [%] |
| Initial | 7.3 | 5.9 | 3.0 | 4.4 | 10.1 | 12.58 | 4.65 | 7.20 |
| d=15 mm | 8.0 | 12.2 | 5.5 | 3.7 | - | - | - | - |
| d=30 mm | 12.1 | 14.1 | 8.5 | 5.5 | - | - | - | - |
| d=45 mm | - | - | 9.8 | 12.3 | - | - | - | - |
| d=60 mm | 8.5* | 6.4* | 12.2** | 6.9** | 12.2 | 15.14 | | |
| d=100 mm | - | - | - | - | - | - | 6.02 | 11.15 |

* results are not relevant due to severely cracked specimen

** results are not relevant, damping probably exceeding 30%

SEISMIC BEHAVIOUR AND LIMITS IN EARTHQUAKE PRONE AREAS

In Eurocodes there are no special provisions in respect to evaluation of the behaviour of chimneys as secondary elements attached to primary load bearing structure. In the following main conclusions from ASCE 4-98 are summarized:

- Coupling is not required if the total mass of the secondary system is 1% or less of the mass of the supporting primary structure. If a coupled analysis will not increase the response of the primary system over that of decoupled analysis by more than 10%, then a coupled analysis is not required.
- When coupling is required, a detailed model of the secondary system is not required, provided that the simple model adequately represents the major effects of interaction between the two parts.
- A coupled analysis of the primary-secondary system shall be performed if the static constraints cause significant load redistribution in the primary system.

In order to overcome these problems Vukobratović and Fajfar (2015) have performed numerical simulation of primary and secondary single degree of freedom systems and interpreted their results in the term of floor response spectra (also known as in-structure spectra). In the parametric study inelastic behaviour of the primary structure was considered, while secondary elements were modelled as linear elastic. In the analysis three types of hysteretic behaviour were considered (EP, Q_0 and Q_{10} see Figure 8). Here Q model with ductility (μ) of 2.0 can represent the behaviour of typical masonry single or apartment house. The natural periods of the (primary) structure and of the equipment (the secondary structure) are denoted as T_p and T_s , respectively. The floor acceleration spectra values is denoted as A_s . The peak acceleration of the structure is denoted as A_p .

In Figure 8 amplification factor A_s/A_p in dependence on T_s/T_p for different models and considering response spectra for soil type B according to EC8-1 classification. It may be seen that for resonance, this amplification factor may be high as 5. It may be also found that amplification factor for Type B of maximum acceleration for floor spectra of primary structure for initial (elastic) state is 1.8, while for DL state is 4.2. This is mainly due to the fact that chimney systems in DL state have similar period of vibration as primary structures and resonance is inevitable. In inelastic state due to increased dampness this amplification (AMP) may be significantly lower (Figure 8-b).

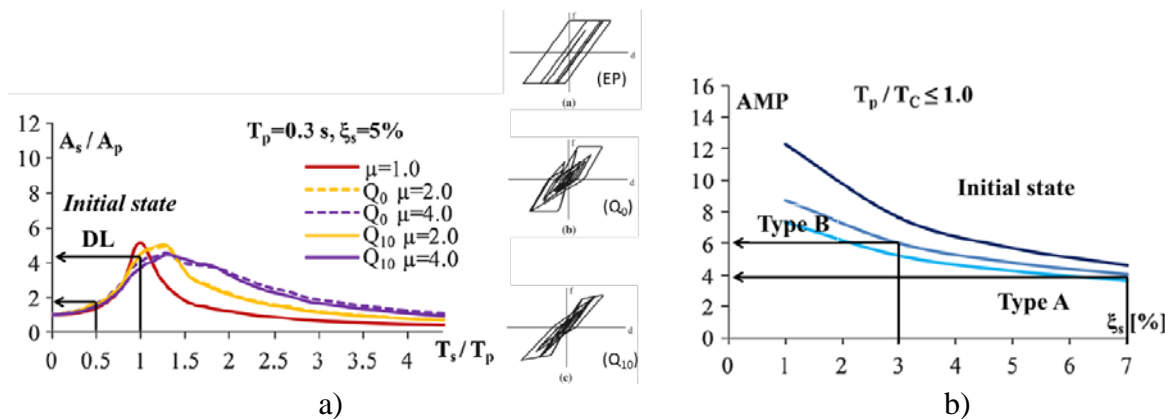


Figure 8: Amplification factors in dependence on performance limits for Type B system for typical masonry house (Q_0 with ductility of 2.0), soil type B a) and Amplification factor for different systems at initial state b) (after Vukobratović et al. 2015)

Considering amplification factors as presented in Figure 8, critical accelerations at floor levels for typical masonry buildings for tested types of chimneys were recalculated and presented in Table 4.

Table 4: Recalculated values for maximum floor accelerations in dependence on the obtained performance limits.

| | H [kN] | W [kg] | A_s [g] | Cor. factor | A_p [g] |
|--------|-----------|-----------|--------------|----------------|--------------|
| Type A | | | | | |
| FC | 1.42 | 287.6 | 0.49 | 4 | 0.12 |
| DL | 2.27 | 237.0 | 0.96 | 4* | 0.24 |
| SD | 1.75 | 130.4 | 1.34 | 4* | 0.34 |
| Type B | | | | | |
| FC | 1.27 | 269.4 | 0.47 | 6 | 0.08 |
| DL | 2.34 | 222.0 | 1.05 | 6* | 0.18 |
| SD | 4.15 | 122.1 | 3.40 | 6* | 0.57 |
| Type C | | | | | |
| FC | - | 316 | - | - | - |
| DL | 10.33 | 130.4 | 7.92 | 4* | 1.98 |
| SD | 6.74 | 130.4 | 5.17 | 4* | 1.29 |
| Type D | | | | | |
| FC | - | 372 | - | - | - |
| DL | 14.12 | 153.5 | 9.20 | 4* | 2.30 |
| SD | 18.68 | 153.5 | 12.17 | 4* | 3.04 |

It may be seen that recalculated values for A_p (regardless the performance limit) may be realistic for top floors of ordinary masonry buildings. On the other hand, obtained values are far higher than adopted values in more recent studies of seismic vulnerability of chimneys (Osteraas et al. 2010; Snoj et al. 2017) though comparable with the results from study of Giaretton et al. (2017) for traditional brickwork chimney systems. It may be also concluded that optimized types of chimney

systems (types C & D) have superb performance in comparison to URM and partly reinforced systems.

CONCLUSIONS

Presence of continuous rebars all along the height of the chimney significantly improve load bearing capacity of the whole system. Presence of continuous reinforcement along all four corners of the masonry units prevented:

- a) the formation of so called plastic hinges at the end of reinforcement and
- b) torsional effect due to asymmetrical reinforcement of the chimney system.

The whole system is stiffer. Failure of improved system occurred at the height of bracing system. This is attributed to the failure of masonry units along the reinforcement at the position of roof hangers. The yielding of hangers occurred before the cracking of masonry units thus provided larger deformations for whole system. This imply that the strength and stiffness characteristics of both masonry units and hanger system are well balanced.

The higher resistance of type D system in comparison to type C can be attributed to the stronger masonry units (higher comp. strength) as well as to the slightly bigger cross-section dimensions. Reinforcement never reached yielding, on the other hand hangers did. Ceramic flue liners and metal spacers stayed undamaged.

ACKNOWLEDGEMENTS

The research work presented herein was carried through industry project financed by industrial partner - Schiedel GmbH Austria and partly co-financed by Slovenian Research Agency through research programme P2-0185.

REFERENCES

ASCE 4-98. (2000), Seismic Analysis of Safety-Related Nuclear Structures.

Bosiljkov V, Antolinc D, Steinecker G & Plaskan S. (2016), Experimental research on the seismic behaviour of contemporary masonry chimney systems. *Proceedings of the 16th International Brick and Block Masonry Conference (IBMAC 2016)*, 26-30 June, Padova, Italy. pp. 2371-2379.

EN 1996-1. (2005), Eurocode 6 – Part 1-1: General rules for reinforced and unreinforced masonry structures, CEN, Brussels, Belgium. June

EN 1998-1. (2003), Eurocode 8: Design of structures for earthquake resistance - Part 1: General rules, seismic actions and rules for buildings; CEN, Brussels, Belgium. June

EN 1998-6. (2005), Eurocode 8: Design of structures for earthquake resistance - Part 6: Towers, masts and chim-neys; CEN, Brussels, Belgium., June

Giaireton, M., Ingham, J.M. & Dizhur D. (2017), Experimental validation of seismic retrofit solutions for URM chimneys, *Bull Earthquake Eng.* DOI 10.1007/s10518-017-0200-0.

Maison, B. and McDonald B. (2017), Analytical study of residential masonry chimney during recent California earthquakes, *16th World Conference on Earthquake Engineering* : January 9th to 13th, Santiago, Chile. pp. 1-12.

Osteraas, J., Krawinkler, H. (2010), FEMA P-58/BD-3.9.7 Background Document, Fragility of Masonry Chimneys, December, U.S. Department of Homeland Security.

Snoj J. & Dolšek M. (2017), Expected economic losses due to earthquakes in the case of traditional and modern masonry buildings. *16th World Conference on Earthquake Engineering* : January 9th to 13th, Santiago, Chile. pp. 1-12.

Vukobratović, V., Fajfar, P. (2015), A method for the direct determination of approximate floor response spectra for SDOF inelastic structures, *Bull Earthquake Eng.* 13/5 pp.1405–1424.



**MASONRY TODAY
AND TOMORROW**

**11 - 14 February, 2018
SYDNEY AUSTRALIA**

www.10amc.com

PULL-OUT TESTING OF NEAR SURFACE MOUNTED STEEL WIRE ROPE IN UNREINFORCED MASONRY

N. A. Misnon^{1,2}, D. Dizhur³, M. Giaretton³ and J. M. Ingham³

¹ PhD Student, Department of Civil and Environmental Engineering, The University of Auckland, 1142 Auckland, New Zealand, nmis681@aucklanduni.ac.nz

² Lecturer, Department of Civil Engineering, Universiti Pertahanan Nasional Malaysia, 57000 Sg Besi, Kuala Lumpur, Malaysia. nooraina@upnm.edu.my

³ Lecturer/Research Fellow/Professor, Department of Civil and Environmental Engineering, The University of Auckland, 1142 Auckland, New Zealand, d.dizhur@auckland.ac.nz; mgia506@aucklanduni.ac.nz; j.ingham@auckland.ac.nz

The use of steel wire rope (SWR) as a near surface mounted (NSM) seismic retrofit technology potentially provides a cost-effective solution to improve the seismic performance of clay-brick unreinforced masonry structures. To establish design guidance for the proposed NSM-SWR technique, the bond strength between SWR and clay-brick substrate was investigated by means of a series of pull-out tests. Various parameters were investigated, including SWR diameter, groove dimensions, SWR bonded length, and adhesive type (i.e., epoxy, cement-based grout, and lime-based grout). NSM-SWR was adhered to an assemblage of solid clay bricks and subjected to monotonic pull-out tests. Pull-out strength and displacement response were investigated using parametric analysis, and the results are presented herein.

Keywords: *Near surface mounted, steel wire rope, bond strength, pull-out test, seismic retrofit technique, unreinforced masonry*



INTRODUCTION

Seismic retrofit technologies for existing unreinforced masonry (URM) buildings continue to evolve to meet demand for improved seismic resistance and to reduce the high seismic vulnerability of these buildings. The use of steel wire rope (SWR), also known as steel cables, is one such innovative retrofit technique that has recently gained interest among researchers due to its advantages of high strength and ductility and reduced cost when compared to other materials. SWR consists of several strands of metal wire twisted into a helix and is used for dynamic (lifting and hoisting in cranes and elevators) or static applications (supporting structures such as suspension bridges or towers). SWR is available in a wide range of diameters from the smallest size being 1.5 mm, up to a maximum diameter of 60 mm, with corresponding ultimate tensile strengths ranging between 1.5 kN and 2103 kN and hence has great potential as reinforcement for existing buildings.

Studies have been previously conducted to investigate the performance of URM structures that were retrofitted with SWR using both unbonded and mechanically bonded techniques and it was established that the use of unbonded SWR to strengthen URM walls results in improved in-plane strength, ductility, and energy dissipation capacity (Chuang et al., 2004; Yang et al., 2012). Chuang et al. (2004) demonstrated that adding two diagonal unbonded 10 mm diameter SWR across one side of a URM wall face resulted in the measured strength capacity being doubled when compared to the strength of the unretrofitted walls. A similar finding was reported by Yang et al. (2012), who used a practical retrofit system comprising of unbonded prestressed wire rope to significantly improve the in-plane shear strength and ductility of URM walls.

Another method is the use of SWR that is mechanically bonded to masonry elements which were subjected to both out-of-plane and in-plane testing. Hračov et al. (2015) installed mechanically fastened SWR in a diagonal configuration on earth brick walls and achieved almost twice the ultimate lateral force and ductility that was recorded for unretrofitted walls. The use of SWR in a 'reticulatus' technique, which consists of adapting a reinforcing mesh to the joint system of irregular stone types with the aim of confining the masonry units, increased compression and flexural capacity of the tested walls (Csikai et al., 2014).

The near surface mounted (NSM) technique has recently received attention by researchers and practitioners because of its easy installation, minimal intrusiveness to building appearance, and ability to allow strengthening products to experience large stresses before failure. Fibre reinforced polymer (FRP) and steel bars are among the most commonly used retrofit products for the NSM technique. These products are typically inserted into a vertical groove cut on the surface of a masonry wall. Recent research addressing the performance of NSM applications (Dizhur et al., 2014; Konthesingha et al., 2014) has shown significant improvements in the behaviour and structural integrity of retrofitted elements. For example, the use of NSM carbon fibre rope resulted in significant increases in loading capacity, deformability, and energy dissipation (Korany and Drysdale, 2004).

The experimental campaign presented herein explored the combined use of the NSM and SWR techniques, known as NSM-SWR. The bond behaviour between substrate and wire rope installed using different adhesive materials (i.e., epoxy, cement-based grout (CBG), and lime-based grout (LBG)) was investigated in terms of capacity and effectiveness. Sixty pull-out tests of NSM-SWR

were undertaken under monotonic loading on 20 masonry assemblages. The influence of the following parameters on the bond stress-slip relationship was studied: SWR diameters, d_r (4 mm, 6 mm, 8 mm and 10 mm); groove dimensions, d_g (varied from $1.5d_r$ to $3.0d_r$); bonded length, l_b (160 mm, 180 mm and 200 mm); and type of adhesive (epoxy, CBG, and LBG).

EXPERIMENTAL PROGRAM

Twenty clay-brick masonry assemblages with approximate dimensions of 225 mm (width) x 230 mm (length) x 265 mm (height) were constructed for use as substrate for the NSM-SWR technique. Three NSM-SWR samples (SWR and adhesive) were installed on each masonry assemblage (one per face) and individually subjected to monotonic pull-out testing. A total of 60 pull-out tests were conducted in accordance with ACI 440.3R-04 (2004) standards. Parameters investigated include SWR rope diameter (4, 6, 8, 10 mm), groove depth ratio (1.5 to 3.0), SWR bonded length, and adhesive type (epoxy, CBG, LBG).

Material properties

The clay-brick masonry assemblages (or cubes) were constructed using recycled clay bricks acquired in the wider Auckland region of New Zealand. Each brick cube was built with six clay bricks, grouped based on a physical scratch test (NZSEE, 2017), and 15-mm mortar joints. The bricks were classified into two groups—Type *A* and Type *B*—based on the compressive strength of the bricks (Table 1). A mortar mix with a ratio of 1:2:9 (cement: lime: sand by volume) was chosen as representative of existing masonry buildings in New Zealand (Russell and Ingham, 2010). Table 1 summarises the mechanical properties of the clay brick, mortar mix, and masonry assemblages determined by laboratory tests. Compression tests of 50x50x50 mm mortar cubes and half bricks were undertaken in accordance with ASTM C109 (2008) and ASTM C67 (2017), respectively. The compressive strength of the masonry assemblages was identified according to ASTM C1314 (2016).

Table 1: Mechanical properties of masonry assemblages

| Brick | | | | | Mortar | | | Masonry |
|----------|--------------|--------------|-----|------|--------------|-----|------|--------------|
| Type | Scratch test | f'_b (MPa) | n | COV | f'_j (MPa) | n | COV | f'_m (MPa) |
| <i>A</i> | Hard | 32.8 | 7 | 0.27 | 2.20 | 21 | 0.53 | ≥ 10 |
| <i>B</i> | Medium | 23.6 | 7 | 0.36 | | | | < 10 |

f'_b = compression strength of clay brick

f'_j = compression strength of mortar

f'_m = compression strength of masonry assemblages

n = number of samples

Galvanized wire strand core (WSC) stainless-steel wire rope, grade 1770, with various diameters, 4 mm, 6 mm, 8 mm, and 10 mm was used for the SWR. Table 2 reports the mechanical properties of the SWR provided in the manufacturer's specifications. Table 3 provides the properties of the three adhesives (i.e., epoxy, CBG, LBG) used during testing provided in the manufacturer's specifications.

Table 2: Mechanical properties of SWR

| Diameter d_r (mm) | Breaking load (kN) | Elongation (mm) |
|------------------------|-----------------------|-----------------|
| 4 | 11.4 | 28.8 |
| 6 | 21.1 | 43.2 |
| 8 | 40.3 | 51.0 |
| 10 | 63.0 | 64.0 |

Table 3: Mechanical properties of adhesive from specification

| Adhesive | Compression strength (MPa) | Shear strength (MPa) |
|--------------------|-------------------------------|-------------------------|
| Epoxy | > 70 | > 10 |
| Cement-based grout | 37.7 | - |
| Lime-based grout | >15 | 0.15 |

Specimen preparation

The SWR was installed on the assemblages after the masonry was cured for 28 days with arrangements as shown in Figure 1. Prior to installation, the SWR were formed into loops to ensure grip with the hydraulic pull-out testing machine. The loops were made in accordance with guidelines provided by the supplier, which state that each loop must have at least three wire grips and a distance six times the diameter of the SWR ($6d_r$). The wire grip must be installed with an appropriate orientation, as shown in Figure 2a. The SWR were cut into designated lengths and cleaned with grease remover to improve the bond with the adhesive.

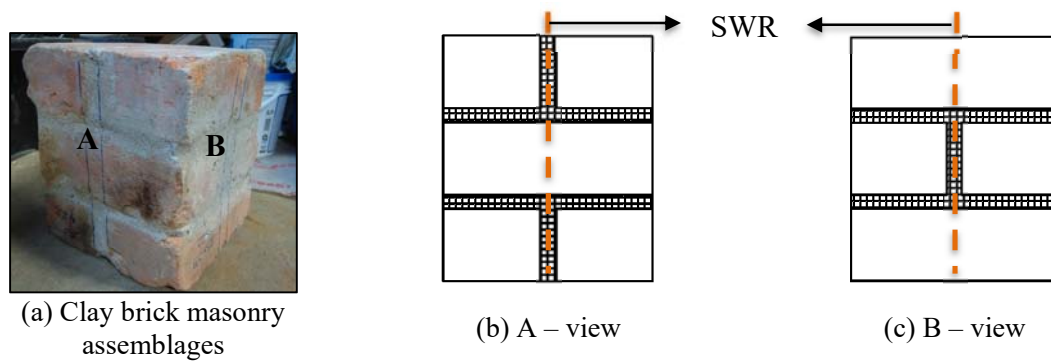


Figure 1: Installation of SWR on clay brick masonry

A groove was cut at the centre of face of the masonry assemblages using a wet-cutting circular saw with a diamond-coated 3-mm-thick blade. Prior to SWR installation, the grooves were cleaned using compressed air and brushed with acetone to remove unnecessary dust that could affect the bond between the adhesive and substrate. Subsequently, the SWR were mounted on the masonry assemblages with adhesive. The bonded length of each SWR from the cube surface was marked and measured (see Figure 2b). Following installation, the specimens were air cured for up to 7 days for epoxy and 28 days for CBG and LBG. Each SWR specimen was installed on a different side of

the masonry assemblage after completing the previous test in order to verify the good condition of the masonry assemblage prior each SWR installation and performing a new test.

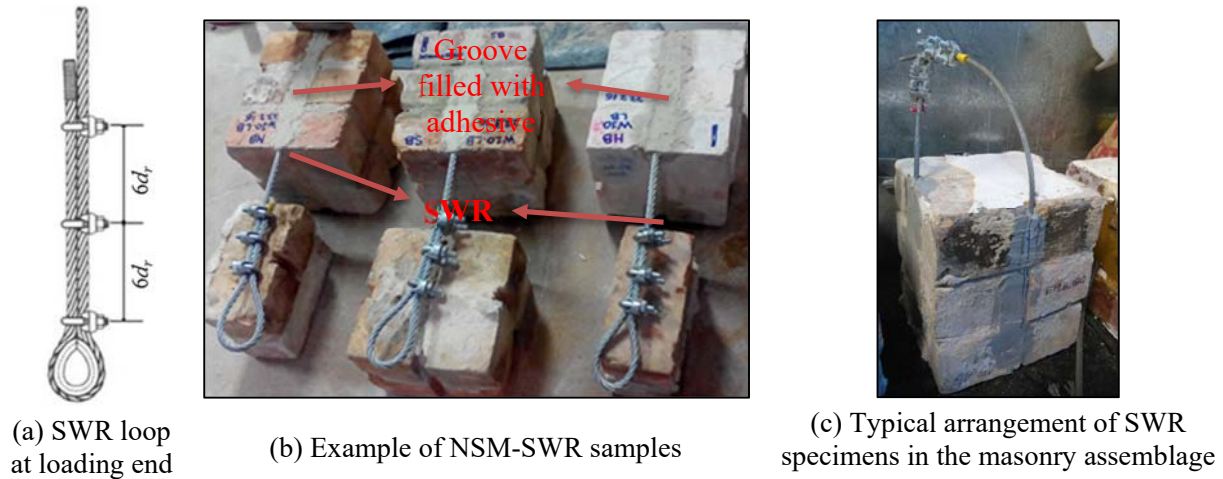


Figure 2: NSM-SWR specimens

Pull-out test set-up

The pull-out tests were performed using a material testing system (MTS) machine with a capacity of 300 kN. Each specimen was centred under loading point of the testing machine in order to ensure no eccentricity occurs during pull-out testing. A clamping system designed to hold the specimens was tightened before each test. The pull-out load was applied to the SWR at a rate of 0.05 mm/s and measured with the electronic load cell of the testing machine. The loaded slip was measured with two linear variable differential transducers (LVDTs). A data acquisition system recorded the data. Figure 3 shows the pull-out test set-up.

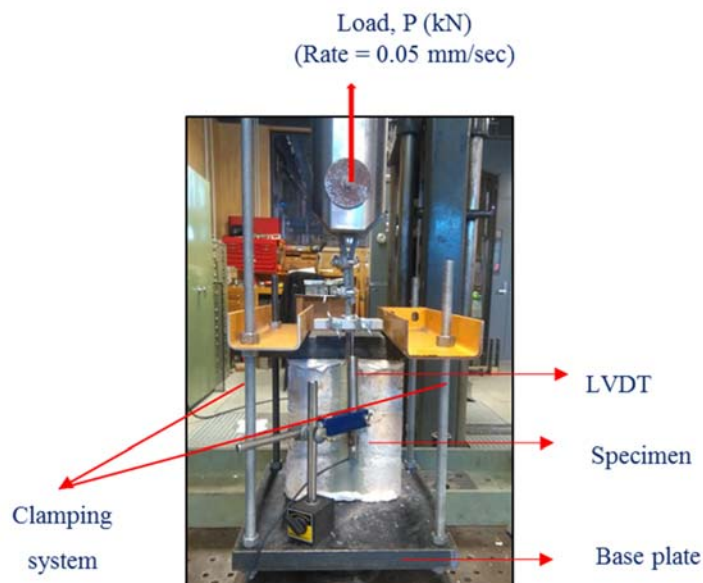


Figure 3: Pull-out test set-up

TEST RESULTS AND DISCUSSION

Typical pull-out load-displacement (L-D) curves were determined from the collected data, and three main regions—SWR twisting (A), full tensioning (B) and failure (C)—were identified in relation to the response stages of the NSM-SWR system. Region (A) corresponds to the initial stage in which the SWR began to twist due to the pull-out loading because of its physical form, which comprises several twisted wire strands. After the SWR was in full tension, an interaction within the retrofit system between the SWR and substrate occurred at region (B). At region (B), the SWR was fully tensioned until it reached the maximum load capacity of the system. Dropping of the load and system failure corresponds to region (C). The system still carried some load due to the existing mechanical bond between the SWR and adhesive. Following the peak loading, the SWR resisted the applied load and “unscrewing” itself from the adhesive resulting in the fluctuation of the load visible in region (C). This response was observed until the total pull-out of SWR occurred.

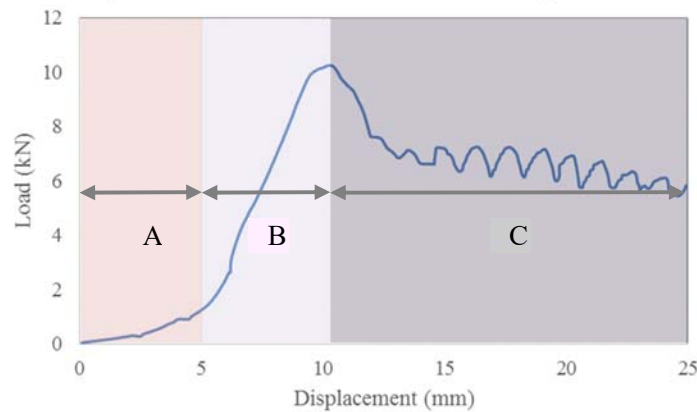


Figure 4: Typical load-displacement curve (sample E12-8-180 (16/16))

Failure modes and test results

Two pull-out failure modes were identified: (i) bond failure at the SWR-to-adhesive interface (SA, see Figure 5a) and (ii) bond failure at the adhesive-to-substrate interface (AG, see Figure 5b). The SA failure mode was observed as a critical failure mode, with about 88% (53 out of 60) exhibiting a similar failure. The SA failure mode was further subdivided into two categories: (a) pull-out failure (PO), and (b) splitting of adhesive (AF). SA failure initiated with crack formation at the top of the loaded end and propagated down the brick cube with increasing applied axial force with either pull-out of the SWR (PO) or sudden detachment of adhesive (AF) at maximum displacement of the tested specimen.

Similar to SA failure, AG failure initiated with crack formation at the top of the loaded end, and sudden detachment of a cone-shaped piece of mortar (Figure 5c) was observed after the maximum load was reached. Due to low mortar strength (2.2 MPa), AG failure was critical for the SWR length installed at the mortar part of the masonry assemblages. SA and AG failure modes can occur as pure interfacial failure due to insufficient mechanical interlocking between the SWR-to-adhesive interface and the adhesive-to-substrate interface, respectively. Table 4 presents the characteristics of each tested specimen and the maximum load applied. The following sections discuss the results.

The subsequent discussion of the influence of bonded length and groove embedment emphasises specimens with epoxy adhesive.

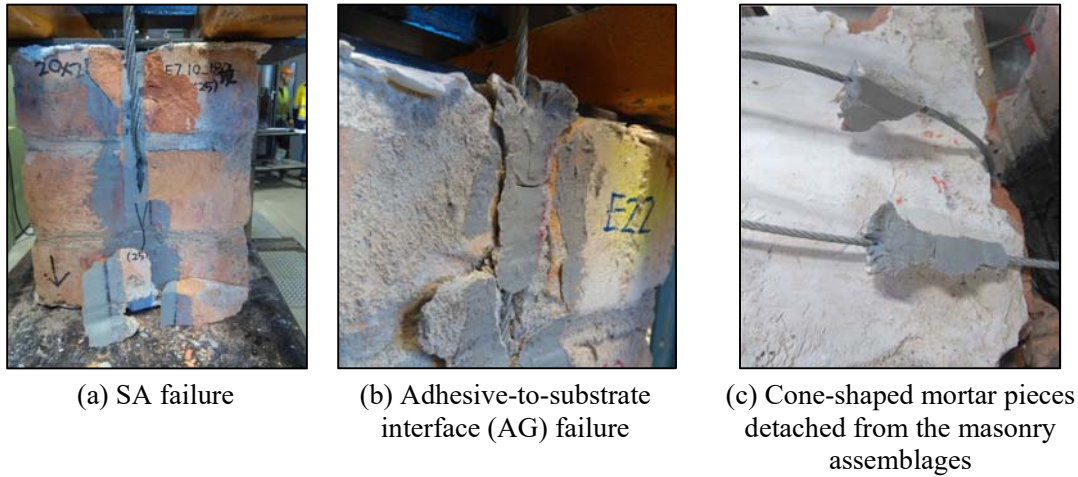


Figure 5: Failure modes observed in specimens following monotonic pull-out testing

Table 4: Geometry of specimens and test results

| Adhesive | Rope diameter, d_r (mm) | Groove embedment, d_g/d_r (mm) | Number of samples* | Average max load, P_{avg} (kN) | CoV (-) | Failure mode |
|----------|---------------------------|----------------------------------|--------------------|----------------------------------|---------|---------------|
| Epoxy | 10 | 1.5 | 3 | 16.29 | 0.09 | SA (3) |
| | | 2.0 | 3 | 15.93 | 0.23 | SA (3) |
| | | 2.5 | 3 | 16.46 | 0.16 | SA (3) |
| | 8 | 2.0 | 3 | 11.79 | 0.13 | SA (2) AG (1) |
| | | 2.5 | 3 | 10.29 | 0.14 | SA (3) |
| | 6 | 2.0 | 3 | 12.54 | 0.17 | SA (1) AG (2) |
| | | 2.5 | 3 | 16.14 | 0.18 | SA (2) AG (1) |
| | 4 | 2.5 | 3 | 8.18 | 0.26 | AG (3) |
| | | 3.0 | 3 | 9.67 | 0.04 | SA (3) |
| CBG | 10 | 1.5 | 3 | 6.48 | 0.57 | SA (3) |
| | | 2.0 | 3 | 2.06 | 0.05 | SA (3) |
| | | 2.5 | 3 | 7.98 | 0.21 | SA (3) |
| | 8 | 2.0 | 3 | 4.19 | 0.25 | SA (3) |
| | | 2.5 | 4 | 3.54 | 0.48 | SA (4) |
| | 6 | 2.0 | 3 | 2.23 | 0.00 | SA (3) |
| | | 2.5 | 3 | 2.42 | 0.04 | SA (3) |
| | 4 | 2.5 | 3 | 2.65 | 0.09 | SA (3) |
| | | 3.0 | 3 | 2.09 | 0.50 | SA (3) |
| LBG | 10 | 1.5 | 3 | 4.46 | 0.14 | SA (3) |
| | 8 | 2.0 | 2** | 0.69 | 0.64 | SA (2) |

*Bonded length tested for each sample type: 160 mm (1), 180 mm (1) and 200 mm (1)

**Samples with 160-mm and 180-mm bonded length only

(#) = Number of samples presenting a particular failure mode

Effect of adhesive/filler and of SWR diameter

Figure 6 plots the (average) maximum load recorded for each type of sample in relation to SWR diameter and adhesive type. Masonry assemblages retrofitted using epoxy adhesive showed higher performance than those strengthened with CBG or LBG. The ultimate load of epoxy specimens was typically higher than that of CBG and LBG specimens (see Table 4), with the difference greater than 65% when considering the same variables. These results may be due to more effective mechanical interlocking between epoxy and SWR compared to CBG and LBG. During pull-out tests, both CBG and LBG samples exhibited a lack of substrate-to-SWR anchorage, and most of the specimens exhibited PO failure. Another factor that may have affected the poorer performance of the CBG and LBG specimens is the tendency of CBG and LBG to expand. This may have resulted in transverse cracks due to shrinkage at the surface of the adhesive pastes along the bonded length of the SWR after the hardening process.

Increasing the SWR diameter generally resulted in increased P_{max} for all types of adhesive. A larger diameter results in more interfacial contact area between the SWR and adhesive, resulting in more bond interaction as well as effect of stronger in the NSM-SWR retrofit system. Further tests are currently underway to investigate the possible influence of brick strength to bond strength of the NSM-SWR retrofit system.

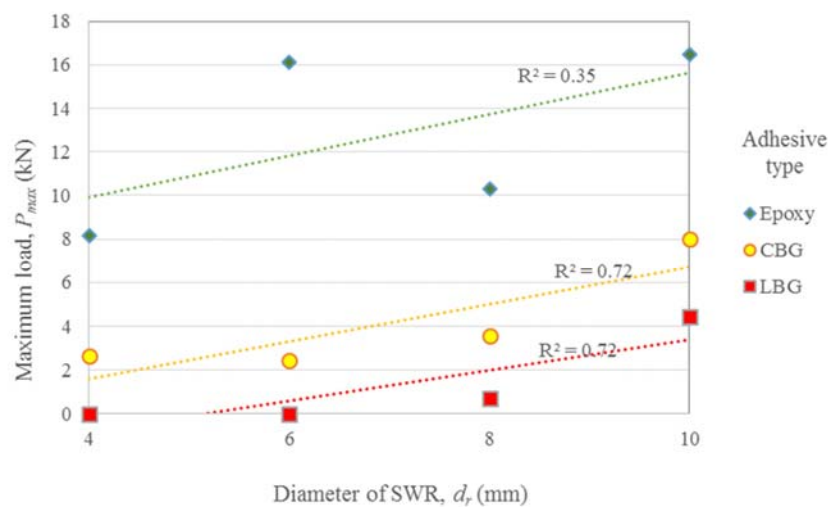


Figure 6: Influence of adhesive type and SWR diameter for specimens with $d_g/d_r = 2.5$

Effect of bonded length on bond strength

Experimental tests were carried out to investigate the effect of the bonded length of the SWR. All variables were kept constant except for SWR diameter and bonded length, l_b . Three bonded lengths (160 mm, 180 mm, and 200 mm) of SWR were mounted. For a given depth of the groove embedment ratio, $d_g/d_r = 2.5$, it was observed that maximum load increased as bonded length increased (Figure 7), with the rate of increment up to 30% for all SWR diameters.

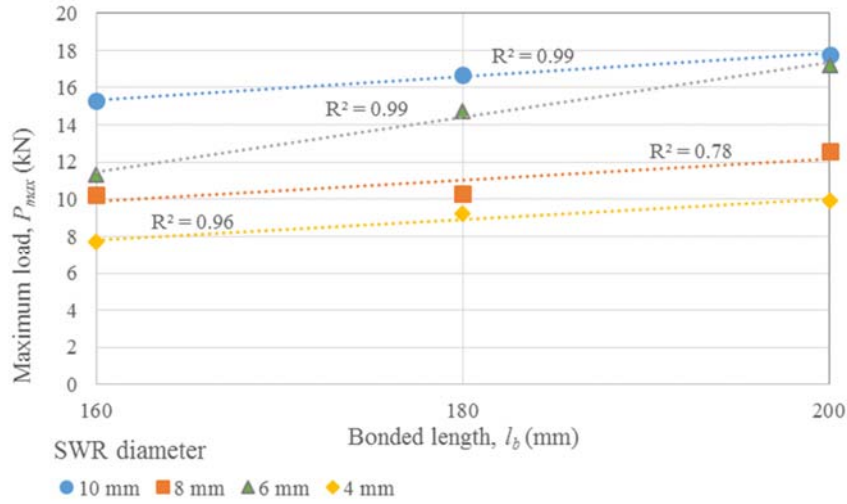


Figure 7: Variation of the maximum load by bonded length for specimens with epoxy adhesive ($d_g/d_r = 2.5$)

Effect of groove embedment on bond strength

The effect of the groove embedment on the SWR-to-masonry bond was studied as a part of the experimental program. The geometry of groove embedment, d_g , was designed according to the SWR diameter, d_r , ($1.5d_r - 3.0d_r$, see Table 4) in order to maximize the bonded area between SWR and adhesive minimising the intrusion of the strengthening intervention into the masonry. The effect of groove embedment is presented as average bond stress, τ , by considering the bonded length, l_b , of the specimens mounted on the masonry assemblages. The bond stress is computed as in Equation 1 below:

$$\tau = \frac{P_{max}}{\pi d_r l_b} \quad (1)$$

where P_{max} is the maximum applied load, d_r is the SWR diameter, and l_b is the bonded length. Figure 8 shows average bond stress results of the specimens with epoxy adhesive. The average bond stress linearly decreased with an increase of the groove embedment ratio, d_g/d_r , for all SWR diameters. This may be due to the non-uniform distribution of the bond stresses along the bonded length. Similar findings were reported for pull-out test of NSM-FRP rods by De Lorenzis et al. (2002).

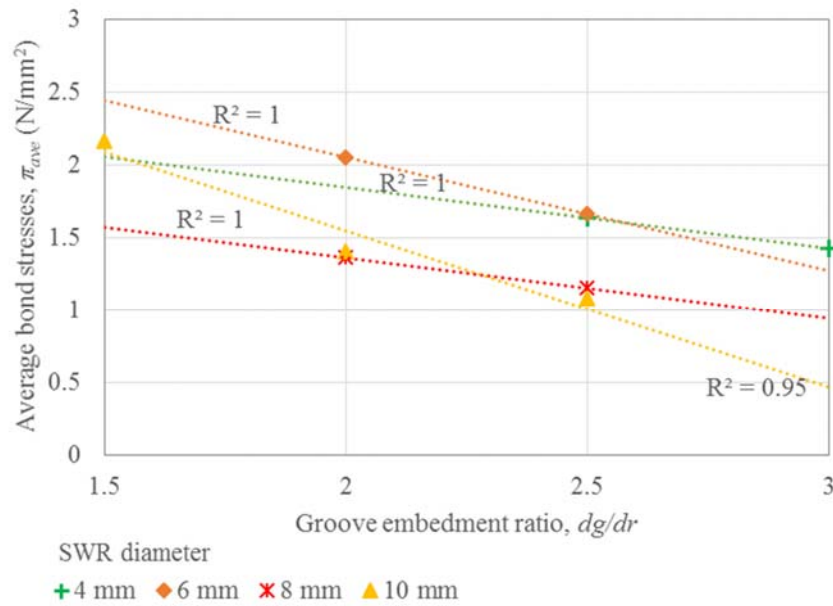


Figure 8: Effect of groove embedment for specimens with epoxy adhesive

CONCLUSIONS

Sixty monotonic pull-out tests were undertaken to investigate the bond performance of the NSM-SWR strengthening technique. The results of the experimental program led to the following conclusions:

- Three regions were identified in the typical load-displacement (L-D) curve in response to the pull-out loading of NSM-SWR: (A) SWR twisting, (B) full tensioning, and (C) failure.
- Two bond failure modes were identified: (SA) SWR-to-adhesive interface and (AG) adhesive-to-substrate interface. The primary mode of failure was SA (53 out of 60 specimens).
- Effectiveness of the bond strength between SWR and masonry assemblages relies on the studied parameters, namely adhesive type, SWR diameter, bonded length, and groove embedment.
- The bond strength of NSM-SWR with epoxy achieved a higher pull-out load than samples with CBG or LBG.
- Increasing the SWR diameter resulted in increased pull-out load value.
- The pull-out load increased up to 30% with an increment of the bonded length.
- The bond stresses decreased with an increment of the groove embedment ratio.

ACKNOWLEDGEMENTS

The authors gratefully acknowledge the assistance of staff in the structural laboratory of the University of Auckland, and to Standen's and MAPEI for material support throughout the research. The Ministry of Education, Malaysia is also thanked for supporting Aina Misnon's PhD study at the University of Auckland.

REFERENCES

- ACI. (2004). 440.3 R-04: Guide Test Methods for Fiber-Reinforced Polymers (FRPs) for Reinforcing or Strengthening Concrete Structures. American Concrete Institute, Farmington Hills, USA.
- ASTM. (2017). C67-17. Standard Test Methods for Sampling and Testing Brick and Structural Clay Tile, ASTM International, West Conshohocken PA.
- ASTM. (2008). C109/C109M. Standard Test Method for Compressive Strength of Hydraulic Cement Mortars (Using 2-in. or 50-mm Cube Specimens), ASTM International, West Conshohocken PA.
- ASTM. (2016). C1314-16. Standard Test Method for Compressive Strength of Masonry Prisms, ASTM International, West Conshohocken PA.
- Chuang, S., Zhuge, Y., & McBean, P. C. (2004). Seismic retrofitting of unreinforced masonry walls by cable system. In *13th World Conference on Earthquake Engineering*, August 1-6, Vancouver, BC, Canada.
- Csikai, B., Ramos, L. F., Bastos, P., Moreira, S. M. T., & Lourenço, P. B. (2014). Flexural out-of-plane retrofitting technique for masonry walls in historical constructions. In *SAHC2014–9th International Conference on Structural Analysis of Historical Constructions*.
- De Lorenzis, L., Rizzo, A., & La Tegola, A. (2002). A modified pull-out test for bond of near-surface mounted FRP rods in concrete. *Composite Part B: Engineering*, 33(8), pp. 589-603.
- Dizhur, D., Griffith, M., & Ingham, J. (2014). Out-of-plane strengthening of unreinforced masonry walls using near surface mounted fibre reinforced polymer strips. *Engineering structures*, 59, pp. 330-343.
- Hračov, S., Pospíšil, S., Garofano, A., & Urushadze, S. (2016). In-plane cyclic behaviour of unfired clay and earth brick walls in both unstrengthened and strengthened conditions. *Materials and Structures*, 49(8), pp. 3293-3308.
- Konthesingha, K. M. C., Masia, M. J., Petersen, R. B., & Page, A. W. (2014). Experimental evaluation of static cyclic in-plane shear behavior of unreinforced masonry walls strengthened with NSM FRP strips. *Journal of Composites for Construction*, 19(3), pp. 1-15.

Korany, Y., & Drysdale, R. (2004). Enhancing seismic flexural resistance of historic masonry walls using carbon fiber rope. *Mas Soc J*, 22(1), pp. 27-38.

NZSEE (2017). *The Seismic Assessment of Existing Buildings. Part C8: Seismic Assessment of Unreinforced Masonry Buildings*. New Zealand: New Zealand Society for Earthquake Engineering.

Russell, A. P., & Ingham, J. M. (2010). Prevalence of New Zealand's unreinforced masonry buildings. *Bulletin of the New Zealand Society for Earthquake Engineering*, 43(3), pp. 182.

Yang, K. H., Joo, D. B., Sim, J. I., & Kang, J. H. (2012). In-plane seismic performance of unreinforced masonry walls strengthened with unbonded prestressed wire rope units. *Engineering structures*, 45, pp. 449-459.



**MASONRY TODAY
AND TOMORROW**

**11 - 14 February, 2018
SYDNEY AUSTRALIA**

www.10amc.com

IN-PLANE TILT TESTS ON DRY STACK MASONRY WALLETES

N. Mojsilović¹ and M. Petrović²

¹ Senior Scientist, Institute of Structural Engineering, ETH Zurich, 8093 Zurich, Switzerland,
mojsilovic@ibk.baug.ethz.ch

² PhD Student, Institute of Structural Engineering, ETH Zurich, 8093 Zurich, Switzerland,
petrovic@ibk.baug.ethz.ch

A research project on the structural behaviour of dry stack masonry wallettes subjected to in-plane base rotation (tilting) is underway at the Institute of Structural Engineering of ETH Zurich. The main goal of the research project is to investigate the influence of bond, aspect ratio and pre-compression level on the behaviour of wallettes. Load tests on two series of dry stack clay brick masonry elements have been completed. The first series consisted of nine wallettes built in running bond and the second one consisted of six wallettes built in stack bond. The length of the specimens was 1200 mm and the thickness of the elements was 115 mm. Three different aspect ratios (height to length of the wall) were considered for the first series, namely 0.5, 1 and 1.5. For the second series only two aspect ratios, namely 0.5 and 1 were considered. Due to the lateral instability of the stack bond wallettes during base rotation it was not possible to perform tests on wallettes with an aspect ratio of 1.5. For both test series three different pre-compression levels of vertical (gravity) load were applied (0, 0.05 and 0.10 MPa). After assembling the specimens on the steel girder base, this was rotated up to failure. Both shear sliding and overturning failure modes were observed. This paper presents the preliminary results of the load tests and discusses the structural behaviour of dry stack masonry elements. A number of conclusions as well as recommendations for future research are given.

Keywords: *dry stack masonry, load tests, masonry, stack bond, tilt test.*

INTRODUCTION

A research project is underway at the Institute of Structural Engineering to investigate the structural behaviour of unreinforced dry stack clay brick masonry wallettes subjected to in-plane base rotation (tilting). The main goal of the experimental part of the research project is to investigate the influence of masonry bond, aspect ratio (height h_w to the length l_w of the wall) and applied pre-



compression (σ_{pc}) on wallettes behaviour. To investigate this, a total of 15 tilting tests have been conducted. These tests are described in the present paper.

Previous experimental research work in this area included tests on dry-stack masonry elements subjected to in-plane and out-of-plane tilting, see e.g. Baggio and Trovalusci (1993), Uzoegbo et al. (2007), Vélez and Magenes (2009), Vasconcelos and Lourenço (2009), Jimenez (2011), Vélez et al. (2014), Casapulla and Portioli (2015). In the referenced work different failure modes have been reported, mainly in-plane sliding and in- and out-of-plane overturning. Some of the work also reported hybrid (a combination of the previously mentioned) failure modes. It should be noted here that majority of the referenced investigations were performed either on small or on scaled masonry elements, whilst the findings presented in this paper have been obtained from tests on full-scale elements.

TESTING PROGRAMME AND MASONRY MATERIALS

Load tests on two series of dry stack clay brick masonry elements have been completed. An overview of the testing programme is given in Table 1. The first series consisted of nine wallettes built in running (R) bond and the second one consisted of six wallettes built in stack (S) bond, see Figure 1.

Table 1: Testing programme and specimen designation

| h_w/l_w | σ_{pc} | | | σ_{pc} | | |
|-----------|---------------|------|-----|---------------|------|-----|
| | 0 | 0.05 | 0.1 | 0 | 0.05 | 0.1 |
| 0.5 | AR1 | AR2 | AR3 | AS1 | AS2 | AS3 |
| 1.0 | BR1 | BR2 | BR3 | BS1 | BS2 | BS3 |
| 1.5 | CR1 | CR2 | CR3 | - | - | - |

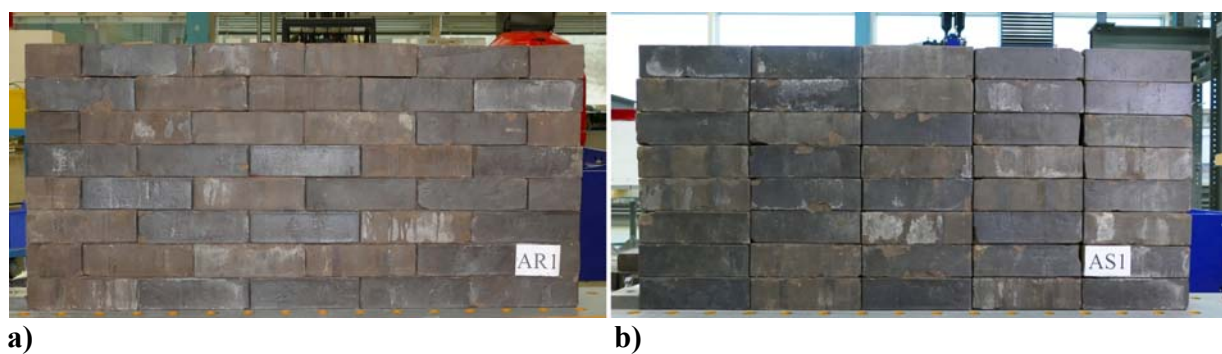



Figure 1: Masonry bond: (a) running and (b) stack bonds

The length of the specimens was 1200 mm and the thickness of the elements was 115 mm. Three different aspect ratios were considered: 0.5 (A), 1.0 (B) and 1.5 (C), thus resulting in the specimens' height of 600 mm, 1200 mm and 1800 mm, respectively. For the second series only two aspect ratios, namely 0.5 and 1 were considered. Due to the lateral instability of the stack bond wallettes

during base rotation it was not possible to perform tests on wallettes with an aspect ratio of 1.5, i.e. height of 1800 mm. Further, three different values of the vertical (gravity) load, σ_{pc} , were applied: self-weight only (designation 1), and additional pre-compressions of 0.05 MPa (designation 2) and 0.1 MPa (designation 3), see Table 1.

Table 2 gives information on the properties of the clay brick unit that was used. The unit's compressive strength, f_b , its dimensions and the weight are presented. The unit's dimensions and weight were determined on 20 specimens. The values given are mean values and the corresponding standard deviation is given in parenthesis.

Table 2: Brick properties

| Unit | Shape | Width [mm] | Height [mm] | Length [mm] | Weight [N] |
|---------|---|-------------|-------------|-------------|-------------|
| VHLZ NF |  | 114.7 (0.3) | 70.8 (0.3) | 240.5 (0.6) | 441.0 (3.0) |

The angle of friction in the bed joint has been determined from the tests on small, two courses high specimens, see Figure 2. Three different specimens were considered and for each of them ten tests were performed. The mean value obtained from the tests on the specimen in running bond (RB) was 32.26° with a corresponding standard deviation of 2.09° . From two different sets of the specimens built in stack bond (SB 1 and SB 2, cf. Figure 2) the mean values of 31.65° and 31.08° were obtained. The corresponding standard deviations were 2.66° and 1.75° , respectively.

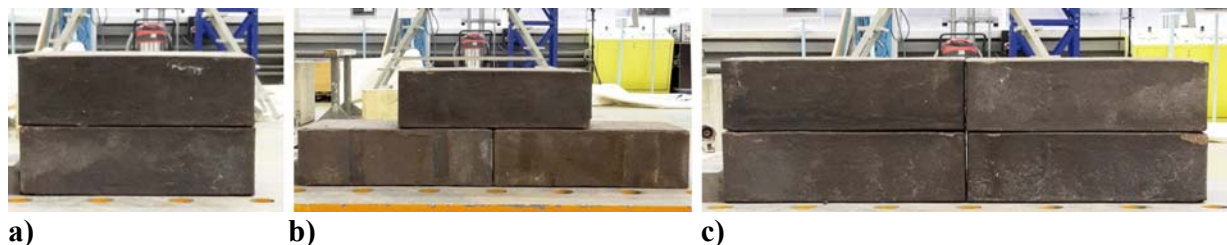


Figure 2: Determination of the angle of friction: (a) RB; (b) SB 1; (c) SB 2

TEST SET-UP

The test set-up is shown in Figure 3. A rotation joint (2) was installed on the base plate (1), which was fixed to the strong floor. The south end of the steel beam (3) was supported by the rotation joint, while the north end was hung on the chain (4), which was used to rotate the beam, i.e. the test specimen (6). To avoid the sliding between the lowest course of the wall and the steel beam, a stopper (5) was fixed on the south side of the wall. The additional weight, which consisted of the upper steel beam (7) and two steel elements (8) and (9) was placed centrally on the top of the specimen. The weights (8) and/or (9) were fixed to the beam (7) using threaded bars, and thus

elements (7) to (9) acted together as a rigid body. In order to enhance the friction between the beam (7) and the specimen, sandpaper was placed between them. During the tests, the weights were secured by the crane and an auxiliary lateral support was mounted to keep the weights in-plane with the wall. To minimize the friction between weights and lateral support Teflon strips were fixed on the side of the weights.

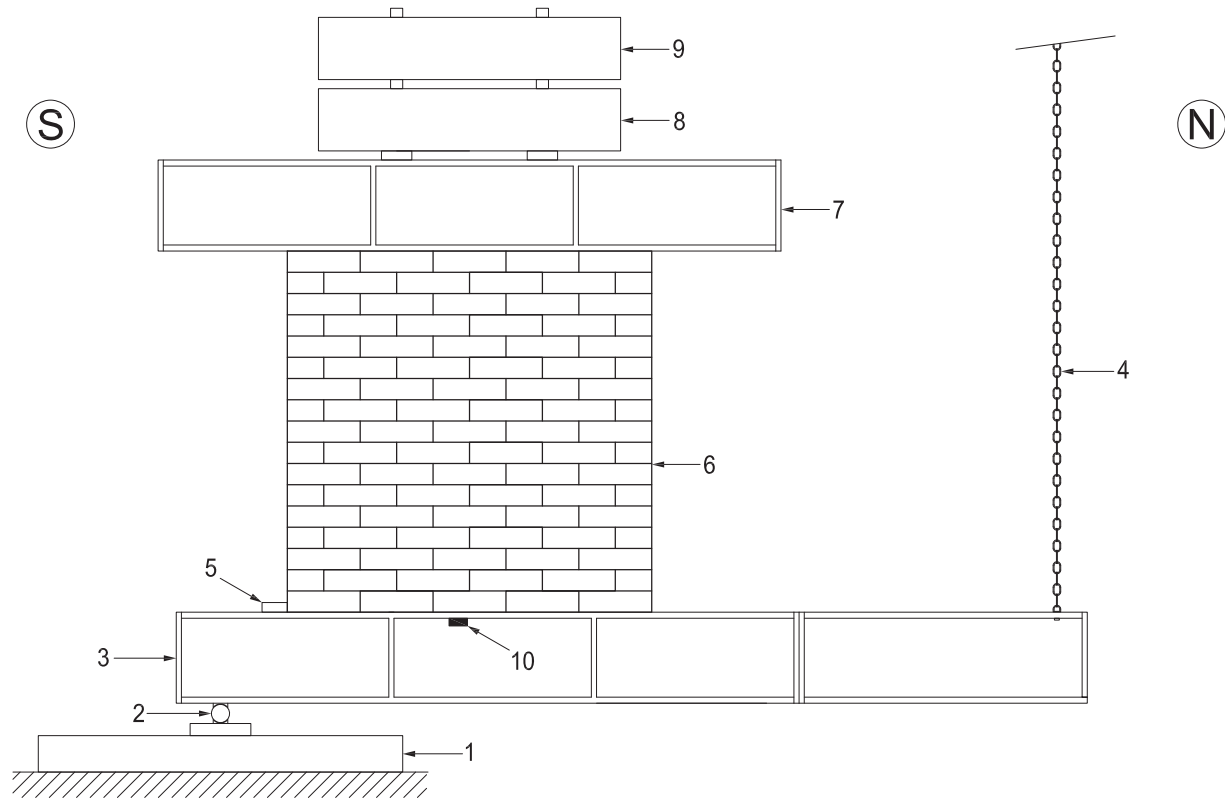


Figure 3: Test set-up

A tilt testing procedure included the following steps: (i) building, i.e. assembling of the wallette on the horizontally placed lower beam; (ii) if needed, loading the specimen with additional weight; (iii) zeroing the instruments, and (iv) slowly increasing the rotation angle α by pulling the chain until the failure of the specimen. Rotation speed was controlled by hand and was kept as even as possible during testing (1 to 2°/min). In some cases, a test had to be repeated due to out-of-plane failure, which was usually caused by the imperfect construction of the dry-stack wall. In detail, due to the production process of the brick's, which includes burning of the clinker stone followed by cooling, the bricks surface was not even, i.e. planar. For this reason, the stack bond specimens with aspect ratio 1.5 could not be performed, since it was not possible to construct such high wallettes. The failure of the wallettes always occurred along the joints and thus the same bricks could be repeatedly used for the construction of the specimens.

Two inclinometers (10) were fixed on both east and west sides of the lower beam and were used to measure the rotation angle, α . The measured data has been recorded continuously. In order to document the tests, a video camera was used to record the experiment and still photos were taken

before the start of each test and after the failure. Since, the only force acting on the wall was the gravity force, which is decomposed into normal and shear force (as a function of α) there was no need for additional force measurements.

TEST RESULTS AND DISCUSSION

Table 3 shows the values of the rotation angles at failure obtained from tests. The average value of both (east and west side) angle measurements is presented. Further, the type of failure is given: shear (S) or overturning, i.e. tilting (T). These two failure modes are shown in Figure 4 for specimens BR3 and AR3.

Table 3: Angle of rotation at failure (in degrees)

| h_w/l_w | σ_{pc} | | | σ_{pc} | | |
|-----------|---------------|-----------|-----------|---------------|-----------|-----------|
| | 0 | 0.05 | 0.1 | 0 | 0.05 | 0.1 |
| 0.5 | 30.54 (S) | 29.53 (S) | 28.00 (T) | 24.33 (S) | 19.22 (T) | 19.23 (T) |
| 1.0 | 24.54 (S) | 20.72 (T) | 19.40 (S) | 14.16 (T) | 12.79 (T) | 11.73 (T) |
| 1.5 | 23.62 (T) | 16.31 (T) | 14.89 (T) | - | - | - |

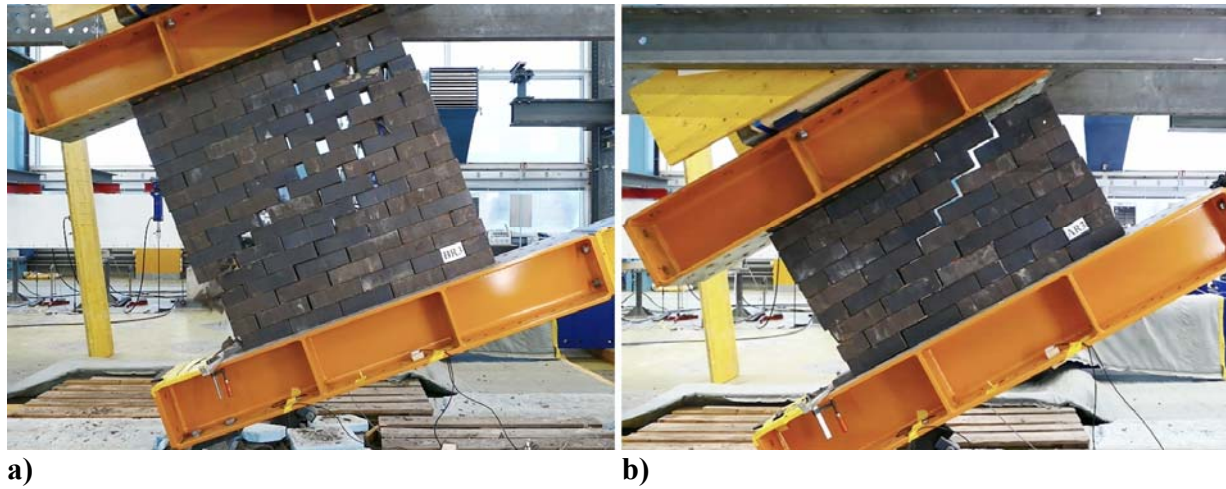


Figure 4: Failure modes: (a) shear and (b) overturning (tilting)

It can be seen from Table 3 and Figure 5 that the highest rotation angle at failure was obtained for specimen AR1 ($\alpha_u = 30.54^\circ$) and was close to the angle of friction obtained from the material tests on small specimens. Further, the difference in ultimate values of α for stack (grey shaded area in Figure 5) and running bonded wallettes is obvious. As expected, the zero brick overlap of the stack bond leads to a lower angle of rotation at failure. Further, the shear failure occurred for small aspect ratios and small pre-compression stresses.

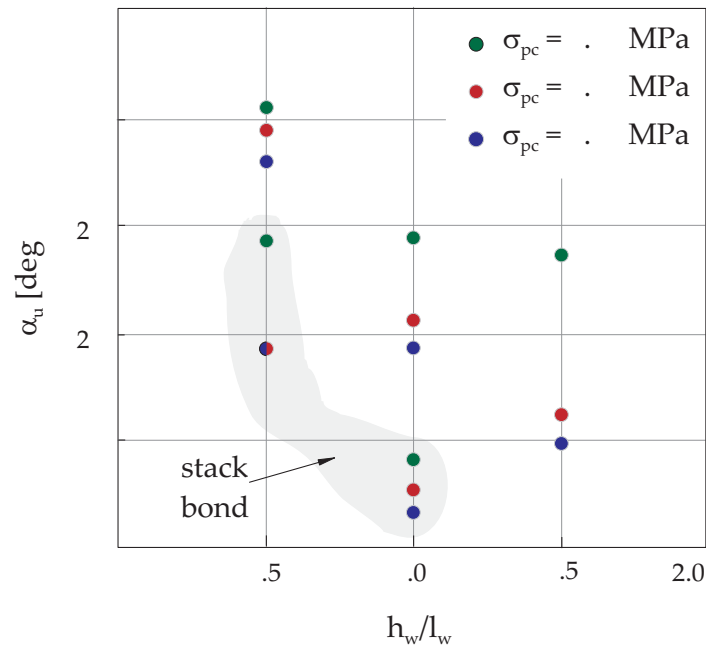


Figure 5: Relationship for failure angle – aspect ratio for all wallettes

The specimens of the first test series (running bond) exhibited both shear failure and overturning while all specimens (except AS1) of the second series (stack bond) failed by overturning. Specimens that failed in shear developed staircase-like cracks, i.e. openings of the head joints, see Figure 6. The less slender specimens were prone to shear failure and those with larger aspect ratio to overturning, cf. Table 3.



Figure 6: Shear failure of specimens BR1 and BR3

Overturning failure of the wallettes built in running bond is shown in Figure 7, the overturning point being the south lower corner of the walette.

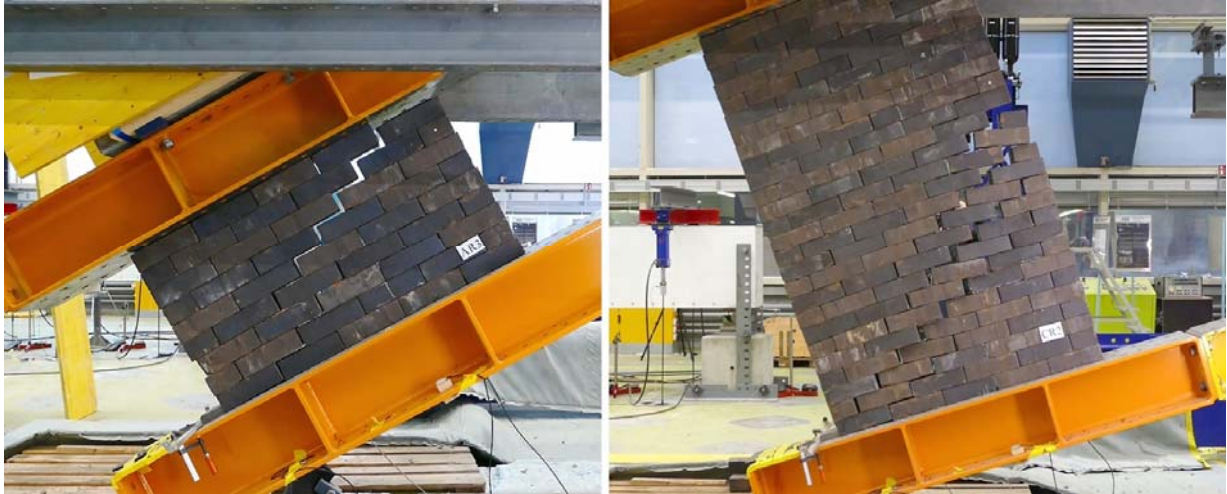


Figure 7: Overturning of specimens AR3 and CR

Figure 8 shows the typical tilting failure of the stack bond specimens. Even at very small rotation angles ($4-5^\circ$) the separation of the stacks was visible. For a majority of the specimens the stacks acted more or less independently of each other. Only for the specimens with the smallest aspect ratio, was a somewhat different behaviour observed. One of them, AS1, clearly failed in shear, see Figure 9, and the two others, AS2 and AS3, changed in the early phase of the test from the deformation mode of sliding to overturning.



Figure 8: Overturning failure of specimens AS3 and BS3



Figure 9: Development of sliding failure of specimen AS1

The influence of the test parameters (bond type, added weight and aspect ratio) can be summarized as follows. The structural behaviour of the wallettes was largely dependent on the shape, i.e. imperfections of the single bricks due to the missing mortar. However, it could be said that running bond masonry elements behaved quasi-homogeneous due to the overlapping of the bricks, while the behaviour of stack bond masonry elements was governed by the single stacks. Adding the weight on top of the wallette (i.e. increasing the pre-compression) increased the height of the mass centre (relative to the bottom of the wallette) and caused the failure angle to decrease. The same is true for the influence of increasing height, i.e. aspect ratio of the specimen, cf. Figure 5. Moreover, the added weight, i.e. the lifting of the mass centre favoured the occurrence of overturning failure.

CONCLUSIONS

An investigation of the behaviour of masonry wallettes subjected to in-plane tilting is underway at ETH Zurich. Preliminary results of tests on two series of elements were analysed and allow a number of conclusions to be drawn:

- The failure angle of base rotation obtained from the tests was nearly the same as that obtained on small (two rows high) specimens
- Both increasing the height of the specimen and the added weight (pre-compression level) reduces the value of the rotation angle at failure and tends to change the failure mode from sliding to overturning
- Masonry bond has considerable influence on the value of the rotation angles at failure

Future research will concentrate on the developing of an analytical in-plane failure criterion that can predict the ultimate (base) rotation angle of dry-stack masonry walls. Further, the study of the out-of-plane behaviour deserves some attention.

ACKNOWLEDGEMENTS

The post-graduate student, Mr. Jan Wachtl, helped in performing the tests. This support is gratefully acknowledged.

REFERENCES

- Baggio C., and Trovalusci P. (1993). Discrete models for jointed block masonry walls. *Proceedings of 6th North American Masonry Conference*, June 6-9, Philadelphia, USA.
- Casapulla C., and Portioli F. (2015), Experimental and analytical investigation on the frictional contact behaviour of 3D masonry block assemblages, *Construction and Building Materials*, 78, pp. 126-143.
- Jimenez D. D. (2011), Analysis of masonry walls: structural design and seismic reinforcement through tilting experiments, Massachusetts Institute of Technology, 131p.
- Restrepo Vélez L. F., Magenes G. and Griffith M. C. (2014), Dry stone masonry walls in bending—Part I: static tests, *International Journal of Architectural Heritage*, 8(1), pp. 1-28.
- Restrepo-Vélez L. F., and Magenes G. (2009), Static tests on dry stone masonry and evaluation of static collapse multipliers, Research Report ROSE 2009/02, Pavia, 72p.
- Uzoegbo H.C., Senthivel R., and Ngowi J.V. (2007), Load Capacity of Dry-Stack Masonry Walls, *TMS Journal*, 25, pp. 41-52.
- Vasconcelos G., and Lourenço P. B. (2009), Experimental characterization of stone masonry in shear and compression, *Construction and Building Materials*, 23(11), pp. 3337-3345.

ENERGY DISSIPATION OF FRAMED SEMI INTERLOCKING MASONRY PANEL UNDER LARGE DISPLACEMENT

M. A. Hossain¹, Y.Z. Totoev² and M.J. Masia³

¹ PhD Student, Centre for Infrastructure Performance and Reliability, The University of Newcastle, Callaghan, NSW 2308, Australia, Md.Akhtar.Hossain@uon.edu.au

² Senior Lecturer, Centre for Infrastructure Performance and Reliability, The University of Newcastle, Callaghan, NSW 2308, Australia, yuri.totoev@newcastle.edu.au

³ Associate Professor, Centre for Infrastructure Performance and Reliability, The University of Newcastle, Callaghan, NSW 2308, Australia, mark.masia@newcastle.edu.au

A Semi Interlocking Masonry (SIM) building system has been developed in the Centre for Infrastructure Performance and Reliability at The University of Newcastle, Australia. The major motivation in developing the system was to improve the seismic performance of masonry infill panels. The SIM panels have significant energy dissipation capacity due to the sliding friction between the SIM units induced during an earthquake. Because all bed joints in a SIM panel are sliding joints, SIM panel can withstand large in-plane displacements without damage. To test SIM panels, a special steel frame with pin connections at each corner was designed and built. The arrangement with pin connections allows application of in-plane shear distortion to the panel of up to 120 mm. The study presented herein focused on the experimental investigation of energy dissipation capacities of three different types of panels (panel with open gap, panel with foam in the gap, panel with grout in the gap). This paper presents the energy dissipation of mortarless SIM panels confined within mechanical steel frame subjected to large in-plane shear distortion. The structural performance of the SIM panels is also analysed and potential displacement patterns are identified under large displacement.

Keywords: SIM, interlocking masonry, sliding joints, energy dissipation, in-plane

INTRODUCTION

Masonry is a complex system consisting of an assemblage of solid or hollow units, mortar or mortar-less joints, grout and reinforced bars, each with different material properties. Masonry behaviour is made more complex by the discontinuity of the units in a mortar-less system and by

mortar joints acting as planes of weakness due to their low tensile and shear bond strength in a conventional mortared system (Hossain *et al.*, 2017). From a constructional engineering perspective, masonry is classified as conventional mortared (bonded) system and non-conventional interlocking mortar-less masonry systems which are subdivided into interlocking and surface bonded system. The term ‘interlocking masonry system’ is defined as a masonry structural wall system in which the constituting masonry units are intentionally shaped so that they are not only dry stacked in a self-aligning manner but also function as structural units (Totoev, 2015).

There have been several attempts to develop mortar-less solid/hollow interlocking blocks in different parts of the world recently. Recently, interlocking mortar-less (dry) masonry systems have been used as an alternative to the conventional mortared masonry systems for panel construction for earthquake resistance. The structural behaviour of the interlocking mortar-less masonry system is not well understood yet, and there is no design specification and/or standard for the design of these systems. Although many interlocking mortar-less block systems have been developed, their full structural potential has not yet been realized due to the lack of information available about the exact behaviour of these new masonry systems under different loading conditions.

Damage occurs in traditional masonry during an earthquake because masonry panels are not efficient in dissipating the energy induced by the earthquake (Hossain *et al.*, 2017). To improve the energy dissipation capacity of masonry, a new system has developed and is called Semi Interlocking Masonry (SIM) (Totoev, 2010). SIM units have limited relative longitudinal movement along bed joints and courses and their interlocking features prevent relative out-of-plane movement. Consequently, stiffness and susceptibility to damage of the SIM panel are reduced and the capacity to dissipate earthquake energy increased (Totoev and Al Harthy, 2016). Two types of SIM units have been developed: Topological and Mechanical as shown in Figure 1. Topological SIM units use the natural contours of the units to allow the in-plane movement between units, whilst the mechanical SIM uses a series of dowels and penetrations to allow the in-plane movement of the units (Lin *et al.*, 2016).



a) Topological SIM Unit



b) Mechanical SIM Unit

Figure 1: Semi-Interlocking Masonry (SIM) Unit, adopted from Forghani *et al.* (2016)

Forghani *et al.* (2016) carried out several tests to determine the water penetration and thermal insulation characteristic of SIM panels using different fillers between the units and the conclusion was that panels constructed with putty exhibit better performance regarding thermal insulation and water penetration than panels constructed without putty between the units. The variation of the coefficient of friction of SIM units with different bedding materials, e.g. linseed oil based putty, tape etc. has also been studied Hossain *et al.*, 2016. The surfaces with putty possess higher coefficient of friction compared to the other tested surfaces.

A larger research project using Mechanical and Topological SIM units on SIM panels has been started recently at the University of Newcastle, Australia. Based on the results obtained by Forghani *et al.* (2016) and (Hossain *et al.*, 2016), the SIM panels were constructed using the putty as a gap filler between the SIM units. The project at obtaining a better understanding on the cyclic behavior of mechanical SIM panels using quasistatic tests.

This paper describes the response of a SIM panel to in-plane cyclic displacements using mechanical SIM units with different treatments for the gap filler between the frame and the top of the panel with particular emphasis on the energy dissipation and displacement characteristics the panel.

EXPERIMENTAL PROGRAM

The testing setup is shown in Figure 2. The steel frame used in this research is made of Australian standard 310UC137 sections and the details of the frame is given by (Healy, 2011). The lateral hydraulic jack cylinder body was mounted on the strong wall and the piston attached to the fixing point on the frame attachment plate using a single pivot pin. Four pin supports were introduced at the four corners of the frame so that the applied cyclic load can be transferred directly to the masonry panel. This system allows the masonry panel to be subjected to displacement of up to 120 mm. The pin jointed frame allows the applied force to be transferred completely to the masonry panel without significant loss due to the frame stiffness.

Instrumentation for the cyclic load testing included ten linear variable displacement transducers (LVDTs) and four electrical strain gauges which were mounted to the steel frame as shown in Figure 2. LVDT1 to LVDT7 were used to monitor the lateral displacements at various locations and LVDT8 and LVDT9 were used to measure diagonal displacements. The measurements from LVDT7 were used to determine the drift of the panel and represents of the overall displacement of the panel. LVDT10 was placed on the right top side pin joint to monitor the out-of-plane movement of the panel. The strain gauges were used to measure the strains in the steel members. Nine targets were also placed on the backside of the panels with a secondary camera, to determine the relative movements of the SIM layers. All transducers were wired to a Datalogger connected to a computer.

The gap filling putty, 3 to 5 mm in thickness, were applied on all horizontal and vertical joints between the SIM units during panel construction. Six panels, 2m × 2m, were their in-plane shear distortion behaviour. However, in this study, only the response of the panels built with Mechanical SIM units is presented. The location of the putty and the dimensions of mechanical SIM unit are shown in Figure 3 (left). Figure 3 (right) shows the putty being applied to the panel.

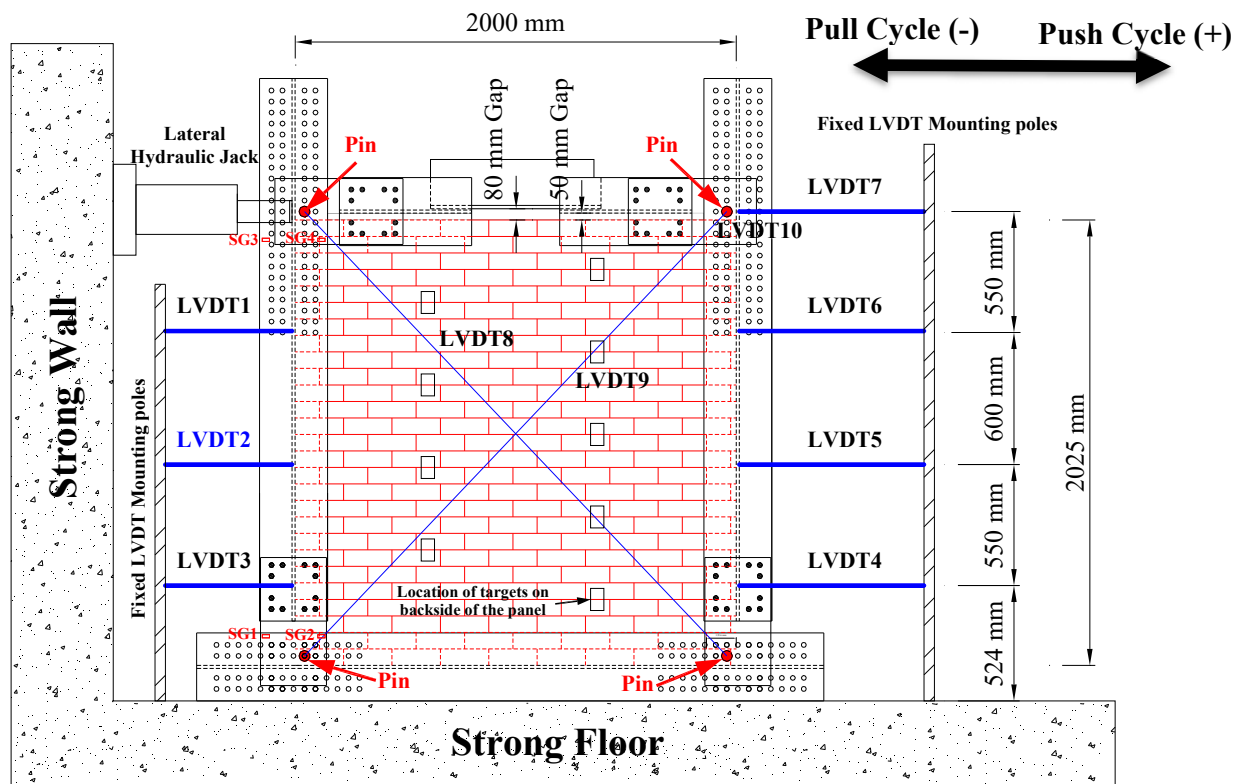


Figure 2: Experimental Details for In-Plane Cyclic Testing of SIM Panels

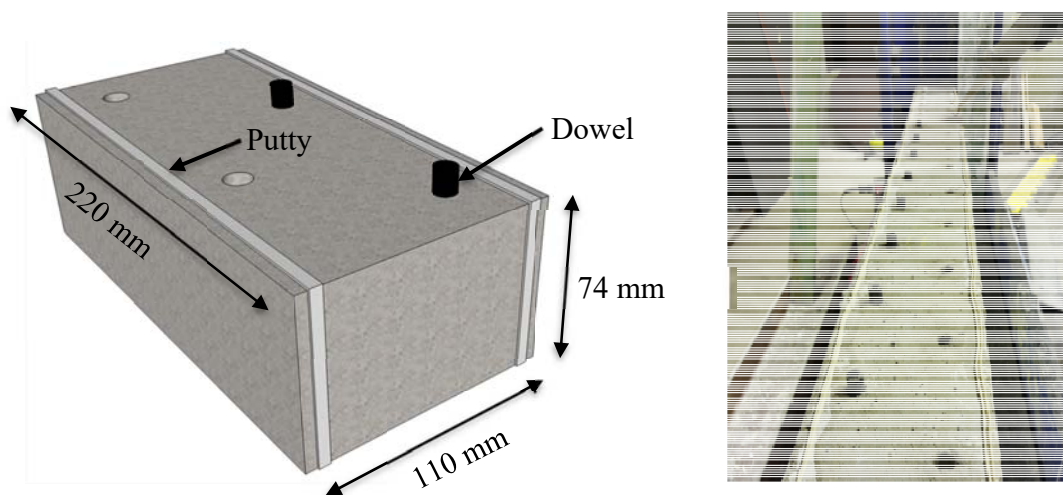


Figure 3: Placement of putty in Mechanical SIM unit (left) and SIM panel (Right)

The Mechanical SIM unit used in this research was made of concrete, which has high compressive strength but significantly low tensile strength. The mean compressive strength of the SIM unit used in this study was 31.5 MPa with a CV = 20%; the density of the units was 2250 kg/m³. After construction of the SIM panels, there was a gap between the panel and the steel frame of

approximately 50mm at each top corners and approximately 80mm gap in the middle of the SIM panels as shown in Figure 4. One of the panels tested (Panel MO), the gap remained open during testing; One Panel (Panel MF), the gap was filled with self-expanding polyurethane Foam (soft gap filler) and in another panel (Panel MG), the gap was filled with cement Grout (hard gap filler) as shown in Figure 5. The foam used was a self-expanding polyurethane foam filler that expands to 2.5 times the initially dispensed foam after being sprayed, which allowed a complete seal to form around panel. The grout used was a mixture of cement and sand with a cement to sand ratio of 1:6. The grout was allowed to set for 28 days before testing. The mean grout compressive strength after 28 days was 37.63 MPa with a CV = 10.37%.

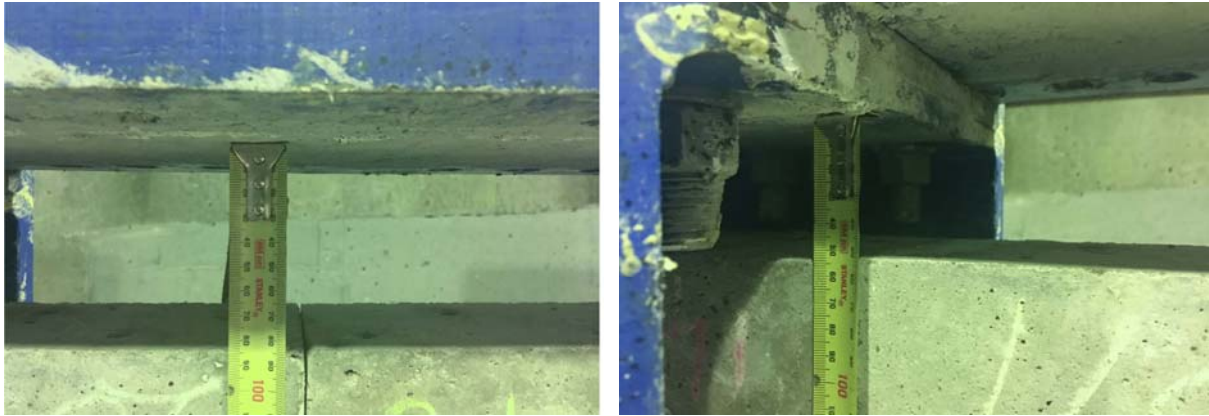


Figure 4: Gap between the steel frame and top-middle of the panel (Left), and gap between the steel frame and top-left and top-right sides of the panel (Right)

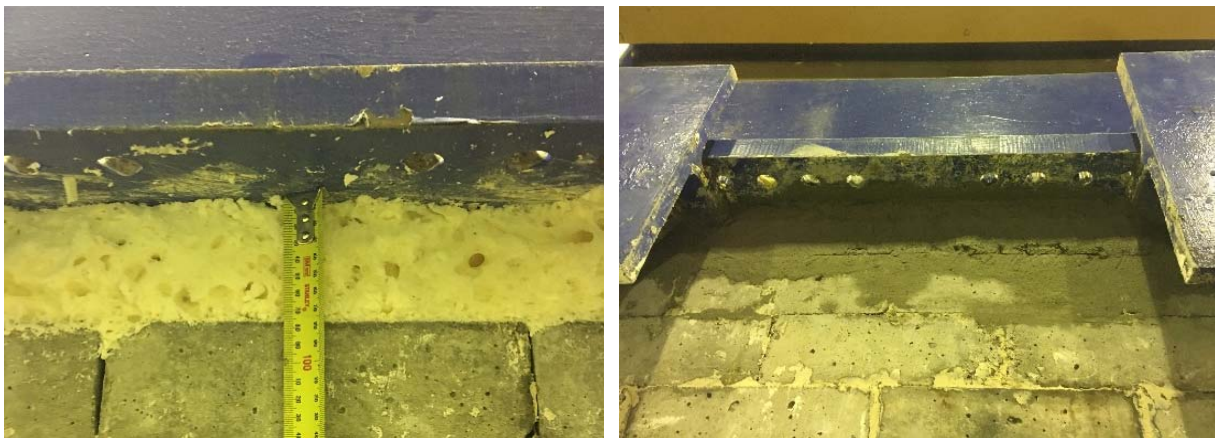


Figure 5: Foam (left) and grout (right) fillings

The bare frame and frame with one panel are shown in Figure 6. A speckle pattern as shown in Figure 6 was applied on the panels, so that the Digital Image Correlation (DIC) could be used to obtain the displacement topology of the panel. The results obtained from DIC analysis are not presented herein.

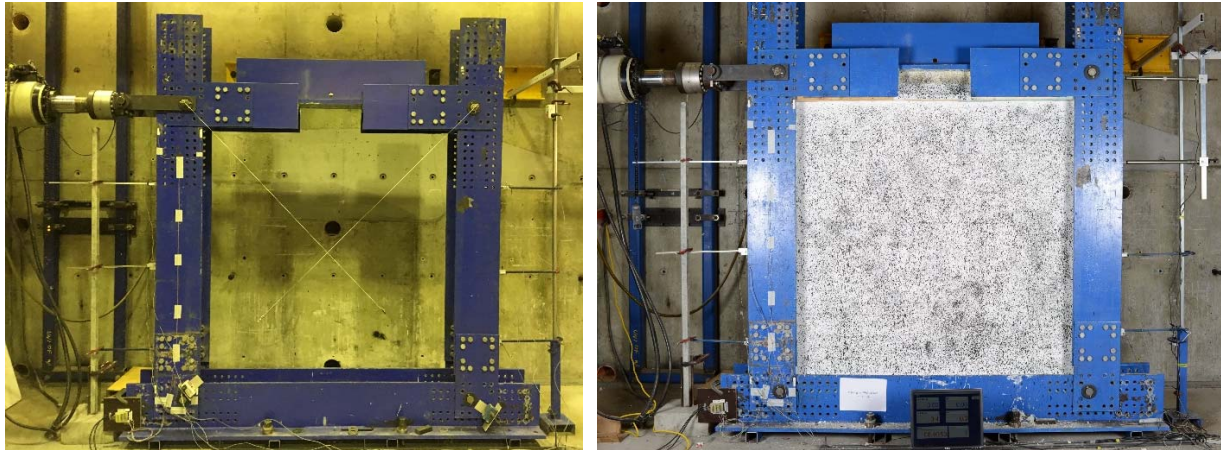


Figure 6: Bare frame (left) and frame with panel showing speckle pattern applied for digital image correlation (Right)

The results presented herein include four in-plane tests:

- (i) Panel Zero: a bare steel frame test as shown in Figure 6(left)
- (ii) Panel MO: a test with the frame and the mechanically interlocking SIM panel with an open gap between the frame and the top of the panel.
- (iii) Panel MF: a test with the frame and the mechanically interlocking SIM panel with low compressive strength foam filling.
- (iv) Panel MG: a test with the frame and the mechanically interlocking SIM panel with grout filling.

The steel frame was then subjected to the lateral displacement history in cyclic form. Cyclic lateral displacements were applied at the top left pin support of the steel frame by a hydraulic jack. Each displacement level was repeated three times, and the measurements of the LVDTs, and visual cracking of the panel and data from the strain gauges were monitored carefully. Figure 7 shows the time history of the applied displacement. The displacement rate was changed, as shown in Table 1 but the loading period was 800 sec for all target displacements except for the 1 mm displacement. The horizontal force was recorded using the internal load cell of the hydraulic jack and the story drift was calculated by dividing the measured displacement at LVDT7 by the story height of 2 m. The test duration varied from 450 to 500 minutes. A detailed description of the testing program is presented elsewhere (Hossain *et al.*, 2017).

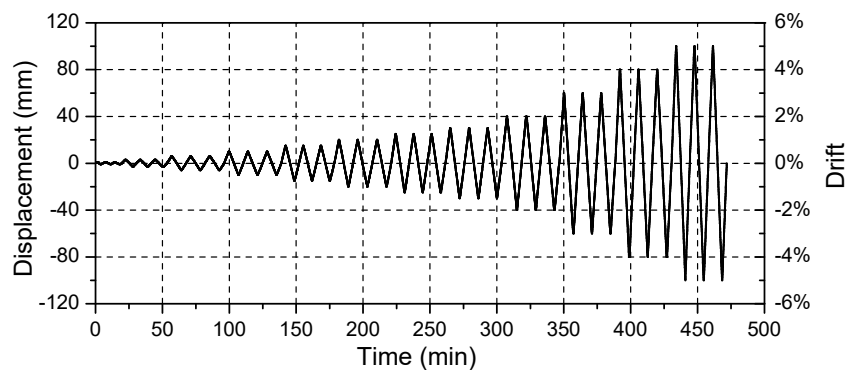


Figure 7: Applied displacement history

Table 1: Cyclic displacement rates

| Displacement mm | Displacement rate mm/sec | Displacement mm | Displacement rate mm/sec | Displacement mm | Displacement rate mm/sec |
|--------------------|-----------------------------|--------------------|-----------------------------|--------------------|-----------------------------|
| 1 | 0.01 | 15 | 0.075 | 40 | 0.20 |
| 3 | 0.015 | 20 | 0.1 | 60 | 0.30 |
| 6 | 0.03 | 25 | 0.125 | 80 | 0.40 |
| 10 | 0.05 | 30 | 0.15 | 100 | 0.50 |

RESULTS AND DISCUSSION

The SIM system primarily depends on friction as a means of energy dissipation during a seismic event. Thus, it is important to obtain an understanding of the load-displacement behavior during the testing. The hysteretic load-displacement loops obtained for each tested specimen are presented in Figure 8. The peak envelope of the force-displacement of the 1st cycle of each displacement level is also shown in Figure 8. Note that the vertical axis scaling in Figure 8(a) is different from others.

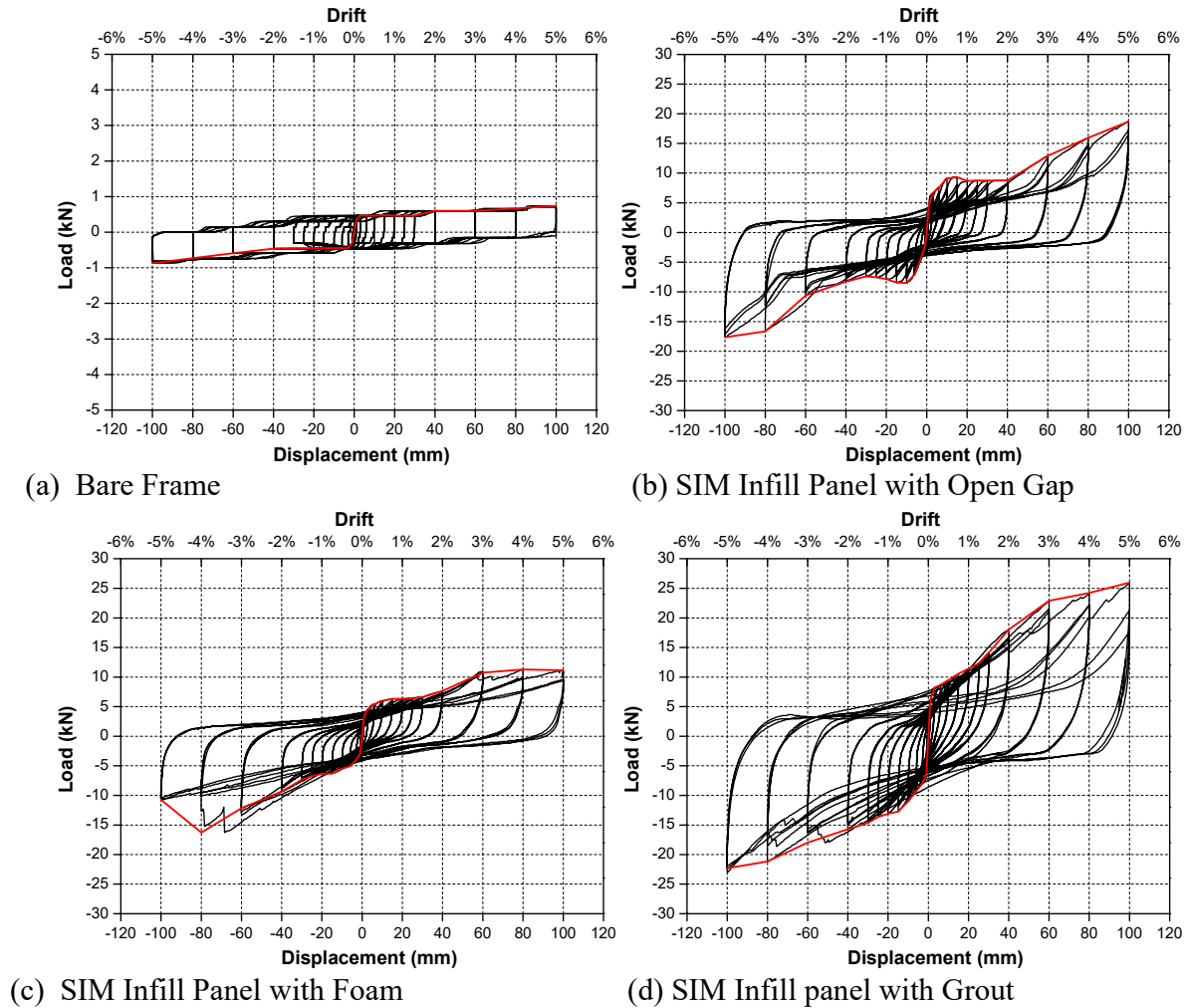


Figure 8: Force-Displacement Hysteresis

There is no noticeable difference in the stiffness degradation between the three cycles at all levels of displacement of Panel zero (bare frame) which indicates that the testing steel frame does not suffer any damage during the cycling at even this larger displacements. In addition, there is a reasonably systematic and stable response for push and pull cycles for all displacement levels.

The energy dissipation capacity of the panel is an important parameter in the design and evaluation of interlocking masonry (Symans *et al.*, 2008). The energy dissipation of cyclic testing can be calculated by the integral of the hysteretic force/displacement graphs. The area of each cycle represents the energy for that particular cycle, which can be calculated using Equation 1 and represented by Figure 9 (Paz, 2012). A summary of the energy dissipation results is presented in Table 2.

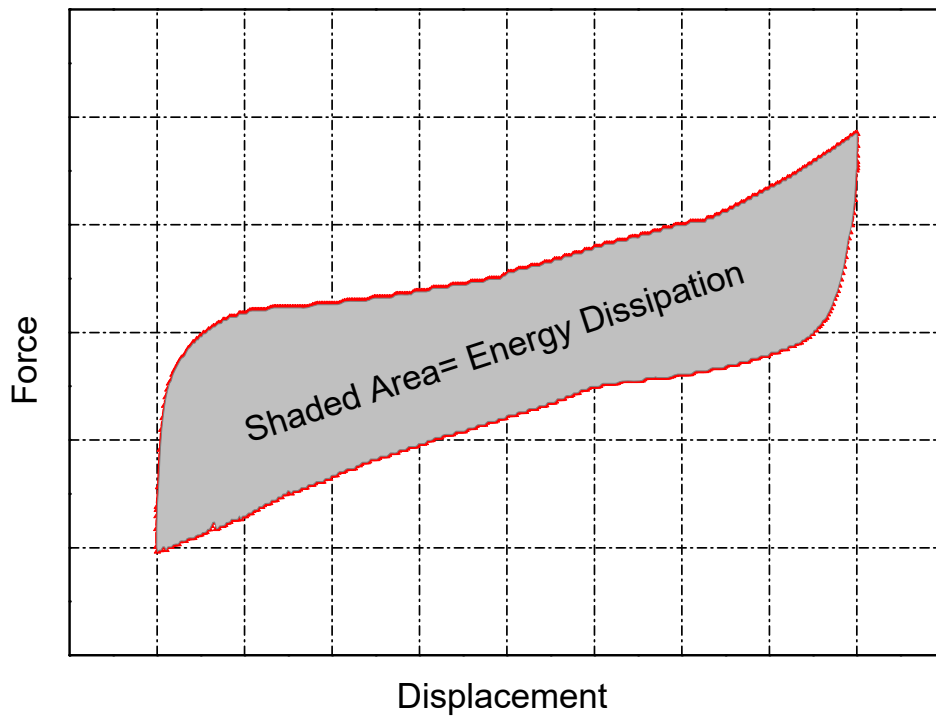


Figure 9: Energy dissipation of a cycle

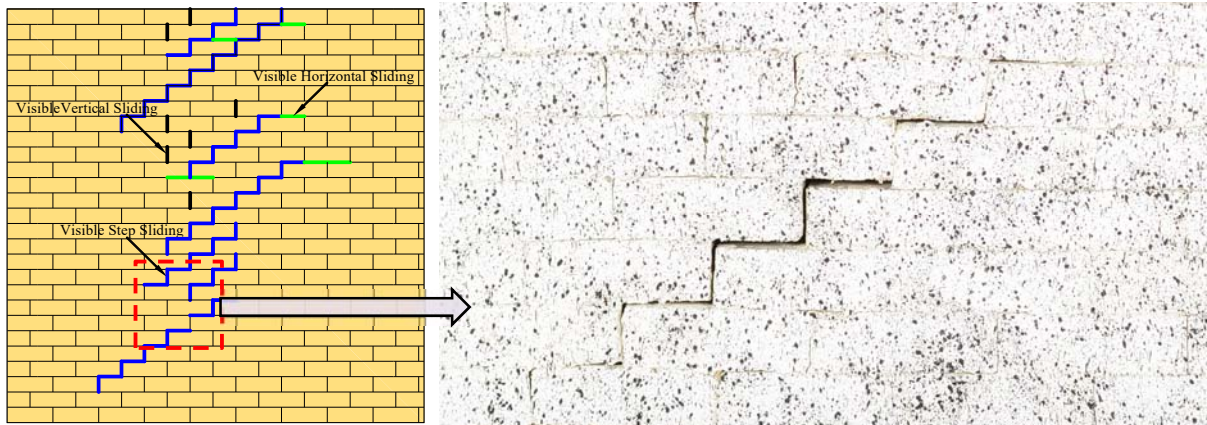
$$E = \int F_s(x).dx \quad (1)$$

where E is the Energy dissipation, F_s is the Shear force and x is the displacement.

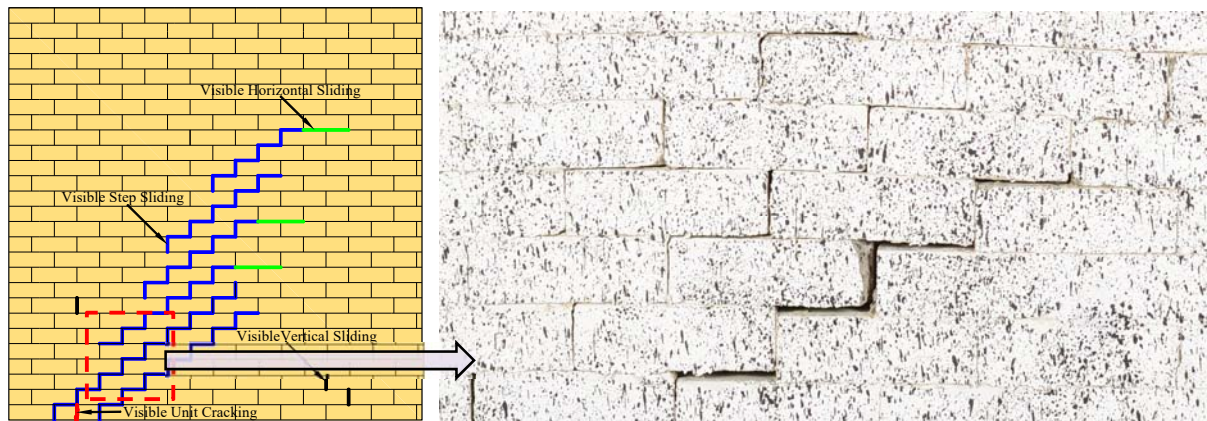
Table 2: Summary of Energy Dissipation (ED)

| Displacement (mm) | Drift (%) | Panel Zero: Bare Frame | | Panel MO: Open Gap | | Panel MF: Foam | | Panel MG: Grout | |
|----------------------|--------------|---------------------------|------------------------------|-----------------------|------------------------------|-------------------|------------------------------|--------------------|------------------------------|
| | | Force (kN) | ED in 3 cycles (kN.mm) | Force (kN) | ED in 3 cycles (kN.mm) | Force (kN) | ED in 3 cycles (kN.mm) | Force (kN) | ED in 3 cycles (kN.mm) |
| 1 | 0.05 | 0.31 | 0.80 | 3.46 | 4.142 | 3.16 | 3.92 | 5.77 | 6.19 |
| 3 | 0.15 | 0.46 | 3.32 | 5.32 | 21.93 | 4.18 | 19.05 | 6.99 | 29.70 |
| 6 | 0.3 | 0.46 | 8.03 | 6.77 | 52.64 | 4.95 | 42.99 | 8.03 | 66.32 |
| 10 | 0.5 | 0.46 | 15.73 | 7.95 | 101.68 | 5.52 | 74.14 | 9.67 | 130.31 |
| 15 | 0.75 | 0.46 | 24.84 | 7.94 | 157.79 | 6.00 | 126.23 | 11.04 | 232.98 |
| 20 | 1 | 0.46 | 34.25 | 7.56 | 201.12 | 6.06 | 180.22 | 11.63 | 343.13 |
| 25 | 1.25 | 0.46 | 42.31 | 7.64 | 254.80 | 6.51 | 243.25 | 12.73 | 471.20 |
| 30 | 1.5 | 0.46 | 50.11 | 7.54 | 310.58 | 6.82 | 309.89 | 13.92 | 619.94 |
| 40 | 2 | 0.54 | 71.13 | 8.07 | 478.63 | 8.11 | 475.37 | 16.01 | 1027.62 |
| 60 | 3 | 0.60 | 103.63 | 11.18 | 875.68 | 11.83 | 960.25 | 19.35 | 1827.82 |
| 80 | 4 | 0.69 | 133.20 | 14.46 | 1297.59 | 11.16 | 1348.13 | 20.80 | 2349.37 |
| 100 | 5 | 0.78 | 166.52 | 17.21 | 1859.50 | 10.36 | 1639.13 | 22.08 | 2649.02 |

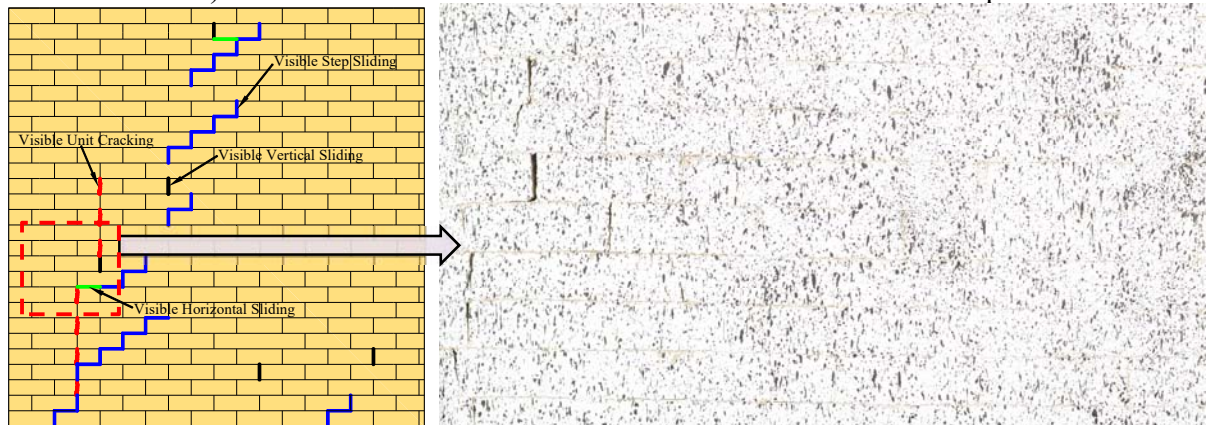
The increase in the energy dissipation in the SIM panels was caused mainly by the relative slip and friction forces developed between the SIM units. This dissipation was amplified when full contact was developed between the frame and the panel. Panel MG possessed higher energy dissipation capacity than the other two tested panels for each displacement level, which is due to the difference in the gap between the top of the panel and steel frame. No SIM unit cracking was observed in the SIM Panel MO. Unit cracking was observed in Panel MF and Panel MG at a displacement of 80 mm (Story drift of 4%), and crack occurrence and width increased thereafter. The final joint opening pattern after 1st cycle at 100 mm pull cycle is shown in Figure 10; one SIM unit and seven SIM units cracked in Panel MF and Panel MG respectively, after 100 mm pull cycles.



a) Panel MO: Mechanical SIM Infill Panel with Open Gap



b) Panel MF: Mechanical SIM Infill Panel with Foam in the Gap



c) Panel MG: Mechanical SIM Infill Panel with Grout in the Gap

Figure 10: Opening of joints and Cracks in the panels

The visible gaps between the SIM units in the step sliding in Panel MO and Panel MF are more pronounced than that in Panel MG as the Panels MO, and Panel MF could move vertically due to the gap between the top of the panels and steel frame. The cumulative energy dissipation of the four panels is summarized in Figure 11.

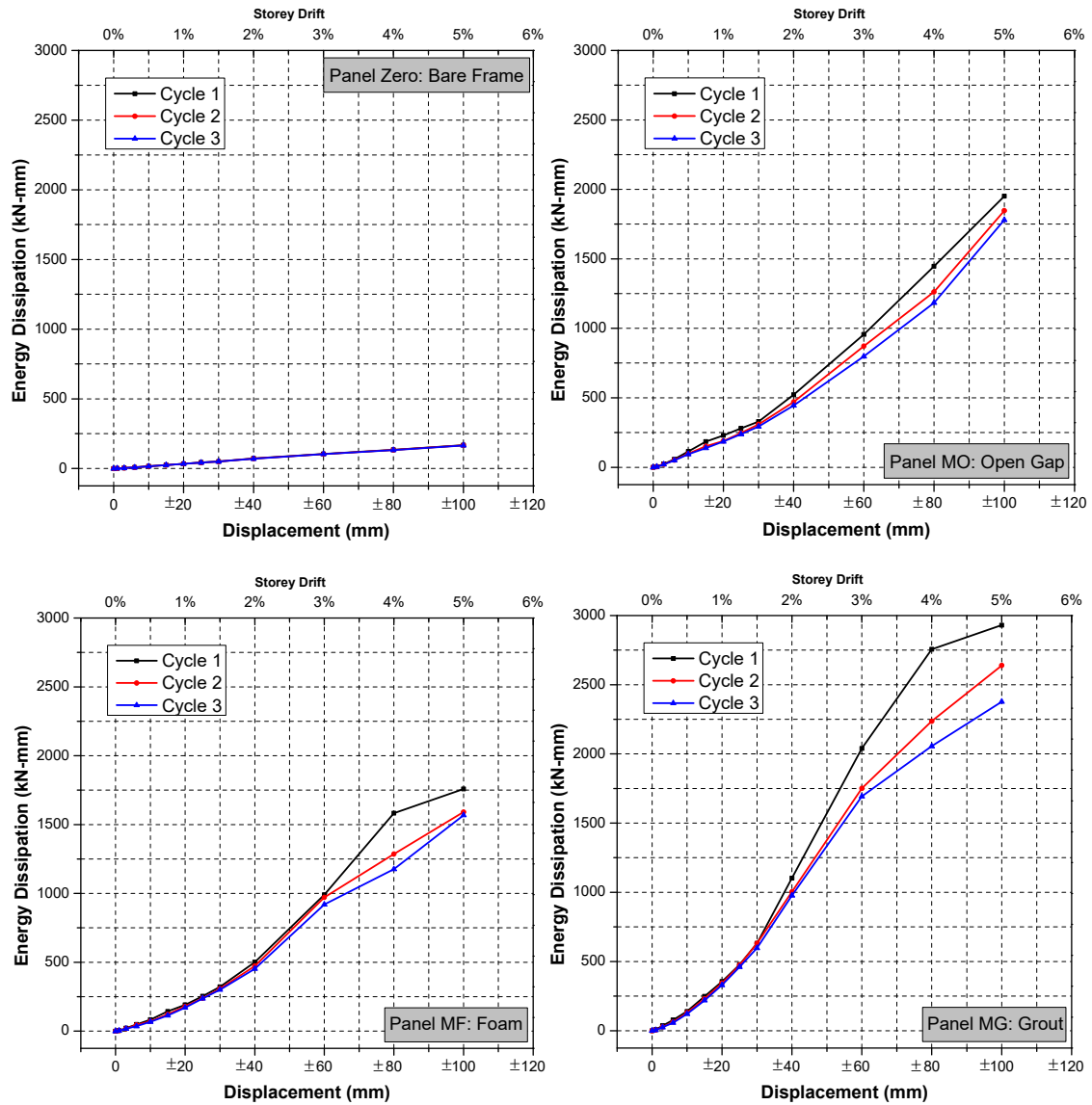


Figure 11: Energy dissipation vs. displacement of the tested panels

For the bare frame (Panel Zero), a linear response for energy dissipation with respect to displacement was observed. This is because the friction in the pin joints is the only contributing factor in the bare frame. It can be observed in Figure 11 that there is no significant difference in energy dissipation among the three tested panels up to about 30 mm displacement. At this initial stage, SIM units engage in sliding gradually from the top of the panel near the pushing column and the compression on the bed joints is not high. After that, most units are sliding and the energy dissipation increases due to increasing compression on bed joints. The gap between the top of the panel and the frame plays important role at this stage. The largest energy dissipation was observed for the SIM panels with a grouted gap. In panels MF and MG cracking of units at 80 mm

displacement resulted in some local relaxation of compressive stresses and corresponding change in the energy dissipation.

CONCLUSIONS

To assess the contribution of SIM panels in terms of energy dissipation, the response of the bare frame and the SIM-infilled frames were studied. The contribution of the pinned connected bare frame in terms of energy dissipation is negligible compared to that of the SIM panels. This happened because of the introduction of the pin supports in the frame. The cracking and gap opening patterns and hysteretic behaviours of the frame with different types of gap filler between the top of the panels and the steel frame have been studied at high displacement levels. Typical diagonal step sliding was observed for the panel without fillers and for the panel with foam filler. The frame with cement grout filler, however did not experience too many cracks. A series of full hysteresis curves were obtained for the panels with mechanical SIM units, which indicates a significant energy dissipation capacity. From the overall assessment viewpoint, based on obtained hysteretic loops, the response envelope and the gap opening pattern, the conclusion is that the cyclic behaviour of the panels with mechanical SIM units has the potential to contribute in dissipating energy during in-plane shear loading.

ACKNOWLEDGEMENTS

This experimental study was possible because of the enthusiastic collaboration of several students and the technicians at the Centre for Infrastructure Performance and Reliability at The University of Newcastle, Australia.

REFERENCES

- Forghani, R., Totoev, Y.Z., Kanjanabootra, S., and Davison, A. (2016). Experimental Investigation of Water Penetration through Semi-Interlocking Masonry Walls. *Journal of Architectural Engineering*, pp. 04016017-1-9.
- Healy, D. (2011). Design of Steel Frame for Repeated Cyclic Tests on Masonry Panels. Retrieved from The University of Newcastle, Australia:
- Hossain, M. A., Totoev, Y. Z., and Masia, M. J. (2016). Friction on mortar-less joints in semi interlocking masonry. *Proceedings of 16th International Brick and Block Masonry Conference*, Padova, Italy.
- Hossain, M. A., Totoev, Y. Z., and Masia, M. J. (2017). In-plane cyclic behavior of Semi Interlocking Masonry panel under large drift. *Proceedings of 13th Canadian Masonry Symposium*, June 4-7, Halifax, Canada.
- Lin, K., Totoev, Y. Z., Liu, H., and Guo, T. (2016). In-Plane Behaviour of a Reinforcement Concrete Frame with a Dry Stack Masonry Panel. *Materials*, 9 (108).
- Paz, M. (2012). *Structural dynamics: theory and computation*: Springer Science & Business Media.

Symans, M., Charney, F., Whittaker, A., Constantinou, M., Kircher, C., Johnson, M., and McNamara, R. (2008). Energy dissipation systems for seismic applications: current practice and recent developments. *Journal of Structural Engineering*, 134 (1), 3-21.

Totoev, Y. Z., and Al Harthy, A. (2016). Semi interlocking masonry as infill wall system for earthquake resistant buildings: A review. *Journal of Engineering Research*, 13 (1), 33-41.

Totoev, Y. Z. (2010). Australian Patent Application No. 2010905681.

Totoev, Y. Z. (2015). Design Procedure for Semi Interlocking Masonry. *Journal of Civil Engineering and Architecture*, 9 (2015), 517-525.



**MASONRY TODAY
AND TOMORROW**

**11 - 14 February, 2018
SYDNEY AUSTRALIA**

www.10amc.com

PSEUDO-STATIC TESTS OF MORTAR-LESS MASONRY JOINT WITH DIFFERENT INTERLOCKING SHAPES

K. Lin¹, H.J. Liu² and W. Hou³

¹ Associate Professor, Shenzhen Engineering Lab for Wind Environment and Technology, Shenzhen Graduate School, Harbin Institute of Technology, Shenzhen 518055, China, linkun@hit.edu.cn

² Professor, Shenzhen Engineering Lab for Wind Environment and Technology, Shenzhen Graduate School, Harbin Institute of Technology, Shenzhen 518055, China, liuhongjun@hit.edu.cn

³ Shenzhen Engineering Lab for Wind Environment and Technology, Shenzhen Graduate School, Harbin Institute of Technology, Shenzhen 518055, China, houwang@hit.edu.cn

The framed structure infilled with mortarless brick (MB) panel exhibits considerable in-plane energy dissipation because of the relative sliding between bricks and good out-of-plane stability resulting from the use of interlocking mechanisms. Two different types of bricks, namely, non-interlocking mortarless brick (N-IMB) and interlocking mortarless brick (IMB), are examined experimentally.

The cyclic behavior of all the investigated joints (N-IMB and IMB) are investigated in consideration of the effects of interlocking shapes, loading compression stress levels, and loading cycles. The hysteretic loops of N-IMB and IMB joints are obtained, according to which, a mechanical model is developed. The Mohr–Coulomb failure criterion is employed to describe the shear failure modes of all the investigated joints. A typical frictional behavior is observed for the N-IMB joints, and a significant stiffening effect is observed for the IMB joints during their sliding stage. The friction coefficients of all the researched joints increase with the augmentation of the compression stress and improvement of the smoothness of the interlocking surfaces. An increase in the loading cycle results in a decrease in the friction coefficients of all the joints. The degradation rate of the friction coefficients increases with the reduction in the smoothness of the interlocking surface.

Keywords: *mortarless brick joints, interlocking shapes, cyclic loads, shear-compression behaviour, experiment*



INTRODUCTION

Reinforced concrete (RC) frame structures with masonry panels are known for their economic feasibility and low technology requirement. However, as Yuen et al. (2015) and Cavaleri et al. (2005) point out, the disadvantage of RC frame in terms of seismic behavior is increasingly highlighted, especially in high seismic-prone regions. To improve seismic behavior, a conceptually novel system for framed masonry panels was proposed in reference by Lin et al. (2005). According to the concept, the frame was infilled with a mortarless brick (MB) panel. An MB panel can dissipate energy because of the relative sliding of each brick and avoid out-of-plane failure through the interlocking mechanism (see Figure 1). A series of experiments on MB panel infilled frame was carried out by the Lin et al. (2005), and the results indicated that the MB panel exhibits considerable energy dissipation during cyclic loading and can significantly improve the seismic behavior of the frame structure. To evaluate the contribution of the energy dissipation and lateral resistance of the MB panel to the frame, an equivalent model was introduced in reference proposed by Lin et al. (2013); the authors found that the energy dissipation of the MB panel results from friction between bricks.

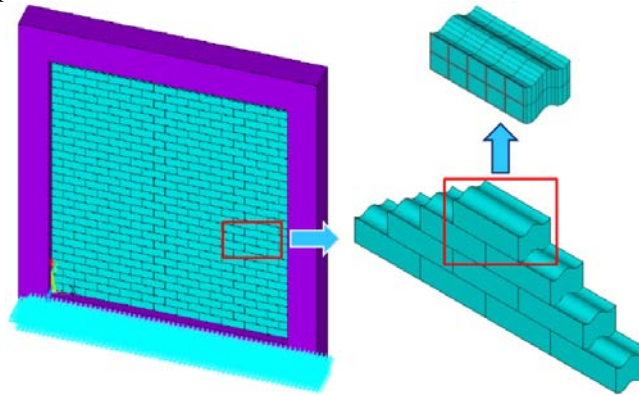


Figure 1: Reinforcement concrete frame with MB panel

Improvement of the energy dissipation of MB panel requires some knowledge on the particular mechanical properties of the novel component. However, previous researches by Basha et al. (2015) and Cai et al. (2014) mainly focused on the shear and compression behaviors of traditional masonry with mortared brick units; their results are unsuitable for dry stack masonry. Studies on the MB panel became active only in the last decade. However, these recent studies mainly focused on the cyclic behavior of non-interlocking mortarless brick (N-IMB) joints. Lourenco et al. (2004) applied the couplet test to investigate the shear–compression behavior of dry stack stone joints. According to their research, the Mohr–Coulomb failure criterion can describe the characteristics of dry stone joints under different compression stress levels; the friction coefficients of the dry-stone joints were obtained experimentally, and the cohesion for the investigated joints could be neglected. Zuccarello et al. (2009) applied the traditional triple test and confirmed that the shear–compression behaviors of N-IMB joints represent the Coulomb friction law. Lin et al. (2012 & 2015) proposed a new modified loading device, which was improved through the traditional triple test, to study the cyclic behavior of N-MIB joints. However, the new loading device induced additional bending moments on the contact surface; the additional bending moments resulted in a pinch phenomenon in the hysteretic loops.

Therefore, the proposed loading device should be improved to avoid the additional moments.

Just as Anand et al. (2014) and Sanada et al. (2008) point out, different from the non-interlocking mortarless brick (N-IMB) panel, the interlocking mortarless brick (IMB) panel exhibits different in-plane/out-of-plane behaviors, damping ratios, and energy dissipations. Sturm et al. (2015) and Rui et al. (2015) studied the shear and compression behaviors of IMB experimentally. Their results indicated that the cohesion of IMB can be neglected, and pre-compression level and interlocking shapes are both important to the shear–compression behavior of the researched interlocking blocks. The cyclic behavior of IMB wall was investigated, severe damage was found at the bottom of the IMB walls because of large drift levels, which indicate that the interlocking shapes need to be improved. Thanoon et al. (2008) studied the effects of the interlocking shapes of blocks on the compressive and out-of-plane behaviors of mortarless block masonry through numerical simulations and experimental tests; however, the influence on the in-plane behavior was not investigated.

The mechanical behavior of the contact between the mortarless bricks, which is a nonlinear problem, can become highly sophisticated by considering the influence of interlocking shapes. Ensuring accuracy during the processing and installation of mortarless bricks in practical engineering is difficult and causes a far less idealized contact between mortarless bricks under practical conditions than those under laboratory test conditions. Moreover, the use of interlocking bricks aggravates the non-idealized characteristics of the contact conditions for mortarless joints. Therefore, the frictional parameters (mainly the friction coefficient) and shear force–displacement hysteretic loops obtained from previously reported shear–compression tests of N-IMB joints are unsuitable for the characterization of IMB joints. Obtaining in-depth insights into the shear–compression characteristics of IMB joints by considering the influence of different interlocking shapes is highly necessary.

A comprehensive experimental investigation of the behavior of IMB joints with four different interlocking shapes was carried out in Harbin Institute of Technology Shenzhen Graduate School. The present study aims to improve knowledge on the mortarless masonry structure under cyclic loading, which is of crucial importance in the evaluation of the energy dissipation of MB panels. Aside from those of interlocking shapes, the effects of compressive stress and loading cycles were also investigated and analyzed quantitatively.

DESCRIPTION OF THE SPECIMEN

Light aggregate concrete (LAC) bricks were selected for the cyclic test. According to the material standard for LAC, the mix proportion (cement: fly ash: ceramsite: sand) of LAC was determined to be 1:0.27:1.7:2.6, with a water cement ratio (w/c) of 0.42. The YAS-5000 compression-testing machine was utilized to perform the uniaxial test to determine the compressive strength of LAC. The average density ($\rho = 1746 \text{ kg/m}^3$) and average compressive strength ($f_c = 31.7 \text{ MPa}$) were obtained for LAC.

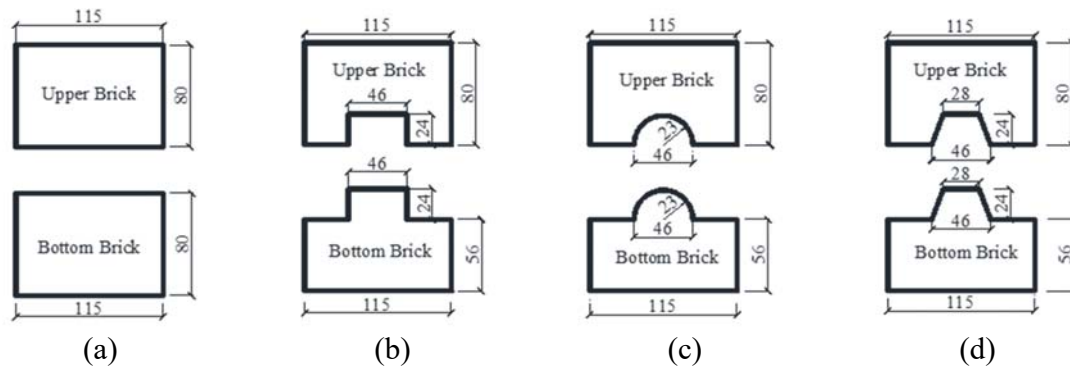


Figure 2: Dimensions and profiles of cross-section for specimens of bricks with various interlocking shapes: (a) non-interlocking; (b) rectangular interlocking; (c) circular interlocking; (d) trapezoidal interlocking

Although IMB can improve the out-of-plane stability of the MB panel effectively, unsuitable interlocking shapes or dimensions would lead to significant stress concentration and potential damage for the MB panel. In this study, the shear-compression characteristics of N-IMB joints and IMB joints with three interlocking shapes, namely, rectangular, trapezoidal, and circular, were investigated through the cyclic loading tests. The length, width, and height of the bricks for the upper and bottom portions are 80 mm×115 mm×80 mm and 375 mm×115 mm×80 mm, respectively, as shown in Figures 2 and 3.



Figure 3: Photos for specimens of the bricks with various interlocking shapes: (a) non-interlocking, (b) rectangular interlocking, (c) circular interlocking, (d) trapezoidal interlocking

DESCRIPTION OF TESTING PROCEDURES

The test setup is shown in Figure 4. The upper brick is fixed in the steel clamping plate, which is connected to the support frame through a rigid drive rod. The bottom brick is fixed in the steel slot, which is bolted on the sliding plate of the loading device. The counter weights, which are employed to apply different vertical compression levels to the upper brick, are fixed on the top of the steel clamping plate through a steel rod. Both the support frame and loading device system are fixed on a steel platform. A linear motor, which can achieve real-time control and provide cyclic horizontal displacement with constant speed, was utilized as the loading equipment. The loading speed of the linear motor ranges from 1 mm/s to 500 mm/s, and the acceleration time is

0.1 s with a repositioning accuracy of 0.02 mm.

The axial deformation of the linked drive rod caused by the horizontal right/left sliding of the bottom brick was measured with four strain gauges symmetrically plastered on the surface of the drive rod to avoid the effects of out-of-plane bending. The deformation (strain) was then converted to axial force of the drive rod, which is equal to the shear force of the sliding mortarless joint between upper and bottom bricks. Lastly, the frictional coefficients, which are equal to shear force divided by the area of the contact surface, were obtained.

Prior to the test, the devices shown in Figure 4 were assembled together as an entire loading system. The leveling adjustment for all loading devices was enhanced during the assembling process to ensure that the brick slides in the same horizontal level all the time. During the test process, leveling adjustment of the loading devices was carried out with a dial indicator. Real-time monitoring of the deformation of two supporting screw rods was employed to ensure the symmetry and level of the dial indicator. All these measures guarantee the accuracy of the measured force. This test involved 16 load cases. Four types of interlocking shapes (i.e., non-interlocking, circular interlocking, trapezoidal interlocking, and rectangular interlocking) and four compression stress levels (i.e., 0.017, 0.028, 0.039, and 0.05 MPa) were investigated. Four loading cycles with an amplitude of 250 mm were applied to each loading case. The loading speed was set to 1 mm/s, which can be assumed as a quasi-static test.

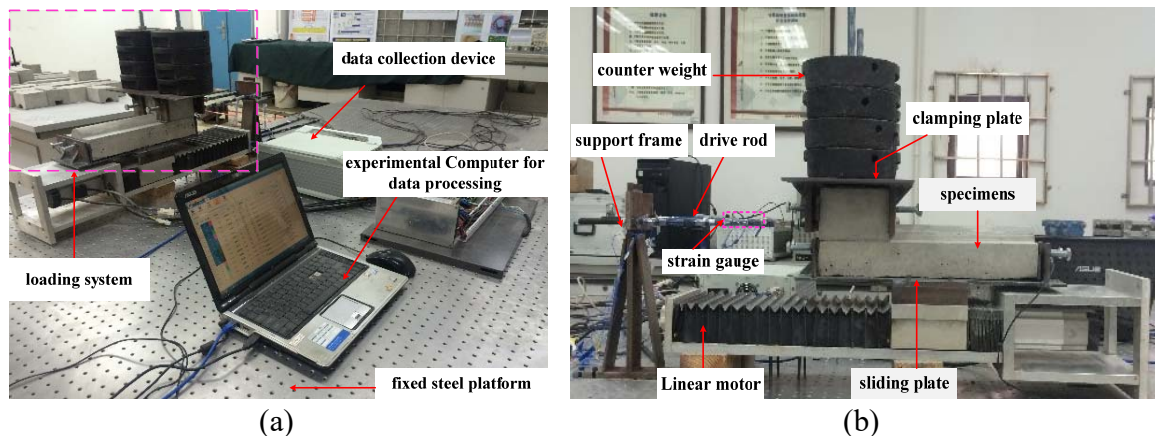


Figure 4: Test setup: (a) entire view, (b) loading system

EXPERIMENTAL RESULTS AND DISCUSSION

Figure 5 shows the typical hysteretic loops of the N-IMB and IMB joints. A mechanical model was established and is shown in Figure 6.

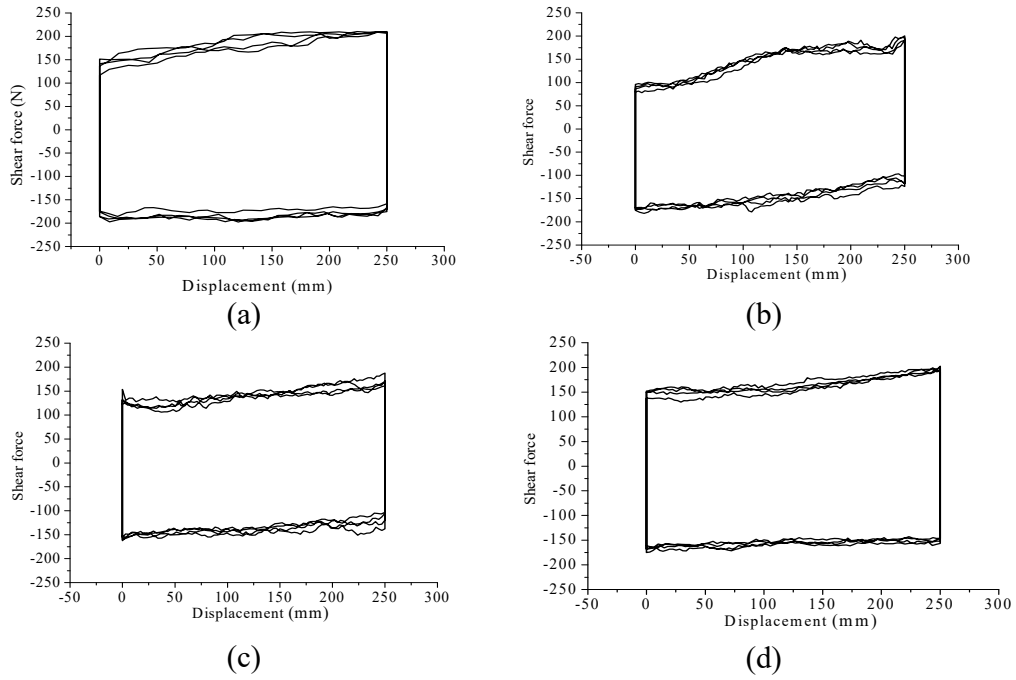


Figure 5: Typical Hysteretic loops for the N-IMB and IMB joints under 4-cycles cyclic experimental tests: (a) non-interlocking, (b) circular interlocking, (c) trapezoidal interlocking, (d) rectangular interlocking

The results indicate that the hysteretic loop can be divided into four stages, namely, initial loading (stage a), constant loading (stage b and stage d), and unloading (stage c). Compared with those of the N-IMB joints, the initial and unloading stages of the IMB joints exhibit similar characteristics. However, for the constant stage, the N-IMB and IMB joints exhibit a significant difference.

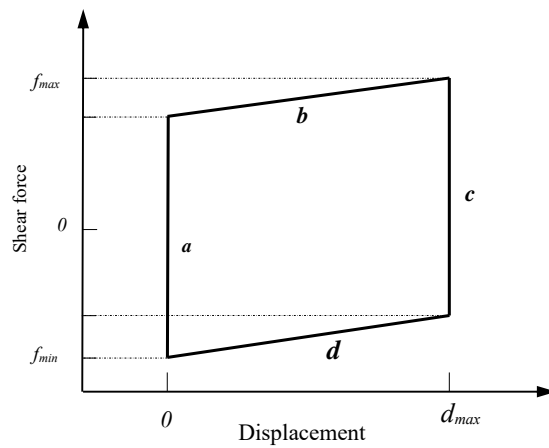


Figure 6: Mechanical model of the hysteric loops for the N-IMB and IMB joints

Unlike that in the N-IMB joints, the shear force of the IMB joints exhibits stiffness hardening

behavior in the constant loading stage (stages b and d), this behavior varied as the interlocking shape changed, shown as in Figure 5 (b) to (d). In consideration of the test process, it is concluded that the stiffness hardening behavior was caused by the loading direction being not parallel to the longitudinal extension of the interlocking portion during the loading process. Therefore, additional compression stress was generated, the shear force of IMB joints increased, and the stiffness hardening behavior appeared.

The average value of the constant stage was selected to calculate shear and compression stresses as follows:

$$\tau = \frac{F}{A}, \quad \sigma = \frac{N}{A} \quad (1)$$

where τ is the shear stress, σ is the normal stress, F is the shear force that is equal to the average force of the constant loading stages, N is the normal force that is equal to the vertical applied force caused by the gravity effects of the countered weights, and A is the vertical projection contact area in the experiment.

The shear stress versus compression stress for all specimens under four-cycle loading is shown in Figure 7. As indicated by the figure, the relationship between shear stress and compression stress for both N-IMB and IMB joints under all researched compression levels complies with the Mohr–Coulomb failure criterion, namely,

$$\tau = c_0 + \mu\sigma \quad (2)$$

where c_0 denotes initial cohesion, which can be assumed as zero for both N-IMB and IMB joints, and μ denotes the representation coefficient. The friction coefficients of both N-IMB and IMB joints with different interlocking shapes are listed in Table 1.

According to Table 1, compression stress level plays an important role on the friction coefficients of the N-IMB and IMB joints. Regardless of the interlocking shapes, as the compression stress increases, the friction coefficient increases by more than 12.5%, and the variation decreases. The maximum increment in the friction coefficient was observed for IMB with circular shape (18%), and the minimum increment was achieved for IMB with rectangular shape (12.5%). The friction coefficient is insensitive to the interlocking shape. Under the same compression stress, when the interlocking shape varies, the variation range of the friction coefficients is less than 10%.

The effect of compression stress on the friction coefficients is primarily caused by the contact degree between two bricks. The upper and bottom bricks do not have tight contact because of the existence of “micro burrs”, and the real contact area between the upper and bottom bricks varies as the compression changes. As the compression stress increases, more micro burrs bite into one another on the contact surface, resulting in an additional contact area and an increment in the shear force of the mortarless joints. Furthermore, with the increase in compression stress, the bite force is overcome during sliding, which also contributes to the increment in shear force.

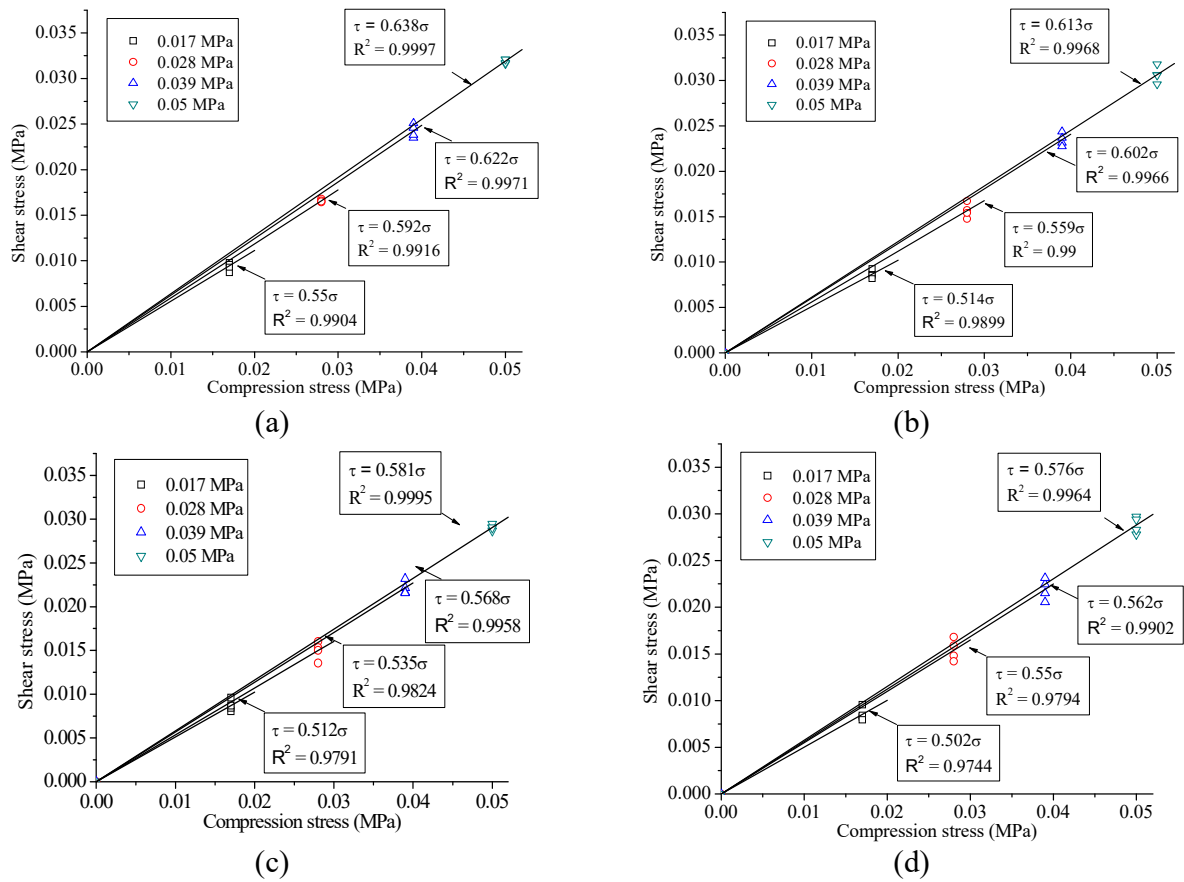


Figure 7: Experimental failure criteria for N-IMB and IMB joints under different compression stress level: (a) non-interlocking, (b) circular interlocking, (d) trapezoidal interlocking, (d) rectangular interlocking

Table 1: Effect of compression stress on the friction coefficient

| Interlocking Shape | Compression Stress | | | |
|--------------------|--------------------|-----------|-----------|----------|
| | 0.017 MPa | 0.028 MPa | 0.039 MPa | 0.05 MPa |
| Non-interlocking | 0.55 | 0.592 | 0.622 | 0.638 |
| Circular | 0.514 | 0.559 | 0.602 | 0.613 |
| Trapezoidal | 0.512 | 0.535 | 0.568 | 0.581 |
| Rectangular | 0.502 | 0.55 | 0.562 | 0.576 |

The effects of loading cycles on the MB joints' behavior were investigated by comparing the experimental results after 4 and 36 cycles. Both the friction coefficient and wear condition on the contact surface were investigated, and a constant compression stress level (0.05 MPa) was selected. The friction coefficients for N-IMB and IMB joints under different loading cycles are listed in Table 2.

The degradation rate (DR) of the friction coefficients was introduced to analyse the influence of

the loading cycles quantitatively. DR can be calculated as

$$DR = \left| \frac{\mu_{36} - \mu_4}{\mu_4} \right| \times 100\% \quad (3)$$

where μ_4 and μ_{36} are the friction coefficients obtained after 4 and 36 cycles, respectively. The DR for IMB with circular interlocking shape has the minimum value (19%), which is close to the value of the N-IMB joints (21%). Meanwhile, the DRs for IMB joints with rectangular and trapezoidal interlocking shapes are much larger (with an average of 33%). The results indicate that DR increases with the decrease in the smoothness of the interlocking surface.

Table 2: Effects of loading cycles on the friction coefficient

| Interlocking Shape | Loading cycles | | Degradation rate (DR) (%) |
|--------------------|----------------|-----------|---------------------------|
| | 4 cycles | 36 cycles | |
| Non-interlocking | 0.638 | 0.502 | 21% |
| Circular | 0.613 | 0.497 | 19% |
| Trapezoidal | 0.581 | 0.405 | 30% |
| Rectangular | 0.576 | 0.369 | 36% |

CONCLUSIONS

(1) A series of cyclic tests was carried out to investigate the compression–shear behavior of MB joints. In these tests, four different interlocking shapes, four compression stress levels, and two loading cycles were investigated. A novel loading test methodology, which is convenient and accurate for cyclic tests, was applied.

(2) The hysteretic loops of the N-IMB and IMB joints under the shear–compression cyclic tests were obtained. A typical Mohr–Coulomb frictional behavior was observed in the N-IMB joints. A significant stiffness hardening effect was found for the IMB joints, the effect was mainly caused by the loading direction being not parallel to the longitudinal extension of the interlocking portion during loading.

(3) Compression stress level plays an important role on the friction coefficients of the N-IMB and IMB joints. Regardless of the interlocking shapes, as the compression stress increases, the friction coefficient increases by more than 12.5%, and the variation decreases. The friction coefficients are insensitive to the interlocking shapes. Under the same compression stress, when the interlocking shape varies, the variation range of the friction coefficients is less than 10%. The influence of compression stress on the friction coefficients is primarily caused by the contact degree between two bricks.

(4) The influence of loading cycles was examined by comparing the experimental results after 4 and 36 cycles. The wear condition was studied, and the degradation rate of the friction coefficient was defined. The results showed that as the loading cycle increases, the wear becomes

increasingly severe. Wear condition has a positive correlation with the DR of the friction coefficient, which means that when more wear occurs, a larger DR is obtained.

ACKNOWLEDGEMENT

The authors are grateful to the financial support from the National Natural Science Foundation of China (51608153, 51508135) and Natural Scientific Research Innovation Foundation in Harbin Institute of Technology (HIT.NSRIF.2017050).

REFERENCES

- Anand K.B., and Ramamurthy K. (2014). Development and Performance Evaluation of Interlocking-Block Masonry. *Journal of Architectural Engineering*. 6, pp. 45-51.
- Basha S.H., and Kaushik H.B. (2015). Evaluation of Nonlinear Material Properties of Fly Ash Brick Masonry under Compression and Shear. *Journal of Materials in Civil Engineering*. 27(8):4014227.
- Cai Y., Shi J.L., Yang W.C., Lv X.Y., and Li D.J. (2014). Research of Masonry Shear Strength under Shear-Compression Action. *Advanced Materials Research*. 1065-1069, pp. 1309-1318.
- Cavaleri L., Fossetti M., and Papia M. (2005). Infilled frames: developments in the evaluation of cyclic behavior under lateral loads. *Structural Engineering & Mechanics*. 21, pp. 469-494.
- GB/T 50129-2011 Standard for the test method of basic mechanics properties of masonry. (2011). Beijing: China Architecture & Building Press.
- Liu H.J., Lin K., Liu P., and Totoev Y.Z. (2014). Numerical Analysis of Out-of-Plane Behavior of Masonry Panel Built with Topological Interlocking Brick. *In Proceedings of the 6th World Conference on Structural Control and Monitoring*. Barcelona, Spain.
- Lin K., Liu H.J., and Totoev Y.Z. (2005). Quasi-static experimental research on dry-stack masonry infill panel frame. *Journal of Building Structures*. 33, pp. 119-27.
- Lin K., Liu H.J., and Totoev Y.Z. (2012). Behavior of mortar-less masonry joint under cyclic shear-compression loading. *Journal of Harbin Institute of Technology*. 44, pp. 6-10.
- Lin K., Liu H.J., and Totoev Y.Z. (2013). Lateral bearing capacity and simplified equations of dry-stack in-filled reinforcement concrete frame structure. *Journal of Civil Architectural & Environmental Engineering* 35, pp. 21-27.
- Lin K., Liu H.J., Liu P., and Huang Y.H. (2014). Out-of-plane behaviour of unreinforced masonry walls with topological interlocking brick. *In Proceedings of the 13th International Symposium on Structural Engineering*. Hefei, China.

- Lin K., Totoev Y.Z., Liu H.J., and Wei C.L. (2015). Experimental Characteristics of Dry Stack Masonry under Compression and Shear Loading. *Materials*. 8, pp. 8731-8744.
- Lourenco P.B., and Ramos L.F. (2004). Characterization of Cyclic Behavior of Dry Masonry Joints. *Journal of Structural Engineering*. 130, pp. 779-86.
- Rui A.S., Soares E., Oliveira D.V., Miranda T., Cristelo N.M., and Leitão D. (2015). Mechanical characterisation of dry-stack masonry made of CEBs stabilised with alkaline activation. *Construction & Building Materials*. 75, pp. 349-358.
- Sanada Y., Yamauchi N., Takahashi E., Nakano Y., and Nakamura Y. Interlocking block infill capable of resisting out-of-plane loads. (2008). *In Proceedings of the 14th World Conference on Earthquake Engineering*. Beijing, China.
- Sturm T., Ramos L.F., and Lourenco P.B. (2015). Characterization of dry-stack interlocking compressed earth blocks. *Materials & Structures*. 48, pp. 3059-3074.
- Thanoon W.A.M., Alwathaf A.H., Noorzaei J., Jaafar M.S., and Abdulkadir M.R. (2008). Finite element analysis of interlocking mortarless hollow block masonry prism. *Computers & Structures*. 86, pp. 520-528.
- Thanoon W.A.M., Alwathaf A.H., Noorzaei J., Jaafar M.S., and Abdulkadir M.R. (2008). Nonlinear finite element analysis of grouted and ungrouted hollow interlocking mortarless block masonry system. *Engineering Structures*. 30, pp. 1560-1572.
- Yuen Y.P., and Kuang J.S. (2015). Nonlinear seismic responses and lateral force transfer mechanisms of RC frames with different infill configurations. *Engineering Structures*. 91, pp. 125-140.
- Zuccarello F.A., Milani G., Olivito R.S., and Tralli A. (2009). A numerical and experimental analysis of unbonded brickwork panels laterally loaded. *Construction & Building Materials*. 23, pp. 2093-2106.



**MASONRY TODAY
AND TOMORROW**

**11 - 14 February, 2018
SYDNEY AUSTRALIA**

www.10amc.com

NONLINEAR DYNAMIC RESPONSE OF DRY STACK SEMI-INTERLOCKING MASONRY WALL UNDER OUT-OF-PLANE LOAD

H.J. Liu¹, K. Lin² and D.X. Peng³

¹ Professor, Shenzhen Key Lab of Urban & Civil Engineering Disaster Prevention & Reduction, Harbin Institute of Technology, Shenzhen 518055, China, linkun.hit@gmail.com

² Assistant Professor, Shenzhen Key Lab of Urban & Civil Engineering Disaster Prevention & Reduction, Harbin Institute of Technology, Shenzhen 518055, China, liuhongjun@hit.edu.cn

³ Shenzhen Key Lab of Urban & Civil Engineering Disaster Prevention & Reduction, Harbin Institute of Technology, Shenzhen 518055, China, hitsz_aconypdx@163.com

The recent earthquakes occurred in China (Wenchuan 2008 and Yushu 2010) have shown that the collapse of masonry walls is the cause of many casualties. In order to improve the out-of-plane stability of the unreinforced masonry panel, a typological interlocking brick system was under research in Harbin Institute of Technology Shenzhen Graduate School. In this system, the shape of interlocking surface (the contact surface between up and down bricks) was considered as a critical point and a series numerical simulation was carried to insight the out-of-plane behaviour of panel.

In this paper, data from a dry stack masonry wall tested under lateral pressure loading by Totoev and Wang (2013) was used to calibrate the finite element model reported in this paper. The failure mode, the out-of-plane strength and pressure-displacement curve was studied. In this test, the wall was built without mortar and with a topological interlocking section as circle. Based on the test, a 3D finite element model was built in ANSYS for further numerical simulation. The modelling method was introduced and the accuracy of model was evaluated by experimental results. Furthermore, the stress distribution and the crack growth in panel were investigated.

In order to investigate the influence of interlocking surface, two kind of interlocking shapes, plane and surface interlocking, were introduced for the tenon. For plane interlocking, rectangular and trapezoidal shapes were used; for surface interlocking, catenary and circular shapes were used. The pressure-displacement curves, stress distribution and crack development were researched. Results shown compared with the plane interlocking shape, the topologically interlocking bricks (TIBs) with surface interlocking shapes achieved more uniform stress distribution while exhibited much lower initial stiffness. The TIBs with surface interlocking also



exhibited lower intensive of cracks which shown considerable potential benefit for infilled RC frame structures.

Keywords: *Masonry panel, out-of-plane, topological interlocking brick, parametric analysis, interlocking shapes*

INTRODUCTION

Because of its economy and low requirement of technology, the masonry was widely used as an infill for the frame structures all around the world. However, the traditional unreinforcement masonry (URM) walls were lack in both tensile and shear behaviour, which leads to the weakness of seismic performance both in the masonry structure and as infilled panel. Most URM or URM infilled panels occurred serious damage after earthquake according to the field investigation (Zhao *et al.* 2009). The urgency of improving its seismic behaviour, both the in-plane and out-of-plan behaviour, was getting more and more attention all around the world.

As the masonry wall is one major part of the frame structure, how to increase the energy dissipation contribution while keep slight rigid effect will be great benefit to the seismic behavior. In our previous research, dry stack masonry (DSM) has been used as infilled panel in frame (Lin *et al.* 2012). The dry stack infilled panel (DSP) can be considered as a composition of frictional damper and dissipation energy by the relative slipping between bricks. Significant energy dissipation can be obtained by the DSP while keep the frame under elastic stage (Lin *et al.* 2014). This novel brick showed significant potential in improving the in-plane seismic behaviour of panel. However, the out-of-plane stability is the other important problem to be solved before its application.

The research on out-of-plane behaviour is far behind the one on in-plane behaviour. Among all the research on out-of-plane behaviour, the arching bearing mechanism was the most common theory, which was firstly proposed by McDowell *et al.* (1956). According to this mechanism, the key factor of the out-of-plane bearing capacity is the compressive strength and thickness ratio of masonry panel, instead of the tensile strength of panel. Based on the arching mechanism, Dawe *et al.* (1989) carried series of out-of-plane experiments. Results shown although the ultimate bearing capacity was lower than the one of traditional masonry panel (built with mortar), it still has considerable load bearing and exhibits significant arch bearing mechanism.

Series research was also carried on the out-of-plane stability of masonry panel under different material composition and/or geometric dimensions (Komaraneni *et al.* 2011; Russo *et al.* 2013). Results show that the out-of-plane capacity was mainly influenced by the compression strength, aspect ratio and boundary condition between panel and frame; the initial cohesion between bricks has slight contribution. An explicit finite element (EFE) formulation based on layered 3D shell element has been presented by Noor-E-Khuda *et al.* (2016a; 2016b). Results shows the EFE model can predicted the out-of-plane behaviour of URM walls successfully, which could be applied for further research. Those researches made the improvement of dry stack masonry been possible. Instead of improve the initial cohesion, special interlocking shapes as introduced in the dry stack panel, shown in Figure 1b. This kind of brick is namely as topologically interlocking brick (TIB).

After the out-of-plane tests of TIB frame was carried out at the University of Newcastle (Totoev *et al.* 2013), this paper focus on the parametric analysis of different interlocking shape with the finite element model. The nonlinear and interaction behaviour of TIB have been modelled using 3D solid element and connection element respectively in ANSYS. The finite element model was firstly verified by experimental results both on the load-displacement curve and failure mode, then used for further parametric analysis to research on the influence of different interlocking shape.

SUMMARY OF EXPERIMENTAL PROGRAM

The out-of-plane test carried by Totoev *et al.* (2013) in the University of Newcastle was selected as a comparison. In this test, the masonry wall was infilled in a steel frame with a dimension of $2\text{m} \times 2\text{m}$. The infilled panel was consist of thirty layers, each layer included ten and a half bricks. The infilled panel was built of TIB. The interlocking shape was defined by the profile of the standard lysaght corrugated steel roofing sheeting, which made the bricks easier to be produced. The dimension of TIB is $230 \times 114 \times 76\text{ mm}$ and the height of circle was 8 mm , as shown in Figure 1. Further detail can be found in reference (Totoev *et al.* 2013).

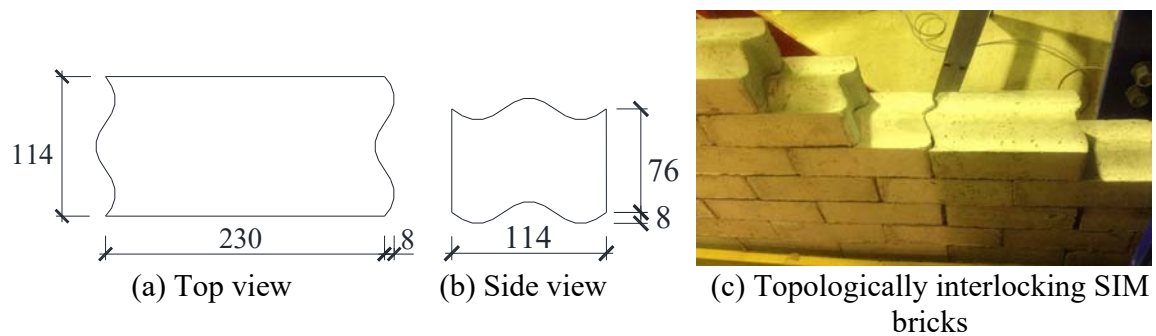


Figure 1: Dimension of the TIB

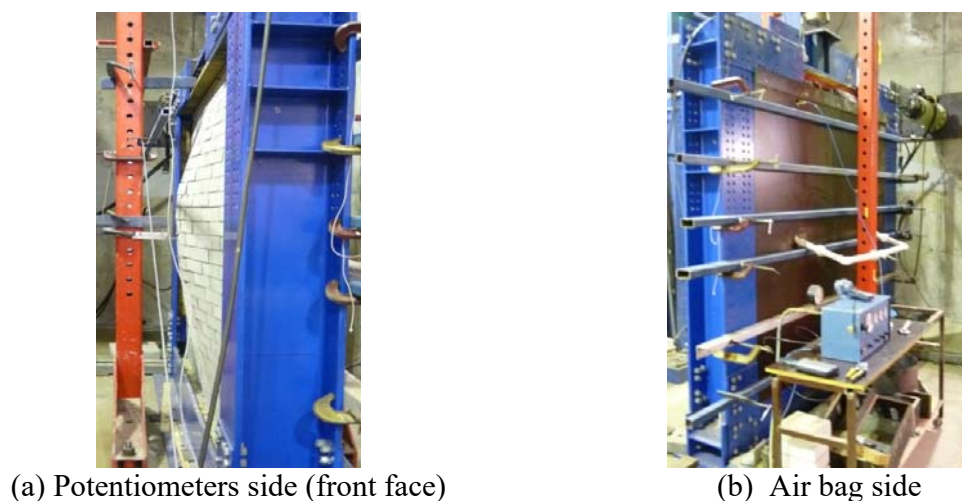


Figure 2: Out-of-plane test set up (Totoev *et al.* 2013)

The arrangement of TIBs was shown as Figure 1 c. The base beam was fixed to the strong floor. The out-of-plane test was pressure controlled. The load was applied by increasing the air pressure in the air bag. The displacements were measured by potentiometers on the other side of the panel. There were no in-plane loads applied during this test. The out-of-plane test was shown in Figure 2.

BENCHMARK MODEL

The software ANSYS was chosen and micro modelling strategy was used in the simulation, shown as Figure 3. In this model, an eight node continuum solid element SOLID65 was chosen for concrete frame and bricks; a contact element pair (CONTA173 and TARGET170) was used to simulate the joints between individual TIB units and between the infilled panel and the frame.

The finite element model was completely constraint in the bottom of frame to meet the practical situation, shown as Figure 3. In order to simplified the analysis, only circle of the horizontal contact surface (top and bottom of the brick) was simulated, the vertical surface was considered as plane, shown as Figure 4. Meanwhile, the calculation precision, the brick was divided into 120 elements as shown in Figure 4 .

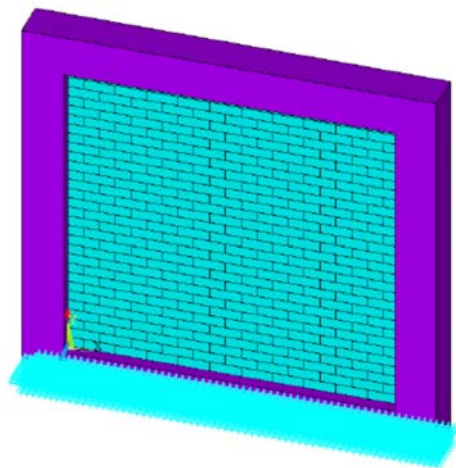


Figure 3: Finite element (FE) model

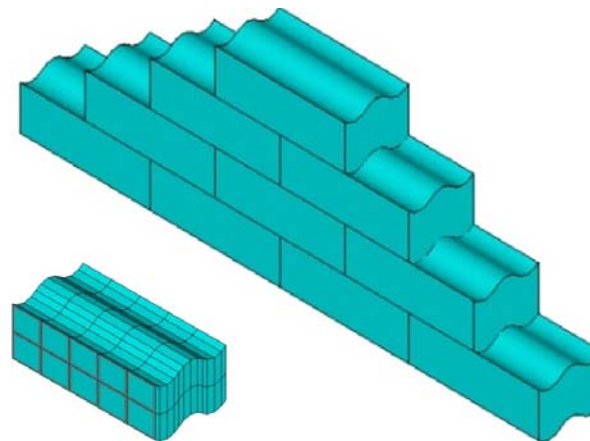


Figure 4: FE Model and meshing of experimental TIB

Table 1: Parameters Used in Finite Element Model

| Brick | | | | | Contact pairs | | |
|-----------------------|------------------------------|------------------------|----------------------------|-----------------|---------------------------------|------------------|-----------------|
| Elastic Modulus (MPa) | Density (kg/m ³) | Tensile strength (MPa) | Compression strength (MPa) | Poisson's ratio | Normal penalty stiffness factor | Contact cohesion | Friction factor |
| 6675 | 25000 | 0.89 | 8.9 | 0.3 | 0.00025 | 0.00001 | 0.7 |

The compressive strength of TIB prism of 8.9 MPa was confirmed by specimen tests (Totoev *et al.* 2013). The elastic modulus of TIB (6675 MPa) was confirmed as 750 times of compressive strength according to the UBC-97 (1997). Most of the parameters for the non-linear models have been confirmed from preliminary material tests, as listed in Table 1. The numerical results were compared to the experimental results and some parameters have been adjusted to achieve reasonable matches to experiments.

A common value of 28000 MPa was used for RC frame. To achieve the nonlinear behaviour of TIB, the Von Mises multilinear isotropic hardening criteria was used to simulate the nonlinear behaviour of TIB, the strain-stress curve was shown as Figure 5 as suggested in Chinese seismic standard (2010).

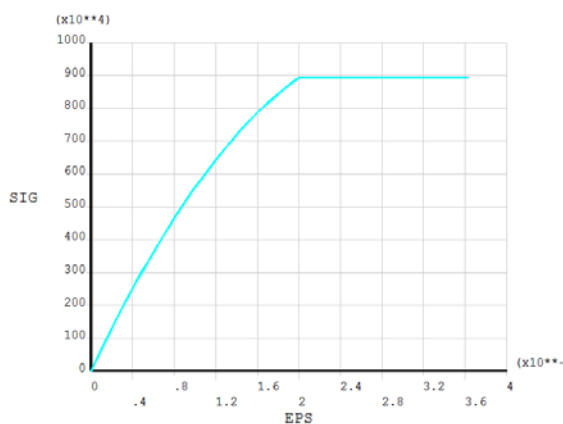


Figure 5: Nonlinear behavior of TIB

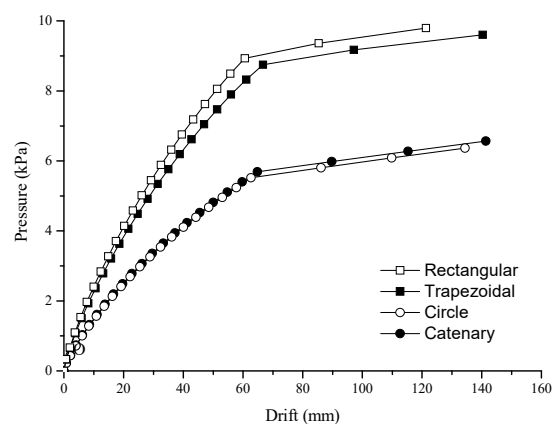
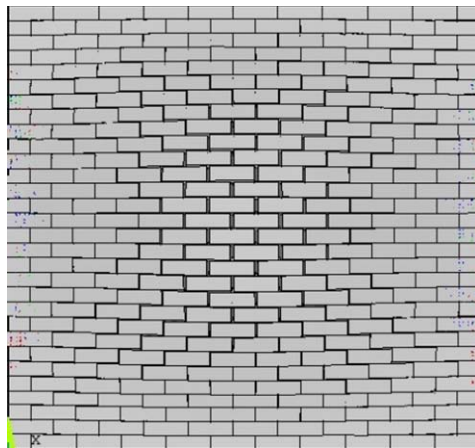


Figure 6: Out-of-plane load-displacement curves for TIB



(a) FE model result



(b) Experimental result

Figure 7: Final crack of TIB panel

The FE model was verified by comparing both the pressure-displacement curve and failure mode with the experimental results. Figure 6 shows the comparison between the middle point's out-of-plane pressure-displacement curves obtained from numerical analysis and the experimental

results. The numerical results fit the experimental results with reasonable accuracy. Figure 7a presents the deformation at the end of numerical simulation. Out-of-plane deformation can be clearly found between individual brick, which reflect the experimental failure mode in good accuracy, shown as Figure 7b.

PARAMETRIC ANALYSIS

In order to investigate the influence of interlocking surface, two kind of interlocking shapes, plane and surface interlocking, were introduced for the tenon.

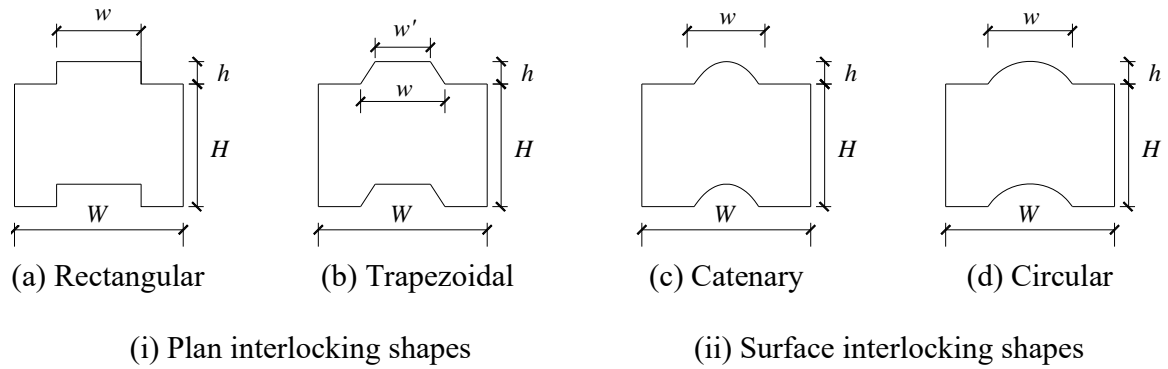


Figure 8: Different interlocking shapes

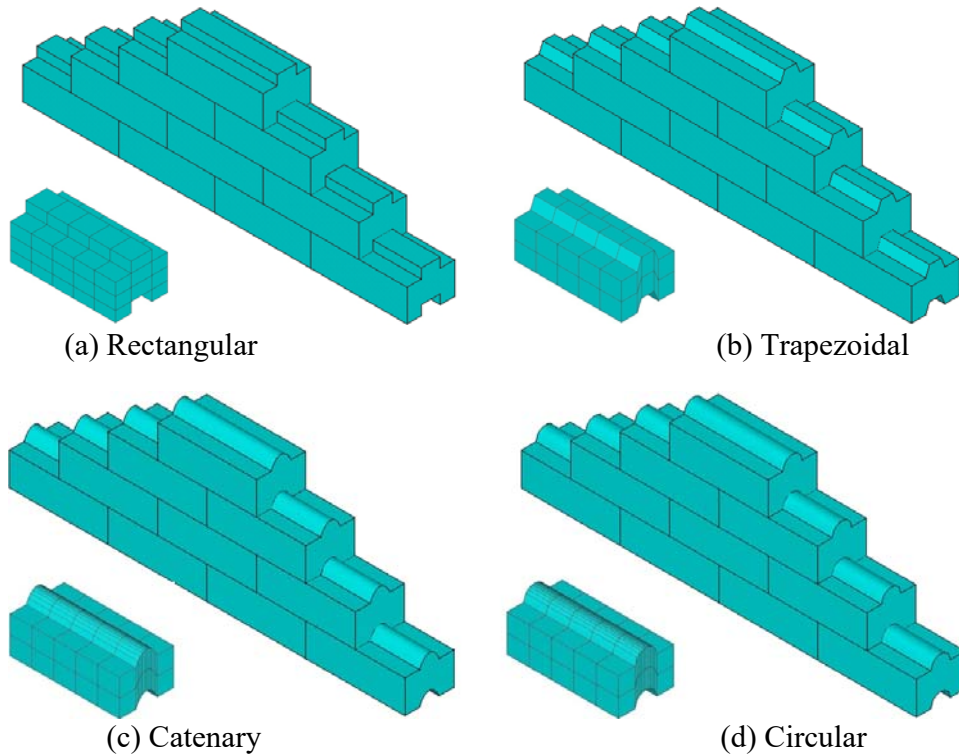


Figure 9: FE Model and meshing condition of different interlocking shape

For plane interlocking, rectangular and trapezoidal shapes were used; for surface interlocking, catenary and circular shapes were used. The geometry dimension schematic diagram was shown as Figure 8. In this figure, W , H is the thickness and height of brick which value is 114 mm and 76 mm (same as the experimental brick); w and h are the width and height of tenon respectively. In this research, the width and height ratio was keep constant for different four interlocking shapes, where $w/W = 0.4$, $h/H = 0.3$, $h/w = 0.5$.

The FE model was built following the same strategy and using same materials as the benchmark model. The FE models and corresponding meshing conditions were shown as Figure 9.

RESULTS

Figure 10 shows the comparison of middle point's out-of-plane pressure–displacement curves for different interlocking shapes. All the pressure-displacement curves exhibited significant bilinear behaviour. The initial stiffness was resulted from the arching mechanism, which was determined by the compression strength of TIB brick and the interlocking mechanisms. The initial stiffness of plane interlocking types (rectangular and trapezoidal) was larger than the one of surface interlocking types (catenary and circular). When the out-of-plane drift over 65 mm, the out-of-plane stiffness of all conditions decreased and exhibited almost same stiffness. The maximum out-of-plane capacity of plane interlocking types (rectangular and trapezoidal) is 50% higher than the one with surface interlocking types (catenary and circular), the average value were 9.7 kPa vs. 6.46 kPa. The ductility of four conditions has slight differences.

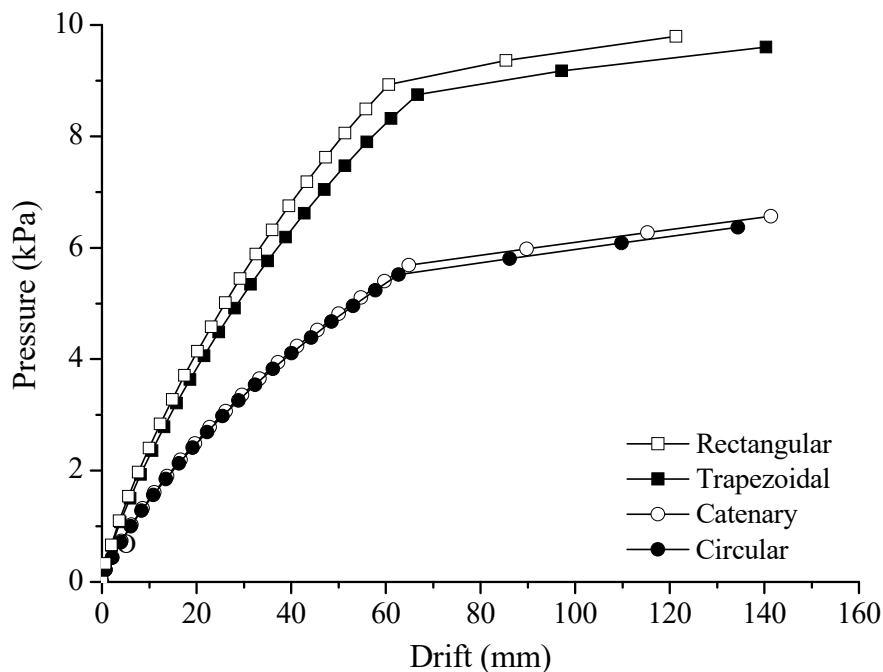


Figure 10: Out-of-plane load-displacement curves for different TIBs

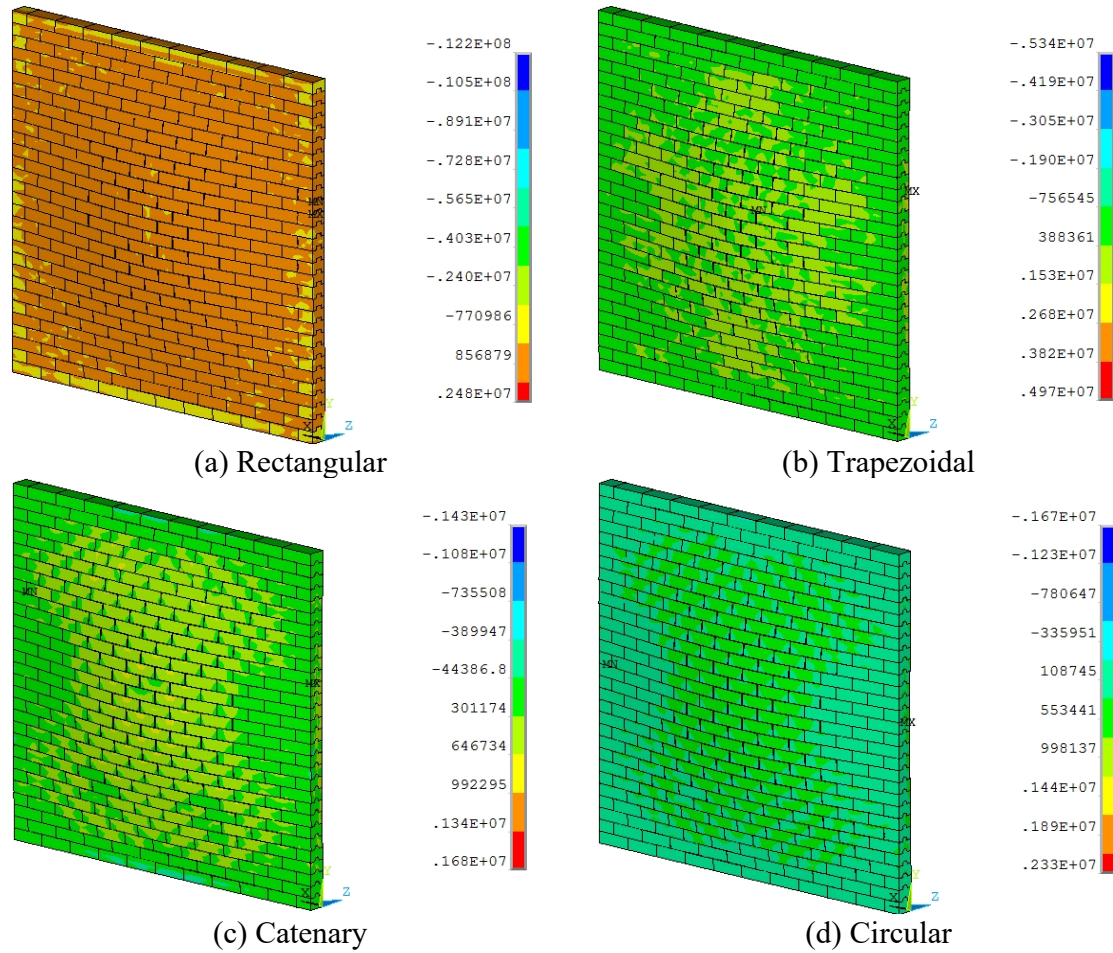
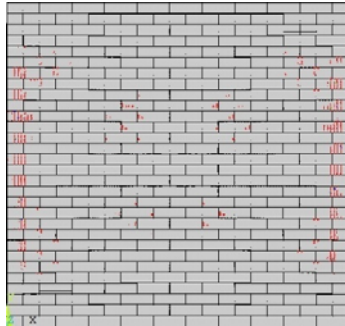


Figure 11: First principal stress of TIB panels

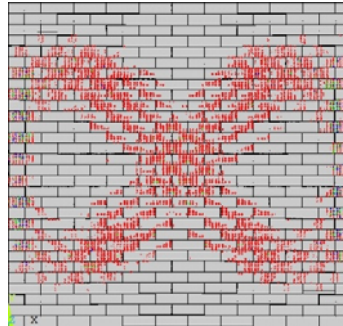
Figure 11 shows the first principal stress distribution in the TIB panels. The stress of surface interlocking is much lower than the one of plane interlocking shapes. The average value of first principal stress in the rectangular interlocking TIB panel was about 2.0 MPa, which indicate that the cracks were easily occurred widespread the whole panel, as shown in Figure 11 a. The first principle stress of trapezoidal TIB panel exhibited “+” mode and the value was around 1.53 MPa, which was slightly smaller than rectangle TIB panel. For the catenary and circular TIB panels, the contribution of first principal were “X” form, the value were 0.64 MPa and 0.55 MPa respectively. This contribution more in line with the two-way slab crack forms.

Figure 10 presents the cracks of concrete for different interlocking shapes under ultimate out-of-plane pressure. According to this figure, the progressive failure can be analysed. At the end of initial stage, there’s almost no crack in the TIB for all the interlocking shapes (“a” series in Figure 12), which indicate the out-of-plane performance keep elastic. At this stage, only some dispersed coverable cracks appears near the connection between panel and columns, which indicate the connection dominate the initial behaviour of panels. As the pressure increasing, more cracks start occurred at middle of the panel and extend as a diagonal “X” from (“b” series in

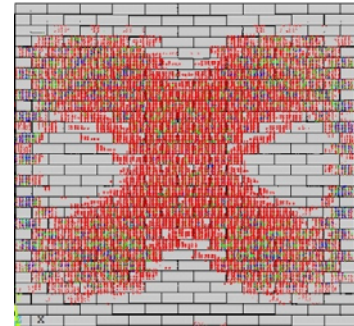
Figure 12). After the “X” cracks extend to vertical zonal cracks, a final “ ∞ ” form can be achieved (“c” series in Figure 12). Different with the plane interlocking TIBs, the intensive of cracks in the surface interlocking TIBs are much lower, which was mostly because smooth interlocking will result in a more reasonable stress distribution and avoid the stress concentrated which postponed the final damage.



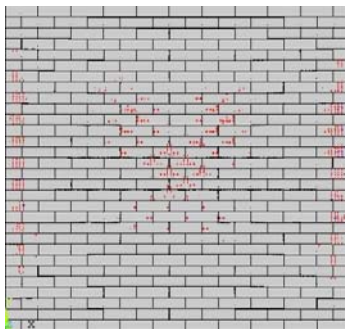
(a) Step 21



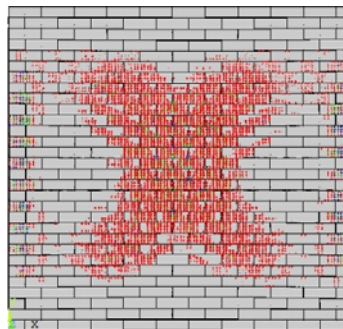
(b) Step 22
(i) Rectangular



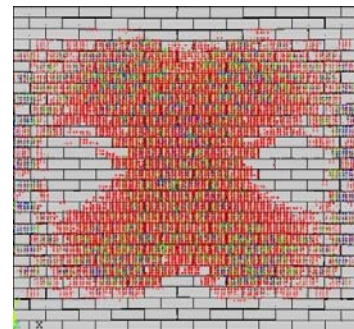
(c) Step 23



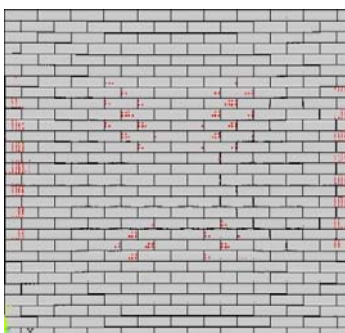
(a) Step 21



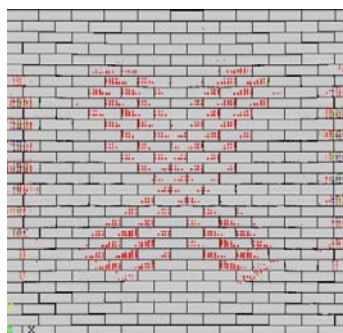
(b) Step 22
(ii) Trapezoidal



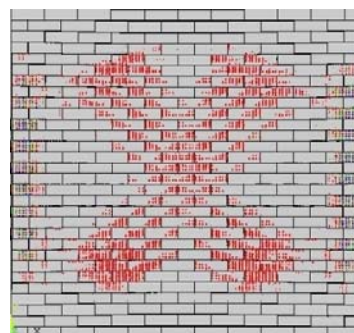
(c) Step 23



(a) Step 21



(b) Step 22



(c) Step 23

(iii) Catenary

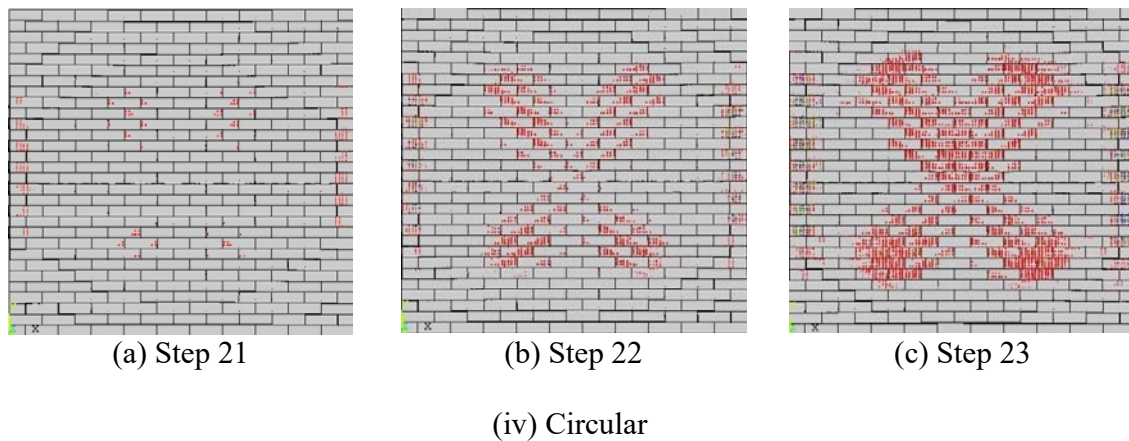


Figure 12: Crack development in TIB panels

CONCLUSIONS

An finite element model of TIB panel was built using ANSYS software. The developed FE model is capable of capturing complex structural response with a good accuracy. Both plane and surface interlocking were introduced in parametric analysis. Four kinds of shapes (rectangle, trapezoidal for plane interlocking; catenary, circle for surface interlocking) were researched. The TIB with plane interlocking tenons shown larger initial stiffness while TIB with surface interlocking tenons exhibit better stress distribution behaviour. The connection between panel and frame has a critical impact on the out-of-plane capacity for all different types of tenons. The surface tenons postpone the damage of the panel because of less stress concentration occurred. The different influence of interlocking tenons will be useful for further performance-based seismic design of TIB panel infilled RC frame structures.

ACKNOWLEDGEMENTS

The authors are grateful to the financial support from the National Natural Science Foundation of China (51608153, 51508135) and Natural Scientific Research Innovation Foundation in Harbin Institute of Technology (HIT.NSRIF.2017050). The material behavior of TIB tests was provided by Dr. Totoev and Ms. Wang in the University of Newcastle, whose kindness is gratefully acknowledged.

REFERENCES

- Dawe J. L., And Seah C. K. (1989), Out-of-plane resistance of concrete masonry infilled panels, Canadian Journal of Civil Engineering, 16(6), pp. 854-864.
- GB 50011-2010 Code for seismic design of buildings [S]. (2010). Beijing: China Architecture &

Building Press.

International Conference of Building Officials. (1997). Uniform building code. *International Conference of Building Officials*.

Komaraneni S., and Rai D. C., et al. (2011). Seismic behavior of framed masonry panels with prior damage when subjected to out-of-plane loading, *Earthquake Spectra*, 27(4), pp. 1077-1103.

Lin K., and Liu H. J., et al. (2012). Quasi-static experimental research on dry-stack masonry infill panel frame, *Journal of Building Structures*, 33(2), pp. 119-127. (in Chinese).

Lin K., and Yuri Zarevich T., et al. (2014). Modeling of dry-stacked masonry panel confined by reinforced concrete frame, *Archives of Civil and Mechanical Engineering*, 14, pp. 497-509.

McDowell E. L., and McKee K. E., et al. (1956). Arching action theory of masonry walls, *Journal of the structural division, ASCE*, 82(2), pp. 915.

Noor-E-Khuda S., and Dhanasekar M., et al. (2016a). An explicit finite element modelling method for masonry walls under out-of-plane loading. *Engineering Structures*, 2016(113), pp. 103-120.

Noor-E-Khuda S., and Dhanasekar M., et al. (2016b). Out-of-plane deformation and failure of masonry walls with various forms of reinforcement. *Composite Structures*, 2016(140), pp. 262-277.

Russo, S., (2013). Testing and modelling of dynamic out-of-plane behaviour of the historic masonry façade of Palazzo Ducale in Venice, Italy, *Engineering Structures*, 46, pp. 130-139.

Totoev, Y., and Wang Z. (2013), In-plane and out-of-plane tests on steel frame with SIM infill. *12th Canadian Masonry Symposium*, Vancouver, British Columbia, Canada.

Zhao, B., and Taucer F., et al. (2009). Field investigation on the performance of building structures during the 12 May 2008 Wenchuan earthquake in China, *Engineering Structures*, 31(8), pp. 1707-1723.

THE OUT-OF-PLANE CAPACITY OF SEMI-INTERLOCKING INFILL PANELS: EXPERIMENTAL INVESTIGATION

O. Zarrin¹, Y.Z. Totoev² and M.J. Masia³

¹ PhD Candidate, Centre for Infrastructure Performance and Reliability, The University of Newcastle, Callaghan, NSW 2308, Australia, orod.zarrin@newcastle.edu.au

² Senior Lecturer, Centre for Infrastructure Performance and Reliability, The University of Newcastle, Callaghan, NSW 2308, Australia, Yuri.Totoev@newcastle.edu.au

³ Associate Professor, Centre for Infrastructure Performance and Reliability, The University of Newcastle, Callaghan, NSW 2308, Australia, Mark.Masia@newcastle.edu.au

The Semi Interlocking Masonry (SIM) system has been developed by the Masonry Research Group at The University of Newcastle, Australia. The main purpose of this system is to enhance the seismic resistance of framed structures with masonry panels. In this system, SIM panels dissipate energy during earthquake excitation through the friction on sliding joints between rows of SIM units. A number of testing programs have been carried out to evaluate the in-plane capacity of different framed masonry panels. However, there was only one out-of-plane test on SIM panel. The main objective of this study is to investigate experimentally the out-of-plane displacement/load capacity of the SIM panel damaged in previous in-plane tests. This paper presents the results of a full-scale SIM panel test made of SIM units with topological interlocking units. The panel was 2000×2025 mm (length × height) respectively and 110 mm thick with full contact to the frame. A lateral load was applied by a hydraulic jack. The load and displacement shape of the panel were recorded at regular increments. The results show that the SIM panels have significant out-of-plane load and displacement capacity.

Keywords: *SIM, Interlocking, Out-of-plane Capacity, Earthquake resistant, Masonry, Sliding joints*

INTRODUCTION

Dissipating earthquake energy is one of the important issues that today's structural engineers are involved with. Several different types of dampers have been invented with a variety of performance characteristics; for example, active, semi-active and passive devices to dissipate the seismic energy. Masonry is a popular material used throughout the world because of its special structural and building characteristics, as well as the cost and availability. However, this material has some limitations for use in seismic regions due to its inherent weakness in tension and shear. These properties combined with the high rigidity and low ductility of the masonry panels cause brittle behaviour during earthquake excitation.

To overcome this deficiency, different materials and methods have been used to reinforce masonry panels. In a frame structure, brittle masonry panels are combined with a ductile frame made of concrete or steel. This method became popular because of economical and practical aspects (Lin et al. 2011). The energy dissipation in traditional framed masonry structures occurs mainly through damage to the frame and infill panels accomplished by the stiffness reduction. This damage could be potentially unsafe and costly to repair. In order to avoid or significantly minimize the damage while improving the energy dissipation, the new masonry panel was proposed (Totoev et al. 2011).

This new mortarless masonry system consists of specially designed bricks capable of relative in-plane sliding of the panel but restrained against out-of-plane sliding. It was named semi-interlocking masonry (SIM) to reflect this specific feature of the new system. A masonry infill panel should be regarded as a structural element that participates in resisting horizontal loads. The rigidity of the panel plays a key role to reach the semi-interlocking brick objective: therefore, increase in flexibility is achieved by reducing the rigidity (Totoev et al. 2011).

There are two main ways to achieve the semi-interlocking effect between bricks:

- 1) Using traditionally shaped bricks with dowels (mechanical semi-interlocking).
- 2) Using specially shaped bricks (topological semi-interlocking) (Wang et al. 2014).

Several in-plane investigations have been performed to evaluate the capacity of different masonry panels (Madan et al., 2004; Uzoegbo et al., 2007; Lin, et al., 2015; Lin et al., 2011; Liu et al., 2016; Hossain et al., 2017). The out-of-plane behaviour of SIM panels has received little attention.

According to the research done by Derakhshan et al. 2008, the initial cracks in the mortarless panels cannot threaten the human life. In fact, mortarless panels are able to absorb more energy than traditional masonry panels. This paper presents results of an out-of-plane full-scale test on a SIM panel made of units with topological interlocking units. A lateral load was applied by a hydraulic jack. The load and displacement shape of the panel were recorded at regular increments. The results show that the SIM panels have significant out-of-plane load and displacement capacity.

TEST SETUP

The panel dimensions were 2000×2025 mm (length × height) respectively. The panel was 110 mm thick with full contact to the frame. The panel was mortarless and made of topological semi-interlocking bricks with dimensions of 220×110×76 mm (Figure 1). These bricks have “33” MPa compressive strength. Linseed oil based putty was used on all bed and head joints to improve buildability, thermal performance and resistance to water penetration (Totoev et al. 2015).



Figure 1: Topological interlocking of SIM bricks

The panel was framed by a universal column steel frame, which was attached to the strong floor (Totoev and Wang 2013). The columns in the frame are 310UC137 section, the base beam is 310UC137 section and a 23 mm plate is welded along the underside of the base. The top beam consists of two-310UC137 sections and a T section using a 250mm by 30mm plate and a 300mm by 20 mm plate welded together (Wang et al. 2015).

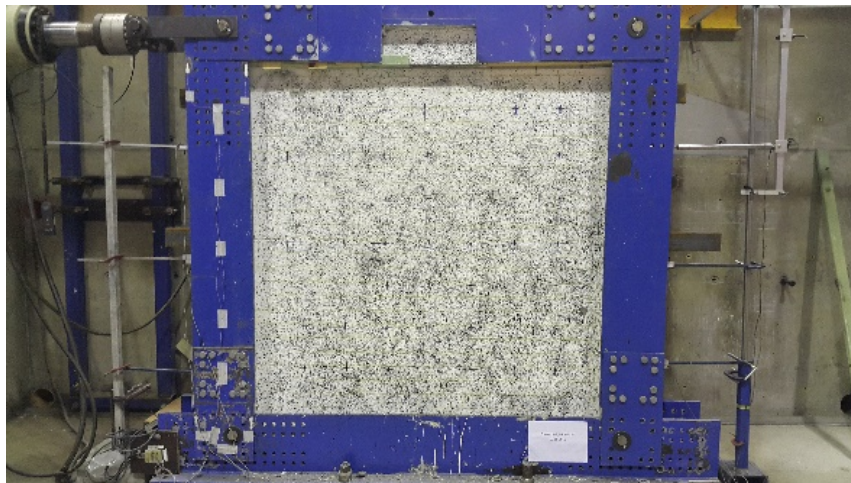


Figure 2: Panel in the steel frame

The lateral load was applied at the centre of the panel by a hydraulic jack through a hexagonal plate (6 mm thickness) as shown in Figure 3a. The plate and jack have been supported by a reaction

structure, which consists of beams (150UB18.0) and fixed to the universal frame by bolts (class 8.8 M20).

The load and lateral displacements of the panel were recorded at regular displacement increments. The edges of the panel were restrained by timber packers between the panel and the frame to simulate simple support. The 65 mm gap at the top has been filled with grout (Totoev et al. 2013). This grout was a mixture of cement and sand (Cement: Sand =1:6). The mean compressive strength of the grout after 28 days was 15.40 MPa (Hossain et al. 2017). This test was performed after the in-plane test. And several cracks can be seen in Figure 3b.

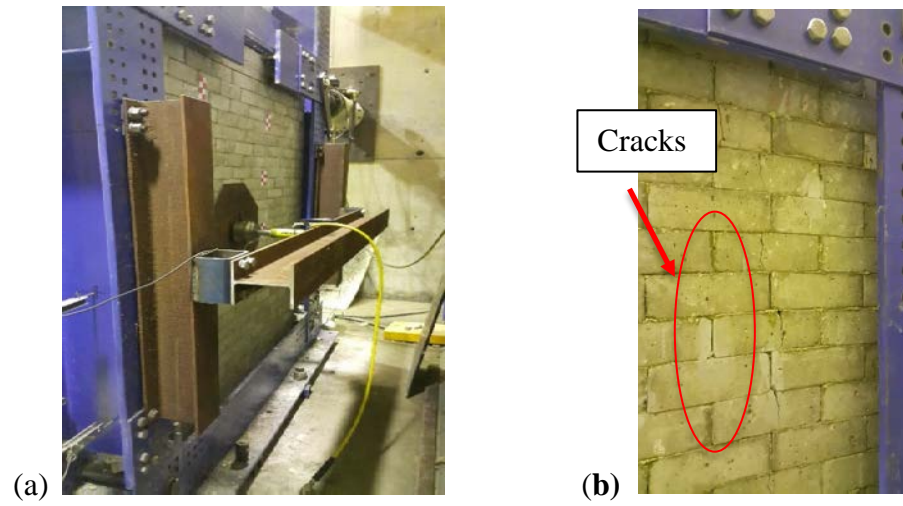


Figure 3: Hydraulic jack setup (a), cracks after previous in-plane test (b)

TEST PROCEDURE

The out-of-plane deflection was measured by Leica Laser Camera (Kennedy 2016) that recorded the lateral displacement by scanning over 10 mm \times 10 mm mesh on the panel. The Theodolite camera was also used to measure the mid-point displacement of the panel (Figure 4). In every 5 mm displacement the total deflection and load on the panel was recorded. Leica Cyclone (Kennedy 2016) and CloudCompare (EDF R. 2017) software were used for analysis of the scans.

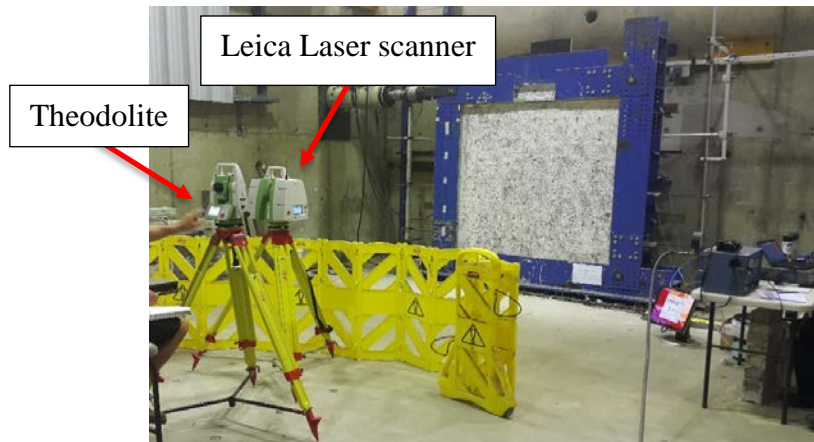


Figure 4: The displacement test setup (Leica Cyclone and Theodolite)

The CloudCompare (EDF R. 2017) software compared each scan's displacement with an initial reference scan taken before any load was applied. The computed lateral distance between dots in every scan is based on the nearest neighbour distance method (EDF R. 2017). Therefore, for each point of the compared cloud (target scan), CloudCompare searches for the nearest point in the first cloud (reference scan) and computes their (Euclidean) distance. If the reference cloud is dense enough, approximating the distance from the compared cloud to the reference cloud is acceptable (EDF R. 2017).

A Quadratic Algorithm (EDF R. 2017) was used by the software to analysis the scans. This algorithm is used for smooth/curvy surfaces and compares one dot of the target scan to six dots of the reference scan and the lateral displacement is calculated by averaging the distances.

MAXIMUM DISPLACEMENT

The out-of-plane displacement of the panel was measured at the key points as shown in Figure 5. Table 1 presents the maximum displacement on seven selected key lines. It is clear from the table that point 25 in the middle of the panel endured the maximum displacement. Figure 6 shows the displacement diagram at an applied load of 27.8 kN. The SIM panel is more flexible compared to traditional masonry panels. The maximum load capacity of the panel was 43.67 kN. The assumption of failure point is based on 20 percent post peak drop in maximum load. Accordingly, the failure point of the panel occurred at 34.84 kN with 149.72 mm displacement. However, the loading of the panel was continued until 174.5 mm displacement without collapsing the panel. This amount of displacement is significantly greater than the panel thickness.

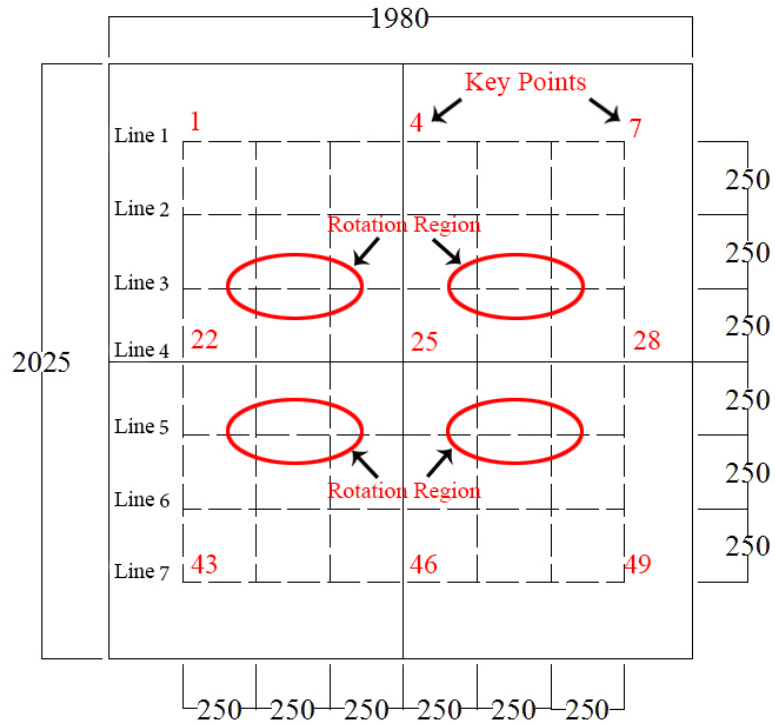


Figure 5: Position of key lines and points on the panel

Table 1: Max displacement for each key line

| Displacement (mm) | Key Points | Key Lines |
|----------------------|---------------|--------------|
| 45.2 | 4 | 1 |
| 94.2 | 11 | 2 |
| 159.2 | 18 | 3 |
| 174.5 | 25 | 4 |
| 148.5 | 32 | 5 |
| 92.8 | 39 | 6 |
| 45.1 | 46 | 7 |

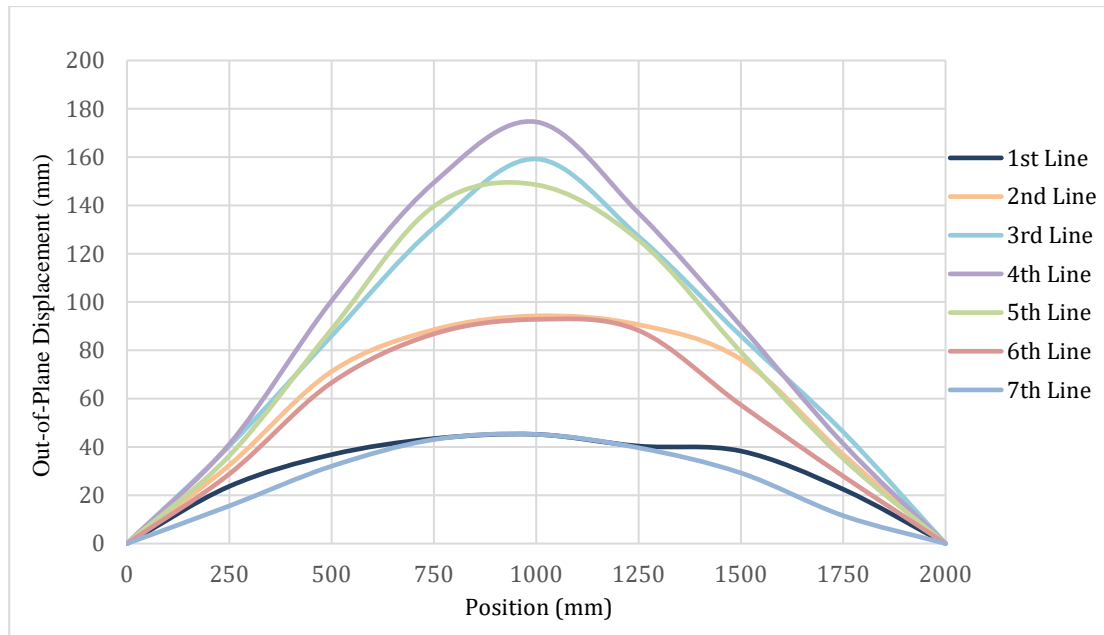


Figure 6: Displacement diagram for selected lines at an applied load of 27.8 kN

Due to filling the gap between the top of the panel and frame with grout, both vertical and horizontal arching was activated. However, only the thrust forces due to horizontal arching caused brick crushing near some head joints when the pressure reached the strength of the bricks (Figure 7). The vertical thrust induced stresses below the bricks compressive strength, hence no damage was observed due to vertical arching.



Figure 7: Crushing of bricks at head joints

The tested SIM panel (Figure 8) was more flexible than traditional masonry panels tested by previous researchers (Griffith et al. 2003; Griffith and Vaculik 2005 and 2007). The panel stability at the maximum displacement revealed that interlocking in the SIM panel could compensate for the lack of mortar perfectly and dissipate more energy without collapsing.

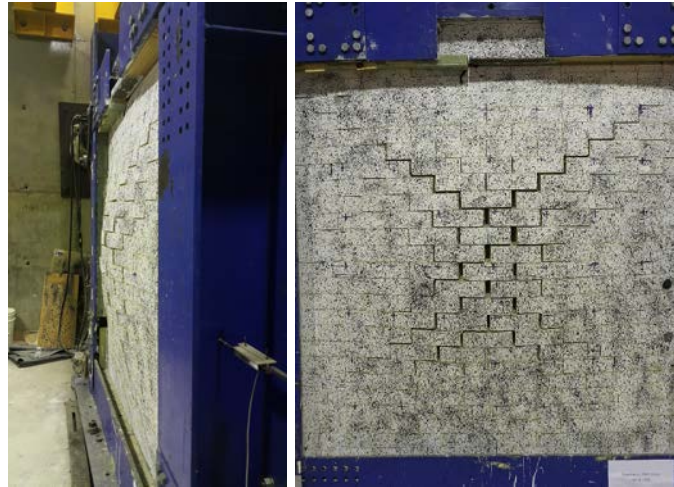


Figure 8: Joint opening pattern on the SIM panel

RESULTS AND DISCUSSIONS

Figure 9 shows the force-displacement diagram for selected points from three rows. The centre point of the panel recorded the highest displacement (174.5 mm). The first two lines belong to the bottom corners (points 43, 49), and the next two lines are the two corners at the top of panel (points 1, 7), and the rest of them show the displacement at the key points according to Figure 5. Besides the cracks from a previous test (in-plane), there were some new cracks at the head joints of bricks. Because of maximum horizontal arching in the middle of the panel, the cracks appeared on the third and fifth lines. Figure 5 indicates the rotation region, where the most cracks and crushing occurred by horizontal arching.

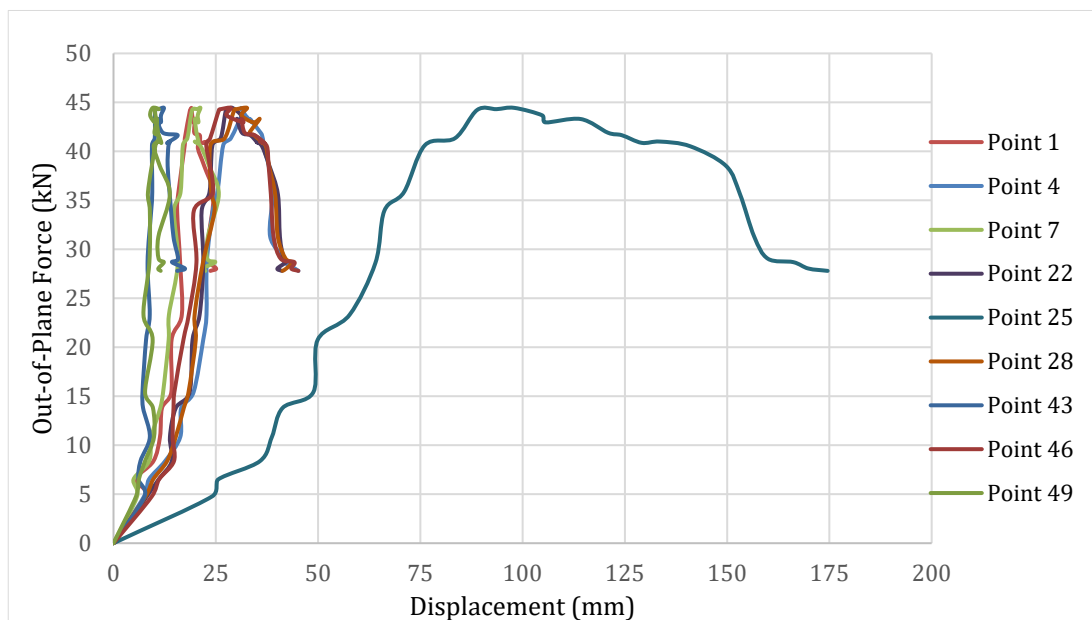


Figure 9: Force-displacement of the selected points

CONCLUSION

The test of out-of-plane semi-interlocking masonry (SIM) panel was performed on a full-scale infill panel subjected to lateral load applied by a hydraulic jack. The jack was operated in displacement control. The SIM panel displayed high flexibility and high capacity for absorbing energy. The interlocking in the panel increased the panel's displacement capacity and decreased the collapse threat compared to traditional mortared masonry construction. The maximum displacement of the panel was more than 170 mm, which is much greater than the panel thickness. After unloading, the panel remained steady.

REFERENCES

- Derakhshan H., and Ingham J.M. (2008). Out-of-Plane testing of an unreinforced masonry wall subjected to one-way bending. *Australian Earthquake Engineering Conference*, Ballarat, Victoria, Australia.
- EDF R., and D T.P., (2017). CloudCompare (version 2.6.1) [GPL software]. Retrieved from <http://www.danielgm.net/cc/>.
- Griffith M., and Vaculik J. (2005). Flexural strength of unreinforced clay brick masonry walls. *Paper presented at the Proceedings of the 10th Canadian Masonry Symposium*, Banff, Alberta.
- Griffith M., and Vaculik J. (2007). Out-of-plane flexural strength of unreinforced clay brick masonry walls. *TMS Journal*, 25(1), 53-68.
- Griffith, M. C., Magenes, G., Melis, G., and Picchi, L. (2003). Evaluation of Out-of-Plane Stability of Unreinforced Masonry Walls Subjected to Seismic Excitation. *Journal of Earthquake Engineering*, 7, pp. 141-169.
- Hossain A., Totoev Y., Masia M., and Friend M. (2017). In-Plane Cyclic Behavior of Semi Interlocking Masonry Panel Under Large Drift. *13th Canadian Masonry Symposium*, Halifax, Canada.
- Kennedy C.R. (2016), Leica Cyclone Basic User Manual.
- Lin K., Totoev Y., and Liu H. (2011), In-Plane Cyclic Test on Framed Dry-Stack Masonry Panel. *Advanced Materials Research*, Vols. 163-167: 167, pp, 3899-3903.
- Lin K., Totoev Y., Liu H., and Wei C. (2015), Experimental Characteristics of Dry Stack Masonry under Compression and Shear Loading, *Materials Science Journal*.
- Madan A., Senthivel R., Uzoegbo H., and Jäger W. (2004). Influence of Masonry Infills on the Dynamic Response of R/C Framed Structures. *Paper presented at the 13th International Brick and Block Masonry Conference*.
- Lin K., Totoev Y.Z., Liu H., and Wei C. (2015), Experimental Characteristics of Dry Stack Masonry under Compression and Shear Loading. *Materials*, 8(12), pp, 8731-8744.

Lin K., Totoev Y.Z., and Liu H.J. (2011), In-Plane Cyclic Test on Framed Dry-Stack Masonry Panel. *Paper presented at the Advanced Materials Research.*

Liu H., Liu P., Lin K., and Zhao S. (2016), Cyclic Behavior of Mortarless Brick Joints with Different Interlocking Shapes. *Materials*, 9(3), pp, 166.

Totoev Y., and Wang Z. (2013). In-plane and out-of-plane tests on steel frame with SIM infill. *12th Canadian Masonry Symposium*, Vancouver, British Columbia.

Totoev Y., Forghani R., Kanjanabootra S., and Alterman D. (2015). Experimental investigation of thermal insulation properties of Semi Interlocking Masonry (SIM) Walls. *Proc., 16th International Brick and Block Masonry Conference*, Padova, Italy.

Totoev Y., Lin K., and Page A. (2011). Numerical Modeling of Framed Dry Stack Masonry Panels. *Eleven Annual NAMC National Conference.*

Uzoegbo H., Senthivel R., and Ngowi J. (2007). Loading Capacity of Dry-Stack Masonry Walls. *The Masonry Society Journal*, 25(1), pp, 41-52.

Wang Z., Totoev Y., and Lin K. (2014). Experimental Study on RC and Steel Frames with SIM Infill. *9th International Masonry Conference*. Guimarães.

Wang Z., Totoev Y., Page A., Sher W., and Lin K. (2015), Numerical simulation of earthquake response of multi-storey steel frame with SIM infill panels. *Advances in Structural Engineering and Mechanics (ASEM15)*.

UNSHAKEN: RETAINING ARCHITECTURAL QUALITIES OF HISTORIC URM CHURCHES AND CHURCH PRECINCTS WITHIN THE NEW ZEALAND SEISMIC RETROFIT PROCESS

Stacy Vallis¹, Sonia Giovinazzi², Shannon Abeling³ and Jason Ingham⁴

¹ Doctoral Candidate, School of Architecture and Planning, The University of Auckland, Grafton, Auckland 1010, New Zealand, sval034@aucklanduni.ac.nz,

² Senior Research Fellow, Department of Civil and Natural Resources Engineering, University of Canterbury, Christchurch, 4800, New Zealand, sonia.giovinazzi@canterbury.ac.nz

³ Doctoral Candidate, Department of Civil and Environmental Engineering, The University of Auckland, Newmarket, Auckland, 1023, New Zealand, sabe321@aucklanduni.ac.nz

⁴ Professor, Department of Civil and Environmental Engineering, The University of Auckland, Newmarket, Auckland, 1023, New Zealand, j.ingham@auckland.ac.nz

The vulnerability of New Zealand's historic unreinforced masonry (URM) church building stock was highlighted following the 2010/11 Canterbury earthquakes (M_w 7.1 Darfield earthquake and M_w 6.3 Christchurch earthquake) and the recent November 2016 Kaikoura earthquake (M_w 7.8). Inherent construction characteristics render these URM structures earthquake-prone and a topic of ongoing discussion concerns the selection of appropriate seismic retrofitting solutions to safeguard and privilege their heritage architectural fabric. URM churches constitute hubs of community activity and it is vital to promote a holistic approach for their conservation, through structural upgrading. Architectural heritage conservation best practice advocates consideration of the historic URM structure along with its architectural setting, in addition to examining the impact of structural interventions. A study of URM churches located within the Anglican Diocese of the Waikato and Taranaki regions was undertaken to explore the application of these established conservation principles, based on the key tenets outlined by the *ICOMOS New Zealand Charter for the Conservation of Places of Cultural Heritage (Revised 2010)*. The initial research phase entailed discussion of the key architectural findings and emerging themes, prior to the development of a framework for assessing various degrees of structural intervention such as post-earthquake risk mitigation or full seismic upgrading.

Keywords: *heritage, church, precinct, architecture, retrofitting, conservation*

INTRODUCTION

“Churches are not only places of worship; they are places for baptisms, betrothals and burials - the important rituals of life, both spiritual and secular.”

(McKay 2015)

The 2010/11 Canterbury earthquakes (M_w 7.1 Darfield earthquake and M_w 6.3 Christchurch earthquake) and the recent November 2016 Kaikoura earthquake (M_w 7.8) highlighted the vulnerability of the unreinforced masonry (URM) church building typology, resulting from the inherent architectural and structural characteristics of URM churches. Furthermore, churches constitute precincts or hubs of community activity whilst functioning as places of worship. Therefore it is vital to consider both their architectural significance and their wider socio-historical importance when undertaking any form of heritage conservation. The concept of ‘setting’, defined by the *ICOMOS New Zealand Charter for the Conservation of Places of Cultural Heritage Value* (2010), advocates consideration of both the historic structure as well as the wider spatial context such as auxiliary outbuildings, accessways and the surrounding landscapes (ICOMOS New Zealand 2010). A shift in focus from individual buildings to groups or precincts of such buildings for heritage conservation via seismic retrofitting can assist in facilitating greater public safety whilst retaining cultural heritage value.

The above argument evoked the following questions: to what extent can the consideration of churches as ecclesiastical precincts assist in the retention of historic architectural qualities during the process of conservation in New Zealand via seismic retrofitting? More specifically, what are the prevalent local ecclesiastical design characteristics and practices that constitute such precincts? Lastly, how does the impact of historic, existing, or proposed retrofitting solutions applied to the historic URM fabric relate to the ICOMOS principles of preservation, restoration reconstruction or adaptation (ICOMOS New Zealand 2010)?

As part of a wider study to determine the seismic resilience of New Zealand churches, a survey of those churches located within the Anglican Diocese of the Waikato and Taranaki regions was undertaken. Of approximately seventy buildings, URM structures numbered only four as the majority of churches featured timber construction. Displaying diversity in both architectural scale and masonry construction type, a closer examination of each building was warranted to extract common architectural themes and variations of these themes, contributing to their overall heritage significance. In terms of seismic risk mitigation, one of the four churches is currently undergoing seismic retrofitting as part of a wider extension scheme and one church features a 1980s retrofit. Although the two remainder URM churches have not undergone any structural modification, both churches illustrate a hybridised masonry and reinforced concrete construction technique which contributes to their seismic resilience.

Archival research coupled with onsite building inspection served as the primary research methodology. Subsequent data-processing and analysis was informed by the development of a data-processing survey template for selected churches. Based on local and international heritage guidance, this methodology assisted the extraction of key heritage considerations for the various masonry construction types and retrofitting schemes. As the first phase of an ongoing study, the exploration of these themes and their implications for cultural heritage value is contained herein. No invasive investigation was undertaken during the on-site inspection.

The discussion begins by briefly foregrounding the current context of post-earthquake conservation of URM structures, by drawing attention to the progress of the Cathedral Church of Christ (Anglican Cathedral) commonly known as the ‘Christchurch Cathedral’ and the Cathedral of the Blessed Sacrament (Catholic Basilica), both located in Christchurch.

URM CHURCHES AND THE NEW ZEALAND POST-DISASTER CONTEXT

The fate of two principal ecclesiastical buildings serves as evidence of significant religious precincts, where monumental URM architecture as well as the wider historic spatial setting and uses together comprise the cultural heritage value. The *ICOMOS New Zealand Charter (2010)* offers guidance for increasing degrees of intervention, beginning with preservation (stabilisation, maintenance, repair), restoration (reassembly, reinstatement, removal), reconstruction, and removal (ICOMOS New Zealand 2010). The scope and application of this guidance varies depending on the particular set of social and economic circumstances.

The Christchurch Cathedral (:) is centrally located within the Christchurch cityscape and derives its cultural heritage value from its stone masonry form as New Zealand’s only Gilbert Scott-designed building, along with its social role in reflecting the values of the city’s founders and functioning as the centre of the Anglican diocese (Heritage New Zealand 1983). Possibly one of the most significant aspects of the building’s original design and completion by 1904, were the debates concerning the use of timber over stone, due to earthquake hazard. Questions of reconstruction were evident as early as the late nineteenth century, when the earthquakes of 1881, 1888, and 1901 resulted in reconstruction of the upper portion of the spire first in firebrick and finally timber, sheathed in copper (Heritage New Zealand 1983).

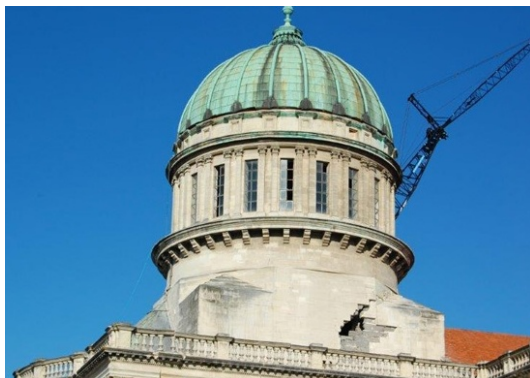


Figure 1: Post-earthquake risk mitigation of Cathedral Church of Christ (Anglican Cathedral) using temporary steel props, 2017

Following extensive damage caused by the 2010/2011 Canterbury earthquakes, and pending a final decision on 9 September 2017, the synod (governing body comprised of priests and laypeople)

responsible for the currently derelict Christchurch Cathedral (:) is confronted by three possible options for future development. Reflecting a range of attitudes and approaches to heritage conservation, these options include: (i) demolishing the remains; (ii) reinstatement or restoration; and (iii) handing the cathedral over to the Government for management on behalf of the citizenry. The decision will be reached by the Anglican synod.

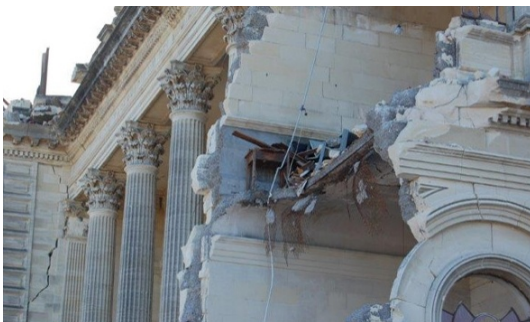
In contrast to Christchurch Cathedral, the Catholic Basilica (**Error! Reference source not found.**) underwent a process of historical documentation and removal of historic fabric, to mitigate the risk posed from falling hazards and for future reinstatement (Lester et al. 2013) (**Error! Reference source not found.**). Two major components of this operation included the recording of masonry fabric, along with the removal of the main dome. The former component involved the implementation of a numbering system corresponding to the various masonry fragments and their original position within the building structure, which were subsequently prepared for storage (**Error! Reference source not found.**). Similarly, the building's dome was systematically dismantled and also stored. The parish is currently awaiting the appointment of a new bishop prior to the confirmation or commencement of any further restoration or reconstruction work.



(a) Intact dome prior to removal



(b) Damage to dome structure



(c) Damage displaying Oamaru stone walls with poured concrete core



(d) Cathedral post-dome removal

Figure 2: Earthquake damage to the Catholic Basilica from the 2010/2011 Canterbury earthquake sequence



(a) Dome about to be lifted



(b) Craning of band element



(c) Dome being placed on ground

**Figure 3: Post-earthquake removal of Cathedral dome
(Photo credit: Opus International Consultants)**

The historic value of the Catholic Basilica derives from the outstanding architectural form, in addition to the socio-historic significance associated with the building. The Neo-classical expression promoted by the architect, Francis Petre (1847-1918), illustrates a local reinterpretation of European design principles and sits within Petre's wider repertoire of domed basilicas across Dunedin, Oamaru, Timaru and Waimate (McLean 2002). Furthermore, the Cathedral's construction method is comprised of locally-sourced Oamaru stone leaves with a poured concrete core, that is both innovative and a distinctive feature of Petre's work. Praised as "southern Irish Catholicism's bastion", the previous and ongoing efforts at conservation and future restoration are reflective of the social significance associated with the Basilica (McLean 2002).



**Figure 2: Post-earthquake documentation of masonry fragments
(Photo credit: Carole-Lynne Kerrigan)**

SURVEY METHODOLOGY

Research into the present state of seismic risk mitigation and/or conservation within the Anglican Diocese of the Waikato and Taranaki's URM churches was informed by compilation of a data collection and processing template. The development and application of the template was based on site observation and reference to best-practice heritage principles presented by various conservation policy documents, such as the *ICOMOS New Zealand Charter (2010)* (*ICOMOS New Zealand 2010*) and the *ISCARSAH Recommendations for the Analysis and Restoration of Architectural Heritage (UNESCO-ICOMOS 2003)*. These principles helped establish an overall understanding of the architectural/contextual 'setting', followed by key stylistic features or variations, and culminating with examining the nature and scope of any structural interventions. The main objective was to complement the information gathered for seismic assessment and to assist in the future selection of retrofitting solutions.

Overarching themes for the analysis of visual impact on historic URM fabric are related to the type of intervention (e.g. bracing diaphragms), along with the effects on experiential or spatial quality and material detailing. More specifically, heritage considerations included the relationship of structural modifications on existing plan configuration, integration with heritage fabric (undertaken internally or externally), expression versus concealment of the structural elements, and lastly, the impacts on architectural detailing (e.g. interior linings) and on the building's exterior. The impacts of any emergency interventions were noted. Whereas these themes were initially conceived in order to gauge the visual, material and experiential impacts of implemented structural upgrading measures, the survey revealed that only one of the URM churches had undergone previous seismic retrofitting. Therefore, a more valuable application of the template was to inform the discussion of historic construction characteristics or proposed structural interventions, rather than solely in reference to existing solutions.

SURVEY OF URM CHURCHES WITHIN THE ANGLICAN DIOCESE OF THE WAIKATO AND TARANAKI REGIONS

McKay acknowledges that "the history of our churches reflects the history of our culture" as New Zealand's colonial churches proved to be manifestations of social and ecclesiastical needs (McKay 2015). Firstly, it is acknowledged that many local churches are adaptations of the Gothic Revival architectural style and were built in timber versus their original European masonry architectural antecedents. Masonry prevailed in regions offering ready availability of the material (Thornton 2003). The surveyed URM examples constitute the minority within an inventory largely containing timber churches and within the context of New Zealand's 297 identified URM church buildings, and offer insight into various aspects of their collective cultural heritage value, as isolated examples within the Waikato and Taranaki regions. The four URM churches that were surveyed and are reported herein are as follows: St. Mary's/Taranaki Cathedral Church of St. Mary (New Plymouth), St. Mary's Church (Hawera), St. Paul's Church (Huntly), and St. Mary's Church (Gordonton). Therefore, the following discussion foregrounds the primary historic architectural and structural features relevant for consideration prior and during the undertaking of any seismic retrofitting work.

The range of architectural scales and construction typologies offers clues to wider patterns of socio-historic development of the Anglican sect within the Waikato and Taranaki regions. The reported

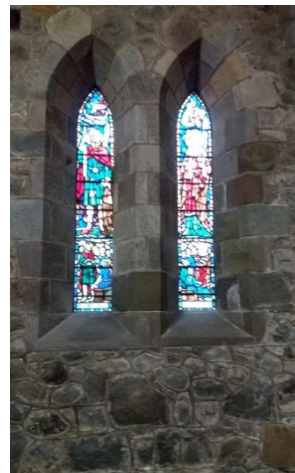
examples display varying degrees of architectural complexity requiring consideration during the assessment and retrofit design processes, as highlighted by Marotta's 2016 seismic vulnerability assessment of New Zealand URM church buildings (Marotta 2016).

A common theme to all Victorian architecture was the correctness of detail and suitability of style for a given building and its use (Stacpoole 1972). Religious differences were evident across various denominations and expressed through Gothic versus Greco-Italianate (Neoclassical) styles, of which the former was preferred by New Zealand's early Anglican sect (Stacpoole 1972). This preference was encapsulated by the 'Battle of the Styles' that took place in Europe during the mid-nineteenth century (Stacpoole 1972). The surveyed examples are all classed as examples of this style, and significance lies in their use within the colonial context.

St. Mary's is acknowledged as New Zealand's oldest stone masonry church and is more formally known as Taranaki Cathedral Church (**Error! Reference source not found.**). The Church is located within the city of New Plymouth. Seismic strengthening design is currently being undertaken, in conjunction with a scheme for extension, and this strengthening has resulted in the Church's closure since January 2016. There is no history of previous structural upgrading or modification to draw upon for reference, and therefore consideration and retention of the building's internal spatial form and construction/material detailing is of paramount importance during the process. The building is listed with Heritage New Zealand (Category 1, List No. 148) (Heritage New Zealand 2017). St. Mary's presents an example of a precinct that hosts a number of architectural elements such as supporting outbuildings or structures (e.g. the existing timber vicarage and Peace Hall, and stone masonry Hatherley Hall). The Church's early role as a garrison building is reflected by the surviving graves belonging to soldiers, and the boundary walls demarcating the churchyard landscape (Alington 1988).



(a) Exposed timber roof



(b) Lancet windows

Figure 3: Pointed arch forms evident in exposed stone masonry and timber architectural elements, Taranaki Cathedral

The succession of alterations and additions to Taranaki Cathedral, which were designed by prominent ecclesiastical architects such as Frederick Thatcher, Benjamin Mountfort, J. Sanderson

and Frank Messenger, generate the varied, albeit cohesive architectural form that is evident today. Conservation works should respect the present building form and may be based on preservation or restoration, rather than reconstruction or adaptation for example. Furthermore, proposed work should retain the detailing that contributes to an ‘Antipodean Gothic’ architectural style, credited to Thatcher for the successful use of European design principles within a new colonial context (Shaw 1991). Key characteristics include the Latin cross plan (long nave extending into chancel and sanctuary, along with the north transept and second aisle), and external features such as the steeply pitched roof, arched window heads, belfry, and unfaced stone walls (**Error! Reference source not found.**). Evidence of masonry repointing and replacement of the original lime mortar with cement is also apparent. In particular, selected methods of roof bracing or diaphragm strengthening should respect the deployment of pointed Gothic arches, which generate a greater sense of verticality, and the expressed interior rafters, purlins, and trusses comprising the roof. These features demonstrate Gothic design philosophy that greatly contributes to the internal spatial experience.



Figure 4: Steeply pitched roof and exposed masonry construction illustrating Gothic Revival stylistic tenets, Taranaki Cathedral

Taranaki Cathedral and St. Mary’s Church (Hawera) share similarity in their respective architectural scales, which is described as featuring three or more naves (‘Typology E’) within Marotta’s classification, (Figure 5**Error! Reference source not found.**) (Marotta 2016). In comparison with Taranaki Cathedral, the architectural setting of St. Mary’s is smaller although is characterised by the inclusion of a parish hall (built 1916), executed in the same construction materials and style as the Church itself. The date of construction of St Mary’s Church is 1903 and the building is currently listed with Heritage New Zealand (Category 2, List No. 862)(Heritage New Zealand 2017).

Like Taranaki Cathedral, a key historic characteristic of St. Mary’s Church lies in the present architectural form, which results from the incorporation of St. James Church within the narthex of St. Mary’s. St. Mary’s was designed by the architectural practice of Messrs. Warren and

Stephenson and unusual features of the Church are the perimeter walls consisting of both double-skin brick and timber-framed portions (Figure 6). Both interior and exterior building form, along with architectural or material detailing, deserve consideration during the undertaking of any proposed structural works. Unlike Taranaki Cathedral, the structural masonry construction is not evident in the interior as the masonry is concealed by timber and plaster backing (Figure 5). Nevertheless, Gothic-design philosophy is apparent in the expressed timber roof structure. The architectural deployment of pointed arches within door and window openings and external buttresses remain consistent with the aforementioned example. No seismic strengthening work has been scheduled, following the installation of a concrete tie-beam during the 1980s. Upon inspection, there is no external or internal evidence of this retrofit, suggesting a highly concealed approach to this work. The extent of repair, removal or reconstruction of any historic fabric is also difficult to gauge from visual inspection alone. However, masonry repointing is believed to have taken place and this work is apparent through the distinct white mortar which dominates the Church's external masonry surface (Figure 7).



(a) Expressed Roof



(b) Plaster and timber backing conceals masonry structure

Figure 5: Expressed versus concealed structure illustrates variations of Gothic Revival principles, St. Mary's (Hawera)



Figure 6: Combination of brick masonry and timber construction, legible in exterior architectural form



Figure 7: Distinctive white mortar detailing

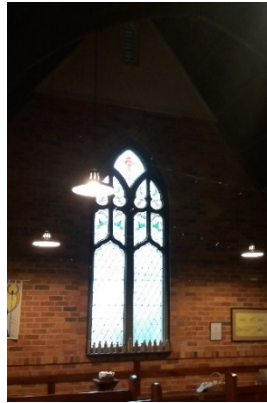
In contrast to the previous examples, St. Paul's (Huntly) and St. Mary's (Gordonton) share a number of stylistic and structural characteristics, which suggest specific considerations for future conservation via seismic strengthening. Both buildings are classed within Marotta's smaller scale church 'Typology A', featuring a single nave and demonstrating brick URM construction (Marotta 2016). The use of reinforced concrete bounding elements that were incorporated into the structural matrix at the time of original construction is apparent. Therefore, these churches may be more specifically classed as 'hybrid' URM buildings, because this technological feature is reflective of a local trend following the devastating effects of the 1931 M_w 7.8 Hawkes Bay earthquake on masonry buildings (Walsh et al. 2014). Currently both buildings are not undergoing any form of seismic strengthening.

St. Mary's Parish is located within the township of Gordonton and was constructed in 1934 (**Error! Reference source not found.**). The architectural firm of Edgcombe & White were responsible for the design. Inclusion of Gordonton cemetery, located within the north-eastern portion of the site, distinguishes the architectural setting, although there are no additional outbuildings. A series of low brick pilasters separates the building site from the road. The church has received national

heritage listing (Category 2, List No. 4303)(Heritage New Zealand 1985). Compared with St. Paul's (Huntly), the building is smaller in scale although displays similar architectural features, classifying it as an example of the Gothic Revival style. Exterior buttresses delineate the transversal walls into four bays, while lancet and rose windows can be respectively found along the rear and altar walls. Some employment of 'constructional polychromy' (a feature of the Victorian period's Gothic Revival style) is also legible in the exterior and interior surfaces, however the door or window detailing remains undefined, unlike St. Paul's (Heritage New Zealand 1990). The use of timber is restricted to the building floors and exposed roof trusses supporting a steeply pitched tile roof. In contrast to St. Paul's (Huntly), the use of bounding elements through the concrete cap beam along the transversal walls and which supports the roof trusses, is visible from the church's interior (Figure 9).



(a) Polychromatic brickwork



(b) Lancet window

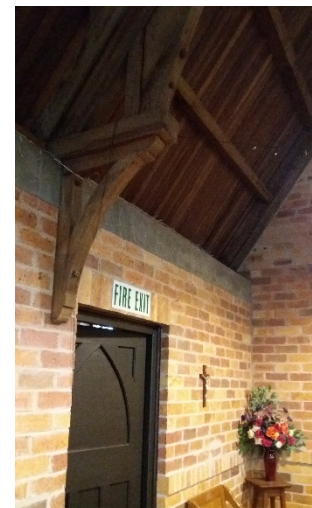


(c) Lancet door

Figure 8: Illustrating Gothic Revival stylistic characteristics: door and window forms, exterior buttresses, exposed construction and 'constructional polychromy', St. Mary's, Gordonton



(a) Beam evident under roof line



(b) Beam visible in nave

Figure 9: Concrete capping beam evident in church interior and exterior

St. Paul's Parish (**Error! Reference source not found.**) is located within the township of Huntly and was also built in 1934. The architectural setting includes a vicarage and church hall, constructed in timber and brick masonry. However these elements do not date to the time of the original church construction. Nevertheless, the whole site is bounded by a low wall, designed using the same material and ornamental forms that are legible within the main church structure. The church has received national heritage listing (Category 1, List No. 4165, Heritage New Zealand) (Heritage New Zealand 1990). Unlike St. Mary's (Gordonton), the concrete bounding elements evident in the church's original plans are believed to be concealed with a brick veneer, as was standard practice during the 1930s, hence displaying a 'concealed' approach for the incorporation of structural elements despite the Gothic Revival philosophy of expressed structure. There have been no structural or spatial additions or alterations. A combination of material detailing and the intact and distinctive architectural forms encompasses the building's heritage significance.

St. Paul's was designed by local architect N. Greenwell and features an innovative use of the locally-produced Huntly brick. Inspired by the Early English Gothic style, Greenwell's architectural adaptation is illustrated through characteristics such as the exterior buttresses, square tower, steeply pitched Marseilles tile roof, crenellated parapets, and pointed lancets evident in the window or door forms. The architectural articulation of the various openings is achieved through the use of constructional polychromy. Six differently coloured brick types generate rich and varied textures across the external form and within the Church's exposed masonry porch, narthex, and nave (Heritage New Zealand 1990). Despite the building's small scale, an internal sense of verticality emanates from the use of pointed arches and the open rimu timber roof supported by three trusses. The altar also features large terracotta-coloured blocks, although the structural performance or role of these elements is currently unknown.

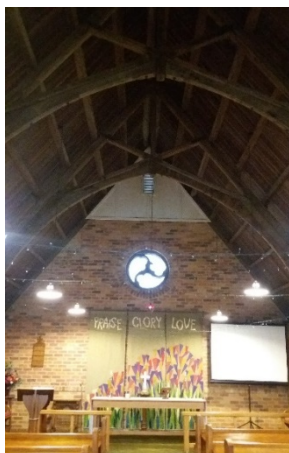


(a) Window, tower, buttress forms accentuated via polychromatic brickwork



(b) Concentric reveal detailing accentuated via polychromatic brickwork

Figure 10: Illustrating Gothic Revival stylistic characteristics in exterior architectural form at St. Paul's (Huntly): lancet windows, exterior buttresses, steeply pitched roof. Use of polychromatic brickwork for architectural detailing



(a) Exposed Timber Roof



(b) Varied Polychromatic Brick Textures evident in Interior

Figure 11: Stylistic Characteristics within Church Interior: Pointed Arch Forms, Rose Window, Polychromatic Masonry, Exposed Timber Roof Construction

All the reported examples feature roof forms and technologies that are of significant architectural heritage value. Whilst falling outside the scope of this study, analysis of New Zealand church roof construction remains an area of little research to date.

CONCLUSION

Churches and church precincts present a unique set of challenges for conservation via seismic retrofitting. The post-earthquake context has revealed varying attitudes that are evident through the identified options for the treatment of the surviving historic fabric by the associated communities. A study of URM churches located within the Anglican Diocese of Waikato and Taranaki enabled the thematic architectural characteristics and considerations for churches with historic, existing and proposed retrofits to be investigated. The findings suggested variations of a predominant stylistic and masonry construction typology, along with differing approaches to the integration of structural elements that cater to seismic risk. However, aside from the availability of locally-produced Huntly bricks, reasons for the use of masonry within a largely timber building stock remains somewhat unclear. Topics for exploration during the next phase of study will involve detailed heritage impact analysis of selected retrofitting solutions on the historic fabric, in conjunction with capturing the perspectives held by the groups involved in this process, such as parishioners, engineers or architects.

ACKNOWLEDGEMENTS

This project was supported by QuakeCoRE, a New Zealand Tertiary Education Commission-funded Centre. This is QuakeCoRE publication number 0228.

REFERENCES

Alington, M. H. (1988). Goodly stones & timbers : a history of St. Mary's Church, New Plymouth. New Plymouth [N.Z.], New Plymouth N.Z. : The Church 1988.

- Heritage New Zealand. (1983). "Cathedral Church of Christ (Anglican)." The List Retrieved 01/08/2017, 2017, from <http://www.heritage.org.nz/the-list/details/46>
- Heritage New Zealand. (1985). "St. Mary's Church (Anglican)." The List Retrieved 28/06/2017, 2017, from <http://www.heritage.org.nz/the-list/details/4303>.
- Heritage New Zealand. (1990). "St. Paul's Church (Anglican)." The List Retrieved 22/06/2017, 2017, from <http://www.heritage.org.nz/the-list/details/4165>.
- Heritage New Zealand. (2017). "St. Mary's Church (Anglican), ." The List Retrieved 27/07/2017, 2017, from <http://www.heritage.org.nz/the-list/details/861>.
- Heritage New Zealand. (2017). "Taranaki Cathedral Church of St. Mary (Anglican)." The List Retrieved 14/08/2017, 2017, from <http://www.heritage.org.nz/the-list/details/148>.
- ICOMOS New Zealand (2010). ICOMOS New Zealand Charter for the Conservation of Places of Cultural Heritage Value. New Zealand, ICOMOS New Zealand: 1-11.
- Lester, J., A. Brown and J. Ingham (2013). "Stabilisation of the Cathedral of the Blessed Sacrament following the Canterbury earthquakes." *Engineering Failure Analysis* **34**: 648-669.
- Marotta, A. (2016). Seismic Vulnerability Assessment of New Zealand Unreinforced Masonry Churches PhD Thesis, Sapienza University of Rome.
- McKay, B. (2015). *Worship: A History of New Zealand Church Design*. New Zealand, Godwit Publishing Limited.
- McLean, G. (2002). *100 historic places in New Zealand*. Auckland, N.Z., Auckland, N.Z. : Hodder Moa Beckett 2002.
- Shaw, P. (1991). *New Zealand architecture : from Polynesian beginnings to 1990*. Auckland, N.Z., Auckland, N.Z. : Hodder & Stoughton 1991.
- Stacpoole, J. (1972). *Architecture 1820-1970*. Wellington, Reed, Wellington, Reed : s.n. 1972.
- Thornton, G. G. (2003). *Worship in the wilderness : early country churches of New Zealand*. Auckland [N.Z.], Auckland N.Z. : Reed c2003.
- UNESCO-ICOMOS (2003). *ICOMOS Charter Principles for the Analysis, Conservation and Structural Restoration of Architectural Heritage*. Zimbabwe, ICOMOS: 1-4.
- Walsh, K. Q., K. J. Elwood and J. M. Ingham (2014). "Seismic considerations for the Art Deco interwar reinforced-concrete buildings of Napier, New Zealand." *Natural Hazards Review* **16**(4): 04014035.

OUT-OF-PLANE RESPONSE OF AN INNOVATIVE MASONRY INFILL WITH SLIDING JOINTS SUBJECTED TO DYNAMIC TESTS ON SHAKING TABLE

P. Morandi¹, R.R. Milanesi², C.F. Manzini³ and G. Magenes⁴

¹ Senior Researcher, Department of Civil Engineering and Architecture, University of Pavia, Via Ferrata 3, 27100 Pavia, Italy, paolo.morandi@unipv.it

² Researcher, Department of Civil Engineering and Architecture, University of Pavia, Via Ferrata 3, 27100 Pavia, Italy, riccardo.milanesi@unipv.it

³ Researcher, EUCENTRE Pavia, Via Ferrata 1, 27100 Pavia, Italy, carlo.manzini@eucentre.it

⁴ Full Professor, Department of Civil Engineering and Architecture, University of Pavia, Via Ferrata 3, 27100 Pavia, Italy, guido.magenes@unipv.it

Within the European FP7 Project "INSYSME", the research unit of the University of Pavia has developed a seismic resistant masonry infill system with original details (Morandi et al. 2015), which subdivides the masonry panel into horizontal stripes, able to mutually slide through suitable "sliding joints"; the stress concentration and the local effects are reduced by means of deformable joints at the infill-frame interface and the out-of-plane stability is governed by the flexural resistance of the masonry stripes and adequate out-of-plane supports at the RC columns. The solution takes advantage to functioning principles already developed in other researches (i.e., Lin et al. (2011), Mohammadi et al. (2011), Preti et al. (2016)). An extensive experimental campaign, composed by tests of characterization, in-plane cyclic tests on one-storey one-bay full scale RC bare frame and two different configurations of infilled frames (with and without a central opening) followed by out-of-plane shaking-table dynamic tests, and a dynamic test on a shaking table of a full scale two-storey building, has been performed. In this paper the results of the out-of-plane dynamic test on shaking-table conducted on the one-storey one-bay full-scale fully infilled specimen are discussed. After the realization of a new test set-up, a very demanding testing protocol, constituted of artificial input motions at increasing intensity, has been applied to the specimen. The out-of-plane response along the height of the wall has been studied through accelerations and displacements time histories measured at each stripe. The out-of-plane experimental performance of this infill system appears to be very promising for real application both in the case of new RC buildings and as replacement of non-structural walls in existing structures.

Keywords: *innovative masonry infill, sliding joints, out-of-plane response, experimental dynamic shaking table test.*

INTRODUCTION

“Traditional” masonry infill construction solutions, where the panels are built in complete contact with the surrounding RC frame without provision of any gap or connection around the boundaries and after the hardening of the RC members, have evinced a series of critical aspects related to in-plane and out-of-plane seismic response, often observed both in the post-seismic surveys (i.e., Manzini and Morandi; 2012) and in the experimental outcomes (i.e., Calvi and Bolognini, 2001, Guidi et al., 2013, Morandi et al., 2017a).

Although a series of researches oriented towards possible novel systems have been recently carried out in order to solve, or at least to limit, the aforementioned critical issues (Morandi et al., 2016), a widely recognized solution, which reduces in-plane/out-of-plane seismic vulnerability of masonry infills guarantying, at the same time, a sufficient thermic, acoustic and durability performance, has not been achieved yet.

Within the European FP7 Project "INSYSME", the research unit of the University of Pavia has developed a seismic resistant masonry infill system with sliding-joints (Morandi et al., 2016) with original details on which a very wide experimental campaign has been conducted. The proposed engineered system, that takes advantage from past researches on “partitioned” infill solutions as the one proposed, i.e., by Lin et al. (2011), Mohammadi et al. (2011) and Preti et al. (2016), aims to control the damage propagation in the masonry infill and to reduce the in-plane interaction between the RC frame and the panel, dividing the infill into four horizontal stripes, able to slide one on each other through properly conformed sliding joints. Moreover, a deformable joint located at the frame/infill interfaces has the objective to reduce the local effects and the stress concentration in the proximity of the interface between the masonry panel and the RC elements. The layout of the system is reported in Figure 1a.

The innovative infill aims to guarantee a sufficient displacement capacity without the creation of a single strut, which is instead common in traditional infill solutions. The combined use of deformable joints at the infill-frame interface and sliding horizontal joints within the infill would guarantee a suitable deformation capacity and reduce both the damage in the masonry and the infill-structure interaction. Moreover, a significant reduction of the local shear demand at the ends of the columns adjacent to the infill due to the subdivision on more stripes is expected. At global level, this system would also allow limiting the concentration of deformations/internal forces in one single storey of the building, reducing the risk of formation of “soft storey” and enable to reduce the negative effects of possible irregular distributions of infills in plan and in elevation. The out-of-plane stability is governed by the horizontal flexural resistance of the masonry stripes and is guaranteed by suitable designed "shear keys" attached to the column, constituted by “omega” shaped steel profiles connected to the RC columns by means of nails shot with a nail gun (Figure 1e); the units at the edges of the infill adjacent to the columns and to the openings are shaped with a recess (C-shaped units, Figure 1b) in order to accommodate the shear keys. The sliding joints (Figure 1c), having a ribbed shape, allow obtaining a mechanical interlocking that, together with a specific high-tension strength plaster placed on both sides of the masonry, should ensure the out-of-plane stability of the panel. The functioning of the proposed infill system is described in more detail in a work by Morandi et al., 2016.

The unreinforced masonry used in the stripes of the infill is realized with vertically perforated lightweight clay units and general-purpose 1 cm thick mortar bed- and head-joints. The plain clay unit (Figure 1d) has a thickness of 25 cm and a percentage of voids of 45%. A mortar of class M5 (nominal compression strength of 5 MPa) has been used in the head- and in bed-joints. A layer of fibre-reinforced plaster of about 2 cm has been placed in order to increase the out-of-plane

flexural resistance of the masonry stripes, without jeopardizing the sliding. The single horizontal sliding joint is made up by two plastic (nylon casted with molybdenum disulphide in order to reduce friction coefficient) corrugated male-female elements, which overlap one on the other (Figure 1c) along the entire thickness of the wall. The infill-frame interface joint, realized with cementitious material, has been adequately studied in order to obtain a mixture that allows reducing the elastic modulus in a range of values ranging between 100 and 150 MPa, while maintaining a value of flexural and compression strength similar to that of a traditional mortar for load-bearing masonry. The thickness of the infill-column joint has been set as 2.5 cm, whereas the thickness of the infill-beam joint set as 3.0 cm.

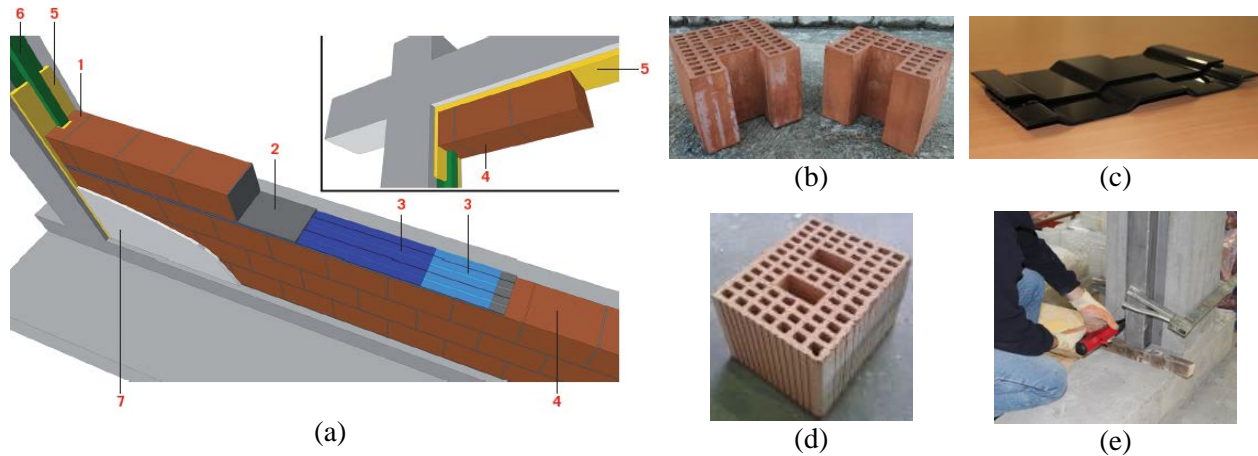


Figure 1: (a) Details of the innovative masonry infill with sliding joints: 1. C-shape units (b); 2. mortar bed-joints; 3. sliding joints (c); 4. clay units (d); 5. interface joints; 6. shear keys (e); 7. plaster.

An extensive experimental campaign, composed by tests of characterization, in-plane cyclic tests on one-storey one-bay full scale RC bare frame and two different configurations of infilled frames (with and without a central opening) followed by out-of-plane shaking-table dynamic tests, and a dynamic test on a shaking table of a full scale two-storey building, has been performed. In this paper, a description of the specimens, of the test set-up and of the experimental protocol used in the out-of-plane dynamic tests on shaking-table conducted on the one-storey one-bay full-scale specimens is discussed, along with the most significant results of the experiment conducted on the fully infilled RC frame.

SPECIMENS, TEST SET-UP, INSTRUMENTATION AND TESTING PROTOCOL

Two different configurations of the innovative infill have been tested: one with and one without a central opening. In

Figure 2, the layout of the fully infilled (called “TSJ1”) and of the partially infilled RC frame specimens (“TSJ2”) is reported. The RC frames have been designed according both to the current European and the Italian seismic code provisions. The out-of-plane tests have been performed on the same infilled frames previously subjected to cyclic in-plane tests (“low-velocity” and “high-velocity”, the latter only on the infill without opening, see Morandi et al., 2017b). The results of

the tests on the specimen with the solid infill are in particular reported and discussed in this paper.

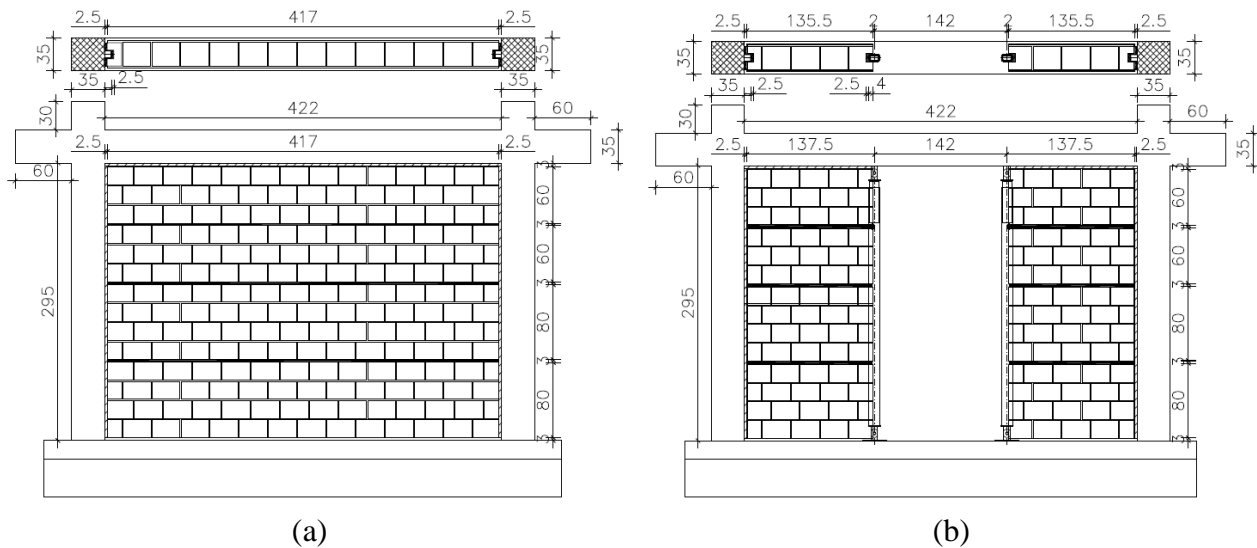


Figure 2: Layout of the (a) fully infilled (TSJ1) and of the (b) partially infilled (TSJ2) RC frame specimens (represented without plaster). Measures in cm.

Experimental set-up and instrumentation for the out-of-plane tests

The out-of-plane tests have been carried out on the shaking table of the TREES lab of EUCENTRE in Pavia, immediately following the in-plane experimentation; therefore, the tested masonry infills have previously sustained a certain level of in-plane damage. A steel reaction frame realized to serve as an out-of-plane restraint during the shaking table tests has been anchored to the shaking table through two 5 cm thick steel plates, with the aim of transferring the shear force coming from the shaking table to the foundation of the specimen. Once the infilled frames have been fixed to the shaking table, the RC top beam of the specimens has been connected through L-shaped steel profiles attached to the cantilever beams of the steel reaction frame, in order to restrain the out-of-plane displacement of the RC structure and only allow the out-of-plane deformation of the masonry infill. For the vertical loads application to the columns, the same self-equilibrated system used during the in-plane tests has been adopted. The out-of-plane setup is sketched and showed in Figure 3.

In order to measure the out-of-plane displacement of the tested masonry panels and to control possible displacement of the surrounding RC frame and foundation of the specimens during dynamic out-of-plane tests, an optical acquisition system and displacement transducers (linear potentiometers) have been adopted, whereas the accelerations have been measured with accelerometers. For the fully infilled specimen three vertical lines of optical markers have been located (at the RC column, at mid-length and at about one fourth of the length of the infill), and 20 potentiometers and 13 accelerometers have been used, as illustrated in Figure 4 and Figure 5.

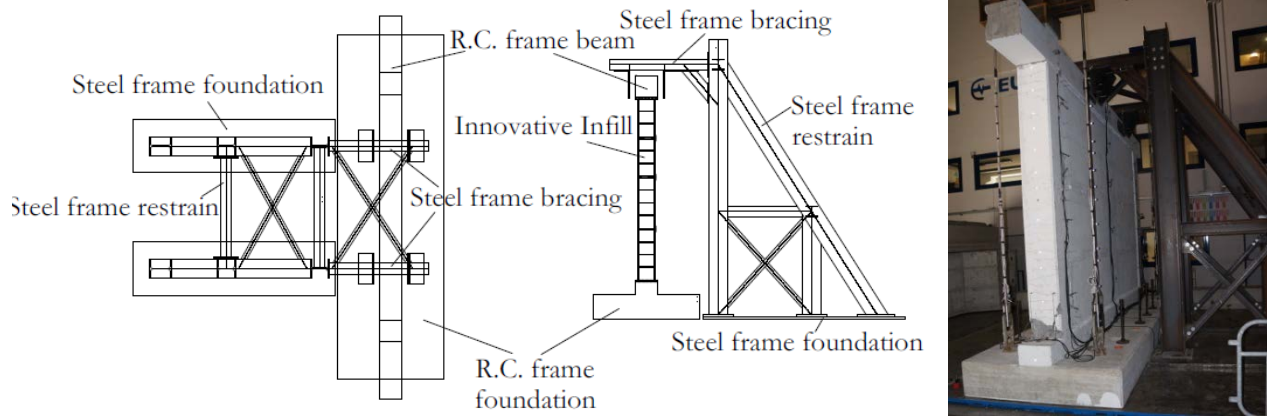


Figure 3: Layout of the out-of-plane setup for dynamic tests on shaking table.

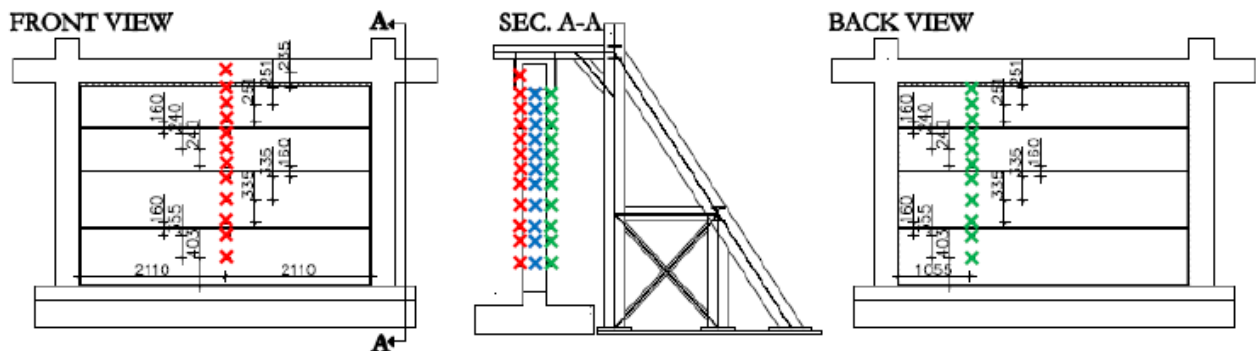


Figure 4: Optical instrumentation installed in out-of-plane tests (TSJ1).

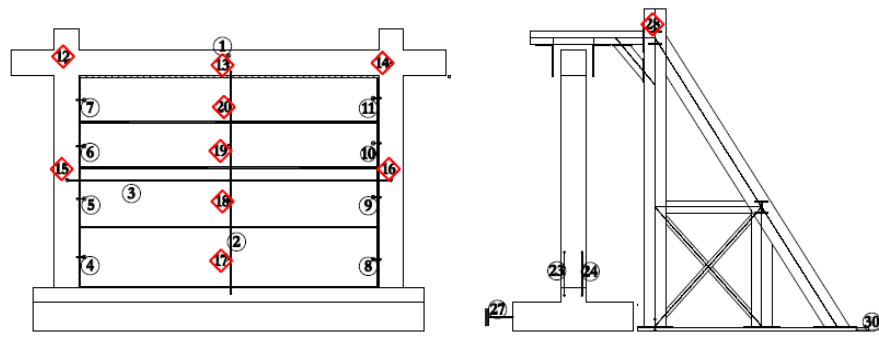


Figure 5: Potentiometers and accelerometers (in red) installed for out-of-plane tests (TSJ1).

Testing protocol

The loading protocol takes as reference FEMA 461 (2007) and Retamales et al. (2011), and has consisted of different artificial ground motions scaled at increasing intensity and with a content in frequency domain selected according both to the results of non-linear dynamic analysis on various RC structures and to the performance of the shaking table in terms of maximum

accelerations, velocities and displacements (Milanesi et al., 2017). An example of the obtained artificial ground motion and the related effective recorded signal, plus the corresponding elastic acceleration and displacement spectra, is reported in Figure 6.

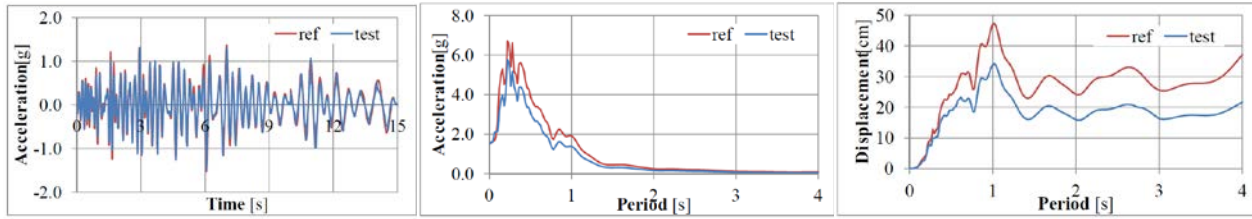


Figure 6: Reference and recorded (shaking-table) Ground Motions and corresponding acceleration and displacement spectra used for out-of-plane dynamic tests: GM 150_060.

Table 1 presents the experimental dynamic testing sequences performed on specimen TSJ1. The table specifies the test number, the dynamic input typology, the tests name, the reference PGA and the one recorded during the test. Before the main Ground Motions (“GM”), white noise tests (“RNDM”) and tuning tests (“TNG”) have been performed, the former mainly for the characterization of the dynamic properties and for a preliminary tuning of the shaking table, the latter mainly for the calibration of the shaking table test parameters; the tuning tests are constituted by scaled signals of the following main runs. Repetitions of the aforementioned sequence have been performed till the attainment of ultimate conditions on the infill specimens.

Table 1: Out-of-plane testing sequence for TSJ1

| Test # | Dynamic input | Test name | Reference PGA [g] | Recorded PGA [g] |
|-----------|---------------------|-----------------------|-------------------|------------------|
| 1 | RNDM | RNDM_01 | 0.03 | - |
| 2 | RNDM | RNDM_02 | 0.10 | - |
| 3 | 50% GM 020 | TNG_020_50% (4x) | 0.10 | - |
| 4 | GM 020 | GM 020 | 0.20 | 0.20 |
| 5 | 25% GM 040 | TNG_040_25% (5x) | 0.10 | - |
| 6 | GM 040 | GM 040 | 0.40 | 0.39 |
| 7 | 12% GM 080 | TNG_080_12.5% (5x) | 0.10 | - |
| 8 | GM 080 | GM 080 | 0.80 | 0.79 |
| 9 | RNDM | RNDM_03 | 0.10 | - |
| 10 | 8% GM 120 | TNG_120_8.5% (8x) | 0.10 | - |
| 11 | GM 120 | GM 120 | 1.20 | 1.23 |
| 12 | RNDM | RNDM_04 | 0.10 | - |
| 13 | 6% GM 150 | TNG_150_6% (5x) | 0.10 | - |
| 14 | GM 150 | GM 150_060 | 1.50 | 1.49 |
| 15 | RNDM | RNDM_05 | 0.10 | - |
| 16 | 6% GM 150_2x040 | TNG_150_2x040_6% (4x) | 0.10 | - |
| 17 | GM 150_2x040 | GM 150_2x040 | 1.50 | 1.58 |

TESTS OF CHARACTERIZATION

In order to evaluate the mechanical properties of the elements of the infill system, a series of tests of characterization on single materials and on masonry specimens has been conducted, in accordance with European standards and codes (for the complete results, see Morandi et al., 2017b). Table 2 reports the outcomes related somehow to the out-of-plane behaviour (mean and coefficient of variation) of vertical/lateral compression and flexural strength of masonry, along with a measure of the “local shear resistance” on the C-shaped units (shear/tensile resistance of the flange of the unit). The masonry has been characterized through tests on specimens without and with plaster; in Table 2, both values are reported, in order to appreciate the influence of the plaster.

Table 2: Summary of the tests of characterization related to the out-of-plane behaviour

| Mechanical properties | Symbol | Mean | C.o.v. |
|---|-----------|-------------------|---------------|
| Tensile/shear strength of “C”- shaped units | R | 3.39 kN | 18.6 % |
| Vertical compression strength of masonry ¹ | f_v | 6.83 (7.02) MPa | 16.3 (16.4) % |
| Vertical elastic modulus of masonry ¹ | E_v | 9686 (9920) MPa | 10.4 (14.0) % |
| Lateral compression strength of masonry ¹ | f_{lat} | 1.89 (2.41) MPa | 10.6 (17.8) % |
| Lateral elastic modulus of masonry ¹ | E_{lat} | 2863 (4597) MPa | 23.4 (1.3) % |
| Flexural strength of masonry ¹ | f_{x2} | 0.308 (0.397) MPa | 10.6 (7.2) % |

¹ For these tests, the values in brackets refer to masonry specimens with plaster.

RESULTS OF THE OUT-OF-PLANE TESTS

Cracking pattern

The sequence of the damage pattern before and after significant runs is reported in Figure 7. The previous in-plane cyclic tests on the specimen were pushed up to 3.00% drift for two times (at low and at high velocity) and had produced some cracks along the sliding joints mainly confined in the plaster, with some little damage in the masonry only at the corner of the bottom stripes. In Figure 7, the cracking pattern caused by the in-plane actions has been indicated with grey and black marks.

The infill subjected to out-of-plane dynamic action has not manifested any significant damage up to run *GM 120*, where vertical cracks had appeared at the thirds of the length of the upper masonry stripes. One of the crack at the top stripe was evident at both sides of the panel. At the following ground motion (*GM 150_060*), the vertical cracks, above all in the less damaged side, have extended such that to be approximately correspondent to those of the other side, with the exception of a crack in the second bottom stripe. Finally, at the last ground motion (*GM 150_2x040*), the previous cracks have extended in both length and width and areas of the infill at the edges of the panel close to the RC columns have been subjected to heavy damage, partly only confined in the plaster, partly involving also the masonry with spalling and partial collapses (see the last two pictures of Figure 7, where the dashed hatch represents damage in the plaster, whereas the solid hatch represents the spalling and the partial collapse of the masonry). These areas at the edges of the panels, involving mainly the second and the third masonry stripes, have

been mainly damaged due to the failure of the “wings” of the “C-shaped” units against the steel shear keys anchored on the RC columns.

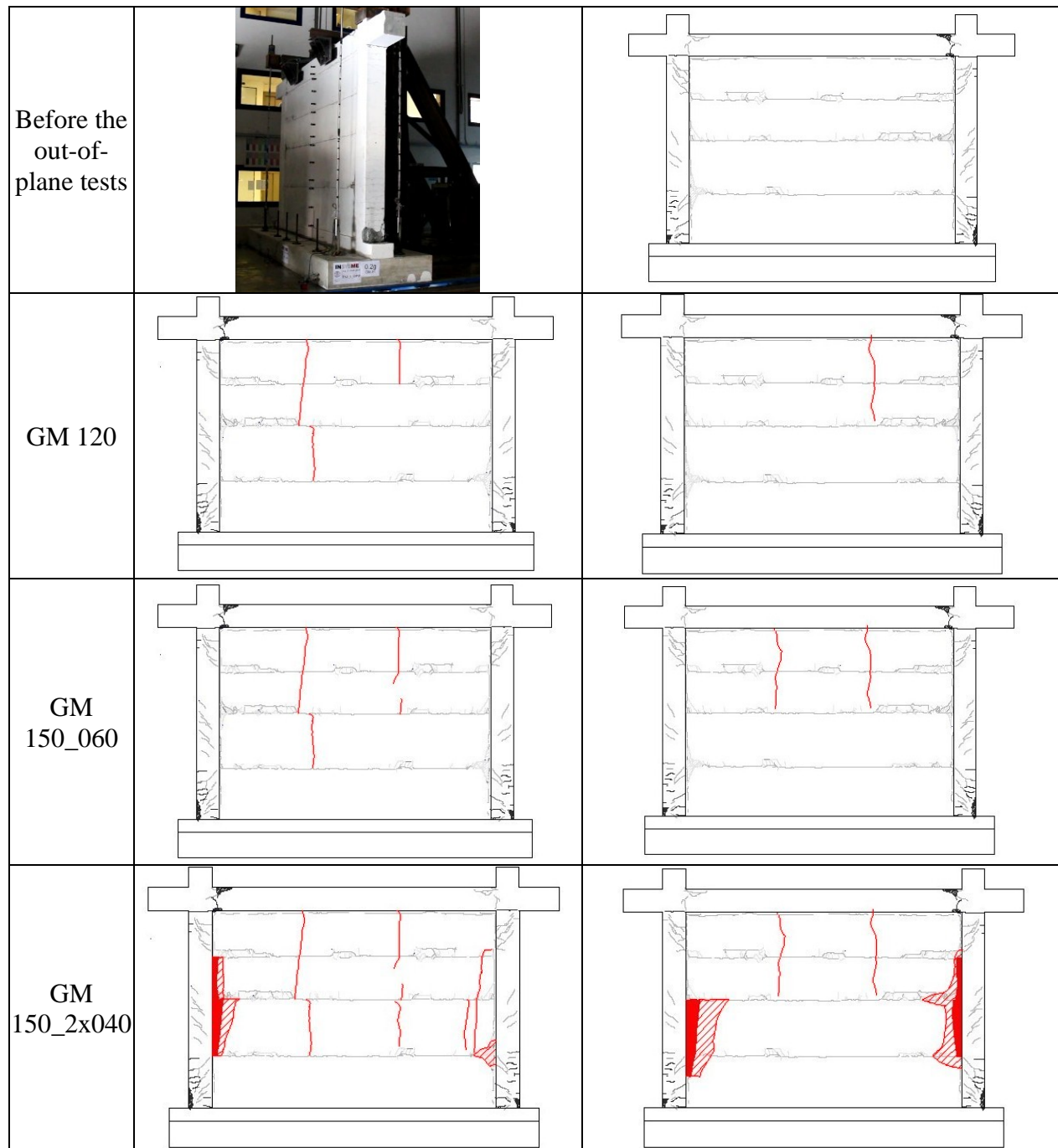


Figure 7: Damage propagation for TSJ1 (highlighted in red) at the two sides. Grey lines refer to in-plane tests carried out previously on the same specimen.

Out-of-plane dynamic identification

The modal identification techniques used are based on the dynamic response measurements of a virtual system under natural conditions, assuming that the excitations have random nature in time and in the physical space of the structure. The fundamental assumption in this type of identification techniques relates to the fact that the excitation imposed on the structure is comparable to a stationary Gaussian white noise stochastic process in the frequency range of interest. However, the response measured on the structure includes the modal contributions of the ambient forces, the contribution of the structural system and the contribution of the noise signals from undesired sources. Furthermore, the measured response reflects the poles (amplitude peaks from the spectral density functions) from the structural system and from the ambient forces, and consequently the identification techniques must have the ability to separate the different components of the signal (Ewins, 2000; Brincker et al., 2000).

Some of the results obtained has been considered in terms of singular values, frequencies of vibrations for each mode identified and of mode shapes for the specimen. In particular, the variation of the first fundamental frequency of vibration (f_1) at different stages of the shaking table testing presented a trend characterized by values of f_1 decreasing as the damage level increases. A similar description of the effect of cumulative damage on the dynamic properties of the specimen is given by the index id_x , obtained as the ratio of the frequency of vibration of the damaged structure with respect to that of the undamaged configuration, being equal to 1 when the structure is undamaged, actually at the beginning of the out-of-plane tests. In Figure 8a, the variation of the id_x index is presented.

Up to test #9 (subsequent to *GM 080*) the modal shape of each detected mode of vibration of the specimen remains essentially unchanged with respect to that identified during test #1; the fundamental frequency of the first mode decreases from 15.5 Hz ($T_1=0.065$ s) to 14.0 Hz ($T_1=0.071$ s), while the frequency of the higher modes remains unchanged. After test #11 (*GM 120*) a significant change in the frequencies and modal shapes of the detected modes of vibration of the specimen can be observed. In particular, the fundamental frequency of the first mode decreases from 14.0 Hz (test #9) to 12 Hz ($T_1=0.083$ s, test #12, subsequent to *GM 120*) and to 11.5 Hz ($T_1=0.087$ s, test #15, subsequent to *GM 150_060*).

In Figure 8b and Figure 8c a comparison between the modal shape of the first mode detected in test #1 and test #15 is reported.

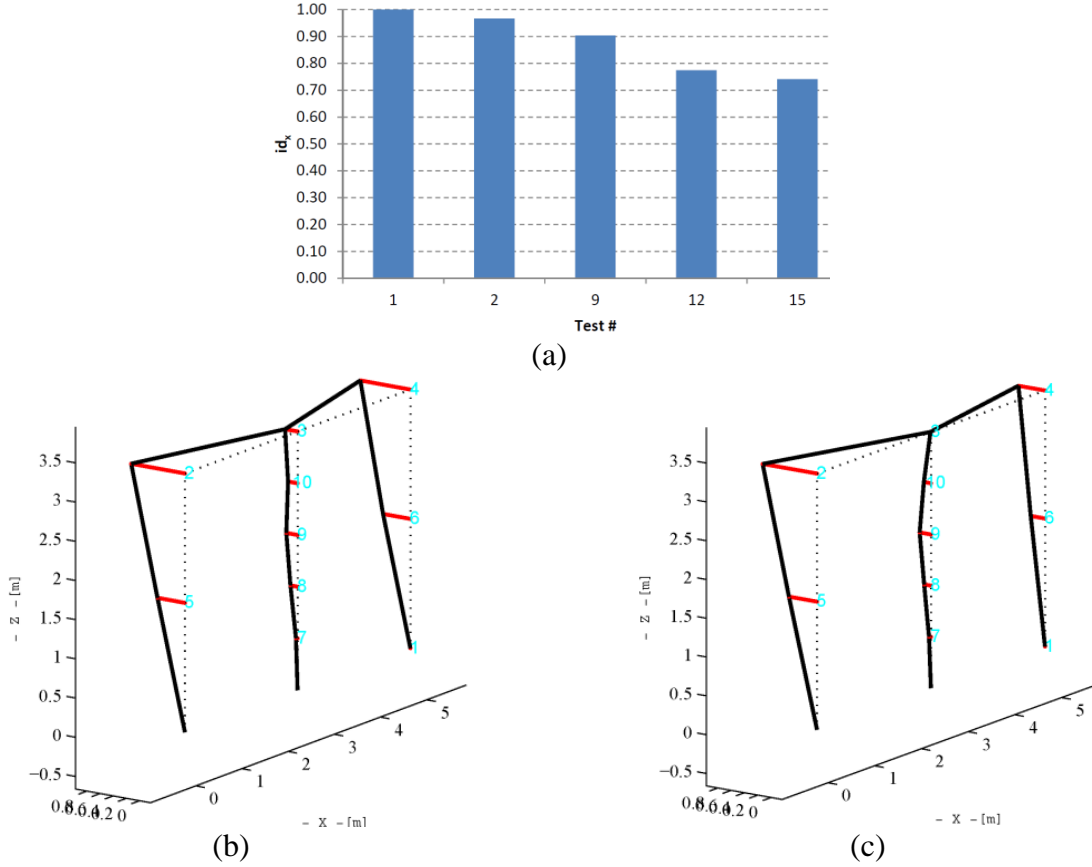


Figure 8: (a) Variation of the damage index i_{dx} . Comparison between the deformed shape of the first mode of vibration detected in: (b) test #1 ($f=15.5$ Hz); (c) test #15 ($f=11.5$ Hz).

OUT-OF-PLANE ACCELERATION AND DISPLACEMENT

The out-of-plane acceleration and the displacement time-histories evaluated for each infill stripe have been measured. Figure 9, Figure 10 and Figure 11 show the acceleration and displacement time histories and their distribution along the height of the infilled frame, evaluated at corresponding positive and negative peaks of the infill top stripe for the case of *GM 150_060*.

The accelerometers used for the evaluation of the acceleration time-histories and distributions along the height of the specimen are highlighted in Figure 5. Optical markers placed in the same positions (that is, the markers located at half-height and half-length of each stripe) have been used for the evaluation of the displacement time-histories, whereas displacement distributions have been evaluated with reference to all the vertical lines of markers installed on the specimen.

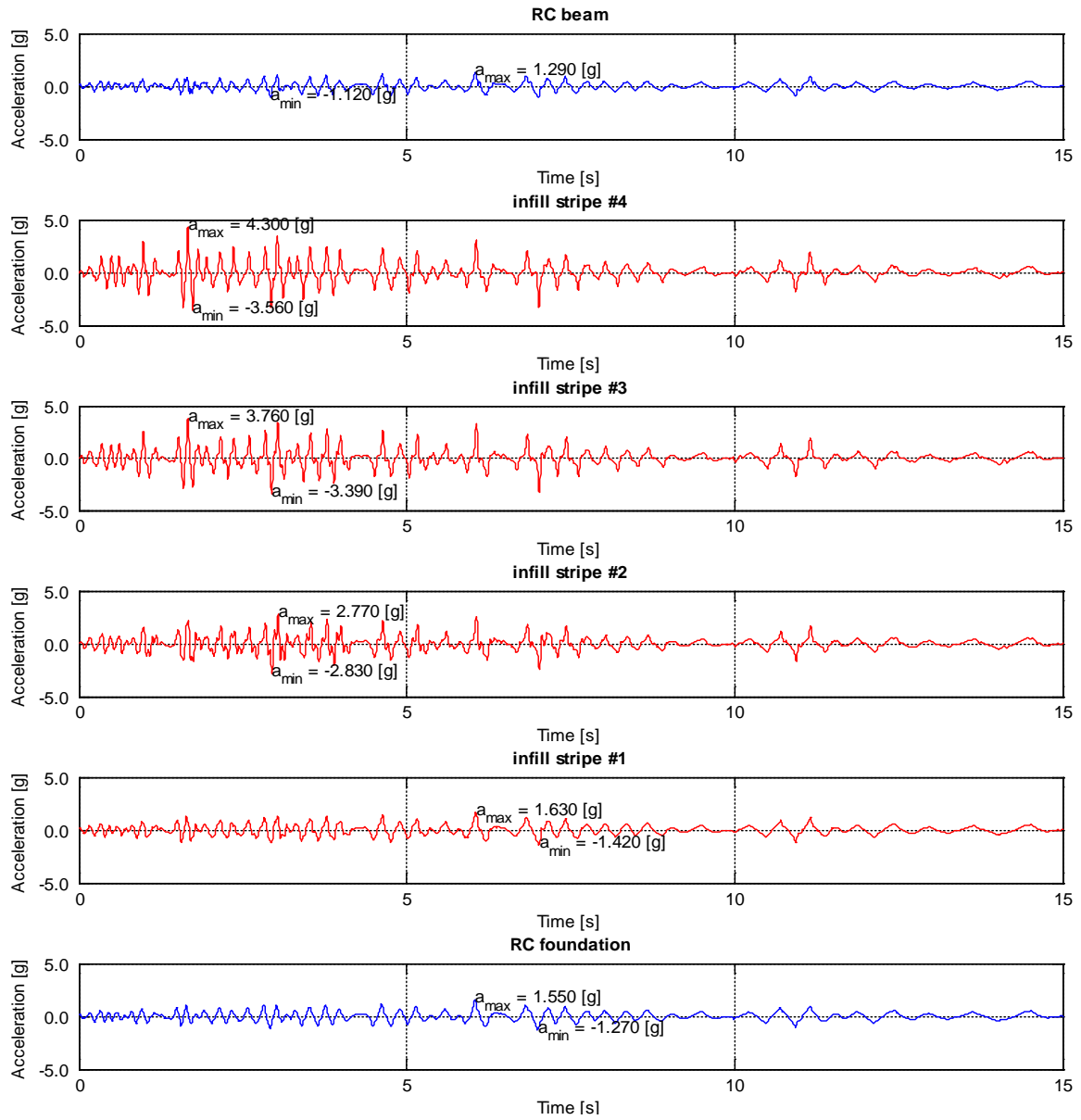


Figure 9: Acceleration time-histories during *GM 150_060*.

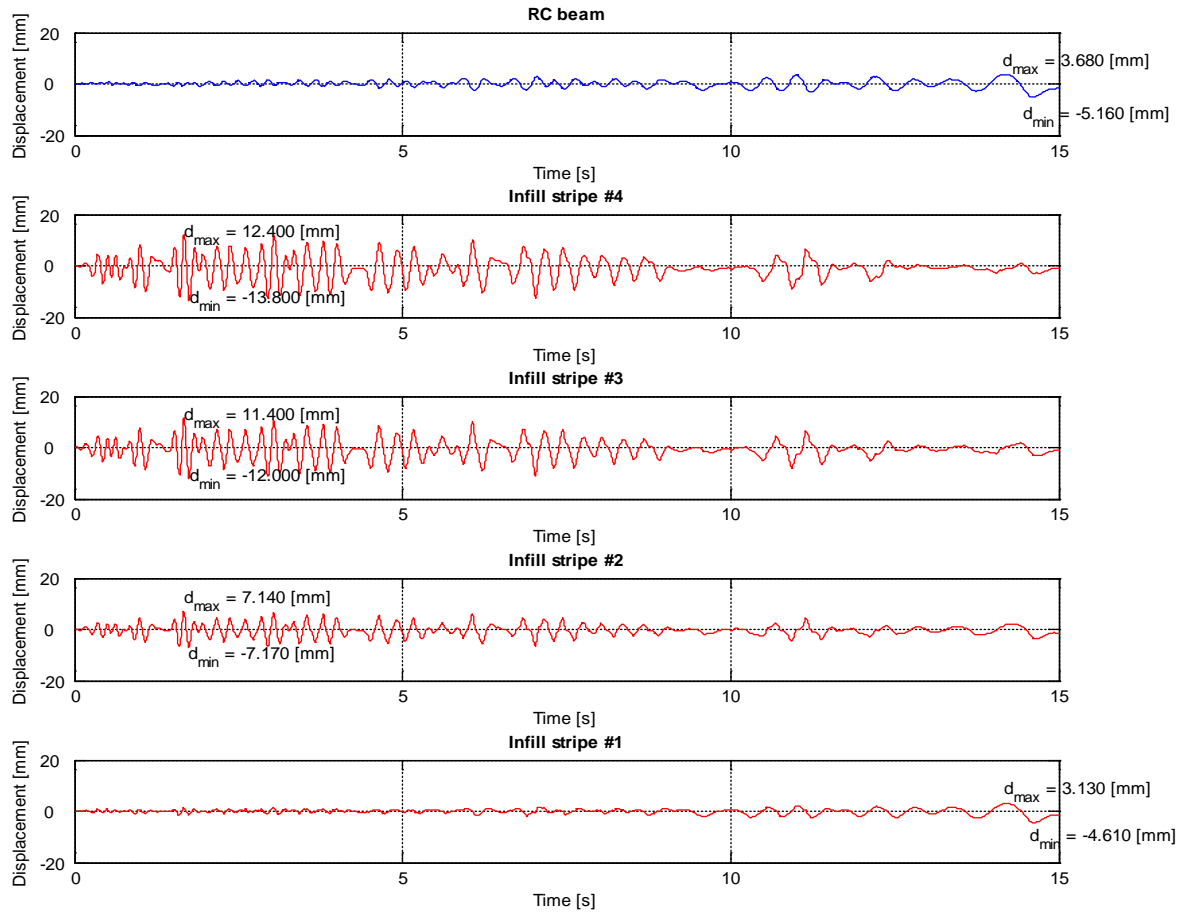


Figure 10: Displacement time-histories during *GM 150_060*.

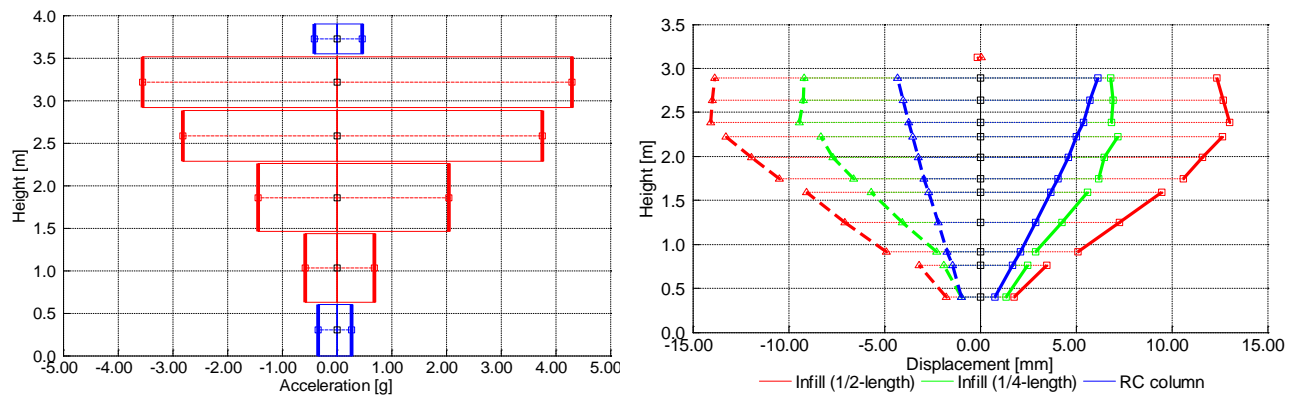


Figure 11: Distribution of accelerations and displacements at positive and negative peak acceleration and displacement, respectively, of infill top stripe (quotes are referred to the top of the foundation): *GM 150_060*.

Figure 12 reports the maximum acceleration and the ratio a_{max}/PGA in the four infill stripes, as a function of the effective PGA of the applied artificial records. In addition, Figure 13 plots the maximum displacements in the stripes versus the applied PGA.

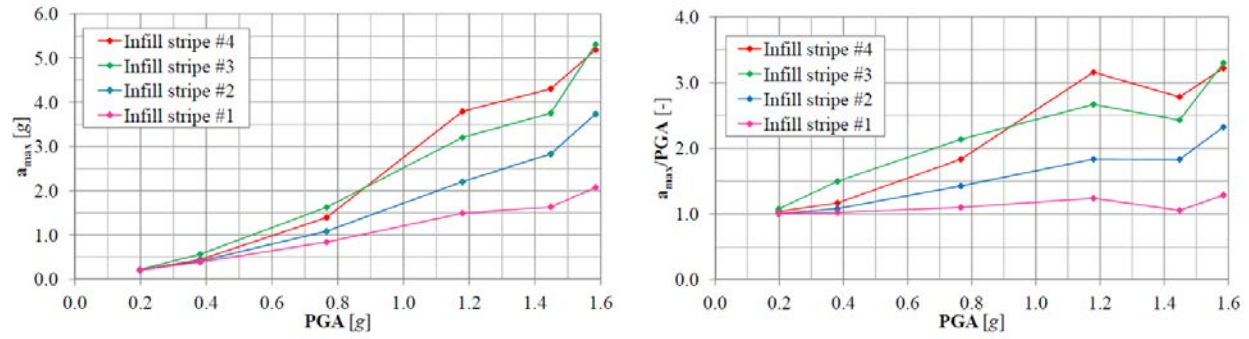


Figure 12: Max acceleration and ratio (a_{max}/PGA) vs PGA (at the RC foundation).

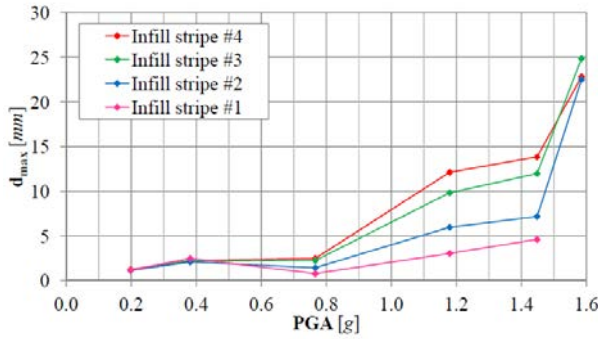


Figure 13: Maximum displacement (relative maximum displacement to foundation displacement) vs PGA (at the RC foundation).

CONCLUSIONS

In this paper, the results of an out-of-plane shaking-table dynamic test conducted on one-storey one-bay RC frame infilled with the innovative masonry infill system developed by the University of Pavia, have been discussed. A specific set-up has been designed and a demanding testing protocol, consisted of different artificial ground motions scaled at increasing intensity, has been applied to the specimen. The out-of-plane response along the height of the infills has been studied through accelerations and displacements time histories measured at each stripe.

Although the same specimen had been already subjected to two in-plane cyclic tests up to 3.0% drift, during out-of-plane dynamic action the infill has not manifested any significant damage up to run *GM 120* (recorded $PGA = 1.23g$), where vertical cracks appeared at the thirds of the length of the upper masonry stripes; partial failure of the specimen has occurred at the last very demanding ground motion (*GM 150_2x040*, recorded $PGA = 1.58g$), where areas of infill at the edges of the panel close to the RC columns, involving mainly the second and the third masonry stripes, have been subjected to severe damage, due to the failure of the “wings” of the “C-shaped” units against the steel shear keys anchored on the RC columns without, however, causing the total collapse of the wall. The location of the cracks suggests the occurrence of an actual horizontal flexural behaviour of the masonry stripes before the attainment of the ultimate resistance of the C-shape units. The out-of-plane dynamic identification has well captured the

increasing level of damage, with a reduction of the natural frequency of the specimen from 15.5 to 11.5 Hz.

Moreover, the out-of-plane response has not been influenced by previous damage, albeit limited, due to the in-plane cyclic tests. This could reasonably allow considering the in-plane and the out-of-plane behaviour as uncoupled, at least for the evaluation of the out-of-plane resistance and stability, unlike what it should be performed for traditional infills (Morandi et al., 2016).

Finally, analysing the out-of-plane acceleration and displacement data recorded on each masonry stripe, it appears evident as the acceleration and displacement demand increases with the height (larger values at upper stripes), up to almost 4.5g and about 15 mm, respectively, at the top stripe at run *GM 150* (before the occurrence of any significant damage) and up to more than 5.0g and almost 25 mm, respectively, at the last input motion (*GM 150_2x040*), when the infill was partially collapsed; therefore, in this latter case, out-of-plane acceleration of more than 3 times the one applied at the base was found. Besides, it is also evident that the displacements of the top stripe are influenced by the beam-infill boundary conditions.

At the light of this experimental evidence, the out-plane performance of this innovative infill in the solid configuration can be therefore considered extremely promising for future possible real application in the construction of new RC structures or in the seismic upgrade of existing buildings when replacement of non-structural walls is feasible.

ACKNOWLEDGEMENTS

The financial support of the European Commission within the project INSYSME "INnovative SYStems for earthquake resistant Masonry Enclosures in rc buildings", grant FP7-SME-2013-2-GA606229, 2013-2016 is acknowledged. ANDIL and its associated companies, and RUREDIL spa are gratefully acknowledged as industrial partners of the project. The contribution of Capaccioli srl for the supply of the sliding joints is also acknowledged.

REFERENCES

Brincker, R., Zhang, L., Andersen, P., (2000), "Modal Identification from Ambient Responses using Frequency Domain Decomposition", *Proc. 18th ISMA*, San Antonio, Texas.

Calvi, G.M., Bolognini D., (2001), "Seismic response of RC frames infilled with weakly reinforced masonry panels", *Journal of Earthquake Engineering*, Vol. 5, No. 2, pp. 153-185.

Ewins, D. J., (2000), "*Modal testing: theory, practice and application*", Research Study Press Ltd, England.

FEMA 461, (2007), *Interim Testing Protocols for Determining the Seismic Performance Characteristics of Structural and Nonstructural Components*, FEMA, Washington D.C..

Guidi G., da Porto F., Dalla Benetta M., Verlato N., Modena C., (2013), "Comportamento Sperimentale nel Piano e Fuori Piano di Tamponamenti in Muratura Armata e Rinforzata" (in Italian), *Research Report*, Dip. Ingegneria Civile, Edile e Ambientale, University of Padova, Italy.

Lin, K., Totoev, Y.Z., Lin, H.J., (2011), "In-plane cyclic test on framed dry-stack masonry panel", *Advanced Materials Research*, Vol. 163-167, pp. 3899-3903.

Manzini, C.F., Morandi, P., (2012), "Rapporto preliminare sulle prestazioni ed i danneggiamenti agli edifici in muratura portante moderni a seguito degli eventi sismici emiliani del 2012" (in Italian), *Research Report*, Vol. 1, pp 1-51, EUCENTRE, <http://eqclearinghouse.org/2012-05-20-italy/>.

Milanesi, R.R., Morandi, P., Dacarro, F., Albanesi, L., Magenes, G., (2017), "In-plane pseudo-static and out-of-plane dynamic testing procedures of infilled RC frames", *Proc. 7th AESE*, pp 271-290, 6-8 September 2017, Pavia, Italy.

Mohammadi, M., Akrami, V., Mohammadi-Ghazi, R., (2011), "Methods to Improve Infilled Frame Ductility", *Journal of Structural Engineering*, Vol. 136, No. 6, pp 646-653.

Morandi, P., Milanesi, R.R., Magenes, G., (2015), "Soluzione innovativa per tamponatura antisismica in laterizio a giunti scorrevoli" (in Italian), *Proc. XVI ANIDIS Conference*, 13-17 September 2015, L'Aquila, Italy.

Morandi, P., Milanesi, R.R., Magenes, G. (2016), "Innovative seismic solution for clay masonry infills with sliding joints: principles and details", *Proc. 16th IBMAC*, pp 1273-1281, 26-30 June 2016, Padova.

Morandi P., Hak S., Magenes G., (2017a), "Experimental and numerical seismic performance of strong clay masonry infills", *Research Report*, 2017/2, EUCENTRE, Pavia, Italy. <http://www.eucentre.it/report-di-ricerca/>

Morandi, P., Milanesi, R.R., Manzini, C.F., Magenes, G., (2017b), "Experimental tests of an engineered seismic solution of masonry infills with sliding joints", *Proc. of XVI WCEE*, 9-13 January 2017, Santiago Chile, Chile.

Preti, M., Bolis, V., Stavridis, A., (2016), "Design of masonry infill walls with sliding joints for earthquake structural damage control", *Proc. 16th IBMAC*, pp 1317-1324, 26-30 June 2016, Padova, Italy.

Retamales, R., Mosqueda, G., Filiatrault, A., Reinhorn, A., (2011), "Testing Protocol for Experimental Seismic Qualification of Distributed Nonstructural Systems", *Earthquake Spectra*, Vol 27, No. 3, pp 835-856.

COMPARISON BETWEEN PREDICTED URM WALL OUT-OF-PLANE DISPLACEMENT-BASED PERFORMANCE AND IN SITU PROOF TEST RESULTS

K.Q. Walsh¹, D.Y. Dizhur², I. Giongo³, H. Derakhshan⁴ and J.M. Ingham²

¹ Department of Civil & Environmental Engineering & Earth Sciences, University of Notre Dame, Indiana, United States, kwalsh8@nd.edu; Frost Engineering and Consulting, Mishawaka, Indiana, United States, kwalsh@frosteng.net

² Department of Civil and Environmental Engineering, University of Auckland, New Zealand, ddiz001@aucklanduni.ac.nz, j.ingham@auckland.ac.nz

³ Department of Civil, Environmental and Mechanical Engineering, University of Trento, Italy, ivan.giongo@unitn.it

⁴ School of Civil, Environmental and Mining Engineering, University of Adelaide, Australia, hossein.derakhshan@adelaide.edu.au

The current study addresses the final stage of a three-part research program in which a variety of unreinforced masonry (URM) walls were physically tested in situ to measure out-of-plane (OOP) behaviour, were assessed for force-based (i.e., strength) performance, and finally were assessed for displacement-based performance. Predictive assessments were carried out using previously published predictive models, and the comparison of experimental to predictive displacement-based performance is the focus of the study reported herein. Displacement-based criteria were applied at selected points on the force-displacement backbone curve. Other researchers have found weak correlation between the results of experimental data sets and the predictive model that is incorporated within multiple internationally recognised standards such as ASCE 41 and FEMA 356 for URM infill wall drift performance.

Furthermore, in situ conditions for URM walls rarely reflect the idealised conditions assumed in analytical predictive models, leading to practicing engineers being uncertain as to which analytical models and inputs are most appropriately applied. In the current study, the predictive results were compared to previously reported experimental results of twelve tests on existing URM walls performed in situ, representing a variety of geometries, boundary conditions, pre-test damage states, and material properties. In general, use of the existing predictive methods results in the over-prediction of the measured displacement parameters, which is likely due to most of the predictive methods being based on historical walls tests in one-way spanning conditions and without rigid

restraints capable of effectuating arching action in the wall, in contrast to the wall test conditions in the current study.

Keywords: *unreinforced masonry (URM), earthquakes, out-of-plane, infill walls, airbag proof-testing, analytical methods*

INTRODUCTION

The earthquake vulnerability of buildings constructed using conventional British architecture with unreinforced fired clay brick masonry (URM) prior to the introduction of modern earthquake loading standards is especially well-known in Australasia (Moon et al. 2014). Nonetheless, few such existing URM structures have been retrofitted to resist design basis earthquake (DBE) forces, despite the prominence of this construction in the form of load-bearing, partition, and infill walls. In particular, significant out-of-plane (OOP) failures of URM walls often occur during moderate and severe earthquake shaking. Predictive analytical models that apply to particular wall configurations have been developed over the past few decades. However, the accuracy of such methods relative to in situ proof testing results has not been widely reported. Furthermore, these predictive methods often involve the assumption of idealised boundary conditions and pre-existing damage states that may not exist in “real world” configurations. Finally, strength-based predictive methods often require knowledge of various material properties that are rarely available to the engineering practitioner and limit the amount of reserve capacity (i.e., equivalent ductility) that can be assumed by the engineer, whereas displacement-based predictive methods do not have these limitations. Hence, a study that compares the accuracy of widely used displacement-based predictive methods and assumed input values to the results of experimental in situ tests is lacking and was the subject of the investigation reported herein. The experimental results considered are derived from the testing program carried out and previously reported by Walsh et al. (2017a, 2017b), including twelve in situ URM walls wherein lateral forces were applied using airbags to simulate distributed OOP demands. The referenced test set of URM walls represented a variety of geometries, boundary conditions, pre-test damage states, and material properties.

PREDICTIVE MODELS FOR THE OOP DISPLACEMENT-BASED BEHAVIOUR OF URM WALLS

Doherty et al. (2002) recommended that experimental curvilinear URM pushover behaviour be idealized by a trilinear model with three different displacement parameters as illustrated in Figure 1. Δ_1 represents the displacement for determining initial stiffness. Doherty et al. (2002) empirically derived ratios of Δ_1/Δ_f from 0.06 to 0.20 for a range of degradation states (with the most severely damaged walls having the highest anticipated ratios of Δ_1/Δ_f). By comparison, Derakhshan et al. (2013a) recommended that a ratio of Δ_1/Δ_f equal to 0.04 be used for undamaged walls. Due to its association with idealised initial stiffness, one may infer that Δ_1 represents the predicted “yield” displacement by which an elastic analysis or identification of the initial period may be carried out. However, Doherty et al. (2002) noted a lack of a definitive yield point in experimental results, and furthermore concluded that the instability collapse displacement Δ_f determined in dynamic, time-history analyses is relatively insensitive to the initial stiffness or the period determined from it. Thus, Doherty et al. (2002) did not explicitly define a definitive yield displacement parameter.

Vaculik and Griffith (2017) considered the predicted yield point for comparison to experimental results to be the average of Δ_1 and Δ_2 empirical values as recommended by Doherty et al. (2002), with Δ_2 being the second trilinear-defining parameter. For idealising the experimental results considered in the current study, Walsh et al. (2017a) identified the yield displacement by assuming an equivalent elasto-plastic system with reduced stiffness in which the initial slope of the idealised trilinear curve was set to intersect with the experimentally measured curve at the first point on the curve which represented a measured force equal to 75% of the maximum post-crack lateral force (Park 1989). By comparison, Derakhshan et al. (2013a) defined Δ_1 such that the initial slope of the idealised trilinear curve intersects the measured curvilinear response at 67% of the maximum post-crack lateral force, and recommended a formula to calculate Δ_1 using the cracked moment of inertia.

Δ_2 in Figure 1 represents the displacement for determining the effective secant stiffness (which will hereafter be referred to simply as the secant stiffness) for use in nonlinear analysis as a substitute structure representation for a multi-degree-of-freedom system (Doherty et al. 2002). Furthermore, other researchers (Griffith et al. 2003; Derakhshan et al. 2014) have recommended that the wall's fundamental vibrational period assumed when estimating the wall's maximum reliable dynamic displacement capacity be defined assuming the secant stiffness at the displacement Δ_2 . Hence, Δ_2 and its corresponding force can be referred to as the “design point” on the force-displacement curve for many types of engineering analyses, especially in the design for the ultimate limit state or for life safety evaluation of existing walls. Doherty et al. (2002) identified that the secant stiffness for URM walls is different than for most other systems due to material strength variability and lack of definitive yield and/or softening points, and recommended empirically derived ratios of Δ_2/Δ_f from 0.28 to 0.50 for a range of degradation states (with the most severely damaged walls having the highest anticipated ratios of Δ_2/Δ_f) in single-leaf walls. By comparison, Derakhshan et al. (2013a) tested multi-leaf (two-leaf and three-leaf) walls with and without overburden loads and recommended a formula for calculation of the ratio of Δ_2/Δ_f , which typically produced smaller ratios than per Doherty et al. (2002) with an upper bound value of Δ_2/Δ_f equal to 0.25. By further comparison, NTC (2008) recommends that Δ_2/Δ_f be assumed equal to 0.40 in engineering assessments, unless limited by potentially unsafe conditions such as floor joist unseating.

Finally, Δ_f in Figure 1 represents the instability displacement under quasi-static loading (hereafter referred to as the static instability displacement). For simply-supported, one-way vertically spanning URM walls without overburden loads nor rigid restraints causing arching action to develop, it has been shown that the static instability displacement is expected to be equal to the wall thickness (Ewing et al. 1984; Doherty et al. 2002; Derakhshan et al. 2013b; Penner and Elwood 2016). However, the static instability displacement is expected to be smaller for one-way vertically spanning walls with applied overburden loads. Also, this displacement value can be significantly larger than the wall thickness for two-way spanning walls (Vaculik and Griffith 2017). In any given overburden load or spanning condition, note that utilizing the full static displacement capacity for a practitioner engineering assessment is non-conservative as much of the wall's displacement capacity is associated with “negative stiffness” (i.e., displacement increases with reducing lateral force; see Figure 1). Numerical dynamic time-history analyses (Derakhshan et al. 2014) have shown that one-way vertically spanning URM wall displacements beyond $0.5\Delta_f$ and $0.25\Delta_f$ for simply-supported and cantilevered walls, respectively, are rarely reversible and generally lead to wall collapse. Furthermore, displacement capacity is extremely sensitive to resonance occurring between the wall rocking and the ground (or floor) motion, such that dynamic URM wall

displacement capacity may vary significantly depending on the ground-motion record and building characteristics being considered in analysis (Wilhelm 2007; Derakhshan et al. 2014).

Displacement-based models recommended for use in determining the three different displacement parameters (Δ_1 , Δ_2 , and Δ_f) for various wall boundary conditions are listed in Table 1. Various alternative methods for predicting the OOP behaviour of URM walls have been documented elsewhere (Ferreira et al. 2015). Recommended methods for predicting force capacities were discussed previously by Walsh et al. (2017a, 2017b), wherein the authors categorised URM wall types generally into “unbounded” and “bounded” wall conditions, with the latter representing URM infill walls which are constrained by relatively rigid elements, such as RC frames, and thus may form compressive strut “arching” mechanisms while deforming OOP. For determining the secant stiffness at displacement parameter Δ_2 , a predictive model developed explicitly for infill walls is presented in assessment standards FEMA 356 (2000) and ASCE 41 (2014), with modifications proposed by Flanagan and Bennett (1999). Currently, there is no research basis known to the authors for distinguishing between “unbounded” and “bounded” URM wall types for estimating OOP displacement parameters Δ_1 and Δ_f . However, in previously reported research on retrofitted URM cavity walls tested in one-way vertically spanning conditions, Walsh et al. (2015) concluded that “bounded” walls with arching action were likely to have lower fundamental vibrational periods than “unbounded” walls. Furthermore, “bounded” walls were determined to have much more significant strength capacity as compared to “unbounded” wall types, controlling for geometry and material characteristics.

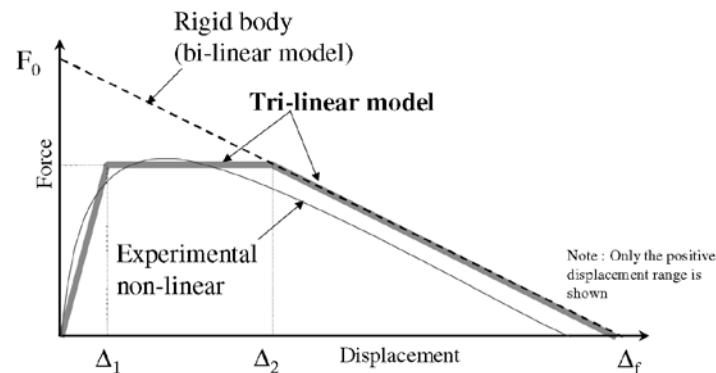


Figure 1: Idealised force-displacement behaviour for URM walls deformed OOP (Doherty et al. 2002)

Table 1: Summary of recommended predictive OOP performance models and associated applications

| Predictive model | Applicable performance metric | Top and bottom edge restraints | Side edge restraints | Model assumptions and applications |
|-----------------------|---|--|-----------------------|---|
| Doherty et al. (2002) | Δ_1 = Displacement for determining initial stiffness (empirical) | Diaphragm or URM wall on contiguous levels | Free (unrestrained)** | <ul style="list-style-type: none"> • one-way vertical spanning only • empirically-derived |

Table 1: Summary of recommended predictive OOP performance models and associated applications

| Predictive model | Applicable performance metric | Top and bottom edge restraints | Side edge restraints | Model assumptions and applications |
|--|---|--|--|--|
| Doherty et al. (2002) | Δ_2 = Displacement for determining secant stiffness (empirical, single-leaf) | Diaphragm or URM wall on contiguous levels | Free (unrestrained)** | <ul style="list-style-type: none"> one-way vertical spanning only empirically-derived |
| Derakhshan et al. (2014) | Δ_2 = Displacement for determining secant stiffness (empirical, multi-leaf) | Timber diaphragm or URM wall on contiguous levels* | Free (unrestrained)** | <ul style="list-style-type: none"> one-way vertical spanning or cantilevered simply supported restraints top and bottom |
| Flanagan and Bennett (1999) [modified from ASCE 2014 and FEMA 2000] | Δ_2 = Displacement for determining secant stiffness (infill walls) | RC slab or RC beam*** | n/a | <ul style="list-style-type: none"> one-way vertical spanning / arching only Derived for use in infill walls with height-to-thickness ratios ranging from 6.8 to 35.3 |
| NZSEE (2015) | Δ_f = Static instability displacement (one-way) | Timber diaphragm or URM wall on contiguous levels* | Free (unrestrained)** | <ul style="list-style-type: none"> one-way vertical spanning or cantilevered |
| Vaculik and Griffith (2017) | Δ_f = Static instability displacement (two-way) | Diaphragm or URM wall on contiguous levels | One or both sides laterally restrained | <ul style="list-style-type: none"> two-way spanning (minimum translational support at bottom edge and at least one vertical edge) |
| <p>*RC bond beams are also present at floor levels in many pre-WWII buildings with load-bearing URM walls and timber diaphragms in Australasia, but without vertical rigid elements (i.e., RC columns) to restrain the RC bond beams against vertical deflection, the RC bond beams are generally not assumed to effectuate compressive strut “arching” mechanisms in the URM walls under OOP loading.</p> <p>** Recommended for best-practice use in the case of isolated piers between window/door openings or for long parapets (with no overburden loads), such that one-way vertical spanning (i.e., horizontal cracking rather than vertical or diagonal cracking) is likely to govern OOP collapse.</p> <p>***URM infill walls may also be bounded by steel framing, but such an arrangement is far less common in Australasia.</p> | | | | |

TEST WALL CONDITIONS

Test walls were located within six different buildings in New Zealand: the Weir House (WH) estate in Wellington (constructed 1932), the Oriental Bay (WO) apartments in Wellington (early 1900s), the Wellington Railway Station (WR, 1937), an automotive garage (AG) in the Auckland CBD (1958), a retail building (AO) located in Orakei, Auckland (1938), and a mixed-used building on Kingston Street (AK) located in the Auckland CBD (1927). Geometries and pre-test damage states are summarised in Table 2.

Loading was applied to all test walls by using an air compressor to gradually inflate 1–3 (depending on the wall length) vinyl airbags that were positioned in a gap of 25–35 mm between the test wall panel and a plywood backing panel. The loaded area from each airbag was approximately 1150 mm by 2050 mm. The plywood backing panel consisted of an assemblage of plywood sheets and timber frames. The applied load from the airbags was transferred from the plywood backing panel to the braced reaction frame using 6 to 8 s-shaped load cells (each with a capacity of 10 kN) which provided the primary source of horizontal stability to the plywood-backed frame panel. The plywood-backed frame panel rested on greased steel plates to allow the panel to slide with minimal frictional resistance to ensure that the entire load was transferred through the load cells and not

resisted by bearing friction. The braced reaction frame consisted of vertical and diagonal timber members screw fixed into the concrete floor slab. The total lateral load, V , at any given time was calculated as the summation of the force recorded by all load cells. Additional information and figures regarding the existing wall conditions and how lateral forces were applied to the test walls using airbags is provided by Walsh et. al (2017a). Some test walls listed in Walsh et al. (2017a, 2017b) were not considered in the current study because it was evident from the force-displacement curves that no plateauing had taken place, and thus the yield displacement could not be defined with any level of confidence.

Table 2: Summary of test wall geometries, boundary conditions, and preparations

| Test ID | Length (mm) | Full in situ height* (mm) | Brick thickness (mm) | Top edge restraint | Side (vertical) edge restraints | Bottom edge restraint | Features and preparations |
|---------|-------------|---------------------------|----------------------|-----------------------|--|-----------------------|---|
| WH2 | 3850 | 2730 | 95 | Gypsum board (free) | RC column and URM return wall | RC slab | Plaster 15–20 mm thick each side, existing minor cracks |
| WH3 | 3480 | 2730 | 95 | Gypsum board (free) | RC shear wall and timber wardrobe | RC slab | Plaster 15–20 mm thick each side, existing minor cracks |
| WO1C | 3900 | 2740 | 110 | Timber (lateral only) | URM return walls both sides | URM / RC | Plaster 15–20 mm thick each side, horizontal and vertical 50 mm deep cut at 1600 mm above floor height and at the horizontal midway mark |
| WR1 | 2180 | 4280 | 108 | 127 mm RC slab | Free (unrestr.) both sides | RC slab on grade | Side edges saw cut free |
| WR2B | 1915 | 4342 | 108 | 127 mm RC slab | Free (unrestr.) both sides | RC slab on grade | Side edges of WR2B saw cut free after testing WR2A |
| WR4 | 1900 | 3100 | 108 | 127 mm RC slab | Free (unrestr.) and tall door | 127 mm RC slab | One side edge saw cut free and other side edge had nearly full |
| WR5 | 2580 | 2980 | 108 | Timber (lateral only) | URM return wall and short door opening | RC slab | |
| WR6 | 1305 | 2980 | 108 | Timber (lateral only) | Free (unrestr.) both sides | RC slab | Side edges saw cut free |
| AG1 | 4400 | 3400 | 112.5 | 280x150mm RC beam | 305x265mm concrete-encased steel columns both sides, contiguous infill on one side | RC slab on grade | Brick masonry veneer (as part of cavity infill wall) removed prior to testing |
| AG2 | 4400 | 3400 | 112.5 | 280x150mm RC beam | 305x265mm concrete-encased steel columns both sides, contiguous infill | RC slab on grade | Brick masonry veneer (as part of cavity infill wall) removed prior to testing, simulated in-plane cracking with 50 mm deep cut in X-shape across entire panel |

Table 2: Summary of test wall geometries, boundary conditions, and preparations

| Test ID | Length (mm) | Full in situ height* (mm) | Brick thickness (mm) | Top edge restraint | Side (vertical) edge restraints | Bottom edge restraint | Features and preparations |
|--|-------------|---------------------------|----------------------|--------------------|--|-----------------------|--|
| AO1 | 3380 | 2655 | 109 | 300x375mm RC beam | 350x350mm RC column (interior) with contiguous infill and 300x300mm RC column (exterior) | Timber | |
| AK2 | 1450 | 2750 | 75 | 300x475mm RC beam | Free (unrestr.) both sides | 300x475mm RC beam | Vertically cut through the 75 mm brick and removed original cavity steel wire ties |
| *Refer to Walsh et al. (2017a) for the distinction between full in situ height and test height | | | | | | | |

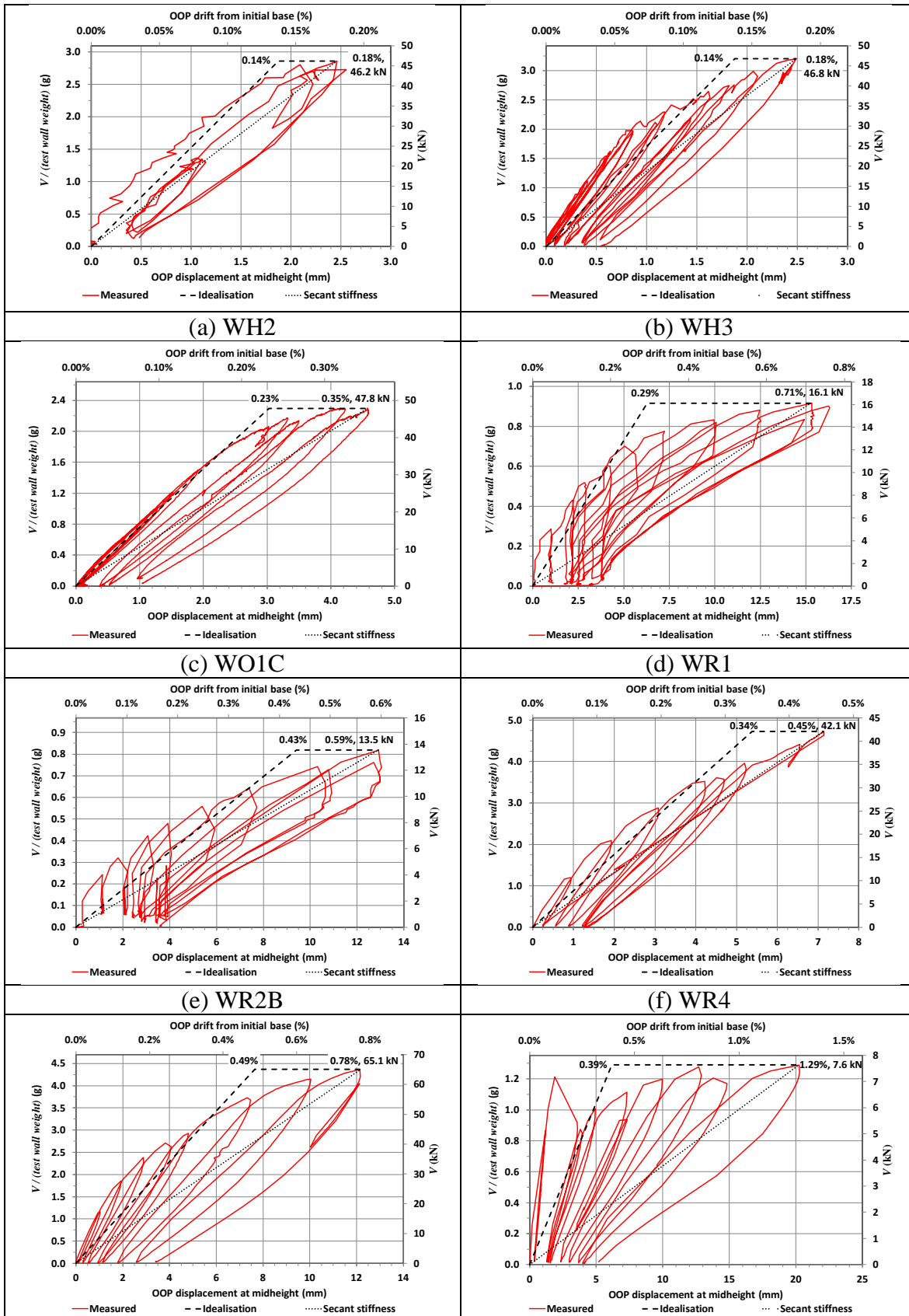
MATERIAL PROPERTIES AND GEOMETRIES

Brick, mortar, and masonry prism samples were extracted from the test walls and tested in accordance with the relevant ASTM standards [see Walsh et al. (2017a) for the complete list of standards and materials properties]. The gross cross-section of bricks was assumed for determining all material strengths. The average measured brick height, brick length, and mortar joint thickness in each relevant building were as follows (all dimensions in mm): 160, 300, and 15 for the Wellington Weir House (WH); 76, 230, and 18 for the Wellington Oriental Bay apartment building (WO); 78, 223, and 13.5 for the Wellington Railway Station (WR); 72, 224, and 11 for the Auckland Garage (AG); and 76, 225.5, and 13.5 for the Auckland Orakei retail building (AO). All masonry walls tested were constructed in running bond pattern with half brick length overlaps. Where needed for predictive calculations, the “equivalent” bed joint shear friction coefficient was assumed to be 1.04 to account for residual moment capacity in horizontal bending along a square bed joint (Vaculik and Griffith 2017).

COMPARISON OF MEASURED AND PREDICTED WALL CAPACITIES

All test walls were laterally loaded semi-cyclically at a quasi-static loading rate. The maximum lateral-force value (expressed as an acceleration with respect to gravity, g) for each wall was determined by dividing the maximum total test lateral force, V , by the weight of the test wall (see Figure 2). In many of the test buildings in which the test walls were required to remain in place after testing, testing was concluded after the peak strength of the test walls had been reasonably assumed to have been reached. In such cases, idealised curves were added to the measured force-displacement curves shown in Figure 2. The idealised curves shown in Figure 2 connect the origin, the idealised yield drift determined by assuming an equivalent elasto-plastic system with reduced stiffness (Park 1989), and the post-crack peak strength “design point”. Tests wall AG2 was able to be tested to complete collapse, and the instability drift was measured using photogrammetry. The values for OOP drift measured with respect to the initial base position are shown in Figure 2 as the ratio (%) of the OOP displacement at mid-height to the vertical distance between the wall base and the mid-height displacement gauge (i.e., approximately half the wall height).

Experimental and predicted values for displacement at yield, displacement at the “design point” for secant stiffness, and static instability displacement were compared, and the relative values are depicted in Table 3. Using the Doherty et al. (2002) empirical average values, the average ratio of predicted to measured yield was 2.65 with a high coefficient of variation (CV) of 0.96. This apparent overprediction may be due to some of the walls tested in the current study not actually being tested to peak strength (note the few force-displacement curves in Figure 2 without measured softening) or due to some of the walls tested in the current study being much stiffer relative to the Doherty et al. (2002) test walls due to two-way spanning conditions as well as arching action from the rigid bounding elements – neither of which was explicitly considered by Doherty et al (2002). Furthermore, this overprediction is largely controlled by three test specimens (WO1C, AO1, and AK2), and if these three data points are removed, the average of the ratios of predicted to measured yield would be 1.39 (CV 0.68). Nonetheless, it is evident from these findings that the empirical average values for parameter Δ_1 as published by Doherty et al. (2002) might be considered a general upper-bound for predicting idealised yield drifts that are assumed to represent an equivalent elasto-plastic system with reduced stiffness, although further research is warranted in this area.



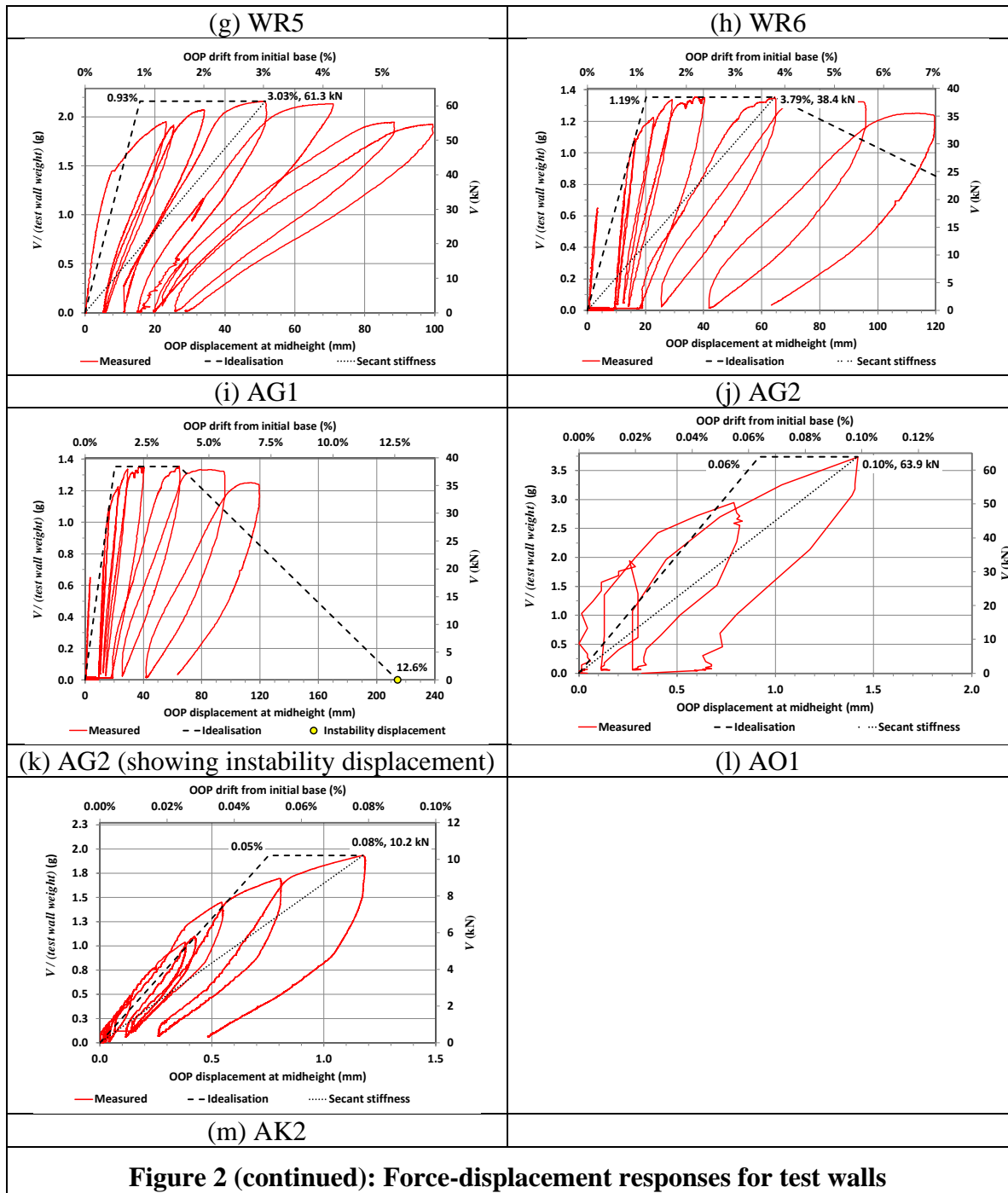


Figure 2 (continued): Force-displacement responses for test walls

“Design points” associated with the secant stiffness were predicted using both the Doherty et al. (2002) empirical average values and the modified version of the standards’ (FEMA 2000; ASCE 2014) analytical equation per Flanagan and Bennett (1999), with the latter pertaining explicitly to infill walls and limited to a height-to-thickness (h/t) ratio of 30. Both predictive methods resulted in high overpredictions of the “design point” displacement relative to the experimental values, with average ratios of predicted to measured results being 7.31 and 20.93, respectively (see Table 3). In particular, use of the standards’ equation, even with the modification, overpredicted the displacement values severely in the current study, although this observation is consistent with the

conclusions reached by Flanagan and Bennett (1999). Notably, both predictive methods were based largely on tests in vertical one-way spanning conditions. In contrast, the walls tested in the current study were configured in mostly two-way spanning conditions, and thus were measured as being comparatively stiff. However, test walls that were able to loaded to more severe damage levels due to intended removal following testing (e.g., AG1 and AG2) were measured as having drifts at peak strength more consistent with the predictive model and with other researchers' experimental data.

Table 3: Comparison of predicted and measured wall performance

| Test ID | Measured drifts ¹ | | | Predicted drifts ¹ | | | | Ratio of predicted to experimental | | | | Assumptions and other notes |
|-------------|------------------------------|--------------------|-------------------------------------|-------------------------------|-------------------------------|-------------------------------|-------------------------------------|------------------------------------|---------------------------|---------------------------|--------------------|---|
| | Yield* (%) | Design point** (%) | Static instability*** (% Δ) | Yield ^A (%) | Design point ^B (%) | Design point ^C (%) | Static instability ^D (%) | Yield | Design point ^B | Design point ^C | Static instability | |
| WH2 | 0.14% | 0.18% | - | 0.42% | 1.95% | - | - | 2.98 | 10.81 | - | - | |
| WH3 | 0.14% | 0.18% | - | 0.42% | 1.95% | - | - | 2.98 | 10.69 | - | - | |
| WO1C | 0.23% | 0.35% | - | 1.04% | 3.21% | - | - | 4.54 | 9.13 | - | - | Moderate damage per Doherty et al. (2002) |
| WR1 | 0.29% | 0.71% | - | 0.30% | 1.41% | - | - | 1.04 | 1.98 | - | - | |
| WR2B | 0.43% | 0.59% | - | 0.30% | 1.39% | - | - | 0.69 | 2.34 | - | - | |
| WR4 | 0.34% | 0.45% | - | 0.42% | 1.95% | 8.1% | - | 1.23 | 4.30 | 17.83 | - | |
| WR5 | 0.49% | 0.78% | - | 0.43% | 2.03% | - | - | 0.89 | 2.62 | - | - | |
| WR6 | 0.39% | 1.29% | - | 0.43% | 2.03% | - | - | 1.12 | 1.58 | - | - | |
| AG1 | 0.93% | 3.03% | - | 0.40% | 1.85% | 9.3% | - | 0.43 | 0.61 | 3.08 | - | |
| AG2 | 1.19% | 3.79% | 12.6% | 1.32% | 3.31% | 9.3% | 13.2% | 1.11 | 0.87 | 2.46 | 1.05 | Severe damage per Doherty et al. (2002) |
| AO1 | 0.06% | 0.10% | - | 0.49% | 2.30% | 5.9% | - | 8.21 | 23.32 | 60.34 | - | |
| AK2 | 0.05% | 0.08% | - | 0.33% | 1.53% | - | - | 6.55 | 19.50 | - | - | |
| Avg. | 0.39% | 0.96% | - | 0.53% | 2.08% | 8.18% | - | 2.65 | 7.31 | 20.93 | - | |
| CV | - | - | - | - | - | - | - | 0.96 | 1.04 | 1.30 | - | |

Notes:

¹ All drifts in this table represent the ratio of lateral displacement to the wall's vertical height below the location of primary horizontal cracking (assumed, and generally observed during testing, to have occurred at half the wall's total height).

* Intended to correspond with the idealised Δ_1 parameter, based on an equivalent elasto-plastic system with reduced stiffness (Park 1989).

** Intended to correspond with the idealised Δ_2 parameter, representing the displacement at peak force for determining the effective secant stiffness for use in nonlinear analysis (Doherty et al. 2002). In contrast, Derakhshan et al. (2014) recommended that secant stiffness be determined at the point of 75% of the rigid-body action threshold force.

*** Intended to correspond with the idealised Δ_f parameter for static wall instability. Measured using photogrammetry.

^A Based on empirical averages for Δ_1 per Doherty et al. (2002) for undamaged/new wall conditions unless otherwise noted in the table. Note that Doherty et al. (2002) did not explicitly define Δ_1 as the definitive yield displacement parameter. In contrast, Vaculik and Griffith (2017) considered the predicted yield point to be the average of Δ_1 and Δ_2 .

^B Based on empirical averages for Δ_2 per Doherty et al. (2002) for undamaged/new wall conditions unless otherwise noted in the table.

^C Based on the equation modified by Flanagan and Bennett (1999) from ASCE (2014) and FEMA (2000). Walls in this table without predicted values in this column were either not considered infill walls, or were infill walls with h/t ratios exceeding 30.

^D Based on the analytical equation proposed by Vaculik and Griffith (2017).

Ductility, as considered here, is the ability of a component to reach its peak strength and continue deforming under demands without weakening. While URM walls are not traditionally considered as having true ductility behaviour due to their brittle materials, they can be considered as having equivalent ductility capacity due to OOP rocking for purposes of identifying quantitatively performance limit states, or for use in linear (i.e., strength-based) assessment procedures. Note that the average measured equivalent ductility of the tested wall specimens in this study would be the ratio of the displacement at the design point to the displacement at yield, or $0.96\% / 0.39\% = 2.5$. By comparison, the average equivalent ductility capacity of the test walls using the predicted values per Doherty et al. (2002) would be 3.9, although this value would be smaller if more walls were considered to be damaged prior to deforming OOP. By further comparison, a provision in the upcoming version of ASCE 41 (2017) identifies more conservatively an equivalent m-factor of 1.5 for URM wall OOP behaviour for use in linear static and linear dynamic procedures (LSP and LDP, respectively). Identification of test walls in the study reported herein with especially low drifts at measured peak strengths (e.g., WR1, WR2B, WR4, and AO1 as shown in Figure 2) validates for purposes of proof testing that such walls were unlikely to have been loaded to their peak strengths, or at the very least, that some amount of equivalent ductility capacity existed beyond the measured peak strengths.

Only one wall in the current study was able to be tested to collapse (AG2). Note that the ratio of predicted to measured static instability displacement was an accurate 1.05 (albeit, this being only one data point). Notably and in contrast to the other predictive methods considered herein, the model used to predict the OOP static instability displacement of this test wall (Vaculik and Griffith 2017) accounted for the two-way spanning conditions that were present in the tested wall.

CONCLUSIONS

Displacement-based predictive methods for determining the OOP capacity of URM walls do suffer from many of the limitations present in the use of strength-based methods. Hence, a study that compares the accuracy of widely used displacement-based predictive methods and assumed input values to the results of experimental in situ tests was the subject of the investigation reported herein. The predictive results were compared to previously reported experimental results of twelve tests on existing URM walls performed in situ, representing a variety of geometries, boundary conditions, pre-test damage states, and material properties. In general, use of the existing predictive methods results in the over-prediction of the measured displacement parameters, which is likely due to most of the predictive methods being based on historical wall tests in one-way spanning conditions and without rigid restraints capable of effectuating arching action in the wall, in contrast to the wall test conditions in the current study. This apparent overprediction may also be due to some of the test walls not actually being tested to peak strength. Hence, the authors strongly recommend that further experimental tests on URM walls be carried out in two-way spanning conditions with and without rigid boundary elements, and where possible, that testing conditions allow for pushing walls to complete collapse in such a fashion that can be accurately measured.

ACKNOWLEDGEMENTS

A portion of the experimental testing was funded by the Building Research Association of New Zealand (BRANZ) through grant LR0441 and the Natural Hazards Research Management Platform (NHRP) through grant C05X0907. The authors are also grateful for the in-kind donations provided by the owners of the tested buildings, including KiwiRail and Mansons TCLM Ltd. Technical advisory for both testing and analysis was provided by Holmes Consulting Group. Students and staff who participated in the various field and laboratory testing efforts include Anthony Adams, Mark Byrami, Marta Giaretton, Mark Liew, Jeff Melster, Alexandre Perrin, Laura Putri, Jerome Quenneville, Ross Reichardt, and Gye Simkin.

REFERENCES

- ASCE (American Society of Civil Engineers) (2014), Seismic evaluation and retrofit of existing buildings, ASCE 41-13, Reston, Virginia, United States, 518 pp.
- Derakhshan, H., Griffith, M., and Ingham, J. (2013a), Airbag testing of multi-leaf unreinforced masonry walls subjected to one-way bending, *Engineering Structures*, 57(12), pp. 512–522, 10.1016/j.engstruct.2013.10.006.
- Derakhshan, H., Griffith, M., and Ingham, J. (2013b), Out-of-plane behavior of one-way spanning unreinforced masonry walls, *Journal of Engineering Mechanics*, 139(4), pp. 409–417, 10.1061/(ASCE)EM.1943-7889.0000347.
- Derakhshan, H., Dizhur, D., Griffith, M., and Ingham, J. (2014), Seismic assessment of out-of-plane loaded unreinforced masonry walls in multi-storey buildings, *Bulletin of the New Zealand Society for Earthquake Engineering*, 47(2), pp. 119–138.
- Doherty, K., Griffith, M., Lam, N., and Wilson, J. (2002), Displacement-based seismic analysis for out-of-plane bending of unreinforced masonry walls, *Earthquake Engineering and Structural Dynamics*, 1(4), pp. 833–850, 10.1002/eqe.126.
- Ewing R.D., and Kariotis J.C. (1981), Methodology for mitigation of seismic hazards in existing unreinforced masonry buildings: Wall testing, out-of-plane, Tech. Rep. ABK-TR-04, ABK, A Joint Venture, El Segundo, California, United States.
- Federal Emergency Management Agency (FEMA) (2000), FEMA 356: Prestandard and commentary for the seismic rehabilitation of buildings, Washington, DC, United States. 518 pp.
- Ferreira, T., Costa, A., and Costa, A. (2015), Analysis of the out-of-plane seismic behavior of unreinforced masonry: A literature review, *International Journal of Architectural Heritage*, 9(8), pp. 949–972.
- Flanagan, R., and Bennett, R. (1999), Arching of masonry infilled frames: Comparison of analytical methods, *Practice Periodical on Structural Design and Construction*, 4(3), pp. 105–110, 10.1061/(ASCE)1084-0680(1999)4:3(105).
- Griffith, M. C., Magenes, G., Melis, G., and Picchi, L. (2003), Evaluation of out-of-plane stability of unreinforced masonry walls subjected to seismic excitation, *Journal of Earthquake Engineering*, 7(SPEC. 1), pp. 141–169.

Moon, L., Dizhur, D., Senaldi, I., Derakhshan, H., Griffith, M., Magenes, G., and Ingham, J. (2014), The demise of the URM building stock in Christchurch during the 2010–2011 Canterbury earthquake sequence, *Earthquake Spectra*, 30(1), pp. 253–276.

Norme Tecniche per le Costruzioni (NTC) (2008), Decreto Ministero delle Infrastrutture, 14 gennaio 2008, G.U. n. 29 del 4 febbraio 2008 - Suppl. Ordinario n. 30. http://www.cslp.it/cslp/index.php?option=com_docman&task=doc_download&gid=3269&Itemid=10 (In Italian).

NZSEE (New Zealand Society for Earthquake Engineering) (2015), Assessment and Improvement of the Structural Performance of Buildings in Earthquakes, Recommendations of a NZSEE Project Technical Group. Incorporated Corrigenda No. 4, Section 10, Seismic Assessment of Unreinforced Masonry Buildings, Wellington, New Zealand, 293 pp.

Park, R. (1989), Evaluation of ductility of structures and structural assemblages from laboratory testing, *Bulletin of the New Zealand National Society for Earthquake Engineering*, 22(3), pp. 155–66.

Penner O., and Elwood K.J. (2016), Out-of-plane dynamic stability of unreinforced masonry walls in one-way bending: shake table testing, *Earthquake Spectra*, 32(3), pp. 1675–97.

Walsh, K., Dizhur, D., Shafaei, J., Derakhshan, H., and Ingham, J. (2015), In situ out-of-plane testing of unreinforced masonry cavity walls in as-built and improved conditions, *Structures*, 3, pp. 187–199, 10.1016/j.istruc.2015.04.005.

Walsh, K., Dizhur, D., Giongo, I., Derakhshan, H., and Ingham, J. (2017a), Effect of boundary conditions and other factors on URM wall out-of-plane behaviour: Design demands, predicted capacity, and in situ proof test results,” *Sesoc Journal*, 30(1), pp. 57–81.

Walsh, K., Dizhur, D., Giongo, I., Derakhshan, H., and Ingham, J. (2017b), Comparison between predicted URM wall out-of-plane strength based capacity and in situ proof test results,” *13th Canadian Masonry Symposium*, June 4–7, Halifax, Nova Scotia, Canada, 12 pp.

Wilhelm, M., Mojsilović, N., and Dazio, A. (2007), Out-of-plane shaking table tests on unreinforced masonry walls, *Proceedings of the 10th North American Masonry Conference*, June 2–5, St. Louis, Missouri, pp. 671–682.

Vaculik, J., and Griffith, M. (2017), Out-of-plane load–displacement model for two-way spanning masonry walls, *Engineerign Structures*, 141, pp. 328–343, 10.1016/j.engstruct.2017.03.024.

AN IMPROVED MACROELEMENT MODEL FOR THE NONLINEAR ANALYSIS OF MASONRY BUILDINGS

S. Bracchi¹, A. Galasco², A. Penna³ and G. Magenes⁴

¹ PhD Candidate, ROSE Programme, UME School, Institute for Advanced Studies, via Ferrata 1, I-27100 Pavia, Italy, Stefano.Bracchi@umeschool.it

² Post-Doctoral Researcher, Department of Civil Engineering and Architecture, University of Pavia, via Ferrata 3, I-27100 Pavia, Italy, Alessandro.Galasco@unipv.it

³ Associate Professor, Department of Civil Engineering and Architecture, University of Pavia, via Ferrata 3, I-27100 Pavia, Italy, Andrea.Penna@unipv.it

⁴ Full Professor, Department of Civil Engineering and Architecture, University of Pavia, via Ferrata 3, I-27100 Pavia, Italy, Guido.Magenes@unipv.it

In the numerical modelling of nonlinear behaviour of masonry buildings by means of macroelement models, it is important to correctly capture the lateral stiffness and strength of the structure. The macroelement model currently implemented in the TREMURI computer program thanks to the presence of nonlinear interfaces lumped at the element extremities allows studying the coupled axial and in-plane bending response of masonry panels, with the inherent limitation of approximating the stiffness associated with at least one of these behaviours. Moreover, the shear strength of the wall can be captured only if a calibration of material properties is performed before the analysis. The paper presents an improved macroelement model to simulate the in-plane cyclic behaviour of masonry walls. The model overcomes some of the limitations of the currently available macroelement. As regards the flexural behaviour, a methodology to capture the correct flexural stiffness of the panel is developed. As regards the shear behaviour, the proposed improved macroelement is able to predict the correct shear strength of the wall, considering multiple shear strength criteria and directly starting from the experimentally measured mechanical properties. The improved model is then implemented in the TREMURI program and its ability of accurately predicting the nonlinear response of masonry structures is verified through the simulation of experimental tests. The paper finally discusses possible applications of the improved model to the analysis of new and existing structures to perform vulnerability studies.

Keywords: *Masonry, macroelement model, nonlinear analysis, flexural stiffness, shear strength*

INTRODUCTION

A significant interest in modelling approaches suitable for static and dynamic analysis of unreinforced masonry structures has recently developed, due to their well-known high vulnerability to seismic actions. The nonlinear behaviour can be modelled using micromodelling techniques (e.g. Alpa and Monetto, 1994), where a refined discretization of units, mortar and interfaces by nonlinear finite elements is proposed, or by equivalent continuum models (e.g. Calderini and Lagomarsino, 2008), in which masonry is idealized as an equivalent homogenized material, derived from the mechanical properties of the components. A good alternative to reduce the computational burden, still obtaining accurate results, is represented by the so-called macroelement approach (e.g. Magenes et al., 2001), where a single element is used to model the response of a masonry element (pier or spandrel beam). The behaviour of an entire masonry wall can then be modelled assembling macroelements, using equivalent frame techniques (e.g. Magenes and Della Fontana, 1998; Belmouden and Lestuzzi, 2009). Among these macroelement models, the one proposed by Penna et al. (2014) is particularly suitable for the analysis of buildings and has been implemented in the TREMURI (Lagomarsino et al., 2013) computer program for the nonlinear analysis of masonry buildings. In this paper, an improved version of this macroelement is developed, with the aim of solving some of the limitations of the current model.

MACROELEMENT MODEL OF MASONRY WALLS

The basic ideas of the two-node macroelement model proposed by Penna et al. (2014) are illustrated in Figure 1. The panel is ideally subdivided into three parts: a central body, where only shear deformations are possible, and two interfaces, where the external degrees of freedom are located, which can have relative axial displacements and rotations with respect to those of the extremities of the central body. The two interfaces can be considered infinitely rigid in shear and have a negligible thickness. Their axial deformations are due to a system of distributed zero-length springs.

These assumptions simplify the macroelement kinematic and compatibility relations allowing for a reduction of the actual degrees of freedom of the model. Since the central part is considered as a rigid body with only shear deformation capability, under small displacement hypotheses, the axial displacements and rotations of the ends can be considered equal to the centroid ones (w_e , φ_e), whereas the transversal displacements of the central body ends must be equal to the corresponding nodal displacements (u_i , u_j). Therefore, the macroelement kinematics can be described by means of eight degrees of freedom, six nodal displacement components (u_i , w_i , φ_i , u_j , w_j , φ_j) and two internal components (w_e , φ_e). No distributed transversal actions are considered and so the internal shear force is constant along the element axis ($V_i = V_j = V$). A no tension model has been attributed to zero-length springs at the interfaces, with a bilinear degrading constitutive model in compression.

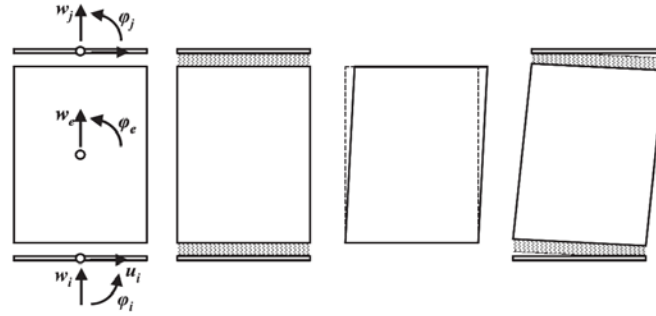


Figure 1: Kinematics of the macroelement (Penna et al., 2014)

However, the current macroelement is characterized by some limitations. The first one is the underestimation of energy dissipation in flexural failure modes. To solve this issue, a new constitutive law of the single spring, characterized by a limited compressive strength and unloading stiffness equal to the elastic one, has been introduced by Bracchi et al. (2017). This allows for an increased energy dissipation and damage accumulation. Figure 2 shows the comparison between the current and new law. The other limitations regard the inability of capturing at the same time both the axial and flexural stiffness of the element and the ability of modelling the shear strength of the wall only if a calibration of the material properties is performed before the analysis. This paper proposes an improved macroelement able to solve these two issues.

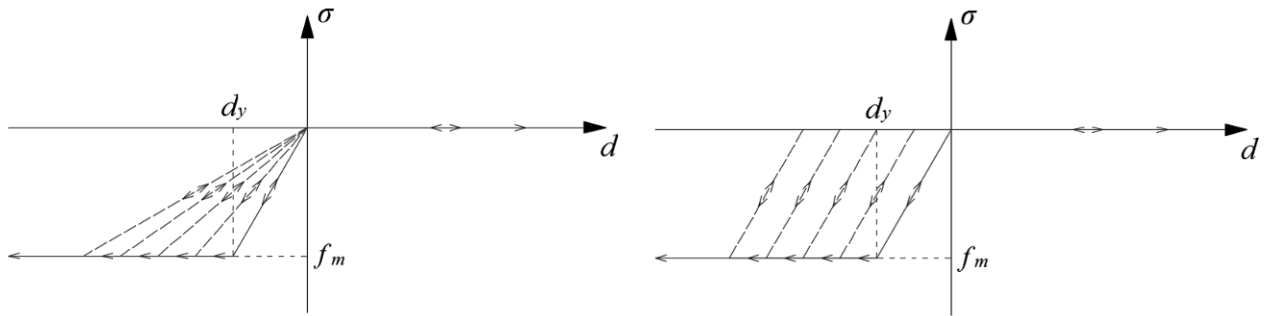


Figure 2: Original (Penna et al., 2014) (left) and improved (Bracchi et al., 2017) (right) constitutive law for interface joint springs

FLEXURAL STIFFNESS

As already explained, in the macroelement of Penna et al. (2014), the axial and flexural deformations are concentrated at the top and bottom interfaces, where two sets of springs, having a stiffness per unit area k equal to $2E/h$ (where E is the elastic modulus of masonry and h is the height of the element), are located. As observed by Petry and Beyer (2015), this formulation allows to correctly reproduce the axial stiffness of a masonry panel, but the flexural stiffness results to be underestimated.

In particular, the flexural stiffness depends on the static scheme of the macroelement, i.e. on its boundary conditions. As an example, in cantilever conditions, the flexural stiffness of the macroelement is equal to $2EI/h^3$ (where I is the moment of inertia of the element), whereas the flexural stiffness of an elastic beam with the same properties is equal to $3EI/h^3$. To correctly reproduce the flexural stiffness of a masonry panel, the flexural stiffness of the macroelement has to be multiplied by a correction factor equal to 1.5. In double-fixed boundary conditions, the flexural stiffness of the macroelement is equal to $4EI/h^3$, whereas the flexural stiffness of an elastic beam with the same properties is equal to $12EI/h^3$. Therefore, in this case, the correction factor of the stiffness turns out to be equal to 3.

In general, the correction coefficient of the flexural stiffness is a function of the boundary conditions of the macroelement, i.e. of the ratio of the moments at top and bottom nodes of the macroelement (M_i and M_j) and is constant if the static scheme is maintained constant during the analysis. However, in the case of a macroelement inside an equivalent frame discretization, different static schemes with respect to cantilever or double-fixed can be found and the ratio of moments M_i and M_j (i.e. the static scheme) can vary during the analysis.

An approximated way of modelling the correct flexural stiffness using the current macroelement formulation, consists in modifying the elastic modulus E set as input in the numerical model. This represents only an approximated solution because, increasing E , the axial stiffness is now overestimated. Furthermore, if the boundary conditions vary during the analysis, the correction can not be changed and, in the case of walls made of various macroelements, the boundary conditions are not known before the analysis. However, this approach has been used up to now to account for the underestimation of flexural stiffness in the current macroelement.

To perform the correction of flexural stiffness automatically for each macroelement in generic boundary conditions (Figure 3), also varying during the analysis, the variable α has to be introduced. This is defined as the ratio between the distance from the section of zero moment and the section of maximum moment in absolute value (h_0) and the height of the macroelement (h).

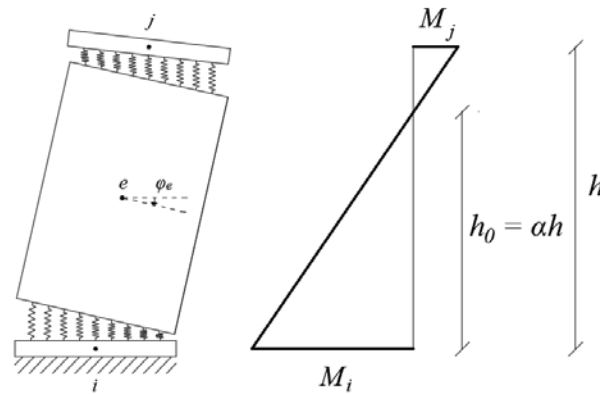


Figure 3: Macroelement in generic boundary conditions

Since the nonlinear problem in the macroelement is formulated in terms of kinematic and not static variables, it is preferable to express the variable α as a function of displacements and

rotations, instead of moments. The relationship between the variable α and the kinematic variables is expressed by Equation (1).

$$\begin{cases} \alpha = \frac{\varphi_i - \varphi_e}{\varphi_j - 2\varphi_e + \varphi_i} & |\varphi_i - \varphi_e| \geq |\varphi_j - \varphi_e| \\ \alpha = \frac{\varphi_j - \varphi_e}{\varphi_j - 2\varphi_e + \varphi_i} & |\varphi_i - \varphi_e| < |\varphi_j - \varphi_e| \end{cases} \quad (1)$$

The correction factor to be applied to the axial stiffness k to obtain the correct flexural stiffness is represented by the variable 3η . To obtain the relationship between η and α , the correct flexural stiffness of the macroelement, expressed as a function of α , has to be equated to the one of a Bernoulli beam with the same properties. Therefore, the correction factor η results to be expressed by Equation (2).

$$\eta = \frac{\alpha}{3\alpha - 1} \quad (2)$$

To implement the correction of flexural stiffness in the macroelement formulation of Penna et al. (2014), the three rotations used in the flexural equilibrium equations have to be corrected by the factor 3η . The correction factor 3η is a function of α and, hence, of the internal rotations φ_i , φ_e and φ_j of the macroelement.

Replacing the original rotations with the corrected rotations in the flexural equilibrium equations of the macroelement formulation described by Penna et al. (2014), i.e. in the calculation of the elastic contributions to N and M and of the correction contributions due to cracking and crushing, the correction of flexural stiffness can be performed automatically inside the macroelement.

SHEAR STRENGTH

The shear damage model of Gambarotta and Lagomarsino (1997), on which the shear behaviour of the macroelement of Penna et al. (2014) is based, was developed for a masonry panel damaging and failing with a mechanism of shear sliding along the whole cross section. Therefore, the shear strength and damage state of the single macroelement is calculated assuming the criterion for shear failure with sliding along the whole cross section, expressing the shear strength V_{res} through Equation (3).

$$V_{res} = lt \left(\bar{c} + \bar{\mu} \frac{N_0}{lt} \right) \quad (3)$$

The macroscopic shear model is hence based on a combination of equivalent cohesion \bar{c} , and equivalent friction coefficient $\bar{\mu}$. The strategy adopted in the improved macroelement is to calculate (or calibrate) the equivalent parameters to reproduce the shear strength foreseen by commonly used shear strength criteria, starting from the local mechanical properties, derived from characterization tests or code prescriptions.

A distinction among piers and spandrels is required. As regards piers, different situations have to be distinguished, based on the failure mechanism. For diagonal shear cracking with cracks passing through the bricks, a possible formulation of the local shear strength, given the tensile strength of bricks f_{bt} , was proposed by Mann and Muller (1982). Magenes and Calvi (1997) transformed the local criterion into a global strength criterion introducing a correction factor taking into account the influence of shear span ratio α_v , defined as the ratio between the distance from the zero moment to the maximum moment section (h_0) and the wall length (l). The shear strength is expressed by Equation (4), as a function of the axial compression force (N_0) acting on the considered section.

$$V_{res} = lt \frac{f_{bt}}{2.3(1 + \alpha_v)} \sqrt{1 + \frac{N_0}{f_{bt}lt}} \quad (4)$$

To find the equivalent parameters \bar{c} and $\bar{\mu}$ to be used in the shear strength formulation adopted in the macroelement, a first-order Taylor polynomial approximation of Equation (4) in the point $N = N_0$ has to be calculated. The equivalent friction coefficient $\bar{\mu}$ is the slope of the obtained straight line, whereas the equivalent cohesion \bar{c} is represented by the intercept.

For shear failure with sliding along bed-joints of the whole cross section, Magenes and Calvi (1997) proposed that the shear strength is given by Equation (5).

$$V_{res} = \frac{lt}{1 + \alpha_v} \left(\bar{c} + \bar{\mu} \frac{N_0}{lt} \right) \quad (5)$$

The shear strength is thus the one obtained using the Mohr-Coulomb formulation, corrected with the coefficient $1/(1+\alpha_v)$ to consider different ratios between height and length and different boundary conditions of the wall. Furthermore, the cohesion and friction coefficient \bar{c} and $\bar{\mu}$ proposed by Mann and Muller (1982) have to be used (Equation (6)).

$$\begin{cases} \bar{\mu} = \frac{1}{1 + \mu \tan \theta} \mu \\ \bar{c} = \frac{1}{1 + \mu \tan \theta} c \end{cases} \quad (6)$$

The correction factor of μ and c is a function of the crack inclination θ with respect to the horizontal, depending on the masonry pattern. In the original formulation, Mann and Muller (1982) proposed a correction factor with $2\Delta_y/\Delta_x$ in place of $\tan \theta$, where Δ_x and Δ_y are the unit length and height, respectively. This corresponds to the crack usually forming in a running bond pattern; however, in this work, the more general formulation of Equation (6) is adopted, to allow the consideration of different bond patterns. In this case, since both the formulations of Equations (3) and (5) are linear, the calibrated values of \bar{c} and $\bar{\mu}$ can be obtained setting the two equations equal.

In the case of shear failure with sliding along bed-joints of a cracked cross section, Magenes and Calvi (1997) proposed that the shear strength is expressed by Equation (7).

$$V_{res} = lt \frac{\left(1.5\bar{c} + \bar{\mu} \frac{N_0}{lt}\right)}{1 + 3\bar{c}\alpha_V / \left(\frac{N_0}{lt}\right)} \quad (7)$$

As done for the case of diagonal shear cracking with cracks passing through the bricks, a first-order Taylor polynomial approximation of Equation (7) in the point $N = N_0$ is performed to calculate \bar{c} and $\bar{\mu}$.

In the case of failure for sliding along the cracked section, an upper limit to the shear strength is often imposed by building codes. As an example, Eurocode 6-Part 1-1 (EN 1996 1-1, 2004) requires that, in the case of filled head-joints, the shear strength f_v (in terms of stress and relative to the compressed part of the section) is lower than a limit value f_{vlt} equal to 0.065 times the strength of the brick f_b . However, in the formulation of the improved macroelement, the specification of the strength limit directly introducing f_{vlt} , instead of f_b , is adopted. Multiplying the limit value f_{vlt} times the compressed length and the thickness of the section, the strength limit results to be expressed by Equation (8).

$$V_{res,lim} = \frac{\frac{3}{2} f_{vlt} lt N_0}{N_0 + 3 f_{vlt} \alpha_V lt} \quad (8)$$

Also in the case of $V_{res,lim}$, the values of \bar{c} and $\bar{\mu}$ are obtained applying the same approach of the previous case. Obviously, the shear strength is the minimum between the one associated to sliding along the joints and to compressive failure of the bricks.

Furthermore, the shear failure can be associated to the attainment of tensile strength of masonry f_{tu} at the centre of the panel. The shear strength is expressed by Equation (9), i.e. using the criterion proposed by Turnšek and Sheppard (1980), corrected by means of the factor $1/(1+\alpha_V)$ proposed by Magenes and Calvi (1997).

$$V_{res} = \frac{f_{tu} lt}{b(1 + \alpha_V)} \sqrt{1 + \frac{N_0}{f_{tu} lt}} \quad (9)$$

The parameter b is a coefficient accounting for shear stress distribution in the centre of the wall and is a function of the ratio between the height (h) and the width (l) of the panel (Benedetti and Tomaževič, 1984). The equivalent shear strength parameters \bar{c} and $\bar{\mu}$ are calculated as done for the other criteria, starting from the first-order Taylor expansion in the point $N = N_0$.

As regards the spandrels, the criteria associated to diagonal shear cracking with cracks passing through the bricks or to the attainment of tensile strength of masonry, have to be used, again depending on the pattern. The choice of these failure mechanisms, instead of the ones

characterized by sliding, is justified by the impossibility, due to interlocking phenomena, of sliding on a vertical joint plane at the end-sections, as observed by Lagomarsino et al. (2013).

Finally, Figure 4 shows an example of interaction diagram of a masonry pier, with the different strength criteria.

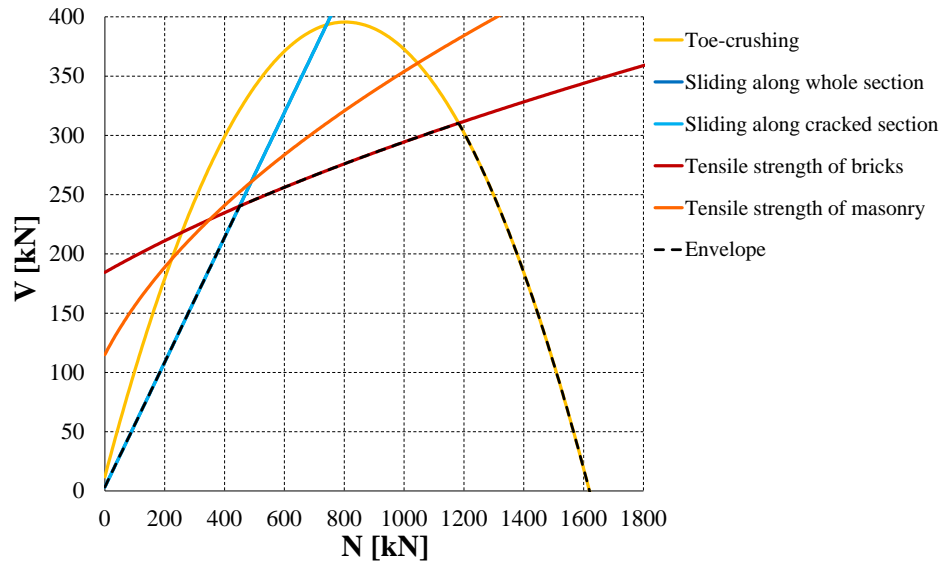


Figure 4: Interaction diagram of a wall with the different strength criteria

The shear strength and equivalent strength parameters vary during the analysis and among the different macroelements of a wall. To implement the calculation of shear strength V_{res} and equivalent strength parameters \bar{c} and $\bar{\mu}$ in the improved macroelement, the following strategy is adopted: firstly, at each analysis step and for each macroelement, the value of axial load N_0 and shear span ratio α_v are determined. The shear strength V_{res} is then calculated as the minimum among the strengths foreseen by the four strength criteria (or among the criteria selected, if not all of them are considered). The equivalent shear strength parameters \bar{c} and $\bar{\mu}$ corresponding to the governing criterion, i.e. the one leading to the minimum strength, are then calculated. These parameters are finally used in the shear damage model to determine the damage state. The shear strength (and failure mechanism) and the equivalent strength parameters are continuously updated during the analysis until the shear strength is reached. After that, the shear strength and equivalent parameters are kept constant and equal to the ones corresponding to the attained strength. It is hence reasonable to think that, when an element has reached the strength, the shear strength (i.e. the failure mechanism) and the equivalent parameters are fixed.

In the case of a macroelement with α greater than one, the shear strength criteria as formulated in the previous section (i.e. starting from the formulas proposed by Magenes and Calvi (1997)) are unreasonably underestimating the actual shear strength and overestimating the shear damage. This is evident comparing the results of experimental tests on masonry façades to the ones obtained from the numerical simulation. This behaviour is explained by the presence of α_v at the denominator of all the strength criteria. When α_v is larger than h/l , i.e. α is greater than one, the shear strength starts to be overly reduced. Since there is no physical reason justifying the

increased reduction of shear strength for panels with α_v greater than h/l , a lower bound for the shear strength is introduced. In particular, for each macroelement, the value of α_v is limited to h/l , which corresponds to limit α to unity. As a final remark, it should be noticed that the correction factor $1/(1+\alpha_v)$ was proposed only for brick masonry. In the improved macroelement, the possibility of adopting or not the correction factor is given, but the final decision is left to the user, based on the type of masonry. Finally, the improved macroelement was implemented in the software TREMURI.

APPLICATIONS OF THE IMPROVED MACROELEMENT

The first application of the improved macroelement consists in the simulation of experimental static tests. In particular, the improved macroelement was used to simulate the response of whole buildings. This case is particularly important since it allows to check the efficiency of the correction of flexural stiffness in the case boundary conditions are different from constant cantilever or double-fixed, depending on the actual moment profile along the height and varying during the analysis. Furthermore, the efficiency of the shear strength prediction at the building scale can be verified.

The test considered is the one performed by Magenes et al. (1995) at the University of Pavia, on a full-scale, two-storeys unreinforced masonry building prototype. The building consisted of four two-wythe solid brick walls: the plan dimensions were 6 m and 4.4 m, with height of 6.4 m, wall thickness of 250 mm and non-symmetric openings. One of the longitudinal (i.e. parallel to the loading direction) walls (“Door Wall”) was disconnected from the adjacent transverse walls, whereas the other (“Window Wall”) was connected to the adjacent walls with an interlocking brick pattern around the corner. The floors consisted of a series of isolated steel beams, designed to simulate a very flexible diaphragm. The specimen was subjected to a quasi-static applied displacement history, meant to simulate the dynamic load. Due to the presence of flexible floors, two separate numerical models for “Door” and “Window Wall” were built and analysed. Since the “Door Wall” was separated from the transverse walls, the corresponding model consisted only of a single wall, whereas, in the case of the “Window Wall”, also the transversal walls were included.

For simplicity, only the “Door Wall” was considered; this was simulated using the current macroelement by Mandirola (2015). The mechanical parameters of the improved macroelement were optimized to best simulate the experimental behaviour; both piers and spandrels were modelled using the improved macroelement. The elastic moduli E and G were set equal to 1490 MPa and 534 MPa, respectively. As regards the shear strength, the criterion of tensile failure of bricks was adopted, being the most consistent with the experimental damage mechanism, with values of f_{bt} equal to 0.82 MPa for all the elements and applying the correction factor $1/(1+\alpha_v)$. Figure 5 presents the results in terms of hysteretic curves and damage patterns at failure. The experimental value of f_{bt} reported by Magenes and Calvi (1997) is equal to 1.07 MPa.

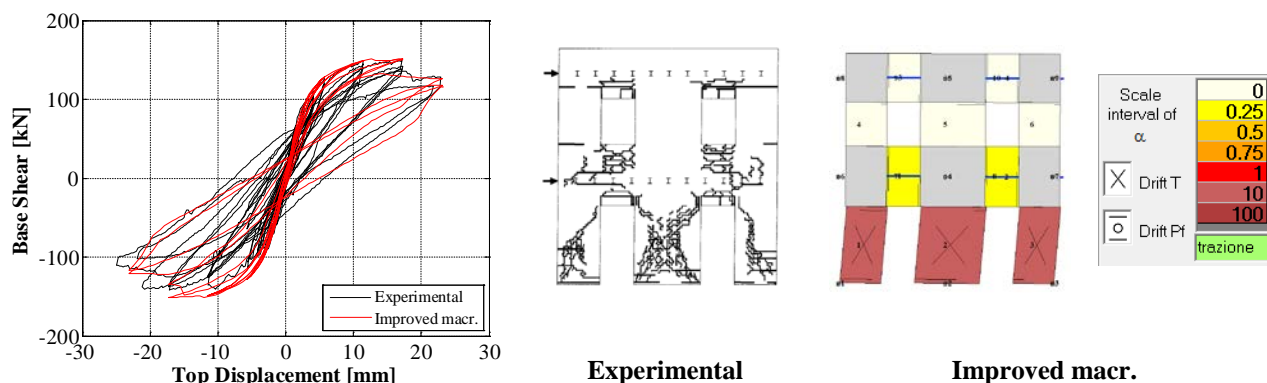


Figure 5: Comparison between the experimental and numerical results obtained using the improved macroelement, in terms of base shear vs. top displacement curves (left) and damage mechanisms at failure (right)

From the hysteresis curves, it can be observed that the improved macroelement is well predicting the shear force decay and energy dissipation, although the strength is slightly overestimated in the negative direction. In terms of damage patterns at failure, the improved macroelement allows to well capture the large damage of piers at the ground level and the absence of damage at the first level, whereas an underestimation of the damage of the spandrels is evident. However, since the failure mechanism of the wall and the hysteresis curves are captured, this simulation led to conclude that the improved macroelement is effective in well capturing the response of buildings.

Other applications of the improved macroelement consist in the simulation of dynamic experimental tests at the building scale (full or reduced). Moreover, the formulation adopted allows the improved macroelement to be still characterized by the low computational burden typical of the current macroelement. Therefore, the improved macroelement can be used to perform nonlinear analyses to study the vulnerability of existing or new buildings, as it is currently been doing in a recent project, aimed at assessing the implicit seismic risk of code conforming structures in Italy (Camilletti et al., 2017).

CONCLUSIONS

In this work, an improved macroelement was proposed starting from the one of Penna et al. (2014). Some of the limitations of the current model were solved: in particular, a methodology to model the correct flexural stiffness was developed, together with the automatic calibration of the equivalent shear strength parameters, starting from different strength criteria available in the literature. These calibrations are performed for each element and at each step of the analysis. The improved macroelement was then implemented in TREMURI and was used to simulate experimental tests. The tests were simulated using the mechanical properties allowing for the best simulations of the experimental results and the improved macroelement proved to be effective in simulating experimental tests on buildings. Furthermore, other possible applications of the improved macroelement were discussed.

Future developments of this work consist in the definition and implementation of more appropriate strength criteria for the spandrels. A methodology to automatically calibrate the macroelement parameters governing the nonlinear shear deformability, starting from experimentally observed quantities, can be also developed. The methodology developed to include different strength criteria can be applied to include other shear strength criteria, prescribed by building codes of various countries. Finally, a larger number of experimental tests can be simulated, also with the aim of better understanding the validity of the adopted shear strength criteria, especially for what concerns the application of the correction factors ($\tan\theta$ and $1/(1+\alpha\nu)$).

ACKNOWLEDGEMENTS

Part of this work was carried out within the framework of the ReLUI Project PR1 - Masonry Structures 2017 and of the Programme n. 15 of the EUCENTRE Executive Project 2017, both funded by the Italian Department of Civil Protection. The authors would also like to thank M. Mandirola for the support in the simulation of experimental tests.

REFERENCES

- Alpa G., and Monetto I. (1994), Microstructural Model for Dry Block Masonry Walls with In-Plane Loading, *Journal of the Mechanics and Physics of Solid*, 42, pp. 1159-1175.
- Belmouden Y., and Lestuzzi P. (2009), An Equivalent Frame Model for Seismic Analysis of Masonry and Reinforced Concrete Buildings, *Construction and Building Materials*, 23, pp. 40-53.
- Benedetti D., and Tomaževic M. (1984), Seismic Assessment of Masonry Constructions, *Ingegneria Sismica*, 1, pp. 9-16 (in Italian).
- Bracchi S., Galasco A., and Penna A. (2017), An Improved Macroelement Model Accounting for Energy Dissipation in In-Plane Flexural Behaviour of Masonry Walls, *Proceedings of 16th World Conference on Earthquake Engineering*, January 9-13, Santiago Chile, Chile.
- Calderini C., and Lagomarsino S. (2008), A Continuum Model for In-Plane Anisotropic Inelastic Behaviour of Masonry, *ASCE Journal of Structural Engineering*, 134, pp. 209-220.
- Camilletti D., Cattari S., Lagomarsino S., Bonaldo D., Guidi G., Bracchi S., Galasco A., Magenes G., Manzini C.F., Penna A., and Rota M. (2017), RiNTC Project: Nonlinear Dynamic Analyses of Italian Code-Conforming URM Buildings for Collapse Risk Assessment, *Proceedings of the 6th ECCOMAS COMPDYN Conference*, June 15-17, Rhodes Island, Greece.
- EN 1996-1-1 (2004), Eurocode 6: Design of Masonry Structures - Part 1-1: Common Rules for Reinforced and Unreinforced Masonry Structures, CEN, Bruxelles, Belgium.
- Gambarotta L., and Lagomarsino S. (1997), Damage Models for the Seismic Response of Brick Masonry Shear Walls. Part II: the Continuum Model and its Applications, *Earthquake*

Engineering and Structural Dynamics, 26, pp. 441-462.

Lagomarsino S., Penna A., Galasco A., and Cattari S. (2013), TREMURI Program: an Equivalent Frame Model for the Nonlinear Seismic Analysis of Masonry Buildings, *Engineering Structures*, 56, pp. 1787-1799.

Magenes G., Calvi G.M., and Kingsley G.R. (1995), Seismic Testing of a Full-Scale, Two Story Masonry Building: Test Procedure and Measured Experimental Response, in “Experimental and Numerical Investigation on a Brick Masonry Building Prototype - Numerical Prediction of the Experiment”, Technical Report, University of Pavia, Pavia, Italy.

Magenes G., Braggio C., and Bolognini D. (2001), Metodi Semplificati per l’Analisi Sismica Non Lineare di Edifici in Muratura, Technical Report, CNR-GNDT, Rome, Italy (in Italian).

Magenes G., and Calvi G.M. (1997), In-Plane Seismic Response of Brick Masonry Walls, *Earthquake Engineering and Structural Dynamics*, 26, pp. 1091-1112.

Magenes G., and Della Fontana A. (1998), Simplified Non-Linear Seismic Analysis of Masonry Buildings, *Proceedings of the British Masonry Society*, 8, pp. 190-195.

Mandirola M. (2015), Numerical Modelling Report, Technical Report, EUCENTRE, Pavia, Italy.

Mann W., and Müller H. (1982), Failure of Shear-Stressed Masonry: an Enlarged Theory, Tests and Application to Shear Walls, *Proceedings of the British Ceramic Society*, 30, pp. 223-235.

Penna A., Lagomarsino S., and Galasco A. (2014), A Nonlinear Macro-Element Model for the Seismic Analysis of Masonry Buildings, *Earthquake Engineering and Structural Dynamics*, 43, pp. 159-179.

Petry S., and Beyer K. (2015), Force-Displacement Response of In-Plane-Loaded URM Walls with a Dominating Flexural Mode, *Earthquake Engineering and Structural Dynamics*, 44, pp. 2551-2573.

Turnšek V., and Sheppard P. (1980), The Shear and Flexural Resistance of Masonry Walls, *Proceedings of the International Research Conference on Earthquake Engineering*, June 30-July 3, Skopje, Macedonia.

FULL-SCALE OUT-OF-PLANE SHAKING TABLE TESTS OF URM WALLS IN TWO-WAY BENDING

F. Graziotti¹, U. Tomassetti², L. Grottoli³, A. Penna³ and G. Magenes⁵

¹ Assistant Professor, Dept. Of Civil Engineering and Architecture – DICAr, University of Pavia and European Centre for Training and Research in Earthquake Engineering - EUCENTRE, Pavia, 27100, Italy, francesco.graziotti@unipv.it

² PhD Student, DICAr, University of Pavia, Pavia, 27100, Italy, umberto.tomassetti01@universitadipavia.it

³ Postgraduate Researcher, EUCENTRE, Pavia, 27100, Italy, luca.grottoli@eucentre.it

⁴ Associate Professor, DICAr, University of Pavia and EUCENTRE, Pavia, 27100, Italy, andrea.penna@unipv.it

⁵ Full Professor, DICAr, University of Pavia and EUCENTRE, Pavia, 27100, Italy, guido.magenes@unipv.it

Insight into damage observations from recent events has confirmed that the activation of out-of-plane (OOP) local mechanism is one of the major causes of structural collapse in unreinforced masonry buildings subjected to seismic excitations. These failures are due to the attainment of displacement levels incompatible with equilibrium configurations for the kinematic chain of the considered mechanism rather than the exceedance of stress capacity in structural elements. The two-way bending OOP failure mechanism, where at least one vertical edge of the wall is restrained, is one of the most surveyed causes of structural damage and collapse. Since very little research on this particular failure mechanism was found in the literature, several tests are envisaged to understand the phenomenon on full-scale calcium silicate walls. The first two tests were conducted on U-shaped calcium silicate brick URM specimens, composed by an OOP panel and the two return walls. One specimen, fixed on four edges, was subjected to 0.10 and 0.05 MPa of vertical stress, the other one, fixed on three edges with the top free, was subjected to 0.05 MPa of vertical stress on return walls. The experimental set-up allowed to tests the two specimens with different boundary and loading conditions. Different incremental input motions sequences were performed on each specimen until its collapse. The research aimed at understanding the complex dynamic behavior of such sub-structure, the failure mechanisms and the effect of boundary conditions.

Keywords: *Shaking table test, out-of-plane, two-way bending, URM, calcium silicate.*

INTRODUCTION

One of the major causes of structural collapse in unreinforced masonry (URM) buildings is the out-of-plane (OOP) local failure, as confirmed by damage observations from recent seismic events. For example, following the Christchurch earthquakes, Giarretton *et al.* (2016) noted three primary types of OOP wall failures in brick URM buildings: (i) vertical (or one-way) bending of the wall (7% of the cases), which tended to occur in longer walls or walls without side supports; (ii) two-way bending (57% of the cases), which required support of at least one vertical edge of a wall; (iii) top portion cantilever type failure with the entire top section of a wall or building façade collapsing, mainly due to a lack of proper connections. Over the last years, a significant contribution to the study of the one-way bending OOP mechanism has been carried on by several researchers including both experimental (Doherty 2000, Graziotti *et al.* 2016a, Penner *et al.* 2016, Simsir *et al.* 2004) and numerical activities (Lam *et al.* 2003, Sorrentino *et al.* 2008).

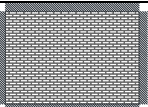
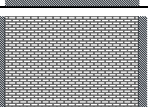
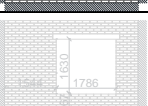




The experimental research on the two-way bending OOP mechanism is, instead, limited to the contribution of airbag quasi-static tests on full-scale specimens (Griffith *et al.* 2007 and Messali *et al.* 2017) and dynamic shaking table tests on half-scale specimens (Vaculik *et al.* 2007). The lack of sufficient dynamic experimental tests suggested that further effort in understanding this particular mechanism is needed. Therefore, this paper presents a couple of two-way bending OOP collapse shaking-table tests on full-scale U-shaped URM specimens. The test is a part of a wider research project aimed at assessing the vulnerability of URM building in the region of Groningen, a region of Netherlands which is not naturally prone to seismic events, in the last two decades has been exposed to induced seismicity. The testing campaign included also included in-situ mechanical characterization tests and laboratory tests comprising: characterisation tests performed on bricks, mortar and small masonry assemblies; in-plane cyclic shear-compression (Graziotti *et al.* 2016b) and two full-scale shaking table tests conducted in 2015 (Graziotti *et al.* 2017a) and 2016 (Graziotti *et al.* 2017b) on two different URM building typologies on the testing facilities of the EUCENTRE laboratory. A further full-scale collapse shaking table test has been performed in 2017 at the LNEC laboratory of Lisbon. The paper describes the testing layout, the protocol and the preliminary results of two-way bending OOP shaking table tests performed on U-shaped specimens. The specimens, having all the same geometry, differed for applied vertical overburden pressure and boundary conditions. The experimental campaign aims to be a solid reference for the development of reliable numerical models to be used for simulating the dynamic response of such walls to arbitrary seismic motions.

DESCRIPTION AND CHARACTERISATION OF THE MASONRY SPECIMENS

Professional masons built the specimens in accordance with the Dutch practice under controlled laboratory conditions. The specimens were 2.75 m high (34 brick layers) U-shaped single leaf walls made of calcium silicate (CS) bricks (density of the masonry equal to 1835 kg/m^3). The size of the CS bricks was $212 \times 102 \times 71 \text{ mm}$ while the mortar bed-joints were nominally 10 mm thick. The plan dimensions of the specimens were $3.98 \times 1.1 \text{ m}$; the former represented the length of the main panel to be tested OOP, the latter was the length of the two return walls, built to restrain the OOP panel on the two lateral vertical edges. The specimens differed in terms of the applied vertical overburden pressure and OOP panel boundary conditions. Table 1 clarifies the specimens' name, the applied vertical overburden pressures and the OOP panel boundary conditions. The OOP panel of the first

specimen (*i.e.* tests CS-010-RR and CS-005-RR) was initially subjected to a vertical overburden stress value (σ_v) equal to 0.10 MPa, later decreased to 0.05 MPa to fully exploit the specimen's capacity. The two return walls, ensuring flexural rigidity, were subjected to a vertical stress value as reported in Table 1. The resulting initial static scheme was double fixed in both, vertical and horizontal edges for both specimen configurations CS-010-RR and CS-005-RR. In these two tests, the upper layer of bricks was rotationally restrained. Even if the scope of the present tests was envisaging idealized boundary conditions, the applied level of imposed vertical overburden pressure could be considered representative of a loadbearing wall located at the second floor of a classical two storeys residential building.

Table 1. Characteristics of test specimens (in grey the tests not already performed 7/2017).

| Specimen ID | σ_v OOP wall [MPa] | σ_v RET wall [MPa] | Horizontal restrain condition | Vertical restrain condition | Scheme |
|-------------------|------------------------------------|------------------------------------|-------------------------------------|-----------------------------------|---|
| CS-010-RR | 0.10 | 0.10 | Fixed (R) | Fixed |  |
| CS-005-RR | 0.05 | 0.05 | Fixed (R) | Fixed |  |
| CS-000-RF | 0 | 0.05 | Fixed (R) Free (F) | Fixed Fixed |  |
| CSW-000-RF | 0 | 0.05 | Fixed (R) Free (F) | Fixed Fixed |  |
| CL-000-RF | 0 | 0.05 | Fixed (R) Free (F) | Fixed Fixed |  |
| CV-000 | CS | 0 | Fixed (R) Free (F) | Fixed Fixed |  |
| | CL | 0 | Fixed (R) Free (F) | Fixed Fixed |  |

The OOP panel of the second specimen (CS-000-RF) was unloaded with the top horizontal edge free of any restrain condition, leading to a fixed-free restrain scheme in the vertical spanning direction; the wall may represent a panel located at the top storey and parallel to the diaphragm-roof spanning direction, without proper connection with the diaphragm-roof system. Three more specimens, already built with the same geometry, will be tested in the summer-autumn 2017: the first one (CSW-000-RF) is characterised by an opening, the second (CL-000-RF) has been constructed in clay (CL) bricks (unit size 211x100x50). The last specimen is a cavity wall with the inner loadbearing structure in CS bricks and the outer leaf in CL bricks. Two L-shaped ties per square meter connect the two masonry leaves.

A detailed overview of the experimental testing campaign on material samples and masonry wallettes was performed at Department of Civil Engineering and Architecture of the University of Pavia. Table 2 summarizes experimental mean values, standard deviations and coefficient of

variation (*C.o.V.*) for the investigated mechanical parameters, namely compressive strength (f_m), Young's Modulus in compression (E), flexural tensile strength of masonry parallel (f_{x2}) and perpendicular (f_w) to bed-joints. The first two parameters were determined on masonry specimens according to EN 1052-1, flexural tensile strength parallel to bed-joints was obtained adopting EN 1052-2, while the last one by means of the bond wrench tests as for EN 1052-5. Moreover, the mortar's compressive (f_c) and flexural strength (f_t) values were determined according to EN 1015-11 and the compressive (f_b) and tensile (f_{bt}) strength of units, as well.

Table 2. Results of characterization tests on mortar and masonry specimens.

| | E | f_m | f_{x2} | f_w | f_c | f_t | f_b | f_{bt} |
|------------------------|------|-------|----------|-------|-------|-------|-------|----------|
| <i>Mean</i> [MPa] | 4784 | 9.74 | 1.29 | 1.04 | 6.27 | 2.18 | 15.31 | 2.61 |
| <i>St.Dev.</i> [MPa] | 862 | 0.76 | 0.11 | 0.17 | 1.58 | 0.60 | 0.93 | 0.38 |
| <i>C.o.V.</i> [%] | 18 | 7.8 | 8.2 | 16.5 | 25.2 | 27.3 | 6.1 | 14.5 |
| <i>Number of tests</i> | 7 | 7 | 6 | 13 | 44 | 22 | 8 | 8 |

TESTING LAYOUT AND DYNAMIC SEQUENCE

The test set-up was installed on a uni-directional shake table and oriented to excite the specimens in two-way bending condition. Figure 2 shows some pictures of the test setup. The steel frame, designed to be rigid, ensured that the dynamic input motion was transferred from the table to the top of the wall with negligible amplification. The specimens were anchored through the reinforced concrete foundation to the shake table by means of steel bolts. The moment restraint condition at the two vertical edges (*e.g.* in the horizontal spanning direction) of the OOP panel in both specimens was ensured by the connection of the wall panel with of two return walls. Regarding the first specimen (CS-010-RR may represent a loadbearing wall in a real structure), the OOP panel was vertically loaded to the desired initial axial stress value through a 4500-mm-long top steel beam pulled down by means of 4 steel squared hollow cantilevers bolted to the beam web and connected to 4 bars in series with a spring system. Four steel braces with mechanical hinges at one end (the extremity connected to the frame) ensured the connection between the top beam and the rigid frame. The braces were rigidly connected to the specimen top beam by means of steel plates in order to avoid any relative rotation. The hinge system, shown in Figure 1b, allowed for the uplift of the upper part of the wall simultaneously transferring the horizontal dynamic input of the shake table to the top of the specimen. The horizontal restraint condition on the top of the OOP wall was guaranteed by L-shaped steel profiles bolted to the bottom of the top beam and clamping the 34th brick layer; high strength mortar was used to fill the gap between the top row of bricks and the steel profiles. The bottom section of the wall specimen lay on a mortar bed-joint resting on the specimen foundation. The stiffness of the spring system (Figure 2f), guarantees that the increased force at collapse condition (when the wall height is maximum assuming a rigid body uplift) is less than 5% of the static initial static pressure. The designed spring stiffness, experimentally tested, was 53.5 N/mm for those used to provide 0.1 MPa and 0.05 MPa of vertical stress; the lever arm effect was taken into account by applying the vertical overburden pressure. The resulting static configuration of the OOP panel was a double-fixed boundary conditions in both, vertical and horizontal directions, with almost constant vertical overburden pressure. In the case of vertically unloaded walls, the top beam was sustained by proper steel supports (Figure 2c) with 30 mm air

gap between the beam bottom and the top horizontal edge of the OOP panel. As shown in Figure 2e, vertical overburden pressure and the top boundary condition in the two return walls have been applied in a similar fashion of the OOP panel case, adopting a top squared hollow profile beam to redistribute the vertical load transmitted by a further squared hollow transverse beam pulled down by means of steel rods in series with a spring system identical to the one earlier mentioned; a mechanical hinge has been adopted at the connection between the two steel profiles in order to avoid any moment transmission to the walls. Four steel plates (two per wall) ensured the connection between the return walls top beam and the OOP panel top beam guaranteeing horizontal displacement compatibility. This allowed for the transmission of the input acceleration also to the upper portion of the return walls, even in the case of unloaded OOP panel. U-shaped steel (Figure 2b, Figure 2c), profiles clamping their free extremity restrained any possible OOP displacement. The entire setup instrumentation consisted in accelerometers, potentiometers, wire potentiometers and tri-dimensional optical acquisition system. Accelerometers were installed in order to record the applied acceleration histories at the specimen foundation, on the top beam, on the rigid frame and on the return walls. Additional accelerometers were installed on the wall OOP panel in order to monitor its dynamic response. Wire potentiometers (WP), attached to the frames, were installed in several positions in order to record its horizontal displacement relative to the shake table; the location of accelerometers and WPs was chosen in relation to the boundary conditions and according to the expected deformed shape. Vertical displacement transducers were also installed on the spring system to monitor the spring shortening and in turn the applied vertical overburden pressure during all the testing phases.

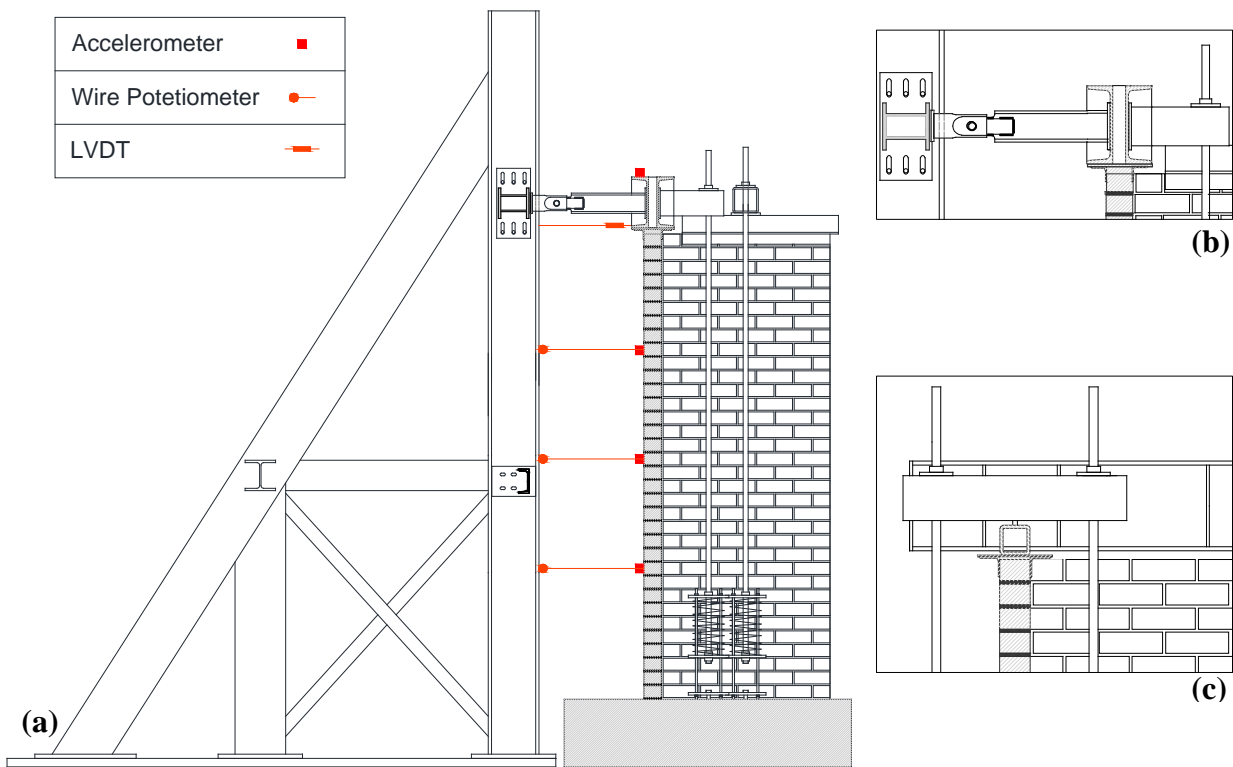


Figure 1: Geometry of the test set-up: general view (a), connection between top beam and rigid frame (b) and return wall loading system (c).



Figure 2: Testing layout: general view (a), loading systems (b, c, d) and spring system (e).

The specimens were subjected to incremental dynamic tests (a series of table motions of increasing PGA values) to fully exploit their capacity investigating displacement shape and failure mechanism. Since one of the purposes of the present test was to compare the results with the performance exhibited by the second storey transverse walls (excited out-of-plane) of the building prototype dynamically tested by Graziotti *et al.* (2017b), the specimens have been subjected to floor accelerograms following a similar testing sequence. Therefore, the actual inputs were the second-floor accelerograms of the full-scale building specimen subjected to incremental dynamic tests with two records: EQ1 and EQ2 (representative of the dynamic characteristics of induced seismicity ground motions of higher and lower return periods, respectively (Graziotti *et al.* 2017b). The floor accelerograms obtained from the EQ1 motion testing sequence, have been substituted to floor motions obtained from an analysis performed on a calibrated TREMURI numerical model (Lagomarsino *et al.* 2013) representing an undamaged building, assuming as input the ground motion recorded near Huizinge on 16th of April 2012 that was the largest magnitude event ever recorded in the area. Regarding the EQ2 testing sequence, for practicality and to allow a better control of the shaking table performance, only the second-floor accelerograms recorded during EQ2-125% and EQ2-200% were adopted as inputs. These two acceleration histories (FEQ2-DS3 and FEQ2-DS4), characterized by “wider” spectra, have been considered well representative of the progressive damage evolution occurring in the full-scale specimen (*i.e.* DS3=Moderate damage, DS4=Extensive damage). A fourth artificial input signal, characterized by wide spectral shape and long duration, was adopted in order to induce a collapse of the first specimen, avoiding the unrealistic scaling of the experimental floor motions. This input signal consisted in a sequence of sine impulses with increasing period in order to excite a wide range of frequencies. The signal was

duplicated and performed in sequence. Table 3 lists the adopted input motions, peak table accelerations (PTA) specifying also the associated ground motion (GM). Figure 3 illustrates their 100% scaled acceleration time histories while Figure 4 shows the associated acceleration and displacement 5% damped spectra.

Table 3. Summary of the employed input motions.

| Input | PTA[g] | Description | GM input |
|-----------|--------|---|----------|
| FHUIZ-DS0 | 0.15 | 2 nd Floor Acc. (Numerical) | Huizinge |
| FEQ2-DS3 | 0.26 | 2 nd Floor Acc. (Experimental) | EQ2-125% |
| FEQ2-DS4 | 0.32 | 2 nd Floor Acc. (Experimental) | EQ2-200% |
| SSW | 0.50 | Artificial Record | - |

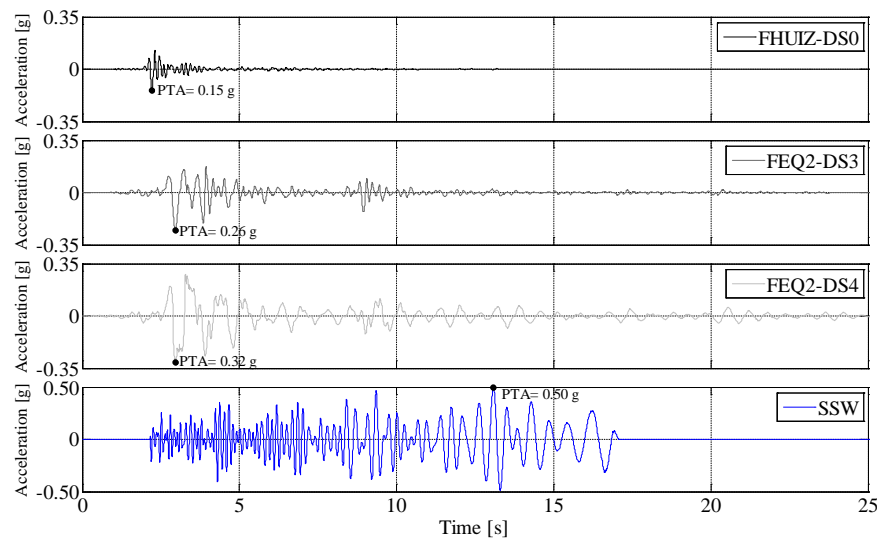


Figure 3: Acceleration time histories of the employed table motions.

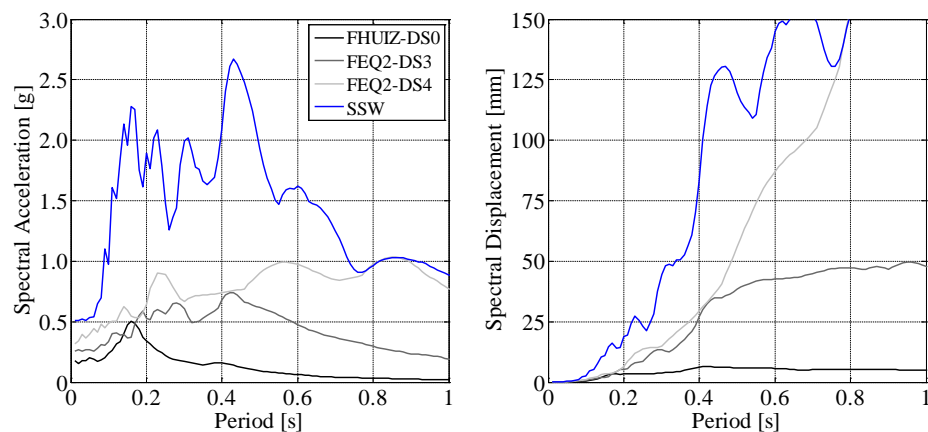


Figure 4: Acceleration and Displacement response spectrum (5% damping).

The testing programme followed the one carried out by Graziotti *et al.* (2017b) in order to allow for a comparison with the out-of-plane walls of the full-scale building prototype. Initially, the specimens were subjected to low amplitude random excitations (WN) in order to identify their

undamaged dynamic properties. This test was repeated after the attainment of cracking. Low intensity calibration runs have been performed as well in order to better control the shaking table. For both specimens, the testing sequence consisted of incremental dynamic tests starting with FHUIZ-DS0, through FEQ2-DS3 and as last FEQ2-DS4.

Table 4 and Table 5 list the testing sequences of the two specimens including the input typology, the scaling factor, the PTA and the associated horizontal displacement recorded at mid-height of the OOP panel (MHD) for CS-010/005-RR and at top of the OOP panel (TD) for CS-000-RF (calibration runs are identified by “-C”). In the case of CS-010-RR specimen case, the vertical overburden pressure has been reduced in order to induce the first cracking of the OOP panel at lower levels of PTA. Consequently, the CS-010-RR specimen remained in the elastic range for the entire testing sequence. After the attainment of cracking, the CS-005-RR wall was subjected to a further input sequence with the SSW table motion in order to reach the collapse. For the CS-000-RF specimen, after the attainment of cracking, a short repetition of the previous input sequence has been performed in order to better understand the dynamic post-cracking behaviour.

Table 4. CS-010-RR and CS-005-RR testing sequences.

| CS-010-RR configuration | | | | | CS-005-RR configuration | | | | |
|-------------------------|-------------|---------------|---------|----------|-------------------------|------------|---------------|---------|----------|
| Test # | Test Input | Input Scaling | PTA [g] | MHD [mm] | Test # | Test Input | Input Scaling | PTA [g] | MHD [mm] |
| 1 | WN | 100% | +0.06 | - | 18 | FEQ2-DS4 | 100% | -0.32 | -0.3 |
| 2 | FHuiz-DS0-C | 50% | -0.07 | +0.1 | 19 | FEQ2-DS4 | 200% | -0.68 | +0.5 |
| 3 | FHuiz-DS0 | 100% | -0.16 | +0.2 | 20 | FEQ2-DS4 | 300% | -1.05 | +0.9 |
| 4 | FHuiz-DS0 | 150% | -0.20 | +0.3 | 21 | FEQ2-DS4 | 400% | -1.18 | +1.3 |
| 5 | FEQ2-DS3-C | 40% | -0.11 | +0.1 | 22 | FEQ2-DS4* | 600% | -1.93 | +8.0 |
| 6 | FEQ2-DS3 | 89% | -0.22 | +0.1 | 23 | WN | 100% | +0.08 | - |
| 7 | FEQ2-DS3 | 100% | -0.27 | +0.2 | 24 | SSWx2 | 75% | +0.39 | +3.1 |
| 8 | FEQ2-DS3 | 125% | -0.31 | +0.2 | 25 | SSWx2 | 200% | +0.99 | +4.5 |
| 9 | WN | 100% | +0.07 | - | 26 | SSWx2 | 250% | +1.39 | +9.1 |
| 11 | FEQ2-DS4-C | 50% | -0.17 | -0.1 | 27 | WN | 100% | -0.05 | - |
| 12 | FEQ2-DS4 | 100% | -0.32 | -0.2 | 28 | SSWx2-C | 150% | +0.92 | +7.2 |
| 13 | FEQ2-DS4 | 125% | -0.38 | -0.3 | 29 | SSWx2-C | 150% | +0.81 | +5.5 |
| 14 | FEQ2-DS4 | 150% | -0.47 | -0.3 | 30 | SSWx2-C | 100% | +0.66 | +5.6 |
| 15 | FEQ2-DS4 | 200% | -0.74 | -0.4 | 31 | SSW | 300% | +1.42 | Fail |
| 16 | FEQ2-DS4 | 250% | -0.91 | +0.6 | | | | | |
| 17 | FEQ2-DS4 | 300% | -0.90 | +0.6 | | | | | |

Table 5. CS-000-RF testing sequence.

| Test # | Test Input | Input Scaling | PTA [g] | TD [mm] | Test # | Test Input | Input Scaling | PTA [g] | TD [mm] |
|--------|-------------|---------------|---------|---------|--------|------------|---------------|---------|---------|
| 1 | WN | 100% | -0.04 | - | 12 | FEQ2-DS4 | 150% | -0.46 | -1.6 |
| 2 | FHuiz-DS0-C | 50% | -0.07 | +0.2 | 13 | FEQ2-DS4 | 175% | -0.54 | -2.0 |
| 3 | FHuiz-DS0 | 100% | -0.15 | +0.5 | 14 | FEQ2-DS4 | 200% | -0.68 | -2.4 |
| 4 | FHuiz-DS0 | 150% | -0.23 | +0.7 | 15 | FEQ2-DS4 | 250% | -0.78 | -3.0 |
| 5 | WN | 100% | +0.08 | - | 16 | FEQ2-DS4 | 300% | -0.95 | -3.4 |
| 6 | FEQ2-DS3-C | 50% | -0.16 | +0.4 | 17 | FEQ2-DS4 | 350% | -1.10 | +4.7 |
| 7 | FEQ2-DS3 | 89% | -0.23 | +0.6 | 18 | FEQ2-DS4* | 400% | -1.28 | +12.8 |
| 8 | FEQ2-DS3 | 100% | -0.25 | +0.7 | 19 | WN | 100% | +0.04 | - |
| 9 | FEQ2-DS3 | 125% | -0.34 | +0.9 | 20 | FHuiz-DS0 | 100% | -0.15 | +5.0 |
| 10 | FEQ2-DS4 | 100% | -0.39 | +1.0 | 21 | FEQ2-DS3 | 100% | -0.24 | +4.9 |
| 11 | FEQ2-DS4 | 125% | -0.38 | -1.3 | 22 | FEQ2-DS4 | 200% | +0.67 | Fail |

*1st cracks reported

TEST RESULTS

The test set-up proved to be effective in allowing the specimens to be tested with the desired boundary conditions and inducing a pure OOP two-way bending action in the walls. A slight overshoot at low period spectral accelerations is detectable analysing the accelerations recorded by the accelerometers on the top beam. The first specimen in the CS-010-RR configuration remained in the elastic range for the entire testing sequence, up to PTA equal to 0.90 g and a maximum MHD of 0.6 mm. In the CS-005-RR configuration, the specimen attained first cracking during FEQ2-DS4 motion scaled up to 600%, with a PTA equal to 1.93 g and an associated peak MHD of 8.0 mm. Highly non-linear behaviour is detectable starting from a MHD displacement of approximately 3 mm. A horizontal crack developed on the bed-joint between the 4th and 5th brick layers, two further diagonal stepped cracks appeared starting from the two top corners forming a V-shape; a vertical crack has been observed dividing the OOP panel into two portions in the horizontal spanning direction and connecting the diagonal cracks with the horizontal one. Figure 5 shows the first cracking pattern of the two specimens.

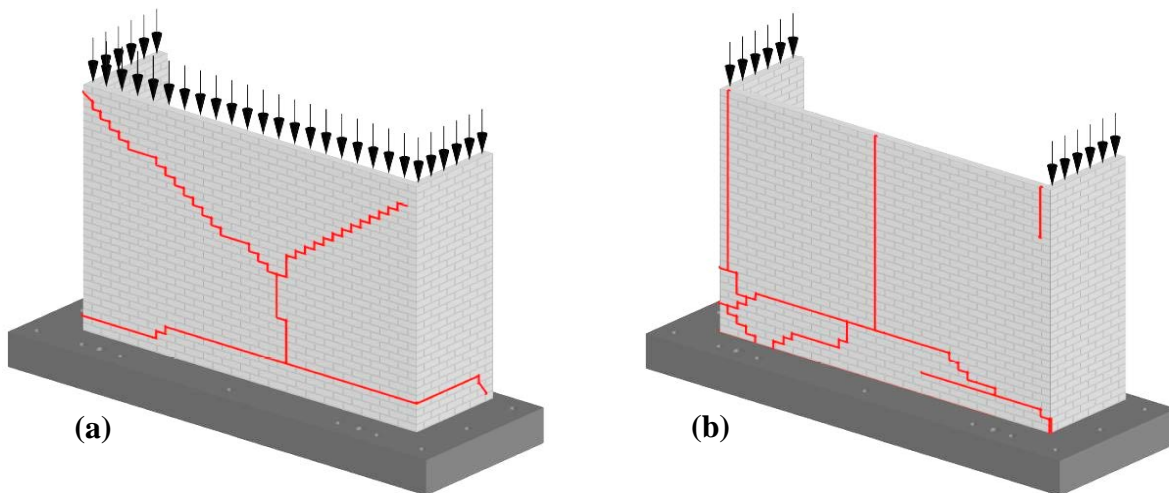


Figure 5: First cracking patterns of CS-005-RR (a) and CS-000-RF (b) specimens detected at the end of the test runs #22 and #18 respectively.

The CS-000-RF specimen reached the first cracking condition during FEQ2-DS4 scaled up to 400% (PTA equal to 1.28g) showing a peak TD of 12.8 mm. Two vertical cracks developed at the connections between the OOP panel and the return walls while a further one split the OOP panel in two portions. Horizontal cracks have been observed in the lower portion of the main panel. Figure 6 shows approximately the deformed shape of the OOP panel at the attainment of MHD for CS-010-RR and TD for CS-000-RF, distinguishing between positive displacement on the left side and negative displacement on the right. The graphs plot a linear interpolation between the points (black spheres) in which displacements were directly recorded.

The CS-005-RR specimen collapsed under the SSW artificial motion scaled up to 300% (PTA equal to 1.42g). The masonry portion of the OOP panel rotated using as pivot points the pre-existing cracks till the attainment of large horizontal displacements leading to the global loss of equilibrium (see Figure 7a). The collapse of the CS-000-RF specimen was observed during FEQ2-DS4 scaled at 200% (PTA equal to 0.67g). The resulting collapse mechanism was the combination of rotation

along the vertical cracks and overturning of the upper portion of the OOP panel (see Figure 7d). Both specimens have shown a relatively brittle behaviour after the attainment of first cracking, with a failure acceleration considerably lower than the cracking one. This phenomenon could have been emphasized by the masonry horizontal flexural strength (f_{x2}) governed by CS unit tensile strength. Figure 7c shows the comparison between the specimens' capacities in terms of wall displacement (MHD for CS-005-RR and TD for CS-000-RF) and PTA for the FEQ2-DS4 motion tests. Moreover, the collapse accelerations and the associated inputs are shown.

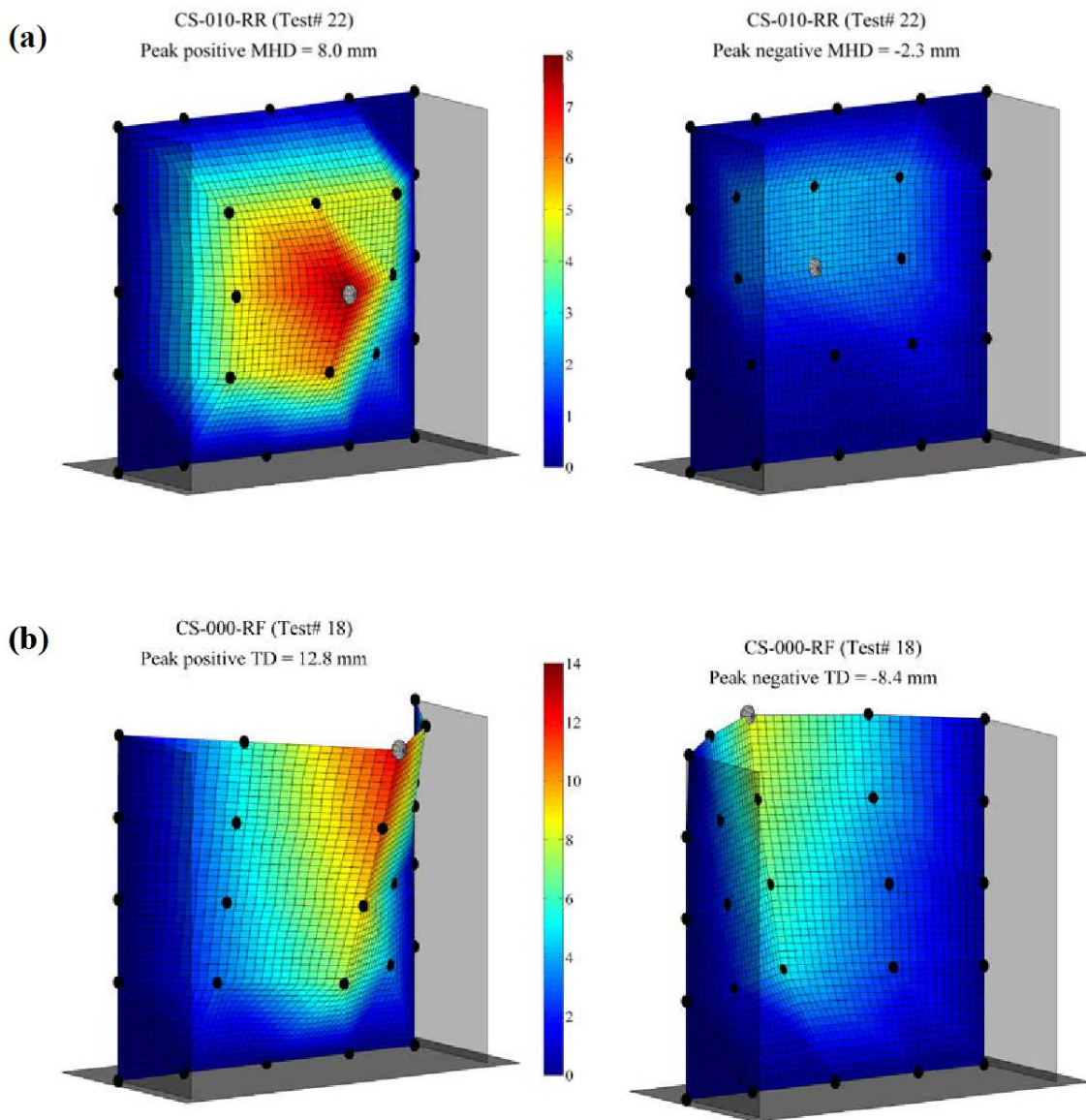


Figure 6: Deformed shapes on first cracking test of CS-005-RR (a) and CS-000-RF (b).

The test confirmed how the boundary condition may affect the OOP response of a panel wall, it is possible to appreciate the differences in terms of stiffness and cracking acceleration between the two specimens. Furthermore, reducing the acting vertical overburden pressure (from the CS-010-RR to the CS-005-RR configuration) did not affect the specimen stiffness.

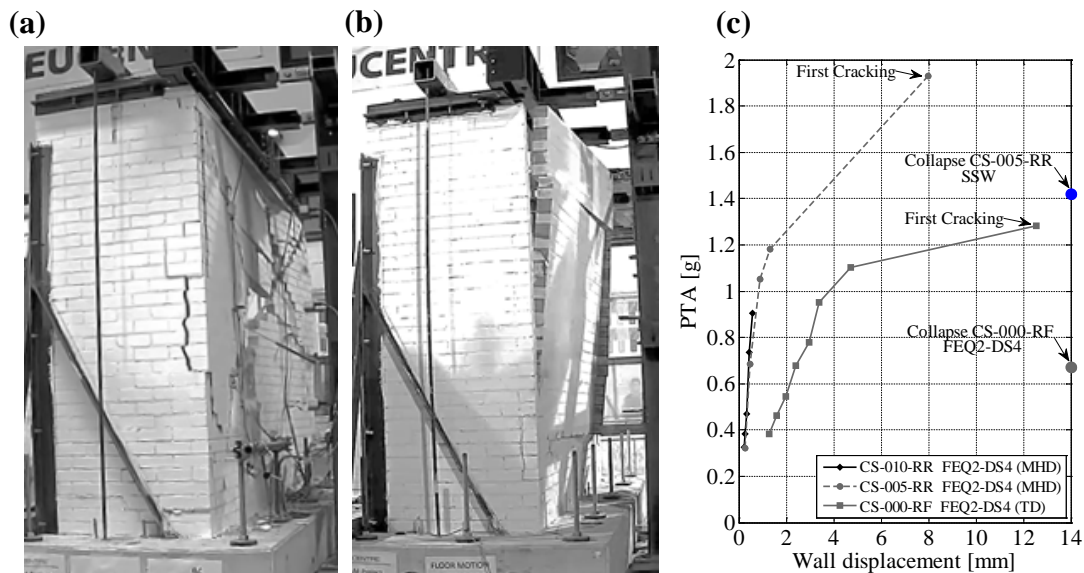


Figure 7: Collapse screenshot of CS-005-RR (a) and CS-000-RF (b) specimens; Comparison between specimens' capacity in terms of wall displacement and PTA (c).

CONCLUSIONS

This paper presents the preliminary results of a two-way bending OOP shaking table test on two U-shaped URM calcium silicate walls. The test-setup allowed to test the specimens under different loading and boundary conditions, assuming as dynamic input motion second-floor accelerograms. CS-005-RR and CS-000-RF specimens attained cracking condition subjected to FEQ2-DS4 input motion scaled up to 600% (PTA = 1.93 g) and 400% (1.28 g), respectively. The CS-005-RR specimen collapsed under the SSW artificial motion scaled up to 300% (PTA = 1.42g). The collapse of the CS-000-RF specimen, instead, was observed during FEQ2-DS4 scaled at 200% (PTA = 0.67g). Contrary to what was observed by past quasi-static tests, both specimens have shown a relatively brittle behaviour after the attainment of first cracking, with a failure acceleration lower of the cracking one. This phenomenon could also have been emphasized by the masonry horizontal flexural strength governed by CS unit tensile strength. Three more specimens with different characteristics will be tested in autumn 2017. All the processed data will be available upon request.

ACKNOWLEDGEMENTS

This paper describes an activity that is part of the “Study of the vulnerability of masonry buildings in Groningen” project at the EUCENTRE, undertaken within the framework of the research program for hazard and risk of induced seismicity in Groningen sponsored by the Nederlandse Aardolie Maatschappij BV. The authors would like to thank all the parties involved in this project, namely EUCENTRE and University of Pavia (DICAr) laboratories that performed the tests, NAM, Arup and TU Delft. Thanks go also to J. Uilenreef, R. Pinho, F. Dacarro, S. Peloso, A. Fragomeli, S. Scherini, S. Dainotti, U. R. Garbaggio, S. Sharma and S. Girello for the practical support.

REFERENCES

- Doherty K.T. (2000), An investigation of the weak links in the seismic load path of unreinforced masonry buildings, PhD Thesis, University of Adelaide, Australia.
- EN 1052-1, 2, 5. Methods of test for masonry – Part 1, Part 2, Part 5. CEN/TC. Eu. Standard: 1998.
- EN 1015-11. Methods of test for mortar for masonry – Part 11. CEN/TC. Eu. Standard: 1999.
- Giaireton M., Dizhur D., Da Porto F. and Ingham J. (2016), Construction details and observed earthquake performance of unreinforced clay brick masonry cavity walls. *Structures*, 6, pp.159-169.
- Graziotti F., Tomassetti U., Penna A. and Magenes G. (2016a), Out-of-plane shaking table tests on URM single leaf and cavity walls, *Engineering Structures*, 125, pp. 455-470 DOI:10.1016/j.engstruct.2016.07.011
- Graziotti F., Rossi A., Mandirola M., Penna A. and Magenes G. (2016b). Experimental characterization of calcium silicate brick masonry for seismic assessment. In: *Brick and block masonry: trends, innovations and challenges*. Proc. of the 16th IBMAC, Padova, Italy. DOI: 10.1201/b21889-215
- Graziotti F., Guerrini G., Kallioras S., Marchesi B., Rossi A., Tomassetti U., Penna A. and Magenes G. (2017a). Shaking Table Test on a Full-Scale Unreinforced Clay Masonry Building with Flexible Diaphragms. *Proc. of 13th Canadian Masonry Symposium*, Halifax, Canada.
- Graziotti F., Tomassetti U., Kallioras S., Penna A. and Magenes G. (2017b), Shaking table test on a full-scale URM cavity wall building, *Bull of Earthq Eng*, in-press, DOI: 10.1007/s10518-017-0185-8
- Griffith M. C., Vaculik J., Lam N. T. K., Wilson J. and Lumantarna E. (2007), Cyclic testing of unreinforced masonry walls in two-way bending, *Earthq Eng & Struct Dyn*, 36(6), pp. 801-821.
- Lagomarsino S., Penna A., Galasco A. and Cattari S. (2013), TREMURI program: An equivalent frame model for the nonlinear seismic analysis of masonry buildings, *Engineering Structures*, 56.
- Lam N.T.K., Griffith M.C., Wilson J. and Doherty K. (2003), Time-history analysis of URM walls in out-of-plane flexure, *Engineering Structures*, 25(6), pp.743–754.
- Messali F., Ravenshorst G., Esposito R. and Rots J. (2017). Large-scale testing program for the seismic characterization of Dutch masonry walls. *Proc. 16th WCEE.*, Santiago Chile.
- Penner O. and Elwood K.J. (2016), Out-of-Plane dynamic stability of unreinforced masonry walls in one-way bending: shake table testing, *Earthquake Spectra*.
- Simsir C.C., Aschheim M.A. and Abrams D.P. (2004). Out-of-plane dynamic response of unreinforced masonry bearing walls attached to flexible diaphragms. *Proc. 13th WCEE.*, Vancouver, Canada.
- Sorrentino L., Masiani R. and Griffith M.C. (2008), The vertical spanning strip wall as a coupled rocking rigid body assembly, *Structural Engineering and Mechanics*, 29, pp.433–453.
- Vaculik J. and Griffith M. C. (2007). Shake-table tests on masonry walls in two-way bending. *Proc. Australian Earthquake Engineering Society*, Wollongong, Australia.



**MASONRY TODAY
AND TOMORROW**

**11 - 14 February, 2018
SYDNEY AUSTRALIA**

www.10amc.com

OUT OF PLANE BEHAVIOUR OF CONCRETE BLOCK MASONRY WALL WITH DIFFERENT BASE SUPPORT CONDITIONS

A.C. Isfeld¹, M. Hagel², A.L. Müller³ and N.G. Shrive⁴

¹ Postdoctoral Scholar, Department of Civil Engineering, Schulich School of Engineering, Calgary, AB, Canada, acisfeld@ucalgary.ca

² Executive director, Alberta Masonry Council, Calgary, AB, Canada, markhagel@albertamasonrycouncil.ca

³ Research Associate, Department of Civil Engineering, Schulich School of Engineering, Calgary, AB, Canada, anna_l_mueller@gmx.de

⁴ Professor, Department of Civil Engineering, Schulich School of Engineering, Calgary, AB, Canada, ngshrive@ucalgary.ca

When assessing the potential for buckling of a masonry wall, the effective height is affected by the deflected shape of the wall and that shape results in part from the end supports. Employing the traditional Euler buckling criteria, the deflected shape and end supports vary the value of the effective height. In Euler theory there are only three support conditions: pinned, fixed and free. However, support conditions for masonry walls and columns are often conservatively assumed to be pinned when in reality the supports are more likely a hybrid of fixed and pinned conditions: the width of the concrete block does not allow free rotation at the base. The effect of the base support conditions on the deflected shape of 1200 mm (3'11") wide by 2438 mm (7'11") high partially grouted block walls was investigated and the results of this testing were compared with detailed finite element micro-models developed in Abaqus and SAP2000.

Keywords: *axial load capacity, buckling load, concrete masonry walls, load eccentricity, slenderness.*



INTRODUCTION

The current Canadian masonry design standard, CSA S304-14 (2014), appears to underestimate the capacity of slender loadbearing masonry walls (Müller et al., 2016). For plain and reinforced concrete masonry walls with low slenderness ratios, material strength generally governs the resistance of the structural element. For this to be the case, the ratio must be less than the limiting value based on end eccentricities, e_1 and e_2 . The slenderness ratio is a function of the effective length factor, k , wall height, h , and wall thickness, t . With increasing wall height, the loadbearing capacity decreases and failure can occur due to buckling. Walls are considered slender when the slenderness ratio exceeds 30 and slender walls are permitted only if the applied factored axial load is less than 10 % of the axial load capacity. When the slenderness ratio is below 30, the resistance for pure axial load is 80 % of the axial load capacity. All walls must be designed to resist a moment greater than or equal to the axial load acting at an eccentricity of 10%. In addition to primary moments causing out-of-plane displacements, additional bending moment develops when the axial load at the supports acts over the displacement. As a result of the additional moment, the displacement increases and leads to a further increase in the moment. The result is a second order P- Δ effect. One reason the Canadian standard underestimates slender wall capacity is the requirement for the conservative assumption of pinned - pinned end conditions when the slenderness ratio is above 30. The effective length factor depends on the support conditions at the top and bottom of the wall and is used to determine the effective height of the wall, kh . For a pinned - pinned support condition, k is 1.0, whereas for a fixed - pinned support condition k is reduced to 0.81. The smallest permissible value for k is 0.80 for walls that are fixed - fixed. Previous testing has focused on walls supported by a pinned connection at their base, which represents a theoretical condition found to deviate from those used in practice (Dizhur et al., 2009, Walsh et al. 2017). To understand the degree to which a reinforced concrete masonry wall can resist moment at its base when no additional effort has been made to ensure a moment connection, testing and finite element modelling of several walls have been conducted.

PREVIOUS TESTING

To assess the margin of safety of the current code, previous experimental studies of reinforced concrete masonry were reviewed and experimental failure loads compared to the capacities calculated using the Canadian standard. Experimental tests have been completed on full-scale slender concrete block masonry walls with axial loading by Yokel et al. (1970), Cranston and Roberts (1976), Drysdale et al. (1976), Fattal and Cattaneo (1976), Hatzinikolas et al. (1978), Suwalski (1986), Hatzinikolas et al. (1991), Mohsin and Elwi (2003) and Liu and Hu (2007). There have been few experimental studies where the walls were tested under a combination of out-of-plane and axial loading; including Yokel et al. (1971), Fattal and Cattaneo (1976), the ACI-SEASC Task Committee on Slender Walls (1982) and Popehn et al. (2008). Tests have been primarily completed with pinned - pinned boundary conditions. Only Yokel et al. (1970) tested walls with the base supported fixed from rotating (pinned - fixed). Cranston and Roberts (1976) examined one wall that was fixed at both the bottom and the top. The bottom support stiffness of the walls tested by Mohsin and Elwi (2003) varied between a pinned support and a partially fixed support with a maximum stiffness of 10000 kNm/rad. Wall heights have ranged from 2.5 to 7.4 m and slenderness ratios have varied from 12.9 to 51.2. In cases where combined loading was used, axial load was applied before the walls were loaded to failure with horizontal out-of-plane pressure.

The review and analysis of experimental failure loads of concrete masonry walls confirmed that the load-bearing capacity predicted by the CSA S304-14 (2014) provisions is conservative. For walls subjected to axial loads only, the predictions become more conservative with increasing wall heights and decreasing load eccentricity. The reason for the underestimation of capacity is the magnification of the acting moment. The magnification depends on the applied axial load and the critical axial load, P_{cr} , which is a function of the effective flexural rigidity and the effective height of the wall. The code equation causes wall height to have a more significant influence when the rotational stiffness at the bottom of the wall is neglected. For masonry walls exposed to a combination of out-of-plane and axial loading, the code is especially conservative for load cases involving large vertical loads. Comparison between the applied moments and the theoretical moments determined with the moment magnifier method showed that the moment magnifier method overestimates the acting moment for large axial loads and large wall heights (Müller et al., 2016).

Based on analysis of the studies above, further testing is needed to provide results for less conservative design for slender masonry walls. While almost all studies involved testing walls with pinned support conditions at both the bottom and the top of the wall, in reality, masonry walls do not have free rotation at the base. The base support is rather a hybrid of fixed and pinned conditions. Addressing the problem of unrealistic boundary conditions, in-situ testing has been completed by Dizhur et al. (2009) to assess the strength and stiffness of brick masonry under quasi static out-of-plane loading, and by Walsh et al. (2017) to assess the seismic out-of-plane behaviour of unreinforced brick masonry with varied geometric configurations and boundary conditions. To identify the influence of restricted rotation on the effective height and the load-bearing capacity of slender, reinforced concrete block masonry walls, testing walls with fixed or partially fixed support conditions at the bottom of the wall is necessary. By measuring the deflections along the wall height, the effective height and thus the k-factor can be determined and compared with those values provided by the code. As there has been little research on slender masonry walls subjected to a combination of out-of-plane and axial loads, more tests should be performed, as this loading case can occur due to wind and seismic loads.

WALL SPECIMEN

Three concrete masonry walls with a height of 2.39 m and a width of 1.19 m were built. They consisted of standard, bond beam, and half block hollow concrete masonry units with an actual thickness of 190 mm. They were face-shell bedded and laid in running bond. The second core from each end of the wall was grouted and vertically reinforced with a M15 (16 mm diameter) reinforcing bar. In addition, the first, fifth and last (twelfth) courses were horizontally reinforced with a M15 reinforcing bar. The cross-section of the wall is shown in Figure 1. The walls were constructed eccentrically on steel C-channels with 600 mm 15 M starter bars welded to the base. Vertical reinforcement was tied and lapped to the starter bars. The steel channel had 4 bolt tabs on each side to secure the walls to the load floor, as shown in Figure 2.

Individual grout cylinders, mortar prisms, and masonry prisms were constructed for compressive testing at 28 days post construction and on each testing date. Individual concrete block units were also tested for compressive strength. Masonry prisms were hollow, 2 units high, and cured under the same conditions as the full walls. Type S mortar was used and cubes were cured beneath polyethylene sheets. Grout cylinders were cured at 100% humidity and 23°C until

testing. Prisms were capped on the face shells with Plaster of Paris as outlined in Annex D (D.4.1) of CSA S304-14 (2014). The top and bottom surfaces of the grout cylinders were ground to achieve a flat surface for testing. The material properties obtained are summarized in Table 1 with the coefficient of variation (C.O.V.) and corrected compressive strengths based on an effective C.O.V. of 10% when less than 10 samples were tested, as outlined in Annex C of CSA S304-14 (2014).

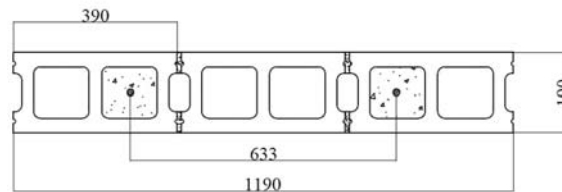


Figure 1: Average Cross-Section of the Walls (Dimensions in mm)

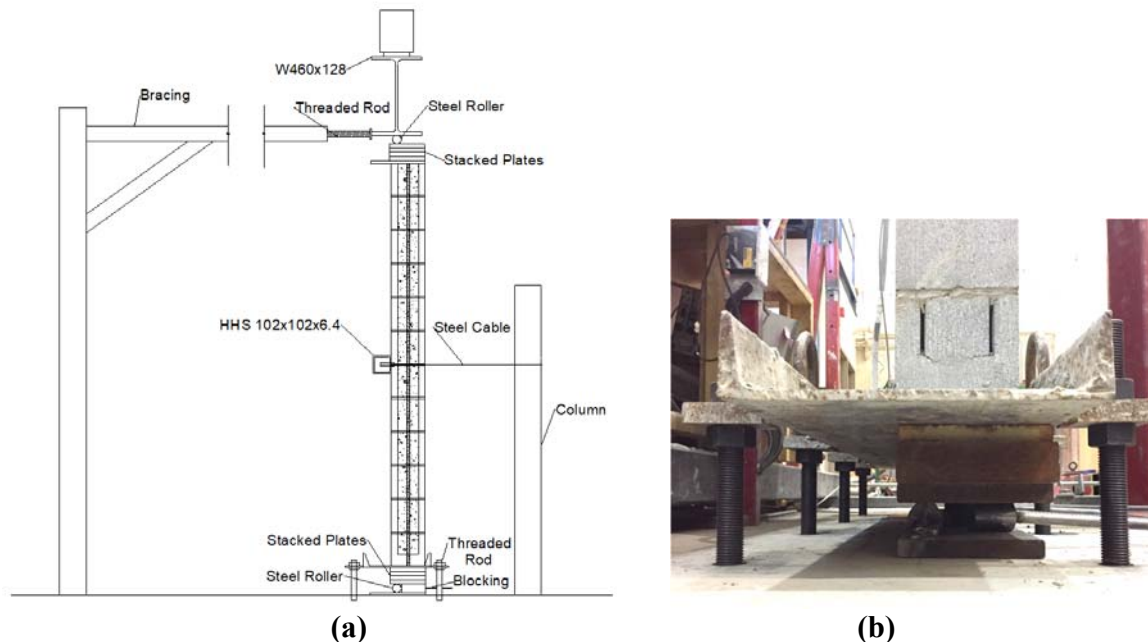


Figure 2: (a) Vertical Section of Wall with Pinned - Fixed Supports and (b) Base Detail

Table 1: Material Test Results

| Material | Avg. Comp. Strength [MPa] | C.O.V. [%] | Effective Comp. Strength [MPa] |
|----------|---------------------------|------------|--------------------------------|
| Block | 22.15 | 7.7 | 18.52 |
| Mortar | 12.35 | 6.6 | 10.32 |
| Grout | 22.22 | 3.4 | 18.58 |
| Prism | 18.21 | 4.9 | 15.22 |

TEST SETUP

The first of the 3 walls was first tested with a fixed support at the base of the wall. The top support permitted rotation about a round steel bar to represent a pinned end condition. Walls were subjected to a combination of eccentric axial load and out-of-plane load, which was applied to

specific levels in order to evaluate the displaced profile. Axial load was applied in displacement control with two actuators up to a total load of 250 kN. The load was distributed over the wall width through an I-beam between the actuators and the 50.8 mm diameter round bar. As indicated in Figure 2(a), horizontal bracing was used to restrain sway of the loading beam. Threaded rods within the bracing system were adjusted to eliminate any out-of-plane displacements that occurred at the top roller during loading. To avoid local material failure it was necessary to spread the line load from the rod to the whole cross-section of the wall at both the top and base of the wall. To facilitate this load spreading, two sets of four steel plates were welded together to have a total thickness of 100 mm each and were placed on top of the last course and below the C-channel on which the walls were built. The C-channel was positioned concentrically below the loading frame, thus placing the wall at an eccentricity of $t/3$. To facilitate future testing with a pinned base support a pinned connection, similar to the top support was provided, and steel blocking used to fill the gap between the steel plates at the base support as seen in Figure 2(b). During the pinned - fixed testing rotations of the C-channel were restrained by threaded rods which connected tabs on the C-channel to the lab floor; nuts were tightened above and below the tabs.

An out-of-plane line load was applied at mid height by means of a box beam that pushed against the wall. Steel cables were fixed to both ends of the box beam and were connected with a turnbuckle. The direction of the cables was changed with pulleys that were attached to steel columns. Tightening the turnbuckle led to tension in the steel cables, which pulled the box beam against the wall. The force in the steel cable was measured with the help of strain gauges that were fixed to the turnbuckle. The tension in the cable was increased to 6.3 kN, thus applying a 12.6 kN out-of-plane force to the wall.

To collect data for the displaced profile out-of-plane displacements were measured at five points (four equally spaced at 480 mm increments, and one 95 mm from the top of the wall) along the wall height using laser displacement sensors, and at the level of the top support using a LVDT. Rotation of the top of the wall with respect to the loading beam was recorded using the relative displacements on either side of the roller using LVDTs. Preliminary testing indicated the sensitivity of the setup to small out-of-plane displacements at the top of the wall due to the flexibility of the bracing. To correct for this displacement the threaded rod was extended until the top support was returned to zero displacement. This was an iterative process and the out-of-plane and vertical loads were adjusted to maintain the test loads.

RESULTS

The out-of-plane displacement profiles for eccentric axial load, and after the addition of the out-of-plane line load are plotted in Figure 3. Straight line segments connect the discrete data points, and third order polynomials allow for enhanced visualization of the displaced profile. Under both conditions the maximum displacement occurs above the mid height of the wall. When eccentric axial load is applied alone, the location of maximum out-of-plane displacement is at 0.8 of the total height. The addition of the out-of-plane line load at $H/2$ causes a significant increase in the out-of-plane displacement and the maximum displacement is at 0.6 of the height.

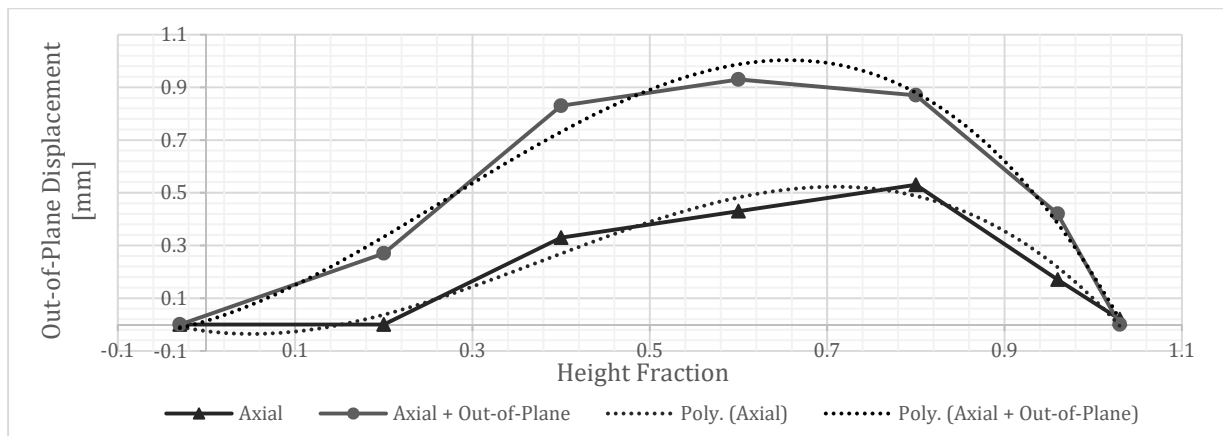


Figure 3: Pinned - Fixed Test Displaced Profile

FINITE ELEMENT MODELLING

Finite element modelling (FEM) was conducted to evaluate the load displacement behaviour and displaced profile of the wall under known loads. FEM of masonry structures is categorized as either macro or micro-modelling (Lourenço, 1996). Macro-modelling can be utilized for structures with known macro properties, usually with the assumption that the components within the structure are fully bonded. Micro-modelling can be used when information is available for the constituent materials but the macro properties are unknown. An accurate micro-model should include all the basic types of failure mechanisms that characterize masonry, such as cracking of the joints, sliding along the bed or head joints, tensile and diagonal cracking of the units, and masonry crushing (Lourenço et al., 1995). Models were developed using the micro-modelling approach, with individual parts in contact, to determine the load-displacement curve, then the parts were merged for comparison to the testing results which was known to be within the linear elastic range. In recent tests the walls have been observed to crack and the models will be updated to reflect this.

MATERIALS

Steel plates were represented with linear elastic material properties ($E = 200 \text{ GPa}$, $\nu = 0.3$) as they are not expected to exceed this range. Reinforcing steel included nonlinear behaviour with the Plasticity model in Abaqus. Nonlinear materials properties were applied to the concrete units, mortar, and grout using the concrete damage plasticity (CDP) model in Abaqus/Standard and Abaqus/Explicit which is based on work by Lubliner et al. (1989). Plasticity theory is used to approximate the behaviour of concrete and other similar materials which do not have a well-defined yield value. The assumption is that scalar damage occurs and the model is designed for applications in which the concrete is subjected to arbitrary loading conditions, including cyclic loading. The model takes into consideration the degradation of the elastic stiffness induced by plastic straining both in tension and compression. The yield function for the CDP model is defined in terms of effective stress and the corresponding stress invariant. Non-associated plastic flow is assumed using the Drucker-Prager hyperbolic function. Tension and compression are defined by separate hardening rules. Stress-strain data were used to define both the compressive and tensile behaviours.

The properties of the quasi-brittle materials used are listed in Table 2, obtained from testing of these materials. The yield strength of the reinforcing steel was 400 MPa and the modulus of elasticity was 200 GPa. Without more detailed testing, approximations were made to represent the material behaviour, and models of the component tests were used to calibrate the values. For each of the three quasi-brittle materials the modulus of elasticity was calculated using Equation 1 (Drysdale and Hamid, 2005), which is related to the material's compressive strength.

$$E = 850f'_c \quad (1)$$

The tensile strength of each quasi-brittle material was calculated using Equation 2.

$$f_t = 0.1f'_c \quad (2)$$

The CDP values given in the Abaqus documentation (ABAQUS, 2016), were implemented for the three quasi-brittle materials. The dilation angle, eccentricity, compressive strength ratio, material constant, and viscosity parameter were 32, 0.1, 1.16, 0.667 and 0.001 respectively.

Table 2: Material Parameters

| Material | f'_c [MPa] | f'_t [MPa] | E [GPa] |
|-----------------|------------------------------------|------------------------------------|---------------------------------|
| Block | 18.5 | 1.85 | 15.7 |
| Mortar | 10.3 | 1.03 | 8.8 |
| Grout | 18.6 | 1.86 | 15.8 |

GEOMETRY

Standard parts were established for units, grout, mortar, and reinforcing steel and repeated in the assembly. Like materials were merged within the assembly when in contact to produce continuous grout and mortar parts. The geometry was based on nominal 200 mm concrete units with an actual size of 390 mm x 190 mm x 190 mm. To facilitate meshing, rounded corners were not used. The geometry was otherwise accurately represented, accounting for the taper of the blocks. The standard unit geometry is shown in Figure 4. The reinforcing steel was modelled using line elements embedded in the grout region. Symmetry was utilized along the centre line of the wall.

BOUNDARY CONDITIONS

For the displacement based models, steel plates were modelled as being in contact with the base and top of the walls. Pinned supports were modelled by having a steel roller in contact with the steel plates, and these rollers were held fixed in space by setting the displacements in all three directions to zero. The fixed support was modelled by fixing the steel plate in space as shown in Figure 4(b). The symmetry condition was applied along the centreline of the wall. For the load based model, the top roller boundary condition was simulated by restraining out of plane displacements along the centre line of the roller contact, thus permitting vertical displacements and rotation at this location (see Figure 4(c)).

LOADING

Models were loaded first in a displacement scheme to obtain full load-displacement curves, then run in a load controlled scheme to plot the displaced profile. In the displacement based models the top roller was displaced a total of 25 mm, by modifying the vertical boundary condition in the loading step, and the model was stopped during the softening portion of the load-displacement curve. For the load based models the top roller was removed and a pressure load was applied over the contact area at that location with a total magnitude of 125 kN (half of the total load used in testing based on the use of symmetry). An out-of-plane load was applied as a pressure at the mid height of the wall over the loading beam contact area with a total magnitude of 6.3 kN.

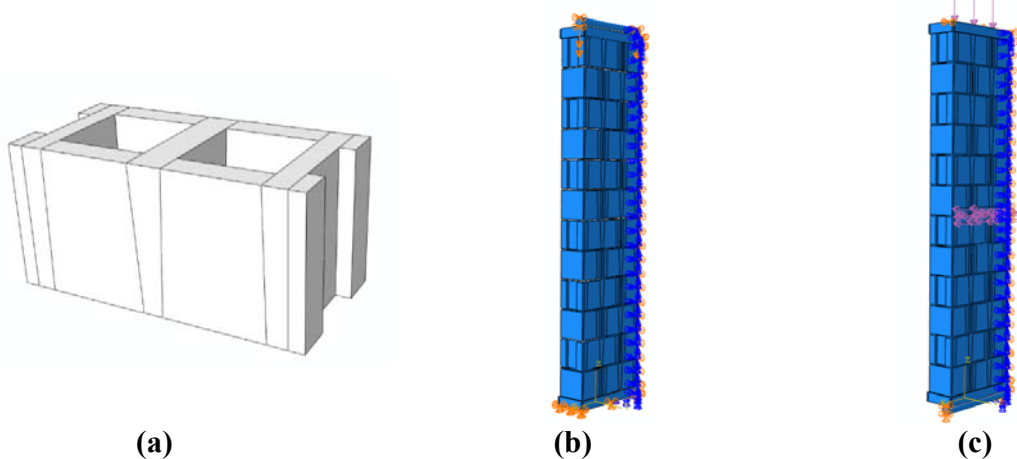


Figure 4: (a) Concrete Unit Geometry, (b) Pinned - Fixed Displacement Based Model, and (c) Pinned - Pinned Load Based Model

MESH REFINEMENT

For the mesh refinement study Abaqus 8-node bilinear brick elements (C3D8) elements were used. To reduce computational demands the mesh refinement study was conducted on a two unit high, grouted prism assembly. The mesh density was varied by assigning a global element size. However, geometric variations caused some elements to deviate from this size. The mesh refinement study on the grouted prism assembly gave convergence of the solution with an average element size of 10 mm, which was applied to the full model (Isfeld et al., 2016).

CONTACT

The bond between the unit and the mortar can often be the weakest link; it is controlled by the unit-mortar interface and can exhibit tensile (mode I) and shear (mode II) failure (Lourenco, 2002). The displacement based models utilized frictional contact between all parts, including units, grout, mortar, and steel plates/rollers. However, the load based models were simplified by merging the masonry components and using full bonding, with frictional contact remaining only between the steel plates and rollers. The results of the models with the conditions of full bonding between parts and frictional contact were compared up to the maximum vertical test load, showing agreement between the load-displacement curves. Contact was included with a frictional coefficient of 0.75 and hard normal contact.

FEM RESULTS

Models were run first with frictional contact between units, mortar, grout and the supporting steel. The load displacement curves for the pinned - pinned and pinned - fixed conditions are significantly different, as may be seen in Figure 5(a). The peak load was 433 kN for the pinned - pinned end condition and 869 kN for the pinned - fixed conditions, showing a 100 % increase when the base support is fixed. As shown in Figure 5(b) the maximum out-of-plane displacement is reduced from 1.4 mm for the pinned - pinned condition to 0.4 mm for the pinned - fixed condition when axial load is applied alone, and from 2.1 mm to 0.6 mm when axial and out-of-plane loads are applied. Comparison of the maximum displacements for the pinned - fixed models with the test results show the models are stiffer than the tested walls for which the maximum displacements were 0.53 mm for axial load only and 0.93 mm for axial and out-of-plane load. This may be attributed to the simplified approach used in determining the elastic modulus of the material components. However, the models were consistent with the testing, having the maximum displacement occur above the mid height of the wall.

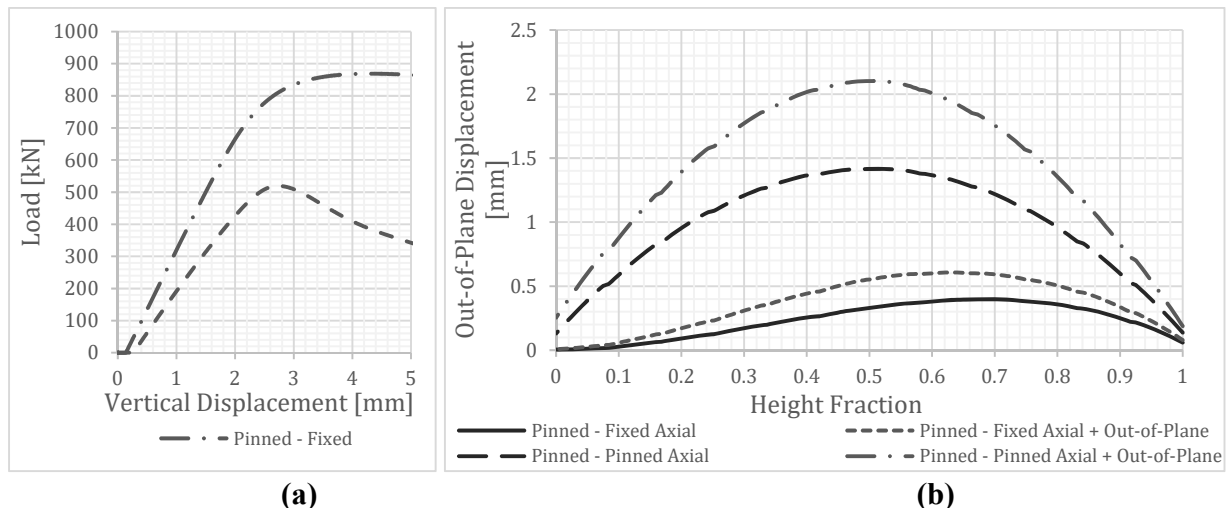


Figure 5: FEM Results (a) Load Displacement Curves and (b) Displaced Profiles

FINITE ELEMENT MODELLING IN SAP2000

SAP2000 is a finite element program that is widely used in practice for structural analysis and design because of its simplicity. Models of the tested walls with the two different base support conditions were created to investigate the correlation between the deflected shape as obtained from the experiments and that obtained from SAP2000 models. Figure 6(a) shows the cross-section of the wall used in the finite element model. Due to the use of face-shell bedding, the model consists of the two face-shells, the grouted cores and the two reinforcing bars. Models were also developed with the whole cross-section including the webs as depicted in Figure 6(b). Both cross sections simplify the actual geometry by excluding bond beams and taper of the units.

The height of the pinned walls was 2.67 m, which consists of 2.39 m actual wall height and 0.28 m for the support at the top and bottom of the wall. For simplification purposes, the material properties of the face-shells and the grouting were assumed to be equal. The compressive strength, f_m , used was 13.2 N/mm², based on interpolation of values given in the Canadian

Standard (CSA 2014). The modulus of elasticity, E_m , was calculated using Equation 1. The model was a two-dimensional frame element that exhibited the properties of the presented cross-section. To apply an eccentricity to the load and the support at the top and the bottom of the wall, insertion points that generate an offset of the frame axis were used. The constraint at the top of the wall only restricted movements in the out-of-plane direction, while the bottom supports also resisted the vertical forces. The fixed support was additionally able to resist bending moments.

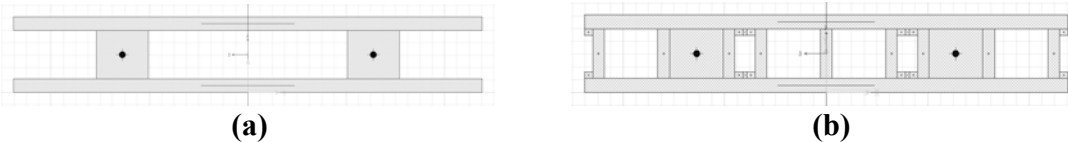


Figure 6: (a) Mortar Bedded and (b) Full Cross-Section of the Model

DEFLECTIONS

The deflected profiles of the walls were determined with a linear-static analysis and are shown in Figure 7. Because of the relatively low wall height, second order effects have little influence and can be neglected. It can clearly be seen that the support condition at the bottom of the wall has a great influence on the deflected shape and the maximum displacement. This finding is consistent with the test results and the detailed FEM. The pinned wall bends in a symmetrical single curvature with a maximum deflection of 2.49 mm in the middle of the wall. The fixed support condition at the base, forces the wall to bend in an asymmetrical double curvature with a much lower maximum deflection of 0.84 mm at approximately 2/3 of the wall height. The rotation at the base of the wall is zero and the point of inflection is at approximately 1/3 of the wall height. This leads to an effective wall height of 0.7 times the actual wall height. In comparison to the pinned wall, the maximum deflection is reduced by 66 %. The deflections of the models with the full cross-section are only slightly less, with a maximum of 2.27 mm for the pinned and 0.75 mm for the fixed support condition.

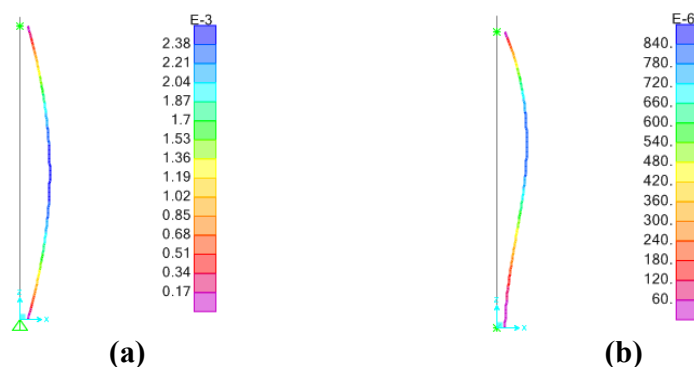


Figure 7: Simplified Cross Section Wall Deflections a) Pinned Base b) Fixed Base

DISCUSSION

The behaviour of a concrete masonry wall when the base support is not forced to behave as pinned was examined. Though no additional measures were taken to ensure a moment connection at the wall base, testing demonstrated a displaced profile similar to that of a fixed base. FEM of the two extreme conditions, pinned - pinned and pinned - fixed show that the actual wall behaviour is likely an intermediate condition at the base rather than fully fixed or

pinned. The assumption of a pinned connection is conservative as the test wall clearly deviates from pinned - pinned with the maximum out-of-plane displacements occurring between 0.8 and 0.6 of the total height when axial and combined axial and out-of-plane loads are applied. Further testing will be conducted considering the base condition as pinned for direct comparison of the walls behaviour. FEM results were consistent between Abaqus and SAP2000 for determining the displaced profile under known loads. A simplified cross section in SAP2000 allows for an efficient modelling approach with only 19 % difference when compared to the detailed micro model created in Abaqus. Further refinement of the material models applied in Abaqus and SAP2000 is required to improve agreement with testing results.

ACKNOWLEDGEMENTS

This research was funded through the Mitacs Accelerate program with the financial support of the Alberta Masonry Council. The authors also appreciate the contribution of material made available by Expocrete, and wall construction by MCAA South. Special thanks to the technical staff at the University of Calgary, Department of Civil Engineering.

REFERENCES

- ABAQUS (2016). ABAQUS 6.16 Documentation, Providence, RI, USA, Dassault Systemes.
- ACI-SEASC Task Committee on Slender Walls (1982). Test Report on Slender Walls. Editor Athey, J.W., Los Angeles, CA. 126pp.
- Canadian Standard Association (2014). S304.1-14 Design of Masonry Structures. Mississauga, Ontario, Canadian Standards Association. Volume, 240.
- Cranston, W. B. and Roberts, J. J. (1976). "The Structural Behaviour of Concrete Masonry Reinforced and Unreinforced." *Structural Engineer* 54. pp. 423-436.
- Dizhur, D., Derakhshan, H., Ingham, J. M. and Griffith, M. C. (2009). In situ Out-of-Plane Testing of Unreinforced Masonry Partition Walls. *Proceedings of 11th Canadian Masonry Symposium*, May 31- June 3, Toronto, ON.
- Drysdale, R. G. and Hamid, A. A. (2005). Masonry Structures Behaviour and Design: Canadian Edition Mississauga, ON, Canada Masonry Design Centre.
- Drysdale, R. G., Sallam, S. E. A. and Karaluk, E. (1976). Design of Masonry Walls and Columns for Combined Axial Load and Bending Moment. *Proceedings of 1st Canadian Masonry Symposium*, June 7-10, Calgary, AB.
- Fattal, S. G. and Cattaneo, L. E. (1976). Structural Performance of Masonry Walls under Compression and Flexure. Washington, US National Bureau of Standards, 73.
- Hatzinikolas, M., Neis, V. V. and Ghosh, S. (1991). Strength Test on Slender Plain Block Masonry Walls with Veneer Wythes, 739-748.

Hatzinikolas, M. A., Longworth, J. and Warwaruk, J. (1978). Concrete Masonry Walls. Editor. Edmonton, AB, 70.

Isfeld, A., Rizaee, S., Hagel, M., Kaheh, P. and Shrive, N. (2016). Testing and Finite Element Modelling of Concrete Block Masonry in Compression. *Proceedings of 13th Canadian Masonry Symposium*, June 4-7, Halifax, Canada.

Liu, Y. and Hu, K. (2007). Experimental Study of Reinforced Masonry Walls Subjected to Combined Axial and Out-of-plane Bending, 1486-1494.

Lourenco, P. B. (2002). "Computations on historic masonry structures." *Progress in Structural Engineering and Materials* 4(3). pp. 301-319.

Lourenço, P. B. (1996). Computational strategies for masonry structures. PhD, Delft Technical University.

Lourenço, P. B., Rots, J. G. and Blaauwendraad, J. (1995). "Two approaches for the analysis of masonry structures: micro and macro-modelling." *HERON* 40(4). pp. 313-340.

Lubliner, J., Oliver, J., Oller, S. and Onate, E. (1989). "A Plastic-Damage Model for Concrete." *International Journal of Solids and Structures* 25(3). pp. 299-326.

Mohsin, E. and Elwi, A. E. (2003). Effect of implied fixity at masonry block wall support interface on stability of load bearing walls. *Proceedings of 9th North American Masonry Conference*, June 1-4, Clemson, South Carolina, USA.

Müller, A. L., Isfeld, A., Hagel, M. and Shrive, N. (2016). Review and Analysis of Capacity of Slender Concrete Masonry Walls. *Proceedings of 13th Canadian Masonry Symposium*, June 4-7, Halifax, Canada.

Popehn, J. R. B., Schultz, A. E., Lu, M. and Storlarski, H. K. (2008). "Influence of Transverse Loading on the Stability of Slender Ureinforced Masonry Walls." *Engineering Structures* 30(10). pp. 2830-2839.

Suwalski, P. D. (1986). Capacity of Eccentrically Loaded Slender Concrete Block Walls. Master of Engineering, McMaster University.

Walsh, K. Q., Dizhur, D. Y., Giongo, I., Derakhshan, H. and Ingham, J. M. (2017). "Effect of boundary conditions and other factors on URM wall out-of-plane behaviour." *SESOC Journal* 30(1). pp. 57-81.

Yokel, F. Y., Mathey, R. G. and Dikkers, R. D. (1970). Compressive Strength of Slender Concrete Masonry Walls, US National Bureau of Standards. 33.

Yokel, F. Y., Mathey, R. G. and Dikkers, R. D. (1971). Strength of Masonry Walls Under Compressive and Transverse Loads, US National Bureau of Standards. 34.



**MASONRY TODAY
AND TOMORROW**

**11 - 14 February, 2018
SYDNEY AUSTRALIA**

www.10amc.com

EFFECTS OF HORIZONTAL REINFORCEMENT DISTRIBUTION ON IN-PLANE PERFORMANCE AND POST-PEAK BEHAVIOUR OF MASONRY SHEAR WALLS

O. Stathis¹, O. Fischer² and S.L. Lissel³

¹ M.Sc. Civil Engineering, Technical University of Munich, Germany, olympios.stathis@gmail.com

² Professor and Chair of Concrete and Masonry Structures, Technical University of Munich, Arcisstrasse 21, 80333 Munich, Germany, oliver.fischer@tum.de
Executive Board Member, B+S Consulting Engineers, Munich, Germany

³ Associate Professor, Department of Civil Engineering, University of Calgary, 2500 University Dr NW, Calgary, AB, Canada, slissel@ucalgary.ca
Project Engineer, B+S Consulting Engineers, Munich, Germany

The effect of horizontal reinforcement on the performance of partially grouted masonry shear walls subjected to cyclic in-plane lateral loading was studied on eight wall specimens with an aspect ratio of 1 ($H = 1.8$ m, $L = 1.8$ m) at the University of Calgary, Canada. This paper focuses on how the even distribution/spacing of the horizontal reinforcement can positively affect significant wall characteristics. Leaving wider spacing between the bond beam reinforcement as suggested by the Canadian design code has proven to be disadvantageous compared to distributing the reinforcement in every course up the height of the wall. The even distribution of the bars up the height of the wall prevents the initial diagonal cracks from propagating. Instead, new small diagonal cracks form all over the wall, leading to a better crack pattern and a comparatively more ductile failure mode. Furthermore, the experimental results showed better energy dissipation, higher ductility, slower stiffness degradation, and lower ultimate strength degradation for the walls reinforced with evenly distributed bed-joint-reinforcement (reinforced in every course) than did the walls with widely spaced reinforced bond beams.

Keywords: *bed-joint-reinforcement, cyclic in-plane lateral loading, masonry shear walls, bond beam spacing, quasi-static testing, energy dissipation, ductility, stiffness degradation, partially grouted*

INTRODUCTION

The poor seismic response of unreinforced masonry walls led to the development of reinforced masonry along with the grouting of the cores and courses. Steel reinforcement increases the



ductility of these walls through a redistribution of lateral loads, whilst guaranteeing better energy dissipation and a less brittle failure. In buildings, typical failure or damage to masonry shear walls under seismic loading occurs due to lateral in-plane movement, which exceeds the resistance of the structure in the horizontal direction.

The research described in this paper focussed on examining concrete masonry shear walls with different types and patterns of horizontal reinforcement such as bond beams and bed-joint-reinforcement (BJR). Although the Canadian design code (CSA 2004) allows the use of widely spaced bond beams; this is not considered good design. Therefore, an experimental comparison of the behaviour of partially grouted shear walls with different reinforcement and spacing patterns is a significant point of interest for this paper. The significant variables used to compare the walls' in-plane behaviour are the displacement ductility, energy dissipation capacity, and stiffness degradation. A special focus is on the post-peak behaviour of the walls tested.

CONSTRUCTION DETAILS

Eight partially grouted masonry shear walls were constructed from hollow concrete blocks and Type S mortar. The walls were constructed in four groups of two identical walls per group. The main difference between wall groups was in the type, amount, and spacing of the horizontal reinforcement. The vertical reinforcement ratio was constant in all walls, consisting of three 15M ($A_{bar} = 200 \text{ mm}^2$) reinforcing bars with a horizontal spacing of 800 mm, as illustrated in Figure 1. These bars were overlapped with three 15M vertical dowels of 600 mm length which were welded to the base beam to connect the wall to the base beam which in turn was fixed to the laboratory floor during execution of the experiments. The reinforced cores were grouted. The main structure of all walls, without taking the horizontal reinforcement into account, is shown in Figure 1.

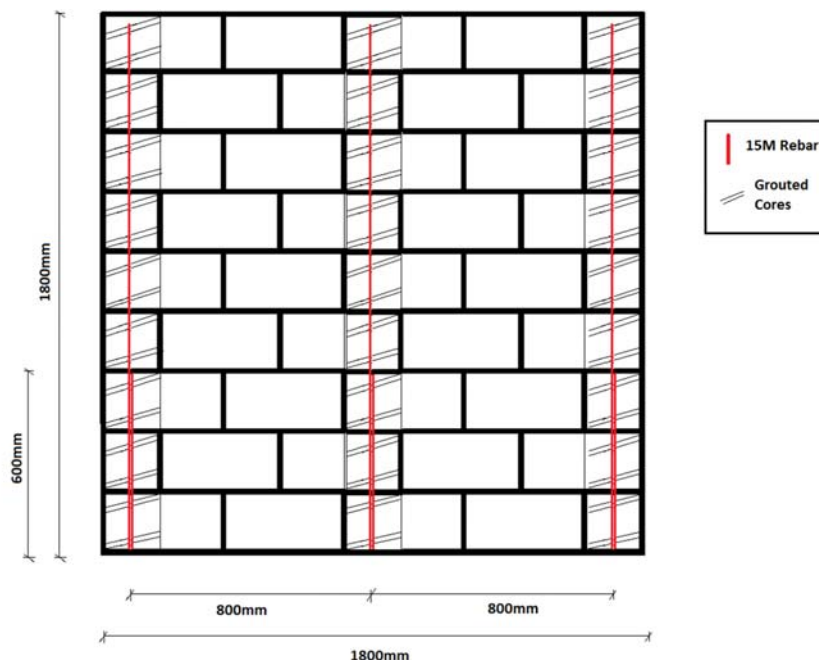


Figure 1: Vertical reinforcement and grouting pattern

All eight wall specimens were constructed by an experienced mason under supervision, using 390 mm x 190 mm x 190 mm (width x height x thickness) hollow concrete masonry blocks in running bond with face shell bedding. The horizontal reinforcement was placed during construction in a bond beam in one of the four groups, and in the bed joints in the other three groups. In the latter case, heavy gauge truss (diagonally oriented cross wires) and/or standard gauge ladder (cross wires perpendicular to main wires) shaped bed-joint-reinforcement was placed in the bed-joints, course by course, during the construction. The vertical reinforcement was placed and the reinforced cores were grouted every few courses during the construction. The nominal dimensions of the walls were 1800 mm x 1800 mm x 190 mm (height x length x thickness), with an aspect ratio of one. This aspect ratio was chosen, combined with high axial loads, to increase the likelihood of a diagonal shear failure mode. The position of the horizontal reinforcement is listed in Table 1.

Table 1: Specification of wall parameters

| Group | Wall | Reinforcement type | Location (Course) | Rebar Size ø | Anchorage Type |
|-------|------|------------------------------------|-------------------|-------------------|----------------|
| A | 1,2 | Bond Beams | 3rd & 6th | 11.3 mm | 90° hook |
| B | 3,4 | Standard Gauge BJR | Every Course | 3.76 mm | - |
| C | 5,6 | Heavy & Standard BJR (Alternating) | Every Course | 3.76 mm & 4.75 mm | - |
| D | 7,8 | Heavy Gauge BJR | Every Course | 4.75 mm | - |

In the group with bond beams, units with knock-out webs were used, so that the rebar could be placed. The mortar used was Specmix Type S preblended mortar containing portland cement, hydrated lime and dried masonry sand, and was mixed with water in the lab before application. The grout used to fill the cores with the vertical reinforcement as well as the bond beams was Specmix Core Fill Grout with Coarse mixture.

TEST SET-UP

The test arrangement was designed to fix the base of the walls while leaving the top of the wall free to translate but not rotate. The specimens were anchored to the floor using four bolts per side in order to prevent sliding on the laboratory floor during testing. Two actuators applied the vertical (axial) load through steel roller plates allowing in-plane movement of the wall's top, whilst maintaining a constant axial load. This load represents the roof or floor loads of a building while also preventing in-plane rotation of the wall. The axial loads for each actuator were adjusted throughout the experiment to counteract the moment that is caused by the lateral force. The total axial load remained constant throughout the experiment. The test set-up is illustrated in **Figure 2**.

The quasi-static cyclic tests were carried out by applying an in-plane displacement controlled lateral load to the shear walls through a steel capping beam. The displacement controlled loading comprised two cycles of displacement and each cycle comprised one pull and one push cycle,

respectively. The peak displacement was held for two seconds. The loading protocol used in this work is shown in **Table 2**.

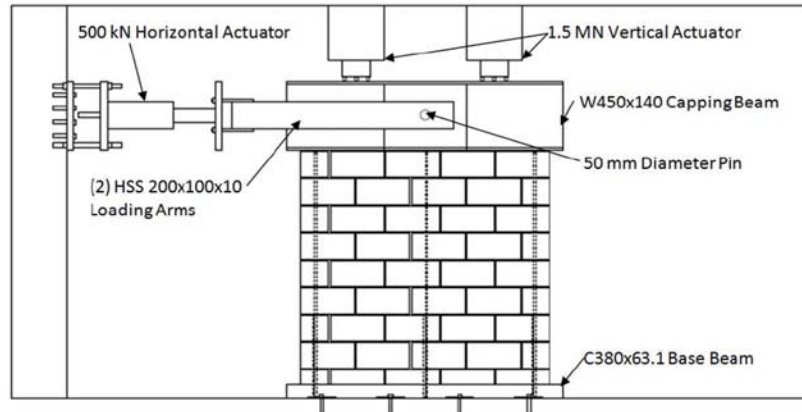


Figure 2: Schematic diagram of the wall and test frame (Lissel & Dickie, 2010)

Table 2: Displacement control loading protocol

| Displacement (mm) | 0 to 1 | 1 to 15 | 15 to failure |
|-------------------|--------|---------|---------------|
| Increment (mm) | 0.25 | 0.5 | 1 |
| Speed (mm/s) | 0.1 | 0.25 | 0.5 |

OBSERVATIONS - CRACK PATTERN

In most cases, the walls experienced a crushing of the right (north) toe which can be attributed to the biaxial compressive stresses. The shear strength of the wall groups differed but was within the material variation in all cases and for both directions. Walls in Group A (10M bond beams in the 3rd and 6th courses) demonstrated a comparatively brittle shear failure mode, whereas the wall groups reinforced in their bed-joints demonstrated a comparatively ductile shear failure. Wall Group A demonstrated a crack pattern characterized by wide cracks generally located where stress concentration between the grouted and ungrouted cores and courses could occur. These larger cracks propagated throughout the test to a great extent causing a more brittle failure than observed in wall groups with evenly distributed bed-joint-reinforcement. Walls in Groups B (Standard BJR) and C (Alternating BJR), and also Wall 7 from Group D (Heavy BJR) demonstrated a crack pattern with smaller cracks evenly distributed throughout the height and length of the wall. Wall 8 from Group D showed similar behaviour to these groups, however some larger cracks and spalling at the left end core have to be taken into consideration. In conclusion, the even distribution of bed-joint reinforcement up the height of the wall prevented the initial diagonal cracks from widening and propagating. Instead, new small diagonal cracks formed all over the wall, leading to a better crack pattern and a comparatively more ductile failure mode. Last but not least, although the amount of reinforcement used in these tests lies within the range where the amount of horizontal reinforcement should have an effect (Rizaei, 2015), the observation from these tests was that increasing the amount of horizontal reinforcement did not have any significant effect on the shear strength of the wall groups. Table 3

summarizes the load-displacement behaviour at three different stages; 1) cracking 2) maximum load 3) ultimate displacement (failure).

Table 3: Summary of Test Results (Only Push Direction Shown)

| Group | Wall type | Wall | Push direction | | | | | | | |
|-------|---|------|----------------|---------------|------------------|----------------|------------------|----------------|------------------|-----------------------------|
| | | | Crack | | | Maximum | | Failure | | |
| | | | H_{cr} (kN) | d_{cr} (mm) | H_{cr}/H_{max} | H_{max} (kN) | $d@H_{max}$ (mm) | d_{max} (mm) | $H@d_{max}$ (kN) | $\frac{H@d_{max}}{H_{max}}$ |
| A | 10M, 90° hook, BB: 3 rd , 6 th course | 1 | 124 | 1.5 | 0.66 | 188 | 8.0 | 8.5 | 183 | 0.97 |
| | | 2 | 140 | 1.5 | 0.77 | 181 | 5.0 | 5.5 | 127 | 0.70 |
| B | Standard Duty BJR at every course | 3 | 125 | 1.5 | 0.77 | 162 | 5.0 | 9.0 | 130 | 0.80 |
| | | 4 | 134 | 2.0 | 0.75 | 178 | 9.5 | 10.0 | 171 | 0.96 |
| C | Alternating BJR at every course | 5 | 141 | 1.5 | 0.77 | 182 | 4.0 | 9.5 | 149 | 0.82 |
| | | 6 | 125 | 1.5 | 0.65 | 192 | 5.5 | 8.5 | 112 | 0.58 |
| D | Heavy Duty BJR at every course | 7 | 140 | 2.0 | 0.77 | 182 | 5.0 | 10.0 | 88 | 0.48 |
| | | 8 | 123 | 1.5 | 0.68 | 181 | 5.0 | 10.0 | 122 | 0.67 |

ANALYSIS - BILINEAR IDEALIZATION

This method introduced by (Tomazevic & Zarnic, 1985), defines the ductility as the ratio of ultimate displacement to the displacement at the idealized elastic limit. The ultimate displacement d_u is the last point where the bilinear curve intersects the descending branch of the experimental hysteresis envelope. In previous studies at the University of Calgary (Hoque, 2013), (Rizaei, 2015), the post-peak ultimate displacement was chosen as the point where the strength dropped to 80% of the maximum strength. If the experimental envelope did not drop to 80%, the ultimate displacement was assumed to be equal to the maximum displacement. The same approach was also followed in this work. In order to apply this kind of analysis, the following parameters had to be determined:

- A_{env} , the area under the experimental envelope
- d_{cr} , the displacement at which the initial stiffness of the experimental envelope changes due to the first significant crack
- H_{cr} , the lateral load at which the first significant crack was observed
- d_e , the displacement at the idealized elastic limit
- H_{max} , the ultimate strength based on the experimental envelope
- d_u , the ultimate displacement reached at a 20% shear strength drop off

- d_{max} , the maximum displacement of the wall before failure occurs

An illustration of the bilinear idealization key parameters is shown in Figure 3.

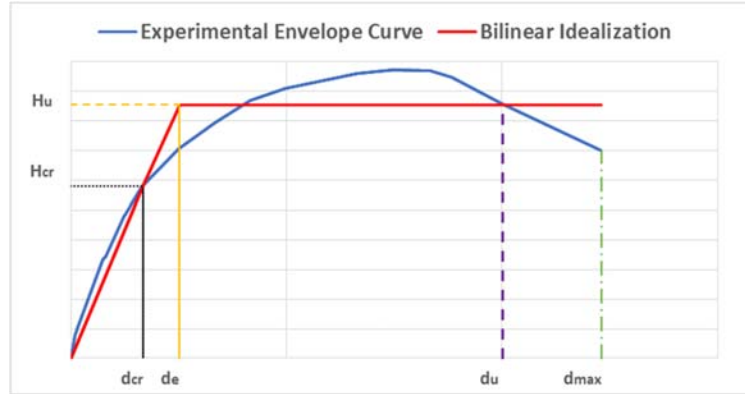


Figure 3: Load-displacement envelope curve and bilinear idealization

The area under the envelope, A_{env} , was calculated by applying the trapezoidal approximation for an area under the curve. The initial stiffness K_e and the ultimate strength H_u were determined from the following equations.

$$K_e = \frac{H_{cr}}{d_{cr}} \quad \text{Eq. 1-1}$$

$$H_u = K_e(d_{max} - \sqrt{d_{max}^2 - \frac{2A_{env}}{K_e}}) \quad \text{Eq. 1-2}$$

The displacement at the idealized elastic limit and the ductility ratio were determined as follows:

$$d_e = \frac{H_u}{K_e} \quad \text{Eq. 1-3}$$

$$\mu_u = \frac{d_u}{d_e} \quad \text{Eq. 1-4}$$

DUCTILITY VALUES

Wall Group A demonstrated significantly lower mean ductility values than any other wall group due to the comparatively low displacement of Wall 1 and the early failure of Wall 2. The ductility of Wall Group B and C ranged between 4.4 and 4.7 in both the push and pull directions. As illustrated in Figure 4, Wall Group D exhibited the highest ductility value of 5.6 among all wall groups in the pull direction, whereas Wall Group C demonstrated the highest ductility value of 4.6 in the push direction. Walls with bed-joint-reinforcement showed an improved ability to undergo greater displacement, thus reaching higher ductility values than did walls with bond beams in the 3rd and 6th courses.

ENERGY DISSIPATION

The dissipated energy E_{diss} of the walls was calculated by using the loading-unloading cycles from the experimental hysteresis loops. The energy dissipated within one loading cycle represents the difference between the energy provided to the wall during the loading phase and the energy released during the unloading phase, and equals the area enclosed within the hysteresis loop as shown in Figure 5(left). The input energy E_{inp} represents the work input by the lateral load

actuator during the displacement of the wall to the maximum displacement of a loading cycle. The input energy is the area under the loading part of the hysteresis loop for one loading-unloading cycle as illustrated in **Error! Reference source not found.5(right)**.

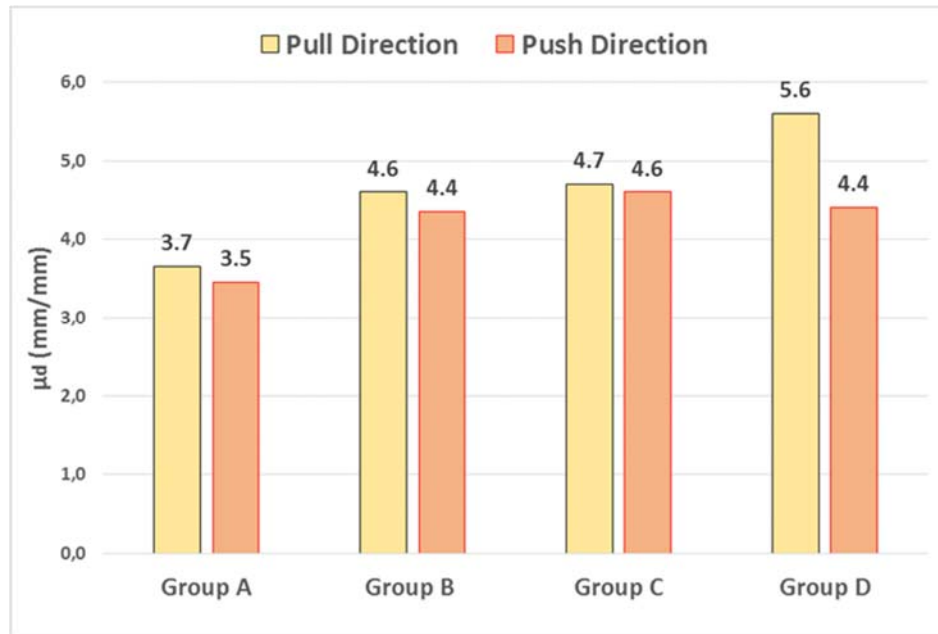


Figure 4: Average ductility values in push and pull direction

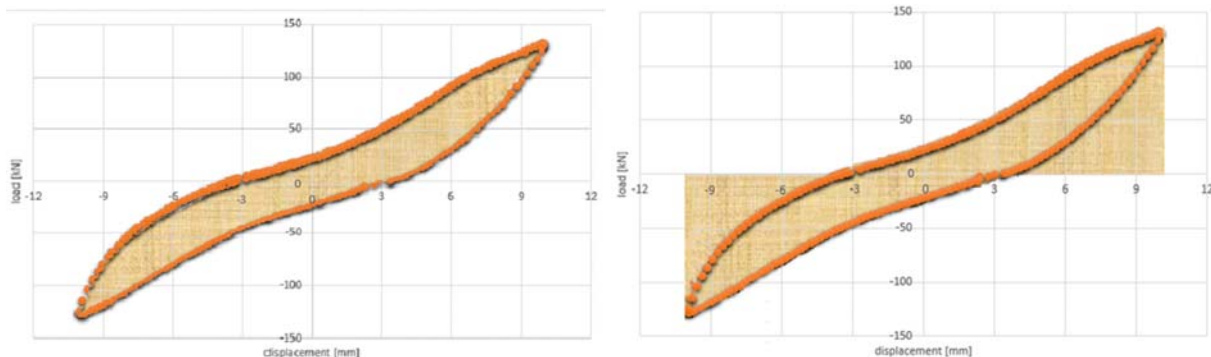


Figure 5: Dissipated energy (left) and Input energy (right) at ultimate displacement in one loading cycle

TOTAL ENERGY DISSIPATION

Error! Reference source not found.4 shows the values of the total dissipated energy, the total input energy, their ratio, and the mean values of the ratio for each wall Group. All these values were calculated at the last displacement cycle. **Error! Reference source not found.4** also illustrates how much input energy each wall dissipated throughout the experiment. This relation can be expressed as the ratio of the accumulated dissipated energy $\sum E_{diss}$ to the input energy $\sum E_{inp}$. Wall 1 exhibited the lowest energy dissipation at 29%, whereas Wall 2, of the same Group had a comparatively higher ratio of 39%. The highest ratio was demonstrated by Walls 7

and 8 of Group D (average 56%) while Wall Group A demonstrated the lowest ratios with a mean energy dissipation capacity of 34%. Despite having the same reinforcement ratio, Wall Group C showed the ability to dissipate a higher amount of the input energy (ratio 44%) throughout the experiment than did Wall Group A with a ratio of 34%. Wall Groups B-D, all having bed-joint reinforcement, demonstrated similar energy dissipation capacities throughout the three states of the experiment. In general, they also demonstrated a higher energy dissipation capacity than Wall Group A.

Table 4: Energy values at the end of the experiment

| Wall ID | | Hor. Reinforcement ratio ρ_h | $\sum E_{diss}$ (kNm) | $\sum E_{input}$ (kNm) | $\frac{\sum E_{diss}}{\sum E_{input}}$ | Mean Values $\frac{\sum E_{diss}}{\sum E_{input}}$ |
|---------|---|---|--------------------------|---------------------------|--|---|
| Group A | 1 | 0.075% | 10.96 | 37.66 | 0.29 | 0.34 |
| | 2 | | 5.79 | 14.87 | 0.39 | |
| Group B | 3 | 0.055% | 15.84 | 35.00 | 0.45 | 0.40 |
| | 4 | | 16.20 | 47.29 | 0.34 | |
| Group C | 5 | 0.075% | 15.93 | 38.43 | 0.43 | 0.44 |
| | 6 | | 14.31 | 30.54 | 0.45 | |
| Group D | 7 | 0.094% | 20.08 | 39.19 | 0.51 | 0.56 |
| | 8 | | 20.80 | 34.16 | 0.61 | |

On the basis of **Error! Reference source not found.**4 and with some reservation due to the small number of specimens, it can be concluded that a higher amount of energy is dissipated with ascending bed-joint-reinforcement ratio. However, a further increase of the horizontal reinforcement ratio, especially above the suggested 1% limit (Rizaei, 2015), does not automatically guarantee better results and should be investigated further.

DISSIPATED ENERGY AT DIFFERENT STAGES OF DAMAGE

This section provides an analysis of the dissipated energy at the three different states of damage. In addition to the amount of dissipated energy, the aim of this section is to show how the dissipated energy is distributed between the cracking state, the state of maximum load, and the state of ultimate displacement on a percentage basis. Table 55 shows the accumulated dissipated energy for each wall at the three different states as well as the total dissipated and input energy values reached. Figure 7 shows the amount of energy dissipated in each state as a percentage of the total energy dissipated.

Wall Group D, the wall with the greatest reinforcement ratio, was able to dissipate the most energy before failure, with the accumulated energy dissipation for this wall group lying at 20.44 kNm. Wall Groups B and C dissipated 78% and 74% of this value respectively. Wall groups reinforced in the bed-joints exhibited a clear ability to dissipate a great amount (between 75-82%) of the total dissipated energy in the post-peak region. Between the first crack and the point of ultimate strength, groups B, C and D achieved values between 16.3% and 22.3%, whereas in the post-peak region the values ranged between 75.7% and 81.9%. Wall Group B and D had comparatively similar performance in all 3 stages of the test. Through this comparison that is illustrated in Figure 6, it becomes evident that Wall Groups B (SBJR), C (ABJR), and D (HBJR) were very consistent, exhibiting comparatively similar behaviour in all three stages. Wall Group A (bond beams) on the other hand, exhibits different behaviour characterized by a significantly higher amount of energy dissipation between the cracking and state of maximum load. However, Wall Group A performs poorly with less energy dissipated in the post-peak region (only 56%) compared to bed-joint-reinforced Wall Groups B, C and D. It is noteworthy that Wall Groups A and C (ABJR) behaved differently in terms of energy dissipation, despite having the same reinforcement ratio. However, it is also worth mentioning that the low amount of horizontal reinforcement used cannot drastically change a wall's behaviour. As the results indicate, the bed-joint-reinforcement had negligible impact on the strength improvement. This may be related to the fact that no yield was recorded. However, the bed-joint-reinforcement efficiently contributed to maintaining the strength and integrity of walls in the post-peak region, as well as improving the energy dissipation.

Table 5: Energy values at three different stages (values in kNm)

| Wall Group | Wall | $\sum E_{diss}$ at cracking stage | $\sum E_{diss}$ at maximum load | $\sum E_{diss}$ at ultimate displacement |
|------------|--------|--------------------------------------|------------------------------------|---|
| A | Wall 1 | 0.26 | 4.94 | 5.76 |
| | Wall 2 | 0.27 | 1.91 | 3.61 |
| | Mean | 0.27 | 3.42 | 4.68 |
| B | Wall 3 | 0.27 | 2.39 | 13.18 |
| | Wall 4 | 0.33 | 2.83 | 13.05 |
| | Mean | 0.30 | 2.61 | 13.11 |
| C | Wall 5 | 0.28 | 2.92 | 12.73 |
| | Wall 6 | 0.31 | 3.84 | 10.16 |
| | Mean | 0.30 | 3.38 | 11.45 |
| D | Wall 7 | 0.38 | 3.57 | 16.12 |
| | Wall 8 | 0.43 | 4.00 | 16.38 |
| | Mean | 0.41 | 3.78 | 16.25 |

STIFFNESS DEGRADATION

In order to evaluate the stiffness degradation, the changes in stiffness ratio, i.e., the ratio between the actual and effective stiffness of the wall K/K_e with respect to lateral displacements, and the displacement normalized with regard to the displacement at the maximum lateral resistance d_{Hmax} , were plotted. The interpolated values of the wall groups in the push and pull directions are illustrated in Figure 7.

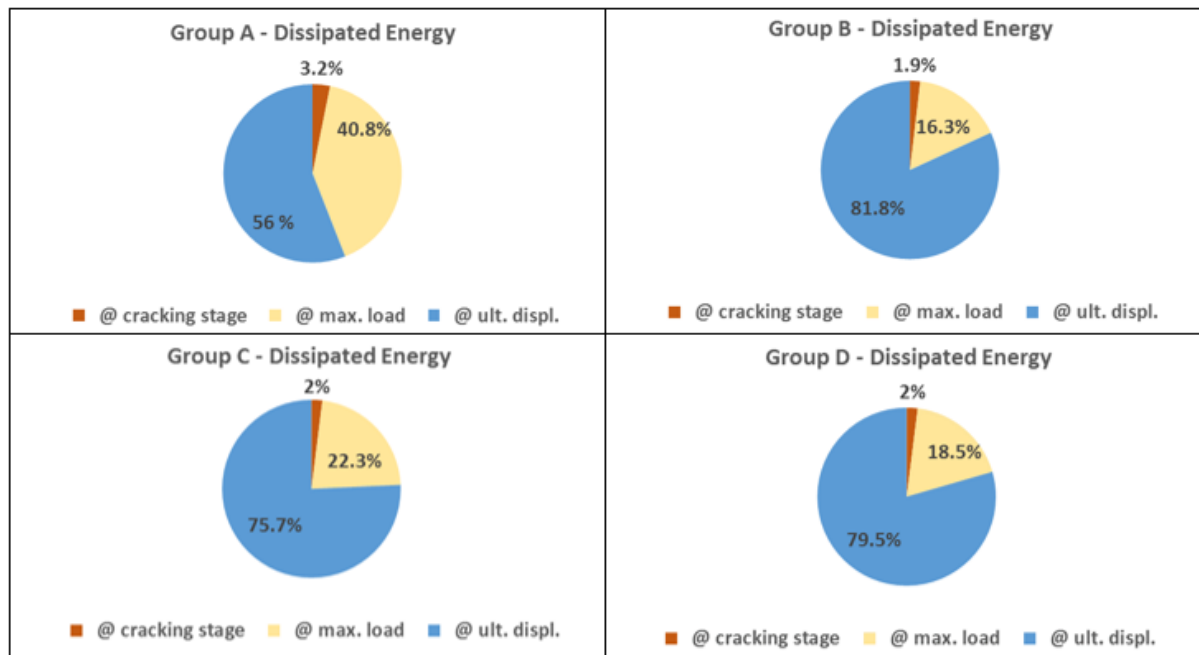


Figure 6: Dissipated energy at the three different stages for Groups A-D on a percentage basis to the total dissipated energy

Similar to the push direction, Wall Group A demonstrated the tendency for the stiffness to deteriorate faster than the other wall groups in the pull direction as shown in Figure 7. Especially in the post-peak region (after d/d_{Hmax} reaches the value of 1), this wall group demonstrated an even steeper stiffness degradation. Wall Group D degraded at a slower rate than the other wall groups followed by Wall Group B. The stiffness of Wall Group C degraded at a similar rate to Wall Group A. However, a difference in deterioration was obvious after the peak strength was reached, where Wall Group C demonstrated slower stiffness degradation. In the pull direction, Wall Group A experienced a sharp decrease in initial stiffness (61%) especially before the state of maximum load. At the state of ultimate displacement Wall Group A demonstrated a comparatively lower further decrease of stiffness (16%) compared to the decrease noticed at the state of maximum load. In the push direction, Wall Groups A and B experienced a stiffness reduction of 66% of the initial stiffness at the state of maximum load. However, in the post-peak region Wall Group B was able to undergo higher deterioration than Wall Group A. Wall Group D (HBJR), on the other hand, exhibited the slowest rate of stiffness degradation compared to any other wall group at the state of maximum load (51% in the pull, 45% in the push). This group also demonstrated a higher reduction in stiffness between the maximum load and ultimate

displacement state (37% in pull). Wall Groups B and C demonstrated similar behaviour to Wall Group D in the post-peak region but were not able to utilize the wall's potential to the same extent.

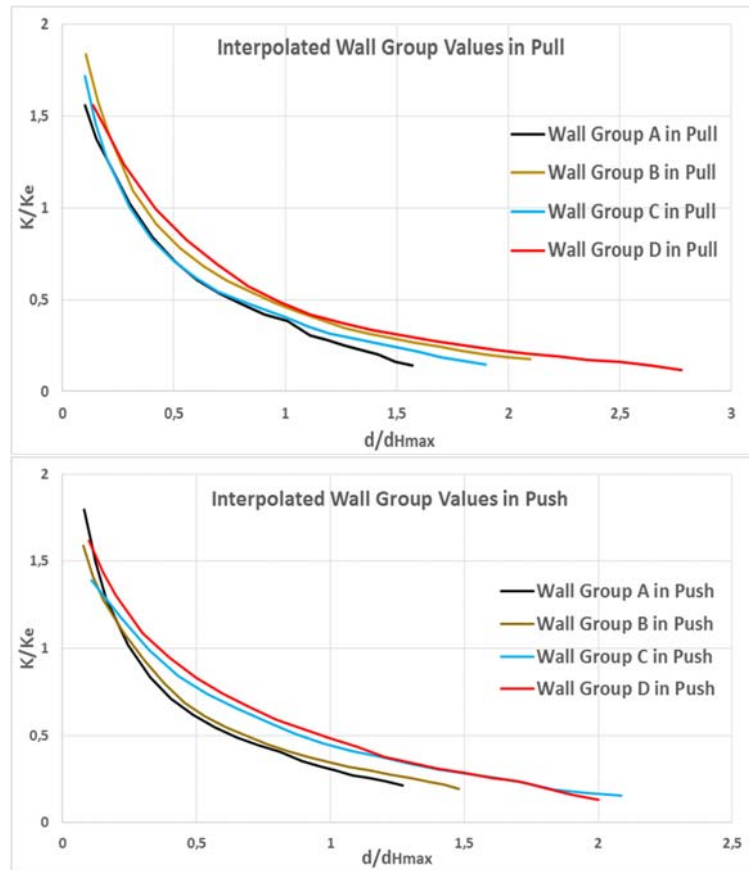


Figure 7: Interpolated stiffness degradation of Wall Groups A-D in pull direction (top) and push direction (bottom)

Wall Group D deteriorated to the highest extent among all wall groups, reaching a low ultimate stiffness value (13% of the initial stiffness) at the end of the ultimate displacement state. In conclusion, the stiffness of Wall Group A deteriorated comparatively quickly and to a higher extent up to the maximum load state, but exhibited very low capacity to degrade further in the post-peak region. Conversely, Wall Group D, followed by Wall Group C, maintained a significantly higher amount of its initial stiffness at the state of maximum load, and deteriorated to a higher extent in the post-peak region compared to Wall Group A. Wall Group D exhibited the ideal behaviour of deteriorating at a slower rate and maintaining a higher amount of the initial stiffness before peak, while demonstrating greater deterioration in the post-peak region. Overall, the walls reinforced in the bed-joints exhibited better stiffness degradation behaviour, in terms of rate and ultimate stiffness value, in the maximum load and ultimate displacement state.

CONCLUSIONS

The spacing of the horizontal reinforcement had a definite influence on the crack pattern. Leaving wider spacing between the bond beam reinforcement as suggested by the Canadian design code (CSA 2004) was proven to be disadvantageous compared to distributing the reinforcement in every course up the height of the wall. The crack pattern in the walls with 10M bond beams in the 3rd and 6th courses was characterized by larger, concentrated cracks that widened throughout the course of the experiment, causing a brittle shear failure. The concentration and poor distribution of horizontal reinforcement in more widely spaced bond beams is not efficient. In the majority of cases, walls with evenly distributed bed-joint-reinforcement exhibited a crack pattern consisting of smaller cracks, spread all over the wall. These walls also demonstrated a comparatively ductile shear failure mode. The even distribution of the bars up the height of the wall prevents the initial diagonal cracks from propagating. Furthermore, the experimental results showed better energy dissipation, higher ductility, slower stiffness degradation, and lower ultimate strength degradation for the walls reinforced with evenly distributed bed-joint-reinforcement (reinforced in every course) than did the walls with widely spaced reinforced bond beams.

It was also reconfirmed that bed-joint-reinforcement can provide the necessary capacity and ductility required as the primary shear reinforcement. The use of bed-joint-reinforcement also had a beneficial impact on the ultimate displacement, which lead to the higher ductility exhibited by these walls.

ACKNOWLEDGEMENTS

The authors would like to thank Expocrete Canada for donating concrete block, Quikrete Canada for donating mortar and grout, and the Masonry Contractors Association of Alberta and the technical staff of the Department of Civil Engineering for their support.

REFERENCES

- CSA S304.1-04, C. (2004). Design of Masonry Structures. Mississauga, Ontario: Canadian Standards Association.
- Hoque, N., 2013. In-Plane Cyclic Testing of Reinforced Concrete Masonry Walls to Assess the Effect of Varying Reinforcement Anchorage and Boundary Conditions. MSc Thesis, Department of Civil Engineering, University of Calgary, Canada.
- Lissel, S. & Dickie, J., 2010. In-plane Shear Test Method for Reinforced Concrete Masonry and Comparison of Test Results. Dresden: 8th International Masonry Conference, Dresden, Germany.
- Rizaei, S., 2015. Assessing Bond Beam Horizontal Reinforcement Efficacy with Different End Anchorage Conditions in Concrete Block Masonry Shear Walls. MSc Thesis, Department of Civil Engineering, University of Calgary, Canada.
- Tomazevic, M. & Zarnic, R., 1985. The Effect of Horizontal Reinforcement on the Strength and Ductility of Masonry Walls at Shear Failure. pp. 1291-1302 ed. s.l.:Proceedings of the Seventh International Brick and Block Masonry Conference.

A FINITE ELEMENT INVESTIGATION ON STRUCTURAL PERFORMANCE OF FULLY GROUTED REINFORCED MASONRY BUILDING

S. Noor-E-Khuda¹ and M. Dhanasekar²

¹ Lecturer, School of Engineering and Technology, Central Queensland University, Perth 6000, Australia.
(Corresponding Author), s.noorekhuda@cqu.edu.au

² Professor, School of Civil Engineering and Built Environment, Queensland University of Technology, Brisbane
4000, Australia, m.dhanasekar@qut.edu.au

It is well known that the reinforced masonry (RM) system with vertical and horizontal reinforcement provide enhanced resistance to lateral cyclonic and seismic loading. All the prevailing international masonry design standards included the contribution of the steel area in their design equations. However, recent studies have shown that the partially grouted RM walls would most likely not perform up to the code expectations. While most investigations considered walls under independent actions ignoring practicable boundary and loading conditions; the research reported herein focused on the structural performance of fully-grouted reinforced masonry (FGRM), multi-storied building. The prototype building adopted a design detail within the provisions of the current Australian masonry standard AS3700-2011. The assessment was carried out through a recently developed explicit finite element (EFE) model. Results on the structural performance of the prototype building is discussed. It is shown that the adopted design detail provided sufficient lateral load resistance and ductility to the FGRM building. The structural design fulfils the structural performance requirements irrespective of the geographic location of the structure within inland Australia.

Keywords: *Fully-grouted, reinforced masonry, multi-storied building, explicit finite element model, lateral loading, in-plane shear.*

INTRODUCTION

With the objective of enhancing the axial and lateral load capacity, masonry walls constructed using hollow blocks are grouted and reinforced both vertically and horizontally, are commonly termed as reinforced masonry (RM) walls. RM walls are predominantly classified as fully grouted (FG) or partially grouted (PG), depending on the extent of grouting and/or close or wide spaced, depending on the reinforcement detailing. The Australian Masonry Standard (AS3700-2011) outlines the FG system as those with all hollow cells grouted and the PG system as the ones with only the cells containing reinforcements are grouted. The structural performance of these systems; load and ductility capacity varies as per the structural configuration. The FG system provides a regular grouted masonry section throughout the length/width of the wall, unlike the PG system that contains weaker un-grouted pockets. Recent research by Dhanasekar and Haider (2008) and Bolhassani et al. (2016), confirms that the PG walls mostly experience cracking along the weaker unreinforced/un-grouted masonry portion and in-cases without yielding the reinforcing bars. While majority of the structural investigation on various RM systems [Dhanasekar and Haider (2008); Dhanasekar et al. (2015 and 2016); Noor-E-Khuda (2016);] engrossed the performance of individual walls the work presented in this paper examines problems of rather practical significance.

Whilst several author's [Dhanasekar and Haider (2008); Noor-E-Khuda and Dhanasekar (2017); Lourenço (2000)] coupled the effect of axial compression and lateral action in their assessments, the combined in-plane and out-of-plane loading interaction caused due to structural irregularity and loading eccentricity is hardly addressed by researchers. Furthermore, the behaviour of the component walls in building structures with practicable reinforcement detail, end support arrangements and under realistic loading conditions can be significantly different than that of the individually analysed walls which triggers the need for the structural performance assessment of multi-storied RM buildings.

With the recent advancement in computational facilities and available sophisticated computer programs, finite element method offer economic and suitable alternate approach to the experimental counterpart. Bolhassani et al. (2016) developed a micro FE model and assessed the structural performance of a one-span, single storied, partially grouted reinforced masonry (PGRM) building and showed promising gain in load capacity and ductility from the detail designed walls. This paper presents the structural performance of a two-spanned & three-storied, fully grouted reinforced masonry (FGRM) prototype building subjected quasi-static lateral loading. The prototype building adopted a structural design within the current AS3700-2011 code provisions; suitable for moderate earthquake loading. The assessment is conducted using an explicit finite element (EFE) model recently developed by the authors. The EFE model incorporated macroscopic masonry properties and successfully simulated the out-of-plane [Noor-E-Khuda et al. (2016a) & (2016b)] and in-plane [Dhanasekar and Haider (2008)] performance of reinforced masonry walls. This paper briefly describes the EFE model and its application to the prototype building. Outcomes from the EFE model are compared with those obtained from the prevailing Australian standards for further justification of the outcomes.

PROTOTYPE BUILDING

Details of the three-storied prototype FGRM building including its geometric, loading and structural configurations are discussed under this section.

The adopted building model enabled the investigation of key parameters necessary for the verification of the structural performance under realistic loading and boundary conditions. All the 150mm thick component walls of the three-storied masonry building considered in this study was fully grouted and reinforced. The typical wall layout is shown in Figure 1. Dimensions of the building measured 8m in length and 4m in width; each storey height was limited to 2.6m, to attain computational economy. The 8m long front wall (Wall B) and the rear wall (Wall A) consisted of door and window openings each measuring 1000mm×2000mm (19.23% of wall area) and 1000mm×1000mm (9.62% of wall area), respectively. On the contrary the orthogonally positioned walls (Wall C) shown in Figure 1.(c), were 4m long solid section. The building was subjected to uni-directional quasi-static lateral loading along the x and the y directions in standalone analyses. When loaded along the x-axis direction [Figure 3], the structure was asymmetric in plan caused by the differences in stiffness between wall A and wall B. The structure was rather symmetrical when loaded along the orthogonal y-axis direction. The building was considered furnished with 150mm thick flat reinforced concrete slabs, including the top floor to facilitate further vertical extension.

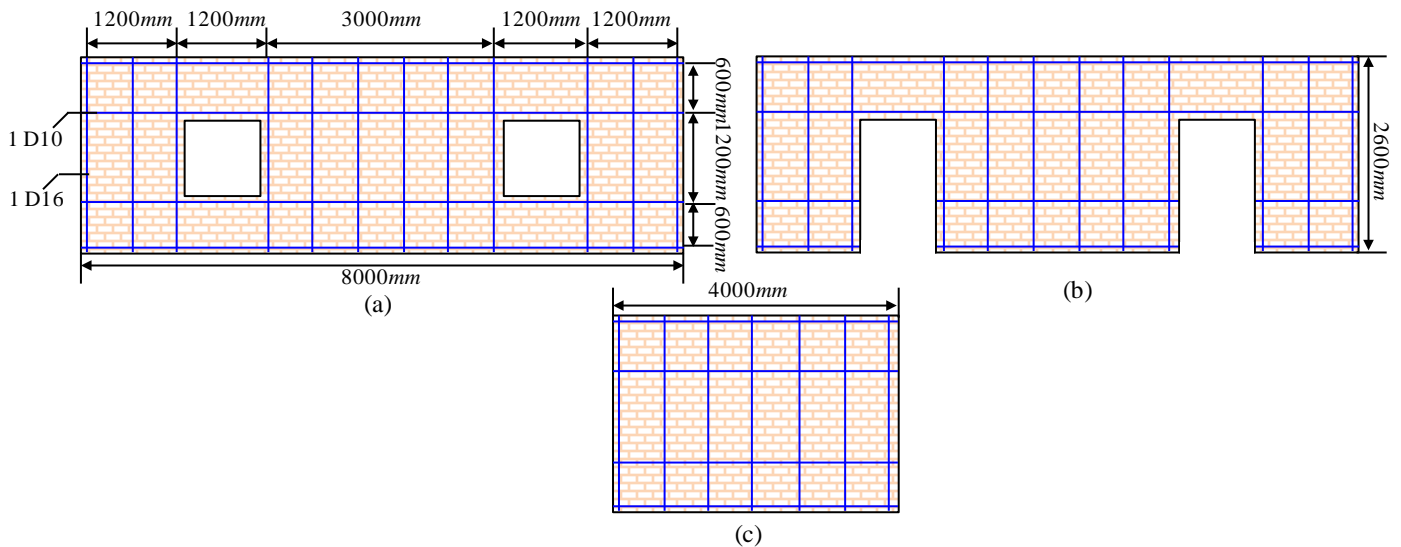


Figure 1: Structural detail; (a) Wall A; (b) Wall B; (c) Wall C

The design of the prototype building and its desired response was directed primarily by the capacity design guidelines outlined in the AS3700-2011 and AS1170.4-2007 code provisions. The adopted design for the prototype building aimed to provide (i) adequate strength, (ii) acceptable level of displacement ductility (min 2.0 for reinforced masonry structures as in Section 6.5, AS1170.4-2007) and (iii) sustain in seismic zones within hazard factor z of 0.3 (AS1170.4 – 2007), which covers majority of the metropolitan and regional Australia. All the component walls were reinforced to fulfil the code requirements for minimal reinforcement. Hence, a vertical and a horizontal reinforcement ratio of 0.002 (0.0023 for wall C) and 0.0008, respectively were used. The same reinforcement detailing (reinforcement spacing, rebar area) was followed in all the

component walls [Figure 1] considering the practicability and ease in construction. Both the vertical and the horizontal reinforcements were equally spaced at 600mm c/c , except those next to the window/door openings. Vertical/horizontal reinforcing bars were provided within 100mm from the structural end of the wall and next to the openings. The horizontal reinforcement band located both above the door and, above and below the window openings contented the lintel band requirements and provided sufficient stability to the walls.

The building was designed for ordinary residential dwelling considering structural importance level 2 (AS1170-2002), a service life span of 50 years and to carry live load of 4kPa . The bottom edge of the ground floor walls were assumed fixed through monolithic connection with the base slab, a common practice for RM walls. Moreover, all the wall intersections was expected to provide full moment resistance.

EXPLICIT FINITE ELEMENT MODEL

The explicit finite element (EFE) model recently developed by the authors is adopted in this study. The model uses a four noded triple – layered shell element (S4R) with seven – point Simpson's integration for each layer. Both the exterior layers of the element representing the masonry face shells was assigned with elastic-plastic unreinforced masonry material properties [Figure 2]. The masonry material model was developed using a user-material model VUMAT subroutine and was written in ABAQUS/Explicit algorithm. The intermediate layer representing the fully grouted cores was assigned with the damaged plasticity material model for concrete. Reinforcement was smeared within the shell section at the designated locations as per the adopted design detail shown in Figure 1.

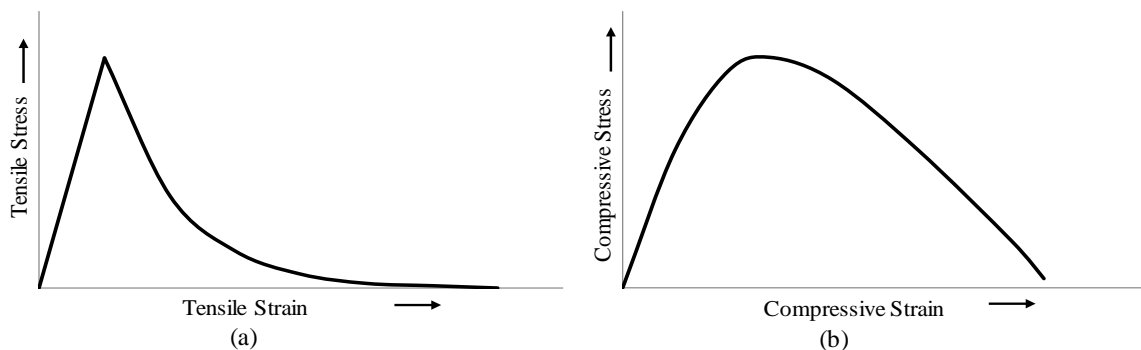


Figure 2: Masonry material response to (a) uniaxial tension; (b) uniaxial compression

The EFE model parameters are calibrated using the four point bending test dataset of a fully grouted reinforced masonry wall of size 1.22m long \times 2.64m high \times 0.15m thick (Abboud et al. (1996)). Details of the model validation is reported in Noor-E-Khuda et al. (2016b). The wall consisted of 2#5 bars (2-16mm) as vertical reinforcements at 610mm centers and 4#3 bars (4-10mm) as horizontal reinforcements at 810mm centres at mid thickness, the adopted reinforcement detail of the prototype building is consistent with the validated model.

Material properties of block, grout and steel considered for the prototype building are identical to those used in Abboud et al. (1996). Double cored hollow concrete block of dimensions 396mm long \times 193mm high \times 143mm thick with face shell thickness of 31mm was considered in all the

walls. Moreover, a premix grout consisting of one part of Type II portland cement, three parts of sand and two parts of 10mm gravel pea coarse aggregate was considered. The compressive strength and the strain corresponding to the maximum stress in masonry were 11MPa and 0.0013 and that of the grout were 18MPa and 0.0018, respectively. The modulus of rupture of grout was 1.9MPa, just over 10% of its compressive strength (18MPa). Steel reinforcement was considered Grade 60 steel conforming to ASTM – A615-84a specifications; the yield stress, modulus of elasticity and yield strain were 462MPa, 174GPa and 0.00267, respectively. The EFE model was shown to accurately predict the deformation, failure and ultimate capacity of in-plane (Haider and Dhanasekar (2008)) and out-of-plane [Noor-E-Khuda (2016 a & b)] loaded reinforced masonry walls.

FE BUILDING MODEL

The finite element mesh of the building model is shown in Figure 3. The 3D model consisted of total 15 walls and 3 roof slabs. Each component FGRM wall was modelled separately using the layered shell element (S4R). The wall-wall and wall-slab-wall interfaces were simulated as perfectly tied. One of the primary challenges in RM modelling is the complications inherited with different materials and as so achieving computational economy. Discretely defining horizontal and vertical reinforcement, and their interfaces on a full-scale building structure seemed time intensive, complicated and tedious. Hence, a smeared definition of the vertical and the horizontal reinforcements was adopted in the EFE model aiming computational efficiency. There were 20238 elements, 21375 nodes and 128250 degrees of freedom in the FE building model. Meshing details of the component walls is given in Table – 1. Under lateral loading the concrete slabs were expected to act as rigid diaphragm and therefore was modelled using R3D4 rigid elements. The bottom horizontal edge of the building marked with the red shades in Figure 3., was fully constrained (i.e., all six translational and rotational degrees of freedom were arrested) to replicate the full moment connection of the RM case.

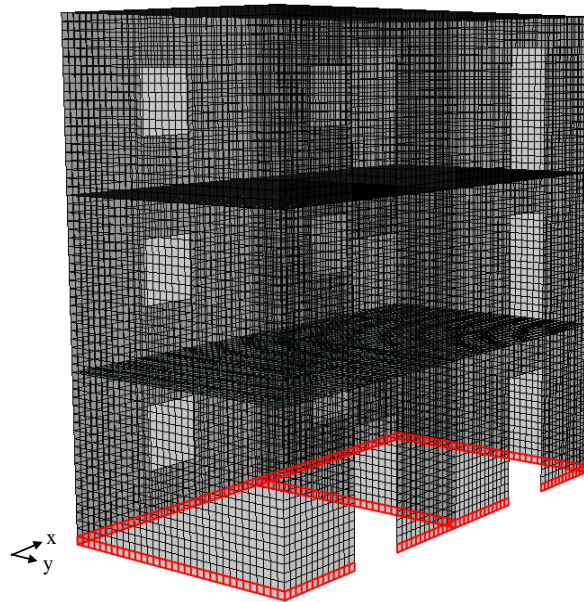


Figure 3: Finite element mesh

Table 1: Finite element mesh detail of component walls

| Component | Element | Node | DOF |
|-----------|---------|------|------|
| Wall (A) | 1346 | 1466 | 8796 |
| Wall (B) | 1234 | 1354 | 8124 |
| Wall (C) | 704 | 759 | 4554 |

FREQUENCY ANALYSIS

Figure 4 shows the vibration mode shapes (mode 1 & 2) of the building structure obtained from subsequent linear elastic buckling and frequency analysis, using ABAQUS. The eigenvalue of the structure in the first and second mode were 150.2 and 194.4, respectively; and the corresponding natural frequencies were 17.66Hz and 19.22Hz, respectively. From the mode shapes [Figure 4], it can be seen that the top floor walls experienced the maximum displacement in the out-of-plane bending mode. Walls located along the plane of loading experienced the least lateral displacement thence expected to provide maximum load resistance. The performance of the prototype building against lateral displacement applied along the y – and the x – axis direction was identified as the critical response.

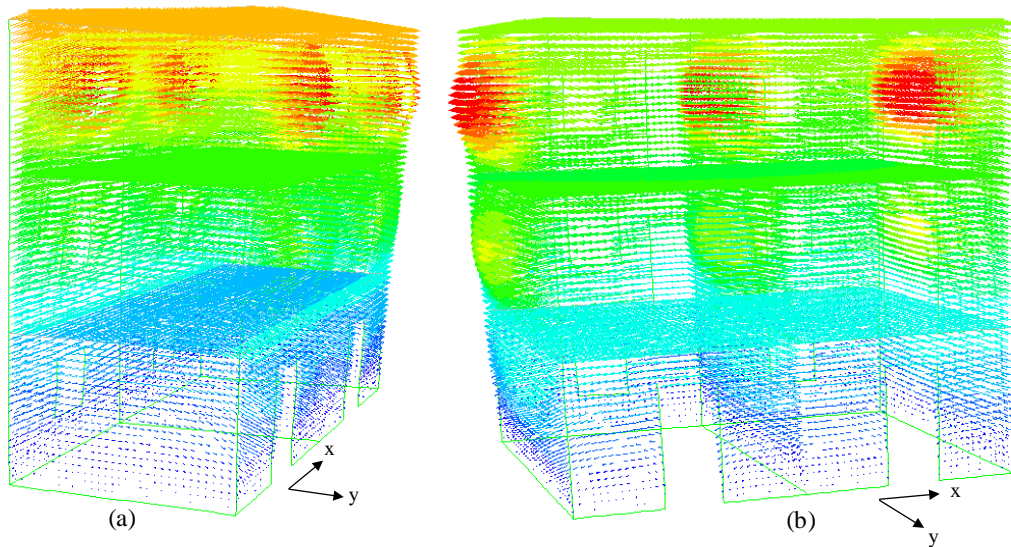


Figure 4: Mode shape obtained from frequency analysis (a) Mode 1; (b) Mode 2

LOADING

All the gravitational and lateral load was applied through the rigid body reference point located at the geometric center of the slab. In the first step, all the superimposed live and dead load from walls/slabs above was gradually applied on the respective storey level which was kept constant throughout the subsequent steps. In the second step, quasi-static lateral displacement was applied through the reference point located on the roof slab, which was linearly increased until the end of the analysis. Separate analysis were performed to investigate the structural response of the

prototype building when loaded along the x – and the y – axis direction, respectively. Each building model was run in the high performance computing facility with generous allocation of CPUS for a set time period of 168 hours, and the outcomes were analysed thereafter.

STRUCTURAL PERFORMANCE OF PROTOTYPE BUILDING

The structural performance of the prototype building under varying loading directions are discussed under this section. Key parameters used in the structural response assessment i.e., base shear, stiffness, ductility and failure modes are covered.

Results from the FE analysis are presented in Figure 5. in-terms of the resisted lateral load and the top floor displacement.

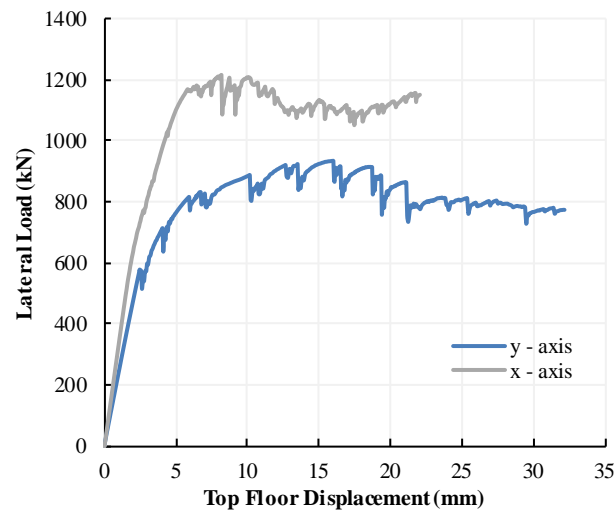


Figure 5: Base shear – top floor displacement

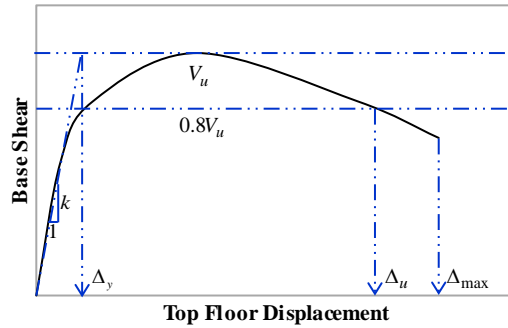
The lateral load presented along the vertical axis of the plot [Figure 5] was calculated as the sum of the reaction forces of the component walls at the ground floor level of the building. It can be seen that the FE model rationally predicted the capacity of the prototype building with varying loading directions. The predicted ultimate load capacity of the structure when loaded along x – and y – axis directions were 1210kN and 933kN, respectively. The critical load was found when the building was loaded along the shorter direction (y – axis) which is in conformity with the frequency analysis outcomes. The building offered the least lateral resistance (22.9% lower than the x-axis direction) when loaded along the y-axis direction.

The influence of the loading direction on the structural performance of the prototype building is discussed under this section. Key structural parameters namely the ultimate load capacity, yield and ultimate displacement, stiffness and ductility demand of the building structure were checked for the seismic performance assessment, shown in Table – 2.

Table 2: Displacement ductility and stiffness of the building

| Direction | V_u (kN) | $0.8V_u$ (kN) | Δ_{max} (mm) | Δ_y (mm) | k (kN/mm) | μ |
|-----------|------------|---------------|---------------------|-----------------|-------------|-------|
| x – axis | 1210 | 968 | 22.06 | 4 | 302.8 | 5.52 |
| y – axis | 933.4 | 746.7 | 32.18 | 4.75 | 196.5 | 6.31 |

The definitions of the ultimate load capacity (V_u), maximum top floor displacement (Δ_{max}) and displacement corresponding to 80% strength capacity (Δ_y, Δ_u) used in the structural performance assessment are shown in Figure 6.

**Figure 6: Idealised load-displacement curve**

The design base shear demand (V_d) of a similar structure constructed at different locations in Australia are measured within the provisions outlined in AS1170.4-2007, is given in Table – 3. The base shear demand demonstrates the adequacy of the adopted design of the prototype building.

Table – 3: Design base shear as per AS1170.4 – 2011

| Location | Z | V_d (kN) | Location | Z | V_d (kN) |
|-----------|------|------------|------------------|------|------------|
| Adelaide | 0.1 | 176.1 | Perth | 0.09 | 158.5 |
| Brisbane | 0.05 | 88.1 | Sydney | 0.08 | 140.8 |
| Darwin | 0.09 | 158.5 | Christmas Inland | 0.15 | 352.1 |
| Melbourne | 0.08 | 140.8 | Cunderdin | 0.22 | 516.4 |

Based on the results shown in Figure 4. and Table – 3, it is obvious that the adopted structural design satisfactorily meets the design seismic load demand in most Australian locations. The lateral load resistance offered by the prototype building was 70% higher than the design base shear demand for a similar structure constructed in Cunderdin, WA. The adopted structural design also fulfilled the displacement ductility requirement of 2.0 for RM buildings.

FAILURE MODE

A brief overview of the structural damage of the prototype building is shown in Figure 7. The logarithmic strain developed in all three stories of the structure at the end of the analysis is presented. Figure 7. (a) and (b) show the structure when loaded along the y- and x-axis directions, respectively. For preciseness strain above the cracking strain of masonry (0.0025) is shown in the plot.

When the prototype building was loaded along the y-axis direction as shown in Figure 7 (a), damage to the structural components of the building was limited to the ground floor region only. Failure of the structure initiated with formation of bed joint cracks next to the window openings on wall B in an out-of-plane mode. Under increased loading, bed joint and diagonal cracks was noticed on the adjacent in-plane walls (wall C).

On the contrary, when the prototype building was loaded along the x-axis direction as shown in Figure 7 (b), all the in-plane walls (wall A & B) experienced combined diagonal and bed joint cracking along the bottom course of the wall. Intensity of cracking was maximum at the ground floor level, although, cracking on walls at other stories could be noticed. Tensile uplift along the bottom course of wall C in an out-of-plane mode was seen in all three stories.

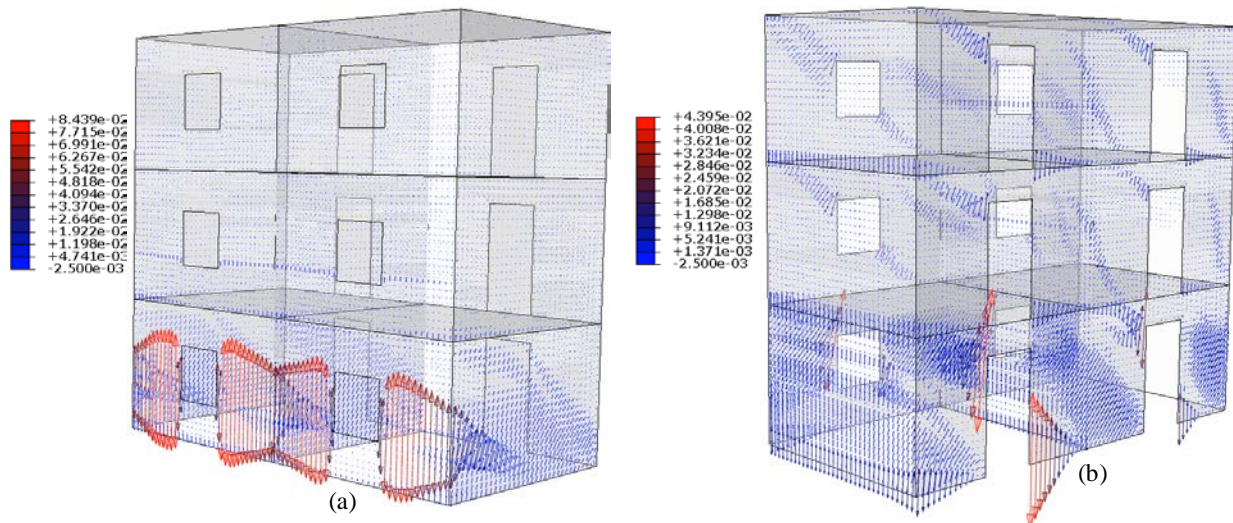


Figure 7: Logarithmic strain plot of building loaded along (a) y-axis; (b) x-axis

CONCLUSIONS

Structural performance of a detail designed fully grouted reinforced masonry (FGRM) prototype building under lateral loading is reported in this paper. The structural design of the building was selected within the design provisions of AS3700-2011. The study was conducted using an explicit finite element (EFE) model where masonry is defined as elastic-plastic macroscopic material. The validated EFE model was used to investigate on the structural performance of the building in terms of load capacity, stiffness and ductility. The EFE model demonstrated its strength and rationally predicted the structural performance of the multi-storied FGRM prototype building loaded along

the alternate x- and y- axis directions. The critical load capacity was observed when the building was loaded along the shorter y – axis direction. The adopted design detail provided sufficient load capacity to the prototype building against the design demand load.

ACKNOWLEDGEMENTS

The authors gratefully acknowledge the software and high performance computing support provided by CQU-HPC team.

REFERENCES

- Abboud, B. E., Hamid, A. A., and Harris, H. G. (1996). Flexural behavior of reinforced concrete masonry walls under out-of-plane monotonic loads. *ACI Structural Journal*, 93.
- AS (Australian Standard). (2007). Structural design actions – Part 4: Earthquake actions in Australia. AS 1170.4, Sydney, Australia.
- AS (Australian Standard). (2011). Australian Standard of Masonry Structures. AS 3700, Sydney, Australia.
- Bolhassani, M., Hamid, A., Johnson, C., Moon, F., and Schultz, A. E. (2016). New design detail to enhance the seismic performance of ordinary reinforced partially grouted masonry structures. *Journal of Structural Engineering (ASCE)*, 142, 04016142.
- Dhanasekar, M., and Haider, W. (2008). Explicit finite element analysis of lightly reinforced masonry shear walls. *Computers and Structures*, 86, pp. 15-26.
- Dhanasekar, M., Thambiratnam, D. P., Chan, T., Noor-E-Khuda, S., and Zahra, T. (2016). Modelling of masonry walls rendered with auxetic foam layers against vehicular impacts. *16th International Brick and Block Masonry Conference*, Padova, Italy.
- Dhanasekar, M., Zahra, T., Jelvehpour, A., Noor-E-Khuda, S., and Thambiratnam, D. P. (2015). Modelling of auxetic foam embedded brittle materials and structures. *The 2nd Australasian Conference of Computational Mechanics (ACCM 2015)*, Brisbane, Australia.
- Lourengo, P. B. (2000). Anisotropic softening model for masonry plates and shells. *Journal of Structural Engineering (ASCE)*, 126, 1008-1016.
- Noor-E-Khuda, S. and Dhanasekar, M. (2017). Masonry walls under combined in-plane and out-of-plane loadings. *Journal of Structural Engineering (ASCE)*. (In-press)
- Noor-E-Khuda, S. (2016). Studies on the out-of-plane behaviour of masonry walls. *PhD Thesis*, Queensland University of Technology, Brisbane, Australia

Noor-E-Khuda, S., Dhanasekar, M., and Thambiratnam, D. (2016a). An explicit finite element modelling method for masonry walls under out-of-plane loading. *Engineering Structures*, 113, pp. 103-120.

Noor-E-Khuda, S., Dhanasekar, M., and Thambiratnam, D. P. (2016b). Out-of-plane deformation and failure of masonry walls with various forms of reinforcement. *Composite Structures*, 140, pp. 262-277.

EXPERIMENTAL STUDIES ON THE EFFECT OF GROUT CONFINEMENT TO THE REINFORCING BARS IN MASONRY WALLS UNDER CONCENTRIC COMPRESSION

M. Song¹ and M. Dhanasekar²

¹ PhD Candidate, School of Civil Engineering and Built Environment, Queensland University of Technology, QLD 4000, Australia, mengli.song@hdr.qut.edu.au

² Professor, School of Civil Engineering and Built Environment, Queensland University of Technology, QLD 4000, Australia, m.dhanasekar@qut.edu.au

The current provisions in the Australian masonry structures standard AS3700 (2011) expect the designers to provide lateral restraining steel reinforcement at spacing not more than the thickness of the wall in order for the vertical steel bars be accounted to resist compression in the reinforced masonry (RM) walls. With a view to examining the appropriateness of this provision, 64 walls of 0.8m, 1.4m and 2.4m heights with varied designs of reinforcement were constructed and tested under concentric compression. It was found that the walls with and without lateral restraining steel performed in a comparable manner. Evidence obtained indicates that the grout is more effective than the prescription of lateral reinforcement in the AS3700-2011.

Keywords: Reinforced masonry, Compression design, Reinforcement buckling & lateral restraining

INTRODUCTION

Masonry is one of the oldest construction materials widely used in residential buildings. The earliest research on reinforced masonry is dated back to 1836 (Roberts et al. 1986), and many reinforced brickwork buildings were constructed in France at the turn of the 19th century. It was observed that the addition of reinforcement can increase the resistance against tensile force from overturning effects and shear force in masonry wall. Steel reinforcement has been developed in various ways to strengthen the masonry structure, common forms are: horizontal reinforcement bars or wires, vertical reinforcement bar and ladder-type or truss-type mortar bed joint reinforcement due to its ease of availability at relatively cheaper prices (Aguilar et al. 1996; Gouveia et al. 2007).

In reinforced masonry, buckling of longitudinal steel bar is identified as one of the key features that can significantly reduce the functionality of structure (Berry et al., 2005). In order to maintain the stability of the steel bar, lateral ties are prescribed in design standards to provide horizontal constraints. However, in real on-site construction, the vertical reinforcements are provided without horizontal ties for reasons of the construction productivity. In this context, the RM walls are market-driven systems where bi-directional horizontal ties are rarely installed, which results in disregarding the contribution of reinforcement to the masonry compression capacity calculations. AS3700 (2011) requires satisfaction of the following criteria for the consideration of the contribution of the vertical steel reinforcement to the compression capacity of the RM walls:

- 1) The vertical steel bars should be located symmetrically in the cross-section;
- 2) The vertical steel bars must be laterally restrained in both horizontal directions by ties of not less than 6 mm diameter, which shall be spaced at centres not exceeding the least cross-sectional dimension of the member (usually thickness of wall) or 400 mm, whichever is the lesser; and
- 3) Have an area, $A_s \geq 0.002A_d$. Where A_s is the total cross-sectional area of vertical reinforcement, A_d denotes the cross-sectional area of the wall.
- 4) Reinforcement quantities in excess of $A_s = 0.04A_d$ shall be used only if the required minimum bar spacing and grout cover can be achieved, and the grout can be properly placed and compacted around the reinforcement.

If any of the aforementioned requirements is not satisfied, the structure shall be designed as unreinforced masonry (URM). As a result, for RM walls where not enough horizontal ties are installed, the contribution of the steel reinforcement will be totally disregarded. Hence, the extent to which the horizontal reinforcement can contribute to the stability of vertical reinforcement and the necessity of arranging horizontal steels become main interest to the masonry industry.

Compression behaviour of RM walls are only sparingly studied Feeg et al. (1979) and Kumar (1995) have examined the effect of vertical steel with various restraining lateral reinforcement for reinforced masonry columns and generally found that the reinforced masonry columns behaved similar to the reinforced concrete columns. Priestley and Elder (1983) studied the effectiveness of the lateral steel to confine the grout of the masonry with a focus on the seismic region application of masonry. Khalaf et al. (1993) through experimental studies on reinforced masonry columns concluded that the lateral restraining bars (similar to stirrups in RC columns) were effective and in the absence of such lateral restraining bars, the vertical bars failed due to buckling prior to failure of the masonry and grout.

Assa and Dhanasekar (2002) proposed a numerical model that explained the effect of the early cracking of mortar joint and bond-slip characteristics between the steel reinforcement and the masonry grout for short reinforced masonry columns under vertical and cyclic lateral loading. In addition, Mullins and Dux (2005) discovered that the compressive capacity was improved by adding reinforcing bars, and the wall exhibited a brittle failure similar to unreinforced blockwork. In 2010, another experimental study examined the concentrically loaded reinforced masonry prisms without lateral ties and it was concluded that the capacity of prisms with unrestrained reinforcement

get a limited increase of about 2% to 13% than the unreinforced prisms, and the failure phenomenon of both the RM and URM walls were identical (Soh, 2010).

This article describes a research program carried out to examine the performance of RM walls with and without different horizontal reinforcement detailing. 64 full scale wall specimens were constructed and tested under monotonous concentric load to investigate the effect of lateral confinement to the compressive behaviour of the vertical steel reinforcement embedded in masonry walls.

SPECIMEN PREPARATION

Test specimens were prepared to examine the effect of slenderness and lateral steel reinforcement provisions as shown in Table 1. All the specimens with 3 different heights were constructed by a professional bricklaying crew of average skills. The cross-section dimensions of all the wall specimens were 600mm long \times 190mm thick \times 800mm / 1400mm / 2400mm high. Two specimens were built for each combination of influence factors (refer to Table 1) as replicates for repeatability of the experimental investigation.

Table 1: Summary of Influence Factors

| Influence Factors | Explanation | Representative Values | Number of Specimens |
|-----------------------------|--|-----------------------|---------------------|
| Slenderness of wall | The ratio of the height (H) to the thickness (T) of the wall | 4.2 | 28 |
| | | 8.4 | 18 |
| | | 12.6 | 18 |
| Lateral steel reinforcement | No lateral steel | | 6 |
| | One direction | 200mm | 8 |
| | | 400mm | 8 |
| | | 800mm | 4 |
| | Two directions | 200mm | 8 |
| | | 400mm | 8 |
| | | 800mm | 4 |

The material properties are listed in Table 2. Both half block and full standard hollow block were employed for mortared masonry walls. The face shell strength of masonry block strength was tested based on AS3700-2011. M3 mortar was mixed on site and was applied on face shell only. Grouts (max 12mm aggregate and 220mm slump) of strengths 20MPa or 25MPa were ordered for each batch of grouting – however, the strength of the delivered grouts varied significantly as shown in Table 2. Moreover, N16 deformed steel bars were used as vertical reinforcement, and R6 bars were used as horizontal reinforcements of both directions to tie the vertical bar with tie wires. The characteristic compressive strength (f'_{mb}) is determined as 5.43 MPa according to Table 3.1 of AS3700-2011, and Joint thickness factor (k_h) is 1.3 according to Table 3.2 of AS3700-2011.

Table 2: Material Properties for Masonry Wall Construction

| Material | Dimension / mm | Strength / MPa |
|--------------------|-------------------|-------------------|
| Masonry Half Block | 190mm×190mm×190mm | 11.5 |
| Masonry Full Block | 390mm×190mm×190mm | |
| N16 Deformed Bar | 16 mm diameter | 500 |
| R6 Round Bar | 6 mm diameter | 250 |
| Concrete Grout | - | 25 / 30 / 35 / 47 |

Each core of the wall specimens was reinforced with one N16 steel bar. In order to investigate the effect of different level of horizontal restraint to the vertical bars, three methods of placement of reinforcing were designed, and classified as grouted walls (as shown in Figure 1(a), (b), (c)) and un-grouted walls:

Grouted walls:

- RM wall with only vertical reinforcing bars (no horizontal reinforcement and ties)
- RM wall with vertical reinforcing bars tied with horizontal steel bars along the length direction of the wall at different spacing (200mm/ 400mm/ 800mm)
- RM wall with vertical reinforcing bars tied with horizontal steel bars along both the length and thickness directions of the wall at different spacing (200mm/ 400mm/ 800mm)

Un-grouted walls:

- RM wall with vertical reinforcing bars tied with horizontal steel bars along both the length and thickness directions of the wall at 200mm spacing. (NOTE: This type of wall specimens was constructed and tested to assess the effect of grout to the compression capacity of the RM walls, although such walls would never be practiced in real buildings.)

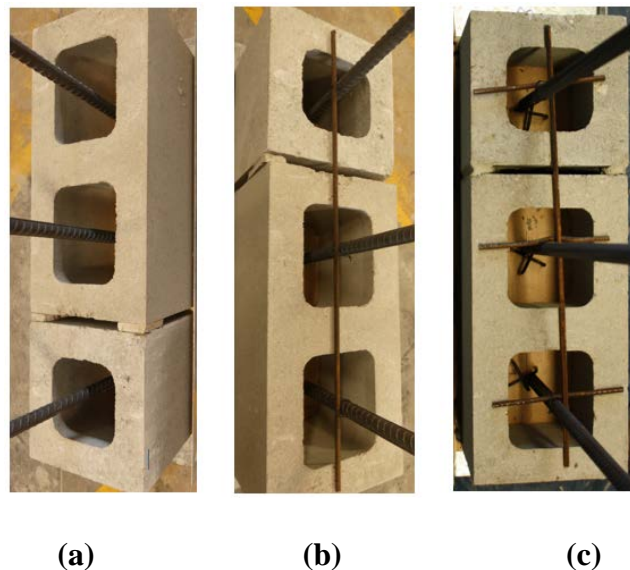


Figure 1: Different reinforcement provisions (a) Only vertical bars; (b) Vertical bars with one direction horizontal bar; (c) Vertical bars with two direction horizontal bars

Specimens were labelled based on the presence or absence of grout, reinforcement setting, specimen height, for example, G30-V1HT(U)-400-800, stands for a 800mm specimen constructed with 30MPa grout, and vertical reinforcements were tied (untied) only in the length direction with the spacing of 400mm. If no horizontal steel was installed, the symbol shall be G30-V0HU-000-800.

To avoid direct contact between the vertical steel bars and the loading platens, the length of the bar was designed shorter than the specimen height in this research. As a result, a vertical clearance of 20mm – 25mm was maintained between the ends of the bar and the ends of the specimen.

A verticality control jig was developed to ensure each steel bar was positioned vertically at its designated location, during laying of each block. Levelling ruler was also used to check the verticality of the bar, as shown in Figure 2(a). Before grouting, soft silicon glue and foam were used to seal the gaps between the web shells at two horizontal ends of the specimen to prevent spilling of the grout through these gaps. The grout was sampled and tested for slump and concrete cylinders were fabricated to carry out strength test after curing and hardening of the cylinders. The grouts in the cores were slightly under-filled to ensure no grout protruding after hardening. After grouting, compaction was accomplished and the top surface of specimen was then covered with plastic cling to provide wet curing environment.

After 28 days curing, cover cling wraps were removed, and epoxy resin – sand mix was spread into the under-filled cores such that the top level is flush with the top surface of the specimen as shown in Figure 2(b). Before testing, plywood strips were inserted in between the loading platens and top and bottom end of the specimen to ensure compressive load was applied uniformly to the full cross section of the specimen.



(a) (b)
Figure 2: (a) Vertical control jig; (b) Top surface flattening with epoxy

EXPERIMENTAL DETAILS

The Loading Portal Frame is shown in Figure 3. The frame was designed to fit the tallest of the walls (2.4m high). A servo-controlled hydraulic actuator was used to provide monotonic static load with 1mm per minute loading rate.

A load cell of 5000kN capacity was mounted under the actuator to record the applied load to the specimens. All specimens were designed with pin-pin boundary condition. The pin end was designed to have two loading plates clamping a steel cylinder, which enabled one direction free rotation of the steel plate connecting to the specimen. L-shaped clamping plates are bolted onto the loading plate to align the centre of the specimen with the centre of the actuator. Displacement control was used with the loading rate set as 1mm per minute. One string pot was used to record the displacement of the travel of actuator, and the compressive load was recorded by a loading cell. Data were recorded and processed in the form of Load cell - Strain gauges.

Testing was stopped when 20% loss of peak load or heavy spalling of face shells or instability of the wall, whichever came first. More than 90% specimens were stopped after the load reduced by at least 20%; Less than 10% of specimens exhibited spalling and two specimens were wrongly tested without removal of the safety steel straps. Time taken to failure varied with different height of specimens, around 5 to 8 minutes.

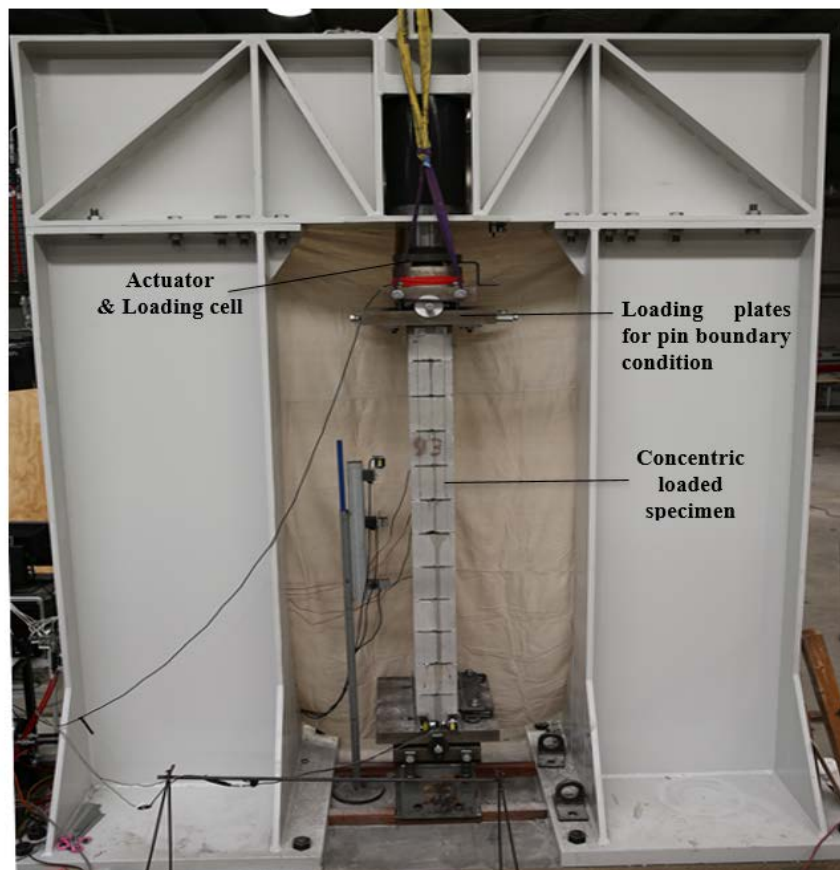


Figure 3: Testing layout for concentric loaded specimens

Steel bars in one of the two replicates of the specimens were strain gauged. Two or three strain gauges were attached at the mid-height of each of the three steel bars for the 800mm and 1400mm specimens; steel bars in the 2400mm high specimens were fitted with strain gauges at sections of $1/3^{\text{rd}}$ and middle height; the layout of strain gauges was kept the same as in Figure 4. Location for each strain gauge was milled flat first and cleaned to remove any debris prior to attaching the strain gauge and then waterproofed. The strain gauges had pre-attached wires from the factory. The wires were taken through the gap between the two courses of the web shells as shown in Figure 4c.

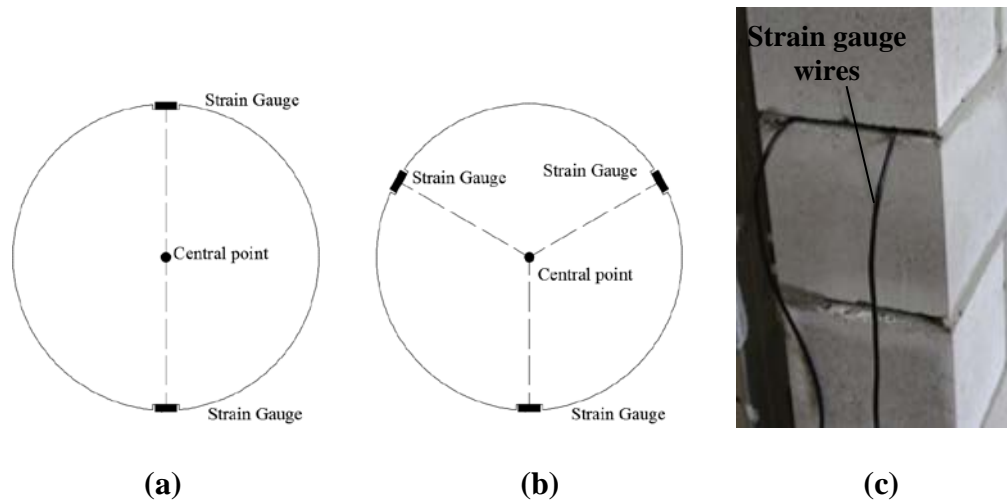


Figure 4: Instrumentation: steel bar cross section layout with (a) two strain gauges; (b) three strain gauges; (c) Strain gauge wires arrangement

FAILURE MECHANISM

Cracks parallel to the direction of loading initiated either at the face shell below the head joint, or below the bed joint mortar with face shell rapturing as illustrated in Figure 5. With the increase of the compression (displacement control), the vertical cracks progressed further. At the same time, cracking noise of the concrete grout was heard, and vertical crack was identified from the exposed grout surface. Moreover, at the two side surfaces which were the narrow surfaces of the wall, web shells exhibited deep beam action.

Cracked face shells did not fell apart due to the bonding with the grout; bond failure between the face shell and the grout was observed occasionally only at the top layer of the specimens, which might have been caused due to insufficient compaction. Moreover, no bonding failure between the steel bar and the grout was observed after the grout was broke opened. Had the bar buckled, bond could have been broken – lack of evidence of such bond failure shows the steel bar – grout system behaved as a composite rather than as individual components, thereby providing support for the hypothesis with which the research was initiated.

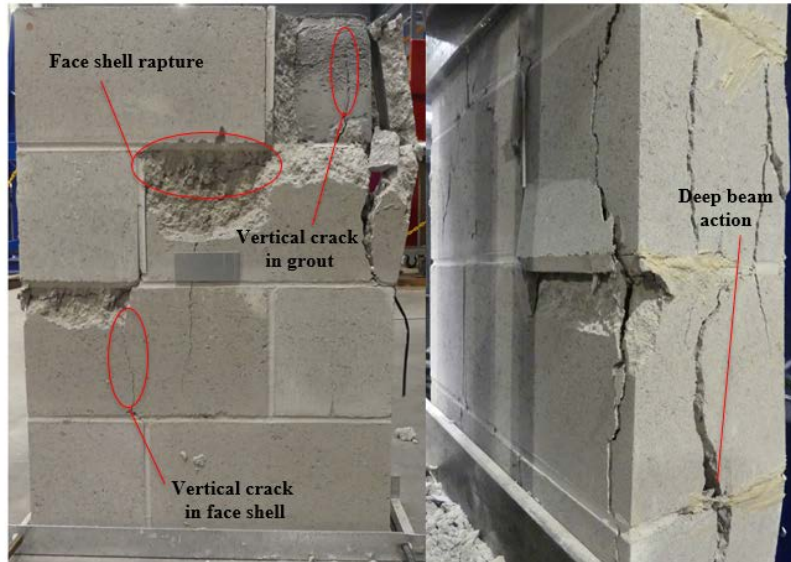


Figure 5: Typical failure phenomenon of RM walls

BEHAVIOUR OF VERTICAL STEEL REINFORCEMENT

The strain of the steel bars when the specimen reached its peak load ($\epsilon_{\text{steel,max}}$) was analysed and presented in Figure 6. Note some strain gauges delaminated or failed to show data – only data from 33 specimens were plotted in this figure. The majority of the steel strains were in the range of 0.002 (corresponds to 400 MPa) and 0.0008 (corresponds to 160 MPa), only few steel bars showed the yielding strain 0.0025 (corresponds to 500 MPa). Thus, it is clear that the strength contribution from the vertical reinforcement when the specimen reach the peak load is limited. No clear tendency can be identified about the effect of different horizontal reinforcement arrangement to the stress level of vertical steel bar and that the stress level randomly varies with different horizontal steel reinforcement.

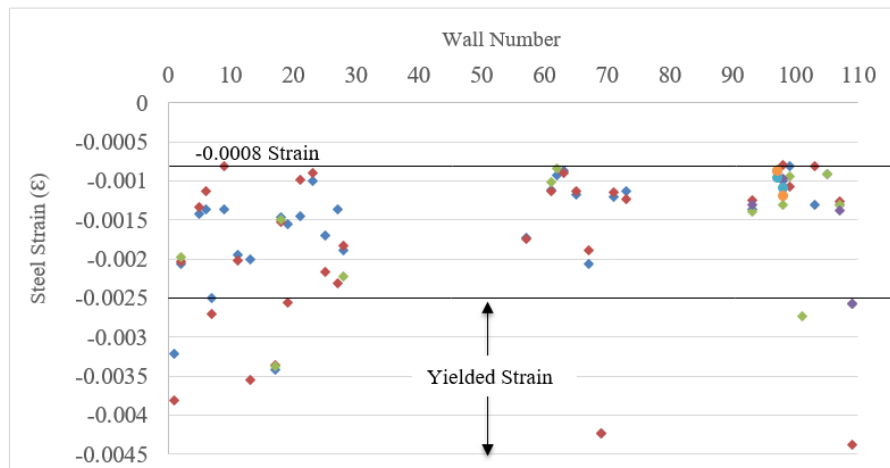
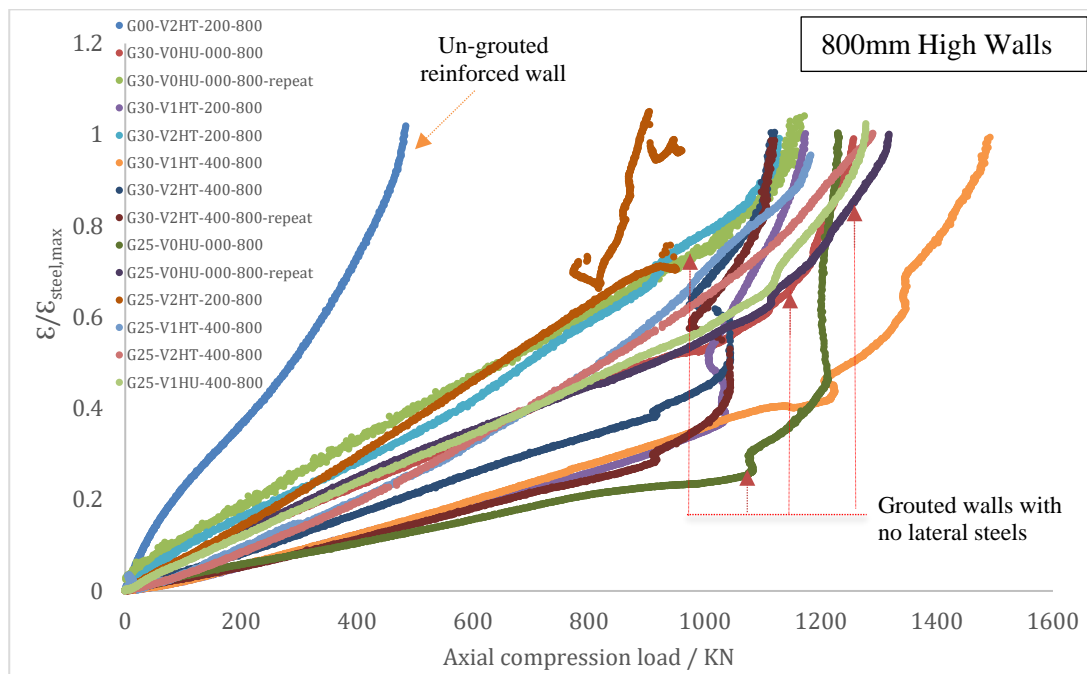


Figure 6: Steel strain when at load bearing capacity of the specimen

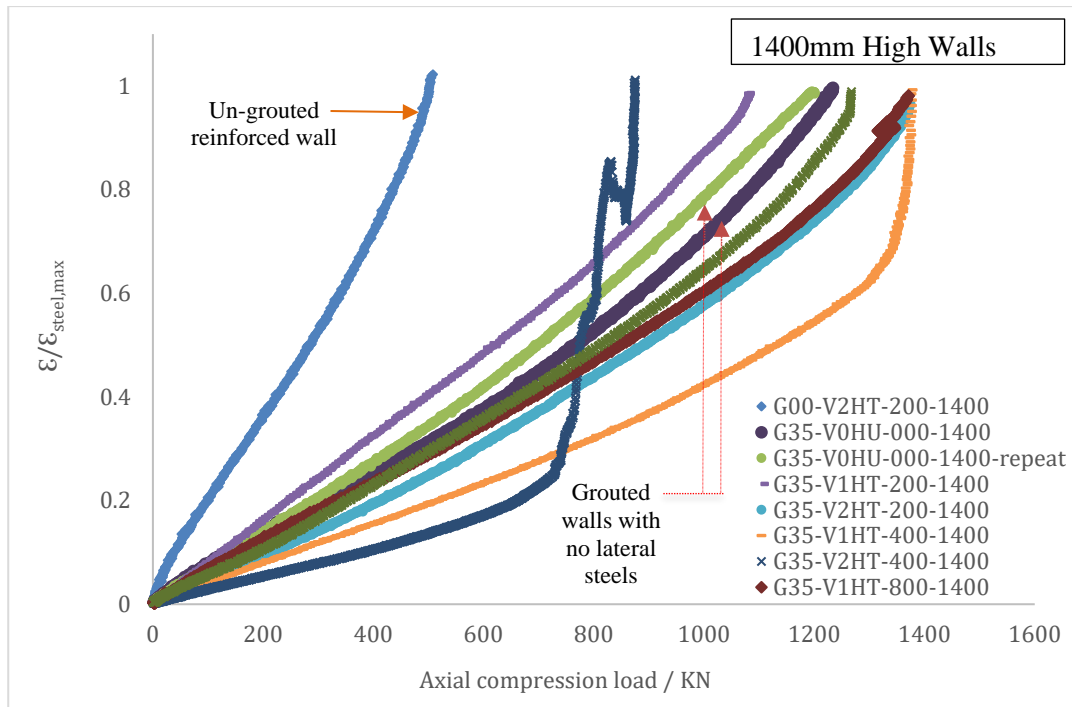
In Figure 7, the normalised strain of steel bars with varied lateral reinforcement patterns are plotted against the compression load (up to the peak load of each specimen) for the 800mm/ 1400mm and 2400mm high walls separately. With the increase in axial compression, the steel strains (non-dimensionalised) increased. In the 800mm high walls, the slope of the curves increased beyond the load of approximately 1000kN owing to cracking in face shell and grout. The 1400mm and 2400mm high walls did not show such a distinct change in slope; however, the increase in steel strain was gradual. Had the bars been buckling, such increase in strain would not have occurred in these steel bars. This result confirms that the bars did not buckle as an independent component – but worked effectively as a composite with the grout; the grout in turn confined the steel bars effectively preventing them from buckling.

The plot also shows that the non-dimensionalised strain of the un-grouted reinforced masonry specimens. These specimens contained lateral steel at 200mm spacing – but were not grouted. Owing to the absence of grout, their ultimate load was lower – but the steel with lateral confining steel on both direction (length and thickness) behaved similar to the steel bars in the grout with or without lateral steel. There was some variability – but all grouted specimens (irrespective of the presence or absence of lateral steel) behaved as identical samples representing a ‘grouted reinforced masonry’ population.

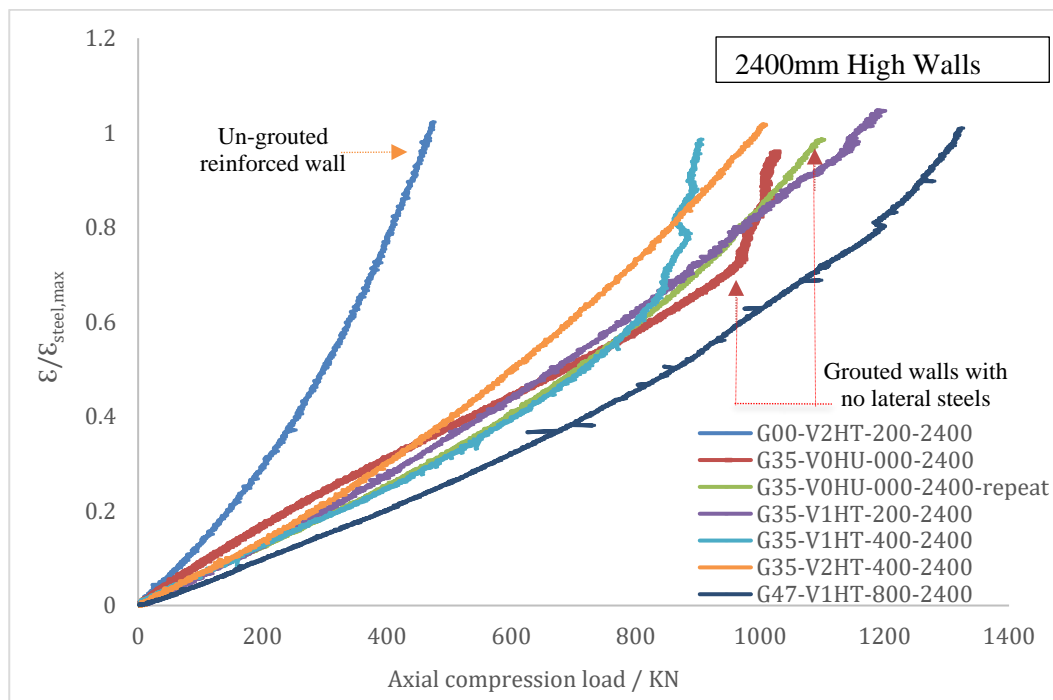
These data indicate that installing lateral reinforcement does not modify the performance of steel reinforcing bars. Furthermore, the steel bars with no lateral confining steels (just confined by the grout) developed strain in a comparable to the bars with lateral steels. Thus, it can be ascertained that the grout around the steel bar can provide sufficient lateral confining effect to the vertical steel until the wall attains peak load.



(a)



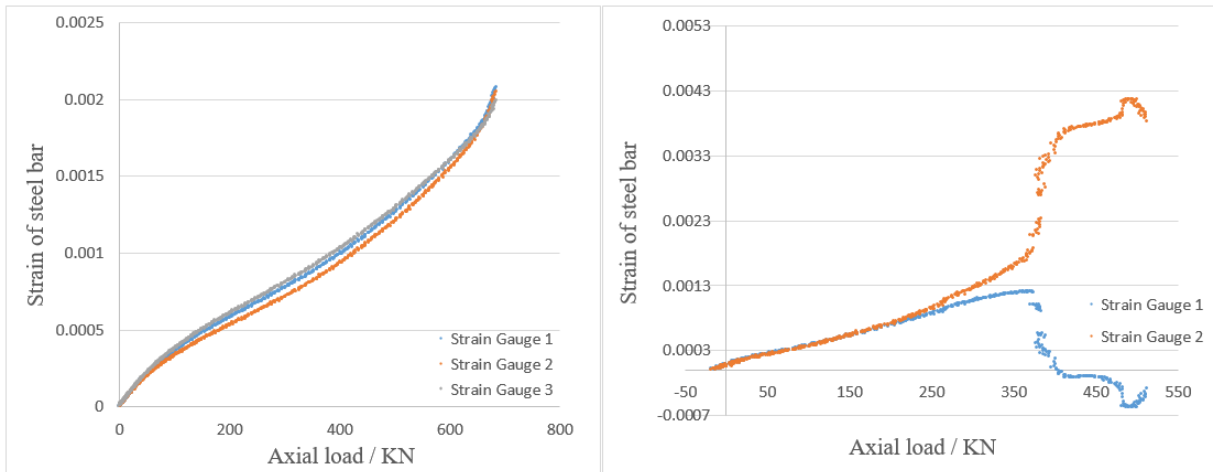
(b)



(c)

Figure 7: Steel strain/maximum strain vs. axial compression load of (a) 800mm walls; (b) 1400mm walls; (c) 2400mm walls

Three out of the four un-grouted walls for each height (800mm/ 1400mm/ 2400mm) showed no buckling phenomenon before the specimen reached its peak load, bar-buckling happened in a 800mm wall, as shown in Figure 8(b). Thus, it can be concluded that the lateral steel reinforcements provided conforming to the AS3700-2011 cannot always effectively prevent bar buckling.



(a) **(b)**
Figure 8: Strain vs. load behaviour of steel bar at middle height of un-grouted masonry (a) specimen without steel buckling; (b) specimen with steel buckling

CONCLUSIONS AND RECOMMENDATION

Effectiveness of grout and lateral restraining steel was studied for reinforced masonry walls through experimental research, the following conclusions were drawn:

- 1) It was observed that the grouted RM walls with and without lateral restraining steel performed in a similar manner.
- 2) No steel bar buckling was observed when only grout was used to provide the lateral restraining.
- 3) It is safe to conclude that without any horizontal restraining, the compacted grout alone can effectively provide lateral restraint for the vertical steel bars and that the current provisions related to reinforced masonry design in AS3700-2011 underestimate the confining effect of grout, further modification for the provisions is recommended to consider the outcomes of this research.

ACKNOWLEDGMENTS

This study is part of a research program funded by the Concrete Masonry Australia Association (CMAA); their financial support is gratefully appreciated. The support of Adbri Masonry in providing masonry blocks is also gratefully acknowledged.

REFERENCES

- Assa, B., & Dhanasekar, M. (2002). A numerical model for the flexural analysis of short reinforced masonry columns including bond-slip. *Computers and Structures*, 80, 547–558.
- Berry, M. P., & Eberhard, M. O. (2005). Practical performance model for bar buckling. *Journal of Structural Engineering*, 131(7), 1060-1070.
- Feeg, C., Longworth, J., Warwaruk, J., (1979), Effects of reinforcement detailing for concrete masonry columns, *Structural engineering research report 76*, University of Alberta, Canada.
- Gouveia, J. P., & Lourenço, P. B. (2007). Masonry shear walls subjected to cyclic loading: influence of confinement and horizontal reinforcement.
- Roberts, J. J., Edgell, G. J., & Rathbone, A. J. (1986). Handbook to BS 5628: part 2. Viewpoint Publ., Palladian Publ. Ltd., London.
- Khalaf, F. M., Hendry, A. W., & Fairbairn, D. R. (1993). Reinforced blockwork masonry columns. *American Concrete Institute Structural Journal*, 90(5), 496-504.
- Kumar, M. (1995), Development of reinforced clay block masonry columns subjected to concentric and eccentric compression, *ME Thesis, Central Queensland University*, Australia.
- Mullins, P. J., & Dux, P. (2005). Compressive strength of reinforced concrete masonry walls. In *Application of Codes, Design and Regulations: Proceedings of the International Conference held at the University of Dundee, Scotland, UK on 5–7 July 2005* (pp. 773-780). Thomas Telford Publishing.
- Priestley, M.J.N and Elder, D.M. (1983), Stress-Strain Curves for Unconfined and Confined Concrete Masonry, *ACI Journal*, 80, 192 - 201.
- Soh, L.T. (2010) Strength of concrete block masonry with unrestrained reinforcement, *PhD Thesis, University of Queensland*, Australia.
- STANDARDS AUSTRALIA. (2011). AS3700 Masonry structures. Sydney, *Standards association of Australia*.
- Zong, Z., Kunnath, S., & Monti, G. (2013). Simulation of reinforcing bar buckling in circular reinforced concrete columns. *ACI Structural Journal*, 110(4), 607.
- Zong, Z., Kunnath, S., & Monti, G. (2013). Material model incorporating buckling of reinforcing bars in RC columns. *Journal of Structural Engineering*, ASCE, 140(1), 04013032.

ANALYSIS OF THE INFLUENCE OF HORIZONTAL REINFORCEMENT AND EFFECTIVE HEIGHT ON THE PEAK STRENGTH OF MASONRY SHEAR WALLS

S. Rizaee¹ and N.G. Shrive²

¹ PhD. Student, Civil Engineering Department, University of Calgary, 2500 University Drive NW, Calgary, AB, Canada, srizaee@ucalgary.ca

² Professor, Civil Engineering Department, University of Calgary, 2500 University Drive NW, Calgary, AB, Canada, ngshrive@ucalgary.ca

The amount of horizontal reinforcement in a masonry shear wall is believed to affect directly the shear strength of the wall. This may be seen from the strength equations in different codes such as CSA S304.1-14, ACI 530-08, AS 3700-2001, NZS 4230:2004, Eurocode 6, BS 5628-2:2005, and models (e.g.: Anderson and Priestley (1992) and Voon and Ingham (2007)). However, according to several recent studies (e.g.: Oan (2015), Hidalgo-Leiva (2016)), horizontal reinforcement does not increase the strength of a shear wall but acts to maintain integrity and strength in the wall after the peak load has been reached. We compare the peak strengths of walls in three sets of experiments. The results suggest that the peak strength is not influenced by the amount and distribution of horizontal reinforcement. The question therefore arises as to why all the codes include shear reinforcement in the estimation of the strength of a masonry shear wall if that reinforcement contributes only after peak load is reached. We also show that the effective height (from varying test boundary conditions) has a direct influence on the shear strength of the wall being tested, which is not reflected in the equations. In addition, some codes and models relate the shear strength of masonry to the applied moment and shear force at the section under consideration or to the height to length ratio of the wall, through a factor of $\frac{M}{Vdv}$ or $\frac{H}{L}$ respectively. This is contrary to limit states philosophy – the strength of the masonry is a material property and should not change with location in the wall: the load at which the masonry fails should depend on the applied loading and wall geometry.

Keywords: masonry shear walls, horizontal reinforcement, partially grouted, influence of effective height

INTRODUCTION

There have been numerous studies on the influence of steel reinforcement on the performance of masonry shear walls beginning with studies like those of Schneider (1959) and Scrivener (1967). More recent studies in this area include those by Rizaee (2015), Stathis (2016), Oan (2015), Seif ElDin and Galal (2015), Hidalgo-Leiva et al. (2016), Bolhassani et al. (2016). The last authors studied the effect of the distribution of reinforcement on the shear capacity of the walls. Walls with single reinforced (SR) and double reinforced (DR) cells with the same reinforcement ratio were tested. In the DR specimens, the reinforcement was distributed more widely, resulting in more grouted courses and columns. There was a 34% increase in horizontal load capacity, 47% increase in ductility and 60% increase in elastic stiffness in the DR specimens compared to the SR specimens: in addition, the failure mode was changed from shear-dominated to flexural-dominated. The authors' numerical model showed that since the partially grouted masonry walls behaved similarly to concrete infilled-frames, the increased grouted courses and columns in the DR specimens improved frame action and confinement and consequently resulted in their better performance. However, it is not clear whether this was due to the reinforcement or the extra grout, because Oan (2015) showed that walls with horizontal bond beams with and without reinforcement had the same strength.

Seif ElDin and Galal (2015) studied the effects of horizontal reinforcement in fully grouted walls. The two specimens were vertically reinforced. One specimen was horizontally unreinforced and the other was reinforced in every other course. The horizontal reinforcement in this study increased the “yield” and ultimate strengths of the wall by 4% and 11%, being insignificant increases considering the normal variability of masonry and that only one specimen of each type was tested. In the study by Hidalgo-Leiva et al. (2016), again the bond beam did not improve the behaviour of the wall, including the maximum capacity, over that of a wall without a bond beam. Thus, these latter two studies provide results in agreement with those of Oan (2015). The experiments conducted by Rizaee (2015), Stathis (2016) and Oan (2015) were therefore reviewed, with a deeper assessment of the influence of horizontal reinforcement on the shear strength of masonry walls.

OVERVIEW OF EXPERIMENTS

Three sets of experiments are considered: set 1 (4 groups) by Rizaee (2015), set 2 (1 group) by Stathis (2016), and set 3 (2 groups) by Oan (2015). The walls were 1.79 x 1.79 x 0.19 m (height x length x width), constructed of 190 x 390 x 190 mm hollow concrete blocks. The walls were grouted and reinforced with 15M reinforcing bars vertically in cores at the ends and in the middle (one core) of the wall. Bond beams were either in the 5th (middle) and 9th (top) courses or the 3rd and 6th (two middle) courses of the walls, grouted and reinforced with 10M or 15M (set 3) reinforcing bars. Based on previous studies by Hoque (2013) and Rizaee (2015), only a few cracks propagated in the 9th course: therefore, in two groups of the walls (groups G and B) the bond beam in the 9th course was grouted but left unreinforced to analyse the influence of reinforcement in this course on the performance of the walls. All wall groups in sets 1 and 2 consisted of two replicas while wall groups in set 3 consisted of three replicas. The walls in sets 2 and 3 were subjected to constant axial load, based on stresses of 2 MPa (set 2) and 0.5 MPa (set 3) over their net area. The loads on the walls in set 1 were adjusted throughout the test (see

below) based on a total load giving an average stress of 2 MPa at the beginning of the test. In sets 1 and 2 the horizontal shear loads were applied in displacement control, being reverse cycles with increasing displacements. In set 3, lateral displacement was applied monotonically at a constant rate in one direction until failure. A summary of varying wall properties and loading is provided in Table 1.

Table 1: Wall Properties and Loading

| Set | Wall group | No. of samples | Bond beam location | Horizontal reinforcement bar size | Vertical stress (MPa) | Boundary condition | Horizontal loading pattern |
|-----|----------------|----------------|-------------------------|-----------------------------------|-----------------------|--------------------|----------------------------|
| 1 | D | 2 | 5,9 | 10M | 2.0 | Fixed-Fixed | Cyclic |
| | F ¹ | | 3,6 | | | | |
| | G | | 5 (reinf.) 9 (unreinf.) | | | | |
| | F* | | | | | | |
| 2 | F' | 1 | 3,6 | | | Fixed-Free | Monotonic |
| 3 | A | 3 | 5,9 | N/A | 0.5 | | |
| | B | | 5 (reinf.),9 (unreinf.) | 15M | | | |

BOUNDARY CONDITIONS

The walls were all tested as shown schematically in Figure 1. Two vertical loading actuators applied constant total loads on the top spreader beam. In set 1, the vertical load applied by each actuator was adjusted in such a way as to induce moments at the top and bottom of the walls and simulate a fixed–fixed boundary condition, shown in Figure 2(a) – the top spreader beam was kept horizontal. The location of zero moment in these specimens was set at 415 mm beneath the top of the walls, making the top and bottom moments unequal. The effective height factor in these specimens is $(1800 - 415)/1800 = 0.77$. In sets 2 and 3, the two vertical actuators applied equal and constant load to the walls throughout the test. In these tests, the boundary condition is fixed-free (cantilever), as shown in Figure 2(b), which resembles half the height of a wall with pin-pin boundary conditions; therefore, the effective height factor is 2.

To normalize for the effects of boundary conditions, all walls were assessed on the equivalent pin-pin end conditions. Therefore, the loads in set 1 are multiplied by $1/0.77 = 1.3$ and in set 2 and 3 are multiplied by $1/0.5 = 2$. The cantilever boundary condition is thought to simulate the conditions on walls in one storey buildings or on the top level of a multi-storey building, while the fixed-fixed condition is thought to simulate the conditions on walls between floors in a multi-storey building – the floor slabs act as diaphragms and keep the top and bottom of the walls in plane.

¹ Wall group F, F*, and F' have the same wall properties. However, Wall groups F and F* are from the study by Rizaee (2015) and wall group F' is from study by Stathis (2016). Vertical load application in groups F and F* (consequently boundary condition) is different than group F'.

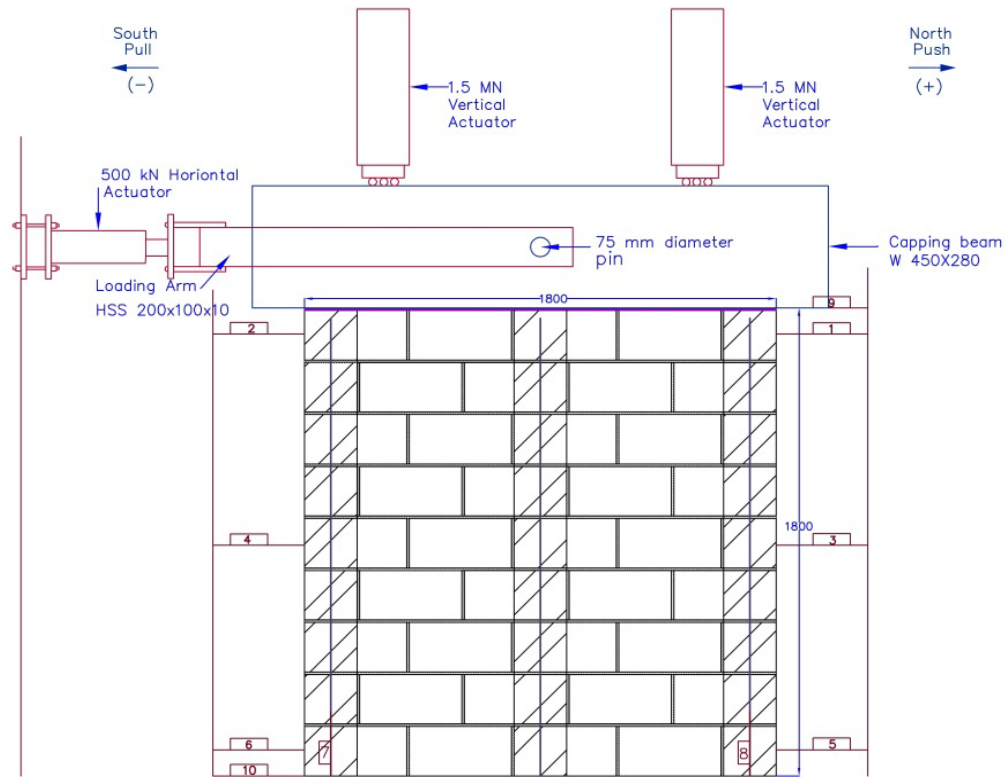
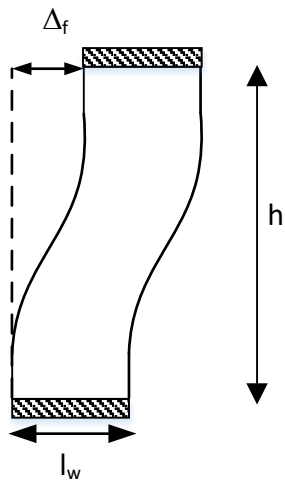
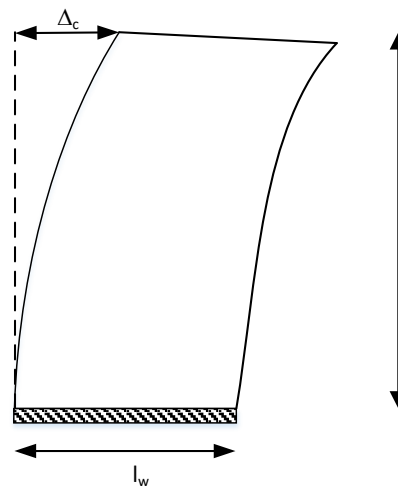


Figure 1: Typical test arrangement



(a) Fixed end boundary condition in set 1



(b) Cantilever boundary condition in set 2 and 3

Figure 2: Boundary conditions

SHEAR MODELS

In order to calculate the in-plane shear strength of masonry shear walls in almost all design standards and proposed models, three components are considered to contribute: the shear strength of the masonry, the increase in shear strength due to “friction” from the applied axial load, and the yield strength of the shear reinforcement. We consider here only the Canadian masonry standard, CSA S304.1-14. A summary of other standards and models can be found in Dickie and Lissel (2009). Equation 1 shows how the shear strength of the masonry is determined according to CSA S304.1-14, while Equation 2 shows that the shear wall resistance is calculated from the shear strength attributed to the masonry, the effect of the applied axial load, and the shear reinforcement.

$$v_m = 0.16 \left(2 - \frac{M_f}{V_f d_v} \right) \sqrt{f'_m} \quad (1)$$

$$V_r = \phi_m (v_m b_w d_v + 0.25 P_d) \gamma_g + \left(0.60 \phi_s A_v f_y \frac{d_v}{s} \right) \leq 0.4 \phi_m \sqrt{f'_m} b_w d_v \gamma_g \quad (2)$$

Where

- A_v = cross sectional area of horizontal reinforcement (mm^2)
- b_w = over all web width (mm)
- d_v = effective depth, which need not be taken as less than $0.8 l_w$ (mm)
- f_y = yield strength of horizontal steel (MPa)
- f'_m = masonry compressive strength (MPa)
- M_f = factored applied moment at the section under consideration (kN.m)
- P_d = applied axial load (kN)
- s = spacing of horizontal reinforcement (mm)
- V_f = factored applied shear at the section under consideration (kN)
- v_m = shear strength attributed to the masonry (MPa)
- V_r = shear resistance (kN)
- γ_g = factor to account for partially grouted or ungrouped walls
- ϕ_m = resistance factor for masonry
- ϕ_s = resistance factor for steel

This equation is based on diagonal shear failure mode. In Equation 1, the shear strength of masonry is defined to depend on the applied factored moment and shear at the section under consideration. There are several issues with this equation. The calculation is possible in the case of a cantilever wall in a single-story building, where M_f is due to the shear force applied at the top of the wall. However, it is not clear how to calculate the shear strength of the masonry in a multi-storey building, with stiff-stiff boundary conditions where shear and moment are applied both at the top and the bottom of a wall. More importantly, why the shear strength of the masonry should depend on factored loads at all is not clear – when the masonry is being constructed, neither it nor the mason are aware of the future factored loads. The equation thus appears contrary to limit states philosophy where the material strength is a material property independent of the loads and is used in the determination of a resistance at any section to be compared with the load effect at the same section.

TEST RESULTS

If the equations in the code are correct, the shear strengths determined in the tests should be normalized to account for the effects of different vertical axial loads, boundary conditions, and masonry compressive strengths. In order to eliminate the effects of axial load from shear strength we subtracted $0.25P_d$ from the peak load. The factor of 0.25 is used in the shear design equation in CSA S304.1-14. This is a somewhat arbitrary factor as Oan (2013) shows a factor of 0.3 and Mann and Muller (1982) indicate values can vary considerably, with their tests on clay bricks giving values between 0.4 and 0.6. The actual compressive load at the time of peak strength was used, which averaged 380 kN in group D, between 408-409 in group F, F*, F', and G, and 90 kN in groups A and B. In order to eliminate the effect of boundary condition the resulting strength was then multiplied by 1.3 in set 1 and by 2 in sets 2 and 3. The new value was finally normalized by dividing by square root of the compressive strength, following the example of many other authors such as Matsumura (1987), Shing et al. (1989), and Voon and Ingham (2006). This should account for the variations in masonry compressive strength between the groups. Thus, we normalized the strengths as:

$$V_{Norm} = \frac{k_{eff} \times (V_{Act} - 0.25 P)}{\sqrt{f'_m}} \quad (3)$$

Weighted prism and unit compressive strength were 16.8 and 29.3 MPa respectively in groups D and F*; 11.4 and 20.1 MPa in groups F and G, 13.0 and 30.2 MPa in group F', and 15.3 and 35.7 MPa in groups A and B. Normalized shear strengths are given in Table 2.

Table 2: Actual Test Results

| Group | Wall | Recorded strength in pull (kN) | Recorded strength in push (kN) | Normalized strength in pull (kN) | Normalized strength in push (kN) |
|-------|------|--------------------------------|--------------------------------|----------------------------------|----------------------------------|
| D | d1 | -208 | 244 | -39 | 49 |
| | d2 | -217 | 223 | -36 | 38 |
| F | f1 | -180 | 211 | -30 | 42 |
| | f2 | -206 | 209 | -40 | 41 |
| F* | f*2 | -225 | 190 | -39 | 28 |
| F' | f'1 | -201 | 188 | -55 | 48 |
| | f'2 | -197 | 181 | -53 | 44 |
| G | g1 | -215 | 175 | -43 | 28 |
| | g2 | -206 | 230 | -40 | 49 |
| A | a1 | | 135 | | 57 |
| | a2 | | 133 | | 57 |
| | a3 | | 126 | | 53 |
| B | b1 | | 142 | | 61 |
| | b2 | | 129 | | 55 |
| | b3 | | 158 | | 69 |

EVALUATION OF TEST RESULTS

We focus only on the effects of reinforcement on the peak shear strength of masonry walls, not on the post peak behaviour of the walls. The purpose is to see if the horizontal reinforcement contributes to the shear strength of the walls as in CSA S304.1-14 and other models.

The test results of the different groups of walls are compared and contrasted to evaluate the effects of varying parameters on the shear strength of the walls. In Table 3 the comparable combinations are categorized and the % of improvement in shear strength in both the pull and the push directions is provided. The values presented in Table 2 show that applying monotonic loading (groups A and B) results in higher ultimate strength than cyclic loading, which is as expected. Regardless of the factor which is varying, the change in shear strength is always in favour of the group A or B subject to monotonic loading - combinations 2, 4, and 6 in Table 3. This makes it hard to judge the influence of the factor which is varying on the shear strength of the walls. The other combinations have the same reverse cyclic horizontal load application. In combination 1, changing the reinforcement location from courses 5 and 9 to courses 3 and 6 has a small positive influence in the pull direction and a small negative influence in push direction, both of which are what one would consider to be normal variation in masonry. In combination 3, placing reinforcement in course 5, vs leaving course 5 and 9 unreinforced, decreases the shear strength by 10%, again within normal variation. Looking at combination 5, placement of reinforcement in course 9 also does not show a consistent influence on strength. This raises the question as to whether the strength of shear reinforcement should be included in the shear strength equation or not.

Table 3: Comparable Combinations

| No. | Comparable groups | Group i | Group ii | Varying factor | % of difference in average pull strength | % of difference in average push strength |
|-----|---------------------|----------------|--------------------------|-----------------------------|--|--|
| 1 | D vs. F, F', and F* | 10M @ (5,9) | 10M @ (3,6) | Reinforcement placement | 15% | -7% |
| 2 | D vs. A | 10M @ (5,9) | 0 @ (5,9), grouted (5,9) | Reinforced vs. unreinforced | | 28% |
| 3 | B vs. A | 15M @ 5, 0 @ 9 | 0 @ (5,9), grouted (5,9) | | | -10% |
| 4 | B vs. D | 15M @ 5, 0 @ 9 | 10M @ (5,9) | Reinforcement distribution | | -29% |
| 5 | G vs. D | 10M @ 5, 0 @ 9 | 10M @ (5,9) | Reinforcement of BB 9 | -10% | 13% |
| 6 | G vs. B | 10M @ 5, 0 @ 9 | 15M @ 5, 0 @ 9 | Reinforcement ratio | | 60% |

In order to determine if there is a statistically significant difference between groups with three or more samples, between groups A and B, and between walls subject to monotonic and cyclic

loading, an ANOVA test was carried out. The assumption in these statistical tests is that the samples are from a normally distributed population and that a wall with specific construction characteristics is a random sample from its population. The ANOVA test showed that there is no statistically significant difference between the strengths of the walls in groups A and B, but that there is a statistically significant difference between the strengths of walls subject to monotonic loading versus cyclic loading, which is as expected.

CONCLUSIONS

Three sets of tests were conducted using two sets of boundary conditions, one having fixed ends and the other having cantilever boundary conditions. The test results were adjusted so that they all represented pin-pin boundary conditions, and were further normalized for different axial stresses and different masonry strengths. We realise that the method we used to normalize the results of the various tests is arbitrary, based on the Canadian code equation, but nevertheless, some normalization was needed. The fact that the normalization procedure used was based on the code equation, but showed the test results of walls subject to each pattern of shear loading to be essentially the same, indicates that the procedure used may well have value and be of the sort needed to compare the results of even more tests. Examining the shear strength given the different arrangements of reinforcement, it is clear that the reinforcement did not change the shear strength of the masonry walls in all the tests examined in a statistically significant way. The fact that the strength of the different masonry walls with different reinforcement amounts and arrangements was found to be independent from both these parameters, as well as axial load and masonry strength, is of great interest as it confirms arguments made before. One must therefore query whether shear wall strength equations should contain a factor for the strength of the shear reinforcement. All the shear reinforcement appears to do is to contribute to maintaining wall strength and integrity after the peak load is reached.

Also looking at the clause 10.10.2 in CSA S308-14 (Equation 1 here) raises the question as to why the strength of masonry is dependent on its location in the wall and the factored loads. In limit states design, the strength of the masonry should be the strength of the masonry. The effect of the loads against which the strength is compared, should be the factor that depends on the loading and the wall geometry and boundary conditions. Thus we believe the area of shear strength of masonry needs re-examining from at least three perspectives. First, the tests used to determine shear strength need to be reviewed and evaluated to determine what they actually measure: this should be compared to the information needed for determining the strength to be used in design. Second, the failure mode and strength of previous tests on masonry shear walls should be re-evaluated, where the results have been normalized for all the variations in boundary conditions, axial stresses and masonry materials, as begun here. Thirdly, the geometry and loading conditions on a shear wall should be assessed for deriving a prediction of the failure mode and strength of the wall.

ACKNOWLEDGEMENTS

We acknowledge the financial support of the Natural Sciences and Engineering Research Council of Canada, the Mitacs program and the Alberta Masonry Council. The work of Ahmed Oan and Olympios Stathis is also sincerely appreciated and gratefully acknowledged.

REFERENCES

ACI 530-08/TMS 402-08/ASCE 5-08 (2008), Building Code Requirements for Masonry Structures, Boulder, CO, USA.

Anderson, D.L. and Priestley, M.J.N. (1992). In Plane Shear Strength of Masonry Walls. *Proceedings of 6th Canadian Masonry Symposium*, June 15-17, Saskatoon, Canada.

AS 3700-2001 (2001), Masonry Structures, Australian Standard, Sydney, Australia.

Bolhassani, M., Hamid, A. A., and Moon, F. L. (2016), Enhancement of lateral in-plane capacity of partially grouted concrete Masonry Shear Walls, *Engineering Structures Elsevier*, Vol. 108. Issue 2, pp. 59-76.

BS 5628-2:2005 (2005), Code of Practice for the Use of Masonry – Part 2: Structural Use of Reinforced and Prestressed Masonry, London, United Kingdom.

CSA S304.1-14. (2014), Design of Masonry Structures, Canadian Standards Association, Mississauga, Ontario, Canada.

Dickie, J. E. and Lissel, S. L. (2009). Comparison of In-Plane Masonry Shear Models. *Proceedings of 11th Canadian Masonry Symposium*. May 31–June 3, Toronto, Ontario, Canada.

Eurocode 6 (2003), Design of Masonry Structures, Brussels, Belgium.

Hidalgo Leiva, D. A., Barbat, A. H., Pujades, L. G., and Acuña-García, D. (2014). Experimental Analysis of In-plane Shear Strength of Reinforced Concrete Masonry Walls and its Seismic Behavior. *Proceedings of 16th International Brick and Block Masonry Conference*, June 26-30, Padova, Italy.

Hoque, N. (2013), In-Plane Cyclic Testing of Reinforced Concrete Masonry Walls to Assess the Effect of Varying Reinforcement Anchorage and Boundary Conditions, MSc. Thesis, University of Calgary, Calgary, Alberta, Canada.

Mann, W. and Muller, H. (1982). Failure of Shear Stressed Masonry- An Enlarged Theory, Tests, and Application to Shear Walls. *Proceedings of the British Ceramic Society*, 30 (Load Bearing Brickwork (7)), pp. 223 – 235.

Matsumura, A. (1987). Shear Strength of Reinforced Hollow Unit Masonry Walls - Difference Between Partially Grouted Walls and Fully Grouted Walls. *Proceedings of 4th North American Masonry Conference*, August 16-19, Los Angeles, California, USA.

NZS 4230:2004 (2004), Design of Reinforced Concrete Masonry Structures, Wellington, NZ.

Oan, A. F. (2013), Diagonal Shear of Partially Grouted Concrete Masonry Panels, PhD. Thesis: University of Calgary, Calgary, Alberta, Canada.

Oan, A. and Shrive, N. G. (2015). The Effect of Horizontal Reinforcement Embedded in Bond Beams in Concrete Masonry Walls. *Proceedings of 12th North American Masonry Conference*. May 17-20, Denver, Colorado, USA.

Rizaee, S. (2015), Assessing Bond Beam Horizontal Reinforcement Efficacy with Different End Anchorage Conditions in Concrete Block Masonry Shear Walls, MSc. Thesis: University of Calgary, Calgary, Alberta, Canada.

Schneider R.R. (1959), Lateral Load Tests on Reinforced Grouted Masonry Shear Walls, Engineering Centre Report, No. 70-101, University of Southern California, California, USA.

Scrivener, J.C. (1967), Static Racking Tests on Concrete Masonry Walls, *Proceedings of International Conference on Masonry Structural Systems*, Austin, Texas, USA.

Seif ElDin, H. M. and Galal, K. (2015). In-Plane Shear Behavior of Fully Grouted Reinforced Masonry Shear Walls. *Proceedings of 12th North American Masonry Conference*. May 17-20, Denver, Colorado, USA.

Shing, P., Noland, J., Klammerus, E., and Spaeh, H. (1989), Inelastic behavior of concrete masonry shear walls, *Journal of Structural Engineering*, Vol. 115, Issue 9, pp. 2204-2225.

Stathis, O. (2016), Effects of Horizontal Reinforcement Distribution on In-Plane Performance and Post-Peak Behaviour of Masonry Shear Walls, MSc. Thesis, Technische Universität München, München, Germany.

Voon, K.C. and Ingham, J.M. (2006), Experimental In-Plane Shear Strength Investigation of Reinforced Concrete Masonry Walls, *Journal of Structural Engineering*, Vol. 132, Issue 3, pp. 400-408.

Voon, K.C. and Ingham, J.M. (2007), Design Expression for the In-Plane Shear Strength of Reinforced Concrete Masonry, *Journal of Structural Engineering*, Vol. 133, Issue 5, pp. 706-733.

NUMERICAL AND EXPERIMENTAL STUDY ON UNREINFORCED MASONRY BUILDINGS WITH VARIOUS OPENING CONFIGURATIONS STRENGTHENED WITH STEEL BANDS

T. Choudhury¹ and H.B. Kaushik²

¹ Research Scholar, Department of Civil Engineering, Indian Institute of Technology Guwahati, Guwahati, Assam, India, t.choudhury@iitg.ernet.in

² Associate Professor, Department of Civil Engineering, Indian Institute of Technology Guwahati, Guwahati, Assam, India, hemantbk@iitg.ernet.in

Unreinforced masonry (URM) buildings are commonly constructed in many Asian countries due ease in availability of materials and economical construction. But these types of buildings are susceptible to severe damage or collapse during earthquakes; therefore, strengthening of such buildings has been a crucial issue since many years. A few codes of practice suggest various schemes to strengthen such buildings without providing sufficient details on design and detailing of strengthening schemes. Though using these schemes increases the lateral load carrying capacity of such buildings, the codes do not provide any method to estimate the actual increase in load carrying capacity. Application of steel bands over URM buildings is tried in the current study as a retrofitting approach to improve their seismic performance. Effectiveness of using steel bands over URM buildings with different opening configurations is an essential issue to be studied. Initially the capacity of a URM building is determined experimentally and results are used to calibrate the numerical model. Over the calibrated model a numerical approach (nonlinear analysis using ABAQUS) is adopted to estimate the lateral load carrying capacity of a URM building with different opening configurations and sizes, and assessment is carried out considering strengthening intervention using steel bands. Though openings drastically alter the lateral load behavior of URM buildings, providing steel bands can be an inexpensive and efficient way of strengthening such buildings without modifying the architecture.

Keywords: *masonry buildings, nonlinear analysis, strengthening, steel bands.*

INTRODUCTION

Traditional masonry structures, which include important heritage buildings, government offices and general residential buildings, are commonly found in most of the Asian countries. Though most of the currently constructed buildings in urban areas are reinforced concrete structures, unreinforced Masonry (URM) building construction still constitute a large proportion of buildings in rural areas due to affordable construction, easily available local materials, and easy construction methodology (Figure 1,a). URM buildings are proven to have good thermal and sound insulation. Being a load bearing structure, the walls are thicker which indirectly make the building fire resistant. Despite of these advantages, URM buildings are considered as one

of the most earthquake prone building typology due to their brittle behaviour and low tensile strength. Such buildings exhibit poor ductility under lateral forces. Therefore, URM buildings constructed in regions of high seismicity are highly vulnerable. In addition, the vulnerability analysis of these buildings was carried out by Ansary (2003); Khan and Khalid (2002); Kumar (2002); Sinha and Brzev (2002) have categorised them under medium-high vulnerability. The capacity of unreinforced brick masonry building decreases due to the introduction of openings in the structure. But quantity, size and position of the openings largely influence the overall capacity of the structure (Shariq et al., 2008). Due to poor seismic performance, a need for strengthening of existing URM buildings has become crucial. Besides, several other past studies (Tomažević et al., 1996; Vicente et al. 2011) used steel ties as a strengthening element, and have shown a substantial improvement in capacity of the structure without contributing an excessive increase in the structure's weight. Hence, to counter the horizontal action due to seismic activity, introduction of steel flats can be a suitable strengthening option since they are easily available and increase in overall construction cost can be significantly reduced (Figure 1. b, c).



Figure 1: (a) Typical Unreinforced Brick Masonry with GI Sheet (Choudhury et. al, 2015) (b)(c) Retrofitted building using steel flats (Kaushik & Dasgupta, 2014)

Hence, the present work consists of experimental and numerical analyses of a single storey URM building with no partition walls. The numerical model was initially calibrated with the results of the experimental model, and the calibrated model was further analysed with different

opening configurations and opening sizes commonly observed in URM. These building models were strengthened using $40 \text{ mm} \times 5 \text{ mm}$ steel flats and their lateral load behaviour was studied and compared with different models. The results of this work can be helpful to determine the performance level, and an approximate amount of capacity increased for URM building with a particular opening typology and size when strengthened with proposed steel band configuration.

BUILDING GEOMETRY AND MODELLING

A full scale, single storey URM building was considered for slow cyclic pseudo-static test (Shahzada et al., 2012). Due to the limited area of the strong floor and the actuator capacity, only single room with one storey building was considered. A single room with the plan dimension of $3\text{m} \times 3\text{m} \times 3\text{m}$ with 10 cm flat RC slab on top was chosen since such size rooms are commonly constructed in rural areas (see Figure 2). A parapet wall of 90 cm high was constructed over the slab and small opening was provided for easy access to the roof. An additional mass of 1 ton was placed on slab to account for the additional masses, for example, water tank over the roof. The sizes of the openings bearing the symbols have dimensions as: **D** = Door ($2.1 \text{ m} \times 0.9 \text{ m}$) and **W** = Window ($1.2 \text{ m} \times 0.9 \text{ m}$).

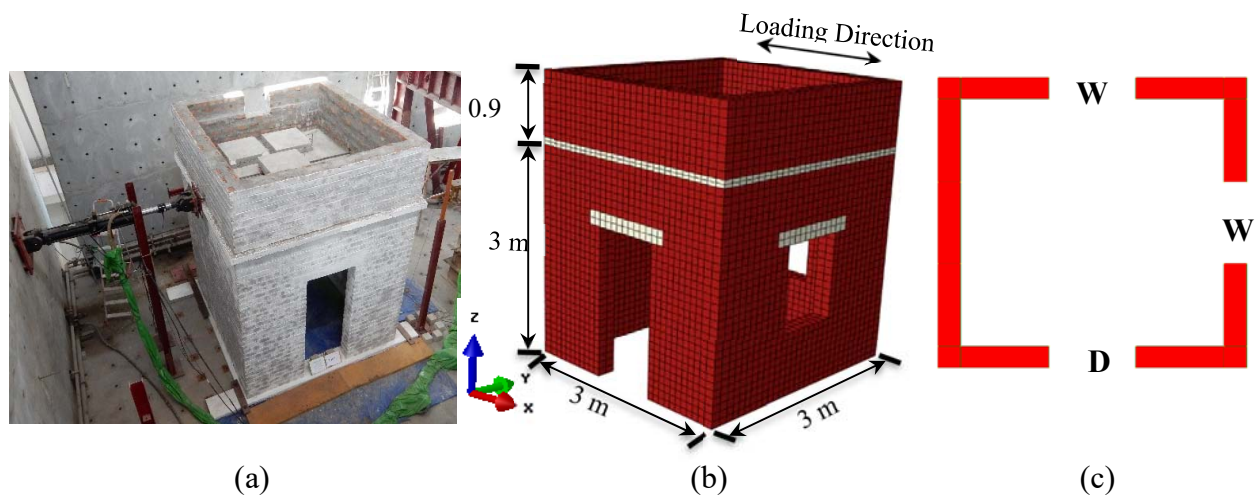


Figure 2: (a) URM building test specimen (b) FE Model and (c) Building Plan

Each wall of the specimen had a height of 3 m , length 3 m and thickness of about 0.24 m . All the walls had double wythes and constructed in English bond, which is commonly used in India. A servo-controlled hydraulic actuator of 250 kN load capacity and 250 mm displacement capacity was used for slow-cyclic pseudo-static testing of the building. The test was carried out in displacement-controlled way by applying three cycles of each target displacement till failure.

The experimental results were used to calibrate the finite element (FE) models of the URM building using Strand7 (Strand 7.2 User's Manual, 2013) as shown in Figure 2,b which was later exported to ABAQUS (ABAQUS: Theory Manual, 2010) for further analysis. Two software were used since Strand7 requires fewer material properties (cohesion value and friction angle), takes lesser computational time to determine the capacity curve and exhibits stability in nonlinear range. But dealing with Stran7 introduces bigger limitations since the softening behaviour of the material is disregarded. Whereas, by means of Concrete Damage Plasticity Model, the softening behaviour of the material can be accounted for in ABAQUS resulting in an acceptable damaged model and capacity curve but the analysis process is highly

time consuming. The FE model consists of 10160 eight-noded brick elements and 15612 nodes. All nodes located at the base of the structure were fully restrained. A concentrated load was applied at the point where the quasi-static load was applied as per the experimental setup. The material properties of the building model, some of which were obtained experimentally, are given in Table 1. The compressive strength of the masonry unit, mortar, and masonry prism were determined as per the relevant Indian standards (BIS 1992, BIS 1995 and BIS 1987a). The tensile bond strength was determined using the method suggested by Khalaf (2005). The initial shear capacity of masonry units was determined following BS EN-1052 (2002).

Table 1: Mechanical properties of the material used in brick masonry building

| Property | Value | Remarks |
|--------------------------------------|------------------------|-------------------------|
| Brick Unit compressive strength | 19.3 MPa | Experimentally obtained |
| Compressive Strength of Mortar (1:6) | 4.84 MPa | Experimentally obtained |
| Masonry Prism compressive strength | 3.18 MPa | Experimentally obtained |
| Tensile bond strength (Z test) | 0.129 MPa | Experimentally obtained |
| Elastic Modulus of Masonry | 1748 MPa | Experimentally obtained |
| Shear Strength (Triplet Shear test) | 0.165 MPa | Experimentally obtained |
| Specific Weight of masonry material | 1637 kg/m ³ | BIS (1987b) |
| Elastic Modulus of Concrete | 24768 MPa | BIS (2000) |
| Density of Concrete | 2400 kg/m ³ | BIS (1987b) |
| Elastic Modulus of Steel | 200000 MPa | BIS (2000) |
| Density of Steel | 7870 kg/m ³ | BIS (1987b) |

Pushover analyses of the URM building model were carried out using Strand7 and ABAQUS in order to systematically evaluate their failure modes and lateral load carrying capacity. Further, FE numerical analyses of the URM building model strengthened using steel bands were also carried out. In the later stage, additional numerical analyses of the URM building model were carried out considering different window sizes and opening configurations. The analyses performed using Strand7 were carried out considering a Mohr-Coulomb failure criterion for masonry with a friction angle of 35° and cohesion value of 0.145 MPa. The non-linear analyses performed using ABAQUS considered the Concrete Damage Plasticity (CDP) model for which the non-linear parameters were taken with dilatation angle as 10°, eccentricity as 0.1, f_{bo}/f_{co} as 1.16, K_c as 0.667 and viscosity parameter as 0.0001, which have been considered based on established literature (Lubliner et al., 1989; Page, 1981). The maximum strength in tension and compression are calculated using the Mohr-Coulomb yield criterion under plane stress conditions. Material non-linearity was defined exclusively for masonry elements, whereas concrete lintels/slabs and steel bands were assumed to behave elastically. Such assumption was made considering the fact that concrete and steel possess strength that is much larger than that of masonry.

EXPERIMENTAL RESULTS AND CALIBRATION OF THE NUMERICAL MODEL

Results of the full-scale URM specimen tested under slow cyclic pseudo-static loading are discussed in this section followed by the numerical calibration of the FE models for the specimen. The experimental test exhibited a mixed failure mechanism consisting of both shear and tensile failure along with twisting mechanism at higher displacement levels (Figure 3). The distribution of Von Mises stresses in the FE model was found to exhibit peaks near the corners

of the openings indicating that damage was more prominent near the openings. The numerical model was then calibrated with the experimental results. The strain contours resulting from the numerical analyses carried out in ABAQUS showed nearly the same crack formation and similar critical regions with that observed in the Experiment (Figure 3). The model was further numerically analysed using Strand7 and the equivalent plastic strain patch, which is one of the outcomes of the numerical simulations, produced nearly similar results when compared with the ABAQUS results. The capacity curves are compared in Figure 4, which again shows a very good agreement between the experimental and numerical curves. More details on both the analysis approaches are provided later. The numerical model of experimentally tested building is referred as Model 1.1, which is later analysed with different opening sizes and configurations.

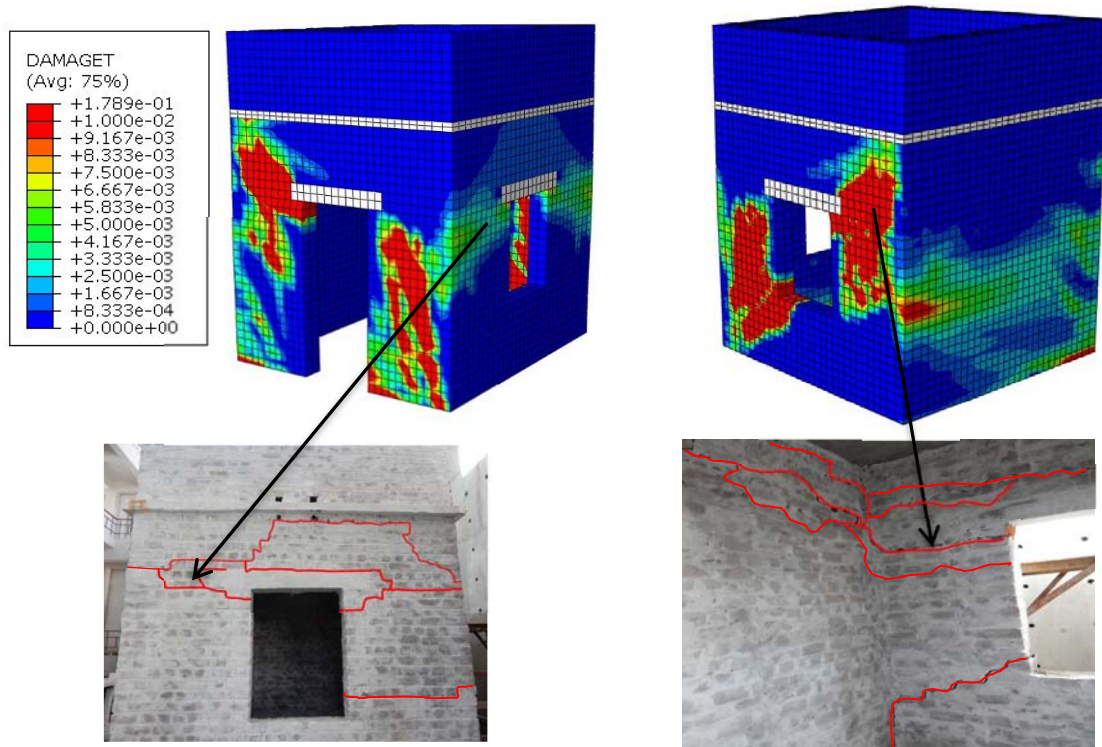


Figure 3: Damaged states of URM building

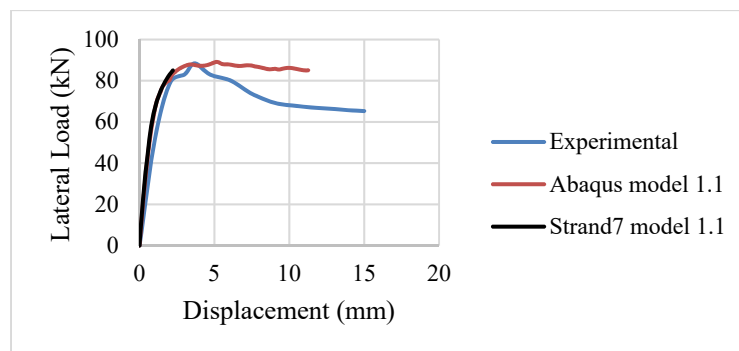


Figure 4: Comparison of capacity curves obtained from Strand7 and ABAQUS with the experimentally obtained capacity curve.

NUMERICAL ANALYSIS WITH DIFFERENT OPENING CONFIGURATIONS

Since it is noticeable that the numerical results matched really well with the experimental results, the calibrated numerical model was further extended considering different opening configurations and sizes. For this purpose, nine FE models were developed considering three different window opening sizes in three different configurations keeping door opening size and configuration same as given below and shown in Figure 5. Three Model sets with different opening configurations were:

Model set 1: $D = 0.9 \text{ m} \times 2.1 \text{ m}$, $W_1 = 0.9 \text{ m} \times 1.2 \text{ m}$ with Plan 1,2,3

Model set 2: $D = 0.9 \text{ m} \times 2.1 \text{ m}$, $W_2 = 1.2 \text{ m} \times 1.2 \text{ m}$ with Plan 1,2,3

Model set 3: $D = 0.9 \text{ m} \times 2.1 \text{ m}$, $W_3 = 0.5 \text{ m} \times 1.2 \text{ m}$ with Plan 1,2,3

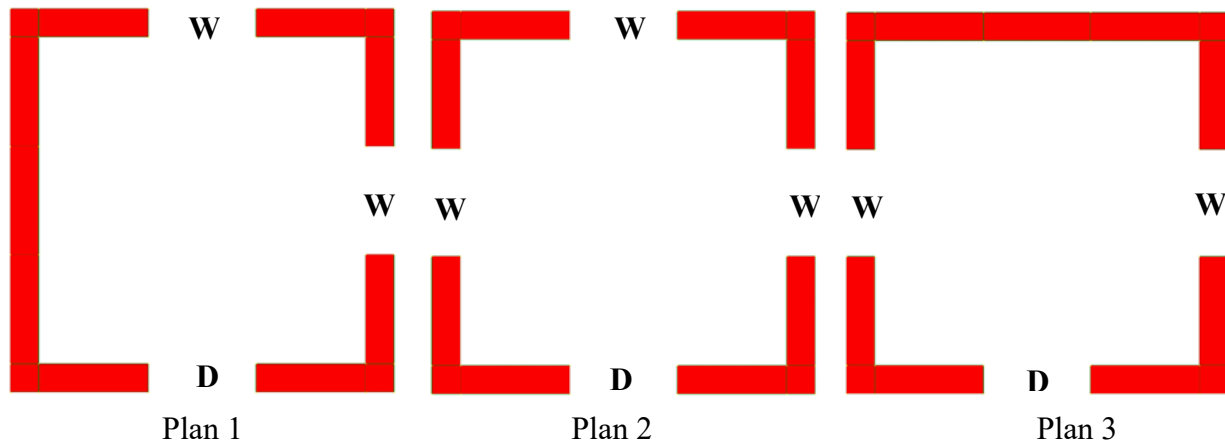


Figure: 5. URM building with different opening configurations

The Plan 1 of Model set 1 was tested under slow cyclic pseudo-static lateral loading in laboratory. The whole set of FE models were subjected to non-linear pushover analysis in both the software for comparison. The same models that were analyzed using strand7 were imported in ABAQUS and analyzed again to get the damage data and to compare their capacity curves obtained from two software. A comparison between pushover curves obtained using both the numerical approaches exhibited nearly similar capacity value but the capacity curves generated by Strand7 do not exhibited much plastic displacement values due to limitations in dealing with softening behaviour of the material. However, adopting the numerical model using Mohr-Column failure criteria with associated flow rule in Strand7 provides an acceptable elasto-plastic curve with much lesser computational time (Choudhury et al., 2015). Such limitations are not there in ABAQUS in which utilisation of CDP model provides more accurate masonry behaviour but takes more computational time. From the results obtained, it is noticeable that the numerical results generated by both the commercial codes, matched quite well.

Since Pushover analysis in strand7 was comparatively faster than that in ABAQUS, it was further used for numerical analysis of rest of the models. The numerical analyses conducted on the models showed a considerable change in capacity with different configuration and opening sizes. Though presence of openings play a major role in stiffness degradation and reduction of lateral load carrying capacity, model with large opening also exhibited large twisting mechanism. In addition, building having lesser number of openings, though of larger size, showed higher lateral load carrying capacity. As expected the models resisted lesser lateral load when the openings were provided along the loading direction. Models with smaller size openings showed insignificant change in load carrying capacity irrespective of the opening configuration. The model with no

window opening along the in-plane direction underwent larger deformation level with negligible twisting mechanism and a small increase in lateral load carrying capacity. Comparing the amount of damage in all the models as shown in Figure 6, the model with smaller opening size exhibited minimum amount of damage with respect to other models. Significant amount of damage was visible in building models with large opening sizes as shown in Figure 7, which represents damage distribution in a particular building configuration with various opening sizes.

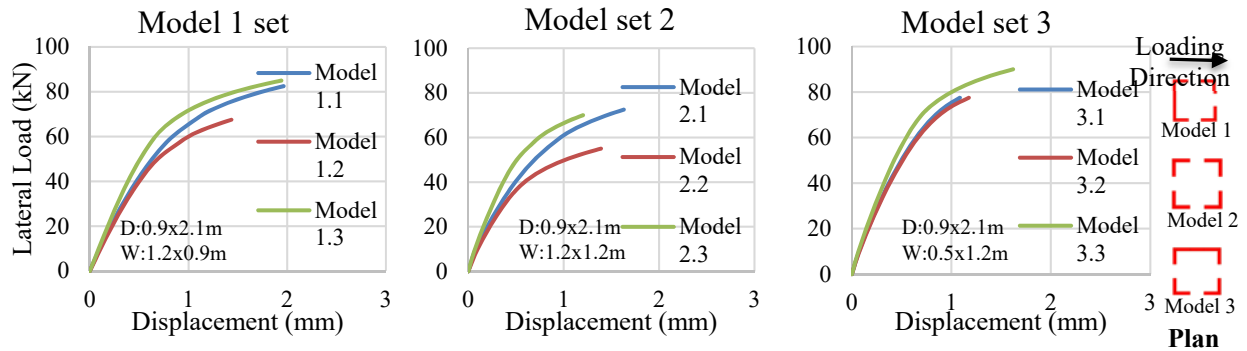


Figure 6: Comparison of capacity curves of three model sets

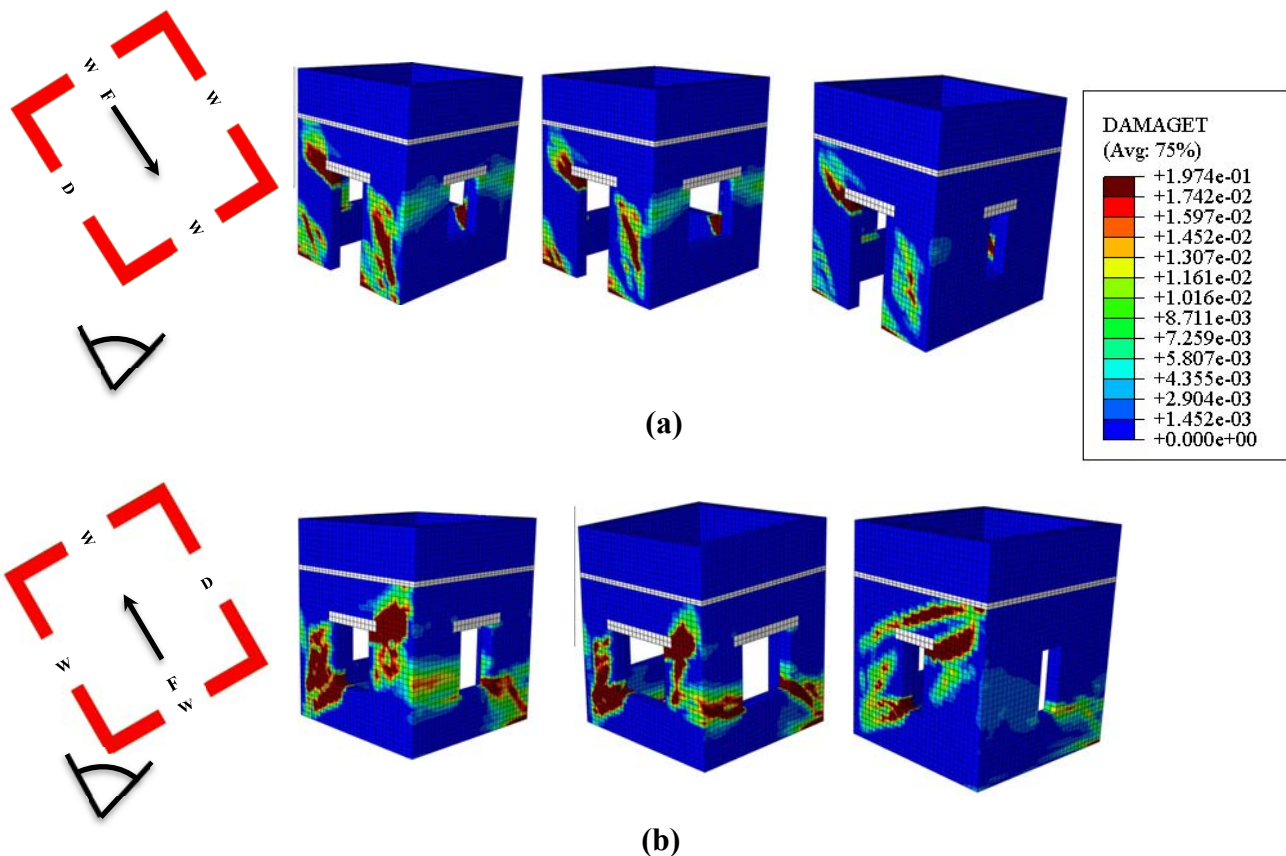


Figure 7: Damage distribution in Plan 2 with various window sizes

STRENGTHENING OF URM BUILDING

From some past earthquakes, it was observed that application of steel bands on masonry walls was quite effective in preventing separation and disintegration of wall elements (Kaushik and Dasgupta, 2014; Kaushik et al., 2006). In addition, it would be interesting to study the

effectiveness of using steel bands in improving the lateral load performance of URM buildings with different opening configurations. In order to achieve this objective, steel bands, in the form of mild steel flats of 40 mm width and 5 mm thickness, were used to strengthen the walls (both internally and externally) of the three building model sets, which were numerically analysed earlier. From the experimental and numerical study of unreinforced masonry it was observed that the damage occur mainly near the corners of the openings (Figure 3 and 7). Hence, horizontal steel bands were used at lintel and sill level of the building models to delay and reduce the development of tensile stresses near the openings. Vertical steel bands were additionally used to connect the horizontal bands for stress transfer as shown in Figure 8.

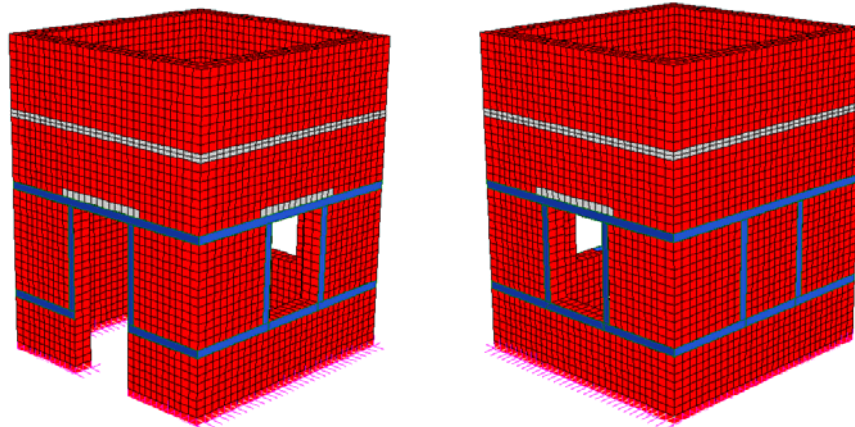


Figure 8: Strengthening of URM building using steel bands

In the already developed FE models, steel flats with cross-section (40mm x 5mm) were simulated as line elements connected to both inside and outside of the wall at a node to node interval of 0.5 m. The numerical analyses results showed a significant increase in lateral load carrying capacity of the structure for each strengthened model sets. Model sets even with large window openings (Model set 2) exhibited higher capacity in comparison to the original unreinforced masonry model (Figure 9, Figure 10).

CONCLUSIONS

In the present study, experimental and numerical testing of full-scale URM building, both un-strengthened and strengthened using steel bands, was carried out. Pseudo-static cyclic test was first carried out on the building and the capacity curve thus obtained was used to calibrate the numerical FE models. The numerical analysis was carried out by performing non-linear static analyses of the building models using two FE commercial codes, namely, Strand7 and ABAQUS. Both the experimental and numerical results provided a good agreement with each other and displayed the same types of failure modes. Strengthening using single steel flats on both faces of the walls showed not only significant increase in lateral load carrying capacity but also a remarkable improvement in displacement capacity of the URM building models.

Besides, a parametric study was also carried out on model sets with different opening configurations and sizes. Nine URM building models categorized as three model sets were created and non-linear pushover analyses of the models were carried out. FE simulation results showed that each model set performed differently in terms of displacement capacity, but introduction of large openings in the walls resulted in reduction in lateral load carrying capacity.

All the building model sets with different opening location and sizes showed remarkable change in lateral load carrying capacity. However, application of steel bands on the walls of the URM building model sets as a strengthening measure resulted in a remarkable increase in both lateral load and displacement capacity. Hence, use of steel flats as a strengthening intervention can be an inexpensive and efficient way of improving the overall capacity of URM buildings.

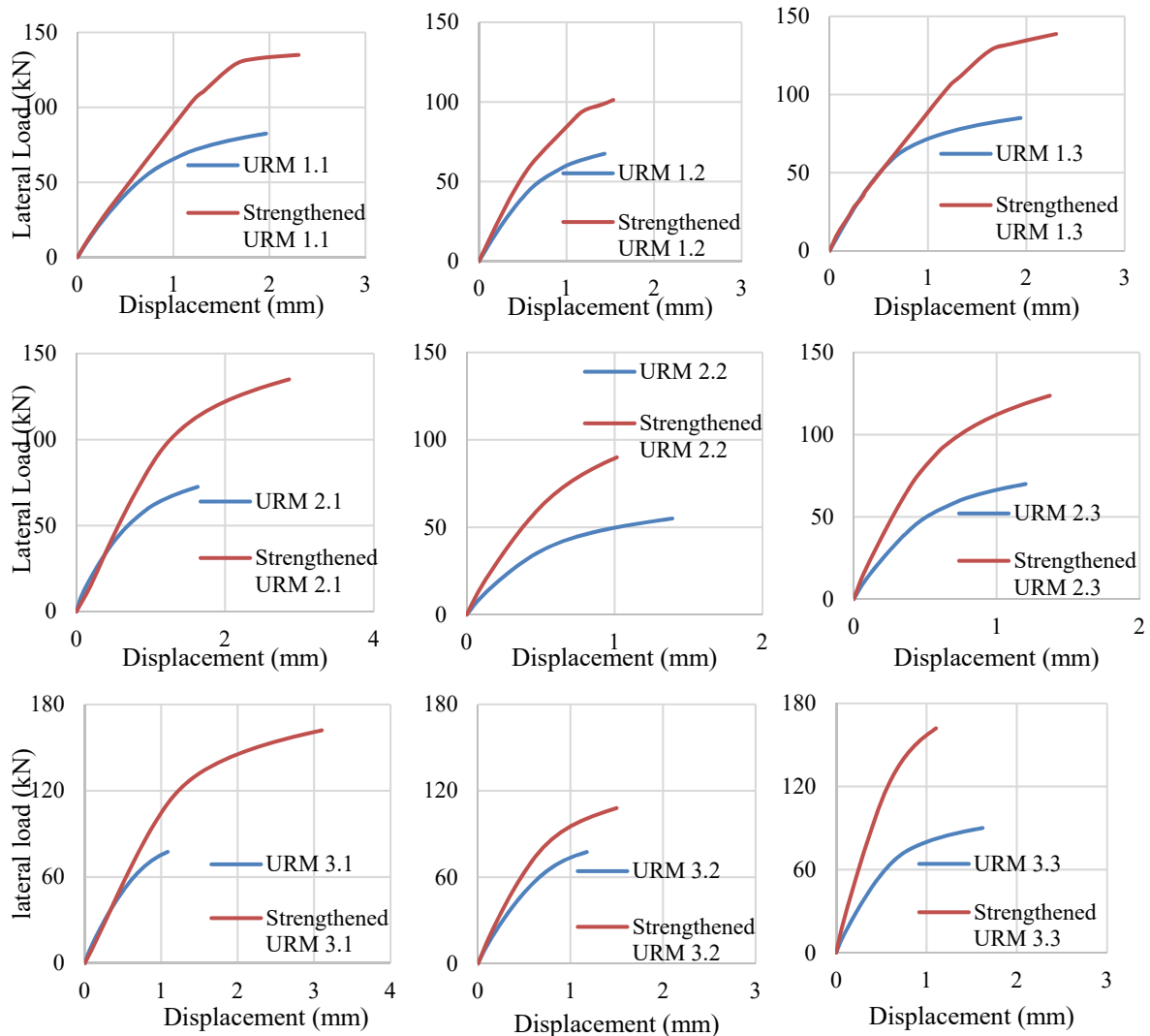


Figure 9: Capacity curves comparison for different models

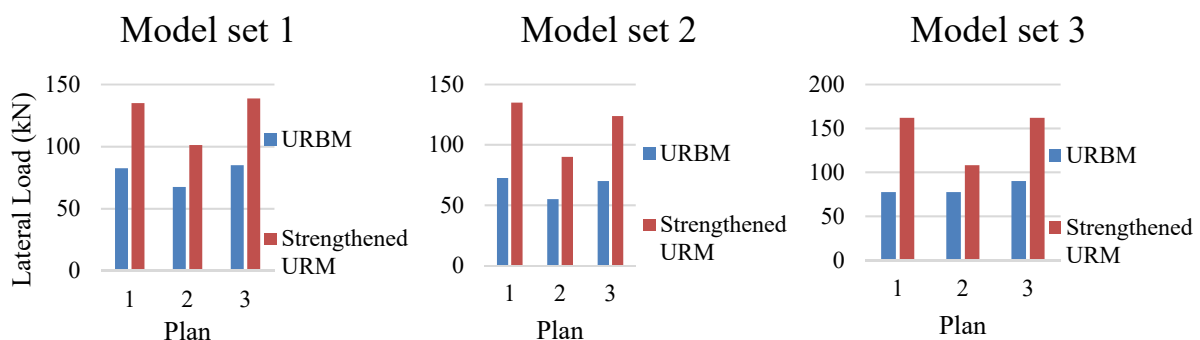


Figure 10: Lateral load carrying capacity comparison for different model sets

ACKNOWLEDGEMENTS

The financial support provided for the experimental study by the Department of Science and Technology, Government of India, is gratefully acknowledged.

REFERENCES

ABAQUS: Theory Manual. (2010). *Version 6.10, 2010*.

Ansary, A. (2003). Housing Report Unreinforced Brick Masonry Buildings with GI Sheet. *World Housing Encyclopedia, EERI(IAEE)*.

BS EN. (2002). Methods of test for masonry - Part 3: Determination of initial shear strength. *BS EN 1052-3*.

Bureau of Indian Standards(BIS). (1995). Indian standard code of practice for preparation and use of masonry mortars. *IS 2250, 5th Revision*, New Delhi, India.

Bureau of Indian Standards (BIS). (1987). Code of Practice for Structural use of Unreinforced Masonry. *IS 1905, 3rd Revision*, New Delhi, India.

Bureau of Indian Standards (BIS). (1987). Code of Practice for Design Loads(Other than Earthquake) for Buildings and Structures. *IS 875(Part 1)*, New Delhi, India.

Bureau of Indian Standards (BIS). (2000). Code of Practice for Plain and Reinforced Concre. *IS 456*, New Delhi, India

Bureau of Indian Standards (BIS). (1992). Indian standard methods of test of burn clay building bricks—Part 1: Determination of compressive strength. *IS 3495, 3rd Revision*, New Delhi, India.

Choudhury, T., Milani, G., & Kaushik, H. B. (2015). Comprehensive numerical approaches for the design and safety assessment of masonry buildings retrofitted with steel bands in developing countries: The case of India. *Construction and Building Materials*, 85, 227–246. <https://doi.org/10.1016/j.conbuildmat.2015.02.082>

Kaushik, H. B., & Dasgupta, K. (2014). Assessment of Seismic Vulnerability of Structures in Sikkim , India , Based on Damage Observation during Two Recent Earthquakes, 27(December 2013), 697–720. [https://doi.org/10.1061/\(ASCE\)CF.1943-5509.0000380](https://doi.org/10.1061/(ASCE)CF.1943-5509.0000380).

Kaushik, H. B., Dasgupta, K., Sahoo, D. R., & Kharel, G. (2006). Performance of structures during the Sikkim earthquake of 14 February 2006. *Current Science*, 91(4), 449–455.

Khalaf, F. M. (2005). New Test for Determination of Masonry Tensile Bond Strength, 17(December), 725–732.

Khan, A. A., & Khalid, M. (2002). Housing Report Unreinforced Brick Masonry Walls In Mud Mortar With Flat Timber Roof. *World Housing Encyclopedia, EERI(IAEE)*.

Kumar, A. (2002). Housing Report Unreinforced Brick Masonry Walls In Mud Mortar With Flat Timber Roof. *World Housing Encyclopedia, EERI(IAEE)*.

Lubliner, J., Oliver, J., Oller, S., & Oñate, E. (1989). A plastic-damage model for concrete. *International Journal of Solids and Structures*, 25(3), 299–326. [https://doi.org/10.1016/0020-7683\(89\)90050-4](https://doi.org/10.1016/0020-7683(89)90050-4)

Page, A. (1981). The Biaxial Compressive Strength of Brick Masonry. *Proceedings of the Institution of Civil Engineers*, 71(3), 893–906. <https://doi.org/10.1680/iicep.1981.1825>

Shahzada, K., Khan, A. N., Elnashai, A. S., Ashraf, M., Javed, M., Naseer, A., & Alam, B. (2012). Experimental seismic performance evaluation of unreinforced brick masonry buildings. *Earthquake Spectra*, 28(3), 1269–1290. <https://doi.org/10.1193/1.4000073>

Shariq, M., Abbas, H., Irtaza, H., & Qamaruddin, M. (2008). Influence of openings on seismic performance of masonry building walls. *Building and Environment*, 43(7), 1232–1240. <https://doi.org/10.1016/j.buildenv.2007.03.005>

Sinha, R., & Brzev, S. N. (2002). Housing Report Unreinforced Brick Masonry Building With Reinforced Concrete Roof Slab. *World Housing Encyclopedia*, EERI(IAEE).

Strand 7.2 User's Manual. (2013). www.strand7.com.

Tomaževič, M., Lutman, M., & Weiss, P. (1996). Seismic Upgrading of Old Brick-Masonry Urban Houses: Tying of Walls with Steel Ties. *Earthquake Spectra*, 12(3), 599–622.

Vicente, R., Rodrigues, H., Varum, H., & Mendes da Silva, J. a. R. (2011). Evaluation of Strengthening Techniques of Traditional Masonry Buildings: Case Study of a Four-Building Aggregate. *Journal of Performance of Constructed Facilities*, 25(3), 202–216. [https://doi.org/10.1061/\(ASCE\)CF.1943-5509.0000164](https://doi.org/10.1061/(ASCE)CF.1943-5509.0000164)

IN-SITU EARTHQUAKE TESTING AND SECURING OF DOMESTIC URM CHIMNEYS

D. Dizhur¹, M. Giaretton², H. Derakhshan³, J. Ingham⁴ and M. Griffith⁵

¹ Lecturer, Civil and Environmental Engineering Department, The University of Auckland,
1023 Auckland, New Zealand, d.dizhur@auckland.ac.nz

² Research Fellow, Civil and Environmental Engineering Department, The University of
Auckland, 1023 Auckland, New Zealand, mgia506@aucklanduni.ac.nz

³ Research Associate, School of Civil, Environmental and Mining Engineering, The
University of Adelaide, 5005 Adelaide, Australia, hossein.derakhshan@adelaide.edu.au

⁴ Professor, Civil and Environmental Engineering Department, The University of Auckland,
1023 Auckland, New Zealand, j.ingham@auckland.ac.nz

⁵ Professor, School of Civil, Environmental and Mining Engineering, The University of
Adelaide, 5005 Adelaide, Australia, michael.griffith@adelaide.edu.au

Failure of domestic unreinforced masonry (URM) chimneys was the first and most frequently encountered evidence of damage observed immediately following the 14 November 2016 Kaikoura earthquake, and previous earthquakes in New Zealand and around the world. The damage typically observed involves the cantilever part of a URM chimney above the roofline, which tends to fall through the roof, outward onto an adjacent building or onto a public sidewalk. In order to mitigate the risk posed by URM chimneys and validate possible securing solutions, in-field experimental tests were undertaken on existing buildings. One URM chimney was tested in Auckland, New Zealand in as-built and retrofitted conditions, while three URM chimneys were tested as-built in Adelaide, Australia. The results from these experimental field testing campaigns are summarised herein.

Keywords: *URM chimney, Kaikoura earthquake, chimney damage, chimney securing, chimney retrofitting, seismic retrofit.*

INTRODUCTION

As a heavy, tall and slender element located above the roofline of a building, unreinforced (URM) chimneys experience large amplifications of earthquake ground motion, frequently making them the first sign of building damage during an earthquake (FEMA P-58/BD-3.9.7 2010). When subjected to earthquake-induced loads, the cantilever part of a chimney above the roofline tends to fall through the roof, outward onto an adjacent building or onto a public sidewalk, posing a significant life-safety hazard to building occupants, neighbours or passers-by, see Figure 1. Numerous past and recent earthquakes around the world (Booth et al. 2004; Giaretton et al. 2017; Dizhur et al. 2017) have reaffirmed and highlighted the hazard that URM chimneys pose.



Figure 1: Examples of damaged chimneys

The high hazard posed by URM chimneys is evident when analysing the recorded insurance claims following past earthquakes in New Zealand. In April 1974 a magnitude 5.0 earthquake with a shallow epicentre struck the South Dunedin area. Despite the low levels of reported earthquake shaking, a large number of insurance claims (approximately 1500, corresponding to about half of the total claims) received by the Earthquake and War Damage Commission were chimney related (Bishop 1974). Following the 2010-2011 Canterbury earthquake sequence, analysis of data provided by the New Zealand Earthquake Commission (EQC) revealed that 90% of all claims and 92% of the total costs related to residential chimney damage were associated with URM chimneys (Giaretton et al. 2017). EQC received approximately 800 insurance claims for damaged or collapsed URM chimneys following the 4 September 2010 Darfield earthquake, almost 10,000 claims after the 22 February 2011 Christchurch earthquake, and a total of 15,400 claims across the entire 2010/2011 Canterbury sequence. At the end of 2011, the total costs for repair, securing, or removal/ replacement of damaged URM chimneys exceeded NZ\$70 million (approximately US\$54 million). Most cases showed that the chimney was the first (sometimes only) building element to structurally fail due to seismic activity (Dizhur et al. 2011; Giaretton et al. 2017), and typically involving only the cantilevered part above the roofline.

More recently, the 2016 Kaikoura earthquake resulted in widespread damage to URM chimneys, see Figure 1b-c (Dizhur et al. 2017). It is highlighted that in the earthquake-affected area many URM chimneys appeared to have been previously removed or lowered to the roofline, likely following the 2013 Seddon and 2013 Lake Grassmere earthquakes (Morris et al. 2013) or even earlier earthquakes (McSaveney 2013).

In order to investigate the performance of four URM chimneys in both as-built and retrofit condition, an in-situ experimental campaign was undertaken in three existing buildings, that served as a supplement to the shake-table testing reported in (Giaretton et al. 2017). The chimney tested in both as-built and retrofit conditions was located in Auckland, New Zealand, while the other three chimneys were tested in Adelaide, Australia, in the as-built condition only.

TESTED CHIMNEYS

Four domestic URM chimneys were tested in existing buildings with the results being presented herein. Chimney A1 was tested in Auckland (New Zealand) with a slightly different test set-up in comparison to chimneys B1, C1, and C2 that were tested in Adelaide (Australia).

URM chimney A1 was located in a residential dwelling (A) that was originally constructed in the 1940's. The dwelling is composed of a clay brick cavity-wall URM ground floor and timber frame first floor, see



(a) View of the subject dwelling



(b) Close-up view of the chimney

Figure 2: Case study building in Auckland (New Zealand) – Chimney A1

Chimney A1 had a single flu with a total height of 8500 mm from ground level to the uppermost point of the chimney. Because of an existing gap between the chimney stack and the top storey, the cantilever part above the roofline was considered 3700 mm high (for perspective see Figure 2) and to ensure the cantilever behaviour, the flushing located at the top storey roof was removed prior testing. The portion of the chimney above roofline had a square cross-section of 470×470 mm and was in good un-weathered condition. The chimney was constructed using strong and dense red clay bricks with a strong lime/cement based mortar mix.

URM chimneys B1, C1, and C2 were located in Darlington, which is a suburb of Adelaide (South Australia), in two clay brick cavity-wall URM single-storey houses, see Figure 3. The houses were built in the 1960s, and closely resembled each other in general aspects, e.g. wall thickness, finishes, cavity wall construction details, wall ties, and roof type. The roofs of these buildings were mildly pitched, made of timber rafters and sheathing, and overlaid with masonry roof tiles. The tested chimneys were single-leaf clay brick, i.e. 110 mm thick, rectangular in

cross section (see Figure 4) and with good brick interlocking at the corners. Chimneys B1 and C2 had, respectively, 1 and 2 internal walls, with only one internal wall in C2 having good interlocking with the perimeter walls (see Figure 4c).

Table 1 reports the chimney dimensions.



(a) Building B – Chimney B1



(b) Building C – Chimneys C1 and C2

Figure 2: Case study buildings in Darlington, Adelaide (South Australia)



(a) B1 (from Building B)



(b) C1 (Building C)



(c) C2 (Building C)

Figure 3: View of the URM chimney cross-sections

Table 1: Dimensions of the tested chimneys and maximum load applied

| Chimney ID | Length ⁽¹⁾ | Width ⁽¹⁾ | Thickness | Unrestrained height | No. of internal walls (t=110 mm) | Estimated mass |
|------------|-----------------------|----------------------|-----------|---------------------|----------------------------------|----------------|
| | L (mm) | B (mm) | t (mm) | h (mm) | (-) | (t) |
| A1 | 470 | 470 | 110 | 3700 ⁽³⁾ | n/a | 1008 |
| B1 | 1200 | 475 | 110 | 1630 ⁽²⁾ | 1 | 976 |
| C1 | 485 | 480 | 110 | 2840 ⁽²⁾ | n/a | 801 |
| C2 | 1435 | 475 | 110 | 1325 ⁽³⁾ | 2 | 975 |

⁽¹⁾ Outside dimension
⁽²⁾ Unrestrained height was from top of walls but below roof because the chimney was not connected to roof
⁽³⁾ Unrestrained height was from roofline (above the wall top) because the chimney was connected to roof

CHIMNEY A1

Chimney A1 was located in Auckland and was tested in as-built and retrofitted conditions.

Test set-up

Initially the clay smoke cap at the top of chimney A1 was removed and the flu was checked to ensure that a clear passage was visible all the way to the fireplace at the bottom, inside the house. Heavy duty rated synthetic straps were attached to the top part of the chimney and to a digital load-cell, which was in turn attached to a 12-volt battery powered winch and anchored to a tree, see Figure 5b. The synthetic loading straps were aligned against the scaffolding in such a way that load was applied horizontally to the chimney, see Figure 5a. This setup enabled easy, controlled load application while having load results immediately available for interpretation. Three Linear Variable Differential Transformers (LVDT) were placed at the top (3.3 m), at mid-height (2.7 m) and at near the roofline of the chimney. Snap-back tests were also performed and three accelerometers were placed: one at the upper most part of the chimney, one attached to the chimney near the roofline, and one inside the house attached to the fireplace, see instrumentation locations (red and blue dots) in Figure 5.

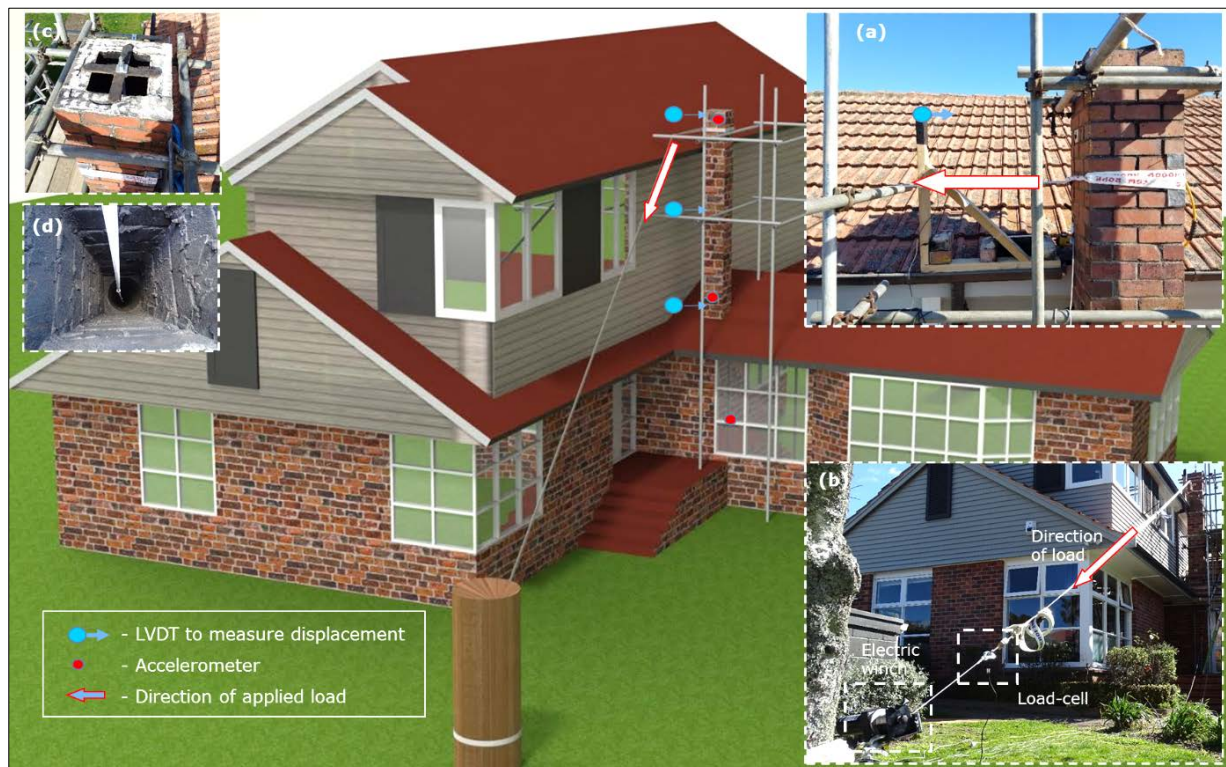


Figure 4: Schematics of loading and instrumentation-setup for chimney A1: (a) Top portion of chimney showing loading direction and location. (b) Location of load-cell and load application mechanism. (c) Top portion of chimney showing cruciform anchor plate for PT retrofit. (d) PT threaded steel rod inserted down chimney flu.

Chimney A1 was first tested in the as-built condition to approximately 1.5% drift level, corresponding to a reduction of ultimate load carrying capacity of approximately 20%. Following the as-built test, a post-tensioned (PT) retrofit was installed inside the URM chimney. The PT system was designed in order to provide ease of installation in a full-scale

chimney (Giaretton et al. 2017). Galvanised threaded D16 ($\varnothing 16$ mm) steel rods in one-metre lengths were inserted down the chimney flu with coupler connections to join individual rods together into a fully functioning single rod that could be post-tensioned (Figure 5d). The dead anchor was located at the base of the chimney underneath the fireplace and consisted of two rectangular 8 mm thick steel plates that were anchored against the four cross sectional sides of the chimney. Similar to the bottom anchorage, at the top of the chimney the live anchor mechanism (Figure 5c) consisted of an 8 mm thick cross plate with the threaded rod centred through a hole and tightened using a washer and a nut. Two tests with different levels of PT were conducted (20 kN and 25 kN of prestress). The prestress was applied to the threaded rod using a hollow hydraulic actuator at the top of the chimney. For all tests, semi-cyclic loading was applied in increments of approximately 0.25 kN.

Construction materials

Fired and dense solid red clay bricks with nominal dimensions of L230 x W110 x H76 mm were placed in a running bond masonry pattern on a 15 mm mortar layer. Visual observations suggested that the mortar was a strong lime/cement-based mortar and in good condition, with no evidence of weathering or deterioration.

Damage observation and test results

The as-built test provided a benchmark for the subsequent retrofitted chimney tests. A force versus displacement graph was produced using the acquired data, see Figure 6. A maximum lateral force of 1.4 kN at a displacement of 16 mm was achieved for the chimney in the as-built condition. The as-built chimney was loaded until reaching a 45 mm lateral top-displacement with approximately 20% reduction in load. Following the testing, a maximum residual displacement of 8.0 mm was recorded.

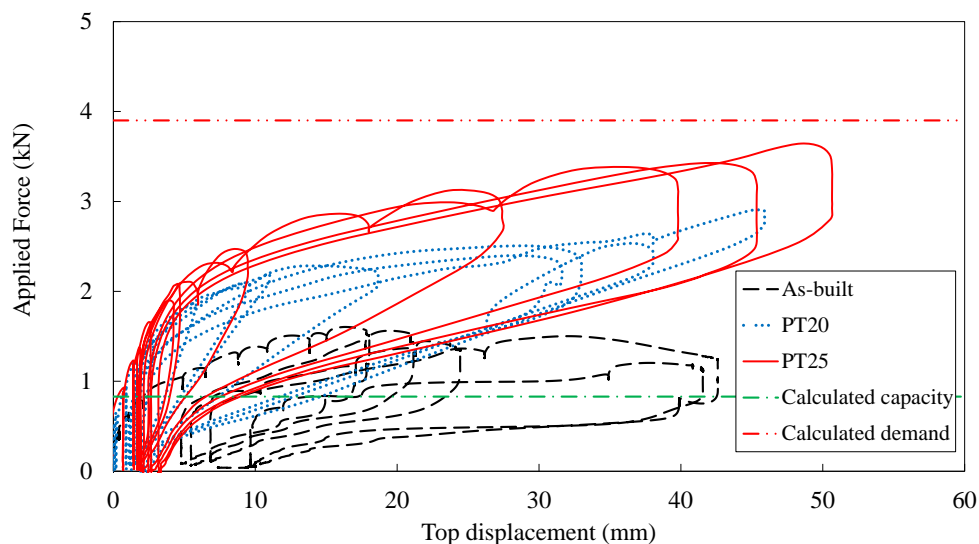


Figure 5: Force versus displacement response of as-built and retrofitted chimney A1

Following the as-built test, the PT retrofit system was installed and vertically stressed to 20 kN (PT20), and the testing procedure was then repeated. Figure 6 shows an approximately 2 times (2.9 kN) increase in capacity for the PT20 chimney at a displacement of 46 mm when compared to the as-built condition. The post-peak residual displacement upon unloading was 2.0 mm.

The chimney was further vertically stressed to a total prestress of 25 kN (PT25). The increased prestress resulted in a 2.6 times increase in capacity when compared to the as-built counterpart. As shown in Figure 6, the PT25 test was stopped when the chimney was laterally loaded to 3.7 kN and a displacement of 52 mm was reached. The PT tests showed a continual increase in strength with increasing lateral displacement due to the chimney arching and consequently stressing the steel threaded rod that was centrally positioned within the chimney. The final recorded residual displacement following PT25 test was 3.0 mm.

During and after testing there was no evidence of movement or damage to the anchoring mechanism at the base of the chimney. A horizontal crack in the chimney was observed two brick courses above the roofline, but no evidence of mortar crushing or masonry deterioration following testing was observed at the crack location or anywhere within the chimney.

Discussion

For the tested URM chimney, the lateral seismic demand was calculated using AS/NZS 1170.5, Section 8: 'Requirements for Parts and Components' (NZS 1170.5 2004) with the section of chimney above the roofline assumed to be supported at the roofline. Key assumptions included the soil type (Soil Type C) and the masonry density being equivalent to 1800 kg/m^3 . $C_p(T_p)$ in accordance with (NZS 1170.5 2004) was calculated as 0.62g (demand conservatively based on crack/rocking initiation of chimney with a period of less than 0.75sec). The equivalent horizontal force of 3.9 kN applied at the location where test load was applied was calculated as the seismic demand at 100% New Building Standard (NBS) loading (Figure 6). Using simple statics and balance of forces, the capacity of the as-built chimney was calculated as 0.9 kN (Figure 6) at the location where the test load was applied. Hence, for the chimney in the as-built condition a capacity/demand (0.9/3.9) of 23% NBS was calculated. Note that the minimum legislative requirement is 34% NBS (The New Zealand Parliament 2004). Based on the as-built experimental test results, the chimney was able to attain a capacity/demand ratio of 36% NBS (1.4/3.9). For PT20 and PT25 tests the chimney was in excess of 74% and 95% NBS respectively (note that the maximum capacity of the retrofitted chimney was not attained because testing stopped at approximately 1.5% drift level).

Although the results showed positive benefits for strengthening URM chimneys against out-of-plane earthquake induced loading, several considerations and factors would need to be addressed before the PT system could effectively be used as a real life retrofit system. Firstly, PT losses experienced by the full system due to creep and settling of the masonry and connections, and initial loosening of live anchorage point, would need to be resolved. For the purposes of this study it was assumed that an existing chimney is no longer in use, but for economic and aesthetical reasons the chimney needed to be retained as part of the dwelling. The effects of heat and fire on the PT system have not been investigated or tested and need to be further addressed if the PT system is to be applied in chimneys that are in use. Data gathered from the Dunedin and Auckland chimney surveys (Giaretton et al. 2017) showed there is a large number of chimneys that are not in use due to installation of more modern heating systems. Typically these chimneys are considered to be an aesthetically valuable part of the structure/building and many house owners prefer for the chimney to remain.

CHIMNEYS B1, C1, C2

Chimneys B1, C1, C2 were located in Darlington, Adelaide and were tested in the as-built condition up to toppling and collapse.

Test set-up

The test set-up consisted of using an excavator to pull each of the URM chimneys horizontally. The applied force was measured using a load cell connecting the excavator boom to the loading frame mounted approximately at the top quarter of the chimney height as shown in Figure 7. The loading frame allowed a horizontal line load to be applied at the centre of the rear face of the chimneys with the aim of subjecting the chimney cross-section to a bending moment about the chimney weak axis.



Figure 6: Typical test on chimneys (Chimney C1)

Construction materials

Fired clay bricks with nominal dimensions of L230 x W110 x H76 mm were solid, frogged (e.g. Figure 8c), and in yellowish colour in building B and had reddish colours in building C. The bricks were placed in a running bond masonry pattern on a 15 mm mortar layer. Visual observations suggested that the mortar was cement-based and in good condition, with no evidence of weathering or deterioration.

To evaluate the masonry bond strength, f_{mt} , 26 in-situ bond-wrench tests were undertaken at various locations of the buildings with the results showing a significant scatter, as evident by the coefficient of variation (CoV) listed in Table 2. It was generally observed that the brick units came away cleanly from the mortar (see Figure 8) which is indicative of poor bonding strength when compared to the mortar tensile strength.



(a) Inner leaf (Building B) (b) Outer leaf (Building B) (c) Outer leaf (Building C)

Figure 7: Brick types and failure pattern during bond wrench test

Table 2: Bond wrench test results

| Dwelling | Location | No. | Mean \bar{f}_{mt} (MPa) | CoV (-) | Char. bond strength f'_{mt} (MPa) |
|----------|-----------------------------|-----|---------------------------|---------|-------------------------------------|
| B | Internal and external walls | 16 | 0.15 | 0.73 | 0.02 |
| C | Outer cavity leaf | 10 | 0.26 | 0.44 | 0.09 |

Damage observation and test results

The initial cracking of the chimneys occurred across a plane that was uneven by one course of bricks, as visible in Figure 4. Subsequent loading of the chimneys resulted in out-of-plane rocking and finally instability. Masonry bond failure occurred at the mortar-brick interface, similar to that observed with the bond-wrench test. The maximum load recorded at failure was 2.45 kN, 1.24 kN, and 2.99 kN respectively for chimney B1, C1, and C2, see Table 1. The test data showed that the loads required to cause cracking were significantly smaller than those required to cause out-of-plane rocking.

Seismic evaluation of chimneys

Analysis of a block diagram representing the chimneys for the two states of stress distributions at the base, cracking and rocking, is shown in Figure 9. The chimney rocking strength is three times the cracking strength. These strength values were calculated assuming the average bond strength, \bar{f}_{mt} , from Table 2 and compared to the measured ultimate strength. It was found that the rocking strength had a better correlation with the measured ultimate strength than did the cracking strength.

The measured ultimate strength of chimneys B1 and C2 (indicated by stars in Figure 10) had an ideal correlation with the rocking calculations, but the rocking calculations for chimney C1 underestimated the measured strength by approximately 25%. The higher measured strength for chimney C1 was attributed to the in-situ timber blocking details at the rocking pivot (see Figure 4b), which provided additional restraint against rotation to the chimney. On this basis, it is recommended for design/assessment purposes that the rocking mechanism be considered for strength prediction, given that the initial cracking did not constitute a failure.

It can be seen from the measured strengths in Figure 10a that the chimneys are safe if located in single-storey buildings in most seismic hazard areas, except for regions at the threshold of 'High' seismicity as defined by ASCE/SEI 41 (2013). In multi-storey buildings (Figure 10b),

the measured strengths are lower than or marginally greater than the seismic accelerations that are expected to be applied to top-storey out-of-plane loaded walls in most Australian capital cities, e.g. for $Z \geq 0.08$. In earthquakes there is potential for the presence of vertical accelerations, which reduces the chimney strength.

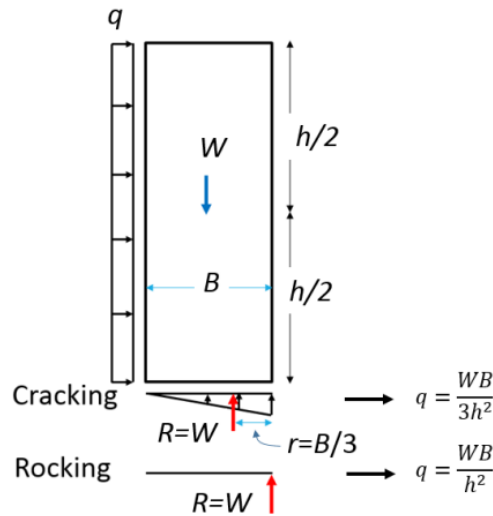


Figure 8: Stress distribution at the chimney base at the instance of cracking and at the onset of rocking; W is the chimney weight and R is the vertical reaction at base

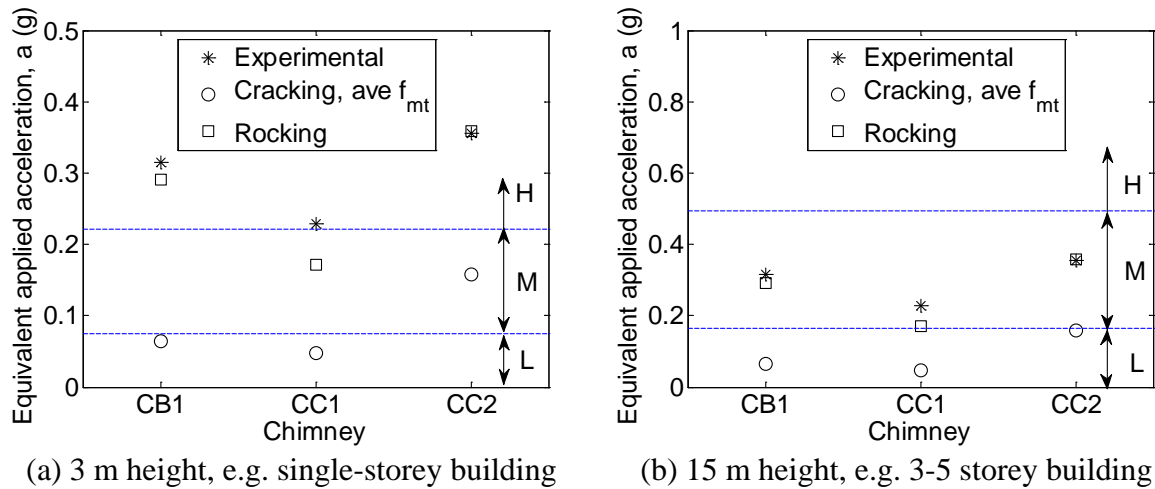


Figure 9: Chimney measured/design strength vs seismic demands (represented by Hazard Factor, Z , and also by L, M, and H notations representing regions with Low, Moderate, and High seismicity as defined in ASCE 2007)

CONCLUSIONS

From the experimental research undertaken, the following points are concluded:

- URM chimneys without a retrofit system pose serious hazards in an earthquake due to their inherent weakness to destabilise, even under shaking generated from minor earthquakes. Due to the heritage value that these chimneys often have, it is more appealing to seismically retrofit the chimney instead of demolish.

- Based on simplified calculations, the tested chimneys do not meet current loading requirements in the as-built condition (<34% NBS).
- Based on attained test results of as-built chimney A, the performance of the as-built URM chimney against the calculated loading demand is 36% NBS.
- The PT system performed as expected by substantially increasing the inherent capacity of the URM chimney and well surpassing the minimum loading requirements of the tested chimney.
- The PT system was simple to install, did not alter the aesthetics of the chimney, and showed a significant increase in strength of the chimney.
- With further research, the PT design can be implemented as a cost-effective retrofit and significantly reduce damage caused due to low to high intensity earthquakes.
- The chimney rocking failure prediction correlated well with the measured strength for two chimneys (B1 and C2) and underestimated the value by 25% for chimney C1.

ACKNOWLEDGEMENTS

The research team is sincerely grateful to Pip and Graham Hunt, as without their trust and support by providing their URM chimney (A1) to test, this research project would not have been possible. Thanks are extended to Patrick Cummuskey from Auckland Council for providing demolition consents and generously helping to secure tested chimney A1.

The authors also gratefully acknowledge the financial support of the Australian Research Council through its Cooperative Research Centre programme and specifically the Bushfire and Natural Hazards CRC. Thanks to the Department of Planning, Transport, and Infrastructure (DPTI), South Australia, for allowing access to buildings B and C prior to their scheduled demolition.

Finally, the authors express their gratitude to J.D. McCauley and to the Adelaide university technical team for their assistance during the testing.

REFERENCES

ASCE/SEI 41 (2013). *Seismic Evaluation and Retrofit of Existing Buildings*. USA: American Society of Civil Engineers. doi:10.1061/9780784412855.

Bishop, D.G. (1974). "The Dunedin Earthquake, 9 April, 1974. Part 2: Local Effects." *Bulletin of New Zealand Society for Earthquake Engineering* 7 (3): 123–29.

Booth, Derek B., Wells, Ray E., & Givler, Robert W. (2004). "Chimney Damage in the Greater Seattle Area from the Nisqually Earthquake of 28 February 2001." *Bulletin of the Seismological Society of America* 94 (3): 1143–58. doi:10.1785/0120030102.

Dizhur, Dmytro, Giaretton, Marta, & Ingham, Jason (2017). "Performance of Early Masonry, Cob and Concrete Buildings in the 14 November 2016 Kaikoura Earthquake." *Bulletin of New Zealand Society for Earthquake Engineering* 50 (2 (Special Issue)): 194–205.

Dizhur, Dmytro, Ingham, Jason, Moon, Lisa, Griffith, Mike, Schultz, Arturo, Senaldi, Ilaria, Magenes, Guido, et al. (2011). "Performance of Masonry Buildings and Churches in the 22 February 2011 Christchurch Earthquake." *Bulletin of the New Zealand Society for Earthquake Engineering* 44 (4): 279–96.

FEMA P-58/BD-3.9.7 (2010). “Fragility of Masonry Chimneys.” ATC-43 Project - Federal Emergency Management Agency (USA).

Giaretton, Marta, Ingham, Jason M., & Dizhur, Dmytro (2017). “Experimental Validation of Seismic Retrofit Solutions for URM Chimneys.” *Bulletin of Earthquake Engineering*, no. In-press, Jul 2017. doi:10.1007/s10518-017-0200-0.

McSaveney, Eileen (2013). “Historic Earthquakes.” *Te Ara - the Encyclopedia of New Zealand*. www.TeAra.govt.nz.

Morris, Gareth J., Bradley, Brendon a., Adam, Walker, & Matuschka, Trevor (2013). “Ground Motions and Damage Observations in the Marlborough Region from the 2013 Lake Grassmere Earthquake.” *Bulletin of the New Zealand Society for Earthquake Engineering* 46 (4): 169–87. NZS 1170.5 (2004). *Structural Design Actions. Part 5: Earthquake Actions - New Zealand*. New Zealand Standards.

The New Zealand Parliament (2004). *Building Act*. M. o. E. D. Department of Building and Housing - Te Tari Kaupapa Whare, New Zealand Government. Wellington, New Zealand, Date of assent: 24 August 2004.



**MASONRY TODAY
AND TOMORROW**

**11 - 14 February, 2018
SYDNEY AUSTRALIA**

www.10amc.com

DYNAMIC TESTING OF MASONRY SHEAR WALLS STRENGTHENED WITH CORE-FILL RETROFITS

A. Papadopoulou¹, O. Fischer² and S.L. Lissel³

¹ M.Sc. Civil Engineering, Technical University of Munich, Germany, a.papadopoulou@tum.de

² Professor and Chair of Concrete and Masonry Structures, Technical University of Munich, Arcisstrasse 21, 80333 Munich, Germany, oliver.fischer@tum.de
Executive Board Member, B+S Consulting Engineers, Munich, Germany

³ Associate Professor, Department of Civil Engineering, University of Calgary, 2500 University Dr NW, Calgary, AB, Canada, slissel@ucalgary.ca
Project Engineer, B+S Consulting Engineers, Munich, Germany

The seismic in-plane performance of masonry walls retrofitted with unconventional core-fill materials is presented. For this purpose, shake table tests on four 1.8 x 1.8 m masonry walls were conducted at the University of Calgary, Canada. A steel fibre reinforced grout (SFRG) and two polyurethanes were examined and their efficacy as core-fill strengthening options was evaluated. The shake table tests were conducted by subjecting each wall to three earthquake signals and subsequently to sinusoidal motions. The earthquake signals varied in their peak ground acceleration (PGA), duration and energy release. The response of the structures was evaluated on the basis of the acceleration and displacement time histories obtained through the instrumentation.

Tests showed a high performance for all walls under excitation with the earthquake signals and no severe visible damage prior to failure. All walls were able to withstand a PGA of 4.9 m/s² (0.5 g) and failed showing a brittle behaviour. Finally, the failure mode was dependent on the core-fill material.

Keywords: concrete block, core-fill retrofit, steel fibre, polyurethane, shake table, seismic performance



INTRODUCTION

Shear walls are essential structural elements in structural masonry and have the ability to resist lateral loads due to winds or earthquakes. They are responsible for maintaining structural integrity and preventing collapse of a building even if severe damage is evident. Modern design standards require steel reinforcement for new construction (CSA 2004), yet many existing buildings do not meet these requirements. The conservation of older and, most importantly, historic buildings has been gaining importance over the past years and the development of alternative methods to strengthen masonry walls without altering them is very desirable. An ideal retrofit would require minimal skill, have minimal aesthetic impact and be relatively inexpensive. In this respect, satisfying structural requirements, while also being straightforward to design is a significant challenge.

This paper presents the in-plane seismic performance of concrete masonry block walls that have been subjected to strengthening with steel fibre reinforced grout and polyurethane core-fills. These materials can be pumped into the internal cores of hollow concrete block walls, filling the internal vertical core without having an aesthetic impact on the exterior of the wall. The surface of the wall remains intact, while the process remains easy, making this retrofit method very desirable. Four 1.8 x 1.8 m hollow concrete block walls constructed from standard 20 cm concrete block units and type S mortar were built and tested under earthquake excitation. Both partial and full filling of the walls were studied. The dynamic behaviour of the retrofitted wall specimens was evaluated through shake table tests. Prior to the full-scale tests on the shake table, materials, as well as prisms, were tested under compression through small scale tests to determine the strength of the individual retrofitting materials. Each wall was then tested under several natural and synthetic ground motions. The response of the structure was captured through accelerometers and laser displacement transducers at various positions on the wall.

MATERIAL PROPERTIES

A closer observation of the properties of the core fill materials should provide a basis for further understanding of their application. Therefore, material properties of the core fill materials as well as the wall components are presented.

The steel fibre reinforced grout mix comprises type CL fly ash and a Masterbuilder's Glenium 7101 superplasticizer. A combination of fine and coarse aggregates was used to create the concrete mix. The Dramix 80/30 BP 30 mm steel fibers manufactured by Bakaert had hooked ends. A similar grout mix was used by Harris (2016) who tested similar walls under quasi-static cycle loading. For a retrofit application in existing buildings where the top of the wall is not accessible, the mix can be pumped in the cores of the wall through a small hole drilled through the face shell in upper part of the wall. Since the SFRG mix is self-consolidating, mechanical vibration of the material is not required after the installation. Compressive tests were carried out on cylinders in accordance with the provisions of CSA A179-14. The mean compressive strength of the specimens was 47.84 MPa.

Two polyurethane materials were also used for the core-fills. The main advantage of these materials is their low weight resulting in lower seismic loads compared to the SFRG

strengthening method. Furthermore, polyurethanes can have a dual function and serve as insulation as well (Korany, Lohonyai & Ross, 2011). Both materials are manufactured and installed by similar processes, but differ in their properties. The speed of installation plays a significant role as it determines the density and hence the quality of the retrofit. The first material, a low density foam (32 kg/m³), is conventionally applied as a lifting foam. The material reacts quickly and hardens minutes after installation. Small voids in the retrofitting material were often visible after the installation and shrinkage was also observed (Figure 1 (left)). The foam, however, adhered well to the concrete blocks. The second material has water-repellent properties. The hydro-insensitive foam is a slowly reactive material with a liquid consistency when installed, which later hardens into a rigid foam. No voids in the materials were visible after installation and no shrinkage was observed (Figure 1 (right)). A very strong adherence to the masonry was also noticeable. For convenience, the core-fill materials will be referenced as lifting foam and hydro-insensitive material in this paper, according to their properties.

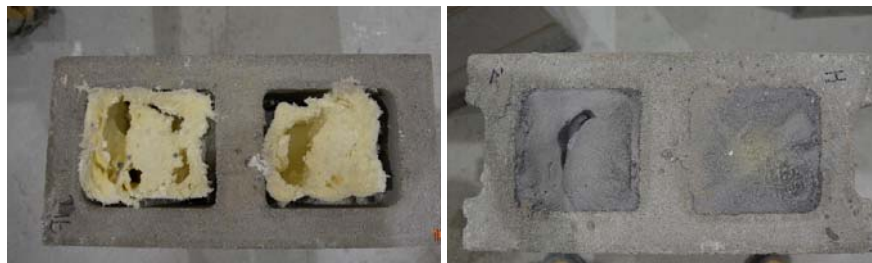


Figure 1: Polyurethane prisms: Lifting foam (left), Hydroinsensitive material (right)

The walls were constructed from 20 cm hollow concrete block units (19 cm x 19 cm x 39 cm) and a Type S mortar. Compressive tests were conducted on 50 mm mortar cubes to determine the quality of the mortar. The cubes showed an average compressive strength of 7.96 MPa.

Finally, compressive tests were conducted on hollow as well as retrofitted prisms. Each prism was built in a stack pattern and was three courses high. Characteristics of the hollow and retrofitted prisms are listed in Table 1:

Table 1: Compressive strength of prisms

| Type of prism/ retrofit | Mean Prism Strength (MPa) | COV % |
|-----------------------------|---------------------------|-------|
| Hollow, unfilled | 4.56 | 14 |
| SFRG mix | 22.08 | 10 |
| Lifting foam | 3.75 | 17 |
| Hydro- insensitive material | 4.89 | 9 |

Observation of the prisms' failure mode and the state of the specimens after the compressive tests can offer further information on the interaction between the retrofit and the concrete block wall. Specifically, insight into the adherence properties of the strengthening materials can be gained. The concrete block was the first material to fail under pressure. The SFRG cores showed a few hairline cracks after testing, but no severe damage. Adherence of the concrete block to the core-

fills was not as strong compared to the polyurethane materials. Nevertheless, it should be noted that SFRG strengthened prisms were subjected to much higher pressure. The hydro-insensitive polyurethane material adhered well to the concrete block, thus the concrete block remained attached to the retrofitted cores and did not fall apart, even after cracking on the surface occurred. The lifting foam also showed high adherence to the concrete block, similar to the hydro-insensitive material. A few specimens also contained visible voids in the cores, which could affect the strength of the walls. The compressive strength of the prisms was not expected to be affected by this fact. The limited standard deviation of the prisms' compressive strength justifies this assumption.

SPECIMEN DESCRIPTION

The four wall specimens were constructed in a running bond pattern with face shell mortar bedding. Strengthening was carried out by partially or fully filling the nine cores of each wall. The two specimens reinforced with SFRG were partially grouted, whereas the specimens being strengthened with polyurethane were fully filled. A cross section of the walls prior the reinforcement process is depicted in Figure 2:

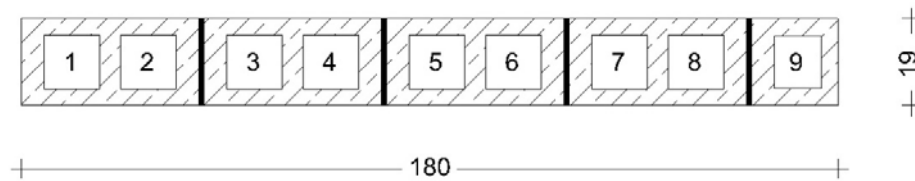


Figure 2: Cross section of masonry with cores

A summary of the characteristics of each specimen is presented in Table 2:

Table 2: Summary of wall specimens

| Specimen | Retrofit | Strengthened cores |
|----------|------------------------|-------------------------|
| Wall A | SFRG mix | 1st, 3rd, 5th, 7th, 9th |
| Wall B | SFRG mix | 1st, 5th, 9th |
| Wall C | Hydro-insensitive foam | 1st - 9th |
| Wall D | Lifting foam | 1st - 9th |

All specimens were tested at an age of 28 ± 2 days. Each specimen was built on an I-beam with anchorage (base beam), which could later be fastened on the shake table to conduct the experiments.

EXPERIMENTAL COMPONENTS

The shake table test arrangement comprises five main components; the shake table, the base and capping beam, the ground motions and the instrumentation. The quality of the results and their analysis is highly dependent on these parameters.

The shake table is a single degree of freedom system constructed as a steel frame consisting of I-beams, which enabled the testing of the wall specimens under dynamic excitation and the evaluation of their seismic performance. Furthermore, a base beam fastened the specimens on the shake table and prevented a failure through sliding. A capping beam consisting of a collection of steel plates was placed on the top of each specimen and was designed to introduce axial load on the wall. It represented a fraction of the load applied to a wall through the upper floors in existing buildings. The weight of the capping beam amounted to approximately 1.5 tonnes.

Both natural and synthetic signals were used for the dynamic excitation. First, a synthetic motion of the Kobe (in 1995) earthquake was chosen. The signal has a small duration and a peak ground acceleration of 0.5 g. The peak ground displacement is 9.53 cm in that motion, almost reaching the capacity of the shake table. The signal was reproduced five times at different intensities ranging from 25% to 125%. Thus, peak ground accelerations up to 0.63 g were reached when testing with this signal. The second signal, a ground motion of the Tohoku (in 2011) earthquake, is characterized by a lower PGA but twice as much input energy, due to the longer duration of the signal. The signal was reproduced four times with intensities ranging from 50% to 125%. Subsequently, a series of sine waves was applied to Walls A, B and C to reach higher accelerations. All records were applied in the in-plane direction to each wall. A list of the selected ground and sinusoidal motions is presented in Tables 3 and 4 respectively:

Table 3: Summary of ground motions

| Name | Earthquake | PGA [g] | PGD [cm] | Duration [s] | Simulated Intensities [%] |
|----------|--------------|---------|----------|--------------|---------------------------|
| Signal 1 | Kobe, 1995 | 0.51 | 9.53 | 41 | 25, 50, 75, 100, 125 |
| Signal 2 | Tohoku, 2011 | 0.36 | 9.46 | 109 | 50, 75, 100, 125 |

Table 4: Summary of sinusoidal motions

| Wall | Sinusoidal Motion | Amplitude [mm] | Frequency Range [Hz] | PGA [g] | Remarks |
|------|-------------------|----------------|----------------------|---------|--|
| A | Sine Wave 1 | 100 | 1 | 0.4 | - |
| | Sine Wave 2 | 50 | 1.5 - 2 | 0.8 | - |
| | Sine Wave 3 | 50 | 2.75 | 1.5 | - |
| B | Sine Wave 1 | 100 | 1 | 0.4 | Start/Ending-phase with lower frequency |
| | Sine Wave 2 | 50 | 1.5 - 2 | 0.8 | Start/Ending-phase with lower frequency |
| C | Sine Wave 1 | 100 | 0.75 - 1 | 0.4 | Start/Ending-phase with lower frequency |
| | Sine Wave 2 | 50 | 1.2 - 2.3 | 1.06 | Start/Ending-phase with lower frequency Rate of increase: 0.1 Hz/5 cycles |

Finally, the response of the specimens was captured by accelerometers and laser displacement transducers. A schematic of the experimental arrangement is presented in Figure 3.

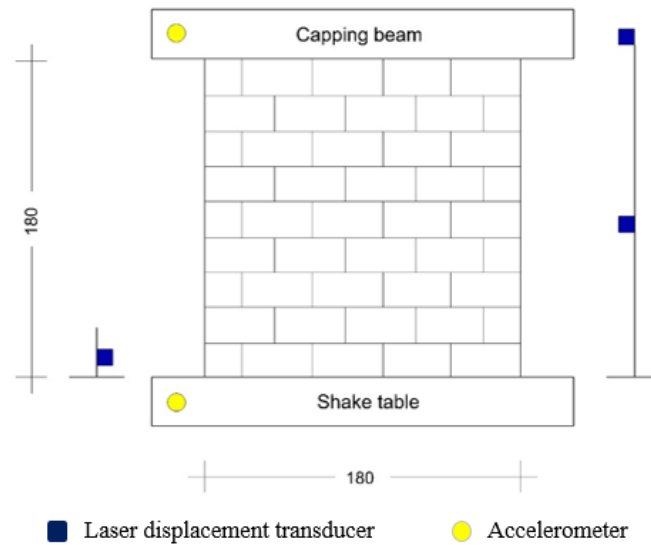


Figure 3: Experimental Arrangements and Specimen

SHAKE TABLE TEST RESULTS

A total of 49 shake table tests were conducted on four unconventionally reinforced masonry walls. The testing of a particular wall was continued until failure or damage indicating imminent failure occurred. Thus, as the number of tests performed on each wall increased, the higher the resistance of the tested wall. The response of each structure, as well as their comparison is based on deformations, force-displacement relationships and observations during testing. Conclusions on the failure mode are also drawn for the walls that were tested to failure.

Observations and Failure Mechanisms

Wall A had the greatest mass out of the four walls and was expected to be the stiffest wall among the specimens. When subjected to the earthquake signals, there were no signs of damage to be found on the surface of the wall. The wall was then excited with two different sine waves showing a peak ground acceleration of 0.4 g and 0.8 g, respectively. Signs of damage, even after such high accelerations, were not evident. This shows the high performance of the wall even under higher earthquake loads. Finally, the structure was subjected to a sine wave with a higher frequency (2.75 Hz) to achieve higher PGA and to observe the failure mode of the wall. Under this type of excitation, the wall started rocking over the first course forming an evident crack, which then propagated and formed cracks between the first and second core of the wall, as well as the eighth and ninth core, separating the two end-cores from the rest of the wall. The central cores kept their integrity, and thus the wall collapsed in four pieces as shown in Figure 4. The failure mode as well as the recorded acceleration and displacement-time histories illustrate the sudden brittle failure of Wall A under the last excitation. After the formation of wider cracks, the lack of rebar causes the wall to lose its integrity. However, this is under an excitation with a very high peak ground acceleration. In general, this retrofitting option showed high performance.



Figure 4: Failure mode for Walls A – D

Wall B, having only three cores retrofitted with the SFRG mix, showed less resistance than Wall A. When subjected to the earthquake signals, the wall showed no noticeable damage for Signal 1; however, hairline cracks started showing in the mortar for Signal 2. Although Signal 1 induced a higher peak ground acceleration than Signal 2, the higher amount of energy being released due to the long duration of Signal 2, resulted in more damage caused by the second signal. Thus, the effect of parameters other than peak ground acceleration, such as duration and input energy, is evident here. Similar observations were also made by Drysdale and Hamid (2005). Damage was restricted to small hairline cracks in the bed joints over the first and second course, where a concentration of the loads applied to the wall is expected. The concrete blocks remained intact during testing with the earthquake signals. Excitation with Sine wave 1 had a similar effect on the specimen as Signal 2. Wall B showed very high performance when being subjected to accelerations up to 0.6 g. Unlike Wall A, Wall B was not able to resist a peak ground acceleration of 0.8 g. The wall failed under the second sinusoidal motion, which included a leap in acceleration values from 0.4 to 0.8 g. The failure mode was identical to Wall A as shown in Figure 4. The acceleration and displacement-time histories display identical values for the recordings up to the point of failure. A deviation between these time histories was noticeable when the acceleration jumped from 0.4 g to 0.8 g and lead to the sudden failure of the wall.

The earthquake signals had a similar effect on Wall C as on Walls A and B. Small hairline cracks formed in the mortar of the first two bed joints, whereas other severe damage or cracking of the concrete blocks was not visible. The wall also showed high resistance when excited with the first sinusoidal motion, thus showing a very high performance. The second sinusoidal wave was

modified and showed different characteristics than the signal previously used on the grouted specimens. The wall was first subjected to an acceleration of 0.4 g, which increased with a rate of 0.1 g/ 5 cycles and resulted in a rocking failure of the wall. The testing was terminated as soon as toe crushing occurred. This type of failure mode is typical for unreinforced masonry walls Drysdale and Hamid (2005), however, the behaviour of Wall C under seismic loads can be attributed to the lightweight nature of its core fill as well as the effectiveness of the selected anchorage. No significant cracks were formed and damage was restricted to crushing of the bottom right corner of the wall. Acceleration and displacement recordings exhibited a gradual but limited increase with each loading step. A notable rise was seen in the last two cycles, where the wall started rocking and the test had to be terminated. This type of core fill offers diverse benefits, including the ability of the wall to deform more, as opposed to walls A and B, which failed suddenly.

Wall D was expected to show the lowest resistance. This wall was only subjected to the earthquake signals as it showed signs of failure at the highest intensity levels of Signal 2. During testing with Signal 1 and the low intensities of Signal 2, the only damage observed was again hairline cracks in the lower bed joints. Vibration of the wall was evident, especially during testing with Signal 2, which has a higher amount of energy release. The failure mode was a rocking failure, similar to Wall C. Rocking occurred at the bottom of the wall, implying a deficit in the anchorage system of the wall. Since testing was terminated before any severe damage occurred, signs of failure were only visible under the bottom course of the wall, where mortar was partially missing due to the sliding and vibration of the wall.

Displacement-time histories

The dynamic response of the retrofitted walls was also evaluated based on the displacement values captured at the bottom, mid-height and top level of the wall. This analysis was based on displacement values obtained from the laser displacement transducers and the walls are approached as a system consisting of two elements, the actual wall and the capping beam, with two degrees of freedom. Analysis of the response of the walls for an excitation with Signal 1 and an intensity of 100% (PGA: 0.5 g) revealed a lack of phase shift or displacement variations between the three lasers and illustrated the absence of larger deformations and significant damage for all four walls up to a peak ground acceleration of 0.5 g. These observations suggest the movement of the walls as a rigid structure. This conclusion is also consistent with the test observations after testing with Signal 1 and the absence of damage, apart from small hairline cracks. Since the majority of all excitation signals were characterized by a peak ground acceleration below 0.5 g, there is no variation in the behaviour of the walls for all intensities of Signal 1 and 2.

Deformation profiles

Deformation profiles are a form of visualization of the deformations taking place. The deformation of the four walls under excitation with Signal 1 (Intensities 25 - 100%) are presented in Figure 5. For Wall A, apart from a seemingly faulty recording for an intensity of 25%, there is no relative deformation over the height of the wall to be observed. Walls B and C show a minor deformation in the lower courses and no relative deformation in the upper part of the wall. The difference in their response lies in their performance with increasing intensity of the signal. While

Wall B shows increasing deformation with increasing intensity, Wall C has an almost identical deformation profile for all intensities. Finally, Wall D is the only structure showing a minor increase in deformation along the height of the wall for all intensities.

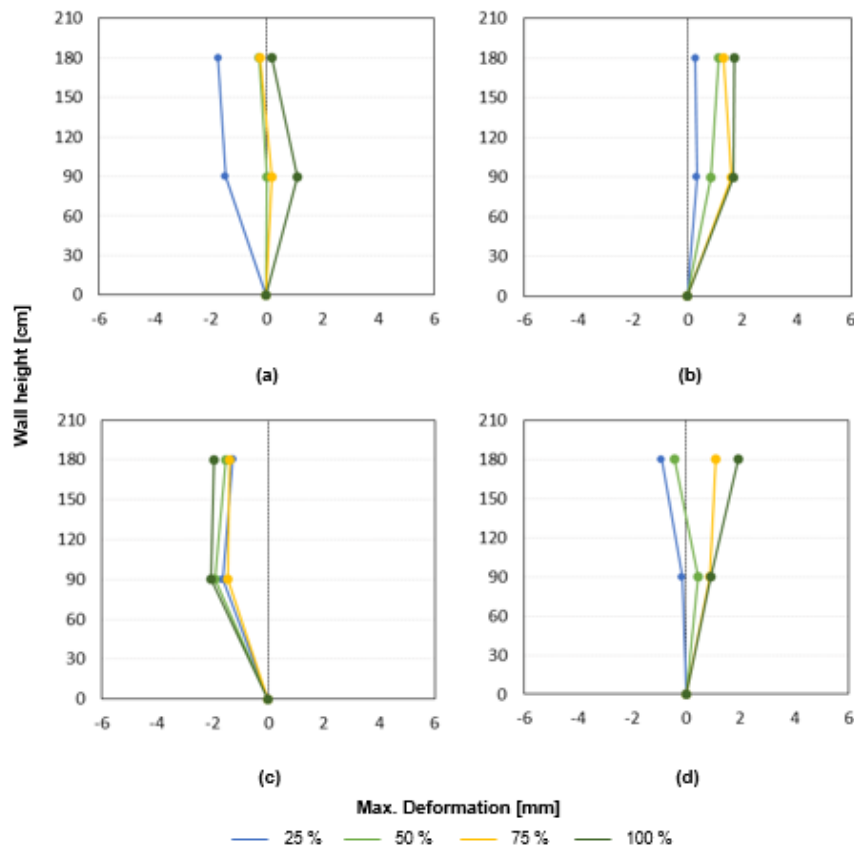
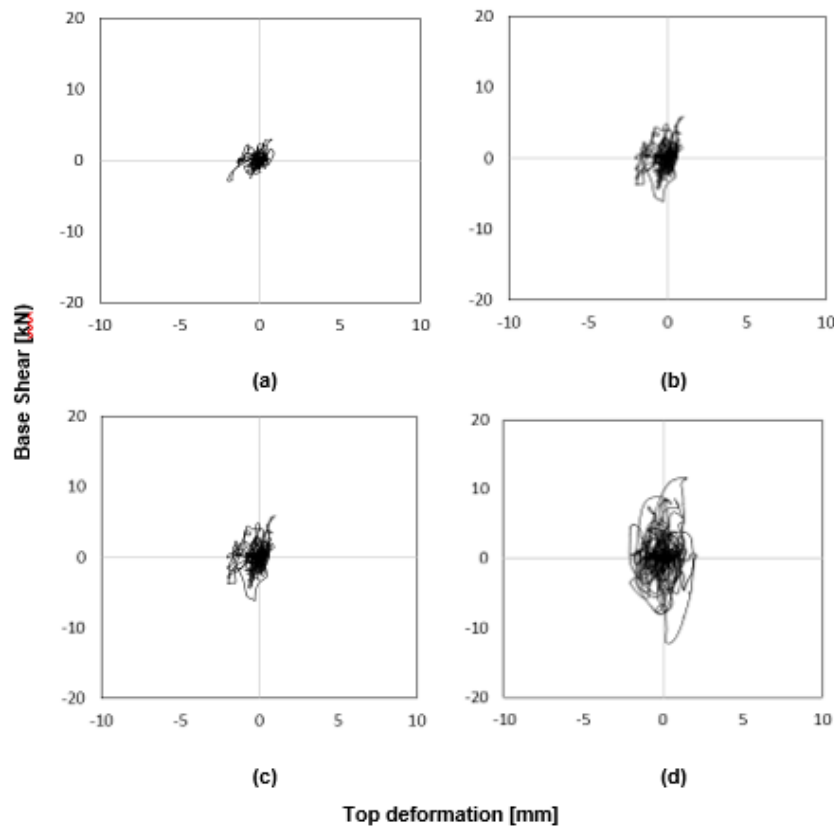


Figure 5: Deformation profiles in elevation for different intensities of Signal 1: Wall A, (b) Wall B, (c) Wall C, (d) Wall D

Force- displacement relationships

In this section, the shear forces developed in the structure as well as the displacement demand are presented on the basis of the acceleration and displacement data recorded. Force-displacement relationships produce hysteresis loops, giving insight into the behaviour of the wall and specifically its energy dissipation and stiffness. Inertia forces acting on the wall were computed as the product of the recorded accelerations and corresponding masses. Damping forces were not considered in the analysis. Since the structure is studied as a double degree of freedom system, forces acting on the wall and the capping beam were computed separately. Hysteresis curves are commonly produced through static testing to evaluate the response of a structure under excitation with gradually increasing displacements. Thus, degradation in stiffness and resistance can be observed for a specific ongoing stimulation. Earthquake signals, however, are characterized by an irregular displacement profile and oscillations taking place around a constantly alternating zero line. Thus, the resulting hysteresis curves show an irregular pattern. Results in this paper are thus

only presented selectively for one specimen. Figure 6 shows the relationship between base shear and top deformation for Wall A under excitation with different intensities of Signal 1. The higher the intensity and thus acceleration, the higher the base shear-forces, however, the deformation is limited, justifying the lack of damage. The response of the wall is in the linear elastic stage with no evident change in the stiffness of the wall. The slope of the resulting curves shows no evident decrease with the propagation of testing and thus no stiffness degradation for this type of excitation.



**Figure 5: Hysteresis loops for Wall A at different intensities of Signal 1:
(a) 25%, (b) 50%, (c) 75%, (d) 100%.**

Seismic resistance

The seismic resistance of the structures can be evaluated by plotting the maximum resisted base shear and the corresponding top displacement for each test (Senaldi et. al., 2014). Wall A resisted the highest base shear forces, with Wall C coming up second in the ranking. Walls B and D were both able to resist forces up to approximately 15 kN. Walls A, B and C showed little increase in deformation as testing progressed, apart from a few deviations resulting from measurement inaccuracies. Wall D was more susceptible to the increase in the intensity of the testing.

Wall A shows minimal increase in deformation with the increase in base shear forces and the testing progression. Wall B shows an increase in deformation with the increase in the intensity of testing and thus, base shear forces. However, the progression of testing (changes between Signal

1, 2 and the sinusoidal motion) has no effect and deformation values remain in the same range for an excitation with Signal 1 and 2. Wall C shows greater deformation values in comparison to Walls A and B and also exhibits an increase in deformation for higher intensities, similarly to Wall B. For Wall D, there is an evident increase in deformation with the increase in intensity and progression in testing. This behaviour can be justified by the less stiff nature of Wall D in comparison to Walls A, B and C.

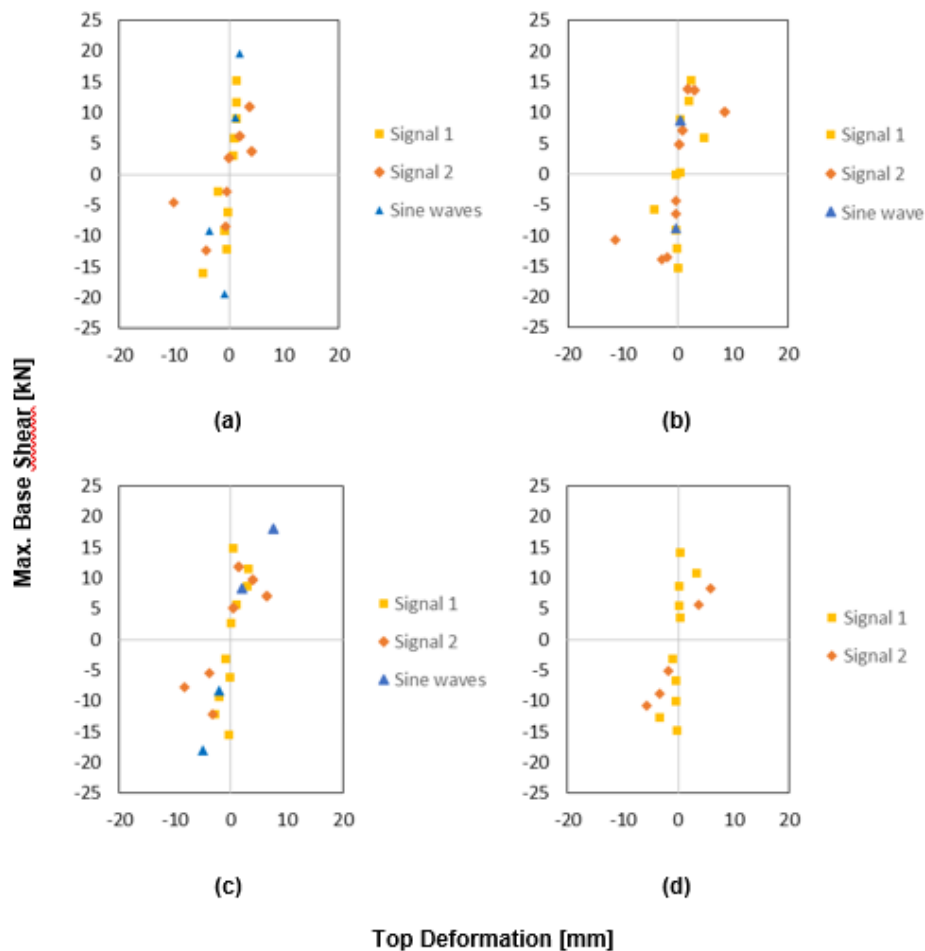


**Figure 6: Seismic resistance curve in terms of base shear and top deformation:
(a) Wall A, (b) Wall B, (c) Wall C and (d) Wall D**

A comparison of the maximum base shear resisted (Base shear_{\max}) and the base shear forces at failure ($\text{Base shear}_{\text{fail}}$) are presented in Table 5. Walls A and B were able to resist higher loads than the base shear forces that ultimately led to the failure of the wall. Both walls, however, were subjected to higher accelerations in a sudden manner, which led to their brittle failure and the accumulation of damage must also be considered. Walls C and D, on the other hand, were subjected to higher acceleration values more gradually. Thus, the base shear forces at failure were higher than the maximum forces resisted for Wall C and comparable for Wall D. Furthermore, polyurethane materials allow the wall to deform more, averting a sudden failure of the structure.

Table 5: Comparison of seismic resistance at max. seismic load and failure

| Specimen | Base Shear_{max} (kN) | Excitation_{max} | Base Shear_{fail} (kN) | Excitation_{fail} |
|-----------------|--|---------------------------------|---|----------------------------------|
| Wall A | 19.56 | Sine Wave 2 | 10.27 | Sine Wave 3 |
| Wall B | 15.29 | Singal 1 _(125%) | 12.09 | Sine Wave 2 |
| Wall C | 18.02 | Sine Wave 2 | 22.59 | Sine Wave 2 |
| Wall D | 14.84 | Singal 1 _(125%) | 14.03 | Singal 2 _(125%) |

CONCLUSIONS

All walls showed high performance under dynamic excitation withstanding PGAs up to 4.9 m/s² (0.5 g) without severe damage. Damage was restricted to small hairline cracks in the mortar prior to failure. The failure mode varied depending on the strengthening material. The SFRG strengthened walls started rocking after cracks formed on the lower bed joints. The specimens strengthened with polyurethane materials showed a rocking failure, which resulted from poor anchorage. All walls moved as rigid objects throughout the testing procedure, showing very limited deformation prior to failure. The SFRG strengthened walls showed almost no deformation prior to failure, whereas the specimen strengthened with the hydro-insensitive material showed limited deformation before the rocking failure.

ACKNOWLEDGEMENTS

The authors would like to thank Poly-Mor Canada for donating polyurethane materials, Bekaert for providing steel fibres, BASF Canada for providing superplasticizer, Expocrete Canada for donating concrete block, Quickrete Canada for donating mortar, and the Masonry Contractors Association of Alberta for their support.

REFERENCES

- CSA A179-14, C. (2014). Mortar and Grout for Unit Masonry. Mississauga, Ontario: Canadian Standards Association.
- CSA S304.1-04, C. (2004). Design of Masonry Structures. Mississauga, Ontario: Canadian Standards Association.
- Korany, Y., Lohonyai, A., & Ross, M. (2011). Application of POLY-MOR Foam as. University of Alberta.
- Harris, T. R. (2016). In-Plane Core Fill Strengthening of Concrete Block Masonry Shear Walls. Doctoral Dissertation, University of Calgary, Civil Engineering, Calgary.
- Senaldi, I., Magenes, G., Penna, A., & Rota, M. (April 2014). Diaphragms on the Experimental Seismic Response of a Full Scale Unreinforced Stone Masonry Building. Journal of Earthquake Engineering



**MASONRY TODAY
AND TOMORROW**

**11 - 14 February, 2018
SYDNEY AUSTRALIA**

www.10amc.com

ENVIRONMENTAL EFFECT ON REINFORCED MASONRY WALLS STRENGTHENED WITH NSM AND CEMENTITIOUS ADHESIVE

Z. Al-Jaberi^{1,2}, J.J. Myers³ and M. ElGawady⁴

¹ PhD candidate, Civil, Department of Civil, Architectural & Environmental Engineering, Missouri University of Science and Technology, 1401 N. Pine Street, zkayc7@mst.edu

² Assistant lecturer, Department of Civil Engineering, College of Engineering, Al-Nahrain University

³ Professor and Associate Dean, Department of Civil, Architectural & Environmental Engineering, Missouri University of Science and Technology, 1401 N. Pine Street, jmyers@mst.edu

⁴ Benavides Associate Professor, Department of Civil, Architectural & Environmental Engineering, Missouri University of Science and Technology, 1401 N. Pine Street, elgawadym@mst.edu

The strengthening of masonry structures using the near surface mounted (NSM) technique with fiber reinforced polymers (FRPs) has gained widespread acceptance recently. Studying environmental conditions on strengthened masonry walls is not straightforward because it is related to FRP, masonry unit, and adhesive material properties, as well as FRP bar–masonry interaction. The behavior of strengthening systems is still of great concern to the industry, especially when exposed to harsh environmental conditions. In this study, an experimental investigation was made to evaluate the flexural behavior of reinforced masonry walls strengthened with NSM-FRP bars and cementitious adhesive when exposed to combined weathering actions. The strengthened walls were exposed to 350 different environmental cycles through a computer-controlled environmental chamber. The exposure cycles consisted of a combination of severe freeze-thaw, extreme temperature, high relative humidity and indirect ultra violet radiation exposure. The exposure regime was selected to simulate the seasonal changes in an environment such as the Midwest in the United States in an accelerated manner. Eight reinforced masonry walls were built for this study. Identical reinforced masonry walls in their unstrengthened form were used as control specimens. Two sets of three specimens strengthened using NSM with different types of FRP bars (glass and carbon) were tested. The first set was tested after at least 28 days as a curing period, while the other set was tested after 72 days of exposure to harsh environmental conditions. In terms of flexural capacity, the specimen strengthened with CFRP strips was affected by environmental conditioning more than the specimen strengthened with GFRP bars.

Keywords: Reinforced masonry, FRP, NSM, cementitious, environment



INTRODUCTION

Strengthening of masonry structures is often required after a certain period of time due to code modifications, construction errors, overloading, destructive environmental exposure or mechanical damage. Fiber reinforced polymer (FRP) techniques have become popular for strengthening in the last decade due to their light weight and non-corrosive makeup.

The near surface mounted (NSM) repair technique has been proposed and applied in the field as an alternative technique to externally bonded (EB) strengthening systems used to increase the flexural capacity for both unreinforced and reinforced masonry walls (Al-Jabari et al., 2015, Al-Jaberi et al., 2015, De Lorenzis et al., 2000, Galati et al., 2006). Typically, epoxy adhesives are used to fill the pre-cut grooves to bond the FRP bar to the structural element. Epoxy has proven to provide excellent bond and durability behavior. In high temperature applications, the guidelines for design of FRP strengthened structures recommend use of fire protection system or insulation to prevent epoxy approaching transition temperature (Soudki and Alkhrdaji, 2005). Using a cementitious-based material as an alternative adhesive agent in the NSM technique is very attractive especially for high temperature applications.

Developed research on strengthening using FRP has focused on the short-term durability performance of strengthened structural elements and has rarely considered the full lifetime of the structure. In addition, durability research has been mostly dedicated to examining environmental degradation factors individually rather than combined in a synergistic manner.

Cold environments and freeze-thaw cycling of NSM FRP have been investigated (Mitchell, 2010). This study presented the experimental results for the flexural and bond performance and freeze-thaw durability of NSM FRP through a series of tests on strengthened slab strips and a series of pull-out bond tests. The results indicated that strengthening using cementitious material as the adhesive for the NSM bar had no discernible negative impact on the performance of the strengthening system. Al-Mahmoud et al. (Al-Mahmoud et al., 2014) investigated the effect of environmental exposure (freeze-thaw cycles and salt water immersion) on NSM CFRP rod strengthened specimens and embedded in cementitious material. The specimens were exposed to up to 300 freeze-thaw cycles; no change in bond strength for NSM FRP rod resulted after this exposure. Soliman et al. (Soliman et al., 2010) conducted a small scale pull-out test to study the bond performance of NSM FRP under 200 freeze/thaw cycles. The main mode of failure for exposed specimens with cement adhesive was splitting of adhesive material with a failure load about 40-56% of that of their counterparts with epoxy adhesive.

High temperature is another factor that affects the behavior of the NSM strengthening system. An experimental study on bond strength of NSM FRP bars under high temperature was reported (Yu and Kodur, 2014). The bond strength was evaluated in the 20-400°C (68-752°F) temperature range. Results from this experimental work indicated that bond strength decreased significantly in the temperature range of 20-200°C (68-392°F) and only retained 30% of the original value at 200°C (392°F). The performance of NSM FRP under high temperature can be improved significantly when inorganic adhesive material is used rather than an ambient temperature cure epoxy. Cementitious-based materials are able to support sustained load for more than four hours when the temperature was 100°C (212°F) and approximately one hour at 200°C (392°F) (Burke et al., 2013). The mode of failure in this study was by debonding at the FRP-cementitious interface. Burke (2008) studied the low and high temperature performance of NSM FRP strengthened concrete slabs. It was concluded that low temperature exposure (-26°C) (-14.8°F)

had no measurable negative effects on flexural behavior. For high temperature exposure 100°C (212°F), the cementitious-based adhesive presented excellent behavior, allowing the strengthening system to remain structurally effective for more than five hours under sustained load. Moisture has been observed to be another important deteriorating agent for specimens strengthened with advanced composites. Pull-off testing was used to evaluate the effect of moisture on FRP-masonry bond (Ghiassi et al., 2012). Constant relative humidity (RH) of 100% at 23°C (73.4°F) was applied on strengthened specimens for eight weeks. The degradation was investigated on the conditioned specimens for two periods (four and eight weeks) of exposure to evaluate the bond performance. The results indicated 15% and 23% reductions in bond strength for conditioned specimens after four and eight weeks of exposure, respectively. Based on this study, moisture exposure can reduce the bond strength of the FRP-masonry elements significantly within a two month period of exposure. The bond failure mode was affected by exposure to accelerated wet/dry cycling. The failure after this exposure condition occurred at the adhesive-substrate interface. In contrast, for the specimens not exposed to wet/dry cycling, the bond failure always occurred in a very thin mortar layer of the concrete (Dai et al., 2010).

There is a lack of long-term data on the performance of strengthened masonry walls under combined environmental exposures. The evaluation of the long-term performance of a strengthened structure requires the assessment of the durability of both the strengthening components and the involved materials under combined environmental action to simulate the natural weathering conditions. This research focused on the effect of combined environmental cycles on flexural behavior of reinforced masonry walls strengthened with the NSM FRP technique and cementitious adhesive. This study was motivated by the need to increase the knowledge on the long-term expected durability of the NSM FRP technique using cementitious material as an alternative choice to epoxy agent. This paper presents an experimental program in which out-of-plane four point load tests are carried out for evaluating the flexure behavior of specimens before and after environmental exposure. The behavior was evaluated in terms of ultimate capacity, secant stiffness, ultimate deflection, and mode of failure.

SCOPE AND GOAL OF THIS STUDY

The purpose of this study is to present the results of reinforced masonry walls strengthened with NSM FRP and cementitious adhesive when exposed to combined environmental conditions. An additional purpose is to study the possibility of change in design flexural capacity or expected failure mechanism due to combined environmental actions. Therefore, this study investigated how the combination of different environmental cycles can affect the long-term behavior of the strengthened walls. Since the effects of the single environmental factors were investigated in previous studies, this study allows evaluating the combined or synergistic effect, which is more representative of structural elements in the field. Eight reinforced masonry walls classified in two sets were built for this study. Each set consisted of three specimens strengthened using different types of fiber (glass and carbon) in addition to the control (stack and running) specimens that were tested. The first set was tested after at least 28 days of a laboratory condition, while the other set was tested after 72 days of exposure to 350 different environmental cycles of freeze-thaw, relative humidity, and high temperature. These cycles are proposed to simulate 20 years of typical in-situ weather conditions in the Midwest region of the United States.

EXPERIMENTAL PROGRAM

This experimental program investigated individual components of the strengthened walls and the out-of-plane resistance of eight reinforced masonry walls strengthened by the NSM technique with cementitious adhesive. The individual components (cementitious adhesive, masonry unit, and FRP bars) and the strengthened masonry walls were subjected to lab conditions and different weathering action in order to compare the results and examine the long-term durability effect.

MATERIALS CHARACTERIZATION

For the NSM FRP technique, two types of FRP bars were used: glass and carbon-epoxy pultruded FRP with a diameter of 10 mm (0.39-in.). The modulus of elasticity, tensile strength, and elongation strain for all these types were determined by the manufacturer as shown in Table 1.

Table 1: Mechanical Properties of FRP Bars and Strip

| Type of FRP | Dimension (mm) | Ultimate tensile strength (MPa) | Elongation at break % | Tensile modulus (GPa) |
|---|----------------|---------------------------------|-----------------------|-----------------------|
| Aslan 200 CFRP bar | 6 | 2241 | 1.81 | 124 |
| Aslan 100 GFRP bar | 6 | 896 | 1.94 | 46 |
| Note : 1.0 GPa = 145.03 ksi; 1.0 MPa = 0.145 ksi; 1.0 mm/mm = 1.0 in./in.; 1.0 mm = 0.039 in. | | | | |

A series of tests were performed to determine each material's mechanical properties. The properties of the materials that were used to construct the specimens are summarized in Table 2.

Table 2: Results of the Material Properties

| Material | Properties | Values (MPa) | Method |
|--------------------------|----------------------------|--------------|---------------|
| Concrete Block | Prism Compressive Strength | 21 | ASTM C1314-12 |
| Mortar Type S | Compressive Strength | 17.5 | ASTM C109-13 |
| Grout | Compressive Strength | 35 | ASTM C1019-13 |
| Cementitious adhesive | Compressive Strength | 55 | ASTM C109-13 |
| Steel Bar | Yield Strength | 471 | ASTM A370-13 |
| | Modulus of Elasticity | 203000 | |
| Note: 1.0 MPa = 145 psi. | | | |

TEST MATRIX AND SPECIMEN PREPARATION

A total of eight strengthened reinforced masonry walls were prepared for this purpose. The specimens for the two sets have the same overall dimensions and longitudinal main reinforcement. The walls were constructed in running and stack patterns and type S mortar using standard masonry blocks 152.5 mm (6-in.). The nominal dimensions of these walls were 1220 x

610 x 152.5 mm (48 x 24 x 6-in.). 2#4 (Area=0.2 in² or 129 mm²/ bar) reinforced fully grouted steel bars were installed four days after wall construction to ensure stability during the vibration process. These control and strengthened wall configurations, in addition to the cross section of the block unit, are shown Figure 1.

The specimen ID consisted of three parts, as shown in Table 3. The first part consisted of two characters (type of FRP and number of FRP bars). The first character represents type of FRP bar: namely “C” for carbon FRP and “G” for glass FRP. The second part referenced the masonry bond pattern; a character “R” represented running bond pattern, and “S” represented a stack bond pattern. The third part identified the exposure condition: namely “L” for laboratory conditions and “EN” for environmental chamber exposure.

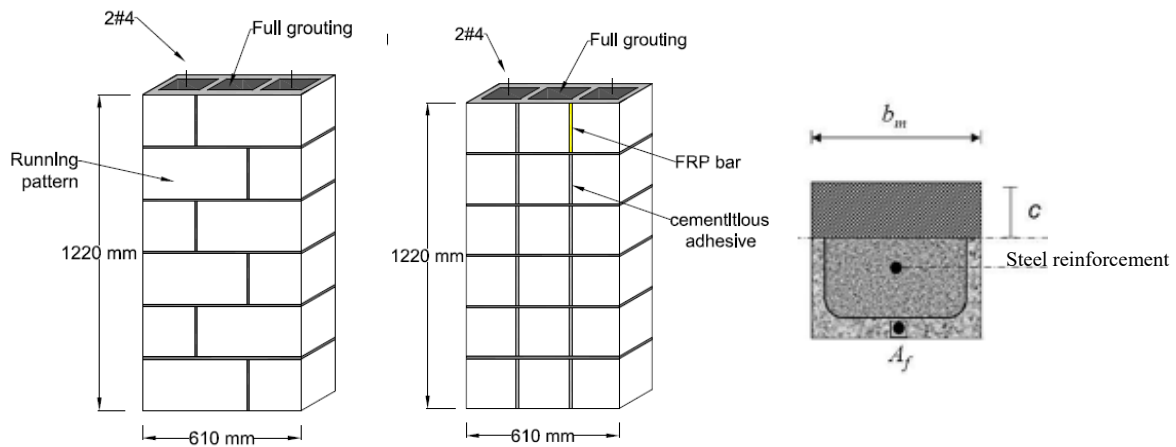


Figure 1: Cross section and reinforced wall configuration

Table 3: Experimental Test Matrix

| Wall | Specimen designations | FRP Type | Number of bars | Groove dimension (mm*mm) |
|------|-----------------------|----------|----------------|--------------------------|
| 1 | Control-R | - | - | - |
| 2 | Control-S | - | - | - |
| 3 | C1-R-L | carbon | 1 | 19*19 |
| 4 | G1-R-L | glass | 1 | 19*19 |
| 5 | G2-S-L | glass | 2 | 19*19 |
| 6 | C1-R-EN | carbon | 1 | 19*19 |
| 7 | G1-R-EN | glass | 1 | 19*19 |
| 8 | G2-S-EN | glass | 2 | 19*19 |

NSM STRENGTHENING PROCEDURE

The NSM FRP installation process needed no surface preparation and involves placing FRP bar into a square groove cut at the tension surface of the masonry wall. A special concrete saw was used to cut the grooves with a dimension more than double the diameter of the bar to avoid

splitting failure of the epoxy cover (De Lorenzis and Nanni, 2002). The FRP bars are deformed by a helical wrap with a sand coating to improve the bond between the bars and cementitious adhesive. The cementitious paste was placed into the grooves to cover 3/4 of the groove height. The FRP bar was inserted in the grooves and lightly pressed to force the bonding agent to flow around the bar and ensure complete bond between the bar and the sides. The groove was then filled with more adhesive and the surface levelled. Construction of masonry walls and curing of cementitious adhesive are shown in Figure 2.



(a)



(b)

Figure 2: Experimental program: (a) Construct Walls and (b) curing of cementitious adhesive

ENVIRONMENTAL EXPOSURES

The exposure cycle consisted of a combination of severe freeze-thaw cycles, extreme temperature cycles, high relative humidity cycles, and indirect ultra-violet radiation exposure. The exposure regime was selected to simulate the seasonal changes in an environment such as the Midwest in the United States in an accelerated manner. A computer-controlled environmental chamber is used to simulate 350 different environmental cycles. This regime consisted of the following:

Freeze-thaw cycles: 100 cycles that simulated the effects of the winter season. Each freeze-thaw cycle consisted of freezing at -17.8°C (0°F) for 50 minutes and thawing at 4.4°C (40°F) for 50 minutes. The transition period between freezing and thawing was 30 minutes.

Extreme temperature cycles: to simulate summer seasonal effects, 150 alternating cycles of extreme temperature from 27 to 50°C (80 to 120°F) was used. Extreme temperature cycles consisted of temperature variation between 27°C (80°F) for 25 minutes and 50°C (120°F) for 25 minutes. The transition period between high and low temperature was 20 minutes.

Relative humidity cycles: the relative humidity were carried out between 60% and 100% and maintained for 20 minutes each, transition period between 100% and 60% humidity was 30 minutes. Relative humidity cycles were carried out at constant temperatures of 15.5°C (60°F) and 26.7°C (80°F).

The order of cycling initiated with 50 freeze-thaw cycles, followed by 20 RH cycles at constant temperature of 15.5°C (60°F), the first set of 40 extreme temperature cycles, then 20 RH cycles at constant temperature of 26.7°C (80°F), the second set of 40 extreme temperature cycles, then 20 RH cycles at constant temperature of 15.5°C (60°F) and the third set of 40 extreme temperature cycles. The exposure regime and specimens in environmental chamber are shown in Figure 3.

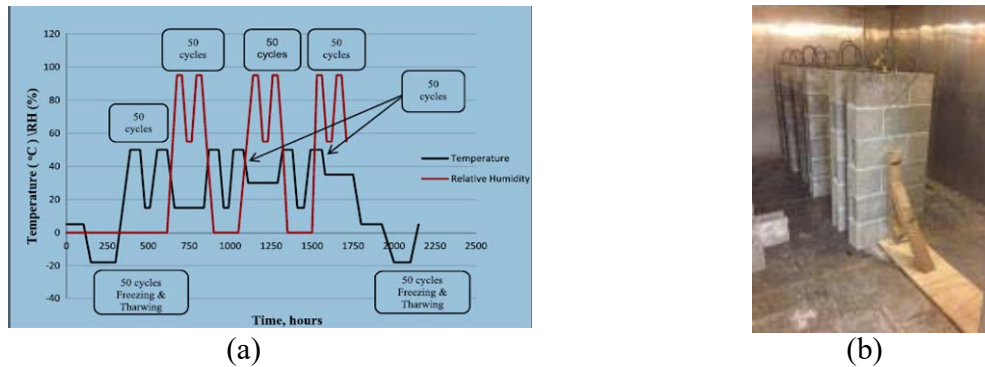


Figure 3: Environmental cycles: (a) exposure regime (b) specimens in environmental chamber

TEST SETUP AND LOADING RATE

Four-point line loading can be used to conduct out-of-plane testing on reinforced masonry walls. The strengthened reinforced masonry specimens used in this study will be tested with simply supported boundaries under cyclic load as shown in Figure 4. An MTS double-acting hydraulic jack with a push-pull capacity of 965 MPa (140 kips) was used to apply a vertical load on the wall panel. This load was transferred to the masonry specimen by means of continuous steel plates and bars along the full width of the external face of the reinforced walls to provide two equal line loads. A piece of thick rubber sheet was inserted at all of the interfaces between the steel plate and masonry wall. The rubber sheet distributed the load evenly and minimized any stress concentration due to unevenness of the wall surface. The distance between these two lines was 200 mm (8-in.). The load was applied in cycles of loading and unloading, as a displacement control, at a rate of 1.27 mm/min (0.05-in./min) through an MTS computer control station up to the load peak value. The displacement amplitude increment was 6.35 mm (0.25-in.); double half loading cycle was applied for each amplitude level as illustrated in Figure 5.

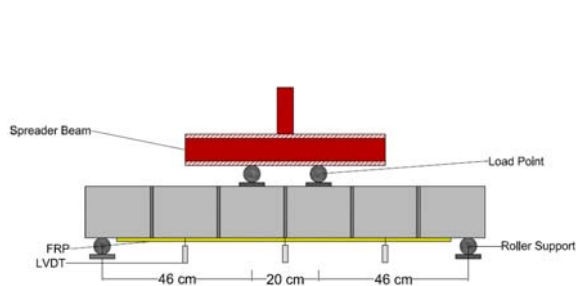


Figure 4: Four point load setup

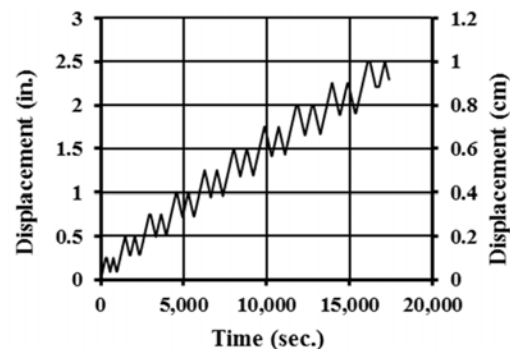


Figure 5: Loading protocol

For the lab conditions specimens, the specimens were ramp loaded after FRP failure happened. Deflections at the mid and third spans were measured using three Linear Variable Displacement Transducers (LVDTs) at each side. In addition, strain gauges were placed on the steel rebar and FRP to record their strains during loading.

TEST RESULT AND DISCUSSION

In order to study the effect of environmental conditions on strengthened reinforced masonry walls; the individual components (cementitious adhesive, masonry unit and FRP bars) and strengthened masonry walls should be evaluated before and after exposure.

CEMENTITIOUS ADHESIVE

The use of cementitious adhesive in place of epoxy as a groove filler has recently been explored in an attempt to lower the material cost and to eliminate the drawbacks of using epoxy. The mode of failure for laboratory set is controlled by the bonding agent property and the debonding failure surface is either in the masonry-adhesive interface or in adhesive layer itself. As a result, the effect of environmental cycles on the cementitious-based adhesive should be considered since this component affects the structural behavior or mode of failure of the strengthened specimens. The mechanical properties of the cementitious adhesive subjected to thermal cycles were determined by using uniaxial compression test. The result showed that the compressive strength of conditioned cementitious-based adhesive was reduced by 9%. This reduction in strength was due to hair cracks developed in the adhesive materials as a result of temperature change during freeze-thaw cycling. For this reason, the mode of failure was expected to govern by cementitious adhesive.

COMPRESSIVE STRENGTH OF MASONRY UNIT

Three individual concrete masonry units were sampled and tested to evaluate compressive strength according to ASTM C140/C140M-16 (Standard Test Method for Sampling and Testing Concrete Masonry Units) under laboratory and environmental conditions. The masonry units are capped in accordance with ASTM C1552, (Standard Practice for Capping Concrete Masonry Units, Related Units and Masonry Prisms for Compression Testing). A fibrous composite laminated cap was used to provide a smooth bearing surface and to distribute the load over the top and bottom of masonry unit. A rigid 610 x 305 x 51 mm (24 x 12 x 2-in.) steel loading plate was used to apply the loads Figure 6. The maximum stress was averaged of three samples for each set. The result showed that the compressive strength of conditioned masonry unit was reduced by 10 %. This reduction in strength attributed to microcracks due to increasing internal voids pressure that generated after freezing the absorbed water.

TENSILE TEST OF FRP BARS

Tensile tests, according to provisions of ACI 440 were conducted by (Micelli and Nanni, 2004) to study the change in longitudinal mechanical properties of FRP. The tensile strength of GFRP bars subjected to the environmental cycles showed a good durability resistance comparing with control bar. Carbon bars showed a degradation in tensile strength by approximately 5% (Micelli and Nanni, 2004). The results of the effect of environmental cycles on individual components are illustrated in Figure 7.

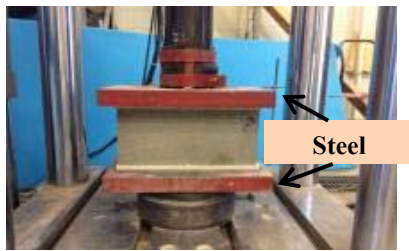


Figure 6: Compressive strength test setup

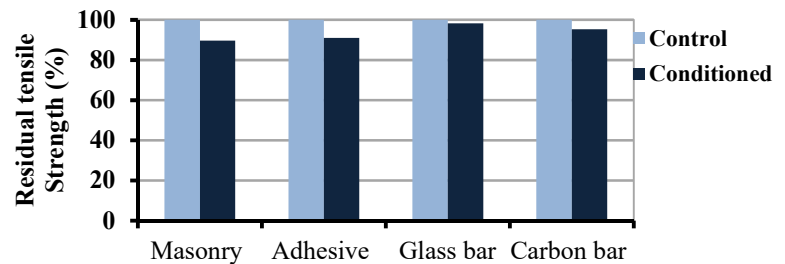


Figure 7: Residual tensile strength (FRP result (Micelli and Nanni, 2004))

STRENGTHENED MASONRY WALLS SPECIMENS

The load versus deflection curve for both sets is illustrated in Figure 8. From the results of individual components, the results for strengthened masonry walls were expected to be affected by the all these components together since the debonding failure surface is in the masonry-adhesive interface or in adhesive layer itself. The general behavior of walls strengthened with FRP system for both sets is still the same. The behavior can be divided into three segments. The first segment of the envelope is pre-crack phase which is varies linearly with a small deflection up to the first mortar crack. Insignificant effect of FRP bars on stiffness of this segment and only a little effect on cracking load were observed. The second segment of envelope is pre-yielding stage. This phase is recognized through the change of the initial slope (i.e. stiffness) and with yielding of the steel reinforcement. The third segment of the load-deflection envelope is the post-yielding segment. It begins with the yielding of steel and ends with failure ofstrengthening system. For the conditioned specimens, the ultimate flexural capacity of the wall strengthened by glass fiber had insignificant change comparing with the wall strengthened with carbon bar. The reduction of ultimate capacity of specimen strengthened with one carbon bar was 34%. The reason behind that could be attributed to the reduction of tensile strength of all components (CFRP bar, cementitious adhesive and masonry unit). The effect of combined environmental cycles led to make the mode of failure more gradual debonding failure comparing with mode of failure for specimen under lab conditions. The stiffness for each specimen was reduced due to the loading-unloading process which is cause initiated micro-cracks in all concrete components (masonry unit, mortar, grout, cementitious material) and increased the deformability of the strengthened walls. The secant stiffness was considered in determining the degradation of stiffness, which is the slope of the line drawn between minimum and maximum loads of first cycle for each displacement interval. For the specimens strengthened with GFRP, the deflection of the laboratory and conditioned specimens was almost the same. Due to environmental

degradation of the concrete components, in addition to any CFRP degradation, the deflection was increased and that led to increase the level of masonry damage. Also the stiffness of conditioned specimens was decrease comparing with laboratory specimens. The results of the ultimate load, deflection, and stiffness reduction percent are presented in Table 4.

CRACKS DURING TEST AND MODES OF FAILURE

Same cracks generated during the test of both sets of specimens. The first flexural tensile crack was a hairline crack that initiated at the block mortar in the maximum moment region. With increasing load, similar cracks developed at other bed joints. Further flexural tensile cracks developed when the specimen loaded at level beyond the cracking load / moment (M_{cr}).

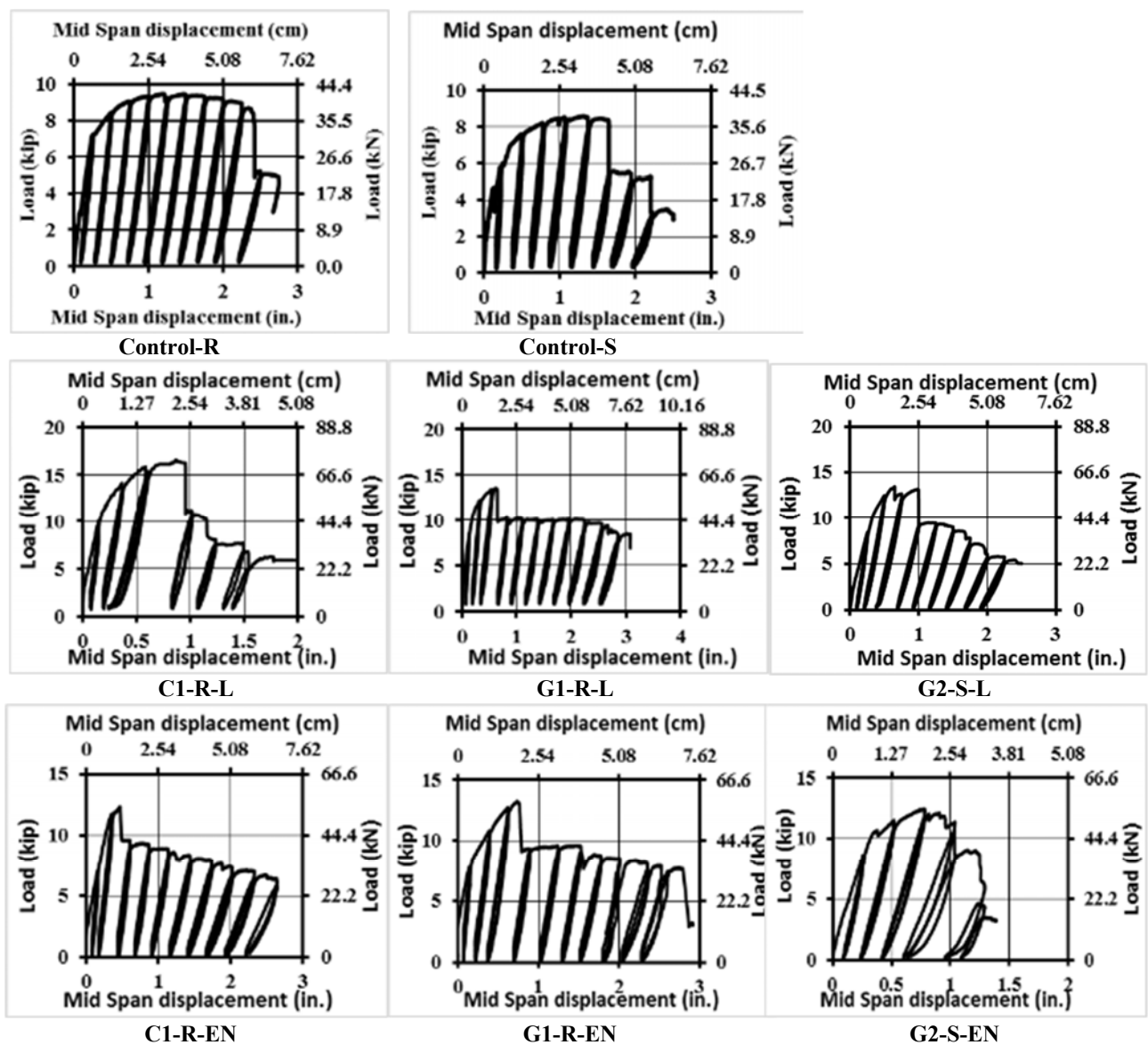


Figure 8: Load-deflection response

Table 4: Percentage of reduction for specimens exposed to environmental action

| Specimen | Capacity | Deflection | Stiffness |
|----------|----------|------------|-----------|
| C1-R-EN | 34% | 41% | 37% |
| G1-R-EN | 5% | 0% | 15% |
| G2-S-EN | 9% | 0% | 5% |

The cementitious material itself, however, cracked during loading. As a result, the embedding material deteriorated gradually and the failure in general is debonding. Flexural shear and shear cracks outside the constant moment region were generated during later stages of loading in addition to concrete unit crushing. Cracks also propagated in specimens reinforced with either CFRP or large amounts of GFRP reinforcement (in this study 2 bar) that were encapsulated with a cementitious material. The masonry cracks were oriented at 45°.

The most common mode of failure that controls the behavior of reinforced masonry walls strengthened with FRP is a debonding failure of the NSM FRP bar rather than FRP bar rupture. The mode of failure for the specimens strengthened with CFRP strip or GFRP bar in this study both before and after environmental cycles was a debonding failure. However, the specimen subjected to environmental conditioning strengthened with CFRP bar failed in a more gradual debonding failure. The observed debonding failure is illustrated in Figure 9.



Figure 9: Observed modes of failure

CONCLUSIONS

An experimental program was conducted to evaluate the effect of combined environmental cycles on the out-of-plane flexural behavior of reinforced masonry walls strengthened using the NSM FRP technique with a cementitious-based adhesive material. For the specimen strengthened with a carbon strip, the environmental conditioning significantly reduced the ultimate capacity and secant stiffness of the first cycle by 41% and 37 % respectively. The reason behind this is attributed to the degradation of the bond and concrete components (masonry unit, mortar, grout, cementitious material), but a microscopic study will be initiated to better define this behavior. The conditioned specimens strengthened with glass bar conversely exhibited an insignificant change in terms of ultimate strength as compared to laboratory conditioned specimens. The mode of failure was the same (debonding failure) for the specimens strengthened with carbon or glass bar before and after environmental cycles.

ACKNOWLEDGEMENTS

The authors wish to acknowledge the support of Midwest Block & Brick in Jefferson City, Hughes Brothers in Seward, Nebraska and HCED (The Higher Committee for Education Development in Iraq) for their support to this project. The authors also wish to thank the technical support staff (CIES) at Missouri University of Science and Technology for their efforts in this research study.

REFERENCES

- Al-Jaberi, Z., Myers, J. J. & ElGawady, M. (2015), Out-of-Plane Strengthening of Reinforced Masonry Walls using Near-Surface Mounted (NSM) FRP Bars with Epoxy and Cementitious Materials. *Advanced Composites in Construction, ACIC*, 195-200.
- Al-Jaberi, Z., Myers, J. J. & ElGawady, M. (2015), Influence of Near-Surface Mounted (NSM) FRP on the Out-of-Plane Behavior of Reinforced Masonry Walls. *12th North American Masonry Conference*.
- Al-mahmoud, F., Mechling, J.-M. & Shaban, M. (2014), Bond strength of different strengthening systems–Concrete elements under freeze–thaw cycles and salt water immersion exposure. *Construction and Building Materials*, 70, 399-409.
- Burke, P. J. (2008), Low and high temperature performance of near surface mounted FRP strengthened concrete slabs. (*Doctoral dissertation*).
- Burke, P. J., Bisby, L. A. & Green, M. F. (2013), Effects of elevated temperature on near surface mounted and externally bonded FRP strengthening systems for concrete. *Cement and Concrete Composites*, 35, 190-199.
- Dai, J.-G., Yokota, H., Iwanami, M. & Kato, E. (2010), Experimental investigation of the influence of moisture on the bond behavior of FRP to concrete interfaces. *Journal of Composites for Construction*, 14, 834-844.
- De Lorenzis, L. & Nanni, A. (2002), Bond between near-surface mounted fiber-reinforced polymer rods and concrete in structural strengthening. *ACI structural Journal*, 99, 123-132.
- De Lorenzis, L., Tinazzi, D. & Nanni, A. (2000), Near surface mounted FRP rods for masonry strengthening: bond and flexural testing. *Proceedings of the international conference on composite engineering*.
- Galati, N., Tumialan, G. & Nanni, A. (2006), Strengthening with FRP bars of URM walls subject to out-of-plane loads. *Construction and Building Materials*, 20, 101-110.

- Ghiassi, B., Silva, M. M., Marcari, G., Oliveira, D. V. & Lourenco, P. B. (2012), Moisture effects on the bond strength of FRP-masonry elements. *6th International Conference on FRP Composites in Civil Engineering, Giorgio Monti*, 1-8.
- Micelli, F. & Nanni, A. (2004), Durability of FRP rods for concrete structures. *Construction and Building materials*, 18, 491-503.
- Mitchell, P. (2010), Freeze-thaw and sustained load durability of near surface mounted FRP strengthened concrete, (*Doctoral dissertation*).
- Soliman, S. M., El-Salakawy, E. & Benmokrane, B. (2010), Bond performance of near-surface-mounted FRP bars. *Journal of Composites for Construction*, 15, 103-111.
- Soudki, K. & Alkhrdaji, T.(2005), Guide for the design and construction of externally bonded FRP systems for strengthening concrete structures (ACI 440.2 R-02). *Structures Congress 2005: Metropolis and Beyond*, 1-8.
- Yu, B. & Kodur, V. (2014), Effect of high temperature on bond strength of near-surface mounted FRP reinforcement. *Composite Structures*, 110, 88-97.



MASONRY TODAY AND TOMORROW

11 - 14 February, 2018
SYDNEY AUSTRALIA

www.10amc.com

MITIGATING IMPACT FAILURE OF MASONRY BOUNDARY WALLS USING AUXETIC COMPOSITES

Mohammad Asad¹, Manicka Dhanasekar², Tatheer Zahra³ and David Thambiratnam⁴

¹ PhD Candidate, Queensland University of Technology (QUT), Department of Civil Engineering & Built Environment, Brisbane, QLD 4000, Australia: m.asad@qut.edu.

² Professor, Queensland University of Technology (QUT), Department of Civil Engineering & Built Environment, Brisbane, QLD 4000, Australia: m.dhanasekar@qut.edu

³ Associate Lecturer, Queensland University of Technology (QUT), Department of Civil Engineering & Built Environment, Brisbane, QLD 4000, Australia: t.zahra@qut.edu

⁴ Professor, Queensland University of Technology (QUT), Department of Civil Engineering & Built Environment, Brisbane, QLD 4000, Australia: d.thambiratnam@qut.edu

Masonry boundary walls protect buildings and structures of national as well as common interests from intruding vehicles. As masonry is weak in tension, the impact due to vehicle intrusions induces tensile stresses in the walls resulting local damage failure. Strengthening masonry walls using various forms of Fiber Reinforced Plastics (FRP) can prevent intrusion but would generate excessive acceleration that can endanger the occupants of the unintended vehicular impact. Furthermore, prevention of local damage can increase the impact force and affect the safety of the wall as it would behave globally. Energy absorption properties of the mitigating system is, therefore, more important than the strength properties. To reduce the accident severity and to save the lives, use of auxetic materials possessing negative Poisson's ratio is promising and hence it has been used as a mitigating measure in this research. Auxetic fabric embedded in fiber cement matrix is used as composite render on both sides of the boundary wall. The wall, supported on three edges except the top was modelled using a layered shell element. Masonry was modelled as a homogenised orthotropic nonlinear brittle material with embedded mortar joints. The wall was modelled with and without the auxetic composite render. Finally, it is concluded from the results that the Auxetic rendering is able to reduce the out-of-plane deformation of the wall significantly during vehicular impact about 8 times as compared to a un-rendered masonry wall.

Keywords: *Sandwiched Auxetic foam, Auxetic fabric, Impact analysis, Masonry walls*



INTRODUCTION

As per recent study conducted in the United States, approximately 60 vehicles per day crash into building in which about 47% of accidental sites are commercial or public buildings or retail stores (Reiter, 2014). Due to such type of crash into building there is threat to the lives inside the vehicle as well as the building. Developing safety measures for buildings against vehicular impact is the prime motive of this study. Safety of vehicles and its occupants is beyond the scope of this study.

Masonry is an essential part of every building whether used as structural element or as boundary fencing walls. Researchers (Felice & Giannini, 2001; Freidenberg et al., 2014; Mauro et al., 2015) performed experiments to understand the local failure mechanism and diagonal cracks developed on masonry wall under out-of-plane loading. During vehicle crash, masonry walls experience local failure (penetration of vehicle into the building), rather than a global failure i.e. failure of whole building/ wall. This local failure is caused by the impact of the vehicle with the masonry walls which tends to generate tensile stresses perpendicular to the direction of impact. This impact is attributed to the effect of Poisson's ratio (ratio of lateral strain to axial strain) of the material. All civil engineering materials, that are used in buildings and engineering infrastructure exhibit Positive Poisson's Ratio (PPR). A relatively new material named auxetic fabric, which exhibits Negative Poisson's Ratio (NPR) is experiencing for blast resisting in military applications (Imbalzano et al., 2016). NPR of the auxetic materials introduces lateral compression when materials are subject to axial compression. Due to this action of the material lateral tensile stresses are eliminated hence impact resistance can be improved. This research is focussed on examining this aspect through advanced finite element modelling methods.

A closer view of the images of some recent incidents is shown in Figure 1. These crashes reveal following observations: (1) the damage in masonry caused by a vehicle is restricted to the intrusion of the impacting vehicle only, and (2) intrusions did not eventuate global failure of the wall or the building.



Figure 1: Vehicle crash with a masonry building (Adapted: <http://www.brisbanetimes.com.au>)

These observations have been found in agreement with the basic laws of mechanics of materials, and dynamic of structures which states: (1) Masonry possesses arching action capability due to

collection of brick units, which has the ability to resist the loading; thus, any openings either intentional (such as windows or doors) or unintentional (damage) caused by impact of crashes will lead to change in load path around the opening without compromising the stability of the whole of the wall; (2) any structure subject to highly non-uniformed strain energy manifested on its surface in a very short time period suffer local damage once this (strain) energy surpasses the local fracture energy of material; (3) If the local damage does not occur by strengthening the wall, then local impact zone possesses higher fracture energy causing strain energy to flow into the weaker parts of structures resulting vibration and damage to these weaker portions. Therefore, it is necessary to design a masonry wall with the optimal dissipation of energy in order to minimise the injuries to the occupants of the building.

The synthesis of available literature reveals that masonry walls retrofitted with Carbon Fibre Reinforced Polymer (CFRP) resist the damage caused due to earthquake loading. The mounting of CFRP layers on the mortar layers in masonry has frequently been used by various researchers (Corbi, 2013; Konthesingha et al., 2013). De Santis and de Felice (2015) used steel fibre reinforced grout to increase the strength of masonry walls and reported that the tensile and shear strengths are enhanced due to the presence of steel fibres in the mix. The existing practice of retrofitting method is based on increasing the strength of wall much higher during an earthquake by introducing a material which possesses positive Poisson's ratio. These materials experience squashing or de-lamination failures due to pressure applied on the material to adjoining interfaces. Auxetic materials possessing NPR when used along with positive Poisson ratio's materials, will overcome de-lamination problem as illustrated in Figure 2. With this background, the Auxetic fabric is selected and tested for its efficacy when subjected to impact loading.

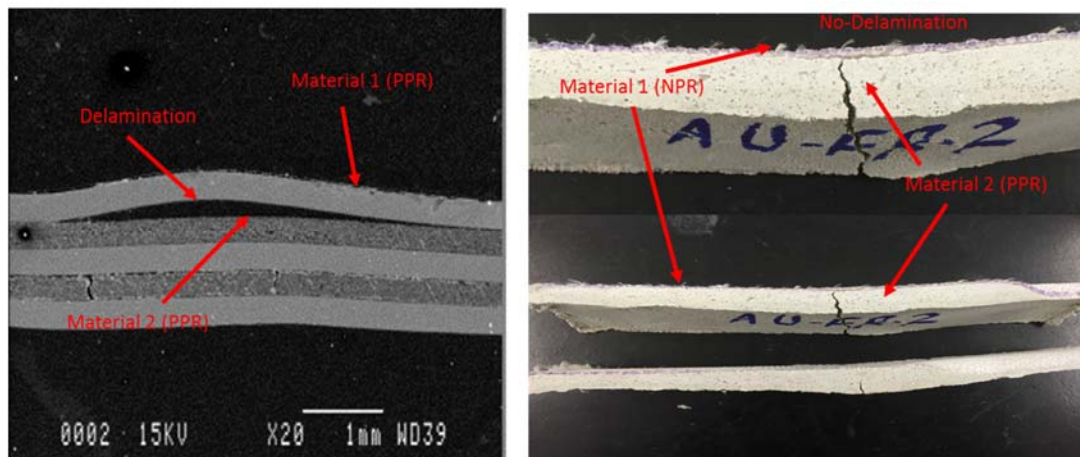


Figure 2: De-lamination between the layers during three-point bending load test (a) PPR composite material (Remmers & De Borst, 2001) (b) NPR composite material (taken from : laboratory test in QUT)

NPR materials contract laterally subjected to axial compression and expand laterally subjected to axial tension (Lakes, 1987a, 1987b). This property helps to improve the mechanical performance in terms of higher fracture strength, resistance to indentation, vibration absorption, shear modulus, and fatigue crack propagation. In the present study, auxetic materials are used as an additive to form a composite render suitable for masonry application.

NUMERICAL SIMULATION AND VALIDATION WITH EXPERIMENTAL RESULTS

For the present study, the numerical simulation was performed on an experimentally tested masonry wall of size 9.15 m long \times 1.07 m wide \times 0.215 m thick (Gilbert et al., 2002). This wall was subjected to low-velocity impacts in the form of the triangular impulse applied through square steel plate placed at mid-height. Laboratory impact test rig as shown in Figure 3(a) was used to apply impact load through a steel plate of size 400 mm long \times 400 mm width \times 50 mm height at mid-height of the wall. The details of the walls are shown in Figure 3(a). The experimental results exhibited that the abutments remained undamaged; therefore, it was considered as the rigid body in the numerical modelling.

The geometry of the wall is modelled as a plate structure in 3D space, a 4-noded 24-DOF (degree of freedom) Quadrilateral Finite Membrane Strain (S4R) element was used with reduced integration and hourglass control. Reduced integration decreases the computational time from 4 point (full integration) to 1 point (single integration). However, for explicit modelling, fully integrated elements are not allowed. Hourglass control needs to be checked for the stability of the numerical solution when reduced integration is used with first-order (4 or 8 corners noded) element. The impact load was applied as a triangular impulse with a peak force of 130 kN at 20.02 milliseconds as shown in Figure 3(b). Figure 3(c) shows the geometry and boundary conditions of the developed model.

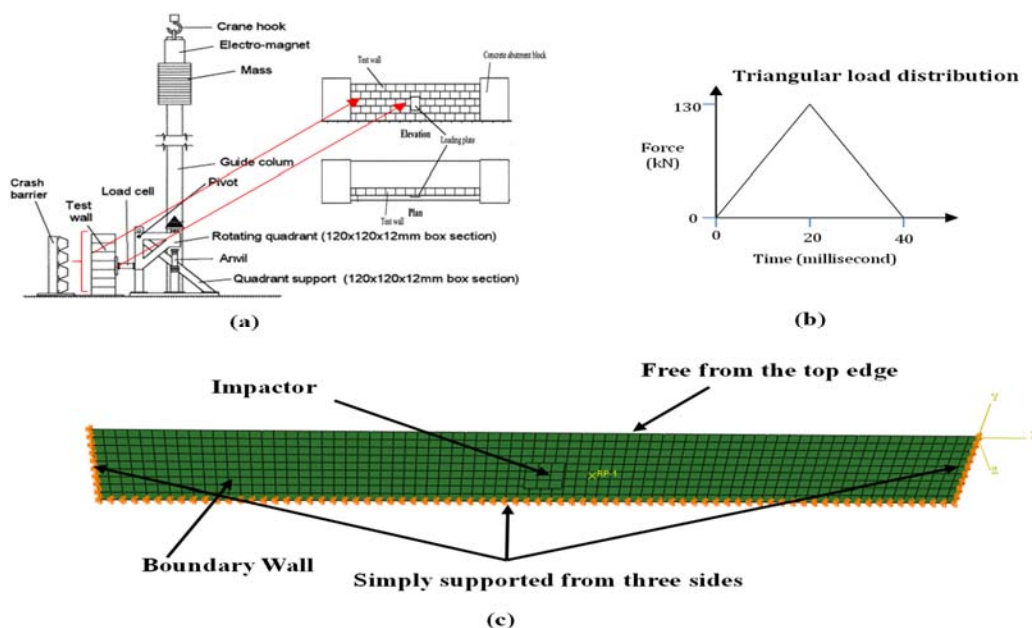


Figure 3: (a) Laboratory impact test rig (Gilbert et al., 2002) (b) Triangular impulse load (Author) (c) Developed model (Author)

Figure 4 depicts the results obtained from the numerical simulations. The experimental failure pattern is also shown in Figure 4(a). Vertical and inclined cracks over the entire height of the wall

in the vicinity of the impact (mid-height) were observed through experiments. Similar failure pattern was obtained from the numerical model as shown in Figure 4(b). It is evident from the crack pattern that increasing the length of wall reduces the effect of the boundary at the support and cracks would be localised in the impact region. With this impact, the left and the right part of the tested brick wall deformed inwardly when subjected to out-of-plane impact load. The deformation of the wall with the maximum deflection as predicted by the numerical model is presented in Figure 4(c). A good agreement is found between the experimental and the simulation results.

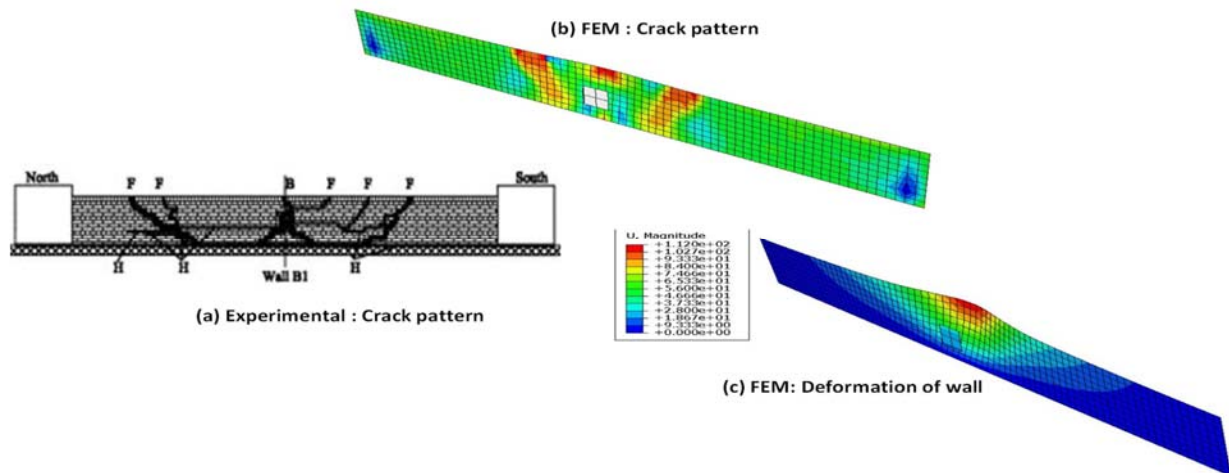


Figure 4: Experimental validation of wall (a) Experimental : crack pattern (reference: Gilbert et al. (2002)) (b) Validation: Crack pattern (c) Validation: Out of plane - Deformation of wall

Another comparison in terms of the displacement versus time graph recorded at mid-height of the wall and offset by 500 mm to the left from the centre of the load applied is shown in Figure 5.

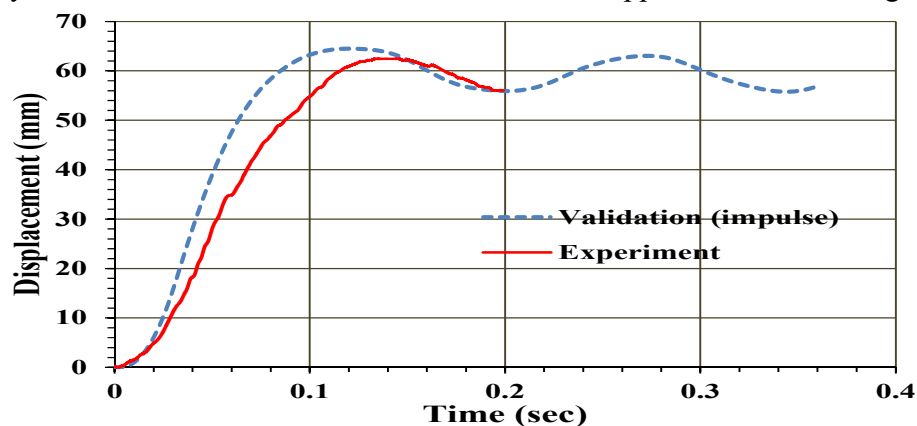


Figure 5: Displacement versus time response of wall

MITIGATING WITH AUXETIC RENDERING

The rendering of auxetic material over the surface of masonry was modelled in the finite element analysis software with the help of composite layered shell modelling technique. For Auxetic rendered masonry wall, seven layers were considered. Each layer of the layered shell element represented one of the material components that constituted the composite Auxetic Rendered Masonry (ARM) wall as illustrated in Figure 6. Layer 4 (mid layer) represented the unreinforced masonry wall whilst the layers 1, 3 (Top) and layer 5, 7 (Bottom) represented mortar material. Layer 2 (Top) and layer 6 (Bottom) were the auxetic material. The whole composite wall can be seen in

Figure 6. In this study, each layer was integrated across the thickness with seven-point Simpson's integration scheme as well as the orientation angle defined relative to the overall orientation of the composite. The use of seven-point Simpson's integration for the multi-layered shell computes results with the best possible accuracy.

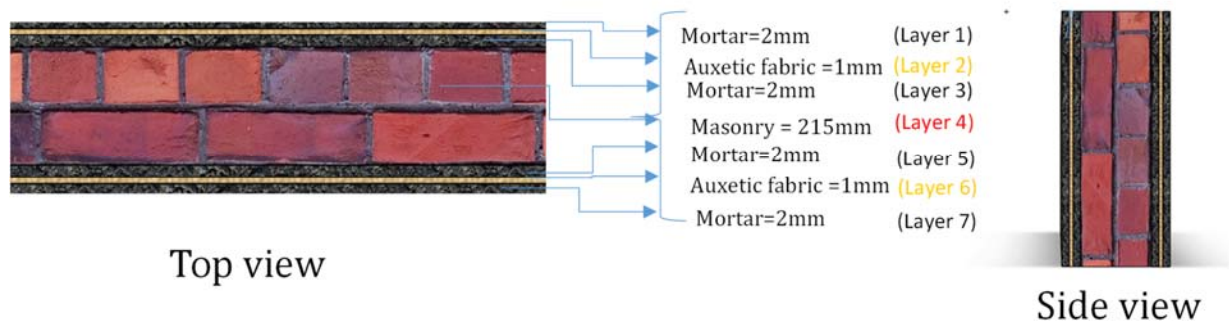


Figure 6: Top and side view of Masonry wall rendered with mortar and Auxetic on front and rear side of wall

Auxetic fabric was purchased from the UK under the brand name AuxeticTM as a mitigating measure for the vehicular impact. The tensile test of the Auxetic fabric was performed in QUT laboratory to understand the complete stress-strain behaviour of the fabric. The Poisson's ratio was observed as negative when the lateral strain correlated with the axial strain. The tensile test was conducted using a 1kN INSTRON 5566 machine, and the test images were studied using digital image correlation (DIC) method. The three (3) tested specimens, testing equipment and typical DIC mesh are shown in

Figure 7.

The experimental tests revealed that the auxetic fabric exhibited elastic-brittle failure - a common phenomenon in most of the metals. Damage Failure Analysis (DFA) was used to examine the initiation of brittle failure in the composite fabric. The DFA simulated the initiation and progression of damage at different layers due to inter-laminar and intra-laminar fabric/ matrix failure. This failure propagation resulted in the degradation of the material stiffness of the fabric as observed at every step of the load increment. A 3D finite element analysis was used with composite layer section to model the composite panel and to define the damage initiation in the model using Hashin's damage criteria (Hashin, 1980). Table 1 summarises the mechanical properties and the

allowable stress for the auxetic fabric under Hashin's damage criteria based on the experimental axial tensile test results shown in Figure 7.

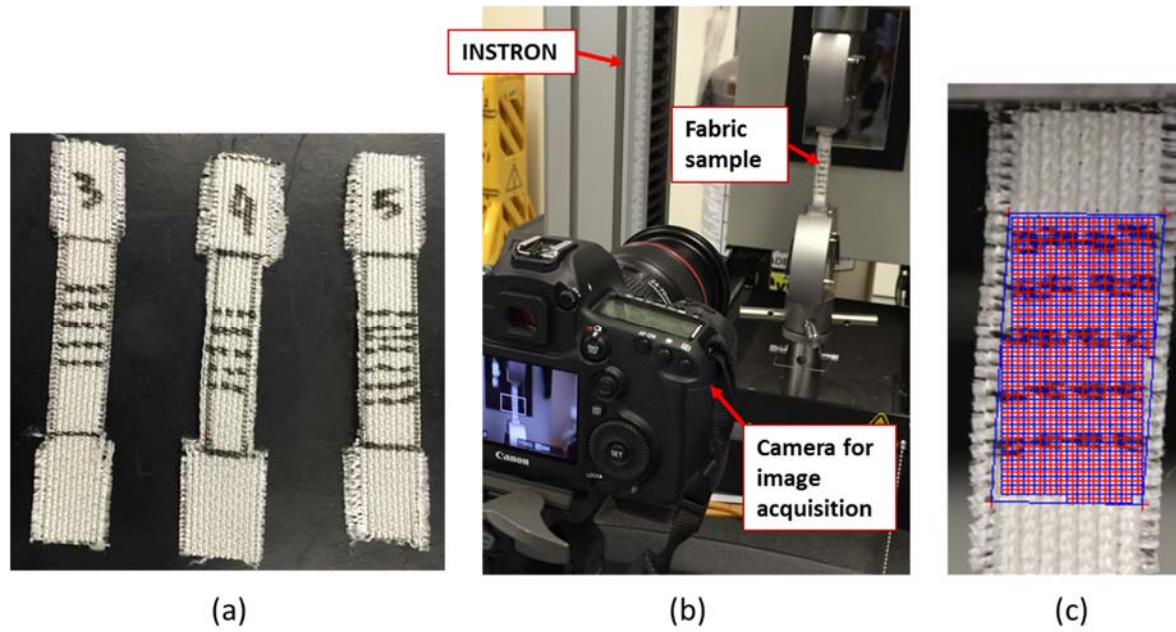


Figure 7: Auxetic fabric testing (a) cut samples (b) test setup (c) DIC mesh

Table 1: Mechanical properties of auxetic fabric

| E_{11} (MPa) | E_{22} (MPa) | G_{12}, G_{13} (Nmm/mm ²) | G_{23} (Nmm/mm ²) | ν_{12} | ρ (tonne/mm ³) |
|--|----------------|--|---------------------------------|-------------|------------------------------------|
| 96.3 | 181.2 | 103.3 | 194.5 | -0.5 | 4.5×10^{-10} |
| Allowable Intralaminar strength of Auxetic fabric | | | | | |
| X_t (MPa) | X_c (MPa) | Y_t (MPa) | Y_c (MPa) | S_L (MPa) | S_T (MPa) |
| 40.4 | 20.2 | 40.4 | 20.2 | 10.1 | 10.1 |

RESULTS AND DISCUSSION

The boundary wall (9.15 m long \times 1.07 m wide \times 0.215 m thick) was rendered with auxetic layer on both sides having a thickness of 1 mm. This rendering was laid to the wall with mortar of 2 mm each on both sides of the wall as shown in 6. The rigid steel impactor of size 800mm \times 400mm \times 50 mm meshed with 200 elements was considered. The size of the impactor was considered slightly bigger than the experimental impactor in order to simulate a front dimension of a vehicle. During impact analysis, the inertial mass and velocity were given as an input to compute external force equivalent to the peak value of triangular impulse load (shown in Figure 3(b)). The inertial mass of the impactor was taken 1500kg (Gilbert et al., 2002a). The constant velocity applied to the impactor was calculated as 6.23 km/h based on the assumed mass of the impactor and the applied peak force of the triangular load.

A comparative study was performed to analyse the effect of auxetic rendering by plotting the deformation versus time graph as illustrated in Figure 8(a). The ARM exhibited a marginal decrease in the localised deformation at the centre of the wall. The maximum deformation obtained was 103.2 mm in URM as shown in Figure 8(b). Whereas in ARM the deformation was spread over larger area as compared to localised collapse of the wall due to the auxetic rendering on both sides which resulted in a decrease of maximum deformation to 80.67 mm as shown in Figure 8(c). Due to auxetic rendering, a marginal reduction of 21.83% in deformation was observed when compared with the un-rendered wall.

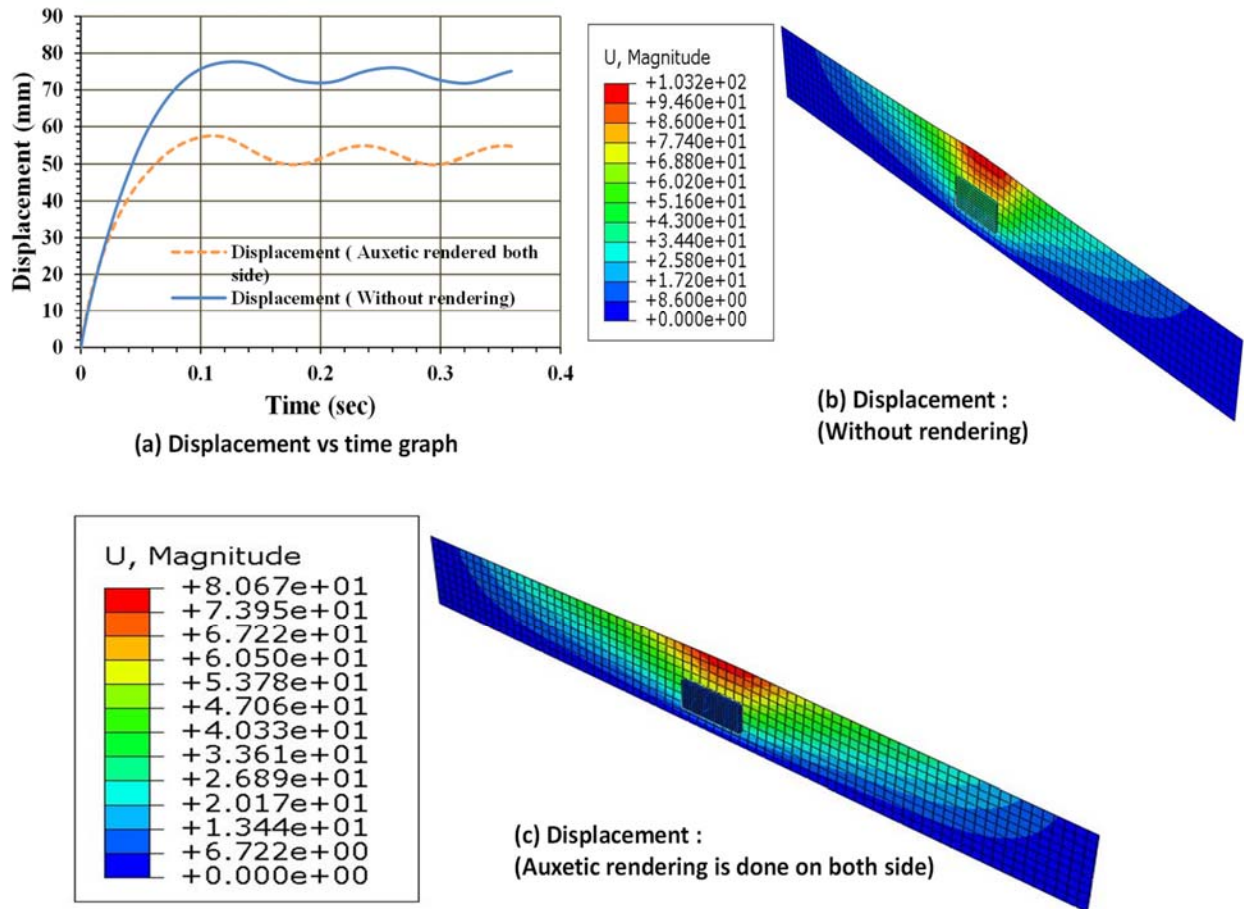


Figure 8: (a) Displacement versus time response of wall at the centre of the wall (b) deformation contour plot of masonry wall without rendering (c) deformation contour when masonry is rendered with Auxetic and mortar layer on both front and rear side of the wall

VARIATION OF ENERGY

In order to study the effectiveness of auxetic rendering on the masonry wall, kinetic, artificial/hourglass, internal and total energy of the whole auxetic rendered and un-rendered masonry wall models is shown in Figure 9. The artificial hourglass energy monitored throughout

the analysis accounts for 4.83% and 6.18% of the total energy whereas the Figure 9(a) and (b) shows the sum of kinetic energy, internal energy and hourglass energy represents the total energy at any time.

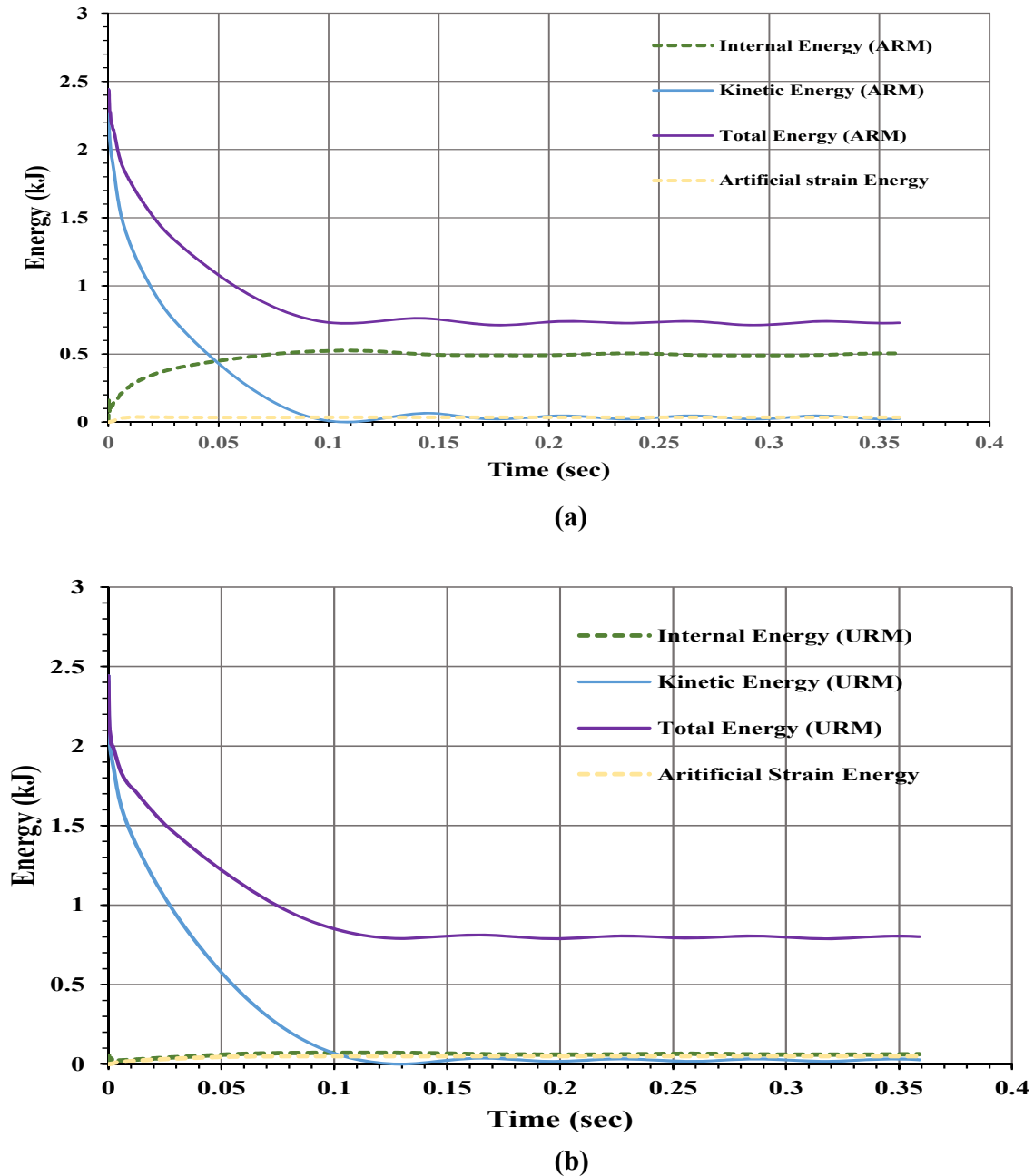


Figure 9: Energy history of (a) Auxetic rendered (b) Un-rendered Masonry wall

The balanced energy equation validated the auxetic rendered and un-rendered masonry wall model. The total internal energy in ABAQUS/Explicit was calculated mainly with the amount of energy dissipated by the model which is a summation of recoverable strain energy, plastic dissipation energy and artificial strain energy (Abaqus, 2014). Figure 10 shows the effectiveness of the auxetic

material in absorbing the energy in plastic phase during the impact due to rendering on both faces of the masonry wall. The rate of absorption of plastic energy was increased by 8 times due to auxetic rendering. With this enhancement in the absorption of energy, the whole masonry wall underwent maximum plastic deformation and resulted in a ductile failure rather than a brittle brick mortar joint failure.

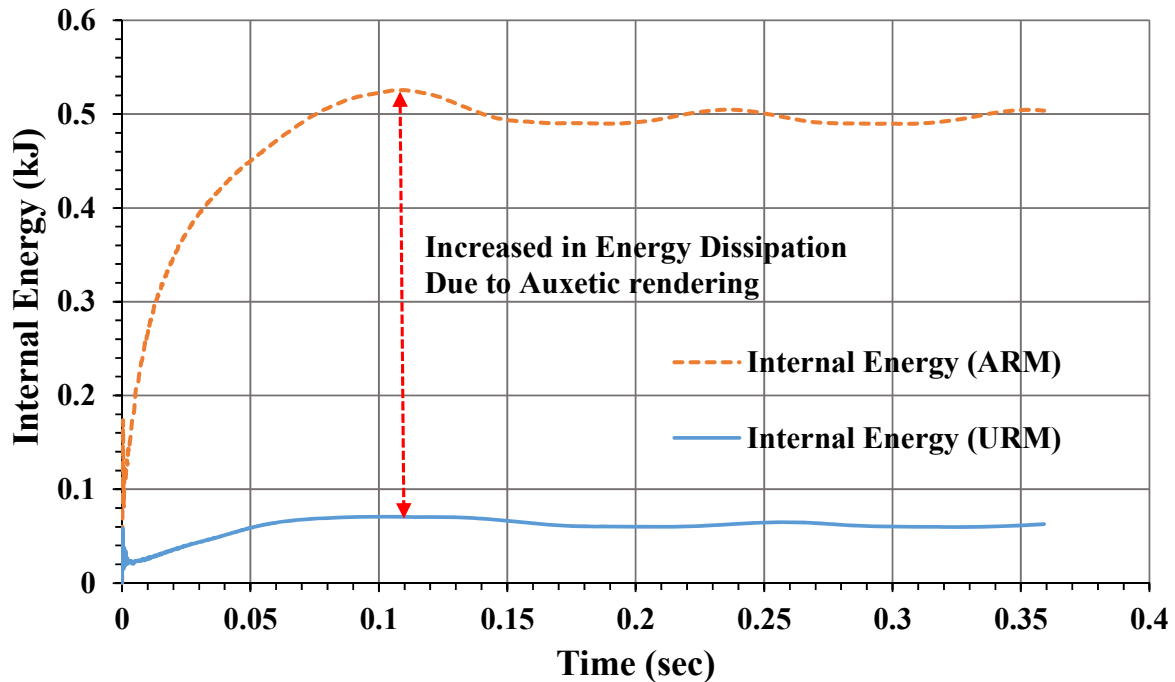


Figure 10: Internal energy versus time graph to compare the energy dissipation due Auxetic rendering on both face of Masonry wall during impact.

CONCLUSION

It was concluded from the results that when the auxetic fabric, a mitigating material was applied to the masonry wall under impact loading, the capacity of the wall increased significantly due to the rendering of the material. Auxetic rendering reduced the deformation by 21.83% when an impactor of mass 1500kg hit the wall at a velocity of 6.23 km/hr. The failure pattern in the un-rendered Masonry wall observed as localised cracking near the impact zone whereas due to auxetic rendering the stress was spread to the whole wall. Auxetic rendering absorbed the impact energy about 8 times more compared with the un-rendered wall. The rendered wall can undergo to resist a considerable amount of plastic deformation even at high impact which ultimately can result in the ductile failure of the masonry wall.

ACKNOWLEDGEMENTS

The scholarship support and the tuition award to the first author from the Queensland University of Technology are greatly acknowledged. The authors also gratefully acknowledge the facilities and support provided by the High-Performance Computing (HPC) Facility lab, Queensland University of Technology.

REFERENCES

- Abaqus, V. (2014). 6.14 documentation. *Dassault Systemes Simulia Corporation*.
- Corbi, I. (2013). Frp reinforcement of masonry panels by means of c-fiber strips. *Composites Part B: Engineering*, 47, 348-356.
- De Santis, S., & de Felice, G. (2015). Steel reinforced grout systems for the strengthening of masonry structures. *Composite Structures*, 134, 533-548.
- Felice, G. D., & Giannini, R. (2001). Out-of-plane seismic resistance of masonry walls. *Journal of earthquake engineering*, 5(02), 253-271.
- Freidenberg, A., Aviram, A., Stewart, L. K., Whisler, D., Kim, H., & Hegemier, G. A. (2014). Demonstration of tailored impact to achieve blast-like loading. *International Journal of Impact Engineering*, 71, 97-105.
- Gilbert, M., Hobbs, B., & Molyneaux, T. C. K. (2002). The performance of unreinforced masonry walls subjected to low-velocity impacts: Experiments. *International Journal of Impact Engineering*, 27(3), 231-251.
- Hashin, Z. (1980). Failure criteria for unidirectional fiber composites. *Journal of applied mechanics*, 47(2), 329-334.
- Imbalzano, G., Tran, P., Ngo, T. D., & Lee, P. V. S. (2016). A numerical study of auxetic composite panels under blast loadings. *Composite Structures*, 135, 339-352.
- Konthesingha, K., Masia, M., Petersen, R., Mojsilovic, N., Simundic, G., & Page, A. (2013). Static cyclic in-plane shear response of damaged masonry walls retrofitted with nsm frp strips—an experimental evaluation. *Engineering Structures*, 50, 126-136.
- Lakes, R. (1987a). Foam structures with a negative poisson's ratio. *Science*, 235(4792), 1038-1040.
- Lakes, R. (1987b). Response: Negative poisson's ratio materials. *Science*, 238(4826), 551-551.

Mauro, A., de Felice, G., & DeJong, M. J. (2015). The relative dynamic resilience of masonry collapse mechanisms. *Engineering Structures*, 85, 182-194.

Reiter, R. (2014). Crash course. *Risk Management*, 61(7), 40.

Remmers, J., & De Borst, R. (2001). Delamination buckling of fibre–metal laminates. *Composites Science and Technology*, 61(15), 2207-2213.



**MASONRY TODAY
AND TOMORROW**

**11 - 14 February, 2018
SYDNEY AUSTRALIA**

www.10amc.com

EXPERIMENTAL AND ANALYTICAL STUDY OF SEISMIC LOW-COST RETROFITTED MASONRY BUILDING

S. Ahmad¹, R. A. Khan², S. Shamim³, M. Asad⁴

^{1,2} Professor, Department of Civil Engineering, Aligarh Muslim University, Aligarh, India.
Shakeel60in@yahoo.co.in

^{3,4} Ex P.G. Student, Department of Civil Engineering, Aligarh Muslim University, Aligarh, India.
mdasadamu@gmail.com

India faces threats from large number of natural hazards such as earthquakes, floods, droughts, landslides, cyclones and tsunamis. During the period 1990 to 2010, India experienced nine damaging earthquakes that have resulted in over 30,000 deaths and caused enormous damage to property, assets and infrastructure. In many cases buildings and structures have proven inadequate to resist earthquake forces and the failure of these can be held responsible for most of the resulting human fatalities. The vast extent of damage and the consequent loss of life associated with these events reflect the poor construction practice in India. The present study deals how to save existing unreinforced masonry structures (without any band such as plinth and lintel band) with the use of low-cost retrofitting techniques. For this, a rectangular masonry building model of dimension (1020mm×910mm×720mm) with wall thickness 56mm on a geometric scale of 1:4 with half size brick was constructed on the shake table. The table generates sinusoidal unidirectional oscillation with the help of motor and oscillator. The responses (acceleration and displacement) were recorded using accelerometers and LVDTs on DEWE-5000 (made in Germany) Data acquisition system. The accelerations recorded at the base level of the shake table model were used as ground acceleration input in SAP2000 software. The analytical responses thus obtained were compared with experimental results and found comparable. The model failed at 750rpm of motor and cracks were marked on the model. Later, the cracks were filled with CONS EPM epoxy and then model was retrofitted using 8mm Fe415 HYSD bars at roof and door level to bring the in-plane wall in compression. Again the retrofitted shake table model was subjected to the varying speed of the motor to obtain the change in responses. The model this time failed at 1400rpm of motor thereby concluding the simple retrofitting technique to be quite efficient and economical. The retrofitted model was again validated using SAP2000 and found quite satisfactory.

Keywords: *Masonry building, retrofitted masonry building, masonry modelling*

INTRODUCTION

Today, Unreinforced Masonry (URM) construction maintains its popularity over many urban areas world-wide. Low cost, durability, widespread geographic availability, low maintenance, thermal insulation, fire protection and easiness to construct makes masonry an appealing construction material for residential buildings. On the other edge, together with the inherent uncertainties in material and structural level, high inertial forces proportional to high mass of the structure makes URM buildings vulnerable to earthquakes. Unfortunately nonlinear response of URM buildings under earthquake induced lateral loads is a challenging task.

According to Abrams (2001) and Laurencio P. et al. (2006) despite being the oldest construction material, masonry is still the least understood in terms of strength, deformation characteristics and other performance related parameters because of its complex behaviour and its non homogeneity. Hong et al. (2004) tested the 1/3-scaled two-story structure under simulated seismic excitation using the shake table and investigated that the shake table test data were useful to trace the changes of structural characteristics from elastic state to post-cracking state. The URM behaved well after the crack was closed to the original position. The test structure that was once damaged but restored to the original shape was subjected to the next level of loading, the structure was able to resist against almost about the same capacity up to the previous load level. Tianyi et al.(2006) tested a full-scale two-story URM building in a quasi-static fashion and investigated that the test URM structure exhibited large initial stiffness, but this stiffness decreased rapidly with small increasing lateral drift. The damage was characterized by large cracks developing at the interfaces between brick and masonry mortar and the failure mechanisms of the test structure were dominated by rocking and sliding of the first-story piers. Bhothara J. et al. (2007) tested a half scale two storey unreinforced brick masonry building with floor and roof structure under longitudinal and transverse shaking. The test results indicated that in-plane walls were damaged in zones having concentration of high shear stress, notably at the walls of the bottom storey. Damage in out-of-plane walls occurred mostly in the zones of high response acceleration and starts from top story.

Furthermore, with the development of computational methods, Finite Element Analysis has become the most important tool for the analysis of structures. According to Keypour et al. (2007), generating a finite element model of the structure requires a good engineering experience to make a reasonable geometrical simplification of the complex geometry and a good assumption of unknown inner-core materials. Finite element micro models require extensive computational facility and complicated failure criterion (Elgawady et al., 2006), as a result finite element micro models are practically applicable to small structural elements in which stress and strain states are heterogeneous. After studying finite element modelling techniques in detail, Lourenco (1996) concludes that “for large structures, the memory and time requirements become too large and, if a compromise between accuracy and economy is needed, a macro-modelling strategy is likely to be more efficient”. In the micro- modelling of masonry special attention has been paid to model the brick-mortar joint interface. A number of plasticity-based continuous-interface models have been developed to model the tension and shear behavior of masonry mortar joints (Lourenco and Rots 1997). Those models account for the interaction between normal compression and shear as well as the shear dilatation often observed in experiments. Mehrabi and Shing (1997) have developed an interface model for analyzing masonry infill that accounts for the increase of contact stress due to joint closing, the geometric shear dilatation, and the plastic compaction of a mortar joint. Khadka (2013) focused on the old traditional buildings, which were constructed more than 100 years ago. A finite element analysis has been carried out in order to reflect the characteristics of

the unreinforced masonry (URM) building. A commercial software SAP2000 was used for the analysis. It was found that the existing forms of the buildings were highly vulnerable for future earthquake.

According to Goodwin C. et al. (2011) seismic improvement is a complex art. He suggested the following strengthening scheme balancing strength requirements with visual impact and economy; Out of plane strengthening of the walls can be made by Inter-Floor Wall Supports by struts, Post-Tensioning provide as a Core Reinforcement and FRP over wall and piers; in-Plane Strengthening can be made by providing the diagonal bracings of steel flats over walls; floor Diaphragm can be retrofitted by diagonal bracings and moment resisting frame either by concrete or steel. Chuang S. et al. (2004) presented the experimental results of three unreinforced masonry walls retrofitted with cable system. He found that the force carried by cable is about 50% of force acted on the whole wall. The improvement of the ultimate lateral load resistance of the retrofitted walls with cable is about 2 times the capacity of un-retrofitted wall. Frumento et al. (2006), is given an overview of the alternative retrofitting solutions presented in the Annex 11E (Italian seismic code), with the intent to create a sound basis for discussion on their possible compatibility with the peculiarities of URM buildings in NZ. Through which he has suggested that the structural connection can be strengthened by tie rod at floor level, insertion of steel rod at joint and ring beams.

EXPERIMENTAL AND ANALYTICAL STUDY

Keeping in view the traditional and conventional construction methods used in non developed regions of the country a typical single storey unreinforced brick masonry model (M_{01}) of dimension 1020mmx920mmx720mm (Figure 1) with wall thickness 56mm on a geometric scale of 1:4 was constructed on unidirectional shake table in the laboratory of civil engineering department, Aligarh Muslim University, Aligarh and the same was modelled in SAP 2000 v17 software for the comparison with the experimental results. Half size bricks (115mmx56mmx35mm) have been used for making the prisms as well as experimental models to be tested on shake table. The Ordinary Portland Cement of Grade 43 and sand with fineness modulus 2.6 was used in proportion of 1:6 for the preparation of cement-sand mortar in the experimental programme conforming to IS 8112:1989 specifications. Three prisms of size (115mmx115mmx 230mm) were casted using 1:6 cement sand mortar. All specimens were air dried before testing after 28 days curing. The material properties such as Compressive Strength, Modulus of Elasticity and Poisson's ratio of brick masonry were found to be 2MPa, 1100MPa and 0.15 respectively. The dynamic load was created by varying the speed of motor. Acceleration and displacements were recorded using accelerometers and LVDTs through DEWE-software placed at shake table, middle and top of the model (Figure 2). The data were recorded from 100rpm to 500rpm at the interval of 100rpm and 500rpm to 800rpm at the interval of 50rpm. Resonance started at 750rpm and visible cracks were found starting from window and door levels propagating to roof level (Figure 3). The same M_{01} model was developed in SAP2000 software using Finite Element Macro modelling. The shake table motion acceleration data was used for the analytical analysis. The walls and slab were modelled using shell elements. The non-structural elements such as wooden door and window were not modelled however; the steel frame in which they were attached was modelled using frame element. At plinth level, there are two steel channel sections of different size which were modelled using shell layered element. The 3D view of analytical model (M_{01}') is shown in Figure 4.



Figure 1: Half size brick model on the shake table (M01)



Figure 2: Accelerometer at top & shake table level and LVDTs at middle and top of the M01 model



Figure 3: Cracks developed in M01 model on shake table

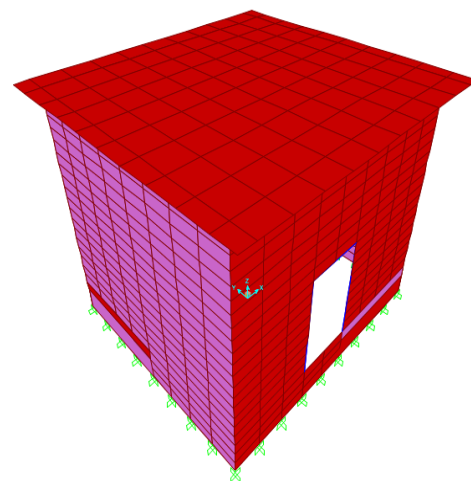


Figure 4: M01' model in SAP2000

Comparison of the results of M_{01} and M_{01}' models are shown in Figure 8 and 9 respectively. The cracks developed in the M_{01} model at 750rpm of motor was filled with CONS EPM epoxy (Figure 10) and then was retrofitted using 8mm Fe415 HYSD bars on inner and outer faces of the walls at roof and door levels (Figure 10-11) to bring the in-plane wall in compression. Holes were drilled in the masonry bricks on all the four corners at door and roof level to ensure proper placements of the bars. Two parallel bars on each inner and outer faces of the masonry walls were placed and tied using perpendicular flats and bolts at both door and roof levels. The connection is shown in Figure 5 and 6. These bars can later be covered using various polymeric covering materials available in market to improve the aesthetic appearance of the structure. The retrofitted model (M_{02}) was also tested on shake table and responses were recorded. The model this time failed at 1400rpm of motor. Figure 7 shows the force v/s speed relation at different

eccentricity values given by the manufacturer of the experimental setup which clearly shows; M_{02} model is capable of taking four times more force compared to the M_{01} model at the eccentricity value of 159.9 degrees. The M_{02} model was again developed in SAP 2000 using finite element tool (M_{02}') as shown in Figure 12-13 for the validation and was found quite satisfactory (Figure 14-16).



Figure 5: Connections showing retrofitting bars

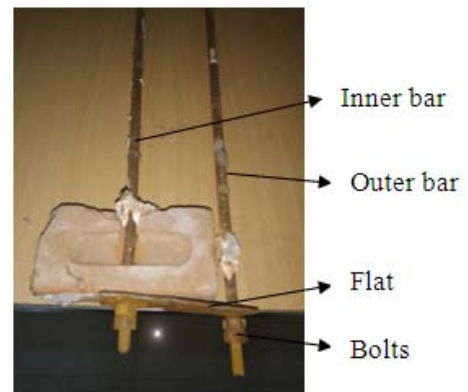


Figure 6: Details of the connection

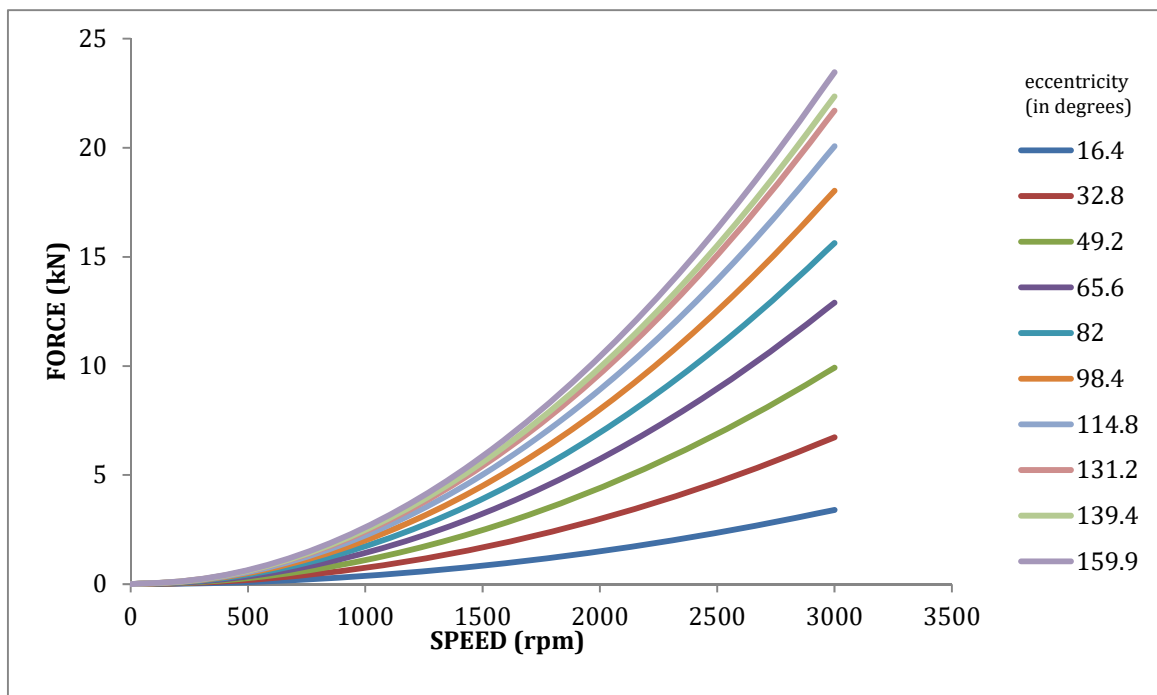


Figure 7: Speed v/s force curves at different eccentricities MO1850 (as given by the manufacturer)

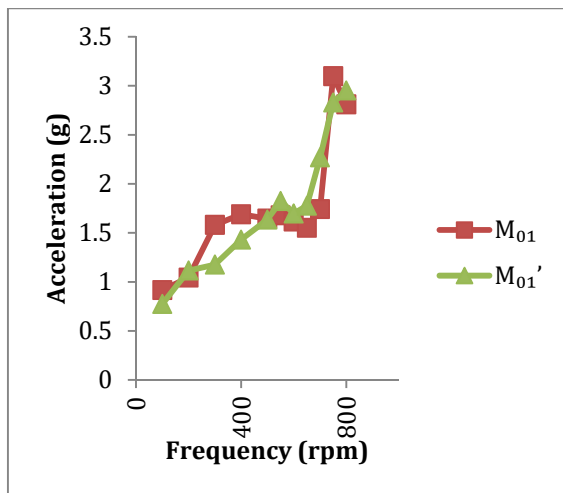


Figure 8: Comparison of acceleration vs frequency for M01 and M01' models

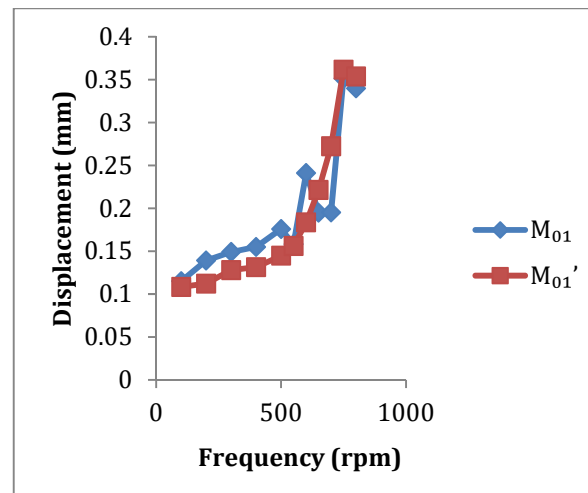


Figure 9: Comparison of displacement vs frequency for M01 and M01' models



Figure 10: Cracks filled with epoxy and retrofitted with 8mm Fe415 HYSD bars from outside (M02 model)



Figure 11: Cracks filled with epoxy and retrofitted with 8mm Fe415 HYSD bars from inside (M02 model)

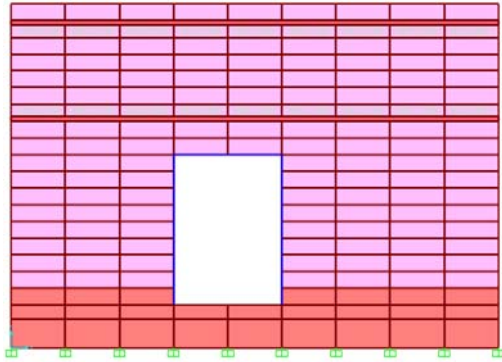


Figure 12: SAP 2000 retrofitted M02' model front view



Figure 13: SAP 2000 retrofitted M02' model rear view

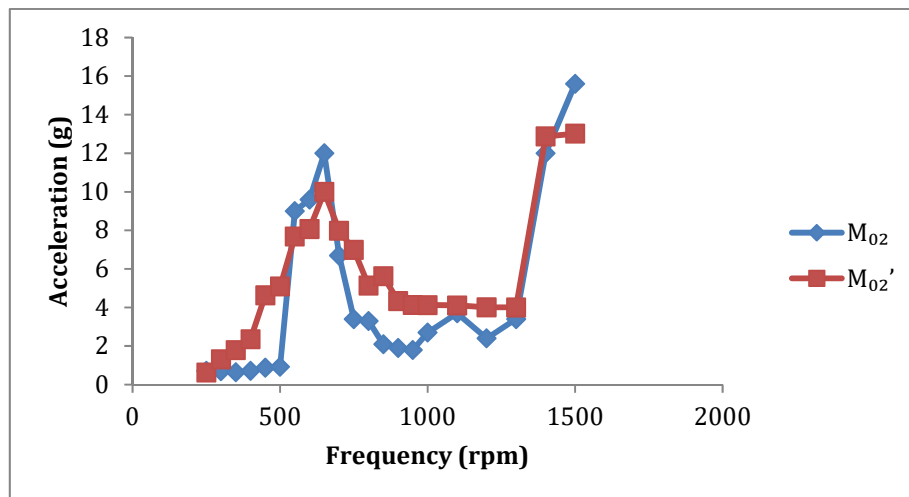


Figure 14: Comparison of acceleration vs frequency for M02 and M02' models

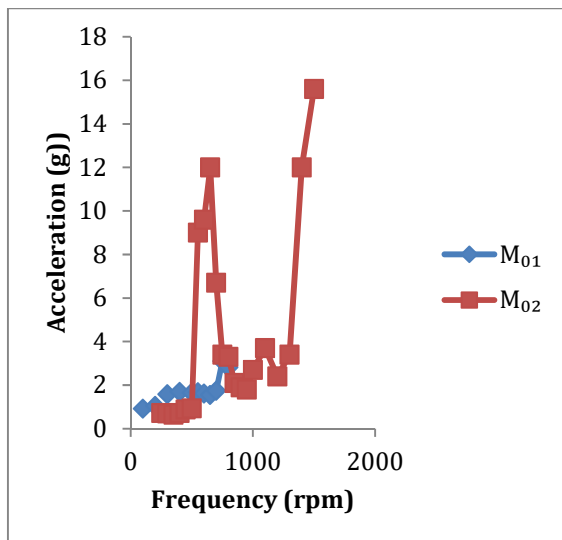


Figure 15: Comparison of acceleration vs frequency for M01 and M02 models

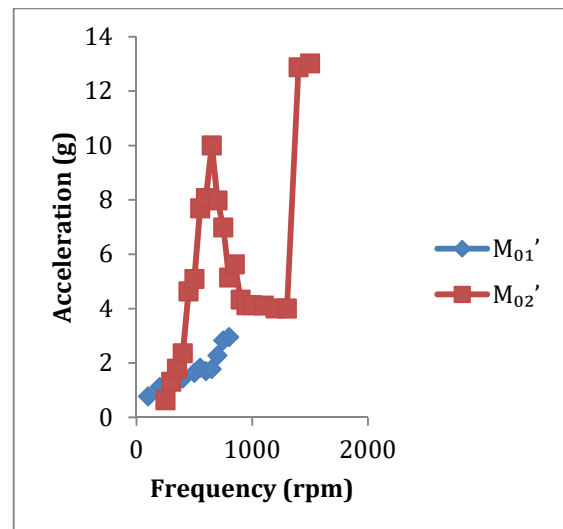


Figure 16: Comparison of acceleration vs frequency for M01' and M02' models

CONCLUSIONS

The responses of un-retrofitted experimental and analytical models (M_{01} and M_{01}') are well comparable. This means macro modelling can be suitably used.

The responses of retrofitted experimental and analytical models (M_{02} and M_{02}') are also well comparable.

The simple and low-cost retrofitted model (M_{02}) takes four times more force in comparison to un-retrofitted model (M_{01}).

This retrofitting technique is quite economical as well as suitable for poor people in earthquake prone areas.

REFERENCES

- Abrams, D.P. (2001). Performance based engineering concepts for unreinforced masonry building structures. *Journal of Progress in Structural Engineering and Materials*, Wiley Interscience, 3:1, 48-56.
- Bothara J.K., Mander J.B., Dhakal R.P., Khare R.K. and Maniyar M.M. (2007), "Seismic Performance and Financial Risk of Masonry Houses" *ISET Journal of Earthquake Technology*, Paper No.493, Vol.-44, No.3-4.
- Chuang S., Zhuge Y., McBean P.C. (2004), "Seismic Retrofitting of Unreinforced Masonry Wall by Cable System". 13th World Conference on Earthquake Engineering, Vancouver, B.C., Canada, August 1-6, 2004, Paper No. 3228.

Elgawady M.A., Lestuzzi P., Badoux M., (2006), “Analytical Model for In-plane Shear Behaviour of URM Walls Retrofitted with FRP,” *Composites Science and Technology*, vol.66, pp. 459-474.

Frumento, Giovinazzi S., Lagomarsino S. and Podestà S. (2006), “Seismic Retrofitting of Unreinforced Masonry Buildings In Italy”, New Zealand Society of Earthquake Engineering (NZSEE) Conference.

Goodwin C., Tonks G. and Ingham J. M. (2011) “Retrofit Techniques for Seismic Improvement of URM Building”, *Journal of Structural Engineering Society New Zealand*, Inc. Vol. 24.

Hong N.K., Kim J. and Mosalam K. (2004), “Seismic Performance of Unreinforced Masonry Building in Low Seismicity Region” 13th World Conference on Earthquake Engineering Vancouver, B.C., Canada August 1-6, Paper No. 953.

Keypour H., Fahjan Y.H. and Bayrakta A. (2007) “Analysis and Strengthening Methods for Historical Masonry Structures”, SEE 5.

Khadka S.S. (2013), “Seismic Performance of Traditional Unreinforced Masonry Building in Nepal”. *Kathmandu University Journal of Science, Engineering and Technology* Vol. 9, No. 1, July, 2013, Pp. 15-28.

Lourenco P.B., Milani G., Tralli A., Zucchini A. (2006), “Analysis of Masonry Structures: Review of and Recent Trends in Homogenization Techniques”. *Canadian Journal of Civil Engineering*, 2007, 34 (11): 1443-1457, 10.1139/L07-097.

Lourenco P.B. (1996), “Computational Strategies for Masonry Structures”, Ph.D. Thesis, Delft University of Technology, Holland.

Lourenço, P. and Rots, J. (1997). "Multisurface Interface Model for Analysis of Masonry Structures." *J. Eng. Mech.*, 10.1061/(ASCE)0733-9399(1997)123:7(660), 660-668.

Mehrabi, A., Benson Shing, P., Schuller, M., and Noland, J. (1996). "Experimental Evaluation of Masonry-Infilled RC Frames." *J. Struct. Eng.*, 10.1061/(ASCE)0733-9445(1996)122:3(228), 228-237.

Tianyi Y., Moon F.L., Leon R.T. and Kahn L.F. (2006), “Lateral Load Testing on a Two-Story Unreinforced Masonry Building, *Journal of Structural Engineering*”, ASCE, vol. 132, no.5, 643-652.

COMMON SENSE APPROACH TO MASONRY QUALITY ASSURANCE

John Chrysler¹, Kurtis Siggard² and Phillip Samblanet³

¹ Executive Director, Masonry Institute of America, jc@masonry.pro

² Executive Director, Concrete Masonry Association of California and Nevada, kurt@cmacn.org

³ Executive Director, The Masonry Society, psamblanet@masonrysociety.org

In the United States and many countries, quality assurance programs have become commonplace to verify that construction complies with the design intent. For masonry, TMS 402, *Building Code Requirements for Masonry Structures* requires one of 3 levels of quality assurance with minimum requirements contained in TMS 602, *Specification for Masonry Structures*. These requirements, when adopted by a building code such as the International Building Code, then define minimum levels of quality assurance for a masonry project. In the 2016 TMS 402/602 these requirements were clarified and enhanced so that designers and construction professionals are aware of the minimum requirements.

This paper will overview the new quality assurance requirements in TMS 402/602-16 and will then look at common sense approaches for inspection, and, where needed, testing of structural masonry. Required and recommended qualifications for structural masonry inspectors and masonry testing technicians will be reviewed as will recommended handbooks and checklists that can be used to provide quick and efficient ways to carry out an effective quality assurance program.

Keywords: *Quality Assurance, Quality Control, Inspection, Testing, Masonry Units, Reinforcement*

INTRODUCTION

If you have read this far into the paper, you are probably asking two questions: 'Why do we need masonry Quality Assurance?' and 'What is this common sense approach associated with Quality Assurance?' Let's start by defining what is meant by masonry Quality Assurance.

Quality Assurance is a term defined as "The administrative and procedural requirements established by the contract documents to assure that the constructed masonry is in compliance with the contract documents" [TMS 402/602]. The TMS 402 definition parallels the concept associated with the Australian National Construction Code definition of Verification Method which means a test, inspection, calculation or other method that determines whether a Performance Solution complies with the relevant Performance Requirements [NCC 2016]. So, what does Quality Assurance or Verification Method mean and how do we satisfy the requirement? First, we must look at what the designer needs to include in the contract documents and second, how the contractor will implement the Quality Assurance program to the satisfaction of the designer.

The basis of this paper is the International Building Code (IBC) [IBC 2018], which, in addition to being the primary building code in the United States is also adopted in some form in at least ten other countries throughout the world [ICC website]. For masonry design and construction, the IBC references the material standard, TMS 402/602, *Building Code Requirements and Specification for Masonry Structures*.

The need and benefit for special inspection and proper quality assurance/quality control is well-documented [Chrysler and Amrhein, 1996, Wakefield, 1996, Beavers and Samblanet, 2001, Samblanet, 2008, Chrysler and Samblanet, 2011]. This paper does not address needs cited in those references, but readers are reminded of the structural benefit of effective and properly executed quality assurance plans; and the problems inadequate design, poor construction, and inappropriate materials can have on the performance of any structure. In recent years, a saying that "poor inspection is often worse than no inspection" highlights concerns that any inspection provides the contractor, owner, designer and building official with the impression that the completed project complies with appropriate building code and intent of the project documents. This paper attempts to provide guidance on how to develop, streamline, and implement an effective Quality Assurance program so that intended performance is realized.

CHOOSING THE APPROPRIATE QUALITY ASSURANCE LEVEL

With the vast differences in exposure, design and construction, a single Quality Assurance program is not applicable to all construction projects. As noted in Chrysler and Samblanet, (2011), where the consequence of failure of a building is higher, such as for a hospital or disaster shelter, more rigorous quality assurance requirements are appropriate while similar quality assurance provisions may be more than needed for a small trash enclosure. Likewise, when more elaborate design methods are used, more extensive documented quality assurance may be warranted, and when prescriptive techniques are used that have historically shown adequate performance, less rigorous quality assurance is likely acceptable. Considering this, TMS Committee 402/602 developed three levels of quality assurance in 1995, which have been maintained, though clarified and enhanced, since first published [Beavers and Samblanet, 2001].

Chrysler and Samblanet, 2011 reviewed various selections that must be considered when determining the appropriate level of Quality Assurance to implement which include the type of building being constructed (through Occupancy Categories at the time that paper was written, and which are now termed Risk Categories) and the method used to design the masonry. Because this sounds like a complicated process, those topics are reviewed briefly here.

ASCE 7-10 [ASCE 7 2010] and IBC (2018) list the Risk Categories which are summarized in Table 1. Risk Categories are a classification on the level of risk associated with unacceptable performance due to potential wind, seismic, flood, snow, ice or other potential loads which could result in structural failure. The designer first chooses the Risk Category based on the building use and size, then must determine the method of masonry design. Even though there are nine design methods listed in Table 2, most structural masonry is designed by either the Strength Design method or the Allowable Stress Design method. Due to these choices - Risk Category (which has 4 possibilities) and masonry design method (which has 9 options) there are 36 possible combinations for determining the appropriate Quality Assurance level that should be applied. However, this quickly reduces to 8 and when considering that Risk Categories I, II and III are combined, and that when Strength Design and Allowable Stress Design are also combined, two choices of Quality Assurance remain for most structural masonry projects.

Table 1-Summary of Risk Categories and Applicable Buildings¹

| Category | General Definition | Examples |
|------------|------------------------------------|--|
| I | Low hazard to human life | Agriculture facilities |
| II | Buildings not otherwise classified | Small/medium commercial facilities Office buildings |
| III | Substantial hazard to human life | Occupancy several hundred Medical care over 50 people Power generating facilities Water and waste utility facilities Detention facilities |
| IV | Essential facilities | Fire, police, rescue, emergency shelter Hospitals, emergency communications Emergency power generating facilities, water storage facilities Air traffic control, emergency hangers Any building having critical national defense functions |

¹ Based on IBC Table 1604.5

Table 2-Minimum Quality Assurance Level^{1,2}

| Design Method | Risk Category I, II or III | Risk Category IV |
|--|----------------------------|------------------|
| <ul style="list-style-type: none"> • Strength Design • Allowable Stress Design • Prestressed Masonry • Masonry Infill • Limit Design Method | Level 2 | Level 3 |
| <ul style="list-style-type: none"> • Veneer • Glass Unit Masonry • Partition Walls | Level 1 | Level 2 |
| • Empirical Masonry | Level 1 | Not Permitted |

¹ Based on TMS 402 Table 1

² In previous editions of TMS 402/602, Level 1 was designated as Level A, Level 2 was designated as Level B, and Level 3 was designated as Level C. These were changed in TMS 602-16 to be consistent with the previous designations used in the International Building Code.

At this point, the code provides direction to the designer for the minimum Quality Assurance level required for the project. Once the Quality Assurance level is determined, Table 3 lists the minimum test verification requirements for the project while Table 4 provides the minimum inspection required. Designers have the option of raising the Quality Assurance level or making individual testing and inspection tasks more stringent than minimum code requirements. An example of this may be for a large retail facility where the minimum required Quality Assurance is Level 2, but the designer elects to specify Quality Assurance level 3. The designer also has the option of specifying a Level 2 Quality Assurance program but may change certain testing or inspection tasks to be more stringent; for example requiring some inspection tasks to be continuously performed rather than on a periodic basis.

With the Minimum Verification Requirements combined into a single table for the three Quality Assurance levels and the Minimum Inspection Requirements also combined into a single table for the three different levels, a designer may want to consider incorporating the applicable tasks of the table into the project documents. Such an approach would preclude the designer from developing a Quality Assurance program from scratch and would also provide confidence that the Quality Assurance program included all of the minimum code requirements.

Consistency in presenting the Quality Assurance program based on the Verification and Inspection Tables would also communicate the requirements to field personnel in a more uniform manner. Doing so should enhance the quality of the final product which is beneficial for everyone.

Table 3-Minimum Verification Requirements¹

| Minimum Verification | Required for Quality Assurance ² | | |
|--|---|---------|---------|
| | Level 1 | Level 2 | Level 3 |
| Prior to construction, verification of compliance of submittals. | R | R | R |
| Prior to construction, verification of f'_m and f'_{AAC} except where specifically exempted by the Code. | NR | R | R |
| During construction, verification of Slump flow and Visual Stability Index (VSI) when self-consolidating grout is delivered to the project site. | NR | R | R |
| During construction, verification of f'_m and f'_{AAC} for every 465 sq. m (5,000 sq. ft.). | NR | NR | R |
| During construction, verification of proportions of materials as delivered to the project site for premixed or preblended mortar, prestressing grout, and grout other than self-consolidating grout. | NR | NR | R |

¹ Based on TMS 602, Table 3

² R=Required, NR=Not Required

That brings up the term 'Periodic'. Continuous means that the inspector is to be present all the time for the particular listed task, but the question is often asked, "How much periodic inspection is appropriate?". While there is no clear answer that can apply to every construction project at all times, there is advice in TMS 602 Commentary which is that the frequency of periodic inspection should be determined by the designer based on the complexity and size of the project. Simply stated, the designer should establish a frequency of inspection (for example, five random hours per week in at least two increments) that would provide the designer a comfort level that materials and workmanship conform to the project documents and code requirements.

Table 4-Minimum Inspection Requirements¹

| Inspection Task | Frequency ² | | |
|---|------------------------|------------------------------------|---------|
| | Level 1 | Level 2 | Level 3 |
| 1. As masonry construction begins, verify that the following are in compliance: | | | |
| a. Proportions of site-prepared mortar | NR | P | P |
| b. Grade and size of prestressing tendons and anchorages | NR | P | P |
| c. Grade, type and size of reinforcement, connectors, anchor bolts, and prestressing tendons and anchorages | NR | P | P |
| d. Prestressing technique | NR | P | P |
| e. Properties of thin-bed mortar for AAC masonry | NR | C ³ /P ⁴ | C |
| f. Sample panel construction | NR | P | C |
| 2. Prior to grouting, verify that the following are in compliance: | | | |
| a. Grout space | NR | P | C |
| b. Placement of prestressing tendons and anchorages | NR | P | P |
| c. Placement of reinforcement, connectors, and anchor bolts | NR | P | C |
| d. Proportions of site-prepared grout and prestressing grout for bonded tendons | NR | P | P |
| 3. Verify compliance of the following during construction: | | | |
| a. Materials and procedures with the approved documents | NR | P | P |
| b. Placement of masonry units and mortar joint construction | NR | P | P |
| c. Size and location of structural members | NR | P | P |
| d. Type, size, and location of anchors, including other details of anchorage of masonry to structural members, frames, or other construction | NR | P | C |
| e. Welding of reinforcement | NR | C | C |
| f. Preparation, construction, and protection of masonry during cold weather (temperature below 4.4°C (40°F)) or hot weather (temperature above 32.2°C (90°F)) | NR | P | P |
| g. Application and measurement of prestressing force | NR | C | C |
| h. Placement of grout and prestressing grout for bonded tendons is in compliance | NR | C | C |
| i. Placement of AAC masonry units and construction of thin-bed mortar joints | NR | C ^(b) /P ^(c) | C |
| 4. Observe preparation of grout specimens, mortar specimens, and/or prisms | NR | P | C |

¹ Based on TMS 602, Table 4

² Frequency refers to the frequency of inspection, which may be continuous during the listed task or periodically during the listed task, as defined in the table. NR=Not Required, P=Periodic, C=Continuous

³ Required for the first 465 square meters (5,000 square feet) of AAC masonry

⁴ Required after the first 465 square meters (5,000 square feet) of AAC masonry

Now comes the challenge of building some common sense into the inspection process. There is a dichotomy in the code to be specific about code provisions, yet to be broad enough to be appropriate for every application.

RECOMMENDATIONS FOR PREPARING A QUALITY ASSURANCE PLAN

Determining the required Quality Assurance level is the first step by the design team in developing an appropriate Quality Assurance plan. Then, specific requirements can be added

to clearly define a project-specific Quality Assurance plan that includes required tests (if any), inspector/testing technician qualifications and duties, procedures for clarification of requirements (for example, RFI's - requests for information), procedures for handling non-compliance by the contractor, and additional tasks that may be required beyond minimum special inspection. For example, if inspection is desired for a flashing system or the application of a clear water repellent, since such items are not covered under special inspection.

Specifications for the project must clearly identify the required materials and properties including, for example: special colors, textures and features of units, the weight classification for concrete masonry units, brick type for clay masonry units and mortar type. Specifications must be up-to-date conveying current requirements. A disappointing, but common trend in recent years, is to cut-and-paste specifications from other projects without updating them for the new project. Sadly, the industry commonly sees old requirements carried over into new project specification, and sometimes the specified requirements are incorrect or do not relate to the project. An all too common example of this are specifications for concrete masonry units that specify the grade and type of the units - such requirements were deleted from ASTM C90 many years ago. Specifying those requirements now is both incorrect and confusing - slowing projects and increasing costs. Therefore, it is critical that the design team prepare the project specifications carefully so that the contractor, inspector, testing agencies and material suppliers know what is needed and expected.

The design team should also clearly understand the purpose and extent of TMS 602. As noted in the preface, TMS 602, when adopted, establishes minimum construction requirements for materials and workmanship used to construct masonry structures - the key words here are 'minimum' and 'structures'. The specification does not include industry 'recommendations' to achieve a better performing masonry project - rather it contains minimum requirements to ensure safety of the structure. It doesn't address things beyond structural safety, so things like fire resistance, moisture control, and thermal performance are beyond the scope of this minimum specification. Designers are encouraged to take TMS 602 and expand it as needed for their specific projects.

Even for the simplest project, TMS 602 is still 'incomplete' on its own, and designers must supplement it by specifying relevant items on the Mandatory Requirements Checklist. This includes listing, where needed, the specified strength of the masonry f'_m , the testing and inspection levels required, and things that are often overlooked such as the location of movement joints. The design team should also review the Optional Requirements Checklist to see if there are items that may apply to their specific project.

Consistent with the need to review the project specifications, project documents must clearly note any required tests that are to be performed, reporting requirements, and criteria for acceptance/rejection. Periodic inspection frequency should be outlined for the specific needs of the project.

One common area of potential conflict occurs with the role, if any, a special inspector may have with evaluating the 'aesthetics' of the project. For most projects, the viewing of items such as the color of units and mortar, blending of units, and tolerances above and beyond the listed structural tolerances in TMS 602, are not tasks assigned to a special inspector. The special inspector should be more focused on issues that affect the structural capacity of the masonry. If such aesthetic items are critical, they need to be clearly specified, likely with the use of an approved sample panel or mock-up, and observed by the project design team.

The design team must also clearly list the tasks of the special inspector; being realistic on the role of the special inspector. An inspector is to inspect, observe and report. Some believe the inspector is to counsel, advise, and oversee the contractor. Except for a few very specific cases, special inspectors should not, and in most cases, may not, direct, stop, or delay the construction process. They may suggest, but the contractor is ultimately responsible for what takes place on the jobsite. If the inspector believes the wrong materials are being used, it can be noted to the contractor, and if the contractor decides to use the materials, the inspector then can only report their observations. It then is between the design team and the contractor to decide if what was done conforms to the project specifications, and if not, whether it matters.

In summary, when developing the Quality Assurance Plan, it needs to be specific to the project and clearly communicated.

TIPS ON IMPLEMENTING THE QUALITY ASSURANCE PLAN

Having qualified testing technicians and inspectors on the jobsite is critical in ensuring the Quality Assurance plan is implemented in an efficient and accurate way. Because of problems in the past with poor testing and inspection by unqualified personnel, requirements have been added into TMS 602 that such personnel are to be 'qualified'. Qualified programs listed in the TMS 602 Commentary include the American Concrete Institute's (ACI) Masonry Testing Technician Certification Program and the International Code Council's (ICC) Structural Masonry Special Inspectors Certification Program. While there may be other means to verify qualification, technicians certified to the ACI and ICC certification programs have demonstrated an understanding for the work they will perform and a general understanding of masonry. Information and guides to help prepare for the ACI Certificated Testing Technician Certification Examination and the ICC Certified Structural Masonry Special Inspectors Certification Examinations are available [ACI 2016, MIA 2015, Samblanet 2008, and Farny, 2015].

Once the testing agency and inspection agency are selected for the project, they must thoroughly review the project documents and requirements to determine how to implement the Quality Assurance program. Determination of the types and extent of testing and inspection is needed early in the process to ensure they are provided when needed. This includes ensuring space and materials are provided for required tests, and that periodic inspection is clearly understood.

The importance of following proper sampling and testing procedures by qualified testing technicians cannot be overstated. Cases where testing technicians with little to no masonry training are sadly all too common. The reported test results are either meaningless, or may be considered appropriate and accurate by the design team even though they were done incorrectly and do not reflect the true condition of the material being tested. Poor, inaccurate testing leads to costly delays that could easily be avoided if performed properly.

Special inspectors are hired to observe the structural masonry being constructed. This obviously means they need to be onsite at the appropriate time during the construction process to observe the work being done. They need to pay attention to those items that have the most influence on the structural integrity of the masonry. These include connections to floors, adjacent walls, and roofs; placement of reinforcement, anchors and ties; and grouting. Other items such as placement of units and mortar joint tolerances are typically not as critical to the

strength of the masonry, and thus may be able to be performed on a periodic basis.

Communication between inspectors and contractors is key, and then, if needed with the design team. Inspectors must remember that their job is to observe, record, and report. Where they see something that does not seem appropriate, or in accordance with the plans and specifications, they should discuss it with the contractor. There may be reasons why the contractor is doing something in a specific way; in some cases, they may not have been aware that things were not being done correctly by their labor. Concisely, accurately and appropriately communicating these issues to the contractor will lead to a positive relationship on the jobsite.

The inspector must also record and report what takes place on the jobsite. Where items appear to be non-compliant, they need to bring these to the attention of the contractor and design team in a timely and appropriate manner so that if needed, corrections can be made. In order to protect the inspector from documenting a situation which could have structural safety implications, the IBC is intentionally careful to term the notices as 'discrepancy' notices, not correction or deficiency notices. This approach forces structural issues to be routed back to the designer for consideration of acceptance or correction.

As with any profession, testing technicians and inspectors must participate in continuing education including keeping current with code requirements, changing materials, and new construction methods. Both ACI and ICC require re-certification and/or continuing education.

ADDITIONAL INFORMATION ON QUALITY ASSURANCE, TESTING AND INSPECTION

Historically, there have been three levels of information associated with codes.

- The Code itself, including Reference Standards
- Code Commentaries
- Industry Information

Individuals responsible for developing the Quality Assurance plan, and those implementing the plan need to be familiar with the related material at each level of information, and on how that information affects their duties and responsibilities.

The Code and Reference Standards, such as AS 3700 and TMS 402/602, are developed and published by those that have an interest in developing design and construction documents for the benefit of the public. The Building Code is developed and monitored by building officials concerned with the proper design and performance of all types of buildings considering the public's health, safety, and welfare. The Reference Standards are developed using specific consensus procedures that must include representation by a balance of designers, code users, and general interest parties willing to participate in the process. Clear balloting procedures that include consideration and resolution of negative/minority positions, review by the public, and other specific criteria are mandatory in the process. In the United States, these Standards are typically created by organizations that have had their rules reviewed and determined to be in compliance by the American National Standards Institute (ANSI) and these groups are thus identified as ANSI Standards Developing Organizations (SDO's). Much of the discussion earlier in this paper describes Code and Standard requirements related to quality assurance.

Code Commentaries add value by explaining the intent of the Committee that developed the Code provisions. The Commentary often provides helpful background information on why the Code Provision is important, what the basis for the provision may be, and occasionally on how to apply the provision. Code commentaries have existed for many years, but have been in the form of a separate document, or positioned behind the code. Recently, the Commentary has been relocated to a column next to the Code so the user can be significantly more aware of the code intent. This format goes a long way in bringing common sense to the meaning and application of code provisions. Designers, contractors, testing technicians, inspectors, and others are reminded to refer to, and use commentary frequently whenever they have questions regarding a specific provision of the Code or a Standard.

Industry information can take on many forms and has varying levels of credibility. The best sources are usually well-known interested parties that are concerned and have expertise with best practices and are not trying to sell a particular product. Organizations and Institutes provide many sources of credible information explaining the intent and application of the Code or material Standards in much greater detail than the Commentary. While such guides, handbooks and tips are not 'Code' they often clarify Code provisions by putting provisions in easily understood language, or by summarizing Code requirements in Tables or in Figures or Photographs. Frequently they provide recommendations on topics not specifically addressed in Codes and Standards.

For masonry testing, ASTM has a wealth of information, and is developing additional online resources with ACI and TMS at the writing of this paper. The Masonry Field Testing Technician and Masonry Laboratory Testing Technician Technical Workbook (ACI 2016) is an excellent resource for testing technicians. The Brick Industry Association, National Concrete Masonry Association, and other trade organizations produce Technical Notes and other resources, downloadable from their websites at no charge, which outline testing procedures and steps that need to be taken to ensure accuracy. For field inspection, the Masonry Institute of America's Reinforced Concrete Masonry Construction Inspectors Handbook, MIA 2015 is the foremost guide on the topic.

A LITTLE COMMON SENSE

Unfortunately, not everything in construction is absolutely 'right' and 'wrong'. There are certain words used in the code that are subject to interpretation. Also, common sense on part of the inspector is needed to help the job progress efficiently. Being too literal in interpretations of Code provisions is often neither productive nor appropriate. One example of where reading to the strictest letter of the Code can slow a project, applying equally to AS 3700, Section 12.8.1 and TMS 602, Article 3.2 F, is that masonry cells to be grouted are clean prior to grouting. Some inspectors in the United States think that the provision means every grain of loose sand must be removed from the cell which is not the intent of the Code. As stated in the Reinforced Concrete Masonry Construction Inspectors Handbook, MIA 2015, clean is meant to be 'reasonably clean' as depicted in Figure 1, without loose deleterious materials such as paper, rags, cans, and other things that could cause obstruction or prevent bond in the cell. A few incidental mortar droppings or some minor sand will not cause structural concern as the loose materials will be blended into the fluid grout during the grouting process.



Figure 1: Acceptable amount of mortar droppings in cavity

Another often misunderstood issue related to masonry grout is the amount of water associated with grout. Large quantities of grout are typically delivered in transit mix trucks from the same producers that furnish concrete. Both AS 3700 and TMS 602 provide for masonry grout to be proportioned (typical for site-mixed grout) or to conform to a minimum compressive strength; 12 MPa (1,750 psi) in AS 3700 and 13.8 MPa (2,000 psi) in TMS 602. Another requirement is the high slump associated with masonry grout (200 to 275 mm (8 to 11 in.)) as depicted in Figure 2, which means a mix design water-cement ratio of 0.65 or greater. This does not conform to the concrete-based design software associated with concrete mix designs, so the ready mix concrete producers use plasticizers and water reducers to minimize the amount of mix water. They ignore the fact that the units absorb a significant amount of water immediately after grout placement. By significantly reducing the amount of water in masonry grout there is insufficient water in the mix design for grout to flow properly and potentially inhibit the normal hydration process.



Figure 2: Proper grout slump with high w/c ratio

Another misperception is related to the placement of reinforcement within a masonry wall. There are two issues that commonly cause confusion. The first is the manner in which reinforcement is to be held in place during the grouting process and the second is the adequacy of the restraint device used to hold the reinforcing steel in place during grouting. Some believe that vertical and horizontal reinforcement must be tied together in masonry. While this is typically done for concrete (to hold the steel in mats and cages), it is not required in masonry. Confinement within masonry units allows for reinforcement positioners as shown in Figure 3 which limits reinforcement displacement during the grouting process. Likewise, bond beam units can hold horizontal reinforcement in place. Tying the vertical and horizontal reinforcing then is not needed and is a waste of time and money.



Figure 3: Masonry reinforcement positioner

Consistent with this, Figure 4 shows congested reinforcement within masonry that has little room for movement. Positioners in this case are neither functional nor required. With the exception of avoiding the use of materials that cause galvanic corrosion, the code has little guidance on reinforcement positioners that may be used. Keep in mind that the only function of the positioner is restraint of reinforcement, within tolerances, before and during the grouting process. Once the grout has taken on initial set, the positioner has done its job and provides no further benefit.



Figure 4: Congested reinforcement-positioners not required

Codes and Standards provide tolerance for placement of reinforcement that are intended to allow minor variations in the placement of the bars while maintaining structural capacity. For example, vertical reinforcement along the length of the wall needs to be within 50 mm (2 in.) of the plan location. AS 3700 requires that reinforcement be perpendicular within 5 mm (0.2 in.) of the detailed location whereas TMS 602 has a greater tolerance of 13 mm (1/2 in.). Properly located reinforcement positioners can easily hold vertical reinforcement within tolerance. However, other methods, such as tying vertical bars to the footing dowels and horizontal bond beam reinforcement, although more stringent than code requirements, can also be adequate in holding the reinforcement within placement tolerances.

These are a few examples where common sense is needed during the construction process, and which still achieves the desired quality without sacrificing the structural capacity of the

masonry. Communication among the designer, contractor, material producer and inspector is necessary so that all parties understand and reach the same final goal-quality masonry construction.

SUMMARY

Increasingly, testing technicians and inspectors are used on masonry projects to ensure quality construction. Developing a clear and concise Quality Assurance plan by the design team is essential to lay the ground work for those on the jobsite. New Code requirements help to identify various minimum Quality Assurance levels. The design team must review the project and supplement the specifications, project drawings and Quality Assurance plan to be specific for the project. With qualified labor, and observers, and a little common sense, the project can proceed quickly and efficiently.

REFERENCES

ACI 2016, CP-70 (16), Masonry Field Testing Technician and Masonry Laboratory Testing Technician Technical Workbook, American Concrete Institute, Farmington Hills, MI, USA 2016

AS 3700-2011, Australian Standard, Masonry Structures, Standards Australia Committee BD-004, 2011

ASCE 7 2010: Minimum Design Loads for Buildings and Other Structures, American Society of Civil Engineers, Reston, VA, USA 2016

Beavers 2001: Beavers, S, Samblanet, P.J., "Inspection of Masonry – A Look at the Requirements in the MSJC and the IBC", Masonry Magazine, Mason Contractors Association of America, Lombard, IL, USA January 2001, pp. 26-29

Chrysler 1996: Chrysler, J., Amrhein, J. "Special Masonry Inspection: The Inspector" Proceedings of the Seventh North American Masonry Conference, The Masonry Society, Boulder, CO, USA 1996, pp. 962-973

Chrysler, 2011, Chrysler, J. and Samblanet, P. "Special Inspection of Structural Masonry Construction - A Review of Current Requirements, Upcoming Changes and Expected Trends in the Future" Proceedings of the Eleventh North American Masonry Conference, The Masonry Society, Longmont, CO, USA 2011.

Farny, 2015: Farny, J.A., Lang, N. Morrison. M, and Samblanet, P.J., "New Programs for Educating and Certifying Masonry Testing Technicians", Proceedings of the Twelfth North American Masonry Conference, The Masonry Society, Longmont, CO, USA 2015.

IBC 2018: International Building Code, International Code Council, Country Club Hills, IL, USA 2014

ICC Website, <https://www.iccsafe.org/about-icc/overview/international-code-adoptions/>

MIA 2015: Reinforced Concrete Masonry Construction Inspector's Handbook, 9th Edition, Masonry Institute of America, Torrance, CA, USA 2015.

NCC 2016, National Construction Code, Volume 1, Commonwealth of Australia and States and Territories of Australia, 2016

Samblanet 2008: Samblanet, P.J. and Chrysler, J., "Masonry Inspector's Certification", TMS Responds, The Masonry Society, Longmont, CO, USA Jul 2008, Vol. 7, No. 1

TMS 402/602: Building Code Requirements and Specification for Masonry Structures (TMS 402/602-16), The Masonry Society, Longmont, CO, USA 2016.

Wakefield 1996: Wakefield, D. A. "Structural Masonry Inspection -A Win-Win Situation" Proceedings of the Seventh North American Masonry Conference, The Masonry Society, Longmont, CO, USA 1996, pp. 974-981

STRUCTURAL BRICK MASONRY IN THE WESTERN UNITED STATES

John Chrysler¹, John G. Tawresey² and Phillip J. Samblanet³

¹ Executive Director, Masonry Institute of America, jc@masonry.pro

² Vice President Retired, KPFF Consulting Engineers, johntaw@aol.com

³ Executive Director, The Masonry Society, psamblanet@masonrysociety.org

Since building structures first appeared on earth, brick masonry units produced by firing clay have always been a building material relied upon to resist the forces of gravity. Recently however, buildings have evolved into steel and concrete frames utilizing brick only as a veneer driven by an aesthetic choice for the exterior wall. But, there are exceptions. In the Western United States, initially driven by seismic criteria and later by cost, structural brick has made a partial comeback. Multi-story load bearing buildings utilizing the compressive strength of brick materials have been constructed in competition with other structural systems. Also, new applications of using brick panelization to reduce the construction schedule and remove clutter from the job site have been employed.

The change in mindset to structural brick has also opened the door to creative concepts for exterior veneer applications. Various new applications have found uses that are termed reinforced veneer, structural brick veneer, laid in place brick panels and brick panels.

This paper presents examples of structural brick masonry projects including examples on structural veneer and panelised brick systems, noting how these systems creatively solved design challenges.

Keywords: *Brick, Structural, Load Bearing, Veneer, Panels*

INTRODUCTION - STRUCTURAL BRICK MASONRY – THE BEGINNING

Building with brick dates back several thousand years as evidenced by archaeological findings of sun dried brick. The first known fired brick dates back to 3000 BC in China (Drysedale, 2008). Fired brick has always been considered one of the longest-lasting and strongest building materials and until the last 100 years has been the building material of choice. Today, in the United States (US) however, most brick is used as veneer clipped to, or in some cases, simply adhered to, a structural backing. While this system works well, it is an inefficient use of the benefits of this beautiful, strong, durable, and fire resistant material.

There is, however, an exception: structural brick masonry. The San Francisco earthquake of 1906 and the Long Beach earthquake of 1933 destroyed many brick buildings (Reference 1), leaving millions of brick in the street, and confronted the brick manufacturing industry with the choice to either address brick structural issues or to go out of business. They chose the former, and started the development of an entirely new approach to brick building construction. While most brick in the US, brick is used simply as a veneer, the Western United States continues to commonly use reinforced brick masonry as a viable building system that has many applications and advantages often not fully recognized elsewhere.

The use of reinforced brick masonry has evolved into many design and construction alternatives that offer designers, contractors and owners new opportunities for cost savings and improved building performance. In the following paragraphs the progression of system developments is presented followed by a summary of some of the lessons learned.

THE BEGINNING – LOAD BEARING

After the 1933 Long Beach earthquake, engineers assumed the design methods for reinforced concrete would apply to reinforced brick and simply added reinforcement into walls and copied concrete design concepts. As time passed, research and engineering experience with the system evolved into many new applications: load bearing single family residences, mid-rise multifamily residences, load bearing panels and exterior building skins classified as brick panels, laid in place brick panels structural brick veneer, reinforced veneer, and rocking veneer.

Early testing by the Structural Clay Products Research Foundation demonstrated the high compressive strength of fired clay masonry (Reference 2). One of the first projects to take advantage of this strength is the Little America Hotel, located in Salt Lake City, Utah (Figure 1). It was constructed in 1975 of 200 x 100 x 300 mm (8x4x12 in.) hollow clay units and remains in use today more than 40 years after it was constructed.



Figure 1: Little American Hotel

Another example is a 12 story residential building in Seattle constructed using 140 mm (6 in.) hollow clay brick, Figure 2. Note that the floor slabs were extended to the exterior of the building to provide a unique appearance and for construction efficiency.



Figure 2: Twelve Story Building in Seattle

In a similar project in Seattle, the floor system was precast concrete hollow core planks. The planks were set on a mortar joint matching the brick face shell thickness. Wet wood shims, slightly thicker than the mortar joint, were placed at 0.6 m (2 ft) on centers in the mortar joint. The initial dead load of the plank rested on the wood shim, as the wood dried it shrunk resulting in an even transfer of load to the mortar joint.

At about the same time, Western States Clay Products Association (WSCPA) initiated a testing program to demonstrate the viability of constructing load bearing masonry residences using 100

x 100 x 300 mm (4x4x12 in.) hollow clay units. The test program again demonstrated the high compressive strength of fired clay masonry and also demonstrated high shear and tensile strengths. The test program resulted in special code provisions that allowed the construction of the load bearing brick residences. Many homes were built replacing the convention wood framing construction.

The high shear and tensile strength led to the realization that fired clay brick masonry could be panelized. Speed of construction is often a driving criterion for a project. In the following example, reinforced load bearing structural brick elements, panels, were constructed off site and placed in record time to construct the project, Figure 3.



Figure 3: Reinforced Load Bearing Panels

Another interesting use occurred when a developer wanted a brick office building. Offices buildings typically have larger distances between load bearing elements than residential applications, often resulting in the selection of a concrete or steel frame structure with floors constructed with steel joists. The developers kept the exterior as brick, by using the brick as formwork for the concrete columns and spandrels. The brick formwork panels were constructed off site and placed; connecting them with appropriate connectors before the reinforcement was placed and concrete was poured into the forms, Figure 4.



Figure 4: Structural Brick used as Form Work for a Concrete Frame

On another building, the shear demand on the wall from the building exceeded the capacity of normal thickness of hollow brick (at the time the thickest brick was 190 mm (8 in.)). The owner still wanted the exterior to be brick, so the brick wall was designed and constructed to accept an additional thickness of sprayed on concrete (gunite). The structural brick wall was constructed using 190 mm (8 in.) hollow brick, which then became the backing for a 300 mm (12 in.) gunited concrete wall, Figure 5.



Figure 5: Structural Brick as a Backup for Gunite

THE EVOLUTION – CURTAINWALL

The tensile strength of structural brick units typically exceeds 7 MPa (1000 psi). This strength provides the opportunity for panelization of elements and transportation of the elements to the project with installation by the project crane. The first known panelized application occurred in 1977 in Portland Oregon. Panels were constructed 150 miles from the project site, shipped by truck and connected to the building with connectors similar to those used for precast concrete panels, Figure 6.



Figure 6: Panelized Brick Curtainwall

Due to the speed and efficiency of panelized brick masonry, there are now many examples of brick panel curtainwall projects in the Pacific Northwest (over 100 known by the author). Each

has a unique story to tell, Figure 7, and use the strength and beauty of brick to meet project needs (Reference 3).



Figure 7: Structural Brick Panel Curtainwall on Koin Tower, Portland OR

EVOLVING SYSTEMS

It became apparent that there are two cost advantages to panelization of brick curtainwalls, speed of construction and use in applications where there is limited access. In other situations, where speed was not a concern and where access was available, the panel system evolved into a “laid in place” panel system, where the need for lifting and transportation was not needed. The concept remained the same as the offsite fabricated panels except they were laid in place on the building. Connectors were engaged into the masonry as the wall was built, Figure 8.



Figure 8: Laid in Place Panel Wall

The next evolution was to eliminate all the ties in a conventional veneer by using more substantial connectors spaced much farther apart. This required changing the non-structural

brick veneer into a structural element with reinforcement. Using hollow brick and reinforcement allows for elimination of ties, which are replaced by more substantial connectors at a greater spacing, while all the remaining details of the conventional veneer remain unchanged. The system is called Structural Brick Veneer and a design guide for the system can be downloaded from the Western States Clay Products Association website (www.wscpa.us), Figure 9.

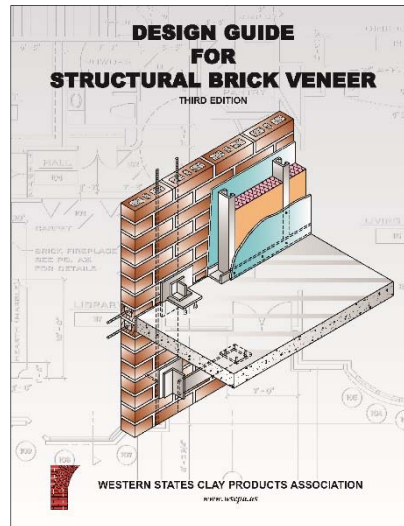


Figure 9: Design Guide for Structural Brick Veneer

Another evolution was to continue with the concept of a conventional veneer, but reinforce and grout the cavity. This system is called Reinforced Veneer, Figure 10. For water control there is no change in flashing detailing or the water and air barrier. Experience has shown that the little water that migrates into this system travels through the grout much the same way as it moves in a vacant cavity, but at a slower rate. It mimics veneer systems that were successfully used for many years, when the cavity was slushed with mortar or grouted. This was before the concept of the clean cavity and rain screen gained acceptance.



Figure 10: Reinforced Veneer

In seismic regions, a major design consideration is for the exterior skin of the building to be able to accommodate the expected building movement without failure. The previously described systems can easily be designed to do this. However, to even better accommodate seismic movements, a new system often described as a “Rocking Veneer” was developed. This system is typically laid in place on neoprene pads that allow the brick panels to rock, while pins are placed within sleeves to maintain position, Figure 11. This system has been used on several recent buildings including a large stadium in Seattle, Washington.

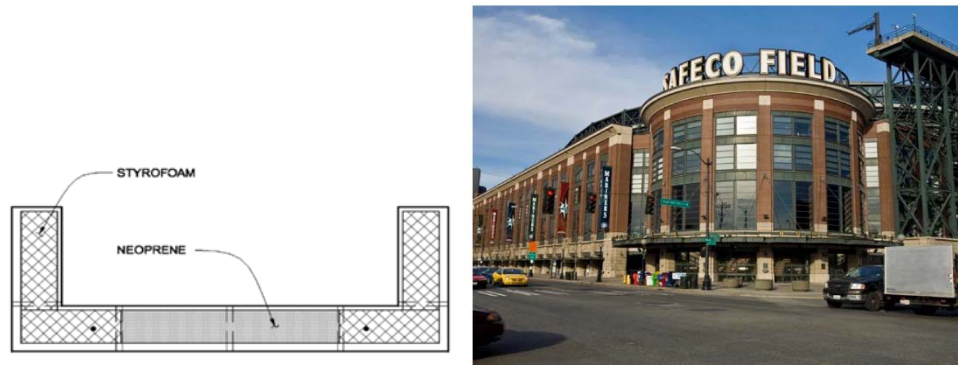


Figure 11: Rocking Veneer

BRICK MASONRY ADVANTAGES

Over the years of evolution of structural brick masonry, many lessons have been learned. The following comments are some that come to mind.

Strength. Fire clay bricks have very different properties than cement based materials. The primary advantage is inherent strength, which is coupled with brick natural beauty, durability, and resistance to fire and the elements. Fired brick compression strengths can be as high as 140 MPa (20,000 psi), and tensile strengths run as high as 21 MPa (3000 psi).

Expansion. Another important difference over cementitious materials is that brick expands over time, while concrete based materials shrink over time. When fresh from the kiln, the units contain no moisture, since any moisture has been expelled during the firing process. The brick at this point is as small as it will ever be. Over time, the fired clay absorbs moisture (even humidity from the air) and like unfired clay, expands. When applying reinforcement to a structural element constructed of clay brick, as the brick element expands, the reinforcement is stretched, imposing compressive forces on the surrounding grout and masonry, which mitigates cracking. When applying reinforcement to a structural element constructed of a cement based material, the cement based material shrinks, putting the reinforcement in compression, which also puts the surrounding materials in tension, which contributes to cracking.

A simple calculation demonstrates the effect:

The TMS 402/602-16 provides a value for brick moisture expansion as $k_e = 3 \times 10^{-4}$ mm/mm (Reference 4). In seismically active regions, the standard also specifies minimum reinforcement ratios for special reinforced masonry shear walls of 0.0013 and 0.0007 in two orthogonal directions. This combination, using strain compatibility and equilibrium results in the following stresses in the masonry and the reinforcement:

The compatibility Equation is equation 1:

$$.0003 - \frac{\sigma_m}{E_m} = \frac{\sigma_s}{E_s} \quad (1)$$

The equilibrium Equation is equation 2

$$\sigma_c A_m = \sigma_s A_s \quad (2)$$

The elastic modulus are: $E_m = 700 f'_m$ and $E_s = 200,000$ MPa and using a brick masonry specified compressive strength of 18 MPa (2600 psi) results in a modular ratio of 15.9.

There are two equations and two unknowns, σ_c and σ_s . Equation 3 is the solution

$$\sigma_s = .0003 \left(\frac{E_s}{1 + n \frac{A_s}{A_m}} \right) \quad (3)$$

Using the minimum steel ratios results in a masonry compressive stress of 0.09 MPa (13 psi) and steel stresses of 58.8 MPa (8500 psi) for the .0013 ratio.

Moisture expansion takes time, sometimes as long as five years after leaving the kiln. Thus, reinforced brick masonry also tends to “heal” over time as the brick expands into any cracks that may have formed.

Design flexibility. The designer has many choices to select shapes and sizes within manufacturing limitations. On large projects, the cost of machining dies for custom shapes for extruded units is small. For example, in a recently constructed hospital in Oregon, the designers were concerned about dropping of mortar into the cells during construction and consequently designed a custom unit with thick face shells and instructed the contractor to bed the mortar in the usual face shell thickness of 25 mm (1 in.), Figure 12. After the wall was grouted solid, grout flowed into the void filling the remaining thickness of the joint, and provided excellent interlock between the grouted core and the brick masonry.



Figure 12: Custom Brick to Prevent Mortar Dropping in the Cells

In reinforced brick masonry, because of the strength of the brick, the area of grout and its strength can generally be neglected during structural design. The purpose of the grout is to bond the brick unit and the reinforcement into a structural system. The increase in the wall compression capacity due to the grout is minimal.

Another example demonstrating flexibility is a large project in Utah where a key objective was to reduce labor cost. This was done by fabricating longer units with a false joint to visually represent conventional brick coursing. The units were flipped at every other course to complete the concept, Figure 13.



Figure 13: Larger Brick with False Joint

Most owners and architects do not like to see a steel ledger angle supporting brick veneer over openings because they are often considered unsightly, and are prone to corrosion. A simple solution is reinforced brick beam, Figure 14. Using mild steel reinforcement is typical, but in extreme climates, may be prone to corrosion. In such cases, replacing the mild steel with

stainless steel is generally recommended. Since stainless steel reinforcement is generally not available and very expensive, using stainless steel all-thread is an economical alternative.



Figure 14: Reinforced Lintel Instead of a Steel Ledge

Coursing is an important aesthetic consideration and corners can provide a challenge to the design. With custom units, on larger projects, the problem can usually be solved. Here is a custom unit used to continue running bond at a corner, Figure 15.



Figure 15: Special Corner Unit

There are many more examples of design flexibility applied to reinforced brick masonry. There seems to be no limit to the creativity of designer and contractors to invent and apply new applications of the system. In recent years there has been continued development of new and exciting uses, including unique soffits, sills, cantilevers, single and double curved surfaces and many different brick patterns. Because the system is structural, it can often perform multiple functions including load-bearing enclosure walls, forms for concrete elements, backing for gunite walls and curtainwalls isolated from the building structure.

CONCLUSIONS

Structural brick masonry has many applications. Its properties are different than reinforced concrete and consequently many unique applications can evolve from applying combinations of innovative design and construction. This is nothing new. For example, a long time ago the designer of the column in Figure 16 used his talents and the flexibility of brick masonry to mimic the stone column. Incorporating reinforcement provides an additional dimension.

There are certain applications where conventional brick veneer may not be practical or efficiently constructed and as shown herein, structural brick veneer offers an alternative that maintains the attractive appeal of a true brick facade.



Figure 16: Roman Column

REFERENCES

Tobriner, 1985: Stephen Tobriner A History of Reinforced Masonry Construction Designed to Resist Earthquakes: 1755-1907, TMS Journal, Vol. 4, No. 2, The Masonry Society, Longmont, Colorado, USA

Compressive, Transverse and Racking Strength Tests of Four-Inch Brick Walls, Research Report No. 9, Structural Clay Products Research Foundation, Geneva, Illinois, USA, 1965

Tawresey, 1978: John G. Tawresey "Reinforced Brick Masonry Panels," Proceedings, ASCE Spring Convention and Exhibit, Pittsburgh, Pennsylvania USA

Building Code Requirements and Specifications for Masonry Structures, TMS 402-16, The Masonry Society, Longmont, Colorado, USA, 2016.

DETERMINATION OF MODEL PARTIAL FACTOR FOR MASONRY UNREINFORCED SHEAR WALLS BASED ON ANNEX D OF EN-1990

H. Salehi¹ and W. Jäger²

¹ PhD student, TU Dresden, Faculty of Architecture, Chair of Structural Design, Dresden, Germany,
hamidreza.salehi@tu-dresden.de

² Professor, TU Dresden, Faculty of Architecture, Chair of Structural Design, Dresden, Germany,
W.jaeger@jaeger-ingenieure.de

Experiments in structural engineering are playing an important role for prediction or characterization of the material properties or behaviour of the structural components. In order to cover all aspect in tests and using the results for design, some methods have been introduced in EN-1990 Annex D for designing based on test data. Calculation of characteristic values and design values of material resistance are the most major aspects.

In this study the recommended methods in Annex D of EN-1990 for resistance of the material will be implemented to extract the partial safety factors for masonry structures based on formulation of design and characteristic values. A database including more than 100 tests on masonry unreinforced shear walls will be used for evaluation of the results. The resistance model for shear wall based on recommendation of eurocode will be considered to be compared with the test results. The main objective will be achieved based on comparison of the model prediction and the test results. The deviation of the prediction from the test is defining the model error or model uncertainty. The test database has the test results for three types of masonry units, Clay brick, Calcium silicate and Autoclaved aerated concrete. The evaluation of partial factor for masonry shear model will be determined based on scatter and the model bias for whole database. Further analysis also will be applied for each type of masonry units for classification of the outcome.

Keywords: *Masonry, shear wall, test, partial factor, model uncertainty*

INTRODUCTION

Experimental studies and test evaluations are fundamental in structural analysis and design of structural components. A precise interpretation of the test result will lead to an acceptable level of prediction for structural behaviour. Currently the basis for most of the design codes like eurocodes are determined based on probabilistic methods and reliability analysis. Test database is one of the essential components in probabilistic methods. In probabilistic methods, engineers are dealing with a set of representative values instead of one single value for each property of structural component. These sets of values are coming from the probability distribution function for each basic variable, which are predicted by evaluation of test data. In addition to the material parameters and the geometry, the modelling of the structural behaviour has a significant influence on the safety of the design. The uncertainty coming from the model can be determined based on comparison of model and tests results. A recommended method for evaluation of the tests results with regards to the structural behaviour model is presented in Annex D of EN-1990. This method will be implemented for evaluation of the partial factor for considering the model uncertainty.

RECOMMENDATION OF EN-1990

The basic code of structural design right now in Europe is the EN-1990 (2002/2010). The basis of design process is defined in this code. The partial safety factor method as applied safety concept in the eurocode is explained in EN-1990.

The main component of partial safety factor method is limit state function. Limit state functions are represented in EN-1990 based on classification of parameters correspond to the resistance (R) and parameters for actions (E). The criteria for verification of the structure is mentioned in EN-1990 based on design values of resistance and action parameters as in equation (1).

$$E_d \leq R_d \quad (1)$$

The design values will be calculated based on recommended values of partial factors. In case of resistance the partial factors are proposed in different eurocodes for different material. In case of actions, the values of partial factors will be selected based on recommendations in EN-1990. The simplified method for representation of resistance design value in EN-1990 is mentioned in equation (2).

$$R_d = R \left\{ \eta_i \frac{X_{k,i}}{\gamma_{M,i}} ; a_d \right\} i \geq 1 \quad (2)$$

Where:

- $X_{k,i}$ is the characteristic value of the material or product property
- η_i is the mean value of the conversion factor taking into account
 - Volume and scale effects,
 - Effects of moisture and temperature, and
 - Any other relevant parameters

$\gamma_{M,i}$ is partial factor covering the uncertainty of the model (γ_{Rd}) and partial factor of material properties (γ_m), $\gamma_{M,i} = \gamma_{Rd} \times \gamma_{m,i}$
 α_d is design value of geometrical data.

In case of actions design values for different types of loading and applying correspondent partial factors the design value will be calculated.

$$E_d = E \left\{ \gamma_{G,j} G_{k,j} ; \gamma_{Q,i} Q_{k,i} ; \gamma_{Q,i} \psi_{0,i} Q_{k,i} \right\} j \geq 1; i > 1 \quad (3)$$

A statistical based method is recommended in Annex D of EN-1990 for determination of resistance model according to tests results. The main concept in this method is based on comparison of the experimental data with the prediction of the resistance model. The calculation will be done through some steps. The first step is to consider a theoretical model for the structure which is represented by basic variables(\underline{X}).

$$r_t = g_r(\underline{X}) \quad (4)$$

Then based on selected theoretical model the prediction of the resistance model will be determined. The comparison of the theoretical values and experimental values will be represented as Figure 1.

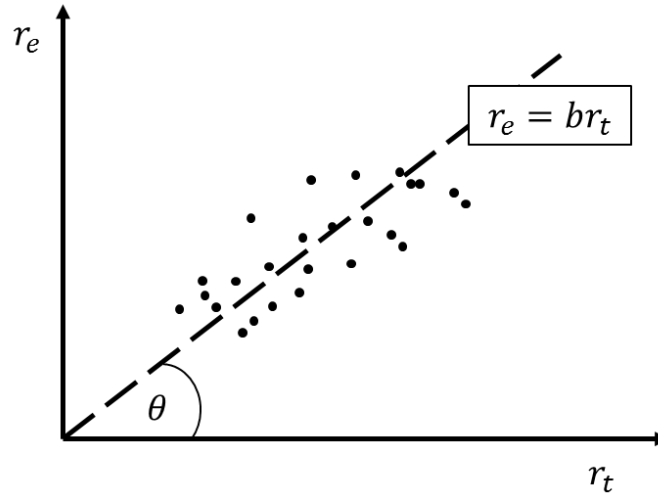


Figure 1: Experimental and theoretical diagram (EN-1990)

The perfect model will predict the resistance of the structure in a way that all the points lay on the line with $\theta = 45$. The scatter of the points from this line is showing the error or deviation of the theoretical value.

For a statistical determination a probabilistic model has to be defined according to resistance model. The probabilistic model which will be applied to the test data based on EN-1990 is represented in equation (5).

$$r = br_i \delta \quad (5)$$

Here b is the “Least Squares” best-fit to the slope. It is representing the model bias which corresponds to the parameter θ . It will be calculated based on equation (6).

$$b = \frac{\sum r_e r_i}{\sum r_i^2} \quad (6)$$

The error term of δ will be defined for each experimental observation and its ratio to the theoretical prediction, as mentioned in equation (7).

$$\delta = \frac{r_{ei}}{br_{ti}} \quad (7)$$

Based on recommendations in the Annex D of EN-1990, it is obvious that the code is considering the lognormal distribution for the error term δ . The following parameter will be defined by the logarithm of δ values. The coefficient of variation correspond to the error parameter will be calculated in accordance with this transformation. This transformation will be conducted with equation (8).

$$\Delta_i = \ln(\delta_i) \quad (8)$$

Consequently the mean and standard deviation for parameter Δ will be calculated based on equations (9) and (10).

$$\bar{\Delta} = \frac{1}{n} \sum_{i=1}^n \Delta_i \quad (9)$$

$$s_{\Delta}^2 = \frac{1}{n-1} \sum_{i=1}^n (\Delta_i - \bar{\Delta})^2 \quad (10)$$

The coefficient of variation for error in the model then will be calculated from the equation (11).

$$V_{\delta} = \sqrt{\exp(s_{\Delta}^2) - 1} \quad (11)$$

The final aim in the Annex D on EN-1990 is to determine the characteristic value or the design value of the resistance parameter. By taking the advantage of calculated design and characteristic values the partial factors can be determined. This is the main concept for this study which is mainly based on recommendations of this annex in EN-1990. The process for the calculation of the characteristic value or design value in this annex is done by considering both contributions of the uncertainty from the basic variables and the model uncertainty. The contributions of these uncertainties will be realized in the calculation process by means of the coefficient of variations for basic variables (V_{X_i}) and the coefficient of variation for model error (V_{δ}).

The calculation of the coefficient of variation for resistance model (V_r), which is in the product function form as in equation (12), will be done based on formula in equation (13).

$$r = br_i \delta = b \{X_1 \times X_2 \dots X_j\} \delta \quad (12)$$

$$V_r = (V_\delta^2 + 1) \left[\prod_{i=1}^j (V_{Xi}^2 + 1) \right] - 1 \quad (13)$$

There is an alternative expression (eq. (14)) in Annex D of EN-1990 for calculation of (V_r) in case of small values (<0.1) for V_δ^2 and V_{Xi}^2 .

$$V_r^2 = V_\delta^2 + V_n^2 \quad (14)$$

The parameter V_{rt}^2 will be calculated with equation (15) in simple production form for the resistance models and in case of more complex models the equation (16) will be implemented.

$$V_n^2 = \sum_{i=1}^j V_{Xi}^2 \quad (15)$$

$$V_n^2 = \frac{VAR[g_n(\underline{X})]}{g_n^2(\underline{X}_m)} \cong \frac{1}{g_n^2(\underline{X}_m)} \times \sum_{i=1}^j \left(\frac{\partial g_n}{\partial X_i} \sigma_i \right)^2 \quad (16)$$

In accordance with the determined coefficient of variation the characteristic value or design value has to be determined. The calculation is classified in two cases, the first one with limited test numbers ($n < 100$) and the second one with large number of tests ($n \geq 100$).

In case one, the statistical uncertainty in parameter Δ will be considered by assuming the t-distribution for this parameter with parameter n as tests number. In this case the characteristic value will be calculated by expression (17).

$$r_k = bg_n(\underline{X}_m) \exp(-k_\infty \alpha_n Q_n - k_n \alpha_\delta Q_\delta - 0.5 Q^2) \quad (17)$$

with:

$$Q_n = \sigma_{\ln(n)} = \sqrt{\ln(V_n^2 + 1)} \quad (18)$$

$$Q_\delta = \sigma_{\ln(\delta)} = \sqrt{\ln(V_\delta^2 + 1)} \quad (19)$$

$$Q = \sigma_{\ln(r)} = \sqrt{\ln(V_r^2 + 1)} \quad (20)$$

$$\alpha_n = \frac{Q_n}{Q} \quad (21)$$

$$\alpha_\delta = \frac{Q_\delta}{Q} \quad (22)$$

where

k_n is the characteristic farctile from Table 1

k_∞ is the value for k_n when $n \rightarrow \infty$ [$k_\infty = 1.64$]

$\alpha_\delta, \alpha_{rt}$ are weighting factors for Q_δ and Q_{rt} respectively.

In case of large number of tests the calculation will be done based on equation (23)

$$r_k = b g_n (X_m) \exp(-k_\infty Q - 0.5 Q^2) \quad (23)$$

Table 1: k_n for 5% fractile value

| n | 1 | 2 | 3 | 4 | 5 | 6 | 8 | 10 | 20 | 30 | ∞ |
|------------------------|----------|----------|----------|----------|----------|----------|----------|-----------|-----------|-----------|----------|
| V _x known | 2.31 | 2.01 | 1.89 | 1.83 | 1.80 | 1.77 | 1.74 | 1.72 | 1.68 | 1.67 | 1.64 |
| V _x Unknown | - | - | 3.37 | 2.63 | 2.33 | 2.18 | 2.00 | 1.76 | 1.76 | 1.73 | 1.64 |

Determination of design values will be the same with characteristic values but in the formula in (17) and (23) the values of k_n and k_∞ will be replaced by $k_{d,n}$ and $k_{d,\infty}$. These values are mentioned in Table 2.

Table 2: $k_{d,n}$ for ultimate limit state design value

| n | 1 | 2 | 3 | 4 | 5 | 6 | 8 | 10 | 20 | 30 | ∞ |
|------------------------|----------|----------|----------|----------|----------|----------|----------|-----------|-----------|-----------|----------|
| V _x known | 4.36 | 3.77 | 3.56 | 3.44 | 3.37 | 3.33 | 3.27 | 3.23 | 3.16 | 3.13 | 3.04 |
| V _x Unknown | - | - | - | 11.4 | 7.85 | 6.36 | 5.07 | 4.51 | 3.64 | 3.44 | 3.04 |

UNREINFORCED SHEAR WALL DATA BASE

The main structural components in construction with masonry materials are masonry walls. Currently applications of unreinforced wall are more common than the reinforced ones. The main requirement, which these types of structures have to provide, is to resist under the normal forces but there are also some cases which the verification of the wall under lateral load is necessary. There are different references on analysis of the shear wall behavior based on probabilistic approaches (see Brehm (2011), Glowienka (2007), Schueremans (2001), Montazerolghaem (2015)) but the evaluation of test data based on recommendation of Annex D for EN-1990 has not considered. A sufficient evaluation has been done in Montazerolghaem and Jäger (2015) for determining the probability distribution function for uncertainty in masonry shear wall models. Determination of a compatible model for the wall behavior needs experimental data. With regard to these data bases and comparison of the model prediction with test result a calibration for model can be done. Afterwards the data base of test data will be implemented in order to determine the partial factor of the model or the uncertainty which is coming from the calculation with the model.

In order to determine the model factor the experimental data from the European research program ESECMaSE (Enhanced Safety and Efficient Construction of Masonry Structures in Europe) ESECMaSE (2006) for masonry structures will be implemented. ESECMaSE is a vast experimental base program which has been conducted in 2004-2008, in collaboration with various European partners. This project is mainly considering with the shear resistance and the deformation of masonry walls made of different types of units and mortar (Montazerolghaem (2015)). The collected data base is well presented in detail in Montazerolghaem (2015) and Jäger,

Ortlepp et al. (Unpublished). The data base consists of 129 tests (full scale) including three different masonry units, 44 tests on CB (Clay Brick), 51 tests on AAC (Autoclaved Aerated Concrete) and 34 tests on CS (Calcium Silicate). The result of tests will be evaluated based on comparison with predicted values of German national Annex DIN EN-1996-1-1/ NA (2012).

The theoretical model in this study for comparison with test data is the recommended method in DIN EN-1996-1-1/ NA. As it is mentioned in Montazerolghaem (2015) and Mann and Muller (1982) there are different types of failure modes for masonry shear walls:

- Friction failure of the bed joint
- Tensile failure (cracking) of the units
- Overturning of single unit
- Flexural (bending) failure of masonry
- Shear compression failure of masonry
- Compression failure of masonry (crashing).

The national recommendation in Germany for verification of masonry walls are represented in DIN EN-1996-1-1/ NA. A specific method is proposed in DIN EN-1996-1-1/ NA-Annex K to be conducted for evaluation of the wall slenderness. The calculation of effective height of the wall will be done based on a factor ψ , which is introduced for different types of boundary conditions. The background for this factor may be found in Kranzler (2008). This factor is particularly considering the restraint ratio at top and bottom of the wall.

The parameter ψ will be applied to the height of the wall in process for slenderness calculation as it is shown in equation (24) . A general classification for ψ factor may be done according to the restraint condition of the wall, the case with fully restraint boundary condition at top and bottom of the wall with $\psi = 0.5$ and the other case as cantilever wall or no restraint at top with $\psi = 1$. A representation of the eccentricity and the wall is illustrated in Figure 2.

$$\lambda_v = \frac{\psi \cdot h_w}{l_w} \quad (24)$$

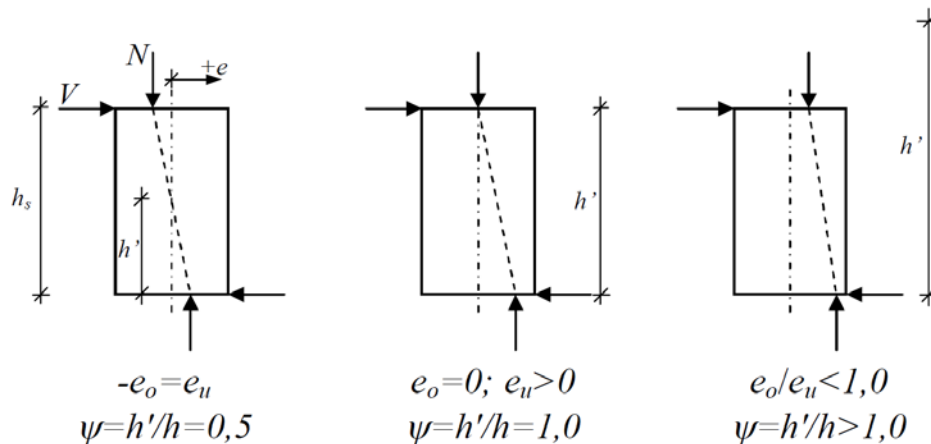


Figure 2: Wall eccentricity at top and bottom and ψ factor (Kranzler (2008))

The DIN EN-1996-1-1/ NA recommendation for determination of shear resistance in case of friction and tensile failure of the units is equation (25)

$$V_{Rdlt} = l_{cal} \cdot f_{vd} \cdot \frac{t}{c} \quad (25)$$

Where

t is the thickness of the wall

c is the shear stress distribution factor and determined as:

$$1.0 \quad \text{for} \quad \frac{h}{l} \leq 1$$

$$0.5(1 + \frac{h}{l}) \quad \text{for} \quad 1 < \frac{h}{l} < 2$$

$$1.5 \quad \text{for} \quad \frac{h}{l} \geq 2$$

l_{cal} is the compression length of the wall and it will be calculated as:

$$l_{cal} = \frac{3}{2} \cdot \left(1 - 2 \cdot \frac{V_{Ed}}{N_{Ed}} \cdot \lambda_v \right) \cdot l \leq l \quad (26)$$

V_{Ed} is the design shear force

N_{Ed} is the design normal force

l is the wall length

f_{vd} is the design value of shear strength with $f_{vd} = \frac{f_{vk}}{\gamma_M}$

γ_M is the partial factor of masonry

The characteristic values of shear strength f_{vk} shall be determined for friction and tensile failure in order to apply in equation (25). The friction characteristic strength for in-plane shear resistance, in case of head joints fill with mortar, may be considered as expression(27) and for tensile failure the equation (28) will be implemented.

$$f_{vlt1} = f_{vk0} + 0.4 \cdot \sigma_{Dd} \quad (27)$$

$$f_{vlt2} = 0.45 \cdot f_{bt,cal} \cdot \sqrt{1 + \frac{\sigma_{Dd}}{f_{bt,cal}}} \quad (28)$$

where

f_{vk0} is the characteristic initial shear strength of masonry,

σ_{Dd} is normal stress

$f_{bt,cal}$ is the computational tensile strength of unit. It may be assumed as a ratio of unit compressive strength.

The other failure mode is shear compression failure. This type of failure happens when the compressive strength in the diagonal strut is exceeded (Montazerolghaem (2015)). In the case of element masonry with thin layer mortar for bed joints and the ratio of overlapping length over unit height less than 0.4 ($l_{ol}/h_u \leq 0.4$) the expression (29) has to be considered for checking of the shear compression failure.

$$V_{Rdl} = \frac{1}{\gamma_M \cdot c} \cdot (f_k \cdot t \cdot l_c - \gamma_M \cdot N_{Ed}) \cdot \frac{l_{ol}}{h_u} \quad (29)$$

where

$$l_c = \left(1 - 2 \cdot \frac{V_{Ed}}{N_{Ed}} \cdot \lambda_v\right) \cdot l$$

l_{ol} is overlapping length

h_u is the unit height

f_k is the characteristic value of masonry compressive strength.

In masonry structures with element masonry, un-grouted head joints and the ratio of $h_u > l_u$, failure on single unit due to the opening of bed joint will be another possible failure scenario. The calculation of shear resistance for overturning of single units will be done according to equation (30) (Montazerolghaem (2015)).

$$V_{Rdl} = \frac{2}{3} \cdot \frac{1}{\gamma_M} \cdot \left(\frac{l_u}{h_u} + \frac{l_u}{h}\right) \cdot N_{Ed} \quad (30)$$

The criteria of flexural failure of the walls subjected to the vertical and horizontal loads simultaneously may be determined based on ultimate limit state of the wall in axial forces (eq. (31)).

$$N_{Ed} \leq N_{Rd} = \Phi \cdot \frac{f_k}{\gamma_M} \cdot l \cdot t \quad (31)$$

$$\Phi = 1 - 2 \cdot \frac{V_{Ed}}{N_{Ed}} \cdot \lambda_v \quad (32)$$

Here the Φ is the reduction factor for considering the slenderness and eccentricity of loadings on the wall and it will be determined based on assumption of rectangular stress block with equation (32). According to both (31) and (32) the shear resistance based on flexural failure mode may be calculated with (33).

$$V_{Rd} = \frac{l \cdot N_{Ed}}{2 \cdot h} - \frac{\gamma_M \cdot N_{Ed}^2}{2 \cdot f_k \cdot h \cdot t} \quad (33)$$

The shear resistance for each test sample in the data base will be determined based on various failure modes according to DIN EN-1996-1-1/ NA-Annex K. The comparison between theoretical prediction values from the code and the observed value from real tests data, will lead to the evaluation of uncertainty, originated from model in the design process.

In the first step of the test evaluation the whole data base will be considered as a general representation of a masonry shear wall behavior under horizontal and vertical load. The diagram of comparison between predicted values and experimental values for all test data is illustrated in Figure 3. Here the influence of the testing uncertainties, like measurement and the specimens, is not involved in the result because; this uncertainty is included in both theoretical and

experimental values. The material parameters in the theoretical values calculation are the values from testing measurements because of that the testing and specimen uncertainties involve in theoretical part too. Therefore, the calculated ratios won't be affected by testing uncertainties. The best fit for a linear function is also considered to represent the relation of experimental and theoretical data as mentioned also in Figure 1.

As it seems in the Figure 3 the fitted line to the database is expressing the overall comparison of experiment and theory. The factor 1.1361 is calculated based on equation (6) and it is representing the inclination of the line. Its value is indicating a conservative prediction strategy in the model for calculation of resistance in this case of shear wall. This is also called as a bias in the model.

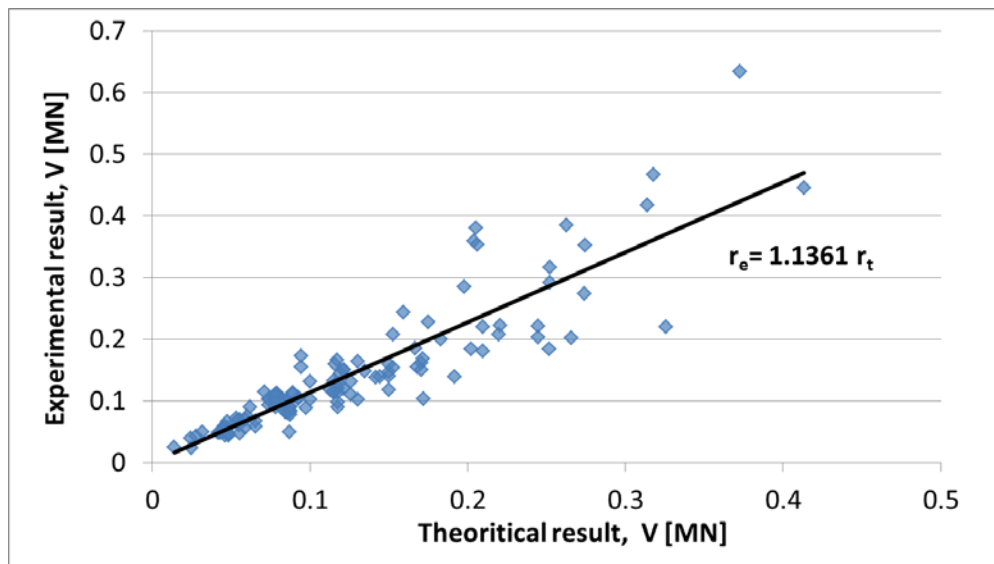


Figure 3: Experimental and theoretical values for masonry wall

In other words it means that most of the experimental data have more capacity than the prediction of theoretical model. This may be interpreted that our model underestimates the resistance of the wall and the real resistance of the wall is always more than the expected value. The other parameter which has to be considered in the model uncertainty is the scatter of the predictions from the fitted line. The representative value for this parameter is the coefficient of variation of model error V_δ which will be calculated based on equation (7)-(11). The result for determination of model error statistical parameters for all database are presented in Table 3

Table 3: Statistical parameter of model error for all database

| $\bar{\Delta}$ | s_{Δ}^2 | V_δ | b |
|----------------|----------------|------------|--------|
| -0.0162 | 0.2257 | 0.2286 | 1.1361 |

According to explanations in previous sections, in this study the aim is to determine the partial factor corresponds to the model error. Therefore in consideration of uncertainty, only the

contribution of model error will be considered. Consequently in equation (14) the term V_{rt} will be ignored, because it is related to the material uncertainty, and the term V_{δ} , coefficient of variation for model error, will be the single parameter in calculation.

Eventually considering the calculated statistical parameters in Table 3 and equation (23), design value and characteristic value of resistance will be determined. The population of experiments data-base is more than 100 and it can be considered as a large number of test data, therefore the equation (23) has been applied for calculation. Afterwards by considering bias of the model in the calculation process, the partial factor for resistance model will be calculated as in equation (34).

$$\gamma_{Rd} = \frac{R_k}{R_d} \cdot \frac{1}{b} \quad (34)$$

In the first case for the whole population of experimental data base the partial factor of model will be $\gamma_{Rd}=1.2073$.

In order to determine more compatible values of partial factor based on masonry unit types, the data base will be classified into subsets based on type of units. As it is mentioned before, test were conducted on three types of units; clay break, calcium silicate and autoclaved aerated concrete. The same procedure of statistical evaluation has been implemented for each subset of masonry unit.

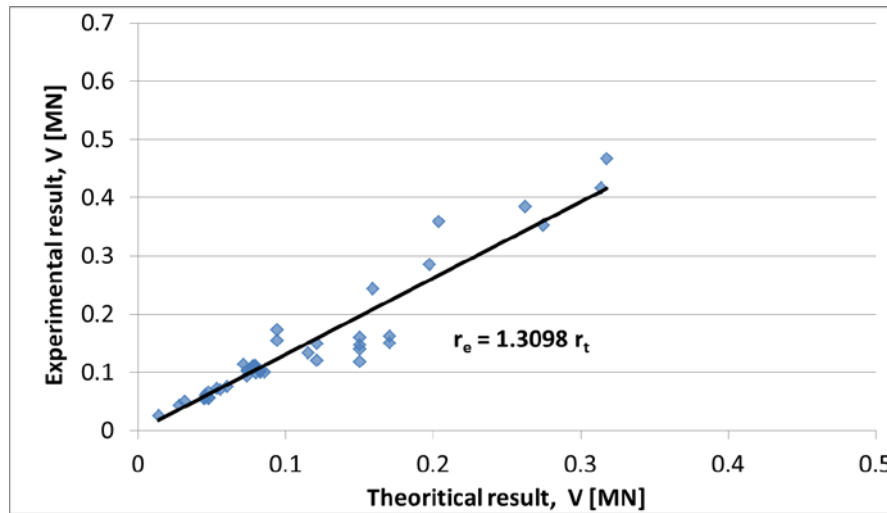


Figure 4: Experimental and theoretical values for CB

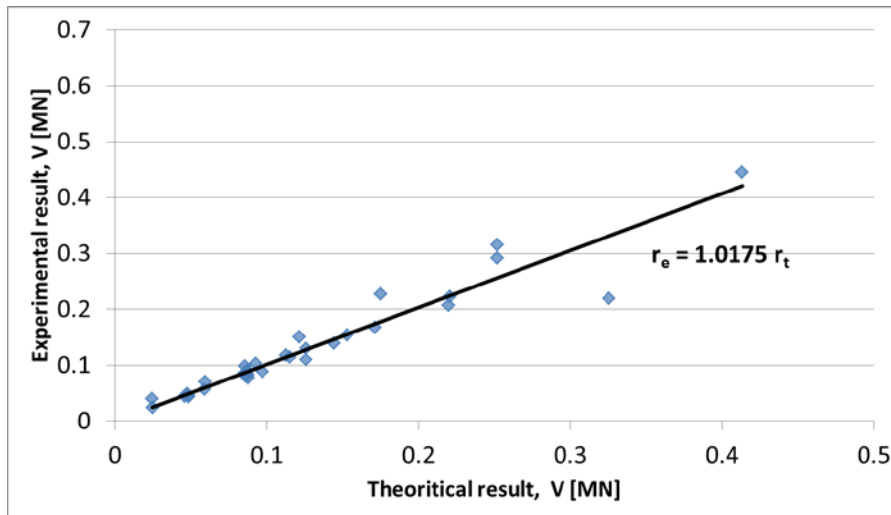


Figure 5: Experimental and theoretical values for CS

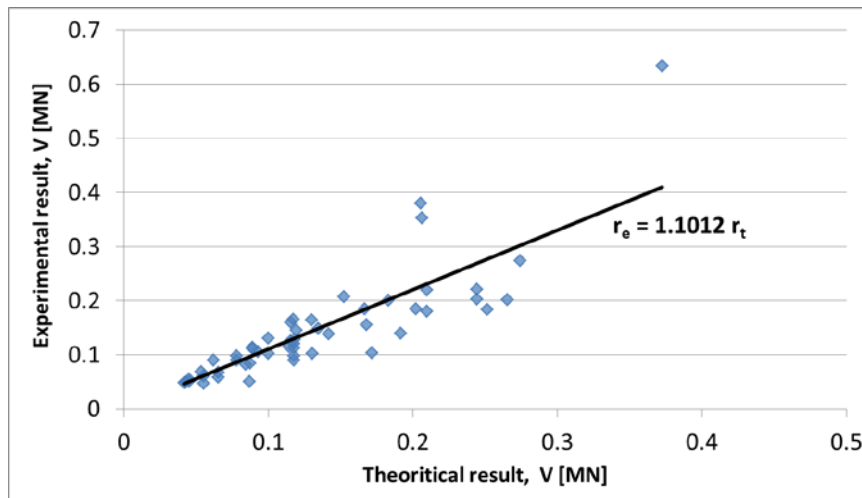


Figure 6: Experimental and theoretical values for AAC

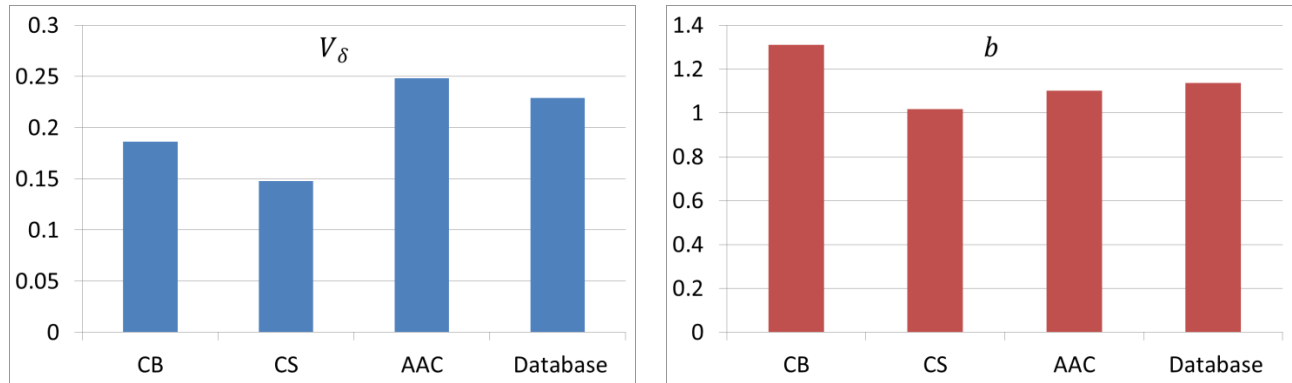
Dividing the original data base to some sub sets will reduce the number of data or population in the statistical evaluation. There is a recommendation in Annex D in EN-1990 about this problem. It is suggesting that, for determining the factor k from Table 1 or Table 2 the value of test number has to be considered as the original database. Therefore, for each subset of masonry unit the same value of k (maximum) will be considered, because the original test database has been considered as large number of test data. Figure 4-Figure 6 are illustrating the analysis of each individual unit type database. According to the analysis, the parameters for calculation of model partial factor have been determined and presented in the Table 4. As it seems the final value of partial factors for each of these unit types are different. There is also a difference between the partial factor of the whole data-base and partial factor of each unit type. The difference is occurred because of various coefficient of variation for model error and model bias.

Table 4: Statistical parameters of model error and partial factor for each unit type

| Unit type | $\bar{\Delta}$ | s_{Δ}^2 | V_{δ} | b | γ_{Rd} |
|-----------|----------------|----------------|--------------|--------|---------------|
| CB | -0.016431 | 0.1844 | 0.186 | 1.3098 | 0.99 |
| CS | 0.004090 | 0.1468 | 0.1476 | 1.0175 | 1.21 |
| AAC | -0.04769 | 0.2444 | 0.2481 | 1.1012 | 1.28 |

In order to make a better observation of the results, in Figure 7 the calculated values for coefficient of variation for model error and model bias are presented. As it seems both of these values in case of AAC are near to the values correspond to the whole database. The smallest values in both cases are from the CS units. On the other hand the maximum value for COV belongs to the AAC and the maximum of bias corresponds to the CB units.

The bias model for CS is nearly one. It means that in average point of view in the case of CS units, the resistance model of shear wall has neither overestimation nor underestimation. In other unit types and also for whole database the bias is higher and more than one, it means that the model is underestimating the material.

**Figure 7: Coefficient of variation of model error and model bias for units and database**

CONCLUSIONS

The basic of structural design in Europe for all types of structural materials is the recommendations of EN-1990. The safety concept which is implemented in this code is based on probabilistic methods and partial safety factor methods. Therefore the main component of this safety format is partial factor. In definition of partial factor for resistance part in structural design, the code is dividing the uncertainty source into two categories, the uncertainty from material properties and the uncertainty from modelling the structure behaviour. The determination of material uncertainty may be conducted through test on each single material. On the other hand the calculation of uncertainty from the model is not simply like material uncertainty. The recommendation in Annex D of EN-1990 has been implemented in this study as a practical process for determination of the model uncertainty. The representative value for model uncertainty is defined in EN-1990 as

γ_{Rd} . This value has been determined according to the experimental database for masonry shear wall and based on failure modes in German national annex DIN EN-1996-1-1/ NA –Annex K.

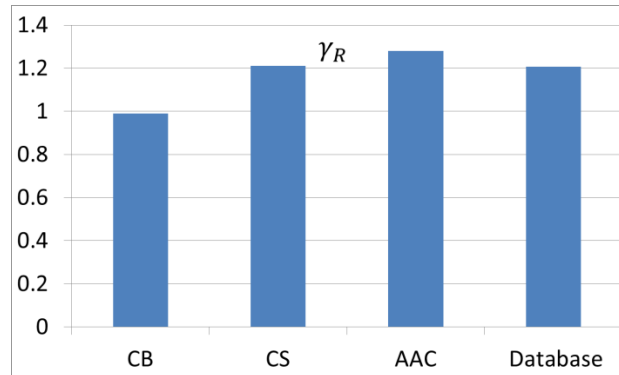


Figure 8: Model partial factor

The final calculation results of partial factors for model uncertainty, based on recommended method in Annex D of EN-1990, are represented in Figure 8. According to the results, the values for CS and AAC units are approximately the same with the value for database, but in case of CB it is nearly one. Partial factor one means that in case of CB the model of shear resistance in DIN EN-1996-1-1/ NA –Annex K works perfectly.

Eventually based on parameters which are involved in the calculation process it can be concluded that two parameters have influence on partial factor of model, bias of model and scatter of the model error. In case of scatter, the coefficient of variation will be the effective parameter in the calculation of partial factor. The higher value of COV will lead to higher value of partial factor. For bias model, the values more than one will be considered as models which are underestimating the resistance and it decreases the value of partial factor, but the bias factor less than one means that the model needs more safety therefore the partial factor will be increased.

The recommended value of partial factor for model may be applied in the calculation of shear wall based on tests on material properties.

REFERENCES

Brehm, E. (2011). Reliability of Unreinforced Masonry Bracing Walls-Probabilistic Approach and Optimized Target Values, TU Darmstadt.

DIN EN 1996-1-1/NA-Nationaler Anhang-Eurocode 6: Bemessung und Konstruktion von Mauerwerksbauten – Teil 1-1: Allgemeine Regeln für bewehrtes und unbewehrtes Mauerwerk (2012). Berlin, DIN Deutsches Institut für Normung.

EN 1990: Eurocode: Basis of structural design (EN 1990:2002 + A1:2005 + A1:2005/AC:2010) (2002/2010). Brussels, European Committee for Standardisation (CEN).

ESECMaSE (2006). Enhanced Safety and Efficient Construction of Masonry Structures in Europe. <http://www.esecmase.org>

Glowienka, S. (2007). Zuverlässigkeit von Mauerwerkswänden aus großformatigen Steinen. TU Darmstadt.

Jäger, W., et al. (Unpublished). Vergleich der normativen Ansätze zum Nachweis von Aussteifungsscheiben im Gebäude nach DIN 1053-1/-100, E-DIN 1053-13, EN 1996-1-1/NA und dem Forschungsvorhaben ESECMaSE hinsichtlich des Sicherheitsniveaus. TU Dresden.

Kranzler, T. (2008). Tragfähigkeit überwiegend horizontal beanspruchter Aussteifungsscheiben aus unbewehrtem Mauerwerk. Inst. für Massivbau TU Darmstadt.

Mann, W. and H. Muller (1982). Failure of Shear-Stressed Masonry. An Enlarged Theory, Tests and Application to Shear Walls. Proc. Br. Ceram. Soc.

Montazerolghaem, M. (2015). Analysis of Unreinforced Masonry Structures with Uncertain Data. Dresden.

Montazerolghaem, M. and W. Jäger (2015). "Characterization of uncertainty (probabilistic models) in verification of unreinforced masonry shear wall / Charakterisierung der Unschärfe (probabilistische Modelle) beim Nachweis von Wandscheiben aus unbewehrtem Mauerwerk." Mauerwerk **19**(4): 287-297.

Schueremans, L. (2001). Probabilistic evaluation of structural unreinforced masonry. Katholieke Universiteit Leuven.

ANALYSIS OF THE VERTICAL LOAD DISTRIBUTION BETWEEN THE STRUCTURAL MASONRY WALLS IN A SMALL SCALE MODEL

M.R.S. Correa¹, W.J. Silva² and J.S. Camacho³

¹ Senior collaborator, Department of Structural Engineering, University of Sao Paulo, Sao Carlos, SP, Brazil,
marcio.correa@usp.br

² Senior Lecturer, Federal Institute of Sao Paulo, Votuporanga, SP, Brazil, engewill@gmail.com

³ Professor, Civil Engineering Department, State Sao Paulo University, Ilha Solteira, SP, Brazil,
jsc@dec.feis.unesp.br

The main aim of the paper is to show the experimental analysis of the vertical load distribution in a small-scale (1:5) clay-block masonry building. The second author personally built the prototype during his PhD program. The four-storey high building was composed of RC slabs on clay block walls, supported by a steel grid settled on a strong slab by means of load cells. Preliminary tests were carried out to assess the properties of the small-scale masonry components. Then a large number of different loads were applied to the building, using water pools, varying: order of load application, level of loaded slab, loaded area on a floor, etc. Each loading scheme produced a set of load cell measurements that evaluated the stress flux along the whole structure. The results showed that the walls work in groups delimited by wall and door openings and that the simple procedure of vertical load homogenization inside each group is consistent with the finite element modelling of the building masonry structure.

Keywords: *Structural masonry, vertical load distribution, small scale model*

INTRODUCTION

The evaluation of masonry walls subjected to vertical loads is an important part of the structural analysis during building design. The interaction of walls influences the way the loads spread downward the building. Many authors, such as Stockbridge (1967), Hendry (1998), Correa and Page (2001), Correa and Ramalho (2004) and Cappuzo Neto (2005), have observed a tendency of homogenization of vertical loads. This phenomenon obviously depends on the shear capacity of the vertical interface of interconnected walls, as widely studied by Lissel et al. (2000), Camacho et al. (2001), Bosiljkov et al. (2004), Oliveira et al. (2011). In brief, the taller the building, the larger

the homogenization of the load. Recently Andolfato et al. (2014) presented a study of the vertical load distribution between the walls in a full-scale four-story concrete blockwork building. The cited authors showed some similarity between experimental and theoretical results inside some wall groups, although the simple design model, that considers uniform vertical stress in a wall group, produced divergent stress values when influenced by significant flexural slab effects.

The present paper shows the main findings of experimental work that involved a series of measurements on a small-scale (1:5) four-storey high masonry building prototype, composed of RC slabs on clay block walls, supported by a steel grid that was settled on a strong slab by means of load cells. Different load cases were applied to the building, measuring the corresponding vertical strains in the load cells. The vertical forces in the load cells were then compared to the ones estimated by different vertical loads applied to the steel grid. The vertical load distribution was developed considering three different procedures: walls without interaction (isolated walls), homogenization inside interconnected walls delimited by door and window openings (group of walls) and linear elastic finite element modelling (FEM).

CHARACTERIZATION OF THE MATERIALS

A special small scale (1:5) clay block was developed by a local producer to be used in the present research. Figure 1 shows natural and fifth-scale blocks. Note the similarity of the cross sections, despite the difficulty of dealing with small dimensions. The whole family of blocks, including half and U-units were manufactured using the same clay of the natural scale ones.

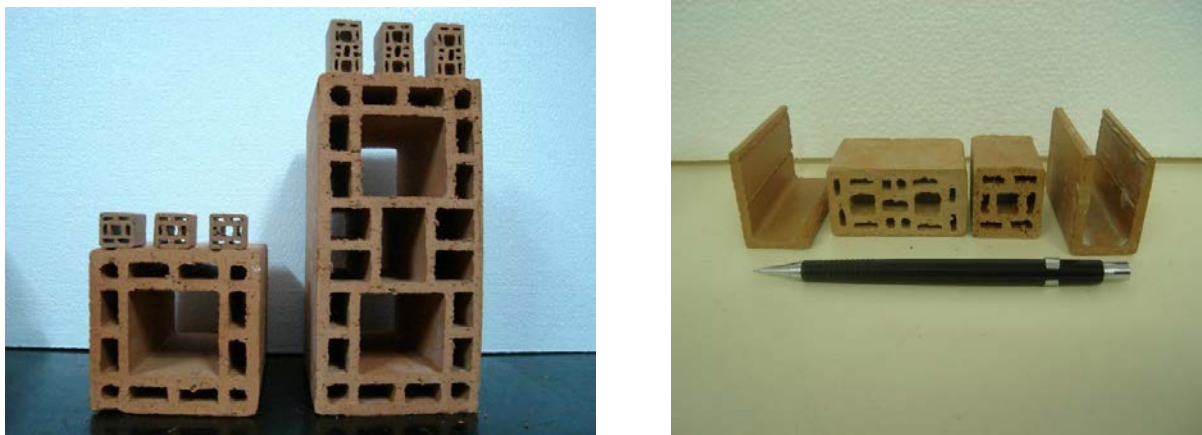


Figure 1: Clay blocks – natural (1:1) and small-scale (1:5)

Table 1 shows basic average properties of the small-scale blocks, determined by a series of tests carried out according to ABNT NBR 15270-3:2005 and ABNT NBR 15812-2:2010.

The same mortar was used throughout the whole experimental program, with a volume proportion of 1:0.5:4.5 (cement:lime:sand) and a water/cement ratio (w/c) of 1.50. Sand was ground in a mill to maintain 0.6mm as the limit for the grain size, which is adequate for thin head and bed joints. Grout was used to fill lintels, bond beams and build slabs. In the first case, the mass proportion was

1:2.48:2.52 (cement:sand:gravel) with a water/cement ratio of 1.02. In the second case, the mass proportion was 1:1.2:1.8 with a w/c of 0.55. Compressive tests were carried out with mortar and grout specimens. Table 2 summarizes the obtained results of the compressive strength.

Table 1: Properties of the small-scale blocks

| Property | Mean values | C.O.V. |
|--|-----------------------|--------------------|
| Dimensions (mm) | 28.09 x 39.47 x 58.07 | 0.3% x 2.0% x 0.3% |
| Gross area (mm ²) | 1631 | - |
| Net area (mm ²) | 1011 | 2.8% |
| Ratio net/gross area | 62% | - |
| Water absorption | 12.59% | 2.5% |
| I.R.A. (g/19355mm ² /min) | 24.14 | 11.9% |
| Compressive strength in gross area (MPa) | 18.10 | 31.5% |
| Young modulus (GPa) | 10.03 | 35.8% |

Table 2: Compressive strength of mortar and grout

| Material | Mean values (MPa) | C.O.V. |
|-----------------------------|-------------------|--------|
| Mortar 1:0.5:4.5 | 4.98 | 15.0% |
| Grout 1:2.48:2.52 (masonry) | 12.98 | 17.7% |
| Grout 1:1.2:1.8 (slab) | 27.48 | 25.8% |

Different specimens were used to estimate the compressive strength of masonry: prisms of two (P2B) and three blocks (P3B), prisms of six blocks (P6B), wallets of five (W5C) and twelve courses (W12C). Some of them are depicted in Figure 2. Auxiliary steel frames were produced to help maintain the dimensions and plumb of the small specimens. Tests on P2B, P3B and W12C resulted in high COVs. In the case of W12C, due to the number of specimens being only two. Because of this, the results for P6B and W5 were considered the most meaningful. Table 3 shows compressive strength and Young modulus for the P6B and W5C.

Table 3: Compressive strength and Young modulus of masonry

| Specimen | Property | Mean values | C.O.V. |
|----------|----------------------------|-------------|--------|
| P6B | Compressive strength (MPa) | 4.91 | 28.2% |
| P6B | Young modulus (GPa) | 2.46 | 41.6% |
| W5C | Compressive strength (MPa) | 6.38 | 10.1% |
| W5C | Young modulus (GPa) | 3.95 | 43.5% |

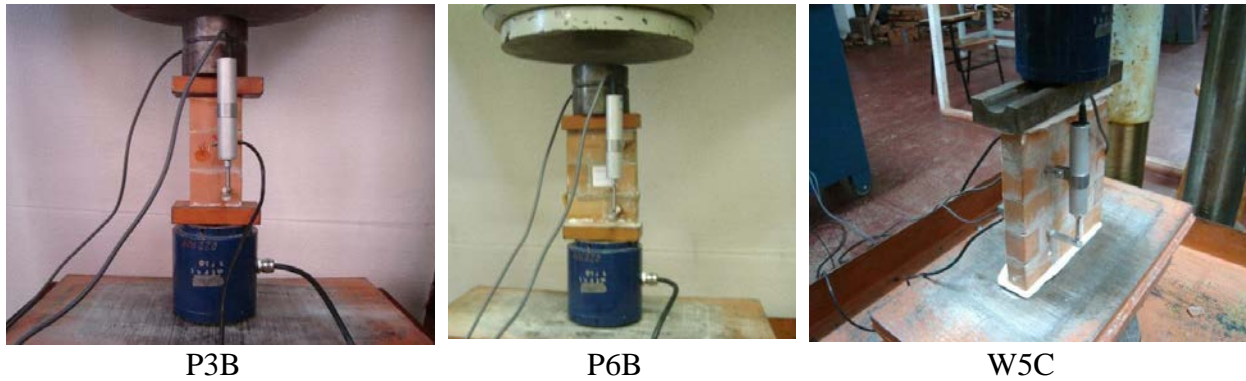


Figure 2: Different specimens for estimating the compressive strength

THE SMALL-SCALE PROTOTYPE

The fifth scale model was inspired by the full-scale building analysed by Andolfato et al. (2014), keeping nearly one fourth of the floor. Figure 3 presents a plain view of the typical floor of the prototype. The building had 4 stories, with a distance of 569 mm (13 courses) between two consecutive floors. Lintel beams were located just beneath the 43.8mm thick slabs. There was no full moment connection between slab and walls. Lintels were disposed at door and window openings. At the top of the building, 6 extra courses were built on the façades. In brief, 62 courses were developed, using 10,742 units. The prototype was personally built by the second author of this paper, taking 8 months. Figure 4 shows a photograph of the building protected by awnings to reduce the thermal influences on the strain measurements. The masonry construction was settled on a grid (box 80mm x 80mm of SAE 1010 steel), supported by 12 load cells (aluminium alloy). The load cells were laid on a 120mm thick slab that corresponds to 600 mm in full scale. All the load cells were previously calibrated, assessing their spring constants. All the electric wires from the cells were connected to the adjacent laboratory, inside PVC tubes. Metallic pools were located inside three rooms of each floor to apply loading by water filling.

THE EXPERIMENTAL PROGRAM

The experimental program consisted of different load schemes, varying loaded rooms and floors. Preliminary assessments were developed to guarantee that the maximum theoretical stress in the walls, in the case of the most loaded scheme, including self-weight of the building, was smaller than 20% of the compressive strength of masonry (see Table 3). This was consistent with the service conditions and guaranteed the meaningfulness of linear-elastic analysis. In the case of the minimum load, instruments were checked to verify sensitivity. Table 4 summarizes the applied loads on each room and floor. Loads were applied progressively and cumulatively in the building. Initially they were applied on each room, from level 1 to 3. Table 5 summarizes the loading schemes and their identification. Secondly, the focus was on each floor, applying loads on all the rooms of a floor, from level 1 to 3. The loading schemes were identified by L1, L2 and L3, respectively. Tests were carried out in days without wind and in periods as short as possible to disregard temperature changes. At the beginning of each test, instruments were zeroed.

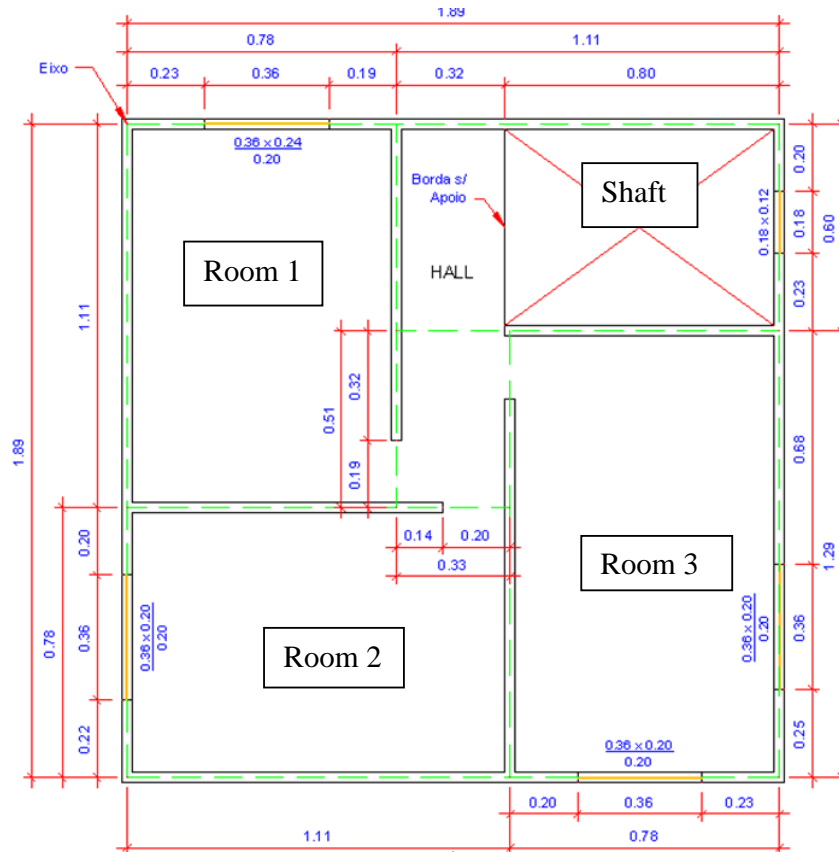


Figure 3: Typical floor of the small-scale (1:5) building – Dimensions in m.

Table 4: Applied loads on the floors

| Floor | Room | Area (m ²) | Load (kN) | Average dist. load (kN/m ²) |
|---------|--------|------------------------|-----------|---|
| Typical | Room 1 | 0.810 | 1.05 | 1.30 |
| | Room 2 | 0.810 | 1.05 | |
| | Room 3 | 0.945 | 1.23 | |

Table 5: Loading schemes by room

| Scheme | Loaded area | Loaded level (identification) | | |
|--------|-------------|-------------------------------|----------|----------|
| 1 | Room 1 | 1 (R1L1) | 2 (R1L2) | 3 (R1L3) |
| 2 | Room 2 | 2 (R2L1) | 2 (R2L2) | 3 (R2L3) |
| 3 | Room 3 | 3 (R3L1) | 2 (R3L2) | 3 (R3L3) |

Table 6 shows a set of results of reactions in the load cells due to loading on room 1. Note the number of the load cells on the left hand side of the table. The vertical loads on the cells are presented in percentage of the total load applied to the prototype. Negative values signify compression and positive ones mean tension. Tables 7 and 8 show similar results for loads applied on rooms 2 and 3, respectively.

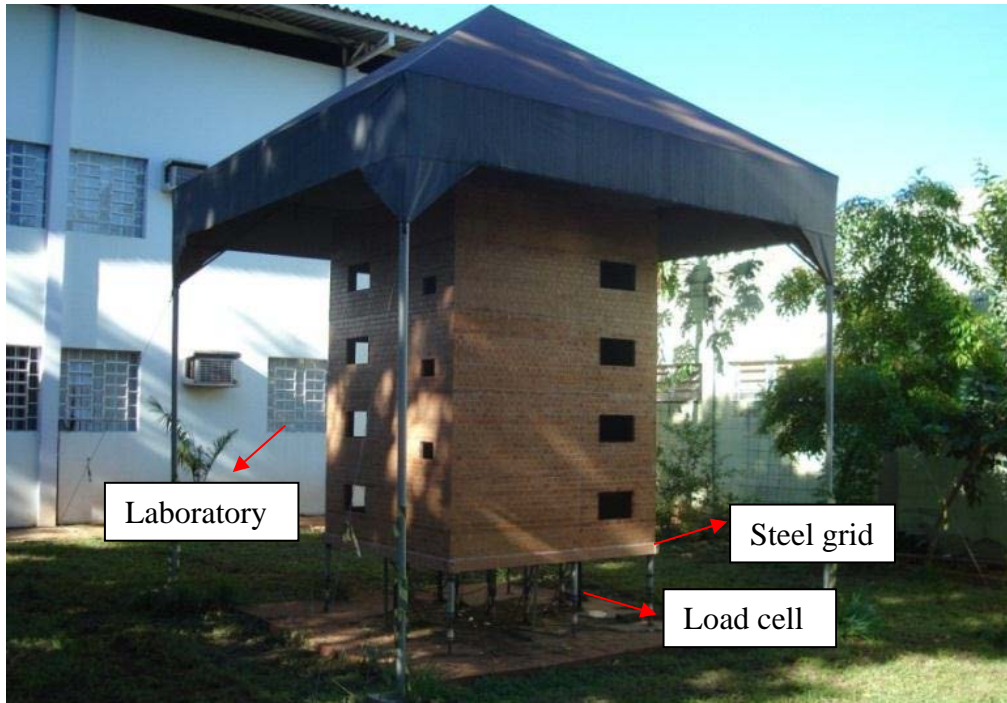


Figure 4: The small-scale building.

Table 6: Results for loading on room 1

| Load Cells | ROOM 1 | | | | Average (%) |
|------------|----------|----------|----------|--|-------------|
| | R1L1 (%) | R1L2 (%) | R1L3 (%) | | |
| 1 | -10.85 | -8.23 | -8.35 | | -9.14 |
| 2 | -22.30 | -22.99 | -21.23 | | -22.17 |
| 3 | -0.84 | -1.51 | -2.56 | | -1.64 |
| 4 | -14.25 | -13.51 | -12.76 | | -13.51 |
| 5 | -8.99 | -8.78 | -9.24 | | -9.00 |
| 6 | +0.83 | +1.48 | +0.72 | | +1.01 |
| 7 | -22.16 | -21.65 | -22.08 | | -21.96 |
| 8 | -7.25 | -6.11 | -5.94 | | -6.43 |
| 9 | -2.90 | -2.23 | -2.52 | | -2.55 |
| 10 | -2.50 | -3.36 | -3.63 | | -3.16 |
| 11 | +0.42 | +1.49 | +1.81 | | +1.24 |
| 12 | +6.73 | +8.68 | +9.15 | | +8.18 |

Table 9 presents reactions for loads applied on all rooms. In a general sense, it is apparent that walls work together. Even in the case of only one loaded room (see Tables 6, 7 and 8), loads spread to load cells far from that room. See, for instance, points 2, 3, 4, 5 and 6 in Table 7. Moreover, this is not only related to the supporting steel grid but to the entire structural system, including the walls

themselves, as indicated by increments of compression in points 4 and 5. Note also that the larger increments do not vary significantly around the mean value. See, for instance, point 7 in Table 6. The C.O.V. of the increments is 1%, which shows that the most important part of the distribution of loads is already done at a distance of two adjacent floors. This is consistent with the findings of Correa and Page (2001), regarding the vertical distance necessary to homogenize the compressive stresses for interconnected walls.

Table 7: Results for loading on room 2

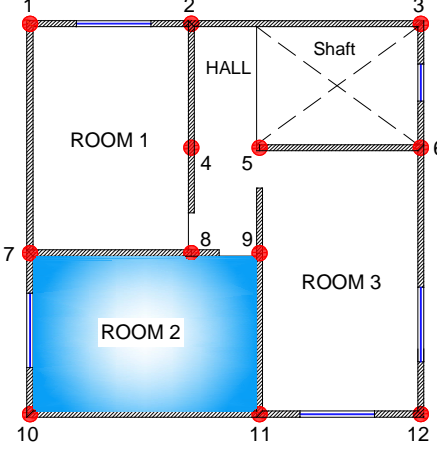
|  | Load Cells | R2L1 (%) | R2L2 (%) | R2L3 (%) | Average (%) |
|---|------------|----------|----------|----------|-------------|
| | 1 | +1.98 | -0.94 | -1.79 | -0.25 |
| | 2 | +0.50 | +0.47 | +0.45 | +0.47 |
| | 3 | +2.50 | +2.97 | +5.86 | +3.78 |
| | 4 | -5.98 | -6.59 | -7.19 | -6.59 |
| | 5 | -4.37 | -5.50 | -5.26 | -5.04 |
| | 6 | +1.96 | -0.46 | -0.00 | +0.50 |
| | 7 | -22.50 | -23.04 | -21.16 | -22.23 |
| | 8 | -12.67 | -9.56 | -9.14 | -10.46 |
| | 9 | -5.91 | -6.04 | -5.77 | -5.91 |
| | 10 | -20.30 | -18.69 | -19.65 | -19.55 |
| | 11 | -15.84 | -20.56 | -19.21 | -18.54 |
| | 12 | -5.50 | -5.19 | -4.51 | -5.07 |

Table 8: Results for loading on room 3

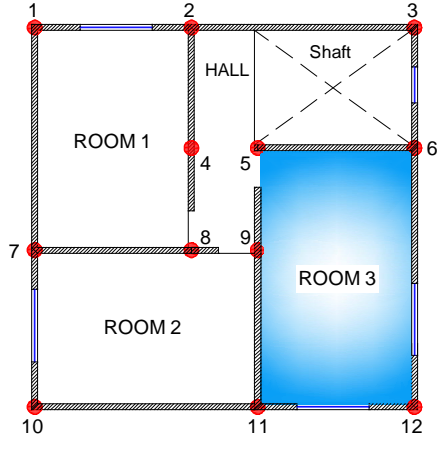
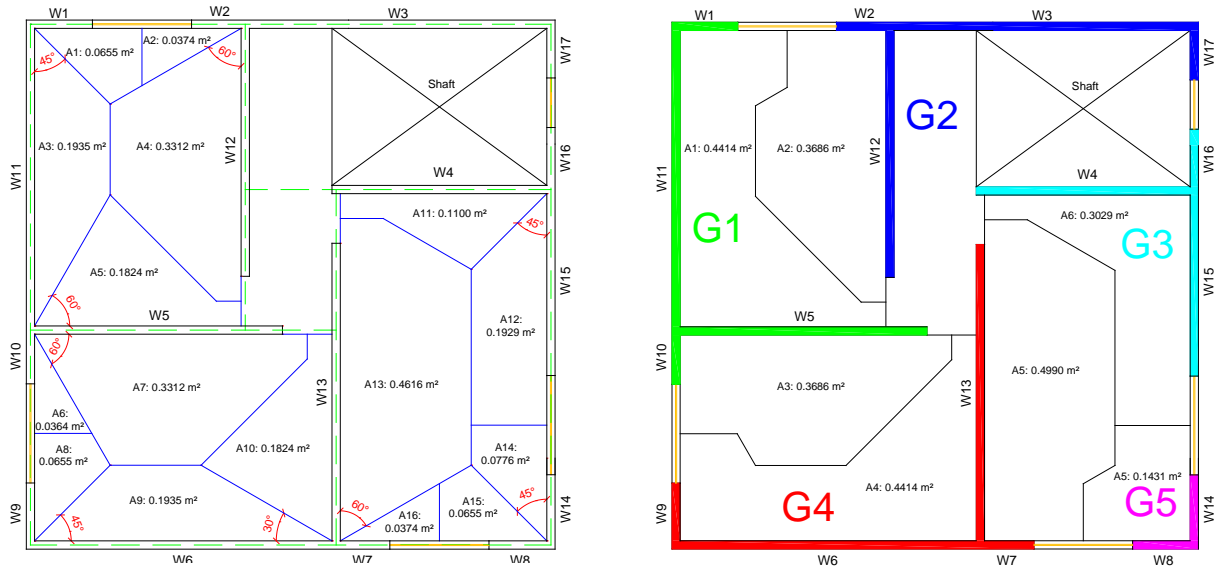
|  | Load Cells | R3L1 (%) | R3L2 (%) | R3L3 (%) | Average (%) |
|---|------------|----------|----------|----------|-------------|
| | 1 | +4.72 | +1.43 | +0.35 | +2.17 |
| | 2 | +1.58 | +3.25 | +3.16 | +2.66 |
| | 3 | -9.90 | -8.66 | -10.17 | -9.58 |
| | 4 | -2.76 | -2.52 | -2.45 | -2.58 |
| | 5 | -12.31 | -11.22 | -10.56 | -11.36 |
| | 6 | -14.01 | -13.83 | -14.82 | -14.22 |
| | 7 | -2.28 | +4.84 | +3.36 | +1.97 |
| | 8 | -5.22 | -5.49 | -5.33 | -5.35 |
| | 9 | -7.80 | -7.82 | -7.94 | -7.85 |
| | 10 | -1.18 | -2.56 | -3.13 | -2.39 |
| | 11 | -19.62 | -18.59 | -19.80 | -19.34 |
| | 12 | -18.62 | -19.49 | -18.94 | -19.02 |

Table 9: Results for loading on all rooms of each floor

| Load Cells | L1 (%) | L2 (%) | L3 (%) | Average (%) |
|------------|--------|--------|--------|-------------|
| 1 | -0.67 | -1.12 | -0.94 | -0.91 |
| 2 | -9.17 | -7.87 | -6.66 | -7.90 |
| 3 | -2.21 | -2.41 | -3.49 | -2.70 |
| 4 | -9.13 | -9.44 | -8.84 | -9.14 |
| 5 | -10.06 | -11.39 | -10.77 | -10.74 |
| 6 | -5.34 | -5.53 | -6.54 | -5.80 |
| 7 | -15.28 | -15.08 | -16.09 | -15.48 |
| 8 | -8.26 | -9.28 | -8.67 | -8.74 |
| 9 | -6.85 | -6.80 | -7.02 | -6.89 |
| 10 | -8.91 | -9.07 | -9.73 | -9.24 |
| 11 | -16.14 | -16.07 | -16.48 | -16.23 |
| 12 | -7.98 | -5.94 | -4.75 | -6.22 |

ANALYTICAL MODELS

Initially, two simple analytical procedures were used to estimate the distribution of loads by the walls of the prototype: isolated walls (IW) and group of walls (GW). In both cases, the loads applied by the slabs were assessed using tributary areas, as illustrated in Figure 5. IW disregards the interaction of walls. GW considers the interaction of interconnected walls, and each group is delimited by door and window openings. The estimated loads at the base of the walls were applied to a steel 3D frame, consisting of horizontal and vertical bars with the characteristics of the steel grid and the load cells, respectively.



Isolated walls

Group of walls

Figure 5: Walls and tributary areas.

Secondly, a finite element model (FE) was elaborated, taking quadrilateral shell elements for representing slabs and walls and 3D frame elements to simulate the steel grid and the load cells. Figure 6 illustrates the FE mesh. The analysis was linear-elastic, using SAP2000® V15. Mesh dimensions were equivalent to a half block and half course in the horizontal and vertical directions, respectively.

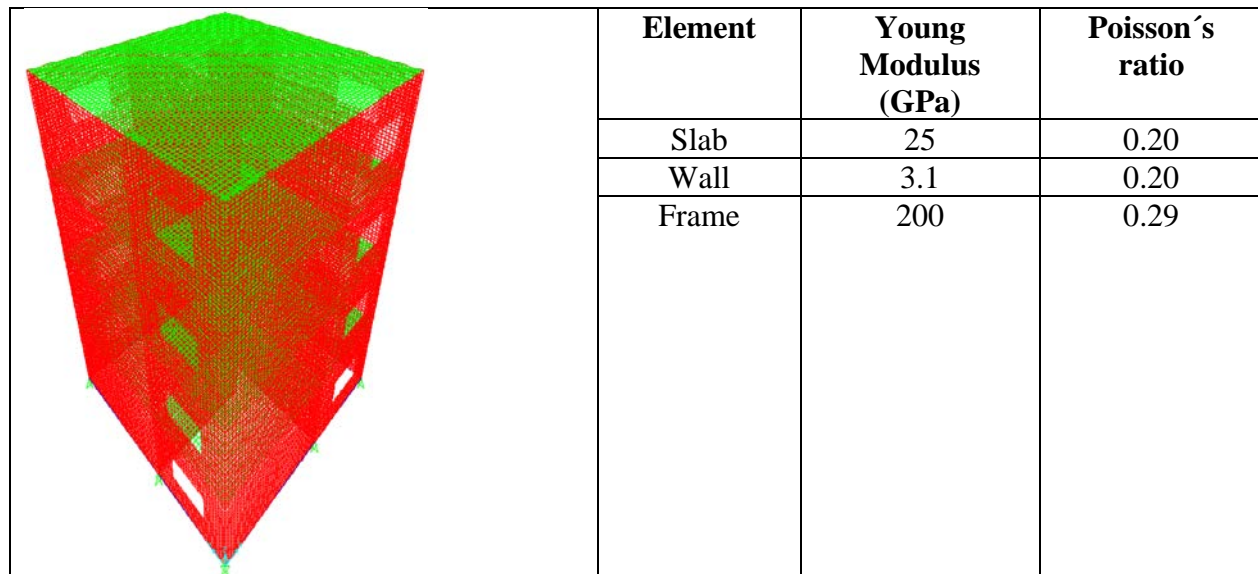


Figure 6: Finite element model

All the experimental load cases were simulated, using the adopted analytical models. The following section will show the comparison of vertical reactions in the load cells, to evaluate the most representative models and to corroborate the idea of the wall group behaviour.

RESULTS AND COMPARISONS

The next tables show theoretical and experimental values of the reactions, as a percentage of the total applied load as aforementioned. Only the results corresponding to the average of the three loaded levels in each case are shown, to avoid presenting a large amount of data. More details can be found in Silva (2014). Tables 10, 11, 12 and 13 correspond to loading on room 1, room 2, room 3 and all rooms, respectively. Note that results related to the analytical models IW, GW, FE are presented beside the experimental ones (EX). Two types of ratios are assessed, one to compare analytical to experimental results, and the other to compare the analytical results of IW and RW to the FE ones. A negative ratio signifies that the reaction changes direction. The average ratio indicates the quality of the approximation; the closer to 1, the better. The comparisons of the analytical models show, in brief, that GW is closer to FE than IW. Note in Table 13 that in the case of loads applied on all rooms, which is what happens in practice, $GW/FE = 1.02$ while $IW/FE = 0.80$. The meaningfulness of GW, compared to IW is higher when loads are applied on one single room (see Tables 10, 11 and 12). In a very simple way, GW represents the interaction of walls as the FE model inherently does.

Table 10: Average theoretical and experimental results for loading on room 1

| Load cells | EXP | IW | GW | FE | IW/EXP | GW/EXP | FE/EXP | IW/EF | GW/FE |
|------------|--------|--------|--------|--------|--------|--------|--------|-------|-------|
| 1 | -9.14 | -14.94 | -11.99 | -17.24 | 1.63 | 1.31 | 1.89 | 0.87 | 0.70 |
| 2 | -22.17 | -14.13 | -19.81 | -19.14 | 0.64 | 0.89 | 0.86 | 0.74 | 1.04 |
| 3 | -1.64 | 0.44 | -10.84 | -1.86 | -0.27 | 6.62 | 1.14 | -0.24 | 5.82 |
| 4 | -13.51 | -25.94 | -11.38 | -18.10 | 1.92 | 0.84 | 1.34 | 1.43 | 0.63 |
| 5 | -9.00 | 0.30 | -1.52 | -1.09 | -0.03 | 0.17 | 0.12 | -0.28 | 1.40 |
| 6 | 1.01 | -0.27 | -0.17 | 1.24 | -0.27 | -0.17 | 1.23 | -0.22 | -0.14 |
| 7 | -21.96 | -21.85 | -25.20 | -23.27 | 0.99 | 1.15 | 1.06 | 0.94 | 1.08 |
| 8 | -6.43 | -15.57 | -14.08 | -11.25 | 2.42 | 2.19 | 1.75 | 1.38 | 1.25 |
| 9 | -2.55 | 4.08 | 2.70 | -0.50 | -1.60 | -1.06 | 0.20 | -8.16 | -5.40 |
| 10 | -3.16 | 2.15 | 1.92 | -3.56 | -0.68 | -0.61 | 1.13 | -0.60 | -0.54 |
| 11 | 1.24 | -0.30 | -0.29 | 0.57 | -0.24 | -0.23 | 0.46 | -0.52 | -0.51 |
| 12 | 8.19 | 0.04 | 0.10 | 2.19 | 0.00 | 0.01 | 0.27 | 0.02 | 0.05 |
| Average | | | | | 0.38 | 0.93 | 0.95 | -0.39 | 0.45 |

Table 11: Average theoretical and experimental results for loading on room 2

| Load cells | EXP | IW | GW | FE | IW/EXP | GW/EXP | FE/EXP | IW/FE | GW/FE |
|------------|--------|--------|--------|--------|--------|--------|--------|-------|-------|
| 1 | -0.25 | 0.53 | -11.66 | -2.06 | -2.12 | 46.64 | 8.24 | -0.26 | 5.66 |
| 2 | 0.47 | -0.48 | -0.28 | 1.27 | -1.01 | -0.59 | 2.68 | -0.38 | -0.22 |
| 3 | 3.78 | 0.07 | 0.18 | 2.86 | 0.02 | 0.05 | 0.76 | 0.02 | 0.06 |
| 4 | -6.59 | 0.05 | -1.26 | -1.07 | -0.01 | 0.19 | 0.16 | -0.05 | 1.18 |
| 5 | -5.04 | 2.66 | 0.39 | -1.02 | -0.53 | -0.08 | 0.20 | -2.62 | -0.38 |
| 6 | 0.50 | -0.35 | -0.30 | 0.38 | -0.70 | -0.60 | 0.75 | -0.93 | -0.80 |
| 7 | -22.23 | -16.02 | -22.35 | -21.58 | 0.72 | 1.01 | 0.97 | 0.74 | 1.04 |
| 8 | -10.46 | -27.55 | -13.79 | -16.76 | 2.63 | 1.32 | 1.60 | 1.64 | 0.82 |
| 9 | -5.91 | -6.38 | -11.75 | -9.34 | 1.08 | 1.99 | 1.58 | 0.68 | 1.26 |
| 10 | -19.55 | -17.33 | -11.51 | -17.04 | 0.89 | 0.59 | 0.87 | 1.02 | 0.68 |
| 11 | -18.54 | -25.86 | -24.67 | -23.23 | 1.40 | 1.33 | 1.25 | 1.11 | 1.06 |
| 12 | -5.07 | 2.73 | 1.87 | -3.39 | -0.54 | -0.37 | 0.67 | -0.81 | -0.55 |
| Average | | | | | 0.15 | 4.29 | 1.65 | 0.02 | 0.82 |

Concerning the correlation to the experimental values, it is apparent that the FE results are generally closer to the experimental ones, compared to the theoretical results obtained with IW and GW. It is worth noting that when loads are applied to only one room (see Tables 10, 11 and 12), IW produces a larger number of different orientation of reactions on load cells compared to experimental values: 47% for IW, 33% for GW and only 6% for FE. Considering the mean value of the average ratios (theoretical/experimental) in all cases as a rough measure of the quality of the analytical model, it is easy to choose FE as the best one (see Table 14). Note that the low value of the IW/EXP ratio indicates alternation of the vertical reaction orientation. In a practical design, if the use of Finite Elements is not yet feasible because of the amount of data preparation and

interpretation, GW seems to be a suitable choice as a simple analytical procedure. The GW procedure can also be improved, as shown by Silva (2014).

Table 12: Average theoretical and experimental results for loading on room 3

| Load cells | EXP | IW | GW | FE | IW/EXP | GW/EXP | FE/EXP | IW/FE | GW/FE |
|------------|--------|--------|--------|--------|--------|--------|--------|-------|-------|
| 1 | 2.17 | 0.05 | 0.16 | 2.55 | 0.02 | 0.07 | 1.18 | 0.02 | 0.06 |
| 2 | 2.66 | -0.35 | -0.34 | 0.57 | -0.13 | -0.13 | 0.22 | -0.61 | -0.59 |
| 3 | -9.58 | 3.97 | 2.26 | -4.52 | -0.41 | -0.24 | 0.47 | -0.88 | -0.50 |
| 4 | -2.58 | 2.67 | 2.89 | 0.51 | -1.04 | -1.12 | -0.20 | 5.27 | 5.70 |
| 5 | -11.36 | -6.97 | -9.49 | -8.68 | 0.61 | 0.84 | 0.76 | 0.80 | 1.09 |
| 6 | -14.22 | -23.50 | -22.22 | -23.01 | 1.65 | 1.56 | 1.62 | 1.02 | 0.97 |
| 7 | 1.97 | -0.37 | -0.41 | 1.07 | -0.19 | -0.21 | 0.54 | -0.34 | -0.38 |
| 8 | -5.35 | -0.19 | -1.41 | 0.62 | 0.04 | 0.26 | -0.12 | -0.31 | -2.29 |
| 9 | -7.85 | -30.68 | -14.07 | -18.83 | 3.91 | 1.79 | 2.40 | 1.63 | 0.75 |
| 10 | -2.29 | 0.51 | -11.82 | -2.44 | -0.22 | 5.16 | 1.07 | -0.21 | 4.84 |
| 11 | -19.34 | -16.46 | -23.07 | -20.21 | 0.85 | 1.19 | 1.05 | 0.81 | 1.14 |
| 12 | -19.02 | -14.28 | -11.86 | -15.10 | 0.75 | 0.62 | 0.79 | 0.95 | 0.79 |
| Average | | | | | 0.49 | 0.82 | 0.82 | 0.68 | 0.96 |

Table 13: Average theoretical and experimental results for loading on all rooms

| Load cells | EXP | IW | GW | FE | IW/EXP | GW/EXP | FE/EXP | IW/FE | GW/FE |
|------------|--------|--------|--------|--------|--------|--------|--------|-------|-------|
| 1 | -0.91 | -4.90 | -8.12 | -5.50 | 5.38 | 8.92 | 6.04 | 0.89 | 1.48 |
| 2 | -7.90 | -5.16 | -7.26 | -6.04 | 0.65 | 0.92 | 0.76 | 0.85 | 1.20 |
| 3 | -2.70 | 1.77 | -2.60 | -1.82 | -0.65 | 0.96 | 0.67 | -0.97 | 1.43 |
| 4 | -9.14 | -7.79 | -3.24 | -6.28 | 0.85 | 0.35 | 0.69 | 1.24 | 0.52 |
| 5 | -10.74 | -1.71 | -4.36 | -4.39 | 0.16 | 0.41 | 0.41 | 0.39 | 0.99 |
| 6 | -5.80 | -9.66 | -8.07 | -8.96 | 1.66 | 1.39 | 1.54 | 1.08 | 0.90 |
| 7 | -15.48 | -13.72 | -16.64 | -15.15 | 0.89 | 1.07 | 0.98 | 0.91 | 1.10 |
| 8 | -8.74 | -15.57 | -10.24 | -9.76 | 1.78 | 1.17 | 1.12 | 1.59 | 1.05 |
| 9 | -6.89 | -13.28 | -8.92 | -10.60 | 1.93 | 1.29 | 1.54 | 1.25 | 0.84 |
| 10 | -9.24 | -5.48 | -8.15 | -8.43 | 0.59 | 0.88 | 0.91 | 0.65 | 0.97 |
| 11 | -16.23 | -16.25 | -18.07 | -16.45 | 1.00 | 1.11 | 1.01 | 0.99 | 1.10 |
| 12 | -6.22 | -4.71 | -4.34 | -6.62 | 0.76 | 0.70 | 1.06 | 0.71 | 0.66 |
| Average | | | | | 1.25 | 1.60 | 1.40 | 0.80 | 1.02 |

Table 14: Test Results

| Parameter | IW/EX | GW/EX | FE/EX |
|--|-------|-------|-------|
| Mean value of the average ratios (all cases) | 0.65 | 1.74 | 1.17 |

CONCLUSION

Using a small scale building with different load cases and comparisons of experimental and theoretical vertical reactions can draw the following conclusions. Considering the theoretical procedures, GW results are closer to FE ones than IW outputs. Comparing analytical and experimental values, it is apparent that the FE is the best procedure to represent the distribution of loads between the masonry walls. When there is a lack of FE modelling, the GW procedure, despite its simplicity, can be used to distribute vertical loads. GW represents the interaction of walls, an important feature of the phenomenon, shown by the experimental program.

REFERENCES

- Andolfato, R.P., Ramalho, M.A., Correa, M.R.S., Haach, V.G. Study of Vertical Load Distribution in Full-Scale Four-Story Masonry Building. *ACI Structural Journal*, v. 111, p. 685-692, 2014.
- Associação Brasileira de Normas Técnicas. Ceramic components Part 3: Structural and non-structural ceramic blocks – Test methods - NBR 15270-3, Rio de Janeiro, 2005.
- Associação Brasileira de Normas Técnicas. Structural Masonry – Clay Blocks Part 2: Execution and site quality control. - NBR 15812-2, Rio de Janeiro, 2010.
- Bosiljkov, V., Page, A. W., Simundic, M. S. G., & Zarnic, Roko (2010). “Shear capacity of the Flange-Web Intersections of Brick Masonry Nonrectangular Sections”, *J. Struct. Eng.*, V. 136, N. 5, May, pp. 574–585.
- Camacho, J. S., Ramalho, M. A.; and Andolfato, R. P. (2001), An Experimental Study of the Interaction among Walls Submitted to Vertical Loads. *Proceedings of the 6th Australasian Masonry Conference*, V. 1, pp. 95-104, Adelaide, Australia.
- Capuzzo Neto, V. (2005). The interaction of clay blockwork masonry walls under vertical loads, PhD Thesis, University of São Paulo, São Carlos, 322p. (in Portuguese)
- Corrêa, M. R. S; Page, A. W. (2001). The interaction of load-bearing masonry walls subjected to vertical loads: Research Report N° 218.12.2001 Callaghan: The University of Newcastle, 61p.
- Corrêa, M.R.S; Ramalho, M.A. (2004). A Simple FE Based Model for Evaluating the Interaction of Load Bearing Walls Subjected to Vertical Loading. *Const. & Building Materials*, v.18, p.77-89.
- Hendry, A.W. (1998). “Structural Masonry”, MacMillan Press LTDA, London, UK.
- Lissel, S.L.; Shrive, N.G.; Page, A.W. (2000). Shear in plain, bed joint reinforced, and post-tensioned masonry, *Canadian Journal of Civil Engineering*, 27 (5), 1021-1030.
- Oliveira, L.M.F; Corrêa, M.R.S.; Ramalho, M.A. (2011). A simplified method to approximate shear stresses at vertical interfaces of interconnected masonry walls. *Proceedings of the 9th Australasian Masonry Conference*, Queenstown, New Zealand, 10pp.
- Silva, W.J. (2014). Experimental and numerical analysis of the vertical loads distribution between masonry walls using a reduced physical model in a 1:5 scale, PhD Thesis, University of São Paulo, São Carlos, 331p.

Stockbridge, J. G. (1967). A study of High-Rise load bearing brickwork in Britain. PhD Thesis, University of Edinburgh, Edinburgh.

AS3700 MASONRY STRUCTURES CODE - A 2018 UPDATE

A.W. Page¹

¹ Emeritus Professor in Civil Engineering, School of Engineering, The University of Newcastle, Callaghan, NSW 2308, Australia, Adrian.Page@newcastle.edu.au

The Australian masonry structures code AS3700-2011 was first produced in 1988 when the previous brickwork and blockwork codes were merged and converted to limit states format. Since that time the standard has been reviewed and updated on a regular basis to reflect progressive advances in the state of knowledge and the development of new techniques and practices. A substantial review of AS3700-2011 has just been completed, and subject to the relevant approval processes, will be compliant with the 2019 edition of the National Construction Code (NCC). As well as various editorial amendments, the new document reflects the outcomes of recent research, particularly in areas related to the compressive behaviour of grouted masonry and reinforced masonry (with substantial increases in capacity); the design of stack bonded masonry; and clarification of the durability provisions for embedded items such as ties, fitments and lintels. This paper provides an overview of the changes to the document and the research background to the revised provisions.

Keywords: *Codes; design; compression; reinforced masonry; stack bonding*

INTRODUCTION

In the 1970s, separate codes for clay brickwork and concrete masonry were developed in Australia to replace the use of overseas standards. In 1988, these separate standards were combined, and extensively revised, to produce the first unified Australian masonry structures code. Masonry design in Australia is therefore covered by this single standard, AS 3700 'Masonry Structures' (Standards Australia, 2011). In the ensuing years the document has been regularly reviewed and revised to reflect advances in research and the state of knowledge (1998, 2001, 2011 and now 2017). Throughout the development and various revisions of AS3700, up-to-date research was taken into account and to facilitate compliance with the National Construction Code (NCC) published by the Australian Building Codes Board (ABCB, 2016), emphasis was also placed on clearly stating the 'high level performance' requirements. For the convenience of users who might prefer simple rules for the design of masonry in small structures,

a complementary standard (AS4773, Part 1 and Part 2) was also produced in 2010 (Standards Australia, 2010).

A substantial review of AS3700-2011 has just been completed, and, subject to the relevant approval processes, will be compliant with the 2019 edition of the National Construction Code (NCC). As well as various editorial amendments, the new document reflects the outcomes of recent research, particularly in areas related to the compressive behaviour of grouted masonry and reinforced masonry (with substantial increases in capacity resulting). Specific provisions for stack bonded masonry and clarification of the durability provisions for embedded items such as ties, fitments and lintels have also been included. This paper provides an overview of the changes to the document as well as the research background to the revised provisions.

The principal revisions in the current review of AS 3700 relate to:

- *Grouted masonry compressive strength,*
- *Compressive strength of reinforced hollow masonry,*
- *Reinforced masonry subjected to concentrated loads,*
- *Stack bonded masonry,*
- *Control joint and wall tie detailing – clarification of some minor inconsistencies between AS 3700 and AS 4773,*
- *Durability of embedded items,*
- *Capacity reduction factors,*
- *Editorial changes to comply with the ABCB Protocol requirements and for consistency with AS 4773-2015.*

COMPRESSIVE BEHAVIOUR OF UNREINFORCED AND REINFORCED GROUTED HOLLOW MASONRY

Recent comprehensive research at the Queensland University of Technology (QUT) into the performance of grouted hollow masonry (Dhanasekar et al., 2017a, b & c) revealed shortcomings in the previous design provisions which resulted in the significant under-prediction of the capacity of both unreinforced and reinforced grouted hollow masonry. The compression tests at QUT on plain and reinforced 200mm grouted hollow masonry involved a large number of units, prisms and 600 mm wide walls, with the detailed study of failure mechanisms, the reinforcement contribution and the effectiveness of the lateral restraint of the compression steel.

A range of variables were considered:

- *Six grout strengths (20 MPa to 50 MPa)*
- *Three wall heights (800; 1400 and 2400 mm)*
- *Concentric and eccentric compression (eccentricities of zero, $t/6$ and $t/3$)*
- *Reinforcement steel strains and percentages*

- *Lateral restraint of reinforcement in the cells of hollow units.*

After the consideration of a comprehensive report to the BD/4 Committee on the QUT research (Dhanasekar 2017) as well as other material, the following revisions were incorporated:

Compressive Strength of Unreinforced Grouted Hollow Masonry

When grouted hollow masonry is loaded in compression, as the load is increased, failure progressively occurs due to grout cracking and the spalling of the outer shells of the hollow masonry units (see Figure 1). The compressive capacity of the combined section is therefore not simply the sum of the compressive capacities of the hollow masonry and grout core and the existing provisions reflected this effect (Scrivener et al.,1988).



Figure 1: Failure of Grouted Hollow Masonry (Dhanasekar, 2017)

The recent QUT research has shown that the contribution of the grout to the compressive strength is more significant than previously thought and the current provisions underestimate the compression capacity by a large margin. The revised strength equation, which still reflects the failure mechanism, is more appropriate. The current AS3700 requirement of limiting the grout strength to 1.3 x the unit strength was also found to be unwarranted. As for the previous provision, the new expression for the basic compressive capacity (F_0) of grouted hollow masonry contains separate terms for the masonry and grout contribution:

$$F_0 \leq \phi \left[f'_m A_b + k_c \left(\frac{f'_{cg}}{1.3} \right)^{0.55+0.005f'_{cg}} A_g \right] \quad (1)$$

Where: ϕ - capacity reduction factor,
 f'_m - characteristic strength of the masonry,
 A_b - the bedded area of the cross-section,
 k_c - strength factor for grout in compression (1.4 or 1.2 depending on unit density),
 f'_{cg} - design characteristic compressive strength of the grout,
 A_g - cross-sectional area of grout.

Note that the characteristic grout compressive strength must be greater than or equal to 12 MPa, and the upper limit on grout compressive strength has been removed.

Contribution of Unrestrained Vertical Reinforcement to the Compressive Strength of Reinforced Grouted Hollow Masonry

Close-spaced or wide-spaced reinforcement in reinforced and grouted hollow masonry walls is usually located in the centre of the cell of the hollow units to obtain the appropriate degree of cover for durability purposes. Under the current AS3700 compression provisions, for the reinforcement to be considered as contributing to the compressive strength, it must be laterally restrained in both horizontal directions to prevent premature compression buckling (See Figure 2). This is obviously not feasible in a single skin grouted hollow masonry wall, and as a consequence the current AS3700 provisions require that this reinforcement be considered to only contribute to the bending resistance.

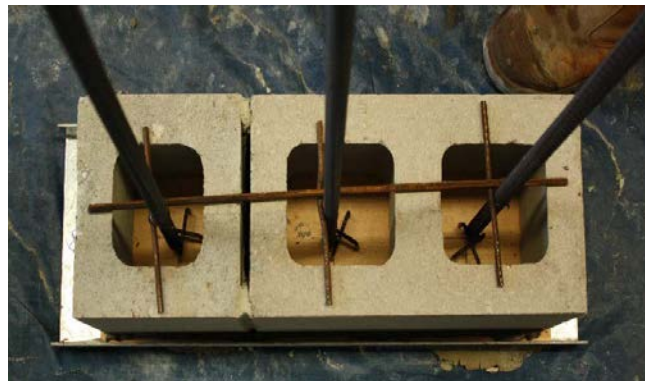


Figure 2: Lateral Restraint of Vertical Compression Steel (Dhansekar, 2017)

The recent QUT research has shown that considerable lateral restraint is provided to the steel by the grout annulus surrounding the vertical reinforcement and the unrestrained vertical steel makes a significant contribution to the compressive capacity. The revised provisions now reflect this fact with a corresponding significant increase in the compressive capacity for wide-spaced and close-spaced reinforced hollow masonry walls. To ensure that an effective grout annulus is obtained around the steel, the revised AS3700 provisions require that the thickness of the annulus around the bar be not less than twice the bar diameter.

Compressive Strength of Reinforced Masonry

The design expression for the compressive capacity of reinforced masonry has been amended in the AS3700 revision to reflect the increased understanding of masonry compressive behaviour from the effects described above. The revised design provisions resulted from a range of full scale tests (see Figure 3), together with the detailed analysis of the results covering a wide range of variables affecting the compressive capacity. This results in a significant increase in the compressive capacity.



Construction & Instrumentation



**Strain Gauged
Reinforcement**



Concentric & Eccentric Loading for 1.4m High Walls

Figure 3: Full Scale Reinforced Masonry Wall Tests (Dhanasekar, 2017)

$$F_d \leq \phi k_{es} \left[f'_m A_b + k_c \left(\frac{f'_{cg}}{1.3} \right)^{0.55+0.005f'_c} A_g + \alpha_r f_{sy} A_s \right] \quad (2)$$

Where: k_{es} - a reduction factor to account for the eccentricity in loading and slenderness of the member in the design of the reinforced masonry, taken as $(1.0 - 0.025S_r)(1.0 - 2.0 e_t)$

S_r - slenderness ratio,
 e - effective eccentricity,
 α_r - reinforcing contribution factor (1.00 for piers, 0.40 for walls),
 f_{sy} - design yield strength of reinforcement,
 A_s - the total cross sectional area of the main reinforcement.

Revised Capacity Reduction Factors

In the revised version of AS3700, several capacity reduction factors have been adjusted to reflect the outcomes of the recent hollow masonry research. The capacity reduction factor for unreinforced grouted masonry has been increased from 0.50 to 0.60, and since hollow masonry with unrestrained vertical steel is now classed as “reinforced” for compression, its capacity reduction factor is now that for reinforced masonry (0.75). (Note that for this latter increase to apply, the steel location and dimensions of the grout annulus around the bar must comply with the code requirements).

The revised Table 4.1 from AS3700 is reproduced below as Table 1.

Table 1: Capacity Reduction Factors (Standards Australia, 2017 Draft)

| Type of masonry or accessory and action effect | Capacity reduction factor (ϕ) |
|--|--------------------------------------|
| (a) Unreinforced masonry: | |
| (i) Compression | |
| (A) Solid or cored | 0.75 |
| (B) Hollow | 0.50 |
| (C) Grouted | 0.60 |
| (ii) Flexure | 0.60 |
| (iii) Shear | 0.60 |
| (iv) Other actions | 0.60 |
| (b) Reinforced and prestressed masonry | 0.75 |
| (c) Wall ties, connectors and accessories: | |
| (i) Wall ties in tension or compression | 0.95 |
| (ii) Connectors across a joint in masonry | 0.75 |
| (iii) Accessories and other actions | 0.75 |

CONCENTRATED LOADS ON REINFORCED MASONRY

When a concentrated load is applied to a masonry wall, in many cases there is significant strength enhancement in the area immediately beneath the load from the restraining effects of the surrounding material. This increase in capacity was already reflected in the unreinforced masonry provisions of earlier versions of AS3700 (Page & Hendry, 1988), but no guidance was provided for reinforced masonry. Similar provisions have now been included for reinforced masonry in the revised edition of AS3700. The strength enhancement beneath the applied load will apply to fully grouted reinforced masonry (when the behaviour will be similar to that for solid masonry), but for masonry which is not fully grouted, no enhancement is permitted.

STACK BONDED MASONRY

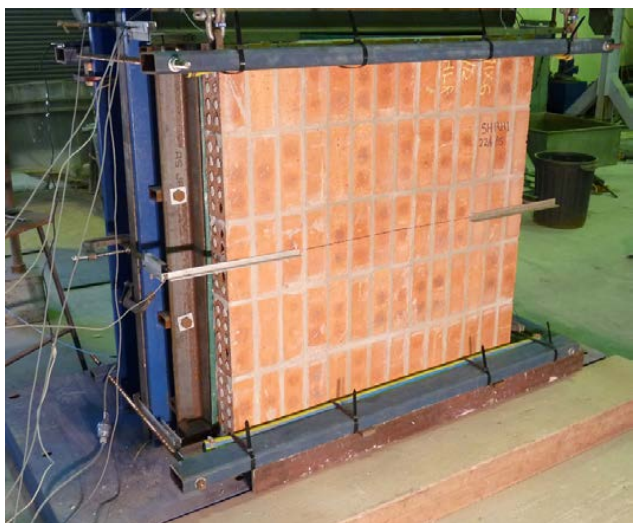
Stack bonded masonry is a form of construction in which the masonry units in adjacent courses are aligned vertically above one another. This bonding pattern leads to continuous vertical joints running the full height of the wall resulting in a weak form of construction particularly when subjected to lateral out-of-plane loading. The use of stack bonded masonry in Australia is not encouraged and consequently, in previous editions of AS3700, no specific design provisions were included. However, architects and other designers are increasingly incorporating stack bonded masonry in their designs either as a veneer or a structural element for architectural effect, taking advantage of the wider range of plain and glazed special bricks. In these cases, specific structural design requirements are needed. Some typical recent examples are shown in Figure 4.

As a result of its increased use, researchers at The University of Newcastle embarked on a comprehensive study of the performance of stack bonded masonry under lateral loading, with the bed joints either plain or reinforced. Panels in both stack bond and running bond were first subjected to lateral loading via an air bag system with top and bottom supports. This was followed by a series of tests with all four edges supported to study potential panel action (see Figure 5).

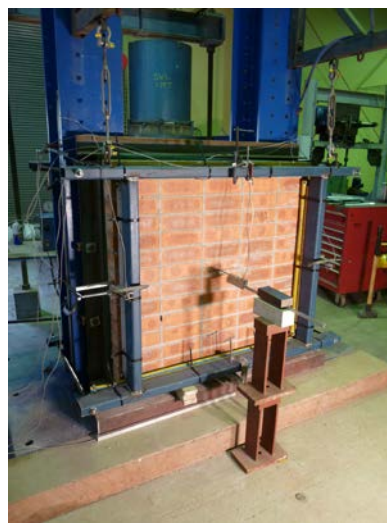


Figure 4: Typical Australian Stack Bonded Masonry Construction

The research at The University of Newcastle has established that, provided the correct design and construction procedures are followed, stack bonding can be used provided it is accompanied by appropriate bed joint reinforcement (Masia et al., 2014; 2015, 2016). The research and design procedures were also confirmed by benchmarking with similar provisions in the United States and Canadian codes (The Masonry Society, 2013; Canadian Standards Association 2014).



One-way bending test- specimen
(Rotated 90° to simulate horizontal bending)



Two-way bending test

Figure 5: Typical stack bonding lateral tests

The new design provisions can be summarised as follows:

- *the bed joint reinforcement must be properly anchored and of the appropriate durability class with an area not less than 0.00035 times the gross area of the wall.*
- *the reinforcement must be continuous between lateral supports and spaced vertically at centres not exceeding six times the thickness of the stack bonded leaf.*
- *the reinforcement must have an overall diameter or thickness not less than 3 mm and not greater than two-thirds of the thickness of the mortar joint.*
- *the masonry is designed as reinforced for horizontal bending and unreinforced for compression, shear and vertical bending.*

DURABILITY OF EMBEDDED ITEMS

Wall ties, connectors and accessories and lintels used in masonry construction must have the ability to maintain their function for the life of the structure without deterioration from corrosion. To ensure that this occurs, AS3700 provides a comprehensive table (Table 5.1) which relates exposure environment to the required durability class for the item in question. The corrosivity of the atmospheric environment has a direct influence on the exposure environment and hence the durability performance. In the revised standard, additional information has therefore been provided on this aspect in the form of an informative appendix (Appendix I) to assist designers in the selection of the appropriate durability class and the specific requirements for obtaining the required level of corrosion resistance. The appendix defines the six ISO 9223 Atmospheric Corrosivity Categories (from C1 for very low corrosivity, through to CX for extreme corrosivity) based on the corrosion rates of metals and relates these categories to conditions in Australia and the AS3700 durability classes (see Figure 6). Appendix I also contains tables for durability

solutions for material or protective coating specification for wall ties, connectors and accessories and lintels.

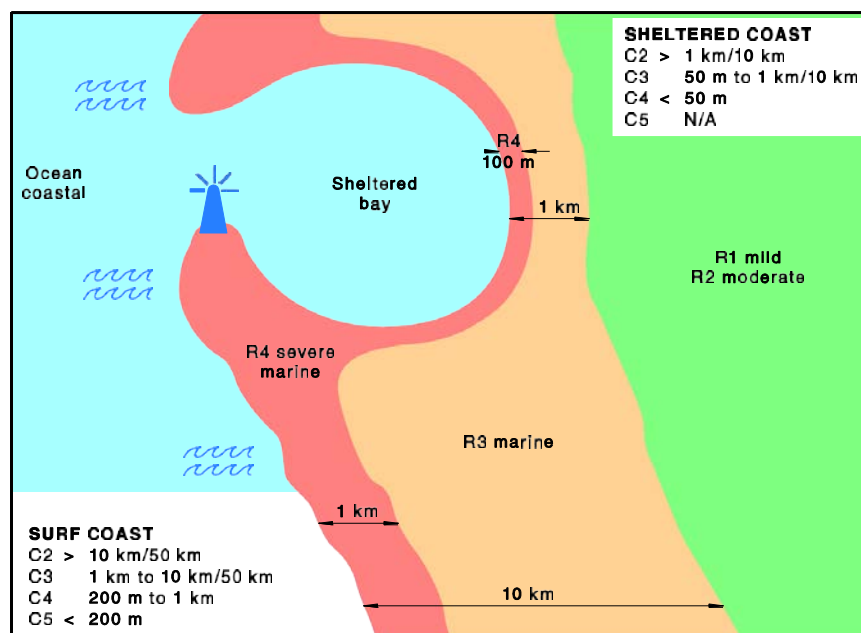


Figure 6: Simplified Corrosivity Category Locations in Australia
(C = corrosivity category; R = corrosion resistance rating)

SUMMARY

The Australian masonry structures code AS3700-2011 was first produced in 1988 when the previous brickwork and blockwork codes were merged and converted to limit states format. Since that time the standard has been reviewed and updated on a regular basis to reflect progressive advances in the state of knowledge and the development of new techniques and practices. A substantial review of AS3700-2011 has just been completed, and subject to the relevant approval processes, will be compliant with the 2019 edition of the National Construction Code (NCC). As well as various editorial amendments, the new document reflects the outcomes of recent research, particularly in areas related to the compressive behaviour of grouted masonry and reinforced masonry (with substantial increases in capacity); the design of stack bonded masonry; concentrated loads on reinforced masonry and clarification of the durability provisions for embedded items such as ties, fixings and lintels.

ACKNOWLEDGEMENTS

As Chair of Committee BD/4 Masonry Structures, the author would like to acknowledge the contributions of all members of the Committee in producing the revised edition of AS3700.

REFERENCES

AS3700-2011 Masonry Structures, (2011), Standards Australia Ltd., Sydney, Australia.

AS4773, Masonry in Small Buildings, Part 1- Design; Part 2 – Construction, (2015), Standards Australia Ltd., Sydney, Australia.

CSA S304-14, (2014), Design of Masonry Structures, Canadian Standards Association, Ontario, Canada.

Dhanasekar M., Ring J., Song M., (2017), Effectiveness of Vertical Steel Reinforcing Bars to Reinforced Concrete Masonry Walls Under Compression, Concrete 2017, Adelaide.

Dhanasekar M., Song M., Ring J., (2017), Response of Reinforced Concrete Masonry Walls to Eccentric Compression, Proc. 13th Canadian Masonry Symposium, Halifax, Canada.

Dhanasekar M., (2017), “A Proposal to Revise Clause 8.5 of AS3700 (2011)”, report submitted to the Masonry Structures BD/4 Committee., QUT School of Civil Engineering and Built Environment, 2 February, 2017 (66 p.).

International Standards Organisation , (1992), Corrosion of metals and alloys- Corrosivity of atmospheres – Classifications, ISO 9223-1992.

Masia M.J., Simundic G., Page A.W., (2014), The Flexural Strength of Stack Bonded Masonry, Stage 1 – a Preliminary Study, Proc. 9th International Masonry Conference, Guimaraes, Portugal, July.

Masia M.J., Simundic G., Page A.W., (2015), The Flexural Strength of Stack Bonded Masonry – an On-going Study, Proc. 12th North American Masonry Conf., Denver, Colorado, May, Paper 0057.

M.J. Masia, G. Simundic and A.W. Page, (2016), Flexural strength of stack bonded masonry in one way horizontal bending: influence of bed joint reinforcement, 16th International Brick and Block Masonry Conference, Padua, Italy, June.

NCC 2016, Vols.1 & 2, (2016), Australian Building Codes Board, Canberra.

Page A.W. & Hendry A.W., (1988), Design Rules for Solid Masonry Subjected to Concentrated Loads, The Structural Engineer, London, Vol 66, No 17/6, September, pp 272–281.

Scrivener, J. C. and Baker, L. R. (1988), Factors influencing grouted masonry prisms compressive strength, Proc. 8th Int. Block and Brick Masonry, 874- 883

TMS402-13/ACI 530-13/ASCE 5-13, (2013), Building Code Requirements and Specification for Masonry Structures, The Masonry Society, Colorado, USA.



**MASONRY TODAY
AND TOMORROW**

**11 - 14 February, 2018
SYDNEY AUSTRALIA**

www.10amc.com

SHOCK TABLE TEST ON MASONRY BUILDINGS STRENGTHENED USING WELDED WIRE MESH AND MICRO CONCRETE

Sachin B. Kadam¹, Yogendra Singh² and Bing Li³

¹ Assistant Professor, Department of Applied Mechanics Walchand College of Engineering, Sangli, Maharashtra 416415, India, sachin.kadam@walchandsangli.ac.in

² Professor and Head, Department of Earthquake Engineering, Indian Institute of Technology Roorkee, Uttarakhand 247667, India, yogendra.eq@gmail.com

³ Director, Natural Hazard Research Centre, Nanyang Technological University Singapore 639798, Singapore, cbli@ntu.edu.sg

Use of Ferro-cement (Welded Wire Mesh in cement concrete/mortar) ‘splints’ and ‘bandages’ is a common method of retrofitting unreinforced masonry (URM) buildings in India. Indian code IS:13935-2009 provides pre-computed amount of reinforcement to be provided in the splints and bandages in URM buildings located in different seismic zones. However, adequacy of this technique is not comprehensively studied so far. In the present study, behaviour of a half-scale burnt clay brick unreinforced masonry building and another similar building but retrofitted using carried out on ‘Shock Table’ test facility available at Department of Earthquake Engineering, Indian Institute of Technology Roorkee. In this facility, an impact is applied at the base of the specimen. The Shock Table motions are impulse type of motion with the characteristics of shorter duration, higher base acceleration and higher frequency content, as compared to actual ground motion.

The pattern of cracking, identification of weaker zones, and modes of failure with increasing intensity of shaking, have been presented and conclusions are drawn with respect to effectiveness of the used strengthening technique. Equivalent frame models (EFM) of the tested buildings have been developed in SAP2000 Nonlinear software and the numerical results are compared with the experimental results. The results suggest that the lateral load resistance of the retrofitted building increases considerably, as compared to the URM buildings. The EFMs are able to predict the peak displacement, quite reasonably but fail to predict the response waveform.

Keywords: *Unreinforced brick masonry; Shock Table Test; Wire-mesh, Retrofit; Equivalent Frame Model*



INTRODUCTION

The adequacy of a retrofitting method can be fully tested either during a real earthquake, or by full scale model testing on a shake-table, simulating the expected ground motion. Non-availability of full/large scale shake-table testing facilities, at many places, necessitates the use of scaled models and simplified testing procedures. These scaled models have been successfully used to compare the dynamic behaviour of URM and strengthened models (Paulson et al. 1991; Nikolic-Brzev and Arya 1996; Tomazevic et al. 2009; Ersubasi and Korkmaz 2010; Sathiparan et al. 2012; Mendes et al. 2014). In India these scale models have been successfully tested on shock-table facility (Arya 1984; Qamaruddin et al. 1984; Qamaruddin et al. 1986; Agarwal and Thakkar 2001; Jagdish et al. 2002). In the present study, two models of half scale brick masonry, one without any strengthening and the other with strengthening using Ferrocement in splints and bandages, have been tested and results are compared with the analytical simulation using macro-modeling approach named “Equivalent Frame Method”. The models have been tested for a series of shocks of gradually increasing intensity on Shock-Table facility available at the Department of Earthquake Engineering, IIT Roorkee. Agarwal (1999), Masood (2006), and Dubey (2011) have shown that the shock-table motions are basically impulse type of motion with the characteristics of small duration, high base acceleration, and high frequency content, as compared to the actual earthquake ground motions. These motions typically have much lower damage potential than a real earthquake motion having identical peak ground acceleration. However, this testing is useful in identifying the pattern of cracking, weak zones in the structure, modes of failure subjected to base excitation, and damage with increasing intensity of shaking; and useful conclusions can be drawn with respect to efficacy of the strengthening technique. A direct comparison of the performance of the URM and retrofitted models can be made by testing both of the models simultaneously subjected to the same shock. To accommodate both these models on same shock-table platform and to keep the total weight within maximum pay load of the shock-table, half scale models made of specially manufactured bricks have been used.

CONSTRUCTION OF MODELS FOR SHOCK-TABLE TEST

To study the effectiveness of strengthening technique using Welded Wire Mesh in cement concrete/mortar for ‘splints’ and ‘bandages’, two models were constructed simultaneously on the shock-table. A skilled mason was employed to construct the specimens with half scale burnt clay bricks of size 118×58×37 mm and 8-10 mm thick mortar joints using 1:6 cement-sand mortar. Curing was done for 28 days and the models were tested in dry condition. Table 1 shows the details of the models. Model 1 represents a single room building built in traditional way without any earthquake resistant feature. Model 2 was constructed with seismic strengthening using Ferrocement strips in splints and bandages.

Table 1: Detail of Conventional and Strengthened Brick Masonry Models

| Sr. No. | Scale of Model | Description of the model |
|---------|----------------|---|
| Model 1 | Half Scale | Traditional brick masonry model in 1:6 cement-sand mortar without any earthquake resistant feature |
| Model 2 | Half Scale | Brick masonry model in 1:6 cement-sand mortar, with strengthening using Ferrocement strips in splints and bandages. |

EXPERIMENTAL SET-UP

The general arrangement of the shock-table test facility, available at IIT Roorkee, has been shown in Figure 1. The test facility consists of i) Permanent way, ii) Shock-table platform, iii) Dead load wagons, and iv) Winch mechanism to pull the wagons as major components.

The permanent way consists of a railway track having three lengths of 12 m each of 44.6 kg/m rails. Thus total weight of one track is 1605.6kg. The rails are laid on prestressed concrete sleepers. The rails are placed at a spacing of 1.676 m at the inner face, and with a grade of about 8%. The rails have been marked at an interval of half meter to control the intensity of impact by positioning and releasing of the wagons at desired location. The prestressed concrete sleepers rest on a well-prepared base, which is about 150 mm thick, made up of stone ballast directly laid on the soil.

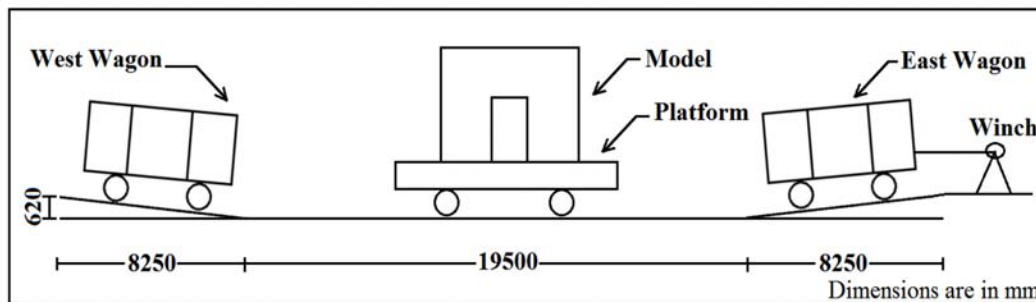


Figure 1: Line sketch of shock-table test facility, available at the department of earthquake engineering, Indian institute of technology (IIT) Roorkee

The shock-table platform consists of an open railway wagon chassis weighing 8.5 tonnes with a rigid steel platform, 7×6 m in plan. Ten helical coil compression springs have been mounted on each end of the Shock-Table platform to moderate the impact from the loading wagon. Each spring's stiffness is of the order of 138 kg/mm with a capacity of 7.5 tonnes. The maximum acceleration of the table has been recorded around 10 g (98.1 m/s²) in some previous conducted tests on the platform. Two loading wagons have been placed on the track on both the sides of the shock-table platform. The East side wagon used to apply the impact which moves along track using winch arrangement as shown in Figure 1. This wagon has been loaded with boulders, sand and reinforced brick slab with the total weight approximating to about 35 tonnes. The West side wagon is stationary and has been loaded with boulders and sand, weighing about 30 tonnes. During the test, the East side loaded wagon has been pulled up the slope and allowed to roll down to give an

impact to the shock-table through springs. In the process, the structure constructed on the shock-table platform gets a few shocks, one main shock by the initial impact and then subsequent shocks by rebounds with the stationary and the loading wagons. A manually operated portable winch has been used to pull the dead load wagons up on the inclined slope. On the grades of about 8% with friction, a pull of about 3500 kg is required. A mechanism to release the loading wagon for rolling down, using a sharp blow from a hammer, has been provided. A safety pin in the release mechanism and stoppers made of steel under wagon wheels have been used to safeguard against accidental release.

TESTING PROCEDURE AND INSTRUMENTATION

The testing procedure consists of imparting shocks of gradually increasing intensity, to the platform on which the model is built, by the heavily loaded East end wagon. One single impact from end wagons imparts a triangular shaped pulse to the central wagon (platform). The first pulse is imparted by the East end wagon and depending on the energy of the impact, subsequent pulses are imparted from rebound with the platform and West end wagons. The intensity of the shock has been controlled, by calibration marks on the rail and the springs mounted on the shock-table. The acceleration time histories of the models were recorded during each shock. The cracks developed at various shocks were marked to study the pattern of cracking and the mode of failure. The models were constructed side by side on the 'Shock-Table' and both the models were subjected to shock type motion at the base simultaneously as shown in Figure 2.



Figure 2: Photograph showing the completed models on shock-table platform

The models were instrumented for measurement of accelerations at top and bottom, during the dynamic testing. For the measurement of accelerations with time, four accelerometers were deployed. These accelerometers were connected to an eight channel data acquisition system for synchronized measurement. Out of these four accelerometers, two were used to measure accelerations of platform (placed on the base of models) and remaining two were used for measurement of accelerations of top of the models (placed on the roofs of the models). The relative

displacement between the platform and the model top during successive shocks was obtained from this acceleration data (using double integration).

EXPERIMENTAL OBSERVATIONS

The building models were subjected to shocks of increasing intensity. The intensity of shocks was controlled by moving the loading (East end) wagon to different distances up the inclined before releasing. For the first shock, the velocity of central wagon (Shock-Table Platform) was not adequate to cause a collision with the stationary (West end) wagon. As a result, only one pulse was applied in the first shock. In successive shocks, the velocity of the platform was adequate to cause a collision with the stationary wagon and two or more pulses were applied. Collapse of the traditional (unreinforced) model occurred after the third shock. The strengthened model was subjected to two more shocks, with maximum acceleration up to 10 g (98.1 m/s^2). The model could not be tested up to collapse as higher accelerations could not be achieved using the available test facility. The traditionally constructed model proved very fragile, but the performance of retrofitted model is substantially improved. Major cracks were seen in the traditional model at the second shock where peak base acceleration of 9.99 m/s^2 was applied during the first pulse and acceleration of 8.38 m/s^2 was applied during the rebound pulse. The maximum roof acceleration of the traditional model was 18.98 m/s^2 in loading cycle and 13.05 m/s^2 during rebound cycle. During this shock, formation of cracks was observed in the traditional model as shown in Figure 3. The cracks starting from the top corner of the door opening extended up to the corner of wall. Similar cracks were also seen in the opposite shear wall having window opening. The solid walls orthogonal to the pulse excitation were subjected to out-of-plane inertia forces. No damage was observed in the retrofitted masonry model, up to this shock, as shown in Figure 3.



Figure 3: Formation of cracks in traditional model whereas retrofitted model was intact after shock 2

In the third shock, the peak acceleration of 24.67 m/s^2 was applied at the base of the models during loading cycle, and an acceleration of 18.96 m/s^2 was applied during the rebound cycle. The maximum roof acceleration of the retrofitted model was 32.85 m/s^2 in loading cycle and 21.43 m/s^2 during rebound cycle.



Figure 4: Front view of the shock-table platform showing the traditional and retrofitted models after shock 3. The traditional model collapsed under this shock

The traditional masonry model collapsed during this shock, and no damage was observed in the retrofitted model as depicted in Figure 4. It was also noted by observing the closer view of the retrofitted model, that no cracks visible by naked eye. In the fourth and fifth shock, the intensity of the impact loading was kept on increasing up to possible capacity of shock table. Maximum possible peak base acceleration in the fifth shock was observed to be 100.67 m/s^2 in loading cycle. There was no damage to strengthened model during shock 4 but minor damage was observed to the strengthened model during fifth shock. Horizontal cracks originating from the base of the door opening appeared on the southern shear walls (Figure 5). Initiation of diagonal cracks was also observed as shown in Figure 5. The initiation of diagonal cracks from the corners of the window opening was also observed on northern side of the retrofitted model. However, there was no visible damage to the east and west side solid strengthened walls.



Figure 5: Front view of shock-table platform showing view of minor cracks developed in retrofitted models after shock 5 on southern side

ANALYTICAL SIMULATION OF SHOCK-TABLE TEST

Macro-modelling technique “Equivalent Frame Model” (EFM), which provides an easier visualization of the structural behaviour and reasonably accurate results with moderate computational efforts has been used in simulation of shock table test. To develop the EFM of a URM wall, Dolce (1989) presented the concept of effective height of piers. The Dolce’s criterion for computation of effective height of piers is shown in Figure 6 and can be expressed as

$$H_{eff} = h' + \frac{1}{3h} D(H - h') \quad (1)$$

where, the values of h' , D , and H for the given pier are referred from Figure 6. The flexural capacity, M_u diagonal shear capacity, V_u^f and the sliding shear capacity V_u^s , of a URM pier can be obtained (Pasticier et al. 2008) as

$$M_u = \frac{\sigma_o D^2 t}{2} \left(1 - \frac{\sigma_o}{k f_d} \right) \quad (2)$$

$$V_u^f = \frac{1.5 f_{vod} D t}{\xi} \sqrt{\left(1 + \frac{\sigma_o}{1.5 f_{vod}} \right)} \quad (3)$$

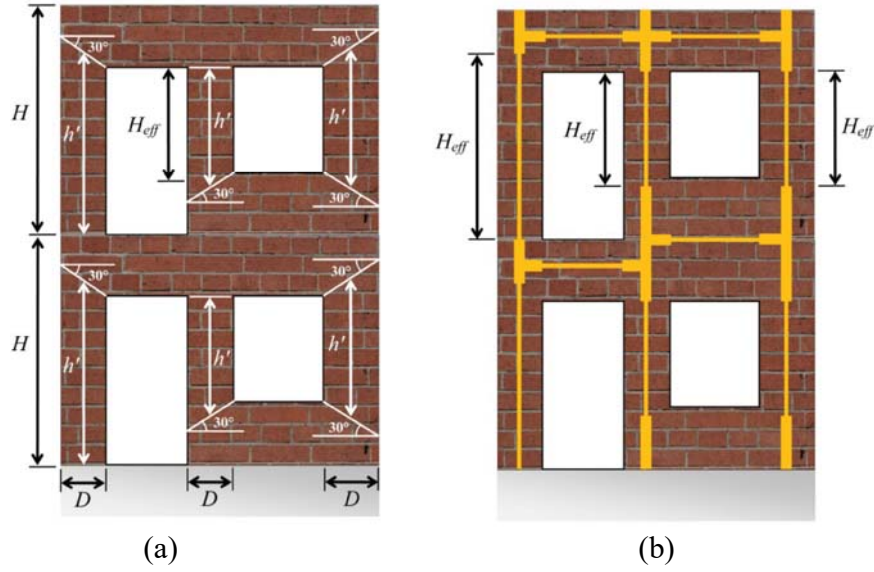


Figure 6: Schematic 2d diagram of a typical masonry wall showing: (a) effective height of piers, as per dolce (1989); and (b) equivalent frame model

$$V_u^s = \frac{1.5f_{vod} + \frac{\mu\sigma_o}{\gamma_m}}{1 + \frac{3H_o}{D\sigma_o}f_{vod}} \quad (4)$$

where, σ_o is the axial stress on the pier, D is the length of the pier, t is the thickness of the pier, k is the coefficient considering axial stress on toe of the pier (generally assumed as 0.85), f_d is the compressive strength of the pier, f_{vod} is the design shear strength with zero axial stress, ξ is the ratio D/t of length to thickness of the pier, μ is the friction coefficient (assumed as 0.4), H_o is the effective height of the pier and γ_m is the factor of safety (assumed equal to 2.0).

The equivalent 3D frame model of the scaled building on shock table platform is shown in Figure 7. The nonlinear behaviour of piers and spandrels has been modelled by assigning plastic hinges (Prasad 2009; Prasad et al. 2009; Singh et al. 2012) at pre-defined locations in the equivalent frame elements. The limitation of the conventional equivalent frame model of URM buildings is its inability to simulate the effect of varying axial stresses on the rocking and shear capacities of piers. This limitation has been overcome in the present study by using a set of two P-M (axial force versus bending moment) interaction hinges to simulate the combined behaviour in rocking, sliding and diagonal shear as proposed by (Prasad 2009) and (Singh et al. 2012).

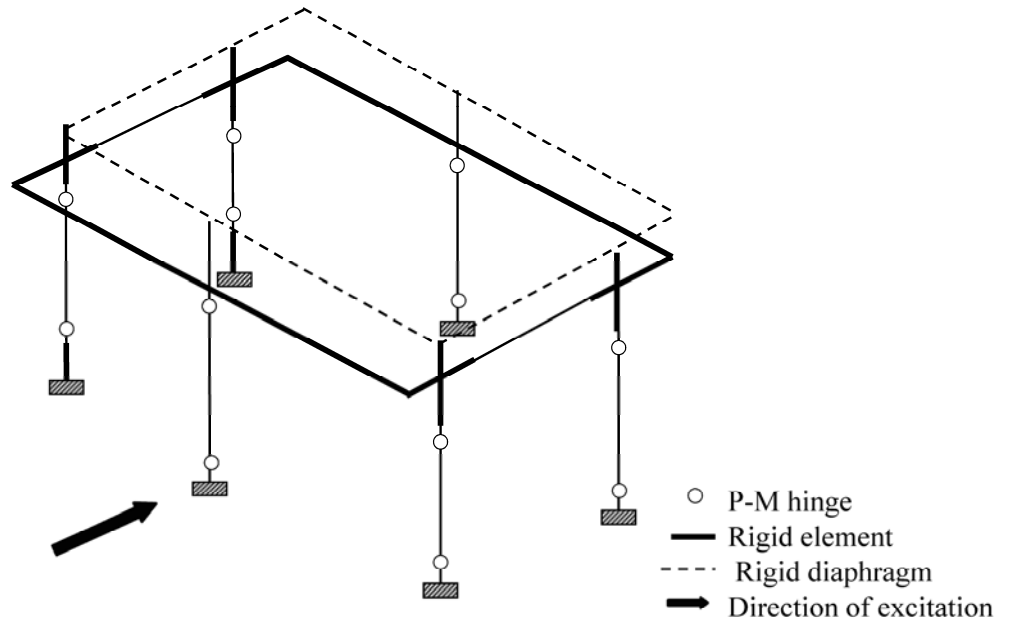


Figure 7: 3D Equivalent frame model of the buildings tested on shock-table platform

The P-M interaction hinges are assigned a yield curve representing the governing failure mode (i.e. the one having minimum capacity) at a given axial force in the pier. It is to be noted that for a given pier, different modes of failure may govern the behaviour at different values of axial force. The capacities of piers in rocking, diagonal shear and sliding shear, for varying axial force have been computed using Equations 2-4.

In order to improve the seismic performance of the existing building, the URM walls have been strengthened in in-plane and out-of-plane action using the Ferrocement strips. The retrofit design has been performed using the concept of permissible stresses as per IS 1905(1987) and IS 456(2000). The amount of reinforcement in splints and bandages has been obtained considering the composite action of the masonry and WWM (Singh 2011). The detailed calculations of the reinforcement in different splints and bandages in a typical wall of the masonry building, are available in Kadam (2015) and not presented here for brevity. In mathematical modelling of simulation of retrofitted masonry the earlier equations proposed by Ghaissi (Ghaissi 2009) has been used as many similar aspects were observed in both these works.

The moment-curvature ($M-\phi$) curve for the composite masonry-micro-concrete-WWM section has been obtained following the ordinary beam theory assuming a linear distribution of strain across the section and compatibility of strain across the cross-section.

The diagonal shear strength of the strengthened masonry pier has been obtained (ASCE 41-06. 2007; FEMA 356 2000; MSJC 2013) as

$$V_{nm} = 0.083 \times \left[4.0 - 1.75 \left(\frac{M_u}{V_u d_v} \right) \right] A_{nv} \sqrt{f'_m} + (0.53 \sqrt{f'_c} t_c d) + (0.5 f_y A_v \frac{d_v}{s}) + (0.25 P_u) \quad (5)$$

where, V_u and M_u are the applied shear force and bending moment, respectively, on the wall section, d_v is the effective length of the wall, usually considered equal to 0.8 times of the total length of the wall. For cantilever walls, the term $\frac{M_u}{V_u d_v}$ is equal to the aspect ratio of the wall. A_{nv} is the net mortared area, f'_c is the compressive strength of mortar, A_v is the area of vertical reinforcement, s is the spacing of the reinforcement, and f'_m is the compressive strength of strengthened masonry which is governed by effective modulus of elasticity of strengthened masonry (E_{rm}). In absence of more accurate estimates, it can be taken as (Ghiassi 2009)

$$f'_m = \epsilon_u E_{msec} \quad (6)$$

where, ϵ_u is the peak strain in masonry and can be considered equal to 0.003, E_{msec} is the secant modulus of elasticity that can be assumed equal to half of the initial modulus of elasticity of the strengthened masonry. The initial modulus of elasticity of the strengthened masonry can be computed (Ghiassi 2009) as follows,

$$E_{rm} = \left(-0.068 \frac{t_m}{t_c} + 1.068 \right) \left(0.243 \frac{E_m}{E_c} + 0.45 \frac{E_b}{E_c} + 0.335 \right) E_c \quad (7)$$

where, t_m is the thickness of the masonry wall, t_c is the concrete layer thickness, E_m is the modulus of elasticity of the mortar, E_b is the modulus of elasticity of bricks, and E_c is the modulus of elasticity of concrete. The strengthened masonry walls with low axial loads and longitudinal reinforcement ratio are prone to sliding shear failure. The capacity of strengthened wall due to sliding shear failure is given by Ghiassi et al. (2012) as

$$V_{se} = \mu_1 P_u + \mu_2 A_{vf} f_{ye} \quad (8)$$

where, P_u is the axial load on the wall, A_{vf} is the area of reinforcing bars perpendicular to the sliding plane, f_{ye} is the expected yield strength of reinforcing bars, μ_1 is the coefficient of friction of brick masonry, and μ_2 is the coefficient of friction of concrete, that can be taken equal to 0.9.

As mentioned earlier, the models have been constructed using half scale bricks, specially manufactured for this purpose. Tests on half scale brick masonry with the same bricks and mortar proportion were performed by Masood (2006). Basic material properties such as compressive strength (f'_c), modulus of elasticity (E) and Poisson's ratio (ν) used in modeling have been considered from this work. Nonlinear Dynamic analysis has been performed to estimate the response of the models, subjected to recorded excitations. As mentioned earlier, the shock-table motion is characterized by high frequency content. Accordingly, a shorter time step (0.0001 sec) has been used in the step-by-step time integration. Rayleigh damping of 10% has been used in both the models which have been subjected to identical shocks recorded at the shock-table platform. The output from the time history analysis was obtained in the form of displacement-time record at roof level. This output displacement has been compared with experimentally obtained displacement.

COMPARISON OF NUMERICAL AND EXPERIMENTAL RESULTS

Figures 8 and 9 show the plastic hinge patterns in the analytical models of the traditional (unreinforced) and retrofitted buildings subjected to different shocks. In the 1995, Structural Engineers Association of California published a document called Vision 2000- Performance based seismic engineering of buildings. It is applicable to the rehabilitation of existing buildings as well as to the design of new buildings. The different limit states, considered as performance level are (Immediate Occupancy) 'IO', (Life Safety) 'LS' and (Collapse Prevention) 'CP' represent the damage states in terms of the thresholds (acceptance criteria) defined in FEMA 356 (2000) for traditional model and as per Ghiassi et al. (2012) for the retrofitted model. It can be seen from the figures that the observed hinge pattern matches very well with the damage observed during testing. For the unreinforced (traditional) building model subjected to Shock 2, the plastic hinges in all the piers reach 'CP' level, indicating imminent collapse as shown in Figure 8 (b). The solution for Shock-3 could not converge for the traditional building, indicating collapse.

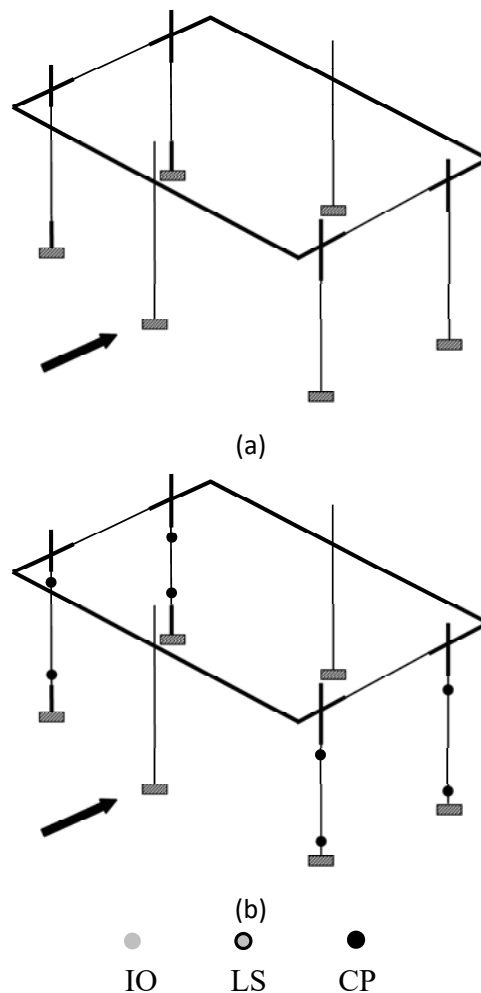


Figure 8: Plastic hinge patterns in traditional building model subjected to: (a) shock-1; and (b) shock-2

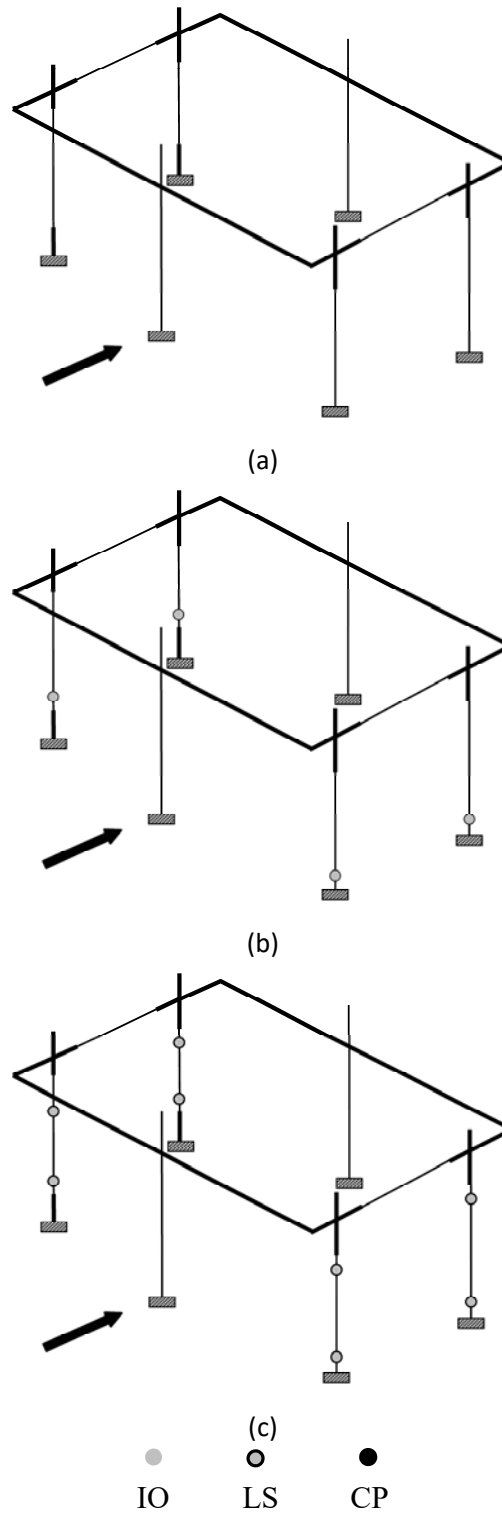


Figure 9: Plastic hinge patterns in retrofitted building model subjected to: (a) shock-3; (b) shock-4; and (c) shock-5

On the other hand, for the retrofitted building, no yielding of plastic hinges occurs until Shock-4 as shown in Figure 9 (a) and 9 (b). For the higher intensity shocks, the plastic hinges in piers show yielding, but did not cross the ‘Life Safety’ performance level even for Shock-5 as shown in Figure 11 (c). This is in good match with the no damage observation for Shock-3 and minor damage observed under Shock-5 for this building during the actual test.

Comparison of numerical and experimental displacement-time plots for shocks of increasing intensity is shown in Figures 10 - 14. Displacements for Shock-1 and Shock-2 are compared for the traditional (URM) model, whereas for larger shocks, the response of the retrofitted model has been compared, as the traditional model collapsed during Shock-3.

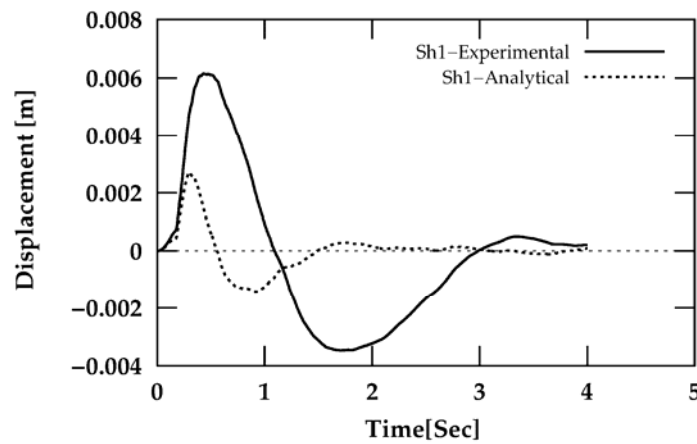


Figure 10: Comparison of displacement response of traditional model for shock-1

Figure 10 compares the analytical and observed displacement response of traditional model subjected to Shock 1. As shown earlier in Figure 8 (a), no yielding in any component was observed in the analysis. As the first shock was of very low intensity, the actual damping mobilized was much lower than the 10% assumed in the analysis. As a result, the analytically estimated response is much lower than the experimentally measured response.

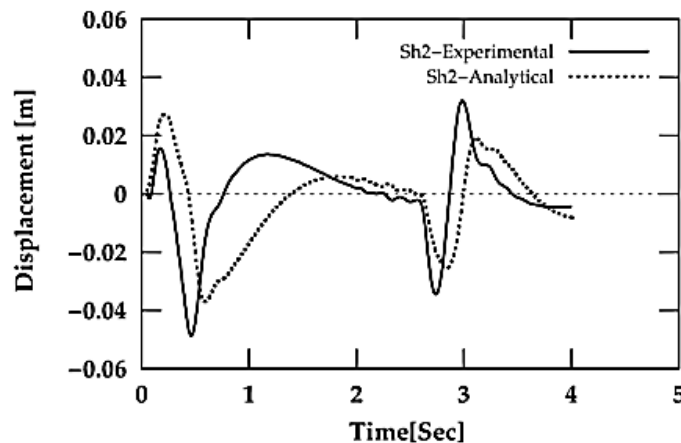


Figure 11: Comparison of displacement response of traditional model for shock-2

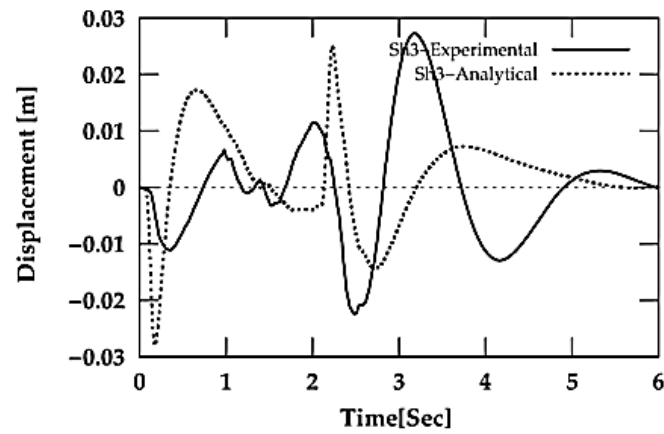


Figure 12: Comparison of displacement response of retrofitted model for shock-3

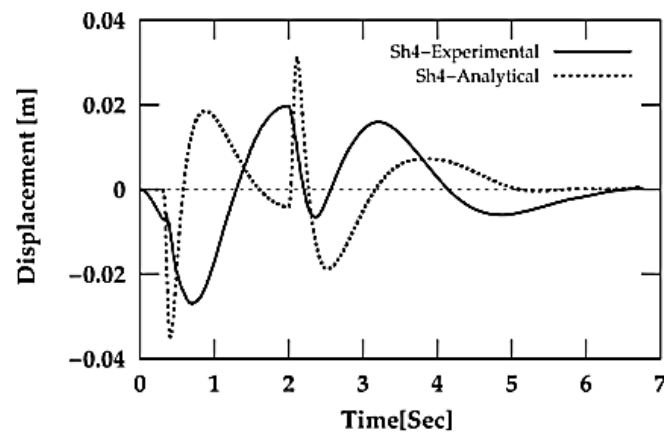


Figure 13: Comparison of displacement response of retrofitted model for shock-4

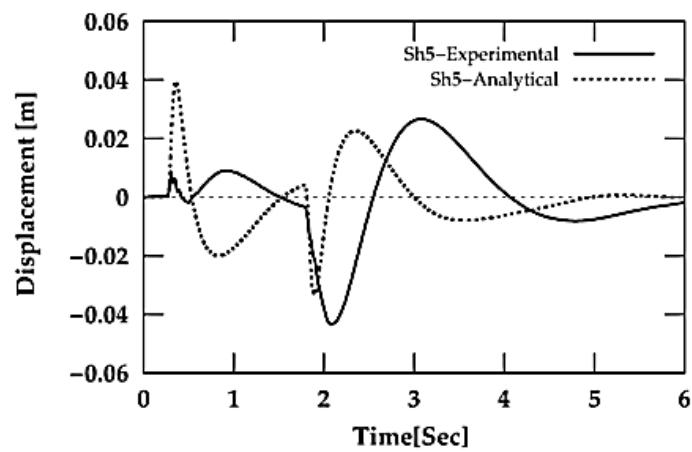


Figure 14: Comparison of displacement response of retrofitted model for shock-5

On the other hand, the numerical and experimental displacements for Shock-2 match quite closely, indicating a close prediction of the stiffness and damping for this level of shaking which corresponds to significant yielding and cracking in the masonry model (Figure 3). The difference in the numerical and experimental displacement waveform increases for the higher intensity shocks. However, the peak displacements observed numerically and experimentally are in good agreement for all the shocks.

SUMMARY

Major cracks were seen in the traditional model at Shock-2 (peak acceleration = 1 g) and collapse occurred at Shock-3 (peak acceleration = 2.5 g), whereas, the retrofitted model survived up to Shock-5 (peak acceleration = 10 g) with minor cracks. It is to be noted that the models can survive much higher peak accelerations in the shock-table test, as compared to the earthquake ground motions, due to low damage potential of the high frequency impulse motions in case of shock-table test. The numerical analysis using Equivalent Frame Approach, predicted the damage levels in both the building models with reasonable accuracy at all the shaking levels, justifying its application for estimating seismic performance of URM and retrofitted buildings. The Equivalent frame models also predicted the peak displacements quite close to those obtained experimentally, for both URM and strengthened buildings. However, the displacement-time waveform could not be predicted accurately.

ACKNOWLEDGEMENTS

The authors would like to acknowledge the financial support received from the Temasek Foundation, Singapore for conducting the study. The support received from the Ministry of Human Resource Development, Government of India, towards the fellowship to the first author is also gratefully acknowledged.

REFERENCES

- Agarwal, P. (1999). "Experimental study of Seismic Strengthening and Retrofitting measures in Masonry Buildings." Ph.D., University of Roorkee, Roorkee.
- Agarwal, P., and Thakkar, S., K, (2001). "A Comparative Study of Brick Masonry House Model Under Quasi-Static and Dynamic Loading." ISET Journal of Earthquake Technology, 38(2-4), 103-122.
- ASCE 41-06(2007). Seismic Rehabilitation of Existing Buildings. American Society of Civil Engineers, Virginia, USA.; 2007
- Arya, A., S. (1984). "Sliding Concept for Mitigation of Earthquake Disaster to Masonry Buildings". Paper read at 8 WCEE, at San Francisco, California,

Dolce, M. (1989). "Schematizzazione e modellazione per azioni nel piano delle pareti (Models for in-plane loading of masonry walls),". Corso sul consolidamento degli edifici in muratura in zona sismica, Ordine degli Ingegneri, Potenza, 1989. (Quoted in Magenes and Della Fontana, 1998)

Dubey, R., N., (2011). "Experimental Studies to verify the efficacy of Earthquake Resistant Measures in Masonry Buildings." Ph.D.Thesis, IIT Roorkee, Roorkee.

Ersubasi, F., and Korkmaz, H. H. (2010). "Shaking table tests on strengthening of masonry structures against earthquake hazard." *Natural Hazards and Earth System Sciences*, 10(6), 1209-1220.

FEMA 356 (2000). "Prestandard and Commentary for the Seismic Rehabilitation of Buildings." Federal Emergency Management Agency, Washington, D.C., USA

Ghiassi, B. (2009). "Homogenization and development of constitutive models for seismic evaluation of brick masonry structures retrofitted with reinforced concrete layer." M.Sc Thesis., Tarbiat Modares Univ., , Tehran, Iran

Ghiassi, B., Soltani, M., and Tasnimi, A. (2012). "Seismic Evaluation of Masonry Structures Strengthened with Reinforced Concrete Layers." *Journal of Structural Engineering*, 138(6), 729-743.

IS456 (2000). "Plain and reinforced concrete - Code of practice." Bureau of Indian Standard, IS 456 ,New Delhi. India.

IS 1905 (1987). "Indian Standard Code of Practice for Structural Use of Unreinforced Masonry (Third Revision),". Bureau of Indian Standards, IS1905,New Delhi,India.

Jagadish, K. S., Raghunath, S., and Nanjunda Rao, K., S., (2002). "Shock table studies on masonry building model with containment reinforcement." *Journal of Structural Engineering*, 29(1), 9-17

Kadam, S. B. (2015). "Seismic Evaluation and Retrofit of Masonry Buildings." Ph.D.Thesis, Indian Institute of Technology Roorkee, India.

Masood, A. (2006). "Out of Plane Behaviour of Unreinforced Masonry Infill Panels." Ph.D Thesis., Indian Institute of Technology Roorkee, Roorkee.

Mendes, N., Lourenço, P. B., and Campos-Costa, A. (2014). "Shaking table testing of an existing masonry building: assessment and improvement of the seismic performance." *Earthquake Engineering & Structural Dynamics*, 43(2), 247-266.

MSJC, (2013). "Building Code Requirements and Specification for Masonry Structures." TMS 402-13/ACI 530-13/ASCE 5-13, The Masonry Society, 2013.

Nikolic Brzev, S., and Arya, A., S (1996) "Seismic Isolation of Masonry Buildings - An Experimental Study." Proc., Eleventh World Conference On Earthquake Engineering.

- Paulson, T., Abrams, D., and Mayes, R. (1991). "Shaking-Table Study of Base Isolation for Masonry Buildings." *Journal of Structural Engineering*, 117(11), 3315-3336
- Pasticier, L., Amadio, C., and Fragiocomo, M. (2008). "Non-linear seismic analysis and vulnerability evaluation of a masonry building by means of the SAP2000 V.10 code." *Earthquake Engineering & Structural Dynamics*, 37(3), 467-485
- Prasad, J. S. R. (2009). "Seismic Vulnerability and Risk Assessment of Indian Urban Housing." Ph.D.Thesis, Indian Institute of Technology Roorkee, India.
- Prasad, J. S. R., Singh, Y., Kaynia, A. M., and Lindholm, C. (2009). "Socioeconomic Clustering in Seismic Risk Assessment of Urban Housing Stock." *Earthquake Spectra*, 25(3), 619-641
- Qamaruddin, M., Arya, A., S, and Chandra, B. (1984) "Dynamic Testing of Brick Buildings models." *Proc., The Institution of Civil Engineers*, 353-365.
- Qamaruddin, M., Arya, A., S, and Chandra, B. (1986). "Seismic Response of Brick Buildings with Sliding Substructure." *Journal of Structural Engineering*, 112(3), 558-572.
- Singh, Y.,(2011) "Seismic Retrofit of Unreinforced Masonry Buildings -Guidelines for Engineers." Centre of Excellence in Disaster Mitigation and Management,IIT Roorkee,India
- Singh, Y., Lang, D. H., Prasad, J., and Deoliya, R. (2012). "An Analytical Study on the Seismic Vulnerability of Masonry Buildings in India." *Journal of Earthquake Engineering*, 17(3), 399-422.
- Tomažević, M., Klemenc, I., and Weiss, P. (2009). "Seismic upgrading of old masonry buildings by seismic isolation and CFRP laminates: a shaking-table study of reduced scale models." *Bulletin of Earthquake Engineering*, 7(1), 293-321



**MASONRY TODAY
AND TOMORROW**

**11 - 14 February, 2018
SYDNEY AUSTRALIA**

www.10amc.com

FLEXURAL TESTS OF CLAY BLOCK MASONRY PRISMS REINFORCED WITH CARBON FIBER (CFRP)

**G.F. Medeiros¹, R. Bordignon², G. Mohamad³, A.B.S. Santos Neto⁴, J.F. Machado⁵ and
V.M. Tombezi⁶**

¹ Doctorate Student, Civil Engineering Graduate Program, Federal University of Santa Maria, Santa Maria, Brazil,
guifleith@upf.br

² Doctorate Student, Civil Engineering Graduate Program, Federal University of Santa Maria, Santa Maria, Brazil,
rodrigo.bordignon@passofundo.ifsul.edu.br

³ Professor, Civil Engineering Graduate Program, Federal University of Santa Maria, Santa Maria, Brazil,
gihad.civil@gmail.com

⁴ Professor, Civil Engineering Graduate Program, Federal University of Santa Maria, Santa Maria, Brazil,
almir.bssn@gmail.com

⁵ Master Student, Civil Engineering Graduate Program, Federal University of Santa Maria, Santa Maria, Brazil,
juliafm.engcivil@gmail.com

⁶ Laboratorist, Civil Construction Materials Laboratory, Federal University of Santa Maria, Santa Maria, Brazil,
vilsontombezi@hotmail.com

Carbon fiber reinforced polymer (CFRP) is a material that could be used with great efficiency in structural strengthening, due to their low weight, high strength and great durability. The present work investigates the reinforcement CFRP in clay blocks prisms by flexural tests. A total of nine masonry prisms were tested. Three of them were tested without reinforcement and the others with the CFRP polymeric material. It was measured the ultimate load, the deflection at the midspan, as well as the tensile deformation of the CFRP reinforcement with two strain gauges. From the tests it was possible to conclude that there was a significant increase in the flexural strength for prisms reinforced with CFRP. The failure mode of the masonry prisms strengthening with CFRP was predominantly shear failure, with no detachment in the carbon fiber contact with the block.

Keywords: CFRP, polymer, carbon, reinforcement, masonry, bending



INTRODUCTION

Among the various structural recovery and reinforcement techniques existing in Engineering, there has been an increasing emphasis on the use of polymeric materials, such as carbon fiber and glass fiber sheets. Carbon fiber reinforced polymers (CFRP) sheets are low thickness materials, which are bonded externally to a given concrete or masonry structure, aiming to increase its tensile strength in bending or shearing. They present high strength, very low weight and great durability (Viapol, 2017).

Researchers have conducted many studies on shear and bending reinforcements in polymeric fibers-reinforced masonry (Anil et al., 2012; Kalali and Kabir, 2012; Bui and Limam, 2014; Gattesco and Boem, 2015; Simoncic et al., 2015). Those studies involve numerical modeling as well as laboratory and field tests, observing the efficiency this reinforcement in masonry. Another matter that has gained great attention from researchers is the verification of bonding between reinforcement and surface, evaluating the detachment phenomena and the adhesion between CFRP and masonry. (Faella et al., 2012; Ghiassi et al., 2013; Ceroni et al., 2014; Carrara and Freddi, 2014; Basilio et al., 2014; Mazzotti et al., 2015; Freddi and Sacco, 2016). One of the techniques to verify the adhesion of the ceramic block and the CFRP is the beam test, positioning the CFRP on the tension side of the beam (Chen e Teng, 2001; Yao et al., 2005; Cruz, 2012).

This article aims to present an experimental study of reinforcement using CFRP in clay block prisms under bending. The interface between the clay blocks and the CFRP will be evaluated, as well as will be defined the increase in mechanical resistance, the characteristic failure modes, the midspan deflection, and tensile deformations. Nine prisms were tested, three of them unreinforced and six using CFRP, with two distinct surface conditions.

EXPERIMENTAL PROGRAM

Beam testing were undertaken on three clay blocks prisms groups, each containing three specimens. One reference group, without reinforcement, and two groups using reinforcement with carbon fiber sheet. The difference between the two reinforced groups was the surface handling, sanding the clay blocks side grooves in one of the groups, while in the other that regularization was not accomplished.

Each prism used in the experiment contained three structural clay blocks of dimensions 14x19x29 cm. The reinforcement with carbon fiber reinforced polymer (CFRP) was conducted on prisms by means of three strips 41 cm long and 5 cm wide, positioned on the tension side, spaced 2 cm, according to Figure 1. Only one layer of the carbon fiber sheet was used (0,166 mm thick).

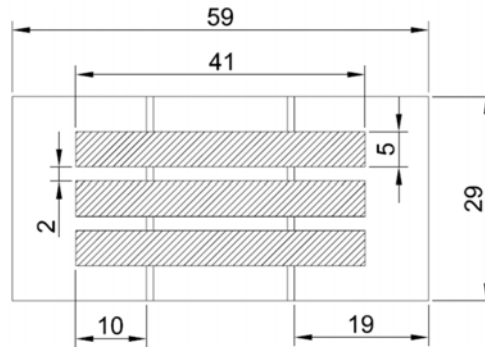


Figure 1: Positioning of the CFRP reinforcement in a three blocks-prism

Reinforced prisms with the surface of the blocks regulated by sanding (Figure 2) are denominated as RRS (Reinforced and Regularized Surface): P1, P2 and P3. Reinforced prisms without the surface of the blocks regulated by sanding are denominated as RIS (Reinforced and Irregular Surface): P4, P5 and P6. Unreinforced prisms are called as UNR (Unreinforced): P7, P8, P9.

The surface handling in the RRS group aimed to increase the contact surface between the fiber and the clay block, with higher adhesion resistance between the two materials. Sanding was accomplished using a grinder with a flap sandpaper disc coupled, according to Figure 2.



Figure 2: Clay block surface regularization for reinforcement application

The detail of the beam test conducted is presented in Figure 3. The supports were positioned at a 54 cm distance from each other, and the load was applied at two points, spaced 17 cm, in the prism central block (middle third of the beam). The loading and deformation data were acquired by the data acquisition system Spider8 and the software Catman. It was used a load cell of 50 kN and a hydraulic press.

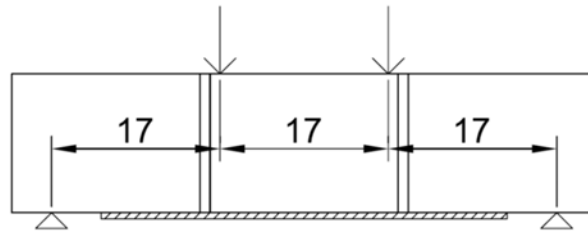


Figure 3: Detail of the masonry prisms beam test

For each prism from the RRS and RIS groups, two strain gauges were bonded onto the reinforcement side strips (Figure 4), aiming to measure the tensile deformations on the carbon fiber. For prisms in the UNR group the strain gauges were also bonded, in order to measure deformations in masonry. Two strain gauges were also used in each prism, with the same positioning used in the reinforced prisms. In order to measure midspan deflection, two dial indicators were used, one on each side of the tested prisms (Figure 4).



Figure 4: Test instrumentation for deformation and midspan deflection measurement

MATERIAL CHARACTERIZATION

The clay blocks used in the test had characteristic compressive strength of the gross area equal to 15 MPa, according to the manufacturer. Laboratory tests indicated the tensile and compressive strength shown in Table 1.

Table 1: Mechanical features of masonry blocks

| Mechanical Feature | Average (MPa) |
|--|---------------|
| Compressive strength of the gross area | 19.04 |
| Compressive strength of the net area | 33.45 |
| Tensile strength | 1.14 |

In the joints, a lime and cement mortar was used, with mix proportions in mass equal to 1:0.13:3.21 (cement: lime: fine aggregate) and water/cement ratio of 0.6. At 28 days, the mortar

presented average strengths shown on Table 2. At the choice of mix proportions, it was aimed that the mortar was strong enough to avoid a joint premature crushing.

Table 2: Mortar mechanical features

| Mechanical Feature | Average (MPa) |
|----------------------|---------------|
| Compressive strength | 25.10 |
| Tensile strength | 6.18 |

Regarding to mechanical features of the CRFP sheet used (Viapol Carbon CFW 300), the data provided by the manufacturer are indicated in Table 3. The fibers are arranged in the sheet in one single direction (unidirectional reinforcement).

Table 3: Carbon fiber mechanical features (Source: Viapol, 2016)

| Mechanical Feature | Value |
|--------------------------------|-------|
| Maximum tensile strength (MPa) | 4900 |
| Elastic modulus (GPa) | 230 |
| Ultimate elongation (%) | 2.1 |

ANALYSIS OF RESULTS

The results obtained with the use of CFRP reinforcement show its efficiency in the increase of resistant capacity of masonry prisms under bending. On average, there was an increase of 198% in the failure load compared to unreinforced prisms, considering specimens in which the clay block surface was regularized (RRS). For prisms with irregular surface (RIS), that load increase reached 147%. The difference of average load obtained between the two reinforced groups reached 21%, with advantage to the group with sanded surface. Maximum loads obtained individually for each of the nine prisms are presented in the Figure 5. Therefore, in both loading application points, half of these values were reached. Table 4 shows the average for each group, as well as the percentage strength increases.

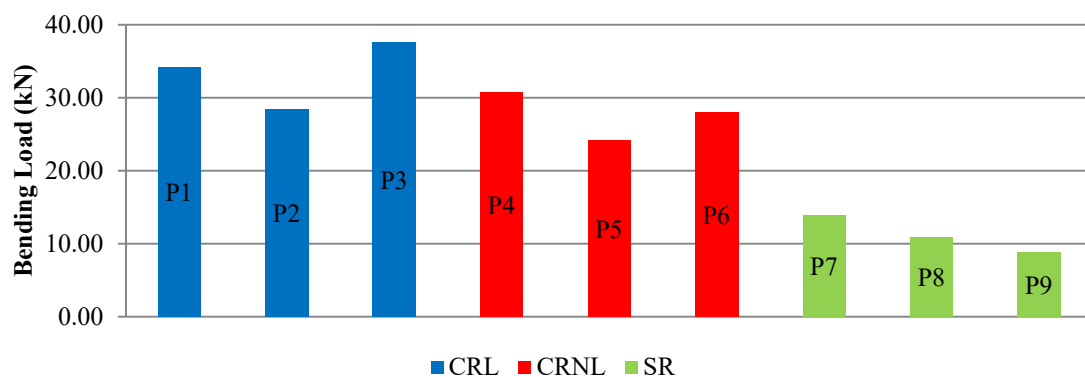


Figure 5: Maximum loads obtained individually for the prisms tested

Table 4: Average maximum loads obtained in the prisms groups

| Group | Average maximum load (kN) | Load increase compared to unreinforced prisms (%) | Load increase compared to reinforced prisms with irregular surface (%) |
|-------|---------------------------|---|--|
| RRS | 33,42 | 198% | 21% |
| RIS | 27,64 | 147% | - |
| UNR | 11,20 | - | - |

After tests, the fiber strips manually removal from the surface showed that bonding, in the RRS prisms case, was much more efficient than in the RIS prisms, as Figure 6 indicates.



Figure 6: Contact surface of the CFRP strips with masonry (RIS and RRS)

All six reinforced prisms of the RRS and RIS groups showed typical shear failure mode (Figure 7). Predominantly, the crack occurred at angle of 45° . For all three unreinforced prisms, crack occurred exactly in the blocks mortar joint, with the mortar-masonry interface detachment. Fiber detachment was not observed.



Figure 7: Failure mode presented by CFRP-reinforced prisms (RRS and RIS)

Loading results and the reinforced prisms failure modes indicated that the bending reinforcement reduced the tensile stresses acting on the masonry prism very efficiently, with no bending failure, no detachment reinforcement-clay block interface and neither tensile failure in the CFRP.

For the prisms displacements analysis, it was considered the average of readings of the two dial indicators used in each test. The average results of the midspan deflection obtained for each of the three prisms groups are summarized in the Figure 8.

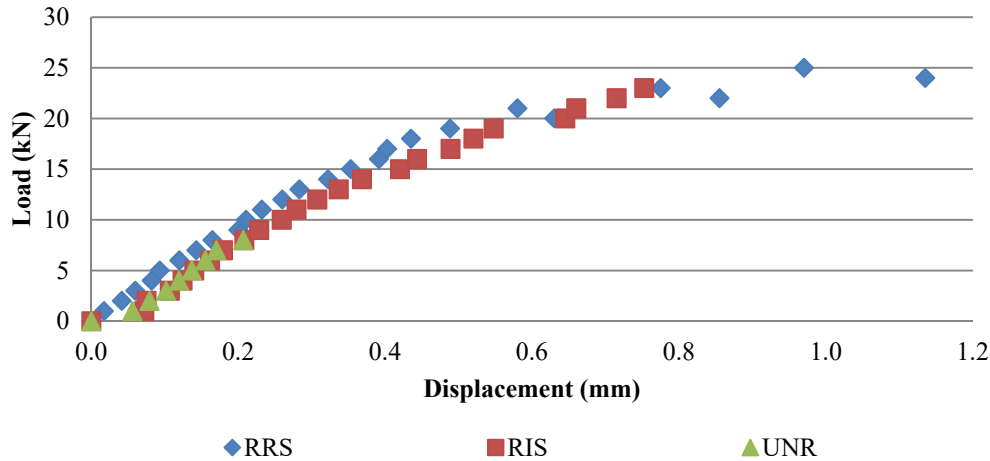


Figure 8: Average midspan deflection for prisms groups

From the Figure 8 it is possible to see that the RRS prisms presented, in general, smaller displacements than the RIS and UNR specimens. Among the samples of the RIS and UNR groups, there was not a considerable difference in the average values.

In the analysis of the deformations of the CFRP reinforcement strips (prisms 1 to 6) or of the region under tensile stress of masonry (prisms 7 to 9), the results presented in Figures 9, 10 and 11 were obtained, considering the average of reading of the two strain gauges, for the RRS, RIS and UNR groups, respectively.

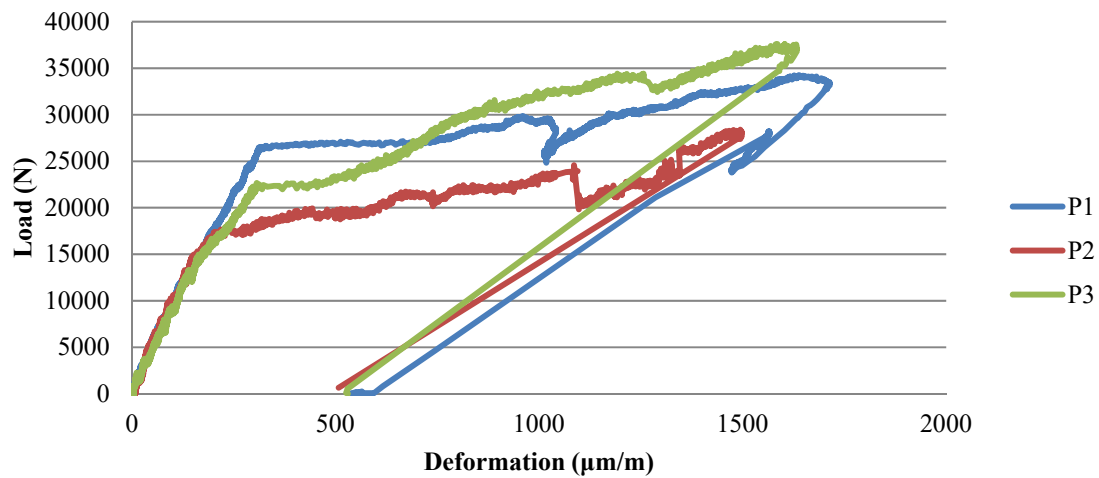


Figure 9: Tensile deformations on carbon fiber (RRS group)

The results in Figure 9 clearly indicate a linear load/deformation ratio for the carbon fiber reinforcement up to bending loadings ranges between 17 kN and 26 kN, which represents the elastic behavior of the material. After this elastic stage, yield limit was reached, with residual deformation in the 500 $\mu\text{m/m}$ range after unloading, due to plastification effects.

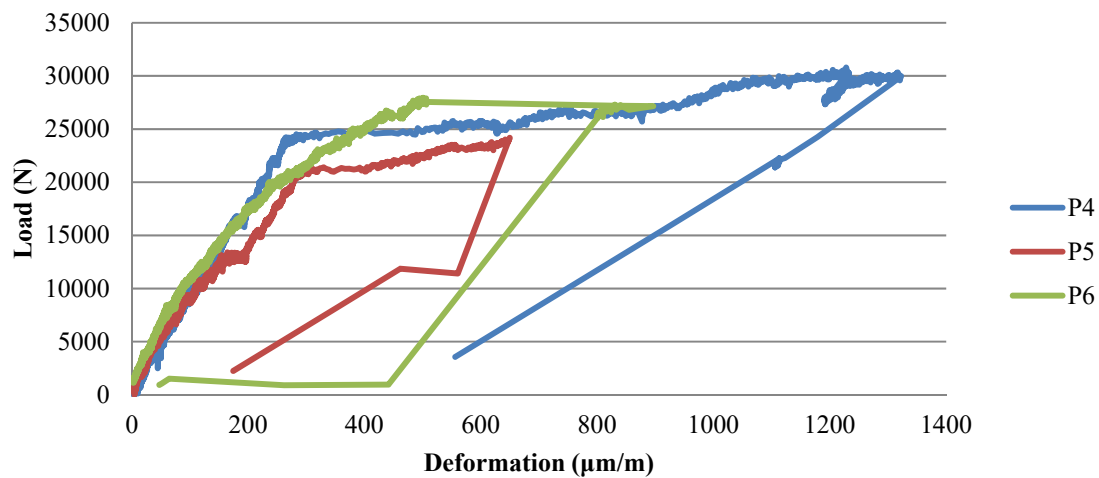


Figure 10: Tensile deformations in the carbon fiber (RIS group)

For the RIS group prisms, a similar behavior was observed (yield limit from 20 kN of bending load). Due to the lower load level reached in the prisms 5 and 6, compared to the RRS group prisms, the same plastic deformation level of the fiber was not reached. For prism 4, which surpassed the 30 kN load at failure, the behavior was similar to prisms 1, 2 and 3, with residual deformation close to 500 $\mu\text{m/m}$.

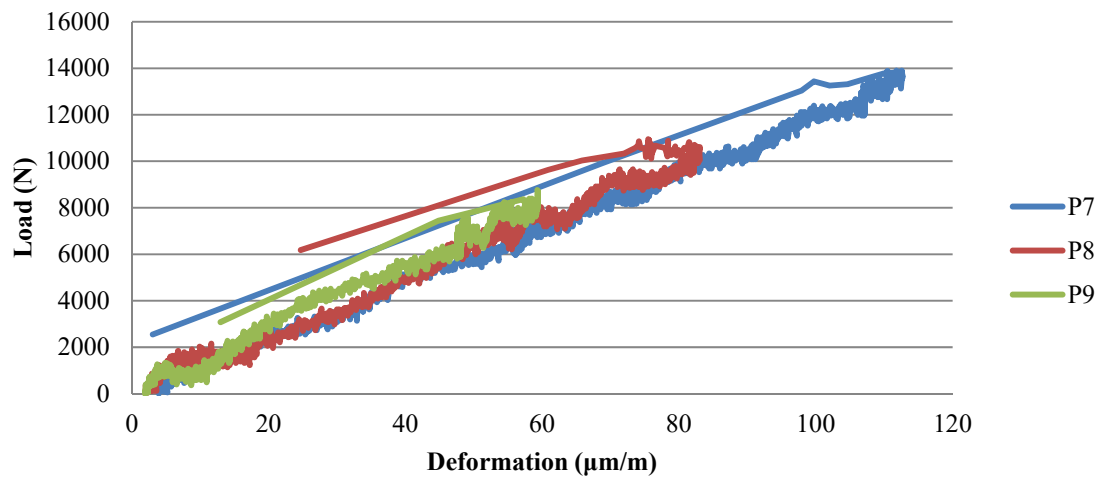


Figure 11: Tensile deformations in masonry (UNR group)

Regarding to the tests without reinforcement (Figure 11), it is clearly observed the elastic behavior of the clay block until the prisms failure, with linear load/deformation ratio. For prisms in the UNR group, the strain gauges were also bonded with the same positioning used in the reinforced prisms, but in contact with the clay block.

The average deformation of the three groups (Figure 12) indicates there is no difference between the load/deformation ratios for clay block and for CRFP. However, it is emphasized that the acting stresses are different, with different areas of material involved in the transversal section.

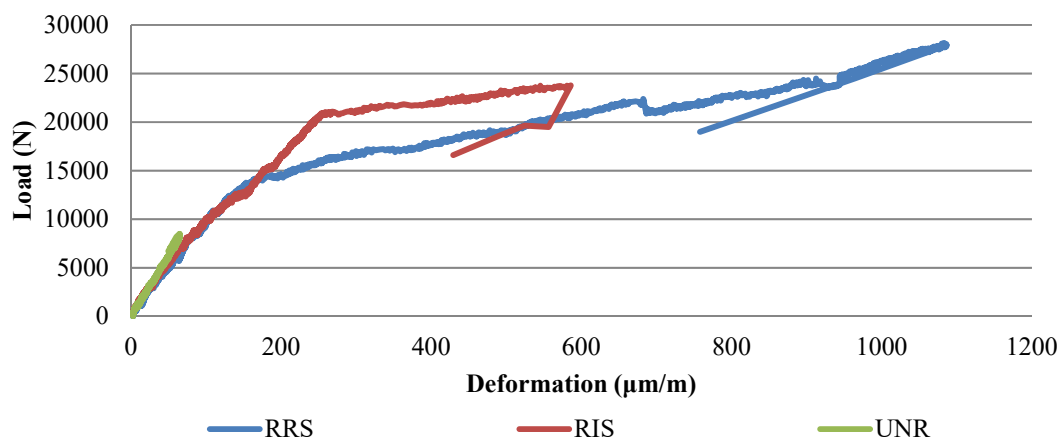


Figure 12: Average tensile deformations considering the prisms groups

FINAL CONSIDERATIONS

This paper has investigated experimentally the behavior of masonry prisms reinforced with CFRP submitted to flexural tests. Three unreinforced prisms and six reinforced prisms were analyzed. From the tests results, it was possible to reach the conclusions listed below.

Generally, a highest strength of the prisms was observed with the use of the carbon fiber sheet, more efficiently when there is regularization of the clay block-reinforcement interface. On average, the load increase caused by the proposed reinforcement area was approximately 198% for the RRS group and 147% for the RIS group.

When comparing the group in which the reinforcement was bonded on the regularized surface (RRS) and the group with irregular surface (RIS), it was observed that the former obtained on average 22% higher load.

Regarding to the failure mode, there was no failure in the system due to bending stresses in the case of the prisms with CFRP bending reinforcement, but shear typical failure.

The deformation on the carbon fiber indicated the elastic behavior up to a bending load range between 20 kN and 30 kN, with load applied at two points (middle third of the beam). When surpassing this load range, yield limit was reached, with plastic deformation approximate to 500 $\mu\text{m/m}$, mainly for the RRS group.

REFERENCES

- Anil O.; Tatayoglu M. and Demirhan M. (2012), Out-of-plane behavior of unreinforced masonry brick walls strengthened with CFRP strips, *Construction and Building Materials*, 35, pp. 614–624.
- Basilio, I.; Fedele R.; Lourenço P. B. and Milani G. (2014), Assessment of curved FRP-reinforced masonry prisms: Experiments and modeling, *Construction and Building Materials*, 51, pp. 492–505.
- Bui, T. T. and Limam A. (2014), Out-of-plane behaviour of hollow concrete block masonry walls unstrengthened and strengthened with CFRP composite, *Composites: Part B*, 67, pp. 527–542.
- Carrara P. and Freddi, F. (2014), Statistical assessment of a design formula for the debonding resistance of FRP reinforcements externally glued on masonry units, *Composites Part B*, 66, pp. 65-82.
- Ceroni, F.; Ferracuti, B.; Pecce, M. and Savoia, M. (2014), Assessment of a bond strength model for FRP reinforcement externally bonded over masonry blocks, *Composites Part B*, 61, pp. 147-161.
- Chen J. F. and Teng, J. G. (2001), Anchorage strength models for FRP and steel plates bonded to concrete, *Journal of Structural Engineering*, ASCE, 127, 7, pp. 784-91.

Cruz, J. S. (2012), *Reabilitação e Reforço de Estruturas*, Lisboa: Instituto Superior Técnico.

Faella, C.; Camorani G.; Martinelli E.; Paciello, S. O. and Perri F. (2012), Bond behaviour of FRP strips glued on masonry: Experimental investigation and empirical formulation, *Construction and Building Materials*, 31, pp. 353–363.

Freddi, F. and Sacco, E. (2016), An interphase model for the analysis of the masonry-FRP bond, *Composite Structures*, 138, pp. 322-334.

Gattesco N. and Boem I. (2015), Experimental and analytical study to evaluate the effectiveness of an in-plane reinforcement for masonry walls using GFRP meshes, *Construction and Building Materials*, 88, pp. 94–104.

Ghiassi B.; Marcari G.; Oliveira D. V and Lourenço P. B. (2013), Water degrading effects on the bond behavior in FRP-strengthened masonry, *Composites Part B*, 54, pp. 11-19.

Kalali, A. and Kabir, M. Z. (2012), Experimental response of double-wythe masonry panels strengthened with glass fiber reinforced polymers subjected to diagonal compression tests, *Engineering Structures*, 39, pp. 24–37.

Mazzotti C.; Ferracuti B. and Bellini A. (2015), Experimental bond tests on masonry panels strengthened by FRP, *Composites Part B*, 80, pp. 223-237.

Nicácio, W. G.; Rêgo E. M. F. Do; Santos G. S. and Oliveira M. H. de. (2013). Análise experimental de prismas de concreto simples reforçados à flexão com compósitos de fibras de carbono. *Proceedings of 55th Congresso Brasileiro do Concreto*, Gramado, Brasil.

Simonic M. J.; Gostic S.; Bosiljkov V. and Zarnic R. (2015), In-situ and laboratory tests of old brick masonry strengthened with FRP in innovative configurations and design considerations, *Bulletin of Earthquake Engineering*, 13, pp. 257–278.

Viapol. (2016), Viapol Carbon CFW 300: Ficha Técnica de Produto. Available at: < http://www.viapol.com.br/media/122330/ft-viapol-carbon-cfw-300-02_07_15.pdf>. Access in: 19 nov. 2016.

Viapol. (2017), Manual de Reforço das Estruturas de Concreto Armado com Fibras de Carbono. Available at: < <http://www.viapol.com.br/media/97576/manual-fibra-de-carbono.pdf>>. Access in: 14 dec. 2017.

Yao, J.; Teng, J. G. and Chen, J. F. (2005), Experimental study on FRP-to-concrete bonded joints, *Composites Part B*, 36, pp. 99-113.

BOND SLIP BEHAVIOUR OF DEEP MOUNTED CARBON FIBRE REINFORCED POLYMER STRIPS CONFINED WITH A DUCTILE ADHESIVE IN CLAY BRICK MASONRY

Ö. S. Türkmen¹, S.N.M. Wijte², J.M. Ingham³ and A.T. Vermeltfoort⁴

¹ PhD Candidate, Department of the Built Environment, Section Structural Design, Eindhoven University of Technology, P.O. Box 513, 5600 MB, Eindhoven, the Netherlands, O.S.Turkmen@tue.nl

² Professor, Department of the Built Environment, Section Structural Designs, Eindhoven University of Technology, P.O. Box 513, 5600 MB, Eindhoven, the Netherlands, S.N.M.Wijte@tue.nl

³ Professor, Department of Civil and Environmental Engineering, University of Auckland, 92019, Auckland, New Zealand, J.Ingham@auckland.ac.nz

⁴ Associate Professor, Department of the Built Environment, Section Structural Design, Eindhoven University of Technology, P.O. Box 513, 5600 MB, Eindhoven, the Netherlands, A.T.Vermeltfoort@tue.nl

Retrofitting clay brick masonry using Deep Mounted (DM) Carbon Fibre Reinforced Polymer (CFRP) strips embedded in grooves filled with a ductile adhesive considerably increases the out-of-plane flexural capacity of slender unreinforced masonry walls. In order to investigate the bond-slip behaviour of CFRP-strips in a viscous-elastic adhesive, an extensive experimental program was initiated. Direct pull-out tests were conducted with clay brick masonry. Two parameters were investigated, namely, the type of adhesive (2 types) and the groove widths (10 and 15 mm). The second part of the experimental program focused on the pull-out capacity when surface treatment (priming or sandblasting) was applied to the CFRP-strips.

In literature dealing with bond behaviour the critical bond length was found using masonry prisms of approximately 350 mm in height. In the current study with CFRP strip application in conjunction with ductile epoxy, the critical bond length was not reached for specimens of nearly 1000 mm in length. This finding was an indication of a significantly improved stress distribution over the length of the embedded CFRP-strip as the appearance of peak stresses was prevented. No premature brick splitting was initiated despite the depth of the groove being 65% of the specimen thickness, whereas in literature this phenomenon was reported for groove depths of only 30%.

Keywords: *bond-slip, pull-out, masonry, reinforcement, seismic, retrofit, CFRP*

INTRODUCTION

In Groningen, an area in the North-East of the Netherlands, earthquakes occur as a result of the subsidence of the ground at relatively shallow depth beneath the earth's surface (*de Waal et al. 2015*). This subsidence is caused by the extraction of gas from the Groningen gas field. As the majority of buildings in Groningen are composed of cavity walls with slender leaves of unreinforced clay brick masonry, and are designed to resist relatively moderate wind loads, it is essential to improve the earthquake resistance of the current buildings in the area to prevent collapse, with likely casualties. Due to the slenderness of the load bearing walls, the lateral load bearing capacity of these walls is mostly critical. Previous research has shown that retrofitting clay brick masonry with deep mounted (DM) Carbon Fibre Reinforced Polymer (CFRP) embedded in viscous-elastic adhesive, considerably increases the out-of-plane flexural capacity when compared to that of unreinforced masonry (*Türkmen et al. 2016, Türkmen et al. 2017, Wijte et al. 2017*). DM is the same concept as the more widely known Near Surface Mounted (NSM) technique, except the CFRP strip is installed deep in the brick, so that the installed tensile component (CFRP) can provide additional flexural capacity and strength for both out-of-plane loading directions.

One of the recommendations following these aforementioned research projects was the necessity of more knowledge regarding the bond-slip behavior of the CFRP strips in the masonry, where the bond is created by embedding the strips in visco-elastic epoxy which is used as a groove filler. It is essential to quantify the interfacial bond-slip relation to allow for accurate modelling and understanding of debonding failures in FRP strengthened structures. There are several parameters that can influence this relation, such as the groove and the strip dimensions, the tensile and shear strength of the groove filler, and the position of the CFRP strip within the member being strengthened. The challenge is to find a suitable configuration at which the bond-slip behaviour provides sufficient flexibility to prevent masonry from premature cracking and results in high pull-out capacities in order to realise effective reinforcement.

The bond behaviour of CFRP systems can be experimentally studied with direct pull-out tests (DPT) and beam pull-out tests (BPT). Because the DPT method is less time consuming and cheaper to prepare and to undertake compared to the BPT test, this method was the starting point to find a configuration that led to the previously stated and desired bond slip behaviour.

SPECIMENS

The kiln fired clay bricks used this research had dimensions $205(\pm 4) \times 97(\pm 2) \times 49(\pm 2)$ mm³ (l×w×h) and had a normalized compressive strength of >15 MPa (manufacturer specs.). For the preparation of ±15L of mortar, 25 kg of M10 masonry mortar mix and 3.5L (±0.25) of water was used. The compression strength of the masonry prisms (14.81 MPa; COV 6.12%) was determined according to NEN-EN 772-1. The Young's modulus of the masonry was 3.1 GPa (COV 2.5%). Mortar prism flexural strength (3.56 MPa; COV 16.5%) and compressive strength (10.65 MPa; COV 20.7%) were determined according to EN-12390-5.

Compression tests carried out on samples extracted from existing masonry buildings show that the mean compressive strength and mean Young's modulus (coefficient of variation between brackets) are 12.7 (0.15) MPa and 9347 (0.27) MPa respectively for clay-solid masonry from before 1945,

and 17.7 (0.38) MPa and 9348 (0.35) MPa respectively for masonry from after 1945 (*Vermeltfoort. 2015*). Thus the masonry used in the current research has a similar compression strength and a significant lower Young's modulus compared to the masonry in Groningen.

The prisms were constructed against a vertical sideboard to ensure minimum vertical deviation and were left to cure for at least 28 days. All masonry prisms consisted of 16 layers of brick in height and had typical mortar joint thicknesses of 13 mm. Even though various studies on pull-out behaviour of NSM FRP (*Willis et al. 2009; Dizhur et al. 2014*) approximate the critical bond length (and thus the required specimen height) as 100 times the FRP strip thickness, it was expected that this rule of thumb was not applicable in the current experimental program due to significant differences in the adhesive used. In order to prevent the specimens from being smaller than the critical bond length, a height of approximately 1000 mm for the prisms was selected.

Using a water cooled circular saw a groove was milled into the masonry prisms to depth d_f (Fig. 1). The dust in the groove was removed with compressed air. The CFRP strips ($20 \times 1.4 \text{ mm}^2$) were cleaned with acetone after cutting the strips into the specified length. If applicable, strain gauges (type PFL-10-11, foil strain gauges having polyester resin backing) were installed on alternating sides (to prevent asymmetric effects) at various locations with more frequent placement towards the loaded end (Fig. 2). The strain gauges were covered with wax to reduce the influence of the adhesive. A layer of primer was applied to the groove to obtain an improved bond of the applied adhesives to the masonry. Afterwards the CFRP strip was inserted into the groove that was partially filled with the flexible adhesive (type A or B) to a level exceeding d_{fs} . The CFRP strip was positioned centrally within the groove with a distance d_{fs}' of 10 mm from the bottom of the groove. The flexible adhesive exceeding d_{fs} was removed. Following the CFRP strip installation, the prisms were left to cure for one day before filling the remaining part (d_{ff}) of the groove with a conventional stiff adhesive. Afterwards another curing period of minimum seven days was maintained (stiff adhesive about 85% of end-strength). The relevant properties of the used flexible and stiff adhesives used, together with the properties of the CFRP strip are provided in Table 1.

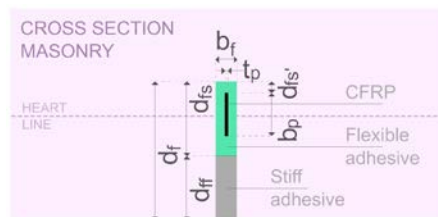


Figure 1: Geometry of the groove and CFRP strip.

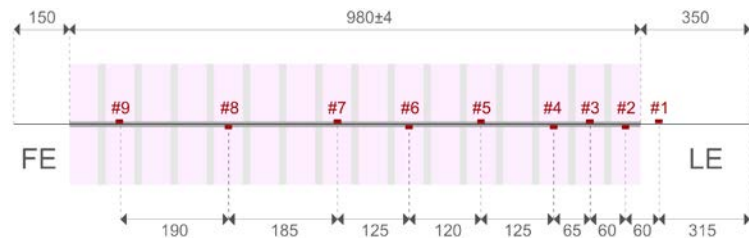


Figure 2: Pull-out specimen and the approximate positions of the strain gauges (indicated with #)

Table 1: Properties of the adhesive used (flexible and stiff) and CFRP

| Component | Compressive strength [MPa] | Tensile strength [MPa] | E-modulus [MPa] | Elongation at break [%] | Poisson ratio [-] |
|----------------|----------------------------|------------------------|-----------------------|-------------------------|-------------------|
| Adhesive A | - | $5.5 \pm 0.2^{(1)}$ | $34 \pm 0.5^{(1)}$ | $89 \pm 8^{(1)}$ | $0.48^{(2)}$ |
| Adhesive B | - | $2.95 \pm 0.1^{(1)}$ | $16.6 \pm 0.1^{(1)}$ | $98 \pm 10^{(1)}$ | $0.47^{(2)}$ |
| CFRP | - | $\geq 2800^{(3)}$ | $\geq 205,000^{(3)}$ | $> 1.35^{(3)}$ | - |
| Stiff adhesive | 45,5 ⁽⁴⁾ | 6,5 ⁽⁴⁾ | 26,000 ⁽⁵⁾ | - | - |

(1) Manufacturer specifications (M.S.) - DIN EN ISO 527 @ 200 mm/min; (2) M.S. - ISO 527 @ 10 mm/min;

(3) M.S. - DIN EN 2561 @ 2 mm/min; (4) M.S. - DIN EN 12190; (5) M.S. - DIN EN 13412

Before the experiment, aluminium plates were glued to both sides of the CFRP strip at the loaded end using high strength instant adhesive. This procedure was a suggestion made by *Dizhur et al. (2014)* in order to facilitate a greater distribution of stress at the grips and thus prevent slippage.

METHODOLOGY

The experimental study for direct pull-tests consisted of two batches. The first batch for direct-pull-out tests consisted of specimens with two different adhesives (Table 2) and groove widths b_f (10 and 15 mm). Each configuration had two specimens from which only one had embedded strain gauges (SG). The CFRP strips had a smooth surface, which was denoted with “S” in the specimen coding. The goal with the first batch was to get more insight on the effect of the adhesive and groove dimensions on the pull-out behaviour of the embedded CFRP strips. The best (high pull-out strength and low corresponding slip) combination of adhesive (A) and groove width (10 mm) was used as standard for the remaining DPT's.

Table 2: Specimens for 1st batch

| Spec. | Adh. | b_f (mm) | SG |
|----------|------|------------|-----|
| A-S15-SG | A | 15 | Yes |
| A-S15 | A | 15 | No |
| A-S10-SG | A | 10 | Yes |
| A-S10 | A | 10 | No |
| B-S15-SG | B | 15 | Yes |
| B-S15 | B | 15 | No |
| B-S10-SG | B | 10 | Yes |
| B-S10 | B | 10 | No |

Table 3: Specimens for 2nd batch

| Spec. | Adh. ⁽¹⁾ | Surface ⁽²⁾ | b_f (mm) ⁽³⁾ | SG |
|-----------|---------------------|------------------------|---------------------------|-----|
| A-RP10-SG | A | RP | 10 | Yes |
| A-RP10 | A | RP | 10 | No |
| A-SB10-SG | A | SB | 10 | Yes |
| A-SB10 | A | SB | 10 | No |

(1) Best performing adhesive 1st batch;

(2) RP = Roughened + primed; SB = Sand-blasted;

(3) Best performing groove width 1st batch

Because the failure of the best configuration of the first batch occurred at the CFRP and adhesive interface, additional pre-treatment of the CFRP was necessary to prevent this under-utilization of the strengthening system. A second batch was initiated to determine whether surface pre-treatment of the embedded CFRP strips would have a positive effect on the bond-slip behaviour. The surface treatment methods consisted of either adding a layer of primer after roughening the CFRP strips with sandpaper, or sand-blasting the CFRP strip. An overview of the tested specimens is provided in Table 3.

TEST SETUP

The direct pull-out tests were conducted on an Instron universal testing machine (Figure 3). The process started by carefully positioning the prism under the loading grips of the testing equipment, with the specimen resting on two support blocks. Hard cardboard was put on the top of the prism to prevent stress concentrations due to a possible non-flat surface of the brick. Afterwards the steel restrain plate on the loaded end was placed on top of the prism (Fig. 4). To prevent undesirable wedge type failure modes when using partial end restraint, a full restraint in the form of a 25 mm thick solid steel plate with three openings was selected. The centrally located opening allowed the loaded end of the CFRP strip to pass through. The smaller two openings allowed the LVDT's to rest on the specimen (Fig. 5). The specimen was then lifted up via the aluminium grip plates. This procedure made it possible for the prism to find its own balance point and thus minimize the eccentricity caused by imperfect installation of the CFRP strips. Using threaded rods, the steel restrain plate was bolted tight to the base of the installation until a pre tension force of 1.5 kN in the CFRP strip was monitored. After resetting the sensors, the experiment was started at a pull-out speed of 0.5 mm/min.



Figure 3: Experimental setup.

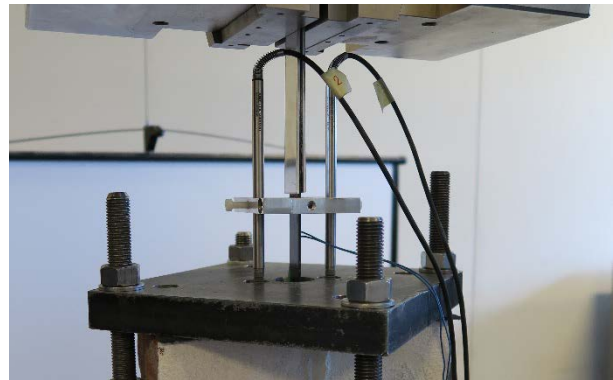


Figure 4: Detailed view of top support, loaded end LVDT's and aluminium plates.



Figure 5: Free end LVDT's.

Prior to the load application process, four LVDT sensors were installed. The upper two sensors measured the loaded end slip (Fig. 2) and the bottom two sensors measured the free end slip (Fig. 4). The mean of the two LVDT's was used to establish the corresponding slip. For the loaded end, the slip was corrected for the elongation over 70 mm of CFRP strip outside the specimen.

TEST RESULTS AND INTERPRETATION

The load-slip diagrams for the first batch of specimens are provided in Figs. 6-9. The abbreviations in the legend stand for loaded end slip (LE), which was corrected for the strain of the CFRP, and free end slip (FE). The notation (-SG) indicates the values for the specimen with embedded strain gauges. The regular specimens and the specimens with embedded strain gauges (-SG) are represented as blue and orange curves respectively. With the non-embedded strain gauges, the modulus of elasticity for the CFRP strip was determined for each experiment separately. The mean of the Young's modulus of the strips was found to be 196 GPa with a C.O.V. of 0.015.

For specimens A-S10(-SG), A-S15(-SG) and B-S10(-SG) with embedded strain gauges a clear decrease in pull-out capacity was observed. This finding was most likely caused by the reduced bonding area due to the placement of strain gauges. The test of specimen B-S15-S was disrupted because the edge of the component on which the free end LVDT's rested (Fig. 5), was clamped on one of threaded rods. This detail introduced an extra tensile force on the CFRP strip, which caused one of the FE LVDT's to fall out and the other one to malfunction. The clamping also explains the measured higher pull-out force measured for this specimen when compared to B-S15, despite the reduction in bond area due to the embedded strain gauges.

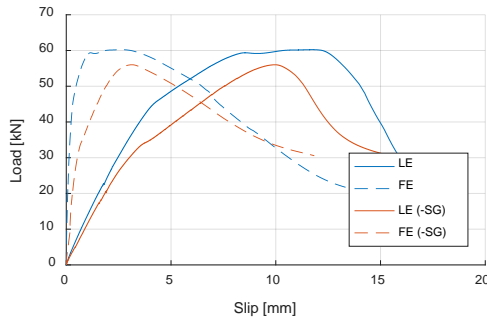


Figure 6: Load-slip diagram A-S10(-SG)

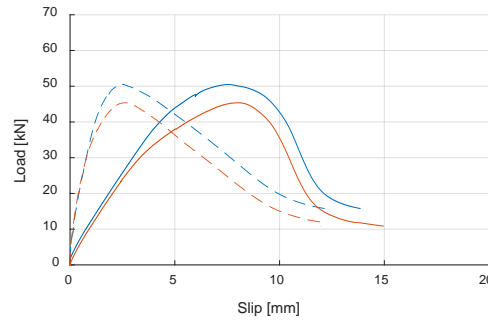


Figure 7: Load-slip diagram A-S15(-SG)

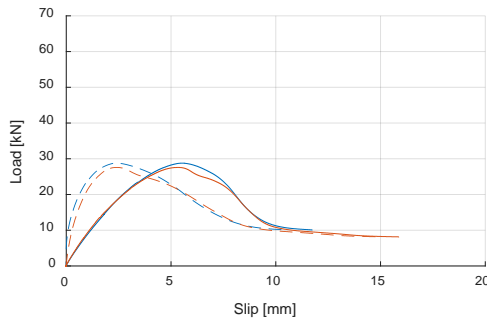


Figure 8: Load-slip diagram B-S10(-SG)

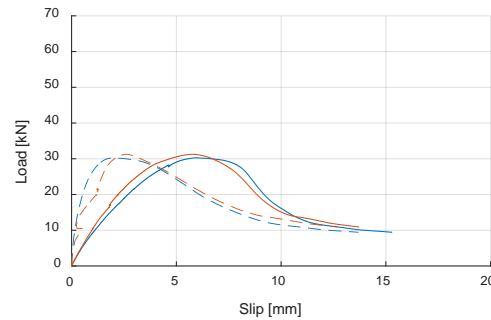


Figure 9: Load-slip diagram B-S15(-SG)

Fig. 10 shows the typical detachment of the CFRP strips from the adhesive, as was observed during these experiments. For all the specimens of this batch, a combined CFRP/adhesive interface failure and cohesive failure of the adhesive occurred. These findings indicated that improvements were

possible on the smooth CFRP strip surface in order to prevent CFRP/adhesive interface failure. With complete cohesive failure on the adhesive, a higher pull-out force was reached.

Despite a groove depth of 65 mm for all the specimens, premature brick splitting was not observed. Only specimen A-S10 developed some hairline cracks during the post-peak process around the CFRP and over the length of the specimen (Fig. 11). These cracks started developing after a 30% decline from the peak pull-out force, at a loaded end slip of 15 mm. For the remaining specimens no hairline crack development was observed. This observation was contradictory to the findings of *Dizhur et al. (2014)*, where pre-mature brick splitting was observed during the direct pull tests for specimens with a groove depth of only 30 mm. Based on the current findings, this premature failure mechanism was likely prevented with the application of a flexible adhesive instead of a stiff epoxy, as the more efficient confinement provided by the surrounding masonry is not the leading cause in premature failure prevention as observed by *Wijte et al. (2017)*.

Based on the load slip diagrams, it was concluded that adhesive A (higher tensile strength and Young's modulus) shows both a significantly higher bond energy (area under load-slip curve) and pull-out capacity than adhesive B. Additionally, a significant improvement of the pull-out capacity was realized when decreasing the groove width from 15 to 10 mm for adhesive A. This difference was not observed for adhesive B. Additional practical advantages of the smaller groove of 10 mm width are increased time-efficiency during installation and ~33% less material usage compared to the wider groove width of 15 mm. Due to these findings and observations, the combination of adhesive A and a groove width of 10 mm was the reference for the second batch of the experiments. The effects of an even smaller groove width than 10 mm were not investigated due to expected difficulties of milling such a small groove in the field.

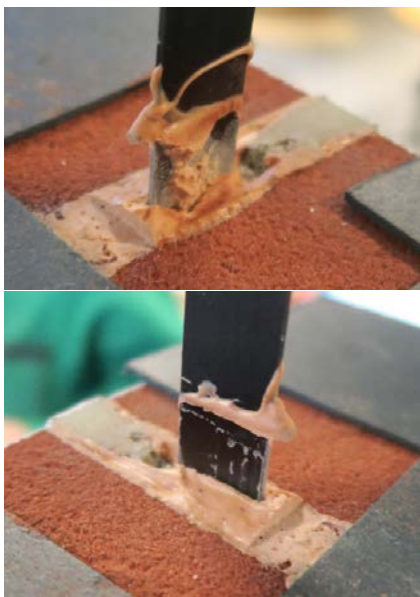


Figure 10: Typical view of loaded end after experiment 1st batch.



Figure 11: Marked hairline cracks during post-peak loading of the front (left) and back side (right).

The load-slip diagrams for the second batch of specimens are provided in Figs. 12 and 13. Comparing these diagrams with the load slip diagram of specimen(s) A-S10(-SG), an increase in

pull-out capacity of $>10\%$ was found. This finding indicated that both surface treatment methods provide a higher strength in terms of pull-out capacity to the smooth CFRP strip surface. This finding was also confirmed by the observed detachment of specimen A-RP10(-SG). Instead of a combined CFRP/adhesive interface and cohesive failure of the adhesive, cohesive failure becomes significantly more dominant (Fig. 14). For specimen A-SB10(-SG) the detachment was observed at the sand-layer/adhesive interface.

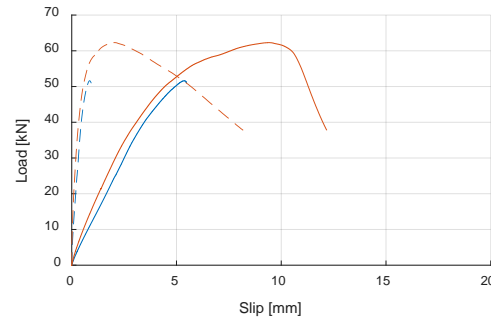
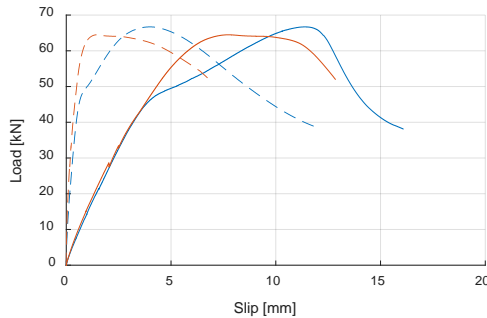


Figure 12: Load-slip diagram A-RP10(-SG) Figure 13: Load-slip diagram A-SB10(-SG)

The first test on specimen A-RP10 failed because the intended pull-out speed was not provided to the software, which resulted in the CFRP strip being pulled out significantly faster (>50 mm/min). The specimen failed at roughly 80 kN pull-out force after the tensile capacity of the CFRP was reached and the strip ruptured. This important accidental finding indicates that a higher pull-out speed has a significant influence on the bond of adhesive A.



Figure 14: Detachment of A-RP10.

Due to gripping problems, specimen A-SB10 slipped from the grips during the experiment. As the embedded region near the loaded end had most likely entered the post-peak region of the local bond-slip behaviour, the specimen was not tested again. Comparing both specimens with embedded strain gauges of this batch, it was observed that there was no significant difference in terms of pull-out capacity. Roughening the strip and adding a primer layer seemed to result in a slight increase in bond energy compared to a sandblasted strip. The former technique has an advantage in terms of application, because sanding the strip is more costly and time-consuming.

BOND DEVELOPMENT

To make a more detailed comparison between the performance of bond behaviour of the roughened/primered CFRP strip and the sandblasted CFRP strip, the development of the bond as a function of embedded length was analysed. In order to establish the local bond and slip behaviour using the embedded strain gauges, the following steps were applied. Based on the active strain gauges, a third order polynomial was constructed for the strain value over the entire embedded length for each moment of measurement (1 Hz). The location of the strain gauges installed over the embedded length of the CFRP strip is provided in Figure 2. Gauge #1 was an exception, because it was installed at the loaded end outside the masonry specimen.

The model was based on dividing the specimen into 980 elements of 1 mm length. For each element the decrease in tensile force in the embedded CFRP strips was approximated using Eq. (1). The decrease in tensile force is in equilibrium with the sum of the bond stress over the length and perimeter of the element (Eq. (2)). Combining equations (1) and (2) resulted in Eq. (3), with the assumption that the CFRP thickness was negligible compared to the width ($b_p + t_p \approx b_p$). Per element the local slip of the CFRP was calculated using the CFRP slip of the previous element, and the strain over the element (Eq. 4). The boundary condition was the slip before the first element (s_0), being the free end slip (s_{free}). Contrary to *Kashyap et al. (2012)* and *Dizhur et al. (2014)*, the calculations of the slip were based on the assumption that the axial strain in masonry and the slip at the unloaded end could not be neglected. Because of the significantly higher embedment length used in this research, the influence of the axial strain of the masonry needed to be taken into account. The tensile force in the strip is in equilibrium with the compression force in the masonry. When a uniform compression stress over the complete cross section of the specimen was assumed, Eq. 5 was found. The axial strain of the composite masonry was determined using the Young's modulus (Eq. 6). The total slip is the sum of the CFRP slip and the masonry axial strain (Eq. 7). To check whether the determined local bond and total slip was able to predict the experimental outcome, the sum of the shear forces of all the individual elements was compared to the measured pull force at the loaded end (Eq. (8)). Finally, the sum of the local slip (s_i) and the free end slip resulted in the theoretical loaded end slip (Eq. (9)).

$$\Delta F_i = (\varepsilon_i - \varepsilon_{i-1}) \cdot E_{CFRP} \cdot b_p \cdot t_p \quad (1)$$

$$\Delta F_i = \tau_i \cdot \Delta L \cdot (2b_p + 2t_p) \quad (2)$$

$$\tau_i = (\varepsilon_i - \varepsilon_{i-1}) \cdot E_{CFRP} \cdot t_p / (2 \cdot \Delta L) \quad (3)$$

$$s_{strip,i} = s_{strip,i-1} + (\varepsilon_{i-1} + \varepsilon_i) / 2 \cdot \Delta L \quad (4)$$

$$\Delta \sigma_{masonry,i} = \Delta F_i / A_{cross,masonry} \quad (5)$$

$$\sigma_{masonry,i} = \Delta \sigma_{masonry,i} + \sigma_{masonry,i-1} \quad (6)$$

$$\Delta_{masonry,i} = \sigma_{masonry,i} / E_{masonry} \quad (7)$$

$$F_{pull,theo} = \sum_{i=1}^n \Delta F_i \quad (9)$$

In order to check whether the proposed calculation steps were valid, a comparison was made between the experimental values and the theoretically calculated values for the pull-out capacity, LE slip and bond energy (Table 4). The comparison took place while the number of active strain gauges was 4 or more (as some strain gauges eventually fell out during the experiment). Looking at the difference in (Δ), no significant differences could be found for the pull-out capacity (<1.3%). The loaded end slip and bond energy showed slightly higher differences (<3.6% and <4.8% respectively), which was likely due to the deformation of the masonry.

Table 4: Experimental and theoretical comparison for pull-out capacity and bond energy.

| Specimen | Pull-out capacity (kN) | | | Loaded end slip (mm)* | | | Bond energy (J)* | | |
|-----------|------------------------|-------|--------------|-----------------------|-------|--------------|------------------|-------|--------------|
| | Exp. | Theo. | Δ (%) | Exp. | Theo. | Δ (%) | Exp. | Theo. | Δ (%) |
| A-S10-SG | 56.00 | 56.11 | +0.20 | 12.41 | 12.38 | -0.27 | 485 | 490 | +1.2 |
| A-S15-SG | 45.37 | 45.26 | -0.25 | 9.70 | 9.50 | +2.05 | 313 | 311 | -0.4 |
| B-S10-SG | 27.57 | 27.80 | +0.81 | 5.69 | 5.89 | +3.60 | 105 | 109 | +3.8 |
| B-S15-SG | 31.26 | 31.46 | +0.62 | 7.84 | 7.88 | +0.45 | 183 | 178 | -2.4 |
| A-RP10-SG | 64.47 | 65.25 | +1.26 | 8.75 | 8.97 | +2.53 | 392 | 410 | +4.8 |
| A-SB10-SG | 62.28 | 62.57 | +0.45 | 10.65 | 10.88 | +2.22 | 495 | 514 | +3.9 |

* Until the moment where 4 or more strain gauges were active.

In order to compare the results for the bond behaviour obtained from the different DPT experiments in a time-efficient way, a graphical representation of the local bond development was proposed in the form of a contour plot. The development of the local bond over the length as a function of the loaded end slip is provided in Figure 16 for specimen A-RP10-SG. The same figure also shows the pull-out force (white) as a function of the loaded end slip.

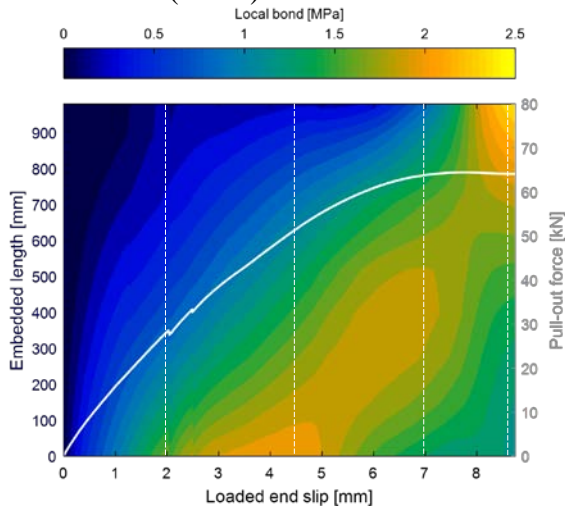


Figure 16. Contour plot of the local bond over the embedded length (coloured) and the pull-out force (white) as a function of the LE slip for A-RP10-SG.

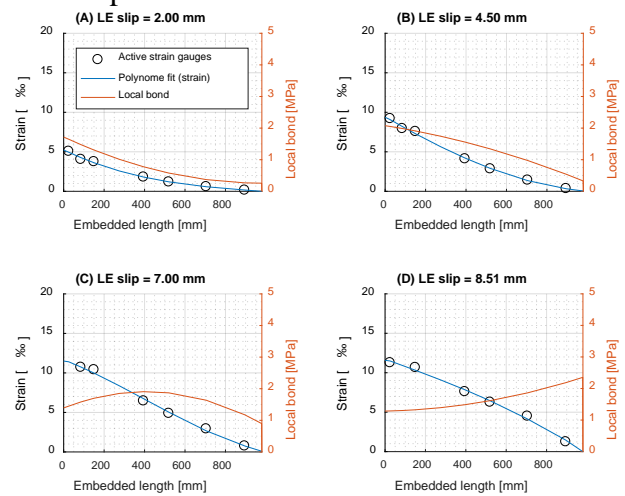


Figure 17. The active strain gauges, the polynome of the strain, and the local bond as a function of the embedded length at four different LE slips for A-RP10-SG.

In order to explain how this figure was obtained and how it should be interpreted, four different moments (indicated with the dashed vertical lines in Fig. 16) are discussed in more detail using Figure 17. At a loaded end slip of 2.00 mm (Fig. 17a) first a polynome for the strain over the embedded length was constructed (blue curve) using the active strain gauges (black circles). Using the previously explained calculation steps, the local bond over the embedded length (orange curve) can be determined. This distribution of the local bond was represented with the vertical color development at 2 mm LE slip value for the x-axis. Here it can be seen that quite early in the process, far before reaching the maximum value for local bond at the loaded end (roughly 2.0 MPa), the adhesive was activated over the entire embedded length. This observation indicates that the embedded length of nearly 1000 mm in this research was shorter than the critical bond length. Because the LE slip increased to 4.5 mm, not only does the area near the loaded end approximate

the maximum value, but the loaded end also starts to get activated more (Fig. 17b). This development can clearly be seen looking at the the region $2.0 \text{ mm} < \text{LE slip} < 4.5 \text{ mm}$ in Fig. 16. Further increasing the LE slip initiates the post-peak process in the near-loaded end area, and moves the stresses more towards the free end (Fig 17c/d). This phenomna is indicated by the shift of the yellowish area from the LE towards the FE between 4.0 mm and 8.5 mm LE slip in Fig. 16.

Looking at the calculated free end slip (7.95 mm) at the moment when the maximum pull-out force is reached for A-RP10-SG, the slip of the CFRP itself accounts for 93.4% (7.42 mm) of the total slip according to the model. This finding means that the axial strain of the masonry of 0.52 mm (6.6%) due to compression cannot be neglected during modelling.

Fig. 18a and 18b present the contour plots of the developing bond for specimens SB10-SG and S10-SG respectively. When compared with A-RP10-SG, specimens SB10-SG and S10-SG show a strong decrease of the local bond towards the loaded end, at an LE slip of about 7 mm. The dark blue regions indicate complete detachment, while for A-RP10-SG the local bond remains approximately 1.2 MPa as can be seen in Fig. 16. From the analysis it can be stated that roughening the strips and adding a primer layer seemed to evoke a significantly better post-peak behaviour when compared to the alternatives with sand-blasting or without surface treatment.

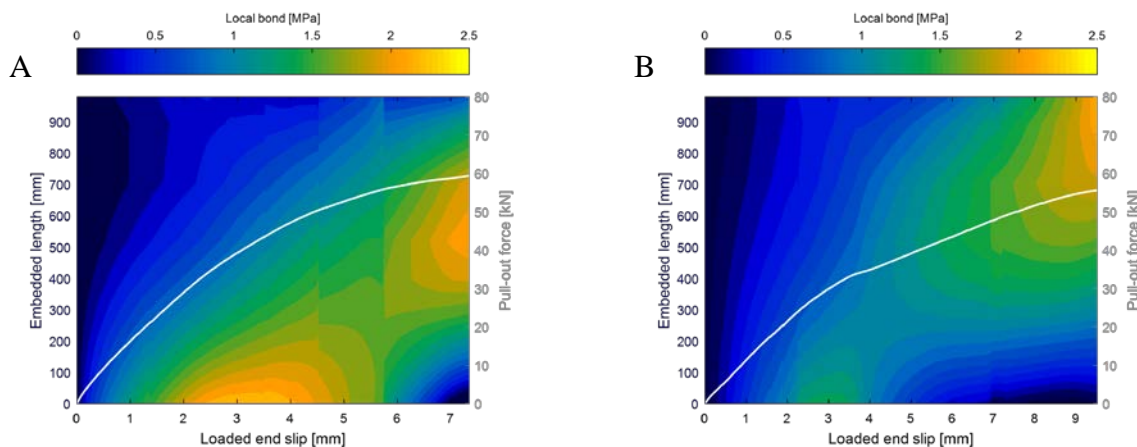


Figure 18. Contour plot of the local bond over the embedded length (coloured) and the pull-out force (white) as a function of the LE slip time for A-SB10-SG (A) and A-S10-SG (B).

COMPARISON WITH PREVIOUS RESEARCH

Looking at the database of all 82 NSM CFRP strips-to-masonry pull tests available in the open literature, the minimum value of the Young's modulus for the applied adhesives is found to be 2,000 MPa (*Seracino et al 2007; Konthesinga et al 2009; Petersen et al. 2009; Willis et al 2009; Kashyap et al. 2012; Dizhur et al 2014*). Adhesive A, which has shown the best performance in the reported study, has a Young's Modulus of only 34 MPa (nearly a factor of 60 lower).

In order to show the significant difference in bond behaviour when applying a ductile adhesive instead of a conventional stiff epoxy, as a final step the performance of A-RP10-SG was compared to specimen B1-4-15-(6/20) tested by *Dizhur et al. (2014)*. Although the two specimens are not

equal in terms of masonry properties and groove/CFRP geometry, this difference has no significant influence on the main objective of comparing the performance of the adhesives. Fig. 19 shows this comparison in the form of bond over the embedded length at the moment of maximum pull-out force. Where a conventional adhesive shows bond concentrations over a limited embedment length (peak around 9.5 MPa), the flexible adhesive used in the reported study shows a nearly uniform distribution (varying between 1-2 MPa). In contrast to the existing database of DPT tests of CFRP on masonry, this observation is the primary factor why no intermediate cracking was observed in this research.

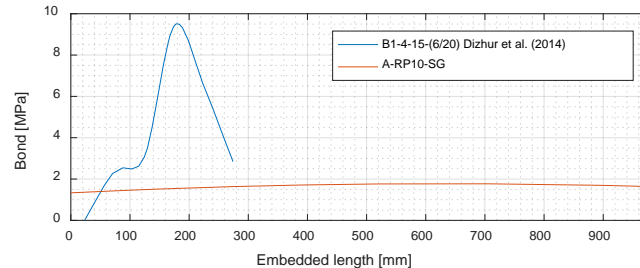


Figure 19. Bond over embedded length at maximum pull-out force for B1-4-15-(6/20) Dizhur et al. (2014) and A-RP10-SG

CONCLUSIONS

Direct pull-out tests were conducted with different flexible adhesives, groove widths and surface treatment configurations. The conclusions of the conducted research were:

1. Adhesive A (higher tensile strength and Young's modulus) performed significantly better than adhesive B for the performed DPT's, both in terms of bond energy and pull-out capacity.
2. Narrowing the groove width from 15 mm to 10 mm led to a higher bond-energy and pull-out capacity for adhesive A.
3. Despite a groove depth of 65% of the brick thickness, no premature cracking was observed. In comparable research with conventional adhesive it was observed that intermediate cracking was the leading failure mechanism at groove depths of only 30%
4. Adding a primer layer to the CFRP strip resulted in a higher pull-out capacity, as the partial CFRP/adhesive interface failure was shifted to a full cohesive failure of the adhesive. The same finding was also applicable for sand-blasted strips.
5. Analysing the bond development showed that roughening the CFRP strip and adding a primer layer not only improved the bond strength, but also advanced the post-peak behaviour when compared to the situation with no surface treatment or sand-blasted surface.
6. Adhesive A used in this study showed a near uniform distribution (1-2 MPa) over an embedded length of approximately 980 mm, where conventional adhesive showed bond concentrations (peak around 9.5 MPa) over a limited embedment length of < 300 mm).
7. Adhesive A used in this study has a significantly lower (factor 60) Young's modulus when compared to the values for the modulus of elasticity found for the used adhesive in the database of all 82 previously conducted NSM CFRP strip-to-masonry pull tests (> 2,000 MPa).
8. The critical bond length for adhesive A was not reached for a 980 mm anchorage length.

9. Contrary to previous research, the axial strain of the masonry could not be neglected when applying a flexible adhesive, as the bond length was significantly higher.
10. The speed at which the DPT was conducted had a major influence on the bond behaviour for adhesive A, as it was found that the adhesive behaves stronger and stiffer.
11. A graphical representation of the local bond development over time was proposed in the form of a contour plot, so that the results from the different DPT experiments could be compared in a time-efficient way for the bond behaviour.

RECOMMENDATIONS

The first recommendation in order to get more insight on the bond slip behaviour of DM CFRP strips confined with a ductile adhesive in clay brick masonry is to conduct more DPT's where the pull-out speed is varied. Secondly, LVDT's should be installed over the height of the masonry specimens to determine the axial strain during the experiment, because the influence of this parameter cannot be neglected. Thirdly, BPT's should be conducted in order to also take flexural behaviour into account. Fourthly, cyclic loads should be applied to investigate degradation effects. Finally, both FE and mechanical models should be developed for engineering purposes.

ACKNOWLEDGEMENTS

The authors wish to thank and acknowledge Royal Oosterhof Holman and SealteQ Group for supporting this research into the behaviour of CFRP reinforcement with ductile adhesive.

REFERENCES

- de Waal, J. A., Muntendam-Bos, A. G., and Roest, J. P. A. (2015). Production induced subsidence and seismicity in the Groningen gas field – can it be managed? *Proc. IAHS*, 372, 129-139.
- Türkmen, Ö.S., Vermeltfoort, A.T. and Martens, D.R.W. (2016). Seismic retrofit system for single leaf masonry buildings in Groningen. *Proceedings of 16th International Brick and Block Masonry Conference*, June 27-29, Padova, Italy.
- Türkmen, Ö.S., Vermeltfoort, A.T., Wijte, S.N.M., Martens, D.R.W. (2017). Experiments to determine the out of plane behaviour of CFRP and ductile adhesive reinforced clay brick masonry walls. *Proceedings of 13th Canadian Masonry Symposium*, June 4-7, Halifax, Canada.
- Wijte, S.N.M., Türkmen, Ö.S., Vermeltfoort, A.T., Martens, D.R.W. (2017). Analytical modelling of the out of plane behaviour of CFRP and ductile adhesive reinforced clay brick masonry walls. *Proceedings of 13th Canadian Masonry Symposium*, June 4-7, Halifax, Canada.
- Vermeltfoort, A.T. (2015). Tests for the characterization of original Groningen masonry under compression and shear loading, Eindhoven University of Technology.
- Willis, C.R., Yang, Q., Seracino, R., Griffith MC. (2009). Damaged masonry walls in two-way bending retrofitted with vertical FRP strips. *Constr Build Mater*; 23:1591–604.

Dizhur, D., Griffith, M.C., Ingham, J.M. (2014). Pullout strength of NSM CFRP strips bonded to vintage clay brick masonry. *Engineering Structures*, Volume 69, pp. 25-36

International Organization for Standardization (2012). *Plastics - Determination of tensile properties*. DIN EN ISO 527.

International Organization for Standardization (1995). *Aerospace series - Carbon fibre reinforced plastics - Unidirectional laminates - Tensile test parallel to the fibre direction*. DIN EN 2561.

German Institute for Standardization (1998). *Products and systems for the protection and repair of concrete structures - Test methods - Determination of compressive strength of repair mortar*. DIN EN 12190.

German Institute for Standardization (2006). *Products and systems for the protection and repair of concrete structures - Test methods - Determination of modulus of elasticity in compression*. DIN EN 13412.

Kashyap, J., Willis, C.R., Griffith, M.C., Ingham, J.M., Masia, M.J. (2012). Debonding resistance of FRP-to-clay brick masonry joints, *Engineering Structures*, Volume 41, pp. 186-198

Seracino, R., Jones, N.M., Ali, M.S.M., Page, M.W., Oehlers, D.J. (2007). Bond strength of near surface mounted FRP strip-to-concrete joints. *J Compos Constr*;11:401–9.

Konthesingha, K.M.C., Masia, M.J., Petersen, R.B., Page, A.W. Bond behaviour of NSM FRP strips to modern clay brick masonry prisms under cyclic loading (2009). 11th Canadian masonry symposium. Toronto, Canada: McMaster University/Canadian Masonry Design Centre; p. 665–74

Petersen, R.B., Masia, M.J., Seracino, R. (2009). Bond behaviour of near-surface mounted FRP strips bonded to modern clay brick masonry prisms: influence of strip orientation and compression perpendicular to the strip. *J Compos Constr*;13:169–78.

HERITAGE HOTEL CASE STUDY: SEISMIC RETROFIT OF AN UNREINFORCED MASONRY BUILDING PRIOR TO THE CANTERBURY EARTHQUAKES

N. A. Misnon^{1,2}, S. Abeling¹, J.Hare³, R. Jafarzadeh⁴, J. M. Ingham⁵ and D. Dizhur⁵

¹ PhD Student, Department of Civil and Environmental Engineering, The University of Auckland, 1142 Auckland, New Zealand, nmis681@aucklanduni.ac.nz; sabe321@aucklanduni.ac.nz

² Lecturer, Department of Civil Engineering, Universiti Pertahanan Nasional Malaysia, 57000 Sg Besi, Kuala Lumpur, Malaysia. nooraina@upnm.edu.my

³ CEO, Holmes Group Limited, Level 2, 254 Montreal Street Christchurch Central, PO Box 6718 Christchurch 8442 New Zealand, johnh@holmesgroup.com

⁴ Service and Asset Planning Specialist-Seismic Retrofit Modelling, Service and Asset Planning Team, Auckland Council, Auckland New Zealand, re_djafarzadeh@yahoo.com

⁵ Professor/Lecturer, Department of Civil and Environmental Engineering, The University of Auckland, 1142 Auckland, New Zealand, j.ingham@auckland.ac.nz; d.dizhur@auckland.ac.nz

The Heritage Hotel (aka Old Government Building) is a prominent unreinforced masonry Italian High Renaissance palazzo building located in Christchurch, New Zealand, that is listed as a Category I historic place. In 1991 the Christchurch City Council purchased the building to prevent its demolition and to preserve its historical significance to the city. In 1995 the Heritage Hotel building was seismically retrofitted to fully meet the NZ Building code (NZS 4203:1992). The retrofit work included partial building demolition, installation of new structural lateral load-resistant systems, and the retrofit and refurbishment of individual building elements. The total cost of the retrofit and refurbishment in 1995 was approximately NZ\$3.75 million. Detailed observations following the 2010/2011 Canterbury earthquakes showed that the building was subject to only minor damage after the September 2010 earthquake. While the February 2011 event caused some damage to exterior stonework and flooding in the basement due to liquefaction, the damage was easily repaired and the building was fully functional by September 2013. The seismic retrofit of the Heritage Hotel allowed for an important heritage aspect of the city to be retained for future generations. Reported herein are details of the seismic retrofit and post-earthquake performance observations.

Keywords: *Seismic retrofit, refurbishment, masonry building, Canterbury earthquakes, heritage building*

INTRODUCTION

Unreinforced masonry (URM) buildings are well known to be vulnerable structures when subjected to earthquake shaking, due to their rigidity and limited capacity to deform. Moderate shaking from earthquakes can cause failure of URM buildings, resulting in catastrophic collapse and potential fatalities. In the February 2011 Christchurch earthquake, 22 URM buildings caused one or more fatalities, with most of the deaths caused by the collapse of URM components such as chimneys and parapets (Canterbury Earthquake Royal Commission, 2012). URM buildings were reported as the most severely affected structural type following the 2010/2011 Canterbury earthquake sequence, and more than 50% of assessed URM buildings were tagged with red placards, indicating that the building had experienced severe damage (Moon et al., 2014). A Canterbury Earthquakes Royal Commission report (2012) presents details of damage to URM buildings.

The 2010/2011 Canterbury earthquakes also revealed success stories of URM buildings that were seismically retrofitted before the earthquake sequence to an adequate strengthening level, which is measured using %NBS (percentage of new building standard). Most retrofitted URM buildings with %NBS greater than 67% were reported to survive the earthquake events with insignificant or moderate levels of overall building damage (Moon et al., 2014). Bailey et al. (2014), Dizhur et al. (2015), and Misnon et al. (2016) report case studies of URM buildings retrofitted with traditional methods as well as new retrofit technologies such as steel bracing and fibre reinforced polymer (FRP) respectively, that performed well in the 2010/2011 Canterbury sequence. The aforementioned case studies indicate the importance of seismic retrofitting of URM buildings to aid in minimising earthquake damage.

A case study of the Heritage Hotel is reported herein, being a seismically retrofitted URM building that performed well in the 2010/2011 Canterbury earthquakes. Prior to the 2010/2011 Canterbury earthquakes the Heritage Hotel was seismically retrofitted to fully meet NZS 4203:1992 (100% NBS), and the building performed well with no significant structural damage observed following the September 2010 and February 2011 events (Gin & Galloway, 2011). Details of the building acquired from interviews and council files after the 2010/2011 Canterbury earthquakes are presented herein.

BUILDING DESCRIPTION

The Heritage Hotel (previously known as the Old Government Building) is a prominent URM building in the Italian High Renaissance palazzo style that is located in the Central Business District (CBD) of Christchurch, New Zealand. The iconic heritage building was originally designed in 1909 by J.C. Maddison and is listed as a Category 1 historic place by Heritage New Zealand (Johnson et al., 1986; Yonge, 1997).

The building is constructed of unreinforced mixed masonry and has a rectangular plan with exterior dimensions of approximately 80 metres by 21 metres and a height of 18 metres (Figure 1a,b). The building was originally constructed with a basement and three floors that had ceiling heights up to 5.4 metres. The foundation of the building is comprised of closely-spaced 7.5 metre precast driven reinforced concrete (RC) piles, with the exception of the west elevation, which has 5.5 metre piles (Johnson et al., 1986). The building has loadbearing clay-brick URM walls. The first and upper floors of the building are URM composed of smooth red solid bricks. The north and west elevations (both street-facing elevations) have heavily

rusticated limestone covering the brickwork at the first floor. The internal and external brick walls are up to 1.1 and 0.9 metres thick, respectively (Johnson et al., 1986; Hare, 1996).

The floors were originally constructed of heavy timber, with the exception of the vaults and toilets, which had concrete floors with thicknesses of 0.45 and 0.25 metres, respectively. The roof of the building originally was constructed of lightweight concrete approximately 0.25 metres thick and had a stone parapet up to 5 metre in height along the perimeter (Johnson et al., 1986; Hare, 1996). On the west façade, Tuscan columns (plain columns without carvings or ornament) span two storeys to support the roof of the distinct main entrance. The building façade is inspired by the Classical style and has regular and symmetric window placement, Corinthian columns, and a heavy balustrade and parapet. The first-floor façade is adorned with dressed limestone, creating a rusticated base and the second- and third-floor façades feature smooth red clay brick and finer detailing (Yonge, 1997).



(a) Exterior view of north elevation



(b) Exterior view of west elevation

Figure 1: Heritage Hotel, 30 Cathedral Square

The most significant interior heritage feature of the building is a central staircase that rises to the full height of the building with landings composed of RC. The staircase is divided on each floor by a long corridor (also a heritage feature) extending from east to west, as shown in Figure 2.



Figure 2: The staircase landing at the centre of the building (image reproduced from Yonge et al., 1997)

BUILDING HISTORY

The Heritage Hotel building was initially constructed to accommodate government offices following the establishment of Christchurch as the capital of the Canterbury District (Johnson et al., 1986). Construction began on 20 November 1911 and was completed in March 1913 (see Figure 3). The building housed government offices for approximately 70 years (Yonge, 1997). After the 1960s, the building experienced a series of natural disasters, including earthquakes and storms, that resulted in damage. An earthquake with moment magnitude M_w 5 occurred on January 1968, causing plaster damage and masonry cracking to the building. The Wahine Storm occurred in April 1968, and an earthquake the following month triggered the development of additional cracks throughout the building. In the early 1970s, noticeable settlement occurred in the southwest corner and was attributed to increased ground motion due to the construction of the nearby Carruca House and Housing Corporation buildings (Johnson et al., 1986; Yonge, 1997).



Figure 3: The Heritage Hotel building in 1913 (courtesy of Christchurch City Libraries)

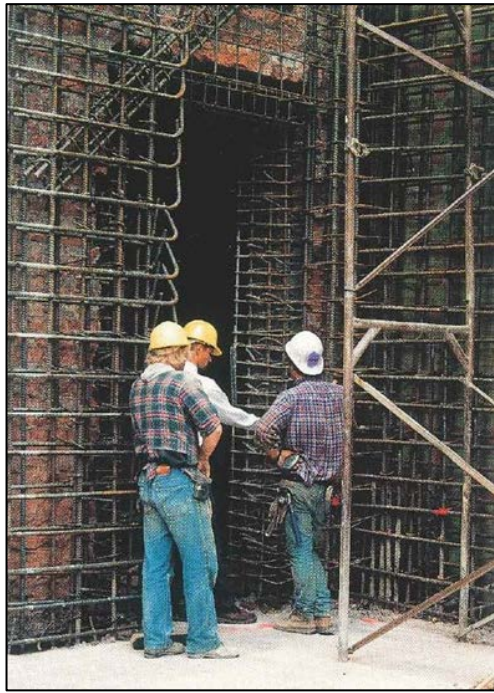
Work was undertaken between the 1960s and 1980s to seismically strengthen the building and repair both internal and external wall damage. The 1960s retrofit work included the removal of the 450-tonne stone parapet and the installation of a smaller RC parapet as well as strengthening the floor to wall connections. Nuralite asbestos cement roofing and standing-seam galvanized roofing were used to weatherproof parts of the main roof of the building in 1979. In 1980, two damaged masonry columns with substantial diagonal shear cracking were replaced with steel substitutes, and significant cracks to the exterior and interior walls were repaired by adding steel ties to the exterior faces and at the south-west roof level (Johnson et al. 1986; Yonge, 1997).

The building was partially occupied for approximately eight years from late August 1980 to 1988, when it was vacated. After remaining vacant for almost three years, demolition was proposed in March 1991 on the basis of a structural assessment by the Ministry for Works and Development (Yonge, 1997). However, strong public support for saving the building influenced the Christchurch City Council (CCC) to purchase it in July 1991 for NZ\$735,000 (Yonge, 1997). Numerous new use options were proposed, including an art museum, movie theatre, casino, and office space. In 1995 a plan for serviced and residential apartments was agreed upon and extensive strengthening and restoration works were undertaken.

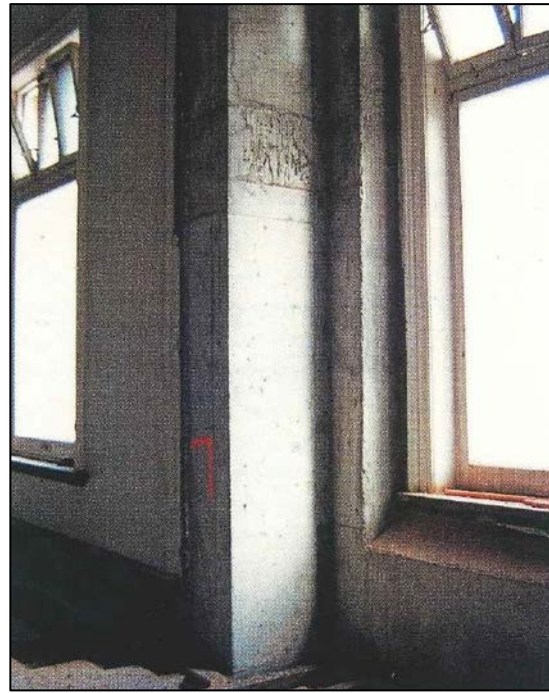
SEISMIC RETROFIT

The Heritage Hotel was originally designed with minimal consideration of lateral loads, specifically seismic loads, and thus a series of natural disasters resulted in damage to and deterioration of the building. After CCC purchased the building, options to seismically retrofit the building were proposed with the aim of improving the structural integrity of the building whilst minimising intrusive intervention to heritage elements (Hare, 1996; Yonge, 1997). Seismic retrofit and refurbishment work was undertaken in 1995 to strengthen the Heritage Hotel to 100% of the NZS 4203:1992 code.

The seismic design work involved partial demolition of the building (Areas 1 and 2 in Figure 4b), followed by the construction of strong RC shear walls in these areas (Figure 5a). These areas were chosen because they previously held toilets and vaults and were deemed to be



(a) New strong RC shear walls act as shear cores anchored back to the building



(b) Example of the addition of an RC skin wall at building corners

Figure 5: Retrofit and refurbish work in 1995 (images reproduced from Yonge, 1997)

The extensive diaphragm upgrading was a key part of the project. Hollowcore concrete flooring with a 100 mm topping was constructed in the new shear core areas, to form rigid diaphragms. The existing timber flooring was strengthened with a new heavily nailed plywood overlay. The timber diaphragms were tied to the shear cores with heavy steel flats running through the floor and into the shear walls. The roof was retrofitted with an RC topping over the existing slab, and a concrete bond beam was cast around the perimeter of the roof.

A new lightweight fibreglass-reinforced cement parapet that replicated the original parapet design was constructed above the bond beam, and steel uprights were cast to support the parapet.

Following demolition of the vault, the existing foundation piles were found to be well reinforced although they had only a compression connection to the existing mass concrete foundation. Thus, new foundation beams were installed where required to sustain loads under the new RC shear walls, with detailing to utilise the full capacity of existing piles and minimise the number of new piles required.

The stone columns of the west façade were diamond cored to their full height, and lightly prestressed cables were inserted to control cracking and provide additional strength. The cables were tied into the foundation and concrete caps were added to the tops of the columns. The retrofit design protected the iconic building façade and the historic central staircase. Full advantage was taken of the existing floor to floor height by adding partial mezzanines to most of the rooms, set back from the heritage façade to avoid visual intrusion. New steel beams were inserted into existing timber floors to support the partial mezzanine levels, and the steel beams were used as floor ties where possible to distribute wall anchor forces into the diaphragm. The

total cost of the retrofit was estimated to be \$3.75 million in 1995, which was approximately the same cost for a new building of similar structural layout at the time.

BUILDING PERFORMANCE FOLLOWING THE 2010/2011 CANTERBURY EARTHQUAKES

A detailed damage assessment of the Heritage Hotel was undertaken immediately following the 2010/2011 Canterbury earthquakes. The assessment was conducted in accordance with guidelines recommended by the New Zealand Society for Earthquake Engineering (NZSEE). The evaluation was initiated to conduct an overall damage assessment, followed by rapid building assessment (NZSEE, 2009).

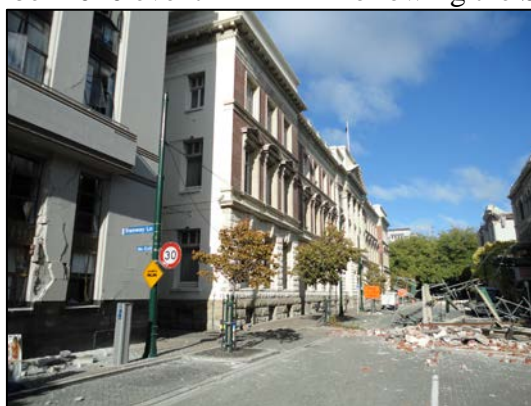
Only minor cracking damage was reported following the September 2010 event, and the building remained operational. Cracks to the external stonework were the most noteworthy damage to the building following the September 2010 event (Figures 6a, b). The building also survived the February 2011 earthquake, with only minor cracking in the URM walls and the south elevation core wall and moderate damage to external stonework observed, both of which were easily fixed. The basement was flooded with water due to liquefaction. The building could have remained operational following the earthquakes, but damage to neighbouring buildings prevented its reopening until late 2013 (Figure 6c).



(a) Small cracks in the exterior stone following the September 2010 event



(b) Crack opening in the exterior stone following the September 2010 event



(c) View of the building following the February 2011 event. The Heritage Hotel survived while buildings nearby collapsed, leaving brick debris on the street

Figure 6: Heritage Hotel damage following the 2010/2011 Canterbury earthquakes

SUMMARY AND CONCLUSIONS

The Heritage Hotel is a registered Category I historic place that represents one of very few successful examples of a seismically retrofitted heritage building in Christchurch. This URM building housed government offices for about 70 years before it was converted to serviced and residential apartments following retrofit work undertaken in 1995 that brought the building to full seismic code at the time of the retrofit work. The important heritage elements had minimal intervention due to partial demolition of areas of low heritage value and the construction of a shear core. The building survived earthquakes in September 2010 and February 2011 with only minor cracks and damage that were quickly repaired. The Heritage Hotel reopened in September 2013 and remains operational to the present.

ACKNOWLEDGEMENTS

This project was supported by QuakeCoRE, a New Zealand Tertiary Education Commission-funded Centre. The authors gratefully acknowledge the assistance of Katie Eberle, a student intern from California Polytechnic State University, San Luis Obispo. The first author also thanks the Ministry of Education, Malaysia for supporting her PhD study at the University of Auckland.

REFERENCES

- Bailey, S., Dizhur, D., Trowsdale, J., Griffith, M., and Ingham, J. M. (2014), Performance of posttensioned seismic retrofit of two stone masonry buildings during the Canterbury earthquakes, *Journal of Performance of Constructed Facilities*, 29(4), pp 1-11.
- Canterbury Earthquakes Royal Commission. (2012), Final Report, Volumes 4. *Canterbury Earthquake Commission, Christchurch, New Zealand*.
- Dizhur, D., Bailey, S., Griffith, M., and Ingham, J. (2015), Earthquake performance of two vintage URM buildings retrofitted using surface bonded GFRP: case study, *Journal of Composites for Construction*, 19(5), pp. 1-9.
- Gin, V., and Galloway, B. (2011), *Heritage hotel - Old Government Building (OGB) Structural Report*, Christchurch: Holmes Consulting Group Limited.
- Hare, H. J. (1996), Case Study: Christchurch Government Buildings Strengthening and Refurbishment, *Bulletin of The New Zealand National Society for Earthquake Engineering*, 29 (3), pp. 141-146.
- Ingham, J. M., Biggs, D. T., and Moon, L. M. (2011), How did unreinforced masonry buildings perform in the February 2011 Christchurch earthquake?, *Structural Engineer*, 89(6), pp. 14-18.
- Johnson, R. D., Lochhead, I., Shapcott, P. M., and Shaw-Brown, D. (1986), *The Architectural Heritage of Christchurch 5. Government Buildings*, Christchurch City Council, pp.15
- Misnon, N. A., Dizhur, D., Mackenzie, J., Abeling, S., and Ingham, J. (2016), Evaluation of Seismically Retrofitted Masonry Substation Buildings, *Proceeding of Australian Earthquake*

Engineering Society (AEES) 2016 Conference, 25-27 November, Melbourne, Vic.

Moon, L., Dizhur, D., Senaldi, I., Derakhshan, H., Griffith, M., Magenes, G., and Ingham, J. (2014), The Demise of the URM Building Stock in Christchurch during the 2010-2011 Canterbury Earthquake Sequence, *Earthquake Spectra*, 30 (1), pp. 253-276.

New Zealand Society for Earthquake Engineering. (2009), Guidelines for Building Safety Evaluation during a State of Emergency. Guidelines for Territorial Authorities. Retrieved from <http://www.nzsee.org.nz/Guidelines/BuildingSafetyEvaluationAug09.pdf>

NZS 4203. (1992), Code of Practice for General Structural Design and Design Loadings for Buildings, Standards New Zealand.

Yonge, M. (1997), Government Buildings Christchurch, 1909-1996, Everbest Printing Co. Ltd., 63pp.

THE CHALLENGES OF DEVELOPING A BOND MODEL FOR FRP TO MASONRY JOINTS—A CLOSER LOOK AT EXISTING TEST RESULTS AND LIMITATIONS OF EXPERIMENTAL DESIGN

J. Vaculik¹, P. Visintin² and M.C. Griffith³

¹ Research Associate, School of Civil, Environmental and Mining Engineering, The University of Adelaide, SA 5005, Australia, jaroslav.vaculik@adelaide.edu.au

² Senior Lecturer, School of Civil, Environmental and Mining Engineering, The University of Adelaide, SA 5005, Australia, phillip.visintin@adelaide.edu.au

³ Professor, School of Civil, Environmental and Mining Engineering, The University of Adelaide, SA 5005, Australia, michael.griffith@adelaide.edu.au

A state-of-the-art review of past experimental research on the bond between FRP composites and masonry substrates was recently performed, identifying some 50 separate studies performed since the early 2000s. Through this process, a database of over 1300 individual tests has been compiled, covering a range of substrates including clay brick, natural stone and concrete block; a range of FRP materials including CFRP (carbon), GFRP (glass), BFRP (basalt), and SRP (steel); and a mixture of externally-bonded and near-surface-mounted retrofits.

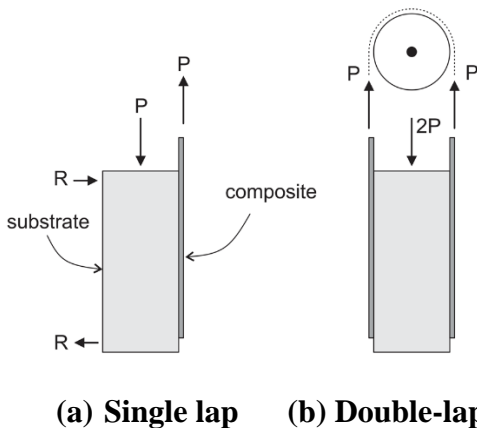
However, despite the large number of tests to date, there are numerous issues that hinder the use of the published data toward the development of a material bond model for design of FRP-to-masonry retrofits. These relate to the inconsistency in test setup and instrumentation, completeness of reporting, and robustness of techniques for extracting local bond properties. A discussion of these limitations is the objective of this paper.

Keywords: *URM, FRP, retrofit, bond model, pull-test*

INTRODUCTION

A significant portion of the world's building stock is comprised of unreinforced masonry (URM) construction, including the majority of historical buildings. Unfortunately, URM construction is particularly vulnerable under seismic loading due to its low tensile strength and heavy mass. A popular method of strengthening unreinforced masonry structures against seismic loads is through adhesive bonding of fibre-reinforced polymers (FRP). The function of FRP retrofits is to provide tensile reinforcement, which can strengthen URM against both in-plane shear as well as out-of-plane flexure (Turco et al, 2006; Willis et al, 2010; Griffith et al, 2013; Konthesingha et al, 2015).

FRP retrofit efficiency is largely controlled by the ability to transfer shear force across the bond between the FRP (hereafter referred to as 'plate') and the masonry substrate. The most widely used test technique for studying the interfacial bond properties is the pull-test, as shown in Figure 1. The basic procedure involved in this test is to adhesively bond an FRP plate to the substrate (brick or masonry) and progressively apply an increasing end slip Δ (via the load P) until shear debonding occurs.



(a) Single lap (b) Double-lap

Figure 1: Common pull-test arrangements

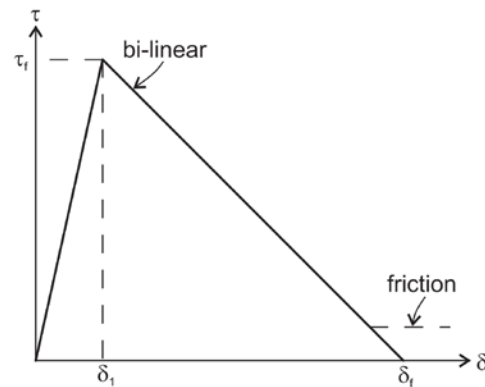


Figure 2: Example of local shear-slip bond model (bilinear model)

The general objective of pull-tests is to investigate the constitutive shear stress versus shear slip (τ - δ) behaviour at the bond interface. Once a τ - δ model is fitted to the experimentally observed behaviour—for example by means of the bilinear model shown in Figure 2—it may be used to predict properties relevant toward design. This can include the debonding load capacity, required anchorage length, and the global load-slip (P - Δ) relationship.

As part of recent work at the University of Adelaide, a large-scale state-of-the art review was undertaken which assembled an experimental database of some 1300 individual pull-tests from approximately 50 studies performed over the past 20 years (Vaculik et al, 2017b). For a full list of these studies the reader is referred to the mentioned paper by the authors. This review has identified that testing to date has covered various combinations of the following:

- Methods of bonding, namely externally-bonded (EB) and near-surface-mounted (NSM) retrofits;

- Masonry materials, including clay brick, concrete block, as well as different varieties of natural stone;
- FRP composite materials, including carbon (CFRP), glass (GFRP), basalt (BFRP), aramid FRP (AFRP), as well as steel-reinforced polymers (SRP).

However, although the amount of experimental work to date has been substantial, the lack of consistent testing methodology and data analysis technique has somewhat impeded the development of generalised material models necessary for codified design (e.g. ACI, 2010; CNR, 2013). The discussion of these issues is the main focus of this paper.

OVERVIEW OF DATABASE

As identified in Vaculik et al (2017b), the majority of existing experimental bond research between FRP and masonry substrates originates from Italy (approx. two thirds), with other notable contributions coming from Portugal, Australia, Poland, Canada, and New Zealand. Notably, the two round robin studies reported in Valluzzi et al (2012) and de Felice et al (2016), as well as the study by Rotunno et al (2015) encompass almost half of all individual tests.

The remainder of this section discusses the scope of the database in terms of test specimens and arrangement. The reader should note that the assembly of the database (≈ 1300 individual tests) described here is ongoing, and thus the quoted percentages of the total number of individual tests are approximate only. For finalised values the reader is referred to Vaculik et al (2017b).

Substrate Types

Clay brick has been the most commonly investigated substrate, covering $\approx 85\%$ of tests. The remainder covers natural stone and concrete blockwork. The fact that such large proportion of experimental work comes from Italy is due to the country's high seismicity and large stock of historically structures. Therefore, there is an expected bias in the work to date toward brick and stone varieties found in this region.

Pull-tests where the prism comprised merely the masonry unit (brick or block) cover $\approx 75\%$ of tests (e.g. Figure 3a). The remainder of tests were performed on masonry prisms built with a combination of the unit plus mortar (e.g. Figure 3b).



(a)



(b)

Figure 3: Pull-tests being undertaken at the University of Adelaide involving NSM GFRP bars embedded in clay brick masonry: (a) short bonded length unit prisms, (b) masonry prisms.

FRP Retrofit Types

The most commonly investigated type of retrofit material has been carbon-FRP comprising approximately half of tests to date. This is followed by glass-FRP which forms about one quarter of tests. The remaining tests investigated basalt-FRP, aramid-FRP, as well as steel-reinforced polymers (SRP).

The range of retrofit types include mainly externally bonded sheets ($\approx 90\%$) followed by NSM strips ($\approx 8\%$). The remainder comprises NSM circular rods and EB strips.

It is worth noting that of the NSM retrofits, the research to date has focused only on clay brick masonry.

Test Arrangement

The pull-test arrangement can be broadly classified into either single-lap or double-lap as shown in Figure 1. In terms of number of tests to date, the spread between single and double lap tests has been approximately even, although the single-lap arrangement has been slightly more commonly used.

The single-lap test (Figure 1a) is the simpler of the two arrangements and has the advantages of the specimens being easier to manufacture and the test being simple to perform. In the most commonly used approach, the plate is actively pulled while an abutting block is used to restrain the prism. The main disadvantage of this arrangement is that eccentricity of the loading produces internal shear

and non-uniform strain profile across the section, which if large enough can affect the slip at the interface. However, these conditions can also be considered representative of wall flexure, and are therefore not unrealistic of typical application of FRP retrofits—i.e. strengthening walls against out-of-plane bending. Furthermore, care should be exercised in the test set-up to ensure alignment between the loading mechanism and the axis of the plate in order to eliminate normal stresses at the FRP-substrate interface.

In the double-lap test (Figure 1b), FRP plates are bonded to opposite faces of the prism and pulled simultaneously. The main benefit of this arrangement is that it removes loading eccentricity and thus minimises flexural strain across the section. The arrangement, however, can introduce other unfavourable effects. For example, the double lap test is commonly performed by looping a single FRP sheet over a pulley as shown in Figure 1b. This causes both laps to be subjected to equal load. However, stochastic variability in local bond properties means that one side will debond before the other. Therefore the specimen needs to be rotationally restrained, otherwise it can suddenly rotate and cause peeling in the non-failed side. Moreover, in such tests it is common practice to determine the debonding load capacity as half the total applied load. Whilst this is correct for the specimen, the fact that the test only ever measures the strength of the weaker side means that conservative bias enters into the results. Addressing this bias would require application of order statistics in the processing of the results; however, to the authors' knowledge, this is not generally done. In this pulley arrangement (Figure 1b), the fact that the stronger side begins to unload once the weaker side achieves its peak load means that loaded-end slip cannot be accurately measured in the post-peak response range.

A small subset of double-lap tests encountered used a double-block arrangement involving either pulling or pushing apart a pair of double-lap prisms. The main advantage of this type of setup is that if the two substrate blocks are directly abutted, then the unbonded length of plate (L_u in Figure 4) becomes minimised. This condition creates what is arguably the most realistic representation of behaviour across a flexural crack in the various test arrangements considered and also leads to minimisation of any snap-through due to build-up of strain energy in the plate (discussed later). However, because such a test arrangement effectively embodies four individual lap joints, an even more severe statistical bias becomes introduced into the test results.

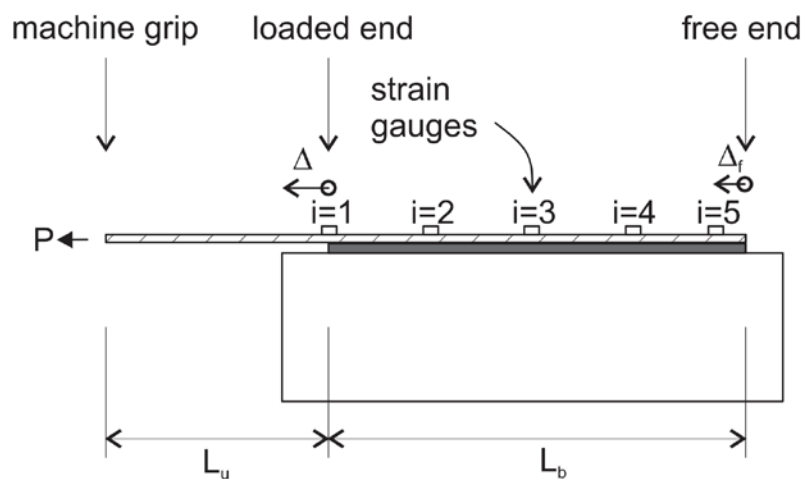


Figure 4. Measurement of axial deformation along the specimen.

Snap-through effect

In order to be able to observe the post-peak response in the load-slip response, any experimental design should attempt to minimise the unbonded length of the FRP plate between the loaded end and the machine grip (L_u as shown in Figure 4). Otherwise, if the flexibility of the plate over the length L_u is too large, reaching peak load can generate a “snap-through” effect as a consequence of elastic strain energy accumulation within the plate. This effect becomes manifested as a sudden jump in slip at the loaded end, which makes the post-peak behaviour unobservable.

Avoidance of premature failure

A basic requirement of the usability of pull-tests toward the development of bond models is that failure occurs through debonding between the FRP plate and substrate. Therefore mitigation of any other forms of premature failure such as FRP rupture is an important consideration in experimental design. Whilst complete elimination of premature failure cannot always be achieved, it should be noted that simply discarding such test results from the data pool leads to bias in the inferred statistics toward underestimating the bond strength.

Instrumentation techniques

As shown in Figure 4, the various forms deformation measurement in a pull-test include strain in the plate (ϵ_p), slip between the plate and substrate at the loaded end (Δ), and slip at the free end (Δ_f). Unfortunately, there is considerable inconsistency in terms of the methods used throughout the tests to date. The form of deformation measurement has important implications toward the method of data analysis as will be discussed in the following section, ‘Approaches for analysis of experimental data’.

The most common method of strain measurement is via strain gauges which provide readings at discrete points along the FRP plate; however, continuous readings using methods such as digital image correlation have become more common over recent years. The main purpose of measuring the strain profile is that it can be differentiated to obtain the shear stress (τ) profile and integrated to obtain the slip (δ) profile along the specimen. By plotting the distribution of τ versus δ allows for a direct means of observing the bond-slip behaviour at the interface. However, the accuracy of this technique is strongly reliant on measurement of a reference slip along the specimen, and the use of strain gauges can also give rise to various complications. For example, the placement of strain gauges directly along the bonded interface can disturb the local bond and thus influence the measurement. This practice should therefore be avoided if possible. Furthermore, local variations in the stiffness of the material or presence of nearby cracks can also influence the gauge readings and thus introduce error.

The measurement of slip (Δ in Figure 4) is also particularly important, since the resulting readings are used in both methods of local bond property extraction (strain gauge readings and inverse analysis) to be discussed in the following section. Unfortunately, review of past works has also encountered inconsistency in the location along the specimen where the reported slip was measured. Although most studies encountered report load-slip curves using the loaded-end slip (Δ) (as shown in Figure 5), other works have instead taken the slip at the machine grip location (refer to Figure 4). It is the authors’ view that ‘slip’ should always refer to the slip at the location at the

loaded end (Δ in Figure 4) to ensure a standardised approach for reporting of results. This would furthermore mean that experimental load-slip plots remain consistent with the convention used in derivation of analytical P- Δ solutions (e.g., Yuan et al, 2004; Caggiano et al, 2012; Vaculik et al, 2017a). Notably, performing a transformation between slip at the machine grip and loaded end is relatively straightforward by calculating the elastic elongation of the unbonded length of FRP (L_u in Figure 4) between the two locations as a function of the applied load.

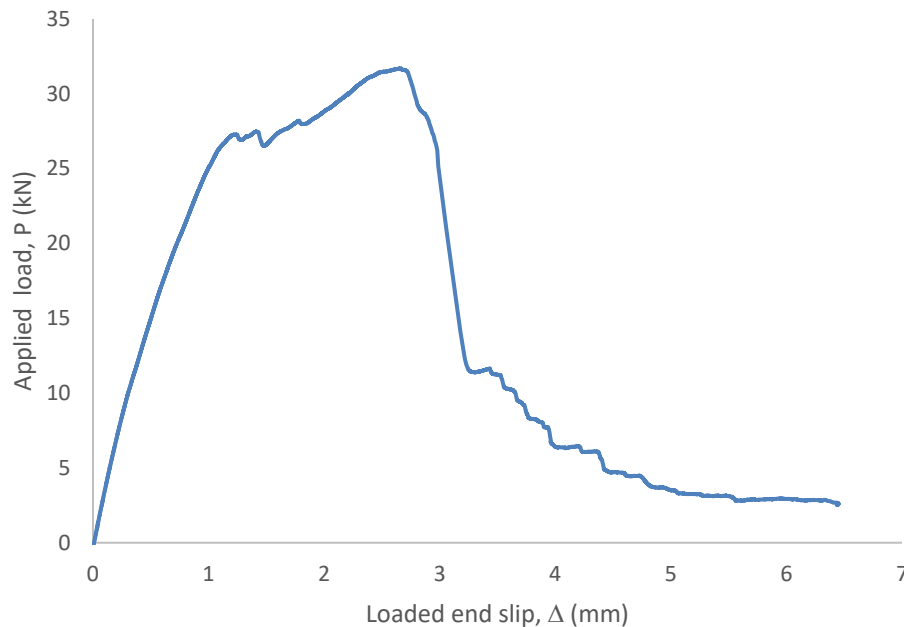


Figure 5: Example of typical experimental load-slip response in a pull-test involving NSM retrofit in clay brick masonry (tests currently underway at the University of Adelaide for the arrangement shown in Figure 3).

Completeness of reporting

Unfortunately, the review undertaken has identified inconsistency in the completeness of reporting in the published works. For example, the compressive strength of the substrate was reported for only $\approx 80\%$ of individual tests, and the elastic modulus for $\approx 60\%$ of tests. The geometry of the test prisms was also often not reported which means that the axial rigidity of the substrate could only be determined in less than 60% of individual tests. Fundamental FRP properties including plate dimensions were also found to be missing in a small number of works.

That these fundamental properties were not reported is significant, because it renders some of the published test data unusable toward the development of codifiable bond strength models (e.g. Kashyap et al, 2012; Carrara and Freddi, 2014; Ceroni et al, 2014). Furthermore, since the bond strength capacity is commonly related with the basic material strength of the substrate, including the compressive strength and tensile strength of the masonry unit (CNR, 2013), emphasis needs to be placed not only on reporting the mean values of these properties, but also the number of specimens tested and the range of variability (e.g. as a coefficient of variation). It is also important that the test methods used for the quantification of these mechanical properties be adequately

described in terms of both the test method and the size of the test specimens (e.g. size of cubes used in compression tests). For example, the tensile strength of the masonry unit can be determined using three alternate techniques: direct tensile tests, splitting tests, and flexural tests, and the type of test used is known to influence the measured value.

APPROACHES FOR ANALYSIS OF EXPERIMENTAL DATA

Data analysis to extract the local bond-slip properties was performed in approximately half the experimental studies performed to date. Data analysis can be subdivided into two broad tiers—calibration of the interfacial fracture energy (G_f), and characterising the local bond-slip properties in terms of a suitable model, for instance the bilinear model shown in Figure 2. The latter tier of analysis is more rigorous but has substantially greater predictive potential as it allows for prediction of both the debonding load capacity as well as the bonded length required to achieve it.

Calibration of Fracture Energy

The interfacial fracture energy G_f is defined as the area under the local τ - δ capacity curve (Figure 2), which is intrinsically related to the debonding force capacity P_{IC} as follows:

$$G_f = P_{IC}^2 / (2L_p E_p A_p) \quad (1)$$

where $E_p A_p$ is the axial rigidity of the plate, and L_p is the plate bonded perimeter. Importantly, P_{IC} is the asymptotic debonding capacity over a sufficiently long bonded length (L_b in Figure 4) such that any further increase in L_b causes no further increase on P_{IC} . This approach can be applied without the necessity to establish the precise shape of the τ - δ model. An important requirement of this approach, however, is that the test has been conducted over a sufficiently long bonded length otherwise the approach underestimates the true value of G_f . Verifying this assumption can be done by any of the following:

- Testing increasing bonded lengths until the debonding force no longer increases;
- Measuring the free-end slip (Δ_f in Figure 4) and ensuring that it remains negligible relative to the loaded-end slip; or
- By establishing the shear stress distribution (via differentiation of strain) and ensuring that the shear stress distribution has not yet reached the free end at the instance of peak load.

Extraction of local τ - δ relationship by strain readings

By assuming a linear variation of strain between adjacent readings, the change in the force in the FRP can be attributed to the force transferred from the strip to the masonry through shear bond stress. Hence, the distribution of shear bond stress along a strips length can be determined indirectly from the strain readings along the FRP plate. In contrast, the slip profile along the specimen is determined through integration of the strain in the plate.

This analysis approach has the notable advantage that it does not require prior knowledge about the shape τ - δ relationship, which makes it well suited toward investigating new retrofitting systems. However, if applied outside of its range of underlying assumptions, the technique can become prone to major sources of inaccuracy. Firstly, considerable error can result from the assumption of

zero slip at the free end when integrating the strain profile to obtain slip, which is often made without verification. This assumption can be particularly inaccurate over short bonded lengths. Secondly, inaccuracies can creep into the results via discontinuity of the strain readings if the strain gauges are spaced too far apart.

Extraction of local τ - δ relationship by inverse analysis

An alternative approach to extracting the local bond-slip behaviour is through inverse analysis, which relies only on the measurement of slip at the loaded end. In applying this method, the user must firstly assume a particular shape of the τ - δ model (Figure 2), and then vary the input parameters (e.g. τ_f , δ_f and δ_l in the bilinear model) until good correlation is observed between the experimental and predicted P- Δ behaviour (Figure 5). The benefit of this approach is that it eliminates the need for strain readings; however it also requires considerably more intense processing of the results. Additionally it can be demonstrated that in order for this approach to produce unique values of input parameters, the procedure needs to consider various characteristics of the P- Δ response, including the peak load, slip at debonding, and the yield slip (Vaculik et al, 2017b).

SUMMARY AND CONCLUDING REMARKS

The development of codifiable procedures (e.g. ACI, 2010; CNR, 2013) for the design of FRP retrofits in unreinforced masonry requires an understanding of the local bond-slip behaviour at the bonded interface. To this end, this paper has summarised the results of a state-of-the-art review of previous experimental investigations using pull-tests. The full review, reported in Vaculik et al (2017b), has assembled a database of some 1300 individual tests from approximately 50 reported studies.

In relation to the scope of testing to date, the review has found that:

- Substrate material includes mostly clay bricks ($\approx 85\%$) with the remainder comprising natural stone and concrete block masonry;
- Retrofit type includes mostly externally-bonded plates ($\approx 90\%$) as opposed to near-surface-mounted plates; and
- Retrofit material includes mostly carbon-FRP ($\approx 55\%$) and glass-FRP ($\approx 25\%$), with the remainder covering basalt-FRP, aramid-FRP, and steel-reinforced-polymers.

This paper has also provided an overview of the differences between the various forms of test arrangement as well as instrumentation technique—the latter having influence on the form of data analysis which can be applied to characterise the local bond-slip properties.

It is also significant that whilst a large number of tests have been identified, only a portion of these can be considered in developing a codifiable material model due to the incomplete reporting of key properties.

ACKNOWLEDGEMENTS

The authors gratefully acknowledge the financial support from the ARC through its Discovery Grant Program (DP140102695) and the Bushfire and Natural Hazards CRC. The findings and views expressed are those of the authors and not necessarily those of the sponsors.

REFERENCES

- ACI (2010). ACI 440.7R-10, Guide for the design and construction of externally bonded fibre-reinforced polymer systems for strengthening unreinforced masonry structures, American Concrete Institute, Farmington Hills, MI, US.
- Caggiano, A., Martinelli, E., and Faella, C. (2012). "A fully-analytical approach for modelling the response of FRP plates bonded to a brittle substrate." *International Journal of Solids and Structures*, 49(17), 2291-2300.
- Carrara, P., and Freddi, F. (2014). "Statistical assessment of a design formula for the debonding resistance of FRP reinforcements externally glued on masonry units." *Composites Part B: Engineering*, 66, 65-82.
- Ceroni, F., Ferracuti, B., Pecce, M., and Savoia, M. (2014). "Assessment of a bond strength model for FRP reinforcement externally bonded over masonry blocks." *Composites Part B: Engineering*, 61, 147-161.
- CNR (2013). CNR-DT 200 R1/2013, Guide for the Design and Construction of Externally Bonded FRP Systems for Strengthening Existing Structures, National Research Council (Italy).
- de Felice, G., Aiello, M. A., Bellini, A., Ceroni, F., De Santis, S., Garbin, E., Leone, M., Lignola, G. P., Malena, M., Mazzotti, C., Panizza, M., and Valluzzi, M. R. (2016). "Experimental characterization of composite-to-brick masonry shear bond." *Materials and Structures*, 49(7), 2581-2596.
- Griffith, M. C., Kashyap, J., and Mohamed Ali, M. S. (2013). "Flexural displacement response of NSM FRP retrofitted masonry walls." *Construction and Building Materials*, 49, 1032-1040.
- Kashyap, J., Willis, C. R., Griffith, M. C., Ingham, J. M., and Masia, M. J. (2012). "Debonding resistance of FRP-to-clay brick masonry joints." *Engineering Structures*, 41, 186-198.
- Konthesingha, K. M. C., Masia, M. J., Petersen, R. B., and Page, A. W. (2015). "Experimental Evaluation of Static Cyclic In-Plane Shear Behavior of Unreinforced Masonry Walls Strengthened with NSM FRP Strips." *Journal of Composites for Construction*, 19(3).
- Rotunno, T., Rovero, L., Toniatti, U., and Briccoli Bati, S. (2015). "Experimental study of bond behavior of CFRP-to-brick joints." *Journal of Composites for Construction*, 19(3).

Turco, V., Secondin, S., Morbin, A., Valluzzi, M. R., and Modena, C. (2006). "Flexural and shear strengthening of un-reinforced masonry with FRP bars." *Composites Science and Technology*, 66(2), 289-296.

Vaculik, J., Sturm, A. B., Visintin, P., and Griffith, M. C. (2017a). "Modelling FRP-to-substrate joints using the bilinear τ - δ rule with allowance for friction—Full-range analytical solutions for long and short bonded lengths." *International Journal of Solids and Structures*, Submitted.

Vaculik, J., Visintin, P., Burton, N. G., Griffith, M. C., and Seracino, R. (2017b). "State-of-the-art review of FRP-to-masonry bond research: Test methods and extraction techniques for local bond properties." *Construction and Building Materials*, Submitted.

Valluzzi, M. R., Oliveira, D. V., Caratelli, A., Castori, G., Corradi, M., De Felice, G., Garbin, E., Garcia, D., Garmendia, L., Grande, E., Ianniruberto, U., Kwiecien, A., Leone, M., Lignola, G. P., Lourenco, P. B., Malena, M., Micelli, F., Panizza, M., Papanicolaou, C. G., Prota, A., Sacco, E., Triantafillou, T. C., Viskovic, A., Zajac, B., and Zuccarino, G. (2012). "Round Robin Test for composite-to-brick shear bond characterization." *Materials and Structures/Materiaux et Constructions*, 45(12), 1761-1791.

Willis, C. R., Seracino, R., and Griffith, M. C. (2010). "Out-of-plane strength of brick masonry retrofitted with horizontal NSM CFRP strips." *Engineering Structures*, 32(2), 547-555.

Yuan, H., Teng, J. G., Seracino, R., Wu, Z. S., and Yao, J. (2004). "Full-range behavior of FRP-to-concrete bonded joints." *Engineering Structures*, 26(5), 553-565.



ISBN 978-0-7259-0018-2